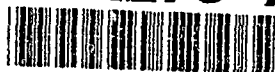


AGARD

ADVISORY GROUP FOR AEROSPACE RESEARCH & DEVELOPMENT

7 RUE ANCELLE 92200 NEUILLY SUR SEINE FRANCE

AD-A275 733



AGARD CONFERENCE PROCEEDINGS 534

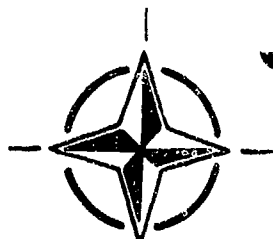
Computational and Experimental Assessment of Jets in Cross Flow

(Evaluation Numérique et
Expérimentale des Jets
dans des Courants Transversaux)

DTIC
ELECTE
FEB 17 1994
S A

*Papers presented and discussions recorded at the Fluid Dynamics Panel
Symposium held in Winchester, United Kingdom, from 19th—22nd April 1993.*

This document has been approved
for public release and sale; its
distribution is unlimited.



NORTH ATLANTIC TREATY ORGANIZATION

94-05240

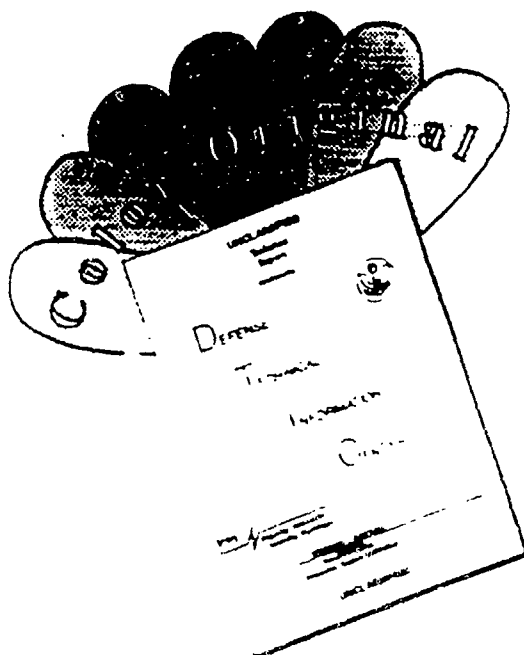


94 2 16 099

Published November 1993

Distribution and Availability on Back Cover

DISCLAIMER NOTICE



THIS DOCUMENT IS BEST
QUALITY AVAILABLE. THE COPY
FURNISHED TO DTIC CONTAINED
A SIGNIFICANT NUMBER OF
COLOR PAGES WHICH DO NOT
REPRODUCE LEGIBLY ON BLACK
AND WHITE MICROFICHE.

AGARD

ADVISORY GROUP FOR AEROSPACE RESEARCH & DEVELOPMENT

7 RUE ANCELLE 92200 NEUILLY SUR SEINE FRANCE

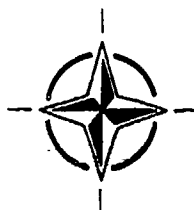
AGARD CONFERENCE PROCEEDINGS 534

Computational and Experimental Assessment of Jets in Cross Flow

(Evaluation Numérique et
Expérimentale des Jets
dans des Courants Transversaux)

Accession For	
NTIS	GRAS
DTIC	TAB
Unannounced	
Justification	
By	
Distribution	
Availability Codes	
Dist	Availability for Special
A-1	

Papers presented and discussions recorded at the Fluid Dynamics Panel
Symposium held in Winchester, United Kingdom, from 19th—22nd April 1993.



North Atlantic Treaty Organization
Organisation du Traité de l'Atlantique Nord

The Mission of AGARD

According to its Charter, the mission of AGARD is to bring together the leading personalities of the NATO nations in the fields of science and technology relating to aerospace for the following purposes:

- Recommending effective ways for the member nations to use their research and development capabilities for the common benefit of the NATO community;
- Providing scientific and technical advice and assistance to the Military Committee in the field of aerospace research and development (with particular regard to its military application);
- Continuously stimulating advances in the aerospace sciences relevant to strengthening the common defence posture;
- Improving the co-operation among member nations in aerospace research and development;
- Exchange of scientific and technical information;
- Providing assistance to member nations for the purpose of increasing their scientific and technical potential;
- Rendering scientific and technical assistance, as requested, to other NATO bodies and to member nations in connection with research and development problems in the aerospace field.

The highest authority within AGARD is the National Delegates Board consisting of officially appointed senior representatives from each member nation. The mission of AGARD is carried out through the Panels which are composed of experts appointed by the National Delegates, the Consultant and Exchange Programme and the Aerospace Applications Studies Programme. The results of AGARD work are reported to the member nations and the NATO Authorities through the AGARD series of publications of which this is one.

Participation in AGARD activities is by invitation only and is normally limited to citizens of the NATO nations.

The content of this publication has been reproduced directly from material supplied by AGARD or the authors.

Published November 1993

Copyright © AGARD 1993
All Rights Reserved

ISBN 92-835-0720-7



*Printed by Specialised Printing Services Limited
40 Chigwell Lane, Loughton, Essex IG10 3TZ*

Recent Publications of the Fluid Dynamics Panel

AGARDOGRAPHS (AG)

Design and Testing of High-Performance Parachutes

AGARD AG-319, November 1991

Experimental Techniques in the Field of Low Density Aerodynamics

AGARD AG-318 (E), April 1991

Techniques Expérimentales Liées à l'Aérodynamique à Basse Densité

AGARD AG-318 (FR), April 1990

A Survey of Measurements and Measuring Techniques in Rapidly Distorted Compressible Turbulent Boundary Layers

AGARD AG-315, May 1989

Reynolds Number Effects in Transonic Flows

AGARD AG-303, December 1988

REPORTS (R)

Shock-Wave/Boundary-Layer Interactions in Supersonic and Hypersonic Flows

AGARD R-792, Special Course Notes, August 1993

Unstructured Grid Methods for Advection Dominated Flows

AGARD R-787, Special Course Notes, May 1992

Skin Friction Drag Reduction

AGARD R-786, Special Course Notes, March 1992

Engineering Methods in Aerodynamic Analysis and Design of Aircraft

AGARD R-783, Special Course Notes, January 1992

Aircraft Dynamics at High Angles of Attack: Experiments and Modelling

AGARD R-776, Special Course Notes, March 1991

ADVISORY REPORTS (AR)

Air Intakes for High Speed Vehicles

AGARD AR-270, Report of WG13, September 1991

Appraisal of the Suitability of Turbulence Models in Flow Calculations

AGARD AR-291, Technical Status Review, July 1991

Rotary-Balance Testing for Aircraft Dynamics

AGARD AR-265, Report of WG11, December 1990

Calculation of 3D Separated Turbulent Flows in Boundary Layer Limit

AGARD AR-255, Report of WG10, May 1990

Adaptive Wind Tunnel Walls: Technology and Applications

AGARD AR-269, Report of WG12, April 1990

CONFERENCE PROCEEDINGS (CP)

High-Lift System Aerodynamics

AGARD CP-515, September 1993

Theoretical and Experimental Methods in Hypersonic Flows

AGARD CP-514, April 1993

Aerodynamic Engine/Airframe Integration for High Performance Aircraft and Missiles

AGARD CP-498, September 1992

Effects of Adverse Weather on Aerodynamics

AGARD CP-496, December 1991

Manoeuvring Aerodynamics

AGARD CP-497, November 1991

Vortex Flow Aerodynamics

AGARD CP-494, July 1991

Missile Aerodynamics

AGARD CP-493, October 1990

Aerodynamics of Combat Aircraft Controls and of Ground Effects

AGARD CP-465, April 1990

Computational Methods for Aerodynamic Design (Inverse) and Optimization

AGARD-CP-463, March 1990

Applications of Mesh Generation to Complex 3-D Configurations

AGARD CP-464, March 1990

Fluid Dynamics of Three-Dimensional Turbulent Shear Flows and Transition

AGARD CP-438, April 1989

Validation of Computational Fluid Dynamics

AGARD CP-437, December 1988

Aerodynamic Data Accuracy and Quality: Requirements and Capabilities in Wind Tunnel Testing

AGARD CP-429, July 1988

Aerodynamics of Hypersonic Lifting Vehicles

AGARD CP-428, November 1987

Aerodynamic and Related Hydrodynamic Studies Using Water Facilities

AGARD CP-413, June 1987

Applications of Computational Fluid Dynamics in Aeronautics

AGARD CP-412, November 1986

Store Airframe Aerodynamics

AGARD CP-389, August 1986

Unsteady Aerodynamics — Fundamentals and Applications to Aircraft Dynamics

AGARD CP-386, November 1985

Aerodynamics and Acoustics of Propellers

AGARD CP-366, February 1985

Improvement of Aerodynamic Performance through Boundary Layer Control and High Lift Systems

AGARD CP-365, August 1984

Wind Tunnels and Testing Techniques

AGARD CP-348, February 1984

Aerodynamics of Vortical Type Flows in Three Dimensions

AGARD CP-342, July 1983

Missile Aerodynamics

AGARD CP-336, February 1983

Prediction of Aerodynamic Loads on Rotorcraft

AGARD CP-334, September 1982

Wall Interference in Wind Tunnels

AGARD CP-335, September 1982

Fluid Dynamics of Jets with Applications to V/STOL

AGARD CP-308, January 1982

Aerodynamics of Power Plant Installation

AGARD CP-301, September 1981

Computation of Viscous-Inviscid Interactions

AGARD CP-291, February 1981

Foreword

One need look no further than the subjects of several recent AGARD meetings: High Lift Aerodynamics (Banff, Fall 1992), Hypersonic Flow (Torino, Spring 1992), Manoeuvring Aerodynamics (Toulouse, Spring 1991), to recognize that AGARD has a strong interest in technology areas in which the basic problem of a jet-in-crossflow plays a role. Yet to find a meeting where the jet-in-crossflow is a primary theme one has to go back to the Lisbon Conference of 1981, "Fluid Dynamics of Jets with Application to V/STOL", AGARD CP-308. In the summary remarks by Dr I.R. Spee of the NLR two conclusions stand out: (i) That there is a need for improved prediction methods and (ii) That the future interest in V/STOL applications is unclear. With the recent ending of the cold war and the realignment of defense needs the future of V/STOL applications is perhaps even more unclear now than it was in 1981.

However, in the past decade the breadth of applications involving the jet-in-crossflow configuration has increased greatly with the renewed interest in hypersonics, the growing demand for increased manoeuvring capability of high performance aircraft and the need for better understanding of problems of mixing in subsonic and supersonic flows. At the same time V/STOL applications have continued to be of interest. Our capability to predict the basic flowfield has grown dramatically and we are now beginning to see computations of jets-in-crossflow interacting with complex configurations of aerodynamic interest. The purpose of this Symposium is to evaluate advances in the field that have occurred since 1981.

In selecting the terms of reference of the conference it was our goal to cast a wide net emphasizing the breadth of jet-in-crossflow applications. This was largely achieved with one exception in the area of thrust vectoring. While there were sufficient papers for one session on thrust vectoring the Programme Committee did not receive any papers on specific applications to thrust vectoring nozzles. One reason appears to be that there are a number of ongoing efforts in this area and results are not ready for public presentation. It may well be that this topic could form the basis of a future symposium. More on this issue can be found in the General Discussion at the end of this volume. The final program was as follows:

- Fundamental Flow Structure (7 papers)
- Experimental Methods (3 papers)
- Thrust Vectoring (3 papers)
- Jet Impingement, Exhaust Gas Reingestion (5 papers)
- Hypersonic Crossflow (3 papers)
- Numerics, Turbulence Modeling (4 papers)
- Vehicle Control (9 papers)
- Internal Flows, Turbine Cooling (4 papers)

The Symposium concluded with general remarks by the Technical Evaluator, Professor Leonard Roberts of Stanford University. This was followed by a lively open discussion during which a number of the issues raised during the Symposium were considered.

The Programme Committee would like to extend thanks to David and Mrs Woodward, the U.K. National Coordinator, Mrs Sheila Martin and all the local organizers as well as the authors for their hard work in preparing for this meeting in one of England's most historic cities.

B. Cantwell, C. Çiray and J. Jimenez
Programme Committee Co-Chairmen

Avant-Propos

Il suffit de lire la liste des thèmes des réunions récentes du Panel FDP, à savoir "l'Aérodynamique des systèmes hypersustentateurs" (Banff, automne 1992), "Les écoulements hypersoniques" (Torino, printemps 1992), "l'Aérodynamique dans la manoeuvrabilité" (Toulouse, printemps 1991) pour se rendre compte du vif intérêt témoigné par l'AGARD pour les technologies où le problème de base d'un jet à écoulement transverse joue un rôle.

Pourtant, il faut remonter à l'année 1981 pour trouver une réunion où les jets à écoulement transverse représente le sujet principal ("La dynamique des fluides des jets et les applications V/STOL" AGARD CP-308). Deux conclusions ressortent des observations finales du Dr I.R. Spee: i) les méthodes de prédiction doivent être améliorées. ii) il est très difficile de prévoir l'intérêt qui sera manifesté pour les applications V/STOL à l'avenir. Avec la cessation récente de la guerre froide et le réajustement des besoins de défense, l'avenir des applications V/STOL est peut-être plus incertain aujourd'hui qu'en 1981.

Cependant, au cours de la dernière décennie, le nombre d'applications mettant en jeu la configuration du jet à écoulement transverse a augmenté considérablement suite au regain d'intérêt pour l'hypersonique, à la demande croissante d'une meilleure manoeuvrabilité des avions de combat à hautes performances et à la recherche d'une meilleure compréhension des problèmes du mélange dans les écoulements subsoniques et supersoniques. En même temps, les applications V/STOL continuent à susciter beaucoup d'intérêt. Notre capacité de prédire le champ d'écoulement de base s'est développée de façon fulgurante et nous constatons les premières interactions entre des calculs de jets à écoulement transverse et des configurations complexes qui intéressent l'aérodynamique. L'objet de ce symposium est d'évaluer les progrès réalisés dans ce domaine depuis 1981.

En définissant les termes de référence de la conférence nous avons voulu faire un grand tour d'horizon afin de souligner l'étendue des applications du jet à écoulement transverse. Ce pari a été tenu à une exception près, dans le domaine de l'orientation de la poussée, car quoiqu'un nombre suffisant de communications ait été soumis, permettant d'organiser une session sur l'orientation de la poussée, le comité du programme n'a reçu aucune communication traitant d'applications spécifiques aux tuyères d'orientation de la poussée. Ceci s'explique en partie par le fait que la plupart des travaux entrepris dans ce domaine sont actuellement inachevés et que par conséquent les résultats ne sont pas disponibles sous une forme présentable au public.

Cependant, ce sujet pourrait bien servir de base à un futur symposium. Le texte des discussions générales qui se trouve à la fin du présent volume traite d'autres aspects de cette question. Le programme définitif a été établi comme suit:

- les structures d'écoulement fondamentales (7 communications)
- les méthodes expérimentales (3 communications)
- l'orientation de la poussée (3 communications)
- l'impact des jets, la ré-ingestion des gaz éjectés (5 communications)
- les écoulements transverses hypersoniques (3 communications)
- les caractères numériques, la modélisation de la turbulence (4 communications)
- le contrôle des véhicules (9 communications)
- les écoulements internes, le refroidissement des turbines (4 communications)

Des remarques d'ordre général de la part de l'évaluateur technique, le professeur Leonard Roberts de l'Université de Stanford ont clôturé le symposium. Ces remarques ont été suivies d'un débat très animé et très ouvert qui a permis de discuter d'un certain nombre de questions soulevées lors du symposium.

Le comité du programme tient à remercier David Woodward, le coordonnateur national pour la Grande-Bretagne, ainsi que Mme Woodward, Mme Sheila Martin et l'ensemble du personnel local pour les efforts qu'ils ont bien voulu consacrer à la préparation de cette réunion organisée dans l'une des villes les plus renommées de l'histoire de l'Angleterre.

B. Cantwell, C. Çiray et J. Jimenez
Co-Présidents du Comité de Programme

Fluid Dynamics Panel

Chairman: Prof. Ir J.W. Slooff
National Aerospace Laboratory NLR
Anthony Fokkerweg 2
1059 CM Amsterdam, The Netherlands

Deputy Chairman: M.C. Dujarric
ASE-Programme HERMES
Bâtiment Copernic
18 Avenue Edouard Belin
31055 Toulouse Cedex, France

PROGRAMME COMMITTEE

Prof. B. Cantwell (Co-Chairman)
Dept. of Aeronautics & Astronautics
Stanford University
Stanford, CA 94305-4035 — United States

Prof. Dr C. Çiray (Co-Chairman)
Aeronautical Eng. Dept.
Middle East Technical University
Inonu Bulvari PK: 06531
Ankara — Turkey

Prof. J. Jimenez (Co-Chairman)
Escuela Tecnica Superior
de Ingenieros Aeronauticos
Departamento de Mecanica de Fluidos
Plaza de Cardenal Cisneros 3
28040 Madrid — Spain

Prof. J.A. Essers
Université de Liège
Institut de Mécanique
Service d'Aérodynamique Appliquée
rue Ernest Solvay 21
4000 Liège — Belgium

Prof. R.J. Kind
Department of Mechanical and
Aerospace Engineering
Carleton University
Ottawa, Ontario K1S 5B6 — Canada

M. PH. Vancamberg
Dept. d'Aérodynamique Théorique
Dassault Aviation, 78 Quai Marcel Dassault
92214 Saint Cloud — France

Dr Ing. H. Korner
Direktor
Institut für Entwurfsaerodynamik der DLR
Flughafen
3300 Braunschweig — Germany

Prof. D. Papailiou
Lab. of Applied Thermodynamics
Dept. of Mechanical Engineering
University of Patras
Kato Kostitsi, Patras 26500 — Greece

Prof. F. Sabetta
Dipartimento di Meccanica E. E. Aeronautica
Universita di Roma "La Sapienza"
Via Eudossiana 18
00184 Roma — Italy

Prof. Dr Ir J.L. van Ingen
Dept. of Aerospace Engineering
Delft University of Technology
Kluyverweg 1
2629 HS Delft — The Netherlands

Prof. Dr H. Norstrud
Division of Hydro- and Gas-Dynamics
The University of Trondheim
The Norwegian Institute of Technology
7034 Trondheim NTH — Norway

Prof. A.F. de O. Falcao
Depart. Engenharia Mecanica
Instituto Superior Tecnico
1096 Lisboa Codex — Portugal

Prof. D.I.A. Poll
Dept. of Engineering (Aeronautical)
Simon Building
University of Manchester
Oxford Road
Manchester M13 9PL — United Kingdom

Dr S. Lekoudis
Director (Acting) Mechanics Div.
Code 1132
Office of Naval Research
Arlington, VA 2217-5000 — United States

PANEL EXECUTIVE

Dr W. Goodrich

Mail from Europe:
AGARD—OTAN
Attn: FDP Executive
7, rue Ancelle
F-92200 Neuilly-sur-Seine
France

Tel: 33(1)47 38 57 75
Telex: 610176 (France)
Telefax: 33 (1) 47 38 57 99

Mail from US and Canada:
AGARD—NATO
Attn: FDP Executive
Unit 21551
APO AE 09777

Contents

	Page
Recent Publications of the Fluid Dynamics Panel	iii
Foreword	v
Avant-Propos	vi
Fluid Dynamics Panel	vii
	Reference
Technical Evaluation Report by L. Roberts	T
SESSION I – INTRODUCTION Chairman: D.S. Woodward	
Fifty Years of Jet in Cross Flow Research by R.J. Margason	1
SESSION II – FLOW STRUCTURE I Chairman: B. Cantwell	
Paper 2 withdrawn	
Transient Flow Features of a Supersonic Jet in a Low Speed Cross Flow by X. Zhang, D.W. Hurst and G.M. Lilley	3
Unsteady Wake Structures in Transverse Jets by R.M. Kelso, C. Delo and A.J. Smits	4
Separated Flow Generated by a Vecteded Jet in a Crossflow by A. Krothapalli and C. Shih	5
SESSION III – EXPERIMENTAL METHODS, TURBULENCE Chairman: C. Çiray	
Scalar Mixing in the Subsonic Jet in Crossflow by S.H. Smith, A. Lozano, M.G. Mungal and R.K. Hanson	6
The Interaction Region Associated with Twin Jets and a Normal Crossflow by N. Toy, E. Savory, S. McCusker and P.J. Disimile	7
Experimental Data for CFD Validation of Impinging Jets in Cross Flow with Application to ASTOVL Flow Problems by P. Behrouzi and J.J. McGuirk	8
SESSION IV – THRUST VECTORING Chairman: H. Korner	
Experimental Investigation of the Interaction of a Thrust Reverser Jet with an External Subsonic Flow by J.-M. Charbonnier, K. Deckers and G. Wens	9
Vecteded Jets-Induced Interference on Aircraft, Prediction and Verification by R.K. Nangia	10
Numerical Investigation of Thrust Vectoring by Injection of Secondary Air into Nozzle Flows by T. Berens	11

SESSION V — FLOW STRUCTURE II

Chairman: J. Jimenez

- Topological Structure of a Jet in a Cross Flow** 12
by A.E. Perry, R.M. Kelso and T.T. Lim
- Paper 13 withdrawn**
- An Experimental Study of Siphonal Jets in a Turbulent Boundary Layer Crossflow** 14
by C.A. O'Riordan, S.G. Monismith and J.R. Koseff

SESSION VI — JET IMPINGEMENT, EXHAUST GAS INGESTION

Chairman: D. Bowers

- Experiments on the Ground Vortex Formed by an Impinging Jet in Cross Flow** 15
by W.B. Blake and V.R. Stewart
- Experiments into the Scaling Parameters Required for Exhaust Gas Ingestion Testing of Vertical Landing Aircraft** 16
by P. Curtis and P.J. Bradley
- Influence of Headwind on Hot Gas Reingestion and Consideration of Pressure Ratio Scaling** 17
by C.J. Penrose
- Unsteady Aspects of Hot Gas Reingestion and Statistical Analysis** 18
by R. Beasley

SESSION VII — HYPERSONIC CROSSFLOW

Chairman: D.I.A. Poll

- Jets Transversaux en Interaction avec des Ecoulements Hypersoniques Raréfiés** 19
par J. Allègre et M. Raffin
- Comparison of the Interactions of Two and Three Dimensional Transverse Jets with a Hypersonic Free Stream** 20
by H.E.G. Powrie, G.J. Ball and R.A. East
- Experiments on Interaction Force of Jets in Hypervelocity Cross-Flow in a Shock Tunnel** 21
by K.W. Naumann, H. Ende, G. Mathieu and A. George

SESSION VIII — NUMERICS, TURBULENCE MODELLING

Chairman: B. Cantwell

- A Numerical Investigation of a Subsonic Jet in a Crossflow** 22
by S.H. Chiu, K.R. Roth, R.J. Margason and J. Tso
- Calculation of Single and Multiple Jets in Cross-Flow with and without Impingement using Reynolds-Stress-Transport Closure** 23
by N.Z. Ince and M.A. Leschziner
- Predictions of Momentum and Scalar Fields in a Jet in a Cross-Flow using First and Second Order Turbulence Closures** 24
by J. Alvarez, W.P. Jones and R. Seoud
- Navier-Stokes Simulation of Two and Three Dimensional Jets in Crossflow, Effects of Grid and Boundary Conditions** 25
by M.Ş. Kavsaoglu, İ.S. Akmandor, S. Çiray and K. Fujii

SESSION IX — VEHICLE CONTROL I

Chairman: Ph. Vancamberg

- Effects, Limits and Limitations of Spanwise Blowing** 26
by W.H. Staudacher
- Pneumatic Management of Blunted-Forebody Flow Asymmetry for High Angle-of-Attack Directional Control** 27
by F.W. Roos, C.L. Magness and D.V. Brown
- Theoretical and Experimental Investigation of a Delta Wing with Turbulent Leading-Edge Jets** 28
by K.J. Craig, L. Roberts, D.I. Greenwell and N.J. Wood

SESSION X — VEHICLE CONTROL II

Chairman: R.J. Kind

- Recent Developments in the Simulation of Steady and Transient Transverse Jet Interactions for Missile, Rotorcraft, and Propulsive Applications** 29
by S.M. Dash et al.
- Numerical Assessment of Aerodynamic Interactions on Missiles with Transverse Jets Control** 30
by M. Dormieux and R. Marsaa-Poey
- First Experimental Assessment of RCS Plume-Flow Field Interaction on HERMES Leading Edge Thruster Configuration** 31
by Th. Pörtner

SESSION XI — VEHICLE CONTROL III

Chairman: F. Sabetta

- Numerical Simulation of a Powered-Lift Landing** 32
by K. Chawla and W.R. Van Dalsem
- A Study of Jet Effect and Ground Effect Interference on a STOL Fighter** 33
by D.J. Moorhouse, J.G. Reinsberg and F.J. Shirk
- Transitional Flight Characteristics of a Geometrically Simplified STOVL Model** 34
by K.R. Roth

SESSION XII — INTERNAL FLOWS, TURBINE COOLING

Chairman: H. Norstrud

- Effects of Free Stream Turbulence on a Jet in a Cross Flow** 35
by T.H. Toften, A.E. Holdø and D. Kapfer
- Paper 36 withdrawn**
- Analysis of Cooling Jets near the Leading Edge of Turbine Blades*** 37
by E. Benz, S. Wittig, A. Beeck and L. Fottner
- Navier-Stokes Analysis of a Swirling Jet in Crossflow** 38
by H. Yağci and M.Ş. Kavsaoğlu

*Contribution from the Propulsion and Energetics Panel.

Reference

SESSION XIII — FLOW STRUCTURE III

Chairman: A.F. de O. Falcao

Etude Expérimentale sur les Interactions entre un Jet Supersonique Chauffé Transversal et un Ecoulement Supersonique Externe par R. Gaillard, P. Geffroy, L. Jacquin et G. Losfeld	39
Inclined Air-Jets used as Vortex Generators to Suppress Shock-Induced Separation by H.H. Pearcey, K. Rao and D.M. Sykes	40
General Discussion	GD

by

L. Roberts
Stanford University
Stanford, California 94305
United States

1. Introduction

The symposium consisted of 37 papers which have been grouped for the purpose of this review, following the General Observations, as those dealing with:

- Flow Structure
- Experimental and Computational Methods, Turbulence
- Thrust Vectoring, Jet Impingement, Exhaust Gas Injection
- Vehicle Control (including Hypersonics)
- Internal Flows

These topics are reviewed in a different order from that presented to retain continuity of subject matter and are followed by Conclusions and Recommendations.

This Technical Evaluation is limited to a brief overall analysis and a summary of the Conclusions and Recommendations.

2. General Observations

The Symposium included papers which ranged from an understanding of the basic structure of the jet in a crossflow, through those concerned with experimental and computational methods for determining the interaction, to papers which treated the more practical aspects such as thrust vectoring, impingement and exhaust gas injection, vehicle control including hypersonics, and internal flows. A review of the history of jets in crossflow was given in the opening paper (paper 1), which traces the research on this interaction over the past fifty years, including its applications to such diverse fields as plume dispersion, combustion fuel injection, reaction control of missiles and aircraft, to its most celebrated application, V/STOL aircraft in transition flight. Primary emphasis was placed on tracing our evolving understanding, both experimentally and computationally, of the flowfield structure.

Many of the papers, particularly those on flow structure and on experimental and computational methods, and on turbulence, were from Universities while important contributions from the National Laboratories and Industry were made on the more practical problems associated with vehicle development. While substantial progress was reported on both experimental and computational aspects of steady flows less was reported on unsteady problems and more effort must be applied to this latter subject before a full understanding of future V/STOL vehicles or of the control by jet flows can be claimed. Although much of the conference was inherently oriented toward military aircraft application it should be realized that the needs of civil aircraft will involve such subjects as aeroacoustics in the future and they may influence the direction of research.

In view of their historical involvement in the development and deployment of the Harrier aircraft and its derivatives a preponderance of papers from the UK and the USA was found, with some papers from GE, FR, BE and TU and no papers from other countries in NATO.

3. Flow Structure

The Sessions on Flow Structure (Sessions II, V and XII) comprised 7 papers (papers 3-5, 12, 14 and 39, 40) covering both experimental and computational studies of subsonic and supersonic jets in a crossflow. In paper 3 the unsteady pressure was measured at high Reynolds number for a supersonic jet, including the effects of the oncoming boundary layer, to identify variations in the sound pressure level with jet pressure ratio and the jet mode (subsonic, under- and overexpanded) giving multiple mode surface pressure fields. The effects of the oncoming turbulent boundary layer were not large.

Paper 4 is concerned with the unsteady generation and convection of vorticity in the wake, using a fluorescent dye and laser cross sectioning techniques, allowing the concentration field in the wake to be reconstructed. The study confirmed and elaborated earlier conclusions that the vorticity emanates from the wall boundary layer. In paper 5 the separated flow structure caused by a rectangular jet was investigated experimentally for several parameters of the jet (Reynolds number, Mach number, vector angle, upstream boundary conditions) and results are displayed for the separated wake behind the jet, when the jet was pointed upstream and downstream, giving different frequencies for the flow.

In paper 12, two studies were reported; a visualization study, using colored dye, in a water tunnel, and a flying hot wire study using a low speed tunnel, to investigate the counter-rotating vortex pair that results from the interaction of the jet with the cross-flow. They show the importance of the separation position in the jet exit tube to the subsequent development of the vortex flows.

In paper 14 a completely different application is investigated (the creation and diffusion of a phytoplankton plume by large populations of filter feeding animals in estuary regions). The effect of bed clams was simulated by large numbers of siphon pairs which alter the mixing characteristics of the phytoplankton-depleted fluid. Variations in concentration were found as a function of siphon height (changing the effective surface roughness) and results were explained in terms of jet stream velocity ratio.

In paper 39 an experimental study of a heated supersonic jet flowing crosswise to a supersonic stream was undertaken in the S5 ONERA wind tunnel. The shock and vorticity structure was shown at $M = 2$, with emphasis on the effects of heating and turbulence.

The use of air jets to suppress shock-induced separation on aircraft wings and empanages was explored in paper 40 where a comparison is made with vane type vortex generators. It was found that the air jet approach allows a greater pressure rise through the shock which now progresses continually over the surface and allows an increase in the downstream pressure recovery at high angle of attack.

In attempting to summarize the Sessions on Flow Structures it should be said that the comparison of CFD and experimental measurement shows good agreement when the flow is dominated by inviscid effects; however when turbulence plays an important part agreement depends on the turbulence model chosen and this can effect some of the inviscid features (eg. the position of a horse shoe vortex in the impingement of jets against a flat plate). Nevertheless, our understanding of the flow structure for steady flows has progressed to the point of application to several problems in aerodynamics in addition to the traditional V/STOL application. Furthermore, our progress in understanding unsteady phenomena continues and should be further pursued particularly in the context of enhanced mixing.

4. Experimental and Computational Methods, Turbulence

The Sessions on Experimental and Computational Methods and on Turbulence (Sessions III and VIII) comprised 7 papers (papers 6-8 and 22-25) and also covered the subject of jets in a crossflow but concentrated on techniques, both experimental and computational and on turbulence modelling required for a good description of the interaction.

In paper 6, experiments were conducted in a wind tunnel, with Planar Laser Induced Fluorescence using acetone as a tracer, giving the scalar mixing of the jet concentration and showing images of the structure not previously reported. The use of smoke illuminated by a laser beam, to visualize in real time and measure the twin jets flowing normally into the crossflow was reported in paper 7. Differences were found in the widely spaced twin jet configuration (compared to the single jet configuration). Measurement variations were found of the probability density, energy spectra and interface location. The measurement gave a detailed mapping of the single and twin jet cases (tandem and in-line). Notably absent in the measured spectra was evidence of "periodic vortex shedding" as reported by earlier works. Paper 8 gave good examples of using LDV in a water channel to investigate the behavior of twin jets. This research concentrated on turbulence measurements required for the validation of CFD codes.

On the computational side paper 22 reported a numerical investigation using different boundary conditions and two turbulence models (Baldwin Lomax and Baldwin-Barth) with the thin layer Navier Stokes results showing good agreement with pressure measurements. The calculation used two grids (a Cartesian and a cylindrical grid for the far and near fields respectively) and successfully showed the presence of a horseshoe vortex near the wall and its influence on the pressure distribution as well as the usual dominant features - the contra-rotating vortices and downstream circulation.

In paper 23 computational results were obtained for a single jet and multiple jets with emphasis on the influence of the turbulence model closure on the results. It was claimed that the results are in better agreement with experiment if the Reynolds stress model given by Gibson and Launder is used in conjunction with a near wall log-law

based model as opposed to the simpler $k - \epsilon$ model. The comparison shows that use of the former turbulence model produces a ground vortex in better agreement with experiment. Results are presented for several fundamentally different 3-d geometries to underscore the importance of the choice of turbulence model closure.

Similar conclusions regarding the importance of choice of turbulence model were shown in paper 24 which was motivated by the behavior of jets in gas turbine combustors. While agreement with experiment was not particularly good it appears that some improvement was obtained when the second moment closure model was used for turbulence. The effects of grid geometry and boundary conditions were investigated in paper 25 where 2-d and 3-d jets were considered. Results are compared using algebraic turbulence models with previous experiments and good agreement is claimed for the gross features.

To summarize these Sessions, it is clear that we now have good techniques to both measure and compute flows, certainly external flows; these are important tools (non-invasive experimental techniques used with good computational techniques). The long pole in the tent is still turbulence modelling and I suspect this will still hold up final progress toward getting full agreement between theory and experiment.

5. Thrust Vectoring, Jet Impingement and Exhaust Gas Reingestion

Sessions on the practical applications to military aircraft (Sessions IV and VI) comprised 7 papers (papers 9-11 and 15-18) and concerned Thrust Vectoring, Jet Impingement and Exhaust Gas Reingestion. The empirical modelling of the interaction between a thrust reverser jet and an external flow was undertaken in paper 9 where the efficiency of the thrust reverser was determined as a function of door design including its opening angle; the influence of the door and side plates on the penetration of the jet and the vortex strength were determined. In paper 10, the jets were represented by a distribution of doublets, sources and sinks, and the vortex path was described empirically; the model was then incorporated into a paneling method to give the interference forces and moments on wings and tails as functions of the jet placement, jet velocity ($\frac{V_j}{V_\infty}$) and wing aspect ratio, in the low speed (transitional) phase of flight.

The control of thrust vectoring by injection was investigated in paper 11 for a hypersonic aircraft. Two-dimensional Euler calculations were carried out to investigate subsonic and supersonic injection of the aircraft forebody boundary layer into the nozzle flow. This allows a determination of the effects of injection on the thrust vector due to changes in pressure and temperature in the nozzle. Stability of the aircraft with α is improved by injection. Paper 15 reviewed past and current experimental studies of the ground vortex produced by jet impingement using fixed ground boards, moving ground belts and moving model tests to give the gross effects of the ground vortex on the aerodynamics for a generic wing-body configuration. Large influences on forces and moments of ground effects were observed. Paper 16 performed experiments to determine the scaling parameters for exhaust gas reingestion for STOVL aircraft and in particular addressed the question of buoyancy or Mach No. scaling versus pressure ratio in this context. It was concluded that for the descent mode of a whole aircraft model the differences in flow field do not appreciably change engine face conditions, thus confirming the scaling parameters originally derived by Cox and Abbott.

In paper 17 the subject of hot gas reingestion was further pursued and the influence of the direction of headwind on engine performance degradation was addressed. The effects of buoyancy and pressure ratio were both considered for Harrier type and ASTOVL (supersonic exhaust) engines with the conclusion that hot gas reingestion is headwind-dependent for some configurations and increases with nozzle pressure ratio. Importantly for full scale/model comparisons ingestion is stochastic in nature and requires the use of statistical methods in its analysis. In paper 18 for ASTOVL aircraft unsteady effects of reingestion were considered and the use of statistical techniques was made to describe the presence of large scale unsteady streaks of hot gas entering the intake. The analysis has been applied to reingestion with under-fuselage diverter arrangements and also provided insight into flow mechanisms using model conditions at nozzle pressure ratios different from full scale while maintaining dynamic similarity.

Sessions IV and VI underscored the importance of good experimental testing in such practical problems as combustion mixing or hot gas reingestion (as evidenced in papers 17 and 18) in conjunction with adequate analysis of the unsteady effects of such phenomena on engine and vehicle performance. Although substantial progress has been made in the numerical analysis of relatively simple geometries for the purpose of conceptual design, experimental testing and the use of appropriate scaling laws together with engineering analysis, will continue to be important to the development of full-scale aircraft.

6. Vehicle Control Including Hypersonics

Sessions on the use of jets to control vehicle motion, including hypersonic vehicles, (Sessions I, IX, X and XI) consisted of 12 papers: papers 19-21 (on hypersonic flow) and papers 23-34 (on the application of jets to subsonic and supersonic vehicles). Regarding the interaction of jet flows with a hypersonic stream, sets of experimental data for trailing edge jets on a 60° delta wing and for transverse jets in a corner flow were given in paper 19. For the delta wing experiment two jets, symmetrically placed on the wing, were used and the efficiency of the jets, which depends on the interaction with the hypersonic flow, at $M = 8$ was determined in terms of the jet momentum and jet position as well as angle of attack. An enhanced normal force and rolling moment were produced. For the corner flow at $M = 20$ the induced wall pressures that result from interaction with the control plumes were found by varying the stagnation pressure of the control jet. These induced pressures result from separation of the corner flow. The investigation of interactions between the jet and a hypersonic stream were continued in paper 20 which used a flat plate approximately 20cm long in an isentropic light piston tunnel at $M = 6.69$ and Reynolds number of 4.27×10^6 /metre. Results in 3-d for different injectant gases show a dependence on upstream separation (and on local flow structure, generally) and on the ratio of specific heats for the gas. Comparison of these features for the 3-d flowfield were made with 2-d results previously reported. In paper 21 a unique model mounting support for the French-German Research Institute shock tunnel was described which allows Mach Number, Reynolds Number and velocity of the hypersonic flow to be produced for millisecond force measurement. Typical interaction coefficients in excess of 2 were measured depending on the location and number of nozzles used and the shape of the surface with which they interact.

Turning now to the lower Mach Number flows (Sessions IX, X and XI) paper 26 gave a summary in the form of a historical review of the use of spanwise blowing to produce improvement in the post stall aerodynamic performance and the stability and control of wings. The conclusions are based on an empirical analysis and the use of spanwise blowing techniques on current and past aircraft.

The blunting of the forebody of an ogive cylinder at high angle of attack in low speed flow suppresses the tendency to develop spurious forces and moments. Proportional sideforce was produced experimentally by blowing through small nose jets for the purpose of control in paper 27, where it was shown that such blowing controls the vortex behavior. Results were given for laminar separation for the blunted configuration in terms of a mass-blowing coefficient and turbulent results were presented using boundary layer tripping techniques showing greater blowing effectiveness for this case and particularly for forward blowing jets. This paper, although not presented, will appear in the Proceedings.

A somewhat similar approach was used in paper 28 where a delta-wing rather than a blunted cone is used with blowing at the leading edges of the wing (ie, blowing tangentially around the blunted leading edge). It was shown experimentally that blowing is similar at high angle of attack to a reduction in angle of attack and a reduction in sweep angle in that both tend to reduce the effects of vortex bursting on loss of lift. Computation of vortex bursting was carried out using the thin layer Navier-Stokes equations and the effects of blowing as well as angles of attack and yaw on the flow over the delta wing were given. The experimental and computational work show that control, by producing a rolling moment, is effected so that wing rock can be eliminated.

In paper 29 a general numerical simulation was used, with Navier Stokes codes, to describe how jet interactions can play a dominant part in the control of missiles and propulsion devices. A computational scheme was presented which accounts for the presence of heavily-laden particulates in the transverse jet; a compressible dissipative $k - \epsilon$ turbulence model ($CDk - \epsilon$) was used. In addition the numerical simulation of helicopter plume interaction with the downwash was considered using Lagrangian vortex tracking procedures combined with Euler/Navier Stokes methodology.

In paper 30 the aerodynamics of lateral control jets on a missile were determined numerically, for both subsonic and supersonic flow, using overlapping grids to conduct the N-S computation with generally good agreement with experimental results.

In paper 31 experimental results were presented of visualization tests of the use of control jets for the HERMES spacecraft. Simulation based on NASA's momentum flux parameters for this configuration used scaling laws derived from the SHUTTLE spacecraft reaction control system. Additionally exploratory pressure measurements were made to describe the control jet interaction with the surface.

Returning to the subject of Vehicle Control at low speed, paper 32 gives a numerical simulation of a powered lift flight of a simplified V/STOL configuration including the lift loss that occurs during descent and its dependence on the behavior of the ground vortex that appears under the vehicle. Time accurate simulations, using the CRAY YMP supercomputer of both straight and level flight, and descending flight, are presented.

A set of overlapping grids was used (ground, jet and delta wing grids) required an upgrading of communication between grids. In the descent case it was found that a number of flow features could cause temporal variations in ground surface pressure (pressure waves) and oscillations in lift when the vehicle is in ground proximity. These include vortex shedding from the jet lip, causing jet oscillations both laterally and streamwise, oscillations in the ground vortex height, and evidence of Karman vortex shedding behind the jet. Comparison of the Strouhal numbers isolated the cause of lift oscillations as probably being associated with variations emanating from the lip of the jet. Fair agreement was found with the previously determined experimental lift coefficient, with the primary effort made to understand the unsteady flow structures.

The practical problem of reducing landing ground roll for the F-16 fighter was reported in paper 33 which analyzed, experimentally, the use of thrust reversers for this purpose. The effect on pitching moment was explored particularly and it was found that a large nose-up pitching moment was experienced on the wind tunnel model at forward deflection of the lower thrust reverser vane. This effect, together with the results using a short ground board in the tunnel influenced the design of the control system used in flight. Subsequent flight test results showed that a nose-down rotation was produced during landing - a result of jet/ground forces very different from those predicted. Control laws were updated to reflect these effects particularly as they affected the thrust reverser operation.

The experimental and computational methods used in a STOVL takeoff study, based on a cropped delta wing with tandem jets, were reported in paper 34. Experimentally, at a maximum free-stream Mach Number of .2 and a maximum nozzle pressure ratio of 3, forces and moments, and steady and unsteady model pressures together with surveys near the tunnel walls, were measured to verify the boundary conditions used in the computations. Comparison was made for a particular set of flow conditions and with choked jets. Gross features such as the coefficients of lift and pitching moment were found and the computation evaluated through more detailed comparisons including the pressure distribution; LDV and Schlieren photographs were also used.

The papers in the Vehicle Control Sessions indicate that the use of jets is promising for increased vehicle control and maneuvering at all speeds but that near the ground thrust vectoring involves more complex aerodynamic phenomena than was first realized, (despite the success of the Harrier in operating partly in this regime).

7. Internal Flows, Turbine Cooling

Finally Session X, devoted to Internal Flows including Turbine Cooling, comprised papers 35-38 and was concerned with experimental and computational approaches to the effects of free-stream turbulence, space averaging of multiple jets, flow inside coolant channels and swirling jets. Paper 35 on the effects of free-stream turbulence investigated, primarily experimentally, its influence on entrainment and mean path of the slightly heated jet at low jet Mach Number. Results show that there are effects of free-stream turbulence intensity on jet development although the trends are insufficiently clear to suggest the primary mechanisms involved. Paper 37 continued the application to turbine blade cooling by air injection. Experimental and computational study indicated that flow inside the coolant channel was influenced by the main flow around the airfoil thus requiring gridding inside the channel. Good agreement of separation with laser measure-

ments was found when simultaneous calculation of the airfoil and the internal flows are carried out. Paper 38 computed the effect of swirl on the jet using algebraic turbulence models with the thin-layer Navier-Stokes equations.

8. Conclusions and Recommendations

1. It is concluded that today's technology adequately meets the need for successful development of military subsonic exhaust V/STOL aircraft; that additional technology is required for the application to aircraft control by solely pneumatic means; and that other applications (e.g. environmentally clean combustion) may be equally important in the future.
2. Agreement between experiment and computation in describing flow structure is generally good for most gross (inviscid) features of simple flows but agreement on the finer details depends upon the choice among various turbulence models. The unsteady interaction of a jet with neighboring surfaces including periodic effects and the mixing process in combustion need more research.
3. There recently have been major improvements in the use of LDV (and in non-invasive techniques, more generally) and significant progress in the use of CFD. Detailed agreement may not always be necessary, depending on the application, and further development of both techniques should be encouraged.
4. In practical applications (such as exhaust gas reingestion) there is a good understanding of the primary effects on current vehicles but their impact on future vehicles is not as well understood.
5. The use of jets for vehicle control appears promising at all speeds when conventional aerodynamic forces are not available. The interaction of the aerodynamics and the control laws is particularly important to the pneumatic control of vehicles and further attention must be given to a proper understanding of this interaction.
6. Further improvement in the understanding of internal flows, particularly the mixing process is needed and can bring about gains in propulsive efficiency of aircraft engines, but can also be applied in other ways. Blade cooling seems to be modelled well if adequate care is taken.
7. Undoubtedly, major changes are taking place in the application of fluid mechanics and, unfortunately, the applications of greatest importance can not be easily identified; nevertheless continued progress in experimental, particularly non-invasive, measurement and in CFD will together give insight into the basic phenomena that will be encountered.

References

1. Margason, R., "Fifty years of jet in cross flow research", NASA Ames, U. S.
2. Withdrawn
3. Zhang, X., Hurst, D. W., Lilley, G. M., "Transient flow features of a supersonic jet in cross-flow", University of Southampton, U. K.
4. Kelso, R., Delo, C., Weisberg, A., Smits, A. J., "Unsteady wake structures in transverse jets", Princeton University, U. S.

5. Krothapalli, A. and Shih, C., "Separated flow generated by a vectored jet in a cross flow", FAMU/FSU, U. S.
6. Smith, S. H., Lozano, A., Mungal, M. G. and Hanson, R. K., "Scalar mixing in the subsonic jet in cross-flow", Stanford University, U. S.
7. Toy, N., Savory, E. and McCusker, S., University of Surrey, U. K., Disimile, P. J., University of Cincinnati, U. S., "The interaction region associated with twin jets and a normal crossflow".
8. Behrouzi, P., McGuirk, J. J., "Experimental data for CFD validation of impinging jets in crossflow with application to ASTOVL flow problems", Loughborough University of Technology, U. K.
9. Charbonnier, J. M., "Experimental investigation of the interaction of a thrust reverser jet with an external subsonic flow, VKI, BE.
10. Nangia, R. K., "Vectored jets induced interference, prediction and verification", Nangia Aero Research Associates, U. K.
11. Berens, T., "Numerical investigation of thrust vectoring by injection of secondary air into nozzle flows", MBB, GE.
12. Perry, A. E., "Topological structure of a jet in a cross flow", University of Melbourne, AUS.
13. Withdrawn
14. O'Riordan, C. A., Monismith, S. G. and Koseff, J. R., "An Experimental study of jets in a turbulent boundary layer crossflow", Stanford University, U. S.
15. Blake, W. B., Stewart, V., "Experiments on the ground vortex formed by an impinging jet in cross flow", WL/FIGC and KSA Technology, U. S.
16. Curtis, P. and Bradley, P., "Experiments into the scaling parameters required for exhaust gas ingestion testing of vertical landing aircraft", British Aerospace, U. K.
17. Penrose, C. J., "Influence of headwind on hot gas reingestion and consideration of pressure ratio scaling", Rolls Royce, U. K.
18. Beasley, R., "Unsteady aspects of hot gas reingestion and statistical analysis", Rolls Royce, U. K.
19. Allegre, J. and Raffin, M., "Control jets interacting with rarefied hypersonic flows", SESSIA/CNRS, FR.
20. Powrie, H. E. G., Ball, G. J. and East, R. A., "Comparison of the interaction of two- and three-dimensional transverse jets with a hypersonic free stream", University of Southampton, U. K.
21. Naumann, K. W., Ende, H. Mathieu, G., and George, A., "Experiments on interaction force of jets in hypervelocity cross-flow in a shock tunnel", German Research Institute ISL, GE.
22. Chiu, S. H., Roth, K. R., Margason R. and Tso, J., "A numerical investigation of a subsonic jet in a crossflow, NASA Ames, U. S.
23. Ince, N. Z., and Leschziner, M. A., "Calculation of 3D jets with cross-flow and impingement", UMIST, UK.
24. Alvarez, J. E., Jones, W. P., Imperial College, and Seoud, R., DRA, U. K., "Predictions of momentum and scalar fields in a jet in crossflow using first and second order turbulence closures".
25. Kavsaoglu, M. S., Akmandor, I. S., Middle East Technical University and Ciray, S., Tai, TU, Fujii, K., Institute Space and Astro Science, Japan, "Navier-Stokes simulation of two and three dimensional jets in crossflow, effects of grid and boundary conditions".
26. Staudacher, W., "Effects, limits and limitations of spanwise blowing", Deutsche Aerospace, GE.
27. Roos, F. W., Magness, C. and Brown, D., "Pneumatic management of blunted-forebody flow asymmetry for high-angle-of-attack directional control", McDonnell Douglas Research Labs, U. S.
28. Roberts, L. and Hong, J., Stanford University, U. S. Greenwell, D. I., and Wood, N. J., University of Bath, U. K., "Theoretical and experimental investigation of a delta wing with turbulent leading edge jets".
29. Dash, S. M., York, B. J., Sinha, N., Hosangadi, A., Lee, R. A., Kenzakowski, D. C., "Recent developments in the simulation of steady and transient transverse jet interactions for missile, rotorcraft and propulsive applications", SAI Corp., U. S.
30. Dormieux, M., Marsaa-Poey, R., "Evaluation numerique des interactions aerodynamiques sur des missiles pilotes par jets lateraux", Aerospatiale, FR.
31. Portner, Th., "First experimental assessment of RCS plume-flowfield interaction on Hermes leading edge thruster configuration", DLR, GE.
32. Chawla, K. and VanDalsam, W., "Numerical simulation of a jet-powered-lift descent, NASA Ames, U. S.
33. Moorhouse, D. J., WL/FIMX, Reinsberg, J. A., SHIRK, F. W., McDonnell Aircraft U. S., "Study of jet effect and ground effect interference problems on a STOL fighter".
34. Roth, K. R., "Transitional flight characteristics of a geometrically simplified STOVL model", NASA Ames, U. S.
35. Toften, T. H., Holdo, A. E., "Effects of free stream turbulence on a jet in a cross flow, University of Hertfordshire, U. K.
36. Withdrawn
37. Benz, E., Wittig, S., University of Karlsruhe, GE, Beeck, A. ABB, Fotner, ch., L., Universitat der Bundeswehr, GE, "Analysis of Cooling jets near the leading edge of turbine blades".
38. Yagci, H., Kavsaoglu, S., "Navier-Stokes analysis of a swirling jet in crossflow", Middle East Technical University, TU.
39. Gaillard, R., Geffroy, P., Jacquin, L. Losfeld, G., "Etude experimental a la soufflerie S5ch de l'ONERA sur les interactions entre un jet supersonique chauffe transversal et un ecoulement supersonique externe", ONERA, FR.
40. Pearcey, H. H., Rao, K., Sykes, D. M., "Inclined air-jets used as vortex generators to suppress shock-induced separation", University London, U. K.

Fifty Years of Jet in Cross Flow Research

Richard J. Margason

Mail Stop 247-2, NASA Ames Research Center, Moffett Field, CA 94035-1000, USA

SUMMARY

The jet in cross flow (JICF) is a basic flowfield which is relevant to a wide variety of applications which are described to provide context for JICF investigations. This paper summarizes material consistent with the scope of topics presented at the 72nd AGARD Fluid Dynamics Panel Meeting and Symposium on Computational and Experimental Assessment of Jets in Cross Flow on 19-22 April 1993 in Winchester, U.K. To focus the present paper, the JICF research was divided into three time periods: (a) early research - up to 1970, (b) research during the 1970's, and (c) research since 1980. The following areas of experimental activity are discussed: the definition of an effective correlation parameter; the jet flowfield including the jet trajectories, cross-section shape, and jet induced pressures; the effects of jet deflection angle, nozzle shape, pressure ratio, velocity decay, and temperature; and the effect of confined flowfield, ground effects, multiple jets, and adjacent surface geometry. In addition, computational methods are discussed including both potential flow based methods, some with empirical and semi-analytical extensions, and Navier-Stokes based computational fluid dynamics (CFD) investigations. Currently modern CFD methods have been able to compute many of the mean flow characteristics of the JICF. Existing CFD methods have not resolved the separated flow region in the near wake of the jet exit. There is also a need for high quality, extensive experimental data which will enable the verification of current and future CFD results and to define unsteady flow characteristics.

LIST OF SYMBOLS

a	speed of sound	h	height or center of vorticity for diffuse vortex model, $h_0/[\text{erf}(\beta h_0)]$
A	area	h_0	half spacing of vortex centers for diffuse vortex model, $2.04[1 - e^{-(V_e s/D)}]$
a,b,c	constants used in empirical equation for the vortex curve (ref. 97)	l_a	analytically determined plume length, $\frac{l_a}{D} = 0.755 \sqrt{\frac{p_{t,j}}{p_\infty}}$
B	width of two-dimensional jet	m, n	exponents used in jet trajectory equation
c	chord	M	Mach number
C_p	pressure coefficient based on either freestream or jet dynamic pressure	M_R	ratio of freestream Mach no. to jet Mach no.
C_{pt}	Pressure coefficient based on jet total pressure	p	pressure
C_R	Callaghan-Ruggeri ratio, $\frac{\rho_j V_j}{\rho_\infty V_\infty}$	q	dynamic pressure, $1/2 \rho V^2$
C_T	thrust coefficient, $T/(q_\infty S)$	Q_{mom}	jet-to-freestream dynamic-pressure ratio, q_j/q_∞
D	jet diameter	r, θ , z	cylindrical coordinates
f	frequency	R, Θ , Z	cylindrical axes
F, G	coefficients used in jet trajectory equation	R	jet radius or effective velocity ratio, $\sqrt{\frac{\rho_j V_j^2}{\rho_\infty V_\infty^2}}$
		Re	Reynolds number, $\rho_\infty V_\infty D / \mu_\infty$
		RV	jet velocity to freestream velocity ratio
		s	distance along jet path from the jet exit; lateral or circumferential distance.
		S	plate or planform area
		St	Strouhal number, fD/V_∞
		St_μ	Effective Strouhal number, $\frac{f B}{V_\infty \sqrt{1 + V_e^{-2}}}$
		t	time
		T	temperature or thrust
		u,v,w	Cartesian velocity components
		V	velocity
		V_e	effective velocity ratio, $\sqrt{\frac{q_\infty}{q_j}}$
		x,y,z	Cartesian coordinates
		X,Y,Z	Cartesian axes
		α	angle-of-attack
		β	diffusion constant for diffuse vortex model, $2.11(s/D)^{-1/2}$
		γ	dimensionless vorticity, $0.72[\text{erf}(\beta h_0)]/V_e$
		Γ	effective strength of each diffuse vortex, $2DV_\infty\gamma$
		ΔL	jet induced lift loss increment
		η, ξ	characteristic coordinates
		Θ	jet temperature to freestream temperature ratio
		μ	coefficient of viscosity

ρ	density
σ	standard deviation
ϕ	angle between Z axis and the normal to the vortex curve
ω	vorticity

subscripts:

B	refers to pressure probe
c	vortex core
C _L	centerline
e	effective

1. INTRODUCTION

The jet in cross flow (JICF) is a basic flowfield which is relevant to a wide variety of applications. The JICF consists a jet exhausting at a large angle into a freestream flow. Variations of the JICF include the jet in a crossflow in-ground effect (JIGE) and cases where there is no freestream velocity: hover out-of-ground effect (HOGE) and hover in-ground effect (HIGE). Specific applications where the JICF represents the primary flowfield feature are described in an effort to provide context for its investigations through the years to obtain its experimental definition and computational solution. Applications include plume dispersion, gas turbine combustor cooling, turbofan thrust reversers, turbojet thrust vectoring, reaction control for missiles and aircraft, and most frequently, the many variants associated with vertical and/or short takeoff/landing (V/STOL) aircraft in transition flight both in- and out-of-ground effect. This paper describes the progress of JICF research and identifies the contributions achieved since a chimney plume study in 1932 and an analytical paper which was written in 1942. The present paper emphasizes the evolution of the understanding of the flowfield physics in the context of both experimental and computational investigations.

This paper summarizes material consistent with the scope of many of the topics presented at the 72nd AGARD Fluid Dynamics Panel Meeting and Symposium on Computational and Experimental Assessment of Jets in Cross Flow on 19-22 April 1993 in Winchester, U.K. After this introduction (section 1), the paper includes the following sections: (2) the flow of a jet exhausting into a quiescent region (HOGE)¹⁻¹²; (3) JICF research¹³⁻²⁸⁴ which is divided into three periods: (a) the early work up to 1970; (b) experimental mean flowfield investigations and refinement of empiricism in potential flow based methods of calculation through about 1980; and (c) recent experimental investigations which begin to provide more detailed data needed to validate contemporary computational fluid dynamic (CFD) calculations as well as CFD studies; (4) the flow of a jet exhausting normal to the ground in a quiescent region (HIGE); and (5) the flow of a jet exhausting normal to the ground in a cross flow (JIGE)²⁸⁵⁻³³³. The paper concludes with section 6 which assesses the current understanding of these flowfields and suggests future research needs.

f	flap
j	jet
max	maximum
min	minimum
o	initial
p.c.	potential core
t	total
∞	freestream

superscripts:

unsteady

2. JET FLOW

Before discussing the JICF, it is useful to review the flow characteristics of a jet exhausting in an ambient region and in a coflowing stream. The free jet flow is sometimes used as a starting condition for JICF analysis. Often, these analyses have used free jet entrainment characteristics as empirical constants.

2.1 Free Jet

A few sketches and flow visualization photographs illustrate the well known features of the jet exhausting into an ambient surrounding. A picture of a nozzle in a water tunnel¹ with some colored milk introduced just upstream of the nozzle is presented in figure 1. The milk is entrained into the jet and mixes in a turbulent mixing region. This flow is illustrated schematically in figure 2 to show the decay and spread as the jet efflux flows away from the nozzle. At the exit plane for a simple, subcritical, convergent nozzle, there is a uniform distribution of both velocity V_j and dynamic pressure q_j near the jet centerline. Two diameters downstream, entrainment of fluid from the ambient surroundings and subsequent mixing is apparent as the profile spreads like an error distribution curve with reduced V and q at the edges of the jet. The jet plume includes a series of transverse ring vortices which entrain fluid. As a result, the cross-sectional area increases with downstream distance.

The precise location of the outer edge of this mixing region is difficult to locate experimentally because the flow is usually turbulent and unsteady as shown in figure 1. At a some distance downstream (typically between 4 and 6 diameters), the peak value on the centerline has dropped below the nozzle exit value. The conically shaped region with undiminished V_j and q_j is known as the potential core. At further increases in downstream distance, the profile assumes the shape of an error distribution curve whose peak value decays inversely with distance. It is difficult to measure with pressure probes beyond about 30 diameters. Another photograph¹ (figure 3) also shows the jet flow exhausting into still water. The air bubbles being entrained into the jet show the flow induction from the quiescent surroundings. This has been called the "douche" (shower) effect. This is another view of the flow illustrated in figures 1 and 2 and shows the nearly radial flow entrainment.

One of the earliest analyses of jet flow was done by Tollmien². This study applied Prandtl's mixing length theory to a homogeneous air jet with adjacent still air for both two-dimensional and axisymmetric jets. There were three assumptions: (1) the tangential shear force was expressed in terms of the lateral momentum of the mixing process; (2) since the width of the jet mixing region increases linearly with downstream distance x , the mixing length l was assumed to be proportional to x (the constant of proportionality c was determined from experimental data); and (3) the turbulence velocity was proportional to the product of the mixing length and the mean velocity gradient. While this analysis provided a good approximation of the mean flow in the fully developed turbulent mixing region, there was no assumption concerning the distribution of turbulence.

Tollmien's analysis was extended by Kuethe³ to account for two parallel streams of different velocities and to represent the initial turbulent mixing adjacent to the potential core region of the jet with a still fluid. Both tangential and normal velocities in the mixing region were obtained. The mixing length l was again assumed to be proportional to the radius of the mixing region: $l = cx$. Experimental measurements were obtained to evaluate this analysis. The initial region ($0 < x < 4$ to 6 diameters) results were faired into Tollmien's solution for large x and shown to provide good agreement with the experimental data. It was found that the sensitivity of the mean velocity-distribution function to the type of turbulence structure assumed was not great. Further work by Liepmann and Laufer⁴ demonstrated a considerable discrepancy between the assumed mixing characteristics and their detailed measurements of the turbulence within the jet.

In an effort to overcome the above discrepancy, Albertson et al⁵ extended the analysis assuming a Gaussian normal probability distribution of velocity in the fully developed region and a modified version in the initial mixing region. A single experimental constant was used throughout the length of the jet efflux. Then using a variety of round and rectangular jets, experiments determined the radial and longitudinal velocity distributions which were used to evaluate the experimental constant. Algebraic expressions and curves were presented for the distributions of velocity, volume flux, and energy flux for each of the jet geometries. In addition, the qualitative representation of the variations of mixing characteristics and a generalized diagram of the mean flow pattern is presented in figure 4. The top portion of the figure shows the streamlines for a two-dimensional jet and the bottom shows the streamlines for a circular jet. The most apparent difference between the two cases is the different half angles of the nominal jet boundaries: (1) 14.0° for the two-dimensional jet; and (2) 11.3° for the circular jet.

In an alternate approach, G. I. Taylor⁶ established the streamline pattern for a variety of jets by replacing the jet with a continuous sink distribution of varying strength along the jet centerline. Validation of this

approach required experimental data to quantify the axial sink distribution. Finding the rate of flow entrainment was a difficult experimental measurement. Most often, assuming radial symmetry, experimentalists have measured the radial distribution of mean velocity, assumed constant density and then integrated numerically to get the local mass flow. At large radial and large axial distances the jet velocity and pressure becomes too low to measure accurately. To overcome this difficulty, measurements near the jet centerline were used to define an analytical form for the overall velocity variation. The difficulty has been finding the most appropriate analytical profile.

A unique technique was developed by Ricou and Spalding⁷ for measuring the axial mass flow rate in the turbulent jet. The jet was surrounded by a porous-walled cylindrical chamber, and air was injected through the wall until the pressure in the chamber was uniform and atmospheric. This was interpreted as the condition where the jet entrainment was balanced by the injected fluid. Mass flow rate measurements of the injected gas provided the magnitude of entrained flow. Subsequently an entrainment law was found relating the mass flow rate, jet momentum, axial distance, and fluid density. Several different gases were injected into a jet of air. These effects as well as buoyancy were accounted for in the final results. When the fluid density is uniform, Reynolds number is high, and the distance z is greater than the nozzle diameter, the mass flow is proportional to the distance z

$$\frac{m}{m_j} = 0.32 \frac{z}{D} \left(\frac{\rho_1}{\rho_j} \right)^{\frac{1}{2}}$$

The entrainment constant was found from the experimental data to be 0.32. This result was used later by many authors to quantify the magnitude of jet entrainment.

Bradbury⁸ derived simple expressions for predicting the spread of turbulent jets exhausting into a parallel stream. Reasonable agreement with experimental data was demonstrated. Viets⁹ modified the Prandtl eddy viscosity model for jets exhausting both in ambient conditions and in a co-flowing stream. The modified model showed improved comparisons with data up to 70 diameters from the jet exit. Catalano et al¹⁰ experimentally investigated an axisymmetric jet in a coflowing stream using a laser velocimeter and obtained both mean and unsteady measurements. While many additional papers could be cited for similar work, it is felt that the sample of papers presented above provides an indication of the type research which has been conducted and the current understanding of free jet flow.

2.2 Jet Exiting From a Plate

The approach taken by Taylor⁶ was extended by Wagnanski¹¹ to the case where the jet emerges at a right angle to an infinite surface. The radial distribution of pressure coefficient C_p on the infinite surface was then computed. These analytical results were compared

with experimental measurements¹² and are presented in figure 5. The measured C_p show a reduction in the magnitude of suction pressure coefficients with increased jet pressure ratio. The analysis predicted the shape of the curve but underestimates the magnitude of the measured pressures.

For the case where the jet emerges at a right angle to a finite surface, a water tunnel flow visualization¹ is presented in figure 6. The jet is shown entraining fluid, some of which is coming from behind the plate. The swirling air bubbles near the edge of the plate indicate that this fluid separates as it flows from behind the plate around its edge into the jet efflux. The pressure distribution induced radially on the plate¹² is presented in figure 7. Near the edge of the plate, the separation region is indicated by an increased suction pressure coefficient. As the separation is relieved inboard of the edge of the plate, the suction pressure coefficient is reduced. The suction pressure coefficient increases again as the induced flow approaches and is entrained into the jet efflux. It is interesting to note that the analytical curve is close to the experimental data inboard of the separation at the plate edge. This shows that the finite plate has a lower induced suction force near the jet when compared with the infinite plate. The experimental data¹² also showed that the magnitude of the integrated suction pressures or lift loss was strongly influenced by the rate of decay of jet dynamic pressure with increasing distance from the jet exit. It was shown that minimum losses in lift (less than 1% of thrust) were obtained from jets which maintain their maximum dynamic pressure for the largest distance (up to 6 jet diameters) away from the nozzle exit. The highest lift loss (up to 4% of thrust) was found with jets which have a potential core less than one diameter in length.

3. JET IN CROSS FLOW

The JICF has received considerable attention because it is the kernel problem for many practical situations. For each case there may be a different emphasis in the flowfield investigation. The main applications can be summarized in the following list:

(1) Initially there were some JICF studies related to plume dispersal from smoke stacks and, more recently, volcanos. Mount Pinatubo in the Phillipines has spread sufficient ash to put a red hue in the sky at sunset in the northern hemisphere. The 'smoke' exits with an upward momentum due to buoyancy into either a stagnation air mass or preferably a cross wind for dispersal. Smoke distribution at both the ground level and downwind are important. This is a pollution problem where smoke concentration is of primary interest. It is customary to evaluate the upward momentum until buoyancy becomes negligible and then to apply a suitable diffusion formulation.

(2) A second application has been effluent dispersal for liquid disposal in streams. This relates to some manufacturing and the current interest in reducing

environmental pollution. Typically the 'jet' represents a pipe or stream flowing into a large lake or river. The research emphasis is diffusion of the 'jet'. The goal is identification of the polluted region and the pollutant concentrations. Another application of this group deals with jets of oil and gas entering the flow in oil wells.

(3) In jet engine combustors, turbines, and others applications, a hot stream of gas can be cooled by injecting jets of cool gas. Injection of fuel is another interest. Since uniform mixing is desired for both applications, it is necessary to study jet penetration and blending of the two streams.

(4) Reaction control jets have been used on rockets and missiles where the jet pressure ratio tends to be very large. There is usually an underexpanded plume which increases the jet induced effect when compared with a sonic, fully expanded jet. Additional applications include control jets on either underwater vehicles or aircraft to produce control moments. In all of these control applications, the jet induced aero-propulsion interactions and their effect on the net control moment are of primary interest.

(5) Perhaps the largest application over the last thirty to forty years is related to V/STOL aircraft and the recent variant, short takeoff/vertical landing (STOVL) aircraft. Many configurations of these vehicles use jets for take-off and landing with varying forward velocities. During the transition between hover and wing borne flight the jets usually induce a loss in lift force and a nose-up pitching moment. The design challenge is to locate the jets to minimize these effects and still balance the aircraft for trimmed flight. In ground-effect there are additional complications: (a) damaging the ground; (b) generating ground wall jets and upwash fountains which modify the aerodynamic forces and moments; and (c) ingesting recirculated hot, exhaust gas in engine inlets.

A jet exhausting into a crossflow generates a complex flowfield with several distinguishable features. When the jet efflux exits the nozzle it is deflected by the freestream to follow a curved path downstream while its cross section changes. For the case of a circular jet, near the nozzle exit, consider the pressure distribution due to potential flow around a rigid circular cylinder (figure 8) where $C_p = 1 - 4\sin^2\theta$. There are stagnation points ($C_p = 1$) upstream ($\theta = 0^\circ$) and downstream ($\theta = 180^\circ$) and minimum pressures ($C_p = -3$) at the lateral edges ($\theta = 90^\circ$ and 270°). As a consequence, the flow spreads laterally into an oval shape. At the same time the crossflow shears the jet fluid along the lateral edges downstream to form a kidney shaped cross-section. At increasing distances along the jet path this shearing folds the downstream face over itself to form a vortex pair which dominates the flow as shown in figure 9.

Associated with the vortex pair is the flow induced into the wake region of the jet from the freestream. This entrainment has been the subject of many investigations. When the locus of maximum vorticity is projected to the symmetry plane the resultant line is called the vortex path. There is also a locus of

maximum velocities in the symmetry plane which is called the jet centerline path. Also shown on figure 9 are the secondary vortices: (2) the horseshoe vortex; (3) the wake vortex street. Some investigators include the vestiges of the free jet ring vortices as a fourth vortex system. Recent investigations which have studied these secondary vortex systems will be discussed in section 3.3.4, "Secondary JICF vortices."

There has been a great amount of research done to characterize the structure of the JICF. Two water tunnel flow visualization photographs from a film by Werlé¹ are presented in figure 10 to provide an appreciation for the complex jet/crossflow interaction. The velocity ratio R for this figure is unknown. These photographs were produced by emitting nine filaments of dye from ports located upstream of the jet exit. As shown in figure 10, the row of ports located laterally upstream of the jet exit was perpendicular to the freestream. Three dye colors were used. The blue dye filament on the centerline flowed to the leading edge of the jet and then divided around both sides of the jet and both parts were entrained into the jet plume on the lee side. Outboard of the centerline the green and red filaments flowed away from the flat plate in the area beside the jet and were also entrained into the lee side. Finally, furthest from the centerline were a second set of green and red filaments which flowed into a saddle point located a few diameters downstream of the jet. The green filament divided into two parts: one part flowed upstream and was entrained into the jet, and the second part flowed downstream near the centerline plane. The most outboard red filament flowed toward the saddle and then downstream to form a wake region. The movie¹ from which these photographs were taken show the three vortex systems (sketched in figure 9) due to the crossflow interaction: (1) the dominant rolled-up longitudinal vortex pair; (2) the horseshoe vortex around the jet exit; (3) and the unsteady wake vortex street shedding immediately downstream of the jet exit. In addition, the free jet ring vortices represent a fourth vortex system.

A particularly complete discussion of the features of JICF was presented by Smy and Ransom¹³. The paper summarized empirical correlations of many of the JICF flow features. In an attempt to focus the present paper the research¹³⁻²⁸⁴ was divided into three time periods: (a) early research - up to 1970, (b) research during the 1970's, and (c) research since 1980. Within each period there were primary foci of the research which are used to organize this discussion. It should be noted that selection of these foci do not imply that these were the only areas studied during each period or that later work did not contribute further advances in understanding.

3.1 Early Research: 1932 to 1970

During the last sixty years JICF applications have been studied extensively in many nations. Systematic investigations began in the 1930's with studies of chimney plumes^{14,15}. In the former U.S.S.R., a variety of applications were identified by Ivanov¹⁶

ranging from smoke stack plumes to an air screen blowing across a door opening to keep warmth in a building. The book's¹⁶ emphasis was furnaces: fuel mixing, fuel injection, air jets to improve combustion, and other related topics. There were 168 references to related work done primarily in the U.S.S.R., U.S.A., and Germany during the period from 1922 to 1957. In V/STOL applications, the Yakovlev Design Bureau developed the subsonic YAK-38 in the 1960's and is currently demonstrating the supersonic YAK-141. The existence of these aircraft suggests that there has been a large research program in their support during the last thirty to forty years.

In a textbook, Kuchemann & Weber¹⁷ described mid-1940's research in Germany for jet induced effects on a jet powered aircraft at high angles-of-attack or with deflected thrust. In 1944 Germany built the first vertical takeoff/landing (VTOL) aircraft, the Bachem Ba 349 Natter. This was a semi-expendable interceptor powered by four solid-fuel rockets for the vertical launch and by a throttleable liquid-fuel sustainer engine for the operational part of the flight. For landing the aircraft was dismantled in flight, and the several sections descended with their own parachutes. After an unsuccessful first flight, the aircraft program was terminated. A second 1940's VTOL concept considered ramjets on rotating wing tips but was not built. However, it was a concept similar to the VJ-101C which was built and flown in the 1960's.

Starting in the late 1940's in the U.S.A. at the NACA Lewis Research Center, Callaghan et al.¹⁸⁻²² conducted a series of experimental investigations oriented toward injection in a jet engine combustor. A primary focus of this work was a description of the penetration of the jet into the freestream and the downstream mixing including temperature effects and effect of the jet orifice shape. Initial interest in V/STOL aircraft provided the impetus for much of the very extensive JICF research investigations conducted in the U.S.A. and Europe during the fifties and sixties²³⁻⁹³. This research was primarily related to the following features of the JICF: jet cross section shape, jet path, and jet induced forces and moments on V/STOL aircraft configurations. Specific reviews of V/STOL aircraft jet interactions were presented in references 23 through 26 and will not be discussed in the present paper. The most complete computational model during this period was developed by Wooler^{39,40,55}; it used doublets and sinks to represent the JICF. Several empirical constants were employed to account for entrainment.

In 1969, a JICF symposium⁴⁸ was held where fifteen papers fairly completely summarized the experimental and computational research conducted during this initial period. At this point, a detailed quantitative description of the flowfield was not available either experimentally or analytically. However, there was broad agreement about the jet cross section shape, appropriate correlation parameter, and jet path.

3.1.1 Jet cross section shape: The formation of a vortex pair from a surface of discontinuity in a separation region was discussed and analyzed by two British papers^{90,91} in the 1930's in relation to lift generated by low aspect wings. These ideas were used in a 1942 analytical study by Chang⁹². This study was concerned with a circular jet of fluid injected normal to a very deep, broad stream and the subsequent jet deflection and shape change of the separation boundary between the jet fluid and the freestream fluid. A potential flow analysis of a deforming fluid circular cylinder was used to describe the roll-up of effluent into a vortex pair. It extended an analytic method⁹⁰ for the vortex wake roll-up of a low aspect ratio wing. The problem was treated as a two-dimensional one which develops timewise along the jet path to represent a steady state three-dimensional flow. The solutions were found to be appropriate only for the initial development of the jet injection. The vortex strengths were consistent with those generated by potential flow past a circular cylinder.

Chang computed (figure 11) the deformation of the boundary. Only one-half of the jet circumference is shown. From $t=0$, where the circumference is circular, the time interval was advanced in steps of 0.10. Contours are shown for t at 6, 9, 11, and 14 time steps. The tick marks on the Y axis show the points where the boundaries cross the axis at each time step. These results were duplicated and extended in 1969 by Margason⁹³ (figure 12). Selected cross sections were scaled to the distance traveled using jet velocity are shown on the second part of the figure for a distance of seven diameters. The roll-up of the jet efflux into a vortex pair which is deflected downstream by the freestream flow is the primary contribution of this calculation. An empirically determined jet path³⁴ was used to locate the jet efflux cross sections at varying (time marched) distances downstream as shown qualitatively on the left side of figure 12. The paper identified the major solution deficiencies as the lack of flow entrainment into the jet wake and incorrect induced pressures in the plane of the jet exit.

There were very limited experimental measurements of the jet cross section shape. Jordinson²⁷ made total pressure measurements to document the flow induced by a jet deflected perpendicular to the freestream. The measured data included the jet path and several jet wake cross-sections normal to the freestream. Other sources of pre-1970 data include Ivanov's book on furnaces¹⁶, Shandorov³⁰, and Keeffer and Baines³³.

3.1.2 Correlation parameter, effective velocity ratio: Early JICF investigations usually characterized the test condition by the ratio of jet velocity divided by freestream velocity $R_V = V_j/V_\infty$. It was soon recognized that this ratio was not appropriate for hot jets. Callaghan et al.¹⁸⁻²² used the product of density ratio and velocity ratio C_R to account for temperature effects in combustors. In addition, V/STOL aircraft investigations were concerned with transition flight

between hover and wing borne flight. It was desirable to have a parameter that ranged from zero at hover to finite values with increasing velocity as flight speed increased. This desire led to the use of the reciprocal of R_V . Another formulation used by Soullier^{70,71} was Mach number ratio, $M_R = M_\infty/M_j$.

Williams and Wood²³ observed that jet induced forces and moments were primarily but not solely a function of velocity ratio R_V . The effects of either Reynolds number based on jet exit conditions or Reynolds number based on wing chord and freestream velocity were secondary. They showed that a better parameter to account for the effects of temperature and compressibility was the 'effective speed ratio' $(V_\infty/V_j)_e = (V_\infty/V_j)(\rho_\infty/\rho_j)^{1/2}$. The reciprocal $(V_j/V_\infty)_e$ is defined as R . These parameters follow from classical arguments that for a prescribed geometry, the jet path and jet induced flows tend to depend mainly on the momentum flux ratio $\rho_\infty V_\infty^2 / \rho_j V_j^2$. Pressure distributions measured on a flat plate (figure 13) which include either a hot jet (300° C) or a cold jet confirm the suitability of this form of the correlation parameter.

In the early 1970's, Harms⁹⁴ conducted measurements of the velocity distributions for cold ($\Theta=1$) and heated ($\Theta=2$) jets both with and without a cross flow. Without a cross flow, it was found that in the fully developed region the hot jet spread more and the potential core was about a diameter shorter when compared with the cold jet results. With a cross flow, velocity distributions were measured at several distances downstream from the jet exit. At $R_V=8$, the vortex curve for the cold jet penetrates to a larger distance into the freestream than the heated jet. At $R=8$, the jet path and the vortex curve are consistent for both the cold and heated jets. Kamotani and Greber¹⁰⁸⁻¹¹⁰ also showed that the velocity centerline locations for both a cold jet and a heated jet coincide as long as the momentum ratio is kept constant. These results further support the use of effective velocity ratio as an appropriate correlation parameter.

In recent years the nomenclature for the most frequently used correlation parameter for aircraft, effective velocity ratio, has been shortened to V_e . Its reciprocal R is most often used in basic fluid flow investigations. The following equations relate the various forms of correlation parameters:

$$V_e = \frac{1}{R} = \sqrt{\frac{\rho_j}{\rho_\infty} \frac{1}{C_R}} = M_R \sqrt{\frac{\rho_\infty}{\rho_j}}$$

For a cold jet where $\rho_j = \rho_\infty$, it can be seen that the simple velocity ratio is appropriate, i.e. $V_e = M_R = 1/R = 1/R_V = 1/C_R$.

For V/STOL applications the magnitude of V_e for transition to wing borne flight depends on the pressure ratio of the lifting propulsion device. For high pressure

ratio jet engines, transition will occur with $V_e < 0.2$; for the Harrier, transition will occur with $V_e < 0.3$; and for lift fans with pressure ratio less than 1.4, transition will occur with $V_e < 0.5$. At hover (i.e. no cross flow), V_e is always zero. While most investigators now use either R or V_e , some researchers use momentum flux ratios which are equal to either of these parameters squared.

3.1.3 Jet trajectory: Another property of JICF which received early attention was determination of the jet trajectory. The path of the jet is associated with the locus of the maximum velocity. Later studies also defined the path of maximum vorticity projected to the symmetry plane (shown on figure 9). Fearn and Weston⁹⁷ showed that while the jet centerline may be measured up to 15 jet diameters along its path, the contrarotating vortices can be detected as far as 45 jet diameters downstream along its path. Margason³⁴ compared empirical expressions obtained by nine investigators for the path of maximum velocity for variable jet deflection angle and variable effective velocity ratio and identified the best correlation. Smy and Ransom¹³ updated the list in 1976. There are a variety of forms used for the analytically derived expressions. Since many of the analytical equations are either very complex or are not closed form only one will be discussed in the present paper. The Wooler⁴⁰ analytically derived equation was found by Smy and Ransom to agree well with experimental data:

$$\frac{x}{D} = \frac{0.19}{V_e^2} \left[\cosh \left(\frac{V_e^2 z}{0.19D} \right) - 1 \right]$$

This equation was improved by taking the Z origin at the end of the jet potential core. For comparison in the present review a series expansion for the hyperbolic cosine was used to put the above equation into the form used by most of the empirical correlations and shown below:

$$\frac{x}{D} = F V_e^n \left(\frac{z}{D} \right)^m + \frac{z}{D} G \cot(\delta_j)$$

This form of the equation is convenient for the case where $\delta_j > 90^\circ$ because the equation is single valued. Some authors have used $z/D = f(x/D, V_e, \delta_j)$. This form gives the penetration distance directly but it can have a two z values when $\delta_j > 90^\circ$ and $x < 0$. Fearn⁹⁹ presented a discussion to guide interpretation of double z/D values. The reader is referred to the original report⁹⁹ for the details. Comparisons of the coefficients (F and G) and exponents (n and m) used in the above equation by various investigators were presented in reference 34 and have been updated for the present paper. They are presented in table I for a jet perpendicular to the freestream where $G=0$ and in table II for a jet at an arbitrary deflection angle to the freestream where G is usually one. These tables show that the F term tends to be either a numerical constant or variable involving a density ratio or $\sin \delta_j$. The n and m exponents tend to vary from 2 to 3. Again, as shown in reference 34, the most robust empirical expression seems to be that by Ivanov¹⁰³.

Table I. Jet trajectory equation terms for $\delta_j = 90^\circ$

Author(ref)	F	n	m
Jordinson ²⁷	2.3	3	3
Callaghan et al. ²⁰	$0.118 \rho_\infty / \rho_j$	2	3.3
Chassaing et al. ⁴¹	$(2.351 + 4V_e)^{0.385}$	2.6	2.6
Storms ³¹	0.195	2	3
Patrick ³⁷	constant	0.85	2.86
Schetz & Billig ³⁸	ρ_j / ρ_∞	2	2.3
Wooler ³⁹	2.645	2.5	2.5
Wooler ⁴⁰	2.63	2	2
Kamotani & Greber ¹⁰⁸⁻¹¹⁰	1.21	1.64	1.58
Fearn ⁹⁷	1.07	3.18	2.99
Snel ¹³³	1.86	2.01	3.01

Table II. Jet trajectory equation terms for arbitrary δ_j

Author(ref)	F	n	m	G
Ivanov ¹⁰³	1	2.6	3	1
Margason ³⁴	$1/(4 \sin^2 \delta_j)$	2	3	1
Shandorov ³⁰	1	2	2.55	$1+V_e^2$
Vakhlamov ³⁵	$1/\sin \delta_j$	2	see below*	1
Vizel&Mostinski ³⁶	$5/(4 \sin \delta_j)$	2	2	1

* $m = 2.53 \zeta + 1.59 \zeta^2 + 0.143 \zeta^3$ where $\zeta = z/D$

3.2 Research During The 1970's

In the 1969 JICF symposium⁴⁸ the need for detailed flowfield surveys was identified as the highest priority research area. As a result, Fearn et al.⁹⁵⁻¹⁰¹ conducted a series of investigations during the 1970's at both NASA Langley and NASA Ames to measure the flowfield and the pressures induced in the plane adjacent to the jet exit for a range of jet deflection angles and several ratios of jet velocity to freestream velocity. Additional investigators^{94-110,117-180} measured other effects: rectangular, elliptic, and more complicated jet exit geometries^{52,66,132,139}; varying jet deflection angle^{98,99,127,142,143}; jet dynamic pressure decay profile^{80,104-107}; jet temperature^{94,102,108-110,118-123}; underexpanded, supercritical jet pressure ratio¹⁴⁸⁻¹⁵¹; and several multiple (usually two jets) jet geometries^{80,130,135,164-166,207,224-227}. In the 1970's, an extensive database was obtained which has provided a basis for understanding the mean velocity flowfield and pressure distributions.

This period was driven by the military interest in rocket reaction control and in V/STOL aircraft where there was a need for pragmatic solutions of jet induced interference effects in the transition flight regime both in- and out-of-ground effect. Many V/STOL aircraft configurations were experimentally tested. The potential flow based computational concepts of Wooller were extended and improved by Adler and Baron¹⁷³ (figure 4). There were some reviews¹⁹⁶⁻¹⁹⁷ and proceedings of several conferences on V/STOL¹¹¹⁻¹¹⁶ include many papers which illustrate progress achieved during this period toward understanding the overall V/STOL aircraft interference effects.

3.2.1 Induced pressures: One well documented aspect of the JICF is the pressure distribution induced on an adjacent flat surface. This has been measured by many investigators (ref 23, 52, 66-71, 78-80, 96, 102, 107-110, and 142-143). In most of the reports the jet-off pressures are subtracted from the jet-on pressures to give the increment due to the jet as the pressure coefficient C_p . While contour plots are probably the most convenient form for data comparisons, there are some errors which affect the interpretation of these plots.

Generally, the C_p contour locations become less definite as the C_p gradient approaches zero which is where C_p tends to zero away from the jet. These errors are caused by measurement limitations and by uncertainty in fairing the sparse data. For example, if the pressure transducer has an error equal to 0.5 percent of full-scale then there is an uncertainty which is shown in figure 14 (a) by the shaded areas. While these bands are small for $C_p < -0.4$, they can be large for $C_p > -0.1$.

A comparison among three investigators^{69,96,&102} (fig. 14(b)) reflects this measurement uncertainty. Another difference is shown in the wake where Fearn's⁹⁶ data tends to be more negative at a given radius for approximately $135^\circ < \theta < 180^\circ$. This may be due to the increased Reynolds number due to a larger jet diameter. Fearn used 10.2 cm diameter jet and the others used 2.5 cm diameter. Comparisons by Fearn in reference 96 with Soullier^{70,71} who used a 12 cm diameter jet show fewer differences.

There are generally three regions on the pressure distributions whose details depend on the effective velocity ratio R . Upstream of the jet exit, there is a positive pressure region which is due to blockage of the freestream by the jet efflux. The second region, generally to the side of the jet exit, exhibits negative pressures which are due to acceleration of flow around the jet and due to jet entrainment. The position of the minimum pressure point moved upstream from about 110° for $R = 2.2$ to about 75° for $R = 10$. The value of the minimum pressure coefficient measured by Fearn⁹⁶ was a function of R and appeared to reach its lowest value of about -4.7 at $R = 6$. These data contrast with potential flow over a circular cylinder where the minimum pressure coefficient of -3 occurs at 90° . The third region, the wake downstream of the jet exit, seems to depend on R and R_e for its shape and extent as discussed previously.

The following changes in the pressure distributions as R increases (V_e reduces) are noted. Below $R \approx 5$ the plots have the shape of a snail where the $C_p = 0$ contour is analogous to the antenna, the positive contours represent the head, and the negative contours represent the shell. At greater R values (fig. 15) the shell grows and the antenna droops to the ground as the head becomes smaller. In the JICF world 'snail' plots have their own mystic.

3.2.2 Jet exit shape: One factor that affects the shape of the 'snail' plot is the shape and orientation of the jet exit as shown in figure 16 where $R = 4$. This has been investigated by McMahon and Mosher^{52,66} and by Weston and Thames¹³⁹. The data for a circular jet⁹⁶ (fig 16(a)) and the aspect ratio 4 rectangular jet data¹³⁹ are shown for both streamwise (fig 16(b)) and blunt (fig 16(c)) orientations. The blunt jet is characterized by a large low pressure region which spreads laterally and downstream; as well as a region of positive pressure which extends relatively far upstream. The pressures induced by the streamwise jet were quite different. The primary effect was a low pressure region which spread laterally with almost no wake region and a small positive pressure region. The circular jet induced pressure distributions are seen to be bracketed by those from the blunt and streamwise jets. The paths of the jet centerline and the vortex curve show the greatest penetration into the freestream for the streamwise jet and the least for the blunt jet. The circular jet paths are between those for the two rectangular jets. For a given jet deflection angle and effective velocity ratio R , the vorticity strength is greater for the streamwise jet than for the blunt jet.

3.2.3 Jet deflection angle: The effect of jet deflection angle δ_j on the jet centerline path has already been discussed (section 3.1.3). The effect of δ_j on the surface pressure distribution was investigated by Taylor¹⁴²⁻¹⁴³ where the angle was varied from 15° to 90° . The decay of the total pressure coefficient C_{pt} on the jet centerline increased with increased deflection angle. As the deflection angle was reduced the negative pressures along the zero degree azimuth approached zero. The positive pressure region immediately upstream of the jet was not well defined; apparently because of a reduced number of pressure ports near the jet exit at lower deflection angles. The 'snail' plot showed a shift downstream of the negative pressure region and an increase in its extent as the deflection angle was decreased. The wake region showed a rapid pressure recovery for deflection angles of 30° or more. Below a δ_j of 30° , the jet wake appeared to attach to the surface and generate a positive pressure region adjacent to the downstream edge of the jet. The size of this region increased as the effective velocity ratio R increased from 6 to 12. Further downstream ($x/D > 7$) the pressures were negative; this indicates the jet is no longer impinging on the surface and that the high local velocities were probably due to flow entrainment into the jet.

Aoyagi and Snyder²¹⁷ obtained surface pressure data for jet deflection angles which ranged from 90° to 45° . The results were consistent with Taylor's data: the pressure field shifted downstream and the entrainment effect decreased with decreasing jet deflection angle. Fearn⁹⁹ presented data showing the changes in the velocity/vorticity flow field which are discussed in section 3.2.8, "Velocity/vorticity profile."

3.2.4 Multiple jets: The effect of dual lifting jets has been investigated by Wooler et al.^{80,164-166} and by Schetz et al.²²⁴⁻²²⁶ to evaluate their effects on jet interference. Both sets of investigations included in-line jet configurations and side-by-side jet configurations. An example of Wooler's in-line jet results are presented in figure 17 where contours of constant total pressure coefficients are shown for a jet spacing of 7.5 diameters at $R = 8$. For this configuration, the downstream jet decays less rapidly than the upstream jet. This difference in decay rates decreases as the jet spacing increases. The deflection in the streamwise direction and the decay of the leading jet appears to be independent of the spacing over the range tested⁸⁰ (2.5 to 7.5 diameters). Surface pressure data indicate that the negative pressures increase with increased spacing between the jets. This result is similar to that generated by a streamwise jet. The combined result is a decreased lift loss when compared with a single jet which has the same total thrust as the pair of jets.

Side-by-side jet configuration results from Schetz et al.²²⁴⁻²²⁶ show that the gross interaction features are characterized by two interrelated effects: (1) significantly enhanced flow velocity (reduced surface pressures) between the jets because of the "channeling" of flow between the jets, and (2) increased (when compared with the single jet) blocking of the crossflow and spillover to the sides which results in increased flow velocities (lower pressures) on the free sides of the jets. The combined result is an increased lift loss when compared with a single jet which has the same total thrust as the pair of jets.

3.2.5 Surface geometry effects: Most of the investigations have concentrated on the pressure induced on a flat plate. Realistic aircraft have the jets mounted in a body of finite size and a rounded shape. Two experimental programs which evaluated jet induced effects on a circular body were reported by Ousterhout^{117,202} and Aoyagi²¹⁵. The Ousterhout investigation used the same 0.95 cm diameter jet in a flat plate model and in a 10.2 cm diameter circular body model. It should be noted that the jet diameter is less than 10% of the circular body model diameter which is much smaller than that for a V/STOL aircraft. As a result these data probably are not representative of a realistic aircraft. The results in figure 18 compare the induced pressures along four streamwise rows. The lateral locations of the rows measured along the surface are the same for the flat plate and the circular cylinder. The data show the following trends: (1) the most negative pressure coefficient peak is found on the flat plate, (2) the rate of longitudinal pressure coefficient decay with increasing lateral distance is similar for the two surfaces, (3) the pressure coefficient profiles for the cylindrical body extend further in the streamwise direction than the corresponding profiles on the flat plate.

The investigation by Aoyagi²¹⁵ used a 1.94 cm diameter jet exiting from a 10.16 cm diameter cylindrical body with an ogive shape nose. This jet to

body diameter ratio, 0.19, is still not representative of an aircraft. Comparison of the pressure distribution obtained with the body of revolution and a flat plate for $\delta j=90^\circ$ and $R=8$ was limited. However, it showed a smaller difference between the flat and cylindrical configurations than Ousterhout showed.

3.2.6 Velocity (dynamic pressure) decay: The decay characteristics of a jet exhausting into ambient conditions are well documented²⁻¹². Typical measurements for hover are presented in figure 19 as the faired curve which show a potential core region about 6 diameters long and a power law decay at increased distances. This figure from Fearn and Weston⁹⁹ also shows the effect of jet deflection angle on the velocity decay for two effective velocity ratios. In all cases the jet decay is faster with a crossflow and have a modest further decay increase as the deflection angle increases to perpendicular.

At hover it was shown by Gentry and Margason¹² that changes in the nozzle internal geometry upstream of the jet exit can change the potential core from 6 diameters down to nearly zero and that the induced lift loss on a plate can increase from one to four percent. For JICF, similar investigations by Fricke et al.⁸⁰ and by Kuhlman et al.¹⁰⁴⁻¹⁰⁷ showed that more rapid jet decay did not cause a significant effect on the induced pressures. A review was conducted by Perkins and Mendenhall²⁰³ of the effects of jet exit profile, exit Mach number, swirl, and turbulence level on jet-induced pressures. Attempts were made to develop correlations; no consistent patterns were apparent from the available data. Later, the effects of swirl and increased temperature were studied experimentally by Kavsaglu and Schetz²⁶⁸. It was found that a high turbulence jet ($u'/V_j > 0.10$) does not have the potential core structure present in a low turbulence jet ($u'/V_j < 0.03$) and has a reduced penetration jet trajectory and reduced induced surface pressures. Swirl was found to have characteristics similar to the high turbulence jet and to also induce large asymmetries in the induced pressure distributions.

3.2.7 Temperature: The velocity decay for temperature ratios Θ of 1 and 2 were found by Harms⁹⁴ to be similar; however, there was a slight reduction in the potential core length for the warmer jet ($\Theta=2$). Flowfield velocity surveys indicate little effect of temperature for a given effective velocity ratio. The path of maximum temperature when compared by Kamotani and Greber¹⁰⁸⁻¹¹⁰ with the path of maximum velocity is shown in figure 20. Here the effective velocity ratio R seems to collapse the maximum temperature centerline for two jet temperatures to one curve. However, for a given R this maximum temperature path penetrates the freestream less than the maximum velocity trajectory. It was found that when the jet temperature increased, the strength and size of the vortex motion increased. As a result, more heat is transferred to the vortex region and the maximum temperature path appears to correspond to the vortex path. For the free jet case, Ricou and

Spalding⁷ found that increasing jet temperature causes more entrainment. A similar effect is noted for the JICF where the increasing jet temperature causes more entrainment and activates the vortex motion. It should be noted that there is no JICF data available for jet temperatures as hot as modern high pressure ratio turbojet engines.

3.2.8 Velocity/vorticity profiles: An example of the measured velocity field⁹⁷ for one location normal to the jet path for an effective velocity ratio of $R = 8$ is presented in figure 21. The data are presented for the entire right half of the cross section and for a portion of the left half of the plane. In figure 21(a), the measured velocities are presented as contours of the velocity component perpendicular to the cross section which are superimposed with a vector plot of the in-plane velocities. In figure 21(b), the in-plane velocities have been integrated to obtain contours of vorticity non-dimensionalized by the maximum vorticity in the plane. In both parts of figure 21 the centerline location and the vortex curve location are noted. It is clearly shown that the maximum upwash velocity occurs at the vortex curve location. These figures also show that, unlike some of the earlier computational procedures (section 3.1.1), there is not a clearly defined boundary between the jet and the freestream.

The vortex pair generated by the JICF appears to be the major flowfield feature. From Fearn and Weston⁹⁷ the path of the vortex curve relative to the jet centerline curve is presented in figure 22 for two values of the effective velocity ratio V_e . Initially the vortex paths were obtained by integrating extensive velocity measurements made at selected planes perpendicular to the jet path. These data are presented as the square symbols near the vortex curve shown in figure 22. Since the upwash velocity in the symmetry plane peaked at the vertical location of the vortex curve, a diffuse vortex model was developed⁹⁵ and used to extract the location and strength of the vortex pair (shown in fig. 22 by triangle symbols). Then these vortex path data were fit using an empirical power equation of the same form as that used for the jet centerline. This is the vortex curve shown on figure 22. Consistent with the discussion in the previous section the vortex curve location is very similar to the temperature centerline.

Fearn and Weston^{95,97} uniquely described the contrarotating vortex pair strength, location, and a measure of their diffuseness. The vortex pair is formed at the jet exit within the jet flow as relatively concentrated vortices whose initial strength is inversely proportional to the effective velocity ratio: $\gamma_0 = 0.72/V_e$. The vortices are deflected by the cross flow and they diffuse at a rate which is a function of the arc length along the vortex curve, but which is a weak function of the effective velocity ratio. The vortices gradually weaken each other by the diffusion of vorticity across the symmetry plane.

From Smy and Ransom's¹³ discussion, the vorticity data from Fearn and Weston^{95,97} are presented in figure 23 in non-dimensional form to show the correlations within the data for effective velocity ratios V_e ranging from 0.10 to 0.25. These vorticity data were taken from the downstream region where the jet curvature is small. In figure 23 (a), the non-dimensional lateral location term of the center of diffuse vorticity is plotted as a function of $V_e^2 s/D$ and is compared with the correlation given by $V_e h_0/D=0.21$. In figure 23 (b), the non-dimensional vorticity term γV_e is also presented as a function of $V_e^2 s/D$ and is compared with the correlation given by $\gamma_0 V_e=0.72$. While there is data scatter, the trend of the data is consistent for both correlations. Vortex diffusion was correlated by $\beta D=2.11/(\sqrt{s/D})$. In figure 23 (c), the vortex core radius r_c/D at which the maximum tangential speed occurs is used to characterize the vortex core size; it is correlated by $r_c/D=1.121/(\beta D)$. The data for the vortex core size is shown to agree with this correlation parameter.

3.2.9 Underexpanded jets: The induced pressure distributions due to an underexpanded sonic jet exiting normal to a flat plate in a subsonic freestream have been investigated¹⁴⁸⁻¹⁵⁰. An example of these data, from Shaw and Margason¹⁴⁸, is presented in figure 24 (a) for momentum ratios (R^2 or Q_{mom}) which range from 0 to 300. The data for the 170° azimuth show that for a selected radial location r/D the pressure coefficient tends to a more negative value as Q_{mom} increases. These distributions indicate a significant loss in jet reaction force and reduced control moment. It was desired to correlate the data for a design method which could account for this loss. The Riemann shock plume geometry was used to identify an appropriate length. Several plume dimensions were tried. The best correlation was achieved using an analytically

determined plume length $\frac{l_a}{D}=0.755\sqrt{\frac{p_{t,j}}{p_\infty}}$ instead of the jet diameter to non-dimensionalize the radial distance as shown in figure 24(b). This correlation permits scaling of the data at a given azimuth to a desired value of momentum ratio.

3.2.10 Effect of lifting jet location relative to a wing: Many experimental investigations of specific V/STOL aircraft have been conducted during the last forty years. A few examples of this research are cited in references 72 through 89. The magnitude of the aero/propulsion interference effects is shown to be dependent on the details of the aircraft configuration. An illustration is provided by the results of a classic investigation by Carter⁸² of the effect of the jet exit location relative to a simple wing. The model had a simple fuselage, an unswept, untapered, aspect ratio 6 wing which used a NACA 4415 airfoil section for both the wing and a 30% chord slotted Fowler-type flap. The model was mounted on a sting using a strain-gauge balance. Two jets, one on each side of the fuselage, were mounted

independently of the wing at the 25% semispan station. The jet exits were positioned at each of the various longitudinal and vertical locations shown by the plus marks on figure 25. The results of the investigation are presented as the increment of interference lift induced by the jets at the various longitudinal locations. The results show that negative lift increments were measured when the jet exits were located ahead of the wing midchord and positive lift increments were measured when the jet exits were located aft of the wing midchord. The fact that the interference effects are most favorable for locations closest to the flap indicates that the jet is helping the wing and flap achieve their full lift potential much like a part span jet flap.

3.2.11 Potential flow based computational methods:

Several potential-flow, vortex-lattice, or panel-method based schemes^{163,164,173-177,204-206,208} have been developed which account for jet-induced interactions. A comparison¹⁶⁹ of five production surface panel methods and one vortex-lattice method¹⁷⁰ demonstrated that good agreement for conventional aircraft aerodynamics can be achieved between any of these methods and experimental data. Several investigators^{55,59,133,163,164,173-175} have extended potential flow based methods to develop approximate predictive JICF methods. One of the earliest and most complete calculation methods for jet induced effects was developed by Wooler et al^{55,164}. This model used a double lifting line to represent a simple wing and a sink-doublet model to represent the jet.

The Wooler method later incorporated the vortex lattice with the sink-doublet jet model to provide a more comprehensive, modular procedure¹⁷¹. For the first module, the incompressible jet model neglects viscous effects other than the entrainment caused by potential flow sinks or doublets. The entrainment of freestream flow into the jet at the pressure force on the jet boundary govern the two equations of motion of the jet. The entrainment parameters were obtained from experimental data such as Ricou and Spalding⁷. Yen¹⁹⁷ presents a complete discussion of the various entrainment parameters used by Wooler and other investigators. The jet cross section was varied from a circle at the exit to an ellipse as the jet is deflected by the freestream. The induced velocity flow field due to the jet is obtained from two singularities: (a) a uniform sink distribution on axes normal to the freestream at discrete locations along the jet centerline represent the entrained flow, and (b) a doublet distribution along the jet centerline represents the blockage and jet-induced circulation effects. Additional procedures were developed to represent nonaxisymmetric jets, jet pairs, and a jet in a nonuniform freestream.

A second module evaluates the jet induced forces and moments using the vortex-lattice method¹⁷⁰ to represent lifting planforms. The method can give good agreement with experimental data for wing-body combinations by including the planform of the body in addition to the wing. Power induced aerodynamic

characteristics were evaluated by using a propulsion-induced camber distribution on the planform to satisfy the flow-tangency condition at the three-quarter chord of the horseshoe vortices of the lattice representation. This vortex lattice program was used to improve the method of ref 164 which only represented the wing by a double lifting line.

Experimental data^{167,168} were used to evaluate these methods. The model had a simple body shape and two wing mounted nacelles mounted inboard on a unswept, tapered wing. Mineck¹⁷² applied Wooler's method¹⁷¹ and obtained good agreement with experimental data from the configuration with the nozzles deflected 90° in the aft position near the wing trailing edge (figure 26). For this case the jet-induced increase in wing lift (i.e., jet-flap effect) dominated and the flow on the wing was attached. In contrast, poor agreement was obtained with the nozzles deflected 90° in the forward position at $x/c=0.11$. This result illustrated the inability of the method to account for separated flow on the wing aft of the forward mounted engine nacelle. Other investigators with similar methods, such as Snel¹³³, have found that the agreement is not good in the wake region. For some cases, an empirical model of the separated wake improved the correlation of computed results with experimental data.

Adler and Baron¹⁷³ improved the Wooler-type method to predict the inner structure of the deflected jet more accurately. Two features of the jet were changed. First, the Chang⁹² method for determining jet cross section shape was incorporated and, second, a method was developed to more adequately represent the non-similar velocity profile within the jet cross section. An entrainment model coupled with velocity decay and cross section shape change and area growth were developed. The ideas of Keffer and Baines³³ where the entrainment is composed of straight jet entrainment and vortical entrainment were used. The vortical entrainment was represented by a vortex pair with local jet growth using a suggestion from Schwartz and Tulin^{187,188}. An example of two jet cross sections are presented in figure 27 for two contrasting conditions of V_e and downstream distance. In both cases, the computed cross section (on the left) compared quite well with experimental results (on the right) from Kaomotani and Greber¹⁰⁸. Similar agreement was shown for conditions which include $4 < R < 12$ and $20^\circ < \delta_j < 90^\circ$. Application of this method to pressure distributions on a flat plate or for aircraft configurations were not shown.

3.3 Research Since 1980

In the early 1980's, the Harrier dramatically demonstrated the value of V/STOL capability in the Falkland Islands conflict. However, with the exceptions of a US/UK STOVL configuration study effort in the late 1980's and the current US STOVL strike fighter (SSF) effort, there has been a slackening of interest in military STOVL applications. This trend has increased

with the dissolution of the USSR. Interestingly, Russia has the only supersonic V/STOL combat aircraft, existing at the present time. It is, apparently, available for flight research and for sale. There has been continuing interest in turbojet engine applications (such as combustor fuel injection, combustor wall cooling, and injection cooled turbine blades) and increased interest in deflected thrust for combat aircraft maneuverability. There was an increased interest in the ground-effect interaction²⁸⁵⁻²⁸⁶ for STOL and STOVL. There were applications^{202,204,206,208-214,223} of potential flow panel methods which represented major extensions of the Wooler and Adler-Baron computational methods. However, these efforts provided only modest improvements in numerical solutions. The research emphasis has shifted to the application of modern computational fluid dynamics (CFD) methods to JICF and to experimental investigations to obtain specific data for use in CFD verification. Several experiments²¹⁵⁻²²² were conducted which used laser velocimetry to measure the JICF flowfield velocities in finer detail.

3.3.1 Extended potential flow computational methods:

An empirical correlation method to predict the surface pressure distribution was developed by Perkins and Mendenhall²⁰²⁻²⁰⁴ for application to a JICF in a flat plate or to a JICF in a body of revolution. The method includes a blockage model, an entrainment model, and viscous correction factors. For the flat plate, where there were adequate experimental data to define the needed correlation parameters, a reasonable comparison was demonstrated. For the body of revolution, there were inadequate data to properly define the correlation parameters.

In an attempt to improve the potential flow based methods, panel methods were coupled with various higher order models for the jet. An investigation by Maskew et al.²⁰⁶ used the VSAERO panel method²⁰⁵ with an iterative panel procedure for wake shape and entrainment for the jet and a source transpiration technique for boundary layers. A separated wake model was attached vertically along the solid potential core of the jet at $\theta=130^\circ$. Limited results for the JICF flat plate case were presented and were consistent with Wooler's results when a wake separation model was used. More complete comparisons with data²⁰⁷ for a jet in a body of revolution were also presented. Here there is a discrepancy downstream of the jet because there was no separated wake model developed for this type of configuration.

In one example Yoo and Strash²¹³ coupled VSAERO to represent the aircraft with a jet model using either ARC3D²⁵⁰ or APPL²⁵¹, a parabolized Navier-Stokes code developed by Roberts. Overlapping boundaries were used to couple the two methods. The model configuration^{167,168} consisted of a simple wing-body with a single lifting jet in the fuselage lower surface. The results were very sensitive to the radial grid density used to represent the jet. Comparisons were made with

pressure data from the model show poor agreement in the jet near field wake region. Away from the jet on the high wing, the computed pressure distributions were similar with and without the jet model.

A similar approach was taken by Howell^{211,212}. The PANAIR panel method²⁰⁹ with the Neumann boundary condition was used to represent the aircraft and a parabolized Navier-Stokes solution with an entrainment boundary condition was used to represent the lifting jet. The jet shape and entrainment were determined using the Adler-Baron method¹⁷³ and unpublished data acquired by Adler. The method was applied to a simple high-wing aircraft configuration with a single lifting jet mounted in the fuselage⁶⁸. A comparison between experiment and theory of jet induced lift as a function of thrust coefficient is presented in figure 28 for the configuration at 10° angle-of-attack. The propulsion induced lift loss is underestimated by about 20% of the thrust. This method extension is unable to account for the separated wake caused by the lifting jet.

A simple solution procedure was developed by Katz and Kern²¹⁴ for a delta wing with a jet blowing through a hole near the 0.5 root chord location to represent an ejector. A vortex lattice code with a separated rolled-up wake for the wing was developed. The jet was modeled by specifying a jet velocity normal to the wing in the ejector opening. It should be noted that the experimental model had a space around the jet where the separation effects could not physically occur. As a consequence the problem of modeling a separation region is greatly reduced. The computed results for the thrust induced lift and drag increments for a range of thrust coefficients at an angle-of-attack of 20° was surprisingly good.

To date, coupled panel method/ higher order jet solutions have demonstrated reasonable comparisons with experimental data upstream and beside the jet exit. These methods have not demonstrated useful results downstream of the jet without an empirical wake separation model. As a result, they appear to offer no improvement over earlier potential flow aircraft /jet methods.

3.3.2 Velocity/turbulence field: Several experimental investigations of the JICF flowfield have been conducted using laser velocimeters^{137,215-222}. The first investigations demonstrated the feasibility of this device for measuring this flowfield. Later investigations produced some useful data which tended to be limited in scope. For example, several reports²¹⁷⁻²²¹ present different parts of the data obtained during a series of NASA Ames Research Center tests in the 7- by 10-Foot Tunnel. A 5.08 cm diameter jet mounted in a flat plate was used with a three-component laser velocimeter. Fearn et al.²¹⁸ discussed the limitations of these data. This report presented four planes of measurements near the jet exit. Snyder and Orloff²¹⁹ presented several additional survey planes. The data included a quantitative measurement of

the weak vortex pair near the flat plate immediately downstream of the jet exit. This result demonstrates the ability of laser velocimetry to resolve the fine flow features in this complex flowfield. In addition, a procedure was developed to follow mean streamlines in the flow while measuring the three velocity components. The raw data also included turbulence information, but these data were not analyzed.

3.3.3 CFD computations: The biggest advance since 1980 has come from the many CFD investigations²⁴⁰⁻²⁷⁵ undertaken to obtain finite difference numerical solutions to the Navier-Stokes equations (NS) for the JICF. Several examples of recent results are examined with an emphasis on their comparisons with experimental data. It was shown by several investigators (ref 191, 194, 241, 261-263, 266, 269, 273, 275) that NS solutions can adequately represent most of the flowfield. The first example¹⁹⁴ of a Navier-Stokes equations finite difference solution for a turbulent jet is presented in figure 29 at an effective velocity ratio R of 4 where the velocities computed in the centerline plane are shown. This computation used a small (24x22x22) nonuniform grid (11,616 grid points) to represent the right half of the flowfield. The left half was accounted for by the use of a symmetry boundary condition. This symmetry approach has been used in most of the computations presented below. The three-dimensional recirculating region and large wake region downstream of the jet are shown as well as the jet spreading and entrainment of surrounding fluid. The jet centerline path compares closely with Keffer and Baines³³ experimental data. Similar agreement with the jet path was shown in computations by Patankar, Basu, and Alpay¹⁹¹. However, the jet decay and wake region were not adequately represented by either computation.

In another NS computation, Oh and Schetz²⁶⁶ used a penalty method finite element method (FEM) where the NS equations were solved using a generalized Galerkin technique. A simple eddy-viscosity turbulence model was used. The finite element mesh was small 30x12x12 (4,320 grid points) and is not directly comparable with grid sizes used for finite difference methods. An example of the induced pressure distribution for an effective velocity ratio R of 4 is presented in figure 30 as a double 'snail' plot. Experimental data²⁶⁸ are shown on the left and the FEM solution²⁶⁶ is shown on the right. The positive pressure regions compare closely. Beside the jet exit, the experimental negative pressure contours are larger in area than the FEM results. The largest difference is in the wake region. The FEM solution has a positive region which is much like that obtained from a simple potential flow solution. This is not a satisfactory solution for estimating induced effects on a V/STOL aircraft. In other FEM parabolized NS computations, Baker et al.²⁴⁴⁻²⁴⁷ also obtained reasonable jet path and cross section shape results but inadequate results in the wake region.

A NS computation by Kaysaoglu et al.²⁶⁹ used a three dimensional, compressible Navier-Stokes code, LANS3D²⁷⁰. The Baldwin-Lomax turbulence model²⁷¹ was used within 5 diameters of the flat plate and the turbulence model of Oh and Schetz²⁶⁶ was used in the jet region. A rectangular grid 59x21x45 (55,755 grid points) was used for a circular jet computation. Along the symmetry plane the jet diameter was represented by 14 grid lines. The jet Mach number was 0.4. The non-uniform jet exit velocity profile was obtained from the characteristic boundary conditions (bc). The inflow (x_{min}) and outflow (x_{max}) used characteristic bc; the top boundary (z_{max}) used M_{∞} of 0.1; and the bottom solid walls used the no slip condition. The surface pressure distribution obtained is compared in figure 31 with experimental data²⁶⁸. The negative pressure region beside the jet is represented well. Although the overall results are reasonably predicted, there are limitations. The computational results do not capture the positive pressure region ahead of the jet and the wake solution.

The previous solutions, which used up to 60,000 grid points, found that the flows especially near the jet exit and in the wake were not adequately resolved. Other computations have used up to 300,000 grid points in an attempt to improve the solutions near the jet exit and on the flat plate surface. Roth²⁶¹⁻²⁶³ used a 55x55x50 (151,250 grid points) Cartesian grid. Chiu et al.²⁷⁵ used the Chimera grid embedding technique²⁷⁶ with two overlapping grids; (1) a 79x33x66 Cartesian grid (172,062 grid points) for the surrounding freestream and flat plate boundary layer and (2) a 51x33x66 cylindrical grid (111,078 grid points) for the jet which was located along the jet vortex curve. The plate pressure coefficient distributions along three azimuthal rays (0°, 90°, and 180°) are presented in figure 32 for both computations and are compared with Fearn and Weston⁹⁶ experimental data. Along the zero degree ray (fig. 32(a)) the increased grid size used by Chiu et al.²⁷⁵ greatly improves the agreement with experiment. Chiu showed that this is probably due to the increased grid density near the edge of the jet. Along the 90° and 180° rays (fig. 32 (b) and (c)), the benefit of increased grid density is less apparent. While there are differences near the jet within two diameters of the exit, there is little to suggest that either increased grid density or the turbulence models used produced improvements in the solutions. Particularly disappointing is the positive pressure computed in the wake along the 180° ray at large distances from the jet.

To date, these computational investigations have shown that the flow near the jet exit and on the surface downstream of the jet exit has not been resolved. This is an area of current activity where both improved experimental understanding of the flowfield and recent advances in computer hardware and algorithms have enabled more elaborate numerical solutions. At this time, comparisons with experimental data demonstrate that there is a need for improved solutions. Whether these results show a need for larger grids (more than

300,000 grid points), more appropriate turbulence models both in and near the jet, or other unidentified improvements is not clear and provide the rational for continued research.

3.3.4 Secondary JICF vortices: The JICF vortex systems are sketched in figure 9. They include the horseshoe vortex. This vortex is analogous to the vortex generated at the wing-body juncture of an airplane. It is much smaller and weaker than the jet vortex pair. The third vortex system is the weakest and needs improved experimental definition. One analogy relates it to the Karman-Benard vortex street. Another concept describes it as an unsteady flow separation region.

Using a laser velocimeter, Snyder and Orloff²²¹ measured the velocities in two wake cross section planes which were within 0.6 jet diameter vertically of the flat plate, ± 10 jet diameters laterally, and located 1 and 2 jet diameters downstream of the exit of a circular jet. Weak wake vortex structures were found in both cross sections. At two diameters downstream the vortices were more clearly developed and were centered less than 0.20 diameters above the plate and laterally at about a jet radius from the centerline plane. These results demonstrate the existence of the wake vortices in time averaged measurements.

The vortex structure of the JICF as sketched in figure 9 has been the subject of more rigorous investigation during the last five years and an improved understanding has been obtained. In an experimental investigation, Fric and Roshko²⁸¹ photographed the four types of vortical structures which exist in the JICF near field and identified their sources. They suggest that: (1) the free jet shear layer lateral ring vortices on the jet circumference evolve from the boundary layer in the nozzle and become distorted as the jet is deflected; (2) the dominant longitudinal counterrotating vortex pair evolves from the shear layer vorticity of the jet; (3) the horseshoe vorticity is due to the adverse pressure gradient just ahead of the jet on the crossflow wall; and (4) the wake vortices, which have been related by some to the vorticity from a solid cylinder, were the least understood and may persist far downstream from the jet exit.

McMahon et al.²⁷⁸ found that the Strouhal numbers for flow past a jet are in qualitative agreement with those for a solid body, provided that the width of the spreading jet some distance from the surface is used rather than the jet exit diameter. Fric and Roshko²⁸¹ used smoke from different sources to mark the vortices and to track the fluid within the vortex cores. They found that the wake vorticity comes from the boundary layer on the wall from which the jet issues and not from the jet fluid. The crossflow boundary layer separates on the downstream side of the jet because it cannot negotiate the adverse pressure gradient which is imposed on it by the flow around the jet. They found that its vorticity is incorporated into the wake vortices, which extend from the wall to the bending jet. As a consequence, they

state that the system of vortices in the wake of a JICF is distinctly different in origin and formation from the vortices which are shed from a solid cylinder. Broadwell and Breidenthal²⁸³ note that the JICF appears to mix better than a free jet. The Fric and Roshko²⁸¹ results imply that the wake may not contribute to the enhanced mixing. Their results suggest that it may be possible to efficiently mix fluid in the crossflow boundary layer with the mean crossflow by taking advantage of the wake formation dynamics.

Moussa, Trischka, and Eskinazi¹²⁴ studied the near field in the mixing of a round JICF. They pointed out that the presence or absence of a wall in the plane of the jet exit is crucial to the behaviour of the entire flowfield. That is, the mixing of a uniform stream with a flow from a hole in a wall is different from with the mixing of a uniform stream with flow from a pipe. The wall separates the JICF wake vortex from the jet pipe wake vortex. Trischka²⁷⁹ measured the shedding frequencies to evaluate these effects for the pipe alone case over a range of vertical locations. Four different but overlapping modes were identified for $V_e < 1$: (1) jet mode; (2) pipe mode; (3) lip mode which extends for a few diameters below the nozzle; and (4) base mode near the region where the pipe intersects the tunnel floor. The pipe mode frequencies were higher than that of the other modes. While the Strouhal number for an infinitely long circular cylinder is 0.21, lower values for the pipe mode were measured for the finite length pipe tested, $St = 0.20$ to 0.19 depending on V_e . There was a clearly measurable difference between the jet and pipe mode for $0.067 < V_e < 0.200$.

In an experimental investigation, Krothapalli et al.²³⁷ studied the recirculation region upstream of a rectangular jet with an aspect ratio 10 using flow visualization techniques. The variation of the separation distance of the horseshoe vortex upstream of the jet due to effective velocity ratio change revealed the existence of two different flow regimes. When $V_e > 0.20$, the wake vortex was symmetric and formed a closed region. When $V_e < 0.20$, there was a Karman-Benard vortex street. When the following Strouhal number definition was used

$$St_u = \frac{f B}{V_\infty \sqrt{1 + V_e^{-2}}}$$

and the variation of Strouhal number with effective velocity ratio was $St_u = 0.18 V_e^{1.25}$. The horseshoe vortex was found to form periodically with a frequency comparable to that of the wake vortex shedding behind the jet.

4. JET IN HOVER IN GROUND EFFECT

Before considering the JICF in ground effect, it is helpful to examine the propulsion-induced effects when a jet-lift aircraft is hovering in ground effect. Figure 33 shows schematically how the ambient air is entrained around the lower surface of a vehicle into the jet; it then strikes the ground and flows outward as a wall jet. The

entrainment induces a download on the vehicle. These phenomena have been studied by many investigators²⁸⁵⁻³³³. For many years, the Wyatt³⁰¹ data have been the standard of comparison for single jet in ground effect lift loss. In recent years many investigators^{322,326} have obtained lower values of lift loss. Investigations of these discrepancies have shown consistent differences. Recently Ing and Zhang³²⁶ identified reasons for these differences and accounted for half of the difference between the results of Wyatt and Corsiglia et al.³²².

The flowfield for the multiple-jet case are more complex as shown in figure 33 where the flow characteristics of the single jet are contrasted with the flow of the multiple jet. The primary difference is the fountain of hot gas between the two jets. This upflow between the jets causes large positive pressures on the lower surface of the fuselage. There is also a circulatory flow between the jets and the fountain.

As illustrations of the fountain effect, the results of two investigations of the upflow are presented. The results by Hertel²⁸⁸ are presented in figure 34. The sketch shows the two nozzles exhausting near the ground with an upflow. Starting at the centerline between the jets, the velocity of the upflow was measured with both jets operating; these results are indicated by the circles. There is a gradual dropoff in the upflow velocity as distance from the line of symmetry increases. Then a reflection plane was placed at the plane of symmetry. The velocities were measured and plotted as the triangles. There is a large upflow velocity at the line of symmetry which drops off sharply as distance from the line of symmetry increases. This shows that the use of a vertical reflection plane is not appropriate for measuring or computing the flow due to jet pairs in ground effect. Further, the results show that there is not a true line of symmetry; instead, there is quite a lot of mixing and interaction between the upflows from the two jets.

The reflection plane also has an effect on the inlet temperature rise. Data obtained by Ryan et al.²⁸⁹ with a small-scale hot-gas ingestion model show this effect (figure 35). The two jets, impinging on the ground with a fountain between them, are moved from a height of 2 diameters from the ground to a height of 10 diameters above the ground. When no reflection plane is located between the two jets, the inlet temperature rise is large at a height-diameter ratio of 2. It drops off sharply and approaches zero at a height-diameter ratio above ten diameters. In contrast, with the reflection plane, there is a temperature rise of about 30° F (17° C) close to the ground, which increases steadily as the inlets move away from the ground. When the nozzles are close to the ground, high velocities on the reflection plane carry the gases up above the inlet and disperse them away from the inlet. Consequently, inlets near the ground are not influenced by the hot gases when the reflection plane is in place. As the exits of the jets are moved away from the ground, the inlets gradually move into the region where these hot gases are carried up,

furnishing results in sharp contrast to the data without the reflection plane. Figures 34 and 35 illustrate the importance of the modeling technique used in investigating these problems either experimentally or computationally.

The fountain effect on a hovering aircraft is generally expected to increase the vehicle lift. However, the magnitude is not always as large as that expected. The probable cause for this lift reduction is shown by the data in figure 36. Vortex-like flows are formed between the fountain and each of the adjacent jets. The pressure distributions on a round plate located in the jet exit plane show that, as expected, the impingement of the fountain flow produces high lifting pressures on the center region of the plate between the jets, but the vortex-like flows between the fountain and the jets induce equally strong suction pressures. Thus, both the lifting pressure and the additional suckdown pressures are much greater than the pressures induced on a single-jet configuration. The question of whether there is a net gain or loss in lift depends on which predominates, the fountain pressures or the suction pressures.

5. JET IN A CROSS FLOW IN GROUND EFFECT

There are applications where the JICF is restricted geometrically which are generally called the jet in a crossflow in-ground effect (JIGE). Examples include the combustor problem and the STOVL aircraft near the ground during take-off or landing. In 1985 and 1987 the NASA Ames Research Center sponsored workshops on JICF in ground effect^{285,286}. Recent review articles by Bray and Knowles^{287,329} present detailed discussions of JIGE research. These papers gather together the more relevant results, especially from the U. K., to provide a summary of JIGE research with an emphasis on computational methods. A key factor in the JIGE problem is the location and strength of the ground vortex as illustrated in figure 37. This ground vortex is similar to the horseshoe vortex for the JICF flat plate problem. The ground vortex is formed where the forward flowing wall jet is opposed by the freestream flow and turned back on itself. Flow visualization and dynamic measurements have shown that this flow is very unsteady.

The ground vortex induces suction pressures on the ground (and on the lower surface of an aircraft) as shown on the top of figure 38. An empirical correlation of the location of the ground vortex separation was developed by Stewart and Kuhn²⁹¹ and is shown on the figure as x which coincides with the location where the pressure is zero. Bray and Knowles^{287,329} identify this point as the ground vortex separation point. The minimum pressure location is defined as the ground vortex core position and the maximum pressure location is defined as the ground vortex penetration point. Curves are presented in figure 38 for two values of effective velocity ratio V_e which show the separation location (where the pressure equals zero on the ground) as a function of height. It is seen that the separation

location moves upstream from the jet as V_e decreases. These data were for a fixed ground plane. Bray and Knowles²⁸⁷ showed that a moving ground plane reduced the penetration distance about 23%. Jet temperature effects are accounted for by the use of V_e as the correlation parameter.

The JIGE was studied numerically by van Dalsem²⁹² using the Fortied Navier-Stokes (FNS) scheme²⁹³. An example of the results are shown in figure 39. At least 140,000 grid points were required to resolve the numerous high-gradient regions such as the ground boundary layer, the jet/freestream shear layer, and the ground vortex. This mixing was reasonably modeled with modified algebraic turbulence models. A number of interesting characteristics of the flow were observed through comparison of the computational results and experimental data, and through the variation of the turbulent flow parameters in the calculations. The numerical simulation predicted the characteristic jet footprint observed experimentally and provided additional insight into the deformation of the jet by the freestream. For example, it appears that the forward penetration of the ground vortex is a strong inverse function of the level of mixing in the ground vortex. The results showed that more work will be required to accurately compute more sensitive low effective velocity ratio V_e flows.

6. FUTURE RESEARCH NEEDS

With the end of the Cold War there is a reduced interest in military applications of V/STOL aircraft. Even though there are a few civil STOVL transport research programs, the present civil aircraft market does not appear to be financially ready for a V/STOL airplane. There is considerable uncertainty concerning JICF research directions in the near future. JICF does provide a good model problem for the advancement of experimental methods and CFD applications. In the U.S. there is an interest in military aircraft applications (STOVL strike fighter (SSF) or combat aircraft with vortex control, reaction control, or thrust vectoring) and aircraft engine applications. Perhaps there will be new interest in other military applications, in civil aircraft applications (such as interaction between commercial aircraft wings and thrust reversers, executive STOVL transport or short haul transport), environmental needs (liquid effluent disposal in streams or smoke stack (volcanic) effluent dispersal), or as yet undetermined research needs which could be supported by future JICF research activity.

Coupled panel method/ higher order jet solutions have demonstrated reasonable comparisons with experimental data upstream and beside a JICF. These methods have not demonstrated useful results downstream of the jet without an empirical wake separation model. As a result, they appear to offer no improvement over earlier potential flow aircraft /jet methods. Currently modern CFD methods have been able to compute many of the mean flow characteristics of the JICF. However, existing CFD investigations have shown that the flow

very near the jet exit and on the surface downstream of the jet exit has not been resolved. This is an area of current activity where both improved experimental understanding of the flowfield and recent advances in computer hardware and algorithms have enabled more elaborate numerical solutions. At this time, comparisons with experimental data demonstrate that there is a need for improved solutions. Whether these results show a need for larger grids (more than 300,000 grid points), more appropriate turbulence models both in and near the jet, or other unidentified improvements is not clear and provide the rationale for continued research. In addition, there have only been limited efforts to resolve the unsteady flow features.

There is a need for high quality, extensive experimental JICF data which will be suitable for the verification of current and future CFD results. At this time only limited laser velocimeter measurements have been made. These results demonstrate the ability of this instrument to greatly improve the quality and precision of steady flow field data. Both steady and unsteady measurements are needed. The effects of nozzle shape, co-annular jets with different temperatures, exit louvers, and swirl typical of lift fans on the jet flowfield and on induced lift need to be investigated to support concepts currently being considered for the STOVL strike fighter (SSF). There is also a need for experimental investigation of the effect of temperatures as high as those developed by modern high pressure ratio turbojet engines.

CFD investigation results showed that more work will be required to accurately compute the JIGE for more sensitive low effective velocity ratio V_e flows. There is a need to experimentally quantify the unsteady character of the JIGE. In the case of two jets in ground effect, experimental results show that there is not a true line of symmetry in the up-flow region; instead, there is quite a lot of mixing and unsteady interaction between the upflows from the two jets. These results illustrate the importance of the modeling technique used in investigating these problems either experimentally or computationally.

7. CONCLUSIONS

The JICF consists of a jet exhausting at a large angle into an unconstrained freestream flow. Variations of the JICF include the jet in a crossflow in-ground effect (JIGE) and cases where there is no freestream velocity: hover out-of-ground effect (HOGE) and hover in-ground effect (HIGE). Applications include plume dispersion, gas turbine combustor cooling, fuel injection, turbofan thrust reversers, turbojet thrust vectoring, reaction control for missiles and aircraft, and, most frequently, the many variants associated with vertical and/or short takeoff/landing (V/STOL) aircraft in transition flight both in- and out-of-ground effect.

This paper described the progress of JICF research and identified the contributions achieved since a chimney plume study in 1932 and an analysis in 1942. The present paper emphasizes the evolution of the

understanding of the flowfield physics in the context of both experimental and computational investigations. Over 300 references are cited to identify only part of the extensive research conducted over the last sixty years.

A large body of qualitative experimental data provides a fairly complete description of the jet in a crossflow. Detailed mean flow pressure and velocity experiments have provided sufficient data for development of several potential flow computations which provide useful preliminary design methods for V/STOL aircraft.

Recent computational fluid dynamics computational efforts were reviewed and their results seem to provide improvements in the estimation of flow field features when compared with earlier potential flow based methods. However, these computational investigations have shown that the flow near the jet exit and on the surface downstream of the jet exit has not been resolved numerically. Whether these results show a need for larger grids (more than 300,000 grid points), more appropriate turbulence models both in and near the jet, or other improvements is not clear. This is an area of current activity where recent advances in computer hardware and algorithms have enabled more elaborate numerical solutions. At this time, comparisons with experimental data demonstrate that there is a need for both higher fidelity steady and unsteady experimental data and improved numerical solutions.

ACKNOWLEDGMENTS: This literature survey has been assisted by the technical library and by other researchers at the NASA Ames Research Center. In the late 1960's, the author started a ten year JICF research collaboration with Dr. Richard L. Fearn and his many students. He graciously made his JICF reference library available for the present paper. It has been an invaluable resource.

REFERENCES

1. Werle, H., "Flows with Large Velocity Fluctuations," motion picture film no. 575, ONERA, Chatillon, France, 1968.
2. Tollmien, W., "Berechnung Turbulenter Ausbreitungsvorgange (Calculation of Turbulent Expansion Processes)," *Zeitschrift für angewandte Mathematik und Mechanik*, vol. 6, 1926, pp. 468-478. (Also available in English as NACA TM No. 1085, 1945.)
3. Keuthe, A.M., "Investigation of the Turbulent Mixing Regions Formed by Jets," *J. Appl. Mech.*, Sept. 1935, pp. A-87 to A-95.
4. Liepman, H.W. and Laufer, J., "Investigations of Free Turbulent Mixing," NACA TN 1257, 1947.
5. Albertson, M.L., Dal, Y.B., Jensen, R.A., and Rouse, H., "Diffusion of Submerged Jets," paper

- no. 2409, *ASCE Transactions*, vol. 115, 1950, pp. 639-697.
6. Taylor, G.I., "Flow Induced by Jets," *J. of the Aeronautical Sciences*, vol. 25, pg. 464, 1958.
7. Ricou, F.P. and Spaulding, D.B., "Measurements of Entrainment by Axisymmetrical Turbulent Jets," *J. Fluid Mech.*, vol. II, pt. 1, Aug. 1961, pp. 21-32.
8. Bradbury, L.J.S., "Simple Expressions for the Spread of Turbulent Jets," *The Aeronautical Quarterly*, May 1967, pp. 133-142.
9. Viets, H., "Turbulent Jet Calculations," USAF-ARL Report 73-0058, Apr. 1973.
10. Catalano, G.D.; Morton, J.B.; and Humphris, R.R.: "Experimental Investigation of an Axisymmetric Jet in a Coflowing Airstream," *AIAA J.*, vol. 14, no. 9, Sept. 1976, pp. 1157-1158.
11. Wagnanski, I., "The Flow Induced by Two-Dimensional and Axisymmetric Turbulent Jets Issuing Normally from an Infinite Plane Surface," *The Aeronautical Quarterly*, Nov. 1964, pp. 373-380.
12. Gentry, G.L. and Margason, R.J., "Jet-Induced Lift Losses on VTOL Configurations Hovering In and Out of Ground Effect," NASA TN D-3166, Feb. 1966.
13. Smy, J. R. and Ransom, E. C. P., "The Structure of Single Jets at Large Angles to a Cross-Flow," Hawker-Siddeley Aviation LTD, HSA-KAD-R-GEN-2288, June 1976.
14. Sutton, O. G., "A Theory of Eddy Diffusion in the Atmosphere," *Proc. Roy. Soc. A*, vol. 135, Mar. 1932, pg. 143.
15. Bosanquet, C. and Pearson, J. L., "The Spread of Smoke and Gases From Chimneys," *Trans. Faraday Soc.*, vol. 32, Dec. 1936, pg. 1249.
16. Ivanov, Yuri V.: "Effective Combustion of Overfire Fuel Gases in Furnaces," The Estonian State Publishing House, Tallin, Estonia, July 1959 (available in English as NASA CN-127612, 1971).
17. Kuchemann, D. and Weber, J., "Aerodynamics of Propulsion," chap. 10, pg. 239, McGraw-Hill, 1953.
18. Callaghan, E. E. and Ruggeri, R. S., "Investigation of the Penetration of an Air Jet Directed Perpendicularly to an Air Stream," NACA TN 1615, June 1948.
19. Callaghan, E. E. and Bowden, D. T., "Investigation of Flow Coefficient of Circular, Square, and Elliptical Orifices at High Pressure Ratios," NACA TN 1947, Sept. 1949.
20. Ruggeri, R. S., Callaghan, E. E., and Bowden, D. T., "Penetration of Air Jets Issuing from Circular, Square and Elliptical Orifices Directly Perpendicularly to an Air Stream," NACA TN 2019, Feb. 1950.
21. Callaghan, E. E. and Ruggeri, R. S., "A General Correlation of Temperature Profiles of a Heated Air Jet Directed Perpendicularly to an Air Stream," NACA TN 2466, Sept. 1951.
22. Ruggeri, R. S., "General Correlation of Temperature Profiles of a Heated Air Jet Directed at Various Angles to an Air Stream," NACA TN 2855, Dec. 1952.
23. Williams, J. and Wood, M. N., "Aerodynamic Interference Effects with Jet Lift Schemes on VSTOL Aircraft at Forward Speeds," AGARDograph 103, Aerodynamics of Power Plant Installation, part 2, Oct. 1965, pp. 625-651 (also RAE Tech. Report No. 66403, 1966).
24. Lee, C.C., "A Review of Research on the Interaction of a Jet With an External Stream," Tech. Note R-184, Res. Lab., Brown Eng. Co., Inc., Mar. 1966 (available from DDC as AD 630 294).
25. Garner, J. E., "A Review of Jet Efflux Studies Applicable to V/STOL Aircraft," USAF AEDC-TR-67-163, Sept. 1967 (avail. from DDC as AD 658 432).
26. Margason, R. J., "Review of Propulsion-Induced Effects on Aerodynamics of Jet V/STOL Aircraft," NASA TN D-5617, Feb. 1970.
27. Jordinson, R., "Flow in a Jet Directed Normal to the Wind," R. & M. No. 3074, British A.R.C., Oct. 1956.
28. Abramovich, G. N., "The Theory of Turbulent Jets," ed. L. Schindel, MIT Press, Cambridge, Mass., 1963.
29. Shandorov, G. S., "The Efflux From a Canal into Stationary and Moving Media," *J. Technical Physics*, vol. 27, no. 1, 1957.
30. Shandorov, G. S., "Calculation of a Jet Axis in a Drifting Flow," *Soviet Aeronautics*, vol. 9, no. 2, 1959 (see also NASA TT F-10,638, 1966).
31. Storms, K. R., "Low-Speed Wind Tunnel Investigation of a Jet Directed Normal to the Wind," Rep. 885, Aeronaut. Lab., Univ. of Washington, Nov. 1965.

32. Hardy, W. G. S., "Non-Parallel Flow Interactions," M.A.E. Thesis, Univ. of Virginia, 1967.
33. Keffer, J. F. and Baines, W. D., "The Round Turbulent Jet in a Cross Wind," *J. Fluid Mech.*, vol. 15, Pt. 4, 1963, pp. 481-496.
34. Margason, R. J., "The Path of a Jet Directed at Large Angles to a Subsonic Free Stream," NASA TN D-4919, 1968.
35. Vakhlamov, S. V., "Computation of the Trajectory of a Jet in a Drifting Flow," *Inzhenerno-Fizicheskiy Zhurnal*, vol. 7, no. 10, 1964, pp. 112-116.
36. Vizel, Y. M. and Mostinskii, I. L., "Deflection of a Jet Injected into a Stream," *Inzhenerno-Fizicheskiy Zhurnal*, vol. 8, no. 2, 1965, pp. 238-242.
37. Patrick, M. A., "Experimental Investigations of the Mixing and Penetration of a Round Turbulent Jet Injected Perpendicularly into a Transverse Stream," *Trans. Institute of Chemical Engineers*, vol. 45, 1967.
38. Schetz, J. A. and Billig, F. S., "Penetration of Gaseous Jets Injected Into a Supersonic Stream," *J. of Spacecraft and Rockets*, vol. 11, 1961, pp. 21-32.
39. Wooler, P. T., "Flow of a Circular Jet into a Cross Flow," *J. Aircraft*, May-June 1969, pp. 283-284.
40. Wooler, P. T., "On the Flow Past a Circular Jet Exhausting at Right Angles from a Flat Plate or Wing," *J. R.Ae. S.* vol. 71, no. 3, Mar. 1967, pp. 216-218.
41. Chassaing, P., George, J., Claria, A. and Sananes, F., "Physical Characteristics of Subsonic Jets in a Cross-Stream," *J. Fluid Mech.*, vol. 62, part 1, pp. 41-64, 1974.
42. Slawson, P. R. and Csanady, G. T., "On the Mean Path of Buoyant, Bent-Over Chimney Plumes," *J. Fluid Mech.*, vol. 28, part 2, 1967, pp. 311-322.
43. Gelb, G. H. and Martin, W. A., "An Experimental Investigation of the Flow Field About a Subsonic Jet Exhausting Into a Quiescent and a Low Velocity Air Stream," *Can. Aeronaut. & Space J.*, vol. 12, no. 8, Oct. 1966, pp. 333-342.
44. Crowe, C. T. and Riesebleter, H., "An Analytic and Experimental Study of Jet Deflection in a Cross-Flow," *Fluid Dynamics of Rotor and Fan Supported Aircraft at Subsonic Speeds*, AGARD CP-69, 1967, paper 16.
45. Gordier, R. L., "Studies on Fluid Jets Discharging Normally into Moving Liquid," St. Anthony Falls Hyd. Lab., Tech. Paper No. 28, Series B, Aug. 1959.
46. Pratte, B. D. and Baines, W. D., "Profiles of the Round Turbulent Jet in a Cross Flow," *J. Hydraulics Div., Amer. Soc. Civil Eng.*, vol. 92, no. HY6, Nov. 1967, pp. 53-64.
47. Platten, J. L. and Keffer, J. F., "Entrainment in Deflected Axisymmetric Jets at Various Angles to the Stream," University of Toronto, Mech. Eng. TP 6808, June 1968.
48. Anon., "Symposium on Analysis of a Jet in a Subsonic Crosswind," NASA SP-218, Sept. 1969.
49. Margason, R. J. and Fearn, R. L., "Jet-Wake Characteristics and Their Induced Aerodynamic Effects on V/STOL Aircraft in Transition Flight," NASA SP-218, Sept. 1969, pp. 1-18.
50. Keffer, J. F., "The Physical Nature of the Subsonic Jet in a Cross-Stream," NASA SP-218, Sept. 1969, pp. 19-36.
51. Hackett, J. E. and Miller, H. R., "The Aerodynamics of the Lifting Jet in a Cross Flowing Stream," NASA SP-218, Sept. 1969, pp. 37-48.
52. McMahon, H. M. and Mosher, D. K., "Experimental Investigation of Pressures Induced on a Flat Plate by a Jet Issuing into a Subsonic Crosswind," NASA SP-218, Sept. 1969, pp. 49-62.
53. Street, T. A. and Spring, D. J., "Experimental Reaction Jet Effects at Subsonic Speeds," NASA SP-218, Sept. 1969, pp. 63-84.
54. Wu, J. C. and Wright, M. A., "A Blockage-Sink Representation of Jet Interference Effects for Noncircular Jet Orifices," NASA SP-218, Sept. 1969, pp. 85-100.
55. Wooler, P. T., "Development of an Analytical Model for the Flow of a Jet into a Subsonic Crosswind," NASA SP-218, Sept. 1969, pp. 101-119.
56. Skifstad, J. G., "Numerical Treatment of Line Singularities for Modelling a Jet in a Low-Speed Cross Flow," NASA SP-218, Sept. 1969, pp. 119-130.
57. Margason, R. J., "Analytic Description of Jet-Wake Cross Sections for a Jet Normal to a Subsonic Free Stream," NASA SP-218, Sept. 1969, pp. 131-140.

58. Braun, G W. and McAllister, J. D., "Cross Wind Effects on Trajectory and Cross Sections of Turbulent Jets," NASA SP-218, Sept. 1969, pp. 141-164.
59. Heltsley, F. L. and Kroeger, R. A., "A General Jet Efflux Simulation Model," NASA SP-218, Sept. 1969, pp. 165-180.
60. Rubbert, P. E., "Calculation of Jet Interference Effects on V/STOL Aircraft by a Nonplanar Potential Flow Method," NASA SP-218, Sept. 1969, pp. 181-204.
61. Rosen, R., Durando, N. A., and Cassel, L. A., "Inviscid Models for the Pressure Induced by a Jet Transverse to a Subsonic Stream," NASA SP-218, 1969, pp. 205-230.
62. Werner, J. E., "The Use of Matched Asymptotic Expansions as an Approach to the Problem of the Jet in a Crossflow," NASA SP-218, Sept. 1969, pp. 231-238.
63. Fearn, R. L., "Mass Entrainment of a Circular Jet in a Cross Flow," NASA SP-218, Sept. 1969, pp. 239-248.
64. Wu, J. C., McMahon, H. M., Mosher, D.K. and Wright, M. A., "Experimental and Analytical Investigations of Jets Exhausting into a Deflecting Stream," *J. Aircraft*, vol. 7, no. 1, Jan.-Feb. 1970, pp.44-50.
65. Mikolowsky, W. T., "An Experimental Investigation of a Jet Issuing in Crossflow," Ph.D. Thesis, Georgia Institute of Technology, Atlanta, GA, May 1972.
66. Mosher, D. K., "An Experimental Investigation of a Turbulent Jet in a Cross Flow," Ph.D. Thesis, Georgia Institute of Technology, Atlanta, GA, GITAER 70-7, Dec. 1970.
67. Vogler, R. D., "Surface Pressure Distributions Induced on a Flat-Plate by a Cold Air Jet Issuing Perpendicularly From the Plate and Normal to a Low-Speed Free-Stream Flow," NASA TN D-1629, Mar. 1963.
68. Vogler, R. D., "Interference Effects of Single and Multiple Round or Slotted Jets on a VTOL Model in Transition," NASA TN D-2380, July 1964.
69. Bradbury, L. J. S. and Wood, M. N., "The Static Pressure Distribution Around a Circular Jet Exhausting Normally From a Plane Wall Into an Airstream," C.P. No. 822, British A.R.C., 1965 (also available as R.A.E. TN no. Aero. 2978, Aug. 1964.).
70. Soullier, A., "Testing at S1.MA for Basic Investigations on Jet Interactions; Distributions of Pressures Around the Jet Orifice," ONERA Document No. 1/253 GY - Part 1/5, April 1968 (Available in English as NASA TT F-14066, 1972).
71. Soullier, A., "Testing at S1.MA for Basic Investigations on Jet Interactions; Distributions of Pressures and Velocities in the Jet Using the Ideal Standard Nozzle (in Unheated State)," ONERA Document No. 1/253 GY - Part 2/5, May 1968 (Available in English as NASA TT F-14072, 1972).
72. Otis, J. H., "Induced Interference Effects on a Four-Jet VTOL Configuration with Various Wing Planforms in the Transition Speed Range," NASA TN D-1400, Sept. 1962.
73. Spreeman, K. P., "Investigation of Interference of a Deflected Jet with Free Stream and Ground on Aerodynamic Characteristics of a Semispan Delta-Wing VTOL Model," NASA TN D-915, Aug. 1961.
74. Margason, R. J., "Jet-Induced Effects in Transition Flight," NASA SP-116, Apr. 1966, pp. 163-176
75. Hickey, D. H. and Ellis, D. R., "Wind Tunnel Tests of a Semispan Wing with a Fan Rotating in the Z Plane of the Wing," NASA TN D-88, Oct. 1959.
76. Hickey, D. H. and Hall, L. P., "Aerodynamic Characteristics of a Large-Scale Model with Two High Disc-Loading Fans Mounted in the Wing," NASA TN D-1650, Feb. 1963
77. Trebble, W. J. G. and Williams, J., "Exploratory Wind-Tunnel Investigations on a Bluff Body Containing a Lifting Fan," Brit. R. A. E. CP No. 597, Apr. 1961.
78. Peake, D. J., "The Pressures on a Surface Surrounding a Jet Issuing Normal to a Mainstream," Nat. Res. Council of Canada Aero. Report LR-410, Nov. 1964.
79. Wooler, P.T., Burghart, G. H., and Gallagher, J. T., "The Pressure Distribution on a Rectangular Wing with a Jet Exhausting Normally into an Airstream," *J. Aircraft*, vol. 4, no. 6, Nov.-Dec. 1967, pp. 537-543.
80. Fricke, L. B.; Wooler, P. T.; and Ziegler, H., "A Wind Tunnel Investigation of Jets Exhausting into a Crossflow," USAF Tech. Rep. AFFDL-TR-70-154, vol. I-IV, Dec. 1970.
81. Margason, R. J. and Gentry, G. L., "Aerodynamic Characteristics of a Five-Jet VTOL Configuration in the Transition Speed Range," NASA TN D-4812, Oct. 1968.

82. Carter, A. W., "Effects of Jet-Exhaust Location on the Longitudinal Aerodynamic Characteristics of a Jet V/STOL Model," NASA TN D-5333, July 1969.
83. Davenport, E. E. and Kuhn, R. E., "Wind-Tunnel-Wall Effects and Scale Effects on a VTOL Configuration with a Fan Mounted in the Fuselage," NASA TN D-2560, Jan. 1965.
84. Rolls, L. S., Drinkwater, F. J. III, and Innis, R. C., "Effects of Lateral Control Characteristics on Hovering a Jet Lift VTOL Aircraft," NASA TN D-2701, Mar. 1965.
85. Hall, L. P., Hickey, D. H., and Kirk, J. V., "Aerodynamic Characteristics of a Large-Scale V/STOL Transport Model with Lift and Lift-Cruise Fans," NASA TN D-4092, Aug. 1967.
86. Rolls, L. S. and Gerdes, R. M., "Flight Evaluation of Tip-Turbine-Driven Fans for Lateral Control in a Hovering VTOL Aircraft," NASA TN D-5491, Oct. 1969.
87. Winston, M. M., "Induced Interference Effects on the Aerodynamics Characteristics of a 0.16-Scale Six-Jet V/STOL Model in Transition," NASA TN D-5727, Mar. 1970.
88. Newsom, W. A. Jr. and Moore, F. L., "Wind-Tunnel Investigation of a V/STOL Transport Model with Six Wing-Mounted Lift Fans," NASA TN D-5695, Mar. 1970.
89. Spreeman, K. P., "Free-Stream Interference Effects on Effectiveness of Control Jets Near the Wing Tip of a VTOL Aircraft," NASA TN D-4084, Aug. 1967.
90. Rosenhead, L., "The Formation of Vortices From a Surface of Discontinuity," in *Proceedings of Royal Society of London, Series A*, Vol 134, 1932.
91. Westwater, F. L., "Rolling Up of the Surface of Discontinuity Behind an Aerofoil of Finite Span," British ARC R and M No. 1692, August 1935.
92. Chang, H.-C., "Aufrollung Eines Zylindrischen Strahles Durch Querwind," Doctorial Dissertation, Univ. of Gottingen, 1942. Also available in English as "The Roll-up of a Cylindrical Jet in a Cross Flow," translated and edited by Nagaraja, K.S. and Schrade, Herbert O., USAF-ARL 73-0131, Sept. 1973.
93. Margason, R. J., "Analysis of the Flow Field of a Jet in a Subsonic Crosswind," in *Analytic Methods in Aircraft Aerodynamics*, NASA SP-228, 1969, pp. 683-702.
94. Harms, L., "Experimental Investigation of the Flow Field of a Hot Turbulent Jet with Lateral Flow," DFVLR Report 1-B 157-73 A 18 (part I) and A 21 (part II), Sept 1973 (available in English as NASA TT F-15707 (part I) and NASA TT F-15,706 (part II), June 1974).
95. Fearn, R. L. and Weston, R. P., "Vorticity Associated with a Jet in a Cross Flow," *AIAA J.*, vol. 12, no. 12, Dec. 1974, pp. 1666-1671.
96. Fearn, R. L. and Weston, R. P., "Induced Pressure Distribution of a Jet in a Crossflow," NASA TN D-7916, July 1975.
97. Fearn, R.L. and Weston, R.P., "Induced Velocity Field of a Jet in a Crossflow," NASA TP-1087, May 1978.
98. Krausche, D., Fearn, R. L., and Weston, R. P., "Round Jet in a Crossflow: Influence of Jet Injection Angle on Vortex Properties," *AIAA J.*, vol. 16, no. 6, June 1978, pp. 636-637.
99. Fearn, R. L. and Weston, R. P., "Velocity Field of a Round Jet in a Crossflow for Various Jet Injection Angles and Velocity Ratios," NASA TP-1506, 1979.
100. Fearn, R. L., Kalota, C., and Dietz, W. E., "A Jet/Aerodynamic-Surface Interference Model," *Proceedings of NADC Workshop on V/STOL Aircraft Aerodynamics*, vol. 1, 1979, pp. 41-63.
101. Fearn, R. L. and Benson, J. P., "Velocity-Field Near the Jet Orifice of a Round Jet in a Crossflow," NASA CR-152,293, Dec. 1979.
102. Thompson, A. M., "The Flow Induced by Jets Exhausting Normally From a Plane Wall Into an Airsteam," Ph. D. Thesis, Univ. of London, 1971.
103. Ivanov, Y. V., "Shape of the Centerline of an Axisymmetric Fan Type Jet in a Cross Flow," *Izv. VUZ. Aviatsionnaya Teknika*, no. 4, Apr. 1963.
104. Kuhlman, J. M., Ousterhout, D. S., and Warcup, R. W., "Experimental Investigation of Effects of Jet Decay Rate on Jet-Induced Pressures on a Flat Plate: Tabulated Data," NASA CR-158,990, Nov. 1978.
105. Kuhlman, J. M. and Warcup, R. W., "Experimental Investigation of Jet-Induced Loads on a Flat Plate in Hover Out-of-Ground Effect," NASA CR-159,004, Feb. 1979.
106. Kuhlman, J. M. and Warcup, R. W., "Jet Decay Rate Effects on Hover Jet-Induced Loads," *J. Aircraft*, vol. 17, no. 8, Aug. 1980, pp. 605-607.
107. Kuhlman, J. M., Ousterhout, D. S., and Warcup, R. W., "Experimental Investigation of Effect of

- Jet Decay Rate on Jet-Induced Pressures on a Flat Plate," NASA CR-2979, 1978.
108. Kamotani, Y. and Greber, I., "Experiments on a Turbulent Jet in a Cross Flow," *AIAA J.*, vol. 10, no. 11, Nov. 1972, pp. 1425-1429.
 109. Kamotani, Y. and Greber, I., "Experiments on a Turbulent Jet in a Cross Flow," NASA CR-72893, June 1971.
 110. Kamotani, Y. and Greber, I., "Experiments on Confined Turbulent Jets in a Cross Flow," NASA CR-2392, Mar. 1974 (see also AIAA Paper No. 73-647, July, 1973).
 111. Anon., "Conference on V/STOL Aerodynamics," AGARD CP-143, Apr. 1974.
 112. Anon., "Conference on Jet V/STOL Propulsion Aerodynamics," vol. I and II, sponsored by Naval Air Systems Command Research & Technology Group, July 1975 (avail. from DCC as AD-A024-023).
 113. Anon., "Conference on Powered-Lift Aerodynamics and Acoustics," NASA SP-406, May 1976.
 114. Anon., "AIAA/NASA Ames V/STOL Conference," AIAA papers 77-565 through 77-618, June 1977.
 115. Anon., "Conference on V/STOL Aircraft Aerodynamics," vol. I and II, sponsored by Naval Air Development Center, May 1979.
 116. Anon., "Conference on Fluid Dynamics of Jets with Applications to V/STOL," AGARD CP-308, Nov. 1981.
 117. Ousterhout, D. S., "An Experimental Investigation of a Cold Jet Emitting from a Body of Revolution into a Subsonic Free Stream," NASA CR-2089, Aug. 1972.
 118. Fan, L. N., "Turbulent Buoyant Jets into Stratified or Flowing Ambient Fluids," Technical Report No. KH-R-15, W. M. Keck Laboratory of Hydraulics and Water Resources, California Institute of Technology, Pasadena, CA, June, 1967.
 119. Abraham, G., "The Flow of Round Jets Issuing Vertically into Ambient Fluid in a Horizontal Direction," Proceedings of the 5th International Water Pollution Research Conference, San Francisco, CA, July-Aug., 1970, pp. III 15/1. III 15/7 (also Delft Hydraulics Lab. Publication No. 81, 1971).
 120. Anderson, J. L., Parker, F. L., and Benedict, B. A., "Negatively Buoyant Jets in a Cross Flow," Report EPA-660/2-73-012, Oct. 1973.
 121. Motz, L. H. and Benedict, B. A., "Heated Surface Jet Discharged into a Flowing Ambient Stream," Report No. 4, National Center for Research and Training in the Hydrologic and Hydraulic Aspects of Water Pollution Control, Vanderbilt Univ., Aug. 1970.
 122. Bosanquet, C. H., Horn, G., and Thring, M. W., "The Effects of Density Differences on the Path of Jets," *J. Fluid Mech.*, vol. 5, Part I, Jan. 1959, pp. 340-352.
 123. Hewett, T. A., Fay, J. A., and Hoult, D. P., "Laboratory Experiments on Smokestack Plumes in a Stable Atmosphere," *Atmospheric Environment*, vol. 5, Pergamon Press, New York, N. Y., 1975, pp. 767-789.
 124. Moussa, Z. M., Trischka, J. W., and Eskinazi, S., "The Near Field in the Mixing of a Round Jet With a Cross-Stream," *J. Fluid Mech.*, vol. 80, part 1, 1977, pp. 49-80.
 125. Eskinazi, S., "Fluid Mechanics and Thermodynamics of Our Environment," chap. 10, section 2, Academic Press, 1975, pp. 304-333.
 126. Bojic, M. L. and Eskinazi, S., "Two-Dimensional Mathematical Model of a Nonbuoyant Jet in a Crossflow," *AIAA J.*, vol. 17, no. 10, Oct. 1979, pp. 1050-1054.
 127. Wu, J., "Near-Field Trajectory of Turbulent Jets Discharged at Various Inclinations into a Uniform Crossflow," *AIAA J.*, vol. 11, no. 11, Nov. 1973, pp. 1579-1581.
 128. Belov, I. V., "A Circular Turbulent Jet in an Unlimited Transverse Flow," *Izvest. VUZ*, Aug. 1975, pp. 130-134 (avail. in English from U.K. National Lending Library for Science and Technology, NIL-M-25268-(5828.4F)).
 129. Holdeman, J. D. and Foss, J. F., "The Initiation, Development, and Decay of the Secondary Flow in a Bounded Jet," *J. Fluids Engng.*, Sept. 1975, pp. 342-352.
 130. Holdeman, J. D. and Walker, R. E., "Mixing of a Row of Jets with a Confined Crossflow," *AIAA J.*, vol. 15, no. 2, Feb. 1977, pp. 243-249.
 131. Schmitt, H., "Deflection of a Round Turbulent Jet in a Cross-Wind," *Archives of Mechanics*, vol. 26, no. 5, Warsaw, Poland, May, 1974.
 132. Schmitt, H., "Deflection of an Oblique, Two-Dimensional, Turbulent Free Jet in a Crosswind," *ZAMM Mechanics of Fluid*, vol. 56, 1976, pp. 227-229.

133. Snel, H., "A Model for the Calculation of the Properties of a Jet in a Cross Flow," NLR TR 74080 U, June 1974.
134. Sucec, J. and Bowley, W. W., "Prediction of the Trajectory of a Turbulent Jet Injected into a Crossflowing Stream," ASME Paper no. 76-FE-8, Mar. 1976.
135. Makihata, T. and Miyai, Y., "Trajectories of Single and Double Jets Injected Into a Crossflow of Arbitrary Velocity Distribution," *J. Fluids Engng.*, vol. 101, June 1979, pp. 217-223.
136. Kashafutdinov, S. T., "Influence of a Transverse Stream on the Exhaust From an Axisymmetric Nozzle," *Izv. Sib. Otd. Akad. Nauk SSSR*, no. 13, Ser. Tekh. Nauk, no. 3, 1974.
137. Crabb, D., Durao, D. F. G., and Whitelaw, J. H., "A Round Jet Normal to a Cross-Flow," ASME paper no. 80-WA/FE-10, July 1980.
138. Sugiyama, Y. and Usami, Y., "Experiments on the Flow In and Around Jets Directed Normal to a Cross Flow," *Bull. JSME*, vol. 22, no. 174, Dec. 1979, pp. 1736-1745.
139. Weston, R. P. and Thames, F. C., "Properties of Aspect-Ratio-4.0 Rectangular Jets in a Subsonic Crossflow," *J. Aircraft*, vol. 16, no. 10, Oct. 1979, pp. 701-707.
140. Antani, D. L., "An Experimental Investigation of the Vortices and the Wake Associated with a Jet in Crossflow," Ph. D. Thesis, Georgia Institute of Technology, Atlanta, GA, Aug. 1977.
141. McMahon, H. M. and Antani, D. L., "An Experimental Study of a Jet Issuing From a Lifting Wing," *J. Aircraft*, vol. 16, no. 4, Apr. 1979, pp. 275-281.
142. Taylor, P., "An Investigation of a Jet Exhausting From a Plate at incidence into a Crosswind," *Vertica*, vol. 1, 1977, pp. 307-315.
143. Taylor, P. and Watkins, D. J., "An Investigation of Inclined Jets in a Crosswind," AGARD-CP-308, Nov. 1981, paper no. 6.
144. Nunn, R. H., "Vorticity Growth and Decay in the Jet in Cross Flow," *AIAA J.*, vol. 23, no. 3, March 1985, pp. 473-475.
145. English, J. W., "The Design and Performance of Lateral Thrust Units for Ships," *Proc. RINA, Quarterly Trans.*, vol. 105, July 1963, pp. 251-276.
146. Taniguchi, K., Watanbee, K., and Kasoi, H., "Investigations into Fundamental Characteristics and Operating Performances of Side Thrusters," Nagasaki Technical Institute, Japan, MTB 010035, May 1966.
147. Norrby, R., "The Effectiveness of a Bow Thruster at Low and Medium Ship Speeds," *Shipbuilding*, vol. 14, no. 156, Aug. 1967, pp. 315-318.
148. Shaw, C. S.; and Margason, R. J., "An Experimental Investigation of a Highly Underexpanded Sonic Jet Ejecting from a Flat Plate into a Subsonic Crossflow," NASA TN D-7314, Dec. 1973.
149. Cassel, L. A., Durando, N. A., Bullard, C. W., and Kelso, J. M., "Jet Interaction Control Effectiveness for Subsonic and Supersonic Flight," U.S. Army Missile Command Report No. RD-TR-69-21, Sept. 1969.
150. Zhang, X. and Hurst, D. W., "Surface Flow on a Flat Plate Induced by a Supersonic Jet Exhausting Normally into a Low Speed Crossflow," AIAA Paper No. 90-3011-CP, June 1990.
151. Allegre, J., Raffin, M., and Caressa, J. P., "Experimental Investigation of Transverse Jet Effects Related to Hypersonic Space Vehicles," *Aerothermodynamics for Space Vehicles*, ESA SP-318, May 1991.
152. Ting, L. and Ruger, C. J., "Oblique Injection of a Jet into a Stream," *AIAA J.*, vol. 3, no. 3, Mar. 1965, pp. 534-536.
153. Monical, R. E., "A Method for Representing Fan-in-Wing Combinations for Three Dimensional Potential Flow Solutions," *J. Aircraft*, vol. 2, no. 6, Nov.-Dec. 1965, Dec. 1965.
154. Werner, J. E. and Chang, H. S., "Analytical Determination of the Induced Flow Due to a Jet in a Subsonic Crossflow," NYU-AA-70-21, Sept. 1970.
155. Werner, J. E. and Chang, H. S., "Analysis of an Entrainment Model of the Jet in a Crossflow," NASA CR-132,324, Mar. 1972.
156. Thompson, J. F., Jr., "Two Approaches to the Three-Dimensional Jet-in-Cross Wind Problem: A Vortex Lattice Model and a Numerical Solution of the Navier-Stokes Equations," Ph.D Thesis, Georgia Institute of Technology, June 1971.
157. Russell, H. L. and Skifstad, J. G., "Application of the Scalar and Vector Potentials to the Aerodynamics of Jets," NASA CR-132,528, Aug. 1973.

158. LeGrives, E. and Benoit, A., "A New Theoretical Model for Representing Jet Penetration into a Subsonic Stream," ONERA TP No. 1116, Jan 1972 (from *La Recherche Aerospaciale*, no.3, May-June 1972, pp. 133-142).
159. Endo, H. and Nakamura, M., "Bending and Development of Three-Dimensional Turbulent Jets in a Crosswind," National Aerospace Lab. TR-216, Nov. 1970 (avail in English as FTD-HC-23-1486-71 (AD-751 093), Aug. 1972).
160. Endo, H., "A Working Hypothesis for Predicting the Path and Induced Velocity of a Jet Exhausting at a Large Angle into a Uniform Cross-Flow," *Trans. Japan Soc. Space Sci.*, vol. 17, no. 36, 1974, pp. 45-64.
161. Chan, D. T.-L., Lin, J.-T., and Kennedy, J.F., "Entrainment and Drag Forces of Deflected Jets," *J. Hydraulics Div., Proceedings ASCE*, vol. 102, no. HY5, May 1976, pp. 615-635.
162. Stoy, R. L. and Ben-Haim, Y., "Turbulent Jets in a Confined Crossflow," *Trans. ASME J. Fluids Engr.*, Dec. 1973, pp. 551-584.
163. Heltsley, F. L. and Parker, R. L., Jr., "Application of the Vortex Lattice Method to Represent a Jet Exhausting from a Flat Plate into a Crossflowing Stream," AEDC-TR-73-57, June 1973.
164. Wooler, P. T., Kao, H. C., Schwendemann, M. F., Wasson, H. R., and Ziegler, H., "V/STOL Aircraft Aerodynamic Prediction Methods Investigation," US AFFDL-TR-72-26, vol. I-IV, Jan. 1972
165. Ziegler, H. and Wooler, P. T., "Multiple Jets Exhausting into a Cross Flow," *J. Aircraft*, vol. 8, no. 6, July 1971.
166. Ziegler, H. and Wooler, P. T., "Analysis of Stratified and Closely Spaced Jets Exhausting into a Crossflow," NASA CR-132297, 1973.
167. Mineck, R. E. and Schwendemann, M. F., "Aerodynamic Characteristics of a Vectored-Thrust V/STOL Fighter in the Transition-Speed Range," NASA TN D-7191, 1973.
168. Mineck, R. E. and Margason, R. J., "Pressure Distribution on a Vectored-Thrust V/STOL Fighter in the Transition-Speed Range," NASA TM X-2867, Mar. 1974.
169. Margason, R. J., Kjelgaard, S. O., Sellers, W. L. III, Morris, C. E. K. Jr., Walkey, K. B., and Shields, E. W., "Subsonic Panel Methods - A Comparison of Several Production Codes," AIAA Paper No. 85-0280, Jan. 1985
170. Margason, R. J. and Lamar, J. E., "Vortex-Lattice FORTRAN Program for Estimating Subsonic Aerodynamic Characteristics of Complex Planforms," NASA TN D-6142, Feb. 1971.
171. Wooler, P. T., "Propulsion-Induced Effects on a Supersonic V/STOL Fighter/Attack Aircraft," Proceedings NADC V/STOL Aircraft Aerodynamics, May 1979, pp. 173-190.
172. Mineck, R. E., "Comparison of Theoretical and Experimental Interference Effects on a Jet VTOL Airplane Model," Proceedings Prediction Methods for Jet V/STOL Propulsion Aerodynamics, July 1975 (avail. from DCC as AD-A024-023), pp. 1016-1034.
173. Adler, D. and Baron, A., "Prediction of a Three-Dimensional Circular Turbulent Jet in Crossflow," *AIAA J.*, vol. 17, no. 2, Feb. 1979 (also Proceedings V/STOL Aircraft Aerodynamics, sponsored by Naval Air Development Center, 1979, pp. 552-585).
174. Beatty, T. D., "A Prediction Methodology for Propulsive Induced Forces and Moments in Transition and STOL Flight," Proceedings NADC V/STOL Aircraft Aerodynamics, May 1979, pp. 64-91.
175. Siclari, M. J., Barche, J. and Migdal, D., "V/STOL Aircraft Prediction Technique Development for Jet-Induced Effects," NAPTC Report no. PDR-623-18, April 1975.
176. Siclari, M., Migdal, D. and Palcza, J. L., "Development of Theoretical Models for Jet Induced Effects on V/STOL Aircraft," Proceedings Prediction Methods for Jet V/STOL Propulsion Aerodynamics, July 1975 (avail. from DCC as AD-A024-023), pp. 998-1015.
177. Foley, W. H. and Sansome, J. A., "V/STOL Propulsion-Induced Aerodynamic Hover Calculation Method," Report no. NADC-TR-78242-60, Feb. 1980.
178. Campbell, J. F. and Schetz, J. A., "Analysis of the Injection of a Heated, Turbulent Jet into a Moving Mainstream, with Emphasis on a Thermal Discharge in a Waterway," Virginia Polytechnic Institute and State University Report VPI-E-72-24, Dec. 1972.
179. Yeh, B. T., "Calculation of the Pressure Distribution Induced by a Jet on a Flat Plate," Department of Air and Space Travel, Aachen, DKVLR DLR-FB 73-02, July 1973 (avail. in English ESRO TT-159, May 1975).
180. L. Grives, E., "Mixing Process Induced by the Vorticity Associated with the Penetration of a Jet

- into a Cross Flow." ONERA T. P. no. 1977-2, May 1977.
181. LeGrives, E., "Mixing Process Induced by the Vorticity Associated with the Penetration of a Jet into a Cross Flow," *J. Engng. for Power*, vol. 100, July 1978, pp. 465-475.
 182. Foss, J. F., "Interaction Region Phenomena for the Jet in a Cross Flow Problem," Universitat Karlsruhe, Karlsruhe, Germany, Sonderforschungsbereich (SFB) Rept. 80/E/161, Feb. 1980.
 183. Sellers, W. L., III, "A Model for the Vortex Pair Associated with a Jet in a Cross Flow," M. S. Thesis, Univ. of Florida, Gainesville, FL, June 1975.
 184. Schollenberger, C. A., "Three-Dimensional Wing/Jet Interaction Analysis Including Jet Distortion Influences," *J. Aircraft*, vol. 12, no. 9, Sept. 1975.
 185. Walters, M. M. and Yen, K. T., "The Aerodynamics of a Jet in a Crossflow," Report no. NADC-78291-60, Dec. 1978.
 186. Strauber, M., "Berechnung von Strahlkonturen mit Hilfe eines Wirbelringmodells," *Zeitschrift fur Flugwissenschaften*, vol. 23, 1975, pp. 394-400.
 187. Tulin, M. P. and Schwartz, J., "The Motion of Turbulent Vortex Pairs in Homogeneous and Density Stratified Media," Hydronautics, Inc. Tech. Rep. 231-15, 1971.
 188. Schwartz, J. and Tulin, M. P., "Chimney Plumes in Natural and Stable Surrounding," *Atmospheric Environment*, vol. 6, 1972, pp. 19-35.
 189. Zandbergen, T. and Joosen, C. J., "Experimental Investigation of Round Jet in a Cross Flow, NLR TR 74013, 1973.
 190. Duvvuri, T., "Theoretical Study of Turbulent Mixing Along Curved Jet Boundaries," USAF-ARL-TR-75-0017, Feb. 1975
 191. Patankar, S. V., Basu, D. K., and Alpay, S. A., "Prediction of the Three-Dimensional Velocity Field of a Deflected Turbulent Jet," *J. Fluids Engng.*, vol. 99, no. 4, Dec. 1977, pp. 758-762.
 192. Bergeles, G., Gosman, A. D., and Launder, B. E., "The Near-Field Character of a Jet Discharged Through a Wall at 90 Degrees to a Main Stream," *J. Heat Transfer*, Aug. 1976, pp. 373-378.
 193. Bergeles, G., Gosman, A. D., and Launder, B. E., "The Prediction of Three-Dimensional Discrete-Hole Cooling Processes," *J. Heat Transfer*, Aug. 1976, pp. 379-386.
 194. Chien, C. J. and Schetz, J. A., "Numerical Solution of the Three-Dimensional Navier-Stokes Equations with Application to Channel Flows and a Bouyant Jet in a Cross-Flow," *Trans. ASME: J. Appl. Mech.*, Vol. 42, pp. 575-579, 1975.
 195. McGuirk, J. J. and Rodi, W., "A Depth-Averaged Mathematical Model for the Near Field of Side Discharges into Open-Channel Flow," *J. Fluid Mech.*, vol. 86, pp. 761-781, 1978.
 196. Platzer, M. F. and Margason, R. J., "Predictions Methods for Jet V/STOL Propulsion Aerodynamics," *J. Aircraft*, vol. 15, no. 2, Feb. 1978, pp. 69-77.
 197. Yen, K. T., "The Aerodynamics of a Jet in a Crossflow," Report no. NADC-78291-60, Dec. 1978.
 198. Hancock, G. J., "A Review of the Aerodynamics of a Jet in a Cross Flow," *Aeronautical J.*, vol. 91, no. 905, May 1987, pp. 201-213.
 199. Baker, A. J. and Manhardt, P. D., "A Numerical Viscous-Inviscid Interaction Algorithm for Prediction of Near-Field VSTOL Jet-Induced Flowfields," Report no. NADC-77167-30, Feb. 1979.
 200. Baker, A. J., Orzechowski, J. A. and Manhardt, P. D., "A Numerical Three-Dimensional Turbulent Simulation of a Subsonic V/STOL Jet in Cross-Flow Using a Finite Element Algorithm," Report no. NADC-79021-60, 1981.
 201. Baker, A. J., Snyder, P. K., and Orzechowski, J. A., "Three-Dimensional Nearfield Characterization of a VSTOL Jet in Turbulent Crossflow," AIAA Paper No. 87-0051, Jan. 1987.
 202. Perkins, S. C. and Mendenhall, M. R., "A Correlation Method to Predict the Surface Pressure Distribution on an Infinite Plate or a Body of Revolution from Which a Jet is Issuing," NASA CR-152,345, May 1980.
 203. Perkins, S. C. and Mendenhall, M. R., "A Study of Real Jet Effects on the Surface Pressure Distribution Induced by a Jet in a Crossflow," NASA CR-166,150, Mar. 1981.
 204. Perkins, S. C. and Mendenhall, M. R., "Computer Programs to Predict Induced Effects of Jets Exhausting into a Crossflow," NASA CR-166,591, June 1984.
 205. Maskew, B., "Prediction of Subsonic Aerodynamic Characteristics: A Case for Low-

- Order Panel Methods," *J. Aircraft*, vol. 19, no. 2, Feb. 1982.
206. Maskew, B., Strash, D., Nathman, J., and Dvorak, F. A., "Investigation to Advance Prediction Techniques of the Low-Speed Aerodynamics of V/STOL Aircraft," NASA CR-166,479, Feb. 1983.
 207. Aoyagi, K. and Snyder, P. K., "Experimental Investigation of a Jet Inclined to a Subsonic Cross Flow," AIAA Paper No. 81-2610, Dec. 1981.
 208. Furlong, K. L. and Fearn, R. L., "A Lifting Surface Computer Code with Jet-in-Crossflow Interference Effects; Vol. I - Theoretical Description; Vol. II - Users Guide for WBWJAS," NASA CR-166,524, Aug. 1983.
 209. Magnus, A. E. and Epton, M. E., "PAN AIR--A Computer Program for Predicting Subsonic or Supersonic Linear Potential Flows about Arbitrary Configurations Using a Higher-Order Panel Method," NASA CR-3251, Apr. 1980.
 210. Roberts, D. W., "A Zonal Method for Modeling 3-D Aircraft Flow Fields With Jet Plume Effects," AIAA Paper No. 87-1436, June 1987.
 211. Howell, G. A. and Snyder, L. D., "Development of V/STOL Methodology Based on a Higher Order Panel Method," NASA CR 166491, May 1984.
 212. Howell, G. A., "Automated Surface and Plume Simulation Procedure for Use with Aerodynamic Panel Codes," NASA CR-177420, May 1986.
 213. Yoo, S. and Strash, D. J., "Zonal Approach to V/STOL Aerodynamics," *J. Aircraft*, vol. 27, no. 10, Oct. 1990, pp. 866-872.
 214. Katz, J. and Kern, D., "Effect of Vertical-Ejector Jet on the Aerodynamics of Delta Wings," *J. Aircraft*, vol. 27, no. 5, May 1990, pp. 408-412.
 215. McLaughlin, D. K., "Laser Doppler Velocimeter Measurements in a Turbulent Jet Exiting into a Cross Flow," AEDC-TR-71-262, Jan. 1972.
 216. Rudinger, G. and Moon, L. F., "Laser-Doppler Measurements in a Subsonic Jet Injected into a Subsonic Cross Flow," *Trans. ASME J. Fluids Engng.*, vol. 43, Sept. 1976, pp. 516-520.
 217. Aoyagi, K. and Snyder, P. K., "Experimental investigation of a Jet Inclined to a Subsonic Crossflow," AIAA Paper No. 81-2610, 1981.
 218. Fearn, R. L., Doddington, H. and Westphal, R., "LDV Studies of a Jet in a Crossflow," Report No. NADC-80238-60, 1981.
 219. Snyder, P. and Orloff, K. L., "Three-Dimensional Laser Doppler Anemometer Measurements of a Jet in a Crossflow," NASA TM-85997, 1984.
 220. Orloff, K. L. and Snyder, P. K., "Using a Three-Dimensional Laser Anemometer to Determine Mean Streamline Patterns in a Turbulent Flow," NASA TM 85,948, July 1984.
 221. Snyder, P. K. and Orloff, K. L., "Three-Dimensional Laser Doppler Anemometer Measurements of a Jet in a Crossflow," NASA TM 85,997, Sept. 1984.
 222. Sislian, J. P. and Cusworth, R. A., "Laser Doppler Velocimeter Measurements of Mean Velocity and Turbulent Stress Tensor Components in a Free Isothermal Swirling Jet," Univ. of Toronto, UTIAS Report No. 281, Mar. 1984.
 223. Fearn, R. L., "Progress Towards a Model to Describe Jet/Aerodynamic-Surface Interference Effects," *AIAA J.*, vol. 22, no. 6, June 1984, pp. 752-753.
 224. Schetz, J. A. and Jakubowski, A. K., "Experimental Study of Surface Pressure Induced on a Flat Plate and a Body of Revolution by Various Dual Jet Configurations," NASA CR 166422, Dec. 1982.
 225. Schetz, J. A., Jakubowski, A. K., and Aoyagi, K., "Surface Pressures on a Flat Plate with Dual Jet Configurations," *J. Aircraft*, vol. 21, no. 7, July 1984, pp. 484-490.
 226. Moore, C. L. and Schetz, J. A., "Effects of Non-Uniform Velocity Profiles on Dual Jets in a Crossflow," AIAA Paper No. 85-1674, July 1985.
 227. Kavsaoglu, M., Schetz, J. A. and Jakubowski, A. K., "Dual Rectangular Jets from a Flat Plate in a Crossflow," AIAA Paper No. 86-0477, Jan. 1986.
 228. Trischka, J. W. and Birkenheuer, N. J., "Computer-Enhanced Analysis of a Jet in a Cross Stream," *AIAA J.*, vol. 21, no. 2, Feb. 1983.
 229. Catalano, G. D., Chang, K. S. and Mathis, J. A., "Investigation of Turbulent Jet Impingement in a Confined Crossflow," *AIAA J.*, vol. 27, no. 11, Nov. 1989, pp. 1530-1535.
 230. Karagozian, A. R. and Greber, I., "An Analytical Model for the Vorticity Associated with a Transverse Jet," AIAA Paper No. 84-1662, June 1984.
 231. Linsell, D. F., "Liquid Crystal Thermography of Surface Effects of Fluid Jets in Crossflow,"

- Royal Naval Engng. College, U.K., RNEL-TR-83004, July 1983.
232. Nunn, R. H. and Linsell, D. F., "Liquid Crystal Thermographic Study of Jet-Crossflow Surface Interactions," AIAA Paper No. 84-2432, Nov. 1984.
 233. Andreopoulos, J., "Measurements in a Jet-Pipe Flow Issuing Perpendicularly into a Crossflow," *J. Fluid Mech.*, Vol. 104, no. 12, Dec. 1982, pp. 493-499.
 234. Andreopoulos, J. and Rodi, W., "Experimental Investigation of Jets in a Crossflow," *J. Fluid Mech.*, vol. 138, no. 1, Jan. 1984, pp. 93-127.
 235. Andreopoulos, J., "On the Structure of Jets in a Crossflow," *J. Fluid Mech.*, vol. 139, Jan. 1985, pp. 163-197.
 236. Sherif, S. A. and Pletcher, R. H., "Measurements of the Flow and Turbulence Characteristics of Round Jets in Crossflow," *J. Fluids Engng.*, vol. 115, Jan. 1989, pp. 165-171.
 237. Krothapalli, A., Lourenco, L., and Buchlin, J. M., "The Structure of the Separated Flow Region Upstream of a Jet in a Cross Flow," AIAA Paper No. 89-0571, Jan. 1989.
 238. Compton, D. A. and Johnston, J. P., "Streamwise Vortex Production by Pitched and Skewed Jets in a Turbulent Boundary Layer," AIAA Paper No. 91-0038, Jan. 1991.
 239. Hatch, M. S., Sowa, W. A., Samuelson, G. S., and Holdeman, J. D., "Jet Mixing into a Heated Cross Flow in a Cylindrical Duct - Influence of Geometry and Flow Variations," AIAA Paper No. 92-0773, Jan. 1992.
 240. Jones, W. P. and Mc Guirk, J. J., "Computations of a Round Jet Discharging into a Confined Crossflow," in: *Turbulent Shear Flows 2*, Springer, 1980, pp. 233-245.
 241. White, A. J., "The Prediction of the Flow and Heat Transfer in the Vicinity of the Jet in Cross Flow," ASME-80-WA/HT-26, 1980.
 242. Demuren, A. O., "Numerical Calculations of Steady Three-Dimensional Turbulent Jets in Cross Flow," *Comp. Meth. App. Mech. Engr.*, vol. 37, May 1983, pp. 309-328.
 243. Demuren, A. O., "Modeling Turbulent Jets in Crossflow," in: *Encyclopedia of Fluid Mechanics*, vol. 2, Gulf Publishing Co., 1985, pp. 430-465.
 244. Baker, A. J., Orzechowski, J. A., and Manhardt, P. D., "A Numerical Three-Dimensional Turbulent Simulation of a Subsonic Interaction VSTOL Jet in Crossflow Using a Finite Element Algorithm," Report no. NADC 79021-60, July 1980.
 245. Baker, A. J., Orzechowski, J. A., Manhardt, P. D., and Yen, K. T., "A Three-Dimensional Finite Element Algorithm for Prediction of V/STOL Jet-Induced Flows," AGARD CP-308, Nov. 1981, paper 26.
 246. Baker, A. J. and Orzechowski, J. A., "An Assessment of Factors Affecting Prediction of Near-Field Development of a Subsonic VSTOL Jet in Crossflow," Tech. Report NADC 81177-60, Sept. 1982.
 247. Baker, A. J., Snyder, P. K., and Orzechowski, J. A., "Three Dimensional Near Field Characterization of a VSTOL Jet in Turbulent Crossflow," AIAA Paper No. 87-0051, Jan. 1987.
 248. Claus, R. W., "Numerical Calculation of Subsonic Jets in Crossflow with Reduced Numerical Diffusion," AIAA Paper No. 85-1441, 1985.
 249. Claus, R. W. and Vanka, S. P., "Multigrid Calculations of a Jet in Crossflow," AIAA Paper No. 90-0444, Jan. 1990.
 250. Pulliam, T. H. and Steger, J. L., "Implicit Finite Difference Simulations of Three-Dimensional Compressible Flow," *AIAA J.*, vol. 18, no. 2, Feb. 1980, pp. 159-167.
 251. Roberts, D. W., "Prediction of Subsonic Aircraft Flows with Jet Exhaust Interactions," AGARD CP-301, May 1981.
 252. Roberts, D. W., "A Zonal Method for Modeling Powered-Lift Aircraft Flow Fields," NASA contract NAS2-12801, Amtec Engineering, Inc., AEI-T88100.01, Dec. 1988.
 253. Roberts, D. W., "A Zonal Method for Modeling Powered-Lift Aircraft Flow Fields," NASA contract NAS2-13357, Amtec Engineering, Inc., AEI-T93100.01, Sept. 1991.
 254. Mongia, H. C., Reynolds, R. S. and Srinivasan, R., "Multidimensional Gas Turbine Combustion Modelling Applications and Limitations," *AIAA J.*, vol. 24, no. 6, June 1986, pp. 890-904.
 255. Holdeman, J. D. and Srinivasan, R., "Modeling Dilution Jet Flowfields," *J. Propulsion and Power*, vol. 2, no. 1, Jan 1986, pp.4-10.
 256. Karki, K. C. and Mongia, H. C., "Recent Developments in Computational Combustion Dynamics," AIAA Paper No. 89-2808, Jan. 1989.

257. Sykes, R. I., Lewellen, W.S. and Parker, S. F., "On the Vorticity Dynamics of a Turbulent Jet in a Crossflow," *J. Fluid Mech.*, Vol. 168, pp. 393-412, July 1986.
258. Needham, D. J., Riley, N., and Smith, J. H. B., "A Jet in Crossflow," *J. Fluid Mech.*, vol. 188, Jan. 1988, pp. 159-184.
259. Harloff, G. J. and Lytle, J. K., "Three-Dimensional Viscous Flow Computations of a Circular Jet in a Subsonic and Supersonic Cross Flow," AIAA Paper No. 88-3703, June 1988.
260. VanOverbeke, T. J. and Holdeman, J. D., "A Numerical Study of the Hot Gas Environment Around a STOL Aircraft in Ground Proximity," AIAA Paper No. 88-2882, Aug. 1988.
261. Roth, K. R., "Numerical Simulation of a Subsonic Jet in a Crossflow," SAE Paper 872343, Dec. 1987.
262. Roth, K. R., "Influence of the Thin-Layer Approximation on Jet in Crossflow Computations," AIAA Paper No. 90-3056, 1990.
263. Roth, K. R., Fearn, R. L., and Thakur, S. S., "Evaluation of a Navier-Stokes Prediction of a Jet in a Crossflow," *J. Aircraft*, vol. 29, no. 2, Mar.-Apr. 1992, pp. 185-193.
264. Shang, J. S., McMaster, D. L., Scaggs, N., and Buck, M., "Interaction of Jet in Hypersonic Cross Stream," *AIAA J.*, vol. 27, no. 3, Mar. 1989.
265. Huang, G.-P., "Model and Computation of Three-Dimensional Turbulent Jets in a Crossflow," Ph.D. Thesis, Ecole Centrale de Lyon, France, June 1989.
266. Oh, T. S. and Schetz, J. A., "Finite Element Simulation of Complex Jets in a Crossflow for V/STOL Applications," *J. Aircraft*, Vol. 27, No. 5, May 1990, pp. 389-399.
267. Shi, Z., Wu, J. M., and Wu, J. Z., "Symmetric and Asymmetric Jets in a Uniform Crossflow," AIAA Paper No. 91-0722, Jan. 1991.
268. Kavsoglu, M. S. and Schetz, J. A., "Effects of Swirl and High Turbulence on a Jet in a Crossflow," *J. Aircraft*, vol. 26, no. 6, June 1989.
269. Kavsoglu, M.S., Akmandor, I. S., Ciray, S. and Fujii, K., "Navier-Stokes Simulation of Two and Three Dimensional Jets in Crossflow," AIAA Paper No. 91-1743, 1991.
270. Fujii, K. and Obayashi, S., "Practical Applications of New LU-ADI Scheme for the Three-Dimensional Navier-Stokes Computation of Transonic Viscous Flows," AIAA Paper No. 86-0513, Jan. 1986.
271. Baldwin, B. S. and Lomax, H., "Thin Layer Approximation and Algebraic Model for Separated Turbulent Flows," AIAA Paper No. 78-257, Jan. 1978.
272. Bruiatskii, E. V. and Kuz'menko, G., "Calculation of the Cross-Sectional Shape of a Jet in a Cross Flow," *Instituti Gidromekhaniki, Kiev, Ukraina, Gidromekhanika*, no. 63, 1991, pp. 15-21.
273. Demuren, A. O., "Characteristics of 3D Turbulent Jets in Crossflow," NASA TM 104337, Apr. 1991.
274. Kim, S.-W. and Benson, T. J., "Fluid-Flow of a Row of Jets in Crossflow," AIAA Paper No. 92-0534, Jan. 1992.
275. Chiu, S. H., Roth, K. R., Margason, R. J., and Tso, J., "A Numerical Investigation on a Subsonic Jet in Crossflow," AIAA Paper No. 93-0870, Jan. 1993.
276. Benek, J. A., Buning, P. G., and Steger, J. L., "A 3-D Chimera Grid Embedding Technique," AIAA Paper No. 85-1523, Jan. 1985.
277. Baldwin, B. S. and Barth, T. J., "A One Equation Turbulence Transport Model for High Reynolds Number Wall-Bounded Flows," AIAA Paper No. 78-257, Jan. 1978.
278. McMahon, H. M., Hester, D. D., and Palfrey, J. G., "Vortex Shedding from a Turbulent Jet in a Cross-Wind," *J. Fluid Mech.*, vol. 48, part 1, 1971, pp. 73-80.
279. Trischka, J. W., "Modes of Turbulent Vortex Shedding from a Pipe-Jet in a Cross-Flow," *AIAA J.*, vol. 17, no. 3, Mar. 1979, pp. 315-317.
280. Kuzo, D. M. and Roshko, A., "Observations on the Wake Region of the Transverse Jet," *J. Fluid Mech.*, vol. 29, 1984, pg. 1536.
281. Fric, T. F. and Roshko, A., "Structure in the Near Field of the Transverse Jet," *Proceedings of Seventh Symposium on Turbulent Shear Flows*, vol. 1 (A90-35176), Aug. 1989, pp. 6.4.1-6.4.6.
282. Coelho, S. L. V. and Hunt, J. C. R., "The Dynamics of the Near Field of Strong Jets in Crossflows," *J. Fluid Mech.*, vol. 200, 1989, pp.95-120.

283. Broadwell, J. E. and Breidenthal, R. E., "Structure and Mixing of a Transverse Jet in Incompressible Flow," *J. Fluid Mech.*, vol. 148, 1984, pp. 405-412.
284. Wu, J. M., Vakili, A. D., and Yu, F. M., "Investigation of the Interacting Flow of Nonsymmetric Jets in Crossflow," *AIAA J.*, vol. 26, no. 8, Aug. 1988, pp. 940-947.
285. "Proceedings of the 1985 NASA Ames Research Center's Ground-Effects Workshop," K. Mitchell - editor, NASA CP-2462, 1985.
286. "Proceedings of the 1987 Ground Vortex Workshop," R. J. Margason - editor, NASA CP-10008, 1987.
287. Bray, D. and Knowles, K., "A Review of Impinging Jets in Crossflows - Experimentation and Computation," AIAA Paper No. 92-0633, Jan. 1992.
288. Hertel, H., "Wandströmungen und Aufströme aus der Umlenkung von Freistrahlguppen" (Wall Flows and Up-Streams Due to the Diversion of Free Jet Groups), Fortschritt Berichte VDI Zeitschrift Fortschr., vol. 12, no. 11, July 1966, pp. 1-72.
289. Ryan, P. E., Heim, R. J., and Cosgrove, W. J., "A Generalized Experimental Investigation of Hot Gas Recirculation and Ingestion for Jet VTOL Aircraft," NASA CR-1147, Sept. 1968.
290. Hall, G. R. and Rogers, K. H., "Recirculation Effects Produced by a Pair of Heated Jets Impinging on a Ground Plane," NASA CR-1307, May 1968.
291. Stewart, V. R. and Kuhn, R. E., "A Method for Estimating the Propulsion Induced Aerodynamic Characteristics of STOL Aircraft in Ground Effect," NADC-80226-60, Aug. 1983.
292. Van Dalsem, W. R., "Study of V/STOL Flows Using the Fortified Navier-Stokes Scheme," Computational Fluid Dynamics, G. de Vahl Davis and C. Fletcher (editors), Elsevier Science Publishers B.V. (North Holland), 1988, pp. 725-735.
293. Van Dalsem, W. R. and Steger, J. L., "Using the Boundary-Layer Equations in Three-Dimensional Viscous Flow Simulation," AGARD-CP-412, Oct. 1986, paper 24.
294. Glauert, M. B., "The Wall Jet," *J. Fluid Mech.*, vol. 1, 1957, pp. 625-643.
295. Bakke, P., "An Experimental Investigation of the Wall Jet," *J. Fluid Mech.*, vol. 2, 1957, pp. 467-472.
296. Bradshaw, P. and Love, E. M., "The Normal Impingement of a Circular Air Jet on a Flat Surface," A.R.C. Reports and Memoranda No. 3205, Sept. 1959.
297. Spreeman, K. P. and Sherman, I. R., "Effects of Ground Proximity on the Thrust of a Simple Downward-Directed Jet Beneath a Flat Surface," NACA TN 4407, Sept. 1958.
298. Kuhn, R. E., "An Investigation to Determine Conditions Under Which Downwash from VTOL Aircraft will Start Surface Erosion from Various Types of Terrain," NASA TN D-56, Dec. 1959.
299. Anon., "VTOL Aircraft Downwash Impingement Symposium" (a compilation of the papers), U.S. Army TREC Tech. Rep. 61-1, Dec. 1960.
300. Shen, Y. C., "Theoretical Analysis of Jet-Ground Plane Interaction," IAS Paper No. 62-144, June 1962.
301. Wyatt, L. A., "Static Test of Ground Effect on Planforms Fitted with a Centrally Located Round Lifting Jet," Ministry of Aviation, ARC CP-749, June 1962.
302. Vidal, R. J., "Aerodynamic Processes in the Downwash-Impingement Problem," *J. Aero. Sciences*, vol. 29, no. 9, Sept. 1962, pp. 1067-1075.
303. Donaldson, C. D. and Snedeker, R. S., "A Study of Free Jet Impingement," *J. Fluid Mech.*, vol. 45, 1971, pp. 281-319.
304. Brady, W. G. and Ludwig, G., "Theoretical and Experimental Studies of Impinging Uniform Jets," IAS Paper No. 63-29, Jan. 1963.
305. deSavigny, R. A. and Hickey, D. H., "Aerodynamics in Ground Effect of a Large-Scale Model with a High Disk-Loading Lifting Fan Mounted in the Fuselage," NASA TN D-1557, Jan. 1963.
306. Vogler, R. D., "Ground Effects on Single- and Multiple-Jet VTOL Models at Transition Speeds Over Stationary and Moving Ground Planes," NASA TN D-3213, Jan. 1966.
307. McLemore, H. C., "Jet-Induced Lift Loss of Jet VTOL Configurations in Hovering Condition," NASA TN D-3435, June 1966.
308. Abbot, W. A., "Studies of Flow Fields Created by Vertical and Inclined Jets Moving over a Horizontal Surface," ARC CP No. 911, 1967.
309. McLemore, H. C. and Smith, C. C. Jr., "Hot-Gas Ingestion Investigation of Large-Scale Jet VTOL Fighter-Type Models," NASA TN D-4609, June 1968.

310. Colin, P. E. and Olivari, D., "The Impingement of Circular Jet Normal to a Flat Surface With and Without Cross Flow," von Karman Institute for Fluid Dynamics, Rhode-St. Genese, Belgium, (avail. as AD688953), Jan. 1969.
311. McLemore, H. C., Smith, C. C. Jr., and Hemeter, P. G., "Generalized Hot-Gas Ingestion Investigation of Large-Scale Jet VTOL Fighter-Type Models," NASA TN D-5581, Jan. 1970.
312. Gauntner, J. W., Livingood, J. N. B., and Hrycak, P., "Survey of Literature on Flow Characteristics of a Single Turbulent Jet Impinging on a Flat Plate," NASA TN D-5652, Feb. 1970.
313. Gubanov, O. I., Lunev, V. V. and Plastinina, L. N., "The Central Breakaway Zone with Interaction Between a Supersonic Underexpanded Jet and a Barrier," translated from *Izvestiya Akademii Nauk SSSR, Mekhanika Zhidkosti i Gaza*, No. 2, Mar.-Apr. 1971, pp. 135-138.
314. Binion, T. W. Jr., "Investigation of the Recirculation of a Flow Field Caused by a Jet in Ground Effect with Crossflow," AEDC-TR-70-192 Sept. 1970.
315. Sparrow, E. M., Goldstein, R. J., and Rouf, M. A., "Effect of Nozzle-Surface Separation Distance on Impingement Heat Transfer for a Jet in a Crossflow," *J. Heat Transfer*, vol. 18, Nov. 1975, pp. 528-533.
316. Bower, W. W., Agarwal, R. K., Peters, G. R., and Kotansky, D. R., "Viscous Flowfields Induced by Two- and Three-Dimensional Lift Jets in Ground Effect," U. S. Navy Report ONR-CR215-246-3F, Mar. 1979.
317. Bower, W. W., Saripalli, K. R., and Agarwal, R. K., "A Summary of Jet-Impingement Studies at McDonnell Douglas Research Laboratories," AIAA Paper No. 81-2613, Dec. 1981.
318. Migdal, D., Hill, W. G. Jr., Jenkins, R. C., and Siclari, M. J., "VTOL in Ground Effect Flows for Closely Spaced Jets," NASA CR 152321, Dec. 1979.
319. Christiansen, R. S., "A Large Scale Investigation of VSTOL Ground Effects," AIAA Paper No. 84-0336, Jan. 1984.
320. Agarwal, R. K., and Deese, J. E., "Aerodynamic of an Airfoil in Ground Effect with a Jet Issuing from its Undersurface," AIAA Paper No. 85-0019, Jan. 1985.
321. Cimbala, J. M., Stinebring, D. R., Treaster, A. L., and Billet, M. L., "Experimental Investigation of a Jet Impinging on a Ground Plane in the Presence of a Cross Flow," Report no. NADC-87019-60, Mar. 1987.
322. Corsiglia, V. R., Wardwell, D. A., and Kuhn, R. E., "Small-Scale Experiments in STOVL Ground Effects," Int. Powered Lift Conference, RAeS, London, Aug. 1990.
323. Iwamoto, J., "Impingement of Under-Expanded Jets on a Flat Plate," *J. Fluids Engng.*, vol. 112, June 1990, pp. 179-184.
324. Liaw, C.-H. P., "Aircraft Aerodynamics with Deflected Jets in Ground Effect," Ph.D. Thesis, Univ. of Kansas, Lawrence, KS, Aug. 1990.
325. Cimbala, J. M., Billet, M. L., and Gaublumme, D. P., "Experiments on the Unsteady Ground Vortex," NASA CR 177566, Aug. 1990.
326. Ing, D. N., "Correlation Between Wyatt and Other Studies on Single Jet In-Ground-Effect Lift Loss," Logico Systems Ltd., Surrey, UK, Report No. 24/91, Jan. 1991.
327. Bellavia, D. C., Wardwell, D. A., Corsiglia, V. R., and Kuhn, R. E., "Forces and Pressures Induced on Circular Plates by a Single Lifting Jet in Ground Effect," NASA TM 102,816, Mar. 1991.
328. Mathis, J. A., "Examination of Energy Spectra Moments in a Developing Turbulent Flow," NIAR Report 91-28, Wichita State Univ., Wichita, KS, Dec. 1991.
329. Knowles, K., Bray, D., Bailey, P. J., and Curtis, P., "Impinging Jets in Cross-Flow," *Aeronautical J.*, Feb. 1992, pp. 47-56.
330. Kuhlman, J. M. and Cavage, W. M., "Ground Vortex Formation for Uniform and Nonuniform Jets Impinging on a Ground Plane," AIAA Paper No. 92-4251, Aug. 1992.
331. Barata, J. M. N., "Fountain Flows Produced by Multijet Impingement on a Ground Plane," *J. Aircraft*, vol. 30, no. 1, Jan.-Feb. 1993.
332. Zhang, X., "A Study of Single Jet Impingement Ground Effect Lift Loss," AIAA Paper No. 93-0869, Jan. 1993.
333. Ing, D. N. and Zhang, X., "Numerical Modelling of a Single Jet Impingement Ground Effect Lift Loss," Logico Systems Ltd., Surrey, UK, Report No. 26/92, Jan. 1993.

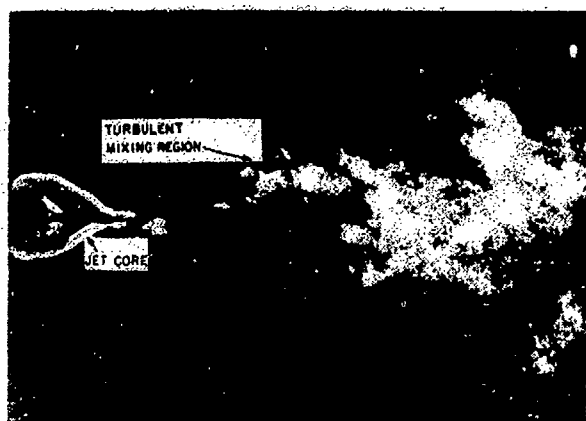


Figure 1.- Photograph¹ of a jet exiting into quiescent surroundings showing the undisturbed jet core and entrainment into the turbulent mixing region.

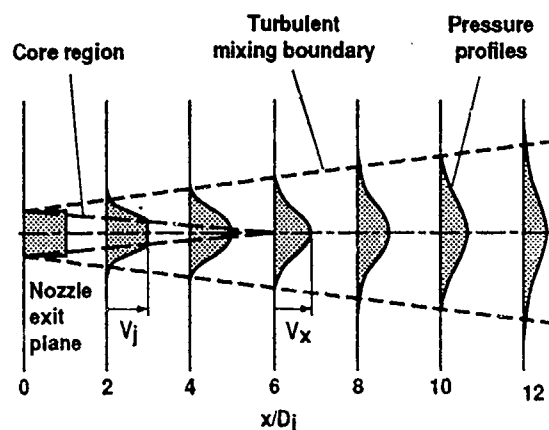


Figure 2.- Schematic of the decay and spread of the jet efflux with distance downstream of the nozzle exit.

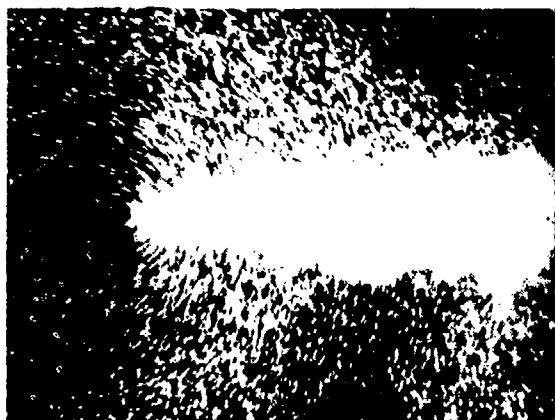


Figure 3.- Photograph¹ of a jet in a water tunnel illustrating with air bubbles the "douche" effect - entrainment of air from quiescent surroundings.

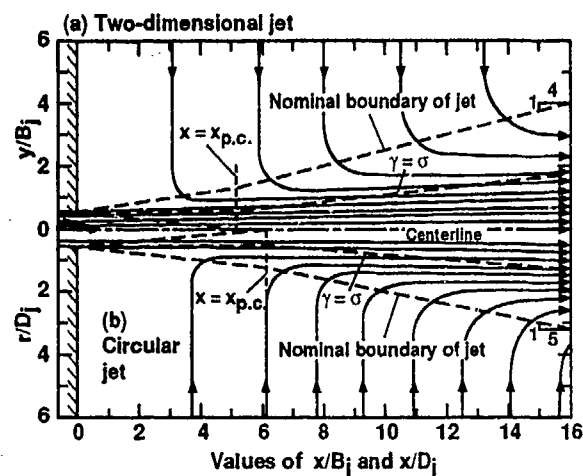


Figure 4.- Curves by Albertson et al.⁵ showing the pattern of mean motion in both the zone of establishment and the zone of established flow for both flow from a jet and a two-dimensional nozzle.

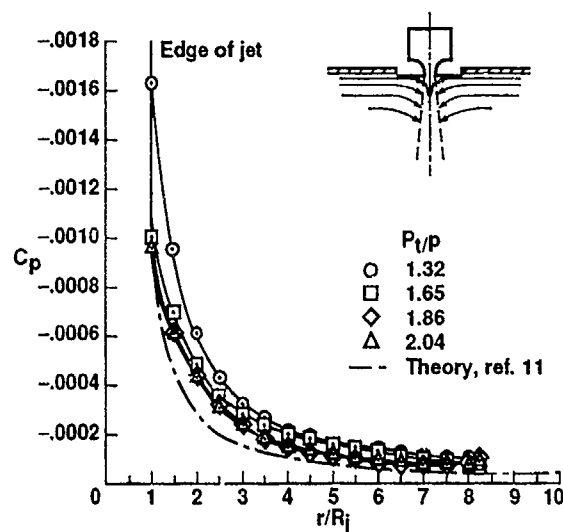


Figure 5.- Radial distribution of pressure induced by a circular jet on an infinite surface¹².

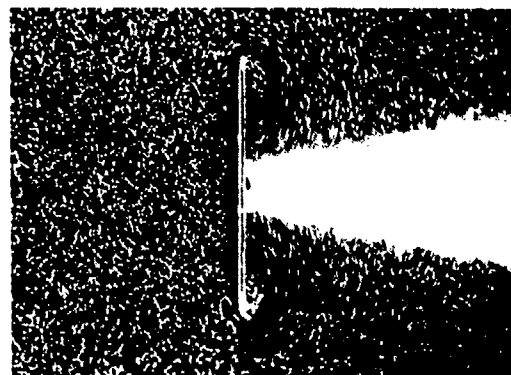


Figure 6.- Photograph¹ of a jet in a water tunnel exiting through a circular flat to illustrate the entrainment from quiescent surroundings around the edge of the plate.

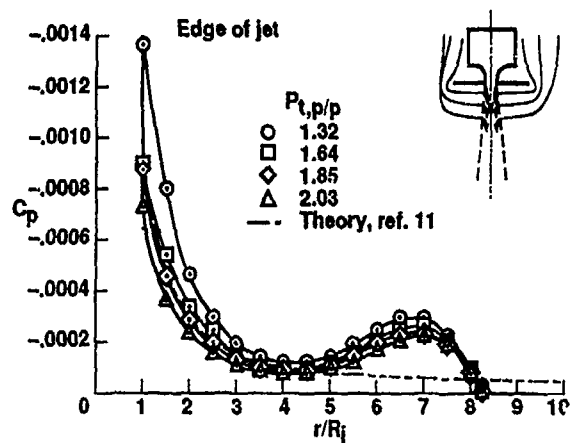


Figure 7.- Radial distribution of pressure induced by a circular jet on a circular plate surface ($r_j/R_p=8.35$, $A_p/A_j=69.5$)¹².

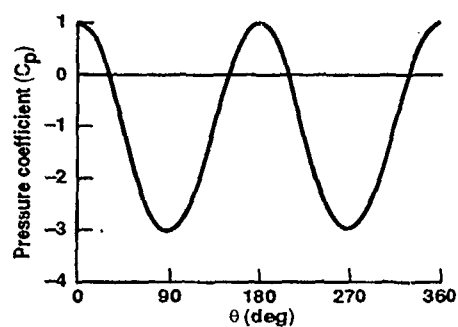


Figure 8.- Pressure distribution around a right circular cylinder in an inviscid, uniform crossflow.

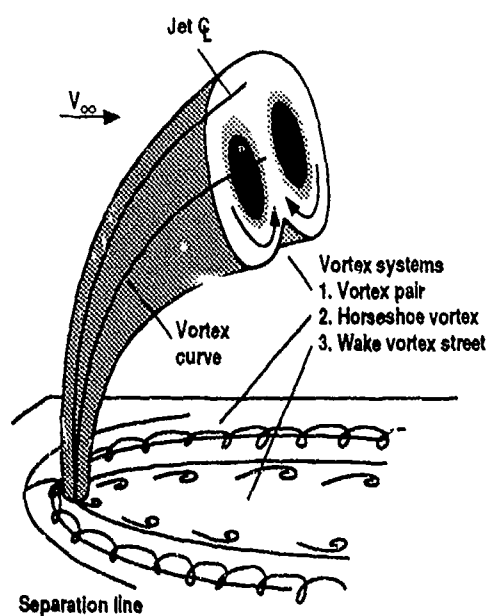
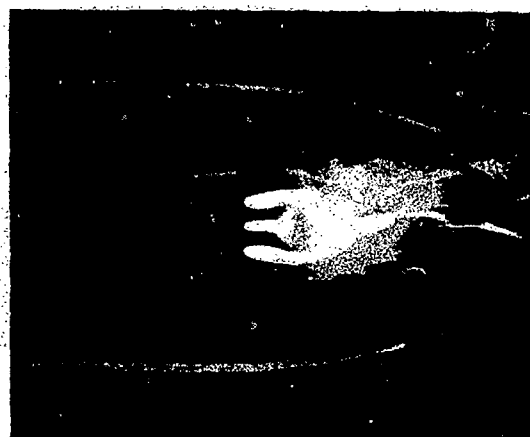


Figure 9.- Sketch of the three vortex systems associated with the jet in a crossflow.



(a) Perspective view.



(b) View down toward the jet exit region.

Figure 10. Photographs of the dye filaments induced around and into a jet exhausting normal to the freestream in a water tunnel¹.

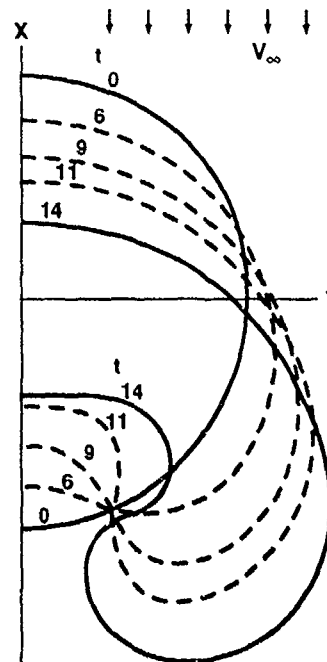


Figure 11.- Chang⁹² results for the rolling up of the vortex flow by a cross flow for half of the jet circumference.

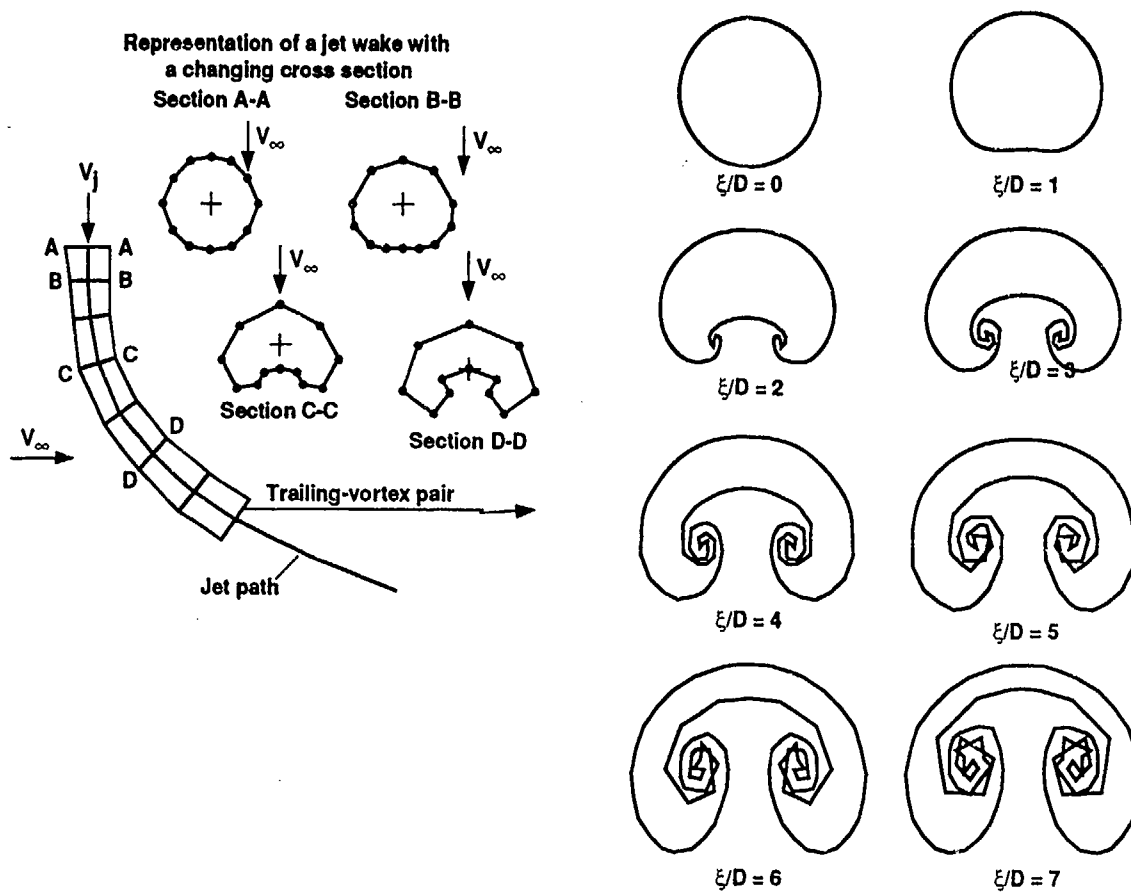


Figure 12. - Selected cross sections for the rollup of a jet in a crossflow into a vortex pair obtained from a Chang potential flow calculation⁹³.

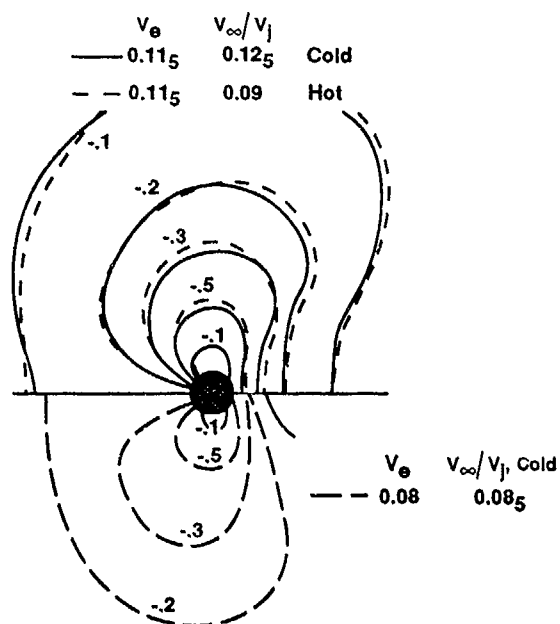


Figure 13.- Williams and Wood²³ correlation of surface pressure distributions induced by cold and hot jets.

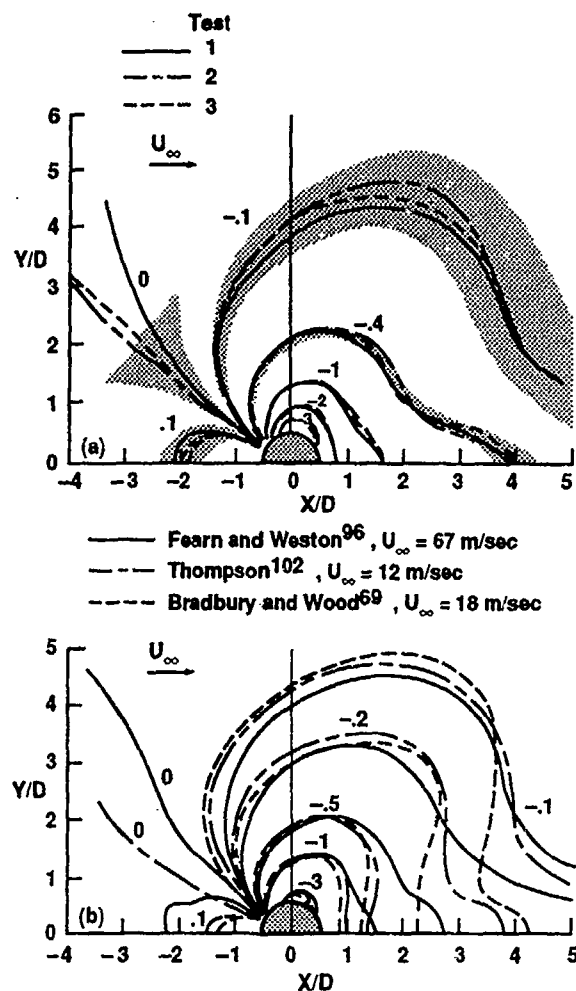


Figure 14.- Surface pressure distribution induced by a JICF where $\delta_j = 90^\circ$ and $V_e = 0.250$.

- (a) Effect of uncertainty due to pressure transducer error ($\Delta C_p = 0.036$)⁹⁶.
 (b) Comparison among three investigations (ref 69, 96, and 102).

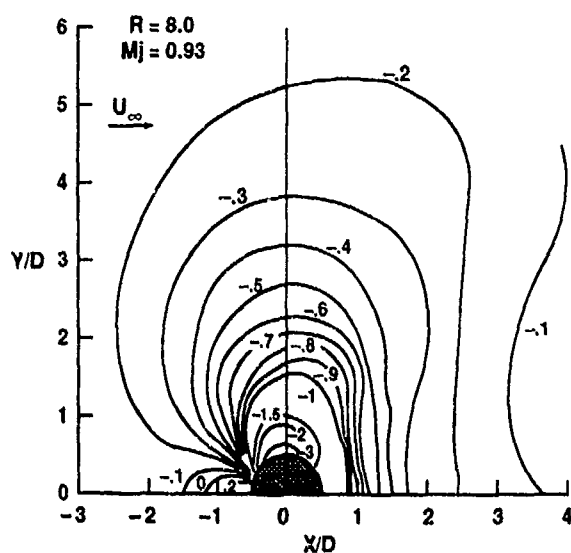


Figure 15.- Surface pressure distribution induced by a JICF⁹⁶ where $\delta_j = 90^\circ$ and $V_e = 0.125$.

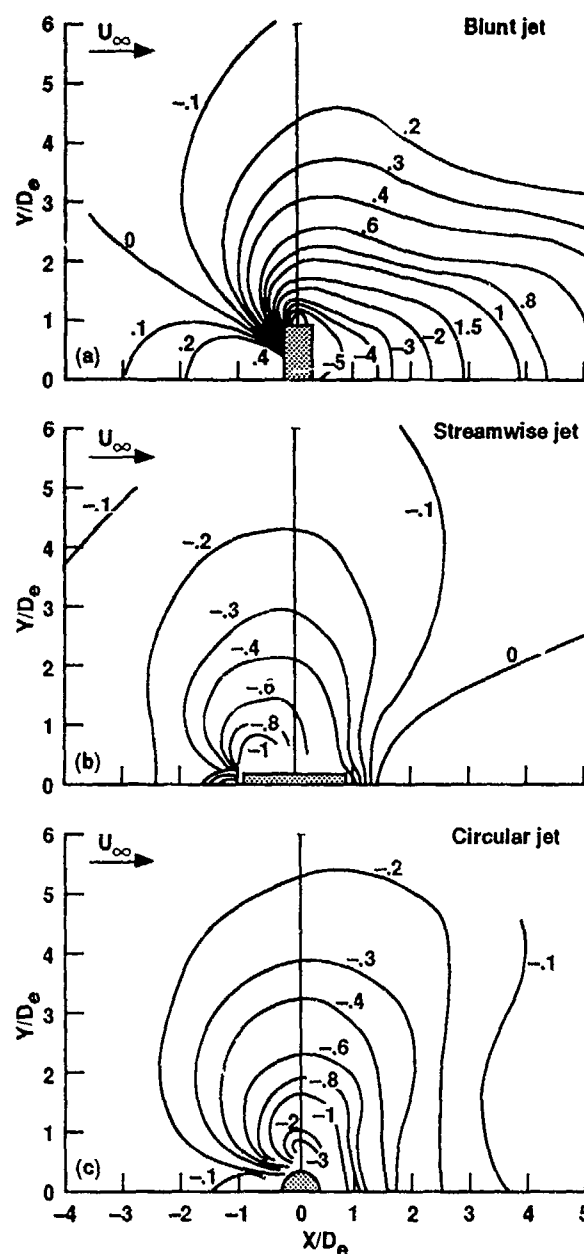


Figure 16.- Effect of jet nozzle shape on the surface pressure distribution¹³⁹ induced by a JICF where $\delta_j = 90^\circ$ and $V_e = 0.25$.

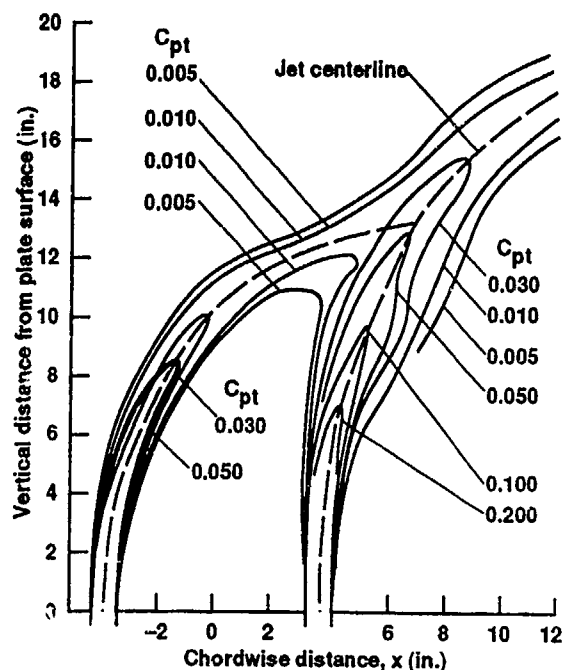


Figure 17.- Contours of constant total pressure coefficients induced by a pair of jets aligned with the freestream (tandem) with 7.5 diameters between jet centerlines ($V_e=0.125$)^{165,166}.

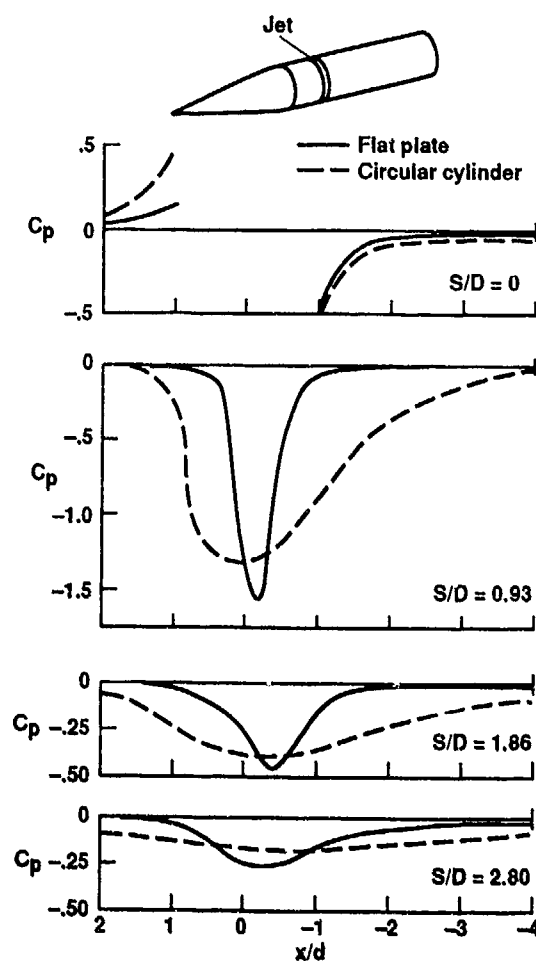


Figure 18.- Effect of the jet exit surface shape on the jet induced pressure distribution¹¹⁷.

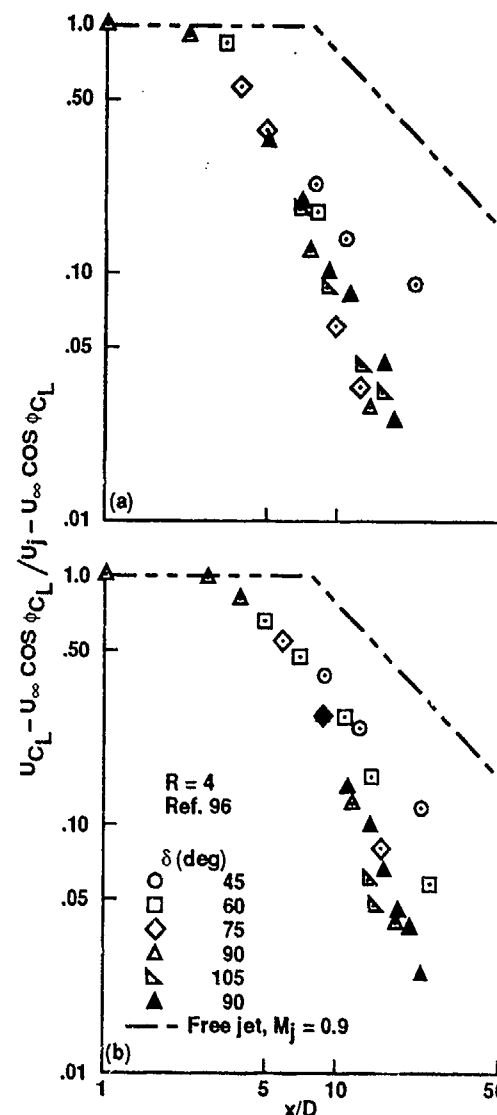


Figure 19.- Decay of jet centerline speed⁹⁹ for V_e of 0.125 and 0.250.

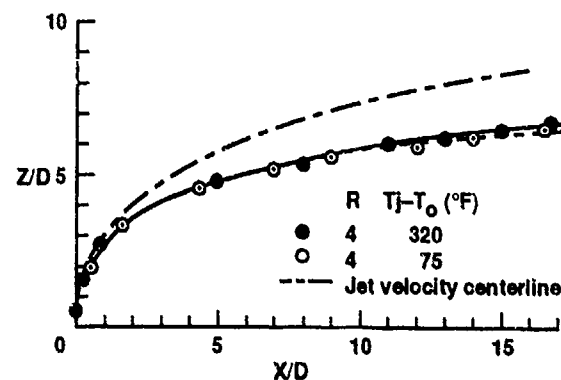
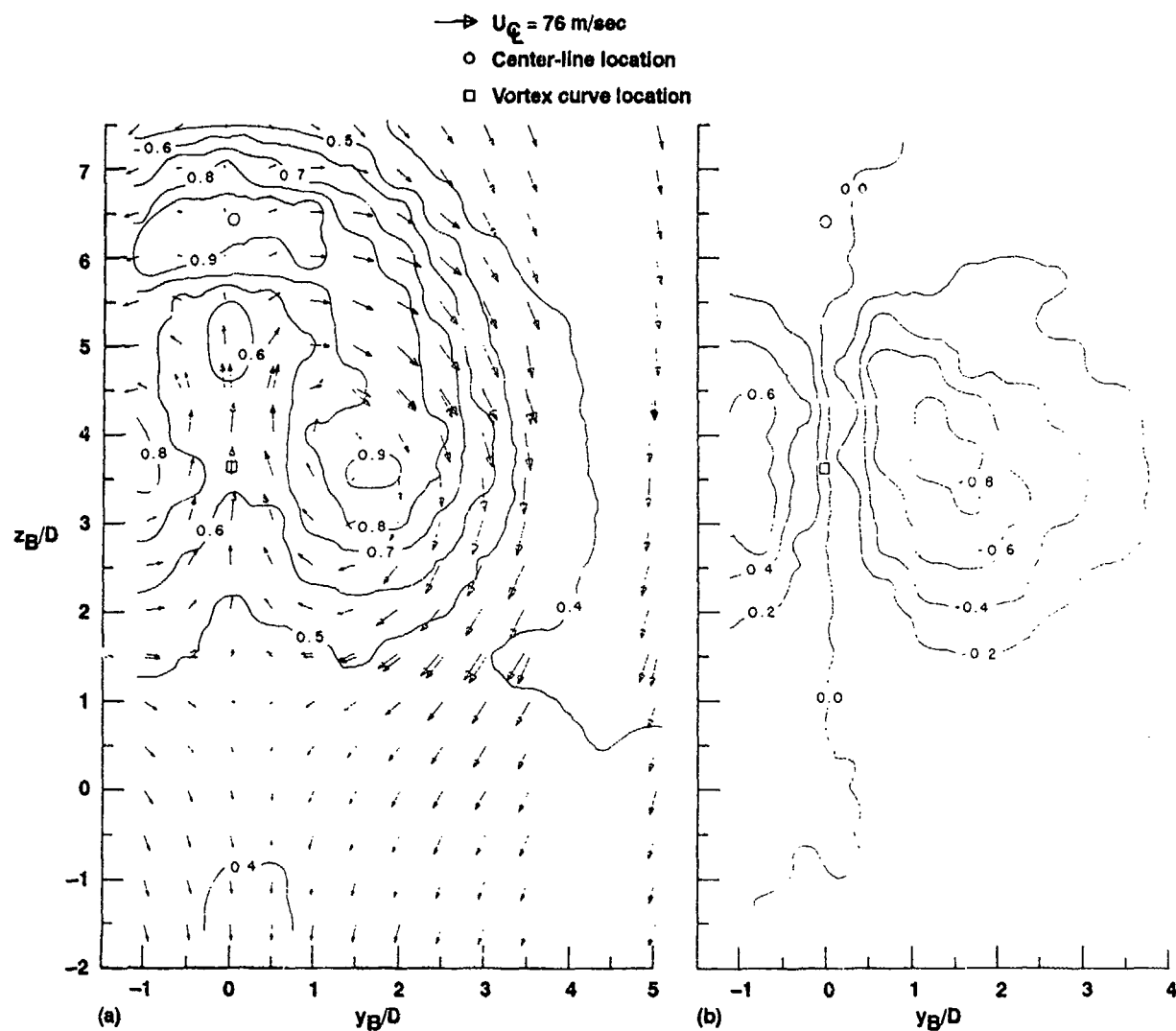


Figure 20.- Location of maximum temperature centerline ($V_e=0.25$)¹⁰⁹.



(a) Measured velocities where u/V_∞ perpendicular to the survey plane is shown by contours and the resultant velocity in the survey plane is shown by vectors.

(b) Vorticity contours computed from measured velocity data. The vorticity is non-dimensionalized by the maximum vorticity in the survey plane.

Figure 21- Jet cross section for $V_e=0.125$, $x/D=7.60$, $z/D=4.81$, and $\phi=42^\circ$ from ref. 97.

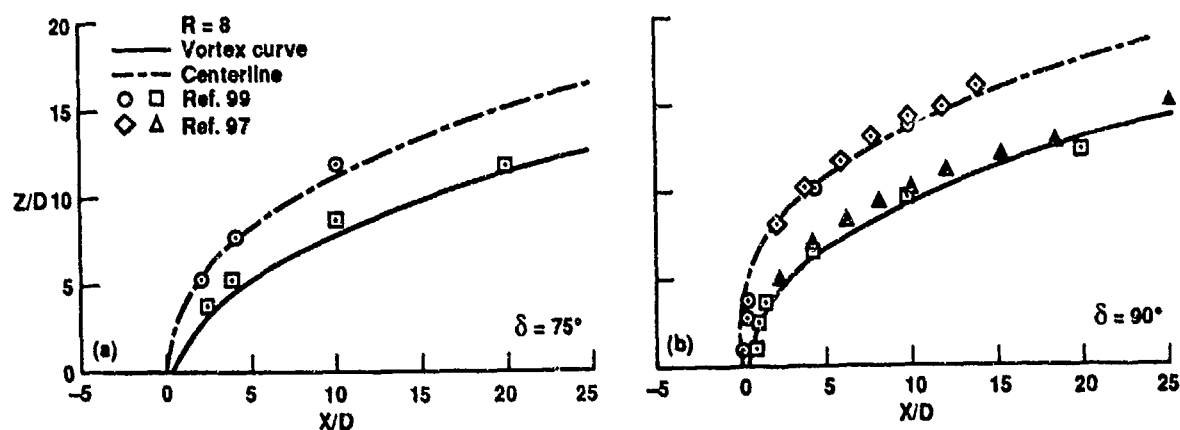


Figure 22.- Measured^{97,99} jet-path centerline and jet vortex curves ($V_e=0.125$). (a) $\delta_j=90^\circ$. (b) $\delta_j=75^\circ$.

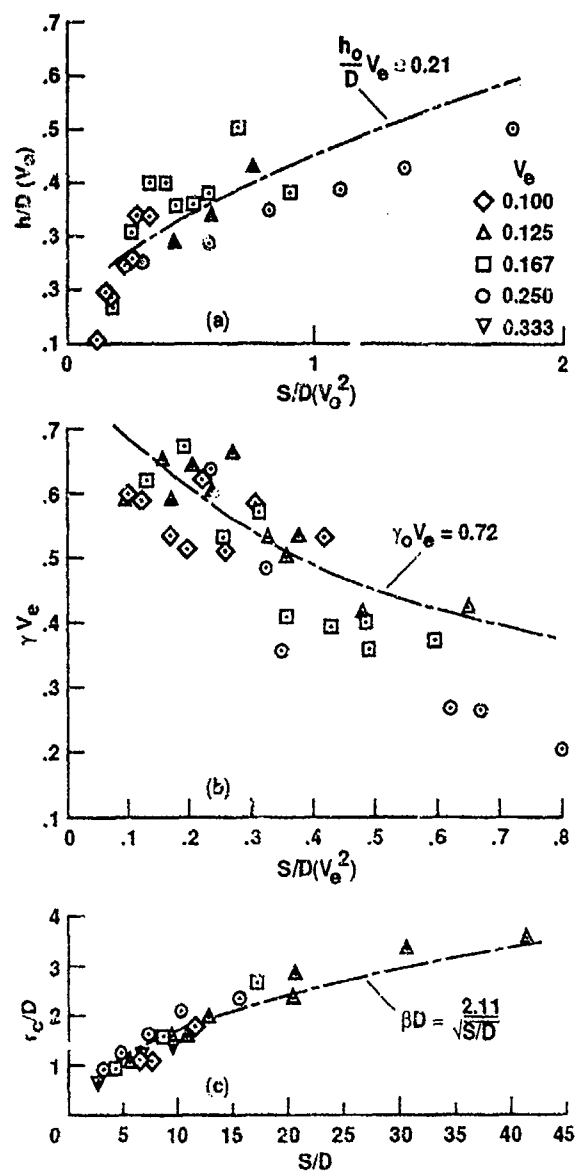


Figure 23.- Normalized vorticity properties from Smy and Ransom¹³ using data from Fearn and Weston⁹⁵.

- (a) Vortex lateral spacing along the jet vortex path.
 (b) Vorticity decay along the jet vortex path.
 (c) Vortex core radius along the jet vortex path.

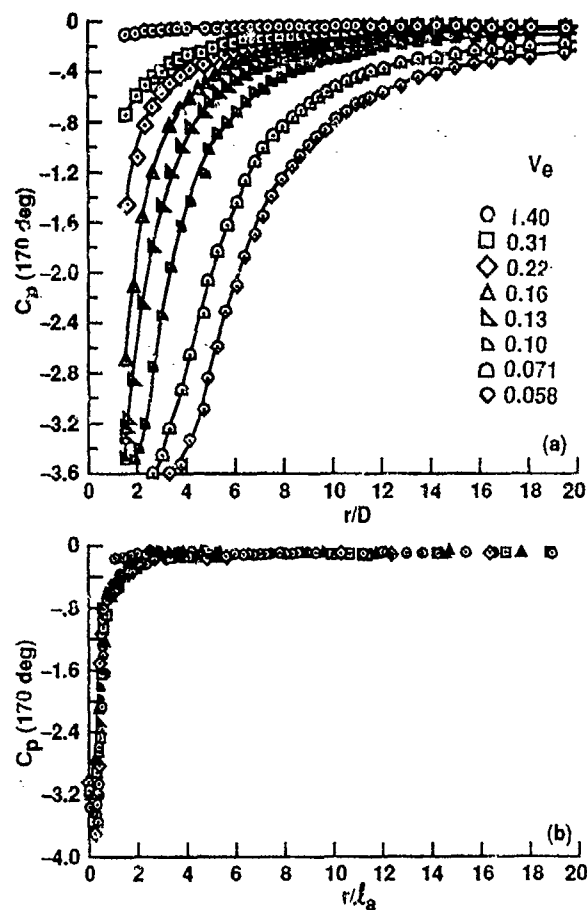


Figure 24 - Induced static-pressure coefficients on a flat plate ($M_\infty = 0.4$)¹⁴⁸.

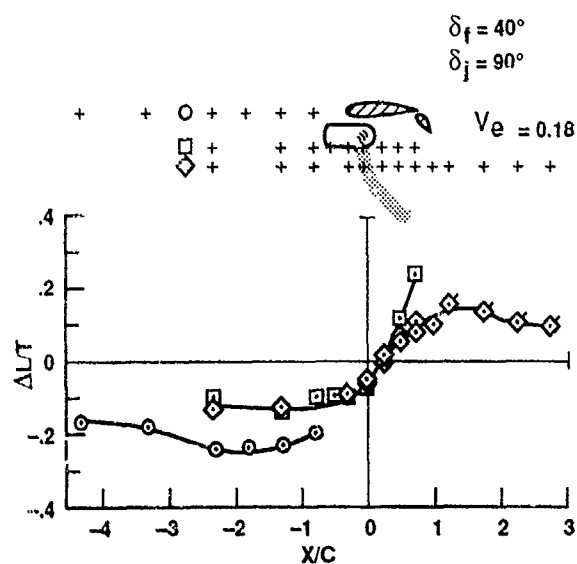


Figure 25.- Effect of varying the chordwise jet location relative to a nearby wing on the induced lift⁸².

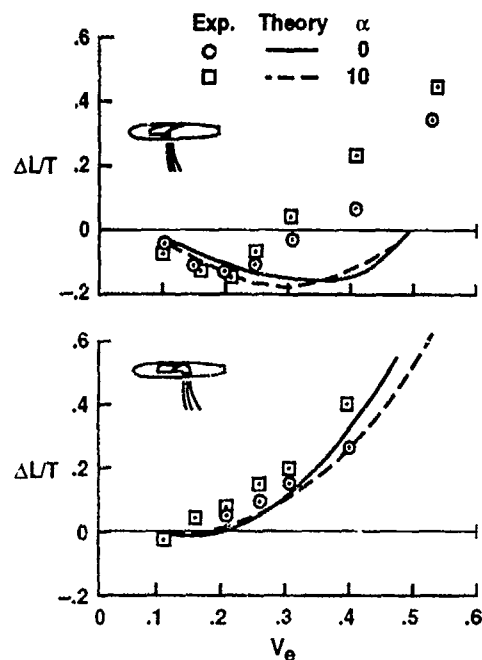


Figure 26.- Comparison between Wooler's method¹⁷¹ and experimental data¹⁶⁷.

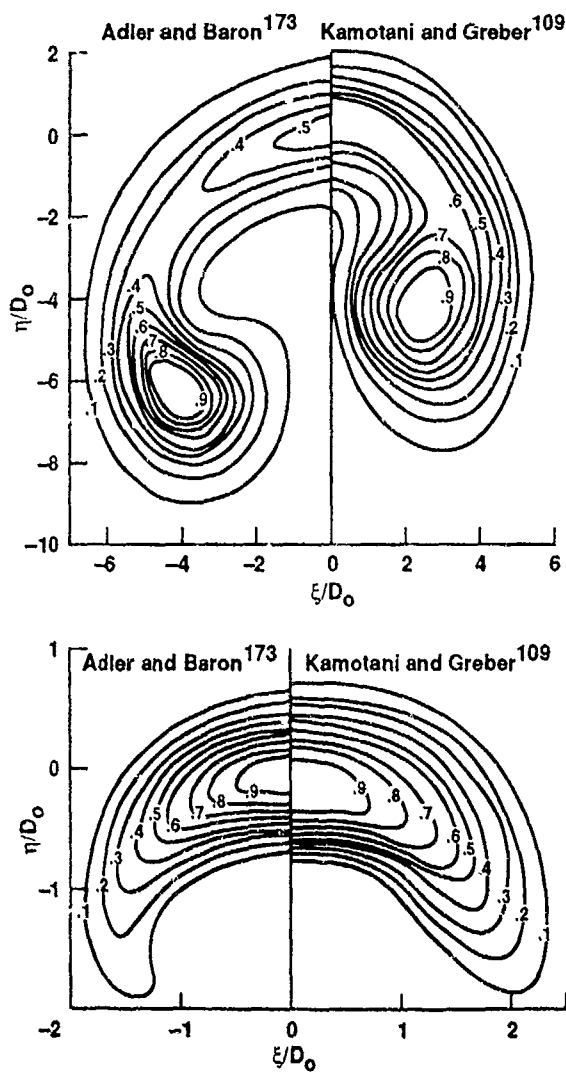


Figure 27.- Comparison between the Adler-Baron method¹⁷³ and experimental data¹⁰⁹ for two jet

cross sections showing constant velocity contours normal to the jet centerline path for $\delta_j=90^\circ$ and $V_e=0.129$.

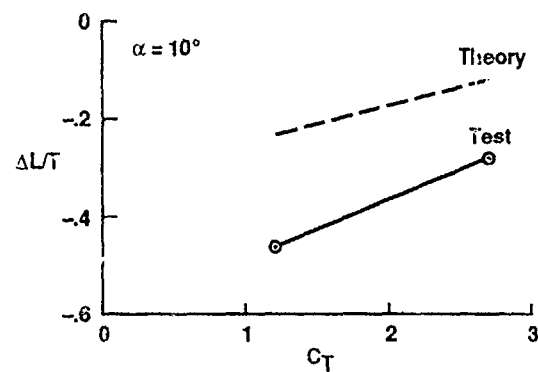
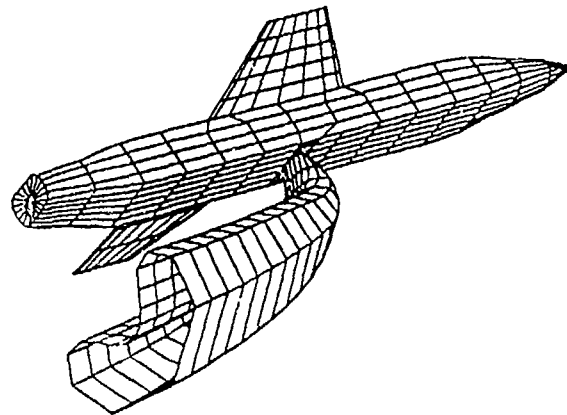


Figure 28.- Comparison of experimental data⁶⁸ and analysis of a V/STOL aircraft in transition flight using the PANAIR panel method²⁰⁹ and a parabolized Navier-Stokes jet wake model²¹².

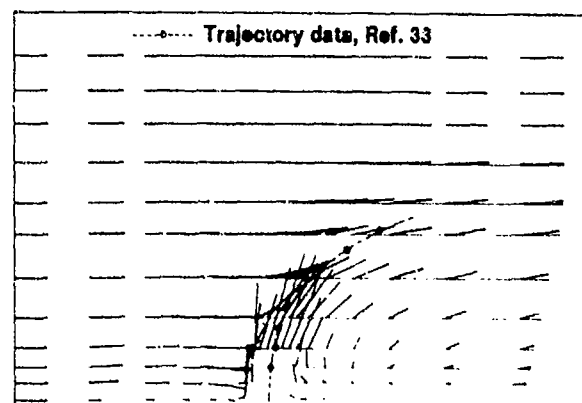


Figure 29.- Calculated¹⁹⁴ velocity vector plot for a JICF in the symmetry plane of jet for effective velocity ratio $V_e = 0.25$.

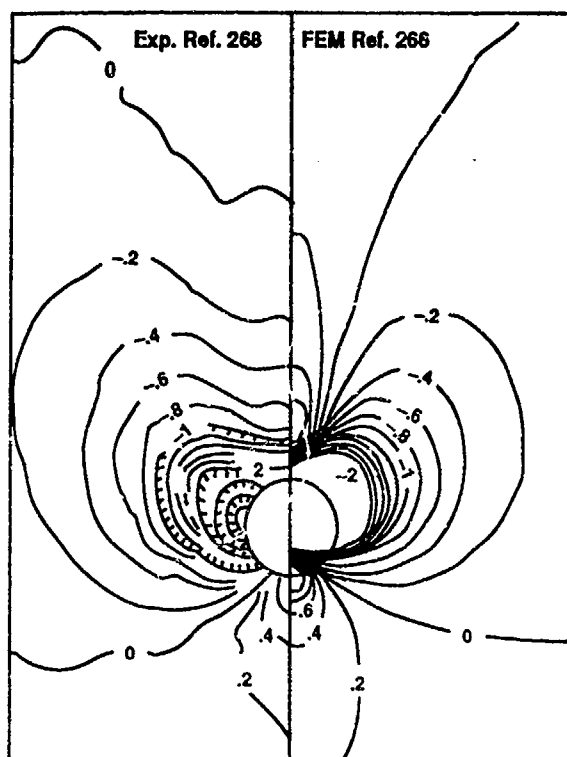


Figure 30.- Comparison of experimental²⁶⁸ and Navier-Stokes computation²⁶⁶ comparison of the pressure coefficients induced by a jet in a crossflow where $V_e = 0.25$.

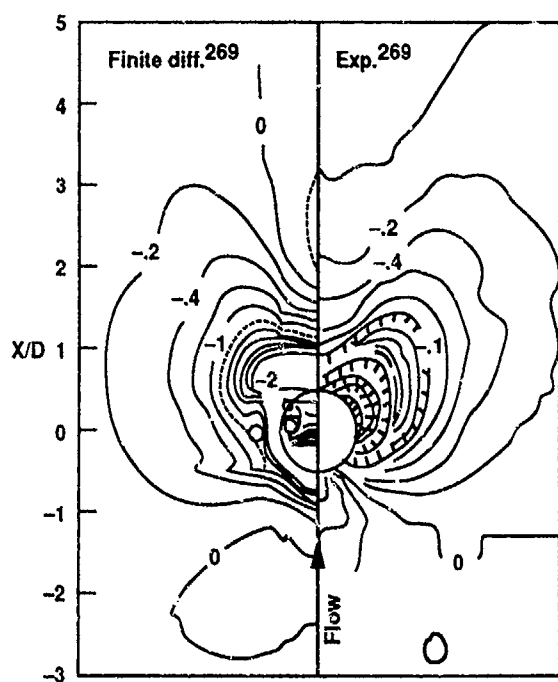


Figure 31.- Comparison of experimental²⁶⁸ and Navier-Stokes computation²⁶⁹ comparison of the pressure coefficients induced by a jet in a crossflow where $V_e = 0.25$.

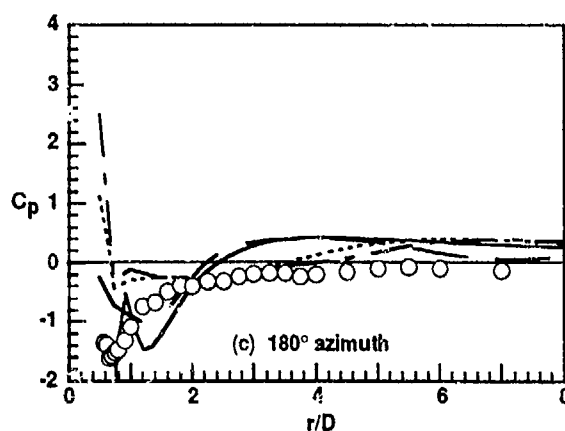
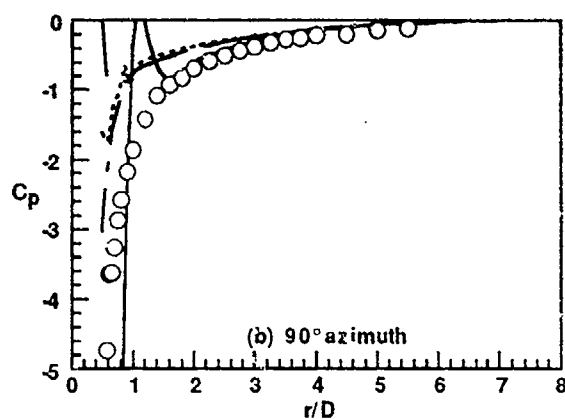
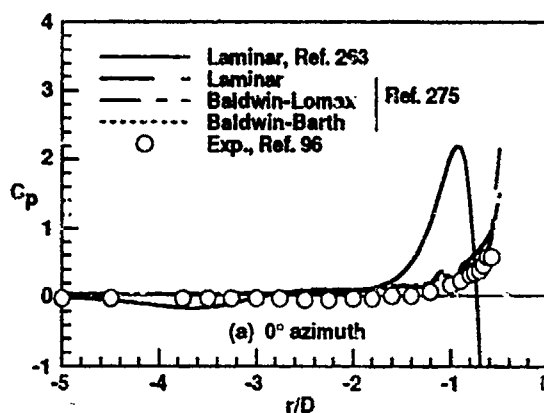


Figure 32.- Experimental⁹⁶ and Navier-Stokes computation^{263,275} comparison of the pressure coefficients induced by a jet in a crossflow where $V_e = 0.167$.

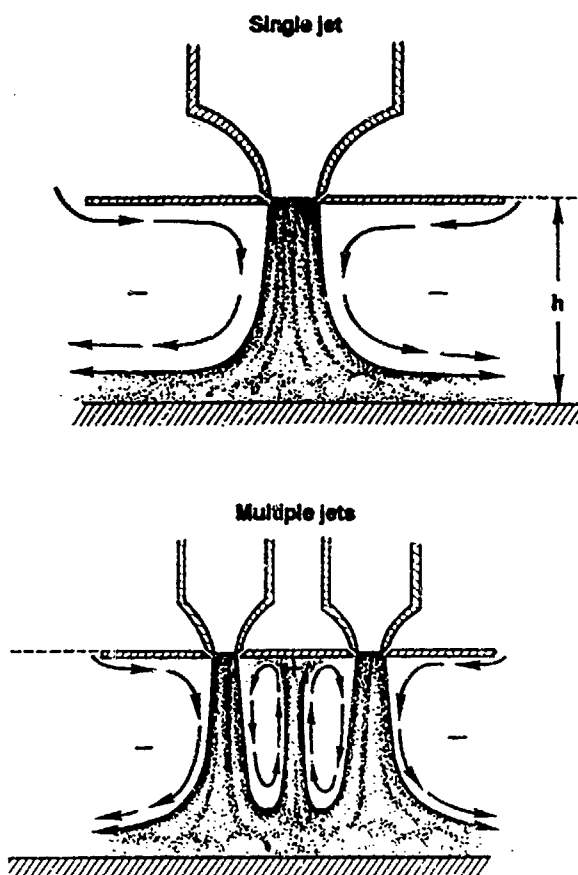


Figure 33.- Sketch of the jet-induced flow for single and multiple jets exiting vertically near the ground.

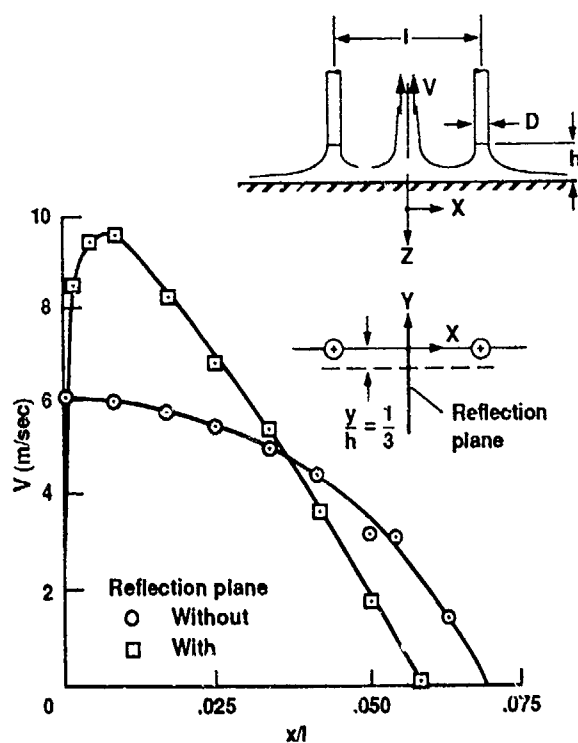


Figure 34.- Effect of a reflection plane on the measured upflow velocities caused by two jets exiting vertically near the ground ($h/D = 3$)²⁸⁸.

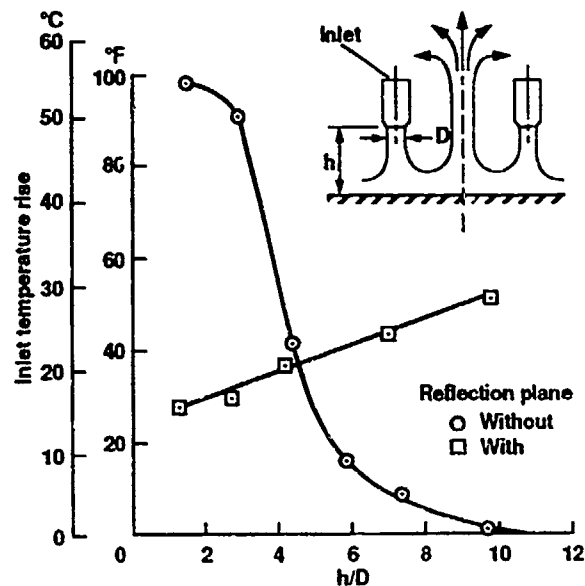


Figure 35.- Effect of a reflection plane on inlet air temperature rise from the fountain flow²⁸⁹.

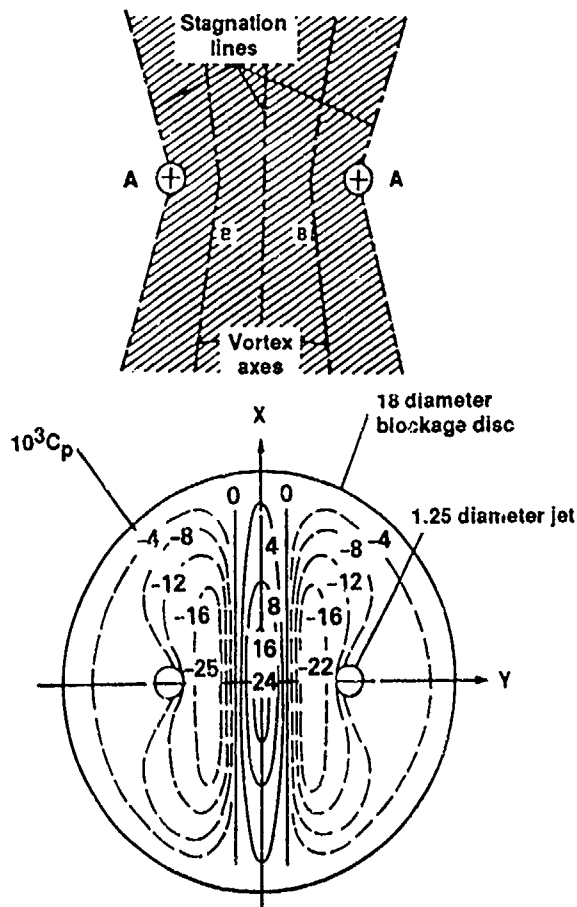
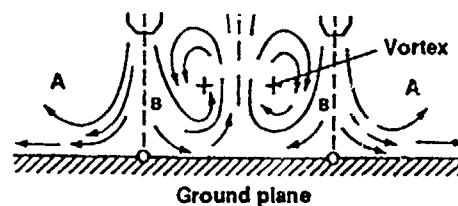


Figure 36.- Flowfield and induced pressure distribution for a twin-jet configuration²⁹⁰.

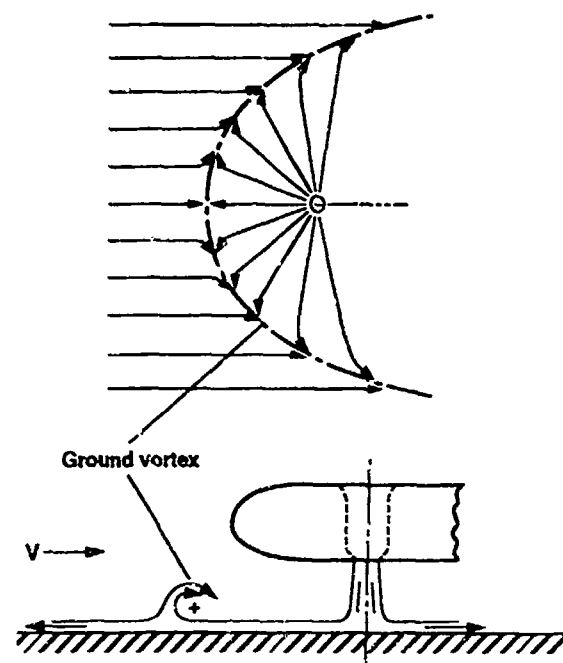
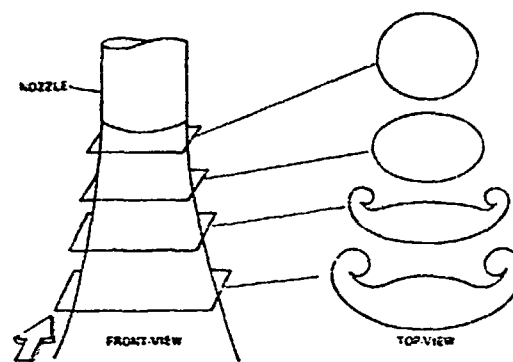
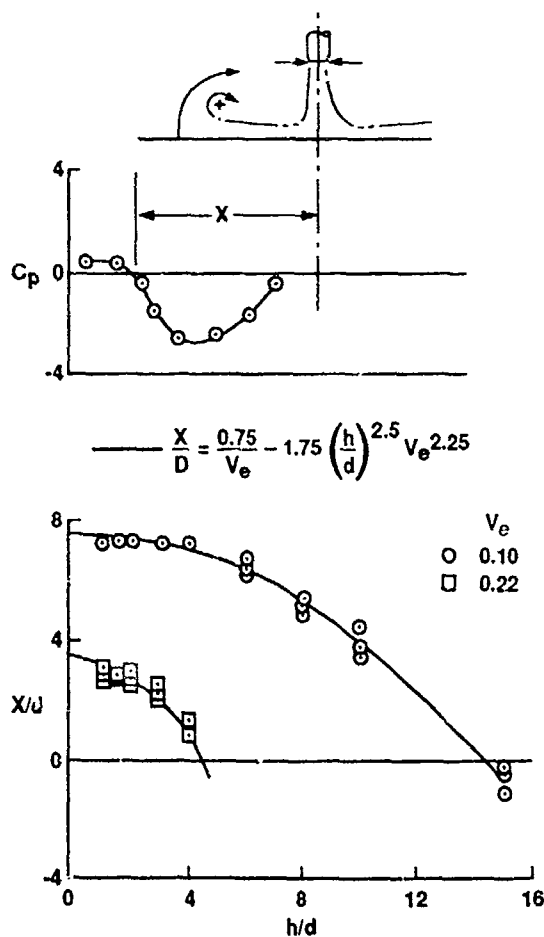
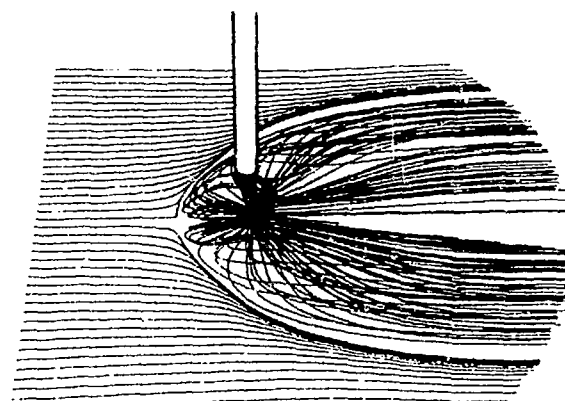


Figure 37.- Formation of the ground vortex.



(a) Observed deformation of the jet due to freestream flow induced pressures.

Figure 38.- Forward projection of the wall jet and ground vortex flowfield²⁹¹.(b) Side view of particle traces for a turbulent jet exiting from a nozzle with $V_e = 0.223$ and $h/D = 3$.Figure 39.- Computational results of a study of jet in ground effect (JIGE)²⁹².

TRANSIENT FLOW FEATURES OF A SUPERSONIC JET IN A LOW SPEED CROSS FLOW

by

X. Zhang^{*}, D.W. Hurst[†] and G.M. Lilley[‡]
 Department of Aeronautics and Astronautics
 Southampton University
 Southampton SO9 5NH
 United Kingdom

Summary

The transient features of a supersonic jet exhausting into a low speed cross flow were studied experimentally. The experiments were conducted in the Southampton University's 3.5 m × 2.6 m low speed wind tunnel. Three supersonic jets at ambient temperatures were used, one being a convergent nozzle and the other two being convergent-divergent nozzles having respectively design Mach numbers, $M_d=1.4$ and 1.7. Each jet issued in the normal direction to a flat plate mounted at zero incidence in the centre of the wind tunnel. The jet pressure ratio varied between 1.2 and 5.0 and the cross flow velocity between 14m/s and 38m/s. Both over-expanded and under-expanded jets were used. The low speed cross flow was found to introduce complex multiple narrow band tones. Changes in the transient flow modes and the levels of the tones were observed from time resolved pressure measurements at various positions on the flat plate.

1. Introduction

Jet/cross flow interaction has applications in many areas of aerospace such as heat transfer, combustion engineering, environmental engineering, V/STOL aircraft, missile and flow control, etc. Research in this area has mainly concentrated on low speed or subsonic jets in a low speed cross flow^{1,2,3} and supersonic jets in supersonic cross

flows^{4,5}. In all these experiments the jet exhausts from a flat plate in a direction normal to the cross flow. For the subsonic jet exhausting into a low speed cross flow, a prominent feature is the presence of a pair of contra-rotating longitudinal vortices, resulting from the momentum exchange between the jet and the cross flow, and producing a strong secondary flow field superimposed on the primary jet flow. The vortices are present at sub and supersonic flows and play an important role in defining the jet trajectory. The jet trajectory and time-mean surface pressure distribution on the flat plate surface have been extensively studied. For a supersonic jet exhausting into a supersonic cross flow, a barrel shock forms around the jet which is usually followed by a Mach disc. These shocks affect the penetration of the jet into the cross flow. Apart from a few cases, the time-dependent surface pressure characteristics have not received much attention.

In contrast with experiments on low speed jets, there have been relatively few studies of a supersonic jet in a low speed cross flow^{7,8,9}. In Shaw and Margason⁷, the time-mean surface flow on a flat plate induced by a supersonic jet in a cross flow was investigated. The effects of the cross flow and the jet pressure ratio were addressed. Again, the time-dependent features of the flow were not studied. However the time-dependent flow field induced by a supersonic jet is caused by different mechanisms from those due to a subsonic jet, and moreover these can have important structural and aerodynamic implications. For an axisymmetric

^{*}Research Fellow, now Lecturer, Department of Mechanical Engineering and Aeronautics, City University, London.

[†]Technical Manager, Wind Tunnel Facilities.

[‡]Professor

supersonic jet, pressure fluctuations inside the jet and its near field consist of components due to turbulent mixing, shock associated noise and narrow band tones where the latter do not exist in a low speed or subsonic jet. Pressure fluctuations due to these three mechanisms have quite different characteristics. The noise due to the turbulent mixing is highly directional¹⁰, with its peak intensity lying between 25° to 45° from the jet direction which is a function of jet Mach number and jet temperature. When the jet is not operating at the nozzle design Mach number shock cells appear in the jet. The interaction between the shock cells and the large scale regular turbulent structures observed in the jet mixing layer produces broad band noise and narrow band tones, e.g. screech. Unlike the noise due to turbulent mixing, the shock associated broad band noise is at its strongest in the upstream direction of the jet. The peak frequency of the noise spectrum is a function of the observation angle¹¹ and due to the Doppler effect its dominant lower frequency components are in the upstream direction of the jet. Apart from the broad band tones, which are observed for both over- and under-expanded jets, screech tones of toroidal (axisymmetrical) and helical (azimuthal) modes¹² are frequently observed. It is noted that the screech tone is at its strongest in the upstream direction of the jet and its frequency is bounded by the lowest frequency component of the broad band noise mentioned above. The screech tone exhibits some distinguishing features, such as a stepped behaviour^{13,14,15}, randomness in the direction of the helical mode, mode modulation¹⁶ and a standing wave like nearfield dynamic pressure distribution^{17,18}.

In this paper, results of the time-dependent pressure measurements on the surface of a flat plate which are induced by a supersonic jet/low speed cross flow interaction are presented and discussed. Particular attention is given to the generation of narrow band tones on the flat plate. The jets employed include choked, over- and under-expanded jets of high Reynolds number and ambient temperature. In all these experiments, the jet has to pene-

trate an oncoming turbulent boundary layer before exhausting and interacting with the low speed cross flow.

2. Description of Experiment

The tests were conducted in the 3.5 m×2.6 m low speed, closed circuit, wind tunnel in the Department of Aeronautics and Astronautics, Southampton University, U.K. The maximum wind tunnel working section speed was 55m/s. To study the effect of the cross flow, the wind tunnel speed was varied between 0m/s and 38m/s. Two tunnel speeds (25.6m/s and 34.4m/s) were used extensively to test the effects of jet pressure ratio. The Reynolds number, Re , based on the freestream cross flow velocity, density and viscosity and the nozzle exit diameter varied between 2.4×10^4 and 6.5×10^4 . In a full length run lasting about 20 to 25 minutes, the air temperature in the wind tunnel rose slightly but was taken as a constant value when the data were processed.

Detailed descriptions of the experiment are given in Zhang and Hurst^{8,9}. A schematic of the test set-up is shown in Fig. 1. A cartesian coordinate system is used to define the measurement space, where the positive x-axis refers to the downstream cross flow direction along the flat plate centre line, the y-axis is the spanwise direction and the positive z-axis is the jet exit direction. The flat plate is 1219 mm long, 914 mm wide, and 12.7 mm thick. The nozzle exit diameter, D , is 25.4 mm and its centre is located 559 mm from the leading edge of the plate. The plate is supported by a steel frame above the tunnel floor in the tunnel working section to ensure a clear view of the flat plate and the jet from the side windows of the tunnel so that flow visualization could be performed. The distance between the plate and the tunnel roof is 1549 mm. Three nozzles were used in the test. They include a convergent nozzle, a con-di nozzle ($M_d=1.4$) and a con-di nozzle ($M_d=1.7$). They are all made from duralumin. The length of the nozzle is 152 mm. The convergent nozzle geometry was based on the

nozzle contour used in the experiments of Seiner and Norum^{19,20}. The jet pressure ratio between the stagnation pressure in the nozzle plenum chamber and the ambient pressure, $P_r (= P_o/P_e)$, varies from 1.2 to 5.

Apart from pressure tapings, a total of 11 pressure transducer ports were installed (Fig. 2). Since the flow was assumed to be symmetrical about the x-axis, only one half of the plate was heavily instrumented by the pressure tapings with the other half reserved for the transducers⁸. All the instrumentation including pressure tapings, pressure transducers, thermocouples and their connections were located underneath the flat plate. These items along with the nozzle block were shielded by a streamlined fairing. A flap was attached to the flat plate at the trailing edge (Fig. 1) to offset the blockage effect of the fairing. Oil flow experiments were carried out to ensure a satisfactory surface flow field without the presence of the jet flow by setting the correct angle for the trailing edge flap. To achieve a satisfactory flow along the leading edge of the plate boundary layer transition was fixed using a 38mm wide sand strip applied to the upper surface of the flat plate immediately downstream of the leading edge.

Two series of time-dependent surface pressure tests were conducted. The first test used four transducers positioned along the positive x-axis ($X=2, 4, 6$ and $8D$). The second test used five transducers on an $R=6D$ half circle ($\phi=180^\circ, 225^\circ, 270^\circ, 315^\circ$ and 0°). In the time-dependent surface pressure measurements, five Kulite XCQ-62-A-100 miniature pressure transducers were employed. The pressure transducers were mounted flush to the plate surface using specially built plugs. Because of the weak signal (about 125 mv full scale deflection) and the long distance between the test rig and data recording unit (10 m), the signals were amplified and filtered to ensure better signal quality and to avoid common mode riding. The signals from four of the five transducers were amplified 1000 times by four FE-359-TA amplifiers, which also served as

transducer power supplies. The amplified signals were then low pass filtered by four Barr & Stroud EF5-02 filters at 20 kHz before being recorded onto tape using a Racal 7D type recorder. The one signal left was amplified 500 times by a Barr & Stroud FE-351-UA amplifier. This transducer's power supply was a Farnell stabilized power supply unit. This signal was filtered by a Rockland Mode 432 LP/HP filter. The reason for using this arrangement was that there were only four Barr & Stroud EF5-02 filters available. The tape recorder had a bandwidth of 20 kHz. AMPEX tapes (12.4 mm) were used as the storage media. Care was taken to ensure good signal quality during its transmission.

To analyze the pressure data, the analogue signals were digitized at 40 or 50 kHz by a MASS-COMP computer and then calibrated. The bandwidths of the spectrum analysis were 19.53 Hz and 24.41 Hz respectively. After comparing results of spectral analysis using data segments of different lengths, it was decided that a one second data segment was long enough to give sufficient accuracy in the analysis. The analyses carried out on the pressure data included auto-correlation and cross-correlation analyses, etc. When the cross-correlation analysis was undertaken, care was taken to correct phase errors introduced by the small mis-alignment in the play-back head of the tape recorder.

Data are presented here in the form of sound pressure level (SPL), power spectral density (PSD), etc., where SPL is defined as

$$SPL \text{ DB} = 20 \log_{10} \left(\frac{p'_{rms}}{2 \times 10^{-5} P_a} \right) \quad (1)$$

where p'_{rms} is the root-mean-square value of the surface pressure. The power spectrum is given as sound power level in DB in a frequency band of width 1 Hz. The reference value of the power spectral density is $2 \times 10^{-5} \text{ Pa}$. The length scale used to correlate the experimental data is the fully expanded jet diameter, D_j , as defined by Tam and Tanna²¹.

In order to study the possible interference of the wind tunnel roof on the time-dependent flow characteristics, a foam sheet was placed on the tunnel roof and the surface pressure fluctuation characteristics were measured using jets from the $M_d=1.4$ con-di nozzle operating at $P_r=1.2-5.0$ without the cross flow. The results were compared with data taken when the foam sheet was removed. Generally, the major jet modes were still observed and the changes in SPL were negligible.

3. Results and Discussion

3.1 Effect of jet operating conditions

Transient flow characteristics of a supersonic jet in a low speed cross flow are closely related to the appearance of shock cells in the jet. In our experiments the jet flow was subsonic, transonic, over- or under-expanded, or fully expanded depending on the jet pressure ratio and nozzle geometry. The corresponding case of the noise radiated from supersonic con-di jets exhausting into ambient air is described by Tam and Tann²¹. In the present experiment, time resolved surface pressures downstream of the jet are measured together with time-mean surface pressures, from which the normal force coefficient, C_F , is evaluated⁸. Fig. 3 gives the variation in the SPL at one position on the flat plate, and in Fig. 4, the variation in the normal force coefficient for the $M_d=1.4$ con-di nozzle, run under subsonic, over-expanded and under-expanded conditions. The apparent scatter of data in Fig. 3 near the sonic condition could be caused by insufficient pressure tapings downstream of the jet exit⁸. When the jet is subsonic, the SPL increases with P_r while C_F decreases. When the jet is supersonic, the changes in SPL and C_F indicate close correlation between the appearance of the shock cells and time-mean flow characteristics. In Fig. 3, the SPL drops near $P_r=3.1$ as the jet approaches the perfectly expanded state, and levels off when $P_r > 4$ where Mach discs appear. Generally, C_F follows the unsteady flow characteristics closely and increases along with SPL in the supersonic regime.

In Fig. 3 and Fig. 4, it is possible to identify some of the changes in C_F and SPL to the appearance of shock cells.

The effect of the cross flow is also illustrated in Fig. 3 and Fig. 4 where it is seen, the SPL experiences relatively small changes when the jet is supersonic. On the other hand C_F becomes less negative as the cross flow velocity is increased. This is the result of the decrease in pressure in the wake region following the jet exit⁸.

The jets generated by the $M_d=1.4$ con-di nozzle cover all the jet modes of interest (subsonic, over-expanded, and under-expanded). Changes in PSD with P_r at a downstream location are shown in Fig. 5 for a constant cross flow velocity. When the subsonic jets are exhausted into the cross flow no narrow band tones are observed on the flat plate. The noise, as detected on the flat plate, comes from the turbulent mixing in the jet and the pressure fluctuation in the boundary layer on the flat plate. A screech tone at 8310 Hz first was observed on the flat plate at $P_r=2.36$, which is associated with an unsteady mode in the jet. At this jet pressure ratio, the jet is over-expanded. As P_r is increased, the shock cell length is increased and it is seen the frequency of the tone drops. At higher pressure ratios, instead of a single peak in the PSD, multiple peaks were observed, indicating that the transient flow field is now dominated by more than one mode. At $P_r=2.52$, two peaks at 6553 Hz and 7588 Hz appear in the PSD. While the 7588 Hz tone is in the same mode as the one reported early, the 6553 Hz one is new. The appearance of multiple modes is induced by the presence of the cross flow (see section 3.5). Tests using the $M_d=1.7$ con-di nozzle indicate the same phenomenon. When the jet pressure ratio approaches the design value the screech tones gradually disappear. After the jet pressure ratio is increased above the nozzle design pressure ratio the jet becomes under-expanded. Again, the tone frequency decreases with P_r as the shock cell length increases and the surface pressure fluctuations become stronger until Mach discs begin to form in the

jet. The PSD at $P_r=3.52$ shows a single peak at 5195 Hz.

The appearance of multiple modes for a given cross flow is not confined to the over-expanded jets only. Tests using the convergent nozzle and the $M_d=1.4$ con-di nozzle show that, when an under-expanded jet is operated near the nozzle design condition, multiple modes are also present. These tones are also affected by the cross flow.

3.2 Relationship between jet unsteady mode and jet operating condition

In addition to the fall in the frequency of the observed tone on the flat plate with rise in P_r as the jet operating condition changes, the mode of the transient flow field also changes. In the present study, the presence of the flat plate provides a reflection surface for the disturbances, which could enhance the excitation of the unsteady modes in the jet. When the jet is over-expanded, the dominant mode is normally toroidal (axisymmetrical). When the jet is under-expanded, the dominant mode is usually helical (azimuthal), with the disturbances travelling clockwise or anticlockwise when viewed in the downstream direction. The mode of the transient flow field is determined through cross-correlation analyses of data taken at the five equal spaced pressure transducer ports on a $R=6D$ half circle on the flat plate (Fig. 2). When the mode is toroidal, the phase shift between two samples is nearly zero without the cross flow and varies linearly according to the streamwise distance between the transducers with the cross flow. When the mode is helical, the phase shift varies in both the cases of zero cross flow and cross flow. In the present experiment, time resolved measurements on the flat plate indicate the presence of a so-called flapping mode²², where the left- and right-hand helical disturbances are excited simultaneously in the jet. The above properties can be used to determine this mode. In Fig. 5, two peaks are observed in PSD at $P_r=2.52$, the dominant tone at 7588 Hz is of toroidal mode and the new one at 6553 Hz is of

helical mode.

Another method of determining the jet structural modes is through the measured SPL. The toroidal mode is found when nearly the same SPL values are observed on the $R=6D$ circle, while the helical mode is found when a substantially higher SPL value is observed in one direction. In Fig. 6 the changes of SPL at $\phi=0^\circ$, 180° and 270° are given at a constant cross flow velocity. When the jet is subsonic ($P_r \leq 2.0$), the SPL values at $\phi=180^\circ$ and 270° are nearly the same. These two positions are located outside the footprint of the wake downstream of the jet exit. The $\phi=0^\circ$ transducer is located in the wake and the SPL value there is subsequently higher than those taken outside the wake region. When the jet is over-expanded, the SPL changes with the shock strength. In this case the dominant mode is toroidal. However, the appearance of the new helical mode results in an increase of the SPL upstream of the jet exit ($\phi=180^\circ$). In the present experimental study the SPL values measured up and downstream of the jet exit are significantly higher than those measured in the direction to the side of the jet exit at $\phi=90^\circ$. This phenomenon points to the existence of excited left- and right-hand helical disturbances in the jet direction²². As the jet approaches the perfectly expanded state, the tones disappear and the higher SPL value downstream of the jet exit is again due to the wake following the jet. The development of the SPL after the jet becomes under-expanded shows that the dominant mode is helical and that the direction of the flapping mode is fixed by the cross flow. The SPL values at the upstream position ($\phi=180^\circ$) and the downstream position ($\phi=0^\circ$) are significantly higher than those measured to the side of the jet exit ($\phi=270^\circ$).

3.3 Wavelength of the screech tone

An important parameter in characterizing the transient features of the flow is the wavelength, λ , of the narrow band tone. In Fig. 7, the wavelengths are presented at a constant cross flow speed for the

three nozzles tested. Apart from the toroidal and helical modes, there are other weak modes in the flow field. The dominant modes, though, are always toroidal or helical. λ is plotted against the jet Mach number parameter, $\beta(=\sqrt{M_j^2 - 1})$. A linear relation exists between the two parameters, λ and β , which is consistent with the observation made with supersonic jets in ambient air.

As the helical mode is the frequently observed mode, attempts have been made in the past to predict its wavelength. Certain useful semi-empirical formulae have been based on the existence of feedback mechanisms^{13,14}. If the temperature difference between the jet and the external environment is taken into account, the wavelength, λ , of the helical mode of an axisymmetrical supersonic jet is given by²³

$$\frac{\lambda}{D_j} = \frac{L}{D_j} \cdot \left(1 + \frac{V_c}{a_o}\right), \quad (2)$$

where L is the averaged shock cell length and is given as

$$L = 0.87 \times 1.22\beta D_j, \quad (3)$$

a_o is the ambient speed of sound and V_c the disturbance convective speed. The fully expanded jet temperature and the external air temperature are taken into account in equation(2). The cross flow velocity is, however, not taken into account. In equation (2), a_o is calculated from the ambient air temperature. V_c varies between $0.65V_l$ to $0.75V_l$, where V_l is the local flow speed. The most commonly used value is 0.7. In the present study, three values, 0.65, 0.7 and 0.75, are used. The local flow speed is taken as the fully expanded jet speed, V_j , which is calculated using the jet pressure ratio and the stagnation temperature of the jet. In calculating V_j , the total pressure loss due to the appearance of the shock in the jet plume is taken into consideration. The averaged shock cell length was not directly measured in the experiment. Instead, previous experimental data were used. The value of L was given by Abdel-Fattah²⁴ as $0.87L_2$, where L_2 is the second shock cell length. Abdel-Fattah's

value was based on tests using a con-di nozzle. The second shock cell length L_2 was given by Pack²⁵ as $1.22D\beta$. However, the value 1.22 was calculated without considering the jet plume size change with a change in the jet modes. In the present study, the fully expanded jet diameter, D_j , was used.

At a tunnel speed of $V_e=25.7\text{m/s}$, predictions of the screech tone wavelength are compared with the experimental data (Fig. 7(b)). The predictions are based on $V_c=0.7V_j$. The wavelength of the narrow band tone of helical mode is predicted rather well for all the test cases. Predictions for other cases in the present test show a similar result. The wavelength of the screech tone is seen to increase linearly with the fully expanded jet Mach number parameter, β . Also included in Fig. 7(b) is the measured wavelength of the helical mode of an axisymmetrical jet produced by an $M_d=1.41$ con-di nozzle²³. It seems that the presence of the flat plate in the current study does not alter the basic excited unsteady mode.

3.4 Mode switch

In performing the time-series analysis, the ensemble averaging method was used to calculate the power spectrum densities. For the flow field where multiple modes exist, an analysis was performed whereby a one second data segment was divided into data blocks. Each data block contained 512 data points. A Fourier transform analysis was applied to each of the data blocks. Results of the analysis show that the multiple modes do not normally co-exist at the same time. A mode switch occurs in a very short time interval and apparently at random. Fig. 8 shows the switch of dominant modes for an over-expanded jet at $P_r=3.4$ produced by the $M_d=1.7$ con-di nozzle. The mode at either 5449 Hz or 6728 Hz could be the only one present in a finite time duration.

3.5 Effect of cross flow

In studying the effect of the cross flow the jet

pressure ratio, P_r , was kept constant and the cross flow velocity was varied between 0m/s and 38m/s. Analyses of the surface pressure data show that the cross flow exercises a considerable influence on both the mode and the level of the transient surface pressure.

When the surface flow is induced by an over-expanded jet in a low speed cross flow, the effects of the cross flow differ according to the jet structural modes involved. When the transient flow is dominated by a single toroidal mode, a rise of the cross flow speed generally changes the narrow band tone observed on the flat plate into a broad band one. The narrow band tone is probably damped by the increased level of turbulent mixing in the jet and the cross flow. The cross flow also introduces fundamental changes in the dominant mode. These changes are demonstrated in Fig. 9. The over-expanded jets were generated from the $M_d=1.7$ con-di nozzle. At the lower cross flow velocities a narrow band tone at 5361 Hz is observed. Minor changes appear with a change in the cross flow velocity. The harmonic at 10684 Hz disappears at $V_e=34.5$ m/s. Finally, a broad band tone centred around 6180 Hz begins to appear. With a further increase of the cross flow speed, the frequency composition is changed fundamentally. Two modes (6142 Hz and 6728 Hz) now exist. At $V_e=34.5$ m/s, the screech mode at 5449 Hz is still the dominant one. However, the dominant mode is switched to the high frequency modes, which is indicated by the two peaks at 6142 Hz and 6728 Hz at the high cross flow velocity of 38.2m/s. The reason for the appearance of these modes is considered to be the result of the changes in the circular jet cross-section into a kidney shaped cross-section after the end of the shock cells as a result of the cross flow. The modal structure of the jet changes and this introduces new modes.

The response of an under-expanded jet to the changes in the cross flow velocity is different from those described above. In Fig. 10 results of a slightly under-expanded jet produced by the con-

vergent nozzle are shown. A toroidal mode at 6279 Hz is observed at the lower cross flow velocities in addition to the dominant helical mode at 5527 Hz. In the present test the multiple modes dominated by the transient flow are rarely observed when the jet is under-expanded. When they do occur the jet pressure ratio is usually low or near the nozzle design pressure ratio. When the multiple modes appear a rise of the cross flow velocity makes the mode weaker. Moreover, the observed narrow band tone associated with the toroidal mode gradually becomes broader and disappears.

The effect of the cross flow on the transient surface pressure is shown in Fig. 11. The effect of the tone mode switch is particularly important when the jet is over-expanded. The SPL measured when the jet is subsonic (Fig. 11a) and in the near perfectly expanded state (Fig. 11c) demonstrates that there are no screech modes and the noise arises from the turbulent mixing. This increases with cross flow velocity. The SPL values measured downstream of the jet exit are higher than those outside of the wake region and it follows that the increased level of turbulent mixing in the wake region contributes to the higher SPL. When the jet is over-expanded (Fig. 11b) the mode switch between the toroidal mode and helical mode brings a sudden rise in SPL upstream of the jet exit. This phenomenon is observed for nearly all the over-expanded jets tested. When the jet is under-expanded (Fig. 11d), the dominant tone is of helical mode and the direction is fixed by the cross flow. As a result, the SPL values measured upstream and downstream of the jet exit on the flat plate ($\phi=180^\circ$ and 0°) are higher than those measured in the spanwise direction to the side of the jet exit ($\phi=270^\circ$). The sudden rise in the SPL value at the upstream position ($\phi=180^\circ$) is further illustrated by the mode changes shown in Fig. 12. The jets in this case are produced by the $M_d=1.7$ con-di nozzle and are also over-expanded. The dominant tones change with the cross flow from a single mode to multiple modes, and this introduces a rise in the SPL value.

4. Concluding Remarks

In the present experimental investigation, the unsteady flow characteristics of supersonic jets issuing in the normal direction to a flat plate mounted at zero incidence in the centre of the wind tunnel were studied. It was found

(1) A close relationship exists between the appearance of shock cells and time-mean normal force coefficient measured on the flat plate.

(2) When the jet is over-expanded the dominant mode in the flow field is toroidal. When the jet is under-expanded the dominant mode is helical.

(3) Multiple modes are induced by the cross flow when the jet is over-expanded or slightly under-expanded. This is considered to be the result of the change in the cross-sectional shape of the jet. When the jet is over-expanded the transient flow field can be changed from that dominated by a toroidal mode to that of multiple toroidal and helical modes. When the jet is slightly under-expanded the transient flow field can be changed from that dominated by multiple modes to that of a single helical mode. The multiple modes are not necessarily co-existing at the same time. A mode switch occurs frequently and at random.

(4) When the dominant mode is helical the presence of the cross flow results in higher SPL values upstream and downstream of the jet exit and lower SPL value to the side of the jet exit.

(5) A linear relation exists between the wavelength of the helical mode, λ , and the jet Mach number parameter, β . The wavelength of the helical mode can be predicted by a semi-empirical formula.

Acknowledgement

This research is supported by Royal Aerospace Establishment under contract D/ERI/9/4/2040/4

33.

References

- [1] Fearn, R. L. and Weston, R. P., "Induced velocity field of a jet in a crossflow," NASA TP-1087, 1978.
- [2] Fearn, R. L. and Weston, R. P., "Velocity field of a round jet in a crossflow from various jet injection angle and velocity ratios," NASA TP-1506, 1979.
- [3] Chiu, S., Roth, K. R., Margason, R. J. and Tso, J., "A numerical investigation of a subsonic jet in a crossflow," AIAA Paper 93-0870, 1993.
- [4] Schetz, J. A., Hawkins, P. F., and Lehman, H., "The structure of highly underexpanded transverse jets in a supersonic stream," *AIAA Journal*, Vol. 5, 1967, pp. 882-884.
- [5] Billig, F. S., Orth, R. C., and Lasky, M., "A unified analysis of gaseous jet penetration," *AIAA Journal*, Vol. 9, Part 6, 1971, pp. 1048-1058.
- [7] Shaw, C. S., and Margason, R. J., "An experimental investigation of a highly under-expanded sonic jet ejecting from a flat plate into a subsonic cross flow," NASA TN D-7314, 1973.
- [8] Zhang, X. and Hurst, D. W., "Surface flow on a flat plate induced by a supersonic jet exhausting normally into a low speed crossflow," AIAA Paper 90-3011, 1990.
- [9] Zhang, X. and Hurst, D. W., "A laser Doppler anemometry study of a supersonic jet in a low speed cross flow," Proceedings of the 4th International Conference on Laser Anemometry, Advance and Applications, Vol. 2, August 1991, Cleveland, Ohio, U.S.A., pp. 403-411.
- [10] Yu, J. C. and Dcsanjh, D. S., "Noise field of a supersonic Mach 1.5 cold model jet," *The Journal of the Acoustical Society of America*, Vol. 51, Part 5, 1972, pp. 1400-1410.
- [11] Harper-Bourne, M. and Fisher, M. J., "The noise from shock waves in supersonic jets," AGARD CP-131, 1973, pp. 11.1-11.13.
- [12] Yu, J. C. and Seiner, J. M., "Nearfield observations of tones generated from supersonic jet flows," AIAA Paper 83-0706, 1983.

- [13] Powell, A., "On the noise emanating from a two-dimensional jet above the critical pressure," *The Aeronautical Quarterly*, Vol. 4, 1953, pp. 103-122.
- [14] Powell, A., "On the mechanism of the choked jet noise," *Proceedings of the Physical Society*, B66, 1953, pp. 1039-1056.
- [15] Norum, T. D., "Screech suppression in supersonic jets," *AIAA Journal*, Vol. 21, 1983, pp. 235-240.
- [16] Seiner, J. M., Manning, J. C. and Ponton, M. K., "The preferred spatial mode of instability for a Mach 2 jet," AIAA Paper 86-1942, 1986.
- [17] Westley, R. and Woolley, J. H., "The near field sound pressures associated with a spinning screech mode," Conference on current developments in sonic fatigue, ISVR, University of Southampton, 1970.
- [18] Westley, R. and Woolley, J. H., "The near field sound pressures of a choked jet when oscillating in the spinning mode," AIAA Paper 75-479, 1975.
- [19] Seiner, J. M. and Norum, T. D., "Experiments of shock associated noise on supersonic jets," AIAA Paper 79-1526, 1979.
- [20] Seiner, J. M. and Norum, T. D., "Aerodynamic aspects of shock containing jet plumes," AIAA Paper 80-985, 1980.
- [21] Tam, C. K. W. and Tanna, H. K., "Shock associated noise of supersonic jets from convergent-divergent nozzles," *Journal of Sound and Vibration*, Vol. 81, 1982, pp. 337-358.
- [22] Seiner, J. M., Manning, J. C., and Ponton, M. K., "The Preferred Spatial Mode of Instability of a Mach 2 Jet," AIAA Paper 86-1942, July 1986.
- [23] Tam, C. K. W., "Jet Noise Generated by Large-Scale Coherent Motion," *Aeroacoustics of Flight Vehicles: Theory and Practice*, NASA Reference Publication 1258, Vol. 1, August 1991, pp. 311-390.
- [24] Abdel-Fattah, A. M., "Discrete tone emission from high-pressure ratio supersonic jets from convergent-divergent nozzle," *AIAA Journal*, Vol. 26, Part 3, 1988, pp. 283-291.
- [25] Pack, D. C., "A note on Prandtl's formula for the wave length of a supersonic gas jet," *Quarterly Journal of Mechanics and Mathematics*, Vol. 3, Part 2, 1950, pp. 173-181.

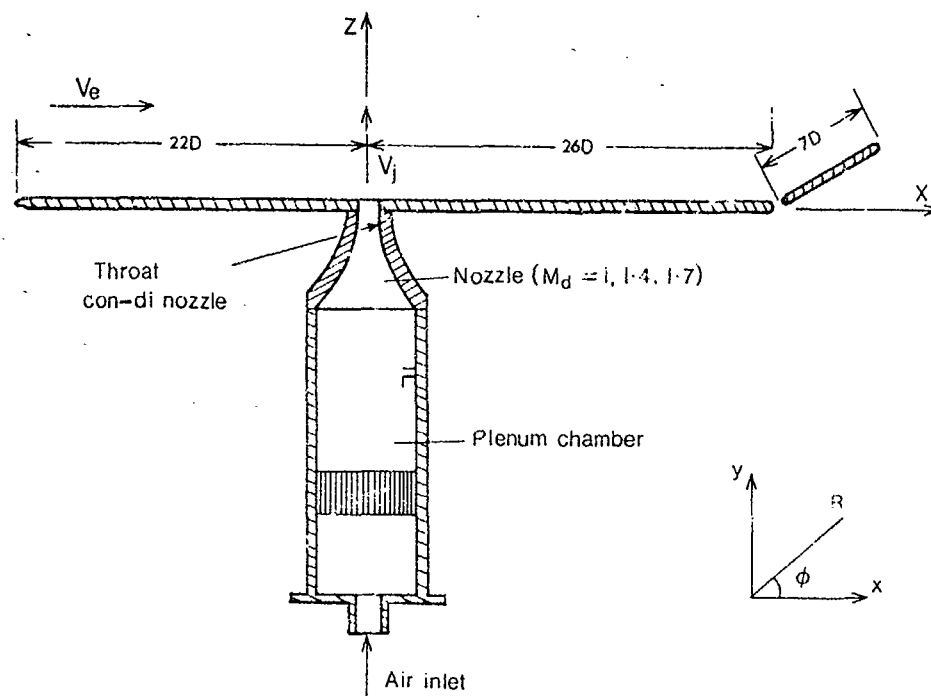


Fig. 1 Schematic of the test set-up with coordinates in the surface of the flat plate.

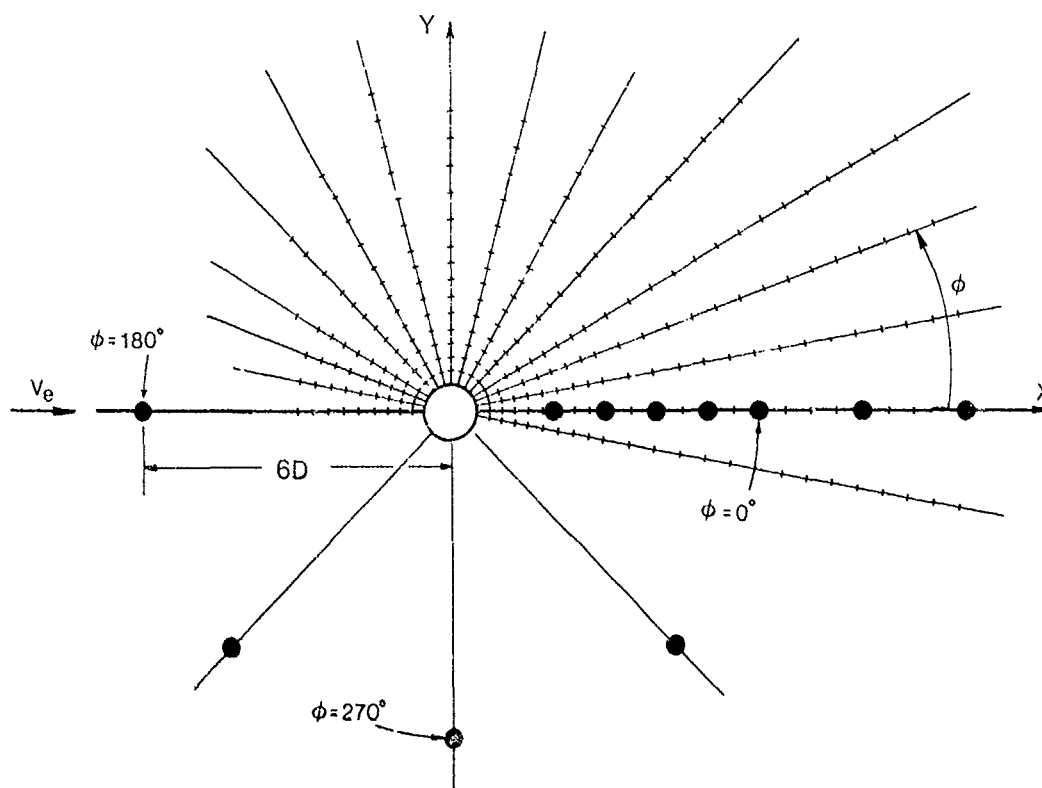


Fig. 2 Positions of pressure transducers and tappings on the flat plate.

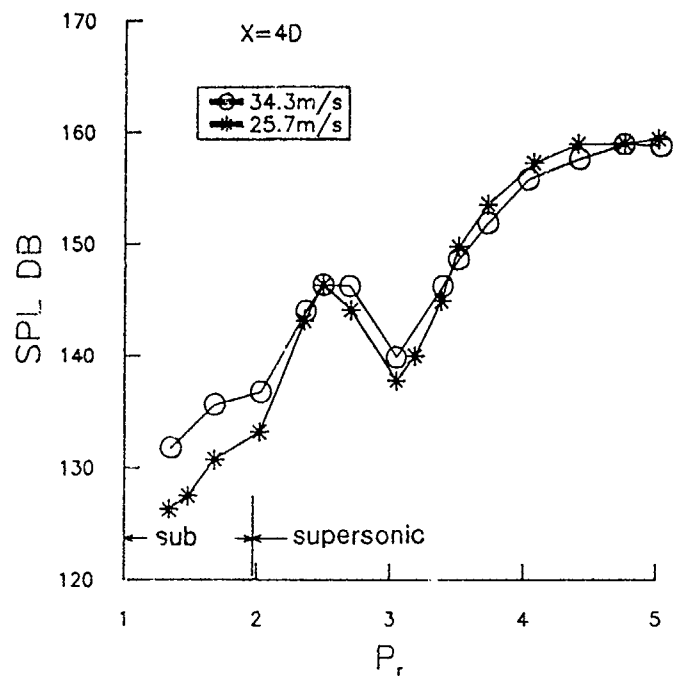


Fig. 3 SPL at two cross flow velocities measured at $X=4D$ on the adjacent flat plate along the x direction downstream of the jet exit. $M_d=1.4$ con-di nozzle.

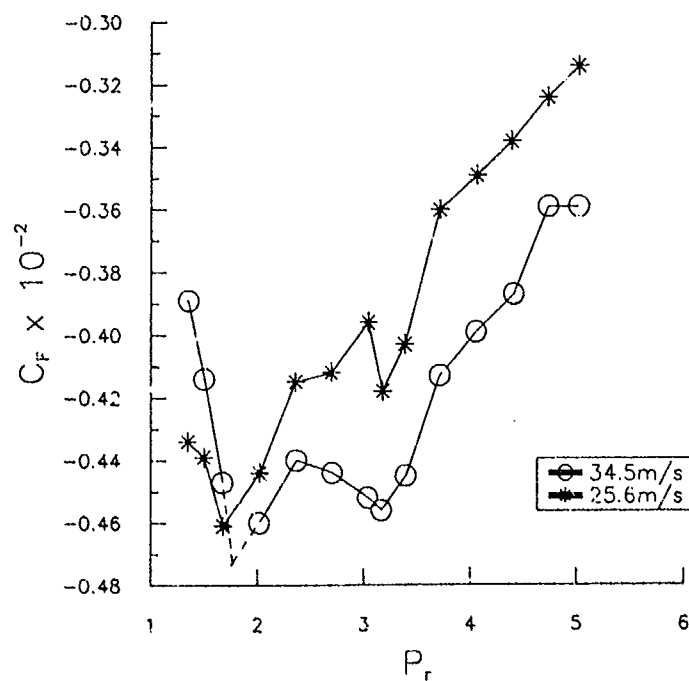


Fig. 4 C_f at two cross flow velocities of 25.6m/s and 34.5 m/s. $M_d=1.4$ con-di nozzle.

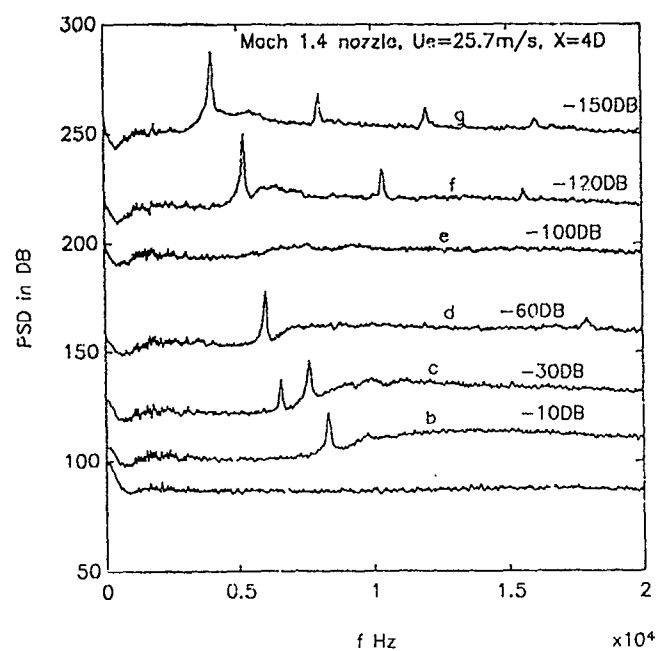


Fig. 5 PSD of surface pressure measured downstream of the jet exit on the adjacent flat plate in the x direction at $V_e=25.7\text{m/s}$, (a) $P_r=1.68$; (b) $P_r=2.36$; (c) $P_r=2.52$; (d) $P_r=2.71$; (e) $P_r=3.19$; (f) $P_r=3.52$ and (g) $P_r=5.04$. $M_d=1.4$ con-di nozzle.

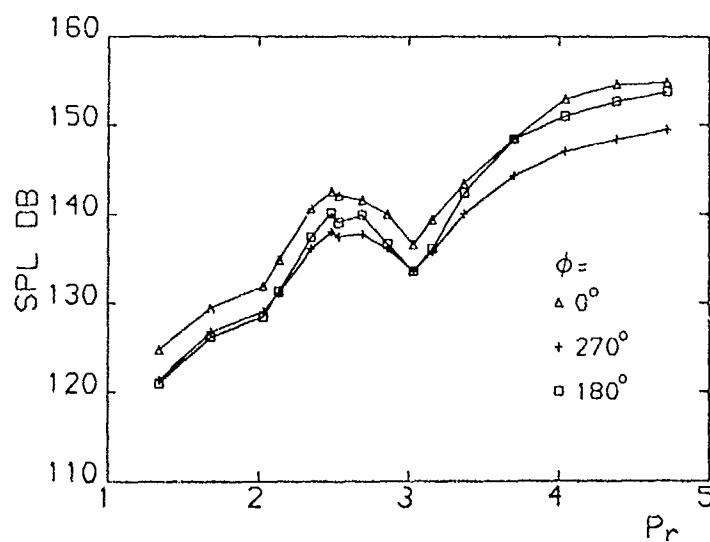


Fig. 6 SPL measured at three positions on the flat plate ($\phi=0^\circ$, 180° and 270°) on an $R=6D$ half circle at $V_e=25.7\text{m/s}$. $M_d=1.4$ con-di nozzle.

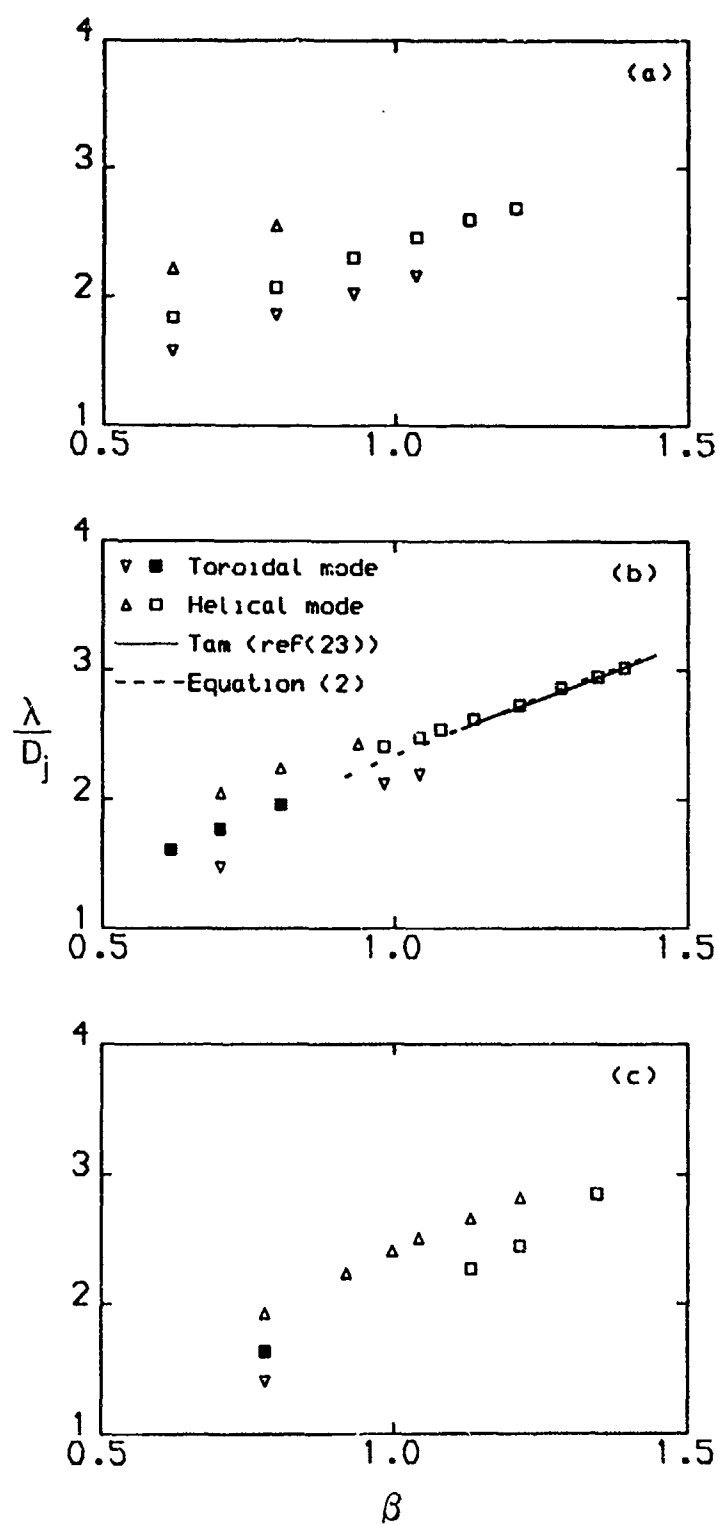


Fig. 7 Changes in mode wavelengths with the jet Mach number parameter, β , at $V_e=25.7\text{m/s}$, (a) convergent nozzle; (b) $M_d=1.4$ con-di nozzle; and (c) $M_d=1.7$ con-di nozzle.

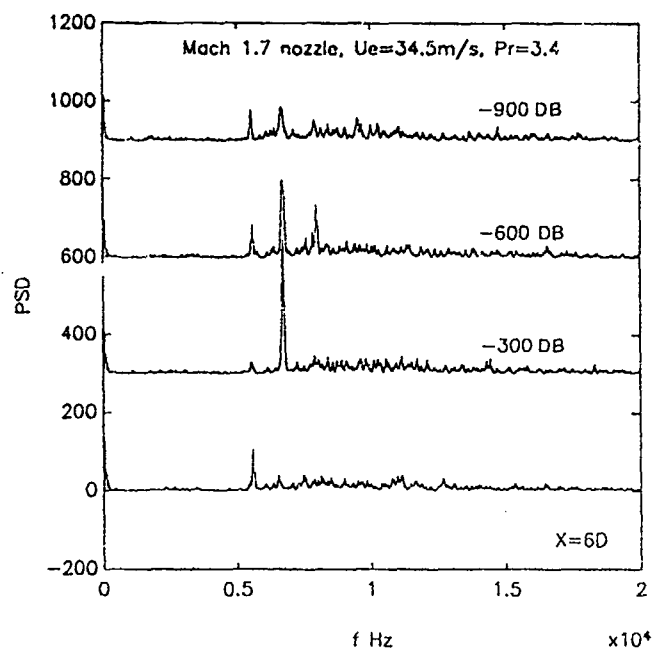


Fig. 8 Mode switch in a multiple mode dominated transient flow field at $P_r=3.4$ and $V_e=34.5\text{m/s}$. $M_d=1.7$ con-di nozzle.

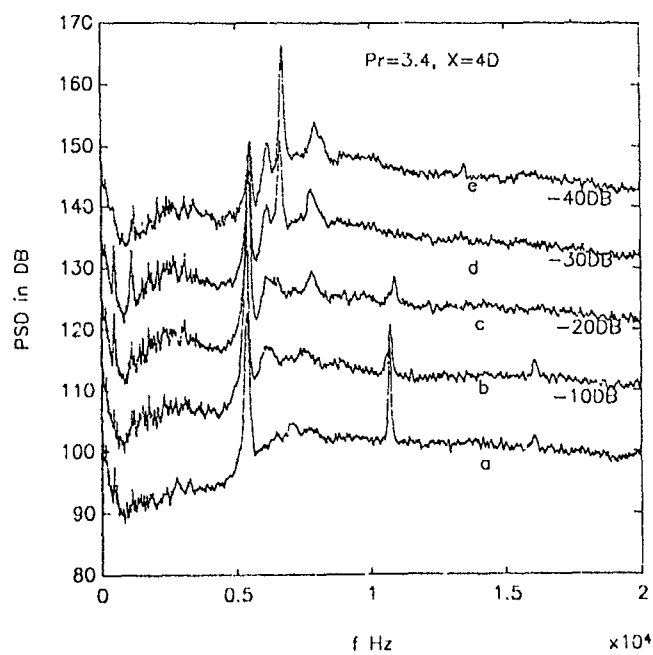


Fig. 9 PSD of surface pressure measured downstream of the jet exit on the adjacent flat plate in the x direction at $P_r=3.4$ (a) $V_e=14\text{m/s}$; (b) $V_e=25.6\text{m/s}$; (c) $V_e=30.8\text{m/s}$; (d) $V_e=34.5\text{m/s}$ and (e) $V_e=38.3\text{m/s}$. $M_d=1.7$ con-di nozzle.

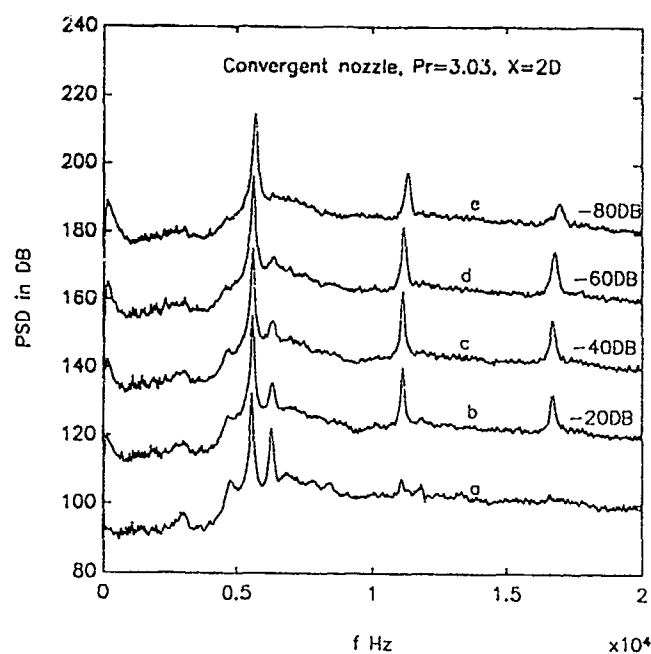


Fig. 10 PSD of surface pressure measured downstream of the jet exit on the adjacent flat plate in the x direction at $P_r=3.03$, (a) $V_e=13.8\text{m/s}$; (b) $V_e=21.3\text{m/s}$; (c) $V_e=25.3\text{m/s}$; (d) $V_e=30.1\text{m/s}$ and (e) $V_e=37.2\text{m/s}$. Convergent nozzle.

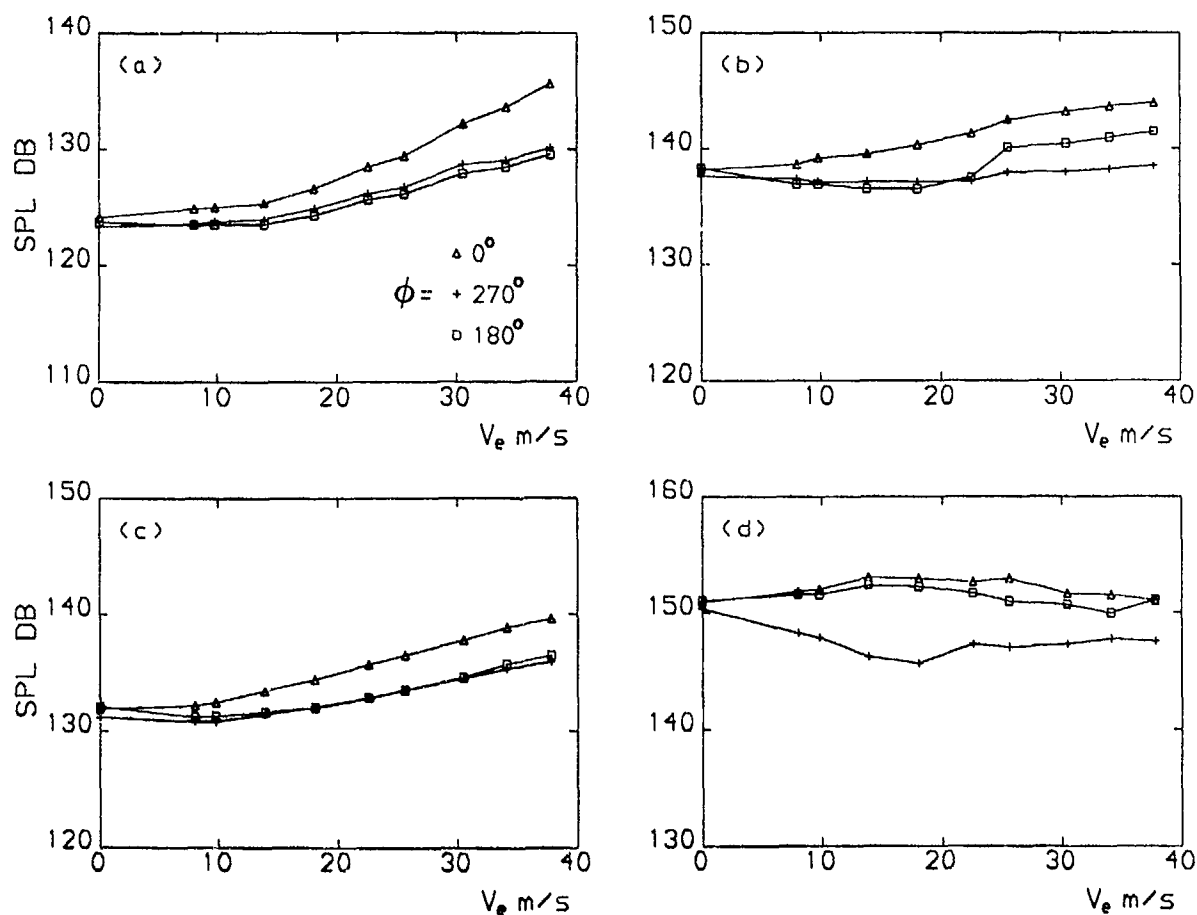


Fig. 11 SPL measured at three positions on the flat plate ($\phi=0^\circ$, 180° and 270°) on an $R=6D$ half circle, (a) $P_r=1.68$; (b) $P_r=2.49$; (c) $P_r=3.03$; and (d) $P_r=4.04$. $M_d=1.4$ con-di nozzle.

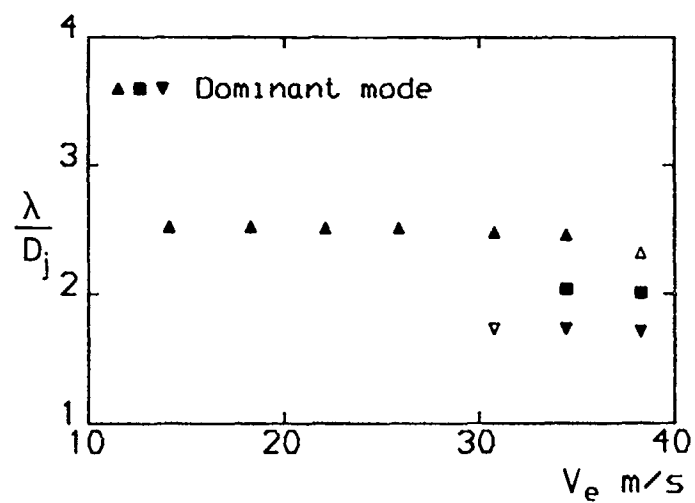


Fig. 12 Mode wavelength of an over-expanded jet at $P_r=3.4$ at various cross flow velocities. $M_d=1.7$ con-di nozzle.

UNSTEADY WAKE STRUCTURES IN TRANSVERSE JETS

R. M. Kelso¹

C. Delo²

A. J. Smits²

¹ C.S.I.R.O. Division of Building, Construction & Engineering,
P.O. Box 56, Highett, Victoria, 3190 Australia.

² Dept. of Mechanical & Aerospace Engineering, Princeton University
Princeton N.J. 08544 U.S.A.

SUMMARY

The unsteady vortex structures in the wake of a transverse jet were studied using a new laser scanning apparatus to obtain three-dimensional images of fluorescent dyes in a water channel flow. By scanning the laser at high repetition rates and by using a high-speed video camera to record the images, the three-dimensional, time-evolving concentration field in the wake can be obtained and later reconstructed. Using this system, the separation and roll-up of the flat plate boundary layer and the subsequent convection of that vorticity away from the wall can be visualized. The relationship between the separation and roll-up on one side of the wake with the separation and roll-up on the other side of the wake can also be studied. On the basis of the reconstructed concentration fields, an attempt is made to describe the mechanisms of wake vortex formation and explain the results of some previous authors.

1. INTRODUCTION

The study of transverse jets is of great relevance to many applications, such as gas turbine engines, V/STOL aircraft exhaust flows and chimney flows just to name a few. An understanding of the structure of these flows is vital if technological developments and accurate predictions of the flow characteristics are to be made. To this end, transverse jets have been studied intensively for many years.

Until recently, however, the unsteady motions in the wake downstream of transverse jets were very poorly understood. Most of the work so far has been concerned with studies of the wake frequencies and the general character of the wake (refs 1 - 4). Despite this work, the actual source of the wake vorticity was not identified. However, recent smoke-wire studies reported by Fric & Roshko (ref. 5) and Fric (ref. 6) have provided conclusive evidence that the wake vorticity originates in the flat plate boundary layer. They pointed out that, in a fluid of uniform density, vorticity can only be created at the surface of the flat plate and the jet nozzle. Their flow visualization studies confirmed that the flat plate boundary layer separates on the downstream side of the jet due to the imposed adverse pressure gradient, and its vorticity is incorporated into the wake vortices which extend from the flat wall to the jet itself. This roll-up process can be seen in Figure 1(a). The arrow indicates a "separation event", a transient boundary layer separation leading to a wake vortex. Note that the wake vortices appear to alternate in circulation in a pattern resembling a von Karman vortex street. Figure 2 shows a streamsurface representation of the unsteady separation and roll-up process. Fric & Roshko suggested that the portions of the wake vortices (separating boundary layer) closest to the jet are entrained and convected by the jet.

Subsequent examination of the flow visualization photographs obtained by Fric & Roshko (ref. 7) suggest that the wake vortex orientation may change from one pattern to another. Whereas Figure 1(a) resembles a von Karman vortex street, as do most of their patterns, Figure 1(b) suggests a significantly different wake flow pattern. Note that Fric & Roshko did not comment on the different appearance of this pattern, which consists of mushroom-like structures, where the vortices appear to be grouped into pairs of opposite circulation.

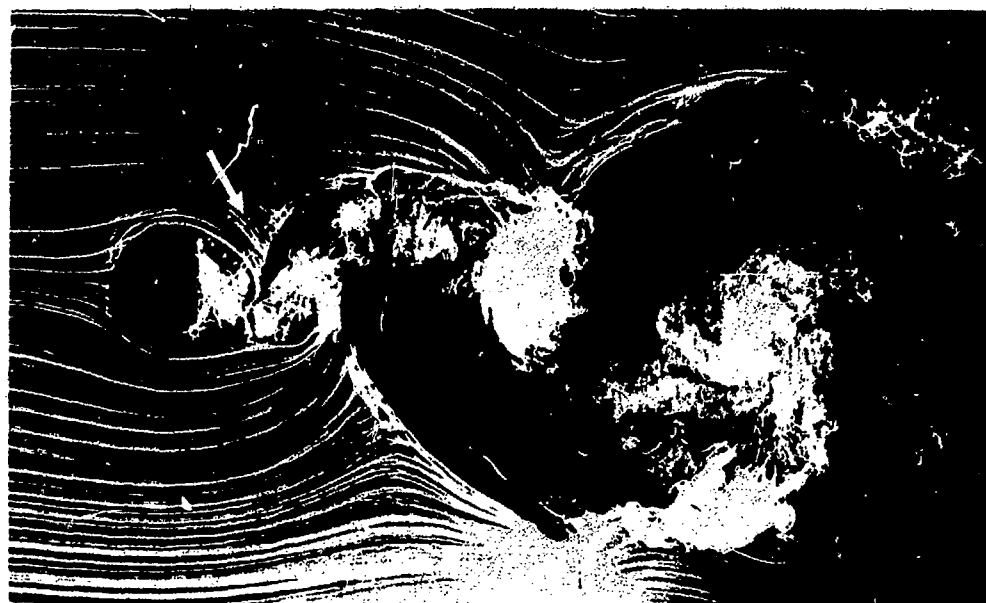
Recent water channel visualization studies by Kelso (ref. 7) and Perry, Kelso & Lim (ref. 8) provide further evidence to suggest that different wake flow patterns may occur. They observed that, under similar flow conditions to those described by Fric & Roshko, when the wake vortices were marked with red and blue dye according to the side of their origin, two characteristic patterns became apparent. In the most commonly occurring pattern, alternating red and blue vortices were observed in the wake whereas in the less common pattern, alternating pairs of like-colored vortices were seen. Unfortunately, the connection between these results and those of Fric & Roshko was not conclusive, although they were suggestive of more than one vortex shedding regime in the wake.

The aim of the present study is to investigate how vorticity is generated and convected in the wake region and how the different wake structures come into being. The study was carried out using a new laser scanning apparatus for 3-dimensional imaging of fluorescent dyes in multiple sectional planes in a water channel flow. By scanning the laser at high repetition rates and by using a high-speed video camera to record the images, the three-dimensional, time-evolving concentration field in the wake can be obtained and later reconstructed. Vortex skeleton interpretations of the visualized flow pattern can then be inferred and the wake structures explained.

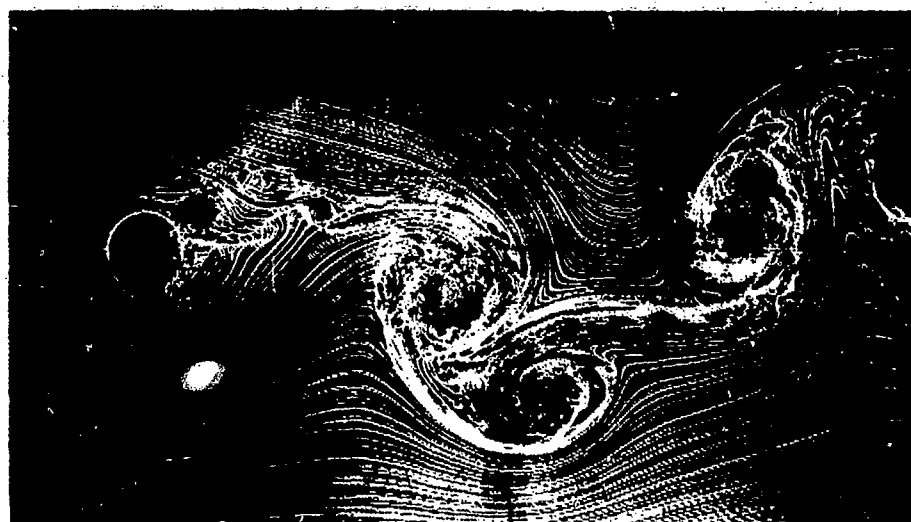
2. EXPERIMENTAL APPARATUS

This study was carried out in the 12" x 18" water channel at the Gas Dynamics Laboratory, Princeton University. Figure 3 shows the geometry of the transverse jet apparatus. The pipe is very short with the fluid entering it from a 5:1 contraction, thus giving a top-hat velocity profile in the case of no cross-flow. The jet discharges from the surface of a horizontal flat plate mounted above the channel floor.

The water channel is equipped with a laser scanning apparatus for 3-dimensional imaging of dyes in multiple sectional planes as described by Delo & Smits (ref. 9). This apparatus, which is shown in Figure 4, incorporates a helical array of 45° mirrors, fixed to twenty faceted faces of



a)



b)

Figure 1. a) Smoke wire visualization of a "separation event" and the accompanying near wall flow. The smoke wire is located adjacent to the flat wall. The arrow indicates a separation event. The overall pattern resembles a von Karman vortex street. $R = 4$ and $Re = 3,800$. After Fric (1990)
 b) Smoke wire visualization of the wake region. The wire is located at $y/D = 0.5$. The pattern consists of mushroom-like structures, where the vortices appear to be grouped into pairs of opposite circulation. $R = 4$ and $Re = 11,400$. After Fric & Roshko (1989)

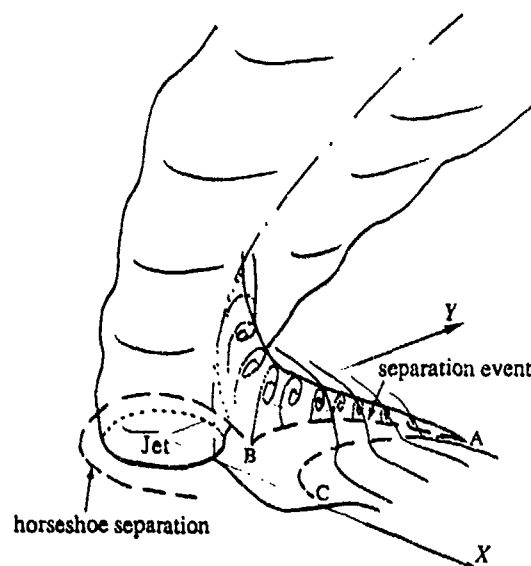


Figure 2. Streamsurface representation of the unsteady separation and roll-up process as interpreted by Fric (1990). It was suggested that the portions of the wake vortices (separating boundary layer) closest to the jet are entrained and convected by the jet.

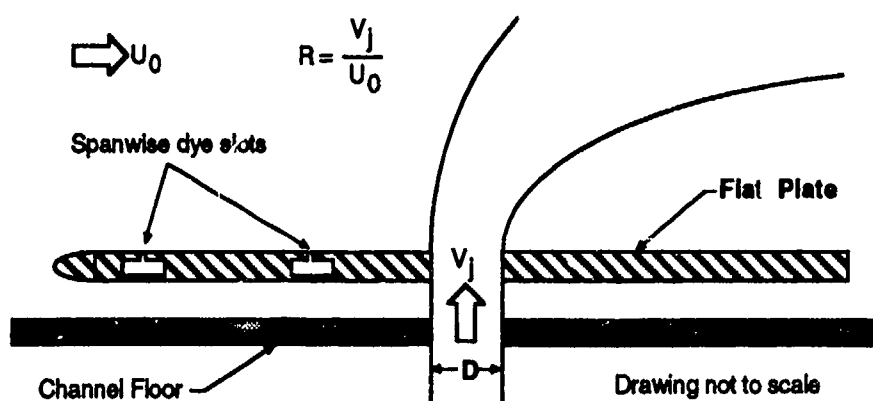


Figure 3. Schematic diagram of the jet apparatus.

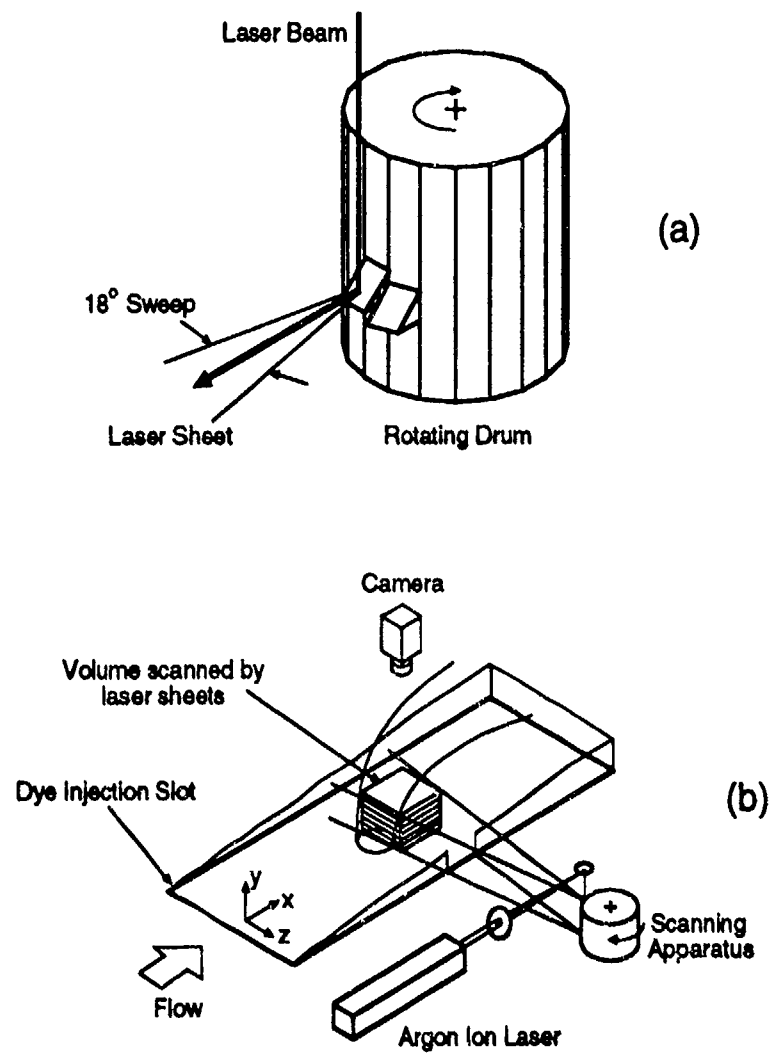


Figure 4. a) Laser scanning apparatus. b) Experimental arrangement.

a rotating drum. When used with a continuous light source such as the Lexel Model 95 argon ion laser used here, the focused laser beam is directed along the axis of the drum, and reflects off each mirror as the drum rotates. The motion of the flat mirror face causes the beam to sweep through an angle of 18° , creating a laser sheet of uniform intensity. The image is recorded by keeping the shutter of the video camera open during the sweep. As the drum continues to turn, the beam reflects off the next mirror forming another sheet at a different height. Because the location of the sheet is determined by the height of the corresponding mirror, the sheet locations are exactly repeatable and they can be accurately determined by a single calibration.

The experiments were performed with a water depth of 205 mm and a free-stream velocity of 150 mm s^{-1} , providing a laminar upstream boundary layer of about 13 mm thickness. The Reynolds number was 3,800 based on the free-stream velocity in the channel and the diameter of the jet. The velocity ratio R , as defined in Figure 3, was 4.3 based on the average jet velocity. The jet exit was located 1.1 m from the leading edge of the plate. Fluoresceine dye (500 ppm concentration) was injected into the boundary layer of the plate from spanwise slots located 216 mm and 890 mm upstream of the jet. The imaged volume measured 96 mm in the streamwise direction by 120 mm in the spanwise direction. There were 20 horizontal laser sheets, spaced 2 mm apart with the lowest sheet at 1 mm above the flat plate and the highest 39 mm above the plate.

The sheets were imaged using a Kodak Ektapro 1000 Motion Analyzer (high-speed video system) fitted with a 12.5 - 75 mm f1.8 zoom lens. The camera operation was synchronized with the motion of the mirrors at all times. The framing rate of the camera was 250 frames per second, corresponding to 12.5 time steps (drum rotations) per second. The two-dimensional images were recorded onto video tape, then transferred to a Personal Iris workstation using a Panasonic AG-6500 editing video cassette recorder and an Imaging Technology Series 151 frame grabber. Wyndham Hannaway image processing software was used to control the frame grabber and to enhance the images. Reconstruction of the images into three-dimensional volumetric images was achieved using software written by a colleague, Jonathan Poggie.

3. RESULTS

The primary output from this investigation is a video showing the time-evolving three-dimensional dye concentration field. To this end, 25 time steps, comprising 500 individual images, were collected on videotape and digitized. These images were reconstructed into three-dimensional volumes which show the evolution of the wake over a period of 2 seconds. Only the most basic image processing was required prior to reconstruction, namely smoothing, noise thresholding and grey-scale stretching. Figure 5 shows a three-dimensional reconstruction of one representative time-step. No correction has been made for the convection of the vortex structures between successive slices (less than 0.6 mm between slices). This will lead to minor distortion of the reconstructed pattern but will not alter the topology or connectivity of the pattern. Note that the pattern shows that a considerable degree of fine-scale motion is present in the flow despite the laminar upstream conditions. Some individual images used in the reconstruction of this pattern are shown in Figure 6. These can be used to trace the connection between the vortex structures in the imaged volume. These images also indicate that the wake motions

occur over a wide range of length-scales. An interesting wake vortex can be seen in the centre of each image. The source of this vorticity can be traced by following the vortex from the top sheets to the bottom. This vortex appears to contain vorticity (of the same sign) from either side of the wake which has lifted away from the flat wall and merged to form a single wake vortex. The main vortex structures in this pattern are described using a series of vortex skeletons in Figure 7. The pattern, which was constructed after careful examination of several preceding time-steps, consists of strands of vortical fluid which convect away from the wall and wrap around a partner of like circulation from the other side of the wake.

4. DISCUSSION

In all, 1700 consecutive time steps were viewed in slow motion to allow the behaviour of the wake to be interpreted. This was not an easy task as the flow is extremely complicated and the presence of dye traces will not always indicate the presence of vorticity. Figure 8 shows the authors' interpretation of the wake vortex roll-up process leading to the von Karman vortex street as shown in Figure 1(a). The pattern consists of a series of vortex loops which are lifted away from the flat wall as the boundary layer separates. Our observations suggest that the downstream side of each loop tends to grow much more rapidly than the upstream side of the loop, probably due to boundary layer vorticity being continually fed into the structures from both sides of the wake as they convect downstream. The upstream side of each loop appears to "merge" or "pair" with the downstream side of the analogous loop from the opposite side of the wake. This may explain the helical appearance of many structures visualized by us and Fric & Roshko. This merging process typically occurs within one diameter of the jet exit, making it difficult to distinguish by any of the more common flow visualization methods. Note that the top portion of the loop may become "entwined" with the shear layer vorticity of the jet itself. The mechanism described here contrasts with the mechanism proposed by Fric & Roshko who suggested that the portions of the wake vortices closest to the jet are entrained and convected by the jet, meaning that the upstream side of each loop would merge with the shear layer of the jet. In Figure 8, vortex tubes are shown as continuous strands. It is possible that breaks may occur at the locations shown.

Figure 9 shows a possible interpretation of the wake vortex roll-up process which leads to the mushroom-like pattern shown in Figure 1(b). Again, this pattern consists of a series of vortex loops, but these loops do not appear to merge with loops generated on the opposite side of the wake. The resulting pattern forms mushroom-like structures when viewed in cross-section. This is, in fact, just one possible scenario leading to this type of structure.

5. ACKNOWLEDGMENTS

R. M. Kelso acknowledges the support of the CSIRO Postdoctoral Fellowship scheme. C. Delo received graduate fellowship support from the Fannie and John Hertz Foundation, and from the National Science Foundation. Thanks are due to R. B. Miles for the use of the laser and F. V. Bracco for the use of the Motion Analyzer. Thanks are also due to J. P. Poggie for the use of his three-dimensional reconstruction software.

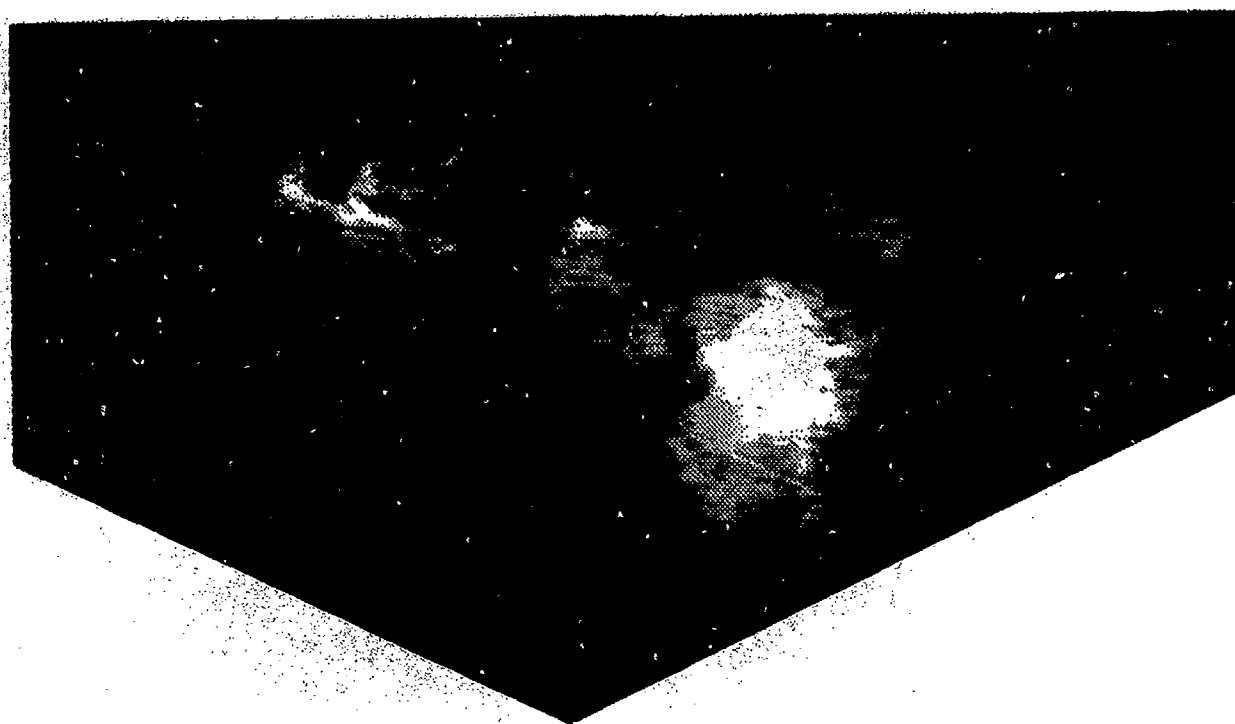


Figure 5. Three-dimensional reconstruction of one representative time-step, shown as an isometric view. Flow is towards the far left. The flat plate and rear side of the jet are outlined. The image is constructed from twenty parallel cross-sections of the wake. No correction has been made for convection of the vortex structures between successive slices.



Figure 6. See caption next page.

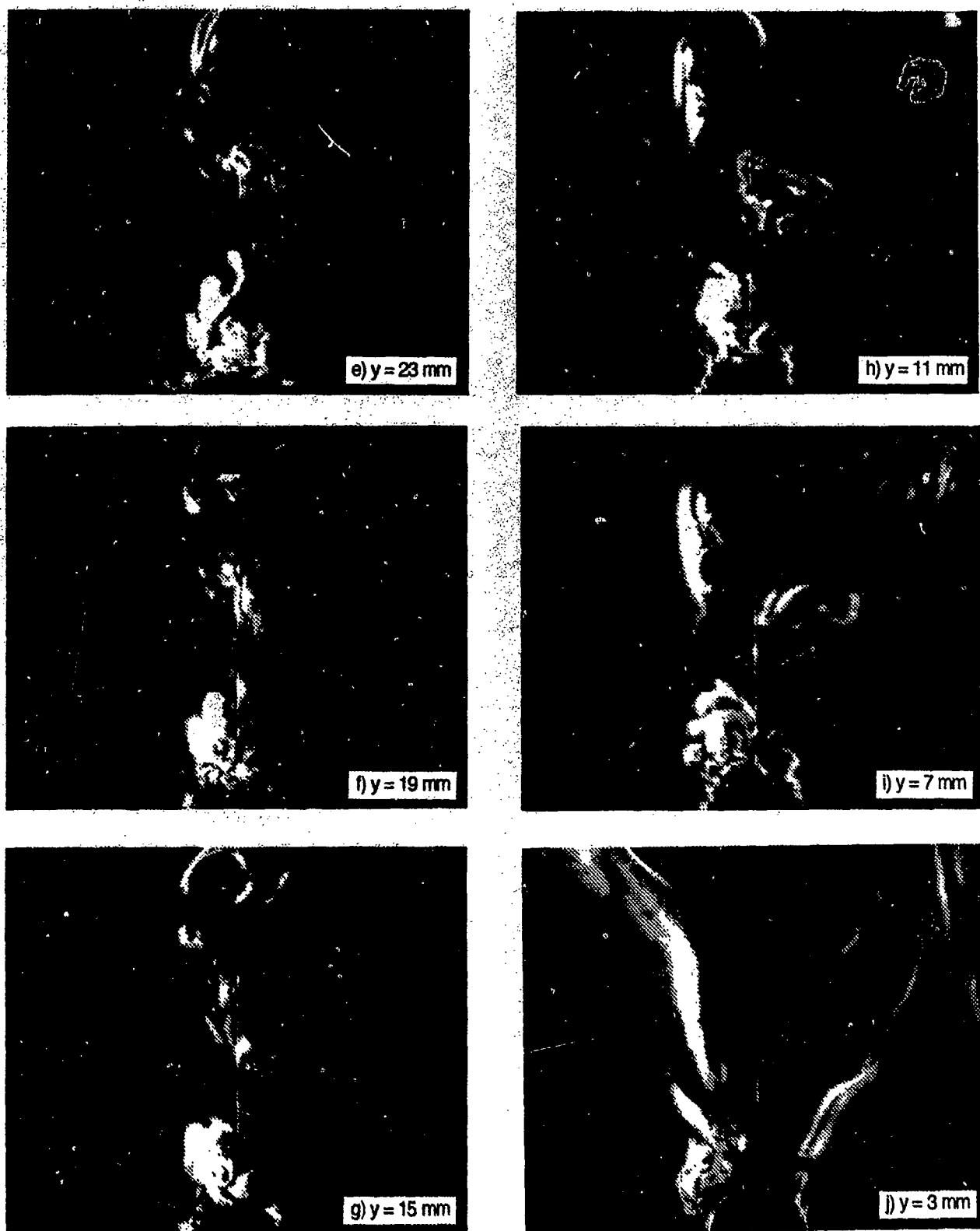


Figure 6 Ten of the twenty laser cross-sections used for reconstructed image shown in Figure 5. The images are parallel to the wall and flow is from bottom to top. The flat plate and rear side of the jet are outlined. The field of view is about 120 mm by 96 mm and the jet diameter is 25 mm. Images a - j show every second cross-section from $y = 39$ mm down to $y = 3$ mm.

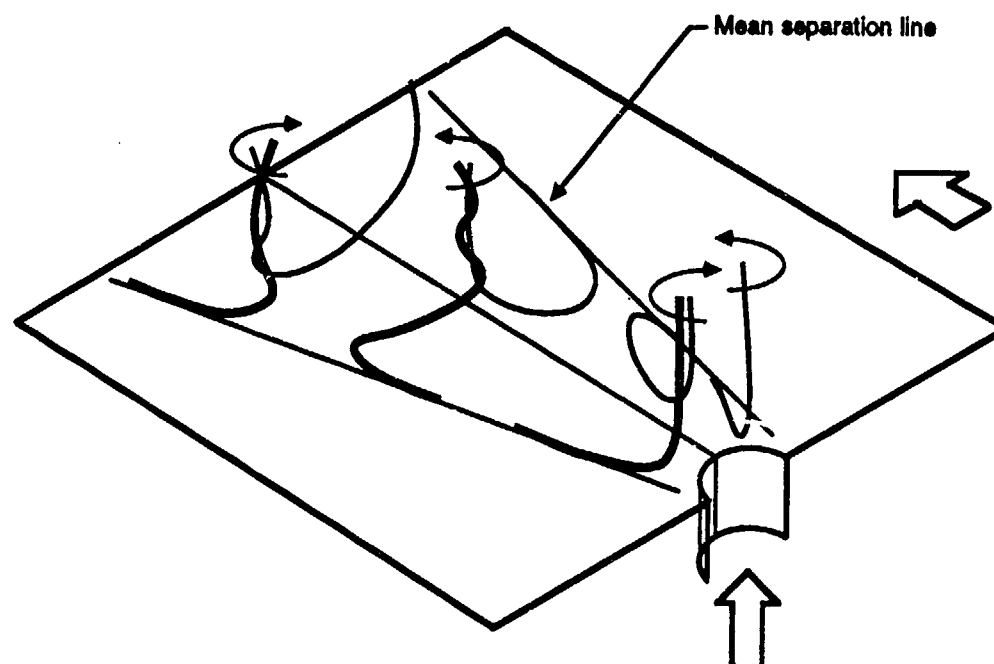


Figure 7. Vortex skeleton representation of the main vortex structures in Figure 7. The skeletons represent only those parts of the wake vortices which were imaged.

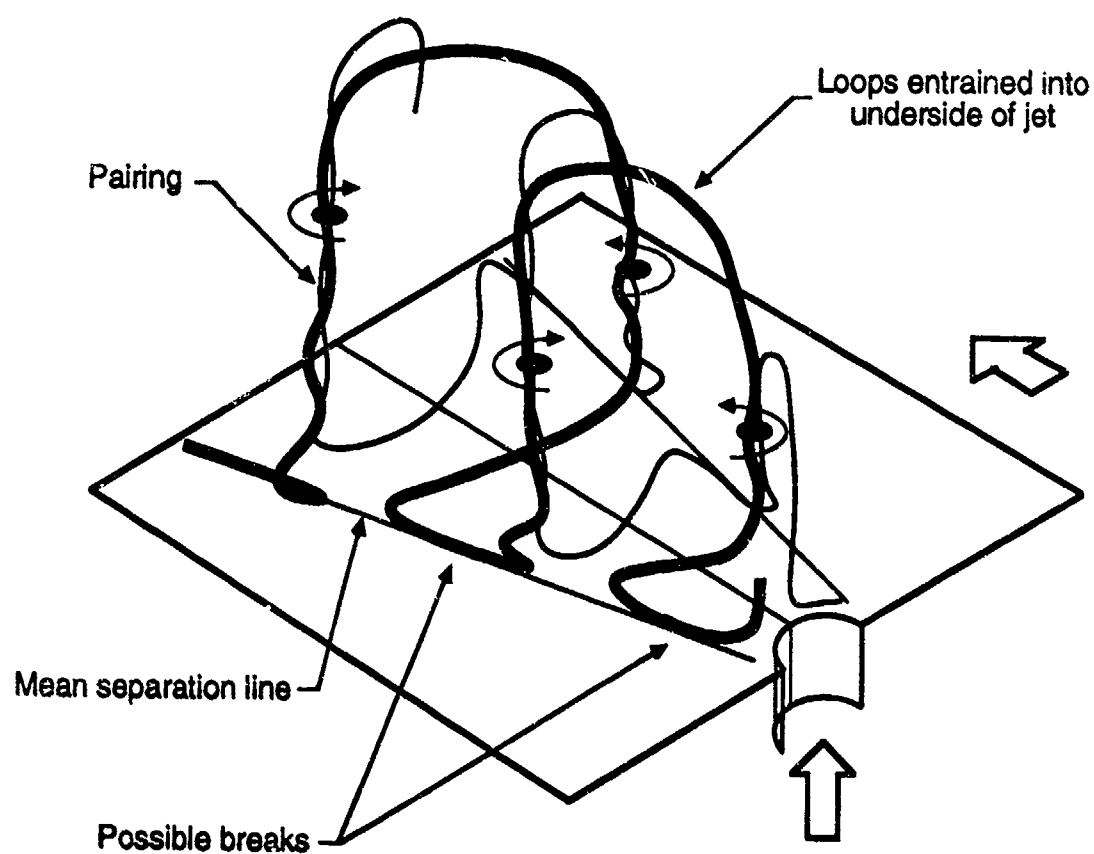


Figure 8. Vortex skeleton representation of the inferred roll-up process leading to the formation of a von Karman vortex street pattern as depicted in Figure 1(a).

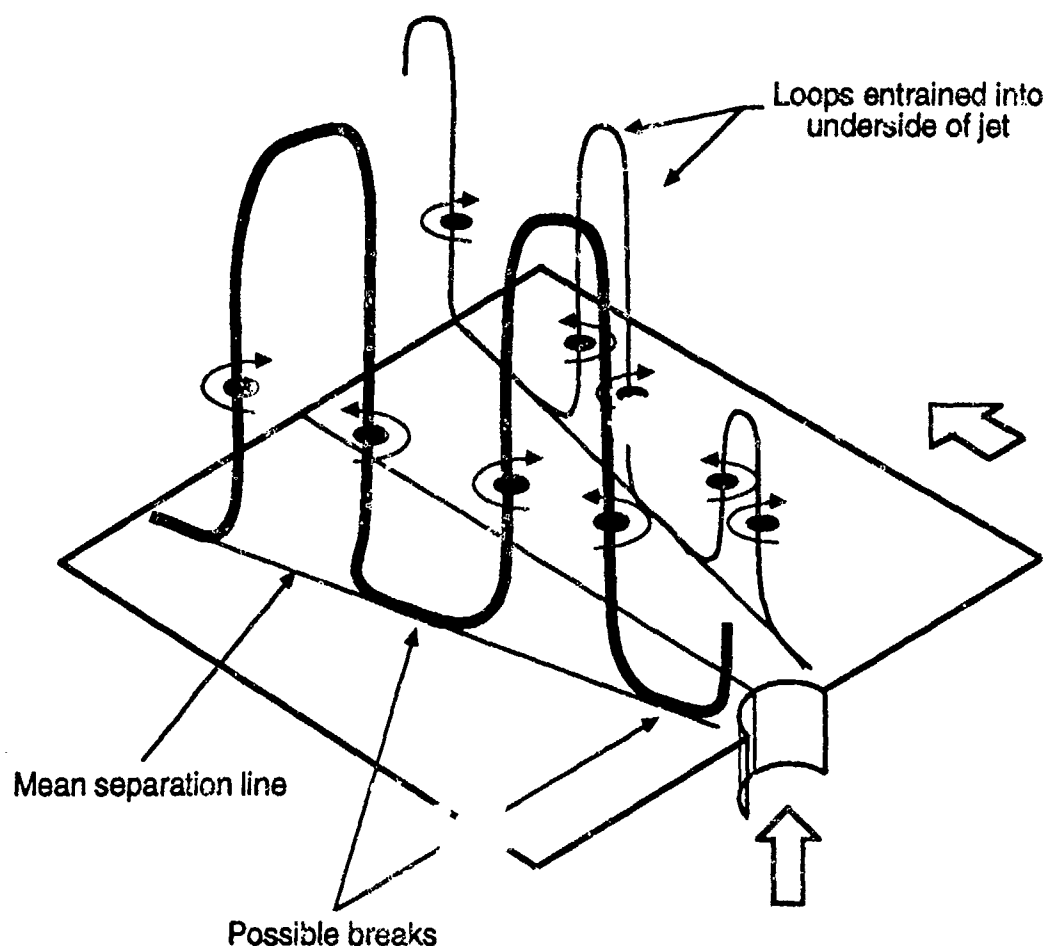


Figure 9. Vortex skeleton representation of the inferred roll-up process leading to the formation of a mushroom-like wake pattern as depicted in Figure 1(b).

6. REFERENCES

1. McMahon, H. M., Hester, D. D. & Palfrey, J. G. Vortex shedding from a turbulent jet in a cross wind. *J. Fluid Mech.* 48, 1971, pp 73-80.
2. Moussa, Z. M., Trischka, J. W. & Eskinazi, S. The near field in the mixing of a round jet with a cross-stream. *J. Fluid Mech.* 80, 1977, pp 49-80.
3. Kuzo, D. M. & Roshko, A. Observations on the wake region of the transverse jet. *Bulletin of the American Physical Society* 29, 1984, p 1536.
4. Wu, J. W., Vakili, A. D. & Yu, F. M. Investigation of the interacting flow of nonsymmetric jets in crossflow. *AIAA J.* 26, 1983, pp 940-947.
5. Fric, T. F. & Roshko, A. Structure in the near field of the transverse jet. *Seventh Symposium on Turbulent Shear Flows*, 1989, pp 6.4.1-6.4.6.
6. Fric, T. F. Structure in the Near Field of the Transverse Jet. Ph.D. Thesis, California Institute of Technology, 1990.
7. Kelso, R. M. A study of free shear flows near rigid boundaries. Ph.D. Thesis, University of Melbourne, 1991.
8. Perry, A. E., Kelso, R. M., Lim, T. T. An experimental study of a round jet in cross flow. Under preparation.
9. Delo, C. & Smits, A. J. Visualization of the three-dimensional, time-evolving scalar concentration field in a low Reynolds number turbulent boundary layer. *Near-Wall Turbulent Flows*. Elsevier Press, 1993.

Separated Flow Generated by a Vektored Jet in a Crossflow

A. Krothapalli and C. Shih
Department of Mechanical Engineering
Florida A&M University and Florida State University
Tallahassee, Florida 32316-2175

I. Abstract

Results of an experimental investigation to determine the characteristics of the separated flow region generated by a subsonic vectored rectangular jet in a subsonic crossflow is presented. Using surface visualization techniques, it was found that the upstream separated flow consist of horseshoe vortices that are formed periodically with a frequency corresponding to that of the vortex shedding behind the jet. The size of the recirculation region around the jet is found to decrease with increasing jet vector angle. The variation of the mean primary separation distance upstream of the jet, with velocity ratio revealed the existence two different flow regimes. The change from one to the other depends on the velocity ratio and the jet vector angle. It is shown that the Strouhal number, based on the vortex shedding frequency and a combination of jet exit and freestream velocities, varies uniquely with velocity ratio.

II. Introduction

The experimental investigation presented in this paper was originally motivated by an interest in short takeoff and vertical landing (STOVL) aircraft configurations that utilize rectangular jets for powered lift. Recently, vectored rectangular jets have been used to improve post stall maneuverability/agility of fighter aircraft. There have been only a few experimental studies which have directly examined the separated flow structure upstream of a jet in a cross flow. In an earlier paper, Krothapalli et.al¹ described the separated flow structure upstream of a subsonic rectangular jet issuing normally from a flat plate into an on-coming subsonic freestream. In continuation of this work, we address here the effect of the jet vector angle, with respect to the freestream, on the separated flow structure and the associated wake flow field.

The classical jet in a cross flow problem has been well researched and several review articles describing the jet structure and its induced pressures on the body from which it is issuing have appeared in the literature^{2,3}. A more in depth study of the flow structure in the near field of an axisymmetric jet in a cross flow has been conducted by Fric⁴. This study convincingly demonstrated that the vorticity within the system of vortices in the near wake of the jet is associated with the separated wall boundary layer. Hence, the flow structure associated with the upstream horseshoe vortex system is important in determining the near wake characteristics. An attempt is made in this study to observe changes brought about by the vector angle of the jet on both the upstream flow structure and the associated near wake.

The main parameters of the problem and their respective ranges considered in this experiment are as follows: The jet exit Reynolds number, based on the nozzle exit width, was varied from 1.3×10^4 to 8×10^4 . A tophat mean velocity profile with laminar boundary layer was maintained at the nozzle exit. The undisturbed boundary layer on the flat plate upstream of the nozzle exit was turbulent. The corresponding free stream Reynolds number, based on the distance from the leading edge of the plate to the nozzle exit, was varied from 3×10^5 to 5×10^6 . The aspect ratio of the jet was 10. The jet vector angle with respect to the freestream was varied from 30° to 150° (see figure 1).

III. Apparatus, Instrumentation and Procedures

The experiment was carried out in two different facilities. Experiments at high freestream and jet Reynolds numbers were carried out earlier (1986) in a close return wind tunnel facility which has a test section 0.6 m wide, 0.6 m high and 1.5 m long. Its free stream velocity can be varied from 5 m/sec to 70 m/sec. Current experiments were carried out in a closed return wind tunnel facility which has a test section 0.35 m wide, 0.55 m high and 1.0 m long. Its free

stream velocity can be varied from 5m/sec to 45m/sec. For the range of free stream velocities considered, the freestream turbulence level, in both wind tunnels, was less than 0.5%. The details of the experimental arrangement and the nozzle assembly for earlier studies were given in reference 1, hence they will not be repeated here. For the current experiment, a new nozzle assembly was designed and built as shown in figure 1. This facility has the flexibility of providing variable jet angles with respect to the freestream from 30° to 150° . The nozzle assembly was mounted on the top wall of the wind tunnel test section. The nozzle exit was positioned in the center of the wall, 50cm downstream of the leading edge of the test section. The breadth and width of the nozzle exit are 10 cm and 1cm respectively. The entire jet assembly was rotated with appropriate modifications to the nozzle exit to provide variable jet angles. A tripping element, consisting of a 2.5 cm wide sand paper, was placed at the beginning of the wind tunnel test section.

Two different flow visualization techniques were used to obtain the main features of the separated flow field: surface oil flow technique using TiO_2 and minitufts in the wake region. The unsteady nature of the separated region was investigated using hot-wire anemometry. The overall phenomenon described in this paper may be considered free of any direct influence from the blockage of the test section by the jet.

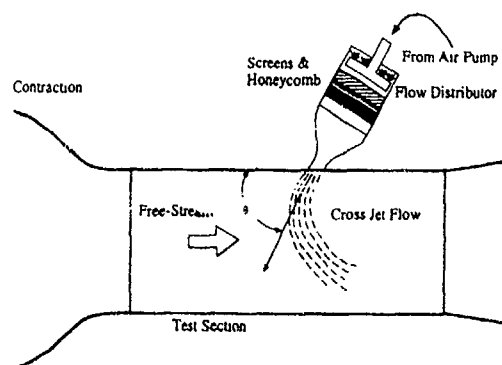


Figure 1. Schematic of the wind tunnel test section with the jet facility.

The test conditions established during these experiments and their corresponding nondimensional parameters are as follows: $5 \text{ m/sec} < V_0 < 40 \text{ m/sec}$; $20 \text{ m/sec} < V_j < 120 \text{ m/sec}$; $1.0 < V_j / V_0 < 10$; where V_0 is the mean freestream velocity and V_j is the mean jet

exit velocity. Boundary layer trips were used at the leading edge of the plate to ensure that the undisturbed boundary layer just ahead of the nozzle exit is turbulent. The mean temperatures of the jet and the freestream were kept constant at 300K.

IV. Results and Discussion

Typical time averaged oil flow visualization pictures of the surface flow near the nozzle exit are shown in figure 2. The corresponding mean freestream and jet exit velocities are 40 m/sec and 120 m/sec respectively. The freestream Reynolds number based on the jet disposition length of 1.17 m was 3.12×10^6 and the jet Reynolds number based on the nozzle width was 0.8×10^5 . The undisturbed boundary layer just ahead of the nozzle exit was found to be turbulent with a thickness, based on $0.99 V_0$, of about 2 cm. The surface flow pattern shows two well defined regions ahead of the nozzle exit, the region of attached flow and the region of separated flow marked by the primary separation line. A secondary separation line is observed between the nozzle exit and the primary separation line. These separation lines are the signature of a horseshoe-type vortex system with two separate vortices rotating in the clockwise direction in the central plane normal to the jet (see reference 1 for details). The formation and rollup of these vortices was found to be a time-dependent periodic phenomenon with the frequency corresponding to the vortex shedding behind the jet. A further discussion on this will be presented later. A similar structure is also observed at other velocity ratios and jet angles, except that the distinction between primary and secondary separation lines becomes less discernible at low (< 1.5) and high (> 8) velocity ratios and at jet angles greater than about 120° .

The surface oil flow patterns in the near wake region show strong dependence on the jet vector angle. For example, in the case of a jet issuing normally into the cross stream, the surface line signature representing horseshoe vortices come together into twin tornado-like vortices that rise up from the surface. When the tornado-like vortices behind the jet are strong, they create a relatively low pressure region immediately behind the jet. The surrounding fluid is then drawn into this region leading to the formation of a narrower wake footprint on the solid wall. The distance of the jet column from the wall, a strong function of the velocity ratio, will influence the axial flow velocity of the

tornado-like vortices. In the case of a vectored jet at $\theta = 45^\circ$, the surface lines associated with horseshoe vortices on the surface move away from the jet forming a much wider footprint on

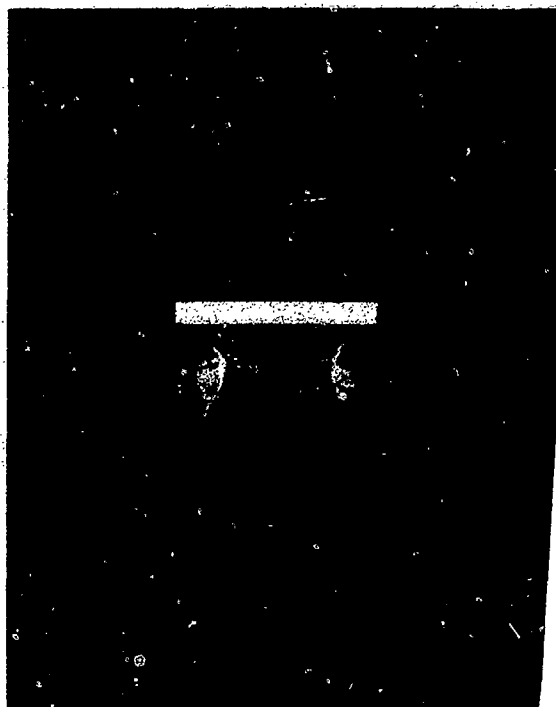


Figure 2a. Surface oil flow picture of the separated region. $V_j / V_0 = 3.0$, $\theta = 90^\circ$

the surface as shown in figure 2b. For example, the width of the surface wake signature at a downstream distance of $1.75L$ is about $3.36L$ as compared to a value of about $1.7L$ for the case of a jet exiting normally from the plate. Further away from the nozzle exit, the separation region continues to expand as shown in figure 2b. The tornado-like vortices appear to be relatively weak and move away from the centerline. The nature of the flow behind the jet may be largely determined by the magnitude of the surface pressure in this region. A similar surface oil flow pattern was also observed for a flow past a rectangular plate (width = 8cm; height = 25cm) at $V_0 = 40$ m/sec, as shown in figure 3. Further experiments need to be carried out to obtain the detailed characteristics of such a wake flow field. For jet vector angles greater than 90° , the separated flow structure looks very similar to the one shown in figure 2a, except the size of the separated region is much smaller.

The main interest in this problem is the determination of the extent of the separated flow region surrounding the nozzle exit. Since there is a plane of symmetry in the flow, the



Figure 2b. Surface oil flow picture of the separated flow region. $V_j / V_0 = 3.0$, $\theta = 45^\circ$



Figure 3. Surface oil flow picture of the separated region generated by a solid rectangular plate (8cm x 1cm) placed at 90° to the free stream. Plate height = 24cm.

distance from the leading edge of the nozzle exit to the primary separation line in the central plane can be used as an estimate of the extent of the upstream separated region. The primary separation line can be easily determined from surface oil flow pictures like those shown in figure 2. This distance from the nozzle exit to the primary separation line is denoted here by S . For the conditions tested, the magnitude of S is insensitive to either the freestream Reynolds number or the jet Reynolds number. Figure 4 shows the variation of S/L , where L is the breadth or long dimension of the nozzle, with the velocity ratio for different jet vector angles (θ). The trend of the data plotted in this manner shows two distinct regimes. The change from one to the other depends on the velocity ratio and vector angle. In the first regime, the separation distance increases monotonically with increasing velocity ratio, which is indicative of the blockage effect of the freestream by the jet. The second regime is characterized by the decrease of the separation distance with increasing velocity ratio. Such a behavior may be related to increased entrainment of the jet at high velocity ratios, which in turn reduces the extent of adverse pressure gradient region upstream of the nozzle exit. However, for $\theta > 120^\circ$ and $V_j/V_o > 4$, the effect of the entrainment seems to be minimal and as a result the separation distance does not vary significantly with velocity ratio.

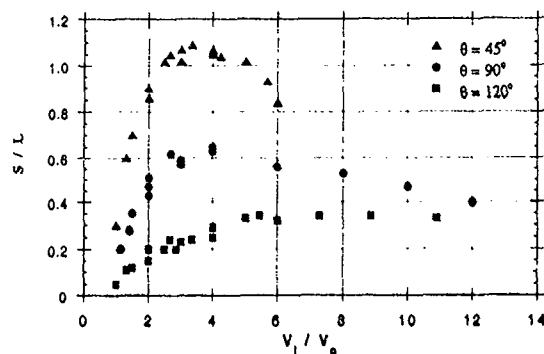


Figure 4. The variation of the nondimensional separation distance with velocity ratio, for different jet vector angles.

The unsteady surface flow structure was obtained using tufts placed on the plate around the nozzle exit as shown in figure 5. Photographs of the tufts were taken with an exposure time of 8 ms at different velocity ratios. Examination of the photographs revealed the presence of two different types of flow structure in the near wake region. Figure 5 presents two

randomly selected photographs of the tuft pattern for a velocity ratio of 3 ($V_j = 120$ m/s; $V_o = 40$ m/sec) and $\theta = 90^\circ$. A symmetric pattern representing a pair of counterrotating vortices is observed. However, a different pattern of tufts is observed when the velocity ratio is increased to about 10 ($V_j = 120$ m/s; $V_o = 10$ m/sec) as shown in figure 6. These photographs suggest the presence of asymmetric vortices similar to those found in a bluff body wake at a corresponding Reynolds number. The two examples shown in figure 5 and 6 are representative of wake flow for a weak jet and a strong jet. The velocity ratio at which the tufts pattern changes from one to the other is a function of the jet vector angle. For example, at $\theta = 45^\circ$, the symmetric flow structure is observed up to a velocity ratio of about 7, while at $\theta = 90^\circ$ an asymmetric vortex pattern occurs for velocity ratios greater than about five. As suggested in reference 1, it is believed that the strength of the tornado-like vortices that are identified in figure 2 will determine the near wake flow field.

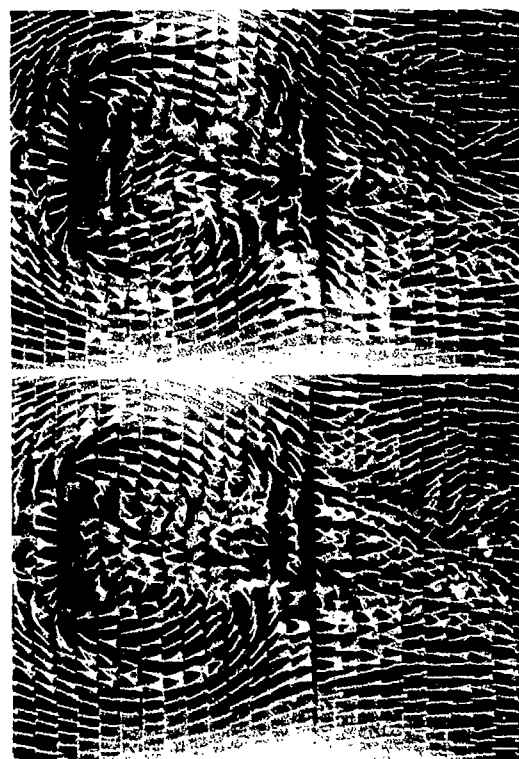


Figure 5. The tufts pattern in the near wake of a jet. $V_j/V_o = 3.0$, $\theta = 90^\circ$

To further explore the unsteady behavior of the flow, hot-wire anemometry was used primarily for the measurement of frequency spectra of the velocity fluctuations both upstream and downstream of the nozzle exit. It is found by

observation that the location of the strongest hot-wire signal depends on the velocity ratio and jet vector angle. The strongest hot-wire signal is defined as the one that gives rise to a well defined peak in its frequency spectrum. Figures 7a and 7b show frequency spectra of the velocity fluctuations at selected positions upstream and downstream of the jet exit. The velocity ratio corresponding to these spectra is 3 ($V_j = 44.7$ m/s, $V_0 = 14.9$ m/s), and $\theta = 90^\circ$. A prominent peak at 24 Hz is apparent in the spectra obtained ahead of the jet (figure 7a) while the peak in the spectra at 24.75 Hz, shown in figure 7b, corresponds to the vortex shedding frequency in the near wake of the jet. The proximity of the values of these frequencies confirms the earlier observation by Krothapalli et. al.¹ that the unsteadiness observed in the recirculation zone upstream of the jet has a frequency close to the vortex shedding frequency behind the jet. Similar observation is made in the entire range of velocity ratios

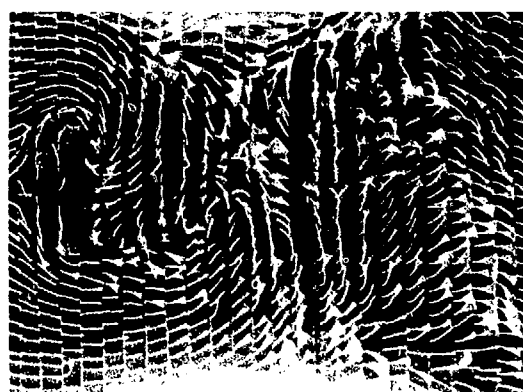
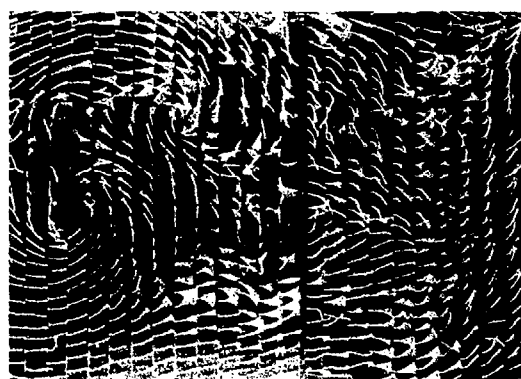


Figure 6. The tufts pattern in the near wake of a jet. $V_j / V_0 = 3.0$, $\theta = 90^\circ$

considered for $\theta \leq 90^\circ$. In order to confirm this finding, figure 8 shows the spectra obtained ahead of the jet and in the near wake at a velocity ratio of 7.5 ($V_j = 43.1$ m/s, $V_0 = 5.75$ m/s) for $\theta =$

45° . However, for $\theta \geq 120^\circ$ the spectra ahead of the jet and in the near wake do not clearly show prominent peaks (Figure 9), suggesting that the unsteadiness in the upstream recirculation zone may be weakly coupled to the vortex shedding behind the jet.

The vortex shedding frequencies in the near wake are obtained from the spectra of hot-wire signals similar to those shown in figures 7 and 8. The amplitude dominant frequency is referred to as the shedding frequency and is used in the calculation of the Strouhal number. Although some variation of the frequency is observed when the hot wire is moved away from the plate, it will not alter the major conclusions drawn from the data. In order to relate the variation of shedding frequency with the changes in velocity ratio, a conventional Strouhal number

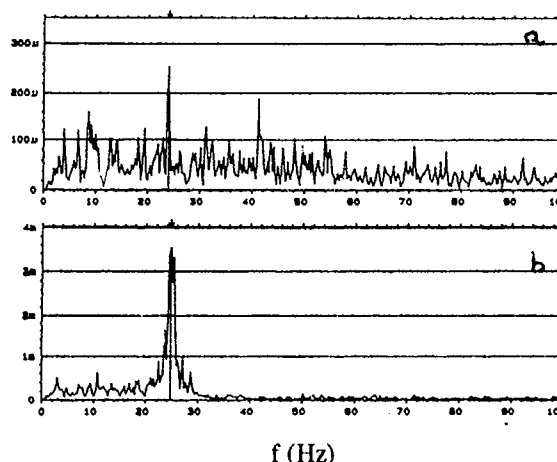


Figure 7. Typical spectra of hot-wire signals upstream (a) and downstream (b) of the jet exit. $V_j / V_0 = 3.0$, $\theta = 90^\circ$

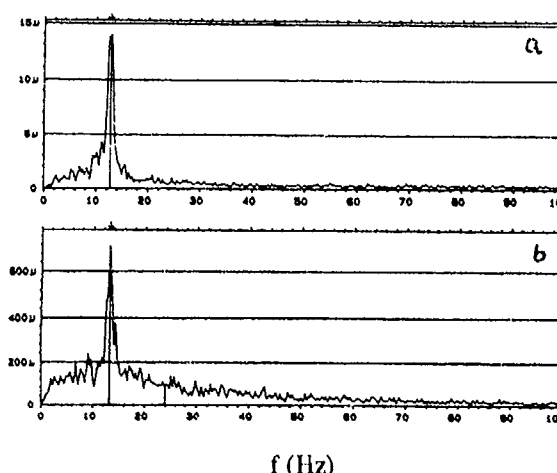


Figure 8. Typical spectra of hot-wire signals upstream (a) and downstream (b) of the jet exit. $V_j / V_0 = 7.5$, $\theta = 45^\circ$

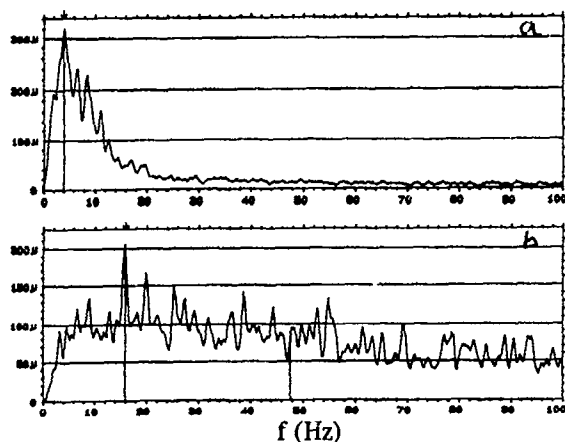


Figure 9. Typical spectra of hot-wire signals upstream (a) and downstream (b) of the jet exit. $V_j / V_0 = 5.3$, $\theta = 120^\circ$

is defined based on the freestream velocity and the nozzle breadth or nozzle exit diameter for a circular jet. Figure 10 shows the variation of this Strouhal number (St) with velocity ratio for a jet exiting normally into the cross stream. The earlier data of Krothapalli et al.¹ are also included in this figure. For the data shown, the freestream Reynolds number ($V_0 L/\nu$) varied from 1×10^4 to 2.7×10^5 . It is found that the variation of St with velocity ratio shows significant scatter beyond the experimental uncertainty. For example, at a velocity ratio of 4, the magnitude of the Strouhal number varies from 0.11 to 0.16. With increasing velocity ratio, the scatter appears to be smaller. Krothapalli et al.¹ have shown that by using a combination of jet exit velocity and free stream velocity the Strouhal number can be redefined as

$$St = fL / (V_j^2 + V_0^2)^{0.5}$$

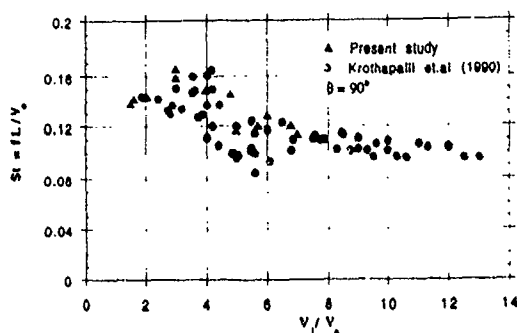


Figure 10. The variation of the near wake Strouhal number with velocity ratio.

Using such a definition, a significant reduction in the scatter of the data can be obtained. Figure 11 shows such a plot with the data covering a broad range of velocity ratios. Also included in this plot are the data obtained by Fric⁴ using an axisymmetric jet. The data plotted in this fashion may provide some guidance in developing a theoretical model. The solid

line shown in the figure corresponds to a functional relationship of the form

$$St = 0.18 (V_j / V_0)^{-1.25}$$

which seems to represent the data well. The effect of the jet vector angle on the Strouhal number is shown in figure 12. At a given velocity ratio, it is observed that the magnitude of the St increases with decreasing angle. An

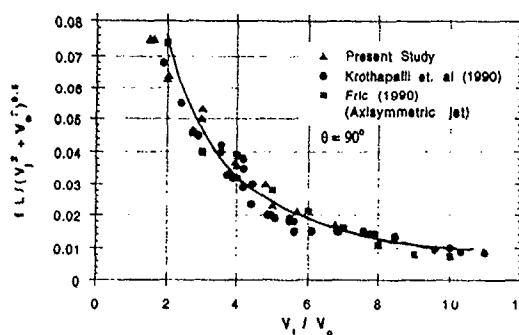


Figure 11. The variation of the modified Strouhal number with the velocity ratio.

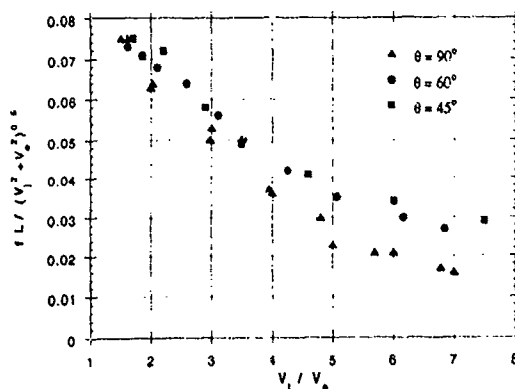


Figure 12. The variation of the modified Strouhal number with velocity ratio for different jet vector angles.

attempt to collapse the data into a single curve was found to be unsuccessful. As described above, for $\theta \geq 120^\circ$, no significant peaks in the spectrum of the velocity fluctuations were noticed. Hence the Strouhal number data for this case is not included in the figure.

V. Conclusions

In the present work an attempt is made to describe the basic flow structure of the separated recirculation region around subsonic vectored rectangular jet into an oncoming subsonic freestream. Using surface flow visualization, it is observed that horseshoe vortices are formed ahead of the jet. These vortices are unsteady in nature with a dominant frequency that corresponds to the vortex shedding frequency in the near wake of the jet. The mean primary separation distance ahead of the jet is found to be a function of velocity ratio and vector angle. The functional dependence depict two distinct regimes, one dominated by the blockage effect of the freestream by the jet and the other by the entrainment process of the jet. The size of the separation region both upstream and downstream of the nozzle exit decreases with increasing jet vector angle.

The surface tufts visualization indicates that the recirculation zone in the near wake has two different vortical structures. The first consists of a symmetric counterrotating vortex pair forming a closed region. The other consists of vortices shedding alternately from each side of the jet quite similar to the flow past a solid bluff body. This type of flow structure occurs in the case of a strong jet. A unique functional relationship exists between the nondimensional shedding frequency (Strouhal number) and the velocity ratio. The relationship $St = 0.18 (V_j / V_\infty)^{-1.25}$ was found to fit experimental data of rectangular and axisymmetric jets issuing normally into crossflow.

VI. Acknowledgments

We would like to thank Mr. Todd La Salle for helping us in the set up of the experiment. The work was partially supported by NASA Ames Research Center, Low Speed Aircraft Research Branch.

VII. References

1. Krothapalli, A., Lourenco, L., and Buchlin, J.M., "Separated Flow Upstream of a Jet in a Crossflow", *AIAA Journal*, Vol 28, NO. 3, 1990, pp. 414 -420.
2. Kuhn, R. E., "The Induced Aerodynamics of Jet and Fan Powered V/STOL Aircraft" *Recent Advances in Aerodynamics*, Springer Verlag, New York, 1986, pp. 337 - 373.
3. Margason, R.J., "Review of Propulsion Induced Effects on Aerodynamics of Jet V/STOL Aircraft", *NASA TN D-5617*, 1970.
4. Fric, T. F., "Structure in the Near Field of the Transverse Jet", Ph.D Thesis, California Institute of Technology, 1990.

SCALAR MIXING IN THE SUBSONIC JET IN CROSSFLOW

S.H. Smith, A. Lozano, M.G. Mungal & R.K. Hanson

High Temperature Gasdynamics Laboratory
Mechanical Engineering Department
Stanford University, Stanford, CA 94305-3032
USA

1. SUMMARY

Results are presented on the structure and mixing of subsonic jets in crossflow. These results are obtained by using planar laser-induced fluorescence of acetone vapor which is carried as a marker of the jet fluid. In addition to providing instantaneous realizations of the jet structure, the data is quantitative in providing instantaneous measures of the jet mixture fraction. We examine jet to crossflow velocity ratios ranging from 6 to 14, corresponding to momentum ratios of 36 to 196. It is found that the instantaneous structure is quite complex, dominated by large-scale motions, and bear little resemblance to ensemble-averaged field. Jet fluid is seen in the wake structure in the curved portion of the jet, even though the amounts are small. Mean and rms concentration fluctuations are presented for select cases.

2. INTRODUCTION

The jet in crossflow is widely used in many technical applications. In several of these, mixing of the jet with the crossflow is of primary importance such as in applications involving gas turbines, fuel injection, SCRAMJETS, VTOL aerodynamics and waste disposal. Compared to other free shear flows (e.g. mixing layers, free jets), the jet in crossflow displays considerably more complexity ranging from jet-like behavior in the near-field to a counter-rotating vortex pair in the far-field and includes the issue of curvature as the flow progresses downstream. Fric & Roshko [1, 2], have provided many detailed visualizations of the near-field and have identified four main vortical structures which comprise the flow: the jet shear layer vortices which evolve on the jet column; the necklace (horseshoe) vortices due to the wall boundary layer which wrap around the jet column; the wake structure which appears downstream of the jet column, connecting the jet to the wall; and finally, the counter-rotating vortex pair which forms downstream in the bent over jet. Fric and Roshko have concluded that, for flush mounted jets, the wake vortices are due to the wall boundary layer fluid, and are in no way related to vortex shedding from the jet column.

Many earlier studies [e.g. 3-7] have provided visualizations and measurements on the velocity field associated with the jet in crossflow. Other studies have dealt with mixing of a passive scalar [8-11] as well as theoretical models [12-16]. Most of the studies which

use passive scalars have reported time averaged quantities with fluctuating quantities only being very recently reported [11]. In this work, we attempt to provide instantaneous measures of the passive scalar field using the latest in non-intrusive diagnostics and to combine the interpretation of these with the detailed picture initiated by Fric & Roshko. Our results should be viewed as work in progress, as we are in a relatively early stage of our investigations.

Planar laser-induced fluorescence (PLIF) has become an attractive technique for concentration measurements in liquid and gaseous flows [17-19] because it is non-intrusive, effectively instantaneous and provides concentration information in a whole plane without integration along the line of sight. Its use of molecular markers allows high spatial resolution measurements with minimal alteration of the flow conditions. There are a large variety of potential tracers for use in liquid flows, but the selection is somewhat reduced when working with gases, and most chemicals currently used in gaseous PLIF concentration measurements (nitric oxide, iodine, biacetyl or acetaldehyde) are not ideal from the viewpoint of toxicity, corrosion, disposal, and carcinogenicity. Recently however, Lozano [20], and Lozano et al. [21] demonstrated the use of acetone as a concentration tracer in a small free air jet. Acetone was shown to be a convenient fluorescent marker when working in air flows, capable of providing high signal-to-noise ratios (SNR). In the present work, acetone is therefore used to obtain concentration images in a subsonic transverse air jet. Detection with a highly sensitive charged coupled device (CCD) camera has improved the data quality, decreasing the minimum detectable signal, increasing the SNR, and enabling the successful instantaneous imaging of large fields of view (17 x 22 cm). Further details on the use of acetone will be provided below.

3. EXPERIMENTAL DETAILS

3.1 Wind Tunnel

To perform the experiments described here, a small wind tunnel was designed and built. The tunnel, Fig. 1, is a vertical structure 220 cm high with a 54 x 54 cm square cross-section. It is suspended from the ceiling of the laboratory and is composed of three parts: the inlet, the test section and the exhaust. The crossflow travels

vertically upward, while the jet is injected horizontally. The 91.5 cm high exhaust section, made of 0.635 cm (1/4") aluminum plate connects to the 5 hp blower that induces the crossflow from the ambient room air. The test section, 91.5 cm tall, is formed by an aluminum frame to which the walls are attached. Two opposite side walls are 0.635 cm (1/4") glass panes, which provide optical access for image acquisition. Note that as acetone fluorescence peaks in the blue, this glass is not required to transmit in the u.v. The third wall, made of aluminum, has a 7.6 cm (3") circular hole for the nozzle. The front aluminum wall is a rectangular frame which can be covered by different combinations of rectangular filler plates of various lengths. One of them contains a 24 x 6.3 cm quartz window to transmit the u.v. excitation laser sheet. This plate can be rotated to allow the laser sheet to cut the flow axially or transversely, and displaced vertically to image different downstream regions of the flow.

The tunnel inlet has a contraction of elliptical profile. One honeycomb plate and four wire-mesh screens are used to homogenize and condition the crossflow. The crossflow velocity is constant, set by the blower to be 7.7 m/s, with a 1% turbulence intensity and less than a 5% velocity variation. The jet/crossflow velocity ratio is modified by varying the jet velocity. The jet inlet, attached to the side wall of the tunnel consists of a cylindrical 16.5 x 25.4 cm settling chamber containing one perforated plate and two honeycomb screens equally spaced, with a 0.5 cm diameter contoured nozzle at the end of the chamber that communicates with the tunnel test section. The jet emerges directly from the tunnel sidewall into the crossflow and its associated boundary layer. At the injection point, the boundary layer is 20.32 cm (8 inches) downstream of the last screen leading to a boundary layer thickness of 0.6 cm (1/4 inch).

3.2. PLIF Diagnostics

Acetone was the tracer of choice for the experiments reported here based on imaging of fluorescence emission. Acetone is a very attractive tracer for PLIF concentration measurements in gaseous flows, owing to its physical and photophysical characteristics. It has a high vapor pressure (~180 Torr at 20°C), which allows for high seeding densities, and its absorption band is broad (225-320nm) with a maximum between 279 and 280 nm. Acetone can, consequently, be excited using different commercially available lasers; the choice for this experiment is a XeCl excimer laser (308nm). Upon excitation, acetone fluoresces over a broad band in the blue (350 to 550 nm), with a peak at 435 nm, an emission efficiency $f = 0.2\%$, and a short lifetime of ~4ns, which enables high temporal resolution imaging without the need for gated cameras. Furthermore, as fast shuttering is not required, images can be obtained with higher SNR, dynamic range and spatial resolution than those attainable with intensified cameras. Acetone also

phosphoresces with a spectrum similar to the fluorescence emission (but extending to longer wavelengths), with a lifetime of 200 ms and efficiency of 1.8%. Phosphorescence intensity depends on temperature and is strongly quenched by oxygen, so possible interferences by the temperature-dependent phosphorescence are completely negligible when air is used as the carrier gas; this is the case with the current jet in crossflow. The fluorescence, however, is independent of temperature, and insensitive to quenching by air. Acetone toxicity is very mild, and its cost is economical. A more detailed description of acetone photophysics can be found in Refs. 20 and 21.

Acetone was seeded by bubbling the carrier air into a sequence of three bottles containing the liquid, in order to fully saturate the carrier air. To filter acetone droplets, a 40µm micropore filter was attached at the container exit. To avoid fluctuations in the acetone seeding density due to the temperature decrease caused by evaporation, the bottles were immersed in a thermostatic bath.

A Questek Series 2000 Excimer Laser, containing a xenon chloride mix, was used to excite the acetone. This laser produces a square beam 2cm wide by 1 cm high tuned to 308nm. The Questek has a maximum energy of 470 mJ/pulse, and it was operated at 400 mJ/pulse for the present set of experiments.

The image collection system was comprised of a Photometrics AT 200 controller (16 bit A/D converter), a thermoelectrically cooled (-40°C) CH250 camera head with a Tektronix TEK 512CB/MPP CCD array, and a Nikon 50 mm F#1.2 lens. This array is a 512x512 pixels, thinned, backside illuminated CCD detector, with a pixel size of 27 µm, and was operated in MPP (multiphase pinned) mode to reduce the dark current. Thinned, backside-illuminated detectors have a much higher quantum efficiency than similar thick, frontside-illuminated arrays. This difference is especially significant for blue light, where efficiencies increase from 10-15% in frontside-illuminated devices to values as high as ~50% at 450 nm and ~55% at 400 nm. The Photometrics 200 system has a reported total noise of 13 e- with a reported gain factor of 4 e-/ADU (analog to digital units).

4. RUN CONDITIONS

The images to be presented below were acquired by illuminating the acetone-seeded jet with the laser sheet in three different ways: (1) side views obtained by slicing the flow axially through the nozzle centerline; (2) plan views obtained by orienting the laser sheet, at a fixed height, parallel to the injection wall; and (3) end views obtained by orienting the laser sheet normal to the injection wall at a fixed downstream distance such that the flow travels through the laser sheet.

The large field of view (17 x 22 cm) meant that the laser sheet could not be recollimated, so in order to minimize divergence and to increase the thinned region of the focus, the optics were kept as far from the tunnel as possible. To this end, a 2 m focal length spherical lens was combined with either a 75 mm cylindrical lens (side views and top views) or a 300mm cylindrical lens (end views). The 2 m spherical lens allowed the focal point to be in the center of the imaged area, while the cylindrical lens created the sheet. The sheet thickness for all views was approximately 1.5 mm. For side views and top views the sheet was approximately 25 cm high in the test section, and for end views the sheet was approximately 15 cm high.

For each of the three run conditions, background and laser sheet profiles were taken, in addition to the jet images. The background images were taken with the laser triggered, but with no acetone present in the tunnel. The laser sheet images were taken by isolating the test section with plastic seals and filling it with acetone; the laser and camera were then triggered to obtain the laser sheet. To correct each flowfield image, ten background images were averaged. This background average was subtracted from ten laser sheet profiles, and they were averaged to create an averaged laser sheet. Finally, for each flowfield image, the averaged background was first subtracted, and then divided by the laser average to create the corrected images.

The number of images acquired are presented in Table 1, below. (Note that select images are presented in section 5, and that the crossflow is kept constant at 7.7m/s.)

Table 1: Velocity Ratio, Jet Reynolds Number, and Number of Images Acquired.

Velocity Ratio	Reynolds Number	side	end	plan
6 to 1	16000	100	100	0
10 to 1	27600	100	100	100
11 to 1	30400	3	3	3
12 to 1	33100	3	3	100
13 to 1	35900	3	3	3
14 to 1	38640	100	100	100

For the images shown below, each pixel imaged approximately 0.5 mm of physical space. This is to be compared with a Kolmogorov scale of 0.7 mm at 26 diameters downstream for the 14:1 case, and using a Kolmogorov constant of 25.

5. RESULTS

5.1 Jet Structure

Three different fixed planes are imaged, and Fig. 2 orients the relationship between each plane to obtain the

side, end and plan views. The side views are planar slices through the jet nozzle centerline and are used as a reference. The end views are located 26 jet diameters downstream, and the top views are 28 jet diameters away from the wall; these values are constant for all jet velocity ratios. Unless otherwise noted, the images are displayed with a 2.0 gamma exponential color table of the form $I_{corr} = I^{1/\gamma}$, where I is the intensity linearly dependent on the acetone concentration, and I_{corr} is the intensity mapped through the color table, to better distinguish the details of the flowfield.

Six instantaneous side views ranging from a velocity ratio of 6:1 to 14:1 are presented in Fig. 3. These views are reminiscent of previous smoke visualizations [3, 5, 9, 10] but differ in two aspects: namely they represent a thin slice through the flow, and they are quantitative. Several features are immediately apparent. (1) The jet penetration increases as the velocity ratio increases. (2) The spreading or width of the jet increases with velocity ratio. (3) Significant intrusions of freestream fluid occurs along the upper jet boundary, associated with the presence of large-scale motions. (4) Of particular interest in these images is the presence of jet fluid in the wake structures, which begins to appear, most clearly, in the 13:1 case.

Although eddies of crossflow fluid penetrating the jet have been previously observed [1,2] the opposite case, which is found in our images (jet fluid entering the wake), has to our knowledge not been reported until the present experiments were initiated [22]. Closer examination of each image suggests however that in the portion of the flow where the jet is most curved, the wake fluid is most apparent, while in the regions of the jet that are bent over and less curved, that little jet fluid is apparent. The 13:1 and 14:1 cases are those for which the curved region is best imaged with the present setup. Future studies using larger jet diameters and close-up views will be able to resolve this question.

The absence of this jet/crossflow interaction was interpreted by Fric and Roshko as evidence that the jet vorticity does not contribute to the wake vorticity. It is possible, however, that they were not able to detect these structures due to a lack of sensitivity in their experiments (smoke-wire visualization). It is also possible that some jet fluid may flow axially into the cores of the wake vortices once they have formed as has been observed in other wake flows [23]. It is also possible that such axial flow may only occur during the times that the jet is curving and stretching the wake vortices, and this may not be the case when the jet is bent over and the stretching is considerably less. Thus our present findings show that jet fluid does indeed enter the wake flow, but that the amounts are small, and that furthermore the effect is most pronounced in the curved regions of the jet.

Figure 4 presents the averaged 14:1 side view next to three independent instantaneous side views. Here the wake occurs in the most orderly fashion that we have observed to date. It appears that the jet fluid in the wake occurs at an angle of about 50 degrees to the wall with a spacing that is approximately two jet diameters in extent. For the velocity ratios shown in Fig. 3, it does not appear that the wake angle is significantly changed.

The end views also show the wake structure. Figure 5 shows five instantaneous 14:1 images next to a 100 ensemble averaged image. Notice that the (feint) wake is often present on the jet centerline and rarely strays off of it. Thus the jet fluid is detected in the centerline cuts shown earlier, but it is unlikely that they would be seen in regions away from the centerline. This figure also shows some common features seen in these end views for this case. There are deep fluid penetrations associated with the counter rotating vortex pair, and a large asymmetry in both vortex size and fluid concentration. In these end views either the left or right vortex momentarily dominates (see the middle column of three, Fig. 5), or they can be approximately the same (lower left image). The vortex pair also can be quite flattened or elongated in comparison to the ensemble average (rightmost column). In all cases however, the wake remains close to the centerline suggesting that its dynamics might be independent of the counter-rotating vortex pair.

Figure 6 shows similar views for the 10:1 case. These are shown to highlight some features which are different from the previous 14:1 case. First, no wake fluid is apparent, consistent with the side views seen earlier at this axial station. Second, the intrusion of freestream fluid into the counterrotating pair is much better defined in this case as is the general observation that the instantaneous and ensemble average seem to bear a closer resemblance to each other, a feature not common in the 14:1 case. In fact examination of other cases of lower speed ratio suggests that such cases are more benign in appearance in comparison to the higher speed ratio cases. The third column of Fig. 6 shows the most deviant images found.

The 14:1 end views showed that one vortex in the counter rotating vortex pair may occasionally dominate, and this is supported by the top views. Figure 7 presents three instantaneous 14:1 top views next to their 100 image average. When viewing these images, it is helpful to remember that the jet is curving into a horizontal laser sheet. As the jet proceeds from left to right, the images display the jet's top, middle and then bottom. In the bottom part the counter-rotating vortices appear, to be referred to here as legs. These views have been chosen to present three specific cases. In one case the bottom leg is dominant; in another case the top leg is dominant, and lastly, both legs are nearly equal. In the last image,

where both legs are fairly equal, the jet most clearly shows a distinct wiggling motion as it moves downstream. Combining these observations with the end views, we conclude that the wiggling motion of the counter-rotating pair extends for considerable axial distances and is of a wavelength that is of the order of the local jet diameter. The concentration of fluid can also be dominant in one leg, compared to the other, for distances as large as our viewing area.

As the jet velocity is decreased, the jet moves farther out of the plane imaged in the top view. This allows the opportunity to see the shapes of the jet protrusions as they enter the imaged plane. In particular Fig. 8 shows four 12:1 images in the standard format. Notice the character of the jet as it enters the plane. The protrusions are fairly straight and banded. The concentration of each band is fairly uniform. Combining this information with the side views seen earlier suggests that the upper edge large-scale intrusions are distributed around the jet periphery and are not localized intrusions.

In summary, the instantaneous images shown here suggest a jet structure which is highly three-dimensional. As the jet curves, jet fluid is brought into the wake vortices and remains fairly close to the jet centerline. Large-scale freestream intrusions occur on the edge of the jet and are radial in extent. As the counter rotating vortices develop, the legs can be of different strengths as well as of equal strengths. The legs also oscillate (wiggle) at a wavelength comparable to the local jet diameter. The higher velocity ratio cases show larger variations in the strengths of the counter rotating vortices, with the lower velocity ratio cases tending to be more similar to the average in shape and extent. This structural picture is generally consistent with earlier views, but adds new features not previously reported. Since our data is quantitative, comparisons with previous measurements will be presented next.

5.2 Quantitative Measures

The averaged side views for both the 10:1 and 14:1 cases have been compared to Pratte and Baines' [8] jet trajectory curve fits for the top edge, bottom edge, and jet centerline, Fig. 9. Each of the three curves has the form

$$\frac{x}{rd_0} = A * \left(\frac{z}{rd_0} \right)^{0.28}$$

where r is the jet-to-crossflow ratio and d_0 is the source diameter, for r ranging between 5 and 35. The letter A is a constant set by Pratte and Baines to 2.63 for the top profile, 2.05 for the centerline profile, and 1.35 for the bottom edge profile. The averaged results agree with Pratte and Baines relationship, which serves to confirm

our approach. It might appear that the jets do not penetrate as deeply as the Pratte and Baines relationship might suggest, but each image shows a slightly downward sloping horizontal reflection near their bottom which is the true horizontal; thus this slight rotation between the camera and jet can account for the reduced penetration.

The centerline concentration profile of the end views are compared to the contours of Kamotani and Greber [10]. They found the centerline scalar profile in the end views formed a self-similar Gaussian profile when the transverse distance is stretched by a characteristic length taken as the half width at half maximum. Their momentum ratios ranged to a maximum of 59.6, corresponding to a velocity ratio in this experiment of 7.7. It is not surprising that the 6:1 and 10:1 velocity ratio give good agreement, Fig. 10, and it is worth noting that the peak of the 14:1 velocity ratio contains deviations from the Gaussian profile, Fig. 11. While we believe that the change in the profile shape is real, we note that the 14:1 profile is shown in a region of the jet that is bent, unlike the lower velocity ratio cases. Further work will explore these differences.

A single rms concentration result is presented here, Fig. 12. It is the rms from end views of the 14:1 velocity ratio and was compiled from 100 images. The results show that the rms is highest in a banded region surrounding the central core of the jet. This result appears to be consistent with the structural picture presented earlier, and results from the large-scale variations which occur around the periphery of the jet. Side view rms results (not shown here) provide a consistent picture, namely that of maximum rms bands occurring at the periphery of the jet.

Finally, Fig. 13 highlights the significant differences between the instantaneous and ensemble-averaged concentration fields. The results are illustrated for the 14:1 case. These images are obtained by mapping the concentration into height and displaying the resulting three-dimensional object. The smooth mean shape and streamwise concentration decay is readily apparent. The instantaneous field, on the other hand, shows the local uniformity of mixing as well as the sharp gradients associated with the jet edges. The wake fluid concentration is seen to be quite small, when compared to the main jet body.

6. CONCLUSIONS

The results presented here provide confirmation of the utility of PLIF imaging in elucidating the fundamental fluid mechanics of the jet in crossflow. Using three orthogonal planar cuts we have been able to provide insights into the instantaneous structure and mixing of the jet in crossflow. Our results suggest a picture in which the jet shows pronounced large-scale intrusions of

freestream fluid around the jet periphery. The counter rotating vortex pair develops in a non-symmetric manner with significant undulations in the streamwise direction. We have also found that jet fluid is likely to appear in the wake vortices in the region of the jet that is undergoing curvature. We have been able to acquire data which confirm and extend previous measures of scalar mixing in this flow. While our work is in an early stage, we plan to extend these results by varying the x/d and y/d laser locations to provide further information and to acquire larger datasets for statistical analysis. We also plan to investigate the jet/wake interaction in further detail and to clarify its physics.

7. ACKNOWLEDGMENTS

This work has been sponsored by the AFOSR, Aerospace Sciences Directorate with Dr. Julian Tishkoff as the technical monitor. SHS is supported by the NDSEG fellowship. We wish to acknowledge useful discussions with A. Roshko on the wake vortices.

8. REFERENCES

1. Fric, T.F. & Roshko, A., "Structure in the Near Field of the Transverse Jet", *7th Symp. on Turbulent Shear Flows*, August 21-23, Stanford, Paper 6-4, (1989).
2. Fric, T.F., "Structure in the Near Field of the Transverse Jet", Ph.D. Thesis, Caltech, (1990).
3. Keffer, J. F. & Baines, W. D., "The Round Turbulent Jet in a Cross-Wind", *J. Fluid Mech.*, 15, 481-496, (1963).
4. McMahon, H. M., Hester, D. D. & Palfery, J. G., "Vortex Shedding from a Turbulent Jet in a Cross-Wind", *J. Fluid Mech.*, 48, 73-80, (1971).
5. Chassaing, P., George, J., Claria, A. & Sananes, F., "Physical Characteristics of Subsonic Jets in a Cross-Stream", *J. Fluid Mech.*, 62, 41-64, (1974).
6. Moussa, Z. M., Trischka, J. W. & Eskinazi, S., "The Near Field in the Mixing of a Round Jet with a Cross-Stream", *J. Fluid Mech.*, 80, 49-80, (1977).
7. Andreopoulos, J. & Rodi, W., "Experimental Investigation of Jets in a Crossflow", *J. Fluid Mech.*, 138, 93-127, (1984).
8. Pratte, B.D. & Baines, W.D., "Profiles of the Round Turbulent Jet in a Cross Flow", *J. Hydraul. Div., Proc. ASCE*, 92, 53-64, (1967).
9. Patrick, M. A., "Experimental Investigation of the Mixing and Penetration of a Round Turbulent Jet Injected Perpendicularly into a Transverse Stream", *Trans. Instn. Chem. Engrs.*, 45, T16-T31, (1967).
10. Kamotani, Y. & Greber, I., "Experiments on a Turbulent Jet in a Cross Flow", *AIAA Jr.*, 10 (11), 1425-1429, (1972).
11. Huang, Z., Low, M. S., Kawall, J. G. & Keffer, J. F., "Structural Features of a Heated Round Turbulent Jet in a Cross-Flow", *Eight Symp. Turb. Shear Flows*, Tech. Univ. Munich, September 9-11, Paper 25-1, (1991).

12. Fearn, R. & Weston, R. P., "Vorticity Associated with a Jet in a Cross Flow", *AIAA Jr.*, 12 (12), 1666-1671, (1974).
13. Broadwell, J.E., Breidenthal, R.E., "Structure and Mixing of a Transverse Jet in Incompressible Flow", *J. Fluid Mech.*, 148, 405-412, (1984).
14. Sykes, R. I., Lewellen, W. S. & Parker, S. F., "On the Vorticity Dynamics of a Turbulent Jet in a Crossflow", *J. Fluid Mech.*, 168, 393-413, (1986).
15. Karagozian, A.R., "The Flame Structure and Vorticity Generated by a Chemically Reacting Transverse Jet", *AIAA J.*, 24 (9), 1502-1507, (1986).
16. Coelho, S. L. V. & Hunt, J. C. R., "The Dynamics of the Near Field of Strong Jets in Crossflows", *J. Fluid Mech.*, 200, 95-120, (1989).
17. Dimotakis, P.E., Miake-Lye, R.C., Papantoniou, D.A., "Structure and Dynamics of Round Turbulent Jets", *Phys. Fluids*, 26, (11), 3185-3192, (1983).
18. Hanson, R.K., Seitzman, J.M., Paul, P.H., "Planar Laser-Induced Fluorescence Imaging of Combustion Gases", *Appl. Phys. B*, 50, 441-454, (1990).
19. van Cruyningen, I., Lozano, A., Hanson, R.K., "Quantitative Imaging of Concentration by Planar Laser Induced Fluorescence", *Expt. Fluids*, 10, (1), 41-49, (1990).
20. Lozano, A., "Laser-Excited Luminescent Tracers for Planar Concentration Measurements in Gaseous Jets", HTGL report No. T-284, Stanford University, Stanford, CA (1992).
21. Lozano, A., Yip, B., Hanson, R.K., "Acetone: a Tracer for Concentration Measurements in Gaseous Flows by Planar Laser-Induced Fluorescence", *Expt. Fluids* 13, 369-376, (1992).
22. Lozano, A., Smith, S. H., Mungal, M. G. & Hanson, R. K., "Concentration Measurements in a Transverse Jet by Planar Laser-Induced Fluorescence of Acetone", *AIAA Jr.*, in press, (1993).
23. Cohn, R. K. & Koochesfahani, M. M., "Effect of Boundary Conditions on Axial Flow in a Concentrated Vortex Core", *Phys. Fluids A*, 5 (1), 280-282, (1993).

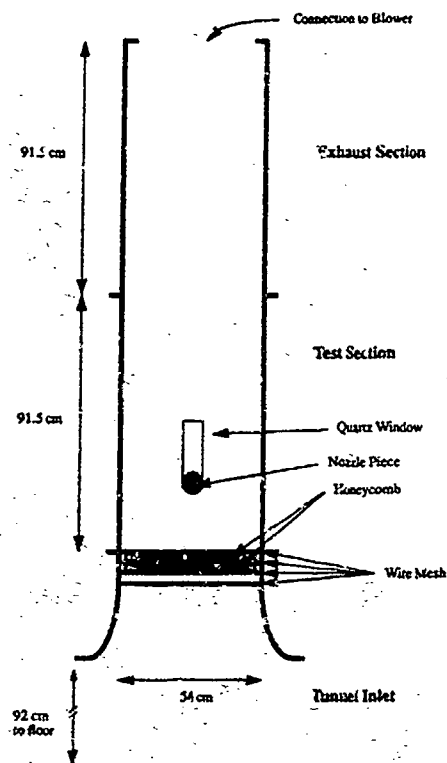


Figure 1: Schematic of the wind tunnel.

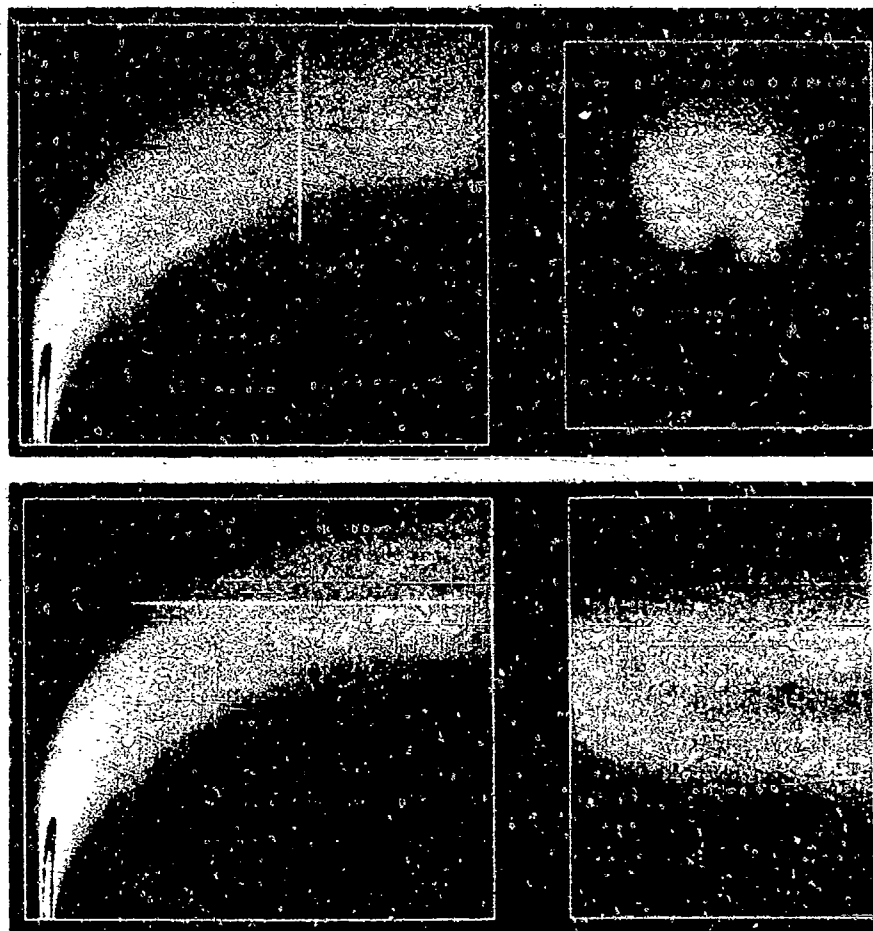


Figure 2: Illustration of side, end and plan views. Line marks position of laser sheet.

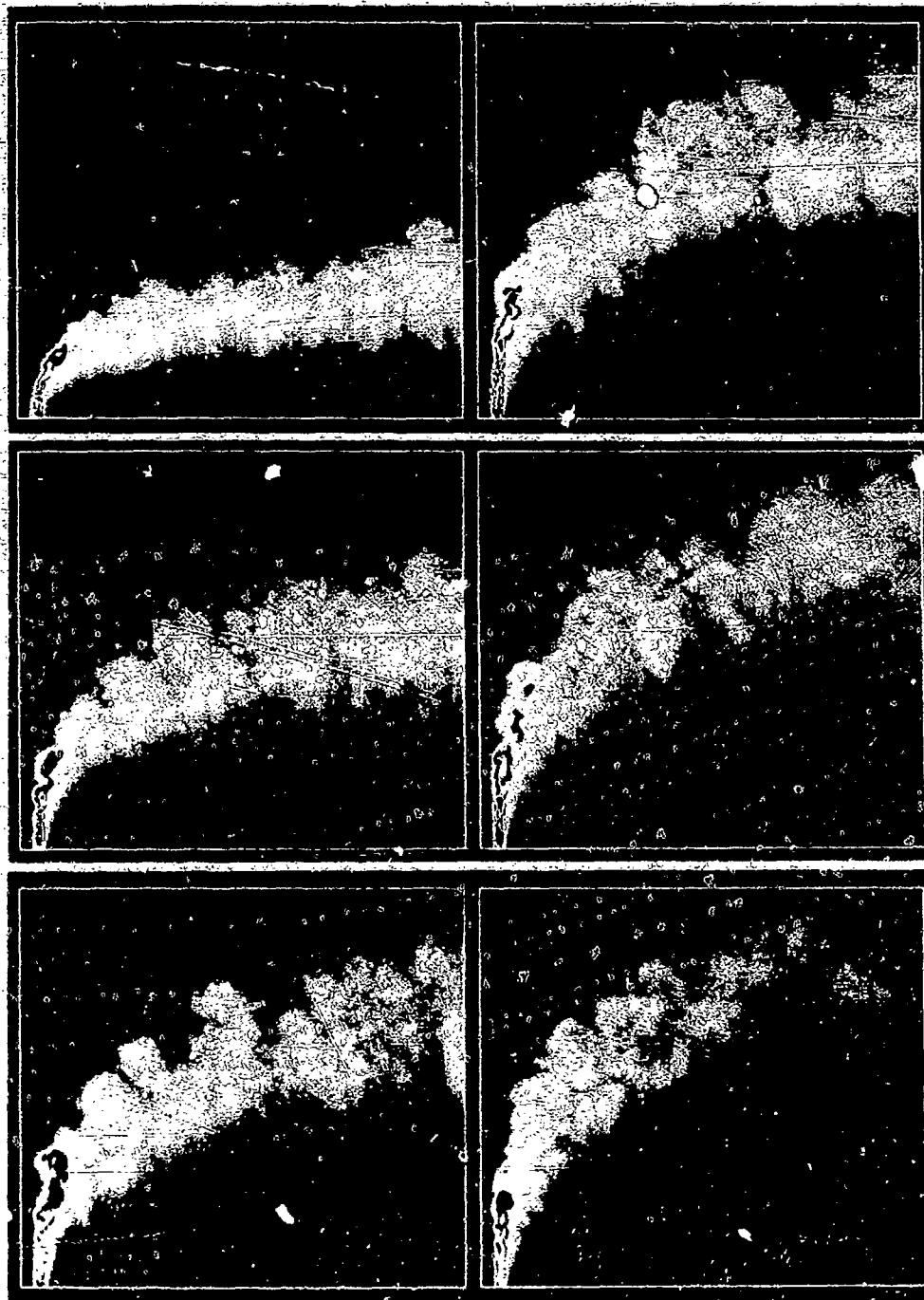


Figure 3: Instantaneous side views for velocity ratio = 6, 10, 11, 12, 13, 14:1 (from top to bottom, then left to right). Field of view is 17 x 22 cm. Jet exit diameter is 0.5 cm. Freestream velocity is 7.7 m/s.

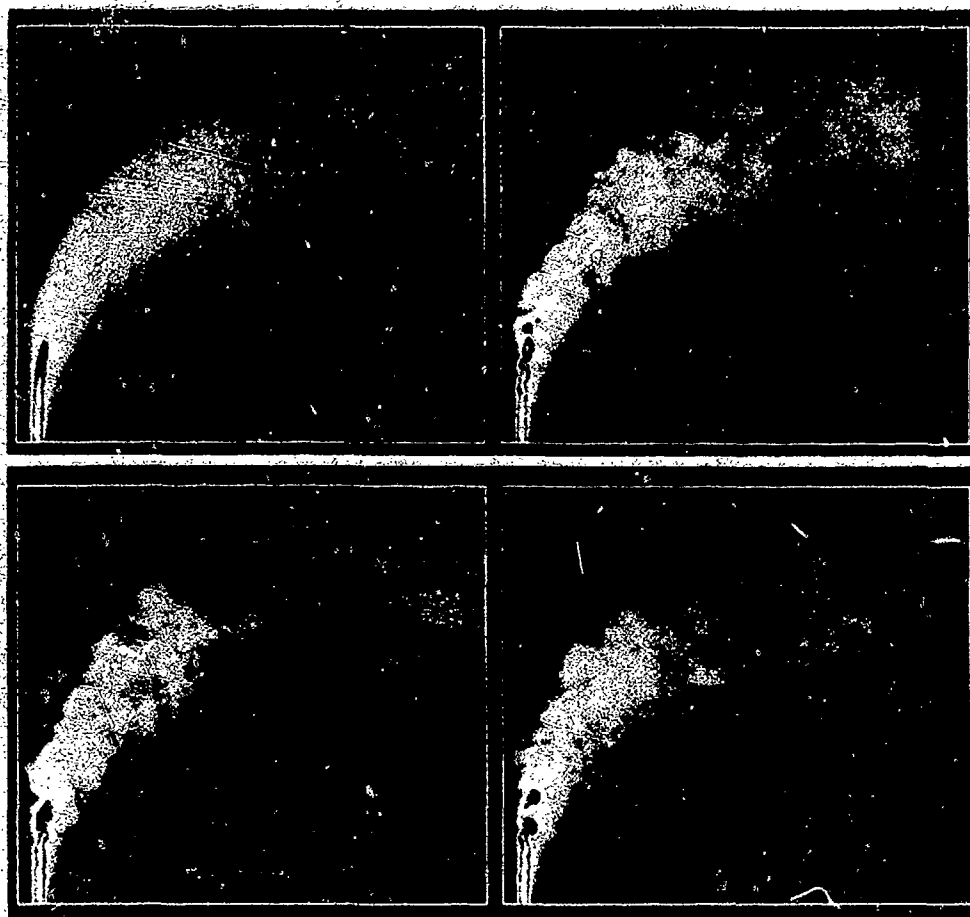


Figure 4: Instantaneous and ensemble averaged side views of 14:1 case showing wake structure.

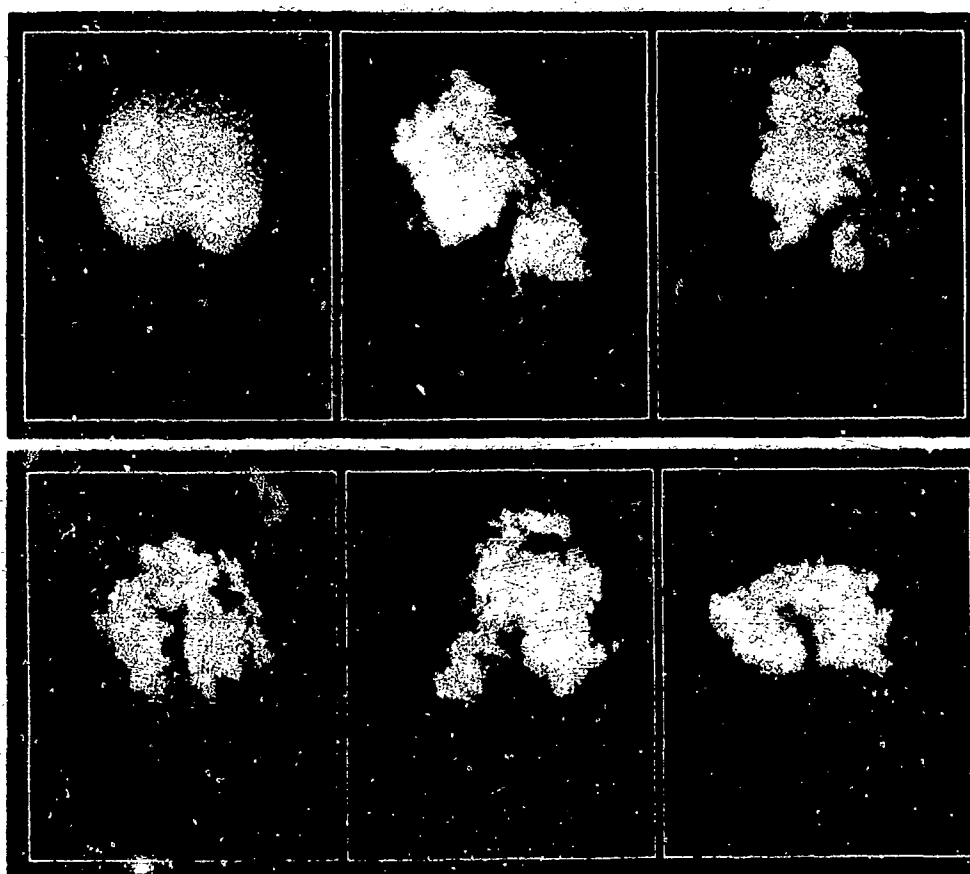


Figure 5: Instantaneous and ensemble averaged end views of 14:1 case.

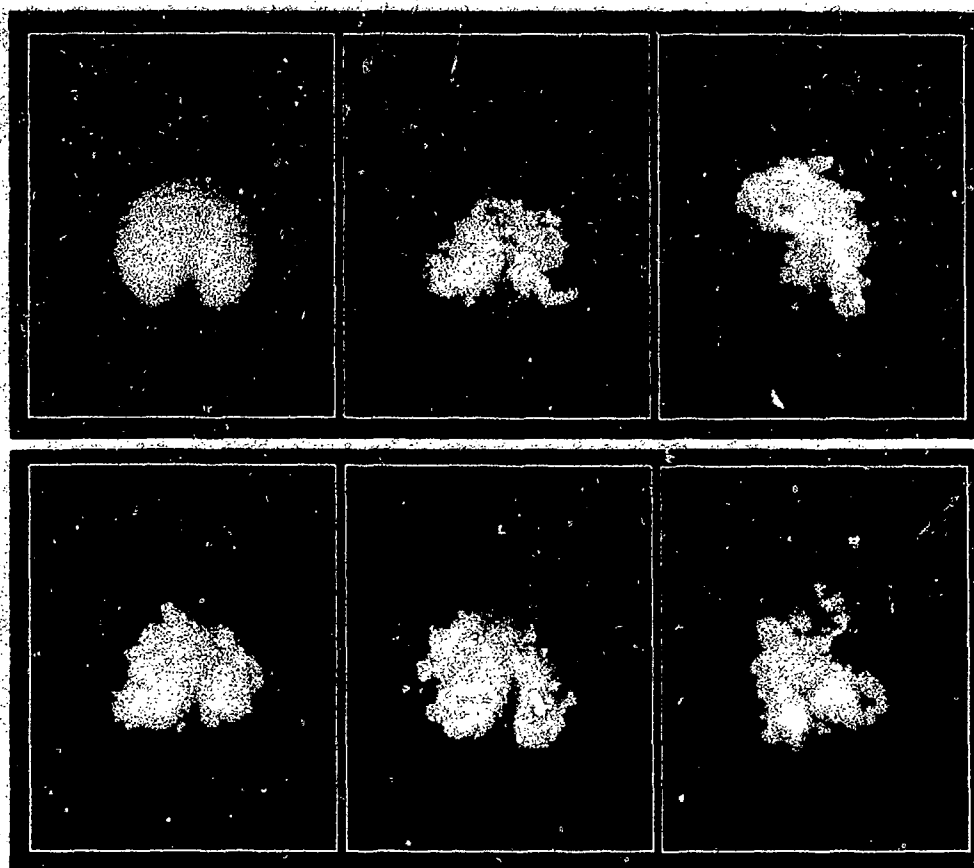


Figure 6: Instantaneous and ensemble averaged end views of 10:1 case.

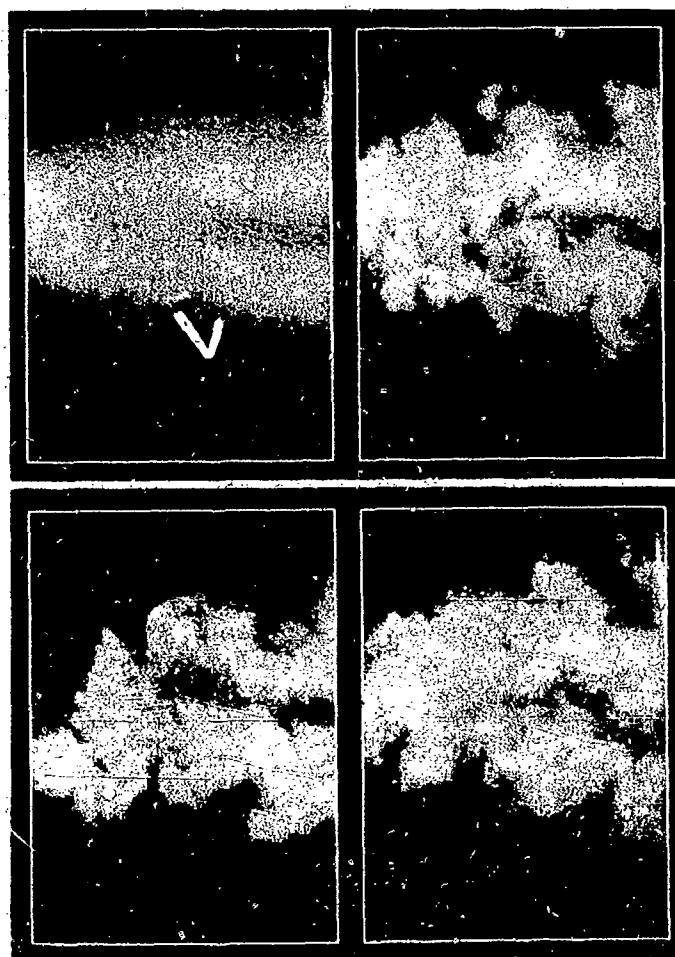


Figure 7: Instantaneous and ensemble averaged plan views of 14:1 case.

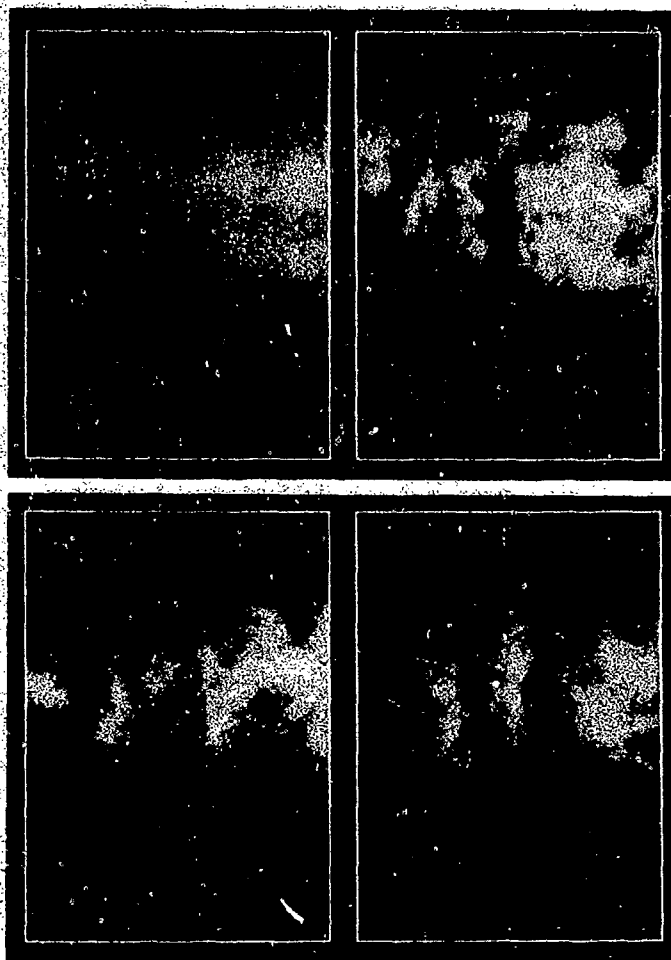


Figure 8: Instantaneous and ensemble averaged plan views of 12:1 case.

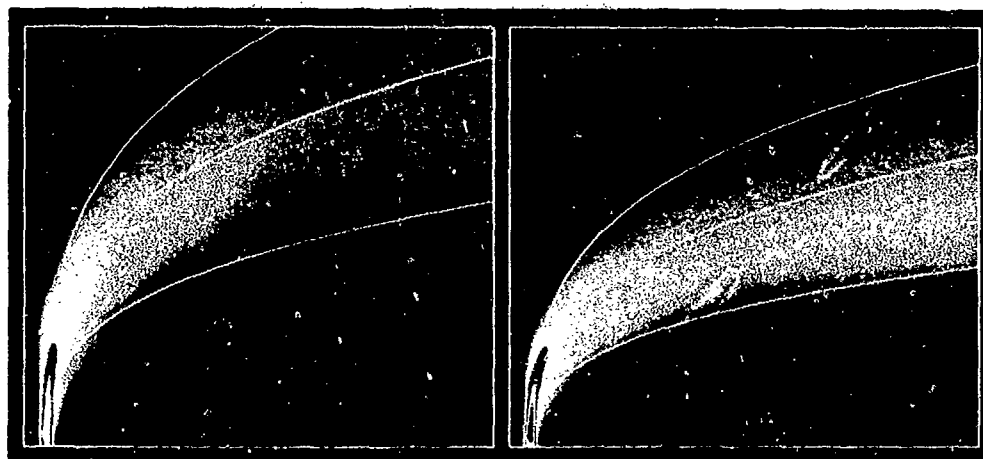


Figure 9: Comparison of 14:1 (left) and 12:1 (right) ensemble averaged side views with Pratte & Baines relationships [8].

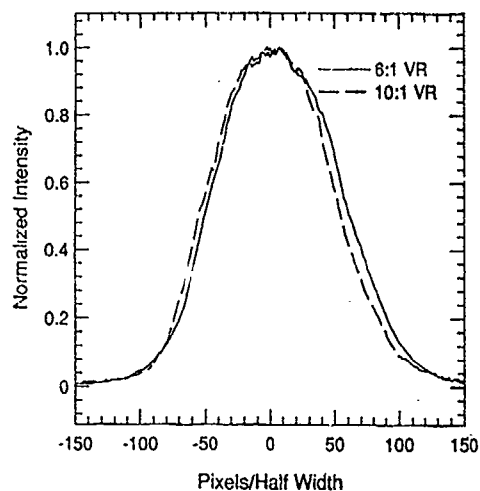


Figure 10: Vertical centerline end view profiles for 6:1 and 10:1 cases. The abscissa is normalized on the half width at half maximum distance.

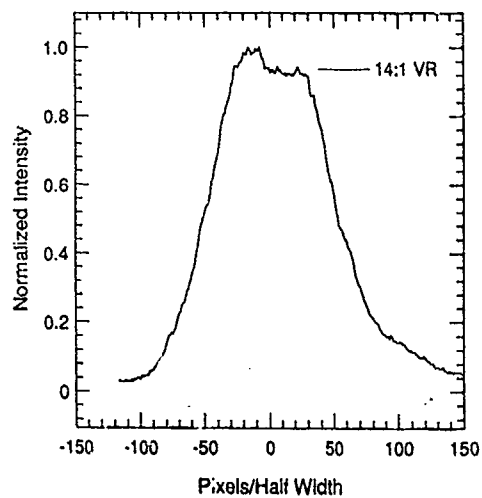


Figure 11: Vertical centerline end view profile for 14:1 case. The abscissa is normalized on the half width at half maximum distance. Note differences with Fig. 10.

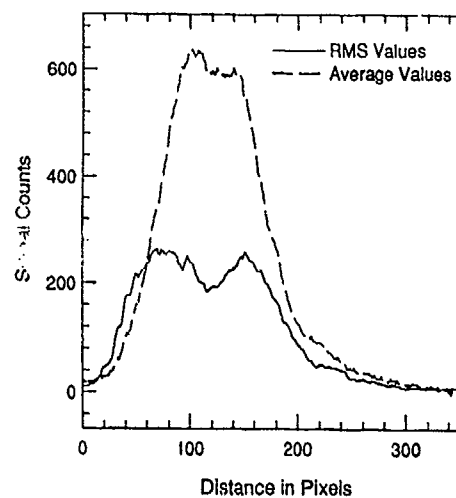
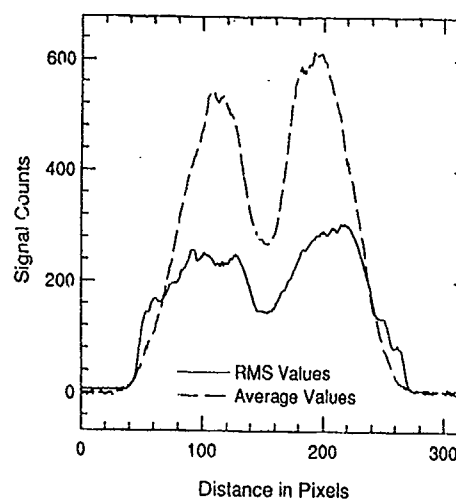


Figure 12: rms field of 14:1 case (image). Plots show horizontal (middle) and vertical (bottom) rms and mean profiles.

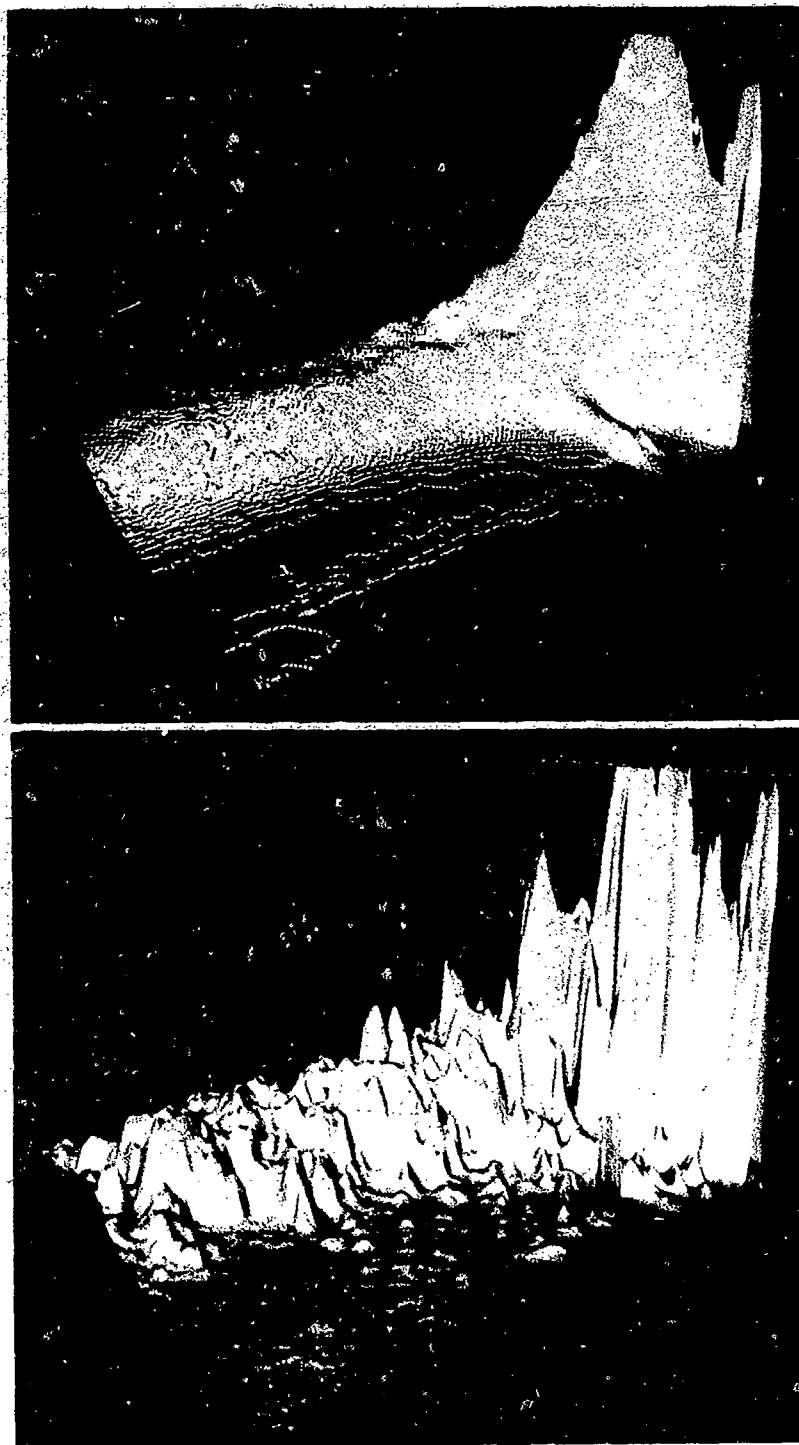


Figure 13: Landscape renderings of average and instantaneous concentrations of 14:1 case. Concentration is mapped into vertical height.

THE INTERACTION REGION ASSOCIATED WITH TWIN JETS AND A NORMAL CROSSFLOW

N.Toy, E.Savory and S.McCusker

Fluid Mechanics Research Group

Department of Civil Engineering

University of Surrey

Guildford GU2 5XH

United Kingdom

P.J.Disimile

Department of Aerospace Engineering and Engineering Mechanics

University of Cincinnati

Ohio 45221

USA

1. SUMMARY

The present work is an experimental investigation of the interaction between twin jets and a normal crossflow using real-time, quantitative, video image analysis of smoke-seeded jets to yield information concerning overall jet growth rates, the widths of the interface regions, intermittencies, p.d.f.s and spectra of the interface fluctuations. The cases covered are side-by-side and in-line jets, with a nozzle spacing of 5 nozzle exit diameters and a jet velocity / crossflow velocity ratio of 8, together with the single jet case. Additional data, in the form of velocity vector distributions from five-hole pressure probe measurements, have been obtained for comparison with the intermittency profiles in planes across the jets for the case of side-by-side jets with a nozzle spacing of 5 diameters and a jet ratio of 6. Finally, a parametric study of the effect on the overall jet penetration of velocity ratio (from 4 to 10), nozzle spacing (from 1 to 5 diameters) and nozzle orientation to the crossflow (from in-line to side-by-side, but with normal injection angle) has been carried out using a new digital image processing system. The velocity data for the side-by-side case shows that the deflected jets are dominated by one single vortex pair such that the inner vortex of each jet pair are not evident. The video analysis of the three main configurations, side-by-side, in-line and single jet, shows that in all cases the width of the mixing region at any downstream location is similar in magnitude to the jet half-width (as defined by the mean interface location). The interface widths are similar for the side-by-side and in-line jets but these are greater than the single jet case. There is some evidence that similarity profiles exist for the intermittency distributions across the interface regions which will enable correlation between the different jet configurations. The parametric study shows that, for a given jet ratio, the in-line jets (0° angle) penetrate further than those set at other angles to the crossflow and that changes of angle between 30° and 60° have less effect upon the overall penetration. For the in-line case it is the second jet, issuing into the lower static pressure region downstream of the first jet, that penetrates furthest into the crossflow.

2. LIST OF SYMBOLS

D	Jet nozzle diameter
E(F)	Energy associated with interface frequency, F
I(x,t)	Intermittency function
k	Wave number ($= 2\pi F/U_R$), m^{-1}
P	Probability density function
Re	Reynolds number ($= U_R D/\nu$)
S	Spacing between nozzle centres
U_R	Crossflow velocity

U_j	Jet velocity
VAR	Variance of interface fluctuation amplitude
VEL	Projected velocity vector in YZ plane
W_j	Mean half width of the jet
x	Arbitrary point located in the flow field
X	Cartesian coordinate in crossflow direction, with origin at geometrical centre of any given nozzle arrangement
Y	Cartesian coordinate in lateral direction
Z	Cartesian coordinate normal to ground plane
α	Jet velocity / crossflow velocity ratio (U_j/U_R)
σ_w	R.m.s. of lateral fluctuation of interface location about the mean value
θ	Angle of twin jet nozzle arrangement to the crossflow direction

3. INTRODUCTION

The classical configuration of a single jet issuing into a crossflow has been investigated by numerous workers and the main features of the interaction have been established. In contrast, the cases of twin side-by-side, in-line or staggered jets have received relatively little attention (refs 1-5). The present authors carried out an earlier investigation of twin side-by-side jets issuing into a crossflow (ref 6). The effects of nozzle spacing (S/D), which was varied from 1 to 5, and jet velocity / crossflow velocity ratio (α), varied from 6 to 10, were examined using a novel technique for real-time video analysis of smoke visualised jets (refs 7,8). The experimental data were given in the form of intermittency contour maps in YZ planes across the jets from which the development of the jets in the downstream direction and the overall penetrations and widths were assessed. It was found that the development of the widely spaced jets (such as $S/D=5$, where the crossflow passes around both sides of each jet) is noticeably different from that of closely spaced jets (such as $S/D=1$, where no crossflow penetration between the jets occurs). In all the cases the inner vortices of the two counter-rotating pairs rapidly disappeared within the first few jet diameters downstream from the nozzles, indicating that the two jets combined to form one large jet displaying single jet characteristics, as noted previously (refs 4, 5).

The present work extends this study by examining a number of aspects of the jet / crossflow interaction. Firstly, some comparative measurements of the velocity field in planes normal to the crossflow have been conducted, using a calibrated five-hole pressure probe, for one particular configuration, namely side-by-side jets with $S/D=5$ and $\alpha=6$. This was carried out in order to ascertain the nature

of the vortex structure within the twin jets. Secondly, one jet nozzle spacing, $S/D=5$, and one typical velocity ratio, $\alpha=8$, has been investigated for three different configurations, namely the single jet, twin side-by-side jets and in-line jets. The quantitative image processing apparatus used in ref 6 has been utilised but in the present study time-histories of the jet/crossflow interface location, or mixing region, have been obtained at different locations to permit determination of the interface statistics, notably intermittency, probability density functions and power spectra. Finally, a parametric study has been carried out to examine the effects upon the overall jet penetration of: jet velocity ratio, jet nozzle spacing and orientation of the nozzles to the crossflow (from in-line to side-by-side, with a normal jet injection angle in all cases). The next section describes the experimental approaches that were adopted in this work.

4. EXPERIMENTAL DETAILS

4.1 Smoke tunnel facility

The experiments were carried out in a purpose built, open-circuit, smoke tunnel facility, illustrated in figure 1, which has working section dimensions of 0.75m height x 0.62m width x 3.6m length and a turbulence level of 0.2%. High efficiency filters are installed at the outlet to remove practically all the smoke particles. A Concept Genie generator was used to produce the smoke in which all of the particles were less than $5\mu\text{m}$ in diameter, with 90% being less than $1\mu\text{m}$. The smoke was introduced into the tunnel, via a small centrifugal fan, and the jets issued from 13.5mm diameter copper nozzles inserted into a common plenum chamber. The generator and plenums were mounted on the tunnel roof in an arrangement which allowed variation in the orientation of the jets to the crossflow direction.

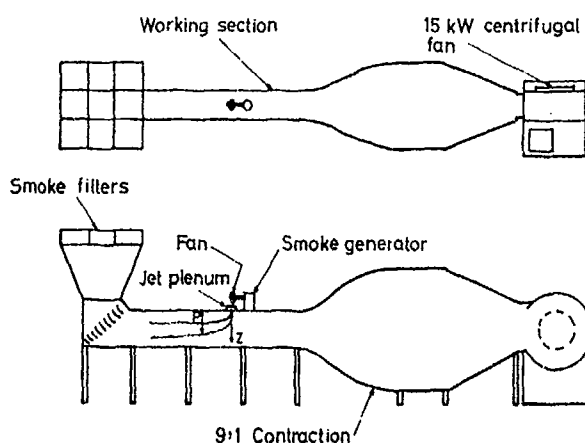


Fig 1 Diagrammatic layout of the smoke tunnel

4.2 Quantitative analysis of jet/crossflow interface region

Details of the jet/crossflow interface structure were obtained at each location by illuminating the flow field at different heights, spaced $2.5D$ apart, using a 10mW He-Ne laser beam directed across the tunnel. The laser, along with a monochrome CCD camera for recording the laser-line traces, was attached to a computer-controlled two-dimensional traversing mechanism, illustrated in figure 2.

The position of the camera and laser were fixed relative to each other with each digitised pixel representing a flow area of approximately $0.58\text{mm} \times 0.58\text{mm}$ (that is, $0.04D \times 0.04D$). Video digitisation and analysis were undertaken by a PDP-11/73 minicomputer-based system using Imaging Technology boards for analogue processing (AP-512), arithmetic logic operations (ALU-512), histogram computations (HF-512) and frame buffer storage (FB-512). Previous work has shown that the video analysis system can be used to obtain quantitative data, including interface statistics, by utilising the smoke as a turbulent/non-turbulent discriminator (refs 7, 8). In the present experiments the fully turbulent jets were seeded with smoke, whilst the crossflow, which was non-turbulent (outside the wall boundary layer) was unseeded. Hence, when the interaction region was viewed by the camera the white portions of each laser illuminated line (smoke present) represented regions of turbulent flow and the black regions (no smoke) represented non-turbulent flow regions.

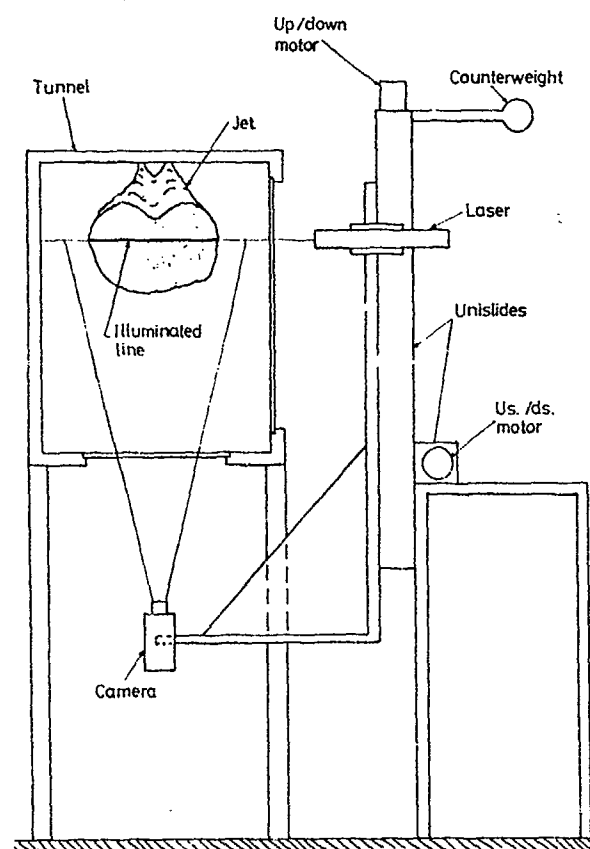


Fig 2 Camera and laser traversing mechanism

Tests were carried out at each location to determine the time history of the position of the interface between the jet and the crossflow (that is, the edge of the smoke seeded region). In each case a time series of 50000 points was obtained and five 10000 point, 250 lag autocorrelations were then computed and summed. A cosine transform was then carried out to produce the power spectrum up to the Nyquist frequency of 25Hz (imposed by the image transfer rate of 50Hz) at intervals of 0.1Hz. The edge time history was also used to compute the probability density function of the interface location, together with the mean, variance, skewness and kurtosis. At each location further

measurements were carried out in which the pixels along each sampled line were interrogated to determine whether smoke was present or not. From a 10000 point line time history the intermittency function was computed for each pixel, defined as

$$I(x,t) = \begin{cases} 1 & \text{if the point } (x,t) \text{ is in a fully turbulent region} \\ 0 & \text{if the point is in a non-turbulent region.} \end{cases}$$

In this context the term "non-turbulent" should be qualified to mean irrotational flow of very low turbulence, that is the freestream value of 0.2%.

The experiments were conducted with a freestream velocity of 1m/s, giving a Reynolds number of 9.3×10^2 based on nozzle diameter. The approaching roof boundary layer had a thickness of 60mm, that is 4.44D. The jet velocity was 8m/s, which gave $\alpha=8$, and measurements were undertaken in lateral YZ planes at downstream locations X/D of 5, 10, 15, 20, 25 and 30 for the single jet case and for twin jets with nozzle spacing S/D=5.

4.3 Quantitative analysis of jet penetration

These experiments were conducted with the same jet rig arrangement and crossflow velocity but, instead of using laser-line illumination, the smoke jets were illuminated by tungsten-halogen narrow slit lighting introduced through the tunnel floor. The slit was aligned to provide plane illumination along the tunnel centre-line ($Y=0$). The smoke jet paths were then viewed by the CCD camera through the side window, covering an area from the nozzle exits to approximately $X/D=35$. In these tests the data acquisition and analysis were carried out by newly-installed image processing apparatus, the Series 151 Imaging Technology system, which emulates and enhances the performance of the 512 Series system. The modular image processing unit is linked to a PC-486 computer via a VME-bus and the software has been developed using an ITEX function library and C-language. For each jet configuration 128 frames of the smoke jet flow were acquired and averaged to give the mean outline of the jet(s). The location of the outer boundary was then determined from this final averaged image by an edge detection algorithm and the data stored on disk for subsequent analysis using logarithmic plots involving the main jet parameters; X/D , Z/D , S/D , α and θ . The scope of the tests covered all possible combinations of the following parameters; nozzle spacing ($S/D=1, 3, 5$ and the single jet case), alignment to the crossflow ($\theta=0^\circ$ (in-line), 30° , 45° , 60° and 90° (side-by-side)) and jet ratio ($\alpha=4, 6, 8$ and 10).

4.4 Comparative velocity measurements

The comparative velocity measurements were undertaken using a five-hole pressure probe, calibrated using the method outlined in ref 9. The probe had a tip diameter of 2.3mm and the side tubes were chamfered back at an included angle of 90° . At each point in the flow all five pressures from the probe, together with the freestream total pressure, were measured relative to a reference pressure (the crossflow static pressure). This was achieved by connecting the pressures, in turn, to a transducer via a Scanivalve fluid switch. A computer controlled the operation of the fluid switch as well as measuring the pressures and computing the necessary coefficients. Preliminary trials showed that the optimum sampling time

for each mean pressure measurement was 30 seconds, whilst the delay time to allow for settling of the pressures after switching ports was 20 seconds. These large timings were essentially due to the relatively low pressures being measured.

In order to calibrate the five-hole probe in the pitch and yaw angular planes a manually operated mechanism was devised in which the probe could be rotated about its tip. A pantograph arrangement was used for one axis (allowing determination of the angle to within 0.5°), whilst the second axis was rotation of the pantograph about a line through the probe tip (with an accuracy of 0.2°). Since the largest angles encountered in a jet in a crossflow are in the pitch (ϕ) direction it was decided that the greatest calibration accuracy should be achieved in this direction by using the second (yaw) axis for pitch. Hence, the pantograph was used for the yaw (β) direction. The calibration procedure was as follows;

(a) At each known probe angular position (ϕ, β) the pressures P_1 and P_4 (pitch), P_2 and P_3 (yaw), P_5 (central tube) and P_d (freestream dynamic) were measured.

(b) The average side tube pressure (P_{av}) was computed

$$P_{av} = \frac{(P_1 + P_2 + P_3 + P_4)}{4}$$

(c) Three coefficients were then calculated

Pitch coefficient, $C_{p_{pitch}} = \frac{P_1 - P_4}{P_5 - P_{av}}$

Yaw coefficient, $C_{p_{yaw}} = \frac{P_2 - P_3}{P_5 - P_{av}}$

Dynamic coefficient, $C_{p_{dyn}} = \frac{P_d}{P_5 - P_{av}}$

(d) This procedure was repeated for the range of pitch and yaw angles likely to be encountered in the flow to be measured (typically within $\pm 30^\circ$) and then two calibration charts were plotted for use in subsequent flow field measurements.

For these measurements the following procedure was adopted.

(a) At any point in the flow P_1, P_2, P_3, P_4, P_5 and P_d were measured

(b) P_{av} , $C_{p_{pitch}}$ and $C_{p_{yaw}}$ were then computed

(c) Using the values for $C_{p_{pitch}}$ and $C_{p_{yaw}}$ the angles ϕ and β were interpolated from the first graph.

(d) These angles were then used to determine $C_{p_{dyn}}$ from the second graph.

(e) The local dynamic pressure ($P_{d_{local}}$) and the magnitude of the velocity vector (Vel) were then calculated using

$$P_{d_{local}} = (P_5 - P_{av}) \cdot C_{p_{dyn}} \quad \text{and} \quad Vel = \sqrt{2/\rho \cdot P_{d_{local}}}$$

where ρ is the fluid density.

(f) Finally, the velocity vector components were determined from the following expressions

$$U = Vel \cdot \cos\beta \cdot \cos\phi$$

$$V = Vel \cdot \sin\beta$$

$$W = Vel \cdot \cos\beta \cdot \sin\phi$$

and the individual components were normalised by the freestream velocity computed from P_d .

The velocity field measurements were undertaken for one configuration, namely side-by-side jets with $S/D=5$ and $\alpha=6$, and the data were compared to those obtained during

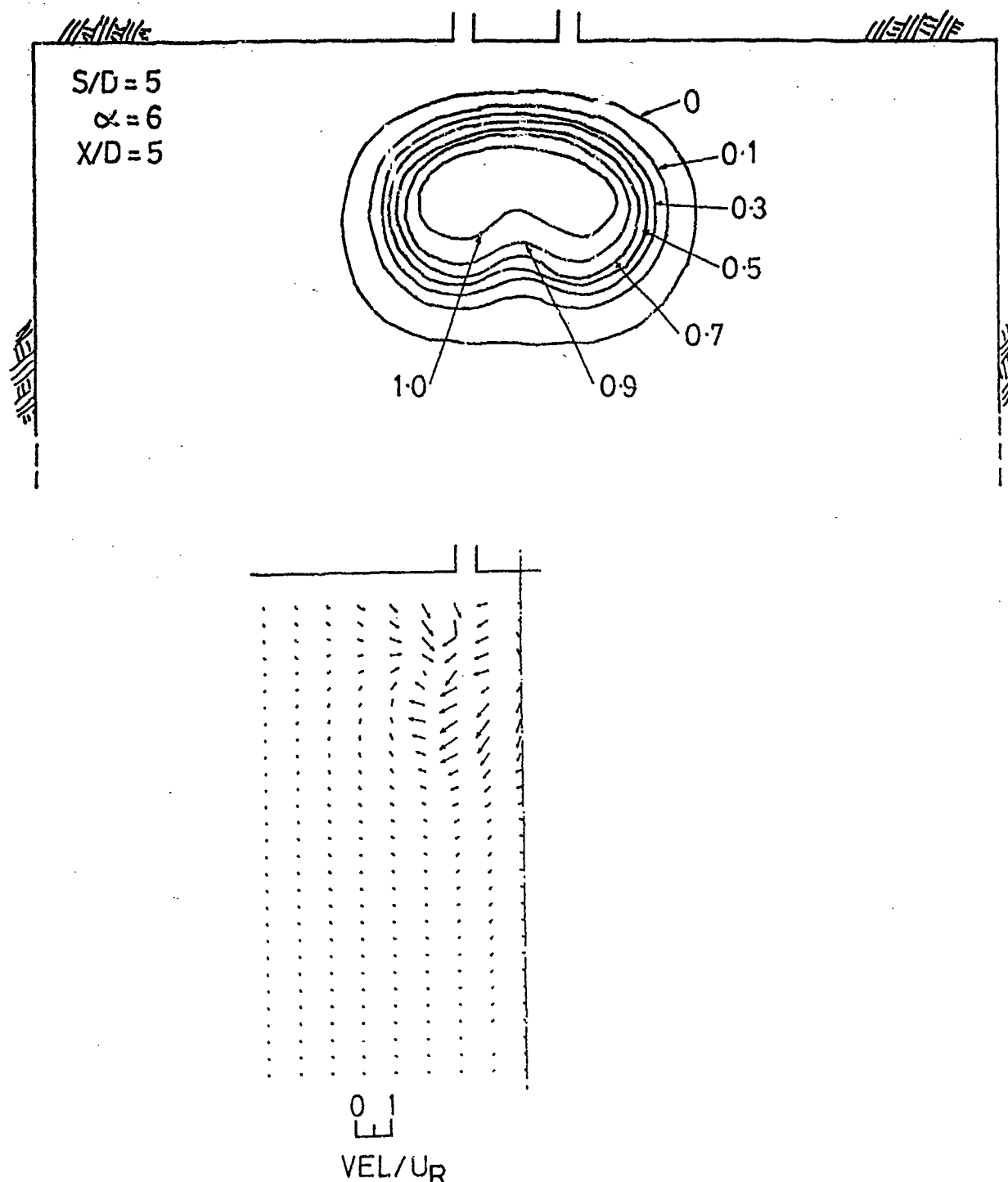


Fig 3 Contours of intermittency and projected velocity vectors in YZ plane at $X/D=5$ ($S/D=5$, $\alpha=6$)

the experimental programme discussed in ref 6. In order to achieve sufficient resolution and accuracy in the pressure measurements it was necessary to use a higher crossflow velocity, of 5.74m/s, giving a Reynolds number of 5.3×10^3 . Four YZ planes, at $X/D=2.5, 5, 10$ and 20 , were surveyed by attaching the probe to a small, single axis, computer-controlled traversing mechanism. It should be noted that, as indicated in ref 10, calibrated five-hole probes are susceptible to errors due to flow turbulence and that these errors are not readily quantifiable for different flow incidence angles. Hence, where it is practical to do so, the probe should be operated in the more accurate self-nulling mode so that all measurements are taken with the device aligned with the mean flow direction, as utilised by the present authors in another investigation using a different wind tunnel, ref 11.

5. RESULTS AND DISCUSSION

Considering first the comparison between the mean velocity and intermittency distributions, the intermittency contour plots and projected velocity vector distributions for two YZ planes at $X/D=5$ and 20 are shown in figures 3 and 4, respectively. Near the nozzle the crossflow penetration between the jets reduces the intermittency on the lower (freestream) side of the combining jets, whilst by $X/D=20$ it is the vortex-induced entrainment of the crossflow which reduces the intermittency on the upper side of the jets. The pattern then established is similar to that of a single jet in a crossflow with a "kidney" shaped profile, containing only one pair of contrarotating vortices. The rapid disappearance of the inner vortex of each pair is also evident in the velocity vector plots. Throughout the set of measured planes from $X/D=5$ to 20 the centre of the

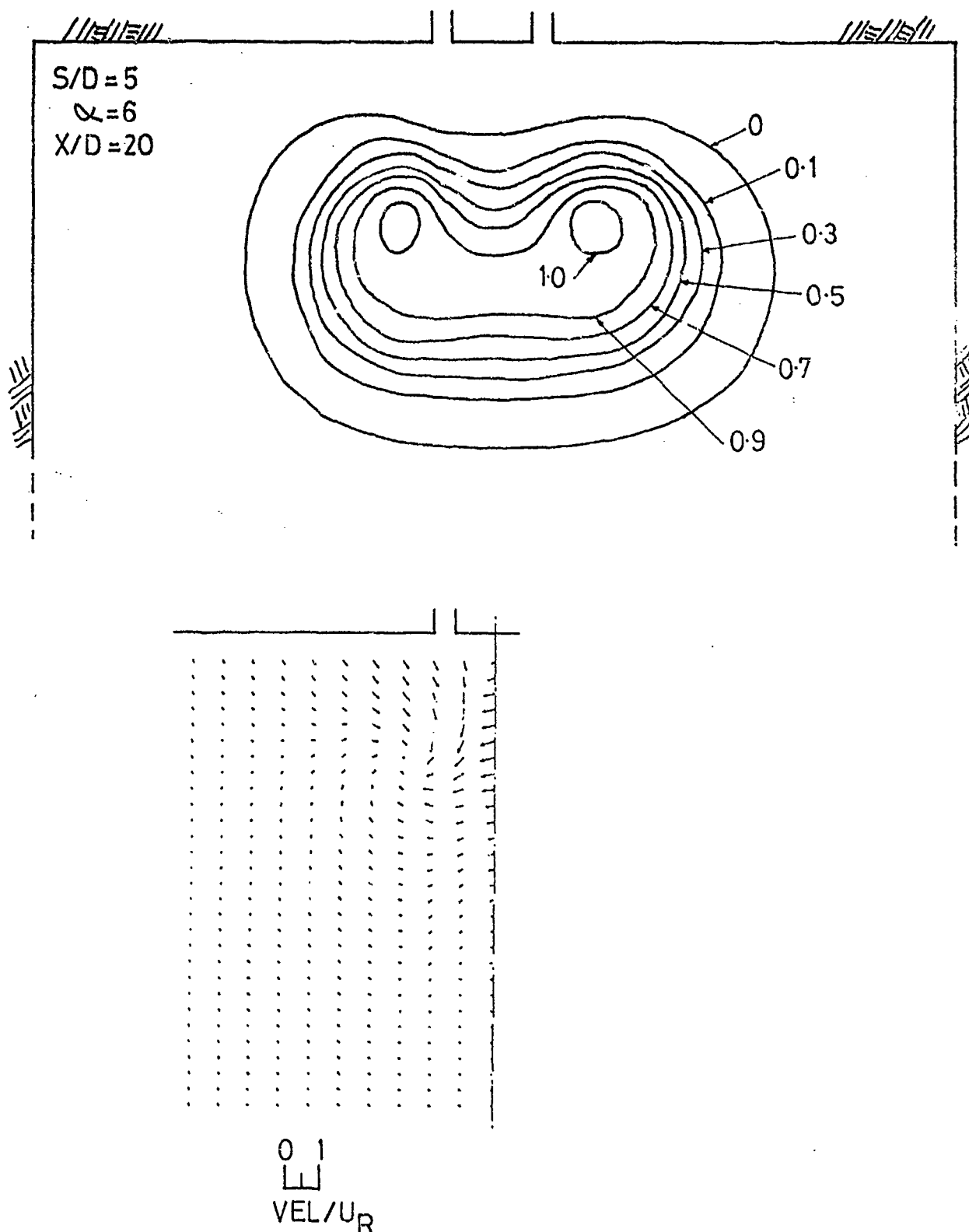


Fig 4 Contours of intermittency and projected velocity vectors in YZ plane at $X/D=20$ ($S/D=5$, $\alpha=6$)

vortex appears to be located at the outer edge of the $I=1$ region in the lateral direction and level with the wall-side of the $I=0.5$ contour in the vertical direction. Figure 5 shows profiles of intermittency and non-dimensional longitudinal velocity along the plane of symmetry ($Y=0$) for the side-by-side jets with $S/D=5$ and $\alpha=6$. It may be seen that the intermittency provides a clear demarcation of the extent of the combined jets in the vertical direction. There is a small peak in the velocity profiles on the wall-side of

the intermittency peaks, most notably at $X/D=2.5$. The velocity increase near the wall is likely to be due to the acceleration of the crossflow between the two jets in that region.

Some typical probability density functions associated with the interfaces for the different jet configurations are illustrated in figure 6 which shows profiles for the single, in-line and side-by-side jet cases, each taken in the YZ

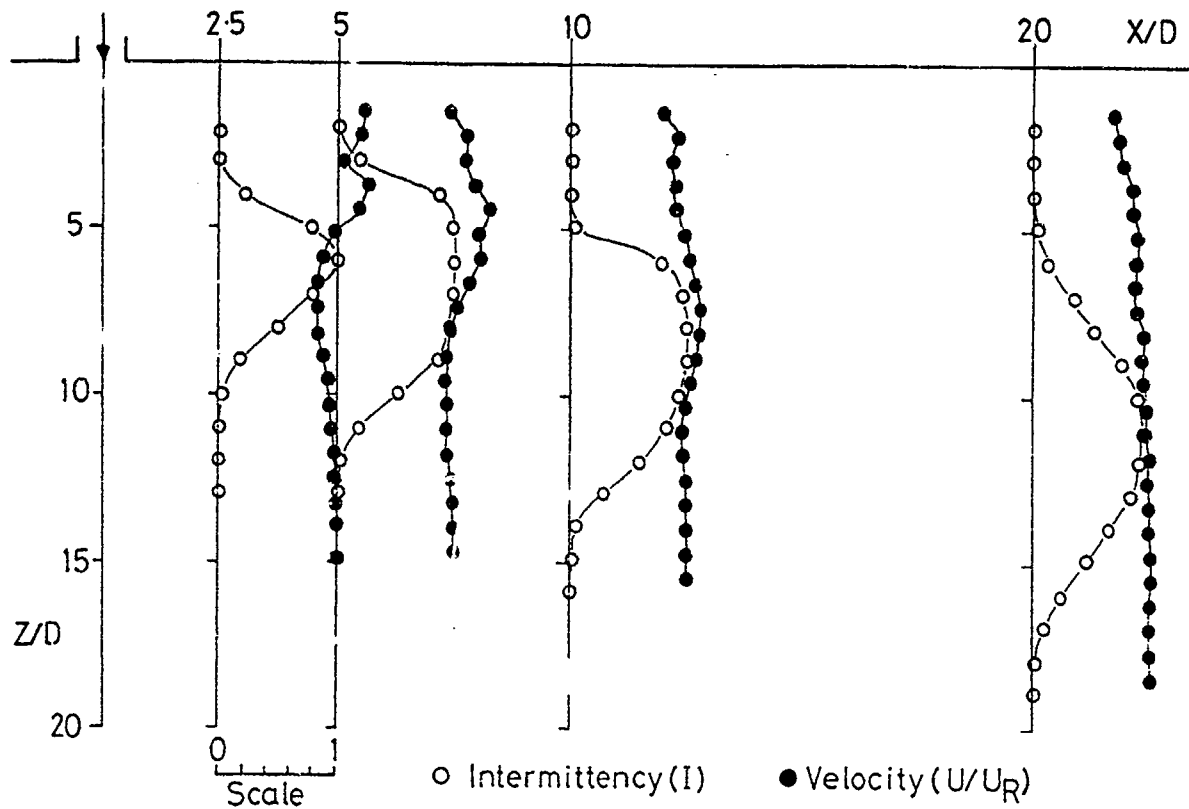


Fig 5 Comparison of intermittency and longitudinal velocity component along jet centre-line ($S/D=5$, $\alpha=6$)

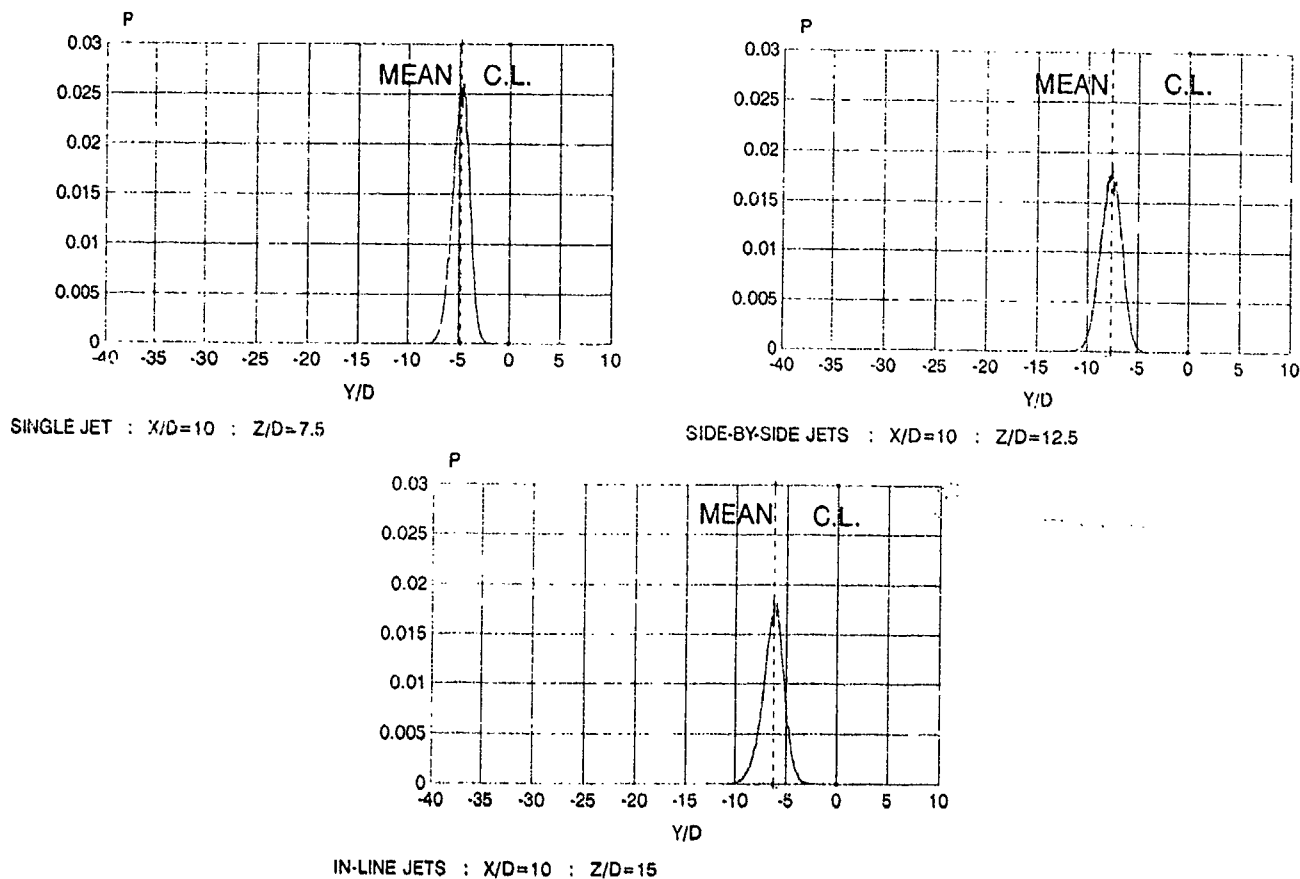


Fig 6 P.d.f. distributions associated with lateral fluctuations of the interfaces for single, in-line and side-by-side jet configurations at $X/D=30$ for $\alpha=8$

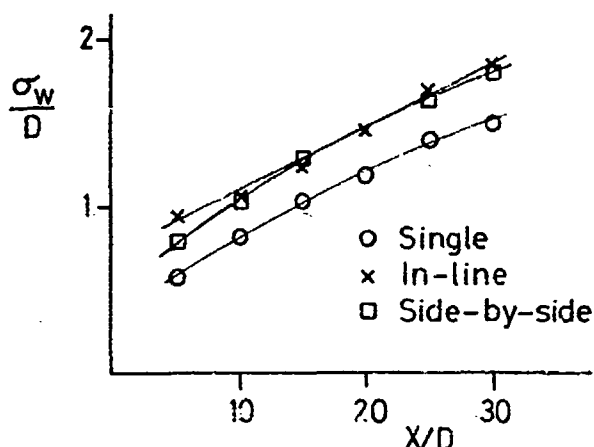


Fig 7 Variation of lateral r.m.s. of interface location with downstream distance for the three cases ($\alpha=8$)

plane at $X/D=10$ along a line at the Z/D location near the region of maximum jet width. These profiles are approximately Gaussian in shape and illustrate that the twin jet interfaces are of similar width but somewhat broader than the single jet interface at the same downstream location. The mean interface location shows that the jet half-width is largest for the side-by-side case, being about 1.5D wider than the in-line case and 3D wider than the single jet configuration. Hence, it is clear that the mixing region associated with two jets is more extensive than that for the single jet. The difference in width between the side-by-side jets and the other cases is due, in part, to the "initial" half-width in the side-by-side case that is provided by the 5D nozzle spacing.

In previous work by the present authors (ref 12) it was noted that the mean lateral locations (defined by the mean of the p.d.f.) and extents of the mixing regions (defined by the inner and outer limits of the p.d.f.) for the three jet cases both increased in the downstream direction. Furthermore, the overall maximum width of the interface at any downstream location was similar for both the in-line and side-by-side configurations and this was greater than that for the single jet case. Figure 7 confirms this trend by illustrating the variation of the lateral r.m.s. fluctuation of the interface about the mean location for the three configurations. The difference between the single jet and the twin jet r.m.s. values is consistently about $0.26D$ indicating that the presence of the two jets promotes greater mixing with the crossflow. The variation in overall jet half width with downstream distance is illustrated in figure 8 for the three different configurations. The edge of the jet is taken to be where the intermittency is zero. As noted earlier, from the p.d.f. data, the combined side-by-side jets are wider than the in-line jets and there is good agreement between the present work and that previously undertaken by the authors (ref 6). The single jet shows a smaller spread than the other cases but, even so, the half-width is greater than that given in ref 13. This is probably due to different definitions for the edge of the jet between the two cases, together with different blockage effects in the experimental arrangements.

Typical examples of the energy spectra associated with the interface fluctuations, taken at $X/D=10$, are shown in

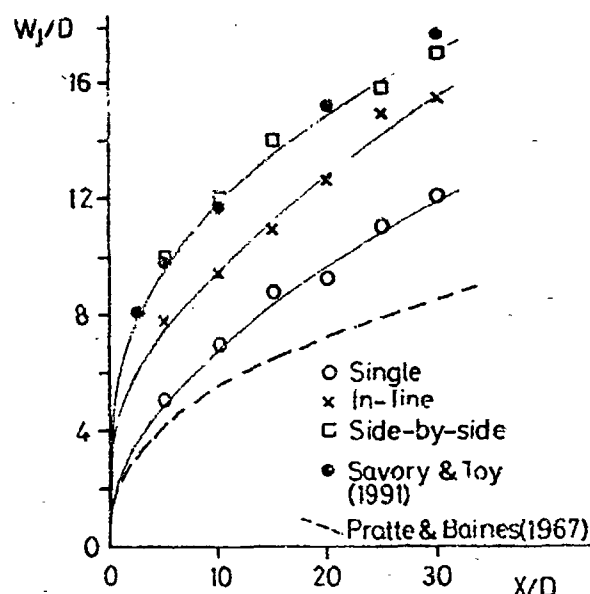
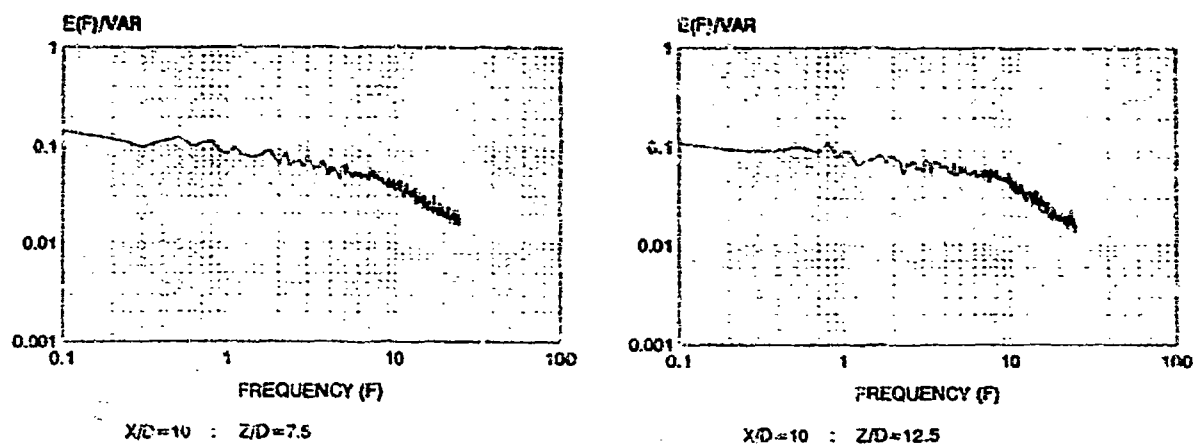
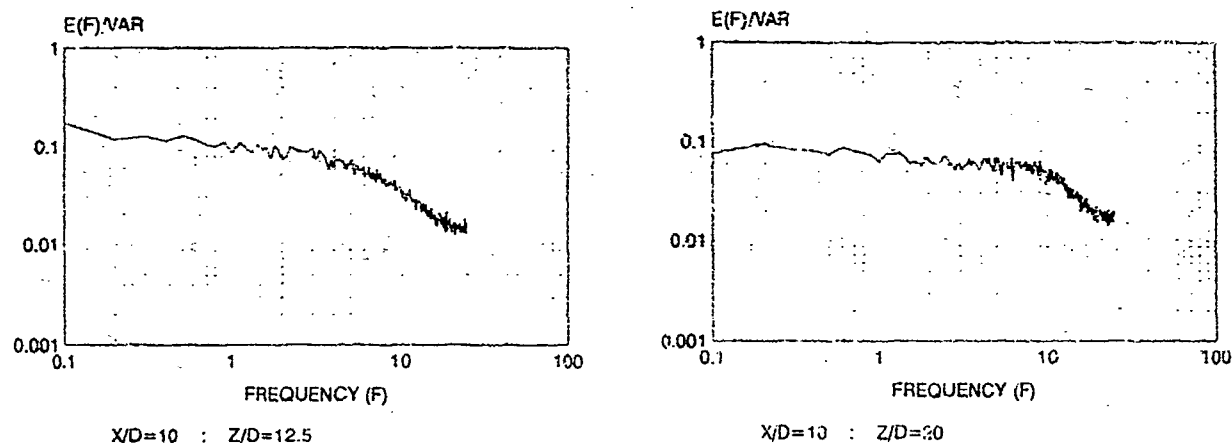
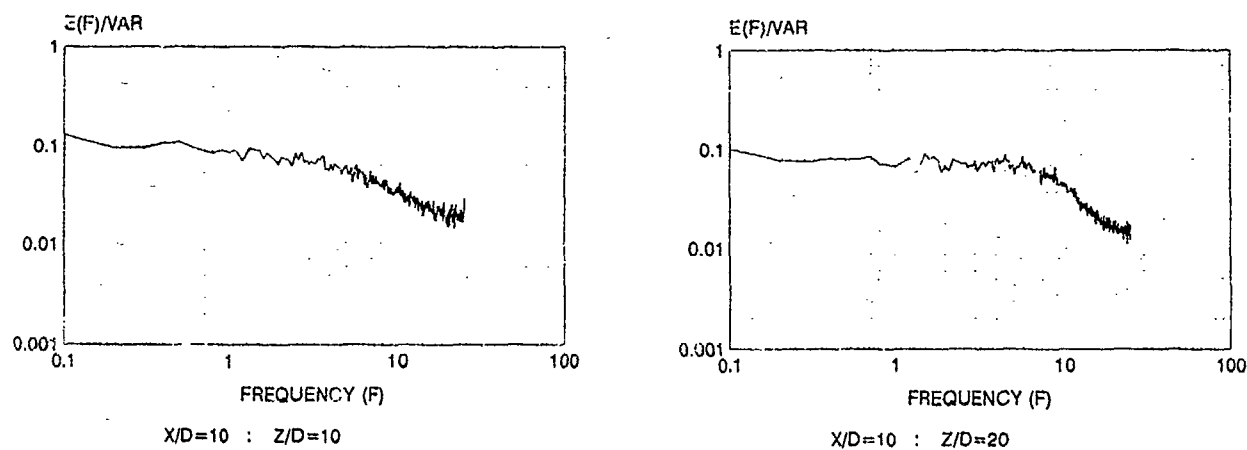


Fig 8 Variation of overall jet half-width with downstream distance for the three cases ($\alpha=8$)

figures 9, 10 and 11 for the single, in-line and side-by-side jets, respectively. In each case two spectra are shown, both just within the jets with one near the top and one near the underside (that is, the ground plane side). In almost all the cases considered there is a distinct transfer of energy to the higher frequencies as the point of measurement is moved from the wall side to the top of the jets. This is indicated in the figures by the extent of the relatively flat portion of the spectra moving from a wave number of about 6 to 50 in the case of the single jet, from 19 to 44 for the side-by-side jets and from 19 to 56 for the in-line jets, together with an increase in the slope of the profiles at the higher frequency end. Further downstream, at $X/D=30$ (not illustrated here), where all the jet flows are more developed, the upper and lower spectra for all three cases become very similar with the wave number shifting from about 6 to approximately 31 towards the outer edge in all cases. The present data are not conclusive but the general trend appears to be an increase in the spectrum slope towards the top of the jets and then a smaller decrease as the outer edge of the interface is approached. This tendency is very noticeable for the single and side-by-side jet cases but less evident for the in-line configuration. A possible explanation for the changes in the energy profiles may be that the flow near the underside of the jets is dominated by the large-scale, low frequency motion associated with the contrarotating vortices whilst the interaction in the top region is largely between the two nominally co-flowing regimes of the jet and the crossflow. The spectra display no evidence of periodic "vortex shedding" associated with the jet flows which has been recorded by earlier workers investigating single jet wakes (refs 14,15). However, as shown in ref 16, the jet does not shed vortices itself but, rather, it draws up vorticity from the separated wall boundary layer near the nozzle (which is due to the adverse pressure gradient in that region). The vorticity is then introduced into the jet wake and the periodicity is broadly similar to that associated with a circular cylinder in uniform flow. However, in the present work the wall boundary layer was not seeded with smoke and so the experimental techniques used would not directly detect any such vorticity.

Fig 9 Interface energy spectra for two heights within the single jet at $X/D=10$ Fig 10 Interface energy spectra for two heights within the in-line jets at $X/D=10$ Fig 11 Interface energy spectra for two heights within the side-by-side jets at $X/D=10$

A significant feature of the flow regime associated with an initially uniform single circular jet issuing freely into still fluid is that the velocity, temperature and concentration distributions in any downstream lateral section may be represented by similarity profiles, as reviewed in ref 17. Such profiles may be adequately defined by Gaussian curves using the maximum value on the jet centre-line as the normalising parameter for the physical quantity, such as velocity, and the half-width of the jet (based upon the distance to where the physical quantity is some fraction of the maximum value, normally either 37% or 50%) as the normalising parameter for the lateral coordinate. However, for the cases of a single jet or multiple jets in a crossflow

the flow is complicated by entrainment associated with the counter-rotating vortex pair. Some measurements of streamwise velocity along lateral lines through a single deflected jet (refs 18, 19) have suggested that some degree of similarity is present between data taken in different downstream planes. In each case the measurement line was through the centre of the jet, following the curve of the characteristic "kidney" shape. However, it has not been possible to confirm whether such similarity profiles exist for twin jet arrangements because of the large number of measurements required to survey complete lateral planes.

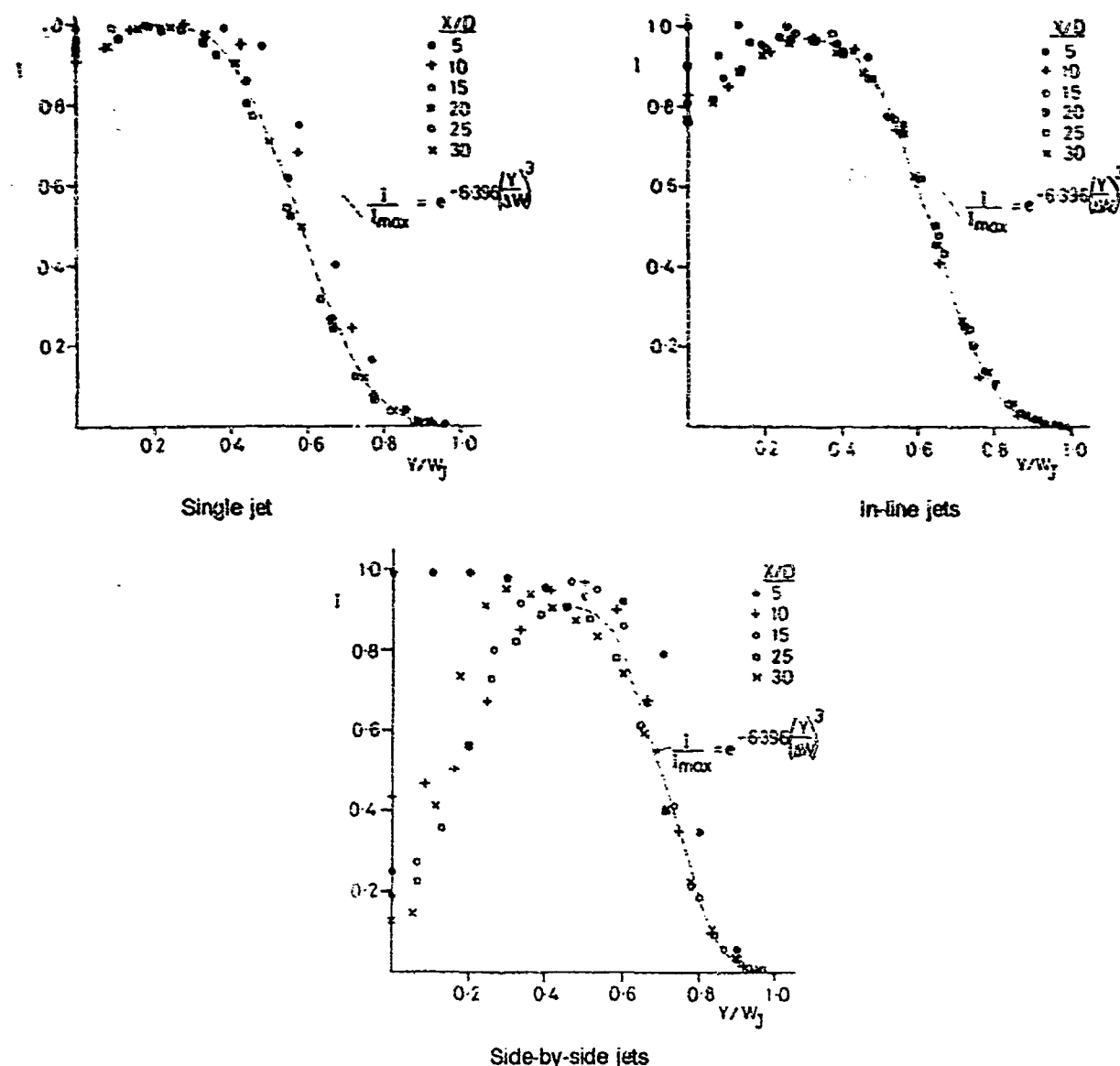


Fig 12 Normalised intermittency profiles across maximum width of the jets ($\alpha=8$)

The present intermittency data has been analysed by considering a characteristic location within any jet configuration which may be used as a reference for all the cases studied. The chosen reference is the data along a line through the jet in each YZ plane, parallel to the ground plane, at a vertical location (Z/D) close to where the maximum jet width occurs. Since measurements were taken at rather coarse spacings of $Z/D=2.5$ the p.d.f. and intermittency distributions in each downstream plane were examined to determine those which were closest to the maximum jet width location. Having ascertained the appropriate profile for each measurements plane the lateral coordinate has been normalised by the jet half-width in that plane, W_j , defined as the distance from the jet centre-line to where $I=0$. This location also coincides with the position where the p.d.f. becomes zero.

These profiles, for the single, in-line and side-by-side cases, are plotted in figure 12. The single jet distribution nearest the nozzle exit, at $X/D=5$, shows that the fully turbulent core of the jet occupies some 40% of the overall width.

However, with increasing downstream distance this "core" decreases such that by $X/D=15$ the curves in the intermittent region associated with the interface tend to follow the same curve. Nearer the jet centre-line, at Y/W_j less than 0.2, there is a decrease in intermittency and this is associated with entrainment of non-turbulent fluid due to the counter-rotating vortices, as noted in ref 6. In the case of the in-line jets there is, again, a fully turbulent region near the exit at $X/D=5$ which extends to some 30% of the jet width. There are more noticeable intermittency deficits near the jet centre-line when compared to those for the single jet case, suggesting that the vortex pair is stronger in the in-line configuration. The precise value determined on the centre-line will be partly due to how close the lateral measurements line is to the actual maximum width location and, hence, where it "cuts" through the vortices. However, on the outward side of the jets, in the intermittent regime, the data collapses well onto a single curve for all the downstream locations examined. For the side-by-side configuration the fully turbulent region at $X/D=5$ occupies about 30% of the overall width, which is similar to the in-

line case. The intermittency deficit on the centre-line is greater than with the other two cases and this is, in part, due to penetration of the non-turbulent crossflow between the two jets and its associated mixing with the inner faces of the jets in the initial region near the exits. Because of this more complex flow field in the nozzle region the jet flow does not become fully developed until further downstream when compared to the single and in-line cases. However, by $X/D=25$ the curves in the intermittent region are beginning to collapse onto a single line. It is notable that the peak intermittency value in this region is now down to about 0.9 and this is likely to be a consequence of the entrainment processes in the near exit region.

It may be seen from the figures that the curves for the developed jet flows may be described by the equation giving the dashed line in each figure. A suitable empirical expression for the profiles in the interface region has been found to be

$$\frac{I}{I_{\max}} = e^{-4.344 \left(\frac{Y}{\Delta W} \right)^2}$$

where I_{\max} is the maximum intermittency value in the profile and ΔW is the lateral distance between the point of maximum intermittency (or the outermost point if there is a region of constant peak intermittency) and the edge of the jet where $I=0$. Hence, ΔW gives a measure of the width of the mixing region in terms of a proportion of the overall jet half-width, being equal to $0.8W$, $0.7W$, and $0.55W$, for the single, in-line and side-by-side jets, respectively. Hence, it is evident that the outer mixing region represents a smaller proportion of the overall width of the combined side-by-side jets than of the in-line jets or of the single jet.

The parametric study is currently in progress but the following trends have been observed in the data;

- (a) For side-by-side jets ($\theta=90^\circ$), at all jet ratios the penetration was greatest for a nozzle spacing $S/D=1$, with the minimum penetration occurring between $S/D=3$ and 5.
- (b) For in-line jets ($\theta=0^\circ$), the penetration was again greatest for $S/D=1$ but the penetration tended to continually decrease with increasing nozzle spacing, at least up to $S/D=5$.
- (c) With the in-line case it was the downstream jet, issuing into the lower static pressure region created by the first jet, that penetrated furthest into the crossflow.
- (d) For a given jet ratio, changes of angle between 30° and 60° had relatively little effect upon the overall penetration.

6. CONCLUDING REMARKS

The velocity data for the side-by-side jets case has shown that the deflected jets are dominated by one single vortex pair, with the inner vortex of each jet pair not being evident. However, further velocity data is required in order to ascertain the nozzle spacings at which two identifiable vortex pairs are present. Ideally, such five-hole pressure probe measurements should be conducted using the nulled mode of operation. Video analysis of the three main configurations, side-by-side, in-line and single jet, has indicated that, in each case, the width of the mixing region at any downstream location is similar in size to the jet half-width (as defined by the mean interface location). These

interface widths are similar for the side-by-side and in-line jets but both are greater than the single jet case.

The present work also suggests that similarity profiles exist for some of the physical flow quantities associated with single or multiple jets in a crossflow. These profiles, along with empirical expressions for jet trajectories, overall jet penetrations and widths, as for example in ref 6, would allow prediction of the jet paths and shapes as well as the flow features within the jets themselves.

The work is continuing and it is intended to begin to examine the internal structures of the jets, utilising the digital imaging approaches outlined in this paper. However, this aspect of the research requires supporting investigations in the form of point measurement distributions of velocities and turbulent stresses which can be most reliably obtained using LDA techniques.

7. REFERENCES

1. Ziegler, H. and Woelfer, P.T., "Analysis of stratified and closely spaced jets exhausting into a crossflow", NACA CR-132297, 1973.
2. Schwendemann, M.F., "A wind tunnel investigation of stratified jets and closely spaced jets exhausting into a crossflow", Northrop Aircraft Division, Hawthorn, CA, USA, Rept NOR73-98, May 1973.
3. Makihata, T. and Miyai, Y., "Trajectories of single and double jets injected into a crossflow of arbitrary velocity distribution", ASME J. Fluids Engng, 105, 1979, pp 91-97.
4. Isaac, K.M., "Experimental and analytical investigation of multiple jets in a cross-flow", PhD thesis, Virginia Polytechnic Inst. and State Univ., Blacksburg, 1982.
5. Isaac, K.M. and Jakubowski, A.K., "Experimental study of the interaction of multiple jets with a crossflow", AIAA J., 23, 1985, pp 1679-1683.
6. Savory, E. and Toy, N., "Real-time video analysis of twin jets in a crossflow", ASME J. Fluids Engng, 113, 1991, pp 68-72.
7. Toy, N. and Wisby, C., "The real time image analysis of a visualised turbulent wake", in "Proc. 1st National Fluid Dynamics Congress", Cincinnati, USA, July 1988, pp 695-702, AIAA Paper No 88-3552-CP.
8. Toy, N. and Wisby, C., "Real-time image analysis of visualized turbulent flows", in "Proc. 11th Biennial Symp. on Turbulence", Univ. of Missouri-Rolla, USA, October 1988, pp A21.1-21.10.
9. Treaster, A.L. and Yocum, A.M., "The calibration and application of five-hole probes", ISA Transactions, 18, 1978, pp 23-34.
10. Christiansen, T. and Bradshaw, P., "Effect of turbulence on pressure probes", J. of Physics E, 14, 1981, pp 992-997.

11. Savory, E., Toy, N., McGuirk, J.J. and Sakellariou N., "An experimental and numerical study of the velocity field associated with a jet in a crossflow", in "Proc. Int. Symp. on Engng. Turbulence, Modelling and Meas.", Dubrovnik, September 1990, pp 165-174.
12. Toy, N., Disimile, P. J., Savory, E., and McCusker, S., "The development of the interface region between twin circular jets and a normal crossflow", in "Proc. of 13th Biennial Symp. on Turbulence, Univ. of Missouri-Rolla, USA, September 1992, Paper B10.
13. Pratte, B.D. and Baines, W.D., "Profiles of the round turbulent jet in a crossflow", ASCE J. of the Hydraulics Div., HY6, 92, 1967, pp 53-64.
14. McMahon, H.M., Hester, D.D. and Palfrey, J.G., "Vortex shedding from a turbulent jet in a crosswind", J. Fluid Mech, 48, 1971, pp 73-80.
15. Moussa, Z.M., Trischka, J.W. and Eskinazi, S., "The near field in the mixing of a round jet with a cross-stream", J. Fluid Mech, 80, 1977, pp 49-80.
16. Fric, T.F. and Roshko, A., "Structure in the near field of the transverse jet", in "Proc. 7th Symp. on Turbulent Shear Flows", Stanford Univ, USA, 1989, pp 6.4.1-6.4.6.
17. Rodi, W., "Turbulent buoyant jets and plumes", Pergamon Press, Oxford, UK, 1982.
18. Keffer, J.F. and Baines, W.D., "The round turbulent jet in a crosswind", J. Fluid Mech, 15, 1963, pp 481-497.
19. Rajaratnam, N. and Gangadharaiah, T., "Scales for circular jets in cross-flow", ASCE J. of the Hydraulics Div., HY6, 107, 1981, pp 497-500.

EXPERIMENTAL DATA FOR CFD VALIDATION OF IMPINGING JETS IN CROSSFLOW WITH APPLICATION TO ASTOVL FLOW PROBLEMS

P. Behrouzi
J.J. McGuirk

Department of Transport Technology,
Loughborough University of Technology,
Loughborough, LE11 3TU, U.K.

SUMMARY

An experimental facility, used to gather validation data suitable for testing CFD model predictions of multi-jet ground impingement flows, is described in the present paper. Water is used as the working medium and LDV measurements of twin impinging jets are reported, both with and without a cross-flowing stream. Emphasis is placed on the presentation of mean and rms velocity contours in the fountain formation region between the jets. The effect of jet splay angle has also been studied. For zero splay or 10° of splay-out the fountain is observed to develop as an upwash flow spatially separated from the two jet flows (jet spacing at 6 jet diameters); for 10° splay-in, a noticeable fountain/jet interaction is observed. Splay-out reduces the strength of the fountain (by around 50%) whereas splay-in has an opposite, strengthening effect for the 7 jet diameter impingement height studied here. The effect of a cross-flow (jet/cross-flow velocity ratio of 10) leads to a clear downwind shift of the fountain origin and inclination of the fountain rise. The results presented offer a sufficiently comprehensive mapping of the mean velocity and turbulence fields to form suitable test cases for the validation of CFD models for ground effect flows.

LIST OF SYMBOLS

D_j	Jet diameter (15mm)
H	Impingement height to ground plane ($7D_j$)
R	Velocity ratio (jet/cross-flow V_j/U_c)
S	Jet spacing ($6D_j$)
U_c	Cross-flow velocity
u	Longitudinal velocity
v	Vertical velocity
V_j	Jet velocity
w	Transverse velocity
x	Longitudinal distance measured positive downstream from jet injection plane
y	Vertical distance measured positive vertically down from jet nozzle exit plane
z	Transverse distance measured positive from symmetry plane bisecting twin jets
θ	Splay angle between jet nozzle centre lines (half total included angle)

1 INTRODUCTION

During its near-ground hovering phase an Advanced Short Take-off and Vertical Landing (ASTOVL) aircraft creates a complex three-dimensional flow field between jet streams, the airframe surface and the ground (see Fig. 1). This complicated flow generally changes the lift forces, (via fountain impingement and suckdown effects), influences hot-gas re-ingestion, and raises fuselage skin temperature (via fountain upwash and ground vortex flows); a proper understanding of this flow is thus important in design of such aircraft. In recent years jet flow field mathematical modelling has moved away from models based mainly on empirical findings towards numerical models of a more fundamental nature, for example Refs. [1], [2], [3]. However, the continued improvement in CFD methods and their successful application to aircraft design requires, for verification, a body of high quality validation data gathered in a range of relevant test case flows. These test cases should focus attention on the fundamental flow components which are important in ground effect flow fields, e.g. multiple impinging jets, ground vortex flow, fountain formation, etc. Over the last decade, this viewpoint has motivated a shift in the emphasis of experimental studies on ground-effect flows, away from measurements intended to provide information on specific configurations of interest to particular project designs, towards more focussed measurements aimed at improving our understanding of particular flow elements. When these measurements are also to serve as benchmark test cases to determine whether particular mathematical modes reproduce these flow elements adequately, then as complete mappings of the flow field as possible are required.

Bray (Ref. 4) has recently reviewed the experimental studies in both the above categories. Although the effects of compressibility via jet pressure and temperature ratios are undoubtedly relevant in practice, the difficulty of making detailed flow-field measurements in the ground impingement zone has meant that the available data is usually restricted to ground plane pressure surveys (e.g.

[4]), or wall-jet traverse information far removed from impingement (Ref. [5]). Measurements of the turbulence field associated with ground-effect flows have usually been carried out in low-speed air-flows (e.g. the ground vortex study of Ref. [6]) or, more commonly, in water flow experiments. Examples of the latter are the ground vortex study of Ref. [1] and the fountain flow measurements of Refs. [7] and [8]. The neglect of compressibility effects is not likely to be serious for ground vortex and fountain flows, since both measurements (Ref. [9]) and predictions (Ref. [10]) indicate that the fountain and ground vortex interactions lie in essentially low subsonic Mach number zones. By choosing to study these flow features in incompressible experiments, emphasis has essentially been placed on the turbulence aspects, so that data from such experiments form fundamental test cases for the validation of the turbulence model component of CFD models for ground-effect predictions.

Although the above comments have indicated that some suitable measurements for ground-effect validation studies have been made, the data-base is by no means large, and the effect of several parameters has yet to be established. If fountain flows are considered, for example, the data of Saripalli (Ref. [7]) formed the first detailed investigation, but are restricted to twin jets of wide spacing ($S/D_j = 9$ and 14) and the existence of a cross-flow was neglected. Barata et al (Ref. [11]) have included a cross-flow, but consider only the case of twin and three-poster parallel jets (i.e. all jet axes parallel and perpendicular to the cross-flow direction). Jet splay, i.e. angling of the jet axes in the plane connecting the jet centres (for convergent jets - splay-in, divergent - splay-out) is believed to influence fountain formation significantly, but no detailed data-base yet exists to document this effect and allow the testing of the ability of current CFD models to reproduce the effect of jet splay.

The objective of the work reported here was to construct an experimental facility especially suited to the collection of flow field data for the validation of CFD models for multi-jet ground impingement flows. In the current paper quantitative experimental results for a twin-jet configuration are presented, taken using non-intrusive LDV techniques to obtain mean and fluctuating velocity fields. The influence of both jet splay and cross-flow are discussed. The next section describes the design of the experimental rig, including details on the flow configurations selected for test and the Laser Doppler velocimeter. Section 3 describes the measurements, and the paper concludes in Section 4 with a summary of the main findings.

2 EXPERIMENTAL FACILITY AND MEASUREMENT TECHNIQUES

The experiments were carried out in a specially designed and constructed water tunnel shown schematically in Fig. 2. The rig is of circulating design. The circuit consists of cross-flow and jet pumps which extract water from a main supply tank and pump it to a large settling chamber (for the cross-flow) or to overhead jet tanks which feed up to three separate jet units. The jet mass flow rates are monitored via rotameters whereas the cross-flow rate is measured by a calibrated orifice plate. turbulence management units are provided in both cross-flow and jet circuits, to provide controlled and well-defined conditions at all inlet boundaries to the test section, as required for boundary condition specification in CFD studies. The turbulence management systems are shown in Fig. 3. Both systems represent a fairly standard combination of perforated plates, honeycomb and coarse and fine mesh screens; the jet unit design follows the suggestions of Saripalli (Ref. [7]). Fig. 4 presents some typical measurements of the mean and rms velocities at jet exit. For the conditions under which measurements were carried out as reported later, the mean velocity was uniform over the central 85% of the jet diameter. The turbulence intensity at the jet exit was around 2%, and in the cross-flow was about 1%. After a contraction section the cross-flow enters a test section made of perspex with the jet units integral with the top plate. For all tests reported here a jet diameter of 15mm was chosen; the test section dimensions are 1.125m long, 0.375m wide and 0.3m high (i.e. 75x25x20 jet diameters respectively). The rig is designed to have an adjustable height via the insertion of a false floor held on supports; this allows impingement distances between 4 and 20 jet diameters to be used. After passing through the test section both cross-flow and jet fluid discharge into a downstream settling tank where an overflow system into the main supply tank ensures a constant back pressure. Valves were included in the circuit so that the rig could also be run without cross-flow, using the settling tanks at both ends as discharge units; the valves allowed equal flow in both directions to be established.

For the measurements reported here a lateral twin-jet configuration was chosen; thus only the two rear jet units as indicated in Fig. 2 were used, so that the line of centres of the two jets (placed symmetrical about the tunnel centre-line) was perpendicular to the cross-flow direction. An impingement height (H/D_j) of 7 jet diameters was selected for test with a jet spacing (S/D_j) of 6 jet diameters. For cases involving jet splay, perspex inserts were used between the jet unit

and the top plate to create 10° of splay-in or splay-out (see Fig. 5).

The cross-flow duct extended $30D_j$ upstream and $45D_j$ downstream of the jet entry plane. In the co-ordinate system used below to report measurements, the origin of the longitudinal (x) co-ordinate (positive in cross-flow direction) is at the jet entry plane; the vertical (y) co-ordinate has its origin in the tunnel roof and is measured positive downwards; finally, the transverse (z) co-ordinate has its origin in the test-section symmetry plane (positive towards the front of the rig). In this system, jet splay occurs by rotating the jet axes in the y-z plane. Measurements were typically taken over a range $-5 < x/D_j < 7.5$, $1 < y/D_j < 6.75$, and on longitudinal planes $z/D_j = 0$ (i.e. the symmetry or fountain formation plane) and $z/D_j = 3$ (i.e. the jet entry plane); each longitudinal plane of measurements consists of around 30 (longitudinal) by 8 (vertical) points. For transverse planes (e.g. $x/D_j = 0$) around 20 transverse data points were taken at each vertical height.

The present results were taken for a jet velocity of 2.5m/s, corresponding to a jet Reynolds number of 37,500 to ensure fully turbulent conditions. When a cross-flow was used the velocity ratio R (jet/cross-flow) was 10, so that the cross-flow Reynolds number based on duct hydraulic diameter was 41,000; measurement of the cross-flow boundary layer thickness at the jet entry plane with no jet flow showed that this corresponded to $0.5D_j$.

The velocity field was measured using a single channel forward-scatter fringe-mode velocimeter with a Helium-Neon laser operated at a nominal power of 5mW. The advantage of using water as the working fluid was that a plentiful supply of naturally-occurring dust particles in the water formed the scattering centres so that no artificial seeding was necessary and strong signals at high data rates (up to 20kHz) were obtained even with the low laser power used. Sensitivity to the flow direction was provided by a DANTEC 55X29 Bragg cell with variable frequency shifting made possible by a DANTEC 55N101 frequency shifter. A 310mm focal length transmission lens was used with a beam spacing of 60mm. Off-axis light collection meant that the effective size of the measuring volume was 2.0mm long x 0.3mm diameter. The signals were processed using a TSI IFA 550 processor connected to a PC and controlled by a ZECH LDV data acquisition interface. No corrections were made for sampling bias; any associated errors were minimised by using high data rates compared to typical velocity fluctuation rates, as suggested by Erdmann and Tropea (Ref. [12]). The signal processor was

operated in trigger mode so that data at fixed time intervals was acquired; a typical data rate used was 2kHz. To minimise statistical (random) errors, the number of individual velocity values used in the experiments to form averages was set at the large value of 40,000 (sampling time 20 secs.) for all data points. This was not necessary in all regions of the flow, but was found essential for meaningful averages in the fountain zone. Finally, the tunnel was run for at least two hours before each test to establish steady conditions; before all main tests the final setting of jet and cross-flow velocities was carried out using the LDV system to guarantee, for example, equal jet velocities, and to ensure repeatable conditions.

3 RESULTS

For the case of twin impinging jets with zero splay and zero cross-flow, Fig. 6 shows profiles of two mean velocity components (u and v) and the rms of the vertical velocity in two longitudinal planes, the first through the longitudinal symmetry plane ($z/D_j = 0$) on which the fountain is formed and the second on a longitudinal plane passing through the jet centre ($z/D_j = 3$). All velocity components are normalised by the jet velocity V_j and all distances by the jet diameter D_j . Examination of the region between -4 and +4 jet diameters centred on the jet entry location shows that good symmetry of the flow is observed, demonstrating the ability of the rig to operate in zero cross-flow. The axial velocity measurements show the strength of the ground sheet flow created by jet impingement; a comparison of Figs. 5a and 5d also identifies the 'reinforcement' phenomenon known to occur in multi-jet impingement ground sheets. The largest axial sheet velocities measured on the jet entry plane (5d) are 20% of V_j whereas this rises to nearly 30% in the fountain plane (5a); this effect has been noted before in Refs. [4] and [5]. The reinforcement and fountain formation effects also cause the ground sheet flow to be effectively thicker on the fountain plane; significant ground sheet velocities are only found within $0.25D_j$ of the ground on $z/D_j = 3$ but axial velocities greater than 10% V_j are found up to $2D_j$ away from the ground on $z/D_j = 0$. Wall jet decay seems to begin from around $4D_j$ distance from the impingement location. Figs. 5b and 5e contrast the flow behavior in the fountain upwash and jet regions respectively. For the $7D_j$ impingement height used here the maximum jet velocity has only decayed to around 90% of its discharge value at a distance of $1D_j$ from impingement. In the fountain however, the maximum upwash (i.e. negative) velocities are found at this height, some 27% of the jet discharge velocity; decay of the fountain peak velocity occurs almost

linearly with height, decreasing to 1/5th of this value in the next 5 jet diameters of rise. An indication of the different turbulence behaviour in fountain and jet is given in Figs. 5c and 5f for the non-dimensional vertical rms fluctuation. The low turbulence in the jet potential core and high shear-produced turbulence in the mixing layers emanating from the nozzle lip are clearly seen in Fig. 5f. Maximum turbulence intensities of around 17% are observed in the shear layers. Similar, but slightly lower, levels are observed at the base of the fountain. This strong turbulence is generated by the impingement process of opposing ground sheet flows; this is therefore likely to be normal stress/normal strain rather than shear generated. It must also be remembered that the peak fountain velocity here is only $0.25V_j$, so local fountain turbulence intensities are more like 50% or larger as has been observed before by Saripalli (Ref. [7]). Note also that the turbulence in the fountain decays more slowly than the mean velocity; rather than decreasing by a factor of 5 as for the mean velocity, the v^2 rms is only reduced by a factor of 2 in the same vertical rise. Finally, note that the smoothness of the data in the fountain peak region ($x/D_j = 0$) is less well behaved than elsewhere, even with a sample size of 40,000; this is probably an indication of large-scale unsteadiness in the fountain flow.

Fig. 7 concentrates on documenting the effect of introducing jet splay on the jet and fountain flow behaviour; both mean and rms vertical velocity contours are shown on the vertical transverse plane passing through the jet centres ($x/D_j = 0$). For the zero splay case (i.e. parallel jets, Figs. 7a and 7b), the results confirm the conclusions drawn from the profile measurements presented in Fig. 6. Note that at a jet spacing of $6D_j$, only a slight blending between jet and fountain flows may be observed, with the shear layer on the inner jet edge spreading slightly faster than on the outside. This leads also to slightly higher turbulence levels on the inside edge, but there is still a clear separation between the high turbulence levels in the jet shear layers and in the fountain zone. Figs. 7c and 7d present the same measurements for the case of 10° of splay-out. The inclination of the jet can be clearly seen in both mean velocity and rms contours. The separate and independent nature of jet and fountain flows is of course enhanced by splay-out. Of some significance is the effect this has on the strength of the fountain in both a mean velocity and a turbulence activity sense. Fig. 7c indicates that the strength of the upwash velocities has been lowered considerably by splay-out. The maximum measured fountain velocity (non-dimensional) at $y/D_j = 6.0$, $z/D_j = 0.0$ was -0.285 for zero splay and -0.163 for 10° splay-out, a reduction of over 40%. The consequences on vertical fountain penetration can be seen by comparing the -0.1 velocity

contour in Figs. 7a and 7c. Similar reductions can be seen in the maximum turbulence levels for the fountain (compare Figs. 7b and 7d). Measured maximum v^2 rms (non-dimensional) at the fountain base for zero splay was $.143$, and this was reduced to $.099$ for 10° splay-out, a reduction of 30%. 10° of splay-in of course reverses all the trends (Figs. 7e and 7f). Jet and fountain are now able to interact strongly; no low turbulence zone separates fountain and inner jet shear layer (cf. Figs. 7f and 7b) and the peak fountain velocities and rms levels at the base are increased by 30% and 15% respectively. Interestingly however, the vertical penetration of the fountain, as judged from the $-0.1 V_j$ contour has changed very little from the zero splay case.

From the turbulence modelling point of view for CFD predictions the level of normal stress anisotropy is an important feature. The vertical rms fluctuation levels displayed in Fig. 7 may be contrasted with the axial rms fluctuation measurements shown in Fig. 8, for parallel jets and both splay conditions, and again on the $x/D_j = 0$ plane. In the jet shear layers the v^2 normal stress is the larger, with peak values greater than the u^2 peak by a factor of 1.4; this is what is to be expected (although slightly greater) for free mixing layer turbulence. At the base of the fountain v^2/u^2 also assumes values of 1.4, in spite of the fact that the fountain origin is near the ground plane, where v^2 levels might be expected to be preferentially suppressed. Decay rates of axial fluctuations in the fountain rise zone are similar to those noted above for v^2 . Fig. 8 indicates that splay out leads to reductions in u^2 turbulence levels which, broadly speaking, follow the trends in the vertical r.m.s. values; apart from the immediate fountain base, the space between the jets is filled with a roughly uniform level of u^2 rms at about 4%. The merging of fountain and inner shear layer turbulence fields by splaying the jets inwards is even more visible in the axial fluctuation measurements; once again anisotropy levels are largest at the fountain base at $1.35 (v^2/u^2)$.

Finally, Fig. 9 indicates the effect of introducing a cross-flowing stream at a velocity ratio of 10; mean and rms of the longitudinal velocity component are shown. The most obvious effect is the departure from left/right symmetry of the zero cross-flow condition (Figs. 9a, 9c) so that the left flowing ground sheet is now decelerated and rolled back by the cross-flow to form a ground-vortex zone. For $R=10$ this extends to around $5D_j$ forward of the jet entry location and has a height of around $2.5D_j$. The cross-flow also shifts the fountain origin downstream by about $1D_j$ as can be seen from the zero contour in Fig. 9b; the contour lines also indicate a down-wind inclination has been introduced. Interestingly, the presence of cross-flow

reduces the longitudinal turbulence levels measured, in spite of introducing a further impingement zone between cross-flow and left-flowing ground sheet.

4. CONCLUSIONS

The main conclusions which have emerged from the work reported here are as follows:

- (1) An experimental facility particularly suited to the study of mean flow and turbulence characteristics of multi-jet impingement ground-effect flows was designed, constructed and commissioned.
- (2) LDV measurements were obtained in this facility for a twin impinging jet flow field. For zero cross-flow and parallel jets, the data are similar to measurements reported previously (e.g. in Ref. [7]), thus validating the experimental facility.
- (3) New measurements have been obtained and reported here for, in particular, the effect of jet splay on the fountain formation process in twin-jet flows. 10° of splay-out was observed to weaken the connection between the central fountain and the jet flows, leading to a reduction of nearly 50% in the maximum measured upwash velocities and of 30% in the turbulence levels.
- (4) The fountain region was noted to be a zone of large local turbulence intensities (greater than 50%), and also a region where normal stress production was dominant, due to the impingement of opposing ground sheet flows. Further, even with very large sample sizes and averaging times, the measurements indicated the presence of large-scale unsteadiness at the fountain base. For these reasons, this is likely to be a difficult flow component for accurate prediction.

5. ACKNOWLEDGEMENTS

This work was funded by British Aerospace (Military Aircraft) Ltd., and the authors would like to express their thanks for this financial support.

6. REFERENCES

1. Barata, J.M.M., Durao, D.F.G., Heitor, M.V. and McGuirk, J.J. "Impingement of single and twin turbulent jets through a cross-flow. AIAA Journal, 29, pp. 595-602, 1991.
2. Childs, R.E. and Nixon, D., "Unsteady three-dimensional simulations of a VTOL upwash fountain" AIAA paper 86-0212, 24th Aerospace Sciences Meeting, Reno, U.S.A., 1986.
3. van Dalsem, W.R., Panaras, A.G., Steger, J.L. "Numerical investigation of a jet in ground effect with a cross-flow" Paper No. 872344, Proceedings of Int. Powered Lift Conference, SAE P-203, Santa Clara, USA, 1988.
4. Bray, D., "Jets in cross-flow and ground effect" Ph.D. Thesis, Cranfield Institute of Technology, 1992.
5. Miller, P. and Wilson, M. "Wall jets created by single and twin high pressure jet impingement" R.Ae.Soc. Aeronautical Journal, pp. 87-100, 1993.
6. Cimbala, J.M., Billet, M.L., Gaublumme, D.P. and Oefelein, J.L., "Experiments on the unsteadiness associated with a ground vortex" AIAA Jnl. of Aircraft, 28, pp. 261-267, 1991.
7. Saripalli, K.R., "Laser-Doppler velocimeter measurements in 3D impinging twin-jet fountain flows" in Turbulent Shear Flows 5, Eds. F. Durst et al, pp. 147-168, Springer Verlag (Berlin), 1987.
8. Barata, J.M.M. "Fountain flows produced by multi-jet impingement on a ground plane" AIAA Jnl. of Aircraft, 30, pp. 50-56, 1993.
9. Abbott, W.A. and White, D.R., "The effect of nozzle pressure ratio on the fountain formed between two impinging jets" RAE Tech.Memo. No. P1166, (1989).
10. McGuirk, J.J. and Page, G.J., "Shock-capturing using a pressure-correction method" AIAA Jnl., 28, pp. 1751-1757, (1990).
11. Barata, J.M.M., Durao, D.F.G. and Heitor, M.V., "Laser-Doppler measurements of multiple impinging jets through a crossflow" 4th Int. Symposium on Applications of Laser Anemometry to Fluid Mechanics, Lisbon, Portugal, (1988).
12. Erdmann, J.C. and Tropea, C.D., "Turbulence-induced statistical bias in laser anemometry" Proc. of 7th Biennial Symposium on Turbulence, Rolla, USA, (1981).

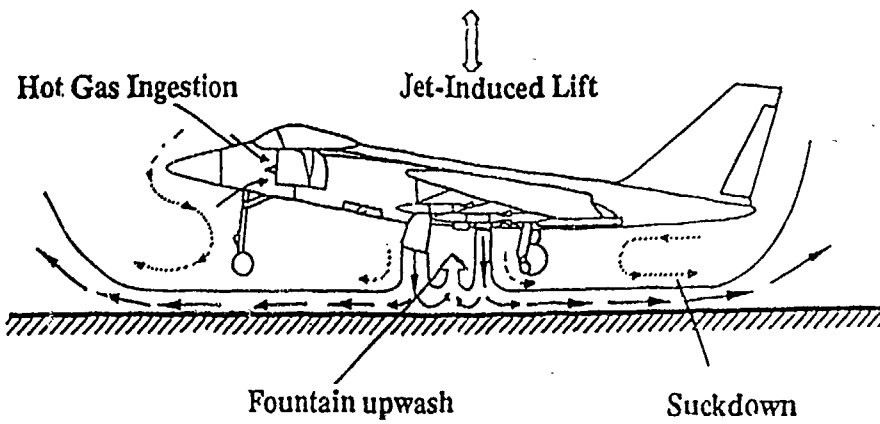


Fig. 1 Major aerodynamic features associated with V/STOL aircraft in the ground-effect zone

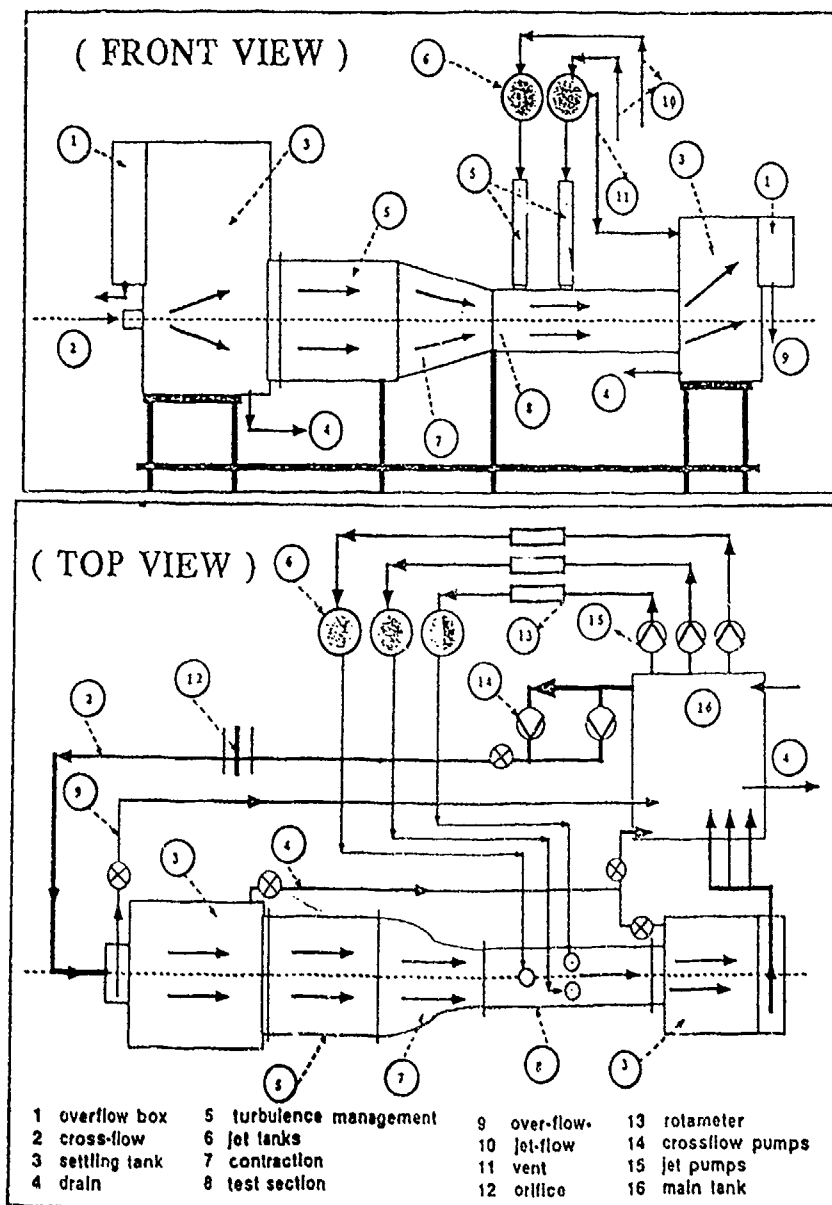
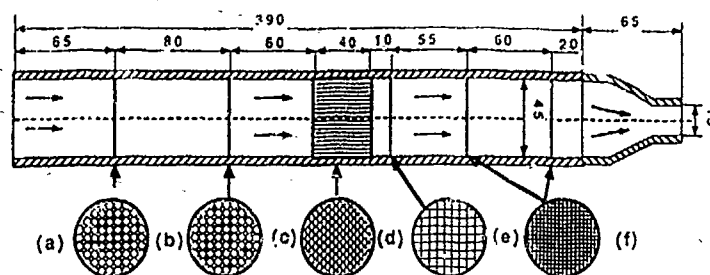
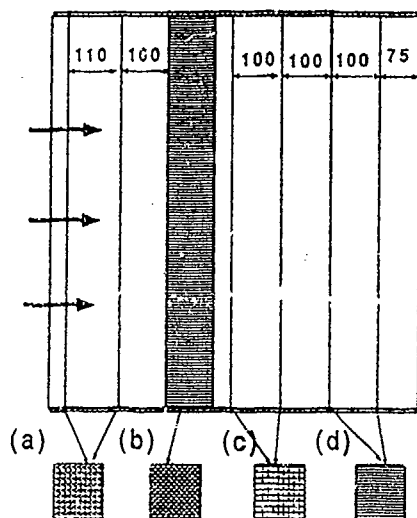


Fig. 2 Schematic of the V/STOL experimental water tunnel



jet unit; (a,b) perforated plates, (c) honeycomb, (d) coarse screen, (e,f) fine screens



cross-flow unit; (a) perforated plates; (b) honeycombs; (c) coarse screens; (d) fine screens

Fig. 3 Schematic of jet and cross-flow turbulence management systems

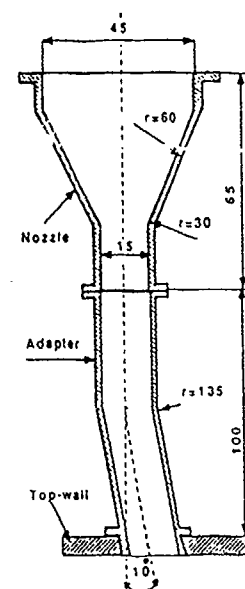


Fig. 5 Jet nozzle adapters to create 10° of jet splay (in or out)

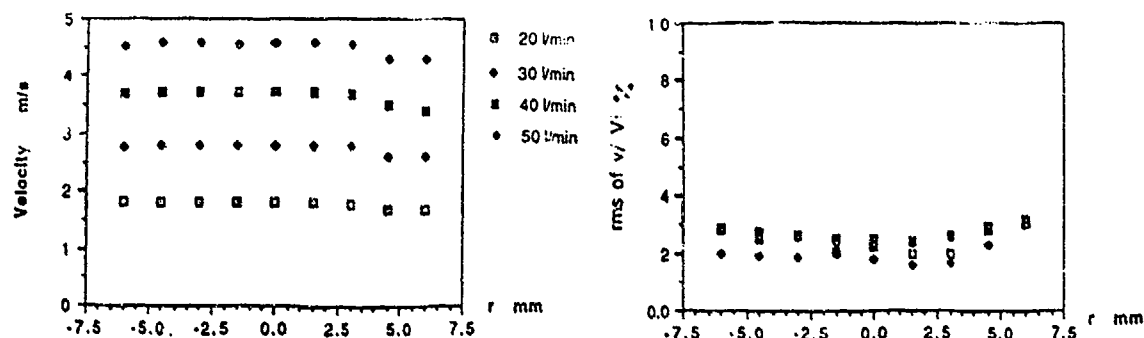


Fig. 4 Mean and r.m.s. velocity profiles at jet exit

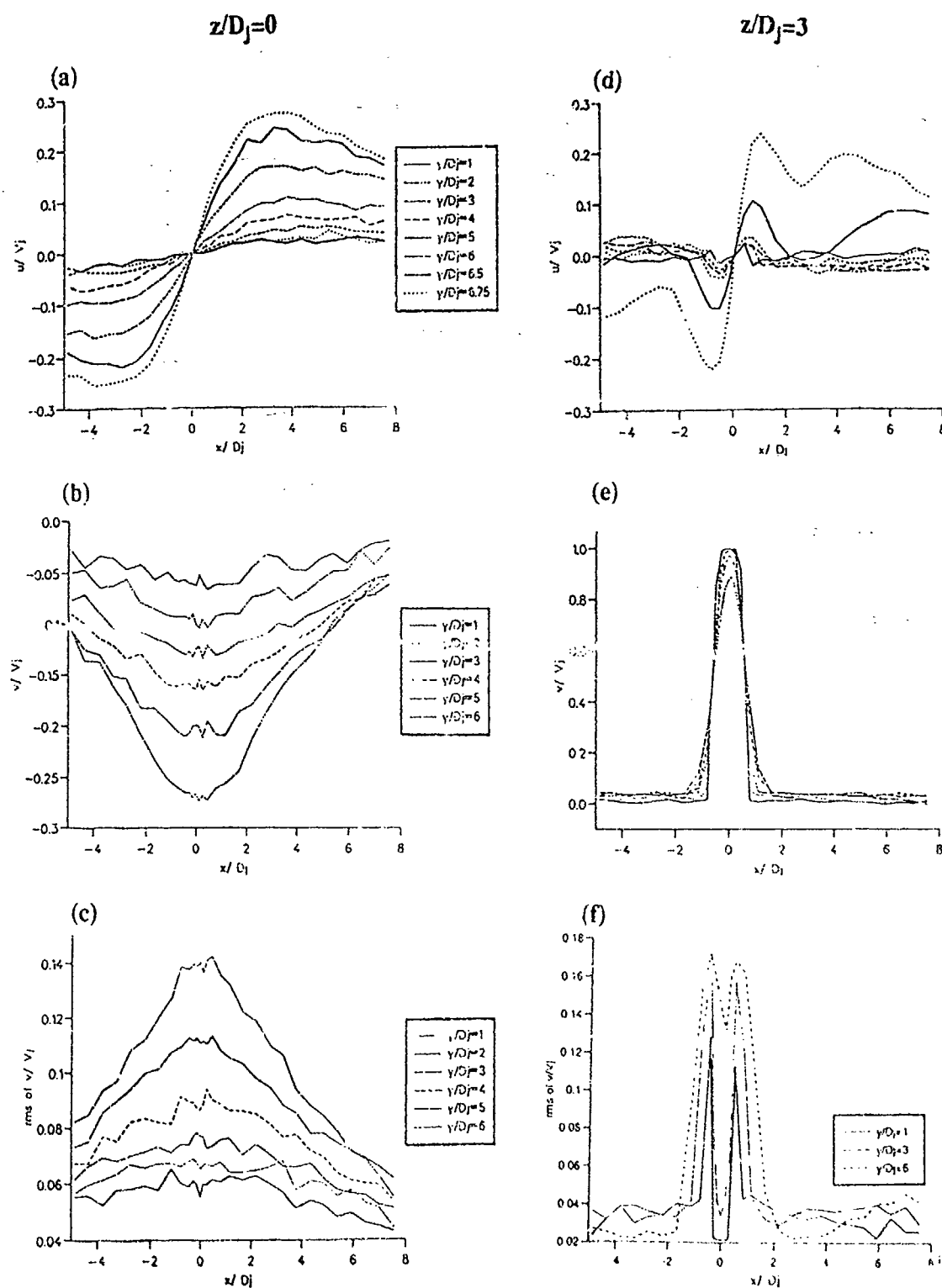


Fig. 6 Mean and r.m.s. velocity profiles for zero splay and zero cross-flow; fountain plane ($z/D_j=0$), mean u and v velocities (6a,6b) and v rms (6c); jet entry plane ($z/D_j=3$), mean u and v velocities (6d,6e) and v rms (6f).

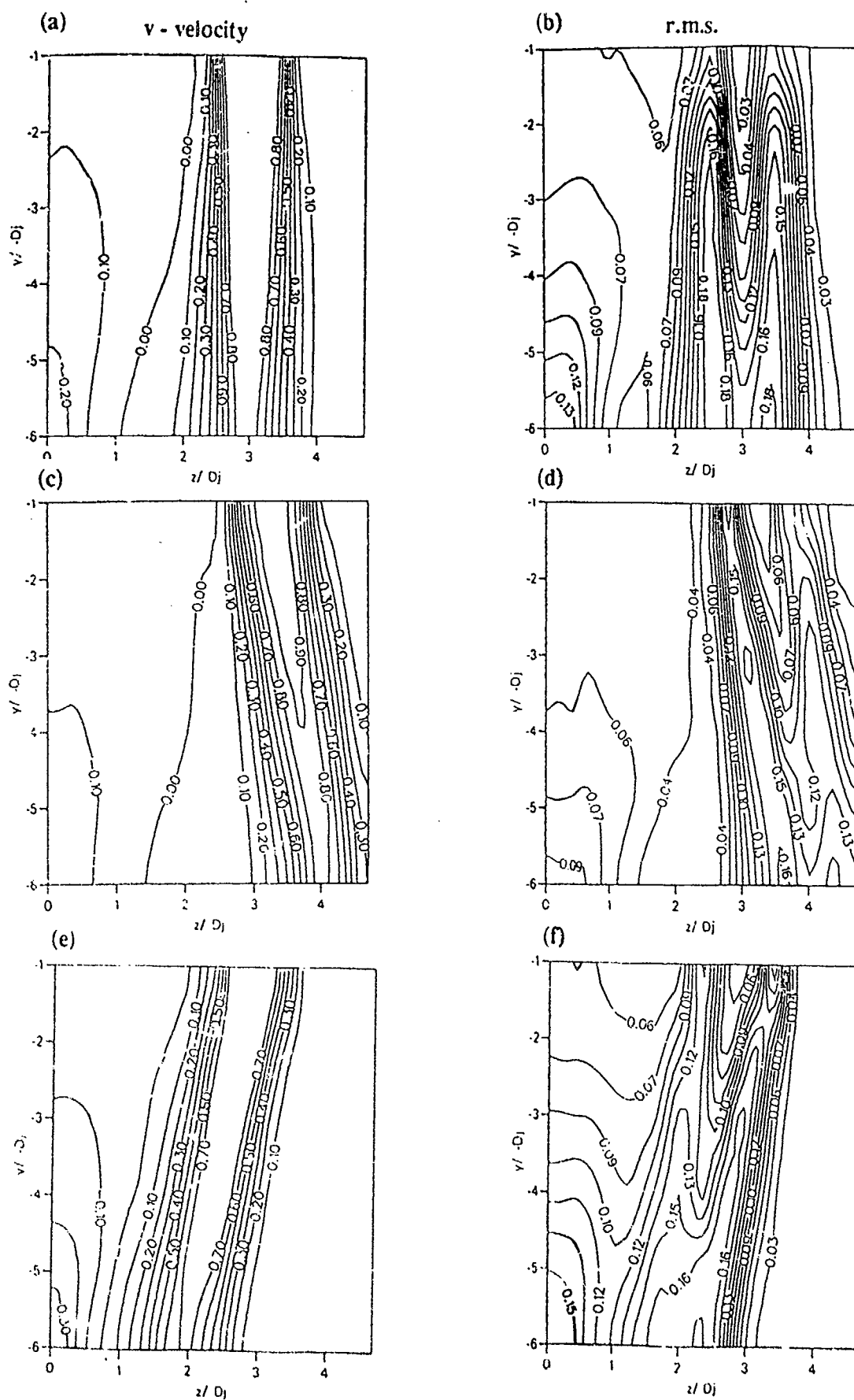


Fig. 7 Effect of jet spray angle on measured mean (a,c,e) and rms (b,d,f) vertical (v) velocity in transverse ($x/D_j=0$) plane

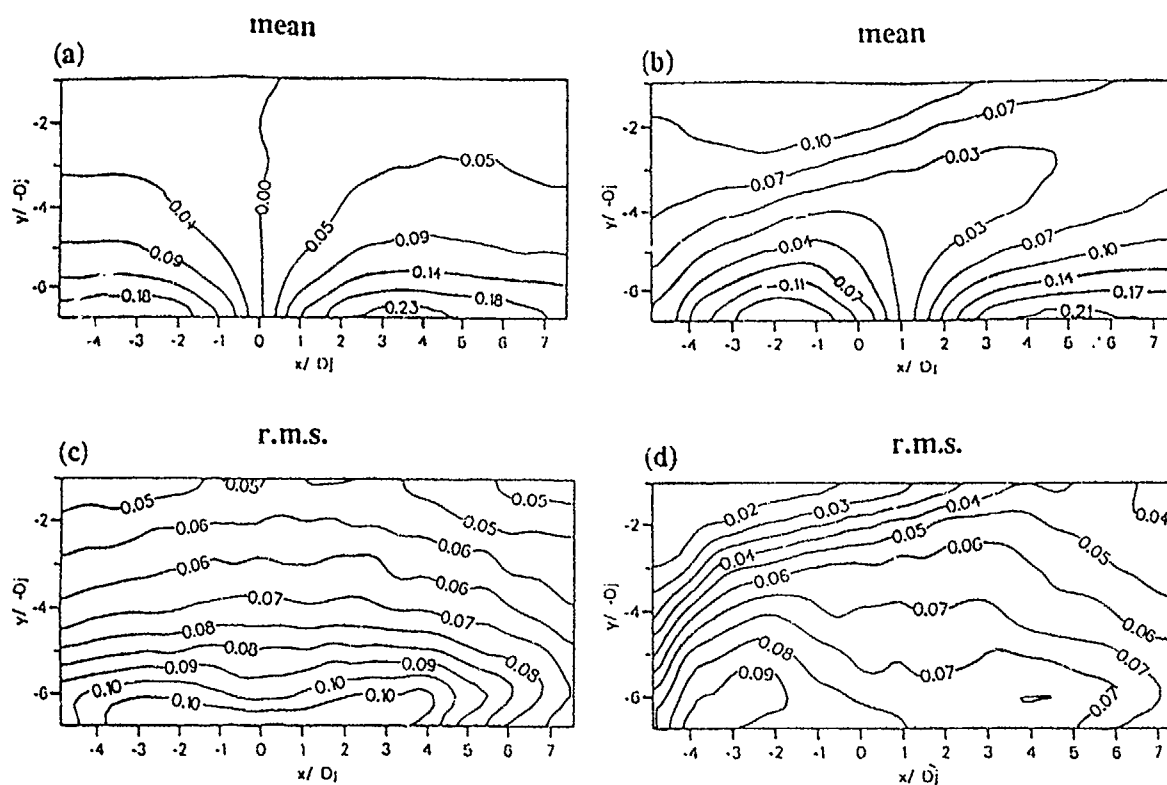


Fig. 9 Effect of cross-flow on measured mean and rms of longitudinal (u) velocity in longitudinal symmetry plane ($z/D_j=0$)
 (a,c) zero cross-flow ($R = \infty$)
 (b,d) with cross-flow ($R = 10$)

EXPERIMENTAL INVESTIGATION OF THE INTERACTION OF A THRUST REVERSER JET WITH AN EXTERNAL SUBSONIC FLOW

J-M. Charbonnier
K. Deckers
G. Wens

von Karman Institute for Fluid Dynamics
Chaussee de Warterloo, 72
B-1640 Rhode-St-Genese
Belgium

SUMMARY

An experimental modelisation of a door type thrust reverser is conducted in a subsonic wind tunnel. The geometry of the model is defined in order to simulate both the internal and external flow of a real thrust reverser. Different door configurations are studied for a selected value of the mass flux injection ratio of 3. Visualisations illustrate qualitatively the jet interaction, and extensive mean velocity and pressure measurements are conducted in sections perpendicular to the upstream flow direction with a five hole probe.

The total pressure losses and the drag force produced by the thrust reverser are deduced from the measurements. As a result, it shows that the smaller opening angle of the door (56°), with a becquet deflection of 15° gives the larger drag force. In addition to the classical pair of counter rotating vortices observed in jet in cross flow interactions, a second pair of counter rotating vortices below the main pair is found. The vorticity field is described with a quite good agreement by a simple vortex model simulating the two pairs of vortices

LIST OF SYMBOLS

U, V, W : velocity components along the axis X, Y, Z.
R : mass flux injection ratio $\rho_j V_j / \rho_0 U_0$
Pd : dynamic pressure
Cpt : total pressure coefficient $(P_t - P_t) / P_{d0}$
Ek : kinetic energy of the secondary flow in a cross section
Deq : hydraulic diameter of the jet orifice
d : opening angle of the door
b : inclination of the becquet
Fdr : effective drag force induced by the thrust reverser
r : radius of the viscous core of the vortex models
 Γ : vortex strength of the vortex models

subscript:

0 : infinite upstream conditions in the cross flow
j : refers to the jet
c : refers to the centre of the vortex
1 : refers to the main vortex pair
2 : refers to the secondary vortex pair

1 INTRODUCTION

It is of interest for aeroplane to improve the efficiency of the systems used to decelerate the plane during the landing in order to reduce the landing distance. Among the various

means that can be applied, thrust reverser systems have been developed, where the thrust of the engine is reversed. Actually, two kinds of thrust reversers are used : the cascade and the door types. Both of them manipulate the engine fan flow to create a reverse thrust, but the second one, which was developed more recently, included the air brake effect created by the deflecting door. During the landing, four doors are opened on the nacelle of the engine, and the engine fan flow is forced to exit through these doors. This simple concept is very promising provide one can predict its efficiency as well as the jet trajectories. A good prediction of the jet trajectory is necessary to avoid the interference of the jet with the aircraft fuselage, the wings or the engine intake.

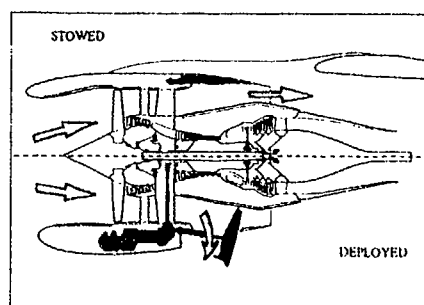


fig. 1: Schematic diagram of a door type thrust reverser (doc. Hispano Suiza)

Despite this jet configuration is similar to the interaction of a jet with a cross flow, the presence of the deflecting doors is likely to modify significantly the behaviour of the jet. Therefore, an experimental modelisation of the door type thrust reverser was initiated two years ago at the von Karman Institute as an extension of the work conducted in the area of jet in cross flow interactions.

For the typical jet to aircraft velocity ratio of 3, there are extensive studies available in the literature for jet in cross flow interaction. A brief review of these studies will point out the major conclusions achieved, that will be useful to discuss the case of the thrust reverser jet. Kamotani and Greber (1972, Ref. 1) made extensive velocity and temperature measurements for both heated and non heated round jets, exhausting through a flat plate with a jet to cross flow momentum flux varying between 15 and 60. They derived correlations for the velocity and temperature trajectories, defined as the location of the maxima of temperature and velocity. It shows that the velocity trajectory is only controlled by the momentum flux ratio.

The main characteristics of the jet in cross flow interaction are the well known counter rotating vortices that are present behind the jet. Fearn and Weston (1974, Ref.2) studied the

behaviour of these vortices for momentum flux ratios varying between 9 and 100. Two vortex models are studied: a simple vortex filament model where the strength and the location of the vortex filament are determined using the velocities measured in the symmetry plane, and a diffuse model where a Gaussian distribution of vorticity is assumed. For this later model, velocity measurements in the whole cross section of the jet are required to compute the strength, the location, and the diffuseness of the vortex. Using this model, Fearn and Weston produced data for the core radius, the strength, the vortex trajectory as a function of the distance from the exit. It shows that the influence of the momentum ratio on the vortex strength is predominant whereas it is negligible on the vortex core size. They also gave a correlation for the vortex curve, defined as the location of the projection of the vortex centres on the symmetry plane. The comparison of the vortex filament model with the diffuse model shows that the simple filament model gives results for the vortex spacing and the vortex strength that are in good agreement with the diffuse model predictions. It implies that one can expect a rather good prediction of the jet characteristics with only the velocity measurements in the symmetry plane, which reduces by a considerable amount the measurements required.

A constraint for these velocity measurements, is to investigate a plane perpendicular to the vortex trajectory, which is a priori not known. Fearn and Weston also show that an angle of $\pm 5^\circ$ between the measurement plane and the plane normal to the plane, will induce a change of only 3% on the vortex strength. Therefore, the constraint on the measurement plane is much less severe, and the measurements in the mean and far field can be done in cross sections perpendicular to the mean flow direction.

Karagozian (1986, Ref. 3) proposes an analytical model for the prediction of vorticity by approximating the force acting on each viscous vortex. The results of this study reinforce Fearn and Weston conclusion on the vorticity generation. Actually, the position and the origin of the counter rotating vortices are widely discussed. Sykes and al (1986, Ref. 4), studied numerically the injection at large injection ratio. On the basis of the results of a Navier Stokes code, they found that the source of vorticity at the jet exit, is the stream wise vorticity present in the boundary of the jet. The same origin was found by Charbonnier (1992, Ref. 5) for an injection ratio lower than 1.

In the jet wake, an especially at high injection ratios, some other vortices were found. They produce an unstationary wake characterised by a Strouhal number around 0.2 (Mac Mahon and al 1971, Ref. 6). Fric and Roshko (1989, Ref. 7) show that these vortices are originating from the boundary layer of the flat plate through which the jet is produced. On each side of the jet, the boundary layer separates due to the high adverse pressure gradient, and create an alternate vortex shedding. In the case of large injection ratio, the wake vortices do not interact strongly with the jet, whereas for small injection ratio, Charbonnier (Ref. 5) demonstrated that such vortices impose a drastic change in the jet behaviour.

In the case of the thrust reverser jet, the presence of a deflecting door behind the jet is likely to modify the vortex generation as well as the jet structures. Actually, the vorticity generated at the surface of the door may have a large influence on the vorticity field downstream. Furthermore, not only the presence of a door, but also the shape of the inlet duct parallel to the main flow will

probably modify the jet behaviour as noticed in the experiment of Pietrzyk and al (1988, Ref. 8) with a short length to diameter ratio of the injection pipe

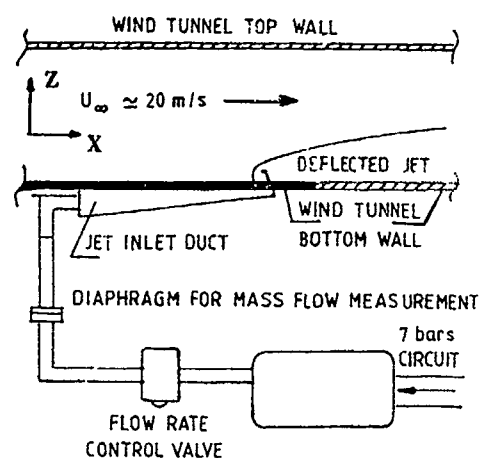


fig. 2: Experimental set-up

As a first approach to the study of a thrust reverser jet, an experimental modelisation of the real geometry is done. These experiments are designed to give first quantitative data in such a configuration, as well as an evaluation of the door geometry on the jet behaviour, and eventually a quantification of the drag force produced. The chapter 2 presents the experimental set up and the measurement technique used during this study. Then in the chapter 3, the reference case of a thrust reverser jet without door is described. The study of a so called reference door is presented in the chapter 4. The investigation of the effect the door and its geometry on the jet interaction are presented in the chapter 5, and an evaluation of the efficiency of the different configurations of thrust reverser doors is given in the chapter 6. Finally, in the last chapter, a modelisation of the vortices is proposed.

2 EXPERIMENTAL TECHNIQUE

A schematic of a real door type thrust reverser is shown on the figure 1. When the door is deployed, the cold engine fan flow is deviated by the door equipped with a small becquet, and forced to exit in the upstream direction. In our study, we do not simulate the exact geometry of the thrust reverser, but we try to keep an injection duct representative of the double flux channel in the real engine. The three dimensional effects induced by the nacelle curvature are neglected as it is modelled by a flat plate. The double flux passage is modelled by a parallelepipedic duct parallel to the plate and located under it, which ends at the downstream side of the jet exit.

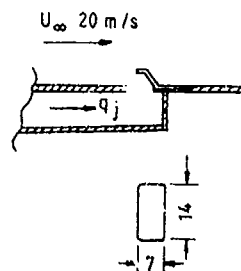


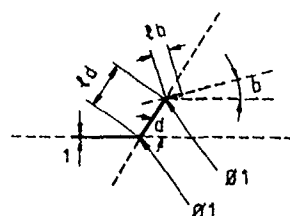
fig. 3: Detail of the door arrangement.

The model is installed in a subsonic Eiffel wind tunnel of $0.28 \times 0.28 \text{ m}^2$ cross section, and it replaces the bottom wall of the test section. The experimental arrangement as well as the flow circuit for the jet are sketched on the figure 2. The mass flow rate $\rho_j V_j$ is monitored by a diaphragm and the cross flow velocity in the wind tunnel is set to 20 m/s . Details of the exit region of the jet with the position of the deflecting door are shown on the figure 3. The rectangular shape of the hole is chosen to be representative of the real case, and the dimensions of $7 \times 14 \text{ mm}^2$ are selected to minimise the wind tunnel blockage effects. The equivalent diameter Deq equals 9.3 mm , the Reynolds number based on the cross flow velocity and this diameter equals $12\,440$. The flat plate boundary layer thickness at the location of the exit without jet equals $1.5 Deq$. The geometrical parameters of the doors tested are defined on the figure 4 and listed in the table 1. In all configurations, the lengths l_d and l_b are respectively equal to 5 mm and 2 mm with a maximum variation of $\pm 0.5 \text{ mm}$. Following the notations used in the table 1, P0 is the configuration without door, called later the reference jet; P2 is called the reference door, and for P3, two vertical plates are added on each side of the jet as sketched on the figure 4.

Conf.	P0	P1	P2	P3	P4	P5	P6
$d(^{\circ})$	-	90	56	56	56	56	66
$b(^{\circ})$	-	0	0	0	15	-15	0
S.P.	-	-	-	yes	-	-	-

table 1 : Definition of the different configurations tested.

Wall streamline visualisations and flow field visualisations using smoke as a tracer and a laser sheet for the illumination were performed on a preliminary set up which is scaled on the model described before, with a jet exit of $9 \times 14 \text{ mm}^2$. Actually, this first model was scaled down in order to reduced the blockage effect, and all the measurements presented here are taken with the model described in the previous section. During the flow field visualisations, the mass flux injection ratio is kept constant equal to 3, but the velocity of the cross flow is reduced to 4 m/s .



WITH SIDE PLATES

fig. 4: Definition of the door geometry

Mean velocities and pressures are measured with a five holes directional probe of 1.2 mm diameter. After calibration, the probe gives the velocity values and directions, as well as the total pressure in a measurement cone of 40° half angle. The probe is mounted on the displacement mechanism of the wind tunnel monitored by a personal computer which also makes the acquisition of the pressure signal.

A particular section at $15 Deq$ is selected to perform most of the measurement in the different configurations. The measures are taken in a half section normal to the cross flow direction to take advantage of the theoretical symmetry plane. For mechanical reasons, the first measurement point is located at 10 mm above the flat plate and the measurement domain is $10 < Z < 145 \text{ mm}$ vertically, and $0 < Y < 75 \text{ mm}$ laterally, by steps of 3 mm .

3 THE REFERENCE JET

The reference jet (configuration P0), is exhausting without door, with a mass flux injection ratio of 3. The figure 5 shows a wall stream line visualisation in the near region of the exit. Upstream of the exit, there is a horseshoe vortex that turns around the jet and is carried out under the jet, as it is mentioned by various experimental studies conducted on jet in cross flow interaction (Andreopoulos, 1985 Ref. 9, Charbonnier, 1992 Ref. 5). In such a case, the two counter rotating vortices on the downstream side of the jet suck in the upstream flow which passes around the jet. The region of reverse flow on the downstream side is ended by a saddle point, the wall stream lines converge toward the symmetry plane and the jet wake is in a certain sense closed.

The secondary velocities and the total pressure coefficient C_{pt} , measured in the half cross section at $X/Deq=15$, are presented on the figure 6. One of the two counter rotating vortices is clearly visible as well as the upward motion induced under the jet, which brings external fluid into the jet wake and then mixes it with the jet flow. The iso pressure plot points out two regions: the wake region where there is a loss of total pressure, and the region above which corresponds to the jet flow with a higher total pressure. The comparison of the two plots shows clearly that the vortices are in the lee side of the jet and that they contribute to mix the high energy flow of the jet with the external flow.



fig. 5 Wall stream line visualisation for the reference jet

Actually, these measurements were also made with the preliminary set up with larger dimensions for the hole ($Deq=12 \text{ mm}$). The comparisons of the two sets of data have shown that there is no significant change in the behaviour of the jet, and the velocity trajectories that can be deduced in both cases agree perfectly together. It gave us a good confidence in the low influence of the tunnel blockage on the jet interaction.

The comparison with the trajectory deduced from Margasson correlation using the mass flux ratio as the velocity ratio (Margasson, 1968 Ref. 10) is found to be about $1 Deq$ under

the experimental point. The same comparison with the correlation of Fearn and Weston (Ref 2) gives an under estimation for the correlation of about 2.5 Deq. The fact that we use the mass flux ratio instead of the momentum flux ratio can explain these differences. More specifically, due to the particular shape of the injection duct, it is likely to have highly non uniform distribution of velocity at the exit with separated regions near the orifice which reduce the effective passage, and eventually will produce a higher equivalent momentum flux ratio.

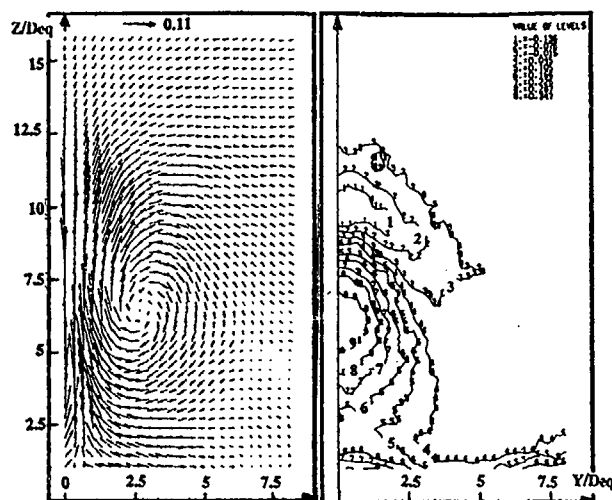


fig. 6 Secondary velocity vectors and iso-total pressure coefficient for the reference jet

Therefore, the use of the mass flux ratio to quantify the injection will allow to integrate into the comparison of the different configurations the changes in the exit region from one door to the other.

4 THE REFERENCE DOOR

The reference door configuration P2 corresponding to an opening angle of 56° is tested for a mass flux injection ratio equal to 3.



fig. 7: Wall stream line visualisation for the reference door

The figure 7 shows a wall stream line visualisation around the jet exit. Compared to the previous case, the topology is totally changed, and downstream of the door. There is no longer only a saddle point, but one node on the symmetry line and two saddle points on each side. The jet wake is not "closed" as in the previous configuration because the wall

stream lines coming from upstream can not enter the region of the wake in that case. The bifurcation lines defining the wake diverge when going in the downstream direction, as well as the wall stream lines that are originating from the node. A flow field visualisation of this configuration is presented on the figure 8, where smoke is injected in the plenum chamber of the jet. Clearly, one can see the door deviating the jet in the upstream direction. Under the action of the external flow, the jet is finally bent and directed in the downstream direction.

For the reference door, three half sections of measurements are performed at $X/Deq=7.5$, 15, and 25. In order to check the symmetry of the jet, as well as the reproducibility of the experimental conditions, a full section is also measured at $X/Deq=15$.

The figure 9 shows the vector plots in the three cross sections. At $X/Deq=7.5$, a strong vortex is visible, and large velocities directed to the wall are present under the vortex. Actually this location is closed to the re-attachment node observed on the wall stream line visualisation, and therefore the negative vertical velocities illustrate the re-attachment region. The next section at $X/Deq=15$ is located after the node, and the vector plots show the presence of a second vortex under between the main vortex and the wall which is not present on the reference jet. This second vortex is attached to the bifurcation line that separates the region of the jet wake which is near the wall from the external flow. In the last measured section at 25 Deq, the two vortices are still present, but the values of the secondary velocities are much smaller than in the first section.

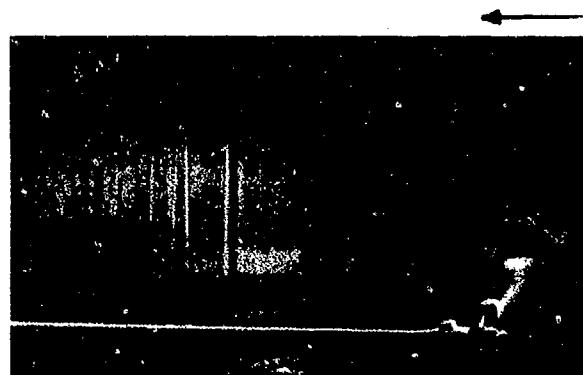


fig. 8: Flow field visualisation in the symmetry plane for the reference door

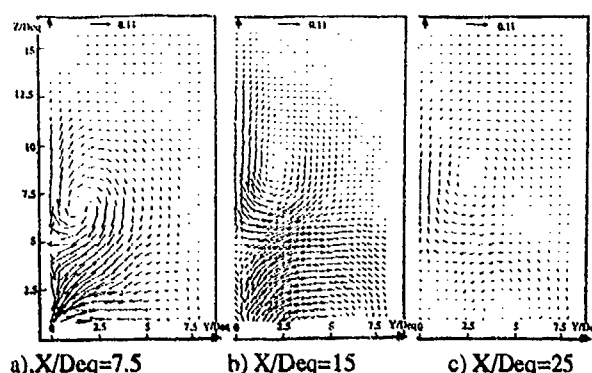


fig. 9: Secondary vector plots for the reference door

The full section measured at $X/Deq=15$ shows that the jet development is symmetric (fig. 10, 11). The good

reproducibility of the test conditions is demonstrated by the comparison of the iso total pressure obtained for the two tests on the right section. On the figure 11, the dash lines on the right correspond to the measurements presented before, and they compare well with the data obtained on the whole section.

The comparison with the reference jet measurements at the same position shows that the secondary velocities are smaller when the door is added. In this case, there is no region of total pressure excess anymore, but only a large region of pressure losses.

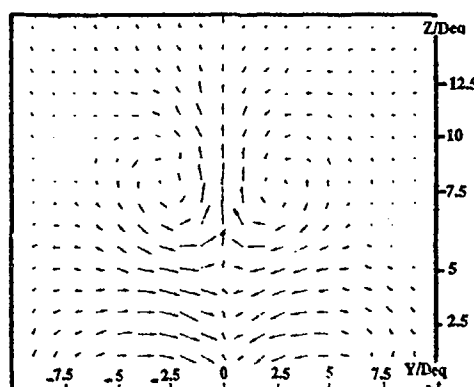


fig. 10: Secondary vector plot for the reference door in the full cross section at $X/Deq=15$

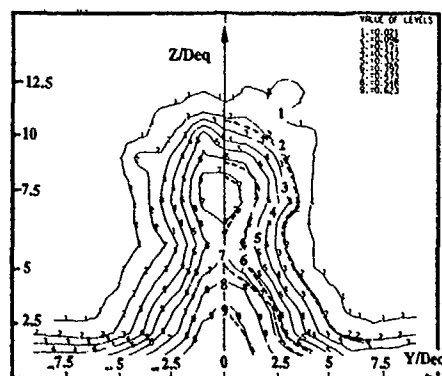


fig. 11: Iso-total pressure coefficient for the reference door in the full cross section at $X/Deq=15$

5. THE EFFECT OF THE DOOR GEOMETRY

As seen on the table 1, the geometry of the door can be changed. The opening angle of the deflecting door can vary between 90° to 56° . For the opening angle of 56° , the becquet can be oriented at 0° , $\pm 15^\circ$ compared to the upstream cross flow direction.

A wall stream line visualisation for the door P1 is shown on the figure 12. The topological pattern is very similar to the pattern observed for the reference door (fig. 7). The effect of the door opening angle is clearly visible on the flow visualisation of the figure 13. For the P0 configuration, the jet is much less deflected to the upstream direction than for the P2 door (fig 8), therefore the vertical spreading and the blockage created by the jet are reduced.

The effect of the opening angle is analysed by comparing the configurations P1, P2, and P6. In all cases, the wall stream

line visualisations are very similar, and, as expected, the second vortex is always present. The figures 14 present the pressure coefficient measured in the symmetry plane at 4 axial positions downstream of the jet exit. In all cases, there is a region of large total pressure losses just downstream of the exit, which is progressively re-energetized by the action of the jet vortices. As a consequence of the opening angle variation, one can see that the larger the angle, the lower the upper frontier of the jet. Moreover, for the 90° opening angle of the door, the wake re-energetisation is more efficient than for the two other configurations. The difference of 10° between the configurations P2 and P6 do not have a significant effect on the wake re-energetisation, whereas it has a small effect on the vertical spreading of the jet.



fig. 12: Wall stream line visualisation for the door P1

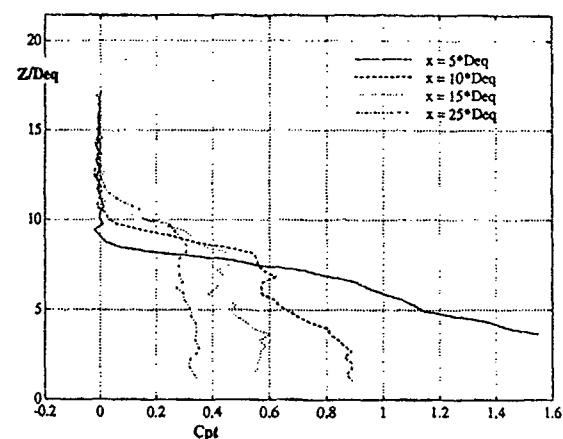


fig. 13: Flow field visualisation in the symmetry plane for the door P1

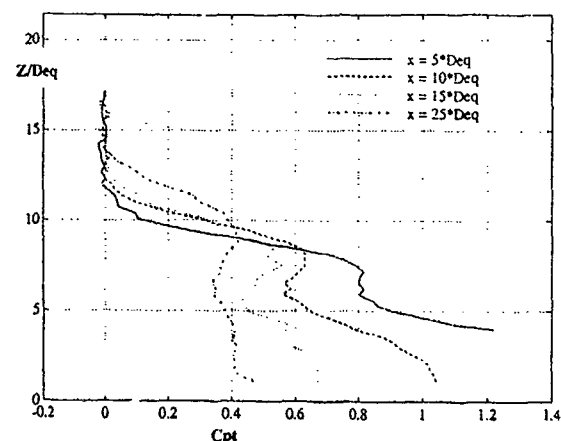
The effect of the becquet orientation is analysed for the reference door opening angle (56°), by comparing the configurations P2, P4, and P5. The figures 15 present the total pressure coefficient in the symmetry plane for the doors P4 and P5. For a becquet orientation of -15° , there is no significant change of the jet frontier and of the wake losses when it is compared to the reference door P2. When the becquet is inclined at $+15^\circ$, the upper frontier of the jet is higher, and the losses are bigger compared to the reference door. Actually, the total pressure losses in the jet wake for the door P4 are about 25% larger than the losses measured for the reference door.

The influence of side plates placed on each lateral side of the exit is also investigated. The configuration P3 corresponds to an opening angle of 56° , without becquet inclination. The aim of the two side plates is to direct the jet as much as

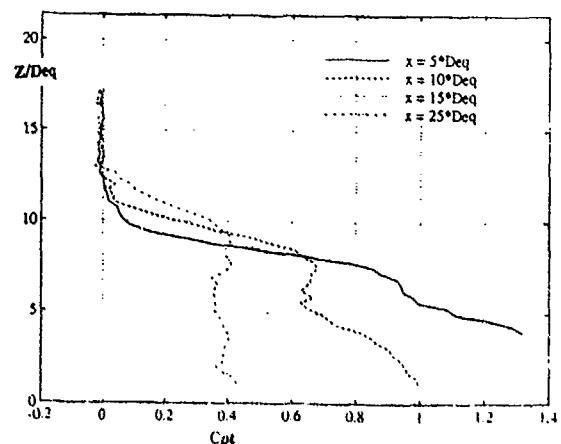
possible in the opposite direction of the cross flow. The figure 16 presents the secondary velocity vectors and the iso total pressure coefficients in the half section at $X/Deq=15$. Comparing with the reference door, the second vortex is stronger in this case, and the area of total pressure losses is larger. As seen on the total pressure coefficient profiles in the symmetry plane (fig. 17), the upper frontier of the jet is higher than in the case of the reference door, but at the same time, the re-energetisation of the wake is more efficient. It is likely to come from the fact that the jet is reaching a higher altitude before being bent and directed in the downstream direction.



a) P1



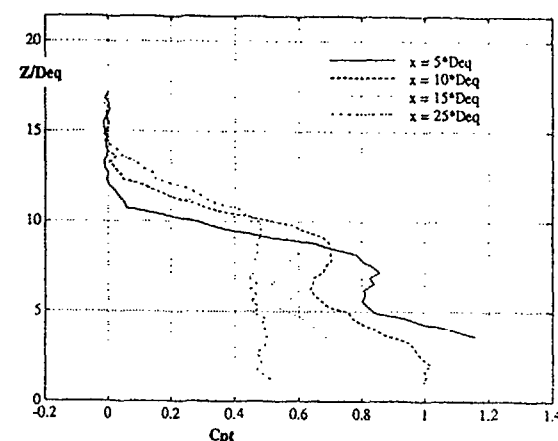
b) P2



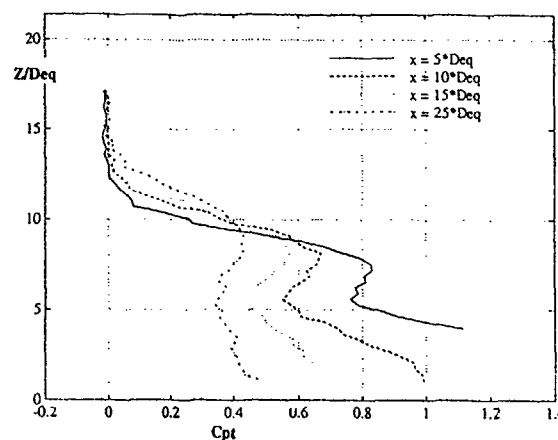
c) P6

fig. 14: Total pressure coefficient profile in the symmetry plane

On the basis of the velocity measurements in the symmetry plane, the velocity trajectory, defined as the location of the maxima of velocity, is plotted for the different configurations on the figure 18. It shows that when a door is present, the jet trajectory is always above the reference jet path. In order to synthesise the comparison of the different configurations, the integration of the pressure losses and of the secondary velocity kinetic energy are computed in the measurement sections at $X/Deq=15$. The values are normalised by the data obtained for the reference jet P0.



a) P4



b) P5

fig. 15 Total pressure coefficient profile in the symmetry plane

Conf.	P1	P2	P3	P4	P5	P6
$E_k/E_k(P0)$	0.45	0.36	0.43	0.44	0.44	0.34
$C_{Pt}/C_{Pt}(P0)$	4.00	4.64	5.00	5.46	5.00	4.10

table 2 : Kinetic energy and total pressure losses normalised by the reference jet values.

The table 2 gives the values calculated for the different doors. The effect of the door is to reduce by nearly a factor of 3 the kinetic energy, and to multiply by more than 4 the total pressure losses. In terms of total pressure, the door P4 gives the higher losses, the side plates (P3) do not increase the losses, and all the configurations with a deflecting angle of 56° are in a band of $\pm 10\%$ variation around the average loss. When the opening angle of the door is increased, the losses are reduced, and there is no significant change of the

total pressure losses between the 66° opening angle (P6), and the 90° opening angle.

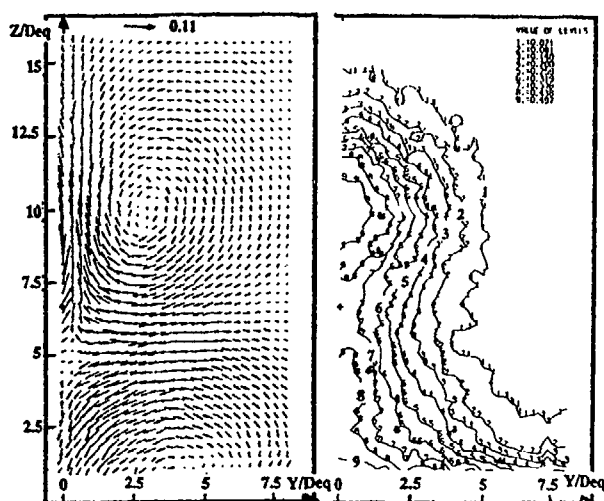


fig. 16: Secondary velocity vectors and iso-total pressure plot for the door P3 at $X/Deq=15$

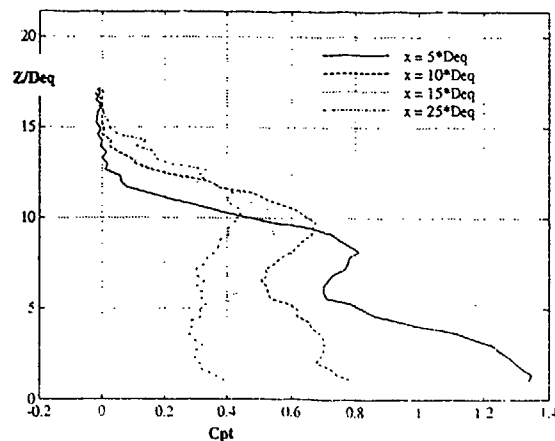


fig. 17: Total pressure coefficient profile in the symmetry plane for the door P3

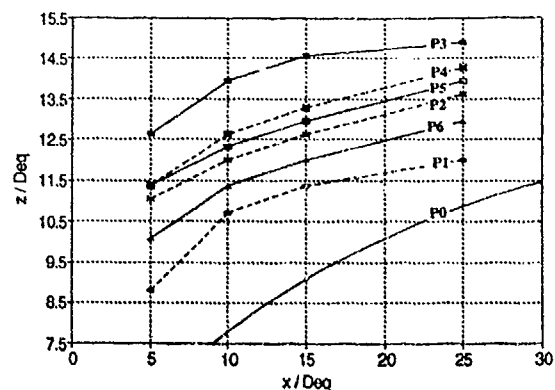


fig. 18: Velocity trajectories for the different configurations

6 EVALUATION OF THE DRAG FORCE PRODUCED

The drag force induced by the thrust reverser is estimated using the integral momentum equation. The figure 19 describes the volume of control used for the calculation. The surface S1 is the upstream section where the flow is uniform, and where the boundary layer is neglected. S2 and S3 are

streamline surfaces, and S4 is the symmetry plane. The surface S5 corresponds the flat plate through which the jet is injected, and the surface S6 is the measured half section. The dimensions of S1 are deduced from the mass conservation applied to the volume of control.

Several assumptions have to be made in order to achieve this computation:

- the air is at uniform and constant density.
- the flow field is stationary,
- the fluxes of the viscous and turbulent stresses through the control volume surfaces are negligible,
- the pressure on the surfaces S2 and S3 is equal to the infinite upstream pressure,
- a turbulent velocity profile is assumed between the wall and the first measurement point in the section S6.

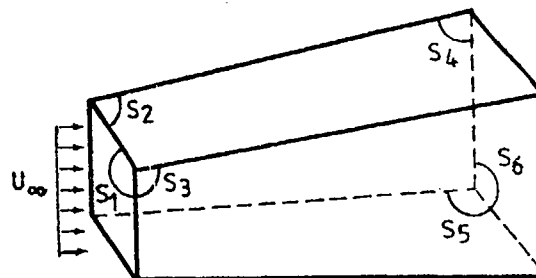


fig. 19: Definition of the volume of control

Therefore, the total drag force which is calculated corresponds to the momentum injected in the upstream direction, plus the force acting on the door, and the friction force on the flat plate. In order to check the calculations, the case of a smooth flat plate without injection is measured and the equivalent total drag force is calculated and compared to the theoretical friction force computed for a flat plate boundary layer. The boundary layer is assumed to be first laminar and then to become turbulent for a Reynolds number of 5.10^5 . The friction force computed on the surface S5 is equal to 0.0462 N whereas the total drag force computed from the measurements equals to 0.0424 N, which is in good agreement with the theoretical value.

Then, the calculation is applied to the reference door, and the measured drag of the flat plate is subtracted to the total drag force to give only the contribution of the thrust reverser system. For this configuration, it is possible to compare the force calculated with a half section of measurements at $X/Deq=15$, with the value obtained for the full section measured at the same location. Furthermore, the two measured half sections at $X/Deq=7.5$, and 25 are also used to compute the effective drag of the thrust reverser. The table 3 presents the results obtained, where the drag force F_{dr} is the effective drag of the thrust reverser jet

X/Deq.	15	15	7.5	25
Section	half	full	half	half
F _{dr} (N)	0.446	0.471	0.555	0.468

table 3 : Effective drag force induced by the thrust reverser for the reference door.

The values computed for $X/Deq=15$ are in rather good agreement, with a variation of $\pm 3\%$ of the average value. The drag force calculated at $X/Deq=25$ is remaining in the

same uncertainty band, whereas the value for $X/Deq=7.5$ is significantly higher (+21%). Actually, at this location, the probe is not able to resolve the high velocity angles in the jet wake near the wall, and therefore the approximation by the turbulent velocity profile is more extended than in the other cases. Furthermore, this approximation is somewhat doubtful in the close wake region, and some other assumptions made, such as on the turbulent stresses, are probably not valid in this case.

The table 4 gives the effective drag force calculated for the other door configurations using the measured half sections at $X/Deq=15$. It confirms what is given by the analysis of the total pressure losses. The opening angle of 56° is the more efficient, and the configuration with the becquet oriented by $+15^\circ$, (P4), produces the larger drag force.

Conf.	P0	P1	P2	P3	P4	P5	P6
Fdr (N)	0.018	0.380	0.446	0.524	0.530	0.500	0.392

table 4 : Effective drag force induced by the thrust reverser.

The force produced by the thrust reverser system is compared to the drag force induced by a cylinder of length L and with a diameter Deq , for the same Reynolds number. The theoretical lengths for this equivalent cylinder are given in the table 5 as a function of the door configuration.

Conf.	P0	P1	P2	P3	P4	P5	P6
L/Deq	2.6	53.4	62.4	73.6	74.2	70.2	54.8

table 5 : Equivalent cylinder reduced lengths.

The advantage of this configuration of reverse jet on a static air brake system is obvious when one compares the equivalent length required to obtain about the same drag.

7. VORTEX MODELLISATION

A simple vortex model is used to describe the vorticity field measured. The vortex has a viscous core where a solid rotation takes place, and outside this core, the tangential velocity is inversely proportional to the distance to the centre. Therefore, the parameters that describe the vortex are the co-ordinates of the centre, the radius of the core, and the strength of the vortex. Two main modellisations are studied: a model with one pair of vortex, and a model with two pairs of vortex. In both cases, the mirror images are considered to simulate the presence of the flat plate.

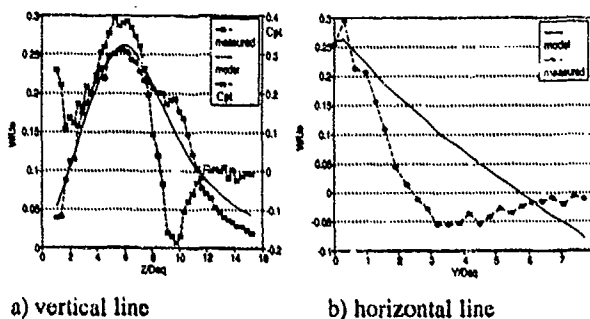


fig. 20: Comparison of the measured and predicted velocities along the reference lines for the reference jet at $X/Deq=15$

7.1 One vortex pair model.

The location of the vortex centre and the strength are deduced by the minimisation of the difference between the measured and calculated vertical velocities on the vertical profile in the symmetry plane. The dimension of the vortex core corresponds to the lateral co-ordinate Y_c of the centre. This model is applied to the reference jet, and the figure 20 shows the comparison between the calculation and the experiment for the vertical component of the velocity on the vertical line in the symmetry plane (20a), and on the horizontal line passing through the vortex centre (20b). On the figure 20a, the total pressure coefficient is also plotted, and it visualises the part of the jet which is not yet mixed. The comparison of the velocities along these two reference lines is rather poor, and this can be explained by the fact that we are not using a measurement plane normal to the vortex curve. Actually, based on the velocity trajectory (fig. 18), one can deduce that in this case the vortex trajectory angle is large and therefore it is likely to explain the differences. Since the trajectory angle is smaller for the other configurations, one can expect a better agreement between the model and the measurements.

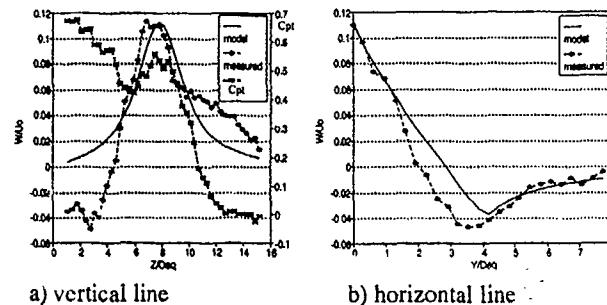


fig. 21: Comparison of the measured and predicted velocities along the reference lines for the reference door at $X/Deq=15$

The same model is applied to the reference door and the figures 21 shows the comparison on the reference lines. The agreement is better but it can be improved by a small modification of the vortex model.

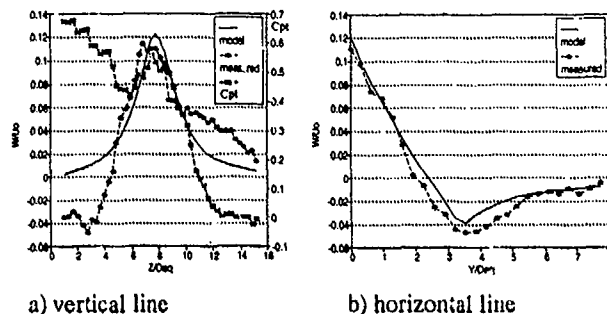


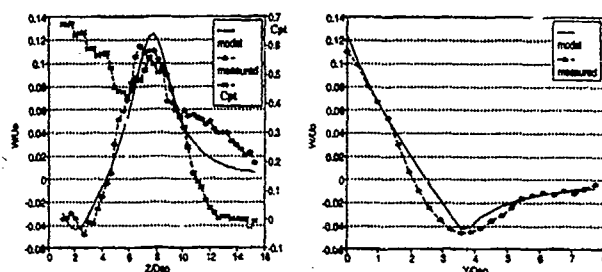
fig. 22: Comparison of the measured and predicted velocities along the reference lines for the reference door at $X/Deq=15$

The optimisation of the vortex parameter is now done on the vertical velocities along the two reference lines instead of using only the symmetry plane line. The figures 22 shows the improvement obtained especially on the vertical velocity along the horizontal line (22b). Nevertheless, some discrepancies are remaining in the symmetry plane under the

jet which are likely to come from the presence of the secondary vortex pair.

7.2 Two vortex pair model.

A second vortex pair with its image is added to simulate the secondary vortex measured for the configurations with doors. The optimisation of the main vortex pair is done as before, by using the two distributions of vertical velocities. By an iterative process, these profiles are also used to determine the position of the centre and the strength of the secondary vortex. The viscous core of the secondary vortex is determined by the minimisation of the error on the horizontal component of the velocity along the vertical line passing through the centre of the main vortex.



a) vertical line

b) horizontal line

fig. 23: Comparison of the measured and predicted velocities along the reference lines for the reference door at $X/Deq=15$

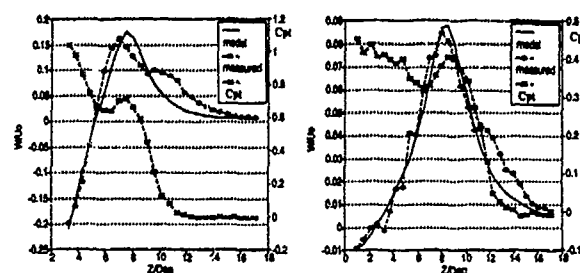
This model is applied to the reference door, and the comparison with the experiment is made along the reference lines (fig. 23). The agreement on the lower side of the jet is now much better. The comparison of the secondary velocity vectors for all measurement points in the section shows that the maximum difference between measured and calculated velocities is equal to 10% of the upstream velocity.

The model is applied to the two other sections measured at $X/Deq=7.5$, and 25. The figure 24 shows a good agreement on the vertical velocity component in the symmetry plane in both cases. The table 6 gives the vortex parameters computed for the reference door at the three locations.

Section X/Deq	7.5	15	25
$Yc1/Deq$	1.9	1.9	2.4
$Zc1/Deq$	7.8	8.0	8.8
r_{01}/Deq	1.9	1.9	2.4
$\Gamma_1/2U_0Deq$	0.61	0.39	0.35
$Yc2/Deq$	1.9	2.2	2.1
$Zc2/Deq$	2.8	2.1	0.7
r_{02}/Deq	1.3	1.7	0.7
$\Gamma_2/2U_0Deq$	-0.84	-0.23	-0.11

table 6 : Parameters for the two vortex pair model applied to the reference door P2

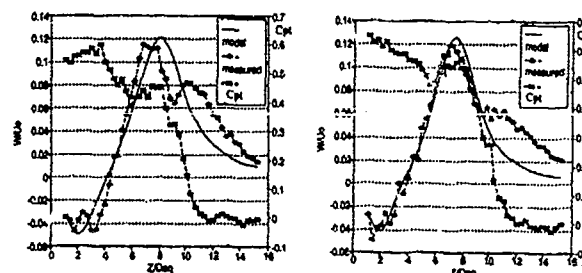
The comparison with the vortex parameter given by Fearn and Weston (Ref. 2), for a jet in a cross flow with an injection ratio of 3, shows that the strengths of the main vortex are smaller for the thrust reverser jet, whereas the spacing between the two main vortices is very similar.



a) $X/Deq=7.5$

b) $X/Deq=25$

fig. 24: Comparison of the measured and predicted velocities along the vertical reference line for the reference door



a) P1

b) P6

fig. 25: Comparison of the measured and predicted velocities along the vertical reference line for the different doors at $X/Deq=15$

Then the model is applied to the other door configurations, and the figure 25 shows that it still provides a good prediction even when the opening angle of the door is changed. The table 7 gives the vortex parameters for the different door configurations.

Conf.	P1	P2	P3	P6
$Yc1/Deq$	2.3	1.9	2.3	2.0
$Zc1/Deq$	8.3	8.0	8.9	7.7
r_{01}/Deq	2.3	1.9	2.3	2.0
$\Gamma_1/2U_0Deq$	0.47	0.39	0.62	0.41
$Yc2/Deq$	2.0	2.2	2.8	1.6
$Zc2/Deq$	2.1	2.1	1.1	2.0
r_{02}/Deq	1.7	1.7	1.3	1.5
$\Gamma_2/2U_0Deq$	-0.23	-0.23	-0.63	-0.14

table 7 : Parameters for the two vortex pair model

The main vortex strength decreases with an increasing opening angle of the door, nevertheless for the configuration P3, where plates are mounted on each side of the door, the variation is opposite and there is a large increase of the vortex strength. For the other parameters, there is no clear tendency of variation with the door configuration.

8 CONCLUSION AND FUTURE WORK

An experimental modelisation of a door type thrust reverser is conducted in a subsonic wind tunnel. The geometry of the model is defined in order to represent both the internal and external flows of a real thrust reverser. Different door configurations are studied for a selected value of the mass flux injection ratio of 3. Visualisations illustrate

qualitatively the jet interaction, and extensive mean velocity and pressure measurements are conducted in sections perpendicular to the upstream flow direction with a five hole probe.

The presence of the door modifies totally the wall stream line topology, as well as the jet wake behaviour. Moreover, a second pair of counter rotating vortices is found between the wall and the well known counter rotating vortices of the jet.

The door opening angle monitors the total pressure losses, and the smaller the angle, the larger the pressure losses. When lateral plates are added on each side of the door, the local pressure loss decreases, but the jet penetration is higher, and finally the losses integrated on a cross section are larger than for the case without side plates.

The drag force produced by the thrust reverser jet is calculated using the momentum conservation equation integrated in a control volume. The larger drag is obtained for the door P4 with an opening angle of 56° and a beccquet deviation of 15° .

A simple vortex modelisation based on two pairs of vortices is used to describe the vorticity field. As for the classical jet in cross flow interaction, the main vortex strength decreases with an increasing distance to the jet exit, and the levels are significantly smaller than for the case without door. The analysis of the different door configurations shows that the main vortex strength decreases with the opening angle of the door, but no clear tendency is found for the other vortex parameters.

Several points arise from this experimental study, that will require an extension of this work.

In terms of optimisation of the door design, smaller opening angles should be tested in order to find the optimal angle.

On the basis of the experimental observation that the penetration height of the reference jet is higher than the value predicted for classical jet in cross flow interaction, the influence of the injection duct design should be investigated separately from the door geometry.

Furthermore, time dependent measurements should be done in order to investigate the possible unstationary behaviour of the jet in this configuration.

Finally, a more fundamental question remains for the transposition of the results to a real case. Actually, the experimental modelisation does not respect the Reynolds number similarity, and therefore the effect of the Reynolds number on the jet interaction should be investigated.

9 ACKNOWLEDGEMENTS

The authors would like to acknowledge Mr F. Lepot, student at the University of Liege (B.), who performed the preliminary experiments, and the technical staff of the Aeronautic/Aerospace Department of the von Karman Institute.

REFERENCES

1. Kamotani, K., Gerber, I., "Experiments on a Turbulent Jet in a Cross Flow", AIAA J., Vol. 10, 1972, pp. 1425-1429.
2. Fearn, R.L., Weston, R.P., "Vorticity Associated with a Jet in a Cross Flow", AIAA J., Vol. 12, 1974, pp. 1666-1671.
3. Karagozian, A.R., "An Analytical Model for the Vorticity Associated with a Transverse Jet", AIAA, J., Vol. 24, No 3, 1986, pp.429-436.

4. Sykes, R.I., Lewellen, W.S., Parker, S.F., "On the Vorticity Dynamics of a Turbulent Jet in a Cross Flow", J. Fluid Mech., Vol. 168, 1986, pp. 393-413.

5. Charbonnier, J.-M., "Analyse et Modelisation de l'Interaction d'un Jet Perpendiculaire de Paroi avec un Ecoulement Principal", These de Doctorat de l'Universite de Poitiers France, 1992.

6. Mac Mahon, H.M., Hester, D.D., Palfery, S., "Vortex Shedding from a Turbulent Jet in a Cross Wind", J. Fluid Mech., Vol. 48, 1971, pp. 73-80.

7. Fric, T.F., Roshko, A., "Structure in the Near Field of the Transverse Jet", in "Seventh Symposium on Turbulent Shear Flows", Stanford University, 1989.

8. Pietrzyk, J.W., Bogard, D.G., Crawford, M.E., "Hydrodynamic Measurements of Jets in Cross Flow for Gas Turbine Cooling Application" in "Trans. ASME", 1988.

9. Andreopoulos, J., "On the Structure of Jets in a Cross Flow", J. Fluid Mech., vol. 157, 1985, pp. 163-197.

10. Margasson, R., J., "The Path of a Jet Directed at Large Angles to a Subsonic Free Stream", NASA TN D-4919, 1968.

VECTORED JETS-INDUCED INTERFERENCE ON AIRCRAFT, PREDICTION & VERIFICATION

Dr. R. K. Nangia

Consulting Engineer
Nangia Aero Research Associates
Maggs House,
78-Queens Road,
Bristol, BS8 1QX, UK

SUMMARY

The prediction of vectored jet-induced effects on V/STOL configurations during transition phase and manoeuvres constitutes an important aspect in the understanding, design, control and operation of such aircraft.

In this paper, a semi-empirical modelling of the jet is used within the framework of subsonic singularity methods. Comparisons with experimental data on a wing-body configuration have been presented. In general, acceptable agreement has been demonstrated. Overall, the emphasis has been on predicting jet interference effects on practical configurations with multi-jet effects; forward and aft nozzles. Configuration effects include tails which operate in a very much stronger jet downwash than the wing.

Optimisation studies can be enabled prior to experimental programmes. This process will allow the design cycle to commence with a good idea of the relative effectiveness of the various controls and the changes needed in the flight control system to cope with partially jet-borne phases of flight. Therefore there is a significant potential for encouraging cost and time savings.

Areas for further work and improvements of the model have been proposed. It is believed that these aspects will have a constructive impact on current and future practical VSTOL and ASTOVL developments.

1. INTRODUCTION

The prediction of vectored jet-induced effects on wing and wing+body+tail (or canard) configurations, Fig.1 (Refs.1-3) during transition phase and manoeuvres constitutes an important aspect in the understanding, design, control and operation of such aircraft. Vectored thrust implies "direct" (resolved thrust force and moments) and "indirect" (induced on aerodynamic surfaces / controls or intakes) effects. The "indirect" effects are often adverse. For satisfactory control of such aircraft ensuring adequate safety margin requires therefore access to a large database with parametric variations not only of the aircraft configuration variables but also of the jet parameters. From the point of view of trim and balance of the thrust-vectoring configurations, the forces arising at the empennage are dictated by stronger jet downwash.

In the past, progress on this subject has been relatively slow because of the evident need to proceed mainly on an experimental basis and the high cost and time factors implicit in wind tunnel tests or full-scale trials. The experiments have ranged from exploring fundamental jet flows (Refs.4-10) to more specialised ones investigating

a particular configuration. Several review papers have been published (e.g. Refs.11-14) The current project scene although more "paced" emphasises cost and time reductions.

The main features of a jet in arbitrary cross-flow and neighbouring surface interference have been appreciated and described by several workers. A jet issuing from a surface deforms under the cross-flow and counter-rotating vortices are formed (Fig.2). The dominant features are, therefore, the entrainment by the jet shear layer and the concentration of vorticity on the downstream side of the jet. In case of neighbouring surfaces, two effects are likely. The first effect is to produce an aerodynamic image of the jet. The second effect exists mainly for the jet in close proximity of the surface or on the surface and causes viscous interactions upstream and downstream of the jet. The high velocities in the initial region of the jet and the associated entrainment effects are not well understood at present. Interpretations are different from various authors.

As yet, the detailed vectored-jet models using field (Navier-Stokes) formulations have not reached sufficient maturity to become tools for routine design and analysis. One recent example by Chiu et al (Ref.15) concerns results from a thin layer Navier-Stokes calculations for a 90° circular jet in cross-flow. The solutions were found to be sensitive to the far-field boundary conditions and the radial grid clustering near the edge of the jet. Some 20,000 iterations were necessary to evolve a solution (although still not fully converged in local detail). The fine clustered grid in the region upstream of the jet exit allowed the horseshoe vortex in the boundary layer near the jet exit to be captured. More importantly for aircraft applications, some of the computed plate pressure distributions compared favourably with the experiment of Fearn and Weston (Refs.5-9) over most of the surface.

A need has been felt therefore for an "effective" (in time, cost and flexibility) semi-empirical jet model to be incorporated within the framework of subsonic singularity methods so that jet-induced forces and moments on a configuration can be predicted with reasonable confidence. Some previous attempts have been noted in Refs.16-20.

This paper deals only with in-flight conditions out of ground effect.

Emphasis in This Paper & Topics Covered

This paper is concerned with a theoretical prediction method for multiple-jet-induced effects on aircraft configurations. The jet model is a synthesis of earlier attempts. Comparisons with experiments conducted on a wing-body configuration at the DRA, have been presented.

© Dr. R. K. Nangia 1993

Presented at an AGARD Meeting on 'Computational and Experimental Assessment of Jets in Cross Flow', April, 1993.

Overall, the emphasis has been on predicting jet interference effects on practical configurations with multi-jet effects (forward and aft nozzles), rather than dwelling on fine detail of the empirical model which has been subjected to progressive development and improvements based on newer evidence, experience from continued applications.

2. SEMI-EMPIRICAL MODEL OF JET

A re-examination of data on the jet plume (Jordinson, Ref.4, Fearn and Weston, Refs.6-9) has lead to a formulation of a semi-empirical jet model depicted in Fig.3. This takes into account the work of Keating (unpublished work at RAE, 1989), Bradbury (Ref.16), Kuchenmann (Ref.17), Smy (Ref.18), Hackett (Ref.19), Wooler (Ref.20), Ashill & Keating (Ref.21) and others (Refs.5, 10, 12). Generally, the experience suggests that the applicability of the model is in geometries where the neighbouring surface is about one jet diameter away from the nozzle. This does not, however, preclude considering cases where this may not be entirely satisfied; because the effects are localised near the nozzle. As experience builds up, limiting of induced velocities can be introduced.

The basic proposition is that the cross-flow momentum is transferred to a streamwise vorticity in a gradual manner releasing the volume of air as an expiration. The strength of the jet is modelled with doublet and source/sink distributions. The vortex path is described empirically.

In Ref.15, it was mentioned that the jet exit conditions may become significant in determining the subsequent roll-up and development of the jet path and the production of forward thrust. This is however, seen as a problem of second-order significance from our viewpoint.

It is known that for a jet issuing from a surface, local viscous interactions are present upstream and downstream of the jet. In the present work, these interactions have not been included. We are seeking a model of jet that will enable consideration and understanding of "practical" flowfields. The jet nozzle is displaced from the wing (or the fuselage) surface and therefore jet near-field effects can be avoided. This does not however imply that we can cater for the local blunt-body flows around the nozzle and body intersections.

A line doublet located along the vortex-line of the jet gives a circular displacement surface with the stagnation lines similar to those found in experimental data (Fearn and Weston, Refs.6-9) as shown in Fig.4. The model therefore implies the imaging effect of the flat plate. However, in relation to the approximations involved in setting up the basic model of jet, the effect of image is relatively small.

For a jet of diameter D and velocity ratio $R = V_j/V$ issuing normally ($\theta_{j0} = 90^\circ$) from the nozzle face at the origin, the jet vortex path (Fig.3) is given by adapting Jordinson (Ref.4) cosh formula with a scaling factor F :

$$(x/D) \cdot F/R^2 = \cosh[(z/D) \cdot F/R^2] - 1.$$

The factor F is taken as 10 for R near 8. Fig.4 shows typical paths according to the formula. Different values of F may be substituted for improving the correlation with experiment at different values of R . The factor F can be also used to describe the jet path.

Fig.5 shows jet vortex paths for different jet velocity ratios R , $\theta_{j0} = 90^\circ$. For the jet issuing at $\theta_{j0} < 90^\circ$, the jet path can be derived with the aid of a virtual jet origin ($\theta_{j0} = 90^\circ$) displaced forward from the real jet origin ($\theta_{j0} < 90^\circ$).

Along the jet geometry defined, the jet semi-empirical representation is based on: doublets for lifting effects and momentum changes, sources to represent the volume displacement of the injected mass flow, and sinks to represent the jet plume.

Forms 1 and 2 of several analytical variations for the doublet strength investigated, are depicted in Fig.6. Experimental results from papers by Fearn and Weston, Thompson are also indicated. The Form 2 agreeing more closely with Fearn and Weston results was considered more plausible and the doublet strength μ_T was generalised in terms of the jet parameters: D and θ_j . Alternatively, numerical forms for doublet strength may also be used.

For introducing the source effects, we need at the nozzle origin a source σ_{v0} which is function of nozzle area and $\cos\theta_{j0}$ plus a line of sinks along the vortex path (distance along jet vortex curve: s) of strength $\sigma_v(\theta_j, s)$ and an allowance for entrainment effects.

To fit the beginning and end of the displacement flux ($\theta_{j0} \leq \theta_j \leq 0$), a plausible (but unproven) expression for the displacement flux, m , (excluding entrainment) is of the form:

$$m \text{ (equivalent at } \theta_j) = A V \frac{R \cos\theta_j}{R \cos\theta_{j0} + \sin\theta_{j0}}.$$

This can be related to the elemental source strength $\sigma_v(\theta_j, s)$ by differentiating along the vortex curve of the jet (variable s).

For an axial jet ($\theta_{j0} = 0^\circ$), the doublets disappear and a source strength at the jet origin σ_{v0} remains. There is an entrainment of air into the jet stream represented by a long string of sinks. An example of these effects in a wind tunnel is given in Ref.21. In free air, there is a lack of suitable information and entrainment effects have therefore not yet been included in the model.

The elemental sources σ_v along the jet vortex path are not easy to integrate in an analytic (economic) manner and a numerical discretisation technique is required to be used when the effects are significant.

For $R = 8$ jet, Fig.7 illustrates the effect of varying jet deflection angle θ_{j0} on the streamwise variations of the jet parameters: height, θ_j , doublet strength μ_T and source strength σ_v . The source term σ_v depends strongly on the variation of θ_j with respect to s . Consequently this term decreases sharply with decreasing jet deflection angle θ_{j0} . The term is appreciable for jet deflection angles θ_{j0} between 75° to 90° but very small for $\theta_{j0} < 75^\circ$. The σ_{v0} term is also small for relatively small jet nozzles and for θ_{j0} near 60° .

With this background experience and considering that the comparable experimental pressure data is for 60° jets, the source effects have not been included in the present analysis. Further work on this aspect has been indicated in future when the model is to be extended generally and to cases where the jet diameter can be considered "large" in relation to the lifting components e.g. tails in immediate vicinity of jets.

Velocities Induced due to Jet

The velocity (cartesian components: u, v, w in x, y, z system) induced at a general point in space due to doublet and source distributions along the jet can be written following the potential flow equations derived in a standard text such as Ref.22.

Early Validation - Pressures Induced on Flat Plate

Fig.8 shows C_p contours induced on a flat plate due to a jet issuing normally ($\theta_{j0} = 90^\circ$). Assuming that the vertical velocity induced by the jet is cancelled by its image in the flat plate, the total C_p follows by doubling up the expression for C_p from the non-dimensional velocity components u and v calculated for one jet as:

$$\text{Total } C_p \text{ (2 Jets)} = 2 C_p \text{ (1 jet)} = 2 (-2u^2 - v^2).$$

The results from present doublet jet model have been compared against Fearn's experimental data (Refs.6-9). It must be mentioned that this comparison is really an extreme case and a rather critical check of the theoretical model since we are estimating the effects due to a jet which is not displaced from the surface and high induced velocities are implied (C_p near -4.0 at the edge of the nozzle). Further, wake effects of the jet on the flat plate surface are also present.

There is, overall a fair to good agreement between the theory and experiment over the region of the flat plate where the jet and surface boundary layer interaction can be considered minimal. The agreement is particularly good for low values of R when the contours are relatively "asymmetric" about the spanwise axis. At higher R , the contours tend towards "symmetry" about the spanwise axis as the jet vertical extent increases. The predictions are once again acceptable for large R and away from the jet and surface boundary layer interaction zones.

These induced C_p comparisons as well as the favourable comparisons on jet stagnation lines have given confidence to pursuing further work and if necessary in future, improved correlations between theory and experiment for given R may be obtained by varying the factor F (and or G). In the current work, we are concerned with "practical" flows where the jet nozzle is displaced from the wing plane by one or two nozzle diameters.

3. INCORPORATION OF THE SEMI-EMPIRICAL JET MODEL INTO LIFTING SURFACE (WING-BODY) APPROACH

Several choices for wing-body model with aerodynamic singularities are possible ranging from simple vortex lattice adaptations to complex higher-order panel methods. In the first instance it is prudent and desirable to keep the modelling aspects simple and concentrate on the jet interference effects for symmetric flow situations.

A circular cross-section body (without boat-tailing) is modelled with source elements, Fig.9 (as in many panel methods). This nominally takes care of the body at zero incidence problem.

Due to close proximity of the jet with respect to the fuselage, potentially large normal and tangential velocities are likely to be induced over the fuselage control points. With the surface sources on the body only, this would require a very large concentration of "strong" panels near the jet. It is therefore appropriate to use a form of internal (fuselage) singularity distribution that

will enable cancellation of the majority of the large normal induced velocities.

An approach, which is possibly more elegant and general, is to introduce a series of 3-D point sources (or sinks) placed inside the fuselage (0.3 to 0.6 times local radius r) at a number of cross-sections in the vicinity of the jet just to image the jet plus fuselage. The number of sources per cross-section equals the number of control points at each cross-section. The number of cross-sections need not be as many as the chordwise stations along the fuselage. It is however, easier to stipulate that for simplicity and continuity, the same number of cross-sections are chosen. The strength of the 3-D sources follows from collocation of normal velocities at the fuselage surface.

An advantage with this procedure is that the flow incidence effects on the body can be included along with the jet effects; the surface panels remain "weak", dealing only with residuals, enabling use of fast efficient algorithms.

The wing was modelled as a thin lifting surface, vortex-lattice with imaging inside the fuselage based on Ref.23 principles. With this technique, the normal velocity body condition is approximately satisfied. The body source panels and internal sources provide the remaining "correction terms".

The adopted procedure offers a very significant step forward towards a practical application. It allows a complete "de-coupling" of the jet effects from the wing-body problem and a modular approach can be set up, although this is only possible because the jet is relatively insensitive to local variations in velocity whereas the wing and body are sensitive to the jet function.

This approach can be easily extended to more realistic modelling of the fuselage. For example, non-circular or elliptic sections can be derived using conformal transformation techniques. The aft parallel body assumption allows the wing image trailing vortices to proceed without intersecting the fuselage. This limitation can be removed, if required, by curving the image trailing vortices. The effect of this will be small in most practical configurations.

Wing thickness effects can be handled as in most panel methods with definition of upper and lower surfaces and this implies an increased paneling.

Extension to asymmetric cases can be visualised; both halves of the configuration will need to be included instead of invoking symmetry half case.

The overall problem is solved by satisfying the boundary condition of zero normal velocity at control points over the fuselage and the wing. An influence coefficient approach is adopted to determine the unknown body source panel strengths and the wing vorticity.

Pressures and loadings are determined after calculating the surface tangential velocities.

We have not included relaxation of trailing wakes in this process at this stage. This is considered a second-order significance problem at present and in principle, it can be handled when required.

4. EXPERIMENTAL MODEL & TYPICAL RESULTS FOR VALIDATION OF THEORY

The validation of the present theory is mainly via the comparisons with a half-model VSTOL configuration tests in the DRA 13 x 9 ft low speed closed section Wind Tunnel (Fig.10).

4.1. Experimental Model

The model was mounted on an underfloor balance, the jet nozzle being connected to "earth" (turntable), so that forces registered were those due to the basic aerodynamics and jet-lift interference, only the forces on the nozzle external structure being ignored. Overall this approach has been considered to be more convenient and less expensive than the other two alternatives, (i) reliance on extensive detailed pressure measurements over the wing which are then needed to be integrated accurately, and (ii) building a model incorporating a "live jet" that is likely to pose problems of accurate balance measurements and calibration of jet thrust.

The fuselage of "oval" cross-section has a slightly drooped nose and is boat-tailed. The characteristic spanwise body dimension (at the wing TE) is $y/s = 0.182$. Wing is mounted in "mid-high" location on the body. The "mildly" cambered and twisted wing is of aspect ratio 3.4, taper ratio 0.325 and has a leading edge sweep of 40° . The wing thickness/chord ratio is 8.5%. Fourteen Pressure measurement on the wing are denoted by A to H, J to N and P. The stations A to M are closely spaced over the inner and middle wing to highlight the essential effects due to the blown nozzle. The nozzle is located at $y/s = 0.2467$. The model however does not have pressure orifices over the fuselage.

The model has been tested through a range of speeds with different nozzles (nominally "large" and "small") and blowing configurations (nozzle position and deflection angle can be preset).

It should be mentioned that the large jet nozzle is less than one diameter away from the fuselage and due to very close proximity, locally high induced velocities may arise. This can cause local separations initially but they can trigger stronger separations over the body and the wing. Pressure measurements over the fuselage would be required to further the understanding of these aspects.

In this paper, results refer to the large nozzle and the qualifier "large" become unnecessary.

4.2. Typical Results, Forward Nozzle, 60° Deflection

Fig.11 depicts the effect of jet blowing ($C_\mu = 0$ and 0.448) on C_p distributions at various spanwise stations on the wing upper and lower surfaces at $\alpha = 0^\circ$. The jet interference on the wing upper and lower surfaces is judged from the differential pressure (ΔC_{pj}) distribution. The local lift (ΔC_{LLj}) distributions have been derived from ΔC_{pj} distributions. To highlight the effect of the jet near-field wing pressures, Fig.12 compares the chordwise pressures at two wing stations A and B lying either side of the nozzle. It is noted that jet interference causes considerable re-distribution of the pressures with the strongest effects appearing near the jet nozzle (wing lower surface). The loss of lift and LE suction is over the whole wing.

4.3. Typical Results, Aft Nozzle, 60° Deflection

Fig.13 shows the effect of jet blowing ($C_\mu = 0$ and

0.448) on C_p distributions at various spanwise stations on the wing upper and lower surfaces at $\alpha = 0^\circ$. The jet interference on the wing upper and lower surfaces is indicated by the differential pressure (ΔC_{pj}) distribution. The local lift (ΔC_{LLj}) distributions have been derived from ΔC_{pj} distributions. Fig.14 compares the chordwise pressures at stations A and B lying either side of the nozzle. As in previous case, the jet interference causes considerable re-distribution of the pressures with the strongest effects appearing near the jet nozzle. The loss in lift extends as far as 70% semi-span. The LE suction increases over the whole LE. Interference lift is positive all along the LE.

Note also from Figs.12 and 14 that the wing pressures at stations A and B for the unblown case are affected strongly by the presence of the nozzle and the associated blunt-body flows. Although the respective shapes are very different, the essential feature is the presence of high suction peaks caused by the blunt-body flows. Pressures on the wing without nozzles *in situ* were not available.

5. PREDICTED RESULTS & COMPARISONS WITH EXPERIMENT

5.1. Theoretical Modelling

The main intention is to derive the jet interference loadings over the wing at this stage and gain an understanding of the strong effects present. Simplifications and panelling in keeping with the theory have been made intentionally (Fig.15). These are:

- An uncambered (flat-plate) wing (semi-span s) is used. This is set at zero incidence on a symmetric circular body at the -45° ("mid-high") location over the fuselage. The xyz axes system is placed with respect to the fuselage nose at (0,0,0). The measurement z_w denotes the vertical distance measured from the wing plane in the jet direction.
- The panelling is 24x8 stations over the fuselage which has $y/s=0.16$. Slight reduction in diameter compensates to some extent for the boat-tailing as well as getting nearer to keeping the minimum distance of the nozzle about one diameter away from the surface.
- The exposed wing panelling is 9 chordwise panels at 10 spanwise stations.

At this stage, the twin-Jet model is regarded as non-interacting, this being approximate will require further experimental information.

Fig.15 shows also the geometry details for the "large" jet nozzle (assuming θ_{jo} set at 60°) in forward (near station 10) or aft (near station 15-16) locations. A slight concern is that jet nozzle is less than one diameter away from the fuselage for both locations (Section 2 and 3).

For convenience, the jet direction notation is kept positive upwards, the wing-body configuration is therefore defined upside down (in the sense that the "cockpit" would be along $-z$ axis).

5.2. Body + Wing, Forward Nozzle at 60° Deflection

Fig.16 shows the vortical velocity induced due to the jet, inner body sources and the resulting chordwise loadings at 10 spanwise stations over the exposed wing.

The contribution due to the fuselage approximately "mirrors" the jet-wing contribution and the magnitude amounts to about a third of the effect due to the jets over the wing.

There is indication of broad "concentration" of interference load over the inner stations, the interference although reducing away from the nozzle is still very significant all along the LE. This confirms the trends measured in experiment (Figs.11-12).

Fig.17 shows the spanwise loading C_{LLC}/C_{av} compared with the experimental loading which has been derived from pressures integration of the data of Fig.11 (Section 4). Gross wing calculations are shown for reference. The theory under-predicts the experiment. In total force terms, as we will see in Fig.20, the agreement is however acceptable. This tends to indicate that a re-distribution of loads had occurred due to presence of fuselage. Partly this is due to the nozzle located very near the LE at wing root which causes a blunt body flow and this may degrade the whole swept-back wing flow. A detailed experiment with pressure measurements on the fuselage would be required to illuminate this aspect.

5.3. Body + Wing, Aft Nozzle at 60° Deflection

Fig.18 shows the vertical velocity induced due to the jet, inner body sources and the resulting chordwise loadings at 10 spanwise stations over the exposed wing. The effects are favourable near the LE of the wing.

As for the previous case, the contribution due to the fuselage approximately "mirrors" the jet-wing contribution and the magnitude amounts to about a third of the effect due to the jets over the wing.

Fig.19 shows the spanwise loading C_{LLC}/C_{av} compared with the experimental loading which has been derived from pressures integration of the data of Fig.13 (Section 4). Gross wing calculations are shown for reference. The theory predicts the experiment acceptably. In total force terms, as we will see in Fig.20, the agreement is also acceptable.

5.4. Comparison of Total Forces

The method has allowed several parametric studies to be undertaken for comparison with experiment. One such study is presented here briefly to indicate the validity and potential. For simplicity, calculations undertaken were for wing only configurations.

Fig.20 shows the effect of varying jet velocity ($R = V_j/V$) on a wing for the two nozzle positions (forward and aft). Lift loss is predicted for both nozzle locations. Comparisons with experiment show very encouraging correlation. The pressure measurement cases discussed in Section 4 are included on this figure ($R=4.585$).

6. SELECTED PREDICTIVE RESULTS

We are now in position to predict some results for cases of practical interest. It must be mentioned that detailed experimental results for validation are not available.

6.1. Forward & Aft Nozzles Operating Together

From a practical viewpoint, we need to know the effects of jet interference due to the forward and

aft nozzles operating together. On practical VSTOL aircraft, design and balance considerations imply substantial differences in thrust levels of the forward and aft nozzles. In the present studies, for simplicity, we have assumed that the forward and aft nozzles operate at the same thrust and that the geometry parameters are the same as previously.

Fig.21 shows the chordwise loadings along the span. As might be expected, there are two peaks corresponding to the forward and aft nozzles.

Fig.22 shows the spanwise loading compared with the cases for the forward and aft nozzles blowing separately. The interference for all nozzles operating is roughly additive of the constituent forward and aft nozzles contributions.

Wing + Body + Tail Configurations

Figs.23 and 24 refer to wing + body + tail configuration. The wing is in "mid-high" location (as in Fig.15) on the fuselage, whilst the tail is in the "mid-low" position. The jet nozzles can be forward or aft. Fig.23 summarises the chordwise interference loadings. Fig.24 shows the jet-interference spanwise loadings on the wing and tail. Note the extremely strong effects felt at the tail location (amounting to 10°-12° "wash" angle). The forward nozzle induces stronger effects on the wing while the aft nozzle causes stronger effects on the tail.

The implications are that in a practical configuration, the tailplane deflections are likely to be very large to balance the interference loads due to vectored jets. Calculations with all jets operating need to be done. These will generally show that to a first approximation, the interference loads arising are additive. This emphasises the need for careful positioning of jets in a given configuration (possibly splaying).

The results given here have demonstrated the ability to provide not only an understanding of the jet-induced effects which are very large on tails but also the ability to offer predictions for realistic configurations.

6.2. Thick Wing

Recently, a series of jet interference studies have been undertaken for a symmetric section thick swept wing of aspect ratio 4.2. The jet direction is downwards for this case and the wing is at $\alpha = 0^\circ$.

Fig.25 shows the effect of forward and aft nozzles, operating separately or together on chordwise pressures induced. Note that the forward nozzles operate at $R = 5$ whilst the aft nozzles operate at $R = 7$. Spanwise variations of normal and axial force and pitching moment due to jet interference are depicted in Fig.26. Note from Fig.25 that jet interference affects mainly the wing lower surface. This also confirms the trends observed in Figs.11 and 12 (Section 4). Fig.26 suggests that for this particular jets configuration, the lift loss is greater due to the aft jets but the pitching moment arising is mainly due to the forward jets.

Fig. 27 illustrates the effect for jet vectoring between 30°, 60° and 90° for an aft nozzle location on the same wing. As shown, the geometry parameters are different from the previous case. Spanwise variations of normal and axial force and pitching moment due to jet interference are depicted. Interference forces and moments increase as jet deflection increases.

Further verifications of the model are planned with controls and flaps. The results for thick wings highlight the ability to undertake very useful parametric studies for practical configurations. Optimisation studies can be carried out prior to experimental programmes. This process therefore has a very significant potential for providing encouraging cost and time savings.

7. FURTHER WORK

The work has provided encouragement for continuation on several aspects. The approach has also highlighted several major gaps in knowledge, indicating therefore the directions of research. Some areas for further work include the following topics.

- **Jet Modelling, Interacting 2, 3 or 4 jets.** The shape of one jet alters due to the presence of another jet nearby either in tandem or side-by-side. Improved knowledge base will lead to a better and more general jet model.
- **Systematic parametric studies of practical configurations with non-planar lifting surfaces at small and large α .** This will allow the design cycle to commence with a good idea of the relative effectiveness of the various controls and the changes needed in the flight control system to cope with partially jet-borne phases of flight.
- **Effect of Wind Tunnel Interference on Jet flows.** For large strength jets not impinging on the tunnel walls, there is a significant effect of the tunnel interference not only in overall terms but also the effect varies along the span of the model. The wind tunnel jet interference needs therefore to be included in the calculations right from the start when making comparisons with experimental data.
- **Jet Effects on Lateral & Directional Characteristics.** Kuhn, Ref.13 has shown schematically that sideslip displaces the jet system laterally. The pressure distribution is shifted towards the downstream side of the configuration generating a jet-induced rolling moment. The rolling moment due to sideslip can be doubled by jet effects. This points towards the possibility of use of differential jet deflections for control. It is open to conjecture that the combination of the inlet-induced directional instability at low speeds plus the large jet-induced rolling moment due to sideslip may have been responsible for the loss of several jet V/STOL aircraft. It is therefore important to determine limiting conditions to optimise control power demands.
- **Control Jet Effectiveness.** The problems created by the jet induced rolling moments can be aggravated by the jet-interference on the effectiveness of the wing-tip roll-control jets. Such control aspects need investigation by extending the current approach.
- **Jet in Proximity of Flaps.** The usual configuration for VSTOL aircraft is a jet in proximity to a strongly deflected TE flaps. The flaps are used to improve STOL performance and in manoeuvre both with jets deflected. Modelling of this aspect is desirable involving the geometry, relaxed wakes and possibility of flow separation.

- **Supersonic Jets.** The investigation of supersonic jets in subsonic cross-flow is a particularly difficult problem in a wind tunnel. The jet being of large velocity ratio is likely to be strongly affected by the wind tunnel constraint.

- **Ground Constraint, High Jet Strengths.** When the jets strike the ground, rolled-up vortex sheets at ground level are required to be introduced. Jet/Ground interactions and Hot Gas Recirculation (HGR) would be too complex for the method used in this paper but some analysis of ground effects on the jet and aircraft aerodynamics may be possible.

Work on these topics should have a constructive and practical impact on current and future programmes for VSTOL aircraft not currently likely with pure CFD methods which are also expensive in time and the costs for experimental studies in depth.

8. CONCLUDING REMARKS

The prediction of vectored jet-induced effects on V/STOL configurations during transition phase and manoeuvres constitutes an important aspect in the understanding, design, control and operation of such aircraft.

Vectored thrust implies "direct" (resolved thrust force and moments) and "indirect" (induced on aerodynamic surfaces / controls or intakes) effects. The "indirect" effects are often adverse. For satisfactory control of such aircraft with sufficient margin for safety requires therefore access to a large database with parametric variations not only of the aircraft geometry but also the jet parameters.

The detailed vectored-jet models using field (Navier-Stokes) formulations have not reached sufficient maturity to become tools for routine design and analysis. This has emphasised the need for "effective" alternative methods (in time, cost and flexibility).

In this paper, a semi-empirical modelling of the jet is used within the framework of subsonic singularity methods, for predicting jet interference effects on practical configurations with non-interacting (at present) multi-jet effects; forward and aft nozzles.

Comparisons with experiment have indicated good agreement with predictions for aft nozzle cases both in forces and pressures. For the forward jet nozzle in close proximity to the wing LE, the predicted forces were in good agreement but the pressures were under-predicted. Therefore, there is a need for improvement in technique and understanding. Further detailed experimentation would also be required.

From the point of view of trim and control of thrust-vectoring configurations, estimates for tail loads can be given. It is important to note that the tail is in a very much stronger jet downwash than the wing.

Jet interference studies undertaken recently for a thick swept wing have demonstrated ability to obtain estimates of forces and moments. Further verifications of the model are planned on practical configurations with controls and flaps.

Optimisation studies can be carried out prior to experimental programmes. This process will allow

the design cycle to commence with a good idea of the relative effectiveness of the various controls and the changes needed in the flight control system to cope with partially jet-borne phases of flight. Therefore there is a significant potential for encouraging cost and time savings.

Areas for further work and improvements of the model have been proposed. It is believed that these aspects will have a constructive impact on current and future practical VSTOL and ASTOVL scene.

ACKNOWLEDGEMENTS

The author has pleasure in acknowledging helpful technical discussions with Mr. J. Hodges, the late (sadly) Mr. R.F.A. Keating, Dr. P.R. Ashill, Dr. B.R. Williams and Mr. P.M. Mordin at DRA. Technical comment by Mr. S.F. Stapelton on the paper is appreciated.

Part of the work was supported by the DRA (formerly the RAE) Aerodynamics & Propulsion Department.

Lastly it should be mentioned that any opinions expressed are the author's own

REFERENCES

1. SEVERAL SPEAKERS, "Towards Harrier III", RAES Conference, See Report by J.M. RAMSDEN, RAES, Aerospace, Feb. 1991.
2. HARRIS, A.E., WILDE, G.L. & SMITH, V.J., MUNDELL, A.R.G. & DAVIDSON, D.P., "ASTOVL Model Engine Simulators for Wind Tunnel Research", Paper 15, AGARD CP-498 (October 1991).
3. LAUGHREY, J.A. & MOORHOUSE, D.J., "Propulsion Integration Results of the STOL Manoeuvre Technology Demonstrator", Paper 30, AGARD CP-498, (October 1991).
4. JORDINSON, R., "Flow in a Jet Directed Normal to the Wind", A.R.C. R & M 3074, 1958.
5. THOMPSON, A.M. "The Flow induced by Jets Exhausting Normally from a Plume Wall into an Airstream", PhD Thesis, Univ. of London, 1971.
6. FEARN, R.L. & WESTON, R.P., "Vorticity Associated with a Jet in a Crossflow", AIAA J. of Air., Vol. 12, No. 12, pp. 1666-71, (Dec. 1974).
7. FEARN, R.L. & WESTON, R.P., "Induced Velocity Field of a Jet in a Crossflow", NASA TP-1087, (1978).
8. FEARN, R.L. & WESTON, R.P., "Velocity Field of a Round Jet in a Crossflow for Various Jet Injection Angles and Velocity Ratio", NASA TP-1506, (1979).
9. FEARN, R.L., "Velocity Field of a Round Jet in a Crossflow for Various Jet Injection Angles and Velocity Ratio", Proceedings of Conference held at University of Stanford in 1983, Published in "Recent Advances in Aerodynamics", Springer Verlaag, 1986.
10. TOY, N. & JAVORY, Z., "An Experimental Study of a Jet in Cross-flow", Surrey University, Guildford, Dec. 1988.
11. KOTANSKY, D.R., "Jet Flowfields", AGARD Report 710, 1984.
12. HANCOCK, G.J., "A Review of the Aerodynamics of a Jet in a Cross Flow", The RAES Aeronautical Journal, Vol. 91, No. 905, pp. 201-13, May 1987.
13. KUHN, R.E., "The Induced Aerodynamics of Jet and Fan Powered V/STOL Aircraft", Proc. of Intern. Symposium, Stanford, Aug. 1983, "Recent Advances in Aerodynamics", Editors: KROTHALLI, A. & SMITH, C.W., Springer-Verlag (1986).
14. MARGASON, R., "Fifty Years of Jet in Cross-flow Research", AGARD FDP 72nd Symposium, Winchester UK, April 1993.
15. CHIU, S., ROTH, K.R., MARGASON, R.J. & TSO, J., "A Numerical Investigation of a Subsonic Jet in a Crossflow", AIAA 93-0870 (1993).
16. BRADBURY, L.J.S., "Some Aspects of Jet Dynamics and their Implications for VTOL Research", AGARD-CP-308, (1981).
17. KUCHEMANN, D. "The Aerodynamic Design of Aircraft", Pergamon, 1980.
18. SMY, J.R. & RANSOM, E.C.P., "Structure of Single Jets at Large Angles to Cross-Flow", BAE Kingston Internal Report, (1976).
19. HACKETT, J.E., "Living with Solid-Walled Wind Tunnels", AIAA-82-0583, 1982.
20. WOOLER, P.T., KAO, H.C., SCHWENDAM, M.F. & ZIEGLER, H., "VSTOL Aircraft Aerodynamic Prediction Methods", AFFDL-TR-72-26, (1972).
21. ASHILL, P.R. & KEATING, R.F.A., "Calculation of Tunnel Wall Interference from Wall-Pressure Measurements", Euromech Colloquium 187, Oct. 1984, DFVLR, Gottingen, (See also RAE TR 85086, (1985)).
22. ANDERSON, J.D., "Fundamentals of Aerodynamics", McGraw Hill, 1984.
23. GIESING, J.P., KALMAN, T.P. & RODDEN, W.P., "Subsonic Steady and Oscillatory Aerodynamics for Multiple Interfering Wings and Bodies", J. of Air., Vol. 9, No. 10, pp. 693-703, October 1972.

LIST OF SYMBOLS

A	= $\frac{1}{4} \pi D^2$, Nozzle cross-section Area
C_{LL}	Local Lift Coefficient
C_p	Pressure Coefficient
C_μ	= $T/(q S)$, Thrust Force Coefficient
D	Jet Nozzle Diameter
F	Scaling Factor, Jet vortex path in free air
L	Lift Force
LE	Leading Edge
q	= $0.5 \rho V^2$, Dynamic Pressure
R	= V_j/V , Jet Velocity Ratio
T	Nozzle Thrust
TE	Trailing Edge
u, v, w	perturbation or induced velocities in x, y, z direction
V	Airstream Velocity
V_j	Nozzle Jet Velocity
x, y, z	Orthogonal Co-ordinates, x chordwise
z_j	Distance along z measured from jet nozzle face
z_w	Distance along z measured from jet nozzle face to wing surface
α	Angle of attack
μ_T	Doublet Strength
μ	= T, Jet Thrust
σ_v	source strength along jet
σ_{v0}	source strength at jet origin
θ_{j0}	Nozzle Jet Deflection angle with respect to free-stream
θ_j	Jet vortex path Deflection angle with respect to free-stream
ρ	Air Density

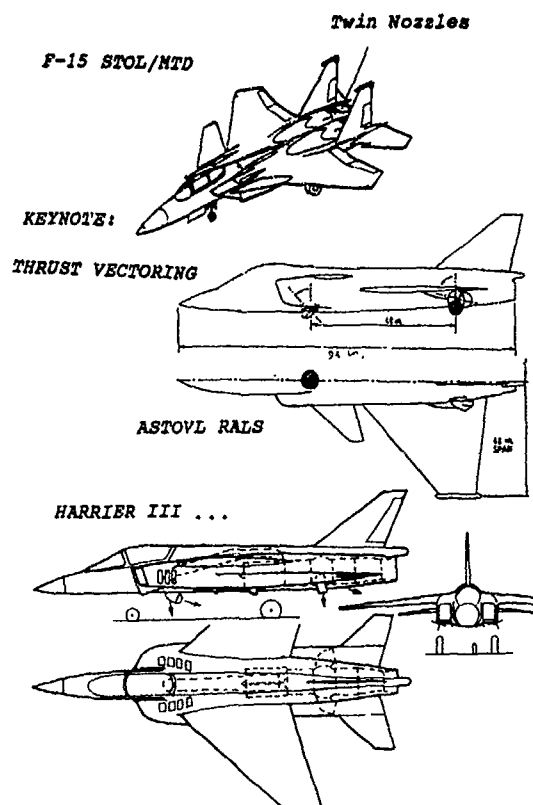


FIG. 1 TYPICAL JET-INTERFERENCE CONFIGURATIONS WITH DIFFERENT LAYOUTS

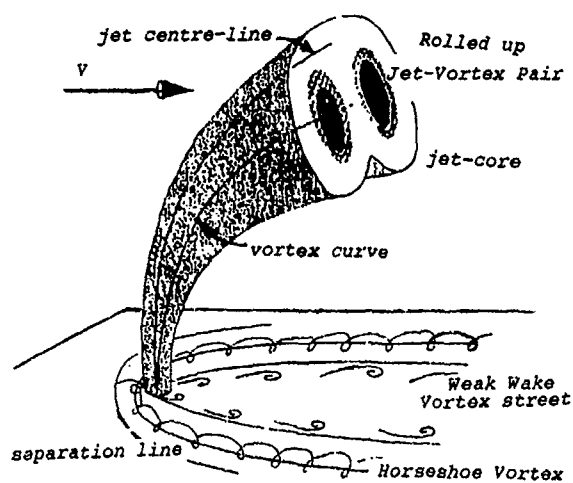


FIG. 2 SKETCH OF JET IN CROSS-FLOW

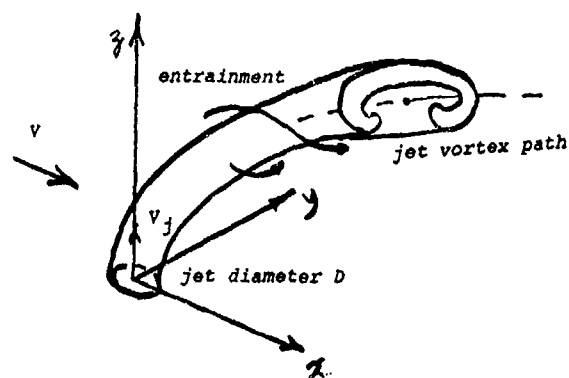


FIG. 3 JET DEFORMING IN CROSS-FLOW, SEMI-EMPIRICAL MODELLING

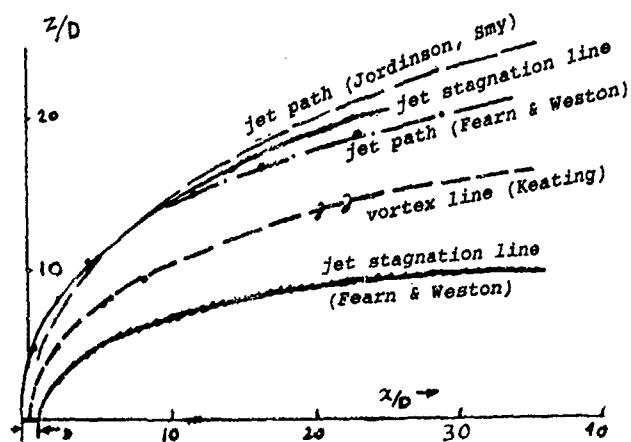


FIG. 4 COMPARISONS OF JET PATHS, $R = 8$, $\theta_{j0} = 90^\circ$ (BASED ON WORK BY KEATING)

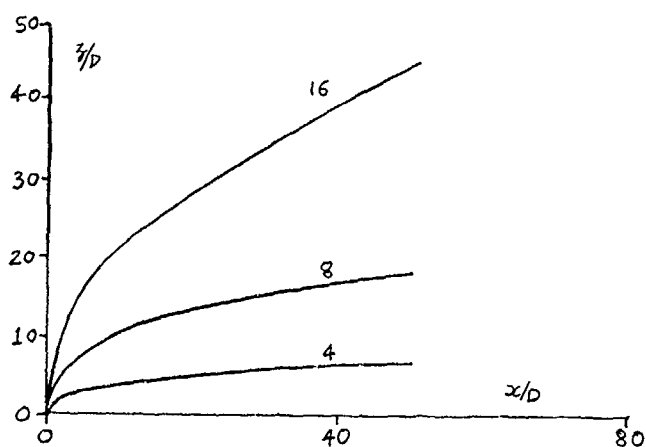


FIG. 5 JET VORTEX PATHS FOR DIFFERENT VALUES OF R , $\theta_{j0} = 90^\circ$

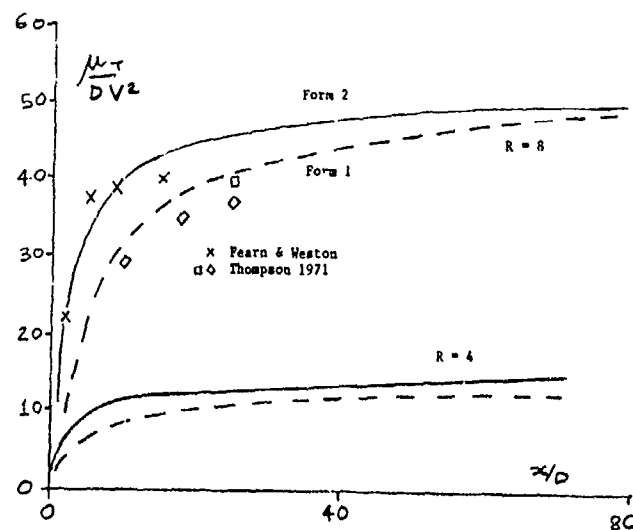


FIG. 6 DOUBLET STRENGTH OF JET $\theta_{j0} = 90^\circ$, $R = 4$ & 8

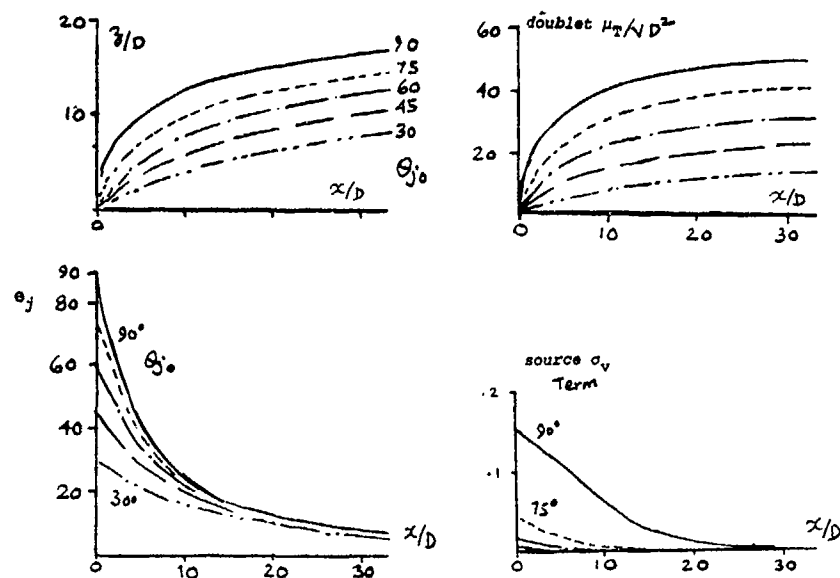


FIG. 7 EFFECT OF θ_{j0} VARIATION ON JET PARAMETERS IN NEAR-FIELD $R = 8$

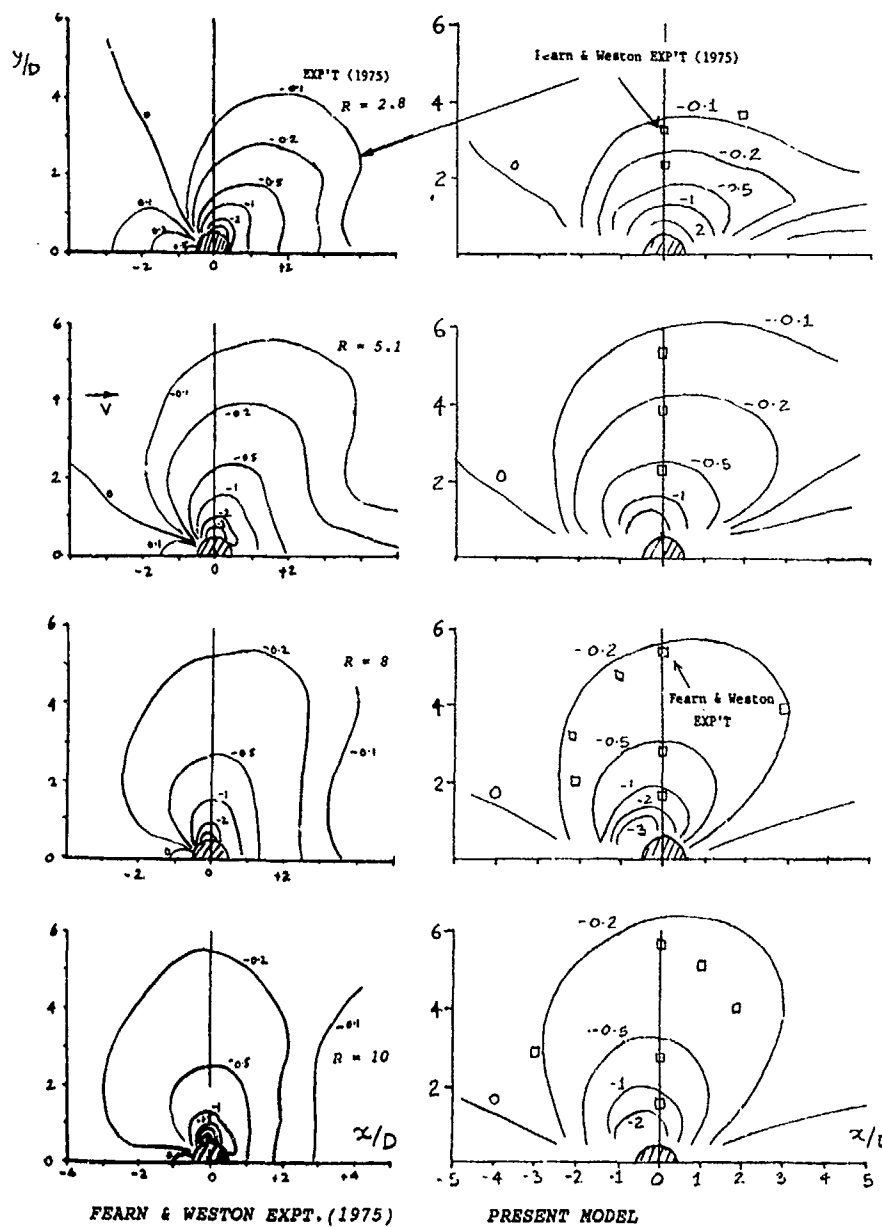
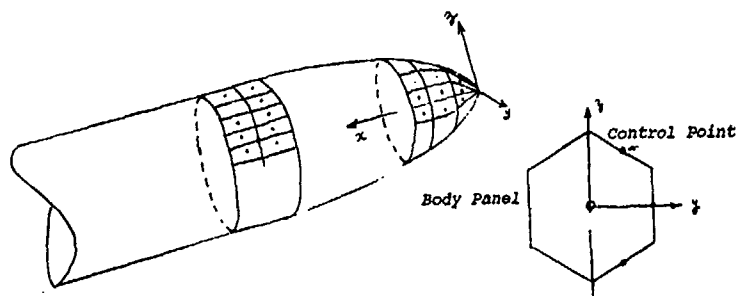
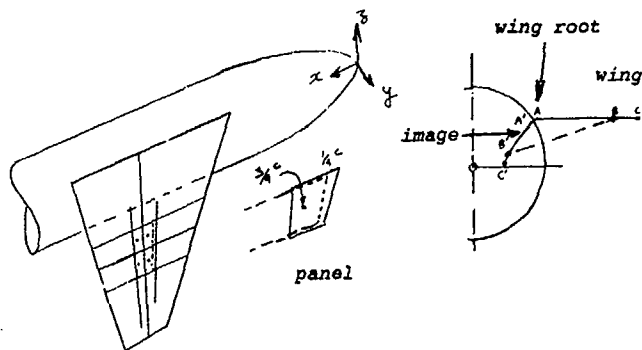
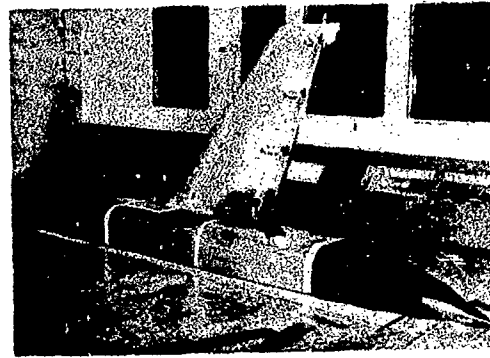


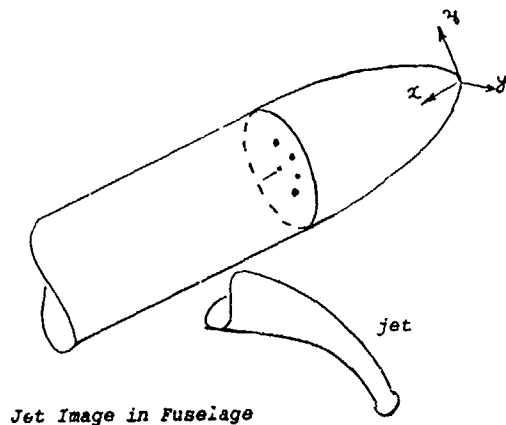
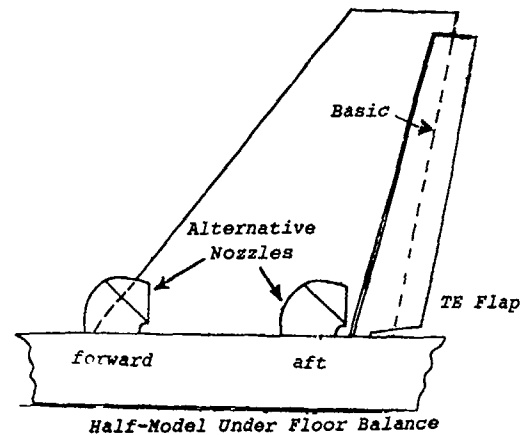
FIG. 8 COMPARISONS OF C_p CONTOURS ON A FLAT PLATE DUE TO JET, R VARIES



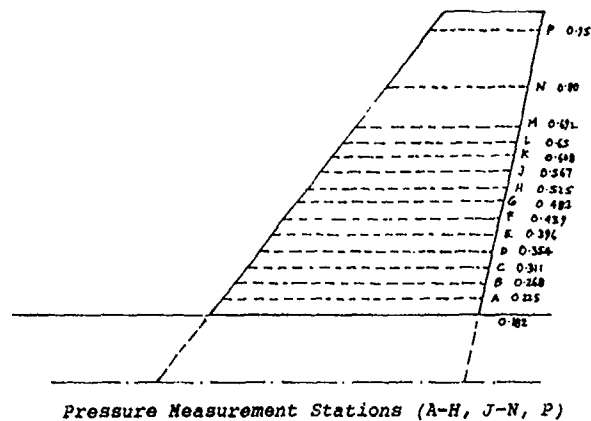
Fuselage Representation



Wing Vortex Lattice & Imaging In Fuselage

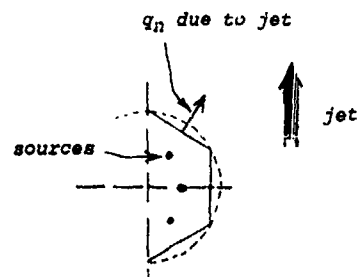


Jet Image in Fuselage



Pressure Measurement Stations (A-H, J-N, P)

FIG. 10 VIEW OF TEST MODEL (WITH TE FLAPS) IN WIND TUNNEL & GENERAL FEATURES



Sources & Sinks Placed Inside Fuselage To Cancel Normal Velocities At The Fuselage Surface

FIG. 9 FEATURES OF THEORETICAL MODELLING

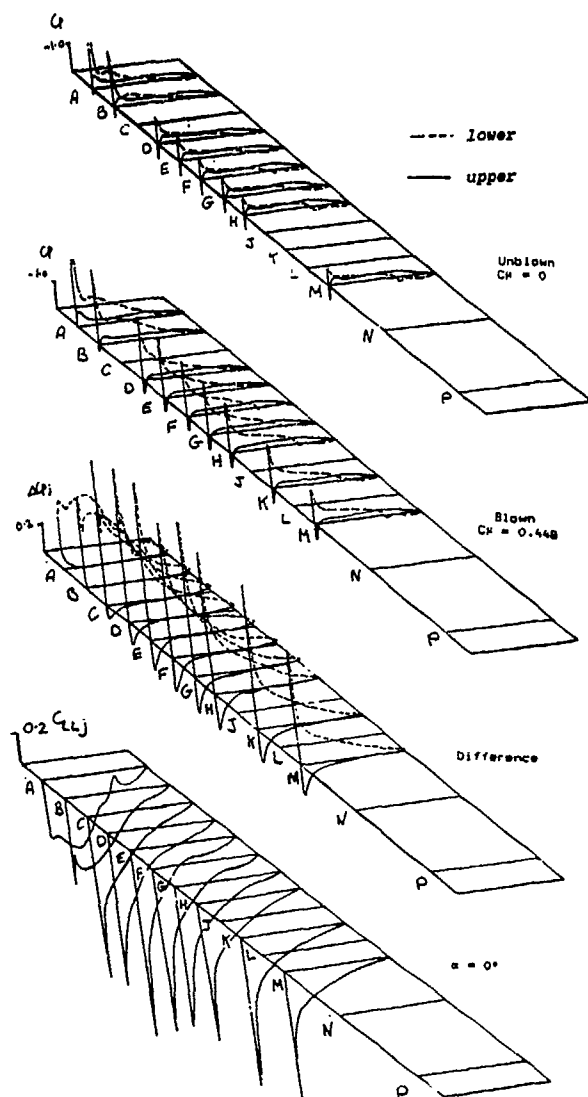


FIG. 11 C_p ($C_\mu = 0$ & 0.448), ΔC_{pj} , C_{LLj} DISTRIBUTIONS, FORWARD NOZZLE, $\alpha = 0^\circ$, $\theta_{j0} = 60^\circ$

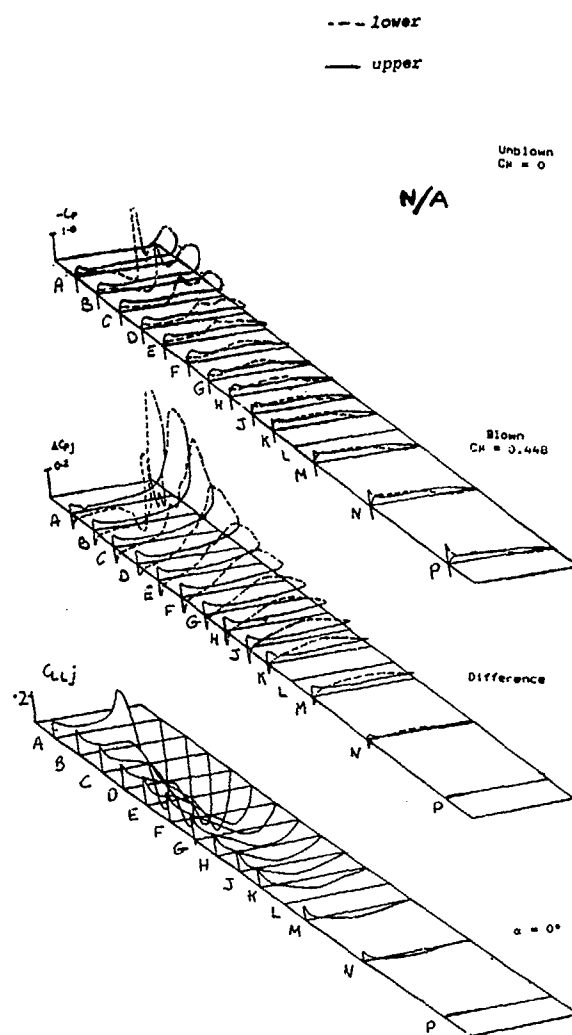


FIG. 13 C_p ($C_\mu = 0$ & 0.448), ΔC_{pj} , C_{LLj} DISTRIBUTIONS, AFT NOZZLE, $\alpha = 0^\circ$

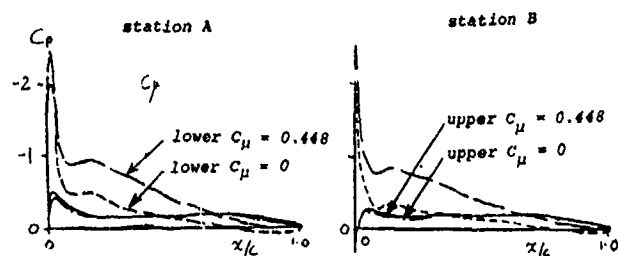


FIG. 12 C_p DISTRIBUTIONS AT STNS A & B, FORWARD NOZZLE, $\alpha = 0^\circ$, $C_\mu = 0$ & 0.448 , $\theta_{j0} = 60^\circ$

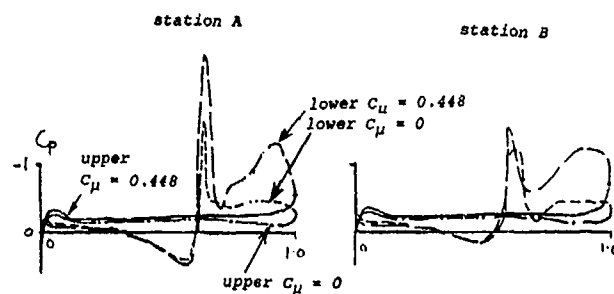


FIG. 14 C_p DISTRIBUTIONS AT STNS A & B, AFT NOZZLE, $\alpha = 0^\circ$, $C_\mu = 0$ & 0.448 , $\theta_{j0} = 60^\circ$

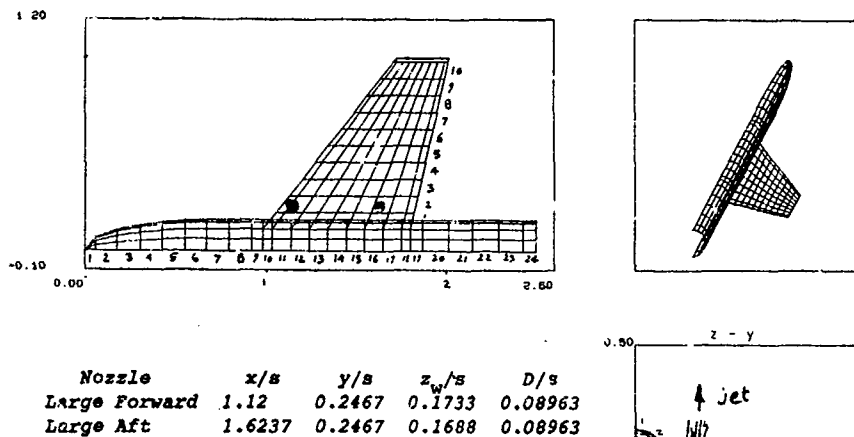


FIG. 15 THEORETICAL MODEL FUSELAGE + WING
& JET NOZZLE DETAILS

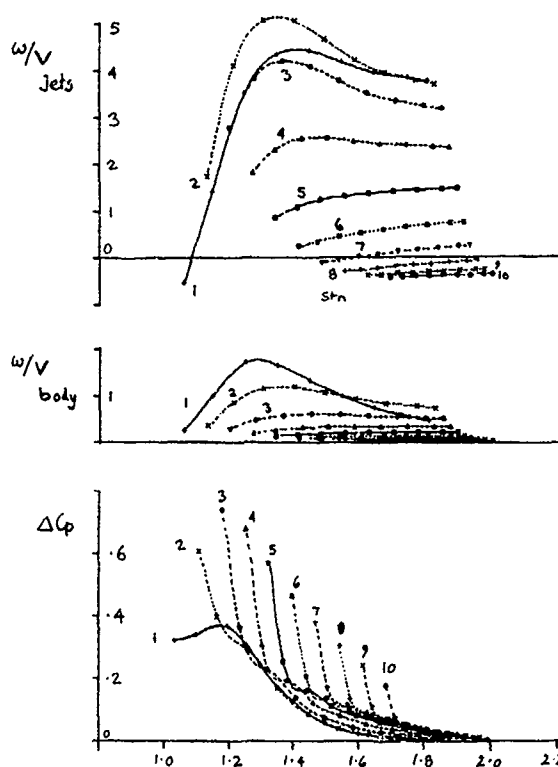


FIG. 16 w/V DUE TO JETS, BODY SOURCES &
CHORDWISE LOADINGS ON WING, FORWARD NOZZLE
 $R = 4.585$, $C_{\mu} = 0.448$, $\theta_{j0} = 60^\circ$

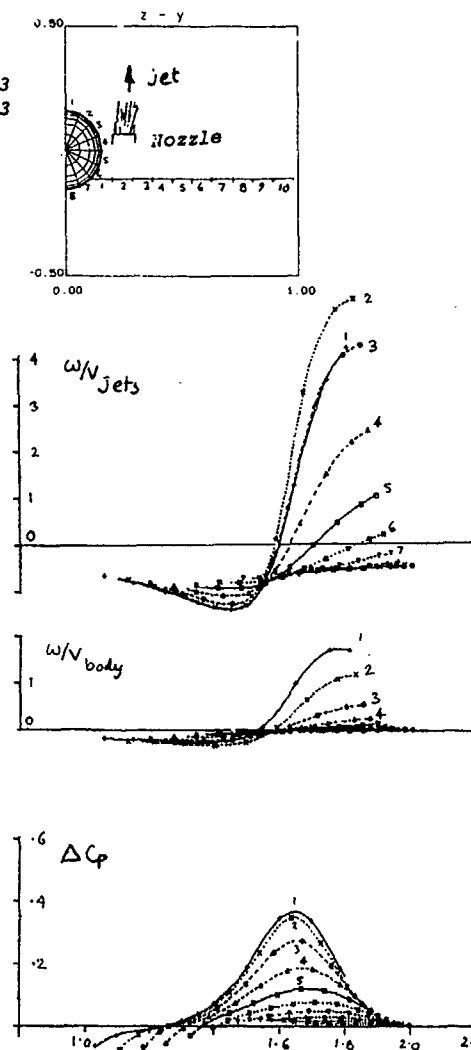


FIG. 18 w/V DUE TO JETS, BODY SOURCES &
CHORDWISE LOADINGS ON WING, AFT NOZZLE
 $R = 4.585$, $C_{\mu} = 0.448$, $\theta_{j0} = 60^\circ$

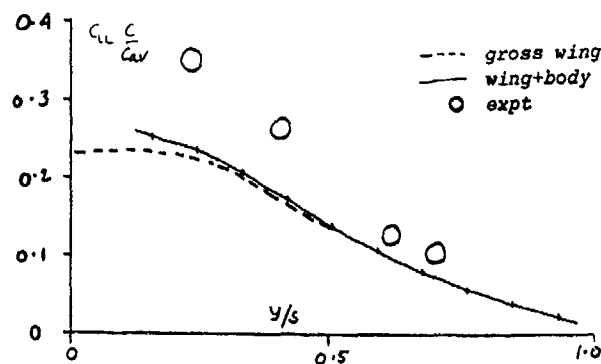


FIG. 17 JET INTERFERENCE $C_{LL} \cdot c/c_{av}$
DISTRIBUTION, FORWARD NOZZLE, THEORY &
EXPERIMENT, $R = 4.585$, $C_{\mu} = 0.448$, $\theta_{j0} = 60^\circ$

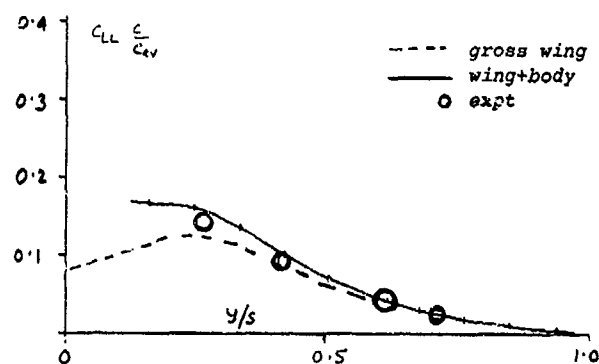


FIG. 19 JET INTERFERENCE $C_{LL} \cdot c/c_{av}$
DISTRIBUTION, AFT NOZZLE, THEORY &
EXPERIMENT, $R = 4.585$, $C_{\mu} = 0.448$, $\theta_{j0} = 60^\circ$

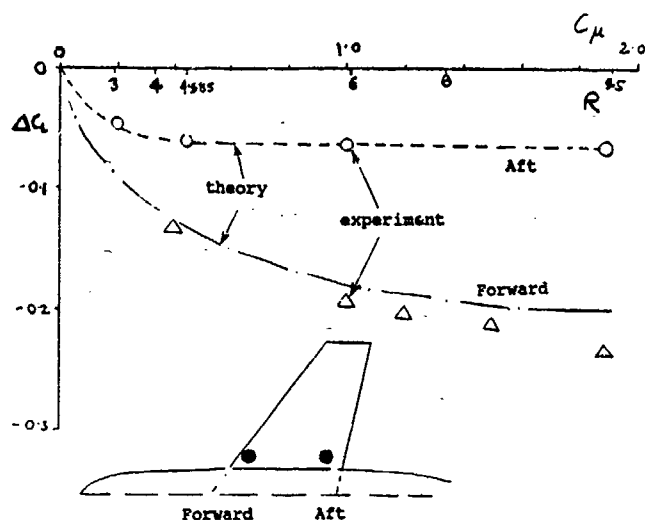


FIG. 20 LIFT LOSS DUE TO FORWARD OR AFT JETS FROM NOZZLES, $\theta_{j0} = 60^\circ$, R & C_μ VARY

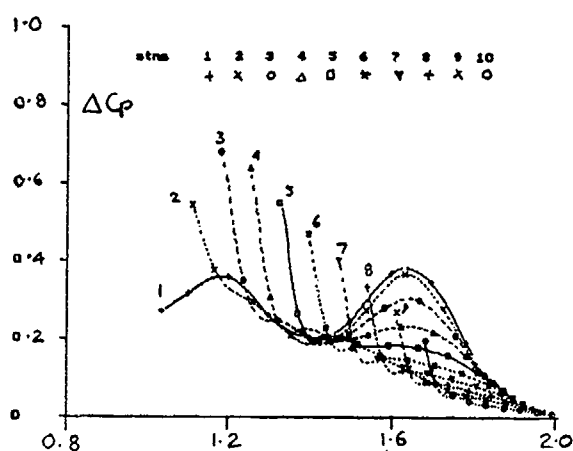


FIG. 21 WING OF (WING + BODY), JET-INDUCED CHORDWISE LOADINGS ALONG SPAN, FORWARD & AFT NOZZLES
 $R = 4.585$, $C_\mu = 0.448$, $\theta_{j0} = 60^\circ$

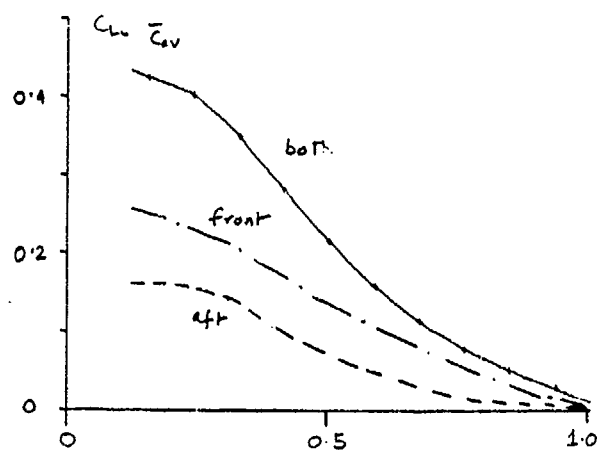


FIG. 22 WING OF (WING + BODY), JET INTERFERENCE $C_{LL} \cdot c/c_{av}$ DISTBN, FORWARD & AFT NOZZLES, $y/s = 0.2467$
 $R = 4.585$, $C_\mu = 0.448$, $\theta_{j0} = 60^\circ$

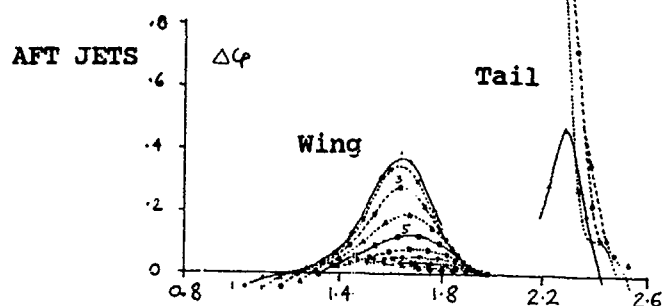
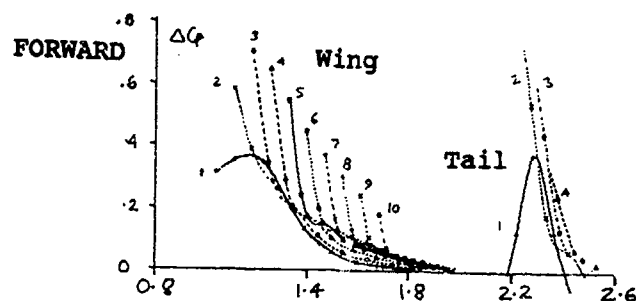
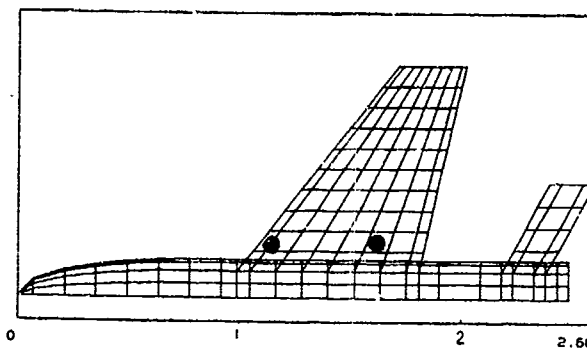


FIG. 23 JET-INDUCED INTERFERENCE ON A WING+BODY+TAIL CONFIGURATION, CHORDWISE LOADINGS

$R = 4.585$, $C_\mu = 0.448$, $\theta_{j0} = 60^\circ$

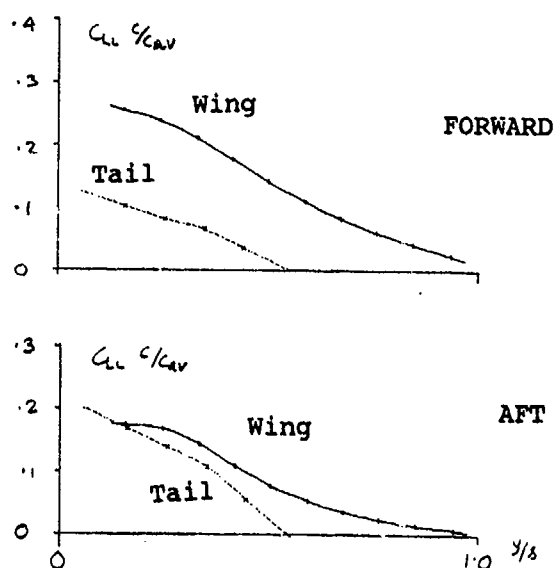


FIG. 24 JET-INDUCED INTERFERENCE ON A WING+BODY+TAIL CONFIGURATION, SPANWISE LOADINGS

$R = 4.585$, $C_\mu = 0.448$, $\theta_{j0} = 60^\circ$

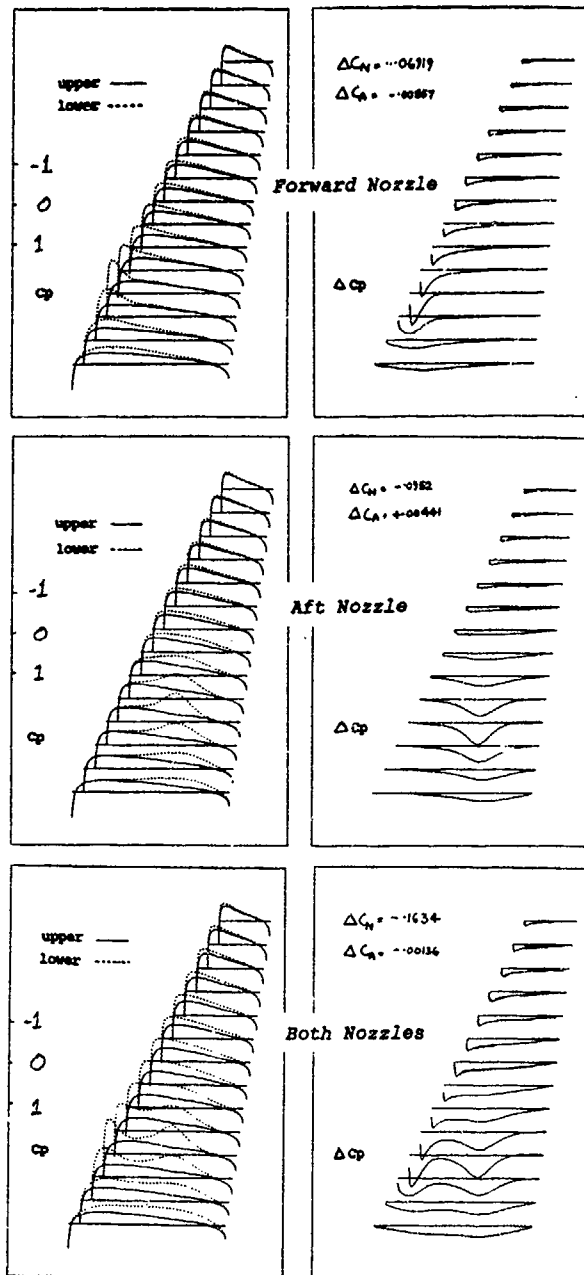


FIG. 25 THICK WING, FORWARD & AFT JETS OPERATING SEPARATELY OR TOGETHER, CHORDWISE PRESSURES INDUCED

Nozzle	x/s	y/s	z/s	D/s	R
Forward	0.16	0.25	0.1	0.065	5
Aft	0.60	0.25	0.1	0.065	7

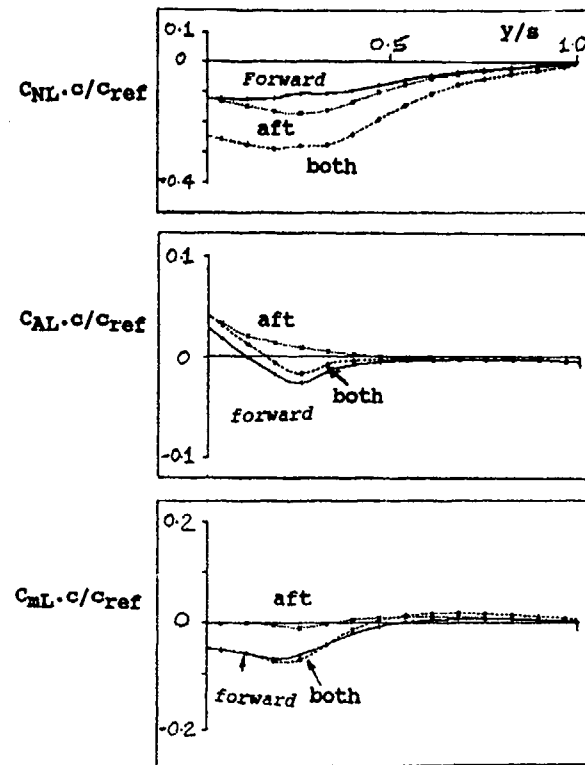
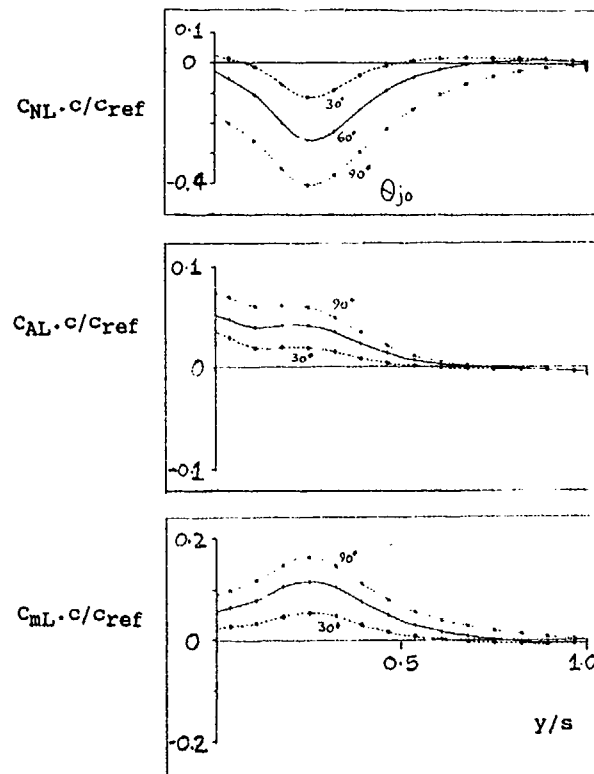


FIG. 26 THICK WING, FORWARD & AFT JETS OPERATING SEPARATELY OR TOGETHER, SPANWISE VARIATIONS OF NORMAL FORCE, AXIAL FORCE & PITCHING MOMENT



Nozzle	x/s	y/s	z/s	D/s	R
Aft	0.65	0.25	0.1	0.1	5

FIG. 27 THICK WING, THE EFFECT OF JET VECTORING ON SPANWISE VARIATIONS OF NORMAL FORCE, AXIAL FORCE & PITCHING MOMENT

Numerical Investigation of Thrust Vectoring by Injection of Secondary Air into Nozzle Flows

T. Berens
Deutsche Aerospace AG
Military Aircraft, LME 213
P. O. Box 80 11 60
D-8000 Muenchen 80
Germany

1. Summary

Injection of secondary air into nozzle flows is an efficient method to control the thrust vector angle of an aircraft. A numerical investigation of thrust vectoring has been carried out for hypersonic aircraft in the transonic flight regime. In this speed range, single duct asymmetrical single expansion ramp nozzles operate far off design due to large nozzle exit areas required for optimal thrust coefficients at hypersonic cruise Mach numbers, thus producing large thrust components in the downward direction.

Injecting secondary air into the nozzle flow in the critical transonic flight Mach number regime can lead to favorable gross thrust vector angles and thus improved thrust efficiency in flight direction.

For a hypersonic aircraft's rectangular convergent-divergent nozzle configuration with a single expansion ramp, 2D Euler calculations of the complete afterbody flow field were carried out in the transonic flight regime, investigating subsonic as well as supersonic injection of the aircraft's forebody boundary layer air into the nozzle flow. Subsonic flow of the injected air along the expansion ramp produces a favorable pressure distribution on the ramp and results in advantageous thrust vectors with small force components normal to the flight direction, and in best thrust efficiency. The interaction between the external flow, the jet plume flow, and the secondary air flow, as well as the behavior of the thrust vector, due to pressure and temperature variations of the injected forebody boundary layer air, are discussed. Also investigated was the impact of the aircraft's angle of attack on the complete nozzle flow field.

List of Symbols

a	speed of sound	[m/s]
Alt	flight altitude	[km]
c_{PGI}	thrust coefficient	[-]

$$c_{PGI,x} = \frac{F_{en,x} + F_{inj,x}}{\left(\frac{F}{\dot{m}}\right)_{en, is} \cdot \dot{m}_{en} + \left(\frac{F}{\dot{m}}\right)_{inj, is} \cdot \dot{m}_{inj}}$$

c_p	pressure coefficient	[-]
-------	----------------------	-----

$$c_p = \frac{p - p_\infty}{\frac{1}{2} \rho_\infty v_\infty^2}$$

\vec{F}	force	[kN]
M	moment	[kNm]
Ma	Mach number	[-]
Ma _∞	flight Mach number	[-]
\dot{m}	mass flow	[kg/s]
NPR	nozzle pressure ratio p_G/p_∞	[-]
p	static pressure	[Pa, kPa]
R	specific gas constant	[J/kg/K]
T	static temperature	[K]
v	velocity	[m/s]
α , AOA	angle of attack	[°]
γ	ratio of specific heats	[-]
ρ	density	[kg/m ³]
σ	gross thrust vector angle	[°]

CFD	Computational Fluid Dynamics
cg	center of gravity
en	relating to engine nozzle
external	relating to external flow along the afterbody
flap	relating to outer contour of lower engine flap
injection, inj	relating to injection of secondary gas
internal	internal performance of engine nozzle and secondary gas injection
is	isentropic
SG	secondary gas
sum	summation
t	total state
x	x-coordinate
z	z-coordinate
∞	ambient condition
7	engine's turbine exit state, secondary gas state in the injection duct prior to injection

2. Introduction

Aircraft which operate in a wide Mach number range up to hypersonic flight velocities are subject to extremely different flight and ambient conditions during take off, along ascent and descent flight trajectories, and while landing. Both the transonic flight Mach number regime and the hypersonic cruise speed range are thrust-minus-drag critical. Integration of the airbreathing propulsion system into the airframe plays a major role for the suc-

cessful development of such aircraft.^{1,2,3} Propulsion integration tasks include the employment of incoming flow precompression by the vehicle's forebody, as well as the installation of asymmetrical variable air inlets and of thrust nozzles capable of handling nozzle pressure ratios (i. e. internal gas stream total pressure to static ambient pressure) ranging from about 2 at low subsonic Mach numbers up to 600 or even higher, depending on air inlet recovery, for a flight velocity of Mach 6. The ratios of maximum to minimum nozzle throat and exit areas both vary from 1 to 6. For hypersonic aircraft with a combined cycle turbo ramjet propulsion system, conventional exhaust systems are incapable of meeting these extreme requirements. Due to limits on flap and seal arrangements,² the capability for wide area variations is infeasible. Matching of the nozzle exit pressure to the ambient state to optimize thrust forces is impossible.

A nozzle configuration with a highly integrated single expansion ramp represents a promising solution to meet these challenging requirements.

Fig. 1 shows the German-proposed Sänger space transportation system^{4,5} with a highly integrated airbreathing propulsion system for the lower stage, as described above. The asymmetrical single expansion ramp nozzle with a large exit area is designed as a part of the aircraft's airframe afterbody in order to minimize underexpansion losses of the engine jet at cruise Mach numbers. This design leads to weight reduction¹ of the expansion part of the exhaust system and to a potential base drag reduction in comparison to a utilization of conventional exhaust systems. A better aircraft performance at hypersonic cruise flight can thus be achieved. Advantages and disadvantages of basic nozzle configurations, including the two-dimensional single expansion ramp concept, are listed in Ref. 1. Key geometric parameters affecting performance and weight of this nozzle type were identified in Ref. 6.

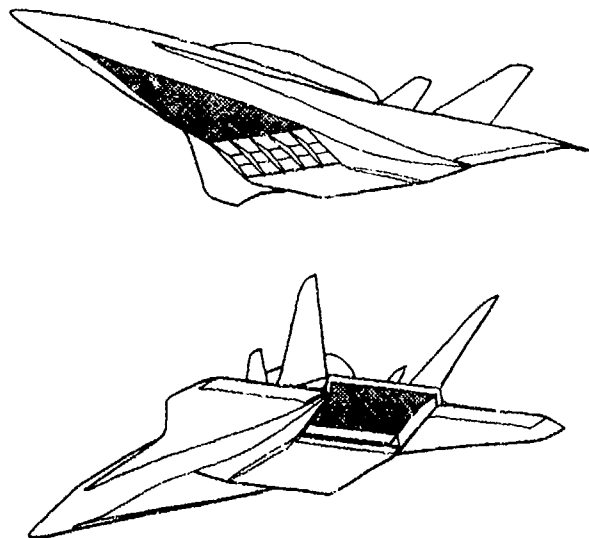


Fig. 1 Integrated airbreathing propulsion system for the lower stage of the German Sänger Space Transportation System

This paper deals with the solution of specific problems in the transonic flight speed range resulting from the employment of single expansion ramp nozzles in hypersonic aircraft.

3. Specific problems with highly integrated nozzles in the transonic flight Mach number regime

In order to achieve optimal thrust coefficients at cruise Mach numbers, hypersonic vehicles require a large nozzle exit area in accordance with high nozzle pressure ratios. During turbo engine operation at transonic flight velocities, however, nozzle expansion ratios are too large, and the nozzle operates far off design. The consequences are thrust losses due to a strong overexpansion of the exhaust gas, unfavorable, downward directed gross thrust vectors, and flow separation in the nozzle/afterbody region, with a negative impact on aircraft trimming and stability.⁷ In this operating mode, large forces in the downward direction are produced, resulting in strong nose-up pitching moments which can no longer be compensated by external aerodynamic means. Fig. 2 shows the range of the gross thrust vector angles for generic nozzles of hypersonic vehicles for proposed Mach number ranges.¹ The gross thrust vector angle is the angle between the gross thrust vector and the horizontal fuselage datum; it is positive for upward gross thrust components.

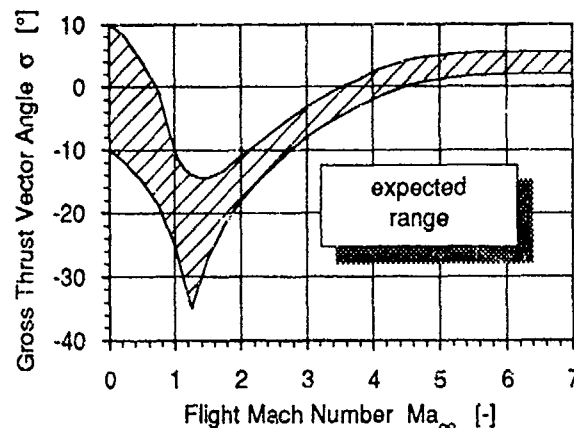


Fig. 2 Expected range of gross thrust vector angles for single expansion ramp nozzles

Using moveable nozzle cowls to adjust the nozzle divergence to the requirements of the pressure ratios in the transonic flight regime results in large incidence angles of these cowls or flaps with large boat tail drag forces. At flight velocities around Mach 1.2, the drag component opposed to flight direction can be as large as 10% of the gross thrust.⁸ In view of the high sensitivity factor between gross thrust and net-thrust-minus-drag, this could be devastating for the feasibility of such aircraft. Nozzle flaps with such high angles of incidence might have to be ruled out. Downward forces induced by a high incident flap have the same magnitude as the cowl's drag⁸ and thus exert a negative impact on the whole aircraft system.

Adjusting the gross thrust vector to the requirements of the transonic flight regime is an important task in the development process of hypersonic aircraft.

4. Injection of secondary gas into nozzle flows in the transonic flight speed range

A method for solving these problems of a hypersonic aircraft's non matched nozzle at transonic flight Mach numbers is the injection of secondary gas into the nozzle flow to fill out the afterbody expansion exit area, which is too large for this operating range. Injection of secondary gas can lead to a favorable pressure distribution along the expansion ramp, resulting in small gross thrust vector angles.^{9,10} Thus, requirements for trimming of the aircraft can be met, and aerodynamic stability can be advanced.

By using as secondary air the vehicle's forebody boundary layer, which due to its turbulent character must be kept away from the engine inlet flow, the diverter drag can be reduced, resulting in better aircraft performance. Also, the use of an ejector nozzle could address the inlet/engine air flow mismatch and high spillage drag at transonic operating conditions.² Taking bleed or bypass air from the inlet as secondary gas could also improve the inlet/engine air flow management at transonic and low supersonic operating conditions.¹¹ To improve the overall performance of injection, the secondary air could be heated up by heat exchangers or even by combustion of fuel before injection, using the oxygen in the secondary air as an oxidizer.

In addition, a secondary gas with relatively low temperature can protect the expansion ramp from the hot exhaust gas of the engine nozzle and can provide cooling for the aft end of the airframe.

This investigation of secondary gas injection into the engine's nozzle flow is addressed to the impact of three major parameters on the afterbody flow field which also have a significant influence on the thrust vector behavior: the total pressure of the secondary gas in the injection duct (or the related duct pressure ratio), the temperature of the secondary gas prior to injection, and the aircraft's angle of attack.

The results of numerical investigations concerning these parameters are discussed after a short description of the CFD tool used and of the boundary conditions employed for the calculations.

5. Description of the Euler Computer Code used for flow analysis

For flow field calculations with the complex interaction of the nozzle plume, the secondary gas injection into the nozzle flow, and the external afterbody flow, the DASA-EUFLEX (Euler code with characteristic FLux Extrapolation) computer code^{12,13} was used, thus solving the inviscid flow equations. Being a cell-centered finite volume scheme, this code stores the data for the flow variables for each cell. The fluxes are evaluated at the cell faces by finding a physical rather than a heuristic solution for the mean values of the flow variables at the finite volume boundaries. This task is carried out by a characteristic eigenvalue decomposition of the flow variables at the cell faces. Employing this asymmetric averaging procedure, new flow variable vectors at the cell faces are created, from which the conventional fluxes are obtained. Since conservative variables are used in the scheme, the

homogeneous solution of the Euler equations contribute to an increase of accuracy with accurate entropy preservation.

A third-order-based interpolation formula is incorporated in order to keep the whole finite volume scheme differentiable. This accounts for high local accuracy at considerably reduced damping. A newly developed differentiable limiter is introduced. It uses the van Albada sensor to detect shocks and other discontinuities where the scheme needs to be switched back to first order whenever a wiggle or a spike is detected in the distribution of the flow variable values during the iteration process. Through input, this limiter can be manipulated to give any arbitrary degree of accuracy.

An optimal, adaptive matrix preconditioning allows higher convergence velocities, reducing the computer's CPU time considerably for the asymptotic steady state approach.

For taking account of real gas effects, the energy equation is augmented with a source term, while the solution scheme can be maintained without any changes. In the source term, the ratio of specific heats γ is included, which is made available either as a spline or as a value taken from a table interpolation for individual calculations. More details about the solution scheme are given in Ref. 12, 13, and 14.

6. CFD model and boundary conditions for the flow field calculations

The afterbody/nozzle flow field was investigated for a hypersonic experimental aircraft,¹⁵ illustrated in Fig. 3 with a coaxial arrangement of turbo and ramjet engines.

The contours of the rectangular convergent-divergent nozzle and the secondary air injection duct are shown in Fig. 4, which also gives the primary measures of the afterbody. In addition, Fig. 4 shows the coordinate system used and the sign convention for forces and thrust vector angles. The thrust vector angle is defined as $\arctan(F_z/F_x)$, thus being the angle between the gross thrust vector F_{sum} and the horizontal fuselage datum. The angle is positive for upward thrust components in the z-direction. The geometry of the two-dimensional afterbody/nozzle configuration is composed of circles and straight lines only. The internal nozzle shape is flat

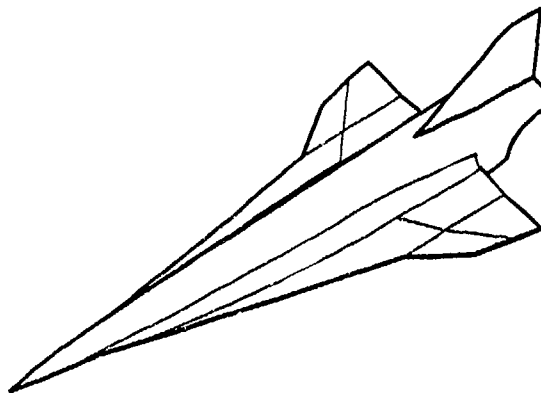


Fig. 3 Hypersonic Technology Experimental Vehicle HYTEX

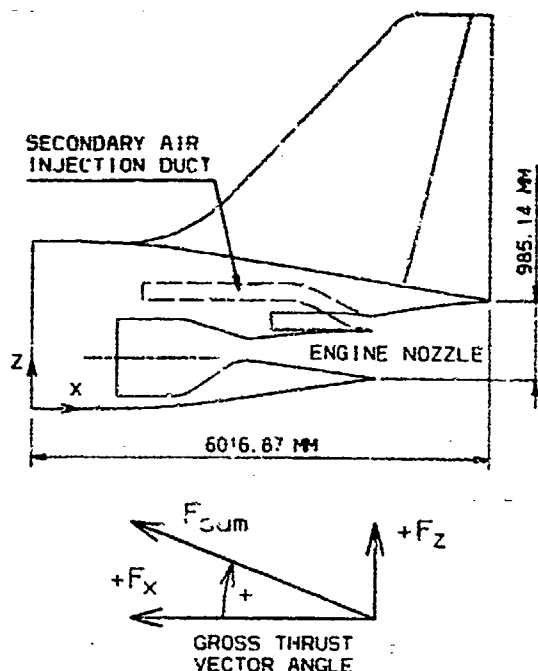


Fig. 4 Afterbody with primary measures and sign convention for forces F and gross thrust vector angles σ

on the lower cowl, and only the upper wall is contoured. For the calculation model, the secondary duct with the solid lines was employed. The shape and course of the duct within the afterbody are dependent on potential integration tasks. An alternative duct shape is illustrated by dashed lines. This shape is of only minor importance for demonstrating effects of the secondary gas injection on the entire nozzle flow field. The contours of the generic nozzle are not optimized for any certain design point. With a contoured ramp on the upper side and a short engine nozzle cowl or flap on the lower side of the afterbody, the nozzle configuration belongs to the internal and external expansion type and is typical for hypersonic aircraft with a strong expansion of the engine's exhaust gas at cruise Mach numbers. The geometry is meant to be variable with respect to area ratios and divergence characteristics, in accordance with flight conditions along the trajectory. Adjustment of the engine nozzle's throat area could be performed by small moveable flaps, which is important in view of weight considerations, especially in the convergent part of the nozzle, where high pressure loads are present. The adjustment of the injection duct's cross section could also be performed by variable flaps. For the presented calculations at $Ma_\infty=1.2$, the geometry of the nozzle, the injection duct, and the expansion ramp remained unchanged.

Numerical values for the thermodynamic states, i. e. the total pressure p_{t7} and total temperature T_{t7} , of the exhaust gas behind the engine's turbine were taken from engine cycle calculations. The presented results of the flow field calculations were obtained taking real gas effects into account. For the exhaust gas and the secondary gas, a γ -distribution as a function of p/p according to Fig. 5 was assumed, derived from a one-dimensional analysis of the jet flow using the computer program of Gordon and McBride.¹⁶

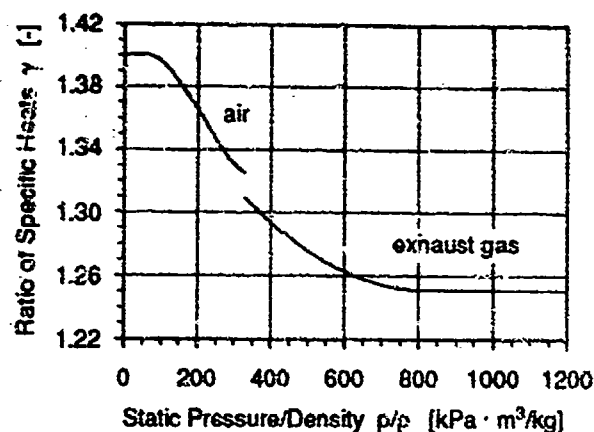


Fig. 5 Ratio of specific heats γ as a function of p/p as incorporated in the computer program

The nozzle flow and the heated secondary forebody boundary layer gas were assumed to be exhaust gas originating from the stoichiometric burning of a mixture of hydrogen and air. Computer program input data for the flight trajectory point at $Ma_\infty=1.2$ and for the thermodynamic parameters of the engine nozzle exhaust gas are listed in Table 1. While the values for these parameters are kept constant throughout all calculations, the thermodynamic states for the injected gas are varied to investigate interactions between the engine nozzle plume flow, the secondary gas injection flow, and the external afterbody flow. These values are given later, together with the description of the numerical results.

The flow region around the afterbody was included in the flow field calculations, because the external flow has a major impact on the nozzle performance, especially at transonic operating conditions. Fig. 6 gives an impression of the grid for the CFD calculations. It consists of 247 lines in the x-direction and 191 lines in the z-direction and covers a computational domain of 22 m by 14 m, corresponding to about 4 times the afterbody length and about 7 times the height of the fuselage. These dimensions were proven to be sufficient for calculations with the EUFLEX computer code in the transonic Mach number regime.¹⁷ The density of the grid lines is higher in the vicinity of the walls and within the engine nozzle, in the secondary gas injection duct, and along the

Ma_∞ [-]	1.2
Alt [km]	9.4
p_∞ [Pa]	28,956
T_∞ [K]	227.0
ρ_∞ [kg/m³]	0.44429
a_∞ [m/s]	302.1
γ_∞ [-]	1.4
R_∞ [J/kg/K]	287.04

p_{t7} [Pa]	259,200
NPR [-]	8.952
T_{t7} [K]	2280
R [J/kg/K]	334.2

fuel: hydrogen
stoichiometric burning
frozen flow

Table 1 Ambient conditions for the flight trajectory point $Ma_\infty = 1.2$ and thermodynamic states at the engine's turbine exit

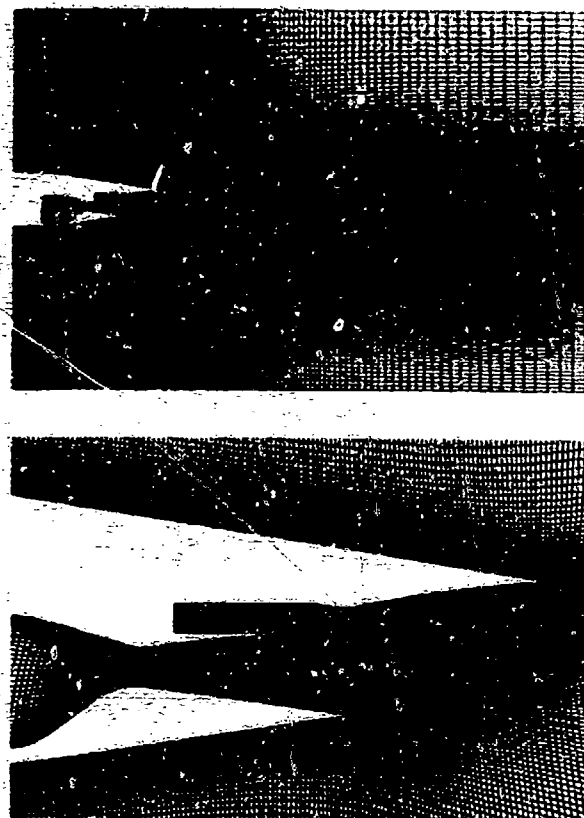


Fig. 6 Grid for afterbody/nozzle flow field calculations with enlarged view of the aft end region

expansion ramp, than in the outer flow field. Fig. 6 also shows the grid in the immediate vicinity of the aft end of the CFD model. All calculations were carried out with the same grid. Since the ambient flow is supersonic, no retroactions of flow phenomena can occur upstream of the afterbody.

7. Results

The results of 2D Euler calculations concerning the injection of secondary gas into the nozzle flow at a flight Mach number of $Ma_\infty=1.2$ are given below.

In an overview, the differences between subsonic and supersonic injection are demonstrated and the consequences for the gross thrust vector evaluated (section 7.1). The influence of the total pressure p_{t7} of the secondary gas on the flow behavior along the expansion ramp and on the complete afterbody flow field, along with the resulting impact on the thrust vector, are given in section 7.2. Test cases with several different total pressures for the secondary gas were studied. In a following step, the effect of heating the secondary gas is described (section 7.3). In section 7.4 the impact of the aircraft's angle of attack on aircraft stability is discussed. The interaction of the secondary gas injection with the external flow field of the afterbody's upper surface is predominant.

Calculations concerning sections 7.1, 7.2, and 7.4 were carried out with a total temperature T_{t7} of the secondary gas of 283 K. The results of sections 7.1 to 7.3 are valid for an angle of attack of 5° , which is in agreement with the nominal value for the ascent trajectory point at

$Ma_\infty=1.2$. All calculations were carried out with the same values of the thermodynamic parameters for the engine's exhaust gas (see Table 1). The results for the nozzle flow were independent of other parameters, namely, the total pressure p_{t7} and total temperature T_{t7} of the secondary gas and the angle of attack, which were varied for each calculation. The numerical values for forces, for the resulting moment with the aircraft's center of gravity as a reference point (coordinates $x_{cg}=-4355.00$ mm and $z_{cg}=1098.64$ mm; compare Fig. 4), and for the mass flow of the nozzle exhaust are given in Table 2. The negative value for M_{cg} denotes a nose-down pitching moment.

F_x [kN]	82.27
F_z [kN]	4.79
M_{cg} [kNm]	-9.40
\dot{m} [kg/s]	50.41
$C_{FGL,x}$ [-]	0.995

Table 2 Results for the engine nozzle for all test cases studied

In addition to the internal performance of the nozzle configuration, the influence of the pressure distribution for the outer surface of the lower engine flap on the thrust parameters is also shown. According to force and moment bookkeeping systems for hypersonic aircraft with highly integrated propulsion systems, airframe aerodynamics should be kept unaffected by engine characteristics. Propulsion effects must be taken separately into account and are to be included in the engine performance data. In this respect, the external cowl of the engine belongs to the propulsion system, since additional forces due to the cowl's angle of incidence associated with nozzle operation modes can occur and can differ from those produced by the nominal geometry.

Many results are given as a function of the total pressure p_{t7} in the secondary duct and not of the pressure ratio p_{t7}/p_∞ , since the general validity of the results for pressure ratios has not been investigated. For the same pressure ratios but different pressures p_{t7} and p_∞ , the impact on the complete flow field might also be different.

Lines for constant flow parameters, i. e. the Mach number and the pressure coefficient c_p , are plotted with an increment of 0.05.

7.1 Subsonic and supersonic injection of secondary gas

A major aspect of these studies is to investigate effects of injection of secondary gas into the nozzle flow on the complete afterbody flow field and of the overall impact on the gross thrust vector. The magnitude of the thrust vector, its angle, and its line of action are dependent on the method of secondary gas injection.

Subsonic injection of the secondary gas occurs if the flow velocity of the gas stays below Mach 1 along the injection duct and throat. If the critical pressure ratio is achieved

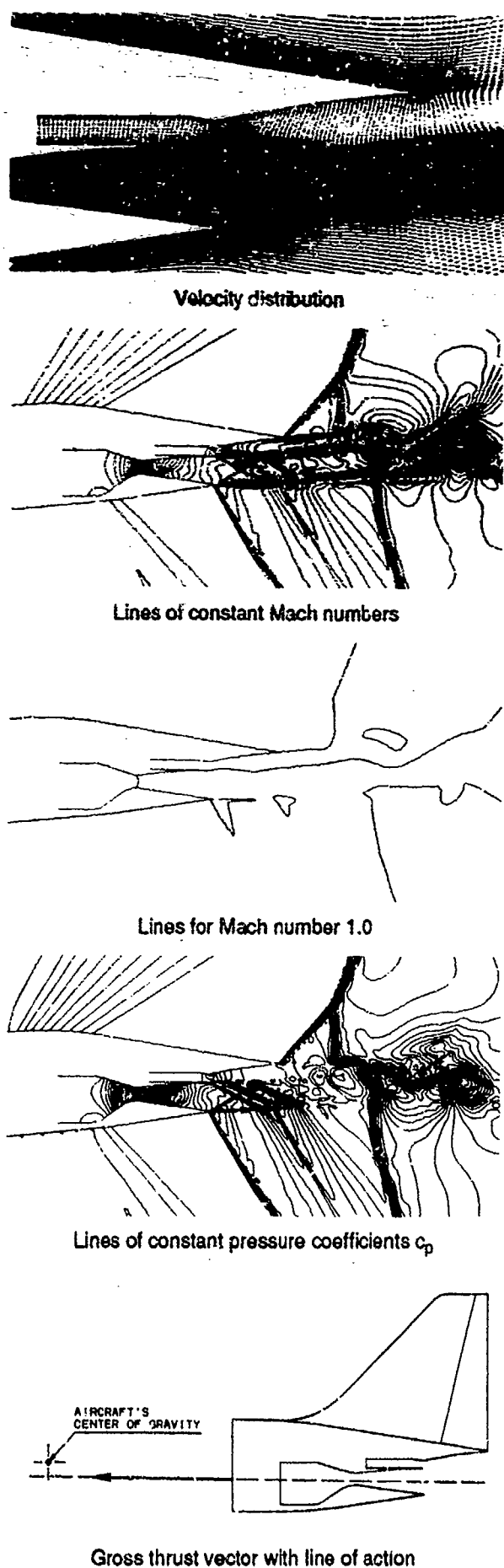
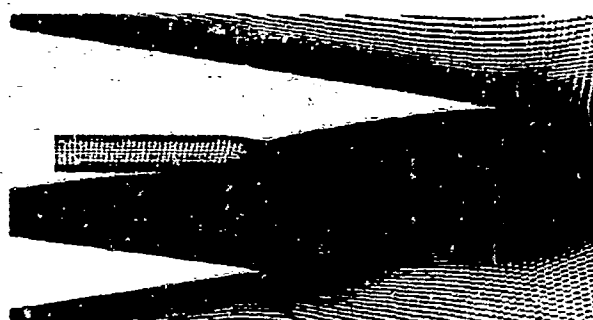


Fig. 7 Results for *subsonic* injection of the secondary gas into the nozzle flow with $p_{17,90} = 27,625$ Pa

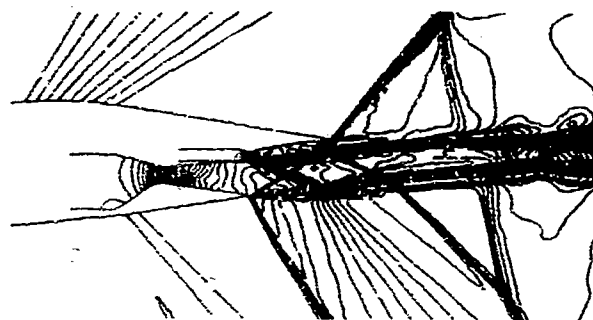
at the injection duct's throat, the flow will become supersonic. In this case one has supersonic injection of the secondary gas, even if a transition to subsonic flow occurs downstream of the throat. Usually, ejector nozzles are designed for supersonic injection, and they produce supersonic flow.

For the calculations carried out, Fig. 7 shows typical results for subsonic injection of the secondary gas into the nozzle flow, corresponding to a total pressure p_0 of 27,625 Pa in the secondary duct. The critical pressure ratio at the injection duct's throat is not achieved. The velocity vectors prove the deceleration of the flow along the expansion ramp. Lines of constant Mach numbers and lines for $Ma=1.0$, as well as lines of constant pressure coefficients c_p are shown for the complete afterbody/nozzle flow field. Basic flow features are evident. Due to the convex geometry of the upper and lower surfaces of the afterbody, expansion waves are present on both sides. The internal flow of the engine nozzle is dictated by its contours. The flow is not symmetrical, due to the internal nozzle shape with a flat lower cowl and a contoured upper wall. Taking the nozzle pressure ratio into account, the nozzle's geometry was designed in such a way that the flow is slightly overexpanded to obtain a jet contraction behind the nozzle's exit. Both the inner and outer plume shocks, as well as the jet shear layer, can be seen in the plots for the Mach number and pressure coefficient distributions. The typical flow structure for overexpanded nozzle flows is present, with alternating shocks and expansion waves reflected by the jet boundaries. For the injected gas jet, shear layers can be seen between this jet and the engine nozzle flow, as well as between the secondary gas jet and the outer flow. The interaction of the secondary gas flow with the external flow of the upper afterbody is revealed by the shock at the end of the upper surface. Further downstream, this shock is deflected by another shock caused by the interaction of the secondary gas jet with the external afterbody flow. The Mach 1.0 lines clearly prove the subsonic behavior of the secondary gas flow. The lines of constant Mach numbers and pressure coefficients impart a complete picture of the flow field.

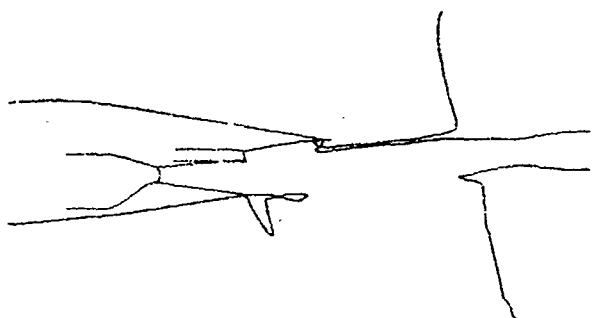
For subsonic injection of secondary gas, the nozzle, the injection duct, and the expansion ramp can be designed in such a way that the cross section of the secondary flow is constant or increases downstream of the injection location, resulting in a constant or increasing pressure distribution along the ramp contour. The flow cross section for the secondary gas can also be influenced by the engine nozzle flow itself. Here the geometry of the nozzle and the nozzle pressure ratio play a major role. As mentioned earlier and as revealed in Fig. 7 by compression shocks and expansion waves, the exhaust gas is slightly overexpanded, leading to a jet contraction behind the nozzle exit. This fact, together with the shape of the single expansion ramp, leads to a broadening of the cross section for the injected secondary gas flow. With subsonic injection, the flow entails a deceleration as well as a pressure increase along the ramp contour downstream of the injection location. The pressure distribution along the ramp produces force components which have a favorable impact on the gross thrust vector and its angle: thrust is increased in flight direction, and small forces normal to the flight direction ensure small thrust vector angles.



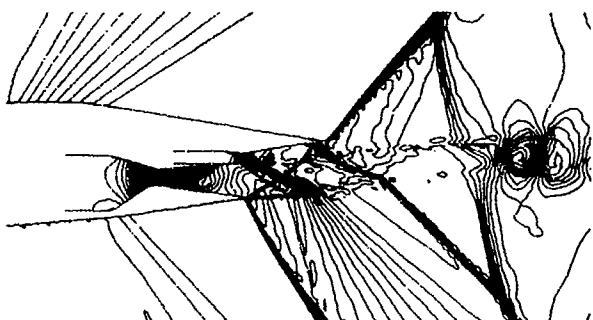
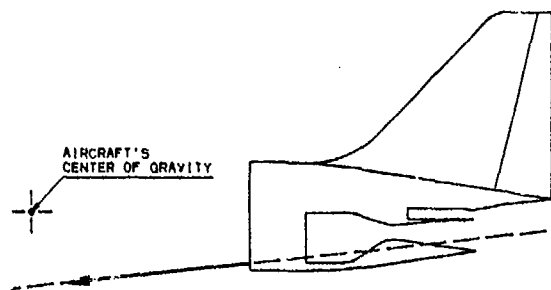
Velocity distribution



Lines of constant Mach numbers



Lines for Mach number 1.0

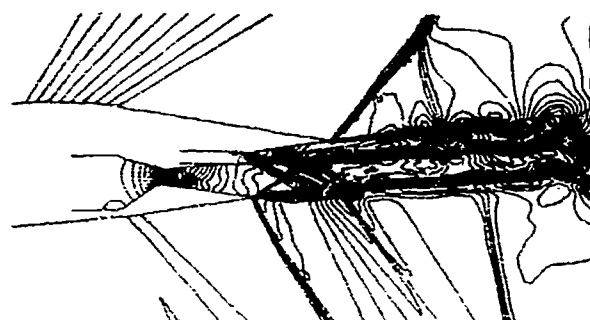
Lines of constant pressure coefficients c_p 

Gross thrust vector with line of action

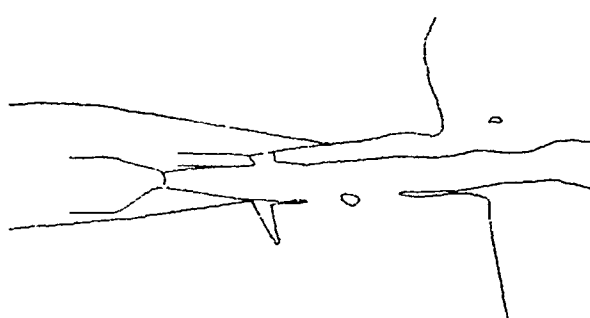
Fig. 8 Results for *supersonic* injection of the secondary gas into the nozzle flow with $p_{17,SG} = 69,250$ Pa



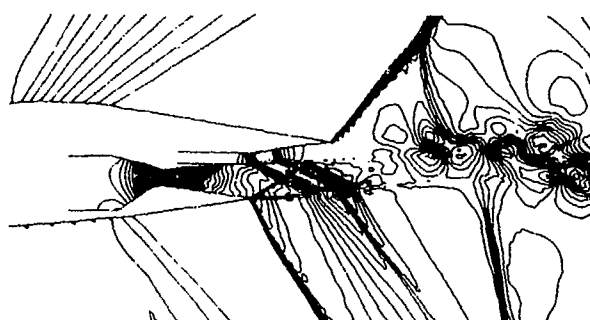
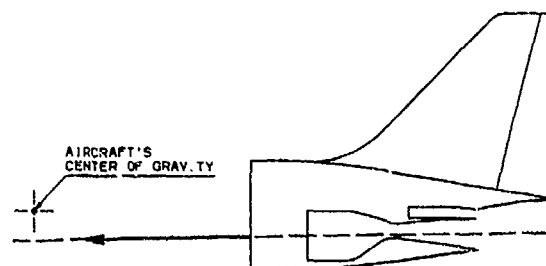
Velocity distribution



Lines of constant Mach numbers



Lines for Mach number 1.0

Lines of constant pressure coefficients c_p 

Gross thrust vector with line of action

Fig. 9 Results for *supersonic* injection of the secondary gas into the nozzle flow and *subsonic* flow along the ramp with $p_{17,SG} = 34,625$ Pa

A very good gross thrust coefficient in flight direction is the result. To avoid separation of the flow, the deceleration of the secondary gas downstream of the injection location must not exceed certain limits. Losses of thrust force due to the slight overexpansion of the exhaust gas are only minor (see Table 2).

In Fig. 8 results for supersonic injection of the secondary gas into the nozzle flow are shown. With the presence of high pressure ($p_{17}=69,250$ Pa) of the secondary air before injection, the critical pressure ratio is achieved at the duct's throat, and supersonic injection takes place. The sonic lines in Fig. 8 show the extent of subsonic and supersonic flow areas. The expansion of the gas downstream of the throat is responsible for low pressures along the single expansion ramp, and the resulting downward forces contribute to a large, negative gross thrust vector angle. At the end of the expansion ramp a shock causes the flow to become subsonic for a small area. If the pressure in the injection duct were somewhat higher, the flow field would be completely supersonic below the expansion ramp.

To prevent a retroaction of aerodynamic disturbances in the afterbody region from travelling upstream through the injection duct and perhaps causing problems at the inlet flow, supersonic flow downstream of the secondary gas injection location may be desirable. In Fig. 9 a flow field is shown in which a supersonic flow region is present downstream of the injection duct's throat (compare lines for Mach number 1.0). In order to obtain a favorable pressure distribution along the ramp and a thrust vector with a small angle, this supersonic region should be small. A shock downstream of the injection location results in subsonic flow along the major part of the ramp. The thrust vector has a larger angle than is the case with pure subsonic flow of the injected gas, and it is negative, but it is still remarkably smaller than the angle for supersonic flow along the expansion ramp. Fig. 9 provides an illustration of the interaction between the engine nozzle plume flow, the secondary gas injection, and the external afterbody flow.

7.2 Pressure variation in the secondary injection duct

The previous section shows that the total pressure p_{17} of the secondary gas has a significant impact on the flow structure of the complete afterbody/nozzle flow field. By varying the pressure in the injection duct, effects on the interaction between the external flow, the engine's jet plume flow, and the secondary air flow were studied. The behavior of the gross thrust vector due to these pressure variations represents a major aspect of this research.

By varying the total pressure p_{17} of the injected secondary gas from 24,625 Pa up to 69,250 Pa, the injected flow exhibiting subsonic behavior at low pressures of 24,625 Pa and 27,625 Pa (Fig. 7) becomes supersonic ($p_{17}=30,625$ Pa), while areas of supersonic flow increase along the expansion ramp at total pressures of 33,625 Pa, 34,625 Pa (Fig. 9), and 69,250 Pa (Fig. 8). The lines for Mach number 1.0 in Fig. 7 to 9 clearly illustrate this effect; the phenomena of the flow field correspond with the examples in these figures and are described in section 7.1. The pressure distributions along the upper contour of the injection duct and along the ramp for the

pressure variations of the secondary gas are shown in Fig. 11 and correspond to the plots of the flow parameters in Fig. 7 to 9. In order to more easily assign the pressure distribution to the model wall, Fig. 10 gives the geometry of the calculation model in the same scale as the x-axis in Fig. 11.

The impact of the secondary gas injection on the thrust forces is given in Fig. 12 to 15.

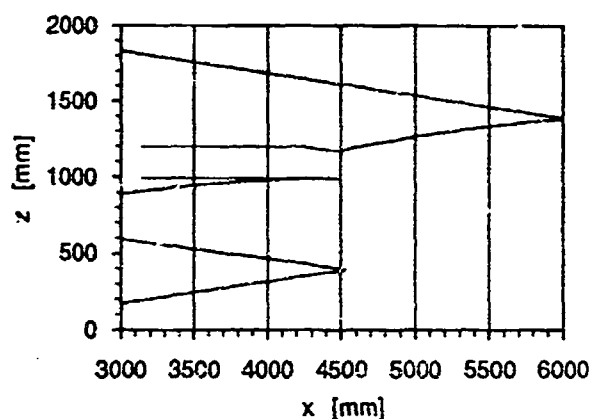


Fig. 10 Contours of the aft end of the afterbody/nozzle calculation model

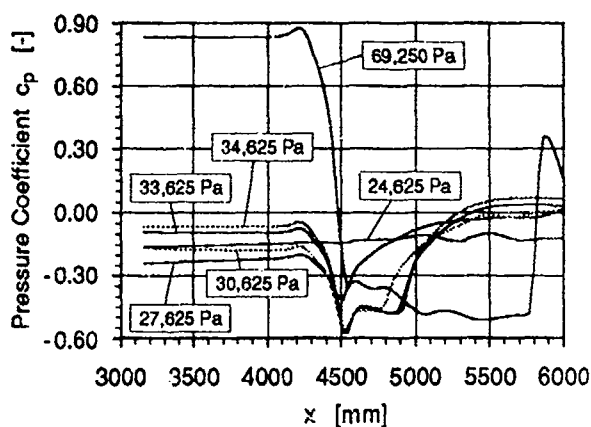


Fig. 11 Pressure distribution for the upper contour of the injection duct and for the ramp with $p_{17,SQ}$ as parameter

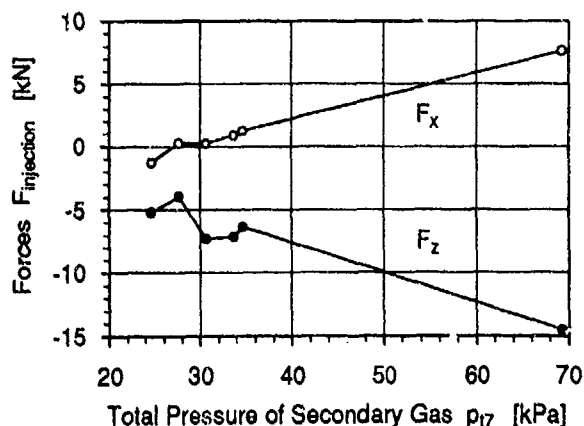


Fig. 12 Forces in x- and z-direction due to injection of secondary gas

While forces in the x-direction, due to injection of secondary gas, increase with increasing total pressure p_{17} of the secondary gas (Fig. 12), forces in the z-direction decrease according to the expansion at the ramp when supersonic flow is present.

As Fig. 13 proves, the magnitudes of the gross thrust vectors become larger with increasing pressure, but as a

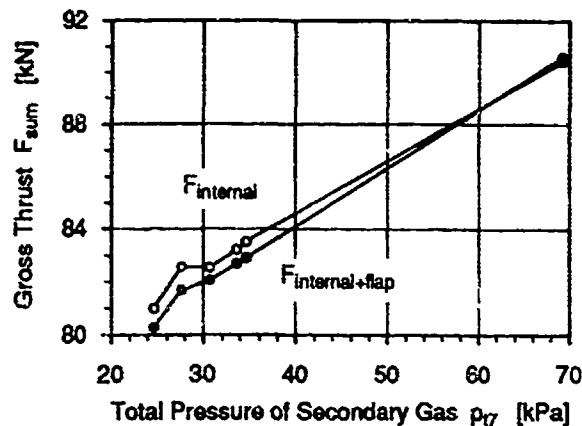


Fig. 13 Gross thrust produced by the complete nozzle configuration

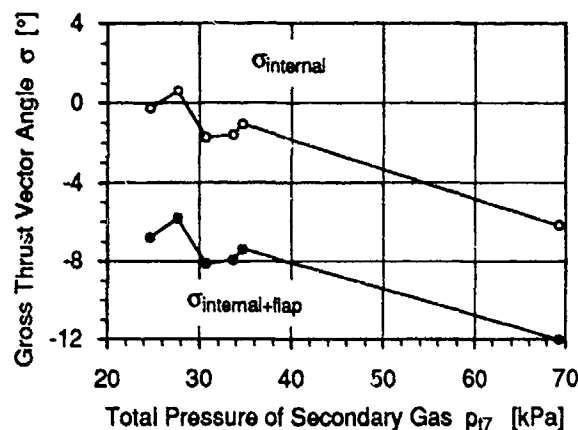


Fig. 14 Gross thrust vector angle produced by the complete nozzle configuration

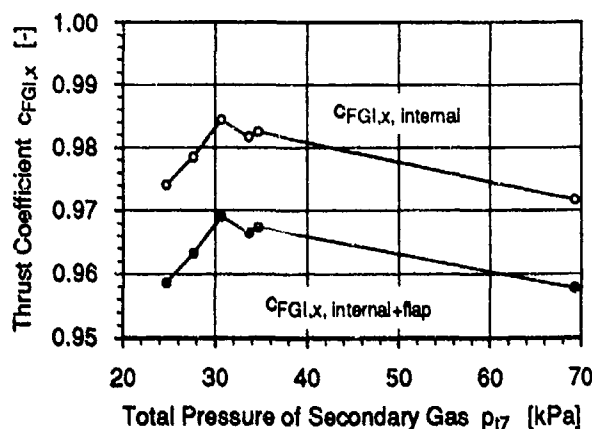


Fig. 15 Gross thrust coefficient in the x-direction

result of negative forces in the z-direction, the vector angle becomes larger, too, turning the gross thrust vector in the negative direction (Fig. 14). Which of these two effects dominates, can be evaluated by looking at the thrust coefficient for the x-direction in Fig. 15. The thrust coefficient as defined in the list of symbols considers the calculated forces in the x-direction due to both the engine nozzle flow and the secondary gas injection flow, as well as the ideal thrust obtained by complete expansion to the ambient pressure of the exhaust gas and of the injected gas. In this way the thrust coefficient becomes a comparable measure of efficiency relative to other nozzle concepts. For pressures of the secondary gas below the ambient pressure, the gas was expanded to the lower pressure at the end of the upper surface of the afterbody to calculate the ideal thrust and the thrust coefficient. In this respect, the thrust coefficient for these calculations reaches its maximum for a total pressure of the secondary gas of 30,625 Pa. At this pressure, supersonic injection of the secondary gas and subsonic flow along the ramp occurs. This fact and the shape of the curve in Fig. 15 indicate that the downward turning of the gross thrust vector due to negative z-forces produced by low pressures at the ramp with increasing total pressure of the secondary gas has a negative influence on the overall nozzle performance. Subsonic flow of the secondary gas along the ramp is responsible for an advantageous pressure distribution, resulting in favorable thrust vector angles and in high thrust efficiency.

In addition to the results for the internal performance of the nozzle and the secondary gas injection, the influence of the pressure distribution on the outer contour of the lower engine flap is included in Fig. 13 to 15.

To complete the description of the flow field calculations, the mass flow of the secondary gas is given in Fig. 16. A total pressure p_{17} of 34,625 Pa results in a mass flow of 13.76 kg/s, which is a reasonably realistic value, according to Ref. 18. For comparison, the mass flow for the engine nozzle runs to 50.41 kg/s (Table 2). How the mass flow rate of the secondary gas or the appropriate pressure in the secondary gas duct can be realized was not the subject of this investigation. The pressure could possibly be regulated by pressure control devices built into the injection duct.

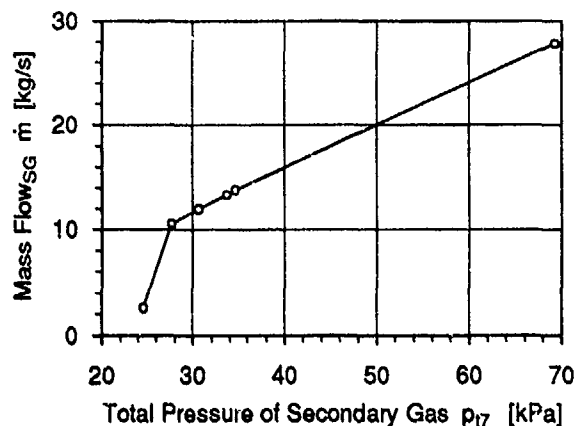


Fig. 16 Mass flow of the secondary gas

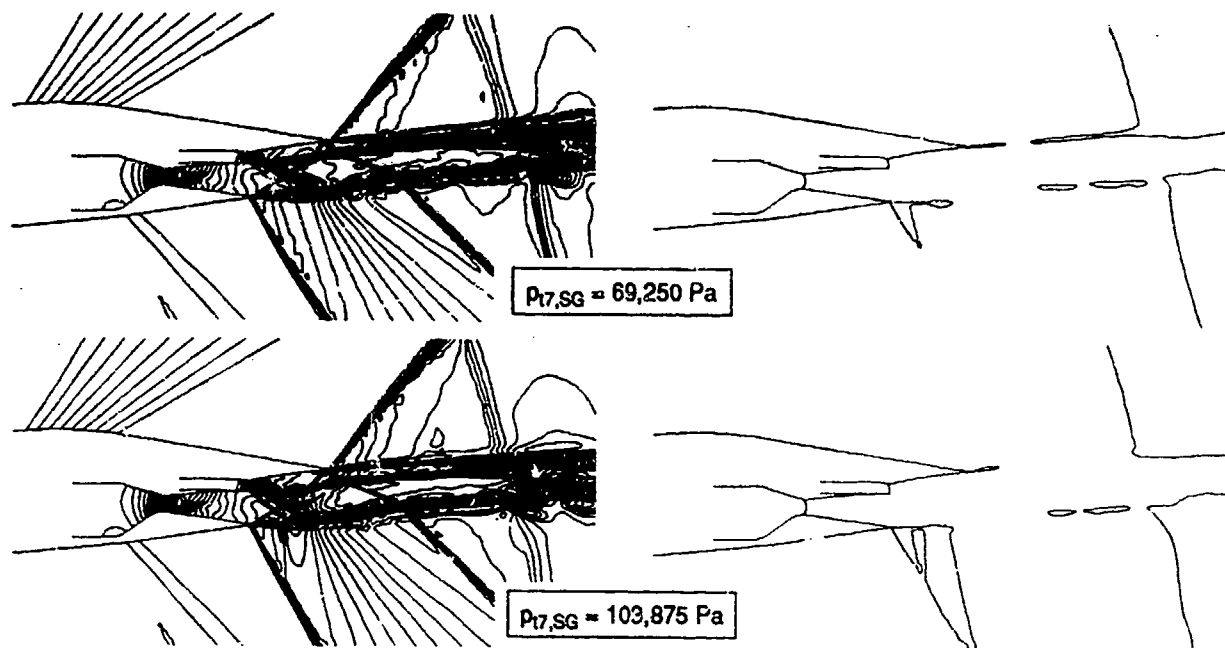


Fig. 17 Lines of constant Mach numbers and lines for Mach number 1.0 for different total pressures $p_{t7,SG}$ of the secondary gas with a total temperature of 1000 K

7.3 Heating of the secondary gas

To investigate the impact of heating the secondary gas before injection into the nozzle flow, flow field calculations were carried out for different total pressures p_{t7} of the secondary gas having a total temperature T_{t7} of 1000 K. For heated secondary gas, a specific gas constant of $R=300$ J/kg/K was assumed.

Fig. 17 shows the flow field with lines of constant Mach numbers for 69,250 Pa and 103,875 Pa. For a description of the flow phenomena, see section 7.1.

Fig. 18 illustrates the pressure distribution along the upper contour of the secondary gas injection duct and the expansion ramp for the four investigated total pressures p_{t7} of the secondary gas. The assignment of the pressure to the geometry of the injection duct and the ramp is facilitated by Fig. 10. A negative gradient for pressures above 69,250 Pa can be seen across the secondary injection duct's throat and further downstream, corresponding with supersonic flow along the expansion ramp, as is also evident in the lines for Mach number 1.0 (Fig. 17). Together with Fig. 17, Fig. 8 and 9 enable a comparison with cold secondary gas (283 K) for total pressures of 69,250 Pa and 34,625 Pa, respectively.

The differences between the flow fields for cold and heated secondary gas are minimal. This can also be verified by observing the forces produced by the injection (Fig. 19), the magnitude of the gross thrust vector (Fig. 20), the vector's angle (Fig. 21), and the thrust coefficient in x-direction (Fig. 22). The reason for this similarity is that two effects compensate each other: higher temperatures on the one hand result in less mass flow on the other hand for a total pressure equal to that of cold flow (Fig. 23). This circumstance leads to similar interactions between the injection of the secondary gas, the nozzle plume flow, and the external afterbody flow field for cold and hot secondary gas at the same pressure level,

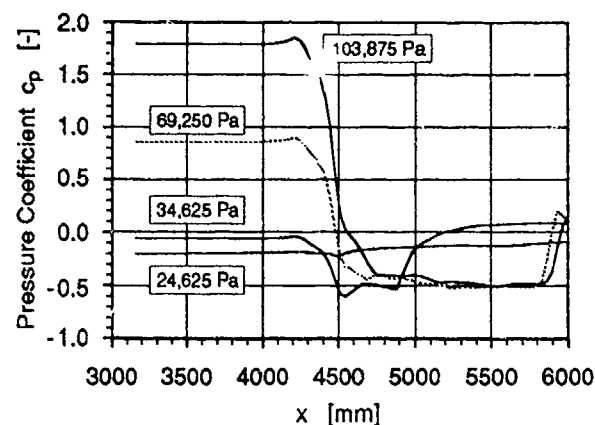


Fig. 18 Pressure distribution along the upper contour of the injection duct and the expansion ramp for different total pressures $p_{t7,SG}$ of the secondary gas with a total temperature of 1000 K

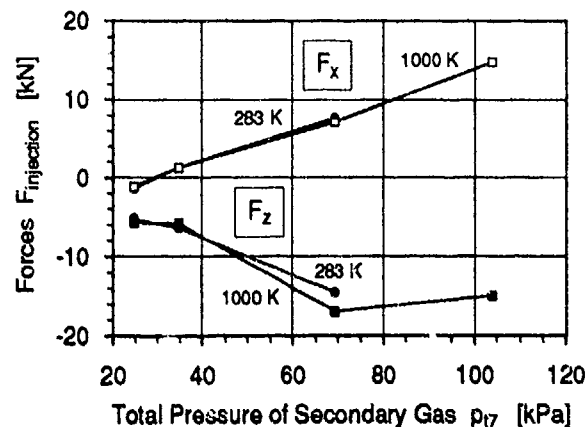


Fig. 19 Forces in x- and z-direction due to injection of secondary gas for $T_{t7,SG} = 283$ K and $T_{t7,SG} = 1000$ K

producing the same results for the thrust vector behavior.

The case with 103,875 Pa for hot gas and the case with 69,250 Pa for cold air, both with large mass flows, refer not so much to the injection of forebody boundary layer air as to parallel design and operation of turbojet and

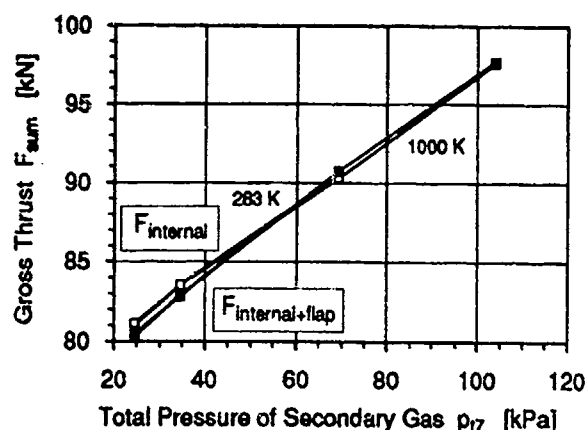


Fig. 20 Gross thrust produced by the complete nozzle configuration for $T_{17,SG} = 283 \text{ K}$ and $T_{17,SG} = 1000 \text{ K}$

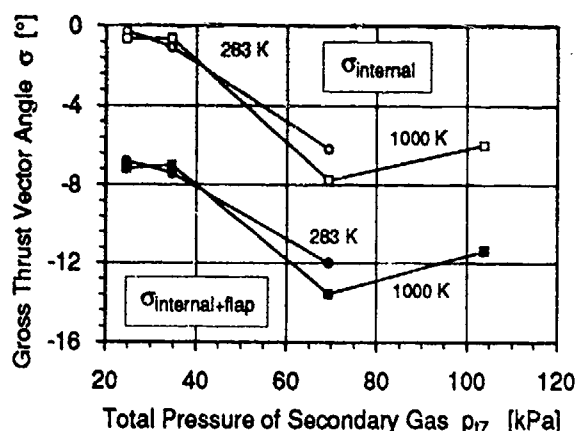


Fig. 21 Gross thrust vector angle produced by the complete nozzle configuration for $T_{17,SG} = 283 \text{ K}$ and $T_{17,SG} = 1000 \text{ K}$

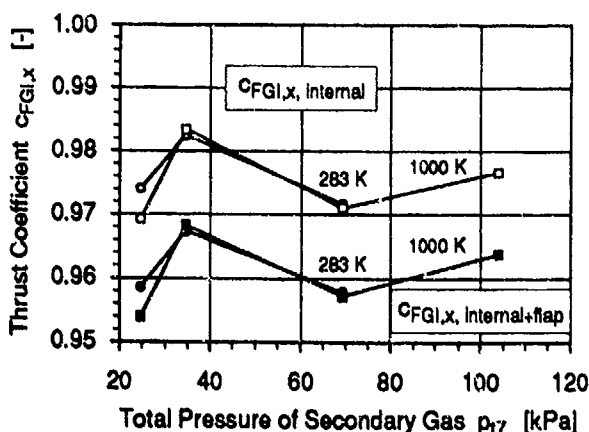


Fig. 22 Gross thrust coefficient in the x-direction for the complete nozzle configuration for $T_{17,SG} = 283 \text{ K}$ and $T_{17,SG} = 1000 \text{ K}$

ramjet engines.¹⁹ They were included in the investigation to demonstrate the effects of very high pressure in the secondary duct.

In Fig. 24 the pitching moments for the nozzle configuration's internal performance are given. The reference point for the moments is the aircraft's center of gravity; nose-up moments are defined as positive. Since the same values for the thermodynamic parameters of the engine's exhaust gas were used for all test cases studied, the moment produced by the engine nozzle remains constant.

Minor differences for the thrust parameters and especially the thrust coefficient (Fig. 22) can be detected at a low total pressure p_{17} for the secondary gas of 24,625 Pa. The differing pressure distributions along the upper contour of the secondary duct and along the ramp, shown in Fig. 25 for 24,625 Pa, are responsible for these discrepancies. The geometry of the ramp is shown in Fig. 10 with the same length scale as in Fig. 25 to facilitate comparison with the pressure distribution. With this geometry of the injection duct, the mass flows for the cold and hot gas are almost identical (Fig. 23). For a total pressure of 69,250 Pa for the secondary gas, thrust values also differ slightly (Fig. 19 and 21) as a result of pure supersonic flow along the expansion ramp when the gas is heated up (Fig. 17). Injection of cold secondary gas leads to a

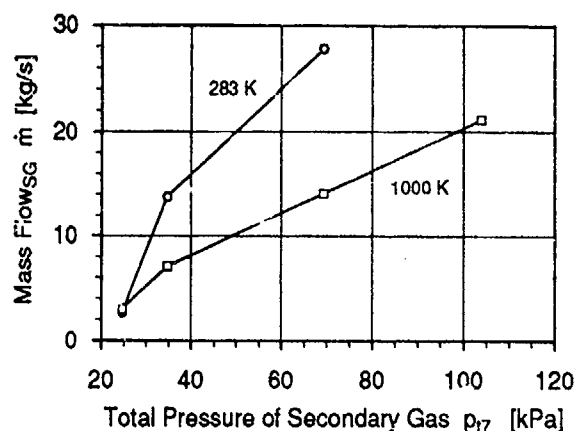


Fig. 23 Mass flow of the secondary gas for $T_{17,SG} = 283 \text{ K}$ and $T_{17,SG} = 1000 \text{ K}$

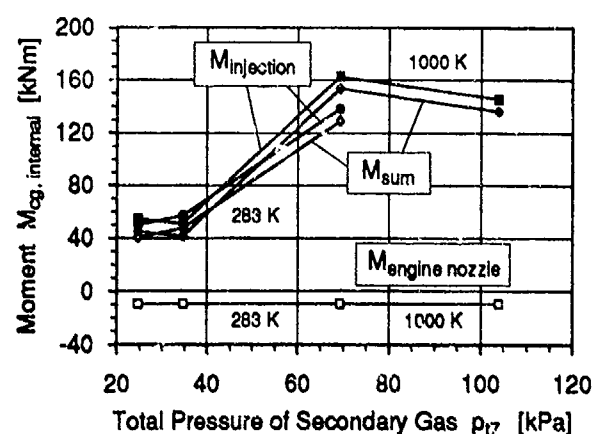


Fig. 24 Moments for the internal performance of the nozzle configuration for $T_{17,SG} = 283 \text{ K}$ and $T_{17,SG} = 1000 \text{ K}$

small subsonic region at the end of the ramp (see Fig. 8 for $p_{17}=69,250$ Pa).

Pressure distributions for $p_{17}=34,625$ Pa and $p_{17}=69,250$ Pa are also shown in Fig. 25, where the results for cold secondary gas are included for comparison.

Another, second way for comparing the results should be discussed: when the mass flow of the secondary gas remains the same for cold and heated gas. According to Fig. 23, cold flow with a total pressure of 34,625 Pa and hot flow with $p_{17}=69,250$ Pa have almost the same mass flow. A comparison of these two test cases favors the cold flow, since the thrust vector angle has a smaller negative value (Fig. 21) and the thrust coefficient is higher

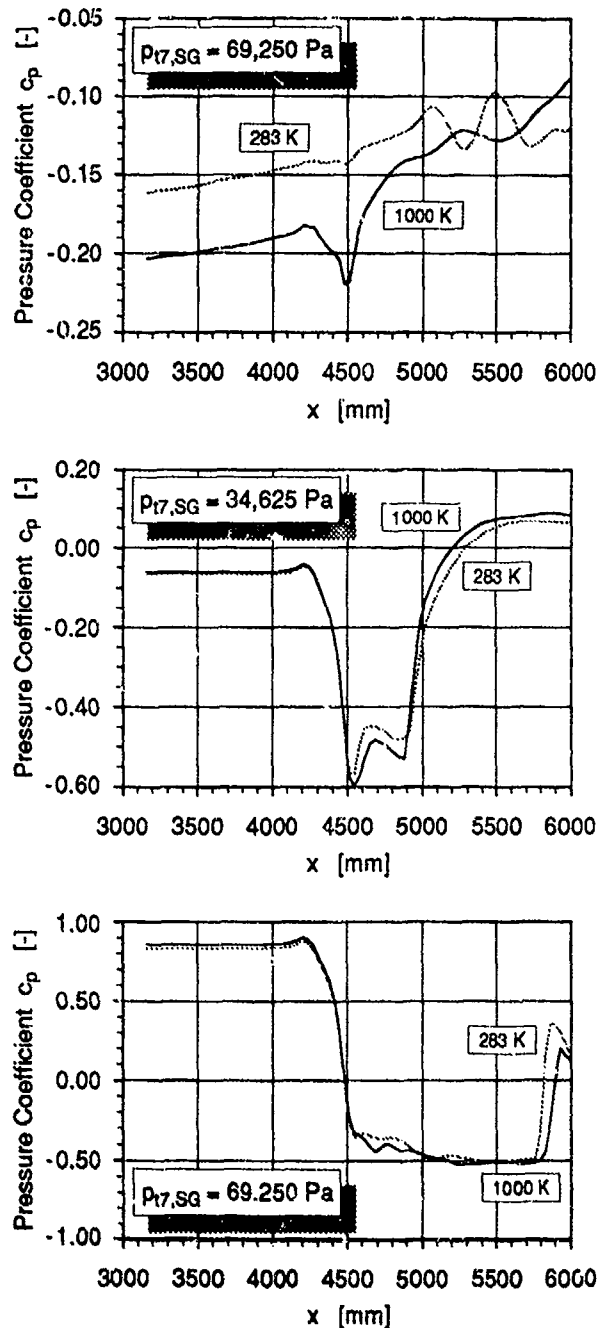


Fig. 25 Pressure distribution for the upper contour of the injection duct and for the ramp at different total pressure levels $p_{17,SG}$ for $T_{17,SG} = 283$ K and $T_{17,SG} = 1000$ K

(Fig. 22). The reason for the better performance with the cold gas injection in this case is found in the subsonic flow along the greatest part of the expansion ramp, which results in a favorable pressure distribution. If an abundance of secondary gas is available, heating might not be necessary to improve the overall efficiency of injection, and the cold flow is sufficient to provide good performance of the nozzle configuration. If the total pressure p_{17} in the secondary gas injection duct is low and very little secondary gas mass is available, heating might have a positive effect to gain thrust and reach a better thrust efficiency.

7.4 Variation of angle of attack

To demonstrate the impact of the aircraft's angle of attack on the afterbody/nozzle flow field and on the gross thrust vector, results are given for a variation of the angle of attack between 0 and 7.5 degrees. The calculations were carried out assuming constant thermodynamic states, i. e. total pressure p_{17} and total temperature T_{17} , for the exhaust gas behind the engine (see Table 1) and for the secondary gas in the injection duct before injection into the nozzle flow ($p_{17}=34,625$ Pa and $T_{17}=283$ K).

The inflow for the inlet and the diverter duct indeed changes with the angle of attack, but the calculations are meant to show the effects on the afterbody/nozzle flow field of only one parameter, which in this case is the angle of attack. Considering the thermodynamic states of the exhaust and secondary air flows according to the inlet and diverter performances in addition to the variation of the angle of attack would lead to effects for the afterbody/nozzle flow field that could no longer be clearly separated and matched to the causes. Moreover, changes in the inlet performance are considered to be very small for the angle of attack variation between 0 and 7.5 degrees, since the precompression of the aircraft's forebody is relatively small at low Mach numbers, and since, together with a detached shock in front of the inlet, the engine's inflow is not substantially affected. The inlet's pressure recovery factor and the distortion are also assumed not to vary considerably.

In order to employ the angle of attack for the calculation procedure, the external geometry of the CFD model had to be modified. At the upstream border of the grid, the upper and lower contours of the fuselage acquire the incidence according to the value for the angle of attack.

Fig. 26 to 33 show the results for the flow field calculations. Lines for Mach number 1.0 are given in Fig. 26. The flow phenomena appearing in the nozzle/afterbody flow are shown in Fig. 9 for $\alpha=5^\circ$ and are described in section 7.1. An increase of the angle of attack has a major impact on the injected secondary gas flow. Due to the stronger expansion of the ambient flow along the upper side of the fuselage with increasing angle of attack, the area of supersonic flow behind the injection duct's throat decreases. The lines for Mach number 1.0 in Fig. 26 best document this flow behavior.

The pressure distribution on the upper wall of the secondary duct and on the expansion ramp is shown in Fig. 27. For a comparison with the model's geometry, Fig. 10 can be referred to.

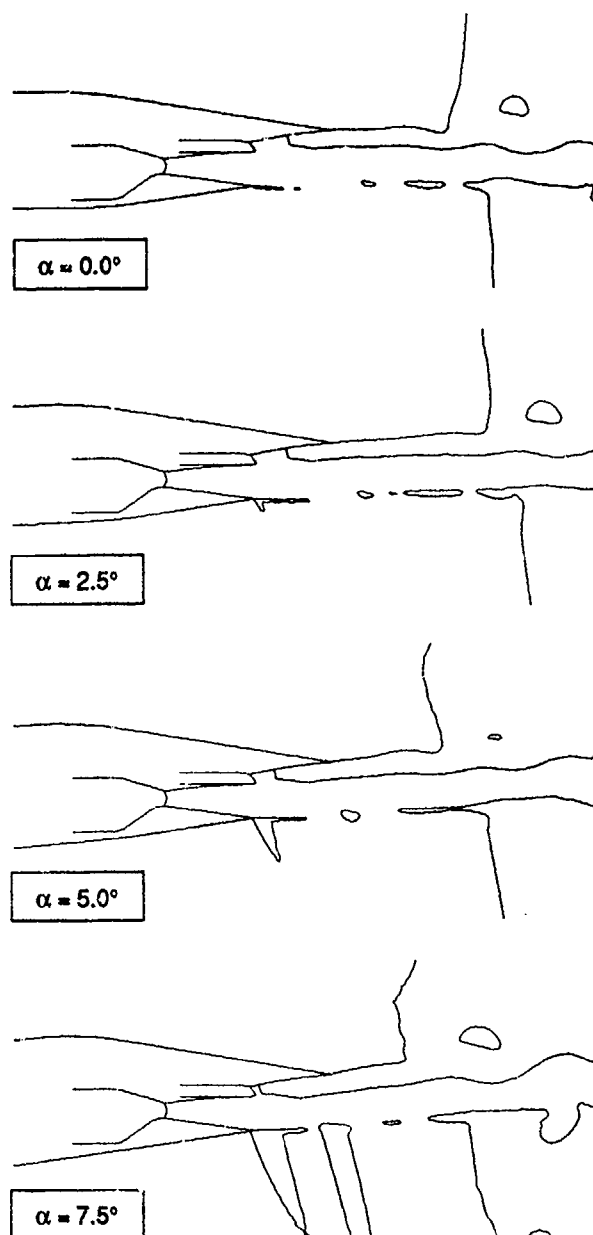


Fig. 26 Lines for Mach number 1.0 for different angles of attack α

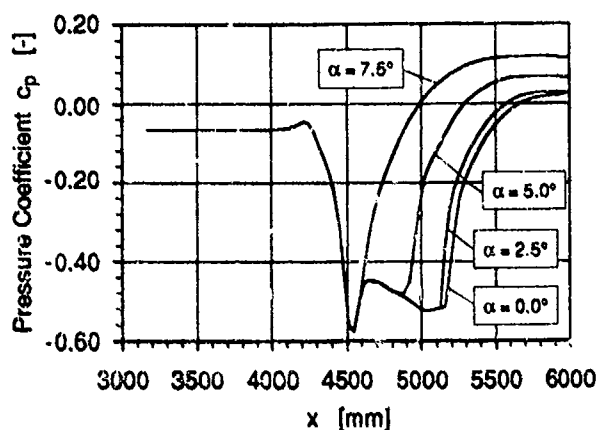


Fig. 27 Pressure distribution along the upper contour of the injection duct and the expansion ramp for different angles of attack

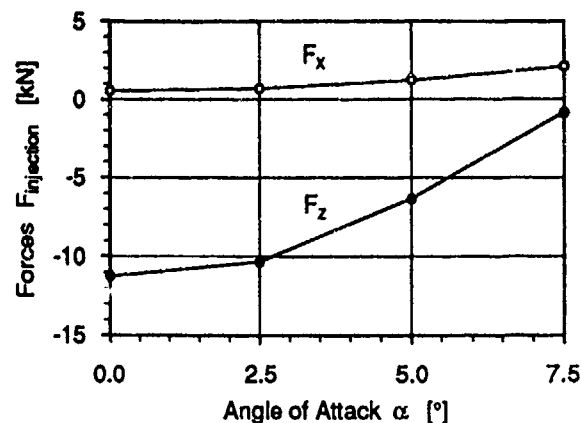


Fig. 28 Forces in x- and z-direction due to injection of secondary gas

The forces due to the injection of secondary gas are shown in Fig. 28. Forces in the x-direction increase slightly with increasing angle of attack, contributing to the aircraft's thrust. Absolute values for the forces in the downward direction become smaller. For the engine nozzle, the conditions remain the same. Values describing the engine performance are given in Table 2.

According to expansion and compression of the ambient flow on the upper and lower surfaces of the fuselage, assuming that no separation takes place, forces in the x-direction decrease for the upper side of the fuselage and increase for the lower side with an increasing angle of attack (Fig. 29). As Fig. 30 documents, forces in the z-direction for both the upper and lower surfaces of the afterbody increase with the same gradient under the premises made for the geometry of the calculation model due to employment of the angle of attack variation.

Nose-up pitching moments decrease for an increasing angle of attack. This behavior of the moment is demonstrated in Fig. 31. For each angle of attack case, the gross thrust vector due to the internal performance of the engine nozzle and the secondary gas injection is shown, together with its line of action determined by the pertinent moment. The length of the vector corresponds with the magnitude of the gross thrust. For increasing angle of

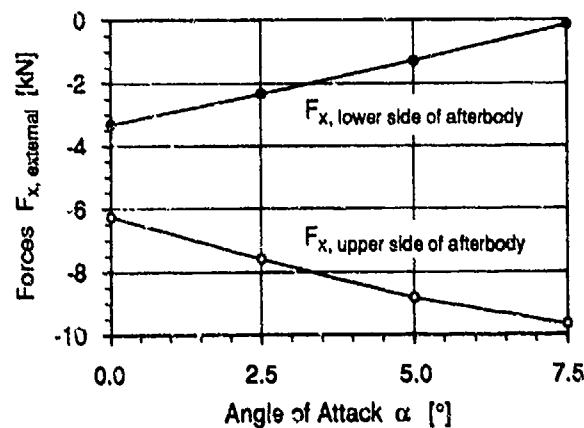


Fig. 29 External forces in the x-direction due to the flow along the afterbody at different angles of attack

tack, the gross thrust vectors show increasing vector angles linked with a decrease of nose-up moments. This behavior of the gross thrust vector enhances the stability of the aircraft.

Corresponding to Fig. 31, the magnitudes of the gross thrust vector and the vector angle are plotted in Fig. 32 and Fig. 33, respectively, for the internal performance of the nozzle and secondary air flow alone and for the internal performance taking account of the external pressure distribution of the lower engine flap.

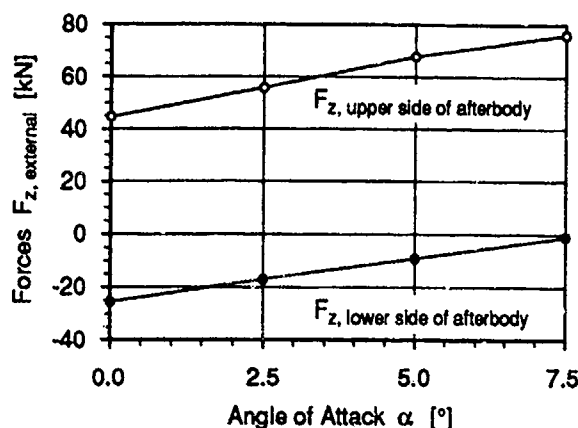


Fig. 30 External forces in the z-direction due to the flow past the afterbody at different angles of attack

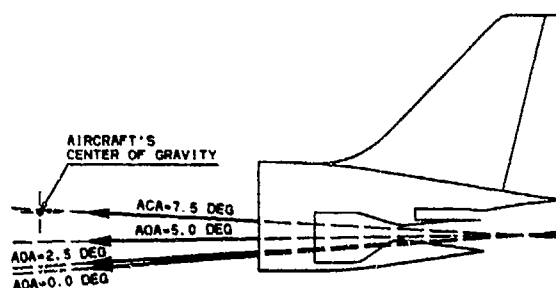


Fig. 31 Gross thrust vectors with lines of action for the internal performance of engine nozzle and secondary gas injection

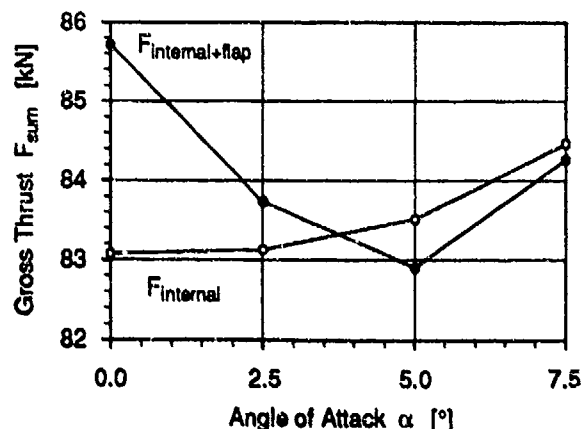


Fig. 32 Gross thrust produced by the complete nozzle configuration

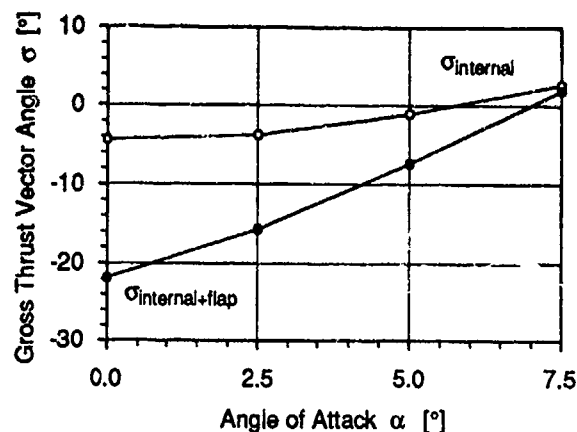


Fig. 33 Gross thrust vector angle produced by the complete nozzle configuration

8. Conclusions

In the transonic flight Mach number regime, injection of secondary gas into the nozzle flow can considerably improve the off-design performance of a single expansion ramp nozzle designed for hypersonic cruise Mach numbers. The thrust vector can be adjusted to the requirements of the inlet forces and of the external aerodynamics.

The vehicle's forebody boundary layer air and/or inlet bleed air could be used as injected secondary gas during take-off and while accelerating to supersonic Mach numbers, until the dual cycle engines are switched from turbojet to ramjet operation mode.

Subsonic injection of the secondary gas results in advantageous pressure distributions along the expansion ramp, yielding thrust vectors with small components normal to the flight direction and very good thrust efficiency. In contrast, supersonic injection and supersonic flow of the secondary gas along the ramp lead to low pressures on the ramp contour, equivalent to large negative thrust vector angles and smaller thrust coefficients. Very good thrust performance is also obtained by supersonic injection of the gas, an immediately following shock, and subsequent subsonic flow along the ramp. This method is quite advantageous, since aerodynamic disturbances in the afterbody region are thus blocked from travelling upstream through the injection duct and influencing the inlet flow.

The influence of the total pressure p_0 of the secondary gas on the afterbody/nozzle flow field as well as the behavior of the gross thrust vector were investigated, studying subsonic injection, the transition to supersonic injection with small regions of supersonic flow at the single expansion ramp, and supersonic injection with supersonic flow along the ramp. A maximum for the gross thrust coefficient is obtained with a small area of supersonic flow downstream of the secondary gas injection duct's throat and with subsequent subsonic flow along the ramp downstream of the shock delineating the supersonic region.

Heating the secondary gas ($T_0=1000$ K) prior to injection into the nozzle flow does not cause major changes in the afterbody flow field structure compared to cold second-

ary gas ($T_g=283$ K), since two effects compensate: higher temperatures on the one hand result in less mass flow on the other hand for a total pressure equal to that of cold flow. This situation creates similar interactions of the secondary gas with the nozzle plume flow and the external afterbody flow, leading to the same thrust vector behavior for the injection of cold and hot secondary gas. A comparison of test cases with heated secondary gas and the same mass flow rate as for cold air favors the cold gas injection. The reason is that, for cold secondary gas, subsonic flow is present along the greatest part of the expansion ramp, giving rise to moderate thrust vector angles and good thrust efficiency in flight direction.

By varying the aircraft's angle of attack, the impact of the external flow on the internal flow field becomes further apparent. For these calculations, constant thermodynamic states were assumed for the engine's exhaust gas before entering the nozzle and for the secondary gas prior to injection into the nozzle flow. Integration of the pressure distribution at the ramp leads to smaller negative forces in the z-direction with an increasing angle of attack. The thrust vector's line of action is turned upward toward the aircraft's center of gravity, thus reducing the magnitude of nose-up pitching moments. Hence, the behavior of the gross thrust vector due to variations of the angle of attack represents a stabilizing effect for the aircraft.

Acknowledgements

This work was supported by the German Ministry of Research and Technology. The participation at the Symposium was made possible by the German Ministry of Defense.

The author gratefully acknowledges the support of A. Eberle, who provided the computer code as a tool to carry out these investigations. The author also thanks his colleagues in the Propulsion Intake/Afterbody department for valuable discussions on the subject. The support of P.W. Sacher is greatly appreciated.

References

- Herrmann, O., "Integration of Turbo-Ramjet Engines for Hypersonic Aircraft", Paper 32, AGARD-FDP Symposium, Fort Worth, Texas, Oct. 7-10, 1991.
- Dusa, D.J., "Turboramjet Exhaust Nozzle Systems", Tenth International Symposium on Air Breathing Engines, Nottingham, England, Sept. 1-6, 1991.
- Ruffin, S.M., Venkatapathy, E., Keener, E.R. and Spaid, F.W., "Hypersonic Single Expansion Nozzle Simulations", Journal of Spacecraft and Rockets, Vol. 29, No. 6, November-December 1992.
- Koelle, D.E. and Kuczera, H., "Sänger Progress Report 1990", Paper No. IAF-90-0175, 41st IAF-Congress, Dresden, Germany, October 1990.
- Kuczera, H. and Hauck, H., "The German Hypersonics Technology Programme", Status Report 1992, Paper No. IAF-92-0867, 43rd IAF-Congress, Washington, D.C., August 1992.
- Kuchar, A.P. and Wolf, J.P., "Preliminary Assessment of Exhaust Systems for High Mach (4 to 6) Fighter Aircraft", AIAA-89-2356, 25th Joint Propulsion Conference, Monterey, Calif., July 10-12, 1989.
- Hindash, I. and Spaid, F.W., "CFD Validation and Wind Tunnel Test for a NASP Single Expansion Ramp Nozzle in the Transonic Regime", 29th Aerospace Sciences Meeting, Reno, Nev., Jan. 7-10, 1991.
- Berens, T., "Berechnung des Strömungsfeldes und Ermittlung des Bruttoschubvektors der HYTEX-Düse bei $Ma_{\infty}=1.2$ ", DASA-LME Internal Technical Note, June 1991, not published.
- Berens, T., "Verfahren zur Schubvektorbbeeinflussung durch Sekundärlufteinblasung in Düsenströmungen im Transschallfluggeschwindigkeitsbereich", DASA-LME Internal Technical Note, July 1992, not published.
- Berens, T., "Berechnung des Strömungsfeldes einer Rechteckdüse mit Expansionsrampe für Hyperschallflugzeuge bei $Ma_{\infty}=1.2$ mit Einlassung der Vorderrumpfgrenzschicht", DASA-LME Internal Technical Note, June 1991, not published.
- Herrmann, O. and Rick, H., "Propulsion Aspects of Hypersonic Turbo-Ramjet-Engines with Special Emphasis on Nozzle/Aftbody Integration", ASME-Paper 91-GT-395, International Gas Turbine and Aeroengine Congress and Exposition, Orlando, Florida, June 3-6, 1991.
- Eberle, A., "Characteristic Flux Averaging Approach to the Solution of Euler's Equations", VKI Lecture Series 1987-04.
- Eberle, A., Schmatz, M. and Bissinger, N.C., "Generalized Flux Vectors for Hypersonic Shock-Capturing", AIAA Paper 90-0390, 28th Aerospace Sciences Meeting, Reno, Nevada, January 8-11, 1990.
- Eberle, A., Rizzi, A. and Hirschel, E.H., "Numerical Solution of the Euler Equations for Steady Flow Problems", Notes on Numerical Fluid Mechanics, Vol. 34, Vieweg Verlag, Braunschweig/Wiesbaden 1992.
- Sacher, P.W., "Hypersonic Technology Experimental Vehicle HYTEX", Review of the German Hypersonic Research and Technology Programme, Bonn April 1991.
- Gordon, S. and McBride, B.J., "Computer Program for Calculation of Complex Chemical Equilibrium Compositions", NASA SP-273, 1976.
- Berens, T., "Einfluß des Rechengebietes und der Netzgröße bei Euler-Rechnungen auf die Resultate für das Strömungsfeld im Düse/Hock-Bereich von Hyperschallflugzeugen bei $Ma_{\infty}=1.2$ ", DASA-LME Internal Technical Note, Sept. 1992, not published.
- Sterr, W., "Diverterdrücke, Diverterdurchsätze und Totaldruckverluste im Grenzschichtkanal bei HYTEX", DASA-LME Internal Technical Note, August 1990, not published.
- John, H. and Herrmann, O., Patentschrift DE 3811614 C1, May 18, 1989.

TOPOLOGICAL STRUCTURE OF A JET IN A CROSS FLOW

A.E. Perry
R.M. Kelso¹
T.T. Lim²

Department of Mechanical and Manufacturing Engineering
University of Melbourne
Parkville, Victoria 3052
AUSTRALIA

SUMMARY:

Experimental studies of round jets in cross flow have been made using flying hot-wire and flow visualization techniques. The velocity ratio of the flow ranged from about 2 to 6 with the Reynolds number up to 6200. The flying hot wire enables time- and phase-averaged measurements to be made in regions of the flow which cannot be measured accurately using stationary wires. These quantitative results together with the complementary flow visualization studies have allowed the mean topological features of the jet in cross-flow to be identified using critical point theory. We believe an understanding of these flow features may give us insight into the large-scale mixing processes which occur in the shear layer of the jet.

LIST OF SYMBOLS

D diameter of the jet
R velocity ratio (V_{jet} / U_0)
 V_{jet} mean (RMS) velocity of the jet
 U_0 free stream velocity of cross flow
y distant from the floor of the tunnel

1 INTRODUCTION

The study of jets in cross-flow is of great practical relevance in engineering applications. In turbomachinery, such flows can be found in turbine blade cooling. Aerodynamic applications include V/STOL aircraft exhaust flows during transition flight, the roll control of missiles. This flow configuration can also be found in industrial applications such as gas burners, chimney flows and piping system just to name a few.

It has long been recognised that when a jet discharges normal to a cross-flow, there is a complex interaction between the two flows, resulting in the deflection of the jet in the cross-flow direction. Far downstream of the pipe outlet, the bent-over jet is dominated by a counter rotating vortex pair which seem to originate at the jet exit.

In the near field, the jet structure consists of ring-like vortices which become distorted with the streamwise distance and in the wake region, alternating vertical vortices of the opposite sign are generated which gives the appearance of a "Karman-vortex-street". Detailed interaction between these flow structures is rather complex and is not fully understood. This has led to numerous experimental and numerical studies (refs 1-7) with the aim of gaining an insight into this rather complex and unsteady flow.

The purpose of this work is to examine the topological structure of the flow which we believe will shed light on the entrainment and mixing processes. Two studies were carried out. One was a flow visualization investigation in a water tunnel and the other was a flying hot-wire study in a wind tunnel. To enable direct comparison with the hot-wire measurements limited smoke visualizations were also made in the same wind tunnel. The flying hot-wire is necessary because this particular flow involves large changes in the velocity vector direction including flow reversal and accurate measurements using stationary hot-wires would not have been possible. A detailed description of this flying hot-wire system is given in Kelso, Lim & Perry (ref. 8). In this paper, we will concentrate on the water tunnel studies, although limited hot-wire measurements are also presented in order to relate to the visual studies. A more comprehensive description of the hot-wire work is currently under preparation. The terminology used here for the topological descriptions is that used by Perry & Chong (ref. 9).

2 EXPERIMENTAL APPARATUS AND METHODS

The flow visualization experiments were carried out in the closed-return water channel at the University of Melbourne. Figures 1 show a schematic diagram of the jet apparatus. The plexiglass working section measured 0.3 m x 0.3m in cross-section and operated at a typical cross-flow velocity of 60 mm/s. The jet was constructed from

Present address: ¹ CSIRO Division of Building, Construction and Engineering,
P.O. Box 56, Highett, Victoria 3190, Australia

² Department of Mechanical and Production Engineering
National University of Singapore
10 Kent Ridge Crescent
Singapore 0511

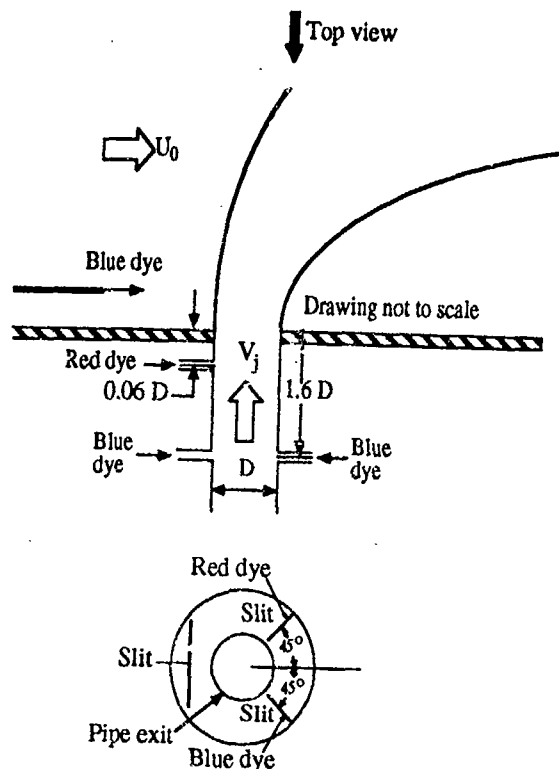


Figure 1. Schematic diagram of the experimental layout (a) side-view of the jet apparatus. (b) Top-view of (a) showing the dye injection slits.

plexiglass tubing with an internal diameter of 25mm, giving a Reynolds number of 1600, based on the cross-flow velocity and jet diameter. The pipe was very short with the fluid entering it from an axisymmetric 36:1 contraction, thus giving a top-hat velocity profile in the case of no cross-flow. A narrow circumferential slot in the pipe wall allowed dye to be injected directly into the pipe to mark the boundary layer. A small dye injection port was also located within the pipe immediately upstream of the pipe exit as shown in the figure. Moveable dye injection tubes were also used to introduce dye into the cross-flow from points away from the wall. In order to mark the boundary layer on the floor of the tunnel, dye was released through spanwise slits as shown in figure 1(b)). Dyes with specific gravity ≈ 1 were used to visualize the flow. No deliberate forcing was applied to any of the flow cases in the water tunnel.

To complement the dye visualization studies, experiments were also carried out in a wind tunnel which used a flying hot-wire so as to overcome the difficulty of velocity vectors undergoing large angular changes and flow reversals. The Reynolds number of the flow was about 6200. Cursory smoke studies showed that the jet flow structures were similar to the water tunnel studies.

3 EXPERIMENTAL RESULTS

Figure 2, plate 1 shows the pattern when blue dye is released from the circumferential slot in the pipe and red dye is released from the upstream port. It is interesting to note from this figure that red dye marks only the upstream side of the jet structures

while blue dye is swept towards the downstream side. This behaviour, as will be discussed in detail later, suggests that there must be a separation line on the inside wall of the pipe. A close examination of the flow pattern also shows that as the cylindrical sheet of blue dye leaves the jet exit, the sheet quickly develops folds on either side of the jet and this folding continues as the jet is deflected in the cross-flow direction.

Figure 3, plate 1 shows the flow pattern when red dye has been released from the port and blue dye has been released from a small tube upstream. Interestingly, it can be seen that the filament of blue dye from upstream stagnates at a "half-saddle point" to be elaborated on later. Figure 4, plate 1 shows a close-up of the red dye which seems to indicate a "vortex-breakdown-like" pattern close to the jet exit. Viewing slow motion images of the breakdown indicates that there is a region of reverse flow in the vortex core normally associated with breakdown. In figure 5, the authors' interpretation of the jet structures is presented. The vortex sheet which surrounds the jet fluid at the exit appears to undergo two sets of roll ups. Figure 5(a) shows Kelvin-Helmholtz-like roll ups forming vortex rings, while figure 5(b) shows the vortex sheet developing roll-ups parallel to the jet axis. This is consistent with the vortex rings tilting and bending in such a way that the net effect is to produce two counter rotating vortex pairs (or CVP) aligned and curving back with jet axis as shown in the schematic diagram of Sherif & Pletcher (ref. 10)

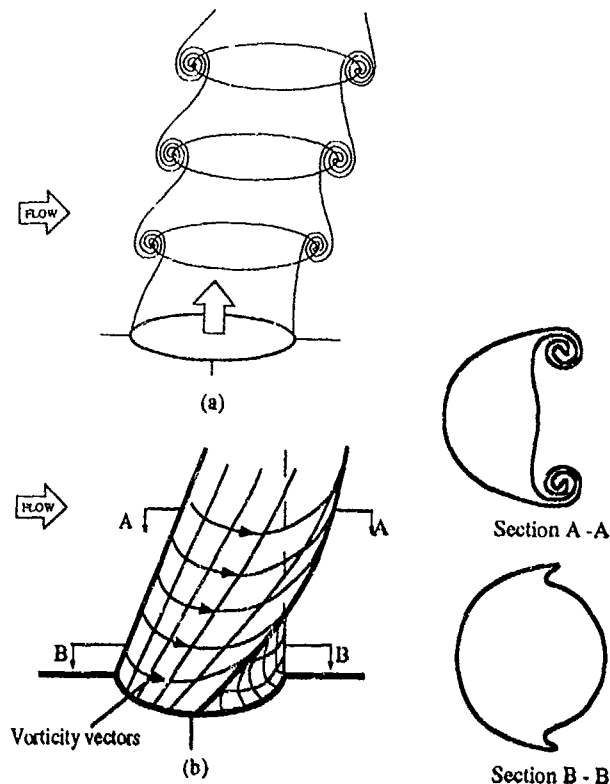


Figure 5. Two roll-up processes close to the jet exit. (a) Kelvin-Helmholtz-like roll-up and (b) folding of the cylindrical jet shear layer.

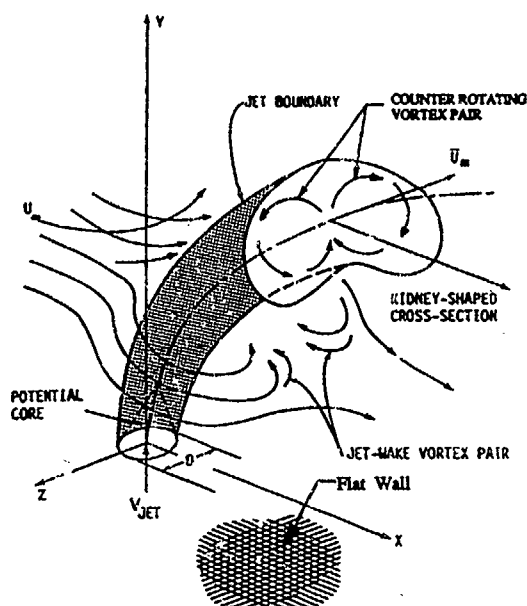


Figure 6. Schematic diagram of jet in cross-flow (from ref. 10)

(see figure 6). The vortex rings on the upstream half of the jet appear to retain their identity as shown clearly in red in figure 2, plate 1. The CVP is shown blue with some red dye also involved (as seen in figure 2) in a region of the jet whose structure so far is shrouded in mystery. Simple vortex skeleton type modelling as outlined by Perry & Chong does not appear to be directly applicable here nor are the patterns seen as periodic as the coflowing jet and wake structure of Perry and Lim (ref.11).

Figure 7(a) shows "flying hot-wire" anemometry studies of a jet in cross-flow at about four times the Reynolds number. We have incorporated a "fold" in the diagram to show how flow in the plane of symmetry is related to the sectional streamline pattern taken on a horizontal plane at about $y=0.42D$ above the surface. Formation of the CVP can be seen. This is a mean flow picture and figure 7(b) shows the authors' interpretation for the complete plane of symmetry flow deduced from more complete hot-wire measurements which extended closer to the wall. An extensive description of the hot-wire measurements can be found in Perry, Kelso & Lim (ref.12).

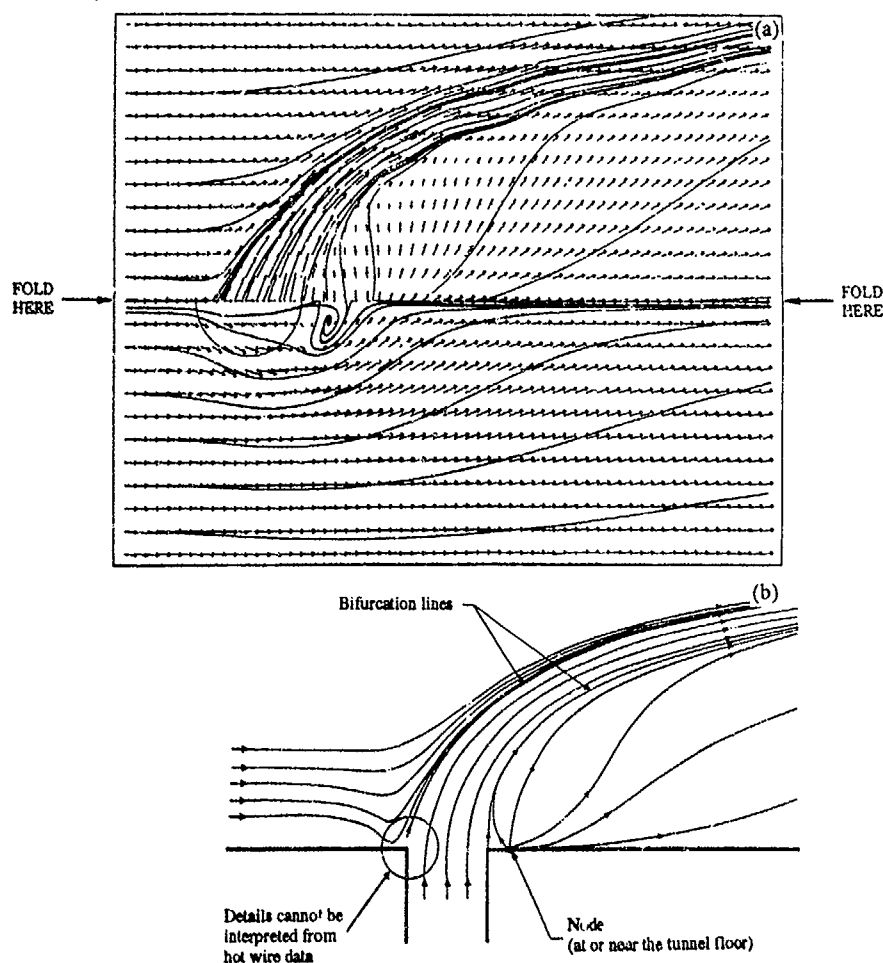


Figure 7. (a) Composite time-averaged vector field and streamline pattern for the unforced jet. Note that the fold-line lies above the tunnel floor at $y/D=0.42$ and in the plane of symmetry (b) Authors' interpretation of the pattern at the plane of symmetry.

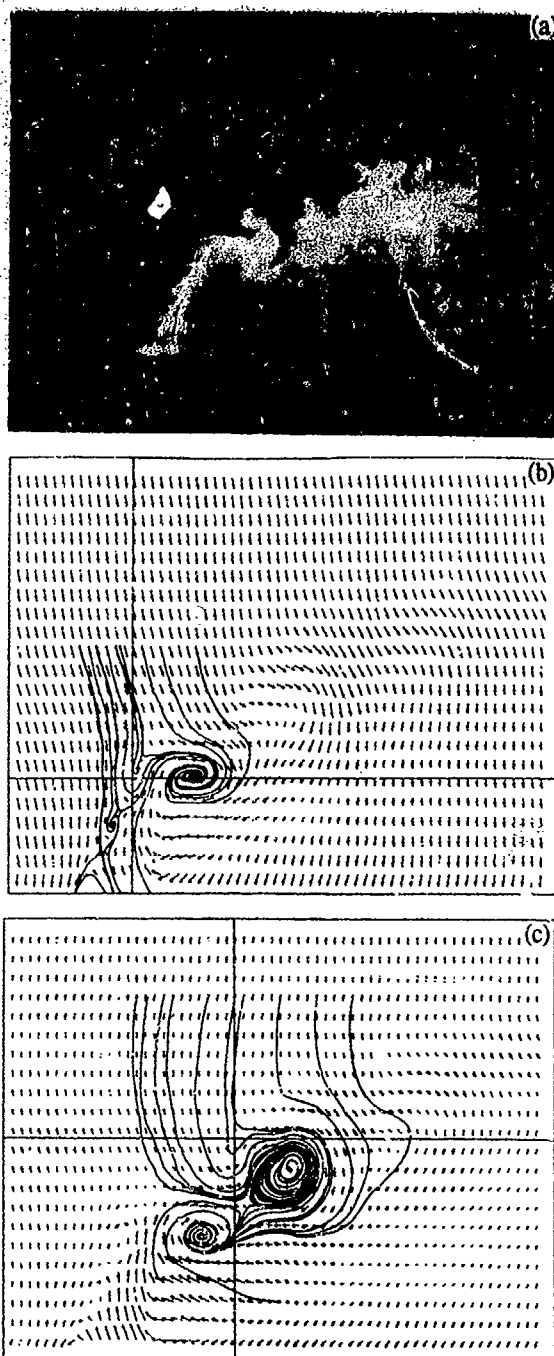


Figure 8. (a) Laser cross-section in the plane of symmetry of the jet performed in the wind tunnel. $Re=6200$, $R=2.2$. (b) and (c) Phase-averaged streamline patterns relative to observers moving with different velocities. "Cross-hairs" identify the part of the flow with which the observer moves.

Overall, the pattern bears a remarkable resemblance to a three dimensional flow separation classified by Hornung & Perry (ref. 13) and Perry & Hornung (ref. 14) as an owl-face of the first kind. The node on the plane of symmetry is probably slightly off the surface and there are other detailed differences but globally the topology is very close. Smoke pattern pictures like that seen in figure 8(a) seems to indicate broadly the same topology as for the water tunnel results although the entire jet outlet is smoke filled and so the results are not as detailed. Also, unlike the water tunnel results, vortex breakdown is not obvious. Figure 8(b) and (c) show phase averaged results of flying hot wire studies. The jet was slightly perturbed to lock in the vortex formation to a fixed frequency. The results in these figure are relative to two different observers, and only eddies moving with the same velocity of the observer are apparent. Also, unlike the cigarette patterns of Perry & Lim and bouyant jets in cross-flow, there is definitely a vortex rollup on the downstream side of the cylindrical vortex sheet

From a detailed examination of dye injection results in the water tunnel, many features seem to originate from inside the pipe. The partially conjectured surface flow topology on the interior of the pipe surface is shown in figure 9. Here a developed surface is shown and the red dye port confirmed the existence of the "reversed flow" region bounded by a negative bifurcation line or

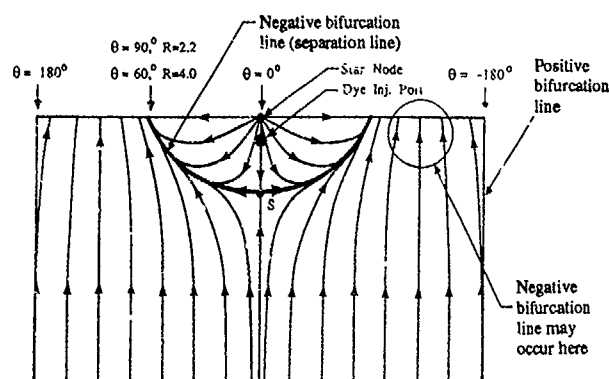


Figure 9. Surface streamline pattern within the jet pipe. The surface is represented as a developed surface; i.e the pipe has been split at the rear, and flattened out.

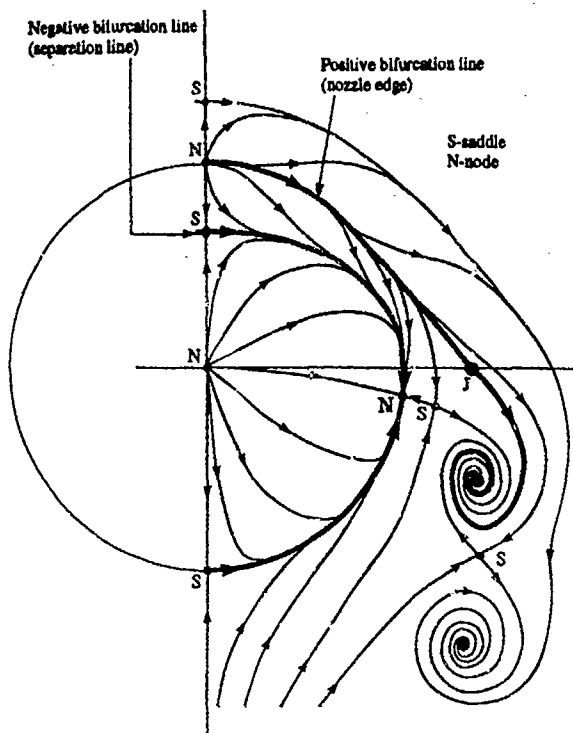


Figure 10. Interpreted and inferred surface streamline pattern shown on a flattened-out rubber sheet which previously covered the inside of the jet-pipe and tunnel floor

separation line. The negative bifurcation line appears to be related to the initial roll up of the blue dye to form the CVP. Figure 10 shows a simplified distorted but topologically equivalent pattern showing how the flow on the inside wall of the pipe is related to the surface pattern on the wall. This method of presentation was suggested by colleague Professor Cantwell. The pattern inside the circle is imagined to be on an elastic membrane which needs to be pushed into the hole and point labelled N is a fictitious node acting as a source for the flow. The pattern on the surface is an instantaneous pattern conjectured from dye traces.

As mentioned earlier, figure 3 shows an intriguing pattern with dye appearing to stagnate in mid-air onto a vortex sheet. It resembles the half-saddle pattern first seen by Perry, Lim & Chong (ref. 15) in coflowing jets and wakes and in the computations of Patnaik et al (ref. 16) and Corcos and Sherman (ref. 17) in plane mixing layers (see also Chen et al (ref. 18)). Figure 11 shows that in detail, we do not really have a half saddle but a cluster of critical points which looks like a half saddle in the large. Furthermore we have the upstream "necklace" or "horseshoe" vortices which form at the surface and the figure shows how these are connected to the vortices associated with the separating shear layer of the jet. Figure 12, plate 1 shows an example of the dye visualization of the necklace vortices. Two patterns are shown in figure 11 with detailed differences at the lip of the pipe outlet. Video movies with dye show that the flow oscillates between these two patterns.

If the shear layer leaving the hole from the upstream lip were taken to have zero thickness, then figure 13 shows how the pattern could be interpreted as a half-saddle. The patterns shown in figure 11 are conjectured from dye studies and are meant to be instantaneous patterns related to an observer at rest relative to the hole. The sequence of ring vortices shown in the dye pictures as shown in figure 2 are not apparent because they are accelerating away but would be seen if the observer were to move with the eddies.

Figure 14, plate 1 shows the dye pattern when red dye is released from the far side slit and blue dye from the near side slit shown in figure 1(b). No dye has been released from the tube where the jet is issuing nor from the upstream slit. These mark the "shed vertical vortices" from the jet. If the jet were to be imagined to be a solid cylinder in cross flow these "shed vortices" would broadly resemble a Karman vortex street. However, as Lighthill (ref. 19) has pointed out, no vorticity can be generated within an incompressible, homogeneous fluid. All vorticity is generated at solid boundaries. The jet in cross flow should not be regarded as a solid cylinder and these dye tests show conclusively that the Karman-street like vortices originate from the vorticity generated at the wall. These somehow join up with the vortices generated in the pipe. The above interpretations agree with those of ref. 4.

4 CONCLUSIONS

One can see that a kaleidoscope of phenomena exists for jets in cross flow even for the simple case of the pipe outlet being flush with the wall. Critical point theory seems to be useful in interpreting the complex eddy structures. There are many vortex systems, all of which are somehow connected. It is clear that the separation pattern inside the tube is important in the initial roll up for the CVP. The vortex rings at the outlet appear to tilt and bend such that they contribute to a component of vorticity for the CVP. Vortex breakdown appears to be occurring in the CVP near the tube outlet. The Karman vortex street like structure come from the vorticity generated at the wall and this vorticity somehow links up with the vorticity generated in the pipe. The necklace vortex system seems to play only a minor role in the overall structure.

So far, in spite of the complexities, we have a broad understanding of the flow structure. The detailed complexities will need to be persuaded. Perhaps direct numerical simulations at low Reynolds number may shed some light on the features which are difficult to resolve experimentally.

5 ACKNOWLEDGEMENT

The authors wish to thank the Australian Research Council for the financial support of this project. Richard Kelso also acknowledges the support of I.C. Shepherd and the CSIRO.

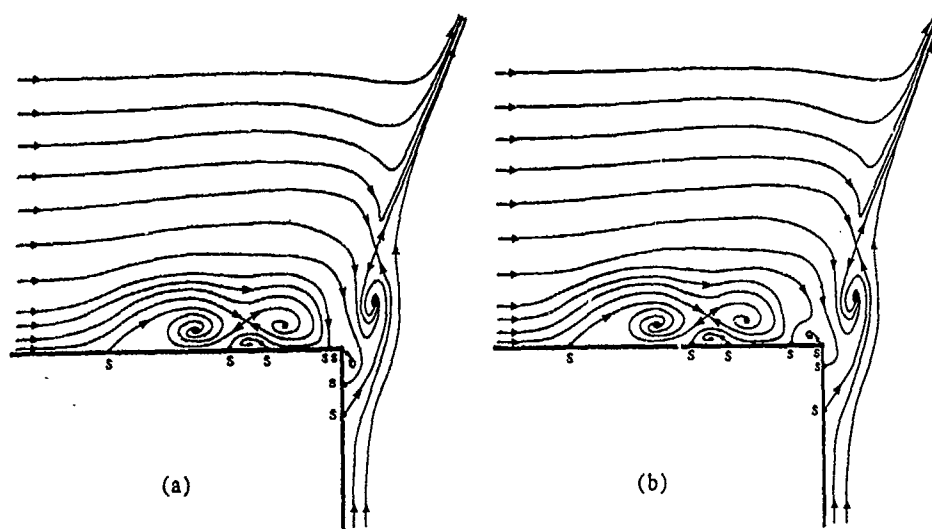


Figure 11. Authors' interpretation of two alternative streamline patterns as seen by a stationary observer.

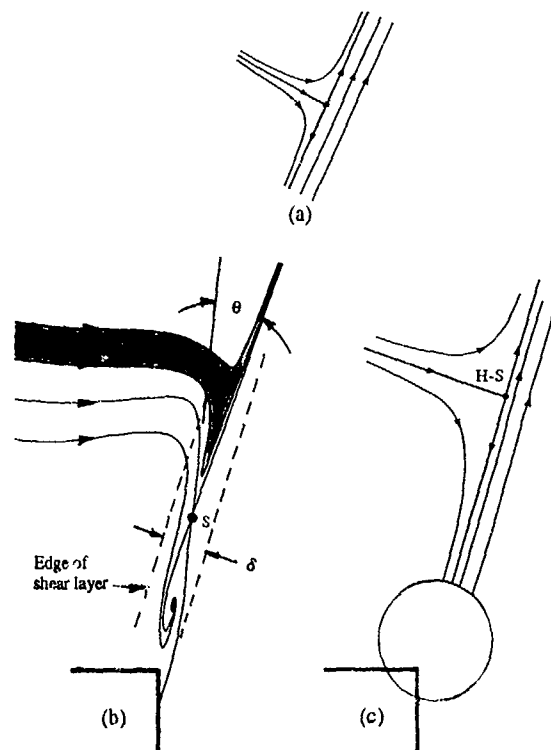


Figure 13. (a) A half-saddle. (b) Details of the saddle point S . δ is the thickness of the shear layer and θ is the angle between the eigenvectors of the saddle point. (c) A limiting case of (b) when δ and θ approaches zero. H-S denotes the half-saddle.

6 REFERENCES

1. Ardreopoulos, J., "On the Structure of Jets in Crossflow", *J. Fluid Mech.*, 157, 1985, pp 163-197.
2. Chassaing, P., George, J., Claria, A. and Sananes, F. "Physical Characteristics of Subsonic Jets in Crossflows", *J. Fluid Mech.*, 62, 1974, pp 41-64.
3. Coelho, S. L.V. and Hunt, J.C.R., "The dynamics of the Near Field of Strong Jets in Crossflows", *J. Fluid Mech.*, 200, 1989, pp 95-120.
4. Fric, T.F. and Roshko, A., "Structure in the Near Field of the Transverse Jet", Seventh Symposium on Turbulent Shear Flows, 1989, pp 6.4.1-6.4.6.
5. Moussa, Z.M., Trischka, J.W. and Eskinazi, S. "The Near Field in the Mixing of a Round Jet with a Cross stream", *J. Fluid Mech.*, 80, 1977, pp 49-80.
6. Scorer, R.S., "Natural Aerodynamics" Pergamon Press, 1958.
7. Sykes, R.I., Lewellen, W.S. and Parker, S.F., "On the Vorticity Dynamics of a Turbulent Jet in a Crossflow", *J. Fluid Mech.* 168, pp 393-413.
8. Kelso, R.M., Lim, T.T. and Perry, A.E., "A Novel Flying Hot-wire System". Provisionally accepted for publication in *Exp. Fluids*.
9. Perry, A.E. and Chong, M.S., "A Description of Eddy Motions and Flow Patterns using Critical-Point Concepts", *Ann. Rev. of Fluid mech.*, 19, 1987, pp 125-155.
10. Sherif, S.A. and Pletcher, R.H. "Measurements of the Flow and Turbulence Characteristics of Round Jets in Crossflow", *J. Fluid Eng.*, 111, 1989, pp. 165-171
11. Perry, A. E. and Lim, T.T., "Coherent Structures of Coflowing Jets and Wakes", *J. Fluid Mech.*, 88, 1978, pp 451-463.
12. Perry, A.E., Kelso, R.M. and Lim, T.T., "An Experimental Study of a Round Jet in a Cross Flow". Under preparation.
13. Hornung, H.G. and Perry, A.E., "Some aspects of three-dimensional separation. Part I : Stream surface Bifurcation", *Z. Flugwiss. Weltraumforsch.*, 8, 1984, pp 77-87.
14. Perry, A. E. and Hornung, H.G., "Some aspects of three-dimensional separation. Part II Vortex Skeleton", *Z. Flugwiss. Weltraumforsch.*, 8, 1984, pp 155-160.
15. Perry, A. E., Lim, T.T. and Chong, M.S. "The Instantaneous Velocity Fields of Coflowing Jets and Wakes", *J. Fluid Mech.*, 101, 1980, pp 243-256.
16. Patnaik, P.C., Sherman, F.C. and Corcos, G.M. "A Numerical simulation of Kelvin-Helmholtz Waves of finite amplitude", *J. Fluid Mech.*, 73, 1976, pp 215-240.
17. Corcos, G.M. and Sherman, F.S. "Vorticity Concentration and the Dynamics of Unstable Free Shear Layers", *J. Fluid Mech.*, 73, 1976, pp 241-264.
18. Chen, J.H., Cantwell, B. J. and Mansour, N.N. "Direct Numerical Simulations of a Plane Compressible Wake: Stability, Vorticity Dynamics and Topology" Thermosciences Division, Dept of Mechanical Engineering, Stanford University. Report no: TF-46
19. Lighthill, M.J. "Attachment and Separation in Three-dimensional Flow. In *Laminar Boundary Layers*, ed. L. Rosenhead, 1963, Oxford University Press, pp 72-82.



Figure 2. Flow pattern obtained when blue dye is injected from the circumferential slot in the pipe and red dye is released from the dye injection port. $Re=1600$, $R=4.0$



Figure 3. Flow pattern produced when the streakline of dye impinges on the shear layer of the jet to produce a half-saddle-like pattern. $Re=1600$, $R=2.2$



Figure 4. Vortex-breakdown-like pattern



Figure 12. Dye pattern showing a top view of necklace vortices.

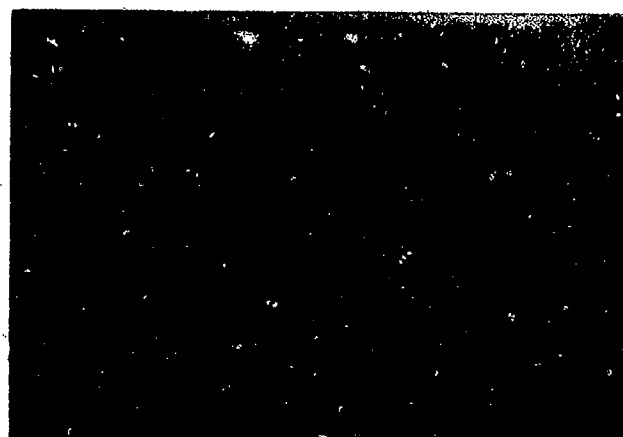


Figure 14. Vertical vortex structure visualized by introducing red and blue dye from the spanwise slits. $Re=2700$, $R=4.0$

An Experimental Study of Siphonal Jets in a Turbulent Boundary Layer Crossflow

C.A O'Riordan, S.G. Monismith, J.R. Koseff
Environmental Fluid Mechanics Laboratory
Stanford University, Stanford, CA 94305-4020 USA

SUMMARY

We conducted experiments in a laboratory flume to study the interaction of bivalve siphonal jets with the turbulent boundary layer which forms in the benthic region of shallow estuaries. Beds of siphonate bivalves (clams) 1.8 meters long were simulated to study the formation of a phytoplankton-depleted layer (concentration boundary layer) over bivalves. Refiltration of excurrent fluid through incurrent siphons, which represents a decrease in aggregate feeding efficiency, was measured for two test beds with $S/d_o=6$ and 16 and siphon pairs oriented perpendicular to the cross flow direction. Results are expressed as a function of the nondimensional distance downstream, x/d_o , the velocity ratio, $VR=u_j/U_\infty$, and the nondimensional animal spacing, S/d_o . We also used laser induced fluorescence to obtain quantitative concentration profiles in order to describe the evolution of the flow and to identify parameters that describe the jet/boundary layer interaction.

Analysis of the height of maximum phytoplankton depletion, or jet penetration, z_{out} , and spreading width of the jet, σ , show that changes in the vertical momentum of the excurrent jet become more important in determining the phytoplankton removal efficiency as VR decreases. Stanton numbers calculated from concentration measurement at the bed do not correlate with those calculated for similar flow over rough boundaries due to the importance of jet/sink dynamics in transferring mass across the concentration boundary layer.

LIST OF SYMBOLS

c_f	skin friction coefficient
C_i	concentration of dye in incurrent fluid
C_o	concentration of dye in excurrent fluid
C_∞	concentration of dye in free stream fluid
δ	boundary layer thickness
δ_i	inner length scale
d_i	incurrent siphon diameter
d_o	excurrent siphon diameter
D	molecular diffusion coefficient
h_s	siphon height above the boundary

J	momentum flux parameter
κ	von Karmans constant
k_s	equivalent sand grain roughness
M	jet momentum flux
n	refiltration fraction
ν	kinematic viscosity
Re_x	Reynolds number based on distance
Re_k	roughness Reynolds number
S	distance between siphon pairs
Sc	Schmidt number, ν/D
St_m	Stanton number for mass transfer
σ	near field width of excurrent plume
u^+	nondimensional mean velocity
u^*	friction velocity
$u(z)$	mean longitudinal velocity
u_j	siphon jet velocity
U_∞	free stream velocity
VR	velocity ratio, u_j/U_∞
z_m	jet length scale
x	distance from leading edge of the bed
z	height above boundary
z^+	nondimensional height above the boundary
z_{out}	height above siphon of maximum dye concentration

1. INTRODUCTION

Benthic communities in estuaries can influence processes in the overlying water column by acting as a sink for phytoplankton biomass. Some studies suggest that benthic suspension feeders (clams, mussels or oysters) may ingest a large fraction of phytoplankton biomass in shallow estuaries (Ref 1) and that in several cases, benthic grazing may deplete phytoplankton biomass in the water column at a rate equal to that of production (Ref 2, Ref 3, Ref 4). In tidal flows, grazing by bivalves may result in the depletion of phytoplankton at the bed when phytoplankton cells which are removed by the bivalves from the boundary layer region are not completely replaced by vertical mixing. Laboratory studies of phytoplankton depletion at the bed have consisted primarily of experiments using suspension feeders without strong excurrent jets (Ref 5). In this study, we are concerned with the formation of phytoplankton depleted regions (concentration boundary layers) over dense beds of siphonate bivalves (animals with incurrent and excurrent

siphons) where the incurrent and excurrent flow dynamics play an important role in mixing.

Our experiments focus on the dynamics of the excurrent jets and the interaction of the jets with the turbulent boundary layer crossflow. Several researchers have demonstrated the importance of hydrodynamics to benthic feeding processes with model studies of one or two siphon pairs (Ref 6, Ref 7) and have found that the behavior of bivalve siphonal jets is similar to that observed for jets in uniform cross flows (e. g. Ref 8). Results in Ref 7 are expressed in terms of the characteristic length scale for a jet in a uniform cross flow, derived from the momentum flux of the jet, M , and the free stream velocity of the cross flow, U_∞

$$z_m = \frac{M^{1/2}}{U_\infty} \quad (1)$$

(Ref 9). Using the definition of momentum flux, we can write this length scale:

$$z_m = \frac{d_o u_j}{U_\infty} \quad (2)$$

where u_j is the jet velocity, d_o is the jet diameter, and U_∞ is the freestream speed of the cross flow. We expect all properties of the flow for a single jet to be described in terms of z/z_m . However, results of flow visualization using a single excurrent jet have shown that the trajectory of the phytoplankton-depleted water cannot be fully described in terms of this parameter (Ref 10) for two reasons. First, because the siphonal jet is immersed in the boundary layer, it experiences a range of velocities through its trajectory. This effect combined with the effect of the vortex system which forms in and around the jet causes the trajectory to flatten, whereas existing theories predict a rising trajectory. Second, the above scaling parameter does not include siphon height, h_s , or siphon orientation, which are controlled by the animal and can alter trajectories significantly. Moreover, the ability to predict the distribution of phytoplankton depleted fluid is complicated by the interactions between siphonal currents of neighboring bivalves. Ref. 7 shows that this interaction can be quite strong even when the bivalve siphons are 10 diameters apart.

In the case of multiple jets in a cross flow, dimensional analysis yields other important parameters. These are the nondimensional jet spacing, S/d_o , siphon height, h_s/d_o , the nondimensional distance downstream, x/d_o , and the velocity ratio, $VR = u_j/U_\infty$ derived from the length scale z_m . Note that in many species of siphonate bivalves the incurrent siphon diameter

is twice the diameter of the excurrent siphon. Therefore, in our analysis we assume that the sink dynamics play a minor role and the jet dynamics dominate the mixing process.

Several researchers have studied the effects of the nondimensional parameters identified above on the mixing of heated or cooled jets in gas flows (Ref 11, Ref 12), and found that the single most important parameter in determining dilution of the jet and heat transfer from the jets to the surface was the momentum flux parameter, J , where

$$J = \frac{\rho_j u_j^2}{\rho_\infty U_\infty^2} \quad (3)$$

They also found that the parameter S/d_o affects jet penetration into the overlying flow, and that as S/d_o increased the jets maintained their structure further downstream. These previous experiments were conducted with one row of jets at most and extrapolation of their results to a large, continuous bed of jets is difficult. Because the interaction of multiple siphon jets with a turbulent boundary layer flow is so complex we do not intend to resolve the entire structure of the flow. Our goal is to examine averaged properties of mass transfer and jet mixing to determine the importance of siphonal currents in phytoplankton depletion at the bed.

We are interested in determining the effect of the interaction of multiple jets on the seston concentration field in terms of the dimensionless parameters listed above. The study presented here is designed to answer the following questions:

(i) Under what physical conditions do concentration boundary layers form over dense beds of bivalves?

(ii) How does the size and density of the jets effect the aggregate feeding efficiency (mass transfer) of a population and the concentration profiles above the bed?

With these questions in mind, we have conducted experiments to study this biological process in simple, well controlled flows using model bivalves.

2. EXPERIMENTAL FACILITY

To simulate bivalve feeding in a tidal cross flow, experiments were conducted in a laboratory flume. The flume is constructed of Plexiglas, PVC pipe, glass and stainless steel, and is 60 cm wide, 60 cm deep, and approximately 10 m long. Flow through the 3 m long test section is

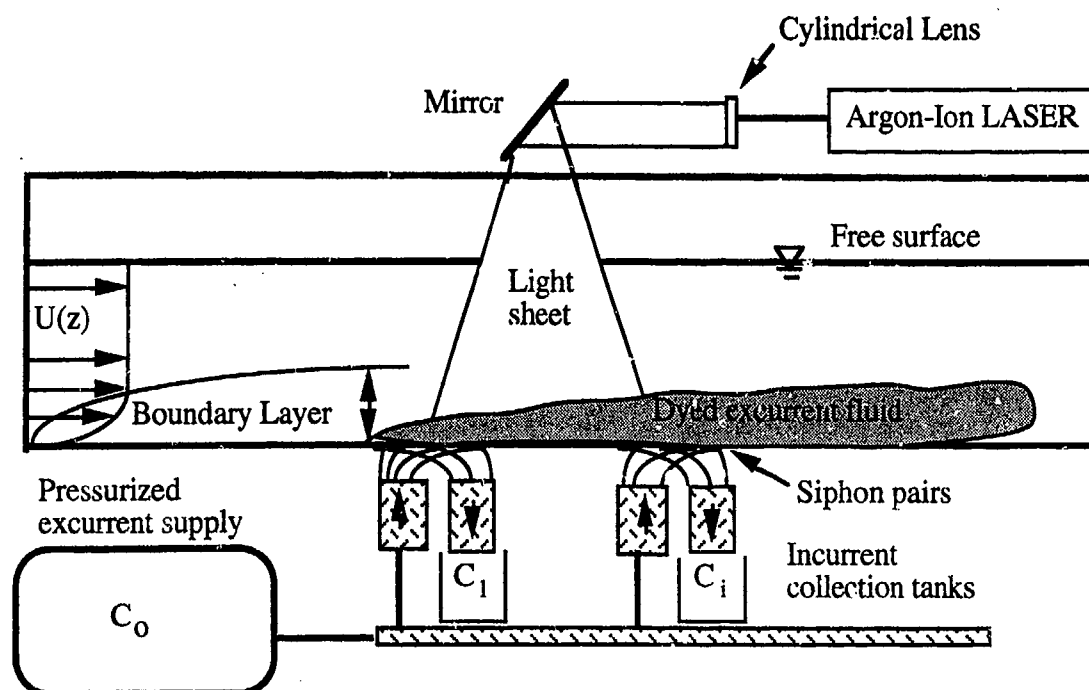


Fig.1 Sketch of experimental test section in the flume facility

controlled by a downstream weir. To ensure a constant free-stream velocity, a 4 m high constant head tank is used to drive the flow through a diffuser into the inlet section. Secondary motions in the flume are reduced by a series of three screens of decreasing sizes in the inlet section. The flow then enters the channel section after passing through a 4:1 contraction.

Flow depth varied between 24 and 28 cm, giving free stream velocities, measured well outside of the boundary layer, of between 8 and 40 cm/s which represents the range of velocities often seen in shallow estuaries. The adjustable weir was calibrated against measured free stream velocities using a single-component, tracker-based laser-Doppler velocimeter (LDV). The flow rate in the channel was then calculated by measuring the height of the water surface above the weir. The turbulent boundary layer in the channel section was tripped using a 3 mm diameter bar 2.2 meters upstream of the test section, shown in Fig. 1.

Shear velocities, u_* , were calculated by fitting the measured velocity profile to the "law of the wall" smooth wall velocity distribution given by Ref 13:

$$u^+(z^+) = \frac{1}{K} \ln(z^+) + 5.5 \quad (4)$$

where the normalized mean velocity is defined as $u^+ = u/u_*$ and the nondimensional height above the boundary: $z^+ = zu_*/\nu$. For this range of cross

flows, u_* , values are approximately 5% of the free stream velocity. The test section surface is hydrodynamically smooth when there is no siphon pumping, and the thickness of the inner region of the boundary layer measured upstream of the test section extended to $z^+ = 300$, or to heights between 30 and 75 mm above the bottom for the range of flow velocities used here.

In the field, benthic bivalve feeding is typically confined to the inner layer, or wall region, of the turbulent boundary layer. This inner layer, defined as $z^+ < 600$, is nearly independent of the outer variables, including boundary layer thickness, δ , and freestream crossflow velocity, U_∞ (Ref 13). Therefore, because we need only to reproduce typical field values of the inner variables, u_* , and roughness height, in our flume, our experiments should represent near-bed hydrodynamics occurring in nature (Ref 7).

Experiments were conducted with false sidewalls along the test bed at a width of 25 cm to provide symmetry planes for the excurrent jets at the edges of the model test section. The reason for doing so was to eliminate lateral entrainment of ambient water on the sides of the test bed.

Full scale physical models of a bed of the bivalve species *Tapes japonica* and *Potamocorbula amurensis* were installed in the test section of the flume. The models consisted of separate tubing for incurrent and excurrent siphons and was based on the model of an individual bivalve used in Ref 7. Fig. 2 shows the siphon pair layout

with S , d_o , d_i , and h_s defined. The siphons were installed in a strip 180 cm long and 20 cm wide in the center of the test section. The strip consisted of nine sections of siphons, each 20 cm x 20 cm. For this study the model siphons were held in a fixed orientation (siphons perpendicular to the cross flow), and siphons were either flush or raised above the bed by 10 mm. Each group of siphons was connected separately via tubing to a pressurized tank which supplied excurrent fluid and to a set of receiving tanks that collected incurrent fluid (Fig. 1). Equal flow through incurrent and excurrent siphons was ensured by the use of calibrated flow meters. Modeling considerations of this type of experiment are discussed in Ref 10.

The dimensions of the models and the experimental conditions are summarized in Table 1.

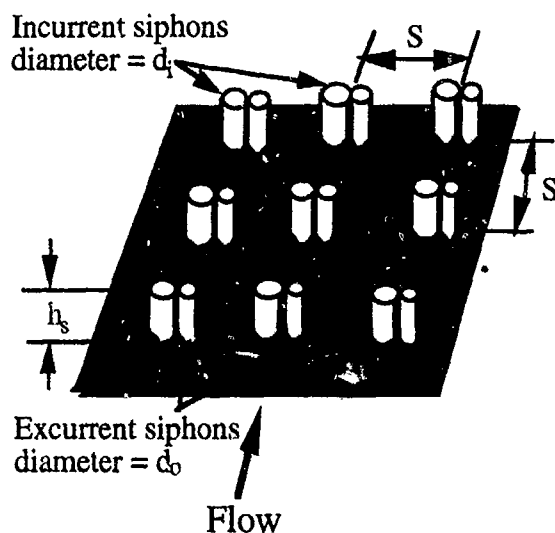


Fig. 2: Perspective view of a portion of the siphon pair array

Table 1. Experimental Conditions

	<i>T. japonica</i>	<i>P. amurensis</i>
d_o (mm)	5.5	3.0
d_i (mm)	2.5	1.5
S (mm)	40	9.5
h_s (mm)	0, 10	0
u_j (mm/s)	98, 197	16, 32
Re_x	170,000-1,500,000	
U_∞ (mm/s)	80-400	
u_s (mm/s)	4-20	

3. EXPERIMENTAL METHODS

Experiments to quantify refiltration (pumping of phytoplankton depleted water from bivalves upstream) by a population of model bivalves were carried out in the test section as shown in Fig. 1. We used sodium fluorescein dye as a tracer to represent phytoplankton-depleted water ejected from excurrent siphons. The excurrent jets of the bivalves were marked with a known dye concentration of about $5 \times 10^{-7} M$ (Molar concentration) which was delivered from a pressurized tank. Incurrent fluid was forced through the incurrent siphons by gravity and was collected from each of the nine banks of model bivalves. Fluorescence of the incurrent fluid was determined and was compared to the fluorescence of the excurrent fluid. Fluorescence measurements were made using a Turner Designs Fluorometer. The amount of refiltration was determined by comparing quantities of the tracer "filtered" by each portion of the bed to the amount of tracer in the excurrent fluid. The results are expressed in terms of a refiltration fraction:

$$n = \frac{C_i - C_\infty}{C_o - C_\infty} \quad (5)$$

where C_i is the fluorescence of incurrent fluid, C_o is the fluorescence of the excurrent fluid, and C_∞ is the fluorescence of the ambient fluid. The refiltration fraction represents the percentage of phytoplankton-depleted fluid an individual bivalve would filter.

Additional information about the average growth of the concentration boundary layer above the bed was obtained from flow visualization using the planar laser-induced fluorescence technique (PLIF - see Ref 14, Ref 15). In this technique, fluorescent dye is illuminated with a thin sheet of laser light and a charged coupled device (CCD) camera is used to capture images of dyed excurrent jet flows (see Fig. 1). Because the intensity of the fluoresced light is proportional to the local dye concentration (Ref 14), this technique gives a quantitative description of the structure of the concentration field. In this case the dye concentration field represents the distribution of phytoplankton-depleted fluid above the bed of bivalves.

The setup for capturing and processing of PLIF images consists of the following; the beam from a 2 watt Ar-Ion laser is passed through a 1 meter

focal length convex lens and a cylindrical lens, creating a 0.5 mm thick laser sheet that is projected into the flow parallel to the free stream direction, illuminating a 20 cm wide vertical section of the flow (PLIF data was recorded at two locations, 0.5 m and 1.5 m downstream from the leading edge of the bivalve bed); a Tiffen orange 15 filter is used before the camera lens to eliminate background scattered light; a Pulnix monochrome CCD camera (640 x 480 pixels) collects the emitted light and converts it to analog NTSC signal; a Perceptics PixelPipe board on a MacIIfx is used to grab and average images with image processing software (PixelTools, Spyglass Transform, GTFS Ultimate, LabVIEW2). Using this system we acquired images with a pixel resolution of $\Delta x = \Delta z = 0.25$ mm. Based on the speed of the crossflow and an estimate of the turbulent fluctuations of the flow (10% of the freestream velocity), the Kolmogorov length scale was estimated to be between $0.11 \text{ mm} < L_k < 0.49 \text{ mm}$. The estimated error of concentration values determined using PLIF is between 5% and 7%.

Relative concentration profiles were calculated from nine second (256 frames) averages by taking vertical sections through images comparing corrected concentration values to the excurrent jet concentration. Digital techniques have been used to correct for the Gaussian laser intensity distribution, light absorption, camera gain, and background dye concentration (see Ref 15). The images are used for analysis of the

structure of the flow and the vertical extent of the concentration boundary layer.

4. RESULTS

4.1 Refiltration

The downstream distribution of refiltration for experiments with siphons flush and $0.2 < VR < 0.8$ is shown Fig. 3.

In each of these cases, a concentration boundary layer develops, as indicated by the increase of the refiltration fraction with distance downstream. Maximum refiltration values for the 1.8 m bed were found to be between 18% for $S/d_o = 16$, and 50% for $S/d_o = 6$. Note that the orientation used in this experiment is predicted to be the most beneficial feeding position, leading to the lowest amount of refiltration (none was found for a single bivalve in this orientation, see Ref 7). An orientation of the siphons parallel to the cross flow may result in substantially greater amounts of refiltration.

When results are normalized by S/d_o we can express the refiltration as a power law defined by:

$$n = \beta \left(\frac{d_o}{S} \right) \left(\frac{x}{d_o} \right)^{0.25} \quad (6)$$

where $0.3 < \beta < 0.6$ depending on the velocity ratio, VR. The data in Fig. 3 that fall below this line are for experiments conducted with raised siphons.

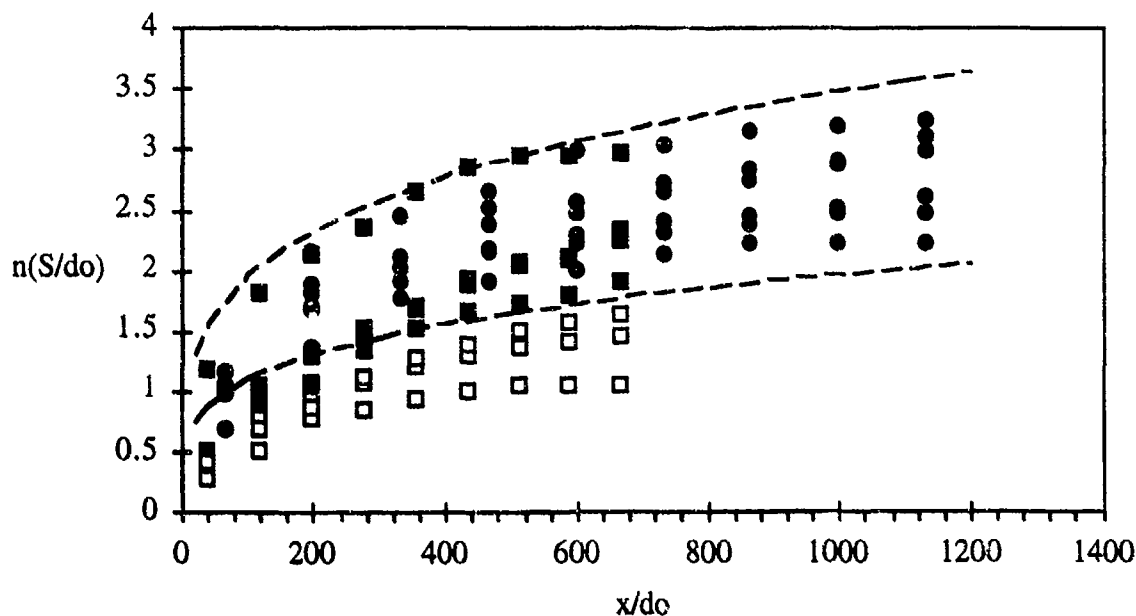


Fig. 3 Results of refiltration experiments with siphons flush and (■) $S/d_o = 16$, (●) $S/d_o = 6$, and (□) $h_s = 10$, $S/d_o = 16$. The dotted lines represent the curves defined by (6).

The dependence of β on VR is difficult to specify. The general trend is that β decreases with increasing VR for flush siphons (see Fig. 4) and $VR > 0.2$. However when siphons are elevated, β increases with increasing VR indicating the importance of siphon height in higher cross flow velocity or lower u_j regimes. In addition, results of experiments with $S/d_o = 6$ show that for $VR < 0.2$ the value of β decreases. This suggests that in the very low VR regime there is an increasing importance of the strength of the crossflow, or the value of u_* in mixing excurrent fluid with the freestream. In the region $VR > 0.8$ it appears that β may approach an asymptotic value regardless of siphon height. (Note that in these experiments we found a linear relationship between U_∞ and u_* just upstream of the jets, therefore we could plot the data as a function of u_j/u_* with equally little scatter).

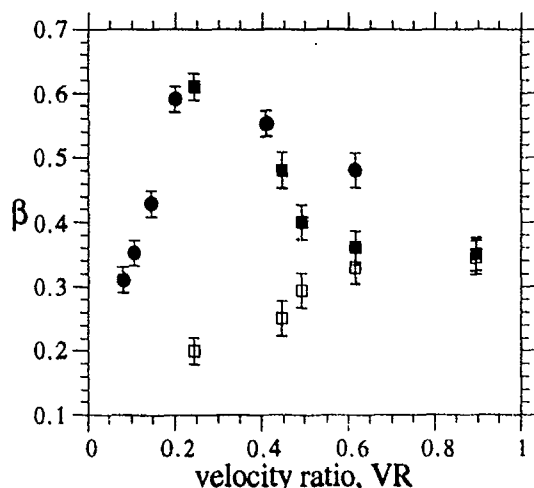


Fig. 4. Values of the coefficient β as a function of VR, with *T. japonica*, $h_s = 0$ (■) and $h_s = 10$ mm (□), and *P. amurensis*, $h_s = 0$ (●).

4.2 CONCENTRATION FIELDS

We can examine the mixing of excurrent jet fluid near the bed which results in refiltration using PLIF. Examining unprocessed video images, we see a strong dynamical interaction between the siphon pairs. Dye from excurrent siphons upstream can be seen entering incurrent siphons downstream. The jets appear to be bent over by the boundary layer cross flow and the interaction results in a series of smaller scale vortices which merge and roll up on each other creating a continuous layer of dye that thickens gradually

with distance downstream (Fig. 5). Turbulent eddies of ambient fluid approximately 3 cm in diameter can be seen penetrating to the boundary. At the lowest crossflow speed (8 cm/s) the dye layer has a vertical extent of approximately 5 cm ($z/d_o = 15$), at a distance 1.5 m from the leading edge of the bed (Fig. 5b). As the cross flow velocity increases, we observed a thinning (in actual height) of the concentration boundary layer and a decrease in the vertical extent of intermittent plumes of dye. At 40 cm/s the dye plumes extended to less than 2 cm ($z/d_o = 8$) above the bed. As VR decreased we observed increasing deflection of the jets until at very low VR the jet appeared to be completely deflected at the edge of the siphon and the excurrent fluid remains attached to the boundary downstream.

We also examined time series of concentration profiles to describe dominant features of the jet/boundary layer interaction. Instantaneous profiles of the concentration field through the center of a single excurrent jet sampled from sequential video frames were compiled into single images.

A time series of vertical concentration profiles 1.5 m from the leading edge for $S/d_o = 16$, $VR = 1.23$ is shown in Fig. 6. The brightest region at the bottom of the image represents the jet core. It ends abruptly in the region where the jet is bent over by the flow. Just above the bright jet region is a zone of lower concentration ambient fluid. This fluid is a result of entrainment of ambient fluid underneath the jet immediately upstream, which has been observed in experiments of a single jet in a cross flow (Ref 8). The flow far above the jet is characterized by plumes of dye originating from excurrent jets upstream which are advected downstream. Large blobs of ambient (clear) fluid penetrate to the jet region of the concentration boundary layer approximately every 5 seconds. Although the time scales of the mixing structures changes when $VR < 1$ we observed that a region of ambient fluid entrainment within the concentration boundary layer persists just above the excurrent jet. It is evident from images such as this one that the region close to the bed is dominated by the dynamics of the jet and the jet/cross flow interaction, whereas the mixing in the outer region of the concentration boundary layer is dominated by advection due to the cross flow.

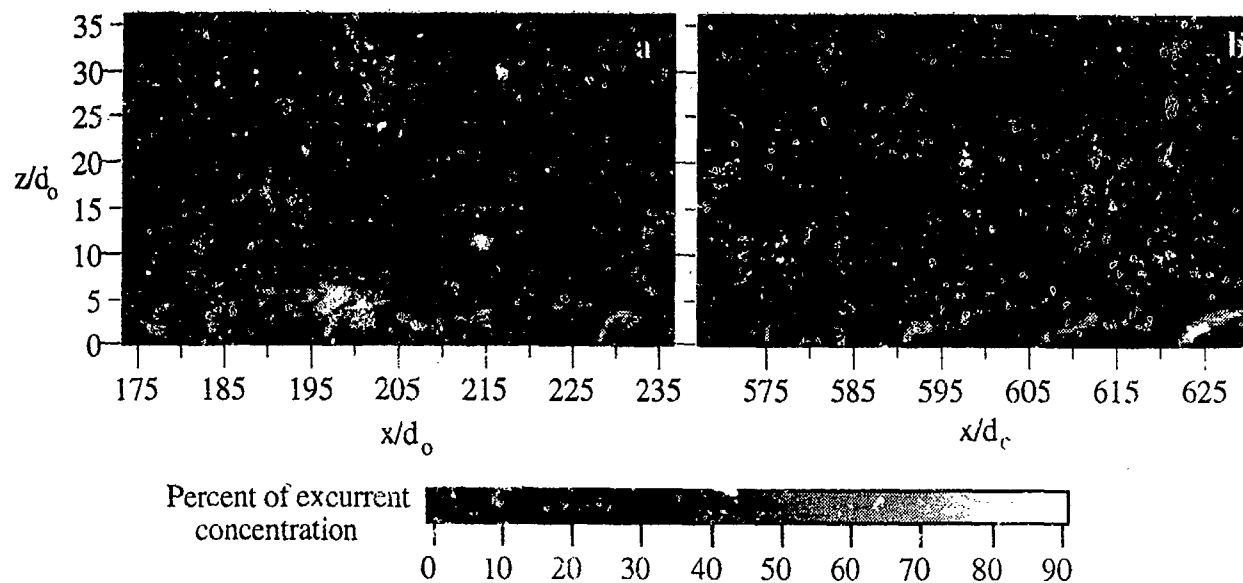


Fig. 5: Instantaneous digital PLIF images with $h_s=0$, $S/d_0=6$, and $VR=1.23$ at a) $x=0.5$ m and b) $x=1.5$ m.

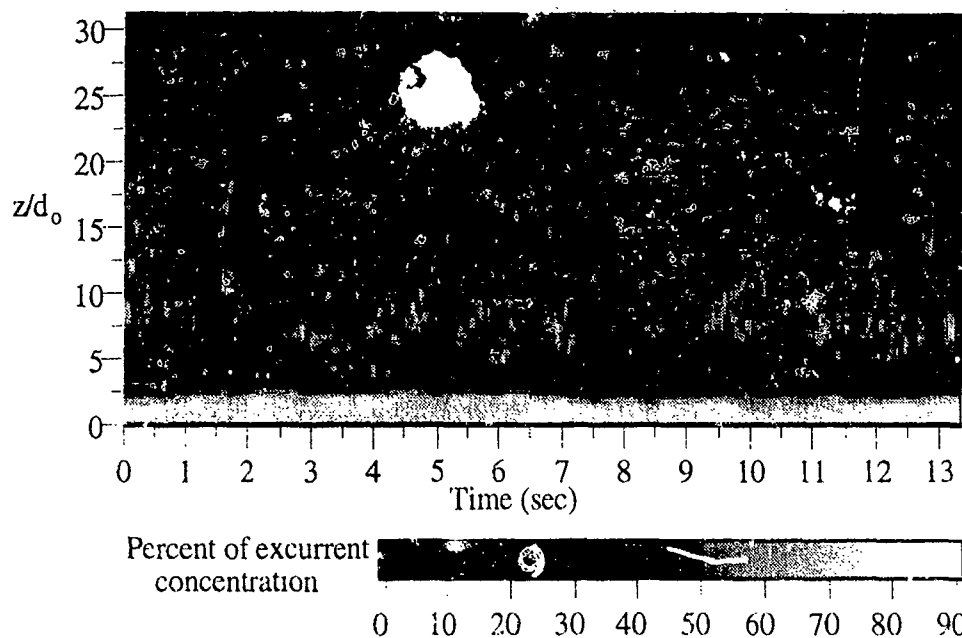


Fig. 6: Digital PLIF image showing a time series of concentration profiles above a model excurrent jet of *Tapes japonica* at $x=1.5$ m with $h_s=0$ and $VR=1.23$.

To summarize our results in terms of the jet/boundary layer interaction, we have normalized the values of jet penetration, z_{out} , and jet spreading width, σ , by the jet in a cross flow parameter z_m (defined earlier), and plotted them as a function of velocity ratio, VR (Fig. 7).

We have defined z_{out} as the height above the siphons at which we see the maximum dye concentration, and σ , as the height above the

boundary at which the concentration drops to 5% of the excurrent jet concentration. This information was obtained from the averaged images of excurrent jets at a distance $S/2$ downstream of the siphon for a range of values of VR and two siphon heights. If the jets within the concentration boundary layer behaved as jets in a uniform cross flow and were only a function of the relative jet strength, then we would expect this nondimensionalization of z_{out} and σ to

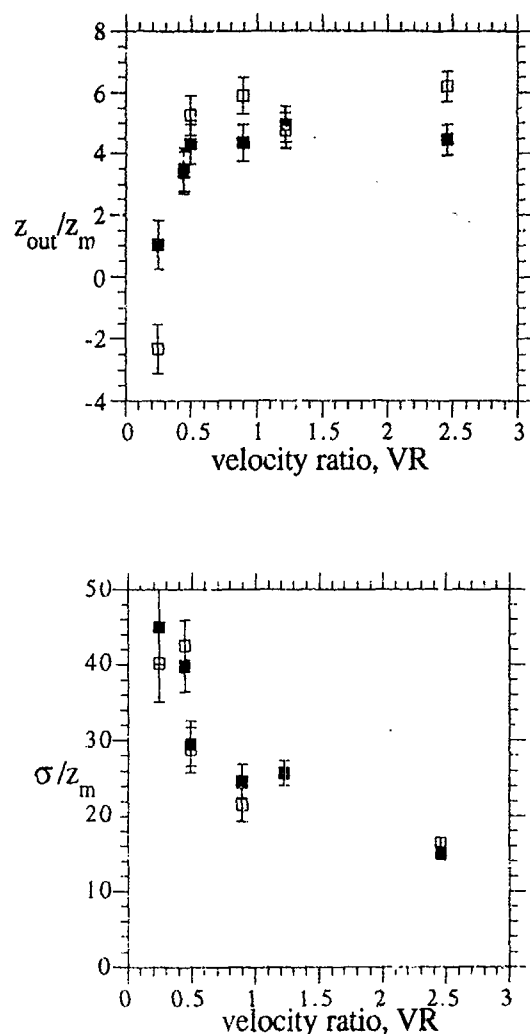


Fig. 7: Jet penetration, z_{out} , and jet spreading width, σ , as a function of VR for *T. japonica* with $h_s=0$ (■) and $h_s=10$ mm (□).

result in a constant value at all VR. Note however, that as the cross flow velocity increases relative to the jet velocity, z_{out}/z_m decreases indicating that the shear in the boundary layer bends the jet over further than predicted for a jet in a uniform cross flow. The dimensionless σ/z_m increases in the region $VR < 0.8$, suggesting the effects of increased mixing. In addition, z_{out}/z_m is slightly higher when siphons are raised suggesting the influence of additional drag on the mean flow which allows the jet to penetrate further into the boundary layer.

However, when VR decreases, z_{out}/z_m becomes negative when the siphons are raised and $VR=0.2$. This is a result of the dye plume being drawn down by the crossflow below the level of the incurrent siphons. At values of $VR > 0.8$, the

values of z_{out}/z_m approach a constant, indicating that jet-in-uniform-cross flow theories can be applied to siphonal currents in this flow regime. Note that the representation in Fig. 7 indicates that we can represent z_{out} and σ as some function of the velocity ratio, or

$$\frac{z_{out}}{d_o} = f(VR) \quad (7)$$

$$\frac{\sigma}{d_o} = f(VR)$$

This is similar to the results of Ref. 16, where they found these parameters to be only a function of VR and distance from the jet.

5. DISCUSSION

5.1 ROUGHNESS AND VELOCITY SHEAR

Lower refiltration values, elevated plumes and increased mixing seen in the experiments using elevated siphons are most likely due to the combination of two factors: roughness and velocity shear. The small scale bed roughness is significantly increased by the protrusion of the tubes from the flume floor, thereby increasing turbulent mixing and wall shear stress (Ref 17).

The second factor affecting mixing is the effect of higher cross flow velocities acting on the jet as it is injected into the flow at a higher location in the boundary layer. Elevated siphons and higher animal pumping rates tend to increase the effective height of the release of the phytoplankton-depleted plume. As the plume is elevated above the bed, it experiences a higher cross flow velocity, and therefore, we would expect increased bending of the jet, increased mixing, and lower refiltration.

Our results indicate a complex interaction of the jet dynamics with that of the turbulent boundary layer. Average concentration profiles from flow visualization (see Ref 10) have shown that the crossflow affects the distribution of excurrent jet fluid in two different ways - through its direct effect on the trajectory of the jets and through its effect on mixing near the bed. This finding is consistent with that of Ref 12. At low VR, they find that little penetration of the jets into the mainstream occurs and the jets are attached to the surface. As VR is increased the jets penetrate further, the jets mix rapidly and the region beneath the jet is ventilated by the mainstream. As noted by other researchers, we have found the most important independent flow parameter to be VR. We have also found that jet

penetration increases with increasing distance between the jets. Ref 12 also found that hole spacing (S/d_o) has a large influence on the heat transfer coefficient. However our study of multiple jets in a crossflow (hundreds to thousands) is on a scale much larger than that which has been examined experimentally to date (2-10 jets). We have found that the parameters VR and S/d_o alone cannot parameterize the behavior of the siphonal jets in the presence of incurrent sinks.

5.2 MASS TRANSFER ANALYSIS

We have used PLIF to observe the structure of the flow near the bed of model siphons and have seen that the water motion, in particular the jet/boundary layer interaction can affect the refiltration ratio by controlling the thickness of the concentration boundary layer which forms over the bed. This has been observed by others in nutrient and phytoplankton uptake studies of corals and sessile organisms (Ref 18). If we assume that the flow over siphonal jets is similar to a turbulent boundary layer over a rough bottom, we can develop an expression for the Stanton number for mass transfer, St_m , based on the analogy between heat and mass transfer (see Ref 19). If we let C_b be the bulk average concentration of phytoplankton in the freestream fluid, and h be the total depth of the flow, then $U_b C_b h$ is the total mass flux passing over the bivalve bed. Let \dot{m} be the rate of transfer of the ambient fluid to the bivalves. We can define the Stanton number for mass transfer as :

$$St_m = \frac{\dot{m}}{U_b(C_b - C_w)} \quad (8)$$

where C_w is the concentration at the wall surface. St_m represents a limitation on the mass transfer rate to the surface.

St_m has been shown to be a function of Re_x , Schmidt number, Sc , surface geometry, and the roughness Reynolds number, Re_k . In applying correlations for Stanton numbers from the heat transfer literature, we have made several assumptions. First, we have ignored the excurrent and incurrent flow dynamics and treat the flow over the siphonal currents as flow over a rough boundary. We have used the total penetration of the excurrent jets, z_{out} , as the heights of roughness elements. We can then define roughness Reynolds number as:

$$Re_k = \frac{u_* z_{out}}{\nu} \quad (9)$$

We have calculated values of u_* based on the skin friction:

$$u_* = \left(\frac{\tau_w}{\rho} \right)^{1/2} = U_b \left(\frac{c_f}{2} \right)^{1/2} \quad (10)$$

We have used the correlation for skin friction given in Ref. 20 for turbulent boundary layers over two dimensional roughness elements :

$$\left(\frac{c_f}{2} \right)^{-1/2} = \frac{1}{K} \ln \left(\frac{84\delta}{k_s} \right) \quad (11)$$

which yields similar values to the correlation for rough pipe flow given by Ref 21 :

$$\left(\frac{c_f}{2} \right)^{-1/2} = -5.1 \log_{10} \left[\frac{6.9}{Re_x} + \left(\frac{k_s}{14.8h} \right)^{1.11} \right] \quad (12)$$

Ref. 20 also gives an expression for the Stanton number based on similarity concepts:

$$St_m = \frac{c_f/2}{Sc_t + (c_f/2)^{1/2}/St_k} \quad (13)$$

where Sc_t is the turbulent Sc in the outer layer. Experimental data for air suggest that the heat transfer equivalent, Pr_t is approximately constant at 0.9 independent of Pr (Ref. 22). The Stanton number for roughness elements, St_k , is given by the correlation:

$$St_k = 5.19 Re_k^{-0.2} Sc^{-0.44} \quad (14)$$

for $70 < Re_k < 2400$. We note that Eq. 14 is only validated for $0.7 < Sc < 6$.

We now compare Stanton number results from our experiments to those expected from correlations for flow over rough boundaries. For the observed values of St_m , we calculated \dot{m} by using the refiltration fraction, n , defined earlier, to represent the normalized concentration of freestream fluid which is transferred to the incurrents. Then,

$$\dot{m} = \frac{(1-n)Q_p}{A_p} \quad (15)$$

where Q_p is the flow per plate or section of the bed and A_p is the total area of the plate. The total flow through the plat is equal to the sum of the flow through the jets, or

$$Q_p = \eta u_j A_j \quad (16)$$

where η is equal to the number of jets per plate and A_j is the area of the jet. We can now write

$$St_m = \frac{\eta(1-n)}{(C_w/C_\infty)} \left(\frac{u_j}{U_\infty} \right) \left(\frac{A_j}{A_p} \right) \quad (17)$$

where the freestream velocity was used to represent the bulk velocity over the bed, C_w is

the average concentration at the wall determined from PLIF images, and the concentration term C_b is taken to be 1. Eq. (17) indicates that we should expect St_m to be proportional to VR.

Results of calculations for experiments with $S/d_0=6$ do show an increase in Stanton number with an increase in velocity ratio (Fig. 8). We can see that although we have included the jet penetration in our calculations for St_m in flow over rough beds, this simplification does not reproduce the observed results. The dynamical effect of the jet/boundary layer interaction appears to play an important role in the mixing of phytoplankton fluid and this process cannot be modeled as flow over a rough boundary. We observed that the fluid at the wall never consists of purely excurrent fluid. In other words, ambient fluid (food-rich fluid) is constantly being mixed down to the bed. The only region in the boundary layer in which we see total food depletion is at the excurrent siphon exit. Therefore the feeding process of the bivalves is not mass transfer controlled and correlations for mass transfer over rough boundaries will not apply well in this case.

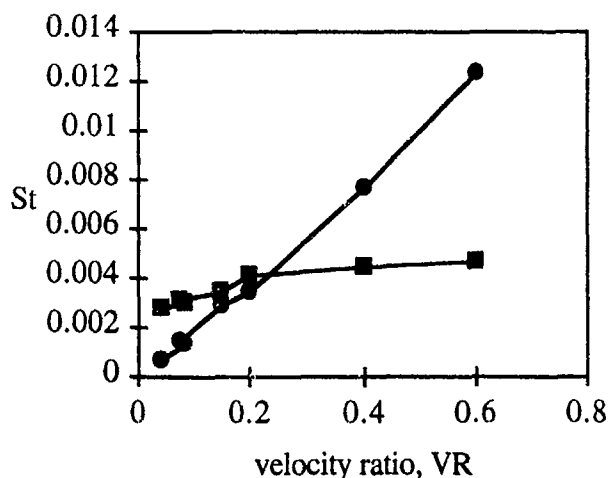


Fig. 8: Stanton numbers for mass transfer at the wall observed for model siphons with $S/d_0=6$ and $h_s=0$ (●), and calculated for turbulent flow over a rough boundary (■).

In addition, it is important to note that the above correlations have been developed for heat and mass transfer at the boundary in gas flows which are characterized by low Schmidt numbers (0.5-1.0). In experiments using fluorescent dye in water the Schmidt number is much higher. For our calculations we have used $Sc=2075$ (Ref. 23). The large Schmidt number used here indicates the relatively large effect of momentum

diffusion to that of mass. Therefore values of Stanton number calculated with a high Sc may not reflect the relative importance of momentum flux in these flows.

6. CONCLUSIONS

The formation of concentration boundary layers (phytoplankton-depleted regions) over beds of model siphonate bivalves can inhibit aggregate feeding efficiency by reducing filtration rates of animals by as much as 50%. The amount of refiltration was found to be a function of VR, S/d_0 , and x/d_0 .

The general trend in the data show that an increase in the siphon height increases roughness and mixing, reducing refiltration fraction. Increasing VR has two effects. First, it increases the flux of dye, or phytoplankton-depleted fluid, into the boundary layer so that there is more fluid available for refiltration. Second, it increases the height of rise of this fluid due to the increased vertical momentum of the jets. When siphons are flush, increasing VR lowers refiltration, because the jets rise higher over the incurrent siphons. However, when the siphons are raised and VR is increased, fluid that was previously drawn down below the level of the incurrent siphons now has more vertical momentum and stays at the level of the incurrent siphons, thereby increasing the likelihood that refiltration will occur. In addition, we found that refiltration is inversely proportional to S/d_0 . Finally, we showed that calculations of Stanton numbers for mass transfer do not correlate well with flow over rough boundaries. Further experiments with measurements of velocity fields will enable us to understand the momentum flux at the bed due to siphonal jets and may help us to define a generalized model for phytoplankton depletion at the bed.

ACKNOWLEDGMENTS

This work has been funded by the NSF, Division of Biological Oceanography, and the Charles Lee Fowell Foundation.

REFERENCES

1. Frechette, M., and E. Bourget, "Food-limited growth of *Mytilus edulis* L. in relation to the benthic boundary layer", *Can. J. Fish. Aquat. Sci.*, 42, 1985, pp. 1166-1170.
2. Cloern, J. E., "Does the benthos controls the phytoplankton biomass in South San

- Francisco Bay?", *Mar. Ecol. Prog. Ser.*, 9, 1982, pp. 191-202.
3. Nichols, F.H., "Increased benthic grazing: an alternative explanation for low phytoplankton biomass in Northern San Francisco Bay during the 1976-1977 drought," *Estuar. coast. shelf Sci.* 21, 1985, pp. 379-388.
 4. Peterson, C.H., and R. Black, "Resource depletion by active suspension feeders on tidal flats: influence of local density and tidal elevation", *Limnol. Oceanog.*, 32, 1987, pp. 143-166.
 5. Butman, C.A., Frechette, M., Geyer, W., and Starczak, V. submitted. "Flume effects on food supply to the blue mussel *Mytilus edulis* L. as a function of boundary-layer flow" *Limnol. Oceanog.*
 6. Ertman S.C. and P.A. Jumars, "Effects of bivalve siphon currents on the settlement of inert particles and larvae", *J. Mar. Res.*, 46, 1988, pp. 797-813.
 7. Monismith, S.G., J.R. Koseff, J. Thompson, C.A. O'Riordan., and H. Nepf, "A study of model bivalve siphonal currents", *Limnol. Oceanog.*, 35, 1990, pp. 680-696.
 8. Fric, T., and A. Roshko., "Structure in the near-field of transverse jet", In: *Proc. 7th Symp. Turbulent Shear Flows*, Stanford Univ., 1989, pp. 6.4.1 to 6.4.6.
 9. List, E.J., "Turbulent jets and plumes" *Annu. Rev. Fluid Mech.*, 14, 1982, pp. 189-212
 10. O'Riordan, C.A., Monismith, S.G., Koseff, J.R.. 1993. An experimental study of concentration boundary layer formation over a bed of model bivalves. *Limnol. Oceanog.*, In press.
 11. Holdeman, J.D., and R.E. Walker, "Mixing of a row of jets with a confined crossflow", *AIAA Journal*, 23, 1985, pp. 1679-1683.
 12. Sherer V., Wittig, S., Morad, K., and N. Mikhael, "Jets in a crossflow: Effects of hole spacing to diameter ratio on the spatial distribution of heat transfer", ASME conf paper: *Int. Gas Turbine & Aeroengine Congress & Expeo*, Orlando, FL, June, 1991.
 13. Hinze, J.O., "Turbulence", McGraw-Hill, 1975
 14. Prasad, R.R. and K.R. Sreenivasan, "Quantitative three-dimensional imaging and the structure of passive scalar fields in fully turbulent flows", *J. Fluid Mech.*, 216, 1990, pp. 1-34.
 15. Kooschesfahani, M.M., and P.E. Dimotakis, "Laser-induced fluorescence measurements of mixed fluid concentration in a liquid plane shear layer", *AIAA Journal*, 23, 1985, pp. 1700-1707.
 16. Savory, E., and N. Toy, "Real-time video analysis of twin jets in a crossflow", *J. of Fluids Engineering*, 113, 1991, pp. 68-72
 17. Grass A.J., "Structural features of turbulent flow over smooth and rough boundaries", *J. Fluid Mech.*, 50, 1971, pp. 223-256.
 18. Jumars, P.A. and Nowell, A.R. "Fluid and sediment dynamics on marine benthic community structure", *Amer. zool.*, 24, 1984, pp. 45-55.
 19. Bilger, R.W. and M.J. Atkinson, "Anomalous mass transfer of phosphate on coral reef flats", *Limnol. Oceanogr.*, 37, 2, 1992, pp. 261-272.
 20. Kays, W.M., and M.E. Crawford, "Convective heat and mass transfer" McGraw-Hill, 1980.
 21. Haaland, S.E., "Simple and explicit formulas for the friction factor in turbulent pipe flow", *J. Fluid. Eng.*, 105, 1983, pp. 89-90.
 22. Dipprey, D.F. and D.H. Sabersky, "Heat and momentum transfer in smooth and rough tubes at various Prandtl numbers", *Int. J. Heat Mass Transfer*, 6, 1963, pp. 329-353.
 23. Dahn, W.J. and K.B. Sutherland, "Direct, high resolution, four dimensional measurements of the fine scale structure of $Sc \gg 1$ molecular mixing in turbulent flows", *Physics of Fluids*, 3, 1992, pp. 1115-1127.

EXPERIMENTS ON THE GROUND VORTEX FORMED BY AN IMPINGING JET IN CROSS FLOW

William B. Blake
Wright Laboratory (WL/FIGC)
Wright Patterson Air Force Base, Ohio 45433
U.S.A.

Vearl R. Stewart
KSA Technology
5689 Plum Orchard Dr.
Columbus, Ohio 43213
U.S.A.

SUMMARY

An inclined jet impinging on the ground creates a wall flow that spreads radially from the point of impingement. If a cross-flow is introduced, the upstream component of the wall flow will separate from the ground and create what has been termed the "ground vortex". The ground vortex has been shown to have a significant impact on aircraft aerodynamics and is one of the major contributors to hot gas ingestion. The paper will review experimental studies of the ground vortex. It will also discuss a recent study which included a generic wing-body configuration for assessing the impact of the ground vortex on configuration aerodynamics. Wind tunnel tests using fixed ground boards, moving ground belts, and moving model tests will be discussed. The emphasis of the data to be presented will be macroscopic, i.e. forward location of the vortex, effects of ground height, etc.

SYMBOLS

A	Jet area
c	Wing mean aerodynamic chord
C_L	Lift coefficient, $L/q_\infty S$
C_m	Pitching moment coefficient, $M/q_\infty S c$
C_p	Pressure coefficient, $(p_{\text{local}} - p_\infty)/q_\infty$
d	Jet diameter, equivalent diameter for non-circular jets, $\sqrt{(4A/\pi)}$
h	Height of jet exit above ground
p_∞	Free-stream static pressure
q_∞	Free-stream dynamic pressure, $1/2 \rho V_\infty^2$
S	Wing area
V_b	Velocity of moving ground belt
V_i	Jet velocity at ground impingement point
V_j	Jet exit velocity
V_∞	Free-stream velocity

V_R	Ratio of jet exit to free-stream velocity, V_j/V_∞
x_i	Distance along ground from jet centerline to impingement point
x_s	Upstream distance from jet centerline to ground vortex separation point
y_j	Distance from plane of symmetry to jet center for side-by-side jets
δ	Jet deflection angle, measured from streamwise direction, positive down.

1. INTRODUCTION

An inclined jet impinging on the ground creates a wall flow that spreads radially from the point of impingement. The wall jet flow does not spread indefinitely; it will ultimately decay from viscous dissipation or be stopped by some intervening mechanism. If a cross flow is introduced, the upstream component of the wall jet will separate from the ground some distance forward of the impingement point. A large separation bubble is created which has been termed the "ground vortex" due to its rotational nature. It is not a vortex in the sense of increasing local velocities as the core is approached. It is a turbulent separation bubble inside which the jet and cross-flow mix.

A ground vortex can be generated by virtually any type of V/STOL aircraft operating in ground effect. The downwash from a helicopter rotor, jet nozzle, lift fan, or ejector can all act as the source of the wall flow from which the ground vortex emanates. The flowfield established by the ground vortex can cause significant changes in aircraft lift and pitching moment. In a sideslip condition, large rolling moments can also be generated. The performance of a helicopter tail rotor in sideward and rearward flight is affected by the ground vortex. In

TABLE 1 - SUMMARY OF GROUND VORTEX INVESTIGATIONS

Investigator	Ref	Year	Facility	Belt	h/d	V_R	Data
Abbott	1	1967	Moving model	-	4,20	25-70	Flow vis.
Colin & Olivari	2	1969	Wind tunnel	No	4	4-11	Flow vis., Pressure
Binion	3	1970	Wind tunnel	No	1,4	6-16	Flow vis., LDV
Schwantes	4	1973	Wind tunnel	No	3,8	12-22	Pressure
Weber & Gay	5	1975	Wind tunnel	No	2.5-8	20-75	Pressure
Stewart & Kuhn	6	1983	Wind tunnel	No	1-25	3-10	Pressure
Stewart	7	1987	Moving model	-	3	8-12	Pressure
Cimbala et al	8	1987	Wind tunnel	No	1-6	2.5-10	Flow vis., Pressure, LDV
Kuhn et al	9	1987	Water tunnel	Yes	2-10	6-30	Flow vis.
Stewart & Kemmerly	10	1989	Moving model	-	3	5-25	Pressure
Cimbala et al	11	1990	Wind tunnel	No	3	6-13	Flow vis., LDV
Stewart & Blake	12	1992	Wind tunnel	Yes	2-25	5-20	Flow vis., Pressure
Kuhlman & Cavage	13	1992	Wind tunnel	No	3,7	5-13	Flow vis., LDV

operations over loose terrain, the ground vortex creates and defines the cloud of debris that can damage engines and reduce visibility. It is one of the primary contributors to hot gas ingestion for both airplanes and helicopters. All of the studies discussed in this paper use a jet nozzle as the source of the wall flow.

2. EXPERIMENTAL RESULTS

2.1 Single Jet

The ground vortex phenomenon has been investigated experimentally by a series of investigators (Table 1). With few exceptions^{6,9,12}, all used a single, circular jet nozzle. A schematic of the flowfield associated with the ground vortex along with the nomenclature used in the paper is shown in Figure 1. The bulk of the tests used flow visualization or ground pressure data to investigate the size and shape of the ground vortex flowfield. Direct comparison between the two techniques^{2,8} has shown excellent agreement.

A typical⁶ centerline distribution of the pressure coefficient measured on the ground is shown in Figure 2. The ground vortex is characterized by a region of negative pressure (in terms of C_p) forward of the high positive impact pressures. The maximum negative pressure is found approximately under the vortex center. The point of zero pressure coefficient has been established as the forward edge of the ground vortex, where the wall jet separates from the ground². A small positive pressure region is found forward of the ground vortex, as the flow

decelerates to move up and over it.

The structure of the ground vortex is seen in the flowfield measurements from Cimbala et al³ (Figure 3). This figure, a time averaged velocity vector plot, provides a visualization of the mean flow in the vicinity of the ground vortex. The ground vortex is elliptical in shape. The velocity profile through the center indicates it is not a classical vortex with increasing velocities near the core.

The forward extent of the ground vortex has been defined as the distance between the jet centerline and the separation point, x_s , by some investigators and as the distance between the impingement point, x_i and the separation point by others. Use of one or the other can be restricted by the test technique. The difference between the two definitions is insignificant at low ground heights ($h/d < 5$) if the velocity ratio is sufficiently large ($V_R > 8$). Both definitions will be used in this paper, depending on the availability of the relevant data.

2.1.1 Fixed Ground Board Tests

The majority of existing data (Table 1), obtained in a wind tunnel without a moving ground belt, include the effects of a ground boundary layer. All of these studies used circular jet nozzles. Stewart & Blake¹² investigated two non-circular nozzles in addition to a circular nozzle. These were a rectangular nozzle of aspect ratio three (major axis perpendicular to the free-stream) and a set of side-by-side rectangular "thrust reverser" nozzles directed 30 degrees forward from vertical (120 degrees from the

aft streamwise direction). The data report from this test has not yet been published. Many of the results are given here for the first time. In the figures that follow, these will be referred to as the "circular", "rectangular" or "thrust reverser" results.

For a circular nozzle, all investigations since that of Binion³ have found the upstream penetration of the ground vortex to be essentially constant up to a height of four jet diameters above the ground ($h/d=4$). The upstream penetration from these data (taken at a height ratio between two and four) are shown in Figure 4. Colin and Olivari² developed a semi-empirical expression for the upstream penetration by assuming the kinetic energy of the wall jet is equal to the kinetic energy in the cross flow at the separation point. Their parameter is based on the flow conditions at the impingement point. Assuming negligible decay of the jet, it can be written in terms of the jet exit velocity as follows:

$$\frac{x_s - x_i}{d} = 1.03(V_i/V_o)^{0.9} \approx V_R^{0.9} \quad (1)$$

Equation (1) also appears in Figure 4, and seems to be near the upper end of the data scatter at low values of the velocity ratio. The bulk of the data in Figure 4 fall in the V_R range of 5-15. For V/STOL aircraft, these values are representative of the operating condition in interest, low speed in ground effect.

As the velocity ratio approaches zero, the free-stream significantly reduces the velocities within the jet. This results in a decrease in the maximum pressure (and velocity) at the impingement point, invalidating the approximation made in Equation (1). At these conditions, the jet is swept downstream before reaching the ground, so no ground vortex will form. The results of Colin and Olivari² indicate zero impingement velocity is reached at a velocity ratio of about three.

The lateral shape of the ground vortex is approximated remarkably well by the simple potential flow model of a source in a uniform stream². To account for differences in penetration due to velocity ratio, we will normalize both the forward and lateral penetration of the ground vortex by the maximum forward penetration at the jet centerline, x_s . The resultant expression for the shape of the vortex is:

$$x/x_s = -(y/x_s)/\tan(y/x_s) \quad (2)$$

Results from the studies where off-centerline vortex data were obtained are shown in Figure 5 along with Equation (2). The most extensive data, obtained from the flow

visualization results of Kuhlman and Cavage¹³, agree well with both the earlier data and Equation (2).

In a small wind tunnel, blockage due to the tunnel sidewalls can affect the ground vortex penetration. Most of the investigations were conducted in large^{2,5,6} or open^{1,4,7,10,12} test sections, where blockage is not a problem. The second investigation of Cimballa et al¹¹ used two jets, 1.5 and 3 inches in diameter, in a test section 48 inches in width. The ground vortex generated by the smaller jet was found to extend further upstream by about two jet diameters compared to the large jet. It was conjectured that with less blockage, the ground vortex flowfield was able to expand and grow more effectively. Kuhlman and Cavage¹³ tested jets 0.375, 0.5, and 1 inch in diameter in a test section 32 inches in width. They found no difference in forward penetration, but a definite reduction in the lateral penetration with the largest jet. For this case, the edge of the vortex passed within four diameters of the sidewall, so some blockage effect would certainly be expected. These results indicate a value of tunnel to jet width of at least forty should be used to alleviate tunnel sidewall blockage effects.

As the height of the jet above the ground is increased, the cross flow will deflect the jet downstream to a greater extent, shifting the impingement point and reducing the amount of flow in the wall jet directed upstream. In addition, the jet will begin to decay. Each of these changes acts to reduce the forward penetration of the ground vortex. The tests which covered the greatest range of height (refs. 6 and 12) measured the forward penetration from the jet exit, not from the impingement point. To account for the height effect, Stewart¹⁴ postulates a modified form of Equation (1) which uses (h/d) in addition to $V_R^{0.9}$ as the correlating parameters. His penetration parameter is $(x_s/d)/V_R^{0.9}$. Figure 6 shows the result. Both data sets correlate very well, with the resultant curve fit yielding:

$$\frac{x_s}{d} = V_R^{0.9} \left[1 + 0.1 \frac{h/d}{V_R^{0.9}} - 0.3 \left(\frac{h/d}{V_R^{0.9}} \right)^2 \right] \quad (3)$$

Since this is referenced from the jet exit, all effects of the free-stream deflection of the jet are contained in the (h/d) terms. The flat slope of the curve near zero height in Figure 6 is indicative of the insensitivity of the vortex penetration to height when the jet is close to the ground.

At a height ratio of about four, the forward penetration of the ground vortex for a rectangular jet is nearly identical to that of the circular jet. Below this height, however, the penetration continues to increase for a rectangular jet.

Above this height, the penetration is reduced more rapidly compared to the circular jet. These effects are shown in Figure 7, which is plotted on the same scale as Figure 6. For the rectangular nozzle, the height relation analogous to Equation (2) is:

$$\frac{x_s}{d} = V_R^{0.9} \left[1.5 - (h/d)/V_R^{0.9} \right] \quad (4)$$

If the penetration parameter is modified to include the trigonometric effects of the deflection, the height relation is given by:

$$\frac{x_s}{d} = V_R^{0.9} \left[\frac{1.5 - (h/d)/V_R^{0.9}}{1 - \sin(\delta - 90)} \right] + (h/d)\tan(\delta - 90) \quad (5)$$

Using this relation, thrust reverser nozzle data are also shown in Figure 7. The data fall exactly on the rectangular nozzle results.

Although not listed in Table 1, several other variables have been studied in ground vortex investigations. Jet turbulence has been investigated in both water⁹ and wind tunnels^{11,13}, with negligible effects on the ground vortex size found in both cases. This is not surprising, since the interaction of the jet with the ground plane is a source of very high turbulence.

The effect of a large plate above or flush with the nozzle exit has also been studied. Kuhlman & Cavage¹³ found the ground vortex flowfield to be unaffected by a plate if it was greater than four diameters above the nozzle exit. Stewart & Kuhn⁶ found a plate mounted flush with the nozzle exit greatly reduced the penetration of the ground vortex if the jet height above the ground was less than four diameters. For larger heights, negligible effects were found. This effect was believed to result from a "trapped vortex" type of flow. Below a critical height, the plate prevents the entrainment of surrounding air into the wall jet. The entrainment action of the wall jet must be satisfied by drawing air from the wall jet and ground vortex itself, creating a "trapped vortex". The free-stream acts to push the vortex further aft. At a jet height of three diameters, Cimballa et al⁶ tested plates flush and two diameters above the nozzle exit. Although their plate (6d x 6d) was smaller than that used in the other two studies, they found a reduction in forward penetration with the plate flush to the nozzle exit, consistent with a "trapped vortex" type flow.

There has been no systematic study of nozzle pressure ratio (nozzle total/free-stream static). All of the jets have

been subcritical except for the results of Stewart & Kuhn⁶, some of which had choked exit conditions.

2.1.2 Moving Model/Ground Belt Tests

The absence of a ground boundary layer decreases the upstream penetration of the ground vortex. This is due to the reduced kinetic energy in the boundary layer that opposes the wall jet compared to a uniform stream (Figure 8). Depending on the thickness of the boundary layer, most or all of the wall jet may lie within it. The wall jet is very thin; the maximum velocity within it occurs below a height of one-quarter jet diameter above the ground. Three studies of the ground vortex used a jet moving relative to the ground^{1,7,10}, where there is no ground boundary layer. With the jet moving relative to the ground, the scrubbing action of the ground causes the jet to decay faster than it would over a fixed ground board⁹. This acts to further reduce the penetration.

Abbott¹, using a jet mounted on a rotating arm, studied the ground vortex with a flow visualization technique. Stewart and Kemmerly^{7,10} used a 1500 ft test track originally developed for wing trailing vortex studies (Figure 9). After acceleration to the test velocity, the jet passed over a ground plane instrumented with pressure transducers. Three rows of transducers were used which yielded time histories of the ground pressures for each run. The upstream penetration found from these moving model tests, along with the fixed ground board data, are shown in Figure 10. The penetration is reduced by approximately one-third compared to the fixed ground board results. The points of zero penetration at very low values of the velocity ratio ($V_R=5$) represent cases where no negative pressures were measured forward of the impingement point. The velocity ratio for no ground vortex formation from the fixed ground board results was about 3.

The off-centerline pressure transducers in the recent tests^{7,10} allowed for study of the lateral extent of the ground vortex. Data from this test are compared to the fixed ground board data and analytical result in Figure 11. Although the moving model yields dramatic differences in the forward penetration, the *normalized* shape of the ground vortex is roughly the same. For the fixed ground board results, the normalization was used to collapse results with varying velocity ratio. We see here that it also collapses the effect of the ground boundary layer.

Two sets of data^{9,12} are available which used a moving ground belt to eliminate the ground boundary layer. If the belt is moving at the free-stream velocity, the scrubbing action found with a moving model is also

duplicated. The belt speed was varied in these tests to allow for a direct comparison of belt-on to belt-off. The reduction in penetration for a moving belt compared to a fixed belt is shown in Figure 12. The reduction is about the same for each nozzle, and appears to increase as the velocity ratio decreases. There is considerable scatter, but the data seem to concentrate about a reduction in penetration of about 20%. The moving model result of two-thirds of Equation (1) is also shown. The reduction in penetration with the moving belt is less than the moving model results, the reason for the discrepancy is not clear at this time.

2.2 Multiple Jets

Data on the ground vortex for multiple jet configurations are very limited. Jet spacings (centerline to centerline) from one and one-half to ten diameters have been tested in both side-by-side and fore-and-aft (tandem) arrangements^{6,9}.

The wall flows from multiple jets meet between the jets and form an upwash fountain flow. For side-by-side jets, the fountain is aligned in the free-stream direction. The fountain formed from tandem jets is perpendicular to the free-stream. For three or more jets, multiple fountains are typically formed. The ground vortex formed from multiple jets is highly dependent on the spacing between the jets. Jets that are widely spaced act as individual jets. As the jet spacing is decreased in a side-by-side arrangement, the fountain and ground vortex both move forward. An empirical relation for this forward movement⁶, valid for jets spaced less than 4.24 diameters apart, is:

$$\frac{x_s}{d} = (\text{single jet}) \left[1 + \frac{2.92}{V_R} \left(2.12 - \frac{y_j}{d} \right) \right] \quad (6)$$

The situation is more complicated for tandem jets. Here, the aft jet is operating in the wake of the front jet. The wall flow from the aft jet only progresses forward to the fountain. For closely spaced tandem jets, Stewart & Kuhn⁶ found an increase in the ground vortex penetration from the front jet compared to the front jet operating in isolation. The water tunnel test of Kuhn et al⁹ found a decrease in the vortex penetration. The reason for the discrepancy is unknown.

2.3 Effect on Vehicle Aerodynamics

The aerodynamic characteristics of a configuration are influenced by the position of the ground vortex relative to the lifting surfaces. A systematic series of tests was

recently completed in the NASA Langley 14x22 ft V/STOL tunnel^{12,14}. A generic configuration was fabricated with two wing planforms that could be tested in one of three longitudinal positions (fuselage station 10, 14, or 18). The wings tested were an unswept rectangular wing and an untapered 30 degree swept wing. The wing span and chord were 27 and 6.75 inches respectively. Figure 13 shows the model with the swept wing in the forward position (fuselage station 10).

Three nozzle shapes were tested with the exit area of each being constant (1.13 sq. inches). These were a circular nozzle 1.2 inches in diameter, a rectangular nozzle of aspect ratio 3 (1.84 in. wide by .613 in. long), and a set of side-by-side "thrust reverser" nozzles vectored 30 degrees forward of vertical ($\delta=120$ deg). The thrust reverser nozzles were of aspect ratio 3 (1.31 in. wide by .435 in. long) and were laterally spaced 2.62 inches from centerline to centerline. All tests were done with the jet nozzle at fuselage station 24.

The combinations of wing position with respect to the nozzle along with a variation in jet velocity ratio (V_R) resulted in ground vortex position variations from well ahead to well aft of the wing. Two balances were used with the primary data from the internal balance which recorded induced forces only. Data on the ground vortex position were obtained using smoke flow visualization in conjunction with a laser light sheet.

The effect of height above the ground on the lift coefficient under various jet/ground belt conditions is shown in Figure 14. The maximum height shown corresponds to about 1.2 wing spans, and will be considered free air for the purposes of discussion. Below a height of about ten diameters, the lift increases for the velocity ratio of 10, with almost no change due to the ground belt. Large lift losses are found for the higher velocity ratio of 20, with a definite reduction in the lift loss when the ground belt is used.

Results such as those shown in Figure 14 were correlated with vortex position as shown in Figure 15. This figure shows data for all three wing positions (unswept wing) at a ground height of four jet diameters. These data are for a fixed tunnel speed so they represent a variety of jet velocities. The same trend is found whether or not the ground belt is used. When the ground vortex is underneath or aft of the wing, small increases in the lift are found. This is probably due to an increase in the effective angle of attack due to the flow moving up and over the vortex. As the ground vortex moves forward of the wing, losses in lift are found that increase with distance. Here, the wing is immersed in the negative

pressure region beneath and aft of the ground vortex. In addition, the effective angle of attack of the wing may decrease due to induced downwash. The effect of height above the ground is shown in Figure 16. As the height increases, the data approach the jet off result. The lift increases found with the vortex aft of the wing decrease, and the large lift losses found with the vortex forward of the wing decrease.

The effect of ground vortex position on lift for the rectangular nozzle is shown in Figure 17. Again, the same trend is found whether or not the ground belt is used. When the vortex is aft of the wing, the magnitude of the lift increase is the same as that found with the circular nozzle. With the vortex forward of the wing, the lift losses are generally smaller than found with the circular. Some of the differences may be due to a different lateral shape of the vortex, although this has not yet been quantified. The effect of height was identical to that found for the circular nozzle.

The effect of ground vortex position on lift for the thrust reverser nozzle is shown in Figure 18. For reference, results from the circular and rectangular nozzles are also shown. Note the change in scale of the abscissa. The forward deflection of the jet results in ground vortex positions much farther forward than found with the unvectored nozzles. While there is more data scatter, the trend is definitely different. For a given position of the ground vortex, the lift losses are much smaller with a thrust reverser nozzle. There are several possible reasons for this. With the thrust reverser nozzle, a fountain will form which lies along the body centerline. This should cause a positive lift increment. A different lateral shape of the ground vortex may also be a contributing factor. The maximum lift loss is about the same for all three nozzles, although the corresponding position of the ground vortex is different for the thrust reverser nozzle.

The effect of ground vortex position on pitching moment for all three nozzle is shown in Figure 19. Data are only shown for the wing in the forward position (fuselage station 10). The reference point for the moment is the quarter-chord of the wing (fuselage station 11.6875). A large difference is again found between the thrust reverser and unvectored jet results. In all cases, nose up moments are found which increase as the vortex moves forward of the wing leading edge. For a given vortex position, the nose up moment is smaller for the thrust reverser. The maximum moment is about the same for all three nozzles. The thrust reverser configuration less of a nose up moment than the unvectored nozzles. Some of this may be due to the fountain formed under the body. The center of pressure of the fountain flow is probably between the

nozzle (fuselage station 24) and the moment center (fuselage station 11.6875), so a nose down moment increment should result.

The differences between the nozzle results shown in Figures 18 and 19 are not due entirely to differences in ground effects. In free air, the lift and moment with the circular and rectangular nozzle results were similar to each other but slightly different than the thrust reverser results. Small losses in lift were found with the unvectored nozzles that increased with velocity ratio. The thrust reverser nozzles produced a similar lift loss at the highest velocity ratio, but at intermediate values, lift increases were found. In all cases the magnitude of the changes decreased slightly as the wing position moved forward.

3. CONCLUSIONS

The ground vortex formed by the interaction of an impinging jet in cross flow has been studied. The following conclusions are made:

- (i) The forward penetration of the ground vortex increases with the ratio of jet to free-stream velocity.
- (ii) The penetration of the ground vortex decreases as the jet height above the ground increases.
- (iii) Below a jet height of approximately four diameters, the penetration is constant for a circular jet. For rectangular and thrust reverser jets, the penetration continues to increase.
- (iv) Use of a moving model reduces the forward penetration compared to a fixed model/ground plane combination. This reduction, approximately 33%, is believed to be due to the effect of the ground boundary layer.
- (v) Use of a moving ground belt reduces the penetration compared to a fixed ground belt, although the difference is less than that found with the moving model.
- (vi) The lateral extent of the ground vortex, normalized by the maximum forward penetration, is independent of velocity ratio and is not affected by the ground boundary layer.
- (vii) The ground vortex flowfield has a large effect on vehicle forces and moments. The effect is a function of the vortex position relative to the

vehicle, regardless of whether a fixed or moving ground belt is used.

- (viii) For the generic wing-body combination tested, large lift losses were found when the vortex was forward of the wing leading edge. Small increases in lift were found when the vortex was under or aft of the wing. Nose up pitching moment increments were found in all cases that increased as the vortex moved forward of the wing leading edge.

4. ACKNOWLEDGEMENTS

This work was sponsored by the U.S. Air Force under contract F33615-89-C-3611. The wind tunnel tests in support of this research were conducted jointly by the USAF Wright Laboratory, KSA Technology, and the NASA Langley Research Center. Mr John W. Paulson, Jr., was the NASA program manager.

5. REFERENCES

1. Abbott, W.A., "Studies of Flow Fields Created by Vertical and Inclined Jet When Stationary or Moving Over a Horizontal Surface," Ministry of Aviation, ARC CP 911, 1967.
2. Colin, P.E., and Olivari, D., "The Impingement of a Circular Jet Normal to a Flat Surface With and Without a Cross Flow," von Karman Institute Final Technical Report, DTIC TR AD688953, January 1969.
3. Binion, T.W., Jr., "Investigation of the Recirculation Region of a Flow Field, Caused by a Jet in Ground Effect with Crossflow," AEDC TR-70-192, September 1970.
4. Schwantes, E., "The Recirculation Flow Field of a VTOL Lifting Engine," NASA TT F-14912, June 1973.
5. Weber, H.A., and Gay, A., "VTOL Reingestion Model Testing of Fountain Control and Wind Effects," Prediction for V/STOL Propulsion Aerodynamics, Vol. 1, NASC, 1975, pp. 358-380.
6. Stewart, V.R., and Kuhn, R.E., "A Method for Estimating the Propulsion Induced Aerodynamic Characteristics of STOL Aircraft in Ground Effect," NADC Rept 80226-60, August 1983.
7. Stewart, V.R., "The Characteristics of the Ground Vortex and its Effect on the Aerodynamic of the STOL Configuration," NASA CP 10008, pp. 1-38, February 1988.
8. Cimbala, J.M., Stinebring, D.R., Treaster, A.L., Billet, M.L., and Walters, M.M., "Experimental Investigation of a Jet Impinging on a Ground Plane in Crossflow," *Journal of Aircraft*, Vol 25, No. 10, October 1988, pp. 923-931.
9. Kuhn, R.E., Del Frate, J.H., and Eshleman, J.E., "Ground Vortex Flow Field Investigation," NASA CP 10008, pp. 61-90, February 1988.
10. Stewart, V., and Kemmerly, G., "Characteristics of the Ground Vortex Formed by a Jet Moving Over a Fixed Ground Plane," AIAA paper 89-0650, January 1989.
11. Cimbala, J.M., Billet, M.L., and Gaublumme, D.P., "Experiments on the Unsteady Ground Vortex," NASA CR 177566, August 1990.
12. Stewart, V.R., Blake, W.B., "A Study of the Effect of a Moving Ground Belt on the Vortex Created by a Jet Impinging on the Ground in a Crossflow," AIAA paper 92-4250, August 1992.
13. Kuhlman, J.M., and Cavage, W.M., "Ground Vortex Formation for Uniform and Non-Uniform Jets Impinging on a Ground Plane," AIAA paper 92-4251, August 1992.
14. Stewart, V.R., "The Effect of the Ground Vortex on the Aerodynamic Stability and Control Characteristics of STOVL Aircraft," KSA Technology report 92-4, October 1992 (to be published as an Air Force TR).
15. Kemmerly, G.T., and Paulson, J.W. Jr., "Investigation of a Moving-Model Technique for Measuring Ground Effects," NASA TM-4080, January 1989.

Figure 1. Formation of Ground Vortex.

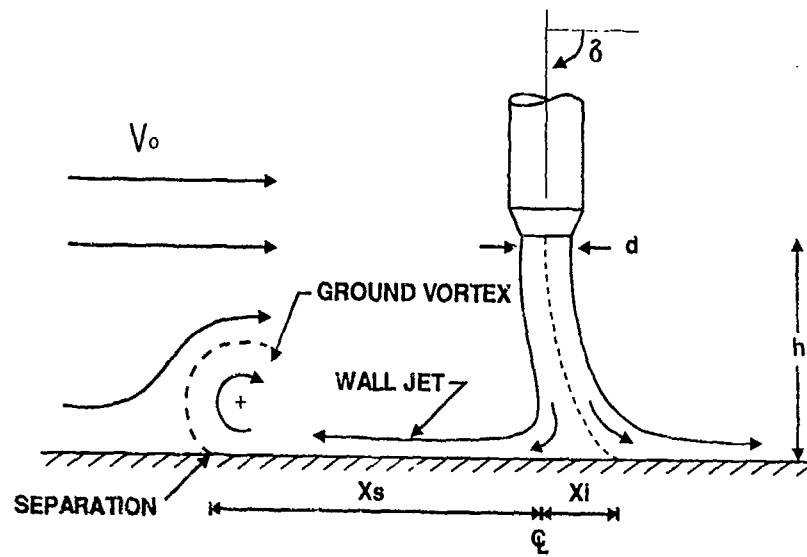


Figure 2. Typical Ground Pressure Distribution (Ref. 6).

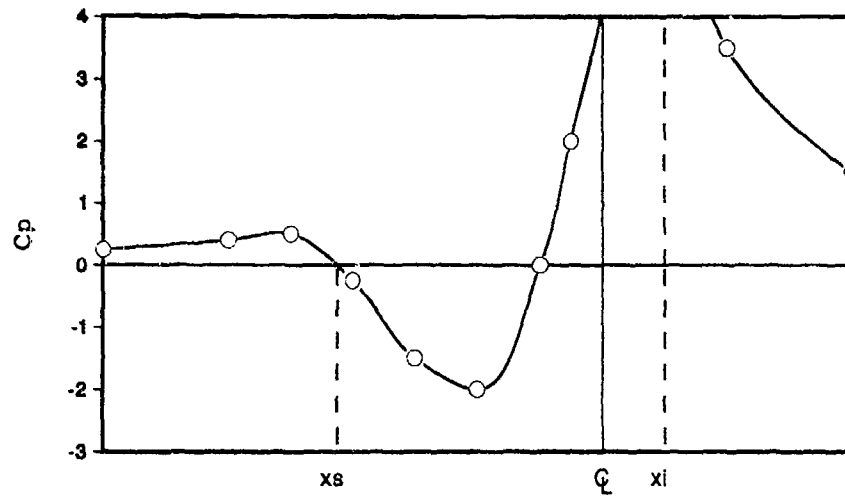


Figure 3. Time Averaged Velocity Vector Plot of Ground Vortex, $h/d=3$, $V_R=5$, Circular Jet (Ref. 8).

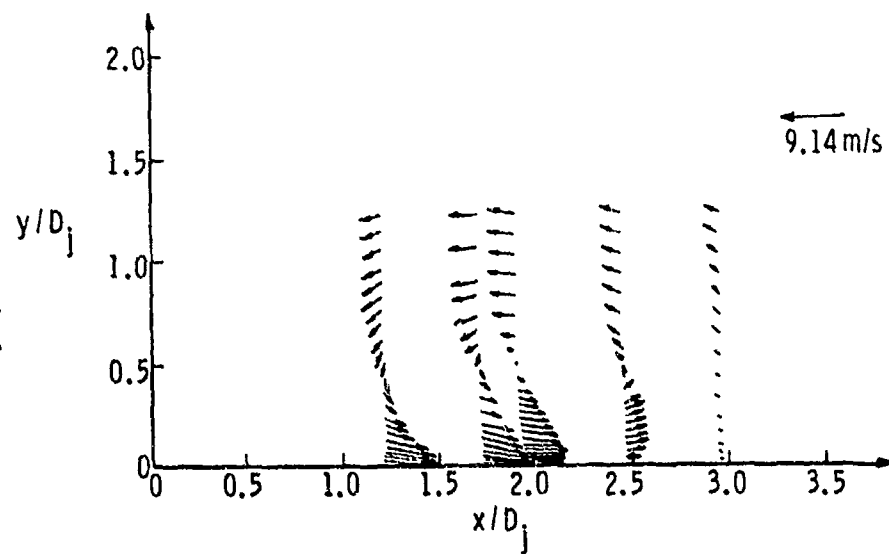


Figure 4. Effect of Velocity Ratio on Vortex Penetration, Fixed Ground Board, $h/d=2-4$, Circular Jet.

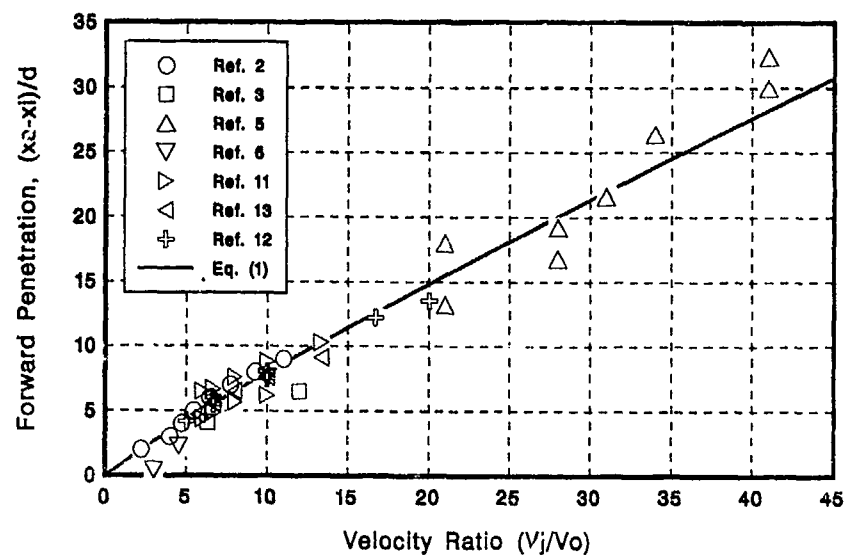


Figure 5. Lateral Shape of the Ground Vortex, Fixed Ground Board, $h/d=3-4$, Circular Jet.

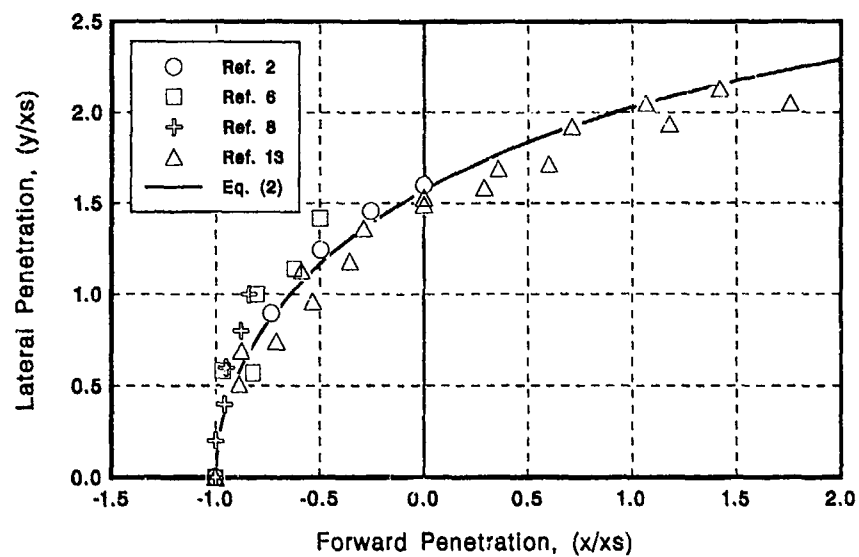


Figure 6. Effect of Height on Vortex Penetration, Fixed Ground Board, Circular Jet.

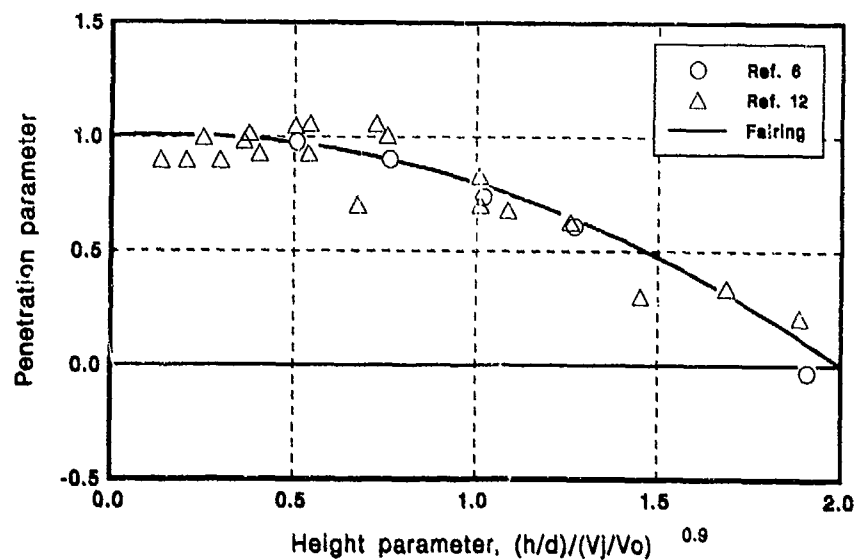


Figure 7. Effect of Height on Vortex Penetration, Fixed Ground Board, Non-circular Jet.

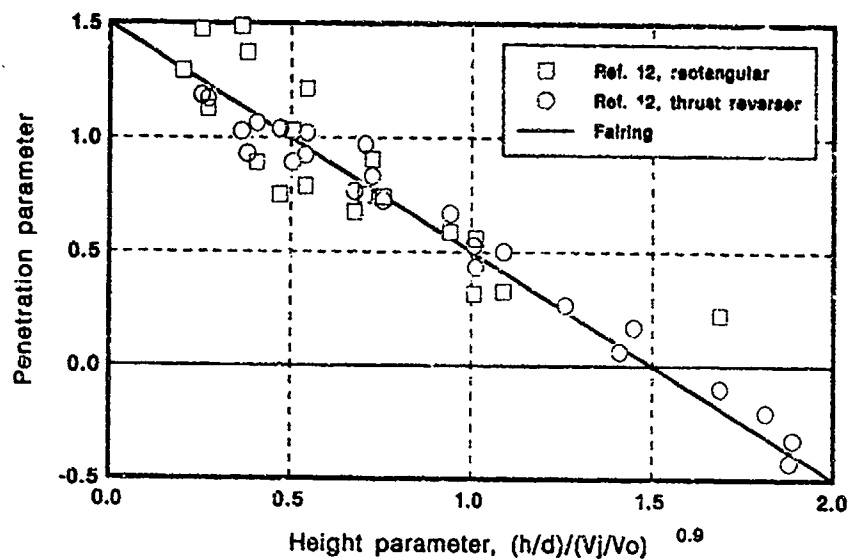


Figure 8. Effect of Ground Boundary Layer on Vortex Penetration.

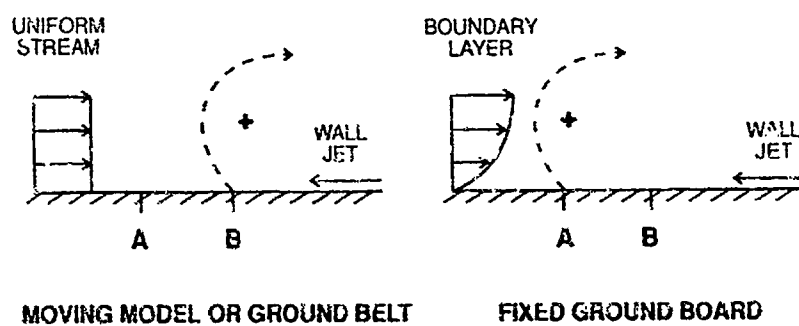


Figure 9. Moving Model Test Set-up (Ref. 15).

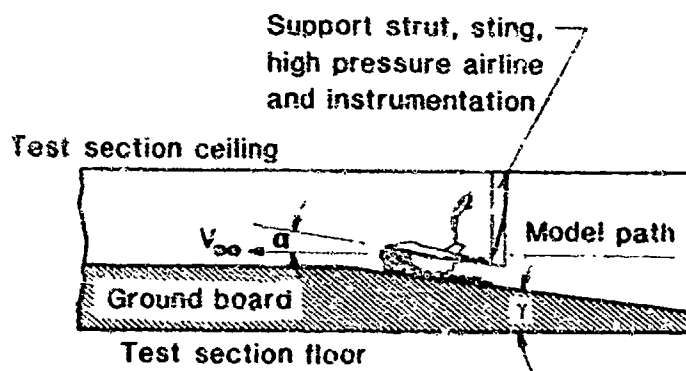


Figure 10. Effect of Velocity Ratio on Vortex Penetration, Moving Model, $h/d=3-4$, Circular Jet.

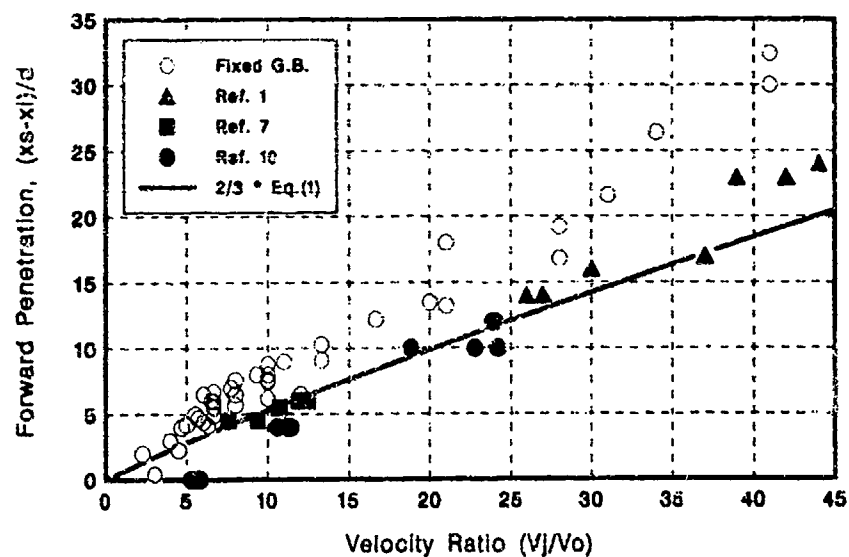


Figure 11. Lateral Shape of the Ground Vortex, Moving Model, $h/d=3$, Circular Jet.

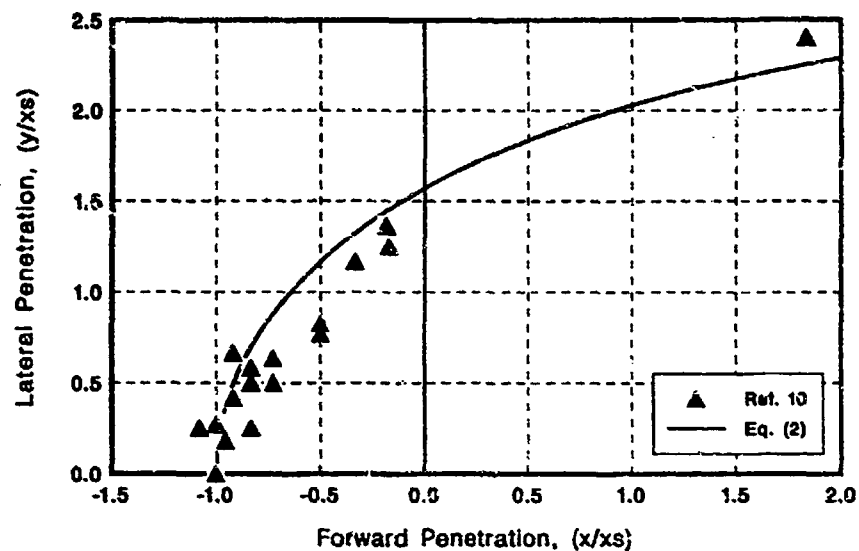


Figure 12. Effect of Moving Ground Belt on Vortex Penetration, $h/d=4$.

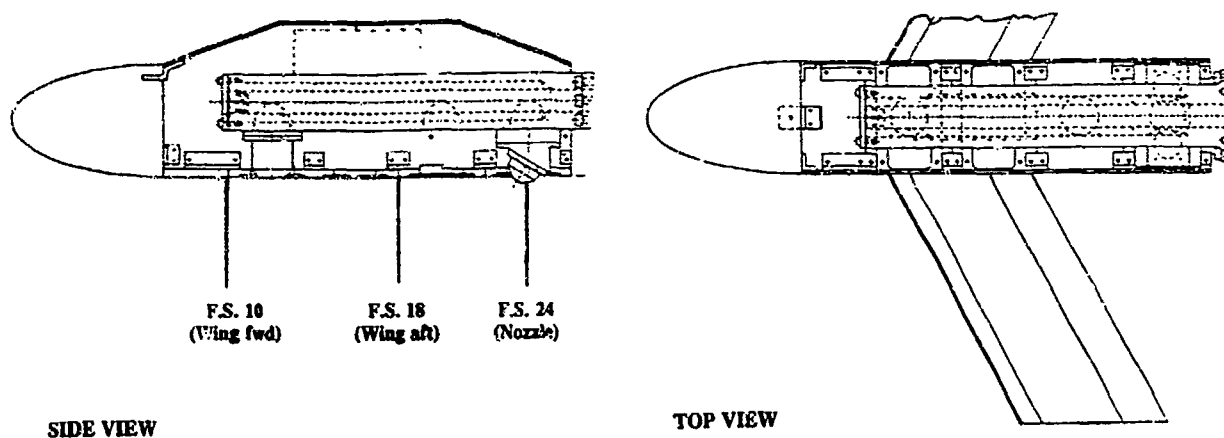
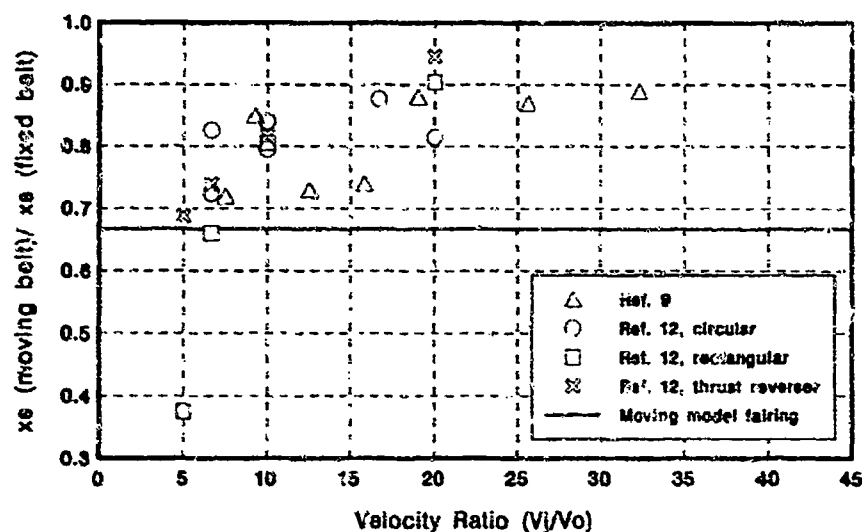


Figure 13. Wind Tunnel Model with 30 deg. Swept Wing.

Figure 14. Effect of Height on Lift Coefficient, Circular Jet.

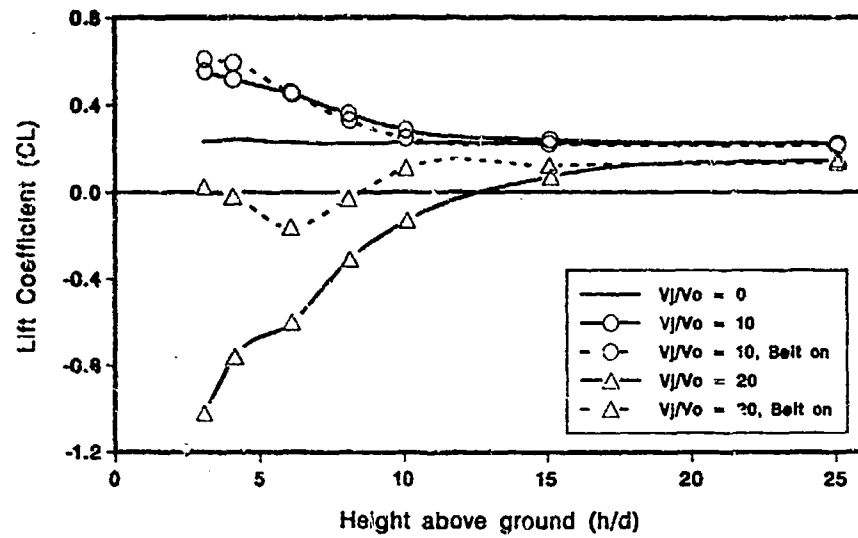


Figure 15. Correlation of Lift with Vortex Position, $h/d=4$, Circular Jet.

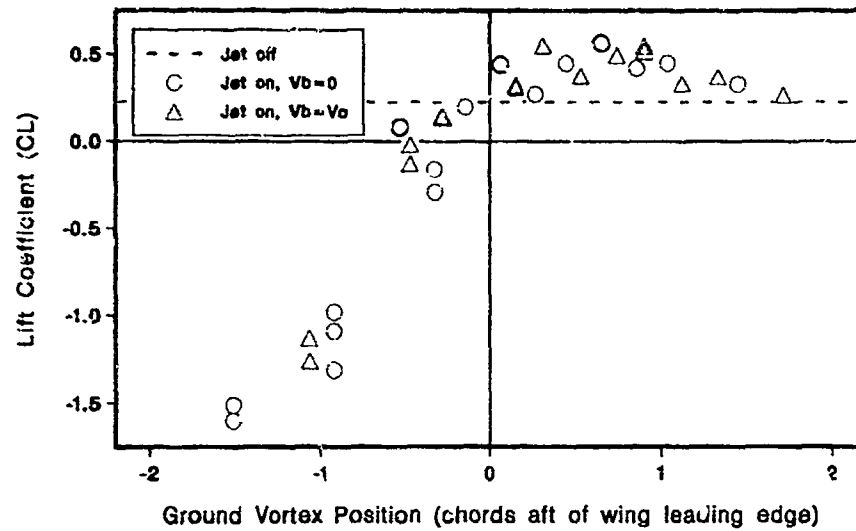


Figure 16. Correlation of Lift with Vortex Position, Circular Jet.

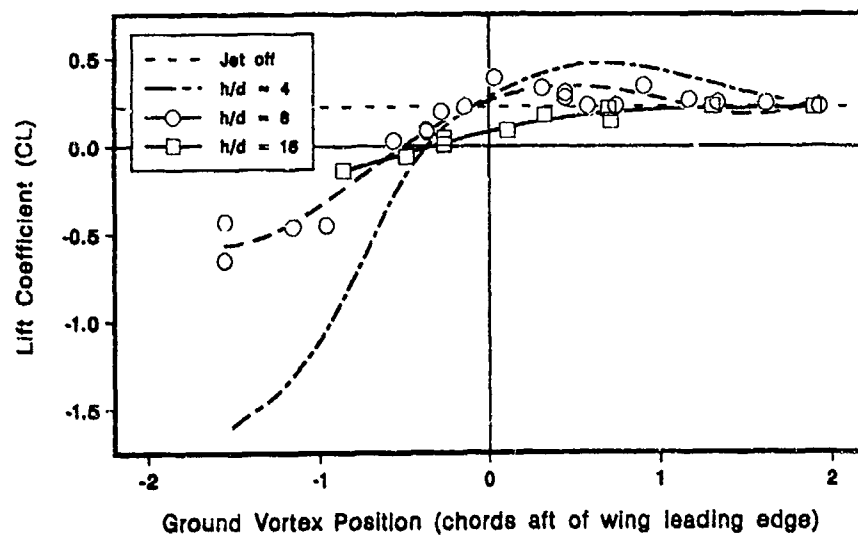


Figure 17. Correlation of Lift with Vortex Position, $h/d=4$, Rectangular Jet.

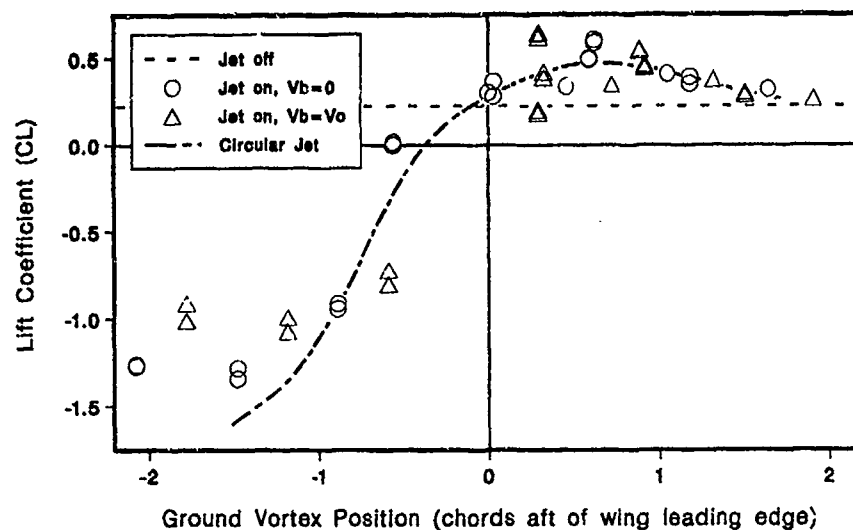


Figure 18. Correlation of Lift with Vortex Position, $h/d=4$, Thrust Reverser.

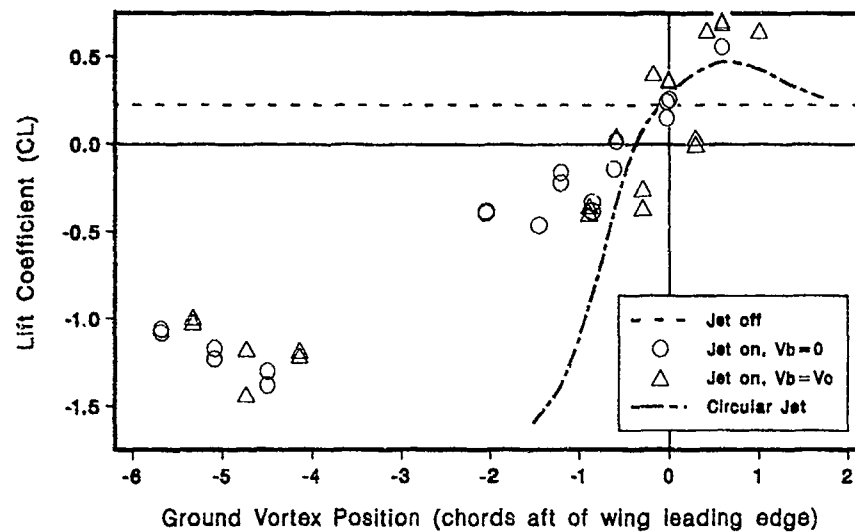
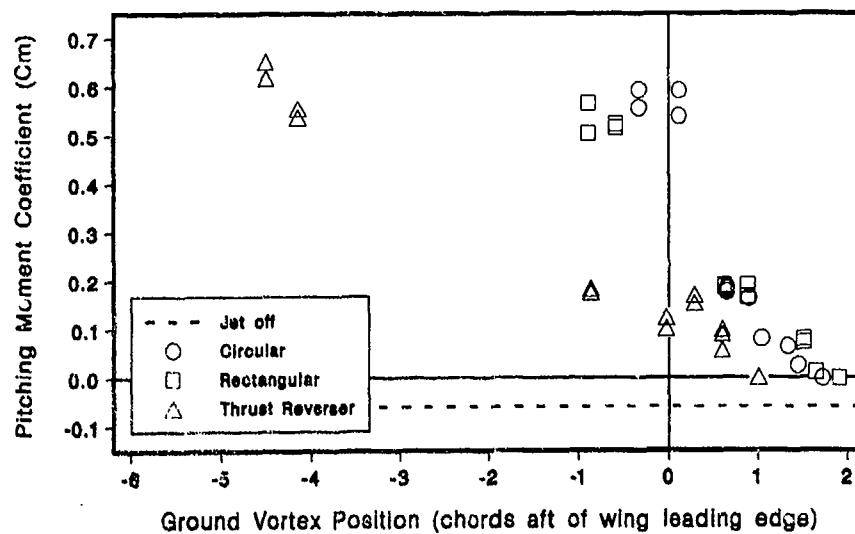


Figure 19. Correlation of Pitching Moment with Vortex Position, $h/d=4$.



EXPERIMENTS INTO THE SCALING PARAMETERS REQUIRED FOR EXHAUST GAS INGESTION TESTING OF VERTICAL LANDING AIRCRAFT

P.Curtis

P.J.Bradley

British Aerospace Defence Ltd.,
Hertford House, Farnborough Aerospace Centre,
Farnborough, Hampshire, UK. GU14 6YU

1. SUMMARY

The phenomenon of Hot Gas Recirculation for vertical landing jet aircraft and the effect of exhaust gas ingestion on aircraft performance is described, along with UK experience of experimental modelling of HGR for aircraft configurations and the scaling of the important parameters.

The conflict between scaling the buoyancy of the flowfield and correct modelling of the pressure field is explored and a number of fundamental experiments addressing this problem are related.

It is shown that in the region close to the jets and when the aircraft is very close to the ground that there are quite large differences between the two scaling criteria; the near-field region requiring full scale pressures for accurate representation. Away from this region the Nozzle Pressure Ratio does not greatly affect the flowfield.

Testing of a generic aircraft model with a number of different configurations shows that once near-field flowpaths have been eliminated the ingestion levels are underpredicted if the flow-field buoyancy is below full scale.

Absolute levels of ingestion are not greatly different between the two scaling criteria, particularly with the large scatter in results which is endemic to the phenomenon. However, it is concluded that for practical configurations, ie. those with low levels of ingestion, scaling of flowfield buoyancy is more correct than scaling of the pressure field; and that this method of scaling is appropriate for use in achieving a low ingestion configuration.

2. LIST OF SYMBOLS

BAe	British Aerospace
BR	Buoyancy Ratio
D	Nozzle Diameter
DRA	Defence Research Agency (UK)
h	Height above impingement
HGI	Hot Gas Ingestion
HGR	Hot Gas Recirculation
NGTE	National Gas Turbine Establishment
NPR	Nozzle Pressure Ratio
r	Radial distance from impingement
STOVL	Short Take-Off/Vertical Land
T	Total temperature
W	Mass flow
θ	Excess temperature ($T - T_a$)

subscripts

a	ambient conditions
j	jet conditions

3. BACKGROUND

3.1 The Phenomenon of HGR

Hot Gas Recirculation is the commonly used term for the ingestion of exhaust gases by jet lift aircraft when performing vertical manoeuvres near the ground. The effects of HGR on gas turbine performance are similar to the ingestion of hot gases from sources such as missile plumes, other aircraft exhausts during close formation flying and steam from a steam catapult, etc. The rise in mean inlet temperature leads to a rise in exhaust gas temperature for a given thrust, thus affecting the life of the turbine. If the exhaust gas temperature becomes too high then a limiter will be invoked to prevent permanent damage to the turbine, thus reducing thrust. This is not desirable in a hovering aircraft.

More importantly even than the effects of mean inlet temperature is the combined effect of inlet temperature

rise rate and engine face temperature distortion (ref 1). These two factors can cause the engine to surge, in much the same way as high instantaneous total pressure distortion. Surges in the hover or during vertical descent are very serious occurrences which can cause the loss of the aircraft.

Hot Gas Recirculation consists of three separate mechanisms.

Far-field recirculation occurs when the ground sheet caused by the impinging lift jets separates due to headwind and its own buoyancy and is blown back towards the intake.

Near-field recirculation is the most damaging mechanism and occurs when the fountain flow caused by multiple lift jets finds a path direct to the aircraft's intake.

Mid-field recirculation covers all other flow paths and can be conveniently thought of as small packets of buoyant gas separating from the edges of the ground sheet or the fountain and being ingested into the intake.

As stated above, all recirculation occurs due to separations, and following very high streamline curvature (ground impingement, multiple ground sheet impingement etc.) It is thus an extremely unstable phenomenon featuring rapid transients. These transients are more pronounced for temperature distortion, for which near instantaneous peaks are as important as they are for total pressure distortion. Figure 1 shows repeatability of temperature rise during six similar descents for the model described later in the paper. This example is fairly typical and illustrates the necessity for rapid response instrumentation in order to capture high frequency fluctuations.

3.2 Modelling HGR

As HGR is such an important factor in the design of jet lift aircraft, reliable methods of modelling the phenomenon need to be found; which for cost purposes usually means sub-scale experiments. Cox and Abbott (ref 2) of NGTE Pyestock (now part of DRA) performed a series of experiments in the 1960's which claimed to show that

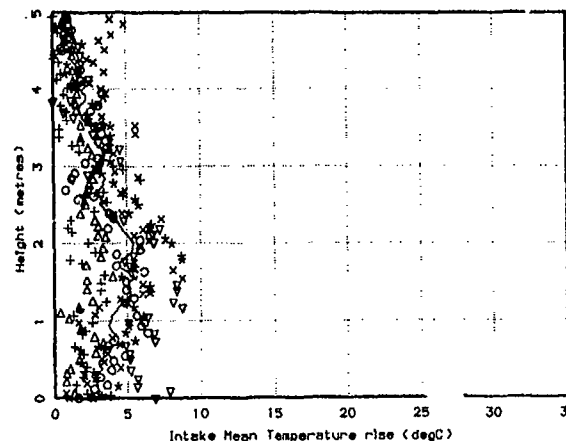


Figure 1. Typical test repeatability

the most important parameter to scale for such experiments was the jet's buoyancy, ie. the pressure forces exerted by the difference in the hot jets' density compared with the ambient air, for which they derived a numerical term, the "Cox Number". They also showed that temperature could be linearly scaled when regarded as "excess temperature", ie. $\theta = T_j - T_a$.

These scaling laws have the effect that if buoyancy is to be maintained at reduced jet temperatures in model testing then jet dynamic pressure will be less than full scale, ie. the pressure field around the aircraft will not be properly simulated. For the engine concepts of the time this was not thought to be a problem and both British Aerospace and Rolls-Royce (in previous corporate guises) constructed test rigs which utilised buoyancy scaling.

To properly model the development of the flowfield around a landing aircraft it is necessary to simulate the motion of the aircraft. Buoyancy scaling helps in this aspect, as the reduced dynamic pressure also scales time and so reduces the rig motion requirement and data acquisition rate.

The linear temperature scaling law was investigated at BAe Kingston and shown to be true for near-field dominated recirculation. However, for mid- and far-field recirculation, where much mixing with the ambient air has occurred, a new law was shown to hold, based on the jet's heat flux. The difference between the two laws is not great with the linear law giving

an overestimate of the order of 20% for typical test conditions.

3.3 Specific Experiments

The validity of buoyancy scaling has been called into question in recent times due to the greatly increased nozzle pressure ratios (NPRs) being proposed for next generation engines. The argument says that highly underexpanded jet flows are so different from low subsonic ones that the flowfield modelling and hence the measured HGR will be significantly different.

To investigate this further a number of experiments have been performed by, and on behalf of, British Aerospace. These included:

A comprehensive study of the effect of NPR for a single convergent nozzle, both as a free jet and a ground jet following perpendicular impingement.

The study of the ground vortex formed by single and twin impinging jets in a cross flow.

The study of ground jet reinforcement between multiple lift jets.

Specific HGR experiments on whole aircraft configurations.

Some results from all these experiments will be presented.

4. SINGLE JET ENTRAINMENT

This investigation was spread over a number of years and was sponsored by RAE Pyestock (now part of DRA). The work was performed at BAe Kingston (refs 3 & 4). Pitot static traverses were made at a large number of stations downstream of a simple convergent nozzle, for a wide range of pressure ratios. Traverses were made in both the free jet and the ground sheet formed by perpendicular impingement of the jet. Measurements were concentrated in the self similar region for ease of analysis.

Figure 2 shows the relative entrainment rates of self similar free jets per nozzle diameter, whilst figure 3 shows the relative mass flow

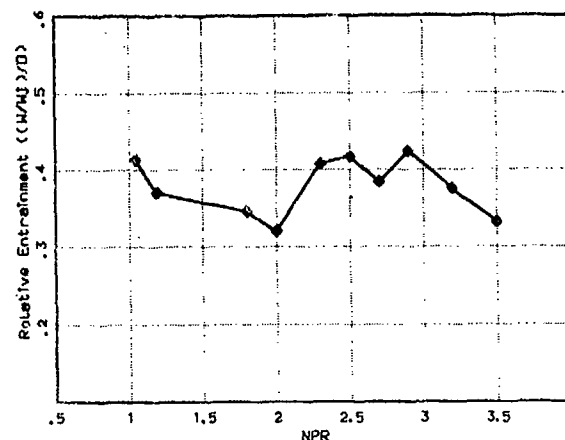


Figure 2. Free jet entrainment

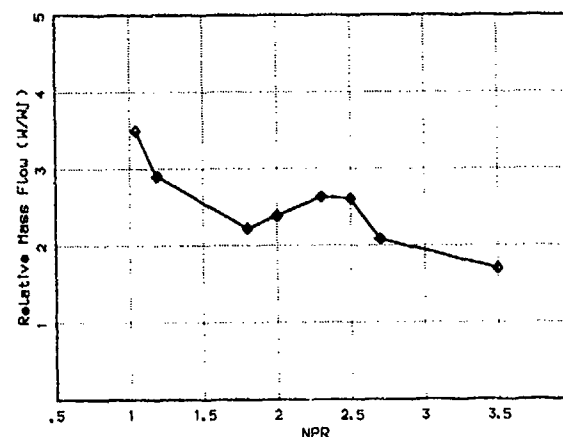


Figure 3. Free jet mass flow at 8D

rates 8D downstream of the nozzle exit, which gives an indication of near nozzle entrainment. For both plots the data has been normalised by the nozzle mass flow for ease of comparison.

It can be seen that there is no simple effect of NPR, with the near nozzle entrainment not necessarily following the self-similar pattern. However, low NPR near nozzle entrainment is highest which indicates reduced strength fountain flows at low nozzle heights. It seems clear that near the choked condition the entrainment starts low and remains low.

Figures 4 and 5 show similar plots for the ground jet. Data for nozzle heights of 4D and 10D is shown as there is considerable difference between them. The near impingement entrainment is measured at $r/D=5$. Interesting points to note are that the entrainment rate is more than double the free jet rate and that in the far-field the effect of NPR is much reduced. The general trend is to

show a reduction of entrainment with NPR.

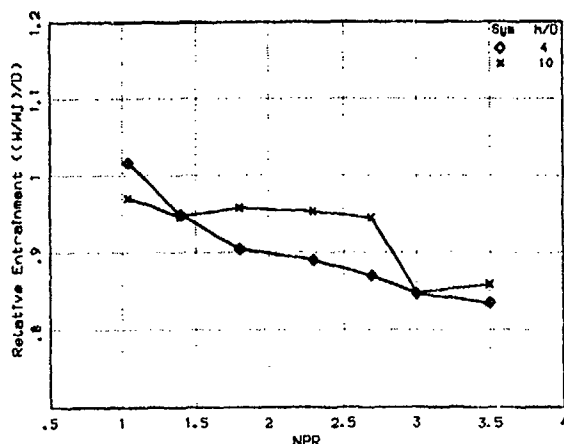


Figure 4. Ground jet entrainment

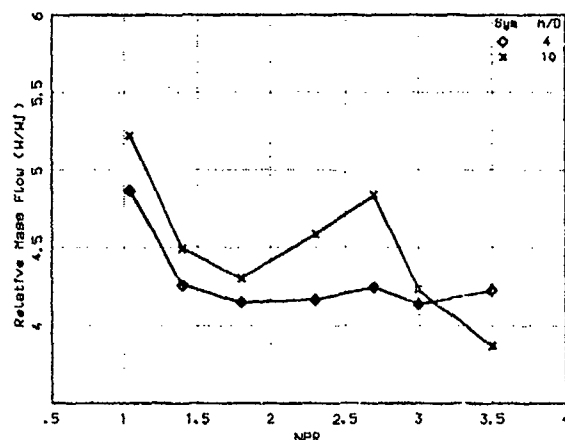


Figure 5. Ground jet mass flow at $r/D=5$

5. GROUND VORTEX PENETRATION

As part of the study into far-field recirculation a number of contracts have been placed on the Royal Military College of Science at Shrivenham to investigate the ground vortex associated with ground jets in cross-wind (refs 5 & 6). A large number of parameters have been investigated, including cross-flow velocity ratio, single and twin jets, moving ground belts, nozzle height and NPR. For the context of this paper, only the effect of NPR will be examined.

Figure 6 illustrates how ground vortex penetration varies with NPR for a single nozzle at a particular cross flow velocity ratio and nozzle height. The pattern is repeated with little variation throughout all the other parameters examined. It can be seen that this data correlates quite well with the jet entrainment data of

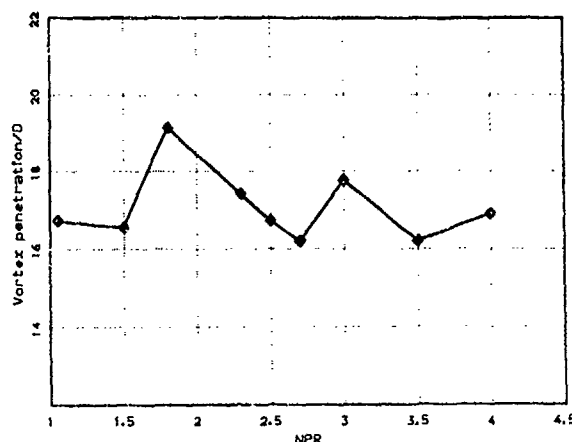


Figure 6. Ground vortex penetration

figures 2-5, ie. at low entrainment rates the penetration is greater. The minimum to maximum variation of penetration seen here is of the order of 17%. Again there is no overall trend with NPR.

6. JET REINFORCEMENT

This investigation concerned the reinforcement of ground jet velocity and depth in the plane of symmetry between two nozzles. Results were compared with single nozzle data and presented as ratios relative to the single jet. The parameters varied included nozzle spacing, height and splay. The work was performed under contract to BAe by Miller and Wilson Aerodynamic Research (ref 7).

One of the more interesting aspects of the work was the extent of the negative reinforcement away from the plane of symmetry; this was unexpected. A limited NPR comparison was performed, using jets of pressure ratio 2.67, 3.67 and 4.67 (the majority of data taken throughout the investigation was at NPR=3.67). For the three pressure ratios it was found that reinforcement, relative to the single jet case, was independent of NPR. Of course, this conclusion cannot necessarily be extrapolated back to fully expanded cases.

7. GENERIC AIRCRAFT MODEL

7.1 Background

As part of continuing investigations into the HGR characteristics of concept aircraft BAe and Rolls-Royce have collaborated on the design,

manufacture and test of an HGR model of a generic STOVL configuration. This model could simulate two different engine cycles and four different lift nozzle configurations (the lift nozzles being remote from the engine). The concepts were somewhat different to any configurations previously tested.

The model was manufactured by Rolls-Royce and tested in two phases on the Ground Effects Rig at BAe Kingston which has subsequently been re-located to BAe Warton. The facility is located in a large hangar and headwind testing is effected by use of a large fan with flow straighteners and simulated ground boundary layer. Such an arrangement has big advantages over a tunnel as the flow paths for any spurious hot gas are too long to ever reach the model.

Measurements were taken from an array of 45 engine face thermocouples arranged as a 15x3 rake. The existing data acquisition system allowed 60 data scans per landing; the data reduction process included thermocouple lag corrections. The data was shared by both companies.

7.2 Phase I Test Conditions

Part of the test programme for the model involved testing at high pressure, rather than the normal buoyancy scaled testing. Full scale pressure could not be used for a number of reasons. The intake could not suck the full mass flow due to choking behind the engine face, where the duct turned through 90° to exit the model. The thermocouples used to measure engine face temperature are fragile, from the requirement for rapid response, and could not survive at full Mach number. The rig could not descend at full scale velocity due to insufficient hydraulic power.

In phase I two configurations were tested at high pressure, referred to here as configurations A and B1. Because front and rear nozzle pressures are different, the different conditions are referred to by their buoyancy ratio, where BR=1 is equivalent to full scale. The table below shows the NPRs associated with the different buoyancy ratios.

Buoyancy Ratio	NPR	
	Front	Rear
1.0	1.15	1.06
0.5	1.30	1.13
0.2	1.76	1.32
0.1	2.53	1.64

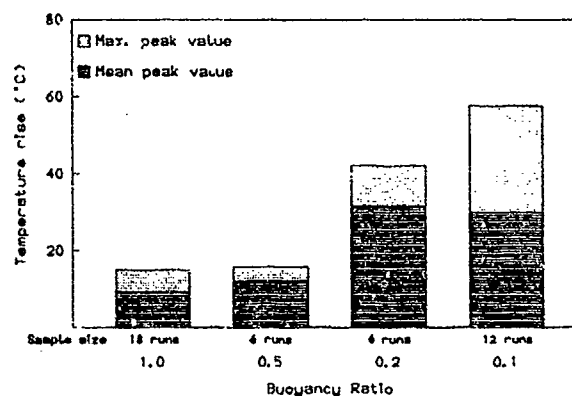


Figure 7. Configuration A in still air

7.3 Phase I Results

Figure 7 shows summary results for intake mean temperature rise over a number of repeats for configuration A in still air. The summary results show both the mean peak value from a series of descents and the absolute peak value measured in this set. This presentation gives a feel for the repeatability mentioned in section 3.1. It can be seen that this configuration gave low HGR under buoyancy scaled conditions, but that the high pressure data gave significantly worse results. Figure 8, however, shows the same comparison at 20 knots headwind, which gives very little difference between the conditions (20 knots headwind was not possible at the lowest buoyancy

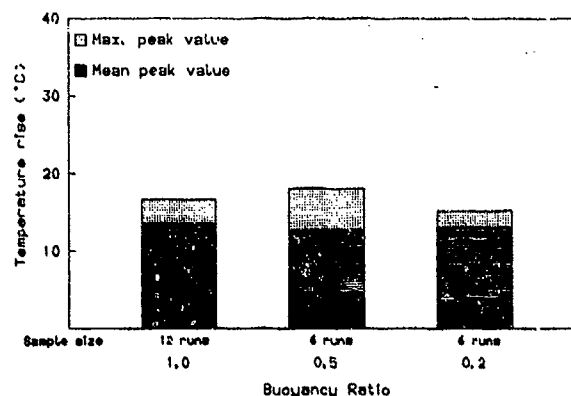


Figure 8. Configuration A at 20 knots headwind

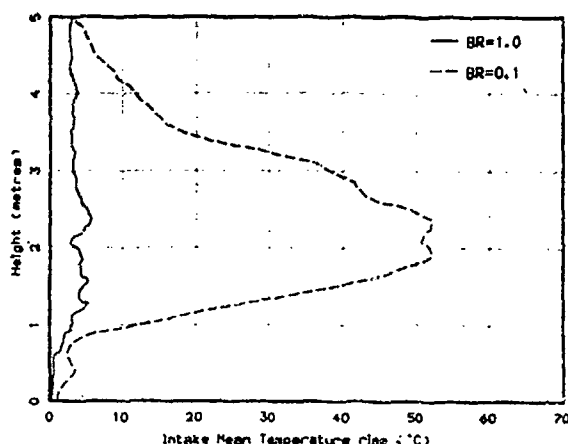


Figure 9. Mean temperature traces for configuration B1

ratio). The pattern was similar for configuration B1, with figure 9 showing the mean line traces with height in still air.

This behaviour was puzzling and led to detailed traverse measurements being taken for the rear nozzles, which were emerging from a plenum. It transpired that the flow from these was non-uniform and that as pressure ratio increased, so the jet angle splayed out by two or three degrees. A sensitivity to splay angle had been demonstrated earlier in the testing, so it was suspected this might be causing the large discrepancies.

7.4 Phase II Test Conditions

Between phase I and phase II, much effort was expended ensuring better quality nozzle flows, with no splay variation with pressure ratio. This could not be achieved for the highest NPR, but acceptable flow quality was achieved up to a buoyancy ratio of 0.15. The table below shows the pressure ratios associated with the conditions tested in this phase.

Confs	Buoyancy Ratio	NPR	
		Front	Rear
A & B2	1.0	1.15	1.06
	0.15	2.02	1.43
C	1.0	1.14	1.15
	0.15	1.97	2.01

Configuration B2 was similar to P1, but differed slightly in the axial spacing of the nozzles.

Configuration C utilised a different engine cycle, giving similar front and rear pressure ratios. Total mass flow and thrust was little different for the two cycles. Consequently, nozzle sizes, and non-dimensional nozzle spacings, were quite different. This configuration was tested in five different sub-configurations where such parameters as rear nozzle splay and underfuselage devices were varied. These are designated C1-C5.

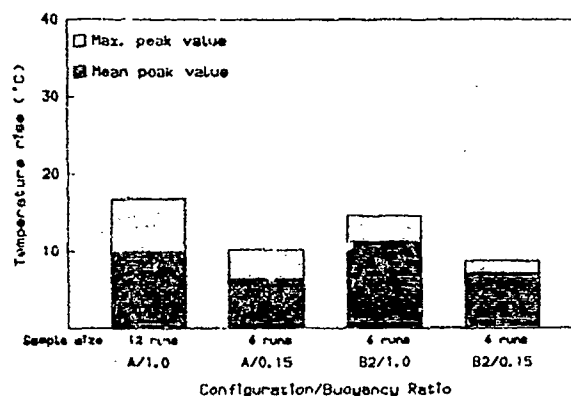


Figure 10. Phase II results in still air

7.5 Phase II Results

Figure 10 shows summary results for configurations A & B2 in still air and should be compared with figure 7. It can be seen that the mean peak values of overall temperature rise are very similar (as are the distortion values which are not illustrated). Figure 11 shows the effect of headwind, where again the two buoyancy ratios give very similar results.

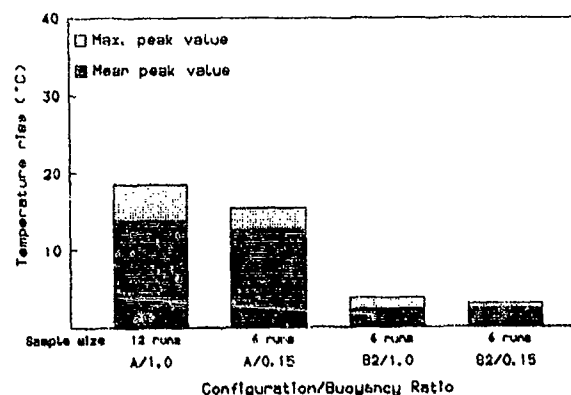


Figure 11. Phase II results at 20 knots headwind

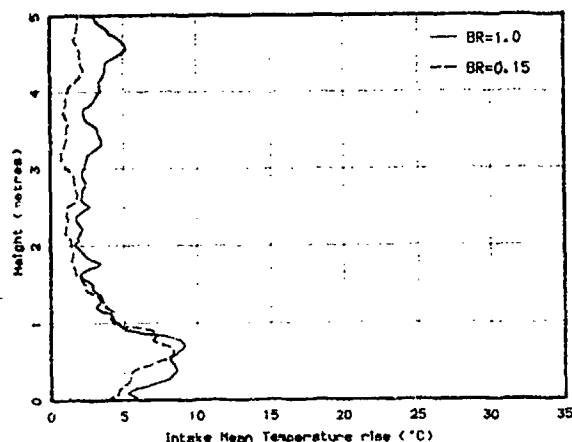


Figure 12. Mean temperature traces for configuration A in still air

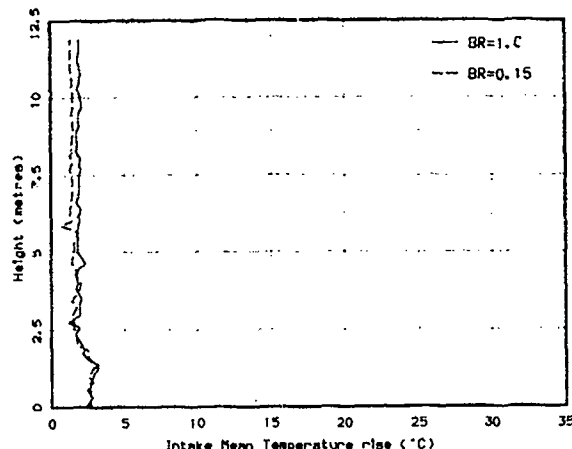


Figure 13. Mean temperature traces for configuration B2 at 20 knots

Figures 12 and 13 show mean line traces of temperature rise against height comparing the two buoyancy ratios for two of the cases. The similarity is particularly good when considering the variability within each set.

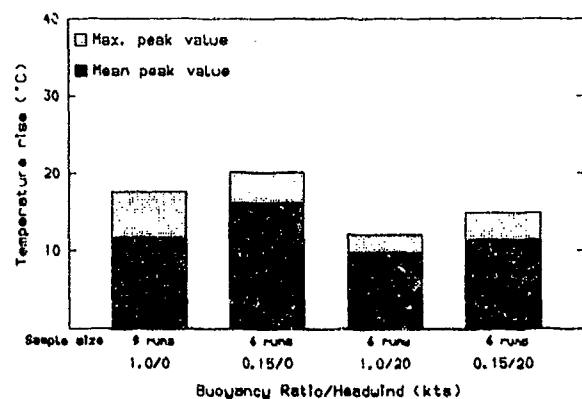


Figure 14. Configuration C5

Summary results for configuration C5 are presented in figure 14. Four of the five sub-configurations have slightly higher HGR at high pressure

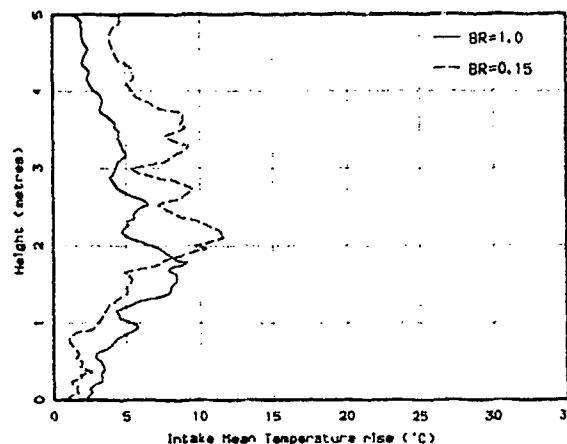


Figure 15. Mean temperature traces for configuration C5 in still air

(of the order of 15%), whereas configurations A & B2 consistently had slightly lower HGR. The absolute differences are small for the low HGR configurations. Figure 15 shows the mean variation with height for configuration C5 and figure 16 the same plot for C4. Although similar, the traces do not compare as well as those in figures 12 and 13.

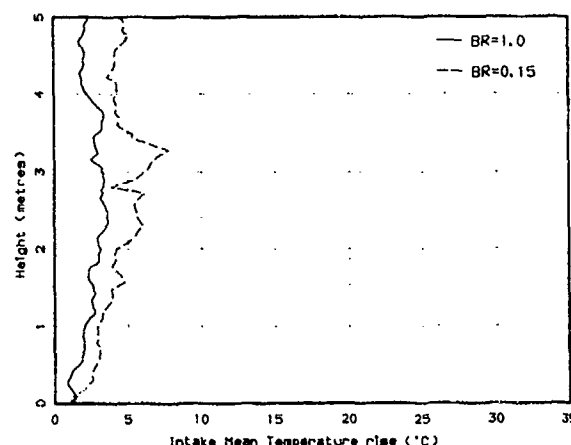


Figure 16. Mean temperature traces for configuration C4 in still air

7.6 Discussion of Results

In section 3.1 three different mechanisms for HGR were proposed. For mid- and far field recirculation the buoyancy of the hot gas is suggested as being most important, while for near-field recirculation the dynamics of the fountain flow are most important. Suppression/control of direct flowpaths to the intake is required for a low HGR aircraft configuration, leading to the conclusion that mid-field recirculation dominates for practical configurations.

Low buoyancy ratio testing (high pressures) should lead to underestimates of the HGR for a mid-field dominated configuration, and this is what is seen for configurations A and B2 in figures 10 and 11. Configuration C, on the whole, shows the opposite trend and particularly so for the high HGR sub-configurations. This suggests that some near-field recirculation is present. In neither case, of course, is it possible to know what is the "correct" answer.

The low HGR configurations were arrived at by testing at buoyancy scaled conditions, which may be inaccurate for high HGR results, but which are perfectly adequate for comparative assessment. Once a low HGR configuration has been developed the results generally support the theory that buoyancy scaling is more accurate. However, the absolute differences between the two scaling methods are small.

8. CONCLUSIONS

The three fundamental experiments showed that flowfield variations due to NPR are not easily described and do not necessarily give even general trends. Two broad conclusions can be drawn from these experiments, however.

In the near-field region, particularly at low nozzle heights, low subsonic NPR gives higher entrainment rates. Fountain flows will tend to be entrained more and so will be weaker than those associated with higher NPR jets.

In the mid- to far-field region NPR has far less effect as velocities and dynamic pressures very rapidly reduce to low subsonic values.

HGR testing of a generic aircraft model at low NPR (buoyancy scaled) and high NPR (low buoyancy) confirms the conclusions from the fundamental experiments, ie. by controlling the near-field and restricting recirculation flowpaths to the non-NPR sensitive regions testing at low buoyancy underestimates the exhaust gas ingestion.

Further, it is seen that the appropriate control over the near-field can be effected by testing at buoyancy scaled conditions, as this is a qualitative rather than quantitative task.

Testing at buoyancy scaled conditions is less demanding on rig capability and instrumentation robustness (a major consideration for the tracking of transients) and is shown to be appropriate and correct for the majority of HGR testing.

9. REFERENCES

1. Williams D.D.:
Hot-Gas Reingestion - Engine Response Considerations.
Paper III.5 of International Powered Lift Conference Proceedings, RAeS (ISBN 0 903409 68 2), August 1990
2. Cox M. & Abbott W.A.:
Studies of the Flow Fields Created by Single Vertical Jets Directed Downwards Upon a Horizontal Surface.
NGTE Memo M.390, October 1964
3. Curtis P.:
Investigation into the Behaviour of a Single Jet in Free Air and Impinging Perpendicularly on the Ground.
BAe-KAD-R-RES-3349, Sept 1987
4. Curtis P.:
Investigation of a Single Jet in Free Air and Impinging Perpendicularly on the Ground - Phase II.
BAe-KAE-R-RES-3607, June 1990
5. Bray D. & Knowles K.:
Experimental Investigation of Jets in Cross-flow and Ground Effect - Analysis of Phase I.
RMCS report TN SMMCE/AeS/0305/3, October 1990

6. Bray D. & Knowles K.:
Experimental Investigation of
Jets in Cross-flow and Ground
Effect - Analysis of Phase II.
RMCS report TN SMMCE/AeS/0305/5,
January 1992
7. Miller P. & Wilson M.:
A Study of VSTOL Flowfields
produced by Normal and Inclined
High Pressure Jet Impingement
MW-TR-91-35, July 1991

Influence of headwind on Hot Gas Reingestion and consideration of pressure ratio scaling

C J Penrose

Powerplant Technology
Rolls-Royce plc
PO Box 3
Filton
Bristol
BS12 7QE
England

Abstract

A major concern affecting the operation of Advanced Short Take-Off and Vertical Landing (ASTOVL) aircraft close to the ground is ingestion by the aircraft intakes of engine hot exhaust gas. This hot gas reingestion (HGR) can produce loss of engine thrust and erode engine stability margins. A prime source of HGR is the flow occupying the region in the 'near' and 'mid' fields around the aircraft. The 'near-field' flow can be controlled by aircraft-mounted anti-HGR devices but these are likely to be less effective in containing the mid-field flow which is greatly influenced by headwind.

Near and mid-field ingestion on Harrier-type configurations has, for many years, been studied by means of model-scale experiments. In most cases in the United Kingdom the experiments have been set up observing scaling procedures which include consideration of the buoyant action of the hot gas and imply tests at low jet velocities with dynamic head similarity maintained. It can be argued that low velocities may not be appropriate for currently-conceived ASTOVL aircraft employing high pressure-ratio supersonic exhausts, and it may be more appropriate to test at full-scale nozzle pressure ratios.

This paper reviews the effects of headwind on HGR for Harrier-type configurations during landing manoeuvres with tests carried out both at low jet velocities consistent with buoyancy scaling ($NPR_F = 1.07$) and at velocities representative of full-scale nozzle pressure ratios ($NPR_F = 2.46$).

The HGR results are examined in relation to expectations of the forward-flowing gas cloud height and penetration distance for the engine exhaust streams while under the influence of headwinds.

The results indicate the sensitivity to headwind to be configuration dependent with the magnitude and height of occurrence of HGR increased for tests at increased NPR's. The analysis techniques employed in the paper recognise the stochastic nature of HGR indicating the need for results to be compared using statistical methods.

The results have considerable ramifications concerning future test techniques that need to be addressed. In particular it should be noted that buoyancy-scaling is only a particular case of dynamic head scaling, albeit at very low model/full-scale jet velocities. This raises the question of the validity of simulating high velocity jets with low velocity equivalents.

List of symbols

ASTOVL	Advanced Short Take-Off and Vertical Landing
CAD	Cushion Augmentation Device (Underfuselage strake / dam assembly)
d	Nozzle diameter
HGR	Hot Gas Reingestion
Ht	Height (measured from 'wheels on')
Kts	Knots
NO-GO VTO	'NO-GO' Vertical Take-Off (Engine 'confidence check' manoeuvre with vertical thrust less than aircraft weight so lift-off prevented)
NPR	Nozzle Pressure Ratio

STOVL Short Take-Off and Vertical Landing

T	Total temperature (absolute)
T_∞	Ambient temperature (absolute)
ΔT	$T - T_\infty$ Temperature rise above ambient - °C
$\bar{\Delta T}$	Mean temperature rise above ambient
ΔT_{120°	Highest mean temperature rise in any 120 sector of the engine face
T_{c120°	Temperature distortion coefficient
	$= \frac{\Delta T_{120^\circ} - \bar{\Delta T}}{\bar{\Delta T}}$

y Horizontal Distance into headwind from nozzle centre-line

VL Vertical Landing
VTOL Vertical Take-Off and Landing

Subscripts

C	Critical
F	Front
i	Intake
J	Jet
R	Rear
S	Vortex separation
120°	Critical Sector Angle for Spatial Temperature Distortion

Superscripts

(-) Mean value

Introduction and background

Rolls-Royce, supplier of the Pegasus powerplant for the successful Harrier Short Take-Off and Vertical Landing (STOVL) aircraft, has long recognised the operational risk posed by recirculation of the engine exhaust gases into the aircraft intakes with the aircraft close to the ground. This hot gas reingestion (HGR) can produce loss of engine thrust and erode engine stability margins which, in extreme cases, can cause engine surge. The flow fields from the twin front and rear exhausts are complex and are traditionally defined in terms of 'near', 'mid' and 'far' fields around the aircraft (Figure 1).

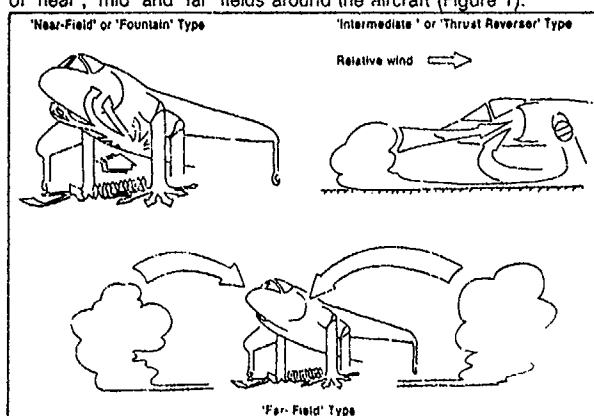


Figure 1

Ingestion into the intakes of hot exhaust gases in the 'near' field flow has been successfully reduced by means of aircraft mounted underfuselage devices designed primarily to reduce suckdown forces caused by the flow entrainment around the aircraft planform with the aircraft in ground proximity. These devices, termed Cushion

Augmentation Devices (CAD's). (Figure 5), capture the transverse and longitudinal 'fountains' of hot gas reflected from the exhaust jets on ground impingement and redirect them into the ground flow sheet. The CAD's are likely to be less effective in controlling the 'mid' field flow which represents gas in both the forward flowing ground sheet and the front jet longitudinal fountain blown back by an oncoming headwind. 'Far' field ingestion is caused by long-time recirculation of the forward flowing ground sheet which rises due to the buoyant nature of the hot gas. This mechanism has not been a problem for Harrier except in cases of landing after prolonged low-level hover or during repeated aircraft landings in one particular area.

Intake HGR on Pegasus powered aircraft from P1127 through Kestrel to Harrier has been studied in the United Kingdom predominantly by means of model-scale experiments with very limited supporting full-scale data. Model-scale tests require the establishment of procedures to set up the test conditions and to scale the model results to full-scale values. Suitable procedures were developed in the UK in the early 1960's, Refs. 1 and 2 which considered the buoyant action of the hot gas, although this mechanism is probably not a necessary requirement for representation of the 'near' and 'mid' field flows. In this procedure the ratios between buoyancy and inertial forces for the model tests are maintained the same as for full-scale, which results in very low jet velocities for the model. Dynamic head similarity is maintained throughout, so headwind, sink rates and landing velocities are similarly reduced. Conditions for a typical 1/15th scale model are shown on Figure 2.

Parameter	Model		Full-scale
	Buoyancy-scaled	Full-scale NPR	
Linear dimensions	1/15	1/15	1
Free-stream velocity m / SEC	1.7	7.6	7.6
Landing velocity m / SEC	0.27	1.22	1.22
Intake Mach number	0.13	0.63	0.63
Intake mass-flow Kg/sec	0.23	0.9	204
Front nozzle pressure ratio - NPR	1.07	2.46	2.46
Front nozzle temperature - K	367	367	416
Rear nozzle pressure ratio - NPR	1.047	1.97	1.97
Rear nozzle temperature - K	723	723	994
Velocity scale	1/4.55	1	1
Time scale	1/3.3	1/15	1

Figure 2

Buoyancy scaling implicitly dictates incorrect simulation of the near-field full-scale flow field. However for subsonic exhausts the limited model/full-scale data available has shown good agreement, albeit where low levels of HGR have been produced with the potential risk of HGR from the rear exhausts screened from the engine inlets by the cool front jets, Ref. 3.

Recent Harrier/AV-8B developments have required Pegasus engines with thrust increases which have produced supersonic front exhaust jets and concerns have been expressed that these jets may not be appropriately modelled by low velocity air streams. Studies have been made into the effect of nozzle pressure ratio (NPR) on fountain strength, Refs. 4, 5 and 6, flow entrainment into the fountain and ground jet, Ref. 7, and the penetration of the ground sheet into an oncoming headwind, Ref. 8. These suggest that fountain flow strengths are increased as NPR is increased and that the penetration of the ground sheet flow into an oncoming headwind, at a given jet/headwind velocity ratio, shows some variation with the absolute jet velocity (or nozzle NPR), see Figure 3 from Ref. 8. The implications of these trends to Harrier developments are discussed in this paper.

Model tests have recently been carried out at Rolls-Royce to establish the potential risk of increased HGR by the adoption of the more powerful engines with higher exhaust jet pressures and temperatures employed in the Harrier 2 and AV-8B. This paper presents the results of the investigations which examined the effects of headwind on a number of airframe configurations including CAD modifications designed to reduce HGR. The tests included NO-GO VTO's and simulated landing manoeuvres. The NO-GO VTO manoeuvre represents an engine 'confidence check' prior to flight, and is carried out with the aircraft overloaded such that the all-up weight exceeds the vertical thrust available thereby preventing lift-off.

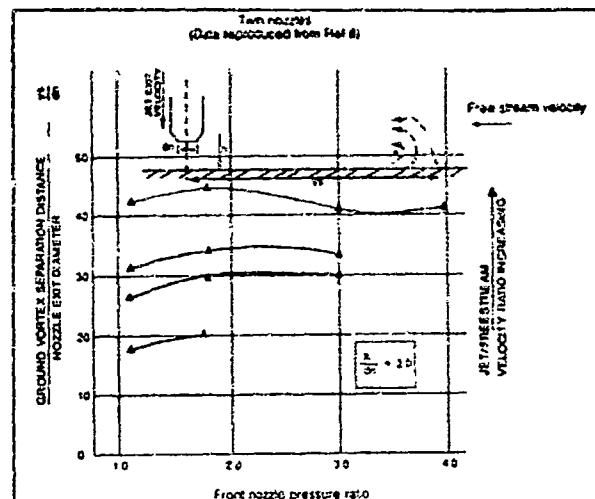


Figure 3

The tests were carried out at low nozzle pressure ratios consistent with buoyancy scaling ($NPR_F = 1.07$) and at full-scale nozzle pressure ratios ($NPR_F = 2.46$).

The flow fields producing HGR are stochastic in nature particularly for the pockets of hot gas shed from the fountain boundary or the edge of the blow back ground sheet. This phenomena was anticipated prior to the tests, Ref. 9 refers, and the majority of tests were accordingly carried out ten times to provide data to allow statistical analysis. This paper illustrates trends between configurations and the effects of headwind which can be derived simply from observation of peak values of HGR from a given manoeuvre or the spread of peaks from a number of successive manoeuvres. The application of statistical analysis methods developed to substantiate (or not) trends determined from small measurement samples and to evaluate extreme values which would be expected to occur during the many manoeuvres required of an operational aircraft are briefly discussed. A more detailed Rolls-Royce analysis using data from the same test series is presented in Ref. 10.

Model and rig

The tests were carried out on a 1/15th scale geometrically representative model of the Harrier 2/AV-8B aircraft fitted to the Vertical Take-Off and Landing (VTOL) rig at the Rolls-Royce test site at Bristol, UK. The model is shown installed on the rig in Figure 4.

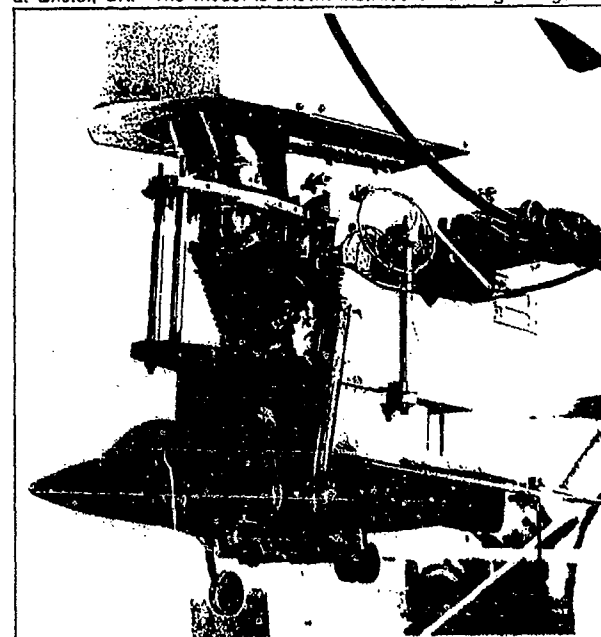


Figure 4

The rig and test facilities are described in Refs. 11 and 12. The model was set at a landing attitude of 7.5° nose-up with the intake auxiliary doors open. Front and rear nozzles were represented set

vertical with outwards splay angles of 5° and 12.5° respectively. The model was provided with the Harrier 2 production standard deep strake and dam (CAD) geometry designated Configuration 1. Modifications designed to provide greater fountain upwash control were manufactured to give deeper strakes, an angled dam and increased dam depth. The configurations tested are shown in Figure 5

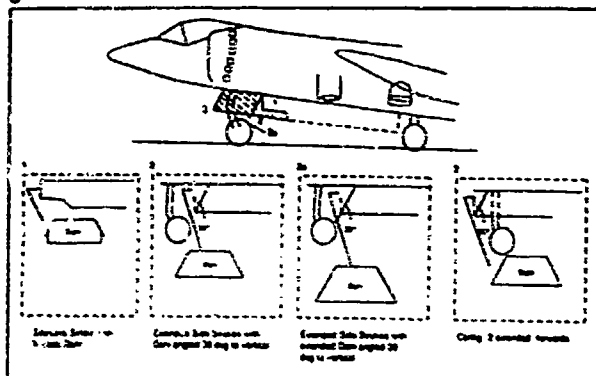


Figure 5

and comprise:

- Configuration (1) - Production standard strake/dam.
- Configuration (2) - Deeper strakes/external dam angled at 30° to the vertical, the same fore-aft location as on the production aircraft.
- Configuration (2a) - As for Configuration (2) but with the dam chord increased in length by 50%.
- Configuration (3) - As (2) with the dam moved forwards with the side strakes extended accordingly.

Instrumentation and data acquisition

Engine-face transient gas temperatures were recorded using an array of fast-response miniature Chromel-Alumel thermocouples formed of wires of $0.002''$ diameter with minimum-mass welded beads arranged in 16 circumferential positions at three radii, see Figure 6.

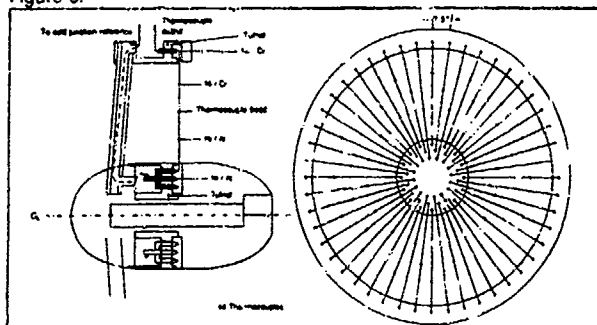


Figure 6

Local temperature measurements were corrected for thermal lag using time-constants relevant to the appropriate engine-face Mach number derived for sample wires precalibrated in the Rolls-Royce Heat Transfer Laboratory in Enstol.

For every manoeuvre the data were recorded in digital form with each individual channel scanned at a rate of 250 Hz for tests at full-scale NPR and at 50 Hz for buoyancy-scaled tests. This system is less costly than continuous individual channel recording, reduces data handling problems and the scanning rate is sufficiently rapid to provide individual channel recording at intervals compatible with the thermocouple time-constant. The scanning intervals provide data at full-scale equivalent height intervals of 75mm during a landing manoeuvre. A description of the data acquisition system is contained in Ref. 11.

Test technique

NO-GO VTO's

Initial experiments were carried out with exhaust conditions preset with the model wheels-on and with air exhausting downstream via flow switching valves located close to the nozzle exits. When conditions were set the valves were rapidly switched to feed air to the vertical nozzles. Following valve switching and flow stabilisation the intake thermocouple readings were recorded for a period of time equivalent to about 30 seconds, full-scale. This time exceeds that for a full-scale NO-GO VTO which is typically 4-6 seconds and provides a good data set for statistical analysis.

Analysis of tests carried out in the above manner indicated that HGR values derived from the NO-GO VTO's with the model on the ground were close to those obtained after a vertical landing manoeuvre had been completed with data recording continued for sufficient time after wheels-on for conditions to equilibrate to those for 'fixed height' wheels-on. This finding was convenient in terms of rig operating efficiency and the procedure to derive NO-GO data at the end of VL manoeuvres was adopted for a large portion of the tests.

A typical trace for a VL followed by a 'NO-GO VTO' for a model test carried out at full-scale NPR's is shown in Figure 7 indicating the

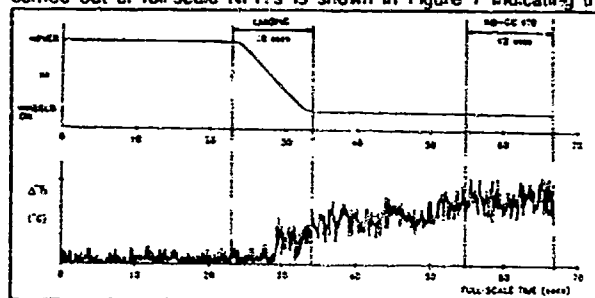


Figure 7

time interval allowed after the VL for conditions to stabilise. The time sample is about 0.8 seconds, model-scale, which is equivalent to 12 seconds (full-scale).

Vertical landings

The vertical landing manoeuvres were carried out at an equivalent landing velocity of 1.2m/sec from a full-scale height of 12 metres with data recording continued for a period of about 30 seconds, full-scale, after wheels-on. This procedure enabled data to be extracted during the landing manoeuvre to wheels-on and subsequently to provide data after landing as NO-GO test results, see above.

Analysis procedures

From an engine performance and stability standpoint it is vital to determine the peak values of mean temperature rise ($\Delta T_{120}^\circ\text{C}$) and circumferential distortion (TC_{120}) at the engine-face, which are defined in Appendix 1 and the derivations of which are discussed in Ref. 9. The peak TC_{120} for a sample landing is shown on Figure 8(a).

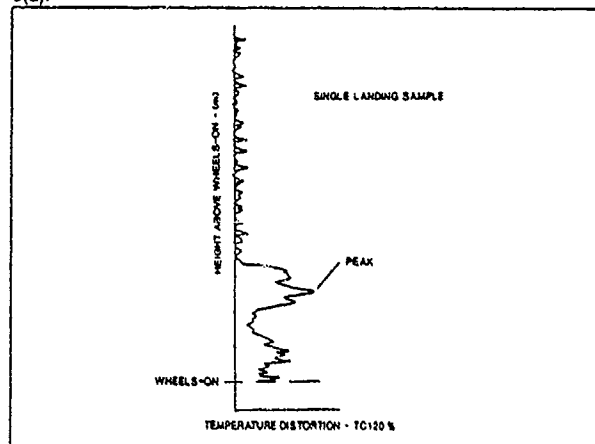


Figure 8a

Due to the stochastic nature of HGR the peak values for a single landing are unlikely to be repeated in subsequent manoeuvres. This is illustrated in Figure 8(b) for a sample repeat landing. Overlays of ten successive landings are superimposed on Figure 9(a) and 9(b) for Configuration 2 tested at buoyancy-scaled ($NPR_F = 1.07$) and full-scale nozzle pressure ratio ($NPR_F = 2.46$).

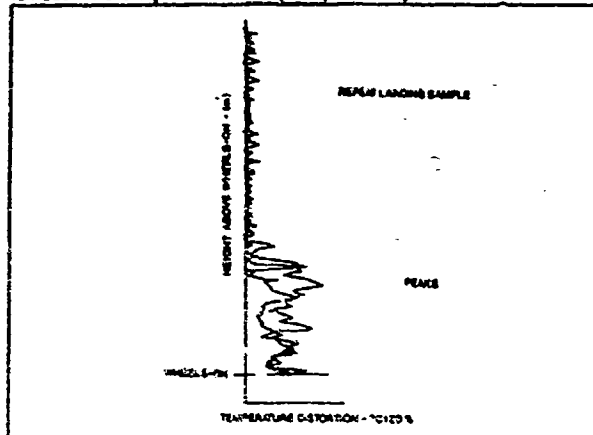


Figure 8b

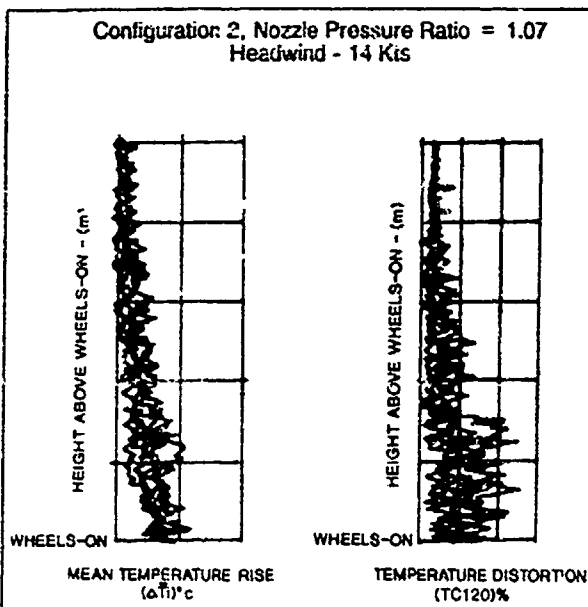


Figure 9a

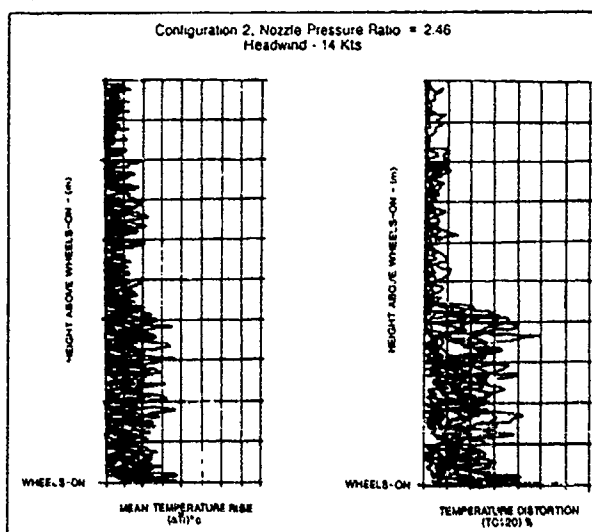


Figure 9b

For a 'first look' analysis examination of the levels and spread of the peak values of mean temperature rise and temperature distortion can be used to assess the relative performance of individual configuration or, for example, the effect of headwind on a given

configuration. This procedure provides only a limited analysis technique and Rolls-Royce is currently developing statistical procedures to identify the significance of differences between peaks for alternative geometries or for headwind effects. These procedures are outside the scope of this paper but are examined in detail in Ref. 10. A limited discussion of the technique is presented later.

Results

Results are presented for tests carried out both at buoyancy-scaled and full-scale nozzle pressure ratio conditions to enable the effects of headwind and nozzle pressure ratio to be established for the various CAD configurations. Results for NO-GO VTO's and vertical landings are presented. Every test point presented in the results figures represents the peak value of mean temperature rise or temperature distortion encountered throughout the particular manoeuvre.

Effect of headwind - NO-GO VTO's

For NO-GO VTO's Figures 10(a) to 10(d) generally indicate a rise in both peak mean temperature rise and distortion as headwind is increased with the levels recorded for the high NPR tests generally exceeding values measured at buoyancy-scaled conditions. This increase with headwind is perhaps to be expected as more of the forward-flowing ground sheet will be blown back into the vicinity of the intakes as headwind is raised. Based on the data samples there are, however, clear differences for buoyancy-scaled, (low jet velocities) and full-scale NPR conditions. For the former the maximum ΔT_i and TC_{120} occur at the highest wind speed tested of 30 Kts whereas for the full-scale NPR tests the maximum ΔT_i and TC_{120} appear to occur at around 12 Kts headwind with little variation in the range 10 Kts to 15 Kts. This is an unexpected result as, for the same jet/headwind dynamic head ratio, the blow back characteristics would be expected to be similar. Two candidate explanations of the different effect of headwind at buoyancy-scaled and full-scale NPR have been considered. Data from Ref. 8, see Figure 3, indicates that tests at the same dynamic head ratio can give some variation in ground jet forward penetration as NPR is increased. The differences have been attributed to decreased entrainment rates for the supersonic jets, Refs. 8 and 7. However, for the tests in question carried out at $NPR_F = 1.07$ and 2.46 the penetration distances appear to be very close and do not, therefore, explain the differences recorded in HGR levels at a given wind speed. It is also evident from Figure 3 that the penetration distances are large, approximately 60 front-nozzle diameters, which suggests good opportunity for mixing of the hot ground sheet with cold ambient air. This in turn suggests little expectation of a large rise in inlet temperature with increasing wind. This is not borne out in the results.

A second explanation must be sought and this may lie in the effect of NPR on the strength of the central fountain between the front jets which increases greatly for tests of $NPR_F = 2.46$ relative to 1.07, Refs. 4, 5 and 6. The increased fountain strength is likely to deflect more hot gas into the vicinity of the intakes to be ingested directly or to be blown in by the oncoming wind. The direct path effect is shown on Figures 10(b) and 10(d) with the hot gas levels progressively reduced as the enlarged and extended CAD's are introduced from Configuration 1, through 2 and 2(a) to 3. This trend is not shown for the low pressure tests where the fountain is controlled with all CAD designs collecting the low energy upwards flowing gas.

The high NPR tests data suggests worst ingestion at a wind speed of about 12 Kts where the flow escaping the CAD's is blown back into the intake. At low velocity the gas penetrates further in front of the intake and is more diluted before ingestion. At higher speeds the reflected gas is blown behind the intake.

Effect of headwind - vertical landings

Trends similar to the NO-GO VTO's are exhibited for the vertical landing manoeuvres, see Figures 11(a) to 11(d) with rises in peak mean temperature rise and distortion as headwind is increased, and with the same differences in the wind speeds at which the peak levels of HGR are encountered for the buoyancy-scaled and full-scale NPR data. This may be explained on the basis that for the VL

the aircraft is descending into the same general flow field as would be eventually set up for the NO-GO VTO. Comparisons of Figures 10(a) and 11(a) and 10(b) and 11(b), however, indicate lower levels of peak mean temperature rise for the VL's than for the NO-GO VTO's. This can be explained on the argument that the aircraft in the VL manoeuvre descends to the ground before the steady-state flow field is fully established as will occur in the prolonged NO-GO VTO. For peak mean temperature distortion values, see Figures 10(c) and 11(c) and 10(d) and 11(d), particularly for the high NPR tests, there are instances of peak distortion levels for some landings which are greater than the worst levels recorded in the NO-GO VTO's. This effect is discussed below.

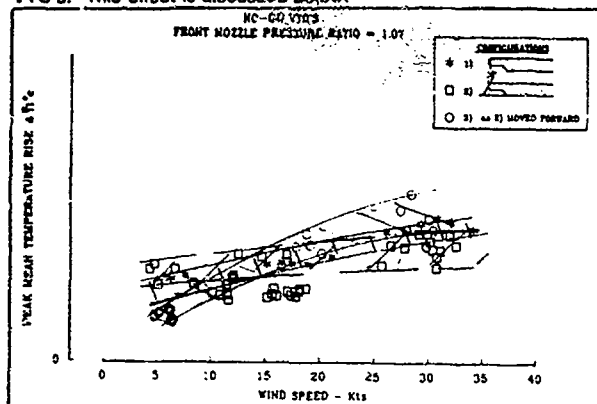


Figure 10a

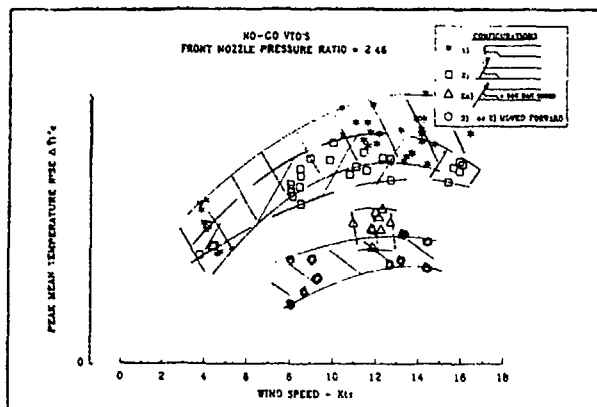


Figure 10b

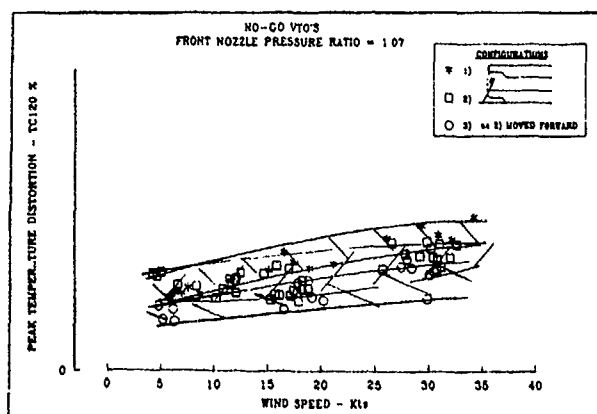


Figure 10c

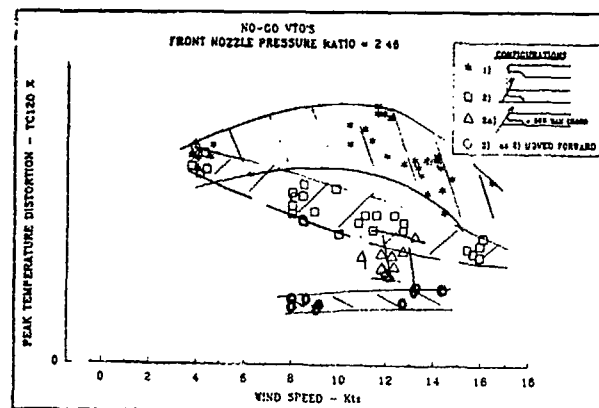


Figure 10d

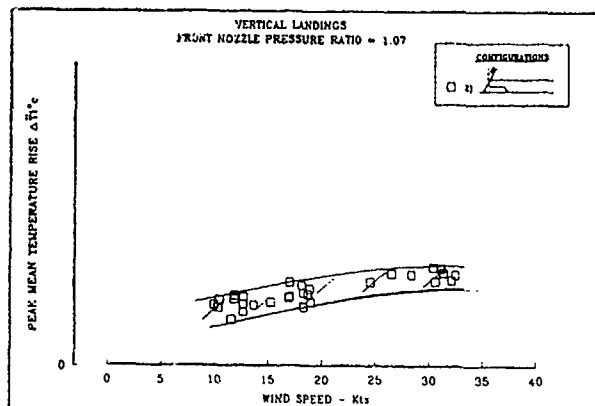


Figure 11a

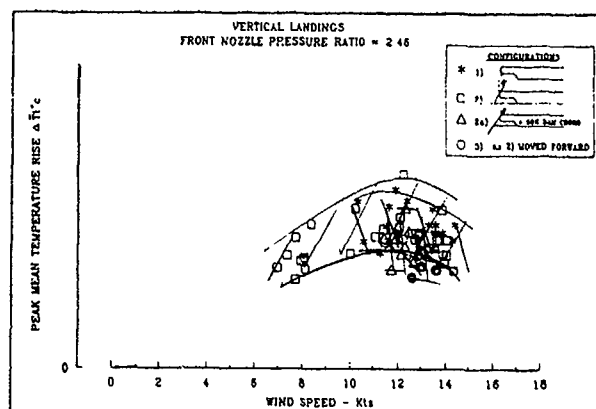


Figure 11b

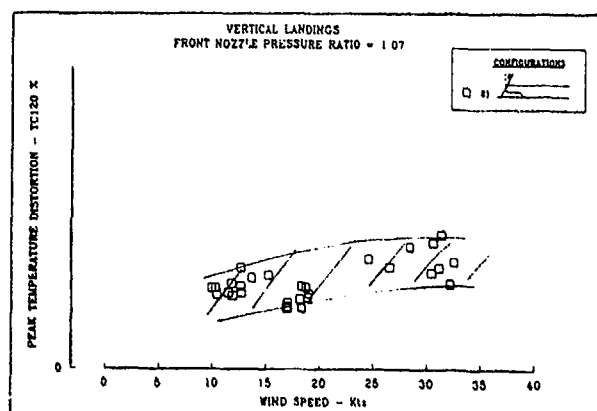


Figure 11c

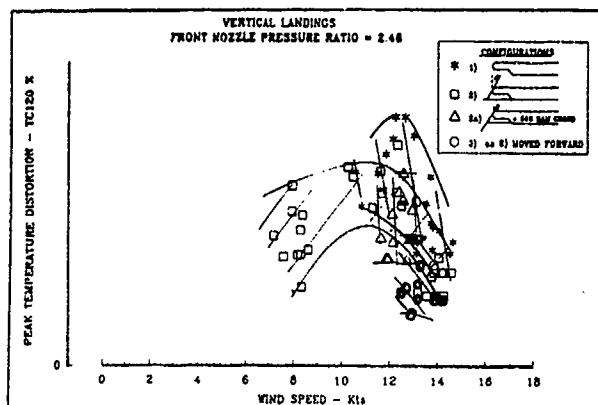


Figure 11d

Variation with height - vertical landings

Further information on the reasons for the occasional high distortion levels for the CAD designs which perform best in the NO-GO can be found on Figures 12(a) and 12(b).

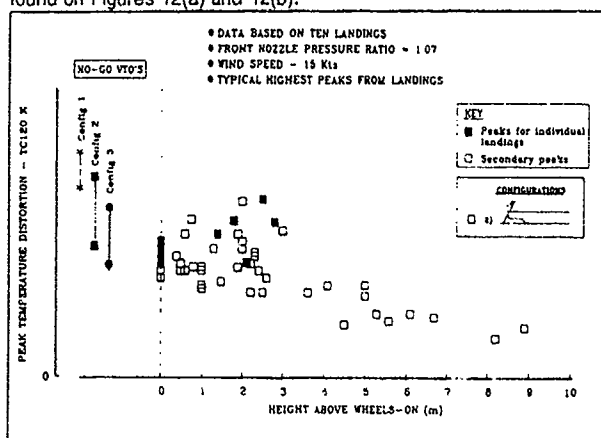


Figure 12a

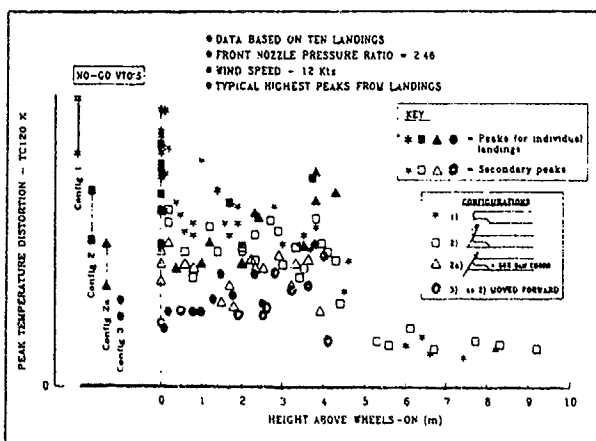


Figure 12b

The figures present results for Configurations 1, 2, 2(a) and 3 at full-scale NPR's (Figure 12(b)) with results for Configuration 2 only available at buoyancy-scaled conditions (Figure 12(a)). These figures, drawn for a full-scale headwind of 12 Kts - 15 Kts, illustrate the peak levels of temperature distortion recorded for every landing shown as solid symbols, but with additional points added which exhibit particularly high levels of distortion for individual landings. It could be noted that for some landings the 'secondary' peaks are greater than the worst levels recorded throughout other landings and some of the levels recorded by the modified CAD's exceeded the worst levels recorded in NO-GO VTO. A possible reason for these isolated peaks is that, during a given landing, while the majority of the gas in the fountain is contained by the CAD some small pockets of hot gas can escape to be sucked in by the intakes. These small pockets of gas create regions of elevated temperatures at the engine-face to produce increased levels of temperature distortion but are too localised to have a significant effect on the mean

temperature rise. For the ten landing data sets available the occurrence of peaks at heights well above wheels-on appears to be more frequent for the CAD geometries which perform best at wheels-on. The statistical significance of this result for the small data samples is discussed in Ref. 10.

The occurrence of peaks above wheels-on during vertical landings illustrates that for a full analysis of the performance of a given configuration it is insufficient to rely solely on 'engine confidence check' NO-GO VTO's. To ensure that the infrequent peaks which might occur at heights well above wheels-on are identified during model tests the following procedures are recommended. Firstly it is necessary to undertake multiple repeat tests of a given geometry to improve the chances of encountering the infrequent peaks. Secondly, it is necessary to develop statistical techniques to evaluate the extreme values which might occur in the many repeat landings carried out by operational aircraft and at what heights they might occur.

Effect of nozzle pressure ratio (NPR) - NO-GO VTO's

The effect of NPR on the absolute levels of intake peak mean temperature rise and distortion for the various CAD configurations in NO-GO VTO's is shown on Figures 13(a) and 13(b).

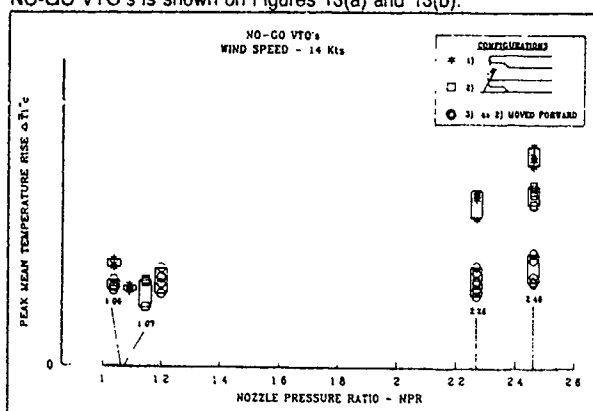


Figure 13a

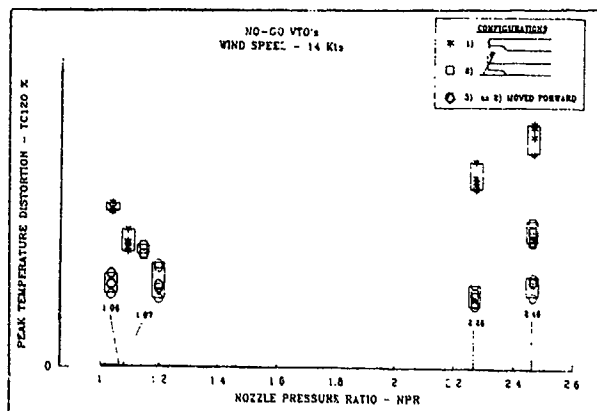


Figure 13b

These figures present cross-plots of the tests included on Figures 10(a) to 10(d) at a chosen headwind of around 14 Kts and also include results from tests on the Harrier model tested at conditions simulating the current Pegasus engine with a full-scale front nozzle pressure ratio of 2.26 (1.06 at buoyancy-scaled conditions). The figures indicate a large increase in both peak ΔT_i and peak TC_{120} at the full-scale NPR's for the least effective CAD, Configuration 1. The increase is progressively reduced through Configuration 2, to Configuration 3 for which the levels of HGR remain near constant at all nozzle pressure ratios. These results indicate that the choice of test technique can produce widely different indications of HGR levels for geometries which are susceptible to near-field ingestion. For 'good' configurations the low levels of HGR attainable will be identified for either test technique. This latter result supports the proposition that 'low-HGR' configurations can be examined using the current buoyancy-scaled test technique which is attractive in terms of rig mechanical requirements and the demands of instrumentation integrity and response. The proposition is, however, flawed in that the 'good' and 'less good' configurations provide

similar results at buoyancy conditions but tests at high NPR are still required to identify whether a given geometry will exhibit increased HGR. A further question to be raised is - which test techniques produce results representative of the full-scale aircraft? This will be discussed later.

Effect of nozzle pressure ratio - vertical landings

Fewer landings than NO-GO VTO's were included in the test programme and buoyancy - scaled data is available for CAD Configuration 2 only. The results are presented in Figures 14(a) and 14(b) at a headwind of 12 Kts from tests at nozzle pressure ratios of 1.07 and 2.46. A similar trend to the NO-GO VTO's, namely an increase in peak ΔT_i and TC_{120} at high NPR is evident but the significance of this result is less clear for landings as the measured peaks occur over a range of aircraft heights.

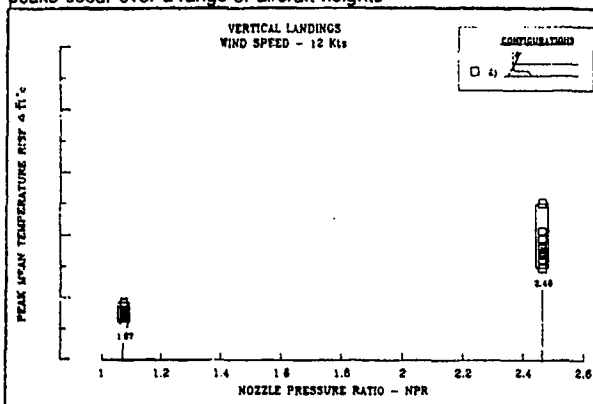


Figure 14a

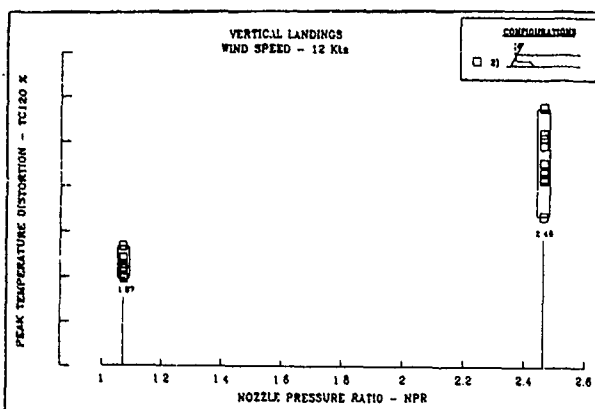


Figure 14b

Statistical analysis

For the small samples available the levels of peak mean temperature rise and distortion recorded from tests at $NPR_F = 2.46$ with changes in CAD geometry for NO-GO VTO's are well defined with little overlap between configurations at a given wind speed, see Figures 10(b) and 10(d). It is evident that application of simple ordered statistical grouping will confirm the significance of true variations between the geometries.

For the landings, where larger samples are generally available, (circa 10) the picture is less clear, see Figures 11(b) and 11(d), where extensive overlaps occur between different configurations at a chosen wind speed. The problem is complicated in that the recorded peaks occur at different aircraft heights above ground. A proper analysis of the significance of differences between configurations requires a more detailed study. Rolls-Royce has attempted this by analysing the results from multiple landings in narrow height bands. Within these bands statistical methods are employed to determine the significance of variations between levels for different geometries and to enable prediction of extreme values likely to occur in multiple manoeuvres through that height. The method is described in Ref. 10.

The methods confirm the indications from the peak values during a landing analysis of the improved performance of the modified CAD's with the aircraft close to the ground. The small samples (circa 10)

make differences between configurations difficult to quantify during landings but the methods suggest that the results for the various geometries all fall in the same set at heights above about 1.5 metres above wheels-on. On this basis the larger number of peaks of heights well above wheels-on recorded for the more effective CAD's are not significant and similar high levels might have been recorded in Configuration 1 had sufficient manoeuvres been completed.

Comparison of model and full-scale

Investigations to examine the model test techniques required to enable accurate prediction of HGR levels for full-scale configuration are severely restricted by the limited full-scale information available, the quality of instrumentation used, environmental variations and the different test techniques employed. Figures 15(a) and 15(b) present data from a range of available model tests and the limited full-scale information acquired.

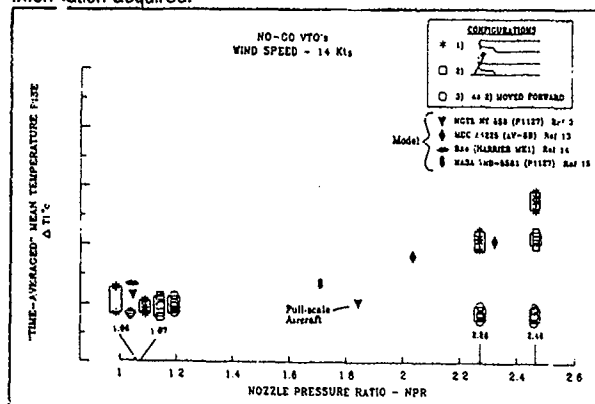


Figure 15a

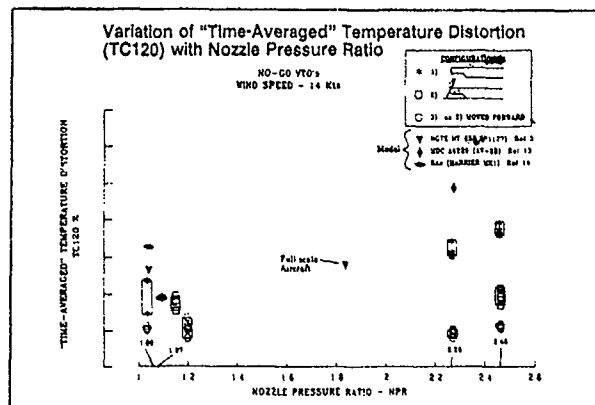


Figure 15b

The results are in the form of time-averaged mean temperature rise and distortion which are derived as the average of successive values of mean temperature rise and distortion recorded over a period of time during simulated NO-GO VTO's or low level hovers. Model data are available from the following sources:

(a) P1127 1/10th scale model tests reported in Ref. 3 carried out at buoyancy-scaled conditions.

(b) AV-8B 1/10th scale hover tests carried out by McDonnell Douglas with the model tested at representative full-scale NPR's, Ref. 13 refers.

(c) Harrier Mk1 1/10th scale model hover tests carried out by British Aerospace with exhaust conditions set up observing the buoyancy-scaling relationship.

(d) A large approximately 1/3rd full-scale model similar to the P1127 tested at NASA Langley with the exhaust to all four nozzles provided by a J85 engine. These data are reported in Ref. 14

(e) The Harrier 2 model NO-GO VTO tests reported in this paper covering buoyancy-scaled and full-scale NPR conditions. Full-scale data are available from a single source only :-

(f) P1127 NO-GO VTO trials reported in Ref. 3.

The configurations all employed longitudinal underfuselage strakes with the exception of (d) while the AV-8B model incorporated a cross-dam similar to Configuration 1 of the present tests. Tests under (b), (d) and (e) had headwind representation while the (a), (c) and (f) studies were at nominally zero headwind.

The following observations can be made from Figures 15(a) and 15(b).

The Harrier Mk1 and P1127 models tested at buoyancy conditions and zero headwind gave slightly higher levels of ΔT_i and TC_{120} than for the present Harrier 2 model tests. These higher values can be attributed to the absence of a dam with the underfuselage strakes channelling the hot gas from the front fountain forwards towards the intake. The effect of the 14 Kts headwind on the present tests is considered to be small, see Figure 10(a), but would, if anything, reduce the HGR levels for the Harrier 2 configuration at the zero headwind condition.

The P1127 full-scale aircraft results (average from 4 events) agree well with the buoyancy-scaled model results (average from 12 events). This was noted in Ref. 3 and formed the basis of the buoyancy scaling techniques subsequently adopted for STOVL aircraft model tests in the UK although the report stated that the observance of buoyancy was not essential for near field HGR. The full-scale results, Ref. 3 should be treated with some caution. The data are based on a very limited thermistor coverage at the engine face, such that pockets of hot gas might have gone undetected. Further the full-scale tests formed part of a series to measure HGR for a range of nozzle aft vector angles during NO-GO VTO's. At 30° aft vector the mean temperature rise results were low and in good agreement with model data. At 15° aft vector, however, the full-scale ΔT_i data was some 60% greater than the model evidence while at zero vector the model results slightly exceed the full-scale evidence, see Figure 15(a).

The large scale NASA model P1127 type configuration gave results similar to the P1127 aircraft when the intake mean temperature rise was scaled on equivalent front jet excess temperature. It should be noted that the NASA tests were carried out with all four nozzles running at an exhaust temperature of about 920K.

The AV-8B model (Configuration 6) tests with representative choked nozzles gave mean temperature rise results close to the present Harrier 2 data with Configuration 1 which is closest to the AV-8B geometry. Temperature distortion levels for the AV-8B were, however, much higher.

It is rather difficult to draw definitive conclusions from the above evidence. There is, however, a clear indication that tests at full-scale NPR on a geometry susceptible to HGR, give HGR levels considerably greater than for tests at buoyancy conditions. The very limited full-scale evidence supports results from buoyancy-scaled tests but with some question marks on data accuracy.

It is noticeable that the increased levels of HGR are recorded for supersonic exhaust conditions whereas the model/full-scale comparisons can be made only for subsonic exhausts. It is considered that the evidence is insufficient to indicate the universal validity of tests either at buoyancy or full-scale NPR's. To best ensure that the model tests indicate worst expectations of HGR for a given geometry with close-coupled exhausts that configuration should be tested both at full-scale and buoyancy-scaled NPR's. In this way sources of HGR attributable to direct 'near field' or 'mid' or 'far' field flow mechanisms can be identified. It is recommended that consideration should be given to 'press-up' trials of the latest Harrier/AV-8B aircraft employing supersonic front exhausts and suitably instrumented to afford comparisons with the recently acquired model data. This will guide the direction of future model test techniques for replacement Harrier aircraft.

Concluding remarks

Peak mean temperature rise (ΔT_i) and distortion (TC_{120}) increases recorded with headwind for NO-GO Vertical Take-offs and landings are greatest for configurations where hot gas reingestion (HGR) reduction measures are least effective. The rises are attributed to hot gas from the front fountain escaping the Cushion Augmentation Device (CAD), formed by the underfuselage strake/dam geometry,

to be blown back by the headwind into the engine intake. Potential sources of HGR due to blowback of the ground sheet are not thought to be the cause of increased HGR with headwind due to the large penetration of the ground sheet forwards before blowback which gives good opportunity for mixing and hence a low expectation of increased temperature of the intake entry air.

CAD configurations which generally produce the most effective HGR control during NO-GO VTO's can produce higher levels of distortion at heights well above wheels-on which present a risk for operational aircraft. The "best" CAD's are believed to permit small pockets of hot gas to escape, with low energy, which are then susceptible to ingestion by the intake, especially with headwinds.

The modifications to the existing Harrier CAD's represent an effective means of HGR control for future Harrier developments with more powerful Pegasus engines although further tests are recommended to reduce the risk of infrequent occurrences of high distortion above ground.

Buoyancy-scaled and full-scale nozzle pressure ratio (NPR) test techniques give similar indications of HGR levels, both peak ΔT_i and TC_{120} , for configurations which exhibit low HGR. Full-scale NPR tests give much higher indications of HGR levels for the less effective CAD designs.

References

1. Cox M and Abbott W A. Studies of the flow fields created by simple vertical jets directed downwards upon a horizontal surface. - NGTE Memorandum M390 October 1964.
2. Abbott W A. Studies of flow fields created by vertical and inclined jets when stationary or moving over a horizontal surface. - NGTE Memorandum M391 October 1984.
3. Allcock A W R and Abbott W A. Full-scale and model studies of exhaust ingestion on the Hawker Siddeley P1127 with special reference to scaling laws. NGTE Note No. NT658 October 1967.
4. Adarkar D B and Hall G R. The 'Fountain' effect and VTOL exhaust ingestion AIAA 68-79.
5. Hall G R and Rogers K H. Recirculation effects produced by a pair of heated jets impinging on a ground plane.

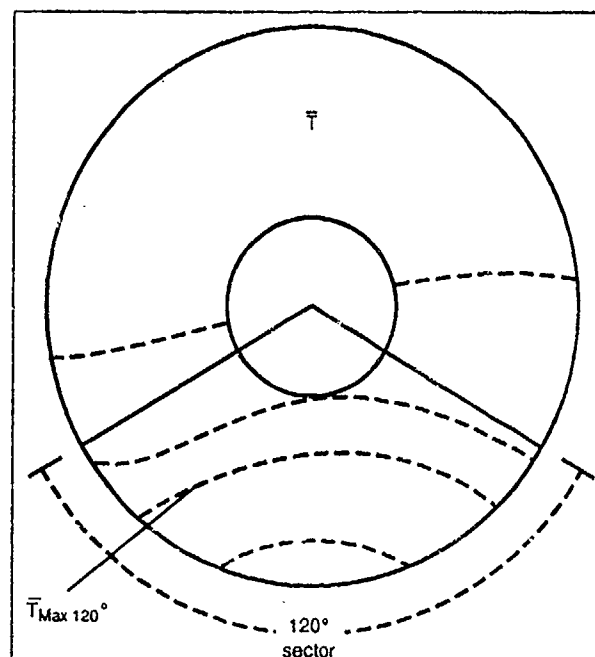
NASA CR-1307 1969.

6. Abbott W A and White D R. The effect of Nozzle Pressure Ratio on the fountain formed between two impinging jets.
- RAE Tech Memo P1166 May 1989.
7. Curtis P. Single jet entrainment - A summary report.
British Aerospace report BAe-KAE-N-RES-3888 January 1992.
8. Knowles K, Bray D, Bailey P J and Curtis P. Impinging jets in cross-flow.
International Powered Lift Conference - London, August 1990 (RAe.S).
9. Williams D D. Hot Gas Reingestion. Engine-response considerations.
International Powered Lift Conference - London, August 1990 (RAe.S).
10. Beasley R. Unsteady aspects of Hot Gas Recirculation and Statistical Analysis. Paper 18. AGARD Symposium on Computational and Experimental Assessment of jets in Cross-flow - Winchester, UK. April 1993.
11. Penrose C J. The requirements for and evolution of a test rig for exhaust gas recirculation studies of V/STOL aircraft Paper No. 35. Sixth European Rotorcraft and Powered Lift Aircraft Forum - Bristol. September 1980.
12. Holmes M, Flitcroft J E and Penrose C J. A Propulsion view of ground effects research. Paper No. 18. AGARD CP-465 Madrid. October 1989.
13. Hall C L and Kamman J H. Hot exhaust gas ingestion characteristics of a small-scale Harrier type V/STOL aircraft model.
McDonnell Douglas Corporation Report No. MDC A4225, August 1977.
14. McLemore C L, Smith C C and Hemeter P G. Generalised Hot Gas Ingestion investigation of large-scale jet VTOL Fighter-type models. NASA TND-5581 January 1970.

Acknowledgements

The author wishes to acknowledge with thanks the assistance of his colleagues at Rolls-Royce, without whom this paper would not have been possible, and to Rolls-Royce plc, for permission to publish this paper. The views expressed are those of the author and are not necessarily those of Rolls-Royce.

Appendix



Spatial Distortion Descriptor - Circumferential Distortion

Distortion coefficient -

$$T_{C120^\circ} = \frac{\bar{T}_{Max120^\circ} - \bar{T}}{\bar{T}}$$

$$\text{or } T_{C120^\circ} = \frac{\Delta \bar{T}_{Max120^\circ} - \Delta \bar{T}}{\Delta \bar{T} + T_\alpha}$$

where $\Delta \bar{T}$ = Mean temperature rise above ambient over the complete engine face

$\Delta \bar{T}_{Max120^\circ}$ = Highest mean temperature rise in any 120° sector of the engine face

Unsteady aspects of Hot Gas Reingestion and statistical analysis

R Beasley

Powerplant Technology
Rolls-Royce plc
PO Box 3
Filton
Bristol
BS12 7QE
England

Abstract

The ingestion of engine exhaust gases into an aircraft intake during jet-lift Advanced Short Take-off and Vertical Lift (ASTOVL) aircraft operation close to the ground is an area of considerable concern and has been the subject of much experimental study.

The recirculatory flows follow complex paths which are strongly influenced by interference with the ground, aircraft structures, adjacent jet streams and by the action of an oncoming headwind. The flows are by nature turbulent at a large scale and unsteady with 'streaks' of hot gas entering the intake in a random manner. This Hot Gas Reingestion (HGR) can erode engine stability margins in a region of aircraft operation where reliable engine performance is critical.

To ensure engine stability sophisticated analysis techniques are required to enable prediction of worst-case destabilising temperature distortion levels for a chosen aircraft/engine combination.

This paper describes the development and application of statistical analysis techniques designed to examine results of model experiments. These techniques enable quantitative conclusions to be reached as an extension to qualitative examination of trends from observed data.

Due to the nature of the flow and distortion parameter, observed HGR data distributions are frequently not normal (Gaussian) and standard statistical techniques cannot be used.

Methods for testing whether a data sample distribution is normal and if there is a significant difference between two sets of data (regardless of distribution shape) have been identified. Use of these techniques enables suitable samples of experimental results to be used for extrapolation to extreme values. The Weibull distribution has been found to produce a good fit to observed data and to be amenable to extrapolation for this application.

The use of these techniques is illustrated by results from a series of model tests demonstrating the potential for considerable reduction in HGR levels by using under-fuselage flow diverter arrangements. These statistical analysis techniques have also been applied to tests with model jet conditions set to different absolute pressure ratios whilst maintaining dynamic head similarity, and to tests carried out at different headwinds. The work has emphasised the need for an adequate number of repeat tests so that a suitable database may be used for extrapolation.

The work described in this paper provides a quantitative method for the analysis of time-dependent HGR phenomena encountered in ASTOVL aircraft operations near-ground with headwind interacting with the various jet plumes.

List of symbols

- ΔT_i Overall mean intake temperature MSC
TC120 Distortion coefficient
ASTOVL Advanced Short Take-Off and Vertical Landing
CAD Cushion Augmentation Device
(Underfuselage strake / dam assembly)
HGR Hot Gas Reingestion

NPR Nozzle Pressure Ratio

NO GO VTO No Go Vertical Take-Off
(Engine 'Confidence check' manoeuvre with vertical thrust less than aircraft weight, so lift-off prevented)

θ Critical sector angle

\dot{T} Intake temperature rise rate

Introduction and background

This paper is a companion to the previous paper presented at this conference (reference 1). The purpose is to develop the theme of the unsteady nature of recirculating gas flows, and to introduce some of the statistical techniques that can be used to analyse test results.

As engine manufacturers Rolls-Royce are responsible for the stability of the engine, which is affected by the ingestion of exhaust gases into an aircraft intake during jet-lift ASTOVL operation close to the ground. In vertical landing and take-off manoeuvres the recirculatory gas paths are complex and are strongly influenced by interference from the ground, aircraft structures, adjacent jet streams and the action of an oncoming headwind. The resulting gas flow patterns are highly turbulent and unsteady. Some "hot streaks" of gas may enter the intake in a random manner, causing a variation of temperature distribution at the engine face.

The phenomenon of this Hot Gas Reingestion (HGR) has been the subject of much experimental and theoretical study. Recent work (reference 2) has shown that the stability response of a jet engine compressor to HGR is controlled by two parameters. These are a distortion coefficient, $TC(\theta)$, where θ is a critical sector angle for the compressor in question, (120 is typically used) and bulk intake mean temperature rise rate, \dot{T} . Figure 1 shows a typical distortion pattern, and a definition of the $TC(120)$ parameter.

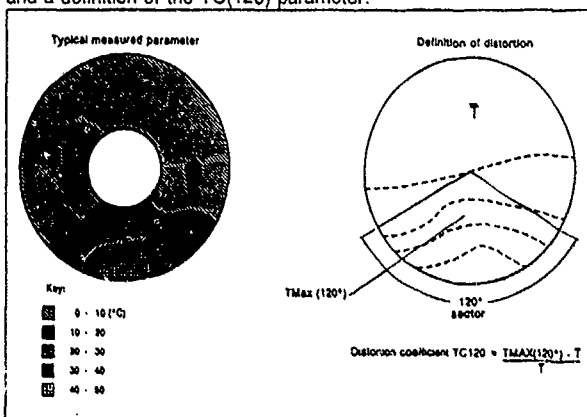


Figure 1

The definition of $TC(120)$ is such that values less than zero cannot exist so the distribution is necessarily bounded to be positive. An additional HGR parameter of importance is overall average intake temperature rise, ΔT_i . This can affect the overall thrust of the engine, and is a useful parameter to examine the bulk HGR processes.

The results of HGR measurements show considerable variation between repeat manoeuvres with the same operational conditions. This is evidence of the stochastic nature of the HGR process, which must be recognised in the analysis method.

Vertical landing and take-off is a safety critical part of the operating flight envelope of aircraft like the Harrier. The engine operates at high power and engine instabilities seriously degrade service life. Additionally, due to the close proximity of the ground there is no room to recover from a loss of thrust, and the resulting heavy landing can have significant effect on airframe integrity. Therefore a key requirement in the design of STOVL-type powerplants is a knowledge of the worst-case destabilising conditions expected. The engine must either be tolerant of these levels, or the aircraft or nozzle configuration must be altered to reduce these levels. This problem becomes increasingly important with increasing thrust levels with hotter, more powerful jets.

Obtaining HGR data is a difficult and expensive process, and full-scale data is very rarely obtained. Therefore results are obtained from model scale tests. For landings, work in the UK (reference 3) has shown the need to represent the dynamics. The issue of scaling laws for HGR tests has been the focus of consideration from the early years of STOVL aircraft (references 4 and 5). Much test work has been carried out at greatly reduced pressure levels, maintaining dynamic head similarity and correctly modelling the buoyant action of the gas. In this procedure the ratios of buoyant and inertial forces are maintained as for full scale. An alternative method is to test at full-scale pressure conditions, (reference 6). Both scale on excess temperature values. There is no established universal procedure, and the results presented in this paper suggest that the test technique depends on which parts of the flowfield dominate the HGR process.

Even at model scale the number of repeat manoeuvres carried out for each set of test conditions is limited, and so methods are needed to statistically examine the data to identify differences between sets of tests, and to extrapolate to find worst-case values. Some of these methods are presented in this paper.

Model data under consideration

A number of different aircraft configurations were tested at model scale, illustrated in Figure 2.

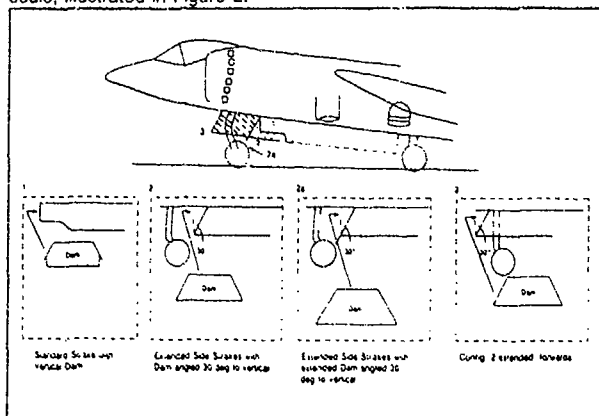


Figure 2

These geometries represent changes to the under fuselage strakes and dams on the aircraft. These devices, known as Cushion Augmentation Devices (CADs) are included on present Harriers to deflect the so-called "fountain" upwards arising from the colliding ground jets and so enhance lift. This deflection of the hot gas acts as a considerable HGR reduction measure. The new geometries tested represent an attempt to optimise this anti-HGR performance.

Configuration 1 represents a current geometry on the Harrier. Configuration 2 has deeper strakes than configuration 1, and the dam is angled at 30 degrees to the vertical. Configuration 2a is as configuration 2, but with the dam increased in length by 50%. A fourth geometry, configuration 3, was tested which was as configuration 2, but with the entire strake/dam arrangement moved forward. Configuration 3 results were not analysed to the same extent as the others.

The analysis presented in this paper concentrates on 3 aspects of the model test results; firstly the effect of geometry, secondly the effect of test nozzle pressure ratio (NPR), and finally the effect of headwind on results. Throughout this paper all results presented

have been suitably scaled to full-scale values, with temperature measurements corrected for thermal lag.

For geometry effects results have been taken from simulated landings tested at full-scale pressure conditions, with temperature scaling based on front nozzle excess temperatures, at headwinds of around 12 knots. At the end of each landing the model was held on the ground, to simulate a NO-GO VTO. A NO-GO VTO is an engine confidence check, where full thrust is applied, but the load weight of the aircraft prevents take-off. Ten repeat landings were carried out with each geometry.

To examine the effect of model test scaling conditions the results of simulated NO-GO VTOs from configuration 1, 2 and 3 were used. ΔT_i and TC(120) values were examined from results at full-scale NPR and buoyancy scaled conditions, tested at the same headwind. The results from NO-GO VTOs were used to eliminate height as a variable.

Finally, the effect of headwind is examined by looking at ΔT_i and TC(120) results from configuration 1 at four different headwinds. Between five and ten repeats were carried out at full-scale NPR conditions for each headwind.

The model tests carried out to examine the potential risk of increased HGR with the more powerful engines in the Harrier 2 and AV8B, introduced in the previous paper, showed low values of temperature rise-rate. Therefore only TC(120) needed to be examined to analyse destabilising effects. The distribution of the TC(120) values was found to be extremely non-normal, and so statistical techniques are required to accommodate small samples without any assumption of a normal distribution.

Analysis methods

A typical trace of TC(120) against height for a single landing, as shown in Figure 3a, has a clearly identifiable peak. When repeat landings for the geometry are overlaid (Figure 3b) the range of different peaks can be seen. This overlay of results clearly illustrates the stochastic nature of the process.

The standard analysis techniques has been to take the peaks from each landing, and show the observed range for each different geometry, as shown in Figure 3c. This is a valid procedure and gives an initial idea of the effect of geometry. In this case changes in geometry have had a considerable effect on the peak levels of distortion.

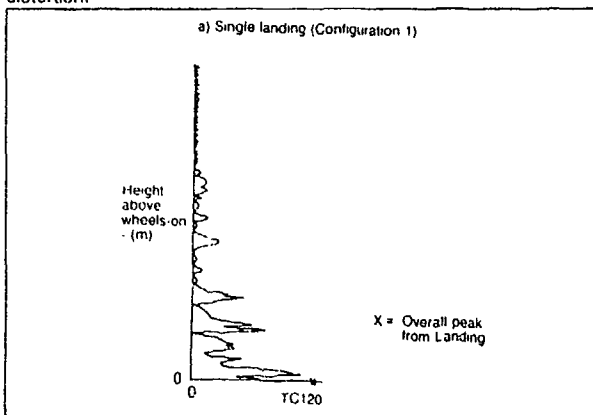


Figure 3a

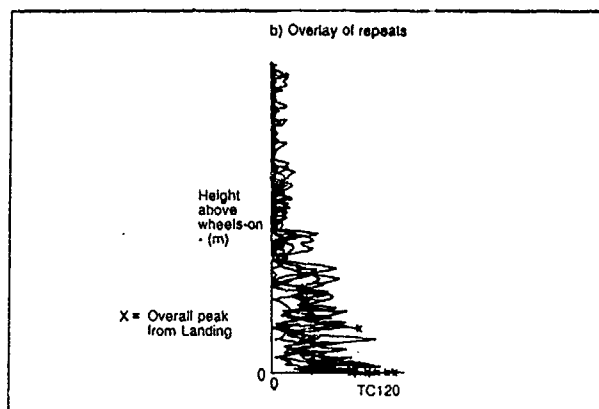


Figure 3b

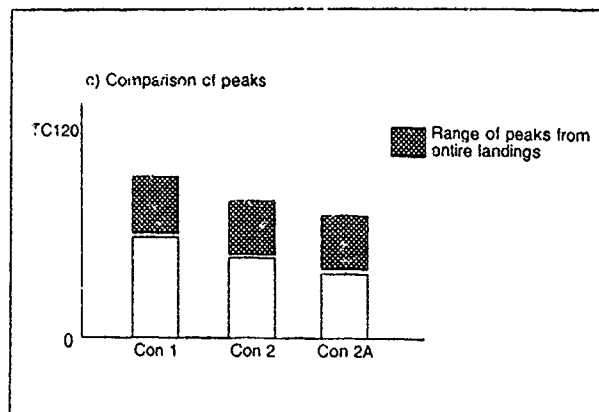


Figure 3c

This simple analysis ignores the effect of height. The results for configuration 1 (Figure 3) showed nearly all the peaks occurring together extremely close to the ground. However for configuration 2a the peaks occurred at various different heights. This is illustrated in the overlay of landing results shown in Figure 4. This result shows that height must be taken into consideration, as peaks at different heights are possibly coming from different mechanisms on different geometries. Therefore a technique has been devised that examines the landing in a series of height bands. An example of the height bands that could be used is shown in Figure 5a. Analysis is performed to predict the peak level in each band Figure 5b shows the different distributions of TC(120) that are found at different heights.

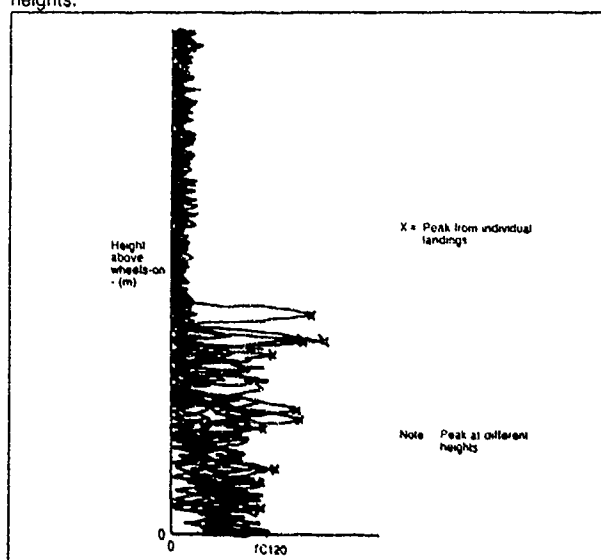


Figure 4

These distributions have been found to be generally non-normal. The effects of this observation are serious, as it means that many standard statistical methods are not applicable to the data. It is no longer possible to use the standard deviation to extrapolate to a known point in the distribution (mean plus n standard deviations) and confirmation of non-normality is needed, and there are a number of

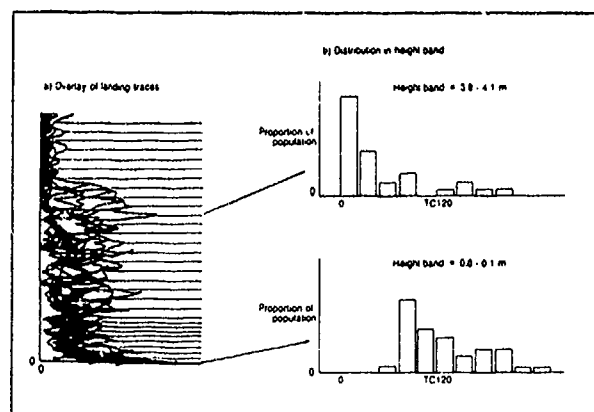


Figure 5

tests that can be used. For the small samples produced by HGR tests the Shapiro-Wilk test (reference 7) has been found to be particularly useful.

For non-normal distributions an alternative means for extrapolating to "worst value" must be found. Previous work on inlet pressure distortion has used Gumbel's extreme value distribution (references 8 and 9) to find expected peaks in intake/engine compatibility studies (reference 10). However, the results of using these extrapolation techniques on temperature distortion values proved most unsatisfactory, producing unbounded and unrealistic solutions. This finding is supported by other work (reference 11) which has shown that 'Gumbel' is not always strictly appropriate for this form of analysis.

An alternative two parameter distribution that is particularly amenable to extrapolation is the Weibull distribution. This is well established as a tool for reliability engineering (reference 12). Once estimates for Weibull parameters have been made extrapolation is readily achievable (see Appendix A).

To produce peak distortion trends with height suitable height bands were selected, within which the Weibull distribution was used to extrapolate to predict the peak in 10,000 landings. 10,000 was taken as a typical life of the aircraft, as well as being a suitably large round number. The considerations made to determine the height bands rely on engineering judgment, as the bands have to be narrow enough to allow quasi-constant values to be assigned where HGR parameters are changing rapidly, but broad enough to smooth out inconsistencies in the data trends due to small sample size. One of the powerful advantages of the Weibull distribution is that it shows up data from different distributions in the quality of the fit. Data from too wide a height band is evidenced by a non-linear fit when the data is presented on a Weibull plot. In order to alleviate these sampling problems it is important that data collection should be as frequent as possible to provide as near an analogue data history as possible.

The analysis may proceed using either all the data within a height band, or simply the peaks from each landing. Stability analysis has concentrated on peaks as it is the distribution of extreme values that is of interest. Peak data is also convenient to use for "first looks" and summaries of data. With the small number of repeat landings there is a danger of results using peaks to be adversely affected by one especially high or low value. This is especially true where overall peak values from a landing occur at different heights. Therefore it is often desirable to expand the data sample to get a better prediction. Using all the data from a landing is one way to do this.

Another useful method is to examine ways of grouping the data. For experiments where different geometries are being tested there may be height regions where aircraft configuration makes no difference. Observation of these regions serves the dual purpose of expanding the data sample, and highlighting the important physical result concerning where geometry does and does not make a difference. Grouping of data can be performed on either peaks or all values. Using all data can ensure that the height bands are kept small.

When test results are grouped it is important to check the assumption that there is no difference between the sets of results.

Due to the small numbers in each group and the non-normal distributions alternatives to the standard techniques have to be applied. Non-parametric tests in general, and the Mann-Whitney in particular, are suitable for this type of problem (reference 13). The Mann-Whitney test compares the rank order of data from two different samples, and states to a given confidence level whether there is a significant variation between the samples. With ten values in each group this test is conservative, and only shows large differences. With increased experience a better idea of the number of values needed to show up subtle variations will become clear. The sensitivity of the test increases dramatically with even small increases in sample size.

Non-parametric tests do not only have applications for extreme value predictions, but can also be used to examine differences between sets of data. For tests at several different physical conditions with controlled test variables, like headwind, a further test is the Kruskal-Wallis test. This is a non-parametric version of regression analysis to see if there is significant variation with the controlled variable.

Variation of peak distortion with geometry and height

The techniques described above were used to analyse the results of model landings for three of the different aircraft configurations shown in Figure 2. The landing traces for each of these configurations, along with the height bands used to perform the analysis are shown in Figure 6.

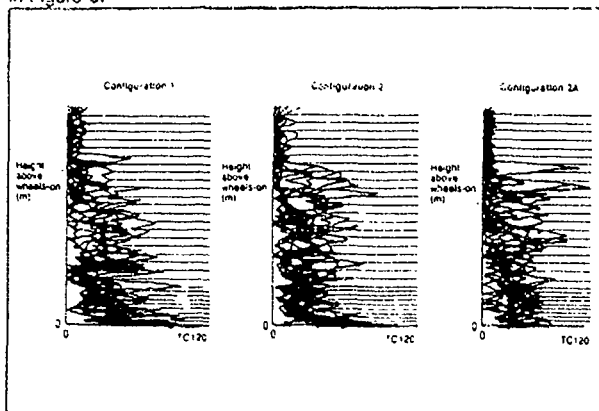


Figure 6

The height bands are the best compromise between large enough bands to ensure a sensible data sample, and small enough to eliminate height as a variable within the band. The tests were all carried out at full-scale NPR.

The Mann-Whitney test was used to show where model geometry was significant. No variation was found above 0.5 m above wheels-on. Due to the small sample sizes these results were checked, and some of the lower heights did not produce acceptable straight line Weibull plots, and so geometries were treated separately below 1.5 metres.

This result is already very interesting and important. The fact that the highest distortion values at mid-landing (around 4 metres) come from configuration 2A and 2 is shown by this statistical analysis to be happenstance, and further repeats on configuration 1 would be expected to produce similarly high values in time. To confirm this the Weibull plot of the height band around 4 metres is shown in Figure 7.

This shows a good straight line fit, given that Weibull plots tend to show some curvature at lower values, backing the assertion that there is no difference between geometries at this height. This is an example of possible false conclusions that could be drawn from carrying out too few landings.

Taking groupings of data where appropriate, predictions for peak TC120 values in 10,000 landings were made for each configuration, using Weibull. The results using peak values and all values are shown in Figure 8.

The trends are the same, but there are differences in absolute levels of distortion, which is not unreasonable.

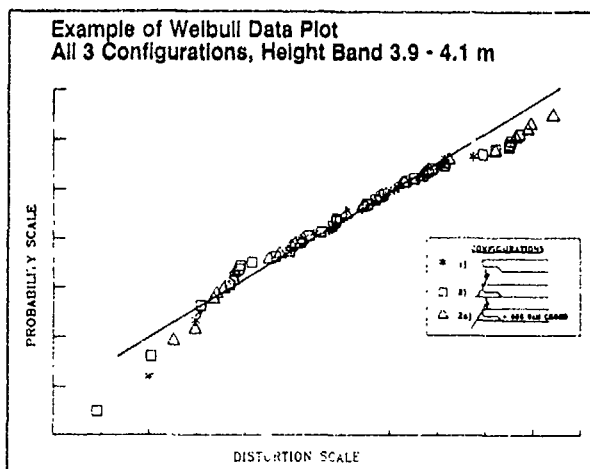


Figure 7

Results from extrapolations from NO-GO VTOs are also shown on Figure 8.

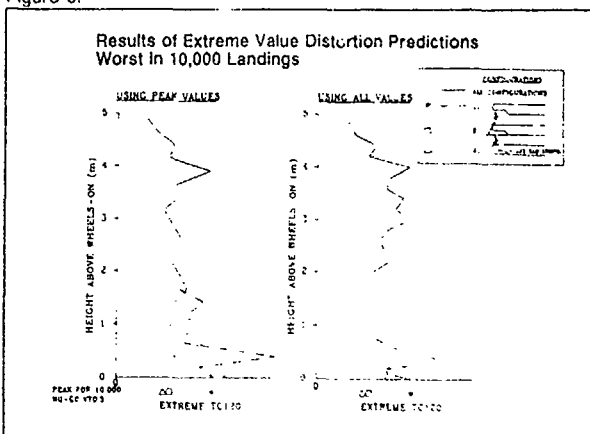


Figure 8

On the ground the two test techniques produce fair agreement except for the configuration 2 data. Examination of the Weibull plot for the landing showed a very poor data fit, due most probably to the small data sample. The NO-GO data formed an acceptable fit and is considered to best represent the performance of configuration 2 near to the ground. Much of the stochastic variation above the ground is due to the interaction of the intake with flowfields set up by exhaust at higher heights, emphasising the importance of dynamic modelling of landings.

These results show that geometry can contribute a very significant reduction in HGR near to the ground, and so can reduce the overall peak distortion level. However there is a cut-off height around 1.5 metres, above which geometry ceases to control HGR levels. This gives evidence of the range of operation where near-field direct path HGR can be controlled by CADs. At heights around 4 metres the hot gas must be coming into the intake via a different flowpath. The distribution at this height is very skewed, with the higher values being rare. The overall ΔT_i values show no bulk HGR, so the distortion must come from small pockets of hot gas separating from the fountain, and intermittently being blown back into the intake.

In terms of aircraft operation, changing from configuration 1 to configuration 2 the overall risk of instability would be reduced, and the worst risk would be at wheels-on. Changing to configuration 2A again would reduce the overall risk of instability, as the area of high distortion near the ground has been removed. However the highest distortion is now significantly above the ground weakening the argument in favour of proposing configuration 2A. Having peak distortion values at height also reduces the value of NO-GO VTOs as a confidence check.

The chance of high (or even worst case) distortion levels at heights where CAD geometry modifications cannot control HGR poses a potential problem to Rolls-Royce as engine manufacturers. As thrust levels and exit temperatures rise candidate engines must either be able to tolerate this distortion, or else other radically different aircraft

installation configurations must be considered. These must fundamentally alter the gas fountain so that pockets of hot gas cannot escape and subsequently find their way into the intake, for example pairs of nozzles converged so that the jets converge before impinging on the ground have been shown effective for earlier model tests of STOVL aircraft configurations.

Effect of model test NPR on HGR levels

The effect of NPR on HGR has been discussed in the previous paper in this series (reference 1). A limited examination using statistical analysis has been conducted for the NO-GO VTO data.

For configurations 1, 2 and 3 tests were carried out at full-scale pressure conditions and at buoyancy scaling conditions maintaining dynamic head similarity. Figure 9 shows TC120 and ΔT_i results from NO-GO VTOs for a nominal wind speed of 12 knots.

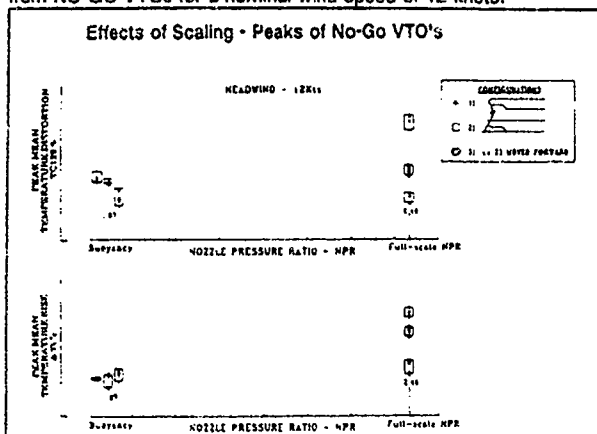


Figure 9

For this data, analysis was required to see if there was any significant variation with NPR, and extreme value extrapolation was not carried out. For configurations 1 and 2 there is no need to apply the Mann-Whitney test as there is no overlap between ΔT_i or TC120 results, and the results are clearly different. The configuration 3 results show no significant difference using the Mann-Whitney test.

Configuration 3 was the best HGR reduction device, and from results with the other configurations this is due to better control of direct path ingestion. For configuration 1 and 2 this fountain effect dominates HGR, and so needs to be accurately modelled (by full-scale NPR testing). For configuration 3 this source is controlled, and buoyancy scaling produces the same results.

Had buoyancy scaled results been greater this would have implied that the action of the hot gas rising was most important, and buoyancy scaling would have been needed. The conclusion of this is that preliminary testing has to be carried out on HGR models at both scaling conditions to find out which method is most appropriate for the particular gas paths occurring. In cases where one method produces higher results this is the most appropriate method. Where the results are the same the most convenient method for the rig can be used.

Effect of headwind on HGR results

Statistical analysis of the influence of headwind has only been carried out for the NO-GO VTO tests since the landing data has too many variables to allow proper analysis with the size of sample available.

The results of NO-GO VTOs on configuration 1 at various windspeeds at full-scale NPR are illustrated in Figure 10. The results of the peaks of ΔT_i and TC120 show slightly different trends.

As there is a controlled parametric variation this data lends itself to a regression analysis. Due to the non-normal nature of the data the Kruskal-Wallis test was used. In order to do this the data had to be separated into groups of similar windspeeds. Values of 4.2, 11.4, 13.7 and 14.6 knots were taken as mean values. For both sets of data the Kruskal-Wallis test showed a significant trend. Pairwise comparisons (using Mann-Whitney) showed that ΔT_i has a low

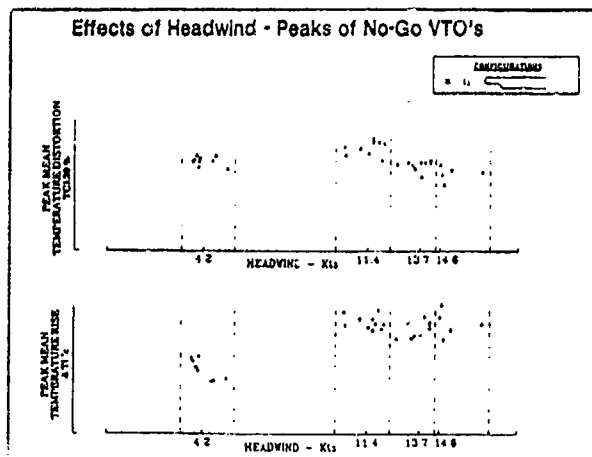


Figure 10

value at 4.2 knots with a significant rise to 11.4 knots, and remains near constant from 11.4 to 14.6 knots. TC120 shows a small rise from 4.2 knots to 11.4 knots, follows by a progressive fall at 13.7 and 14.6 knots with levels lower than at 4.2 knots.

The physical conclusion from this is that there is a critical windspeed for high HGR. At low winds little gas is blown back (hence ΔT_i lowest), but some pockets of gas are as indicated by comparatively higher distortion levels. Higher winds have less effect in reducing bulk reingestion, but smooth out hot pockets into a more uniform gas pattern.

Concluding remarks

Relating to physical HGR results:

- Under-fuselage strake / dam configuration can only affect Hot Gas Reingestion up to a limited height on the current Harrier 4 nozzle configuration. There remains a region of considerable risk beyond the range of control by under-fuselage geometry.
 - Scaling techniques are very important, and the method used should be appropriate to the dominant gas flow field. This work has emphasised the difference between various HGR source processes.
- The analysis technique has shown:
- The stochastic nature of the process makes the use of statistics vital. Quantitative conclusions can be produced rather than qualitative impressions.
 - Powerful statistical techniques exist that can be applied to the data to yield deeper understanding and greater confidence in conclusions.
 - The number of repeat landings needed is crucial. For landings the evidence here is that ten is only just adequate and 15 or more would be necessary to examine the fine details of dependencies suggested by results. NO-GO VTO testing produces a bigger data sample at the same conditions, so fewer repeats are needed.

Acknowledgements

I wish to acknowledge the assistance of my colleagues at Rolls-Royce, especially to Chris Penrose for providing the data, the staff of the Warwick University Manufacturing Group who introduced me to non-parametric tests, and to Rolls-Royce plc for permission to publish this paper.

The views expressed in this paper are those of the author, and do not represent any commitment by or policy of Rolls-Royce plc.

References

1. Penrose C J
Influence of headwind on Hot Gas Reingestion, and consideration of pressure ratio scaling.
Paper 17 of AGARD Symposium on Computational and Experimental Assessment of Jets in Cross Flow Winchester, England
April 1993
2. Williams D D
Hot Gas Reingestion - Engine response conditions
International Powered Lift Conference, London
August 1990 (R Aero S)
3. Penrose C J
The scaling of model test results to predict intake Hot Gas Reingestion for STOVL aircraft with augmented vectored thrust engine.
NASA Ames Ground-Effects Workshop
NASA-CP-2462
August 1985
4. Cox M and Abbott W A
Studies of the flowfields created by simple vertical jets directed downwards upon a horizontal surface.
NGTE memorandum M390
October 1964
5. Abbott W A
Studies of flowfields created by vertical and inclined jets when stationary or moving over a horizontal surface.
NGTE memorandum M391
October 1964
6. Hail C L and Kamman J H
Hot exhaust gas ingestion characteristics of a small scale Harrier type VSTOL aircraft model.
McDonnell Corporation.
Report number MDC A4225
August 1977
7. Shapiro S S and Wilk M B
An analysis of variance test, for normality and complete samples
Biometrika, S2, S92-611
1965
8. Gumbel E J
Statistics of extremes
Columbia University Press
New York
1958
9. Jacobs J L, Kneile K R
Statistical prediction of maximum time-variant
Inlet distortion levels
ARO Inc Report
AEDC-TR-74-121
January 1975
10. Hercock R G
Effect of inlet flow distortion of engine stability
Paper 20 of AGARD CP 324
October 1982.
11. Elshamy M
Bivariate extreme value distributions
NASA Contract Report 4444
1992
12. Abernathy R et al
Weibull analysis handbook
AFWAL-TR-83-2079
13. Part-time MSC lecture notes
Applied statistical methods
Warwick University Manufacturing Group
April 1991

Appendix A - Weibull distribution

In this application the Weibull distribution has been used to test for differences between populations, and to provide a simple means of extrapolating non-normal data.

The Weibull distribution (reference 12) may be defined mathematically by

$$F(x) = 1 - \exp[-((x-x_0)/\eta)^\beta] \quad A-1$$

where η is a characteristic value
 β is a slope value
 x_0 is the minimum value of the distribution

Typically, for distortion values, x_0 is zero, as that is the physical lower bound for distortion values.

With a population of n values of x_i , n and β can be estimated by a maximum likelihood technique, using

$$\frac{\sum_{i=1}^n x_i^\beta \ln(x_i)}{\sum_{i=1}^n x_i^\beta} - \frac{1}{\beta} = \frac{1}{n} \sum_{i=1}^n \ln(x_i) \quad A-2$$

which gives $\hat{\beta}$, by iteration from an initial estimate and then:

$$\hat{\eta} = \left[\frac{\sum_{i=1}^n x_i^{\hat{\beta}} \ln(x_i)}{\hat{\beta}} \right]^{\frac{1}{\hat{\beta}}} \quad A-3$$

To produce a plot of the data, either Weibull paper can be used, or equation A-1 can be increased.

Probabilities can assigned by

$$F(x_i) = P_{x_i} = \frac{i}{N+1} \quad A-4$$

Where i is the rank order of the x_i value ($1 = \text{lowest}$) equation A-1 can be rewritten.

$$\ln \ln (1/(1 - F(x))) = \beta \ln (x-x_0) - \beta \ln \eta \quad A-5$$

which is a linear equation

$$y = mZ + c \quad A-6$$

$$\text{with } y = \ln \ln (1/(1 - F(x))) \quad A-7$$

$$\left. \begin{aligned} Z &= \ln(x-x_0) \\ \text{and } m &= \hat{\beta} \\ C &= -\hat{\beta} \ln \hat{\eta} \end{aligned} \right\} \quad A-8$$

Producing a plot like this can be used to examine the distribution, to see if a single distribution is being modelled.

Extrapolation can be achieved by inverting equation A-1, giving

$$x = x_0 + \eta \left[\ln \left[\frac{1}{1 - F(x)} \right] \right]^{\frac{1}{\beta}} \quad A-9$$

For an extreme value,

$$F(E) = \frac{E}{E+1} \quad A-10$$

can be inserted into A-9, with 10,000 typically being used for E .

JETS TRANSVERSAUX EN INTERACTION AVEC DES ECOULEMENTS HYPERSONIQUES RAREFIES

J. Allègre, M. Raffin

S.E.S.S.I.A./C.N.R.S.
Laboratoire d'Aérodynamique
4ter, route des Gardes
92190 Meudon (France)

RESUME

Les jets transversaux peuvent être utilisés pour assurer, sous certaines conditions, le contrôle directionnel des véhicules spatiaux. A haute altitude, ils prennent le relais des gouvernes classiques, dont l'inefficacité s'accroît avec l'accroissement de la raréfaction de l'écoulement extérieur. Les jets transversaux ont été étudiés expérimentalement en soufflerie, au laboratoire d'Aérodynamique du CNRS, à Meudon, dans le cadre de leur interaction avec des écoulements hypersoniques raréfiés. L'efficacité des jets et les mécanismes des interactions aérodynamiques y ont été examinés pour deux types de configurations.

La première configuration est celle d'une aile delta munie de jets transversaux engendrés à partir de tuyères soniques disposées en amont du bord de fuite de l'aile. Les essais sont réalisés en présence d'un écoulement hypersonique d'air caractérisé par un nombre de Mach de 8,1, un nombre de Reynolds de 11 000 et un paramètre de raréfaction $V = 0,077$.

La seconde configuration est celle d'un écoulement d'angle (corner flow) soumis à l'action d'un jet transversal issu d'une tuyère hypersonique. Cette tuyère est intégrée à l'une des deux parois qui constituent le dispositif d'angle. Les essais sont conduits en soufflerie dans des conditions d'écoulements hypersoniques d'azote caractérisés par un nombre de Mach voisin de 20 et des pressions dynamiques comprises entre 20 Pa et 620 Pa, permettant ainsi de couvrir des niveaux de raréfaction compatibles avec les conditions de rentrée.

Pour de tels régimes intermédiaires où prédominent les effets de viscosité et les effets de déplacement de couche limite, les résultats des mesures des coefficients aérodynamiques montrent, pour l'aile delta, dans quelle mesure les dispositifs de guidage directionnel par jets sont efficaces et peuvent contribuer au contrôle de la trajectoire d'un véhicule spatial en atmosphère raréfiée.

Dans le cas de l'écoulement d'angle, la mesure des répartitions de pressions pariétales fixe l'étendue de la zone d'influence du jet transversal et précise l'effet du niveau de raréfaction des écoulements sur l'interaction.

SUMMARY

Control jets are used on space vehicles in order to replace or complement mechanical aerodynamic controls at high altitudes. As a matter of fact, the efficiency of mechanical controls decreases drastically with higher rarefaction levels of the external flow.

Control jets have been experimentally investigated in wind-tunnels, at laboratory d'Aérodynamique of CNRS, Meudon. Jets are in interaction with external hypersonic rarefied flows. Jet efficiency and associated interaction mechanism have been analyzed for two types of configurations.

The first configuration is a delta wing with transverse control jets issued from sonic nozzles located close to the trailing edge. Tests are performed with an external hypersonic air flow characterized by a Mach number of about 8, a Reynolds number of 11 000 and a rarefaction parameter $V = 0,077$.

The second configuration is a corner flow interacting with a transverse jet issued from one hypersonic nozzle. This nozzle is inserted in one of the two walls which make up the corner model. Tests are made under external hypersonic nitrogen flows characterized by a Mach number of about 20 and dynamic pressures ranging from 20 Pa to 620 Pa, covering rarefaction levels associated with reentry conditions.

For such rarefied flow regimes, dominated by viscous effects and boundary layer displacement effects, measured aerodynamic coefficients demonstrate for the delta wing configuration, how efficient are the control jets and how they can contribute to control the space vehicle trajectory in rarefied atmosphere.

Considering the corner flow configuration, distributions of measured wall pressures show which area is affected by the transverse jet and which is the effect of the flow rarefaction on the interaction process.

NOTATIONS

C_N	coefficient d'effort aérodynamique normal à l'aile delta
e	écartement entre les jets transversaux sur l'aile delta
L	corde de l'aile delta
M	nombre de Mach
p_w	pression pariétale
p_∞	pression de l'écoulement à l'infini amont
Re	nombre de Reynolds
Re_L	nombre de Reynolds fondé sur la longueur de la maquette
T_w	température pariétale
V	$= M/\sqrt{Re_L}$, paramètre de raréfaction
x	abscisse mesurée le long de la maquette
α	angle d'incidence de l'aile delta.

INFLUENCE DE LA RAREFACTION DE L'ÉCOULEMENT EXTERIEUR

En fonction de l'altitude de vol d'un véhicule spatial, le changement de raréfaction de l'écoulement conduit à l'établissement de différents niveaux d'interaction entre la surface du véhicule et l'écoulement extérieur.

A des altitudes faibles, correspondant à un régime d'écoulement continu, les systèmes de guidage classiques par dispositifs aérodynamiques mécaniques tels que gouvernes et élévons, suffisent à assurer le contrôle aérodynamique de l'engin.

A de très hautes altitudes, correspondant à des régimes d'écoulement moléculaire libre ou proche moléculaire libre, les dispositifs aérodynamiques mécaniques deviennent inefficaces et sont remplacés par des systèmes de contrôle par réaction (RCS) tels les jets transversaux. Le libre parcours moyen de l'écoulement extérieur étant suffisamment grand, on ne peut s'attendre qu'à une très faible interaction entre le jet transversal sous-détendu et l'écoulement extérieur.

Pour des altitudes intermédiaires, qui correspondent en particulier aux conditions de rentrée d'un engin spatial, les écoulements sont caractérisés par le régime de forte interaction visqueuse et par le régime de "merged layer".

Les dispositifs aérodynamiques mécaniques ne sont plus suffisamment efficaces pour engendrer, à eux seuls, les efforts aérodynamiques nécessaires. La perte d'efficacité des surfaces aérodynamiques de contrôle s'explique généralement par le fait qu'elles se situent dans des régions caractérisées par d'épaisses couches limites. Pour palier l'inefficacité des dispositifs mécaniques, le guidage par jets transversaux permet d'induire des poussées de guidage complémentaires. A ces régimes d'écoulements intermédiaires, on peut également s'attendre à un effet d'interac-

tion entre le jet transversal et l'écoulement extérieur. Cette interaction génère localement un accroissement de pression pariétale et, en conséquence, une force aérodynamique d'interaction qui s'ajoute à la poussée du jet transversal. C'est dans le cadre de ces régimes d'écoulement de forte interaction visqueuse et de "merged layer" que se situent les études expérimentales entreprises sur l'aile delta et sur l'écoulement d'angle.

MODELE SIMPLIFIE D'INTERACTION

Dans le cas d'un écoulement raréfié caractérisé par un régime de forte interaction visqueuse, le type d'interaction entre un écoulement hypersonique extérieur et un jet transversal peut être décrit schématiquement en considérant à titre d'exemple le cas d'une plaque plane avec jet transversal (fig. 1).

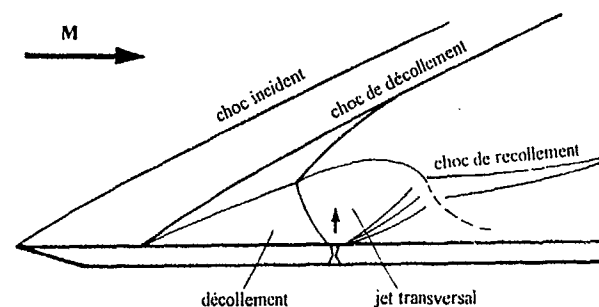


Fig. 1 - Modèle d'interaction

La plaque étant parallèle à la direction de l'écoulement hypersonique extérieur, le jet transversal agit comme une barrière vis-à-vis de cet écoulement. Il en résulte la formation, à l'amont de l'orifice d'injection, d'une zone de décollement et d'un choc de décollement. La zone de décollement se caractérise, au niveau de la plaque, par un accroissement de la pression pariétale. En aval du jet transversal, la détente de l'écoulement entraîne un abaissement localisé de la pression pariétale.

Le niveau de détente du jet transversal, son volume et ses effets sur la distribution de pression pariétale dépendent dans une large mesure des conditions de raréfaction de l'écoulement extérieur. Une plus grande raréfaction accentue en particulier le niveau de détente du jet transversal avec augmentation corrélative de la zone de décollement.

AILE DELTA MUNIE DE JETS TRANSVERSAUX

En fonction de la raréfaction des écoulements, et donc de l'altitude de vol, le contrôle directionnel d'un planeur né-

cessite la présence de dispositifs spécifiques de guidage, tels que les gouvernes aérodynamiques classiques ou les jets de contrôle, dont il convient de prévoir l'efficacité au cours des différentes phases de trajectoires, notamment à haute altitude où les effets de décollement laminaire sont prépondérants.

Des travaux conduits aux Etats-Unis sur le "Space Shuttle" ont permis d'apporter des éléments d'information sur l'efficacité des dispositifs de contrôle par jets transversaux (Réf. 1). Les prédictions d'efficacité de guidage par jets ont été confrontées, pour certaines configurations, à des mesures en vol (Réf. 2). Les comparaisons montrent parfois, notamment aux grandes valeurs du nombre de Mach, des différences importantes relevées entre les efficacités prédites et mesurées des dispositifs de guidage.

Des recherches ont également été réalisées par le passé au laboratoire d'Aérodynamique du CNRS, à Meudon, sur des ailes delta dans le cadre d'un écoulement hypersonique raréfié en régime de forte interaction visqueuse. Les études ont porté sur la caractérisation de l'efficacité de dispositifs du type spoiler de bord de fuite (Réf. 3) et sur l'efficacité du contrôle aérodynamique par jets transversaux (Réf. 4). On rappellera ici quelques résultats expérimentaux obtenus lors de ces études en se limitant à l'analyse de l'effet des jets transversaux. L'utilisation de ces jets est compatible avec les faibles niveaux d'efforts aérodynamiques s'exerçant sur l'aile en atmosphère raréfiée. En marge de certains développements analytiques (Réf. 5) les données expérimentales peuvent contribuer à mieux appréhender les phénomènes. Les résultats présentés montrent l'action des jets transversaux et renseignent sur la structure des écoulements liés à l'interaction.

Les essais ont été conduits dans un écoulement hypersonique d'air raréfié caractérisé par un nombre de Mach de 8,1, par des pression et température d'écoulement de 9,3 Pa et 50 K. Le nombre de Reynolds de 11 000 calculé sur la corde de l'aile delta et le paramètre de raréfaction $V = 0,077$ définissent un régime de forte interaction visqueuse. Les gradients de Mach au sein de la veine d'essai étaient négligeables en raison de l'utilisation d'une tuyère évolutive.

Les maquettes utilisées sont des ailes delta de 60° de flèche et 50 mm de longueur, munies de deux orifices soniques d'injection, de 2 mm de diamètre, localisés à 3 mm en amont du bord de fuite. Ces jets transversaux sont disposés symétriquement de part et d'autre de l'axe longitudinal de l'aile. Sur le plan pratique, un soufflage simultané des deux jets ou le soufflage d'un seul des deux jets permet de communiquer soit un mouvement de tangage, soit un mouvement de roulis et lacet. Les résultats présentés ici portent sur le soufflage simultané avec un débit d'air injecté fixé à 0,1 g/s pour l'ensemble des deux jets transversaux.

Les écartements des jets sont compris entre 10 mm et 40

mm et correspondent à des distances représentant entre 0,2 et 0,8 fois la longueur de l'aile. Les visualisations obtenues par dépôt d'huile montrent, pour l'incidence nulle, que les décollements induits par les injections sont d'autant plus accentués que les orifices d'injection sont plus rapprochés (fig. 2). Dans le cas de l'écartement maximal $e/L = 0,8$ des jets transversaux, deux régions décollées distinctes entourent les deux orifices de jets. Les zones sont de faible étendue et les résultats de pressions pariétales et d'efforts aérodynamiques confirment la faible efficacité attendue pour cette configuration particulière d'injection. L'efficacité de l'interaction est plus importante pour des jets transversaux rapprochés de l'axe de l'aile.

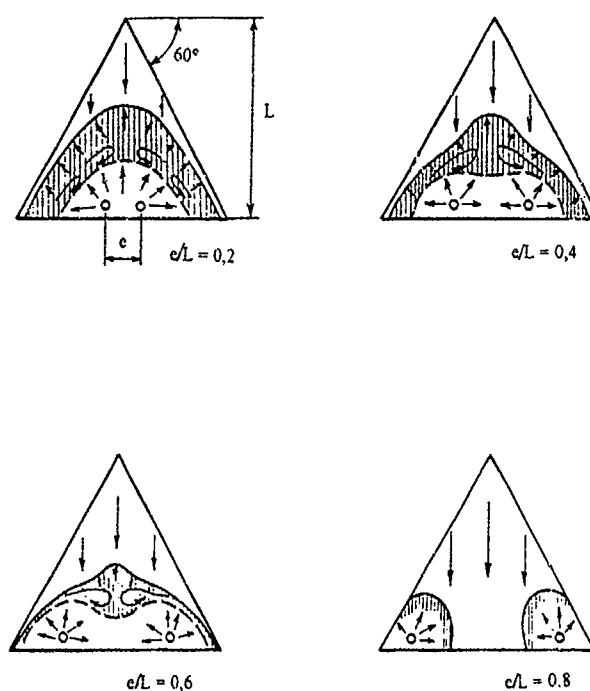


Fig. 2 - Visualisation de l'écoulement de surface par film d'huile ($\alpha = 0^\circ$)

Les répartitions de pressions pariétales, mesurées le long de l'axe de l'aile et rapportées à la pression de l'écoulement à l'infini, sont portées sur les figures 3, 4 et 5 pour les incidences respectives de 20° , 0° et -20° . Les répartitions sont tracées pour les deux écartements de 10 mm et 40 mm entre les jets transversaux. A l'incidence de 20° , les décollements induits par les jets transversaux sont importants, le plus faible écartement entre les orifices d'injection entraînant le niveau de pression pariétale le plus élevé au sein de la zone décollée. A l'incidence nulle et à l'incidence de -20° , l'effet résultant de l'injection fluide demeure là encore prédominant pour le plus faible écartement. Des visualisations de l'écoulement de surface par film d'huile ont montré que, plus l'écartement entre les

orifices d'injection augmentait, moins l'interaction entre les deux zones décollées devenait importante. A la limite, pour l'incidence de -20° et l'écartement de 40 mm, les deux zones décollées n'interfèrent pratiquement plus entre elles, se traduisant, dans ce cas, par un accroissement très limité de la pression pariétale.

Les mesures de forces aérodynamiques sont réalisées au moyen d'une balance à trois composantes munie d'un conduit d'alimentation en air des jets transversaux. Elles confirment l'évolution constatée des pressions pariétales. Les résultats ont montré que le coefficient de force axiale n'était pas affecté par la présence des jets transversaux. En revanche, la figure 6 donne la variation du coefficient de force normale à l'aile pour les deux configurations de jets distants de 0,2 et 0,8 fois la longueur de l'aile. La connaissance des variations des forces normales est utile, en particulier, pour caractériser l'efficacité des jets sur le contrôle directionnel de l'aile. Pour une incidence fixée, la présence des jets transversaux entraîne une variation de force normale qui comprend, d'une part, la force de réaction propre des jets et, d'autre part, la force d'interaction.

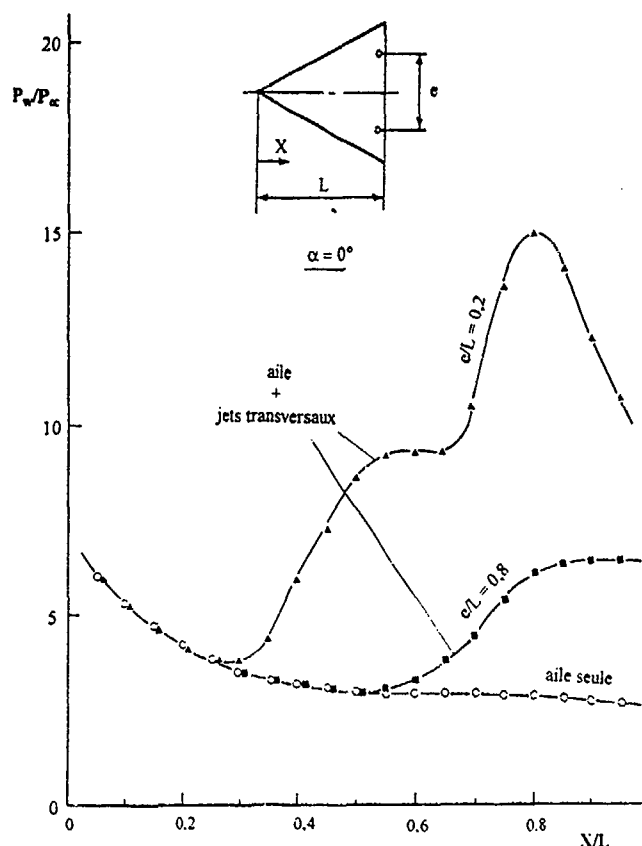


Fig. 4 - Répartitions longitudinales de pression pariétale ($\alpha = 0^\circ$)

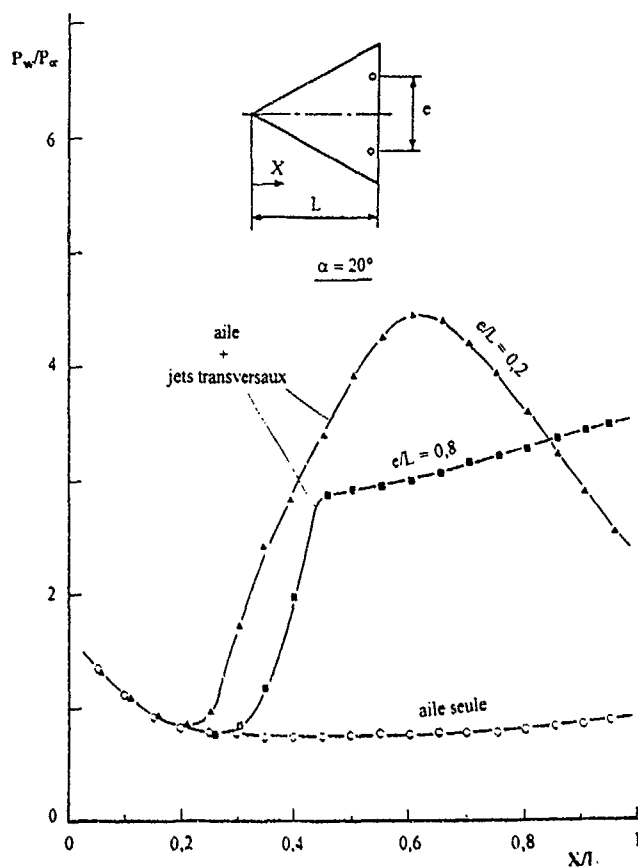


Fig. 3 - Répartitions longitudinales de pression pariétale ($\alpha = 20^\circ$)

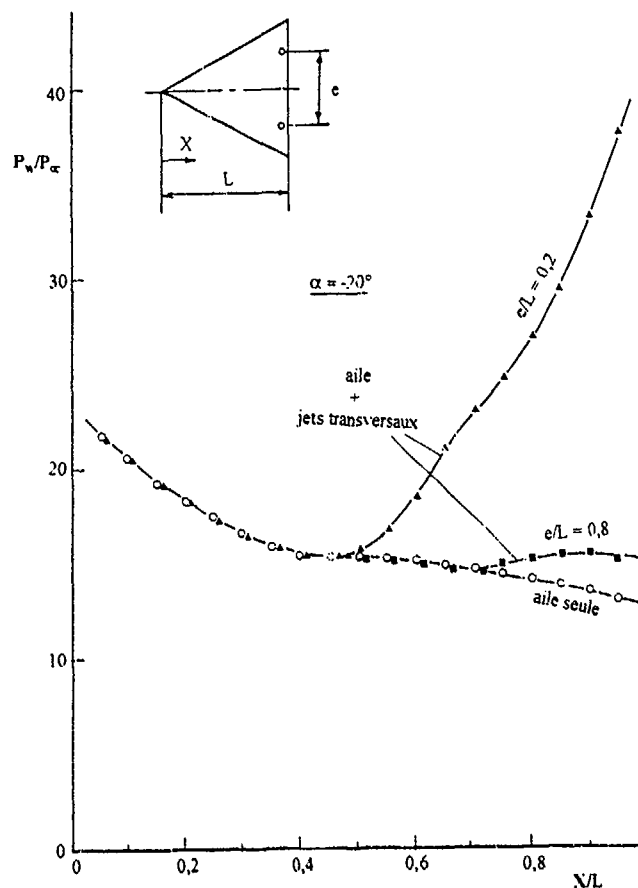


Fig. 5 - Répartitions longitudinales de pression pariétale ($\alpha = -20^\circ$)

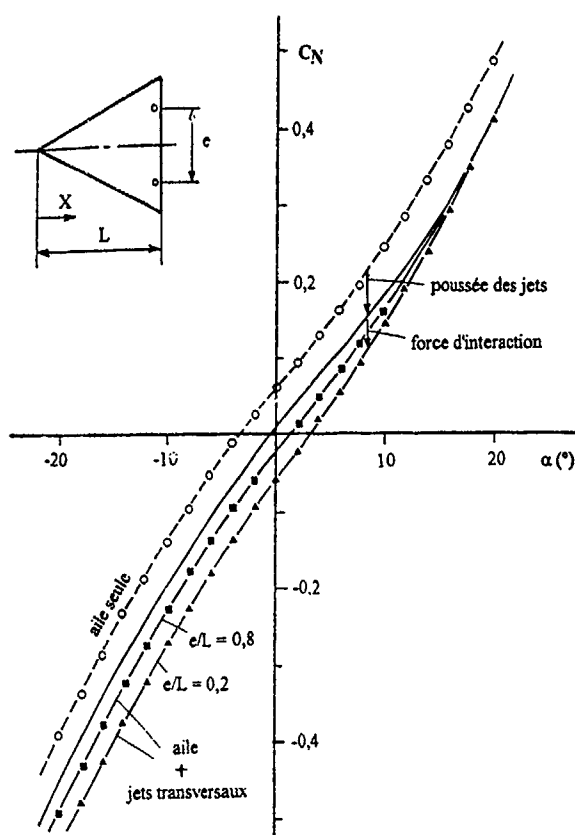


Fig. 6 - Coefficient de force aérodynamique normale à l'aile

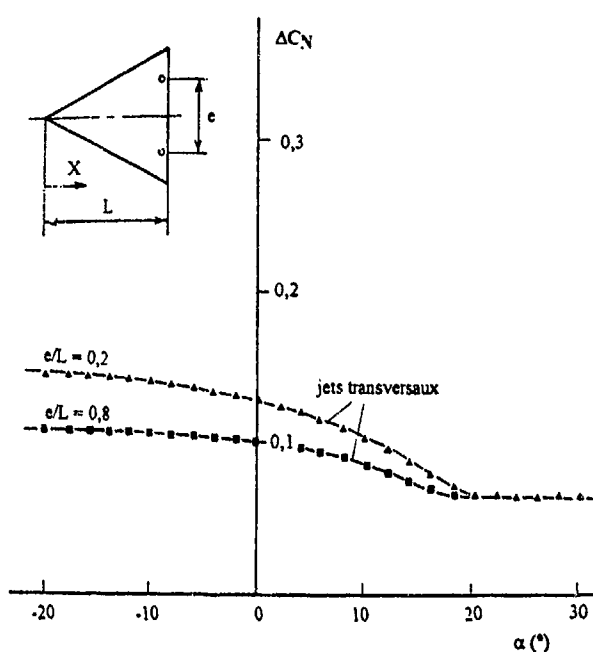


Fig. 7 - Variation de force normale due à l'effet des jets transversaux

Cette dernière est plus accentuée dans le cas de l'écartement minimal des deux jets. Par rapport à la configuration de l'aile sans injection, les variations enregistrées du coefficient de force normale sont portées sur la figure 7. Aux incidences supérieures à 20° , la variation du coefficient de force normale correspond à la poussée propre des jets transversaux ; aucune interaction sensible n'existe dans ces conditions entre l'écoulement extérieur et les jets.

Pour les incidences inférieures à 20° , le mécanisme d'interaction entre les jets et l'écoulement extérieur donne lieu à une amplification de la poussée des jets. Le facteur d'amplification représente le rapport entre la force normale totale s'exerçant sur l'aile et la poussée des jets transversaux.

Aux incidences supérieures à 20° , le facteur d'amplification reste voisin de l'unité. Aux incidences inférieures à 20° , l'interaction s'accroît avec l'incidence de l'aile, ce qui conduit à une augmentation corrélative du facteur d'amplification. Ce dernier dépasse la valeur de 2 aux incidences négatives et dans le cas de l'écartement minimal entre les jets transversaux.

Les résultats présentés apportent quelques données quantitatives sur l'efficacité du contrôle directionnel par jets de l'aile, en régime de forte interaction visqueuse. L'analyse du mécanisme d'interaction entre les jets transversaux et l'écoulement hypersonique extérieur montre, en particulier, que l'effet des jets est d'autant plus marqué que ces derniers sont plus rapprochés de l'axe de symétrie de l'aile. Ils engendrent alors un décollement plus accentué s'accompagnant d'une forte élévation de pression pariétale qui contribue à la force aérodynamique de guidage.

ÉCOULEMENT D'ANGLE ET JET TRANSVERSAL

A haute altitude, lors de la phase de guidage par jets d'un véhicule spatial, les écoulements issus des tuyères propulsives sont fortement détendus en raison du niveau de raréfaction de l'écoulement extérieur. Par voie de conséquence, les jets occupent un volume important et interfèrent avec les parois environnantes soit directement, soit par l'intermédiaire de chocs d'interaction induits par la rencontre des jets de contrôle et de l'écoulement hypersonique extérieur.

La force aérodynamique de guidage qui en résulte est ainsi engendrée par l'action directe et indirecte des jets. Elle comprend la poussée propre des tuyères propulsives mais aussi une force dite d'interaction qui dépend du mécanisme d'interaction souvent complexe entre : les jets de guidage, l'écoulement extérieur et les parois du véhicule.

L'étude expérimentale présentée fait l'objet de campagnes d'essais dans la soufflerie à gaz raréfié du laboratoire d'Aérodynamique de Meudon. Par rapport au modèle d'interaction simplifié représenté figure 1, la géométrie d'un vé-

hicule spatial fait apparaître des protubérances et des éléments de paroi directement exposés à l'action des jets propulsifs de guidage. Pour établir quelques analogies avec le type réel d'interaction, on a été conduit à définir un modèle d'interception entre le jet sous-détendu, l'écoulement hypersonique extérieur et les parois environnantes (Réf. 6). Ce modèle, élaboré comme cas test pour établir des confrontations entre répartitions de pressions pariétales calculées et répartitions de pressions pariétales mesurées en soufflerie est présenté sur la figure 8.

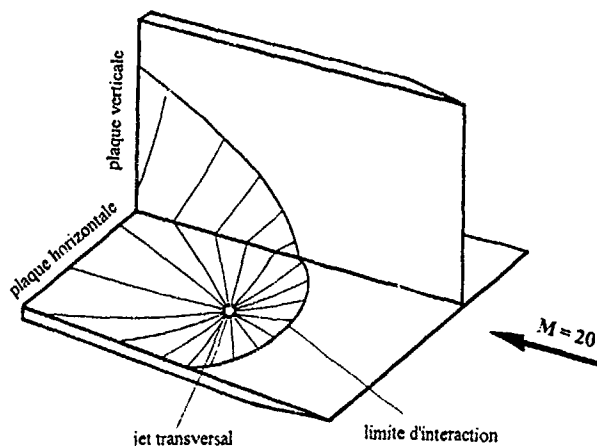


Fig. 8 - Ecoulement d'angle et jet transversal

La maquette de 120 mm de longueur se compose de deux plaques planes perpendiculaires. La plaque horizontale, de 80 mm de largeur, est placée parallèlement à la direction de l'écoulement incident. Elle est pourvue d'une tuyère hypersonique, d'axe vertical, dont la section de sortie affleure la surface de la plaque. Cette tuyère, située à 60 mm en aval du bord d'attaque, engendre le jet transversal d'azote. L'autre plaque, verticale, de 60 mm de hauteur, est, elle aussi, parallèle à la direction de l'écoulement incident. Elle est distante, selon le cas, de 15 mm ou de 30 mm de l'axe du jet transversal permettant de faire varier ainsi les conditions d'interaction aérodynamique. Les bords d'attaque des deux plaques planes sont biseautés et perpendiculaires à la direction de l'écoulement extérieur. Les plaques sont équipées de prises de pression reliées à des capteurs de grande sensibilité en vue d'obtenir les répartitions de pressions pariétales le long de quelques lignes caractéristiques. Les emplacements des orifices de pression sont portés sur la figure 9 dans le cas d'un écartement de 15 mm entre le jet transversal et la plaque verticale.

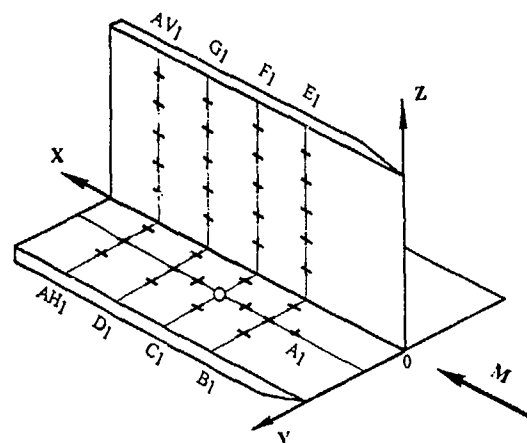


Fig. 9 - Axes de référence et orifices de pression

Les interactions entre jet transversal et écoulement incident ont été étudiées pour différents niveaux de raréfaction des écoulements. Le jet transversal d'azote est issu d'une tuyère hypersonique conique, à nombre de Mach nominal de 5,96, avec un demi-angle de divergence de 9° et des diamètres au col et en sortie tuyère mesurant respectivement 0,213 mm et 1,53 mm. La température génératrice du gaz est de 300 K et la pression génératrice fixée à 4, 12 et 20 bars selon les conditions choisies pour l'injection. Pour ce qui est de l'écoulement extérieur d'azote, les niveaux de raréfaction retenus sont ceux d'écoulements hypersoniques à Mach 20 caractérisés par les nombres de Reynolds successifs de 3 420, 10 056 et 87 324, nombres de Reynolds fondés sur la longueur de la maquette. Les pressions dynamiques correspondantes de 19,5 Pa, 58,5 Pa et 621,6 Pa, sont compatibles avec certaines conditions de rentrée d'un véhicule spatial pour lesquelles se posent les problèmes de guidage par jet.

Plusieurs paramètres gouvernent le processus d'interaction entre le jet transversal, l'écoulement extérieur et les surfaces environnantes. L'étude expérimentale prend en compte la variation de quelques-uns des paramètres tels que le niveau de raréfaction de l'écoulement extérieur, la quantité de mouvement du jet transversal et l'éloignement relatif entre le jet transversal et la paroi environnante.

Les exemples de résultats de pression pariétale fournis dans le présent document sont limités au cas d'un écoulement extérieur caractérisé par un nombre de Mach de 20,2 et par une pression dynamique de 19,5 Pa. Les pressions pariétales mesurées le long de l'axe longitudinal passant par l'orifice d'injection sont relevées sur la figure 10 pour différentes conditions du jet transversal. Avec injection, les répartitions de pressions pariétales font apparaître une augmentation de pression à l'amont de la tuyère d'injection (zone de décollement) et une diminution de pression

localisée à l'aval de l'injection (zone de détente). A l'amont de l'injection, il n'a pas été mis en évidence de plateau de pression mais une augmentation continue de la pression pariétale au fur et à mesure que l'on se rapproche de la tuyère.

Si au niveau de la plaque horizontale les répartitions mesurées de pressions pariétales ne font ressortir que des variations de pressions limitées à quelques pascals, à l'inverse, sur la plaque verticale, les variations sont nettement plus accentuées (fig. 11 et 12). Des essais systématiques réalisés en présence d'un jet transversal, avec et sans écoulement extérieur, ont montré que l'effet majeur ne résulte pas de l'action directe du jet sur la paroi verticale mais du processus d'interaction induit par l'écoulement extérieur. Jet transversal et écoulement extérieur génèrent un choc d'interaction qui interfère à la fois avec la plaque horizontale et avec la plaque verticale. Les traces d'interaction du choc avec les parois correspondent à une augmentation localisée de la pression pariétale. Cette augmentation est détectée sur les axes F1 et G1 des figures 11 et 12.

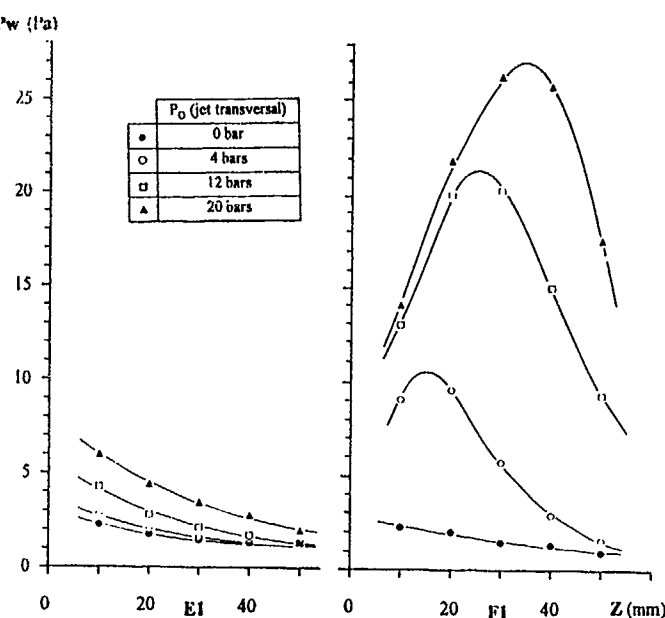


Fig. 11 - Répartitions de pression pariétale (plaque verticale)

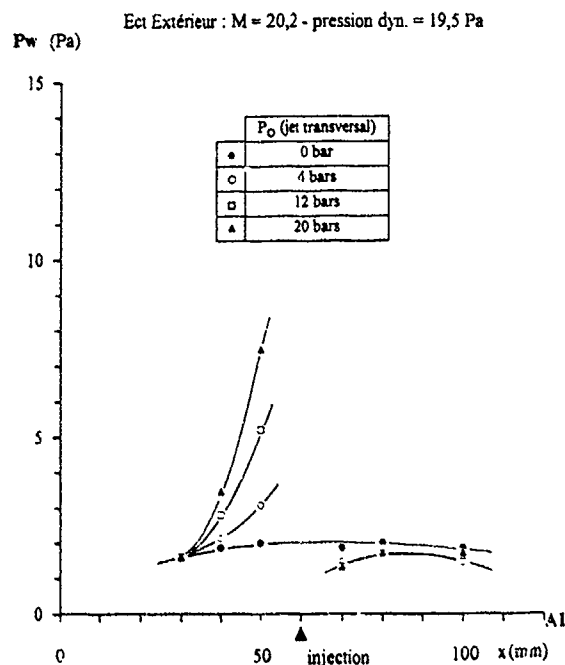


Fig. 10 - Répartitions de pression pariétale (plaque horizontale)

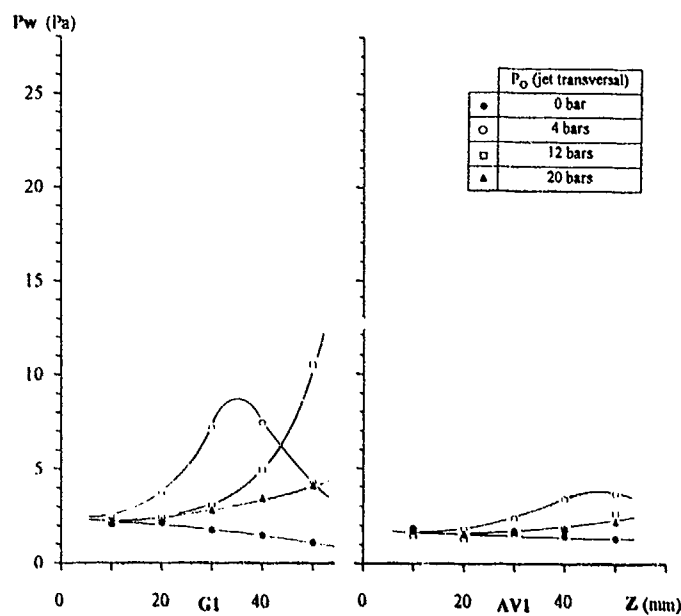


Fig. 12 - Répartitions de pression pariétale (plaque verticale)

L'accroissement de la pression génératrice du jet transversal engendre une hauteur de pénétration plus importante du jet. Corrélativement, les zones d'interaction sont plus marquées, le choc d'interaction s'intensifie en accentuant l'augmentation des pressions pariétales au niveau des parois interceptées.

Les limites des régions d'interaction sont tracées sur la figure 13 en considérant trois niveaux de raréfaction de l'écoulement extérieur et une même condition d'injection du jet transversal. La limite amont des interactions est déduite des mesures de pressions pariétales mais également de la visualisation des écoulements de surface par film d'huile pour les écoulements les moins raréfiés. L'importance des régions décollées dépend du niveau de raréfaction de l'écoulement extérieur et, pour les cas étudiés, une plus faible densité de l'écoulement conduit à des zones de décollement plus étendues.

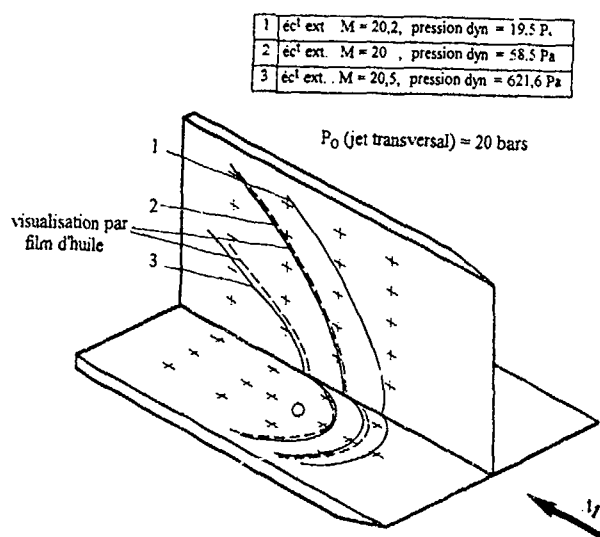


Fig. 13 - Limite amont de la zone d'interaction

CONCLUSION

Dans le cadre d'écoulements raréfiés, les études expérimentales présentées apportent leur contribution en vue de mieux connaître le processus d'interaction entre jets transversaux et écoulement extérieur.

Des essais ont été conduits sur une aile delta munie de jets transversaux de bord de fuite, cette aile étant placée dans un écoulement hypersonique à Mach 8,1. Le nombre de Reynolds de 11 000 fondé sur la longueur de l'aile et le paramètre de raréfaction de $V = 0,077$ définissent un régime de forte interaction visqueuse pour lequel les effets de viscosité et de déplacement de couche limite sont très importants. En atmosphère raréfiée, les résultats fournissent des données quantitatives sur l'efficacité du dispositif de guidage directionnel de l'aile par jets transversaux. L'effet

des jets ressort de l'analyse des variations de pressions pariétales relevées à la surface de l'aile et de la mesure des forces aérodynamiques. Parallèlement, des visualisations permettent de mieux appréhender le mécanisme d'interaction entre jets transversaux et écoulement extérieur, et précisent l'étendue de la zone de décollement, siège de phénomènes tridimensionnels. La force aérodynamique normale à l'aile qui contribue au contrôle directionnel du planeur comprend, d'une part, la force de poussée développée par les jets transversaux et, d'autre part, une force aérodynamique d'interaction. Cette dernière résulte de l'élévation de pression pariétale enregistrée au sein de la zone décollée qui s'établit à l'amont des jets. Les mesures montrent que l'effet des jets transversaux est en général d'autant plus important que ces derniers sont plus rapprochés de l'axe de symétrie de l'aile. Le décollement qu'ils engendrent est alors plus accentué et s'accompagne d'une élévation plus marquée de la pression pariétale.

Dans le cas d'un écoulement d'angle avec jet transversal, le modèle retenu permet d'évaluer le processus d'interaction entre le jet transversal, l'écoulement hypersonique extérieur et les parois environnantes. L'interception du jet transversal par l'écoulement extérieur conduit à la formation d'un choc d'interaction dont l'intensité et l'emplacement dépendent à la fois des conditions du jet transversal et de celles de l'écoulement extérieur. Ce choc joue un rôle prédominant car, en interagissant avec les parois environnantes, il modifie les champs de pressions pariétales en créant des forces aérodynamiques d'interaction. Les essais sont conduits en soufflerie dans des conditions d'écoulement hypersonique à Mach 20 pour des niveaux de raréfaction compatibles avec certaines conditions de rentrée. Pour les écoulements explorés, les résultats font ressortir l'effet de raréfaction de l'écoulement extérieur et montrent que, dans le domaine étudié, la zone d'interaction est d'autant plus étendue que la raréfaction de l'écoulement est importante.

La prédiction de l'efficacité du guidage aérodynamique par jets transversaux implique une bonne connaissance des mécanismes d'interception entre jets et écoulement extérieur. Ceci nécessite à la fois un support analytique et expérimental, en particulier pour les altitudes élevées où les effets de raréfaction modifient sensiblement la structure d'interaction. Les données sur l'aile delta et sur l'écoulement d'angle contribuent ainsi à mieux cerner les effets d'interaction tout en fournissant un support pour des confrontations ultérieures entre grandeurs expérimentales et grandeurs calculées.

REMERCIEMENTS

L'étude a été partiellement réalisée grâce au soutien financier de l'Agence Spatiale Européenne.

REFERENCES

1. KANIPE D.B., Plume/flowfield jet interaction effects on the Space Shuttle Orbiter during entry. J. Spacecraft, 20, 4, Juillet 1983.
2. ROMERE P.O., KANIPE D.B., YOUNG J.C., Space Shuttle entry aerodynamic comparisons of flight with preflight predictions. J. Spacecraft and Rockets, Janvier-Février 1983.
3. ALLEGRE J., LARTIGUE D., SCIBILIA M.F., Rarefied hypersonic flow characteristics of delta wings with trailing edge spoilers. AIAA J., 10, 7, Juillet 1972.
4. ALLEGRE J., MATRAND C., SCIBILIA M.F., Traînée de corps portants pilotés à haute altitude. AGARD Conf. on Aerodynamic Drag., Reprint. 124, Izmir, Turquie, 10-13 Avril 1973.
5. PORTNER T., Simulation requirements for RCS plume-flowfield interaction modelling on a winged reentry vehicle. First European Symposium on Aerothermodynamics for Space Vehicles, ESA/ESTEC, Noordwijk, Pays-Bas, Mai 1991.
6. ALLEGRE J., RAFFIN M., CARESSA J.P., Experimental investigation of transverse jet effects related to hyperconic space vehicles. First European Symposium on Aerothermodynamics for Space Vehicles, ESA/ESTEC, Noordwijk, Pays-Bas, Mai 1991.

Comparison of the Interactions of Two and Three Dimensional Transverse Jets with a Hypersonic Free Stream

H.E.G.Powrie, G.J.Ball and R.A.East
Department of Aeronautics and Astronautics
University of Southampton
Southampton SO9 5NH.
United Kingdom.

SUMMARY

The interaction between a three dimensional (circular) sonic jet and a Mach 6.69 cross flow on a flat plate has been investigated experimentally. The results are compared with data from a two dimensional (slot) sonic jet in the same flow. In both cases the undisturbed flow on the plate is laminar. Heat transfer and oil flow visualisation have been used to identify separation and reattachment within the flow field which, for the case of circular injection, has revealed a number of vortex cells in the region ahead of the jet. For the two dimensional interaction there is only evidence of one vortex pair in this region, however a complex flow downstream of the slot jet has been observed. The influence of injectant gas type on the two dimensional interaction flow field is limited to a weak molecular weight dependence implied by separation length data. In contrast, for three dimensional injection, jet gas composition is found to have a marked effect on the size of the interaction flow field, as well as influencing surface heat transfer rate in the vicinity of the injector.

LIST OF SYMBOLS

A	=	area
d	=	nozzle exit diameter
L	=	model length (upstream of jet exit)
M	=	Mach number
P	=	pressure
R	=	reattachment
S	=	separation
w	=	slot width
X	=	distance upstream of jet exit
γ	=	specific heat ratio
ϕ	=	momentum flux

Subscripts

j	=	jet exit
s	=	separation
0	=	stagnation
∞	=	freestream

1. INTRODUCTION

When a transverse jet is directed into a hypersonic cross flow, the ensuing interaction causes a change in surface pressure in the vicinity of the injector. Integration of this modified pressure distribution results in a force which can be several times larger than the nominal jet thrust. One application of this jet induced force is vehicle attitude control. Such a system is particularly advantageous in situations where conventional aerodynamic surfaces cannot function properly. This may be due either to the low density of the surrounding medium or to the considerable aerodynamic heating effects associated with large flight speeds. Even when the external flow is so rarefied that the interaction force is negligible, the thrust of the jet is still available for vehicle control. A well known example of control jet application is orbital flight manoeuvring and re-entry of the Space Shuttle. Other potential uses are for high velocity and/or high altitude atmospheric vehicles.

From the early 1960s to the mid 1970s the jet interaction phenomenon was the subject of numerous experimental investigations (see¹ and references therein). In general, schlieren or shadowgraph pictures and pressure measurements were used to establish the main effects of jet and freestream parameters on the flow field as well as generating an extensive control force data base. Despite this effort there are few results available for laminar hypersonic flows, a combination which will be encountered by re-entry and high altitude vehicles over some portion of their flight path. As an accurate forecast of control jet performance can only be achieved with the aid of relevant experimental data there is a need to extend the existing data base, particularly in the high Mach number/low Reynolds number flow regime. There is also a demand for more detailed information about the interaction flow field to assist development and validation of CFD codes.^{2,3}

This paper describes a recent experimental study of sonic axisymmetric injection into a laminar, hypersonic freestream flow. In addition to traditional flow visualisation and pressure measurements, liquid crystal thermography complemented by surface oil flow have provided extra information on flow field topology and the effects of the interaction on surface heat transfer. Using these techniques

detailed measurements of the separated region have been made with various injectant gases to gain more knowledge about the role of the jet within this part of the flow field. New information about the separated flow region and the influence of injectant species are presented. The data are compared with results previously obtained from a two dimensional sonic jet issuing into the same flow.⁴

2. DESCRIPTION OF THE FLOW FIELD

The main features and resulting pressure distribution of a two dimensional, sonic jet issuing into a hypersonic flow are shown in Figure 1. In the present work, the jet is highly underexpanded and the undisturbed boundary layer is laminar. The jet acts as an obstruction to the oncoming flow, causing the boundary layer to separate from the surface some distance upstream. A separation shock originates at this point which generates a rise in pressure to a plateau (P2) in the separated flow region. Downstream of this there is a peak (P3) followed by a further pressure rise (P4) in the immediate vicinity of the jet. In order to satisfy boundary conditions, there must be at least two counter-rotating vortices present within the upstream separated region. The presence of the peak P3 may be due to the local stagnation region at the point where the two counter-rotating vortices impinge upon the plate surface, as indicated in Figure 1. A relatively weak interaction shock exists just ahead of the jet.

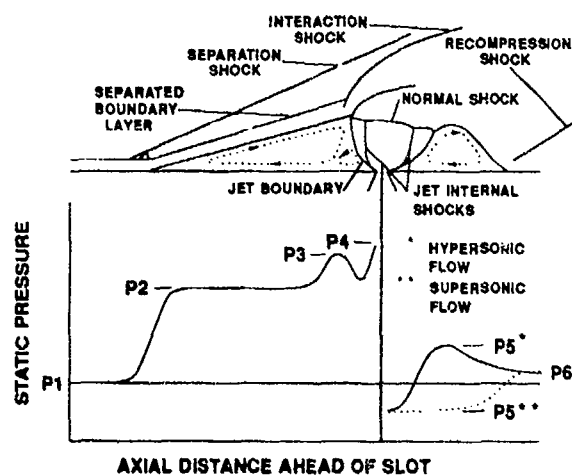


Figure 1 Schematic of the 2-D Jet Interaction Flow Field

Aft of the jet there is another region of separated flow. Experimentally this part of the flow field is usually found to have a static pressure (P5) below that of the undisturbed boundary layer and hence makes a negative contribution to the control force. Nevertheless, several investigators^{5,6} have reported a favourable contribution when the cross flow is hypersonic. This is true for both laminar and turbulent regimes. Downstream of this region, the jet and outer flows reattach as indicated by a recompression shock and accompanying static pressure change to P6.

Several differences exist in the upstream separated flow field if the undisturbed boundary layer is turbulent.¹ In this case the separation angle is larger than for laminar

conditions and consequently the pressure rise across the shock (P2) is greater. However the size of the separated region is less, which reduces the extent of the pressure plateau P2, with sometimes only a single peak discernable.

Under the present test conditions our observations show that the centreline flow for a circular jet interaction is broadly similar to that observed in the two dimensional case. Attributes such as the separated boundary layer and ensuing separation shock are observed from schlieren visualisation although the interaction shock ahead of the jet is slightly stronger than before. However, as the obstacle presented to the freestream flow by the jet is now of finite width, the flow deflects around the jet producing a 'horseshoe' pattern of counter-rotating vortices. This results in a highly three dimensional flow field which is demonstrated by the curved shape of the primary separation region.

Studies of axisymmetric injection into turbulent supersonic boundary layer flows⁷⁻¹⁰ have revealed a flow field which is dominated by the interaction shock ahead of the jet. In these cases the shock is a strong, detached bow shock and the extent of flow separation upstream of the jet is greatly reduced in comparison to that described above. Hence any increased surface load will be almost entirely due to the pressure rise across the normal portion of the bow shock. Consequently the influence of various parameters within the interaction flow field may differ from those in the type of flow currently under investigation.

3. EXPERIMENTAL WORK

3.1 Wind Tunnel Test Facility

All the work described in this paper was performed in the Southampton University Light Piston Isentropic Compression Tube which provides a free stream flow of nitrogen at Mach 6.69 for up to one second. For these experiments the tunnel was configured to operate at a Reynolds number of 4.27 million per metre and stagnation temperature and pressure of 628 K and 12.55 bar respectively.

3.2 Model Design

The two dimensional jet model consists of a flat plate (114mm long by 51mm wide) with a sharp leading edge. The slot is located 75mm downstream of the leading edge and spans the full breadth of the plate. It is internally profiled to form a convergent two dimensional nozzle. Injectant gas is fed at room temperature via a plenum chamber directly beneath the nozzle. The jet stagnation pressure is measured by a transducer connected to the plenum by means of a small hypodermic tube. The centreline pressure profile upstream of the slot is monitored by surface static pressure tapings.

The circular jet model is also a flat plate, 204mm long and 102mm wide. A simple convergent, conical nozzle is employed for the current series of tests. The centre of the nozzle is located on the plate centreline, 135mm from the leading edge. Gas injection and stagnation pressure measurement is similar to that for the slot jet model. The

plate is furnished with more than 120 pressure tappings in order to map the pressure distribution.

Based on the distance from the leading edge to the jet exit, the plate Reynolds numbers are 3.2×10^5 (for slot injection) and 5.7×10^5 (for circular injection). For both models, visualisation of the heat transfer rate at the plate surface (without injection) revealed no indication of transition. In view of this it is believed that the boundary layer is laminar at separation for all cases reported.

3.3 Experimental Procedure

The parameters varied were jet gas species and jet stagnation pressure. The injectant gases used were Nitrogen, Helium, Argon and Methane. This selection provides variation in both molecular weight and specific heat ratio as shown in Table 1. For slot injection, side plates were installed during some tests to inhibit transverse spillage from the recirculating flow region.

Gas	N ₂	He	Ar	CH ₄
γ	1.40	1.67	1.67	1.31
W	28.02	4.00	39.95	16.04

Table 1 Properties of Injectant Gases (at S.T.P.)

The effects of the various jet parameters on the two and three dimensional flow fields were examined extensively. Schlieren pictures were used to identify the main features of the flow field. Heat transfer at the plate surface was visualised using Liquid Crystal Thermography (LCT). (LCT entails applying a layer of temperature sensitive liquid crystal to the model surface. Variations in local heat transfer rate from the flow to the model appear as regions of differing colour). This technique was used in conjunction with oil flow visualisation to examine the finer details of the interaction region. Location of primary separation (the point at which the freestream flow leaves the plate surface) was also determined from oil flow pictures. The centreline surface static pressure distribution was measured for a large number of two dimensional and three dimensional cases. This was done for each injectant gas over a range of injection pressures.

4. PRESENTATION OF JET INTERACTION DATA

Historically, a variety of parameters have been applied in an attempt to correlate jet interaction data. For the majority of experiments the ratio of jet to freestream momentum (flux) has proved the most effective and is defined as follows¹¹:

$$\frac{\phi_j}{\phi_\infty} = \frac{P_j \gamma_j M_j^2 A_j}{P_\infty \gamma_\infty M_\infty^2 A_\infty} \quad (1)$$

However, for cases where M_∞ , M_j , γ_∞ and γ_j are fixed this

may be reduced to:

$$\frac{\phi_j}{\phi_\infty} \propto \left(\frac{P_j A_j}{P_\infty A_\infty} \right) \quad (2)$$

During the present analysis, although there is variation in γ_j (from 1.31 to 1.67), there was noticeably less scatter in the two dimensional data for the various injectants when displayed as a function of the momentum flux parameter defined in equation (2). Therefore this parameter has been used to present the data in this paper. Note also that for slot injection $A_j = w$ and $A_\infty = L$.

5. RESULTS AND DISCUSSION

5.1 Two Dimensional Interaction Data

5.1.1 Surface Flow Visualisation

Liquid crystal thermography (LCT) has been used in conjunction with oil flow visualisation to examine in detail the structure of the two dimensional interaction flow field. Figure 2 shows a schematic of a thermograph and an oil flow picture at the same test conditions including surface flow interpretation. The point at which the external flow separates from the surface is clearly visible from the oil flow picture. Although the equivalent position on the thermograph is not as sharply defined, flow separation is apparent from a decrease in surface temperature which marks the beginning of the relatively cool separated region. The surface temperature within this region is approximately constant except for a hot area just ahead of the jet.

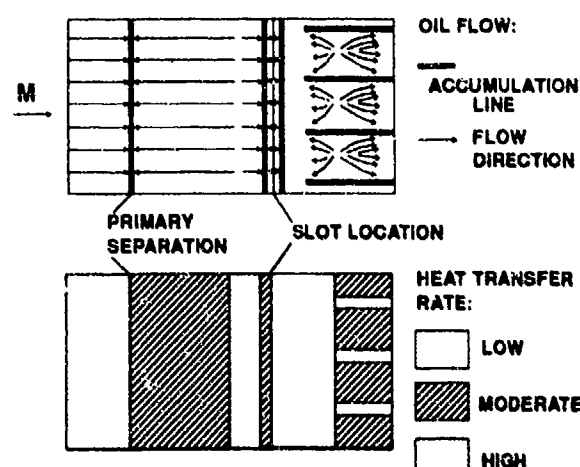


Figure 2 Schematic of Slot Jet Surface Flow Visualisations

Examination of the oil flow at this point reveals a reattachment line which occurs within this high heating zone. Flow reattachment here is consistent with the presence of a second, counter-rotating vortex. There is a narrow band of lower heat transfer between the downstream edge of the hot feature and the jet lip. A line of accumulated oil also exists at this point. We interpret

these features as evidence that the jet fluid attaches to the plate surface at the jet exit, the accumulation of oil representing the point at which the jet flow leaves the surface. A similar feature is seen at the rear edge of the slot which is interpreted in the same manner.

Aft of the slot, the flow field becomes rather complex. Downstream of the jet flow separation point, oil flow pictures indicate streamwise oil striations repeated quasi periodically in a spanwise sense. An analogous pattern is seen in the liquid crystal thermograph, where the hottest regions occur between the oil striations. Both of these patterns indicate that longitudinal vortices are present in the downstream flow region as sketched in Figure 3. Reattachment of the outer flow is indicated by the presence of oil flow 'nodes' which occur between the oil striations at a streamwise position corresponding to an increase in surface heat transfer as indicated in Figure 2. The oil flow pattern shows that the oil striations exist upstream of the reattachment point which implies that the vortices exert some influence within the downstream separation bubble.

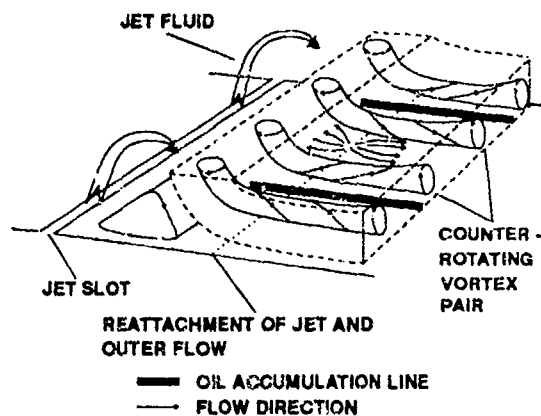


Figure 3 Interpretation of Flow Downstream of the Slot Jet

This highly three dimensional reattachment process is apparent in all slot jet configurations investigated. The presence of the vortices is thought to be due to the Görtler instability mechanism¹² operating in the curved separated shear layer and has been observed in other reattaching jet interaction flows.¹³

5.1.2 Separation Length

The centreline separation length ahead of the slot was determined from oil flow pictures. Four injectant gases were employed over a range of jet stagnation pressures. All the data are for constant slot width and are plotted in a normalised form (X/L) as a function of momentum flux parameter (Figure 4). With the exception of Helium, it can be seen that data reduce almost to a single line - even though γ_i varies from 1.31 to 1.67.

By considering the results for Helium and Argon it is possible to eliminate any specific heat ratio effects ($\gamma_i = 1.67$ for both) and at the same time highlight molecular weight effects. The data in Figure 4 demonstrate that

Argon produces a slightly larger flow separation than Helium for the same jet stagnation pressure and slot width, which is consistent with observations from schlieren pictures.

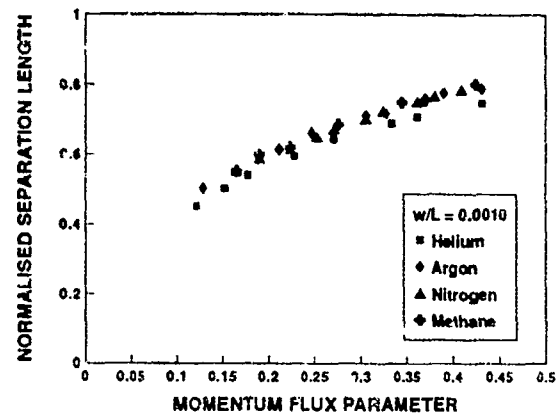


Figure 4 Slot Jet Separation Length Data For Different Injectants

5.1.3 Surface Static Pressure

Figure 5 shows a typical centreline surface pressure distribution for slot injection. The pressure distribution is normalised with respect to the undisturbed plate pressure (measured in the absence of injection). The locations of primary separation and reattachment within the upstream separated region (determined from oil flow visualisation) are also shown; the pressure rises to the point at which the flow separates from the plate surface and then further increases until a plateau is reached. Just ahead of the jet the pressure increases again. It is possible that this rise corresponds to the reattachment of the counter-rotating vortices just ahead of the jet, although there is insufficient resolution in the data for this to be conclusive. There is little difference between pressure data for the various injectant gases when the stagnation pressure and slot width are held constant.

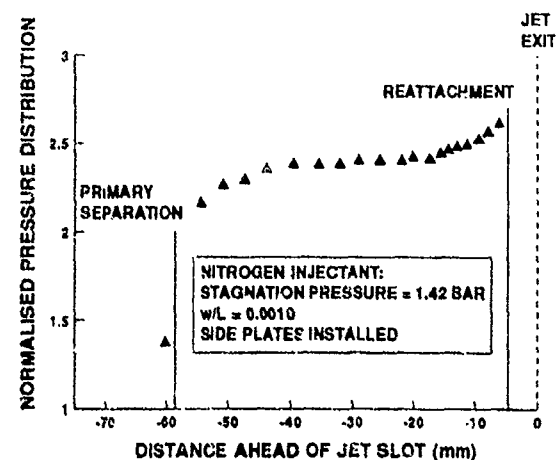


Figure 5 Surface Static Pressure Distribution Ahead of the Slot Jet

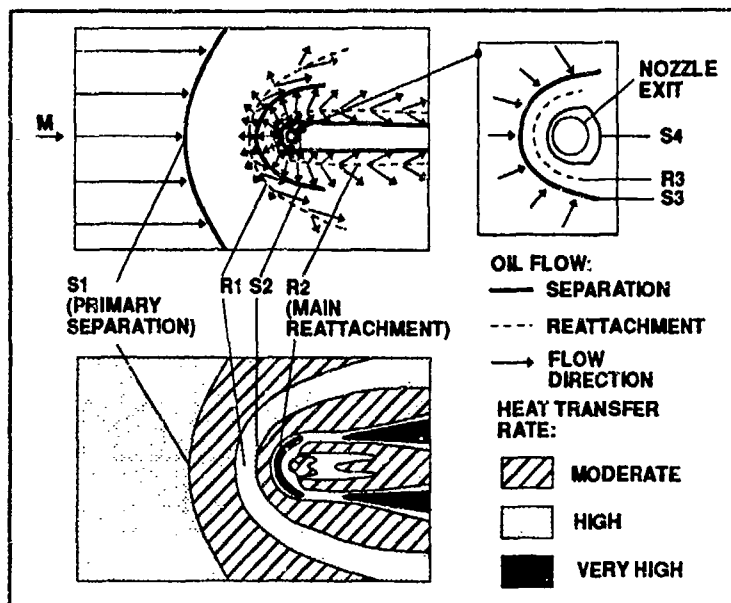


Figure 6 Schematic of Surface Flow Visualisation from Circular Injection

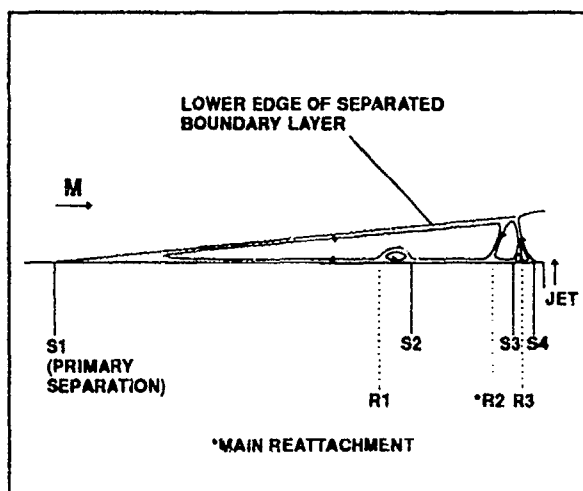


Figure 7 Interpretation of Centreline Flow Ahead of the Circular Jet

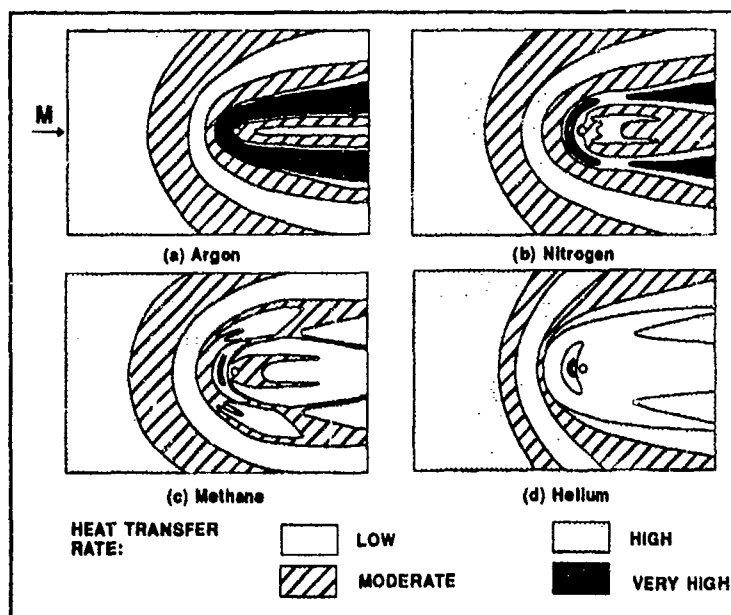


Figure 8 Heat Transfer Rate Visualisation for Different Injectant Gas Types (Circular Jet)

5.2 Three Dimensional Interaction Data

5.2.1 Surface Flow Visualisation

Surface visualisation of the flow field resulting from circular injection revealed a number of complicated features that were not observed in its two dimensional counterpart. In order to illustrate these, a schematic of oil and liquid crystal thermograph pictures, at the same flow conditions, is shown in Figure 6. Working in the same manner as for the slot injection case, four separation lines upstream of the injector can be identified (these are labelled S1 to S4 in Figure 6, S1 being furthest upstream). It is believed that the separation line (S4) around the nozzle exit is, as in the two dimensional case, the point at which the jet fluid leaves the plate. From enlargements of oil flow pictures in the vicinity of the injector it is possible to distinguish flow reattachment (R3) between the two separation lines immediately ahead of the jet (S4 and S3). Moving upstream of separation S3, a very strong region of reattachment (R2) is evident both from oil and heat transfer pictures. This is referred to as the 'main' reattachment. Between this point and the location of primary separation (S1), it is possible to identify another separation (S2) and reattachment (R1) from the surface flow visualisation patterns. For the case of Helium injection, there is evidence that an additional separation and reattachment are present within the interaction region. However, further investigation will be necessary in order to confirm details.

A possible interpretation of the centreline flow from Figure 6 is sketched in Figure 7 which depicts six counter-rotating vortices. This is similar to observations by Shang et al³ on an ogive cylinder in a laminar hypersonic flow, which revealed the presence of two vortex pairs in the upstream separated region.

The thermographs also indicate that the amount of heat transfer in the vicinity of the jet is dependent on the injectant gas. This is illustrated in Figure 8 which shows, in schematic form, typical heat transfer patterns for the four different injectant gases. The most striking feature is the second (main) reattachment region around the jet. In the case of Argon injection the surface heat transfer in this region is always very high. For Nitrogen, the region just ahead of the jet is also a very high heat transfer region, however as the horseshoe vortex progresses downstream there is a slight decrease in heat transfer followed by an increase towards the downstream edge of the plate. Methane creates a similar pattern to Nitrogen except that the process, on average, results in slightly lower surface temperatures. Although Helium produces a small zone of high heat transfer upstream of the jet, the surface temperature of the rest of this area is noticeably lower, except for a hotter region at the end of the plate. These results imply that there is a significant degree of mixing between jet and freestream gases in the separated flow region, which in turn is affecting the local surface heat transfer rate.

5.2.2 Centreline Separation Length

Attempts to collapse separation length data onto a single line using parameters such as those defined by equations (1) and (2) were not successful. Normalised centreline

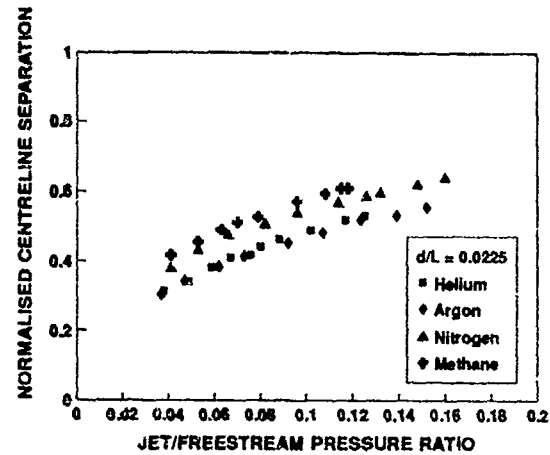


Figure 9 Centreline Separation Length Data (Circular Injection)

separation distances (X_s/L) determined from oil flow visualisation are presented in Figure 9 as a function of jet to freestream stagnation pressure ratio ($P_{0j}/P_{0\infty}$). This figure demonstrates the dominant effect of the injectant specific heat ratio on the extent of the upstream separated flow region. Axisymmetric freejet studies¹⁴ show that the cross sectional area of the jet will increase as the injectant specific heat ratio (γ) is reduced. This means the size of obstacle that the jet presents to the flow will increase with injectant gas type as follows - Helium/Argon, Nitrogen, Methane (see Table 1 for the various γ). In turn, the extent of the interaction flow field will increase as the jet's size increases. This explains the trend observed in Figure 9. Obviously this effect is not seen in the two dimensional interaction results, as the spanwise width of the jet is effectively infinite and therefore independent of injectant gas type. These axisymmetric data demonstrate the importance of the size of the jet for the three dimensional interaction flow field.

5.2.3 Surface Static Pressure

Figure 10 shows a centreline static pressure profile for the circular jet injection in which data are normalised by the

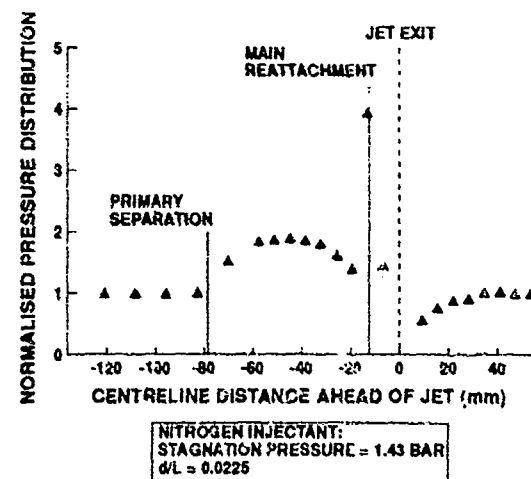


Figure 10 Centreline Surface Pressure Distribution Ahead of the Circular Jet

undisturbed plate pressure. The positions of the primary separation (S1) and the main reattachment (R2) ahead of the jet (measured from an oil flow picture) are included. The upstream centreline pressure distribution bears some resemblance to the two dimensional flow; the pressure increases on the plate to the point at which flow separates, then there is a further rise up to a pressure plateau. In the vicinity of the jet, the three dimensional pressure distribution shows a drop from the plateau value followed by a rapid rise to a peak just ahead of the jet. The size of this peak is larger than any pressure observed in the slot jet case and may be as much as six times the undisturbed plate pressure. The position of this peak corresponds with the location of the main reattachment (R2) ahead of the jet as indicated in Figure 10.

Unlike the two dimensional interaction data there are differences between the centreline pressure distributions for the various injectant gases at fixed pressure ratio (P_0/P_∞) and nozzle geometry. Typical data for each injectant gas are shown in Figure 11. The data confirm observations from flow visualisation methods that the size of the flow field depends mainly on the injectant ratio of specific heats. However, it should be noted that Helium, although producing a shorter separation region, yields the highest plateau pressure ahead of the jet.

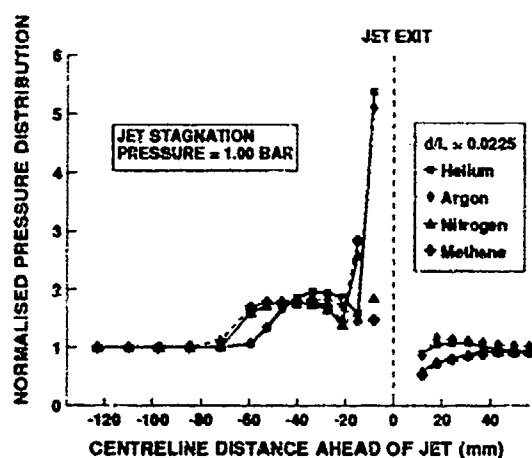


Figure 11 Centreline Pressure Distributions for Different Injectant Gases

Downstream of the jet the static pressure is less than the plate pressure, increasing to a plateau preceded by a slight overshoot. It is evident that the values of the surface pressures in this region are dependent on the injectant gas; Methane produces the lowest downstream pressures then Nitrogen, Helium and Argon.

6. CONCLUSIONS

New experimental data have been presented for a circular sonic jet issuing into a laminar hypersonic cross flow. These have been compared with existing results for a two dimensional jet in the same flow.

Superficially there are similarities between the centreline flow field created by the circular jet and that of the slot jet. However, for the two dimensional interaction the effect of

injectant species is small, which is not true for the three dimensional interaction. In the latter case, as the injectant ratio of specific heats is increased then the cross sectional area of the jet decreases. Consequently the size of the obstacle that the jet presents to the oncoming flow decreases and the hence the extent of the interaction flow field is reduced. This influence of injectant specific heat ratio is not observed in the two dimensional injection case because the spanwise width of the jet is effectively infinite.

Flow visualisation has revealed a complicated region upstream of the circular jet in which a number of counter-rotating vortices have been observed. Also, an effect of the injectant gas composition on the heat transfer rate in the proximity of the jet has been detected. For the two dimensional case there is only evidence of one counter-rotating vortex pair and no indication that heat transfer rate in the vicinity of the slot is dependent on injectant gas.

ACKNOWLEDGEMENTS

The authors are grateful for the technical assistance of Mr. R.P. Clarke during this experimental programme.

This work has been carried out with the support of DRA, Farnborough, U.K..

REFERENCES

- ¹Spaid, F.W. and Cassel, L.A., "Aerodynamic Interference Induced by Reaction Controls", AGARDograph No. 173, 1973.
- ²Brandeis, J., "Numerical Study of Jet Interaction at Super- and Hypersonic Speeds for Flight Vehicle Control", ICAS Proceedings, Beijing, September 1992, pp 1847-1857.
- ³Shang, J.S., McMaster, D.L., Scaggs, N. and Buck, M. "Interaction of Jet in Hypersonic Cross Stream", AIAA Journal, 27, 1989, pp 323-329.
- ⁴Powrie, H.E.G., Ball, G.J. and East, R.A. "Experimental Study of a Two Dimensional Control Jet with a Hypersonic Flow", IUTAM Conference on Aerothermochemistry of Spacecraft and Associated Hypersonic Flows, Marseille, September 1992. (Proceedings to be published).
- ⁵Spaid, F.W. "Two Dimensional Jet Interaction Studies at Large Values of Reynolds Numbers and Mach Numbers", AIAA Journal, 13, 1975, pp 1430-1434.
- ⁶Kaufman, L.G. "Hypersonic Flows Past Transverse Jets", J. Spacecraft, 4, 1967, pp 1230-1235.
- ⁷Orth, R.C. and Funk, J.A. "An Experimental and Comparative Study of Jet Penetration in Supersonic Flow", J. Spacecraft, 4, 1967, pp 1236-1242.
- ⁸Billig, F.S., Orth, R.C. and Lasky, M. "A Unified Analysis of Jet Penetration", AIAA Journal, 10, 1971, pp 1048-1058.

⁹Schetz, J.A., Weiraub R.A. and Mahaffey R.E. "Supersonic Transverse Injection into a Supersonic Stream", AIAA Journal, 6, 1968, pp 933-934.

¹⁰Chambers, R.A. and Collins, D.J. "Stagnation Temperature and Molecular Weight Effects in Jet Interaction", AIAA Journal, 8, 1970, pp 584-585.

¹¹Rausch, J.R. and Roberts, B.B. "Reaction Control System Aerodynamics Interaction Effects on Space Shuttle Orbiter", J. Spacecraft, 12, 1975, pp 660-666.

¹²Blackwelder, R.F. "Analogies Between Transitional and Turbulent Boundary Layers", Phys. Fluids, 10, 1968, pp 2807-2815.

¹³Maurer, F. "Three Dimensional Effects in Shock Separated Flow Regions Ahead of Lateral Control Jets Issuing from Slot Nozzles of Finite Length", AGARD CP 4 (Part 2), 1966, pp 597-634.

¹⁴Crist, S., Sherman, P.M. and Glass, D.R., "Study of the Highly Underexpanded Sonic Jet", AIAA Journal, 4, 1966, pp 68-71.

EXPERIMENTS ON INTERACTION FORCE OF JETS IN HYPERVELOCITY CROSS-FLOW IN A SHOCK TUNNEL

K.W. Naumann, H. Ende, G. Mathieu, A. George
French-German Research Institute ISL
5, Rue du General Cassagnou, 68301 Saint-Louis, France
Postfach 1260, 7858 Weil am Rhein, Germany

SUMMARY

This paper presents experiments on side-jet control efficiency in the hypervelocity flow of the ISL shock tunnel. The parameters of the test flow represent almost truly Mach number, Reynolds number, velocity and density of tropospheric hypervelocity flight. The experiments are carried out with a model, which is equipped with pyrotechnical charges, a settling chamber, laterally blowing jets, and a set of small accelerometers. The pyrotechnically supplied side-jets also are roughly adequate to those used in sound vehicles. Extensive jet gas diagnostics yield the parameters of the gas and the nozzle flow. The accelerometers incorporated in the model allow direct millisecond aerodynamic force measurement. To provide free-flight during the testing time, a fast-acting mounting support releases the model and grips it again when the test flow has passed the model. Using measured acceleration and Pitot pressure histories allows direct straightforward time-dependent evaluation of the aerodynamic coefficients. The procedure is insensitive against disturbances in the starting phase of the flow or moderate flow variations. The results quantify the force, which is produced by interaction of side-jets and ambient flow, and acts on the surface of the model. At the tropospheric hypervelocity conditions of our test, the interaction force on a flat plate substantially increases jet thrust. Moreover, the results quantify the time necessary to establish quasistationary flow for the actual test conditions.

LIST OF SYMBOLS

A	m^2	area
a	g	acceleration
$a_{k,j}$	g	acceleration in k -direction due to jet force
$a_{k,\infty}$	g	acceleration in k -direction due to ambient flow force
$a_{k,t}$	g	total acceleration in k -direction
C_i		interaction coefficient, $(F_{z1} + F_{zj})/F_{zj}$
C_k		aerodynamic coefficient in k -direction
C_D		drag coefficient
C_L		lift coefficient
C_p		pressure coefficient
C_{ps}		pressure coefficient at the stagnation point
F	N	force
$F_{k,i}$	N	force in k -direction due to

		interaction of jet and ambient flow
$F_{k,j}$	N	force in k -direction due to jet thrust
f		number of internal degrees of freedom of a gas
L_M	m	model length
l_{trs}	m	test flow slug length
m	kg	mass
M	$g/mole$	molecular mass
Ma		Mach number
p	Pa	pressure
\hat{p}_0	Pa	stagnation pressure behind a normal shock
R	J/kgK	specific gas constant
Re		Reynolds number
s	m^2	vector with a length equal to the area of a surface element, directed normally to it.
t	s	time
t_{fo}	s	time at test flow onset
t_{qs}	s	time at which quasistationary flow is established
W	m/s	velocity
X, Y, Z		model-fixed cartesian coordinates
γ		ratio of specific heats = c_p/c_v
θ		shock angle
ϕ		streamline deflection angle
ρ	kg/m^3	density

Subscripts

E	nozzle exit value
i	interaction of side-jet and ambient flow
j	jet flow
k	directional index
M	model
S	surface
se	separation
O	stagnation value
∞	ambient flow

Superscripts

$*$	critical value (at $Ma = 1$), nozzle throat value
\wedge	value behind a shock

1. INTRODUCTION

The aim of the experiments described in this paper is to identify and to quantify the relevant parameters of side-jet control, in order to optimize the control efficiency of endoatmospheric hypervelocity projectiles and vehicles.

For these vehicles side-jet control may be useful from different reasons:

At velocities over about 1500 m/s in the lower atmosphere these vehicles are exposed to heavy aerodynamic heating. This affects most severely thin and exposed structures /1/, such as fins or flaps, and may also affect delicate mechanical structures of controls or actuating devices. As a consequence it is desirable to have comparatively "simple" shapes without thin movable surface structures and gaps. This can be achieved by side-jet control, because all what affects the surface shape are the nozzle openings.

Another reason to consider side-jet control for endoatmospheric hypervelocity vehicles is, that efficiency tends to increase with increasing flight Mach number (for this and the following see /2/ and the literature cited therein). In this context efficiency means the component in jet thrust direction of that additional force, which is produced by the interaction between the jet and the ambient flow and acts on the surface of the vehicle. Figure 1 shows a principle sketch of the interaction flow field: The jet leaving the nozzle affects the ambient flow like an obstacle. It produces a bow shock wave, which surrounds the jet and hits the vehicle surface. Behind this bow shock we find increased pressure, which also acts on the vehicle surface. In front of the jet the boundary layer separates. The separation zone of horseshoe shape generates an oblique shock and an area of increased surface pressure as well. In general the interaction of bow shock and boundary layer causes more or less significant separation. In the wake region of the jet we usually find a considerable region of reduced pressure.

Let now p_s be the local pressure acting on the vehicle surface, $p_{s,\infty}$ the local partial pressure acting on the vehicle surface due to ambient flow alone ($p_{s,\infty} = p_s$ if no jets are active), and $p_{s,i}$ the additional local partial pressure acting on the vehicle surface due to interaction of jet and ambient flow, i. e.

$$p_{s,i} = p_s - p_{s,\infty} \quad (1)$$

If we neglect friction effects, the surface force acting on the vehicle is

$$F = \int_S p_s ds \quad (2)$$

which can be split into F_∞ and F_i :

$$F = F_\infty + F_i = \int_S p_{s,\infty} ds + \int_S p_{s,i} ds \quad (3)$$

Of particular interest for considerations on side-jet control efficiency is the component in that direction, where the

manoeuver should be effected, say z . Usually this is also the direction of the main component of the side-jet thrust $F_{z,j}$.

Increasing the efficiency means increasing $F_{z,j} + F_{z,i}$. Since there exists just a limited potential to maximize $F_{z,j}$, the decisive parameter is $F_{z,i}$.

Unfavorably $F_{z,i}$ depends on many parameters, and their respective influence and interdependence cannot be entirely quantified. If we just consider the flight velocity, i. e. flight Mach number, it is clear, that the relative pressure rise due to the bow shock and the separation shock is much higher for higher Ma than the relative pressure drop in the wake region behind the jet. Moreover, the lateral propagation of the bow shock depends strongly on Ma. A high flight Mach number impedes the propagation of the bow shock to the opposite side of the vehicle, where the subsequent pressure rise acts into the wrong direction. Hence it is clear, that with subsonic or transonic vehicles the efficiency of side-jet control is poor. In any case it is advisable to confine the bow shock-surface interaction on surface parts, whose orientation secure the right direction of $F_{z,i}$.

In order to quantify this efficiency, a widely used parameter is the interaction coefficient, defined

$$C_i = (F_{z,j} + F_{z,i})/F_{z,j} \quad (4)$$

This parameter has the detrimental property, that it increases with decreasing $F_{z,j}$, and that one can achieve any high value, if the useful jet thrust is made sufficiently low. This should be kept in mind, and will be recalled in subsequent discussion.

A second aspect of efficiency is the drag force, F_x . At hypersonic or hypervelocity conditions the ratio of lift/drag is worse than for subsonic conditions. Even for waveriders it is limited to a value of about 5 for practical shapes /3/, and the same holds for control surfaces. If the cruise speed has to be constant, the additional drag due to a control action $F_{x,i}$ has to be compensated by additional thrust, i. e. fuel mass. If $F_{z,i}$ of side-jet control is sufficiently high, this control technique can also be efficient with respect to overall fuel consumption /4/.

A further reason to consider side-jet control is, that high velocity of flight necessitates short response time for manoeuvring projectiles /5/. Particularly if only little total impulse is needed, small impulsive thrusters can be advantageous.

Without regards to useful interaction force side-jet control can favorably be used with endo-exoatmospheric vehicles, or with very slow vehicles. In both cases aerodynamic control is not very effective because of

low dynamic pressure, and side-jets or thrust vectoring are the only means to keep control of the vehicle.

Side-jet control of subsonic vehicles concerns mainly VTOL- and STOL-vehicles or maneuvering fighters at very high angle of attack, and is not the subject of our investigation.

Side-jet control of supersonic/hypersonic endoatmospheric vehicles concerns mostly missiles and projectiles /2, 6/. Because of the complexity of the interaction flowfield, the majority of the publications describe experimental work /2/. From the many investigations on flowfield visualization, the qualitative knowledge on the structure of the interaction flowfield is good /2/. Not so numerous are measurements on $F_{z,1}$.

The reasons are:

- ▷ Force measurements with side-jets are expensive, even if the jets are supplied with ordinary gas. The same holds for the deduction of aerodynamic force by pressure mapping.
- ▷ Combustion gases must not be ejected in the majority of test facilities, because they contain aggressive components, which damage the facility or vital components of it.
- ▷ Endoatmospheric hypervelocity flow conditions can only be simulated in shock tunnels or similar short-duration facilities, and just for some milliseconds.

Hence we decided to develop for ISL shock tunnel "B" (see Fig. 2) a technique for direct aerodynamic force measurement of models, which are equipped with laterally blowing jets, and which are exposed to the test flow /7/.

In what follows we describe the first experiments and results on side-jet control efficiency in the tropospheric hypervelocity flow of ISL shock tunnel "B".

2. EXPERIMENTAL SETUP

2.1 Shock Tunnel Facility

A principle sketch of ISL shock tunnel "B" /8/ is shown in Fig. 2, and Tab. 1 gives the test flow conditions. We use the compressed, heated and accelerated test gas in the "straight-through" mode. A divergent expands and accelerates the already supersonic test gas. Compared with the more common process of bringing the test gas at rest at an end-wall, and expanding it through a Laval nozzle, this procedure has the advantage, that the flow in the test chamber is more uniform, and that the heating of the test gas is less. Disadvantageous is the shorter test time, which is short of about two milliseconds, counting from the very beginning of flow in the test chamber. The maximum time available for triggering purposes is 13 ms.

2.2 Millisecond Aerodynamic Force Measuring Technique

Measurements on aerodynamic force in shock tunnels or similar test facilities are in

general more expensive than in wind tunnels with flow durations of seconds or minutes. This holds also for pressure mapping, since the short test time does not allow the use of scanning valves, and each measuring point needs its own transducer. Moreover, a prominent property of hypervelocity flowfields are strong gradients of the state parameters, which need to be resolved by appropriate narrow spacing of the measuring points. Since side-jet control produces a highly 3-dimensional flowfield, direct force measurement is desirable.

At test facilities like ours conventional balances for measurement of aerodynamic force cannot be used, because measuring time is of about the same order or less than the response time of the model/support/balance arrangement. In this case the measured stress is produced as well by external aerodynamic load and inertia effects of model and support /9/. Up to now 5 or more oscillation cycles during test time are needed in addition to sophisticated data reduction procedures to evaluate the aerodynamic force /10/. This becomes more complicated, if the aerodynamic load history is not linear or is unpredictable. This may occur particularly in the starting phase of tests with models of complex structure, or in general, if the models are equipped with installations to produce thrust or side-force. Consequently a technique using free-flying /11/ or softly suspended models /12, 13, 14/, together with direct acceleration measurement, has to be used. An important constraint is, that the interior of the models is kept sufficiently free to allow the installation of side-jets and on-board propellant supply. A detailed description of this technique gives /7/.

2.2.1 Function and Technical Realization

The key feature of the aerodynamic force measurement technique is a special mounting support. Figure 3 schematically shows the function cycle during an experiment. Initially the chuck of the mounting support is closed, fixing the model at its stem with its correct position and attitude. Just before test flow onset, it releases the model for the time of measurement, thus preventing parasitic tank and support oscillations from inflicting model motion. After the testing time it closes and grips the model again, before afterflow accelerates it too much.

Figure 4 shows the second mounting support with the first side-jet model and the test chamber. For driving the opening mechanism of this support we use a charge of 220 mg of gunpowder, because this allows a simple design and is available in ISL.

Model acceleration is measured by a set of small piezo accelerometers. The small velocity and displacement of the model during a time of few milliseconds of test flow allow the use of thin wires between model and recorder or control device. Moreover, centripetal acceleration is small and does not affect transducer output. The models may be of comparatively high cross-section area load, say 100 - 1000 kg/m², because dynamic pressure of roughly 1 MPa accelerates these models sufficiently. Furthermore, thin umbilical

wires cause no considerable restraint on model motion. The wires run through stem and support, well protected against the flow.

Up to now we use small quartz accelerometers PCB 309A with built-in amplifiers. They are mounted adhesively on small discs made from a mixture of resin and micro-balloons. This is necessary to damp the excitation of resonant oscillations of the accelerometers, which mainly result from shock loading of the model structure by the starting test flow, or, less momentous, from the start of the side-jets.

2.2.2 Data Registration and Evaluation

The main equipment used for data registration, triggering of recorders and ignition is shown in Fig. 1. Any of the signals of the heat or pressure transducers mounted along the shock tube can be used for triggering purposes. With a Maurer transient memory we record 8192 data points with 500 kHz sampling frequency and 10 bit storage depth. This covers the whole relevant time of experiment for check of correct functioning of all parts involved. We use no filters in the measuring cascade, because they might suppress short overload peaks or the oscillations mentioned above. For this reason we solely use numerical filtering procedures.

The HP-computer is sufficient for all data evaluation procedures and calculations. For any component "k" of model motion we take the respective acceleration and Pitot pressure histories to calculate the corresponding aerodynamic coefficient history directly. The model acceleration a_k typically depends on model area A_k , model mass m_k , the dynamic pressure of the flow $\rho_\infty W_\infty^2/2$ and the coefficient C_k . Using

$$a_k = (0.5 \rho_\infty W_\infty^2 C_k A_k) / m_k \quad (5)$$

and measured Pitot pressure \hat{p}_0 with

$$0.5 \rho_\infty W_\infty^2 = (\hat{p}_0 - p_\infty) / C_{ps} \quad (6)$$

$$(\hat{p}_0 - p_\infty) / C_{ps} = \hat{p}_0 f(Ma_\infty, \gamma) = \hat{p}_0 / C_{p0} \quad (7)$$

$$0.5 \rho_\infty W_\infty^2 = \hat{p}_0 / C_{p0} \quad (8)$$

we get

$$C_k = (C_{p0} a_k m_k) / (A_k \hat{p}_0) \quad (9)$$

Accordingly the output of the accelerometers are typically normalized with the output of the Pitot pressure transducer and then multiplied by $C_{p0} m_k / A_k$, which depends only on model properties, Ma_∞ and γ . The procedure is straightforward, yields time-dependent coefficient histories, and compensates to some extent flow variations, if the flow is quasistationary and maintains a roughly uniform Mach number.

2.3 The Side-Jet Model

Figure 5 shows frontal views of the first and the second side-jet model. Table 2

gives the data of models 1. The basic parameters of the models are the same, but the new model 2 has better mechanical strength, is prepared for the installation of an internal fast-opening device, and its wing has a swept-back leading edge. The latter is important for flow visualization studies: The rectangular wing of model 1 produces strong tip vortices, and it is not possible to identify details of the separation zone. Hence the pictures shown in chapter 3.2 are already taken from model 2, whereas all other experiments are carried out using model 1. If not stated otherwise, all descriptions mind model 1.

The sketch of Fig. 6 shows the location of jets and accelerometers relative to the centre of gravity of model 1. Figure 7 shows the fully instrumented body of this model, with 2 nozzles, and Fig. 8 shows the single parts.

The most important part of the model is the body. It contains all necessary installations to produce the side-jets, i. e. two pyrotechnical charges, a common plenum chamber and 1 to 3 parallel, exchangeable nozzles. The maximum plenum chamber pressure is about 50 MPa. All accelerometers are mounted on the body, in excavations, as can be seen in Figure 7. With a minimum number of 6 accelerometers 6 components of model motion can be measured, if the transducers can be placed exactly on the X-, Y-, and Z-axes of the model /9/. For our experiments just 3 components are required. Since there is no space available on the X- and Z- axes of our model, the minimum number of accelerometers is 6 as well. Nevertheless, 14 accelerometers are installed to have redundant information, if any of the delicate wires is damaged, and in fact we can check lift, drag, pitch, roll and yaw motion.

The pyrotechnical charges of about seven gram in total are composed of layers of different high-explosive gun powders. The objective is to obtain a moderate pressure rise during a starting phase of 2 to 4 ms, and a constant level pressure for the time of test flow. The use of gun powder is simple from the technical point of view, because we need no high-pressure gas supply, which is likely to complicate any technique of aerodynamic force measurement. On the other hand, the gas mixture depends on the combustion conditions, particularly pressure and temperature. Since pyrotechnics is to some extent a matter of chance, the evaluation of the nozzle flow conditions needs particular studies.

The plate-wing and the upper side of the body form a flat surface. At zero pitch this is aligned with the oncoming ambient flow along the axis of the test chamber. The model itself produces considerable lift acceleration $F_{z,\infty}$ of the order of 1000 m/s². Jet thrust and the model lift act in opposite direction and balance each other to some extent. Since we intend to evaluate $F_{z,i} = F_{z,t} - F_{z,\infty} - F_{z,j}$, it is necessary that $F_{z,\infty}$ and $F_{z,j}$ are of about the same order of magnitude, in order to obtain good resolution.

The experiments show, that the small distance between the thrust axis of the jets and the centre of gravity does not cause significant rotational accelerations, as also does not the moment of the lift force. Hence we may treat the model as a point mass.

3. EXPERIMENTS

The experiments on side-jet interaction force comprise experiments on the nozzle flow parameters, aerodynamic force measurement, and flow visualization by differential interferometry.

3.1 Evaluation of the Jet Flow Parameters

As stated above, combustion of gun powder produces a mixture of gases. Its composition depends on the combustion conditions, particularly pressure and temperature. Of course the combustion conditions in our model are not the same as in breeches, and gas mixture differs from the known values. Moreover, the ideal gas relation between γ and f is not valid, and a significant amount of soot is produced.

Figure 9 shows the histories of the jet plenum chamber pressure, $p_{0,j}$, of different runs, using the same kind of pyrotechnical charges. We see, that rise time, peak pressure and decay time differ substantially.

The measurement of the gas temperature $T_{0,j}$ is affected by the comparatively large surface of the stagnation chamber, its complex shape, and presumably ongoing burning of the powder in swirling flow. Hence we can not get data, that could help to quantify the stagnation gas conditions.

The successive approach is to measure the flow velocity $W_{j,E}$ in the aperture of nozzles with different area ratios $A_{j,E}/A_j^*$, and as well thrust F_j and temperature $T_{j,E}$. Here we use two nozzles with $A_{j,E}/A_j^* = 9.75$ and 1, respectively.

Figure 10 shows a sketch of the experimental setup used for the velocity measurements. We use a single-ray laser Doppler velocimeter, with spectrometric analysis of the Doppler shift of the scattered laser light, using an autostabilized Michelson interferometer (see /15/ and the literature cited therein for detailed information). This technique has the advantage, that it works with the continuously scattered light of many small particles, which pass the measuring volume simultaneously and permanently. For our measurements the soot from the gun powder gave good results, as can be seen from Fig. 11. Notice, that the flow velocity does not change much with time, and also not much with $p_{0,j}$ for an individual run. Figure 12 shows the history of $Ma_{j,E}^* = W_{j,E}/a_j^*$ of the conical nozzle ($a_j^* = W_{j,E}$ of the sonic nozzle). With $Ma_{j,E}^* = 2.10$ and $A_{j,E}/A_j^* = 9.75$, using

$$\frac{A_{j,E}}{A_j^*} = Ma_{j,E}^* \left[1 - \frac{(\gamma-1)}{2} (Ma_{j,E}^{*2} - 1) \right]^{\frac{1}{\gamma-1}} \quad (10)$$

we obtain $\gamma = 1.42$. The dependence of γ on $A_{j,E}/A_j^*$ is weak: if the nozzle boundary layer had a displacement area of 10% of $A_{j,E}$, γ still would be a little over 1.4. From γ and $A_{j,E}/A_j^*$ we calculate $Ma_{j,E}$.

The density of the nozzle exit flow $\rho_{j,E}$ can be calculated using the measured thrust force,

$$\rho_{j,E} = F_j / (A_{j,E} W_{j,E}^2) \quad (11)$$

and with γ and $Ma_{j,E}^*$ or $Ma_{j,E}$, we get $\rho_{j,0}$ and ρ_j .

The gas temperature $T_{j,E}^*$ of the jet is measured optically, by the emission-/absorption method using the wavelength 2.7 $\mu\text{m}/16/$. This technique can only be used with sonic jets, because $T_{j,E}$ must have a certain minimum level. Figure 13 shows the histories of $T_{j,E}$ and $p_{j,0}$ of two shots. From $T_{j,E}^*$ and γ we get $T_{j,0}$, and from this, $p_{j,0}$ and $\rho_{j,0}$ follow molecular mass $M_{j,0}$ and specific gas constant $R_{j,0}$. Table 3 gives a synopsis of the jet gas parameters.

By calculating the total mass of gas in the combustion chamber, it turns out, that the density evaluated above is less than that calculated with the assumption, that all powder has burnt until the time of measurement (i. e. within the first millisecond). This means, that 72% \pm 6% of the gun powder have been burnt until this time. Indeed, a considerable amount of soot can be observed either in the combustion chamber and the nozzles, or on flow visualization pictures, where even unburnt powder grains can be seen.

Since the measurements on jet gas diagnostics have to be done in the plain laboratory, $p_{j,0}$ of nmodel 1 is limited to 10 MPa for safety reasons. Accordingly the numbers of Tab. 3 may not represent the gas conditions at 50 MPa exactly. We plan to repeat these measurements at 50 MPa with model 2.

3.2 Flow Visualization in the Shock Tunnel

For flow visualization we use differential interferometry (for detailed information see /17/ and the literature cited therein). Two light beams pass the flow field, there separated by a certain distance from each other, and brought together on a detector surface, which in our case is a photographic film. The difference in optical length of the two light paths produces interference patterns, either fringes, or changes in light intensity if the fringe spacing is chosen to be infinite. In this case the pictures look like schlieren pictures.

Figure 14 shows such a differential interferogram of the established flow field

generated by ambient flow (see Tab. 1) and one jet from a conical nozzle located in position b) of model 2 (see Fig. 5). Figure 15 shows a similar picture with three conical nozzles located in positions a), b) and c). The time of exposure is 0.5 μ s.

The picture of Fig. 14 shows most of the well-known basic phenomena, as they are given in Fig. 1. We can identify the jet bow shock, the small separation bubble in front of the jet, and the accompanying oblique shock. Besides this, we can see the leading edge shock of the model, and an unburnt gunpowder grain, with its own bow shock wave. We cannot identify the jet boundary, despite the short exposure time, and the wake region also does not exhibit significant details. The image of the bow shock in front of the jet fades near the surface, probably as a consequence of the 3-dimensionality of the flow field, or of mixing from jet and separation bubble flow. Irregularities of the bow shock shape indicate, that there might be pulsations in the interaction flowfield.

At the first glance the picture of the interaction flowfield with 3 jets (Fig. 15) exhibits a large separation bubble in front of the jets, which extends almost up to the leading edge of the plate-wing. Since the difference in length of the optical path of the light beams is integrated along their path through the test chamber, the individual jet bow shocks cannot be identified, and their image is less sharp. The jet boundaries and the wake region also show no significant details.

Looking at the front separation bubbles enables us to evaluate the difference between the single-jet and the three-jet interaction. In both cases the inclination of the (central) separation streamline θ_{ss} is 14 degrees, in coincidence with other findings [2]. In contrast to this the inclination of the separation shock θ_{ss} differs: With the single-jet interaction $\theta_{ss} = 20$ deg., which is the value for a shock at a cone with a semivertex angle of 14 deg. and $Ma_\infty = 4.7$. For the three-jet interaction $\theta_{ss} = 23$ deg., which is the value for a shock at a wedge of 14 deg. This means, that for the three-jet interaction at least near the centreline locally two-dimensional separation conditions are effective.

3.3. Experiments on Interaction Force in the Shock Tunnel

All experiments described here are carried out with each pitch, yaw and bank angle = 0 deg., i. e. $x = X$, $y = Y$, and $z = Z$. Since the accelerometers are aligned with X and Z , all calculations are done in body-fixed coordinates. The cut-off frequency of the numerical low-pass filter [7] applied to the signals presented is 2 kHz or more unless otherwise stated.

3.3.1 Model Acceleration Due to Ambient Flow

Evaluation of $F_{z,i}$ must be carried out by distinct tests. At the beginning we measure the acceleration of the model due to

ambient flow alone, $a_{z,\infty}$. From these tests we obtain the relationship between $\hat{p}_{0,\infty}$ and $a_{z,\infty}$, i. e.

$$a_{z,\infty} = (\hat{p}_{0,\infty}/C_{p0}) (C_{zA_H})/m_H = f(\hat{p}_{0,\infty}) \quad (12)$$

Figure 16 shows histories of model accelerations $a_{z,\infty}$ and $a_{x,\infty}$, and $\hat{F}_{0,\infty}$, filtered numerically with 3 kHz. When the model is set free, we notice some disturbance of the $a_{z,\infty}$ and $a_{x,\infty}$ histories resulting from the opening process. During the subsequent period of 3 ms the model is "falling free" in the vacuum of the test chamber, and the parasitic accelerations attenuate. After this the test flow onset is clearly indicated by the rise of the Pitot pressure signal. For the following time of 1.5 ms Pitot pressure trace and acceleration signals show according histories. Irregular motions of the model indicate the end of free-flight, when the model reaches the stop.

Figure 17 shows the corresponding C_L and C_D histories of the side-jet model, evaluated according to equation (9). Notice, that after 0.4 milliseconds C_L attains its constant value, and that C_D needs 0.6 ms. The faster establishing of C_L compared with C_D is a general effect present in our experiments. A reasonable explanation is, that the drag is more affected by base flow phenomena, which need more time to establish. Nevertheless, by attaining fairly constant values the coefficient histories prove, that in this case, testing time is sufficient to establish quasistationary flow. The according test flow slug length consumed from time of test flow onset t_{fo} until time of established quasistationary flow t_{qs} is

$$l_{t_{qs}} = W_\infty (t_{qs} - t_{fo}) \quad (13)$$

With $W_\infty = 1700$ m/s we obtain $l_{t_{qs}} = 0.7$ m for C_L and $l_{t_{qs}} = 1.0$ m for C_D . Compared with the length of the model (without stem) of 0.14 m the test flow slug length needed to establish test flow itself as well as quasistationary conditions around the model is $5L_H$ for C_L and $7L_H$ for C_D .

3.3.2 Model Acceleration Due to Jet Thrust
The relationship between jet stagnation chamber pressure and model acceleration in still air, i. e.

$$a_{z,j} = f(p_{0,j}) \quad (14)$$

cannot be established generally, because reproducibility is inadequate, as is stated above. To overcome this restriction, we ignite the jet charges just before the test flow onset. For one to two milliseconds we measure $a_{z,j}$ in vacuum to obtain the actual relationship according to (14). Because the jets blow much longer than the test flow, $f(p_{0,j})$ is almost

constant for the time of experiment (see Fig. 18), and this factor can well be used also for the subsequent period of test flow with jets blowing.

3.3.3. Evaluation of Interaction Acceleration

Figure 19 shows the history of normal total acceleration $a_{z,t}$, together with those of $p_{0,j}$ and $\hat{p}_{0,\infty}$ from the same test, with 2 jets in positions a) and c), and with ambient flow. From $p_{0,j}$ we calculate $a_{z,j}$ as described above, and from $\hat{p}_{0,\infty}$ using (12), with known C_{p0} and C_z , we calculate $a_{z,\infty}$. These are shown in Fig. 20, together with $a_{z,t}$. From these we get the history of interaction acceleration

$$a_{z,i} = a_{z,t} - (a_{z,j} + a_{z,\infty}) \quad (15)$$

which is shown in Fig. 21, together with $a_{z,j}$ and $a_{z,\infty}$, for comparison. We notice, that in this case interaction of jet and ambient flow, after about 1 ms of starting time, creates an interaction force, which is of the order of the jet thrust. The history of the interaction coefficient

$$C_i = (F_{z,i} + F_{z,j})/F_{z,j} \\ = (a_{z,i} + a_{z,j})/a_{z,j} \quad (16)$$

is shown in Fig. 22. During the starting phase of the jet, before test flow onset, it is of course unity. When the interaction flowfield is established, its value is about 2.

Figure 23 gives C_i , dependent on the ratio $p_{0,j}/\hat{p}_{0,\infty}$, for experiments with one nozzle located in b), two nozzles in a) and c), and three nozzles in a), b) and c). The vertical error bars represent 2/3 of the oscillation amplitude of the signals, filtered by a low-pass filter with cut-off frequencies ranging from 500 to 1500 Hz, for the time of quasistationary conditions. The horizontal bars represent the change of $p_{0,j}/\hat{p}_{0,\infty}$ during this period. We notice, that the difference between the configurations with one and two jets is small. This indicates, in coincidence with theoretical considerations /18/, that the two jets act in the main individually. From Fig. 15 we know, that the high value of C_i of the experiment with three jets has at least partially to be attributed to the narrow spacing of the jets. The respective influence of pressure ratio and jet spacing will be clarified by additional tests.

The time necessary to establish the quasistationary jet interaction flowfield is about 1 ms from test flow onset (Figs. 21 and 22). This means, that in this case $l_{trs} = 1.7 \text{ m} = 12L_h$. The history of $a_{z,i}$ indicates a steady increase of $F_{z,i}$ in this case, where the jet is already blowing when the test flow arrives. The results support the thesis, that the time, or l_{trs} , needed

to establish quasistationary conditions in hypersonic flow increases according to the extent, to which a coefficient is affected by base-flow or wake-flow phenomena. It is not straightforwardly dependent on the grade of geometrical complexity of a design /19/.

As stated in the introduction, it is very important to keep in mind, that $F_{z,j}$ (being proportional to $Ma_{j,E}^*$) makes the denominator of equation (16). Hence high-performance thrusters, as we used them, tend to lessen the value of C_i . In the literature force measurements with circular supersonic nozzles are rare /6, 20/. Compared with these measurements, $F_{z,i}$ revealed by our experiments is stronger. The reasons for this are yet mentioned in the introduction, and just recalled for clarity:

- The force measurements /6, 20/ were carried out with slender bodies with circular cross-section. Moreover, the nozzle was placed either near the centre of gravity /6/ or at the nose /20/. For those configurations $F_{z,i}$ is known to be small /2/, because the bow shock propagates to the flanks and the opposite side of the body. There its interaction causes adverse effects, whereas the low-pressure wake region behind the jet is totally effective.

- Ma_∞ was less /6, 20/, i. e. transonic /20/ or ranging from subsonic to 4.5 /6/. It is widely known /2/, that interaction becomes more effective with increasing Ma_∞ , and that it is most adverse at transonic conditions.

4. CONCLUSION

With our millisecond aerodynamic force measuring technique we obtain quantitative data about the force, which is produced from interaction of side-jets and ambient flow, and acts on the surface of the model. We notice, that at hypervelocity conditions this interaction force can equal the thrust of supersonic nozzles. Investigations with different surface shapes and nozzle configurations are planned to elucidate and quantify the influence of these parameters.

In addition, we plan to measure the velocity of the deflected jets $W_{j,d}$, because this parameter represents the exchange of impulse between ambient flow and jets. Accordingly knowledge on this parameter can advantageously be used for the development of theoretical models, or for the validation of codes. Since the soot of the gun powder is well suited for laser Doppler velocimetry in the jet opening, it should also give good results in the interaction region. Moreover, only the jet flow is seeded. Hence we can be sure, that the measurement represents solely the jet flow portion of the interaction flow field.

Another parameter to investigate is $W_{j,E}$. According to the reasons mentioned in the

introduction, most of the experiments presented in the literature are performed with stored gas, where $T_{0,j} = T_{\infty}$ and $W_{j,E}$ is low. At ISL we are presently working on a technique to supply the side-jets with pure gases, without disturbing the free-flight of the model. The aim is to provide the scaling laws for the better use of those data.

ACKNOWLEDGEMENT

We gratefully acknowledge the support of Dipl.-Ing. U. Werner and Dipl.-Phys. H. Mach, Spectroscopy Group, ISL, for carrying out the temperature measurements at the nozzle exit.

REFERENCES

- 1 Naumann, K.W. and Smeets, G., "Aerodynamic Heating of KE- and Hypervelocity Projectile Structures", in "Proc. 12th Int. Symp. on Ballistics", San Antonio, TX, 1990. ISL CO 202/91, 1991.
- 2 Naumann, K. W. and Srujijes, J., "Die Flugbahnsteuerung mittels seitlich austretender Strahlen. Literaturübersicht (*Le pilotage des engins sur leur trajectoire au moyen de jets éjectés latéralement. Synthèse bibliographique*)", ISL R 117/85, 1985 (in german and french).
- 3 Schindler, L. H., "Waveriders", in: "Tactical Missile Aerodynamics", Hensch, M. J. and Nielsen, J. N. (Eds.), Progress in Astronautics and Aeronautics, Vol. 104, AIAA, 1986.
- 4 Naumann, K.W., "Steuerung mittels seitlich austretender Strahlen (*Pilotage par jet éjectés latérale-ment*)", ISL CO 255/88, 1988 (in german and french).
- 5 Fleck, V., "Fast Steering of the Angle of Attack: A Contribution to the Guidance of High Velocity Projectiles", ISL CO 220/89, 1989.
- 6 Regard, D., Leplat, H., Champigny, P., "Pilotage des missiles par jets transversaux", AAAF 28ème Colloque d'Aérodynamique Appliquée, ISL, Saint-Louis, France, 21.-23. Oct., 1991.
- 7 Naumann, K. W., Ende, H., Mathieu, G., "Technique for Aerodynamic Force Measurement in Shock Tunnel." J. Shock Waves 1, pp. 223-232, 1991.
- 8 Smeets, G., Naumann, K.W., "Erzeugung von Strömungen für aeroballistische Untersuchungen in den ISL Stoßrohren (*Production d'écoulements pour études aérobalistiques dans les tubes à choc de l'ISL*)", ISL R 113/86, 1986 (in german and french).
- 9 Bernstein, L., "Force Measurements in Short-Duration Hypersonic Facilities", AGARDograph 214, 1975.
- 10 Jessen, C., and Grönig, H., "A Six Component Balance for Short Duration Hypersonic Facilities", in: "New Trends in Instrumentation for Hypersonic Research", Boutier, A. (Ed.), NATO ASI Series E, Vol. 224, Kluwer, 1992.
- 11 Dayman, B. jr., "Free-Flight Testing in High-Speed Wind Tunnels", AGARDograph 113, 1966.
- 12 Vidal, R.J., "Model Instrumentation Techniques for Heat Transfer and Force Measurements in a Hypersonic Shock Tunnel", Cornell Aero. Lab. Rept. AD-917-A-1, 1956.
- 13 Wittliff, C.E., and Rudinger, G., "Summary of Instrumental Development and Aerodynamic Research in a Hypersonic Shock Tunnel", Cornell Aero. Lab. Rept. AD-917-A-2
- 14 Reddy, N. M., "Aerodynamic Force Measurements in the IISc Hypersonic Shock Tunnel", in: "Shock Tubes and Waves, Proc. 14th Int. Symp. on shock Tubes and Waves", Archer, R. D. and Milton, B. E. (Eds.) Sydney, 1984.
- 15 Smeets, G., "Velocity Interferometry", ISL CO 216/90, 1990.
- 16 Mach, H., Werner, U., "Ein neues modifizierte Emissions-/Absorptionsverfahren zur spektroskopischen Temperaturmessung heißer Gase, ISL R 115/92, 1992
- 17 Smeets, G., "Interferometry", ISL CO 214/90, 1990.
- 18 Naumann, K. W., "Vergleichende Untersuchung zu auftriebserzeugenden Hyperschall-Flugkörpern mit Seitenstrahl-Steuerung. Die Steuerung des Anstellwinkels mittels seitlich austretender Strahlen. *Etude comparative d'engins hypersoniques portants, pilotés par jets latéraux. Commande de l'angle d'incidence par éjection des jets latéraux*", ISL R 109/87, 1987 (in german and french).
- 19 Naumann, K. W., Ende, H., Mathieu, G., George, A.; "Millisecond aerodynamic force measurement with side-jet model in the ISL shock tunnel." AIAA 92-3963, 1992, AIAA-J., 1993 (in preparation).
- 20 Lee, E. E. jr., and Willis, C. M., "Interaction Effects of a Control Jet Exhausting Radially from the Nose of an Ogive-Cylinder Body at Transonic Speeds," NASA TN D-3752, 1967.

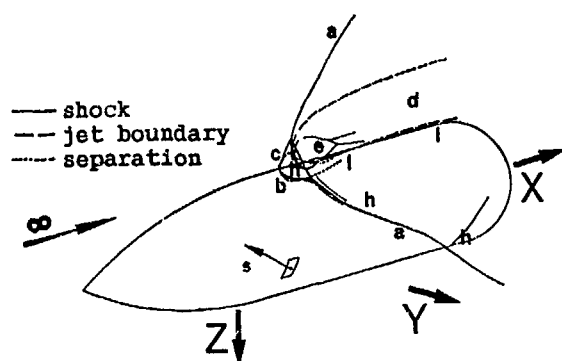


Fig. 1: Principle sketch of the interaction flowfield. a) bow shock, b) separation bubble, c) separation shock, d) jet wake, e) jet internal shocks, h) elevated surface pressure, l) lowered surface pressure

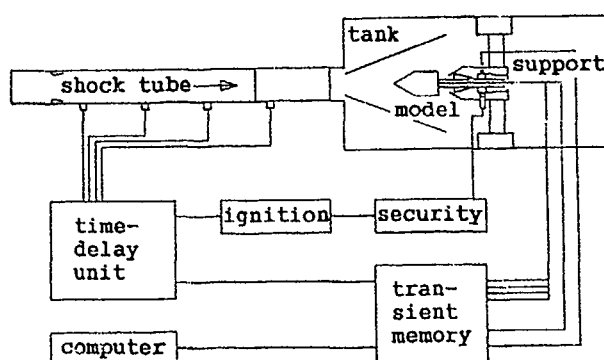


Fig. 2: Simplified sketch of ISL shock tunnel "B".

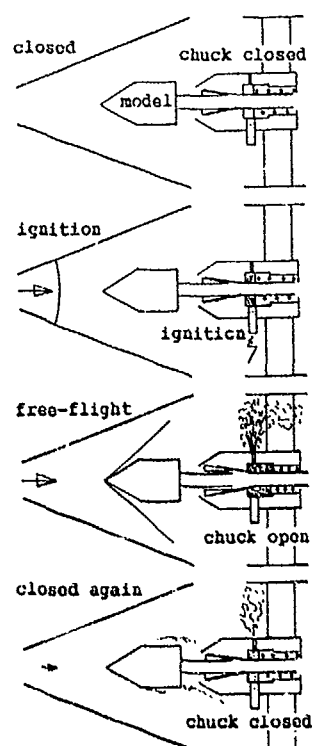


Fig. 3: Function cycle of the mounting support during an experiment.

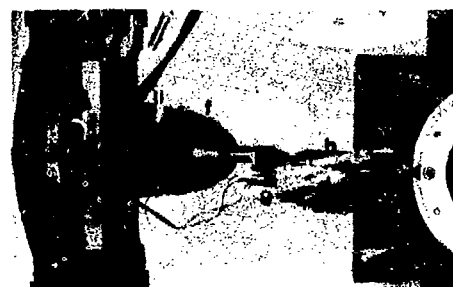


Fig. 4: Mounting support "2" with side-jet model "1". b) side-jet, d) model, f) mechanical support, g) pyrotechnical charge, h) test chamber, i) divergent.

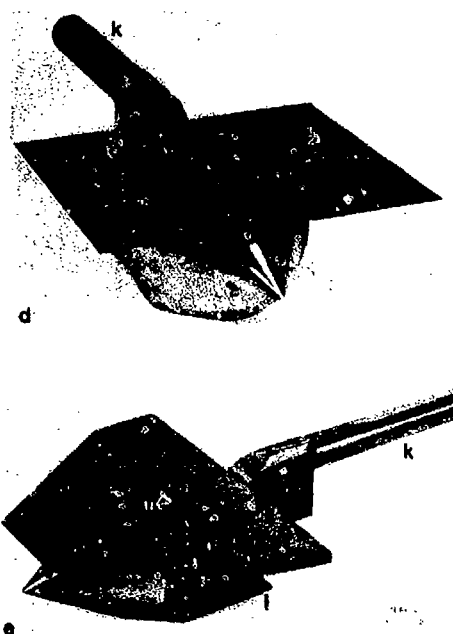


Fig. 5: Frontal view of side-jet models d) "1" (above) and e) "2" (below). a) b) c) jet positions, j) plate-wing, k) hollow stem, l) excavations for accelerometers.

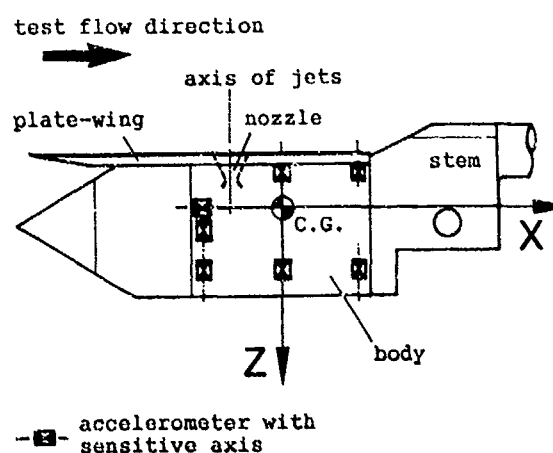


Fig. 6: Location of accelerometers and nozzles relative to C.G. (model "1").

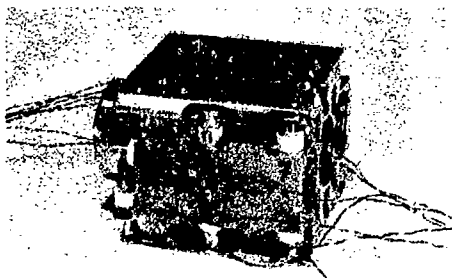


Fig. 7: Body of side-jet model "1". a) c) nozzles, m) accelerometer, n) damping disc.

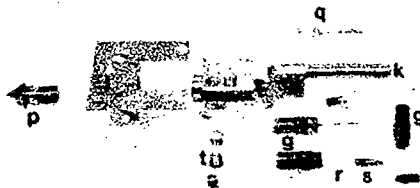


Fig. 8: Parts of side-jet model "1". g) gun powder receptacle, j) wing, k) stem, p) tightening screw of the wing, q) wrench for nozzles and plugs, r) fuse s) fuse-cartridge, t) plugs.

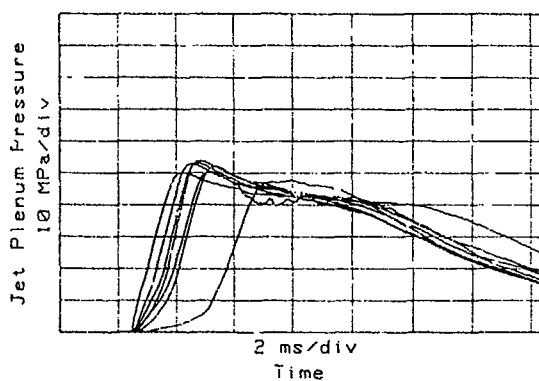


Fig. 9: Plenum pressure histories with one jet, for the same charges.

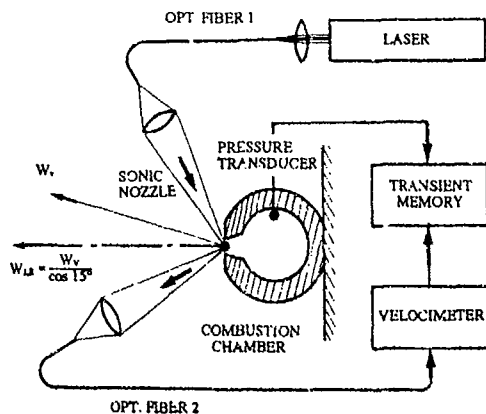


Fig. 10: Sketch of the experimental setup for the measurement of nozzle exit flow velocity.

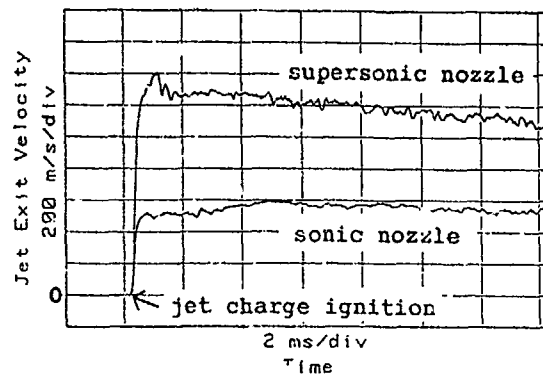


Fig. 11: Histories of nozzle exit velocity.

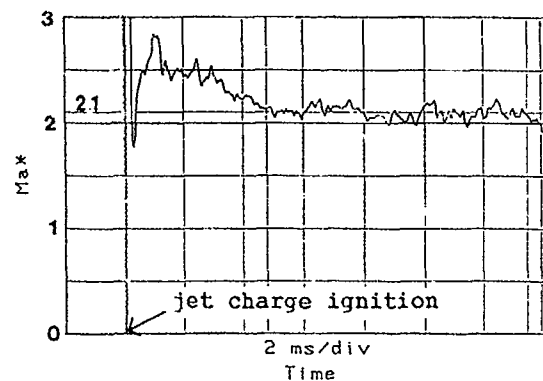


Fig. 12: History of averaged $Ma_{j,E}^*$.

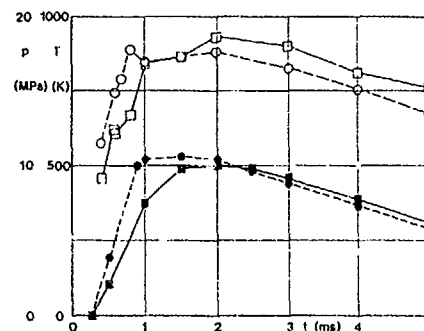


Fig. 13: Histories of $T_{j,E}^*$ (open symbols) and $p_{j,0}$ (solid symbols) of two shots.

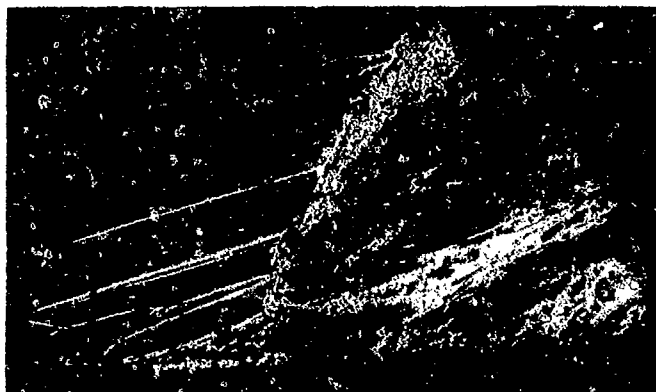


Fig. 14: DI-picture of established flow with 1 jet. a) bow shock, b) separation bubble, c) separation shock, d) jet wake, e) jet position, f) leading edge shock, g) powder grain.



Fig. 15: DI-picture of established flow with 3 jets. a) bow shock, b) separation bubble, c) separation shock, d) jet wake, e) jet position, f) leading edge shock, g) powder grain.

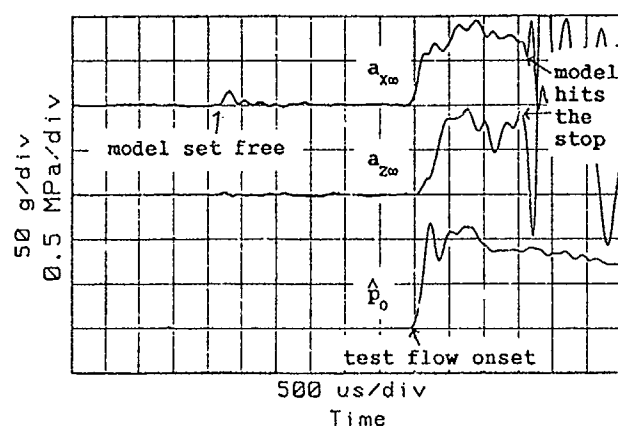


Fig. 16: $a_{x,\omega}$, $a_{z,\omega}$ and $\hat{p}_{0,\omega}$ from an experiment without jets.

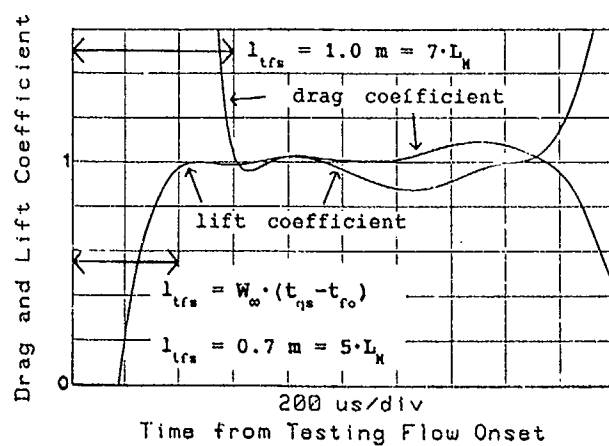


Fig. 17: C_D and C_L of the side-jet model, filtered with 800 Hz.

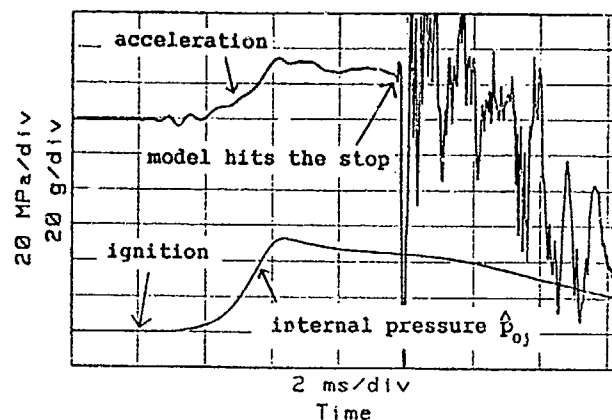


Fig. 18: $a_{z,j}$ in still air and $p_{j,0}$.

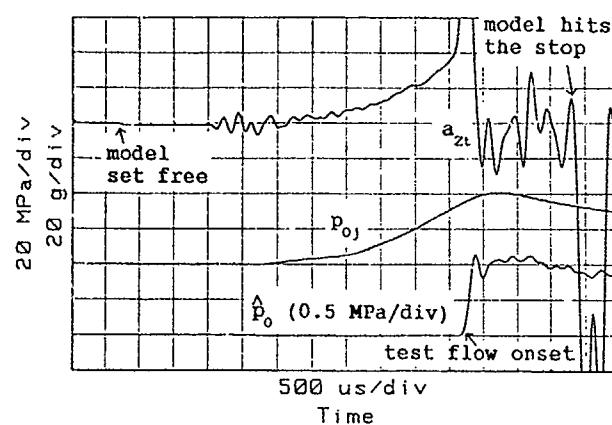


Fig. 19: $a_{z,t}$, $p_{j,0}$ and $\hat{p}_{0,\omega}$ from an experiment with 2 jets.

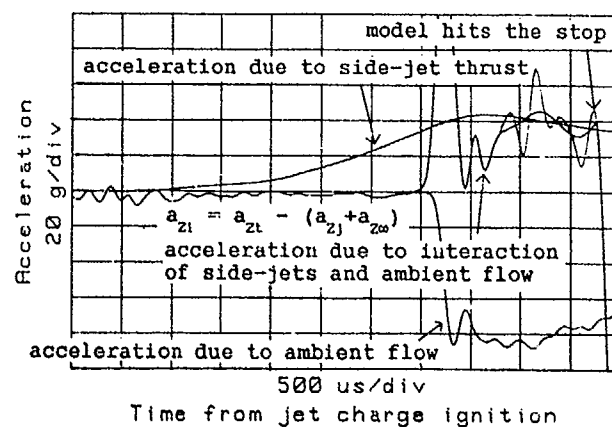


Fig. 20: Accelerations $a_{z,t}$, $a_{z,\omega}$ and $a_{z,j}$.

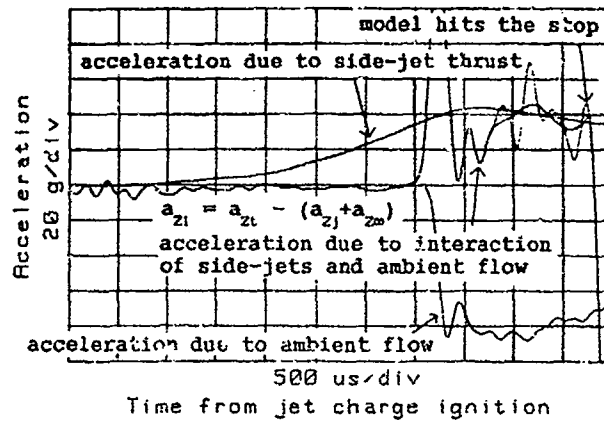


Fig. 21: Accelerations $a_{z,i}$, $a_{z,\infty}$ and $a_{z,j}$; bold line of $a_{z,i}$; cut-off frequency = 1.3 kHz.

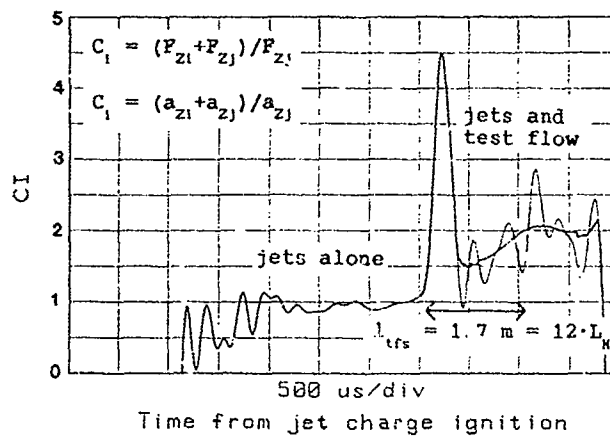


Fig. 22: History of C_1 for 2 jets; bold line: cut-off frequency = 1.3 kHz.

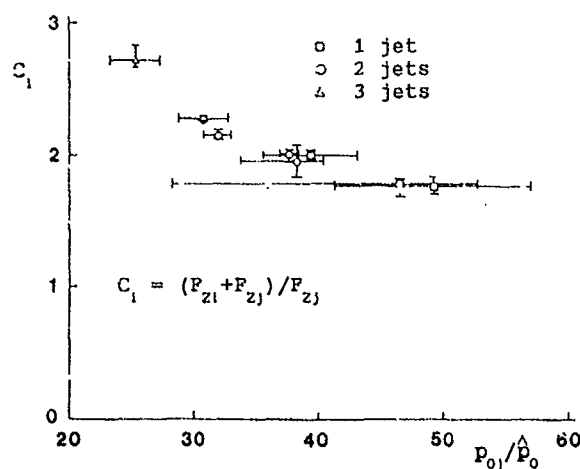


Fig. 23: C_1 dependent on $p_{j,0}/p_{0,\infty}$.

Test Flow Parameters

Quantity	Value	Unit
Velocity W_∞	1690	m/s
Density ρ_∞	0.48	kg/m ³
Pressure p_∞	44.5	kPa
Mach number Ma_∞	4.7	
Reynolds number Re_∞	$45 \cdot 10^6$	1/m
Temperature T_∞	310	K
Gas	N_2	

Tab. 1: Test flow parameters.

Data of Model "1"

Quantity	Value	Unit
Model mass	3160	g
Model span	140	mm
Model length without stem	140	mm
Maximum internal pressure	50	MPa
Nozzle centerline spacing	20	mm

Tab. 2: Data of model "1".

Jet Gas Parameters at $p_{j,0} = 10$ Mpa

Parameter	Value	Unit
Plenum density $\rho_{j,0}$	30	kg/m ³
Plenum temperature $T_{j,0}$	1080	K
Ratio of specific heats, γ	1.42	
Specific gas constant R	308	J/kgK
Molecular mass M	27	g/mole
Nozzle throat diameter D_j^*	4	mm
Nozzle exit diameter $D_{j,E}$	12.4	mm
Nozzle Mach number $Ma_{j,E}$	4.0	
Nozzle exit flow vel. $W_{j,E}$	1250	m/s
Nozzle exit flow pr. $p_{j,E}$	69	kPa
Nozzle exit flow dens. $\rho_{j,E}$	0.90	kg/m ³
Nozzle exit flow temp. $T_{j,E}$	250	K

Tab. 3: Jet gas parameters at $p_{j,0} = 10$ MPa.

A NUMERICAL INVESTIGATION OF A SUBSONIC JET IN A CROSSFLOW

Stephen H. Chiu

Space Systems/Loral, M/S G-81, 3825 Fabian Way, Palo Alto, CA 94303, USA

Karlin R. Roth and Richard J. Margason

Mail Stop 247-2, NASA Ames Research Center, Moffett Field, CA 94035-1000, USA

Jin Tso

Aero. Engineering Dept., Calif. Polytechnic State University, San Luis Obispo, CA 93407, USA

SUMMARY

The flowfield induced by a single, subsonic jet exhausting perpendicularly from a flat plate into a subsonic crossflow has been numerically investigated. The test case was chosen to match available experimental data where the jet Mach number was 0.78 and the freestream Mach number was 0.13. Time-averaged solutions were obtained using the thin-layer Navier-Stokes equations and two overlapping grids. The solutions were sensitive to the radial grid clustering near the edge of the jet and to the far-field boundary conditions. Experimental data comparisons were required to determine the most appropriate jet grid and satisfactory boundary conditions. Globally the solutions converged in about 6000 iterations. The computational results accurately showed the deflected jet and associated contrarotating vortices. The fine clustered grid in the region upstream of the jet exit allowed the horseshoe vortex in the boundary layer near the jet exit to be captured. Most importantly for aircraft applications, the computed plate pressure distributions compared favorably with the experimental data over most of the surface. However, in the wake region immediately downstream of the jet exit where there is extensive flow separation, some discrepancies with experimental data were observed. Two turbulence models were used in this study: (1) the zero-equation, two layer Baldwin-Lomax turbulence model; and (2) one-equation Baldwin-Barth turbulence model. The turbulence models gave results which generally compared no better with experimental data than the laminar computation results.

LIST OF SYMBOLS

a speed of sound
a,b,c constants used in empirical equation for the vortex curve (ref. 8)
a,b,c,d boundary condition designations, see table II for descriptions
B grid factor in Roberts algebraic grid generation model

C_p pressure coefficient based on freestream dynamic pressure
D jet diameter
e total energy per unit volume
E,F,G inviscid flux vectors of Navier-Stokes formulation
J Jacobian
L2 norm residual of the right hand side of finite difference formulation
M Mach number
p pressure
P,R,S viscous flux vectors of Navier-Stokes formulation
Pr Prandtl number
Q vector of conservative variables of Navier-Stokes formulation
R reciprocal of effective velocity ratio
R, θ ,Z cylindrical coordinates
 r_c center of radial clustering, $r/D = 0.5$
 \bar{r} radial coordinate index
Re Reynolds number, $\rho_\infty V_\infty D / \mu_\infty$
t time
u,v,w Cartesian velocity components
U,V,W contravariant velocity components
 V_e effective velocity ratio
x,y,z Cartesian coordinates non-dimensionalized by D
 Δr increment between adjacent radial coordinates
 γ ratio of specific heats
 κ coefficient of thermal conductivity
 μ coefficient of viscosity
 ξ, η, ζ generalized coordinates
 ρ density
 τ generalized time variable; grid stretching parameter
 ϕ angle between Z axis and the normal to the vortex curve
 ψ $\zeta_x^2 + \zeta_y^2 + \zeta_z^2$

subscripts:
i radial index, 1 for the smallest jet grid spacing which is located next to $r/D = 0.5$
max maximum
min minimum
x,y,z components in Cartesian directions
 ∞ freestream

1 INTRODUCTION

The jet in a crossflow (JICF) has been the subject of numerous experimental and computational investigations¹⁻²³. A common geometry for these investigations has been a single, subsonic jet exhausting perpendicularly from a flat plate into a subsonic crossflow (figure 1). The available experimental results²⁻¹⁴ for this simple geometry provide a relatively well defined qualitative and quantitative description of the JICF and its associated flowfield. As shown schematically on figure 1 there are three vortex systems which characterize this flow. The jet efflux is deflected by the freestream and rolls into a contrarotating vortex pair which dominates the flow. When the locus of maximum vorticity is projected to the symmetry plane the resultant line is called the vortex path. There is also a locus of maximum velocities in the symmetry plane which is called the jet centerline path. The upstream recirculation region generates a horseshoe vortex system which is analogous to the vortex at the wing-body juncture of an airplane. The vortical flow in the wake-region has been defined experimentally¹² to be similar to vortex shedding from solid bluff bodies. A recent investigation¹³ using a rectangular jet has shown that the upstream recirculation is unsteady and periodic. The frequency of this periodic motion appeared to be the same as that produced by the vortex shedding in the near wake. The Strouhal number based on the vortex shedding frequency varied uniquely with the velocity ratio.

Many numerical analyses¹⁵⁻²³ have attempted to predict the flow field induced by a jet exiting perpendicular to a crossflow from a flat plate. Good agreement has generally been achieved between computations and experiments for the jet trajectory, the contrarotating vortex pair, and the overall recirculation region downstream of the jet. However, due to the turbulent and separated flow on the flat plate and near the jet circumference, difficulties remain in predicting the surface pressure distribution and fine flow structures like the horseshoe vortex in the boundary layer of the plate. This has prompted the present investigation whose goal is to improve the existing computational results for the pressures induced on the flat plate.

The emphasis on accurate surface pressure prediction is motivated by the relationship of JICF to the lifting jets of Short Takeoff - Vertical Landing (STOVL) aircraft. The jets typically induce a reduction in lift and an increase in nose-up pitching moment during the transition between jet-borne and wing-borne flight. On the AV8A Harrier V/STOL²⁴ the lift losses range from a few percent of thrust in hover to as high as 30 percent of thrust at the velocity typically required for transition to or from conventional flight at altitudes away from the

ground. The corresponding induced nose-up pitching moments range from zero near hover to as high as a value equal to the thrust times the effective jet diameter near transition.

2 GOVERNING EQUATIONS

The flowfield induced by a JICF is characterized by large pressure variations, a pair of diffuse contrarotating vortices, a separated upstream region containing a horseshoe vortex, tornado-like vortices on the lee side of the jet and a three-dimensional, turbulent wake containing both separated and reversed flow. Thus, the three-dimensional Reynolds-averaged Navier-Stokes equations are required to adequately simulate this flowfield. These equations can be written in conservation, non-dimensional form.

In order to develop a numerical tool that may capture the pertinent flow features using a reasonable amount of computer resources, simplifications to the full three-dimensional Navier-Stokes equations must be made. First, since the Reynolds number of the flow is high, the thin-layer Navier-Stokes equations are used in the numerical simulation. Similar to the method used in boundary layer theory, the thin-layer approximation uses order of magnitude arguments to drop all viscous terms that contain derivatives that are parallel to the body surface. However, unlike boundary layer theory, the thin-layer approximation retains all three momentum equations and no limitation is put on the pressure field. Thus, the thin-layer equations permit the calculation of separated and reversed flows as well as flows with large normal pressure gradients. Further, they are valid in both inviscid and viscous flow regimes. Previous laminar, steady flow computational studies have captured the global features of the JICF using grid sizes less than 200,000 for the full domain. For computational efficiency, this simulation also assumes steady flow.

The three-dimensional Navier-Stokes equations with thin-layer viscous terms retained in all three coordinate directions are cast in generalized coordinates and written in conservation law form as follows:

$$\frac{\partial Q}{\partial \tau} + \frac{\partial E}{\partial \xi} + \frac{\partial F}{\partial \eta} + \frac{\partial G}{\partial \zeta} = \frac{1}{Re} \left(\frac{\partial S}{\partial \xi} + \frac{\partial R}{\partial \eta} + \frac{\partial P}{\partial \zeta} \right)$$

where Q is the vector of conservative variables, E , F and G are the inviscid flux vectors and the viscous flux vectors are S , R and P . The generalized coordinates ξ , η , ζ and τ are functions of the Cartesian coordinates x , y , z and time, t . The conservative variables and the flux vectors are given by

$$\begin{aligned}
 Q &= J^{-1} \begin{bmatrix} \rho \\ \rho u \\ \rho v \\ \rho w \\ e \end{bmatrix} & E &= J^{-1} \begin{bmatrix} \rho U \\ \rho u U + \xi_x p \\ \rho v U + \xi_y p \\ \rho w U + \xi_z p \\ (e+p)U - \xi_t p \end{bmatrix} \\
 F &= J^{-1} \begin{bmatrix} \rho V \\ \rho u V + \eta_x p \\ \rho v V + \eta_y p \\ \rho w V + \eta_z p \\ (e+p)V - \eta_t p \end{bmatrix} & G &= J^{-1} \begin{bmatrix} \rho W \\ \rho u W + \zeta_x p \\ \rho v W + \zeta_y p \\ \rho w W + \zeta_z p \\ (e+p)W - \zeta_t p \end{bmatrix} \\
 S &= J^{-1} \begin{bmatrix} 0.0 \\ \psi u_\zeta + \frac{1}{3}(\zeta_x u_\zeta + \zeta_y v_\zeta + \zeta_z w_\zeta) \zeta_x \\ \psi v_\zeta + \frac{1}{3}(\zeta_x u_\zeta + \zeta_y v_\zeta + \zeta_z w_\zeta) \zeta_y \\ \psi w_\zeta + \frac{1}{3}(\zeta_x u_\zeta + \zeta_y v_\zeta + \zeta_z w_\zeta) \zeta_z \\ \psi \left[0.5(u^2 + v^2 + w^2)_\zeta + \kappa \text{Pr}^{-1}(\gamma-1)^{-1}(a^2)_\zeta \right] \\ + \frac{1}{3}(\zeta_x u + \zeta_y v + \zeta_z w)(\zeta_x u_\zeta + \zeta_y v_\zeta + \zeta_z w_\zeta) \end{bmatrix}
 \end{aligned}$$

The viscous flux vectors in the η direction, R , and in the ξ direction, P , may be obtained by substituting η and ξ for ζ in the expression for S .

The conservative variables are based on density, ρ , the three cartesian velocity components, u , v and w , and the total energy per unit volume, e ; these variables are nondimensionalized by ρ_∞ , a_∞ and ρa_∞^2 respectively where a_∞ denotes the freestream speed of sound. The pressure, p , is defined as

$$p = (\gamma-1)[e - 0.5\rho(u^2 + v^2 + w^2)]$$

In these equations, U , V and W are the contravariant velocity components and J is the Jacobian of the coordinate transformation which is calculated using the metric terms, ξ_x , η_z , ζ_t , and so on. The viscosity is expressed by μ , the Prandtl number is expressed by Pr , the coefficient of thermal conductivity is given by κ and the ratio of specific heats is denoted by γ .

3 NUMERICAL METHOD

The present investigation used the multi-grid, overset-mesh flow solver designated OVERFLOW²⁵. Within this solver an implicit, three-factor, diagonalized, central difference scheme, also known as the diagonalized Beam-Warming scheme²⁶⁻²⁸ was selected to solve a thin-layer formulation of the three-dimensional, compressible Navier-Stokes equations. In the computations, thin-

layer terms were applied in all three coordinate directions. This solution scheme which is also contained in the ARC3D²⁹ code is first order accurate in time and second order accurate in space. Second and fourth order artificial dissipation terms are used. A spatially varying time step was employed to accelerate convergence to a steady state solution. For most of the solutions, the time step was started at 0.01 for 50 iterations, increased to 0.1 for the next 1950 iterations, increased to 0.5 up to 4000 total iterations, then increased to 1.0 for more than 4000 iterations.

OVERFLOW uses the Chimera grid embedding technique^{30,31}. Since the JICF has bilateral symmetry for steady flow, the present investigation used two overlapping grids (fig. 2) on a symmetrical half plane. A Cartesian grid with 79x33x66 points in the X , Y and Z directions respectively was used for the surrounding freestream and boundary layer flow on the flat plate. Then a cylindrical grid with 51x33x66 points in the R , Θ , and Z directions respectively (for grids 2, 3, and 4) was embedded for the jet plume. This grid increased in diameter along the Z direction and deflected along the jet vortex curve which was given by Fearn and Weston's⁸ empirical description

$$z = aR^b c$$

The empirical parameters are $a = 0.3515$, $b = 1.122$, and $c = 0.4293$

Both the rectangular plate grid and the cylindrical grid were designed for turbulent flow and were clustered in the expected high shear regions near the plate and near the edge of the jet plume. Approximately 30 grid points were clustered vertically within the plate boundary layer. Adjacent to the plate, the finest z spacing is 6×10^{-5} . Preliminary computations of laminar and turbulent flow over the flat plate (jet off) were made using this grid distribution. The turbulent results obtained using either the Baldwin-Lomax model³³ or the Baldwin-Barth model³⁴ were in close agreement with experimental data³⁵.

Four jet plume grids were generated algebraically with care taken to ensure near-orthogonality everywhere. Grid points were clustered at the shear region between the jet and external flow using an algebraic model developed by Roberts³²

$$r_i = r_c \left\{ 1 + \frac{\sinh[\tau_i(\bar{r}_i - B)]}{\sinh(\tau_i B)} \right\}$$

where

$$B = \frac{1}{2\tau_i} \ln \left[\frac{1 + (e^{\tau_i} - 1)(r_c/D)}{1 + (e^{-\tau_i} - 1)(r_c/D)} \right]$$

The grid spacing at the edge of the jet exit r_c is the finest increment in the jet grid. It is controlled by the stretching parameter τ_1 which varies from zero (no stretching) to large values which produce the most refinement near $r = r_c$. As a measure of grid refinement, the increment between the jet edge and the adjacent radial location is designated Δr_1 . This feature seems to describe the key difference among these grids. Both Δr_1 and the associated stretching factor τ_1 are listed in Table I. The coarsest increment is used in grid 1 ($\Delta r_1/D = 0.006$). Grids 3 and 4 used an increment which is one-tenth as large ($\Delta r_1/D = 0.0006$) and grid 2 used an increment which is less than one-fiftieth as large ($\Delta r_1/D = 0.00011$). Grids 1, 2, and 3 were used to evaluate the effect of grid point clustering near the edge of the jet where there is a step change in velocity at the jet exit. Grid 4 was added to reduce the radial grid increment near the jet centerline. Quadrants of grid 1 and grid 4 are presented in figure 3 for the $z_{\min}=0$ plane. The coarsest stretching was used in grid 1. Grid 2 had the finest grid spacing. Figure 3 shows the difference in grid density near the edge of the jet.

User specified mesh connection data, the rectangular grid and the jet grid, were input to the PEGSUS³⁰⁻³¹ code to construct the overset mesh. Communication between the grids occurs at outer boundaries and at hole boundaries. The outer boundaries of the jet grid were used to make a hole in the rectangular grid with the solution interpolated from the jet grid to the rectangular grid at the hole boundary. The flow equations are solved alternately in each grid.

Laminar and turbulent computations were made for the freestream flow region, external to the jet plume. For turbulent calculations, either the algebraic Baldwin-Lomax model³³ or the one-equation Baldwin-Barth model³⁴ was used within the rectangular grid. Only laminar flow solutions were obtained within the jet grid. Here μ is obtained using Sutherland's equation.

The choice of boundary conditions, which will be denoted as bc, was explored to establish those most suitable for the present investigation. For the jet plume grid, all calculations used the following bc:

- (i) the jet exit velocity profile was specified using the measurements of ref. 8;
- (ii) the flat plate surface was modeled as a viscous adiabatic wall;
- (iii) lateral symmetry was applied across the $y=0$ plane;
- (iv) Chimera interpolation from the rectangular grid was used elsewhere.

For the rectangular grid, all of the computations used a viscous adiabatic wall for the flat plate surface and assumed lateral symmetry across the $y=0$ plane. Four

different sets of bc were tested for the other four surfaces of the rectangular grid. These surfaces are the inflow (upstream) boundary ($x_{\min} = -8$), the outflow (downstream) boundary ($x_{\max} = 24$), the outer lateral boundary ($y_{\max} = 10$), and the top boundary ($z_{\max} = 20$). These bc are described in Table II using the designations (a, b, c, or d) which identify the bc sets on the data figures. The prescribed flow variables bc consisted of a uniform momentum term, u , equal to freestream at all grid points except at the flat plate surface where the velocity was set to zero. The prescribed flow variables bc at the top boundary used freestream velocity over the entire surface. The subsonic inflow/outflow bc were implemented as follows: zeroth order extrapolation of pressure was used upstream while ρ , u , v , and w were held constant; and downstream, the pressure was constant and ρ , u , v , and w were extrapolated. The Riemann invariant bc were applied as locally one-dimensional in terms of the normal velocity at the rectangular grid outer boundaries as described in reference 28.

4. NUMERICAL PARAMETER VARIATIONS

For this paper, only results obtained for a jet to freestream velocity ratio, R , of 6 are presented. They illustrate the effects of number of iterations, jet grid radial point distribution, boundary conditions, and turbulence model.

4.1. Convergence

The convergence of the results is shown by the residual history of the calculations (fig. 4). The L_2 norm starts at approximately 5×10^{-8} and decreases to about 2×10^{-9} after 6000 iterations. It then tends to vary about that level for up to 20,000 iterations. Thus, globally the solution appears to be converged by about 6000 iterations. Comparisons³⁶ of the predicted surface pressures with experimental data⁷ at selected azimuths confirmed this conclusion.

4.2. Grid Effects

4.2.1 Jet path: The jet centerline path (locus of maximum jet velocity) is presented in figure 5. The computations were done with laminar flow in the jet grid. For the present grids and turbulence models in the rectangular grid, the results indicate no significant differences among the various solutions. In all cases the computed jet centerline path did not penetrate the freestream as far as the experimental data for downstream distances greater than 5 diameters. This reinforces the conclusion that adequate simulation of the jet deflection is relatively insensitive to the details of the numerical model.

4.2.2 Plate pressures: In computing the JICF, the most sensitive area is the flat plate adjacent to the jet exit. At the plate, turbulence modeling influences the computed results for $r/D > 0.67$. While for $r/D < 0.67$, the computed flow is laminar. Three azimuthal rays were selected to compare the calculated results with experimental results⁷. The geometric orientation is shown in figure 6 for the 0°, 90°, and 180° azimuths. In figures 7 through 9, the results for pressure coefficient distribution as a function of r/D are presented for the 0° azimuth, the 90° azimuth, and 180° azimuth.

The effects of the radial coordinate distribution for the jet grids were evaluated for each of the jet grids described in the Numerical Methods section. The effect of jet grid on the pressure coefficient distributions are presented for the 0° azimuth (fig. 7(a)), 90° azimuth (fig. 7(b)), and 180° azimuth (fig. 7(c)). These solutions were obtained using the Baldwin-Lomax turbulence model and 11,150 iterations. At 0° azimuth the grid 1 results do not provide agreement with the experimental data, while much better results are obtained with the other three grids. The rectangular grid and the jet grid are overset between $r/D = 0.67$ and 1.00. The C_p solutions show a discontinuity near $r/D = 1.0$ only at the 0° azimuth. The reason for this discontinuity is unknown. At 90° azimuth, the grid 1 solution is poorest; while grids 3 and 4 are better and grid 2 is best. This result is expected because grid 2 has the finest grid spacing at the edge of the jet (see table I). At 180° azimuth all of the grids agree with the experimental data only between r/D of 2 or 3 and 4. This poor correlation is not unexpected because of the massive flow separation along this ray.

These solutions suggest a dense grid is needed near the edge of the jet and that a minimum increment of 0.0001 diameter can provide reasonable agreement with experimental data. However there are additional factors which affect the correlation, and the present investigation does not completely identify them. It should be emphasized that appropriate experimental data were crucial in the assessment of which numerical solutions provided the most satisfactory representation of the flow physics.

4.3 Boundary Conditions

As described in the Numerical Method section, the boundary conditions used in this study are summarized in Table II. In all of these solutions, grid 4 and the Baldwin-Lomax turbulence model were used. The pressure distribution results at 10,000 iterations are presented for 0° azimuth (fig. 8(a)), 90° azimuth (fig. 8(b)), and 180° azimuth (fig. 8(c)). At 0° and 90° azimuths, bc (a) and (b) solutions provide good correlations with experimental data. The bc (c) and (d) both used inflow/outflow on the z_{\max} surface and bc (d) also used inflow/outflow on the x_{\min} surface. Both of these bc give unsatisfactory results when compared with

experimental data. At 180° azimuth, all of the solutions provide a only fair correlation with the experimental data for radii greater than 2 diameters. The solutions obtained from OVERFLOW provided better correlations with experimental C_p data when prescribed variable bc (a) and Riemann bc (b) were used. The bc which used the inflow/outflow boundary conditions (c) and (d) provided unsatisfactory solutions.

4.4 Turbulence Models

The effect of turbulence modeling on the solutions was evaluated using grid 4, bc (a), and 10,000 iterations. At the beginning, it was thought that this portion of the calculations would be the focus of the present investigation. However turbulence models did not appear to be a major factor in obtaining the best correlation with experimental data. As a reference calculation, the laminar solution is compared with solutions which used the Baldwin-Lomax turbulence model³³ and the Baldwin-Barth turbulence model³⁴ in figure 15. At 0° azimuth (fig. 9(a)), all of the solutions provide good agreement with the experimental data. At 90° azimuth (fig. 9(b)), the Baldwin-Lomax turbulence model solution produced the best correlation with experimental data. At 180° azimuth (fig. 9(c)), none of the solutions agreed with the experimental data. These results show that the turbulence models in the rectangular grid region don't seem to improve the fidelity of the solutions. There are other factors (grids and bc) which need to be resolved before a totally adequate solution for V/STOL or STOVL aircraft application is obtained.

5 OVERALL FLOWFIELD RESULTS

The present numerical investigation has produced a large quantity of results and has demonstrated the importance of both jet grid spacing and boundary conditions. The emphasis in the previous sections was to show the factors which affect the satisfactory solution for pressure distribution on the flat plate. In the present section, results will be presented to show that the major portion of the flowfield solution is in substantial qualitative agreement with experimental results. Where experimental data are available, it is also possible to demonstrate quantitative agreement.

The flowfield particle traces (fig. 10) show the entrainment of freestream flow into the plume and the roll-up process forming the vortex pair. The freestream flow is from left to right on the figure. The jet (dark blue particles) flows from the exit in the flat plate perpendicular to the freestream. The red particle traces describe the flow near the flat plate. The dark blue particles which are emitted from the downstream half of the jet tend to roll-up into the vortex pair. The light blue particles originate along a vertical line located several diameters upstream of the jet in the symmetry

plane. Some of these particles are entrained into the jet near the jet centerline path and a few particles are subsequently entrained into the vortex pair. The remainder of the light blue particles flow around the jet to the saddle. Then the light blue particles flow to either the recirculation region downstream of the jet and into the jet centerline path or into the vortex pair.

5.1 Vortex Pair

As shown schematically in figure 1, a vortex pair is the dominant feature of the jet plume. The computed vorticity fields for two right half-plane cross sections are presented in figure 11 at the locations and angles indicated in the figure titles. The cross sections are taken at large angles ϕ to the freestream which are nearly perpendicular to the vortex path. The result of the shearing motion between the jet and the crossflow is shown by the roll-up of the flow into concentrated vorticity contours (fig. 11(a)). Initially there is a thin shear layer formed on the windward side of the jet. Further downstream (fig. 11(b)) the shear layer diffuses into a kidney-shaped vortex pair which is clearly shown by the vorticity contours. In figure 12, the velocity vectors show reversed flow in the wake downstream of the jet. This fluid is then entrained into the jet plume. The jet flow entrainment in the symmetry plane from the wake downstream of the jet is shown by the strong upwash velocities near the edge of the jet in the symmetry plane between the vortices.

5.2 Horseshoe Vortex

Ahead of the jet, the approaching flow is deflected downward near the flat plate and becomes reverse flow very close to the flat plate surface. The horseshoe vortex forms in this upstream separation region, wraps around the jet, and flows downstream. The horseshoe vortex is shown for the symmetry plane in figure 13 using particle traces near the flat plate. The horseshoe vortex has been resolved. Probably, this is a consequence of the dense shear layer grids used in the present calculation. Demuren³⁷ has also identified this feature in a numerical calculation.

5.3 Surface Pressure Distribution

The pressure distribution on the flat plate has been difficult to resolve computationally. The present solutions which used turbulence models did not give significantly better results than the laminar solution. The Baldwin-Lomax model results are shown in figure 14 by color contours. Superimposed onto the contours are several azimuthal rows of small circles whose location and colors correspond to pressure tap locations and pressure coefficients for experimental data⁷. The agreement between the computation and experiment are very good everywhere except for a small region immediately downstream of the jet exit. Since the

Baldwin-Lomax model has not been demonstrated to be effective in massively separated flow this is an expected deficiency.

A final comparison is presented in figure 15 which shows the computational surface particle trace for $R = 6$ (fig. 15(a)) and an experimental oil flow photograph¹¹ obtained at $R = 5.5$ (fig. 15(b)). The overall pattern of these two results is similar. The particles/oil flows around the jet and into the lee region where there is a saddle located on the centerline downstream of the jet. There is also an oil/particle accumulation line formed which extends downstream. In figure 15(a), the particle traces define a region that appears to be the origin a vortex which is not shown in the experimental oil flow (fig. 15(b)). This vortex appears to be freestream flow from the wake vortex entrained into the jet. In real flow it is an unsteady feature which continuously moves.

6 CONCLUDING REMARKS

The present numerical investigation has produced a large quantity of results and has demonstrated the importance of both jet grid spacing and boundary conditions (bc). The grid variation solutions suggest a dense grid is needed near the edge of the jet and that a minimum radial increment of 0.0001 diameter at the jet circumference can provide reasonable agreement with experimental data. Results showed that the major portion of the flowfield solution is in substantial qualitative agreement with experimental results. Where experimental data were available, it was also possible to demonstrate quantitative agreement for selected grids, bc, and turbulence models. The horseshoe vortex upstream of the jet exit has been resolved. This is a consequence of the dense shear layer grids used in the present calculation. The vortex pair in the deflected jet is also resolved. There is a thin vorticity layer formed on the windward side of the jet; further downstream it diffuses into a kidney-shaped vortex pair.

The emphasis in the present paper was to show the factors which affect the satisfactory computation of the pressure distribution on the flat plate. This was evaluated using numerical parameter variations in a systematic series of calculations. The solutions obtained from OVERFLOW provided the best correlation with all of the experimental C_p data when either of two bc were used: (a) freestream variables were specified for the upstream and top boundaries and an extrapolation outflow bc was used at the lateral and downstream boundaries; or (b) characteristic conditions based on Riemann invariants. At the beginning of this investigation, it was thought that the effect of turbulence models would be the focus. However they did not appear to be a major factor in obtaining the best correlation with experimental data.

The pressure distribution on the flat plate has been a difficult region to resolve computationally. The present solutions which used turbulence models did not give significantly better results than the laminar solution. The agreement between the computation and experiment is very good everywhere except for a small region immediately downstream of the jet exit. These results show that while the turbulence models improve the fidelity of the solutions, there are other factors (such as boundary conditions and jet grid radial distribution) which need to be resolved before an adequate solution for V/STOL or STOL aircraft application is obtained. It should be emphasized that appropriate experimental data were crucial in the assessment of which numerical solutions provided the most satisfactory representation of the flow physics.

REFERENCES

1. Anon., "Analysis of a Jet in a Subsonic Crosswind," NASA SP-218, Sept. 1969.
2. Ruggeri, R. S., Callaghan, E. E. and Bowden, D. T., "Penetration of Air Jets Issuing from Circular, Square and Elliptical Orifices Directly Perpendicularly to an Air Stream," NACA TN 2019, Feb. 1950.
3. Jordinson, R., "Flow in a Jet Directed Normal to the Wind," R. & M. No. 3074, British A.R.C., Oct. 1958.
4. Keffer, J. F. and Baines, W. D., "The Round Turbulent Jet in a Cross Wind," *J. Fluid Mech.*, Vol. 15, part 4, 1963, pp. 481-496.
5. Ivanov, Yuri V., "Effective Combustion of Overfire Fuel Gases in Furnaces," The Estonian State Publishing House, Tallin, Estonia, 1959 (available in English as NASA CN-127612).
6. Bradbury, L. J. S. and Wood, M. N., "The Static Pressure Distribution Around a Circular Jet Exhausting Normally From a Plane Wall Into an Air-stream," C.P. No. 822, British A.R.C., 1965 (also available as RAE TN No. Aero. 2978, Aug. 1964).
7. Fearn, R. L. and Weston, R. P., "Induced Pressure Distribution of a Jet in a Crossflow," NASA TN D-7915, July 1975.
8. Fearn, R. L. and Weston, R. P., "Velocity Field of a Round Jet in a Cross Flow for Various Jet Injection Angles and Velocity Ratios," NASA TP-1506, Oct. 1979.
9. Thompson, A. M., "The Flow Induced by Jets Exhausting Normally From a Plane Wall Into an Air-stream," Ph. D. Thesis, Univ. of London, Sept. 1971.
10. Kamotani, Y. and Greber, I., "Experiments on a Turbulent Jet in a Cross Flow," *AIAA J.*, Vol. 10, No. 11, Nov. 1972, pp. 1425-1429.
11. Soullier, A., "Testing at S1.MA for Basic Investigations on Jet Interactions; Distributions of Pressures and Velocities in the Jet Using the Ideal Standard Nozzle (in Unheated State)," ONERA Document No. 1/253 GY-5 parts, May 1968 (available in English as NASA TT F -14072, Jan. 1972).
12. McMahon, H. M., Hester, D. D., and Palfery, J. G., "Vortex Shedding From a Turbulent Jet in a Cross-Wind," *J. Fluid Mech.*, Vol. 48, part 1, Jan. 1971, pp. 73-80.
13. Krothapalli, A., Lourenco, L., and Buchlin, J., "On the Separated Flow Upstream of a Jet in a Cross Flow," AIAA Paper No. 89-0571, Jan. 1989.
14. Werlé, H., "Flows with Large Velocity Fluctuations," ONERA film no. 575, 1966.
15. Wooler, P. T., "Development of Analytical Model for the Flow of a Jet into a Subsonic Crosswind," Symposium on Analysis of a Jet in a Subsonic Crosswind, NASA SP-218, Sept. 1969, p.101-118.
16. Adler, D. and Baron, A., "Prediction of a Three-Dimensional Circular Turbulent Jet in Crossflow," *AIAA J.*, Vol.17, No. 2, Feb. 1979, pp.168-174.
17. Baker, A. J., Orzechowski, J. A. and Manhardt, P. D., "A Numerical Three-Dimensional Turbulent Simulation of a Subsonic V/STOL Jet in Cross-Flow Using a Finite Element Algorithm," NADC Report 79021-60, Sept. 1981.
18. Chien, C. J. and Schetz, J. A., "Numerical Solution of the Three-Dimensional Navier-Stokes Equations with Application to Channel Flows and a Bouyant Jet in a Cross-Flow," *Trans. ASME: J. Appl. Mech.*, Vol. 42, Sept. 1975, pp. 575-579.
19. Claus, R. W., "Numerical Calculation of Subsonic Jets in Crossflow with Reduced Numerical Diffusion," AIAA Paper No. 85-1441, July 1985.
20. Sykes, R. I., Lewellen, W.S. and Parker, S. F., "On the Vorticity Dynamics of a Turbulent Jet in a Crossflow," *J. Fluid Mech.*, Vol. 168, May 1986, pp. 393-412.
21. VanOverbeke, T. J. and Holdeman, J. D., "A Numerical Study of the Hot Gas Environment Around a STOL Aircraft in Ground Proximity," AIAA Paper No. 88-2882, July 1988.
22. Rotli, K. R., "Application of a Three-Dimensional Navier-Stokes Model for a Subsonic Jet in a Crossflow," Doctoral dissertation, Univ. of Florida, Dec. 1988.

23. Kavsoglu, M.S., Akmandor, I. S., Ciray, S. and Fujii, K., "Navier-Stokes Simulation of Two and Three Dimensional Jets in Crossflow," AIAA Paper No. 91-1743, June 1991.
24. Margason, R. J., Vogler, R. D., and Winston, M. M., "Wind Tunnel Investigation at Low Speeds of the Kestrel (XV-6A) Vectored-Thrust V/STOL Airplane," NASA TN D-6826, July 1972.
25. Renze, K. J., Buning, P. G., and Rajagopalan R. G., "A Comparative Study of Turbulence Models for Overset Grids," AIAA Paper No. 92-0437, Jan. 1992.
26. Pulliam, T. H. and Chaussee, D. S., "A Diagonal Form of an Implicit Approximate Factorization Algorithm," *J. Comp. Physics*, Vol. 39, No. 2, Feb. 1981, pp. 347-363.
27. Beam, R. M. and Warming, R. F., "An Implicit Factored Scheme for the Compressible Navier-Stokes Equations," *AIAA J.*, Vol. 16, No. 4, Apr. 1978, pp. 393-402.
28. Pulliam, T. H. and Steger, J. L., "Recent Improvements in Efficiency, Accuracy, and Convergence for Implicit Approximate Factorization Algorithms," AIAA Paper No. 85-0360, Jan. 1985.
29. Pulliam, T. H. and Steger, J. L., "Implicit Finite-Difference Simulations of Three-Dimensional Compressible Flow," *AIAA J.*, Vol. 18, no. 2, Feb. 1980, pp. 159-167.
30. Benek, J. A.; Buning, P. G.; and Steger, J. L., "A 3-D Chimera Grid Embedding Technique," AIAA Paper No. 85-1523, July 1985.
31. Tramel, R. W. and Suhs, N. E., "PEGSUS 4.0 User's Manual," AEDC TR-91-8, June 1991.
32. Roberts, G. O., "Computational Meshes for Boundary Layer Problems," Proceedings of the Second International Conference on Numerical Methods in Fluid Dynamics, Vol. 8, pp. 171-177, Aug. 1971.
33. Baldwin, B. S. and Lomax, H., "Thin Layer Approximation and Algebraic Model for Separated Turbulent Flows," AIAA Paper No.78-257, Jan. 1978.
34. Baldwin, B. S. and Barth, T. J., "A One Equation Turbulence Transport Model for High Reynolds Number Wall-Bounded Flows," NASA TM 102847, Aug. 1990.
35. White, F. M., "Viscous Fluid Flow," McGraw-Hill Publishing Co., 1974.
36. Chiu, S., Roth, K. R., Margason, R. J., and Tso, J., "A Numerical Investigation of a Subsonic Jet in a Crossflow," AIAA Paper No. 93-0870, Jan. 1993.
37. Demuren, A. O., "Characteristics of 3D Turbulent Jets in Crossflow," NASA TM 104337, Apr. 1991.

Table I. Jet grid radial spacing parameters.

GRID	$\Delta r_1/D$	τ_1
1	0.00600	12
2	0.00011	16
3	0.00060	14
4	0.00060	14*

* Note: One radial point is added to Grid 3 at $r/D = 0.11818$ to obtain Grid 4.

Table II. Summary of rectangular grid boundary conditions used on four outside grid surfaces.

boundary condition (bc)	inflow $x_{\min}=-8$	top $z_{\max}=20$	outer $y_{\max}=10$	outflow $x_{\max}=24$
a	prescribed	prescribed	extrapolated	extrapolated
b	characteristic	characteristic	characteristic	characteristic
c	inflow/outflow	inflow/outflow	inflow/outflow	inflow/outflow
d	prescribed	inflow/outflow	inflow/outflow	inflow/outflow

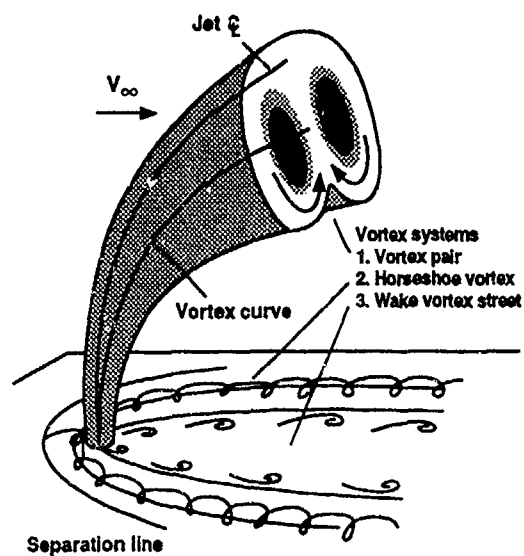


Fig. 1. Sketch of the three vortex systems associated with the jet in crossflow: (1) rolled up jet vortex pair; (2) horseshoe vortex; (3) weak wake vortex street.

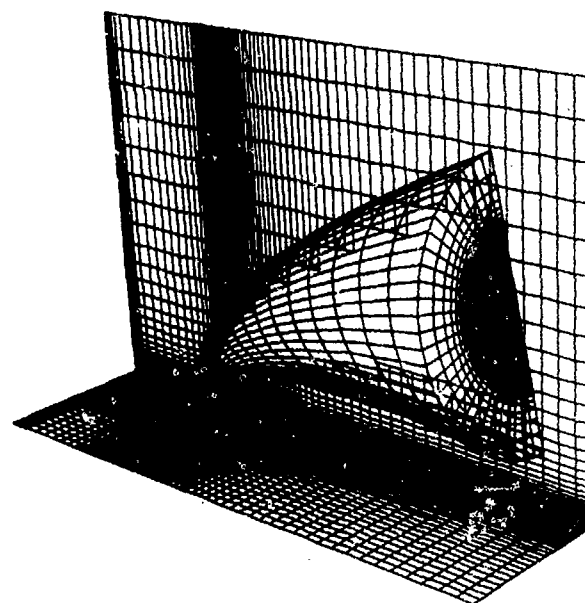
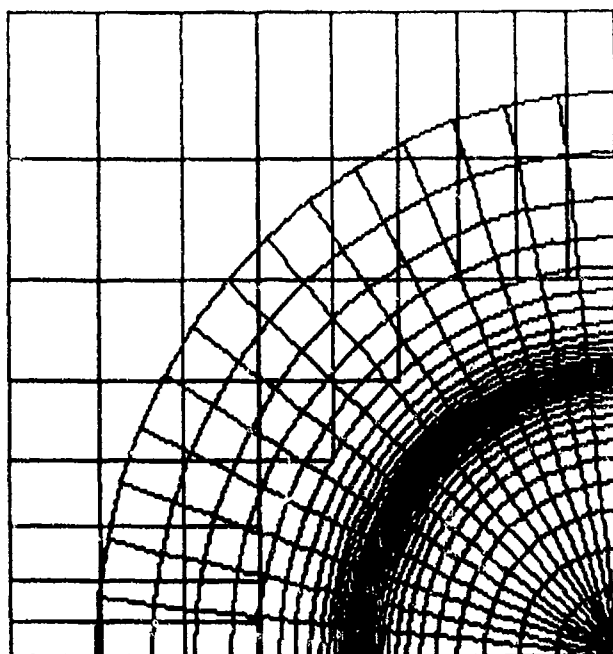
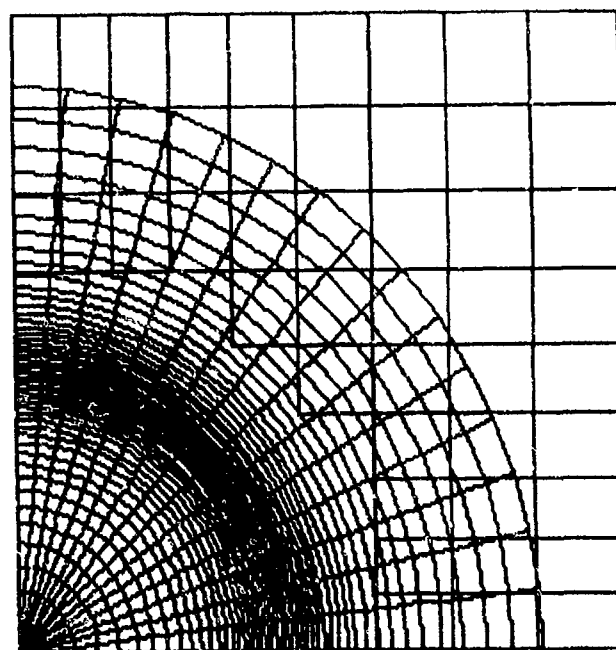


Fig. 2. Chimera grid structure showing cylindrical jet grid and rectangular freestream grid.



(a) Jet grid 1 ($\Delta r_1/D = 0.006$ and $\tau_1 = 12$).



(b) Jet grid 4 ($\Delta r_1/D = 0.0006$ and $\tau_1 = 14$).

Fig. 3. Cylindrical jet grids showing overset with rectangular (Cartesian) grid at $z=0$.

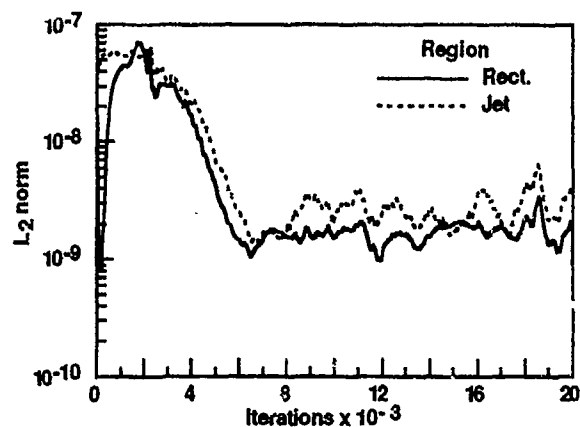


Fig. 4. Convergence history for steady state calculation for velocity ratio 6 with laminar flow using grid 2 and OVERFLOW code.

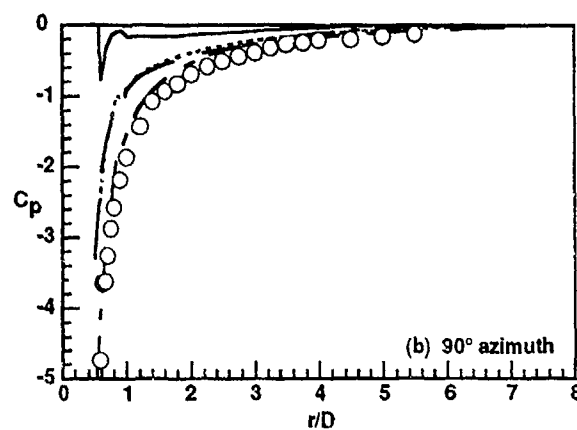
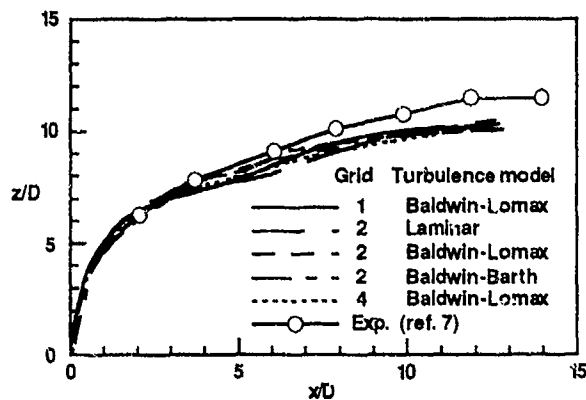
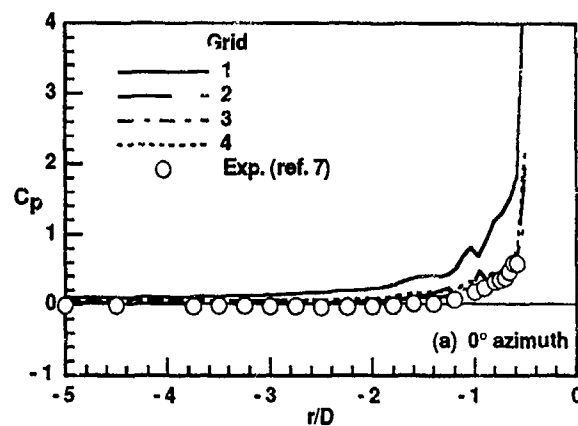


Fig. 5. Comparison of calculated and experimental⁷ jet centerline paths for velocity ratio 6.

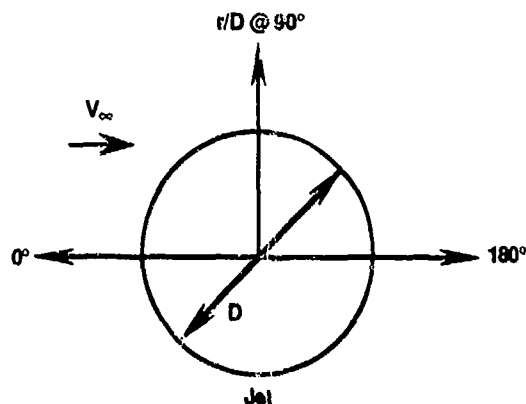


Fig. 6. Location of three radial rays (0°, 90°, and 180°) relative to the jet exit and the freestream.

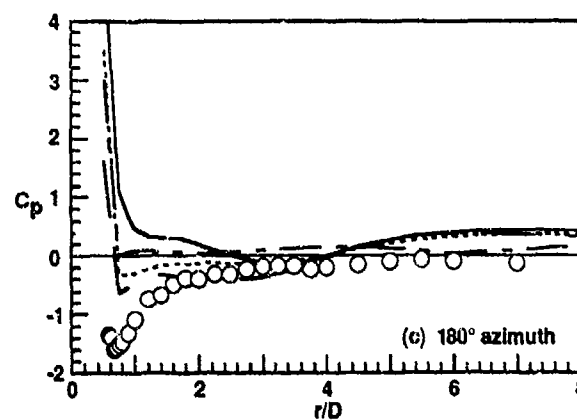


Fig. 7. Effect of several grids using OVERFLOW on radial variation of pressure coefficient (experimental data ref. 7).

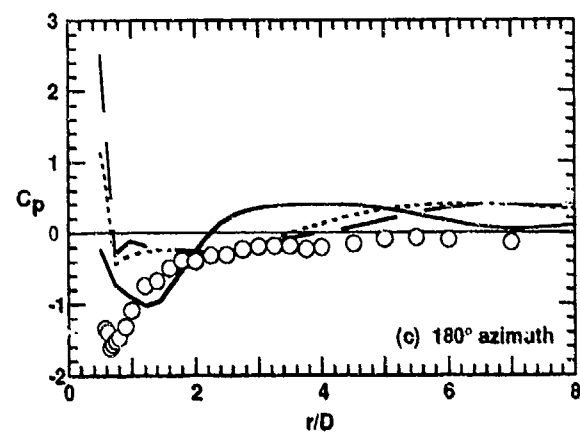
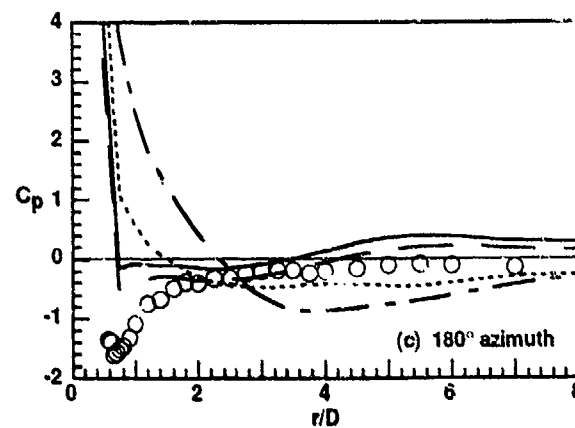
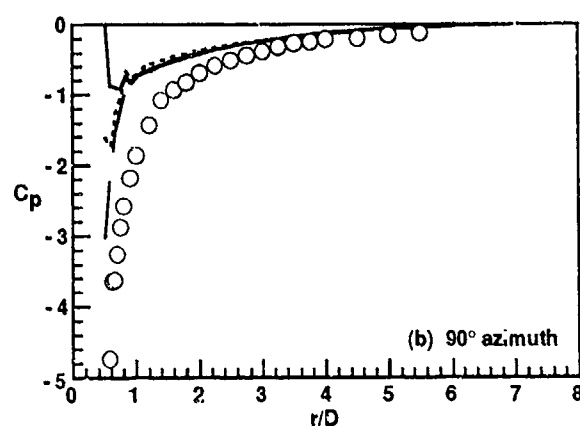
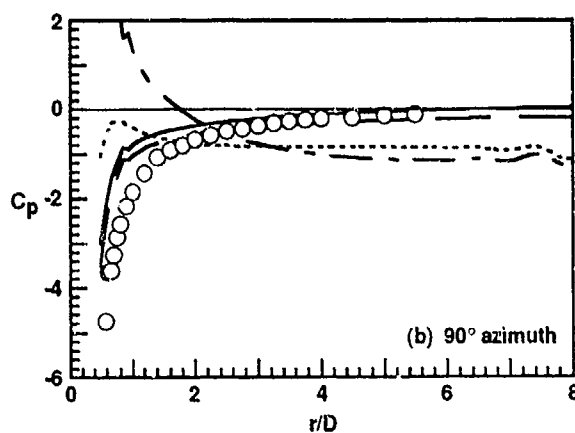
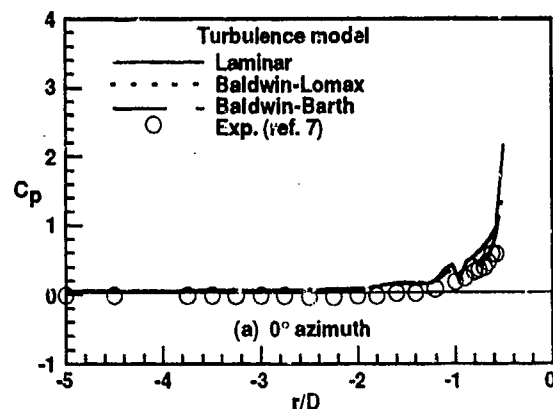
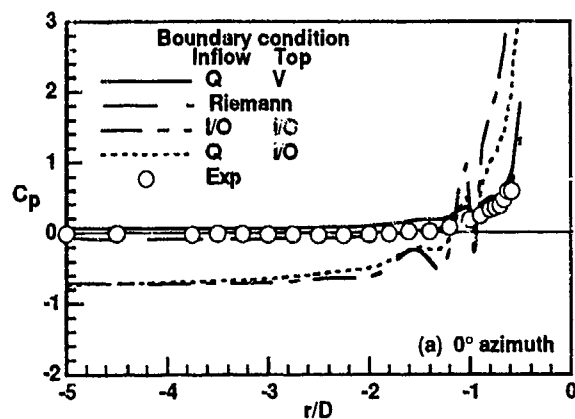
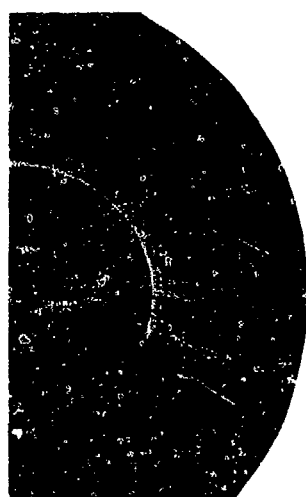


Fig. 8. Effect of boundary conditions using OVERFLOW on radial variation of pressure coefficient (experimental data ref. 7).

Fig. 9. Effect of turbulence models using OVERFLOW on radial variation of pressure coefficient (experimental data ref. 7).



Fig. 10. Particle traces showing entrainment for computed flowfield using the Baldwin-Barth turbulence model.



(a) Vorticity contours for cross section centered at $x = 0.7$, $z = 2.25$, and $\phi = 78^\circ$.



(b) Vorticity contours for cross section centered at $x = 3.07$, $z = 4.25$, and $\phi = 61.5^\circ$.

Fig. 11. Vorticity contours for selected jet wake cross sections.

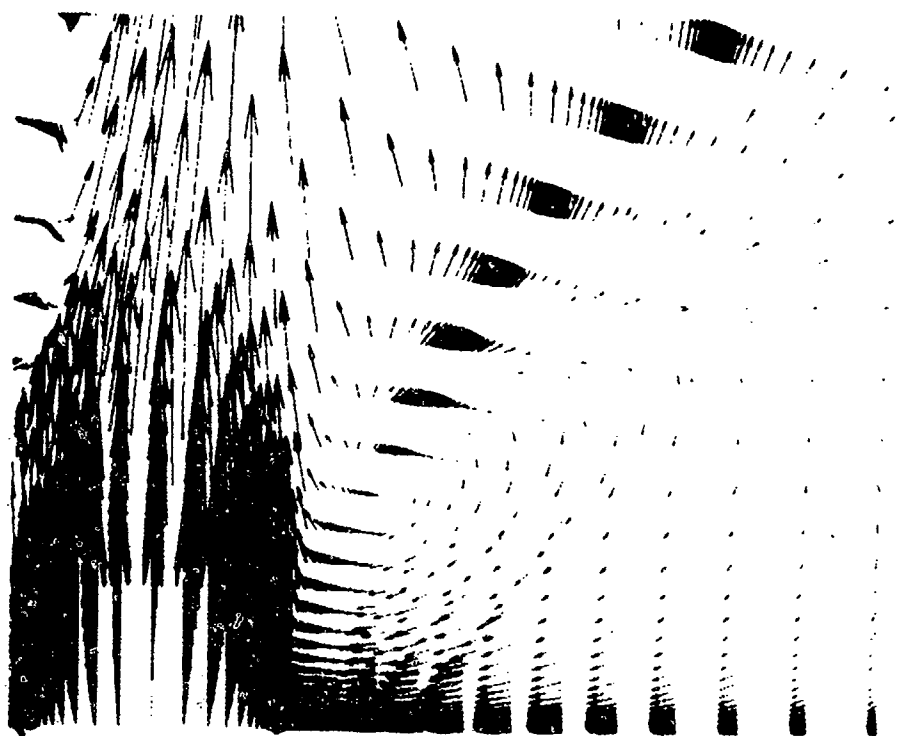


Fig. 12. Enlargement of velocity vectors showing the jet exit and downstream recirculation in the symmetry plane.

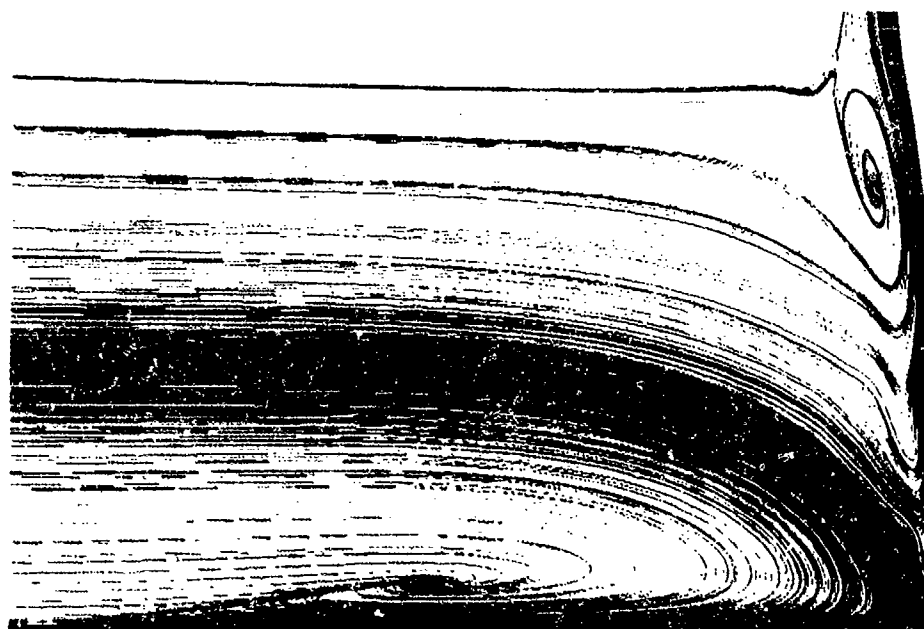


Fig.13. Particle trace lines showing the corner flow structure of the horseshoe upstream of the jet exit in the symmetry plane.

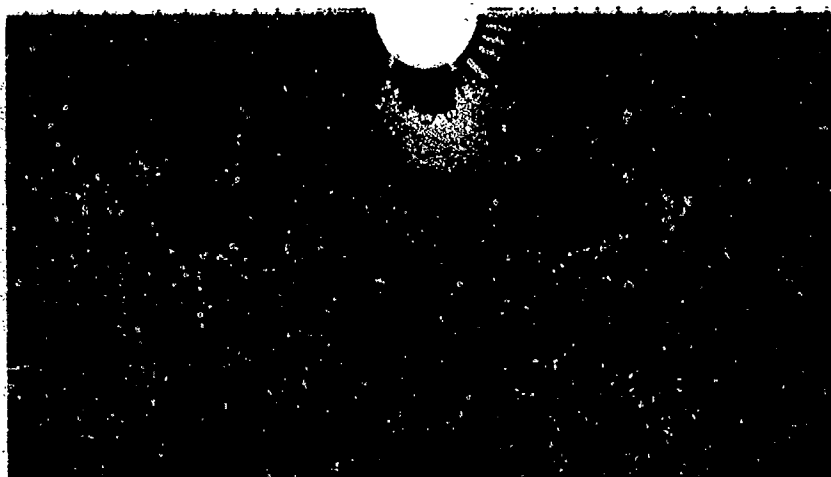
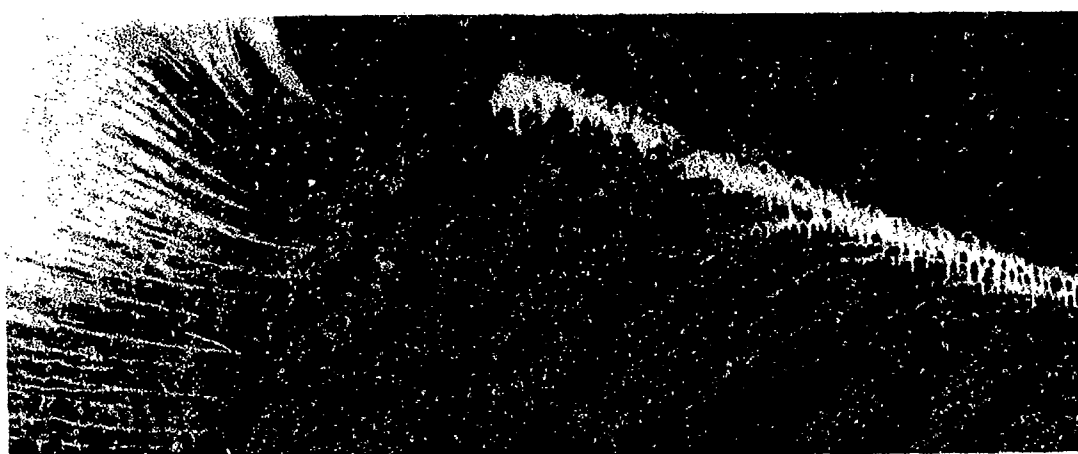


Fig. 14. Experimental⁷ and computational solution comparison of the pressure contours induced by a jet in a crossflow on the flat plate.



(a) Computed surface particle traces.



(b) Experimental¹¹ oil flow photograph.

Fig. 15 Comparison of computed and experimental images of the surface flow on the flat plate near the jet exit.

CALCULATION OF SINGLE AND MULTIPLE JETS IN CROSS-FLOW WITH AND WITHOUT IMPINGEMENT USING REYNOLDS-STRESS-TRANSPORT CLOSURE

N.Z. Ince and M.A. Leschziner
 Department of Mechanical Engineering
 University of Manchester Institute of Science and Technology
 Manchester M60 1QD, UK

SUMMARY

A finite-volume algorithm, incorporating a non-diffusive quadratic scheme for the approximation of convection and full second-moment (Reynolds-stress-transport) turbulence closure, is applied to a free jet in moderately strong cross-flow and three jet configurations combining impingement with weak cross-flow, one geometry involving a twin-jet and another a triple-jet arrangement. The primary objective is to identify the merits and weaknesses of Reynolds-stress modelling, in contrast to one based on the isotropic eddy-viscosity approach, in the present complex 3D environment. While open questions remain, due principally to uncertainties arising from boundary conditions and insufficient numerical resolution in isolated highly sheared regions, the present calculations provide clear indications, in accord with earlier studies in both 2D and 3D flows, of the superiority of the anisotropic closure. It is also demonstrated that a careful treatment of the jet-discharge conditions can be highly influential in respect of predictive realism.

1. INTRODUCTION

Cross-flow imparted to any simple two-dimensional jet provokes a range of complex strain features which pose major challenges to any computational modelling framework in existence. For a start, the flow becomes intensely three-dimensional, with consequent profound implications regarding computational economy, the achievable level of grid resolution and the required accuracy of the discretisation scheme used to approximate transport in directions quite different from the grid coordinates. From a physical point of view, the cross-flow induces cross-jet pressure gradients - hence deflection of the sheared jet fluid, provokes vorticity realignment and vortex stretching - hence cross-jet circulation, and gives rise to a highly turbulent and vortical, possibly periodic wake region which

usually involves reverse flow.

When, in addition to cross-flow, jet impingement occurs - as would be the case in VSTOL operation at ground proximity - a strong radial wall jet forms at the impingement wall, and its interaction with the cross-flow gives rise to an extensive horse-shoe-shaped ground vortex, as shown schematically in Fig. 1.

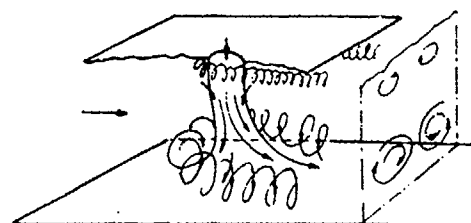


Fig. 1: Schematic representation of impinging jet in cross-flow

Yet more complicated is a situation in which two or more jets are injected into a cross-flow and impinge on the ground. In this case, the collision between the wall jets formed after impingement gives rise to strongly three-dimensional fountains which, among other consequences, lift vorticity from the impingement wall towards the jet-discharge level thus creating strong distortions to the strain field in that region too.

With analytical, integral and inviscid approaches (e.g. Coelho and Hunt [1], Dormieux et al [2]) set aside, computational modelling of jets in cross-flow has been pursued, almost invariably, within the framework of Reynolds-averaged schemes combining finite-volume discretisation and turbulence-transport models. First efforts of this type go back the late 1970's when Patankar [3], White [4] and Bergeles et al [5] computed the characteristics of single jets, the last precluding reverse flow. More recent studies include those of Demuren [6] - directed towards multiple jets in the context of film cooling, Van Daslam [7] - concerned with impinging jet in crossflow, but using a very simple algebraic

turbulence model, Ince and Leschziner [8,9] - involving cross-flow and/or impingement and focusing on the sensitivity to turbulence modelling and boundary conditions, Demuren [10] - considering efficiency gains derived from the multigrid technique for a single jet, McGuirk et al [11] - dealing with cross-flow, impingement and compressibility, and Savory et al [12] - highlighting the evolution and decay of streamwise (cross-jet) vortices.

On the assumption that numerical resolution is adequate - by no means an easily achieved requirement - the greatest level of predictive uncertainty within a Reynolds-averaged formulation arises from the turbulence model. The large majority of computational studies performed hitherto for jets in cross-flow have adopted the eddy-viscosity hypothesis in combination with a two-equation representation of associated isotropic turbulence scales - usually the turbulence energy (the square of a velocity scale) and its rate of dissipation (implying a length scale). While this rather simple modelling approach, evolved by reference to simple shear flows, has shown remarkable, indeed, surprisingly good performance in a wide range of complex condition, there is now a solid body of evidence demonstrating important weaknesses of the approach in many circumstances. Specifically, a number of studies focusing on two-dimensional flows (see Launder [13] and Leschziner [14] for recent reviews), which feature curvature, recirculation and swirl, have shown that eddy-viscosity models are unable to capture properly the complex interaction between these strain characteristics and the turbulence structure. In contrast, Reynolds-stress (*second-moment*) models often yield considerably better representations. Clearly, curvature, recirculation and vorticity also feature prominently in three-dimensional jets subjected to cross-flow and impingement, and it must be assumed that predictive weaknesses observed in eddy-viscosity calculations of these flows are partly attributable to the isotropic nature of the turbulence models used.

Full Reynolds-stress calculations for general three-dimensional flows are still rare, and studies of this type directed specifically towards jets in cross-flow have only been reported by Ince and Leschziner [8] and Demuren [10], the latter primarily concerned with computational economy

rather than predictive performance. A further study by Lin and Leschziner [15] focuses on dilution jets injected into a swirling chamber flow. The calculations of Ince and Leschziner [8], applied to three single jets examined by Fearn and Weston [16] and the impinging jet of Barata et al [17], suggest that the merits of second-moment closure extend to three-dimensional conditions, although the evidence is, at present, insufficiently strong to justify a confident statement.

The present paper is a contribution to ongoing validation efforts designed to identify strengths as well as weaknesses of current second-moment closure forms, leading to the formulation and implementation of more advanced forms (Fu et al [18], Craft [19]). Calculations are here presented, principally, for two jet configurations: an impinging twin-jet in weak cross-flow (Barata et al [20]) and a single free jet in moderate cross-flow (Andreopolous and Rodi [21]). To assist the discussion and to highlight consistency with earlier observations, a narrow selection of results obtained for the single impinging jet of Barata et al [17] are also included.

2. COMPUTATIONAL FRAMEWORK

The calculations reported in this paper have been performed by using a 3D curved-orthogonal finite-volume code developed by Lin & Leschziner [15]. The code solves the Reynolds and continuity equations in an iterative manner by way of a pressure-correction algorithms over a staggered cell arrangement, and incorporates the standard k-ε turbulence model of Jones and Launder [22] and the second-moment closure of Gibson and Launder [23]. Both models were used in conjunction with log-law-based wall laws. The latter model may be represented compactly by the following equations written in Cartesian-tensor form:

$$\frac{D\overline{u_i u_j}}{Dt} = \frac{\partial}{\partial x_k} \left(\left(\nu + c_s \frac{\overline{u_k u_k}}{k} \frac{k}{\epsilon} \right) \frac{\partial \overline{u_i u_j}}{\partial x_k} \right) + P_{ij} + G_{ij} + \Phi_{ij} - \frac{2}{3} \delta_{ij} \epsilon \quad (1)$$

in which

$$P_{ij} = - \left\{ \overline{u_i u_k} \frac{\partial U_j}{\partial x_k} + \overline{u_j u_k} \frac{\partial U_i}{\partial x_k} \right\}$$

is the rate of stress production,

$$\Phi_{ij} = \Phi_{ij1} + \Phi_{ij2} + \Phi_{ijw}$$

represents pressure-strain interaction where,

$$\Phi_{ij1} = \frac{-c_1 \varepsilon}{k} \left(\overline{u_i u_j} - \frac{1}{3} \delta_{ij} \overline{u_k u_k} \right)$$

is the "Rotta" term,

$$\Phi_{ij2} = -c_2 \left(P_{ij} - \frac{1}{3} \delta_{ij} P_{kk} \right)$$

is the "isotropisation-of-production" term, and

$$\begin{aligned} \Phi_{ijw} = & \left[c_1' \frac{\varepsilon}{k} \left(\overline{u_k u_m} n_k n_m \delta_{ij} - \frac{3}{2} \overline{u_k u_i} n_k n_j \right. \right. \\ & \left. \left. - \frac{3}{2} \overline{u_k u_j} n_k n_i \right) \right. \\ & \left. + c_2' \left(\Phi_{km2} n_k n_m \delta_{ij} - \frac{3}{2} \Phi_{ik2} n_k n_j \right. \right. \\ & \left. \left. - \frac{3}{2} \Phi_{kj2} n_k n_i \right) \right] \frac{k^{3/2}}{c_\mu \varepsilon x_n} \end{aligned}$$

represents wall-related influences on the pressure-strain process, in which $n_k \equiv$ wall-normal unit vector and $x_n \equiv$ normal distance from the wall. The above set is closed by the rate-of-dissipation equation:

$$\begin{aligned} \frac{\partial \rho U_k \varepsilon}{\partial x_k} = & c_1 \frac{\partial}{\partial x_k} \left(\frac{\overline{u_k u_i}}{\varepsilon} k \frac{\partial \varepsilon}{\partial x_i} \right) \\ & + 0.5 \frac{\varepsilon}{k} c_{\varepsilon 1} P_{kk} - c_{\varepsilon 2} \frac{\varepsilon^2}{k} \end{aligned} \quad (2)$$

The constants appearing in the above set are summarised below:

c_1	c_2	c_3	c_5	c_1'	c_2'	c_4	c_t	$c_{\varepsilon 1}$	$c_{\varepsilon 2}$
1.8	0.6	0.5	0.22	0.5	0.3	2.5	0.15	1.9	1.45

In efforts to improve the predictive performance of the above second-moment closure, specifically in relation to the spreading rate of 2D plane and round jets, Launder et al [24] proposed and tested a form of the ε -equation which is sensitized to

turbulence anisotropy via related invariants. Specifically, the modification involves a reduction of the coefficient $c_{\varepsilon 1}$ in equation (2) to unity and the following functional relationship of $c_{\varepsilon 2}$ to the anisotropy invariants A_2 , A_3 and $A = 1 - 3/8 (A_2 - A_3)$:

$$c_{\varepsilon 2} = \frac{1.92}{(1 + 0.6A\sqrt{A_2})} \quad (3)$$

where, $a_{ij} = (\overline{u_i u_j} / k - 2/3 \delta_{ij})$, $A_2 = a_{ij} a_{ij}$, $A_3 = a_{ij} a_{jk} a_{ki}$. This new form has emerged from and proven itself in 2D jet studies, and has been adopted here as part of the 'standard' second-moment framework.

In previous computational studies focusing on 3D jets [8], the present authors demonstrated that the use of a first-order approximation for convection, within the so-called *hybrid scheme*, leads to substantial numerical errors with the size of grid which can normally be tolerated on economical grounds. Therefore, the calculations reported herein were carried out with the essentially non-diffusive QUICK scheme of Leonard [25]. Implementation of this scheme in conjunction with second-moment closure is challenging in terms of iterative stability, and a number of stability-promoting measures had to be employed, the most important being the use of the TVD-like *Local Oscillation Damping Algorithm* (LODA) of Zhu and Leschziner [26] and a partial representation of turbulence transport by anisotropic apparent viscosities.

3. CASES INVESTIGATED and COMPUTATIONAL DETAILS

Results are reported here for two types of flow, the first being a single/twin/triple impinging jet arrangement subjected to weak cross-flow and the second a free jet in cross-flow. Fig. 2 gives a schematic representation of the two cases.

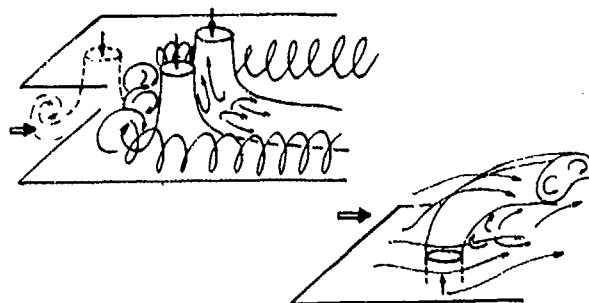


Fig. 2: Geometries investigated

The first group of flows was studied experimentally, all within the same laboratory facility, by Barata et al [17] for single-jet operation, and later by Barata et al [20] with two and three jets. For all cases, the wind-tunnel height was $5D$, D being the jet-nozzle diameter, and the velocity ratio R - defined as the jet velocity divided by the cross-flow velocity - was 30. Experiments were conducted with water, and the measurements were obtained with LDA. Computational results will be presented, principally, for the twin-jet configuration; single-jet results have been reported elsewhere [8] and will be drawn upon here only in so far as they are judged to aid considerations of consistency of performance. Only one result will be included for the three-jet arrangement, for both experiment and calculation do not reveal important features which are not already encountered in the twin-jet arrangement.

Following grid-dependence tests, the final computations contained herein were made over a grid consisting of $60 \times 45 \times 50$ lines. Within this Cartesian framework, the jet exit was represented by a castellated contour, with careful attention being paid to maintaining the correct discharge area, mass-flow rate and momentum flux.

Experimental data for the second case were obtained by Andreopoulos and Rodi [21] with hot-wire anemometry in air. Measurements were made of mean and fluctuating velocity components for three ratios of jet-to-crossflow velocities: 0.5, 1.0, and 2.0. Calculations with a $52 \times 54 \times 30$ mesh have been performed for all three conditions, but space constraints preclude the inclusion of results for more than one case, $R=2$.

Preliminary test calculations for jets in moderately strong cross-flow had shown - and this will be demonstrated below by examples - that the distortion of the jet by the cross-flow across the jet-discharge plane is an important factor affecting predictive performance. Hence, the usual practice of prescribing a uniform discharge velocity profile, in the absence of experimental data, is often inappropriate, particularly at low R -ratios. One superior alternative is to prescribe a total-pressure condition, which allows the numerical procedure to adjust the velocity across the discharge plane in consonance with static-pressure variations. An even better approach is to

incorporate parts of the ducted flow leading to the jet exit into the calculation domain. Most of the results reported here have been obtained with a total-pressure condition. However, results are also reported for uniform jet-discharge velocity as well as with the jet pipe included in the calculation, in order to identify the importance of the jet-discharge conditions on the predicted behaviour within the cross-flow region. Some aspects of this issue had been previously considered by the authors [8] in relation to the jets measured by Fearn and Weston [16].

Boundary conditions at fluid inlet planes, other than those discussed above, were taken from experimental data wherever possible. Distributions of some turbulence quantities, including dissipation and Reynolds stresses, were estimated on the basis of turbulence-equilibrium and isotropy considerations. At far-field exit planes, invariant static-pressure conditions were prescribed, while at walls, no-slip and impermeability conditions were combined with log-law-based wall laws.

4. RESULTS and DISCUSSION

4.1 Impinging Jets

It is instructive to start by recalling briefly some earlier results obtained for Barata et al's single-jet case. Thus, Fig. 3 compares predicted velocity-vector fields across the jet-bisecting plane with streaklines constructed from measured velocity profiles. The most prominent feature is the ground vortex formed as a result of the wall jet, which arises from impingement, interacting with the oncoming cross-stream. The computed solution obtained with the $k-\epsilon$ /QUICK combination appears to seriously over-estimate the length of the ground vortex, while the use of the second-moment closure (denoted by DSM) yields a significant improvement, presumably as a consequence of this model's ability to represent realistically the sensitivity of turbulent diffusion in the wall jet and ground vortex to curvature in the shear layer; this is, in fact, a clearly identifiable and recurring theme in 2D shear layers, but extrapolation to complex 3D conditions is not without risk. Unfortunately, further data available for comparison consists only of some velocity profiles in a restricted portion of the wall-jet region, and these do not

suffice to draw firmer conclusions than that derived above from the streakline structure. In this context, it is informative to mention that recent calculations by the authors [9] for a twin-impinging jet *without* crossflow measured by Saripalli [27] have provided an indication that the interaction between curvature and turbulence in the wall jets forming a central fountain led to a significant overall increase in the spreading rate of the fountain. The implication is that turbulence destabilisation in the curved shear layer on the wall-jet's underside is an important mechanism affecting the evolution of the fountain.

The complexity of the flow field increases considerably in the case of twin-jet impingement in a cross-flow. This is conveyed by Fig. 4 which shows velocity fields across planes A-A and B-B (defined in the inset of Fig. 4), the latter cutting across the fountain which forms as a result of the collision of the wall jets originating from impingement. The fountain is highly three-dimensional, spreading due to the combined action of pressure and diffusion. Moreover, the fountain itself impinges on the top wall, giving rise to secondary wall jets on the upper wall, fluid from which is then partially entrained into both the fountain and the main circular jets. The ground vortex is clearly visible in the jet plane but not on the fountain plane, as the fountain tends to lift the vortex and diffuse it in the vicinity of the upper wall.

Fig. 4 contains two solutions for the velocity field across the jet plane A-A: one obtained with the $k-\epsilon$ model and the other with the Reynolds-stress closure. A comparison between these fields and corresponding ones shown in Fig. 3 reveals predictive consistency in terms of the influence of turbulence modelling on the structure of the ground vortex: it is recognized that in both cases the second-moment closure predicts a considerably shorter ground vortex, the associated physical mechanism having already been discussed in relation to the single-jet solution.

The consequences of introducing a third jet upstream of the fountain, in the symmetry plane between the two jets above, are also identified in Fig. 4. Superficially, the effect is modest: the wall jet emanating from the upstream impingement interacts with the fountain, but does not decisively affect the latter's structure. This conclusion is

supported by detailed quantitative comparisons with experimental data. It is on the basis of these comparisons that further results for the triple-jet case have been omitted from this paper.

Fig. 5(a) provides a comparison of profiles of principal (vertical) velocity component along three different lines lying in plane C-C (see Fig. 4) which cuts across one jet and one-half of the fountain. Both turbulence models give a fair representation of the measured flow, but the stress model appears to return an excessively narrow and pointed profile close to the stagnation point, implying a reduced spreading rate. Similar differences between the models have been observed in calculations for the twin-jet of Saripalli [9,20], although in that case the stress model gave results in close agreement with experiment. Both models predict considerably lower velocities in the fountain than those measured, with the stress model giving a somewhat larger spreading rate and lower peak fountain velocity; this is, again, in accord with observations in the aforementioned case of Saripalli, but there the stress model gave, yet again, close agreement with the experimental data.

The interaction between the jet and the fountain creates significant levels of asymmetry in the profiles of the Reynolds normal stresses, as is seen from Fig. 5(b). It is evident that the Reynolds-stress model returns a far better representation of the measured asymmetry as well as of the level of normal-stress anisotropy, particularly in the jet. In the fountain region, neither model does particularly well, but the Reynolds stress form returns higher stress levels, in better accord with experiment and consistent with the larger Z-wise spreading rate. Unfortunately, no measurements of shear stress were undertaken along plane C-C.

A correct representation of the fountain structure is of considerable practical importance as well as being particularly challenging from a turbulence modelling point of view. This structure is conveyed in Fig. 6 (a), (b), (c), (d) and (e), respectively, by profiles of streamwise velocity (U), upward velocity ($-V$) and Reynolds stresses u^2 , v^2 and \bar{uv} , all along plane B-B shown in the inset in Fig. 4. While both models may be said to return a fair representation of the fountain

structure (except in respect of shear stress), considering the complexity of the flow, there are clear indications that the Reynolds-stress model fares better. First, Fig. 6(a) shows that this model correctly predicts the level of deflection of the fountain by the cross-flow. This is also implied in Fig. 6(b) by the lower level of discrepancy in the amount by which the computed V-profiles are displaced relative to the measured ones. The Reynolds-stress model also yields closer agreement with experiment in respect of normal stresses, although the level of $\overline{u^2}$ is too high close to the impingement point, probably due to a known defect in the wall-related pressure-strain model $\Phi_{ij,w}$ [equation (1)] which always manifests itself in impingement and reattachment regions. The only major disappointment relates to the shear stress \overline{uv} which is puzzlingly low, particularly that returned by the k- ϵ model. With attention focused on the structure predicted by the Reynolds-stress model, it might be reasonably assumed that the broadly correct levels of the transverse turbulence intensity $\overline{u^2}$ [Fig. 6(c)], coupled with the somewhat too low shear strain [Fig. 6(b)], would lead to insufficient levels of shear stress. However, the levels shown in Fig. 6(e) are surprisingly low and, more importantly, inconsistent with the excessive spreading rate of the fountain, unless this spreading is here dominated by inviscid processes. This is an inconsistency which remains to be resolved.

4.2 Free Jet

Space constraints only allow results for one velocity ratio, $R=2$, to be included, and the associated velocity field across the jet's symmetry plane is given in Fig. 7. As seen, this result was obtained with a part of the jet pipe included. The rationale of doing so is identified in Fig. 8. This shows three velocity profiles across the jet-discharge plane pertaining to solutions presented later: one is uniform, the other arose from prescribing an invariant total-pressure condition across the jet exit and the third is the variation predicted when the jet pipe is included. Evidently, there is a considerable amount of distortion at the jet exit due significant cross-jet pressure variations. These distortions increase as the velocity ratio R decreases. Indeed, at $R=0.5$, it has been found that reverse flow *into* the pipe occurs at the upstream end where the cross-flow 'collides' with the jet.

The influence of the jet-discharge conditions on the solution is conveyed in Fig. 9 by way of predicted vertical profiles of streamwise and transverse velocities and turbulence energy at two streamwise positions, $x/D=4$ and $x/D=10$, all arising from the k- ϵ eddy-viscosity model. The essential points to note are, first, that prescribing a uniform jet-discharge-velocity profile creates a marked and inappropriate shift of all distributions in the downstream direction, and second, that prescribing a total-pressure boundary condition yields results which are close to those arising with the jet pipe included. In the case $R=0.5$, the former treatment is inappropriate, and it has been found essential to include the jet pipe in the calculation domain.

Results illustrating the sensitivity to turbulence-model characteristics are given in Figs. 10 and 11. First, Fig. 10 shows the contours of jet excess temperature (or jet-fluid concentration) obtained in order to clearly identify the jet trajectory. Superimposed on the contour plots, one arising from the eddy-viscosity model the other from the Reynolds-stress closure, is a line identifying a trajectory correlation by Komotani and Greber [28]¹. As seen, the maximum jet temperatures predicted with both models agrees well with the correlation. This is an expected outcome, for the bending process is largely governed by inviscid features - the interaction between pressure gradients and fluid inertia.

Fig. 11 compares transverse profiles of velocity, both streamwise and transverse components, turbulence energy and shear-stress profiles at three streamwise positions. Reference to Fig. 7 shows that the profiles in Fig. 11, effectively, traverse the wake region below the jet and penetrate the lower jet edge. The structure of this region is very complex due to upstream reverse flow and the suction of fluid into the leeward jet underside from lateral regions. Numerical tests have shown the predicted wake structure derived from the Reynolds-stress model to be fairly sensitive to the turbulence state at the downstream (leeward) edge of the jet-discharge plane. This region is not as well resolved as would be desirable because of mesh-density constraints, a limitation which is aggravated by

¹ Strictly, the correlation pertains to the locus of maximum jet velocity, but this is difficult to determine with any degree of accuracy.

the staggered storage locations of shear stress and turbulence-energy. The solutions do demonstrate, however, that considerable improvements in predictive realism can be derived from second-moment modelling. Some features in the profiles shown in Fig. 11 are consistent with known characteristics displayed by 2D solutions obtained with second-moment model forms, others are not. The most striking feature is the dramatically lower level of transverse velocity under the jet, which, at first sight, is consistent with the tendency of curvature to reduce entrainment at the strain orientation prevailing in the lower jet edge. The reduced level of upward entrainment promotes forward motion in the vicinity of the centre-plane of fluid being sucked towards this plane from both (lateral) sides of the jet. This interaction is evident from the U-velocity profiles, and it tends to reduce shear on the jet's underside. The stress model also returns improved turbulence-energy levels with lower peaks at the jet underside, which is consistent with the reduced level of shear strain. On the other hand, the stress model is seen to predict higher levels of peak shear-stress in the lower jet shear layer, which contradicts the simple '2D' view on curvature-induced reduction in entrainment, and points to a complex interaction between the stresses in the highly 3D flow conditions prevailing here.

5. CONCLUSIONS

Numerical solutions have been presented for jets in weak and moderate cross-flow, some involving strong normal impingement. Exceptionally for a numerical study of complex 3D flows, the procedure employed herein combined non-diffusive discretisation and a second-moment closure with an anisotropy-sensitized dissipation equation.

The study has demonstrated that considerable care has to be exercised in respect of the jet-discharge conditions, particularly at high cross-flow velocities. Ideally, parts of the jet pipe would be included in the calculation domain. At the very least, a total-pressure-based boundary condition should be adopted, allowing pressure-induced distortions in the exit velocity to be accommodated.

The comparisons between calculations and experimental data, including turbulence quantities,

broadly support earlier conclusions that second-moment closure returns a superior representation of most flow features, in comparison to the k- ϵ eddy-viscosity form. This support is somewhat weaker in the case of the free jet, in which the quality of resolution of the turbulence field at the leeward jet side, close to the jet-discharge edge, is particularly influential and a source of error in the present application.

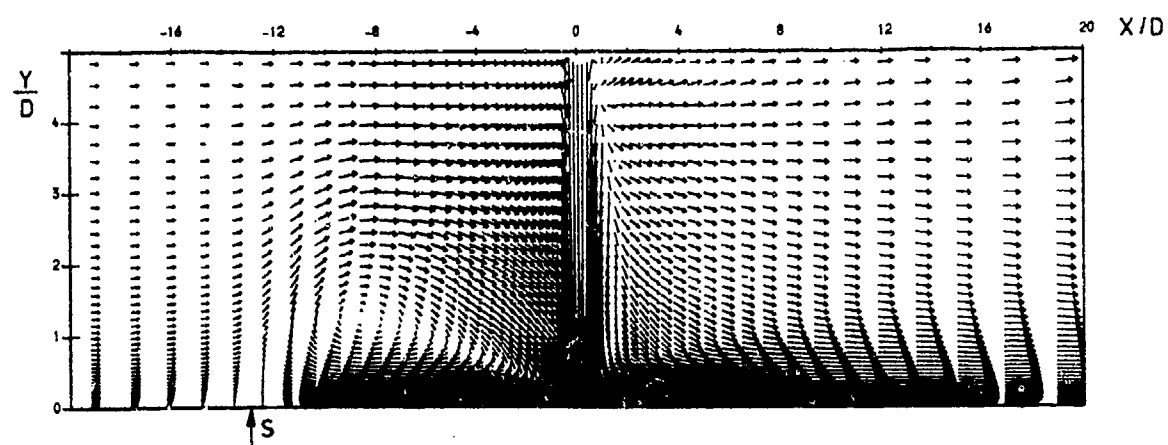
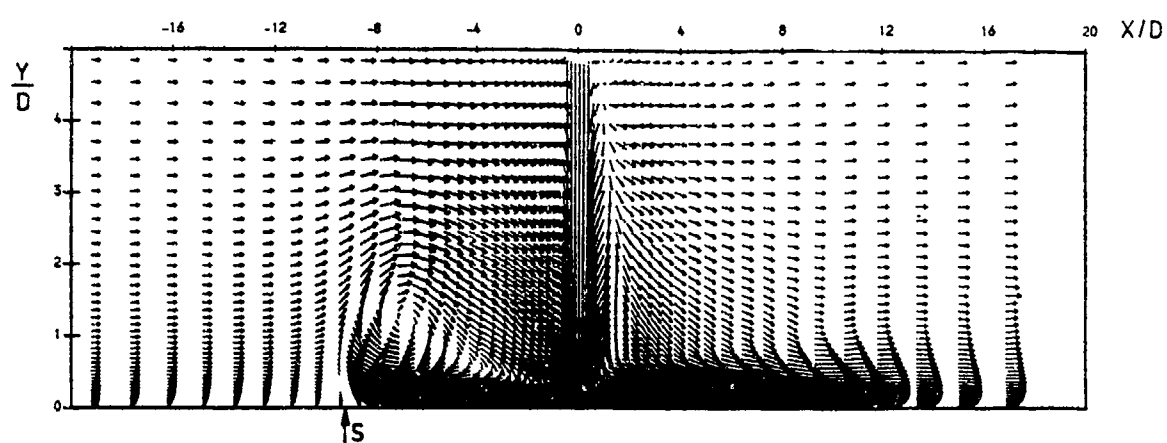
ACKNOWLEDGEMENT

Parts of the study documented in this paper were supported by British Aerospace (Military Aircraft Ltd.). Some of the calculations were performed on the Amdahl VP1100 and VP1200 computers with allocations granted by the Manchester Computer Centre and the Science and Engineering Research Council.

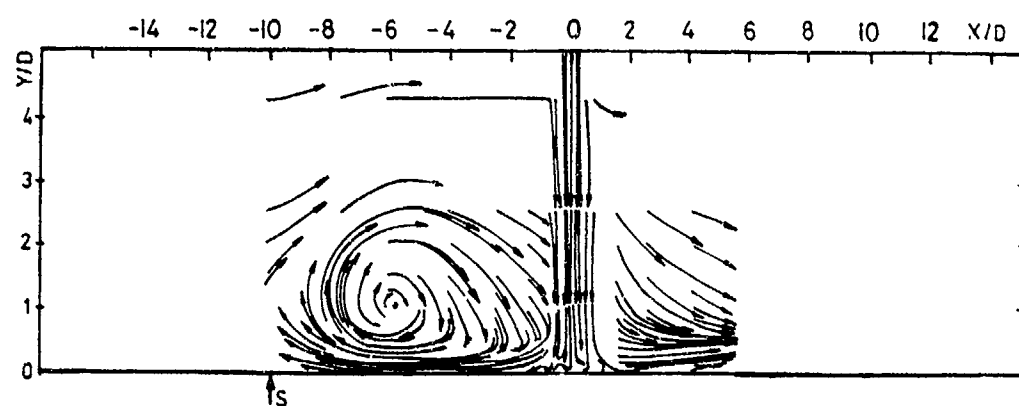
REFERENCES

1. Coelho, S.L.V. and Hung, J.C.R., *J. Fluid Mech.*, Vol. 200, pp. 95-120, 1989.
2. Dormieux, M., Guillen, P. and Abgrall, R., "Numerical simulation of transverse jet flows by a non reactive two species multidomain Euler flow solver", 28th Aerospace Sciences Meeting, Reno, Nevada, January 1990.
3. Patankar, S.V., Basu, D.K. and Alpay, S.A., *J. Fluids Engrg.*, 99, pp. 758-762, 1977.
4. White, A.J., "The prediction of the flow and heat transfer in the vicinity of a jet in cross flow", ASME Winter Annual Meeting, Chicago, IL, 1980.
5. Bergeles, G., Gosman, A.D. and Launder, B.E., *Numerical Heat Transfer*, 1, p. 217, 1978.
6. Demuren, A.O., *Comput. Meths. in Appl. Mech. and Engrg.*, 37, pp. 309-328, 1983.
7. Van Daslem, W.R., "Study of V/STOL flows using the fortified Navier Stokes scheme", *Computational Fluid Dynamics*, (de Vahl Davis and Fletcher eds.), Elsevier, pp. 725-735, 1988.
8. Ince, N.Z. and Leschziner, M.A., "Computation of three-dimensional jets in crossflow with and without impingement using second-moment closure", *Engineering Turbulence Modelling and Experiments*, (Rodi and Ganić eds.), Elsevier, p. 143, 1990.

9. Ince, N.Z. and Leschziner, M.A., "Second-moment modelling of incompressible impinging twin jets", Proc. 5th UMIST Colloquium on CFD, Mech. Eng. Dept., Thermofluid Division, p. 6.7, 1992
10. Demuren, A.O., "Calculation of 3D turbulent jets in crossflow with a multigrid method and a second-moment closure model", Engineering Turbulence Modelling and Experiments, (Rodi and Ganić eds.), Elsevier, p. 155, 1990.
11. McGuirk, J., Page, G.J., Sakellariou, N., Flitcroft, J.E., Abbott, W., White, D.R. and Tattersall, P., "Prediction and measurement of jet flowfield features for ASTOVL aircraft", Proc. Royal Aeronautical Society Int. Power Lift Conf., London August 1990.
12. Savory, E., Toy, N., McGuirk, J.J. and Sakellariou, N., "An experimental and numerical study of the velocity field associated with a jet in a crossflow", Engineering Turbulence Modelling and Experiments, (Rodi and Ganić eds.), pp. 165-174, 1990.
13. Launder, B.E., Int. J. Heat and Fluid Flow, 10, pp. 282-300, 1989.
14. Leschziner, M.A., J. Wind Engineering. and Industrial Aerodynamics, 35, pp. 21-47, 1990.
15. Lin, C.A. and Leschziner, M.A., "Computation of three-dimensional injection into swirling flow with second-moment closure", Proc. 6th Int. Conf. on Numerical Methods in Laminar and Turbulent Flows, Swansea, pp. 1711-1725, 1989.
16. Fearn, R.L. and Weston, R.P., "Induced velocity field of a jet in a crossflow", NASA TP 1087, 1987.
17. Barata, J.M.M., Durao, D.F.G., Heitor, M.V. and McGuirk, J.J., "The turbulence characteristics of a single impinging jet through a crossflow", Proc. 6th Shear Flow Symposium, Toulouse, 1987.
18. Fu, S., Launder, B.E. and Leschziner, M.A., "Modelling strongly swirling recirculating jet flow with Reynolds-stress transport closures", Proc. 6th Symp. of Turbulent Shear Flows, Toulouse, 1987.
19. Craft, T.J., "Second-moment modelling of turbulent scalar transport", PhD Thesis, University of Manchester, Institute of Science and Technology, 1991.
20. Barata, J.M.M., Durão, D.F.G. and Heitor, M.V., J. Fluids Engrg., 114, p. 231, 1992.
21. Andreopoulos, J. and Rodi, W., J. Fluid Mech., 138, p. 127, 1984.
22. Jones, W.P. and Launder, B.R., "The prediction of laminarisation with a two-equation model of turbulence", Int. J. Heat Mass Transfer, 15, p. 301, 1972.
23. Gibson, M.M. and Launder, B.E., "Ground effect on pressure fluctuations in the atmospheric boundary layers", J. Fluid Mech., 86, pp. 491-511, 1978.
24. Launder, B.E., "An introduction to turbulence modelling at UMIST - 1992", Proc. 5th UMIST Colloquium on CFD, Mech. Eng. Dept., Thermofluids Division, 1992.
25. Leonard, B.P., "Comp. Meths. Appl. Mech. Engng., 19, p. 59.
26. Zhu, J., and Leschziner, M.A., Comp. Meths Appl. Mech. Engng., 67, pp. 355-366, 1988.
27. Saripalli, K.R., Turbulent Shear Flows 5, (F. Durst, B.E. Launder, F.W. Schmidt and J.H. Whitelaw eds.), Springer, pp. 146-168.
28. Komotani, Y. and Greber, I., AIAA J., 10, pp. 1425-1429, 1972

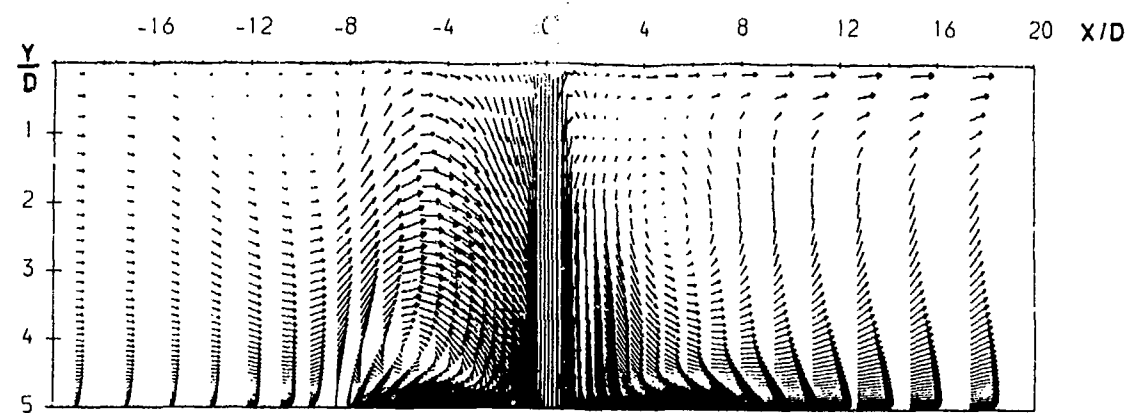
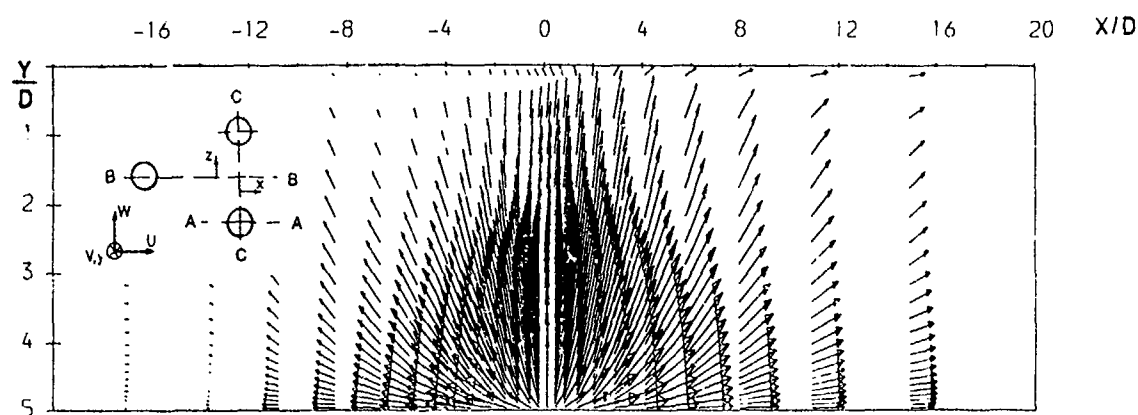
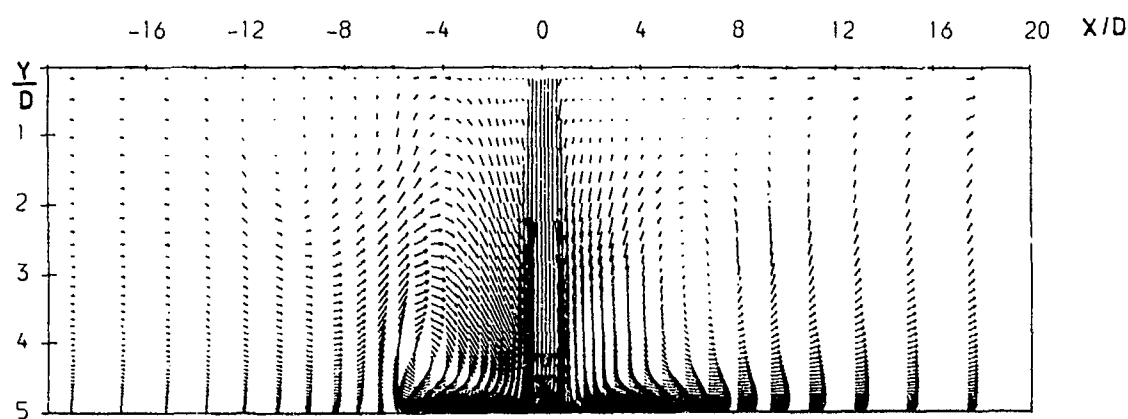
(a) $k-\epsilon$ model

(b) DSM



(c) Experiment

Fig. 3: Single impinging jet; velocity fields across jet centre-plane

(a) Twin jet, plane A-A, $k-\epsilon$ model(b) Twin jet, plane B-B, $k-\epsilon$ model

(c) Twin jet, plane A-A, DSM

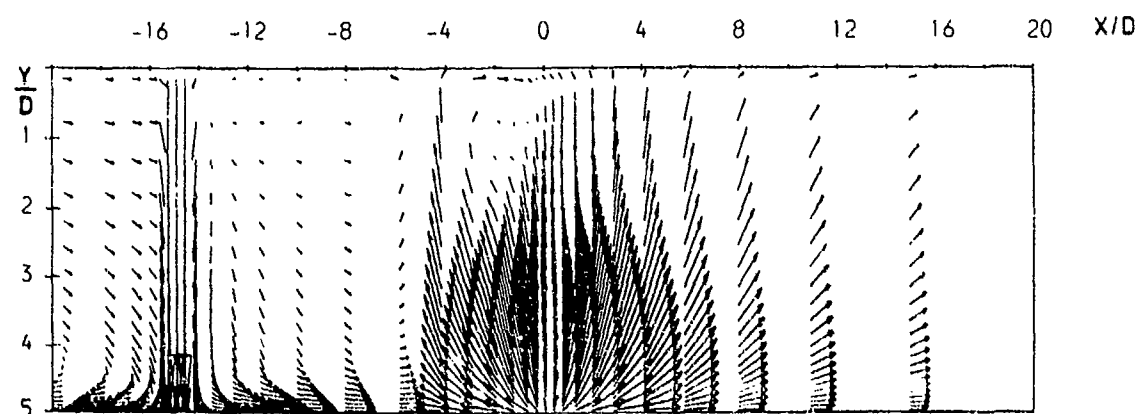
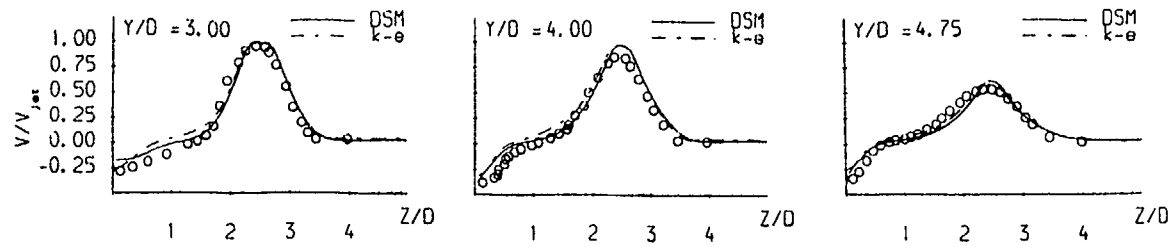
(d) Triple jet, plane A-A, $k-\epsilon$ model

Fig. 4: Twin and triple impinging jets: velocity fields across jet and fountain centre-planes



(a) Profiles of main velocity component across jet plane C-C

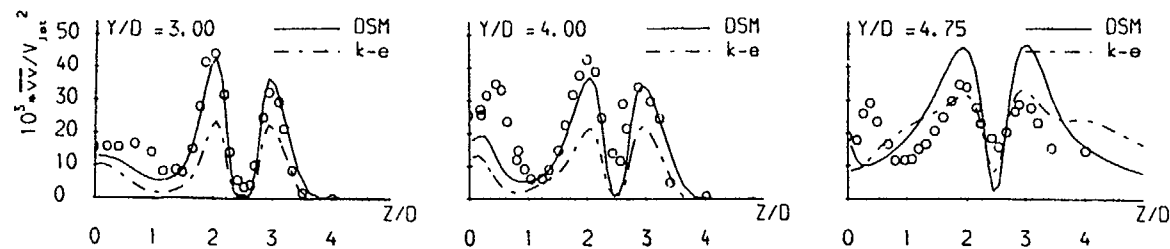
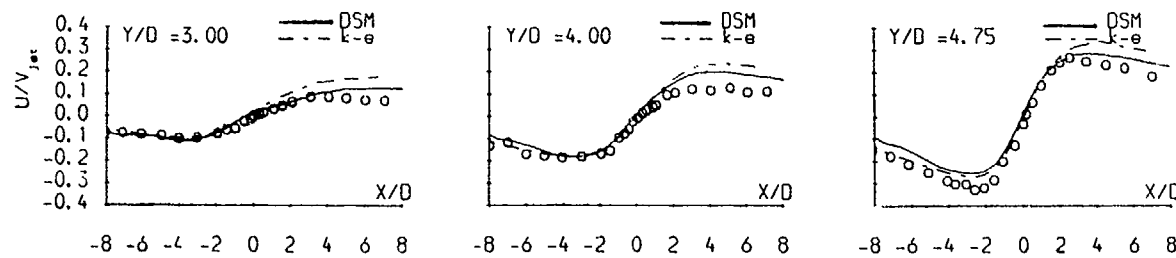
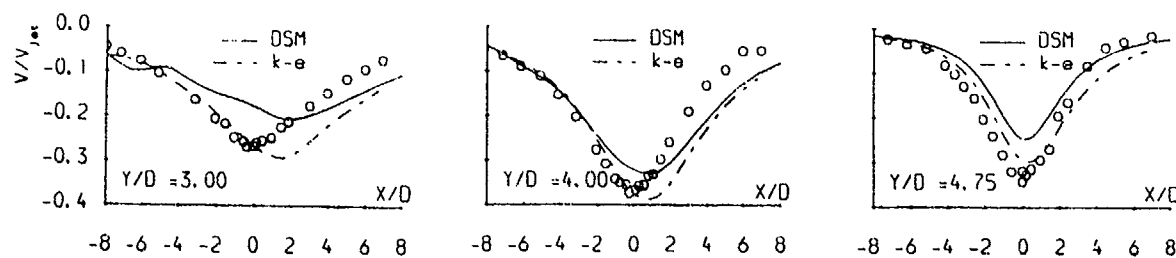
(b) Profiles of main normal stress $\overline{u'^2}$ across jet plane C-C

Fig. 5: Twin impinging jet: response to turbulence modelling in jet region



(a) Profiles of streamwise (U) velocity component across fountain plane B-B



(b) Profiles of main (V) velocity component across fountain plane B-B

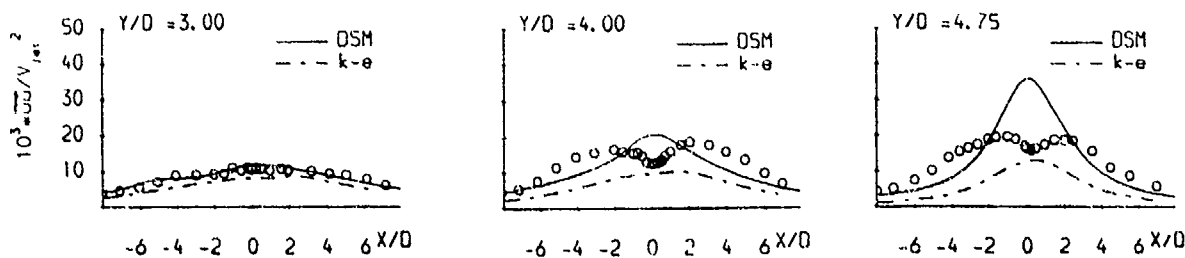
(c) Profile of secondary normal stress $\overline{u'^2}$ across fountain plane B-B

Fig. 6: Twin impinging jet: response to turbulence modelling in fountain region

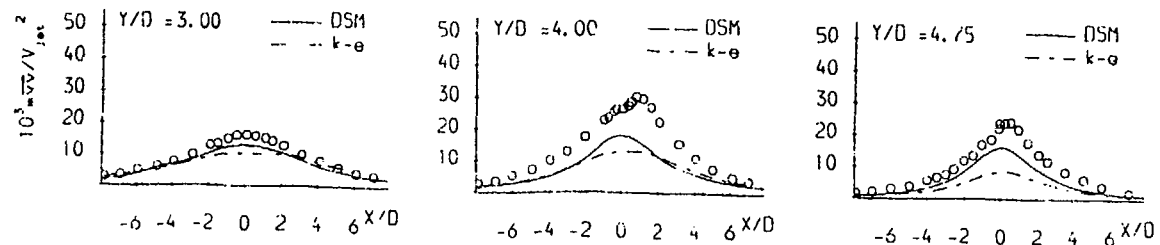
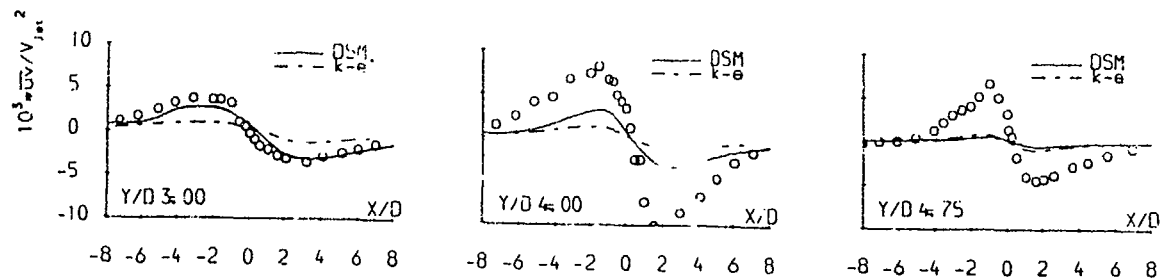
(d) Profile of main normal stress $\sqrt{v^2}$ across fountain plane B-B(e) Profiles of shear stress \bar{uv} across fountain plane B-B

Fig. 6: (continued) Twin impinging jet: response to turbulence modelling in fountain region

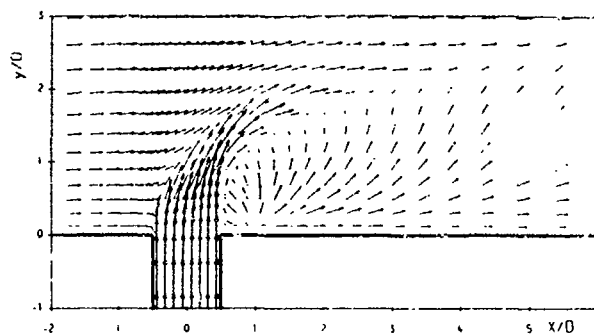


Fig. 7: Single free jet: velocity field across jet-centre plane

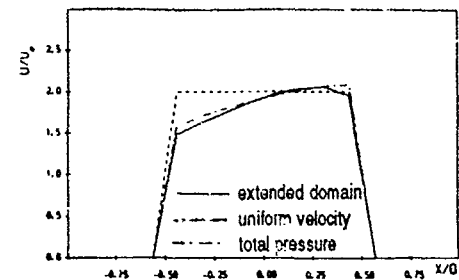


Fig. 8: Profiles of main velocity across jet-discharge plane

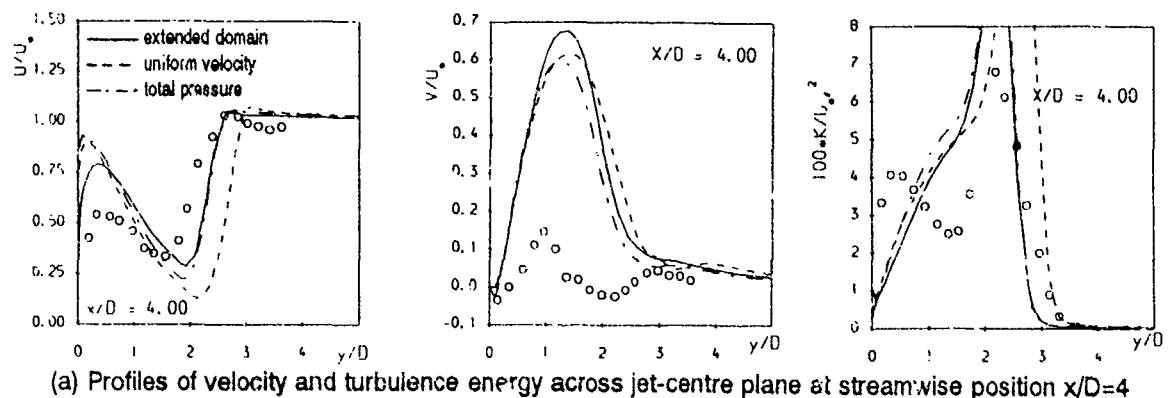
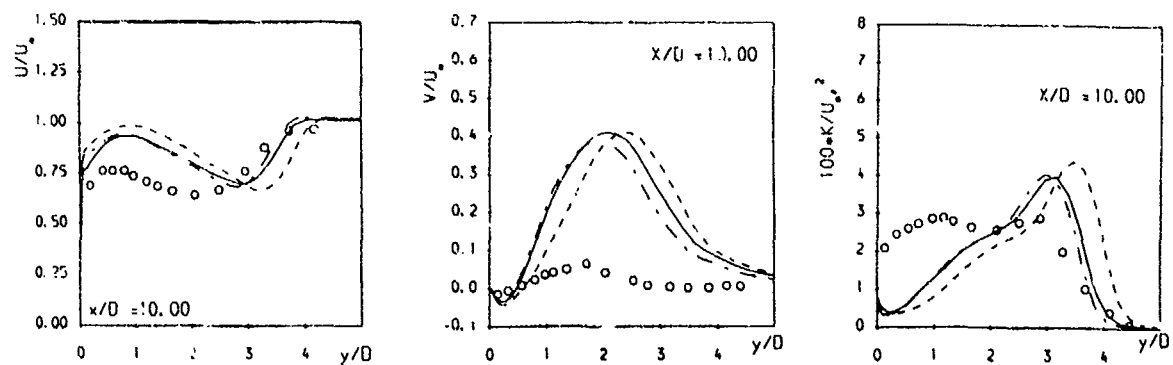
(a) Profiles of velocity and turbulence energy across jet-centre plane at streamwise position $x/D=4$ (b) Profiles of velocity and turbulence energy across jet-centre plane at streamwise position $x/D=10$

Fig. 9: Single free jet: response to aerodynamic boundary conditions across jet-discharge plane

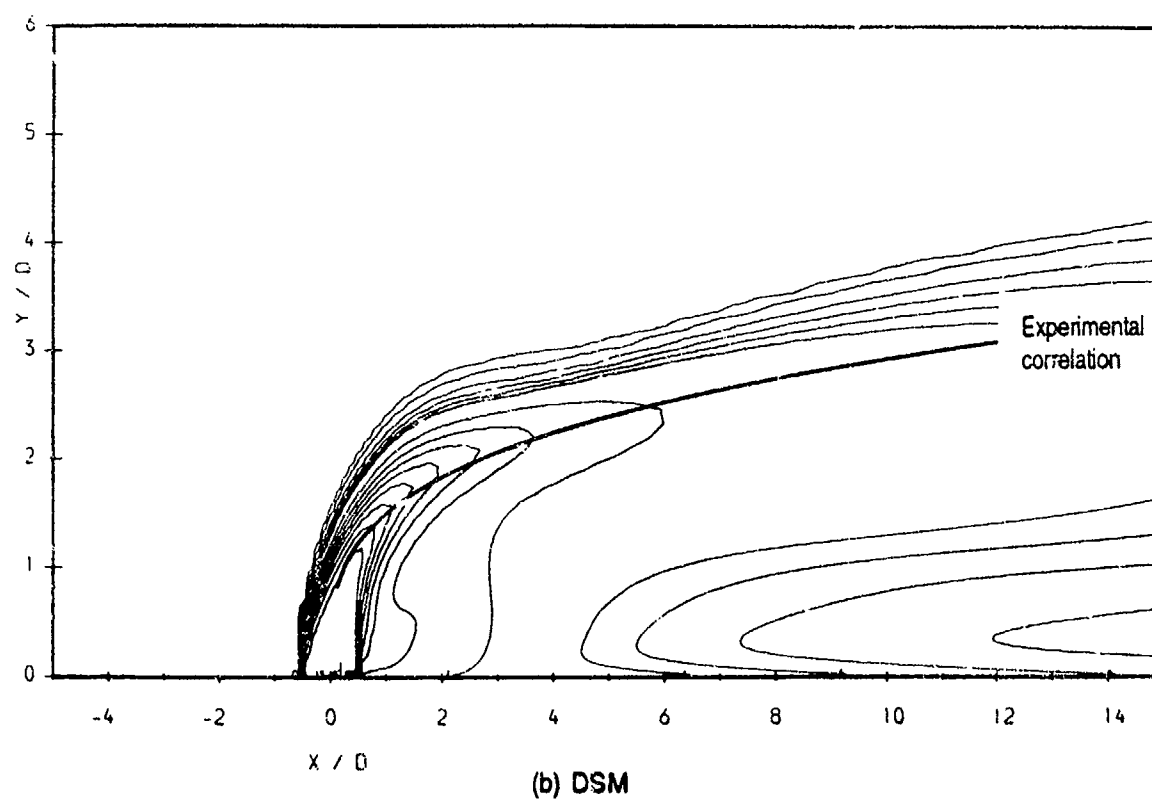
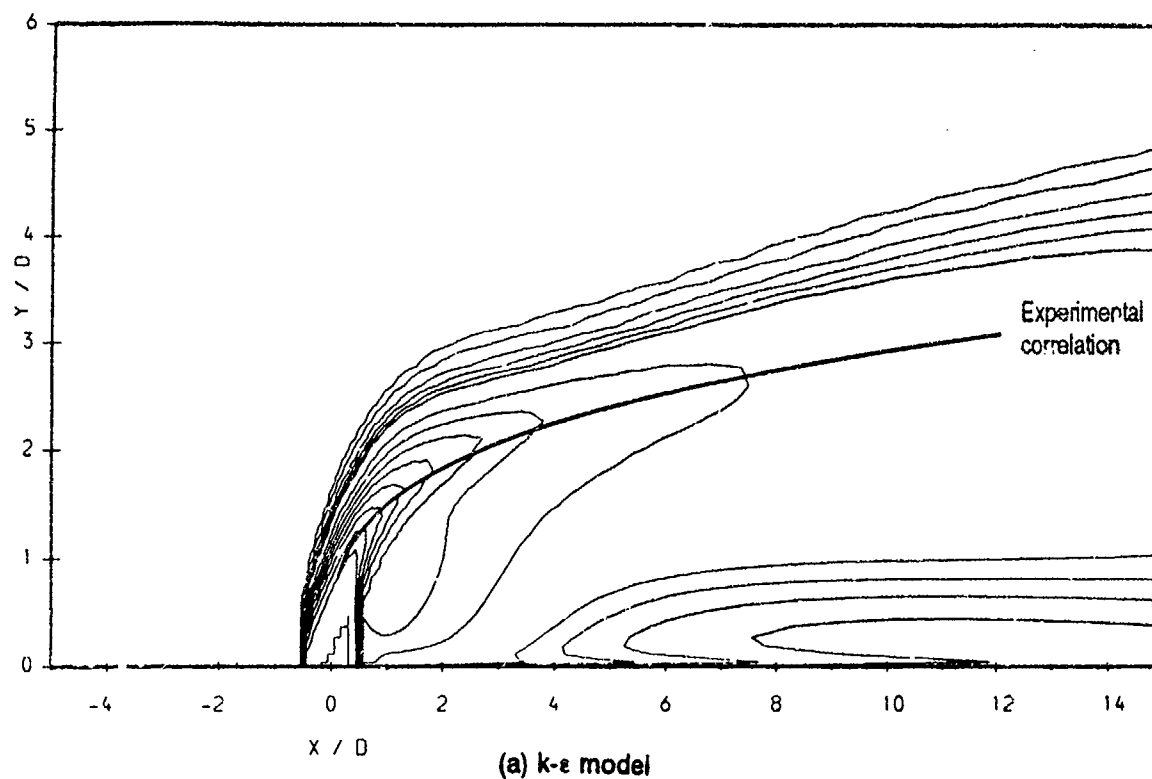
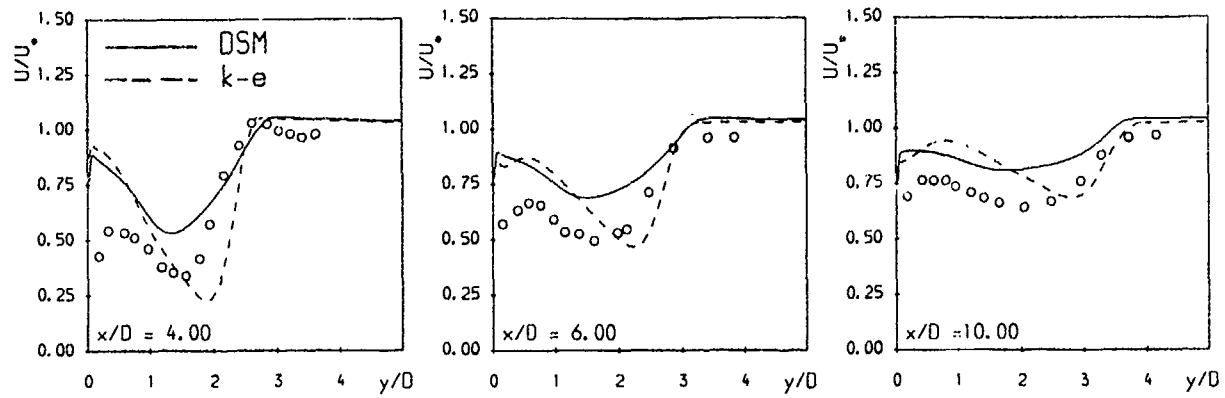
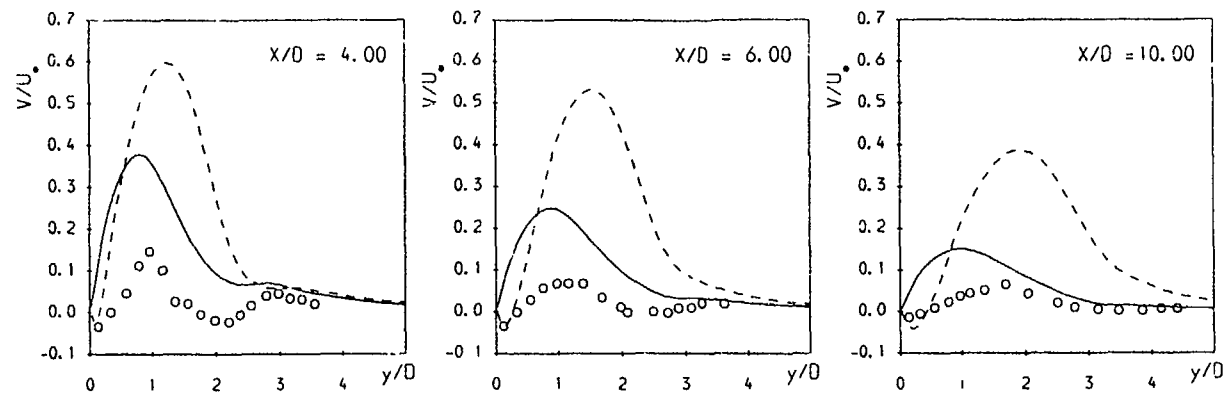


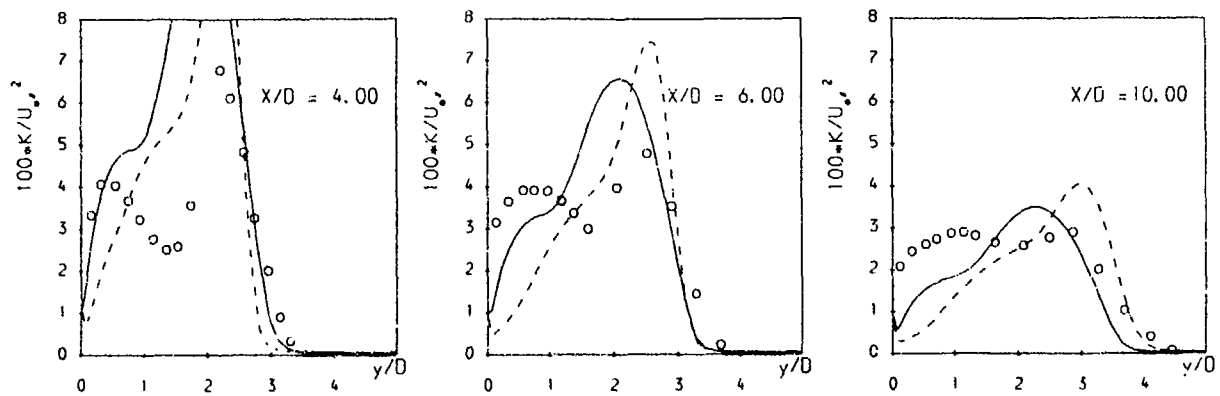
Fig. 10: Single free jet isotherms of excess jet temperature and trajectory (locus of maximum temperature)



(a) Profiles of streamwise (U) velocity across jet-centre plane at three streamwise positions



(b) Profiles of transverse (V) velocity across jet-centre plane at three streamwise positions



(c) Profiles of turbulence energy across jet-centre plane at three streamwise positions

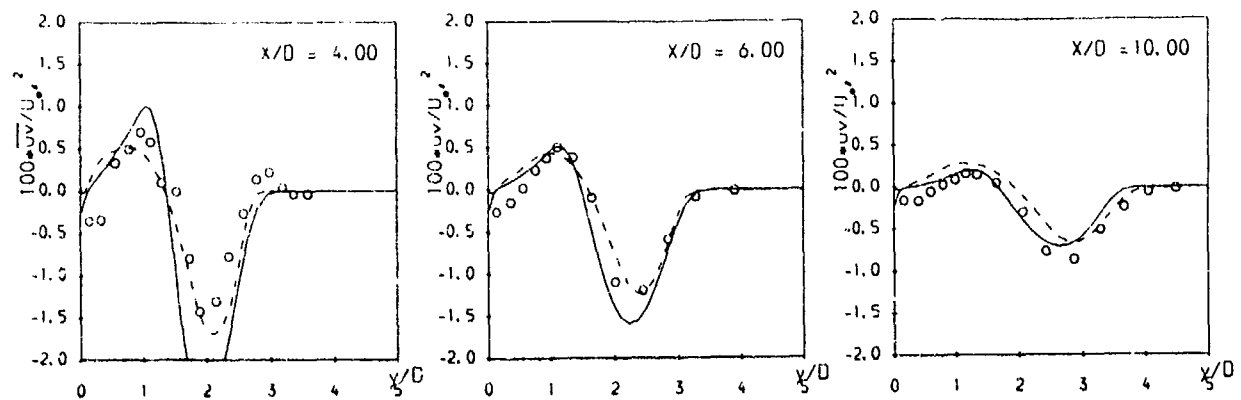
(d) Profiles of shear stress uv across jet-centre plane at three streamwise positions

Fig. 11: Single free jet: response to turbulence modelling

Predictions of Momentum and Scalar Fields in a Jet in Cross-Flow using First and Second Order Turbulence Closures

J. Alvarez and W.P. Jones

Chemical Engineering Department, Imperial College, Prince Consort Road, London SW7 2BY

R. Seoud

Engine Systems Division, Aerospace and Propulsion Department, DRA, Pyestock, Hants. GU14 0LS
UK

SUMMARY

The k- ϵ model and a second moment closure have been applied to the calculation of a slightly heated jet issuing into a cross-flow. Two jet to cross-flow velocity ratios were considered. An assessment of the model performance is made difficult by the high turbulence intensities observed in the recirculation region in the lee of the jet and consequent uncertainty in the hot-wire measurements. Overall the second moment closure gives slightly better agreement but the difference between the results obtained with the two models is not large. For the low velocity ratio, results are extremely sensitive to the boundary conditions prevailing at jet inlet. The predicted mean temperature profiles appear to be more strongly dependent on the predicted velocity fields than on the scalar field closure.

LIST OF SYMBOLS

U_i	Mean velocity components (also U,V,W)
x_i	Coordinate components (also x,y,z)
u_i	Fluctuating velocity components (also u,v,w)
ρ	Fluid density
P	Mean pressure
$u_i u_j$	Reynolds stress tensor
$u_i \phi$	Scalar flux
δ_{ij}	Kronecker delta
k	Turbulent kinetic energy
ν	Kinematic molecular viscosity
ν_t	Turbulent eddy viscosity
ϵ	Dissipation rate of turbulence kinetic energy
τ	Time scale
τ_{ij}	viscous stress tensor
μ	Molecular viscosity
σ_ϕ	Turbulent Prandtl/Schmidt number
Φ	Transported scalar property
U_∞	Cross-flow velocity
V_j	Jet velocity
D	Jet diameter
R	Velocity ratio U_∞/V_j

1. INTRODUCTION

Over the past fifty years the description of the interaction of a jet discharging into a cross-flow and its further development has been the subject of a large number of experimental and theoretical works. An understanding of

the flow is relevant to many engineering fields ranging from film cooling of surfaces subjected to high temperatures to a wide number of environmental problems such as the discharge of polluting, flammable or lethal gases into the atmosphere. However, it is the widespread applicability of the flow in the aerospace industry -V/STOL aircraft in transition from vertical to forward flight, guiding of flying devices and combustion chamber design for gas-turbine engines- which has motivated much of the research in this field.

The numerical solution of the Reynolds averaged Navier-Stokes equations together with turbulence closures based on the eddy-viscosity concept represents a widely used method for predicting this configuration and provides a detailed and comprehensive description of the flow [1-14]. However, the approach is subject to a number of potential errors and discrepancies between predicted and measured results often arise. In some cases these discrepancies can be attributed to numerical errors associated with the discretisation of the equations -in particular the convection terms for which the highly diffusive first order accurate upwind scheme has often been used- and to a lack of the appropriate computer resources needed to deal with meshes involving a large number of nodes. Limitations in the eddy-viscosity approach are undoubtedly also a major source of error. For these reasons recent work has focused on the application of higher-order accurate schemes for discretising the convection terms and on second moment turbulence closures which overcome the limitations inherent to eddy-viscosity modelling.

Leonard's second-order accurate convection scheme, QUICK [15], has been tested in conjunction with the k- ϵ model by Savory et al. [10], Ince and Leschziner [11] and Alvarez and Jones [14]. As is well known QUICK can give rise to boundedness problems (wiggles) in regions where solutions vary rapidly and this effectively prevents its use in the equations describing definite-positive and turbulence quantities. Savory et al. [10] and Alvarez and Jones [14] used QUICK in the momentum equations while hybrid upwind-central differencing was applied in the k and ϵ equations. In order to apply QUICK in the k and ϵ equations, Ince and Leschziner [11] constructed a scheme (LODA) that blends QUICK and the unconditionally stable upwind differencing. However, Alvarez [16], in a similar approach, observed that this blending scheme, while generating bounded solutions, resulted too often to upwind differencing and consequently corresponded to a first-order accurate scheme over a substantial region. Alvarez and Jones [14] also applied the bounded and second order accurate TVD scheme of Van Leer [17] to the discretisation of the

convection terms. They found that (i) the TVD scheme generated solutions of comparable accuracy to those obtained with QUICK and which remained bounded, i.e. no wiggles; consequently it was applicable equally to the mean flow equations and to turbulence quantities and (ii) it was computationally much more efficient than QUICK since the latter required a much larger degree of under-relaxation and, hence, computer time for solution.

Demuren [12] and Claus and Vanka [13] attempted to minimise the numerical error by undertaking calculations with a very large number of nodes (2.5×10^6). In order to improve the computational efficiency a multigrid technique was incorporated into the calculation procedure.

While the k-ε model gives good results in a number of cases, deficiencies in the quality of the predictions have been reported and these have been attributed to the inability of eddy viscosity models to accurately represent turbulence anisotropy in complex mean strain fields. Eddy viscosity models, such as k-ε, relate the Reynolds stresses linearly to the local mean rate of strain and neglect, amongst other influences, the transport to which the stresses are subjected. Moreover, measurements indicate that a region with negative eddy-viscosities exists in the surroundings of a jet in cross-flow [18] and this represent a further limitation since negative eddy-viscosity are not permitted in the model.

Calculations with second moment Reynolds-stress transport equation models have been reported by several groups of workers [11,12 and 14]. Ince and Leschziner [11] used the second-moment closure of Gibson and Launder [19] in conjunction with LODA but only a limited number of results were presented. Demuren [12] incorporated the closure proposed by Launder et al. [20] and reported a poor performance in the configuration studied. Alvarez and Jones [14], approximating the convection terms in all transport equations with the TVD scheme of Van Leer, reported calculations with three second moment closures, those of Gibson and Launder [19], Gibson and Younis [21] and Jones and Musonge [22]. It was found that the performance of Gibson and Launder closure was relatively poor whilst the other two resulted in an improved quality of the predictions with the Jones and Musonge closure providing somewhat better agreement with the experimental data.

Computations of the scalar -temperature or concentration-field have also been reported by a number of workers [1,3,4-7,9]. However, in all these cases a gradient transport model was adopted to represent scalar fluxes.

Amongst the large amount of data on a jet in cross-flow existing in the literature, the measurements reported by Ramsey & Goldstein [23], Andreopoulos and Rodi [18] and Andreopoulos [24] provide a detailed coverage of the velocity, scalar and turbulent fields. For this reason, they are regarded as appropriate for the evaluation of the k-ε model and second moment turbulence closures applied to the calculation of the velocity and scalar fields of a jet-in-cross-flow to which the present work is directed.

2. CALCULATION METHOD

2.1 Basic equations

The Navier-Stokes equations along with mass conservation describe the behaviour of any Newtonian fluid. For constant

density flows, the Reynolds averaged form of these equations can be written

$$\frac{\partial U_j}{\partial x_j} = 0 \quad (1)$$

$$\frac{\partial U_i}{\partial t} + U_j \frac{\partial U_i}{\partial x_j} = -\frac{1}{\rho} \frac{\partial p}{\partial x_i} + \frac{\partial (\tau_{ij} - \overline{u_i u_j})}{\partial x_j} \quad (2)$$

where τ_{ij} is the viscous stress tensor given by:

$$\tau_{ij} = \nu \left(\frac{\partial U_i}{\partial x_j} + \frac{\partial U_j}{\partial x_i} \right) \quad (3)$$

The above equations describe the velocity and pressure fields but if a passive scalar, such as temperature in a slightly heated jet, is considered a further equation has to be added:

$$\frac{\partial \Phi}{\partial t} + \frac{\partial (U_j \Phi)}{\partial x_j} = \frac{\partial (J_j - u_j \Phi)}{\partial x_j} \quad (4)$$

here Φ represents any transported scalar quantity, $u_j \Phi$ is the turbulent scalar flux and J_j is the kinematic molecular scalar flux, negligible at high Reynolds and Peclet numbers, but given by:

$$J_j = \frac{\nu}{\sigma_\Phi} \frac{\partial \Phi}{\partial x_j}$$

2.2 Turbulence Models

Turbulence closures at two different levels have been used in the present study to represent the Reynolds stresses and scalar fluxes appearing in equations (2) and (4).

2.2.1 First moment closure

The Reynolds-stress, $\overline{u_i u_j}$, is approximated with the standard k-ε model [18], viz:

$$-\overline{u_i u_j} = \nu_t \left(\frac{\partial U_i}{\partial x_j} + \frac{\partial U_j}{\partial x_i} \right) - \frac{2}{3} k \delta_{ij} \quad (5)$$

where $k = \frac{\overline{u_i u_i}}{2}$ and $\nu_t = C_\mu \frac{k^2}{\epsilon}$

For the scalar fluxes a similar gradient assumption is invoked, i.e.

$$-\overline{u_i \Phi} = \frac{\nu_t}{\sigma_\Phi} \frac{\partial \Phi}{\partial x_i} \quad (6)$$

where σ_Φ is a turbulent Prandtl/Schmidt number.

The turbulent kinetic energy k and its rate of dissipation ϵ are obtained from the modelled transport equations:

$$\frac{\partial k}{\partial t} + U_i \frac{\partial k}{\partial x_i} = \frac{\partial}{\partial x_i} \left(\frac{\nu_t}{\sigma_k} \frac{\partial k}{\partial x_i} \right) - \overline{u_i u_j} \frac{\partial U_i}{\partial x_j} - \epsilon \quad (7)$$

and

$$\begin{aligned} \frac{\partial \epsilon}{\partial t} + U_i \frac{\partial \epsilon}{\partial x_i} &= \frac{\partial}{\partial x_i} \left(\frac{\nu_t}{\sigma_\epsilon} \frac{\partial \epsilon}{\partial x_i} \right) \\ &- C_{\epsilon 1} \frac{\epsilon}{k} \overline{u_i u_j} \frac{\partial U_i}{\partial x_j} - C_{\epsilon 2} \frac{\epsilon^2}{k} \end{aligned} \quad (8)$$

where values of the empirical constants are:

$C_\mu = 0.09$	$C_{\epsilon 1} = 1.44$	$C_{\epsilon 2} = 1.92$
$\sigma_k = 1.0$	$\sigma_\epsilon = 1.3$	$\sigma_\Phi = 1.0$

2.2.2 Second Moment Closure

The Second Moment Closure formulated by Jones and Musonge, presented in [22] and latter improved [25], has been adopted for the Reynolds stresses. It can be written as:

$$\frac{\partial u_i u_j}{\partial t} + U_i \frac{\partial u_i u_j}{\partial x_1} + \left(\frac{\partial U_i}{\partial x_1} u_j + u_j \frac{\partial U_i}{\partial x_1} \right) = C_s \frac{\partial}{\partial x_1} \left(\frac{k}{\epsilon} \frac{\partial u_i u_j}{\partial x_k} \right) + A_{ij} - \frac{2}{3} \delta_{ij} \epsilon \quad (9)$$

where A_{ij} , the fluctuating pressure redistribution term, is given by

$$A_{ij} = -C_1 \tau^{-1} \left(\frac{\partial u_i u_j}{\partial x_1} - \frac{2}{3} \delta_{ij} k \right) + C_2 \delta_{ij} \frac{\partial U_1}{\partial x_m} + C_3 \left(\frac{\partial u_i}{\partial x_j} + \frac{\partial u_j}{\partial x_i} \right) + C_4 \left(\frac{\partial U_i}{\partial x_j} + \frac{\partial U_j}{\partial x_i} \right) k - \left(\frac{3}{2} C_2 + C_3 \right) \left(\frac{\partial U_1}{\partial x_j} + \frac{\partial U_1}{\partial x_i} \right)$$

where the values of the model constants are

$$C_1 = 3.0 \quad C_2 = -0.44 \quad C_3 = 0.46 \quad C_4 = -0.23$$

At this level of closure the turbulence energy dissipation rate, ϵ , is obtained from:

$$\frac{\partial \epsilon}{\partial t} + U_i \frac{\partial \epsilon}{\partial x_1} = C_\epsilon \frac{\partial}{\partial x_1} \left(\frac{k}{\epsilon} \frac{\partial \epsilon}{\partial x_m} \right) - C_{\epsilon 1} \frac{\epsilon}{k} \frac{\partial U_1}{\partial x_m} - C_{\epsilon 2} \frac{\epsilon^2}{k} \quad (10)$$

where the model constants are assigned the values:

$$C_s = 0.22 \quad C_\epsilon = 0.18 \quad C_{\epsilon 1} = 1.40 \quad C_{\epsilon 2} = 1.90$$

In order to ensure that the above model satisfies realizability and predicts non-negative normal stresses under all circumstances, the terms involving C_2 and C_4 are multiplied by a function F expressed as:

$$F = \text{Minimum}\{1.0, 5R\}$$

where

$$R = 1 + \frac{9}{8} (b^3 - b^2)$$

and where

$$b^2 = b_{ij} b_{ij}, \quad b^3 = b_{ij} b_{ik} b_{jk}$$

with

$$b_{ij} = \left(\frac{u_i u_j}{k} - \frac{2}{3} \delta_{ij} \right)$$

R varies between 0 and 1. It takes the value of unity in isotropic turbulence and is zero in the two-dimensional turbulence limit.

The modelled form of the scalar flux equation proposed by Launder and Samaraweera (26) has been used to obtain the

$u_j \phi$ correlations. It reads

$$\frac{\partial u_j \phi}{\partial t} + U_j \frac{\partial u_j \phi}{\partial x_j} + \left(\frac{\partial U_j}{\partial x_1} \phi + u_j \frac{\partial U_j}{\partial x_1} \right) = C_s \frac{\partial}{\partial x_j} \left[\frac{k}{\epsilon} \left(\frac{\partial u_j \phi}{\partial x_1} \right) \right] - C_{\phi 1} \frac{\epsilon}{k} u_j \phi + C_{\phi 2} u_j \phi \frac{\partial U_j}{\partial x_j} \quad (11)$$

and the value of the constants are

$$C_{\phi 1} = 3.0 \quad C_{\phi 2} = 0.33$$

2.3 Numerical Procedure

The numerical solution method utilises a staggered mean velocity (also shear stress and scalar flux in the second moment closure calculations) storage arrangement to prevent odd/even node uncoupling of the solutions. A linearised implicit conservative difference scheme was used with the pressure being obtained by a pressure correction algorithm. The time dependent forms of the equations were solved with steady flow solutions being obtained by calculating for a sufficient time interval. The second order accurate and unconditionally bounded TVD formulation of Van Leer [17] was used to discretise the convection terms while central differences were used for all other spatial derivatives. Under the assumption of a constant (positive) velocity and mesh spacing and following the node notation given in figure 1, the discretisation of the convection term can be written in the form

$$U_j \frac{\partial \Phi}{\partial x} \approx \frac{U}{\Delta x} \left[(\Phi_i - \Phi_{i-1}) + \frac{\Psi_{i+1/2}}{2} (\Phi_{i+1} - \Phi_i) - \frac{\Psi_{i-1/2}}{2} (\Phi_i - \Phi_{i-1}) \right]$$

where

$$\Psi_{i+1/2} = \frac{r_i + |r_i|}{1 + |r_i|}, \quad \Psi_{i-1/2} = \frac{r_{i-1} + |r_{i-1}|}{1 + |r_{i-1}|},$$

and

$$r_i = \frac{\Phi_i - \Phi_{i-1}}{\Phi_{i+1} - \Phi_i} \quad \text{and} \quad r_{i-1} = \frac{\Phi_{i-1} - \Phi_{i-2}}{\Phi_i - \Phi_{i-1}}$$

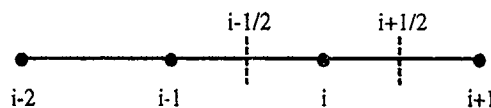


Figure 1. Nodes distribution

The TVD scheme has been implemented in the manner suggested by Zhu [27]; the upwind contribution was treated implicitly with the anti-diffusion component involving the limiter Ψ being handled explicitly.

The boundary conditions applied assumed symmetry along the central, lateral and upper planes of the domain boundary and fixed values were specified at the inflow plane and the jet. At the outflow plane a zero-gradient boundary condition was imposed and at the lower wall boundary solutions were patched onto fully turbulent, local equilibrium wall law profiles.

A full description of the computer program used and method of implementation is provided in [16].

3. TEST CASES

In a previous publication, Alvarez and Jones [14] computed the flow configuration investigated experimentally by Crabb [28] to evaluate the efficiency of the second-order TVD discretisation scheme of Van Leer and to appraise the performance of the Jones and Musonge velocity field turbulent closure. The results displayed a reasonable level of agreement with measured profiles; for mean profiles the agreement was similar to that obtained with the k - ϵ model but the second moment closure provided a better representation of the turbulence field. In order to complement that work, further calculations have been completed with the aim of assessing a second moment closure for scalar properties and to investigate the

performance of the Reynolds stress closures in a case where the near field of the jet in cross-flow is influenced more strongly by turbulence rather than by inviscid dynamics. For this reason the low velocity ratio case ($R=0.5$) of Andreopoulos and Rodi, for which extensive data on mean and turbulent quantities is available, has been selected. This has also been used together with the data of Ramsey and Goldstein to investigate the $k-\epsilon$ model and the second moment closure for the scalar (temperature).

The two test-cases selected have been computed using the $k-\epsilon$ model and the second moment closures. Details of the experimental conditions, computational domain and grid size are given in Table 1. In figure 2, the configuration is illustrated together with the orientation of the coordinate system. In both sets of experiments the velocity distributions were measured by hot-wire anemometry.

Table 1.

	Ramsey & Goldstein [23]	Andreopoulos & Rodi [18]
D (cm)	2.35	5.0
V_j (m/s)	60	6.95
U_∞ (m/s)	30	13.9
R	2	0.5
$T_j - T_\infty$ (°)	55	4
calculation domain	$-2 \leq x/D \leq 9$ $0 \leq y/D \leq 6$ $0 \leq z/D \leq 3$	$-2 \leq x/D \leq 9$ $0 \leq y/D \leq 6$ $0 \leq z/D \leq 3$
grid-size	72x39x21	88x27x20

Also, the buoyancy forces, arising because of the difference in temperature between the jet and the cross-stream, are negligible compared to inertial forces and can therefore be ignored.

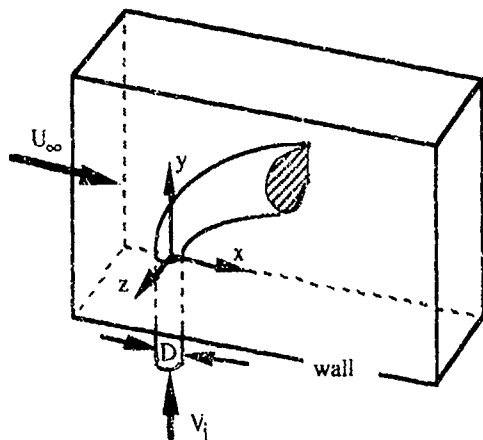


Figure 2. Jet in cross-flow configuration

4. RESULTS

A recirculating region in the downstream vicinity of the jet is one of the features of the jet in cross-flow configuration and is confirmed by measurements by laser-Doppler anemometry [23] and flow visualization studies, for example [22, 29-30]. For a velocity ratio $R=2$, Sugiyama and Usami [29] reported a region of reverse flow extending from the edge of the jet to approximately $x=3D$. Since hot-wire anemometry is not sensitive to flow direction, the measurements downstream and close to the jet inlet must be subject to some uncertainty. This is particularly so for the Ramsey & Goldstein flow, case 1, where a recirculation zone

is likely to have arisen and the measurements taken between the jet and the wall at $x=1.37D$ and $x=3.06D$ are of doubtful validity.

Figure 3 shows a comparison of velocity field predictions with experimental data for the Ramsey and Goldstein flow where all velocities have been normalised with the cross-stream velocity. The differences between the mean profiles predicted with the $k-\epsilon$ model and the second moment closure are somewhat larger than those for the case reported in [14]. The major difference is that the second moment closure predicts the recirculation to extend over a larger region. With the $k-\epsilon$ model the velocity is everywhere positive at $x/D=3.06$ whereas the second moment closure predicts that the recirculation extends just beyond this position in seeming agreement with Sugiyama and Usami's observation. Overall, however, the differences between the two predictions are not too large though the second moment closure gives somewhat better results near the wall.

The measured and predicted profiles of the normal stress, $\overline{u^2}$, are also shown in figure 3 where, as it can be observed, the $k-\epsilon$ model gives much lower values than those predicted by the second moment closure. Overall the results with the latter model are much closer to the measurements particularly near the wall though the maximum arising in the jet at $x/D=3.06$ and $y/D \approx 2.5$ is overpredicted by a factor of around two.

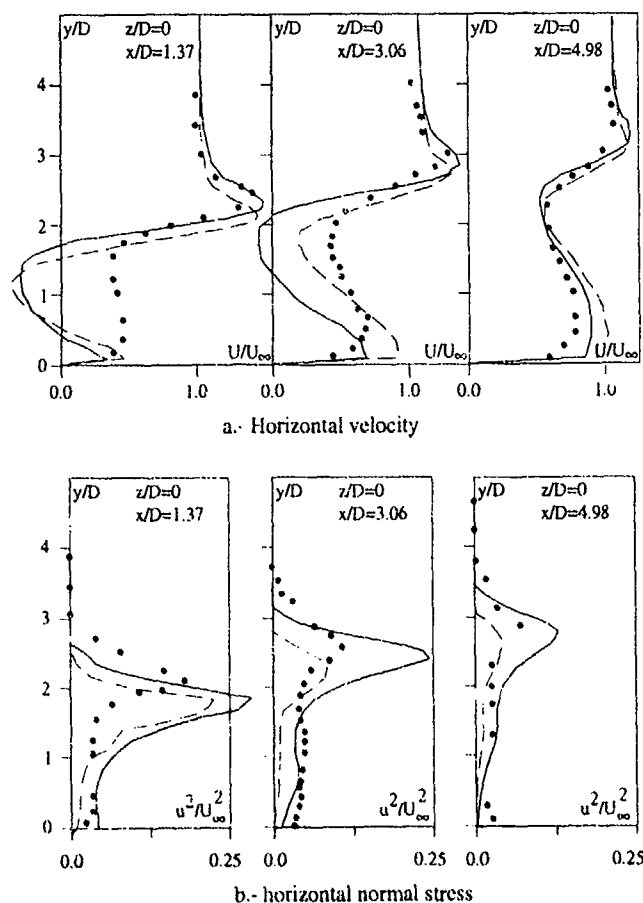


Figure 3. Mean and fluctuating horizontal velocities
 Reynolds-stress turbulence model (—).
 $k-\epsilon$ turbulence model (---).
 Ramsey and Goldstein's Measurements (••••)

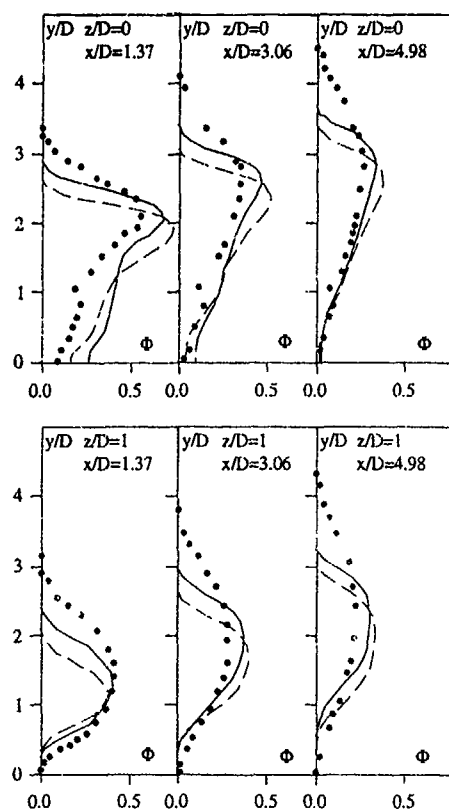


Figure 4. Mean temperatures at $z = 0$ and D . Launder & Sammarawera's turbulence model (—). $k-\epsilon$ turbulence model (---). Ramsey and Golstein's Measurements (••••)

Calculations of the scalar field using the $k-\epsilon$ model and the second moment closures for the scalar equation are presented in figure 4. This figure shows temperature profiles at three downstream distances in the planes corresponding to $z/D=0$ and $z/D=1$. With the exception of the first station in the central plane ($z/D=0$, $x/D=1.37$), both models give similar predictions in the region between the wall and the jet and these are reasonably close to the measured profiles. However, the jet is predicted to spread too slowly into the fluid flowing above it with the consequence that predicted temperature gradients are much steeper than those measured in the region above the jet. This deficiency in the predictions is more evident in the cross-section temperature contours shown in figure 5. It can be observed that the variation of temperature in the vertical and lateral direction is more rapid in the predictions than in the measurements as is clearly shown by the proximity of the contours at the bounds of the jet. Nevertheless, it is again the second moment closure which overall predicts a somewhat more realistic behaviour.

The measurements of mean and turbulent velocities reported by Andreopoulos and Rodi [18] are augmented with two other sets of results obtained in the same configuration: (i) Andreopoulos [24] reports temperature and turbulent heat-flux data and (ii) Andreopoulos [31] measured mean and turbulence quantities at the jet which serve to provide boundary conditions for the calculations.

Since the data provided at the jet exit only covers the central plane, values for the remainder of the jet exit had to be estimated [16]. The non-dimensional mean temperature $\frac{T-T_c}{T_j-T_c}$ and mean heat fluxes $\frac{V}{V_j} \frac{T-T_c}{T_j-T_c}$ have been integrated over the jet inlet to determine their averaged values of 0.73

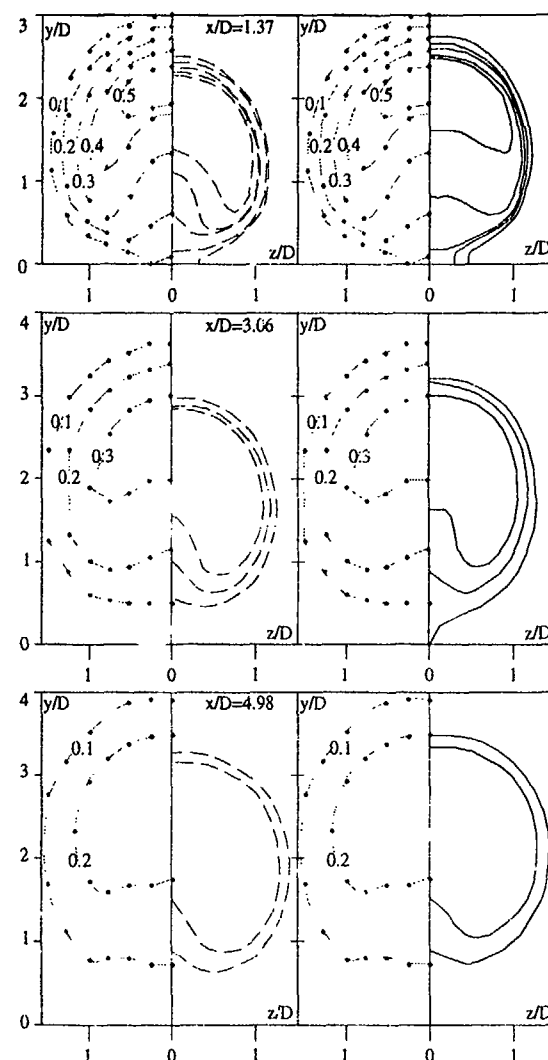


Figure 5. Mean-temperature contours Φ/Φ_j at cross-stream planes. (captions as in previous figure)

and 0.61 respectively. Unfortunately, Andreopoulos could not determine their exact values since there were not enough velocity measurements in the exit plane at different spanwise positions.

Figures 6-8 show at various downstream positions the variation of mean velocities with the distance from the wall. Both turbulence closures predict similar U -, V - and W -profiles above the jet inlet at the central plane though further downstream some discrepancies arise. A possible explanation of this similarity above the jet exit is that inviscid dynamics exert a larger influence than turbulence in the behaviour of the flow, during the initial part of the jet development.

The calculated U and V velocity profiles at the rear edge of the jet inlet ($x/D=0.5$) in the central plane are in excellent agreement with measurements. However, upstream of this station both velocities are consistently overpredicted, with larger discrepancies arising at stations located near the front edge of the jet. Furthermore, this disagreement extends down to the jet inlet which is somewhat surprising since the inlet velocities were specified from measured profiles. A closer examination of the measurements, however, reveals that the inlet profiles reported by Andreopoulos [31] appear not to be entirely consistent with the velocities measured by Andreopoulos and Rodi [18].

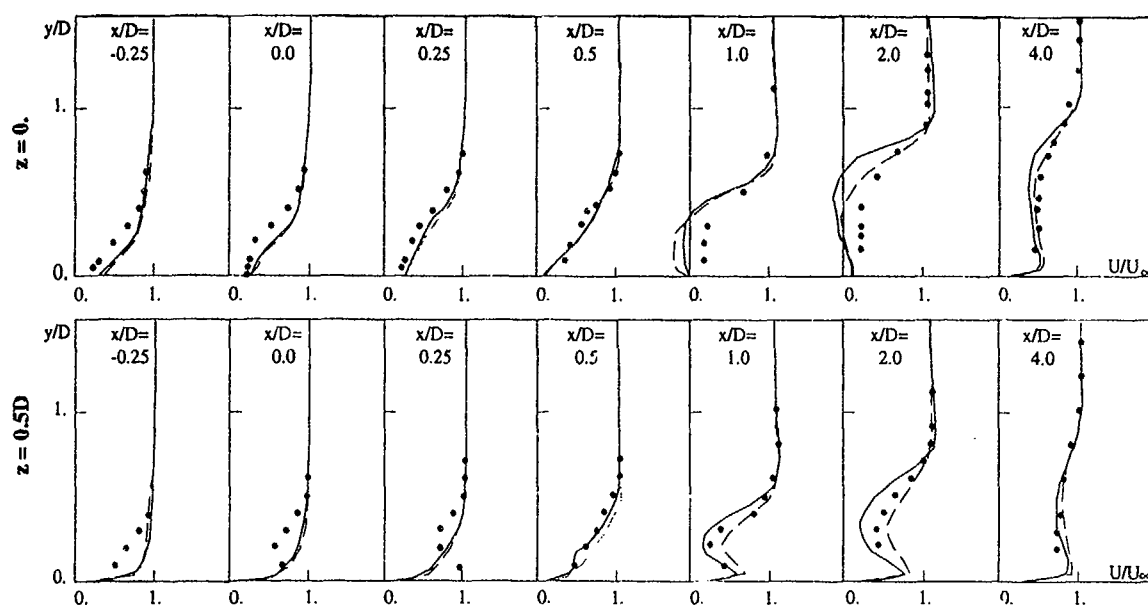


Figure 6. Mean U-velocity at $z=0$, and $z=0.5D$. $R=0.5$. $k-\epsilon$ model (---), RSM (—). Andreopoulos and Rodi's data ($\bullet \bullet \bullet$).

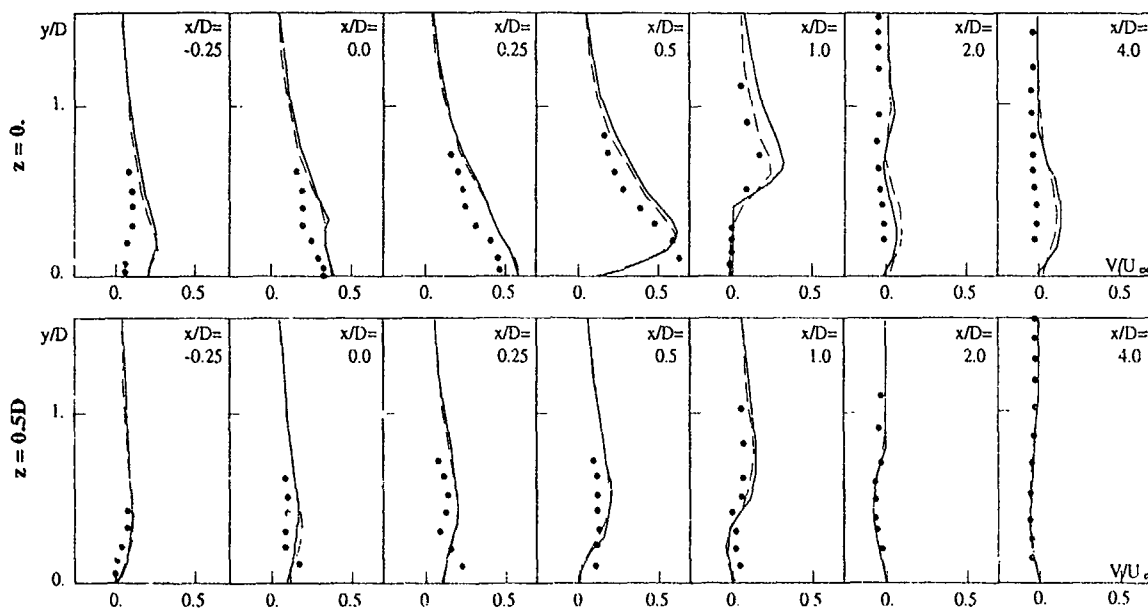


Figure 7. Mean V-velocity at $z=0$, and $z=0.5D$. $R=0.5$. (Symbols as in figure 6)

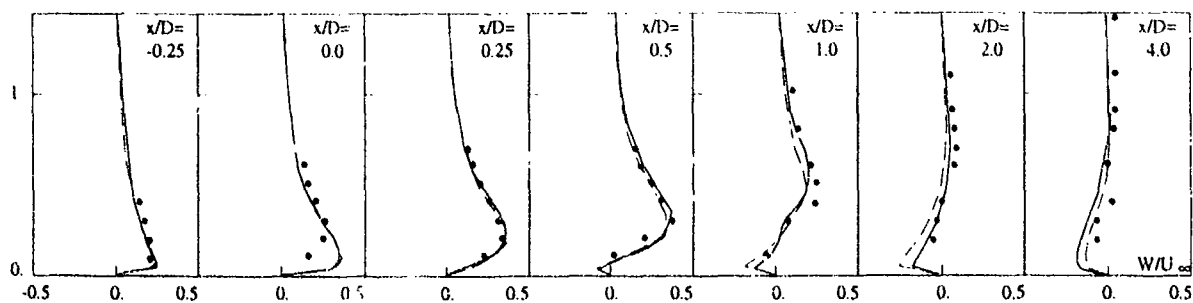


Figure 8. Mean W-velocity at $z=0.5D$. $R=0.5$. (Symbols as in figure 6).

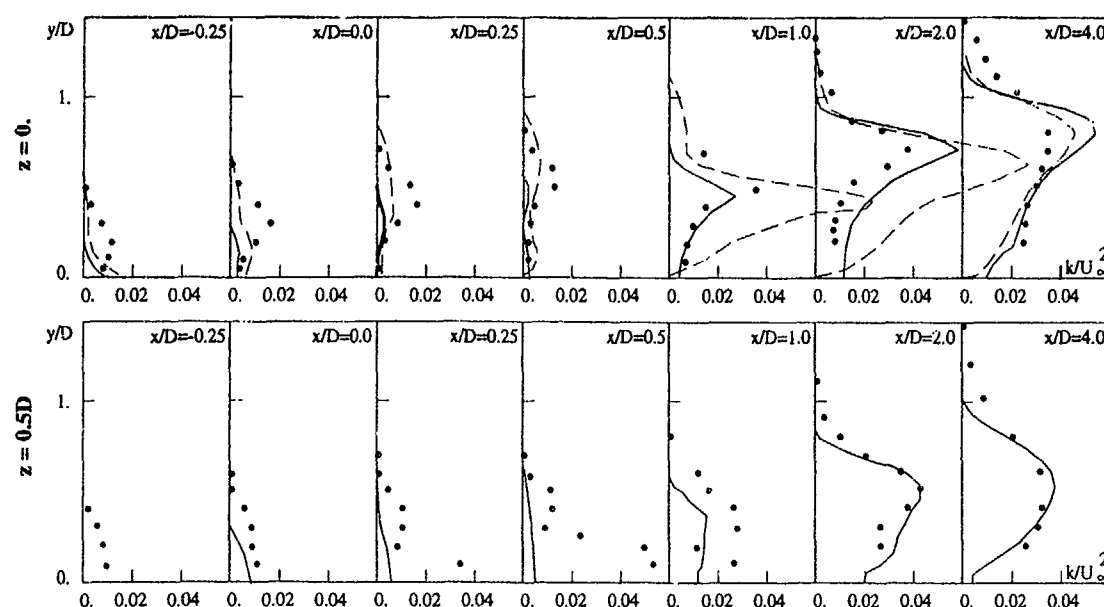


Figure 9. Turbulent kinetic energy at $z=0$, and $z=0.5D$. $R=0.5$. (symbols as in previous figures).

The only major discrepancies between predictions and measurements occur in the profiles in the wake region at $x/D=1.0$ and 2.0 . This is a region of high local turbulent intensity in which a region of recirculation may exist and consequently the measurements must be subject to some uncertainty here. It is probably not possible, therefore, to draw conclusions concerning the models in this region.

The measured V -velocities have appreciable values only in the central plane and upstream of $x/D=1$, elsewhere they are small or negligible. Both turbulence models give similar predictions and slightly overpredict the measurements everywhere throughout the domain but correctly predict the measured jet trajectory with the predicted velocities becoming small beyond $x/D=2$.

The W -velocity profiles (figure 8) in the plane $z=0.5D$ are predicted equally well by both turbulence closures and the level of agreement with measurements is remarkable good. The profiles at $x=D$, $2D$ and $4D$ clearly show an inward motion towards the symmetry plane near the wall and a slight outward motion further away from it, consistent with a vortex motion with a clockwise rotation appearing in this flow configuration.

Figure 9 shows the turbulent kinetic energy profiles at two spanwise planes, i.e. $z=0$ and $z=0.5D$. In the region over the jet inlet, both turbulence closures underpredict the measured data with the $k-\epsilon$ model results being in slightly closer agreement. The turbulent kinetic energy production in this

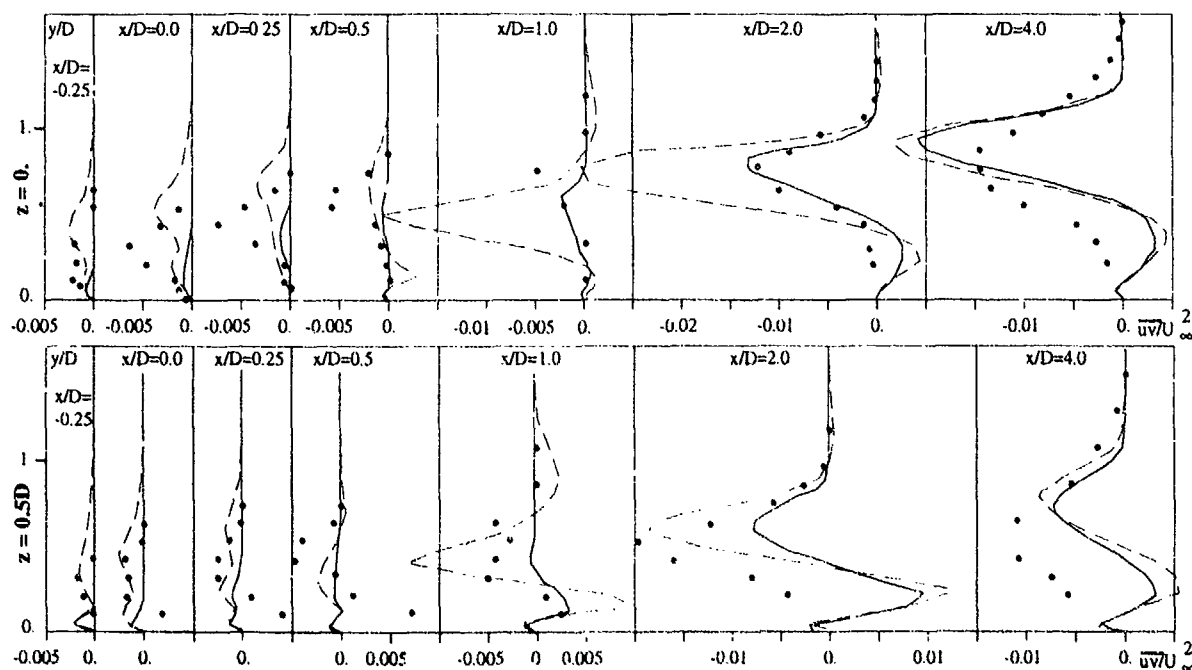


Figure 10. \overline{uv} shear stress at $z=0$, and $z=0.5D$. $R=0.5$.

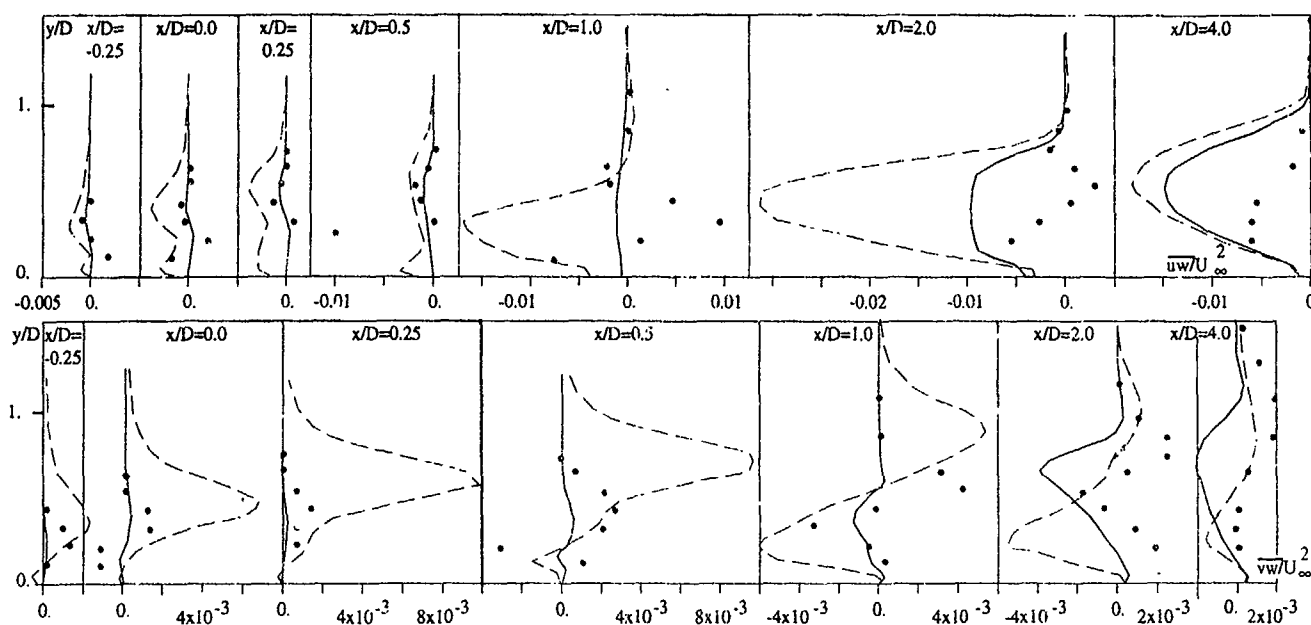


Figure 11. \overline{uw} - and \overline{vw} -shear-stress profiles at $z/D=0.5$.

region is dominated by the mean-velocity gradient component $\partial U/\partial y$. Hence, it can be argued that the disagreement between measurements and predictions of the turbulent kinetic energy are connected, at least partially, with the error in the predicted U -velocity field in this region. For example, in the plane $x=-0.25D$ (figure 6) and for $y/D > 0.25$, it can be observed that both models predict practically undisturbed cross-stream flow, which implies a low turbulence level. Experimentally, however, the influence of the jet is observed up to about $y/D=0.5$ and this is consistent with the measured k -profiles (figure 9). A similar behaviour can also be observed at other stations above the jet inlet.

For the region downstream of the jet inlet where the flow is turbulence-dominated, the Reynolds stress model gives predictions of turbulent kinetic energy which are in very good agreement with measurements. In contrast, the k - ϵ model overpredicts the values everywhere downstream of the inlet by an appreciable amount.

Figure 10 shows the development of the turbulent shear stress \overline{uv} . For reasons of clarity, a scale 4 times larger than that for the kinetic energy has been used. As for the k -profiles, the values in the immediate surround of the jet inlet are not well predicted by any of the turbulence models and the largest values of \overline{uv} appear downstream at the jet-wake interface. In the central plane and downstream of $x/D=1.0$ the results obtained with the second moment closure are much closer to the measurements than the k - ϵ results though appreciable discrepancies are evident.

It is a common feature of the jet in cross-flow configuration that, in the wake region, the fluid close to the wall moves faster than that further away. This has been observed by Crabb [28] for velocity ratios $R=2.3$ and 1.15 where the trend was observed up to 20 diameters downstream of the jet inlet. Andreopoulos and Rodi detected this behaviour for velocity ratio $R=2$, but oddly they did not for $R=1$ and 0.5 . Examination of the production term in the \overline{uv} -shear stress equation (11) suggests that major contribution comes from

$\sqrt{2} \frac{\partial U}{\partial y}$ with the consequence that a decrease of the U -velocity with increasing y would tend to correspond to a region of positive \overline{uv} shear stress close to the wall, as it has been predicted by both turbulence models -relative maxima are predicted close to the wall in both the central and $z=0.5D$ planes- but this is not reflected in the measurements.

Profiles of the two shear stresses, \overline{uw} and \overline{vw} , are shown in figure 11. In this case the level of agreement achieved with both models is poor and there is little to choose between them. Although the reason for this poor agreement cannot be established with certainty, it is almost certainly related to the discrepancies in the predicted mean velocity field discussed earlier.

Figure 12 shows the temperature distribution at $z=0$. In the predicted velocity field the jet does not penetrate sufficiently immediately above the inlet and consistent with this the calculated temperatures in the region above the jet inlet are lower than those obtained experimentally. This can be seen, for example, at $x/D=0$ where both the k - ϵ and the second moment scalar model give similar profiles. An inconsistency, again, seems to appear at $x/D=0.5$ in the data measured by Andreopoulos; at the pipe exit a value very close to unity was measured, whereas at the first location measured above and close to the jet inlet a much smaller value of 0.6 was reported. Although, a recirculation region exists behind the jet, it is very difficult to see how such a rapid variation in temperature could arise in the experiment.

At $x=D$ both models produce similar results and the upper boundary of the jet is acceptably well reproduced while the rest of the jet which has already spread to the wall is overpredicted by about 10%. At the other two further downstream stations, where the maxima of the measured temperature profiles occurs close to the wall, the k - ϵ model predictions are slightly closer to the measurements than those of the second-moment-closure model which seems to maintain the jet maxima over a longer distance.

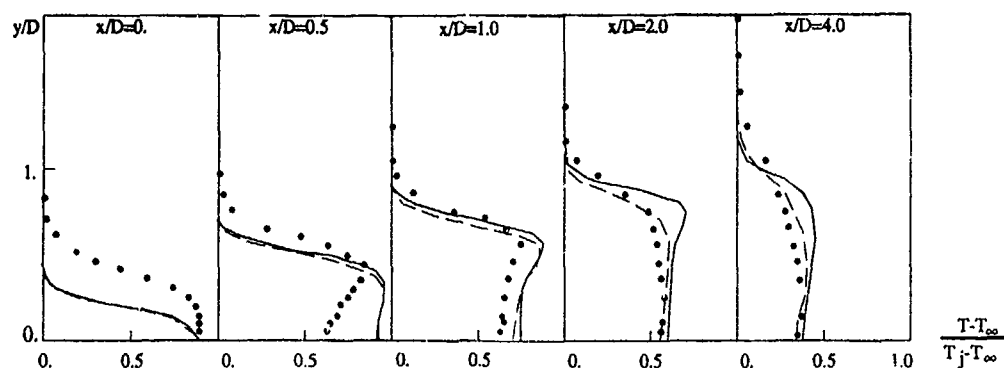


Figure 12. Mean temperature at $z=0$, $R=0.5$.
k- ϵ model (—). Launder & Samaraweera's model (---)

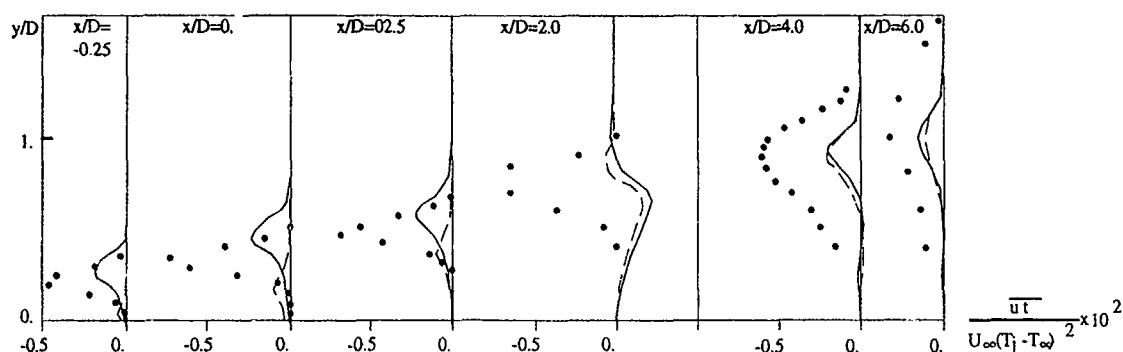


Figure 13. $\overline{u'v'}$ heat-fluxes distribution at the central plane. $R=0.5$.

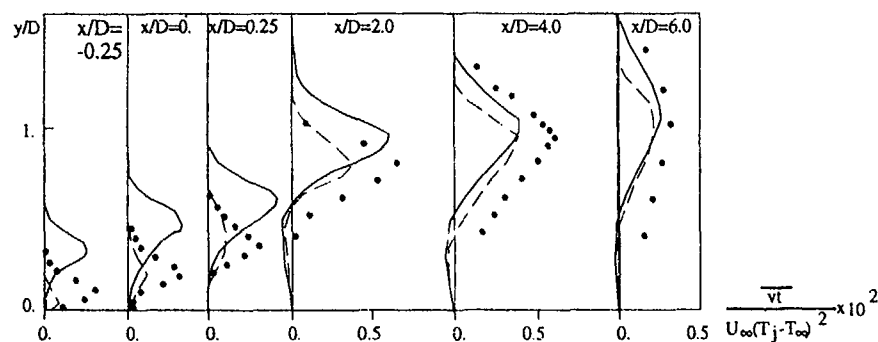


Figure 14. $\overline{v'v'}$ heat-flux distribution at the central plane.

The predicted and measured heat-flux profiles in the central plane are shown in figures 13 and 14. The measured profiles of $u\phi$ are substantially underpredicted by both models though slightly better agreement is evident for the y-direction flux, $v\phi$. Overall, however, the level of agreement is poor. The predicted mean temperature and heat flux profiles are clearly very strongly influenced by the calculated mean velocity field and the discrepancies in this may be responsible, at least in part, for the poor agreement.

5. CONCLUSIONS

The application of the k- ϵ model and a second moment closure to the calculation of the velocity and temperature fields in the surrounds of a jet discharging into a cross-flow for two jet to cross-flow velocity ratios reveals that:

(i) The recirculating region predicted with the Reynolds-stress closure is larger than that obtained with the k- ϵ model for both velocity ratios. The appraisal of the two models performance in this region by comparison with the available measurements is somewhat difficult since the experimental data was obtained with hot-wire probes which are insensitive to flow directions and can give large errors in regions of high local turbulent intensity. The measurements suggest that the local turbulence intensity in this region reached values of up to 85%.

(ii) For the higher velocity ratio, the Reynolds-stress model predicts a slightly larger penetration than the k- ϵ model and is in closer agreement with measurements.

iii) The differences found between the measured and calculated U , V , k and uv fields in the vicinity of the jet inlet for the low velocity case, are clearly associated with uncertainty in the boundary conditions at the jet exit.

(iv) Differences have been reported in the scalar fields obtained with the k- ϵ model and the second moment closure. Some of these, however, are clearly related to the differently predicted mean velocity fields with each model.

It can be concluded that overall both models result in a similar level of agreement with measured profiles.

ACKNOWLEDGMENTS

Support for the work reported in this paper was provided by the Procurement Executive of the Ministry of Defence and this the authors are grateful to acknowledge.

REFERENCES

1. J.C. Chien and J.A. Schetz (1975). "Numerical solution of the three-dimensional Navier-Stokes equations with applications to channel flows and a buoyant jet in cross flow". *J. Appl. Mech.*, vol 42, p 575.
2. S.V. Patankar, D.K. Basu and S.A. Alpay (1977). "Prediction of the three-dimensional velocity field of a deflected turbulent jet". *J. Fluids Engng*, vol 99, p 758.
3. G. Bergeles, A.D. Gosman, B.E. Launder (1978). "The turbulent jet in a cross stream at low injection rates: a three-dimensional numerical treatment". *Numerical Heat Transfer*, vol 1, p 217.
4. W. Rodi and S.K. Srivatsa (1980). "A locally elliptic calculation procedure for three-dimensional flows and its application to a jet in a cross-flow". *Comp. Meth. Appl. Mech. and Eng.*, vol 23, p 67.
5. W.P. Jones and J.J. McGuirk (1980). "Computation of a round turbulent jet discharging into a confined cross-flow". *Turbulent Shear Flows 2*, p 233. Springer-Verlag.
6. A.J. White (1980). "The prediction of the flow and heat transfer in the vicinity of a jet in crossflow". ASME Winter Annual Meeting, Chicago. Paper 80-WA/HT-26.
7. R.W. Claus (1983). "Analytical calculation of a single jet in crossflow and comparison with experiment". NASA Tech. Mem. 83027.
8. R.I. Sykes, W.S. Lewellen and S.F. Parker (1985). "On the vorticity dynamics of a turbulent jet in a crossflow". *J. Fluid Mech.*, vol 168, p 393.
9. M. Fairweather, W.P. Jones & A.J. Marquis (1989). "Predictions of the concentration field of a turbulent jet in a crossflow". *Comb., Sci. & Tech.*, vol 62, p 61.
10. E. Savory, N. Toy, J.J. McGuirk and N. Sakellariou (1990). "An experimental and numerical study of the velocity field associated with a jet in a crossflow". *Proc. 1st Symp. Eng. Turb. Mod. and Exp.*, p 165.
11. N.Z. Ince & M.A. Leschziner (1990). "Computation of three-dimensional jets in crossflow with and without impingement using second-moment closure". *Proc. 1st Symp. Eng. Turb. Mod. and Exp.*, p 143.
12. A.O. Demuren (1990). "Calculation of 3D turbulent jets in crossflow with a multigrid method and a second-moment closure model". *Proc. 1st Symp. Eng. Turb. Mod. and Exp.*, p 155.
13. R.W. Claus and F.P. Vanka (1990). 28th Aerospace Science Meeting, paper 0444.
14. J. Alvarez and W.P. Jones (1993). "Computation of a jet discharging into a cross-flow with a second-moment turbulence closure and a low-diffusive convection-discretisation scheme". *Proc. 2nd Symp. Eng. Turb. Mod. and Exp.* (to appear).
15. B.P. Leonard (1979). "A stable and accurate convective modelling procedure based on quadratic upstream interpolation". *Comp. Meth. Appl. Mech.*, vol 19, p 59.
16. J. Alvarez (1992). PhD Thesis. University of London (in preparation)
17. B. Van Leer (1974). "Towards the ultimate conservative difference scheme. II. Monotonicity and conservation combined in a second-order scheme". *J. Comp. Phys.*, vol 14, p 361.
18. J. Andreopoulos and W. Rodi (1984). "Experimental investigation of jet in crossflow". *J. Fluid Mech.*, vol. 138, p 93.
19. M.M. Gibson and B.E. Launder (1978). "Ground effects on pressure fluctuations in the atmospheric boundary layer". *J. Fluid Mech.*, vol. 86, p 491.
20. B.E. Launder, G.J. Reece and W. Rodi (1975). "Progress in the development of a Reynolds-stress turbulence closure". *J. Fluid Mech.*, vol 68, p 537.
21. M.M. Gibson and B.A. Younis (1986). "Calculation of swirling jets with a Reynolds stress closure". *Phys. Fluids*, vol 29, p 38.
22. W.P. Jones and P. Musonge (1988). "Closure of the Reynolds stress and scalar flux equations". *Phys. Fluids*, vol 31, p 3589.
23. J.W. Ramsey and R.J. Goldstein. (1971). "Interaction of a heated jet with a deflecting stream". *J. of Heat Transfer (ASME)*, November 1971.
24. J. Andreopoulos (1983). "Heat transfer measurements in a heated jet-pipe flow issuing into a cold cross stream". *Phys. Fluids*, vol 26, p 3201.
25. W.P. Jones and A. Pascau (1989). "Calculation of confined swirling flows with a second moment closure". *J. Fluids Eng.*, vol 111, p 248.
26. B. E. Launder and S. Samaraweera (1979). "Application of a second-moment turbulent closure to heat and mass transport in thin shear flows 1. Two-dimensional transport". *Int. J. Heat Mass Transfer*, vol 22, p 1631.
27. J. Zhu (1991). "A low diffusive and oscillation-free convection scheme". *Communications in Applied Numerical Methods*. Vol 7, p 225.
28. D. Crabb (1971). PhD Thesis. University of London.
29. Y. Sugiyama, Y. Usami (1979). "Experiments on the flow in and around jets directed normal to a cross-flow". *Bulletin of the JSME*, Vol 22, No 174, p 1736.
30. J. Foss (1980). "Interaction region phenomena for the jet in cross-flow problem". Rep. DFB80/E/161, Univ. Karlsruhe.
31. J. Andreopoulos (1982). "Measurements in a jet-pipe flow issuing perpendicularly in a cross stream". *J. Fluids Eng.*, vol. 104, p 493.

Navier-Stokes Simulation of Two and Three Dimensional Jets in Crossflow, Effects of Grid and Boundary Conditions

Mehmet Şerif Kavsaoğlu *
İbrahim Sinan Akmandor **
Middle East Technical University
Dept. of Aeronautical Engineering
06531 Ankara, TURKEY

Süleyman Çıray †
TUSAŞ Aerospace Industries,
P.K. 18, 06690, Kavaklıdere,
Ankara, TURKEY

Kozo Fujii §
Institute of Space and Astronautical Science
Yoshinodai 3-1-1, Sagami-hara,
Kanagawa, 229 JAPAN

Abstract

Flowfields of two and three dimensional subsonic jets injected into a crossflow were solved by using a three dimensional Navier-Stokes code (LANS3D)²⁵. Baldwin-Lomax²⁶ turbulence model and the algebraic curved jet turbulence model of Oh and Schetz¹⁴ were used depending on the location in the flowfield. Application of characteristic boundary conditions based on Riemann invariants were found to be useful for the convergence of solutions. Computations made using flat bottom grids showed local pressure singularities around the jet exit. It was shown that these singularities could be removed by using grids with a cavity for the jet entrance. Grid skewness was a particularly effective parameter on the prediction of surface pressures.

Introduction

Injection of jets into a crossflow has numerous applications ranging from waste discharge into rivers to VTOL aircraft. A general description of these flows can be found in Schetz¹ and Abramovich². There are a large number of parameters involved such as jet to crossflow velocity ratio, jet injection angle, single or multiple jets, jet exit geometry, Reynolds and Mach numbers, jet exit velocity and turbulence profiles, swirl, etc. In Figure 1 flowfield description of a round jet injected into a crossflow can be seen⁷.

Experimental data base for the two dimensional jets in a crossflow problem is quite rare^{3,4}. How-

ever, computationally this problem may be more challenging than the three dimensional case due to higher gradients and difficulty of obtaining truly two dimensional experimental data for comparison. On the other hand 3-D jet in a crossflow problem have been studied quite extensively⁵⁻⁹. Reviews of the previous experimental works are available elsewhere^{1,2,10,11,13,14}. Among the most recent contributions investigation of a supersonic jet into a subsonic crossflow¹⁵ can be mentioned. In spite of the many available experimental data still some more experimental work may be needed, particularly for determining the turbulence field in the plume of the jet and in the wake behind the jet.

First Navier-Stokes solution of the jet in a crossflow problem was reported by Chien and Schetz¹⁶. A 2-D solution was made by McGuirk and Rodi by using $k-\epsilon$ turbulence model. Two equation turbulence models was used

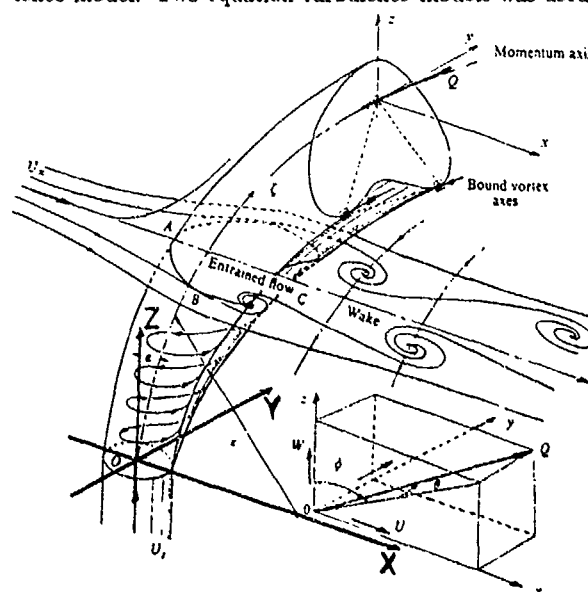


Figure 1. Flowfield description of a round jet in a crossflow⁷.

* Associate Professor

** Associate Professor

† Research Assistant, presently at ARVIN NAA,
1531 Thirteen Street, Columbus, Indiana 47201,
U.S.A.

§ Associate Professor, High Speed Aerodynamics
Division

by Patankar et al.¹⁸ and White¹⁹, TKE model was used in Sykes et al.²⁰ Finite element solution of the parabolized model was reported by Baker et al.²¹ A three dimensional elliptic code using a standard $k - \epsilon$ turbulence model has been widely employed in combustion modelling^{22,23}. Recently an incompressible finite element simulation was reported by Oh and Schetz¹⁴ using an algebraic turbulence model adapted for curved jets.

In the present work 2-D jet in a crossflow experiments of Mikhail, Chu and Savage³ and a case from the circular jet in a crossflow experiments of Kavsaoglu and Schetz²⁸ were chosen as test cases. In the present approach three dimensional, thin layer, Reynolds averaged, compressible Navier-Stokes Equations written in strong conservation form are solved by using LANS3D algorithm^{24,25}. The algebraic turbulence model suggested by Oh and Schetz¹⁴ was used in the jet region. Baldwin-Lomax²⁶ model was used for the other viscous turbulent flow areas which are not covered by the first model. Preliminary runs by using grids with flat bottom showed singularities on surface pressure distribution at the edges of the jet exit. These singularities were removed by using new 2 and 3 dimensional grids which have cavities at their bottom surfaces for jet entrance. Application of characteristic boundary conditions using Riemann invariants at the flow in and flow out planes were found to be helpful for the convergence of the solutions. Computations were performed at IBM 3090 150 E scalar computer installed at TUSAŞ Aerospace Industries (TAI) or at IBM 3090 180 S vector computer installed at Middle East Technical University (METU).

Numerical Method

In this study LANS3D^{24,25} algorithm was used for the solution of compressible thin layer Reynolds Averaged Navier-Stokes Equations written in strong conservation form (for shock capturing purposes). These equations which are transformed from the (x,y,z,t) cartesian coordinates to the general time dependent curvilinear coordinates $\{ \tau = t, \xi = \xi(x,y,z,t), \eta = \eta(x,y,z,t), \zeta = \zeta(x,y,z,t) \}$ read

$$\hat{U}_\tau + \hat{E}_\xi + \hat{F}_\eta + \hat{G}_\zeta = k\hat{S}_\zeta / \text{Re}$$

where

$$\hat{U} = J^{-1} [\rho, \rho u, \rho v, \rho w, e]^T$$

is the vector of dependent variables, J is the Jakobian of the transformation, Re is the Reynolds number, \hat{E} , \hat{F} , \hat{G} are the inviscid flux vectors and \hat{S} is the thin layer viscous flux vector. $k=1$ for viscous flows and $k=0$ for inviscid flows. Complete description of the thin layer equations is documented in Ref. 25. LANS3D program uses

an LU-ADI factorization algorithm with diagonally dominant LU factorization^{24,25}.

Convergence, stability and smoothness of the solutions may depend on the implicit and explicit smoothing factors (ϵ_i and ϵ_e)^{25,29} and also the CFL number:

$$CFL = \frac{\Delta t \sigma_{max}}{\min(\Delta\xi, \Delta\eta, \Delta\zeta)}$$

σ_{max} = maximum eigenvalue.

Boundary Conditions

Various types of boundary conditions were used depending on the location. Here the boundary conditions will be explained in general. Their specific use, if there was any, for two and three dimensional jets will be explained in the corresponding chapters.

Characteristic Approach for the Flow In and Out Planes

For the flow in and flow out planes one dimensional characteristic boundary conditions were used^{29,30}. The associated hyperbolic system of equations is³¹:

$$\partial_t \hat{Q} + A \partial_x \hat{Q} = 0$$

where,

$$\hat{Q} = \begin{pmatrix} \rho \\ \rho u \\ e \end{pmatrix}$$

and

$$A = \begin{bmatrix} 0 & 1 & 0 \\ \frac{(\gamma-3)u^2}{2} & (3-\gamma)u & \gamma-1 \\ [(\gamma-1)u^3 - \gamma \frac{eu}{\rho}] & [\gamma \frac{e}{\rho} - \frac{3(\gamma-1)u^2}{2}] & \gamma u \end{bmatrix}$$

written in flux form, or

$$\hat{Q} = \begin{bmatrix} \rho \\ u \\ p \end{bmatrix} \quad \text{and} \quad A = \begin{bmatrix} u & \rho & 0 \\ 0 & u & \rho^{-1} \\ 0 & \gamma p & u \end{bmatrix}$$

written in primitive variable form. In these expressions ρ is density, u is streamwise velocity component, e is the total energy per unit volume, and p is pressure. Recall that the eigenvalues of the flux Jacobian matrix A are $u, u+a, u-a$. These eigenvalues indicate how information is fed into the domain (Table-1.).

Crossflow Entrance Plane

At the entrance, the crossflow is subsonic and uniform, thus two of the boundary conditions were supplied

	INFLOW		OUTFLOW	
	Subsonic	Supersonic	Subsonic	Supersonic
Number of B.C. to be specified (Analytical B.C.)	2	3	1	0
Number of B.C. by extrapolation (Numerical B.C.)	1	0	2	3

Table 1. Inflow, outflow characteristic boundary conditions³¹.

as input parameters. These are the entrance Mach number, M_∞ and pressure p_∞ . Freestream speed of sound and density were taken as unity ($a_\infty = 1$, $\rho_\infty = 1$). At this boundary the flow is uniform and steady, thus Riemann invariants were used²⁹.

$$R^\pm = V_n \pm \frac{2}{\gamma - 1} a$$

is constant on Mach lines which have slopes

$$\frac{dt}{dx} = \frac{1}{V_n \pm a}$$

where V_n was chosen to be the normal component of the scaled contravariant velocity:

$$V_n = \frac{\eta_x u + \eta_y v + \eta_z w}{(\eta_x^2 + \eta_y^2 + \eta_z^2)^{1/2}}$$

The R_+ Riemann constant was found from the free-stream conditions. R_- was extrapolated from the interior of the flow domain. For this plane $v = w = 0$ and referring to Figure 2, the boundary conditions were set as follows;

$$R_2^- = u_2 - \frac{2}{\gamma - 1} a_2$$

$$R_\infty^+ = u_\infty + \frac{2}{\gamma - 1} a_\infty$$

$$u_1 = 0.5 (R_\infty^+ + R_2^-)$$

$$a_1 = 0.5 \frac{\gamma - 1}{2} (R_\infty^+ - R_2^-)$$

From, $a_\infty = 1$ and $\rho_\infty = 1$

$$a_1 = \sqrt{\gamma \frac{p_1}{\rho_1}}, \quad p_1 = \frac{\rho_1^\gamma}{\gamma}$$

$$\rho_1 = a_1^{2/(\gamma-1)}$$

$$p_1 = \frac{\rho_1^\gamma}{\gamma}$$

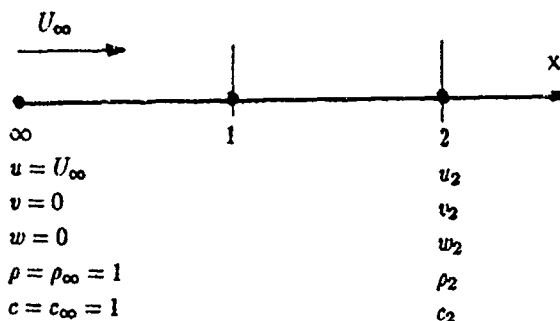


Figure 2. Application of the boundary conditions for the crossflow entrance plane.

$$e_1 = \frac{p_1}{\gamma - 1} + 0.5 \rho_1 u_1^2$$

Indices:

- 1: first station in X direction,
- 2: second station in X direction,
- ∞ : infinity.

Jet Entrance Plane

For 2-D runs these boundary conditions were set in a straightforward way by setting

$$u_1 = 0, v_1 = 0, w_1 = w_{jet}, \rho_1 = \rho_2, a_1 = a_\infty = 1$$

Indices:

- 1: first station in Z direction,
- 2: second station in Z direction,
- ∞ : infinity.

For 3-D runs this boundary conditions were also set in a similar fashion to that of crossflow entrance planes by using the Riemann invariants. Infinity conditions were specified as follows;

$$u_\infty = 0, v_\infty = 0, w_\infty = w_{jet}, \rho_\infty = \rho_2, a_\infty = 1$$

Exit Plane

At the exit the flow properties were less uniform and the unsteady one dimensional characteristic and compatibility equations were used. Writing the equation

$$\partial_t \hat{Q} + A \partial_x \hat{Q} = 0$$

in the transformed uncoupled form by multiplying the equation by X^{-1} , where X is the matrix whose columns are the eigenvectors of A .

$$X = \begin{bmatrix} 1 & \rho/a & \rho/a \\ 0 & 1 & -1 \\ 0 & \rho a & \rho a \end{bmatrix}$$

the equations become

$$X^{-1} \partial_t \hat{Q} + \Lambda X^{-1} \partial_x \hat{Q} = 0$$

where Λ is the diagonal matrix of the eigenvalues. For simplicity we will assume that the X^{-1} has constant elements (during one iteration level):

$$X^{-1} \partial_t \hat{Q} = \partial_t (X^{-1} \hat{Q})$$

$$X^{-1} \partial_x \hat{Q} = \partial_x (X^{-1} \hat{Q})$$

the equation becomes

$$\begin{bmatrix} \rho_t - a^{-2} p_t \\ u_t + (\rho a)^{-1} p_t \\ -u_t + (\rho a)^{-1} p_t \end{bmatrix} + \begin{bmatrix} u & & \\ & u+a & \\ & & u-a \end{bmatrix} \begin{bmatrix} \rho_x - a^{-2} p_x \\ u_x + (\rho a)^{-1} p_x \\ -u_x + (\rho a)^{-1} p_x \end{bmatrix} = \begin{bmatrix} 0 \\ 0 \\ 0 \end{bmatrix}$$

this frozen coefficient form of the nonconservative Euler equations has been put in the form of a set of scalar wave equations. By observing the system of equations above, it can be seen that the quantities;

$$d\rho - a^{-2} dp = 0 \quad \text{along} \quad \frac{dt}{dx} = \frac{1}{u} = \lambda_0 \quad (\text{pathline})$$

$$du \pm (\rho a)^{-2} dp = 0 \quad \text{along} \quad \frac{dt}{dx} = \frac{1}{u \pm a} = \lambda_{\pm} \quad (\text{for Machlines})$$

which are the compatibility equations of the unsteady, one dimensional inviscid flow, are not changing along the pathlines and Machlines which are the characteristic lines. The characteristic and compatibility equations are discretized at the exit boundary using a first order backward difference (see Figure-3. for subscript notation).

$$\Delta t_0 = \lambda_0 \Delta x = \lambda_0 (x_4 - x_3); \text{ for pathlines}$$

$$\Delta t_{\pm} = \lambda_{\pm} \Delta x = \lambda_{\pm} (x_4 - x_1); \text{ for } + \text{ Machlines}$$

$$\Delta t_{\pm} = \lambda_{\pm} \Delta x = \lambda_{\pm} (x_4 - x_2); \text{ for } - \text{ Machlines}$$

$$p_4 - a_4^2 \rho_4 = p_3 - a_3^2 \rho_3; \text{ along pathlines}$$

$$p_4 + (\rho a)_+ u_4 = p_1 + (\rho a)_+ u_1; \text{ along } + \text{ Machlines}$$

$$p_4 - (\rho a)_- u_1 = p_2 + (\rho a)_- u_2; \text{ along } - \text{ Machlines}$$

the inverse marching procedure described in Ref. 30 was applied to the nondimensional equations (Fig. 3). That is for any point on the exit boundary, the correct slopes of the characteristics are first found by interpolating between local velocity and Mach number of two adjacent points at the previous time level. Once the slopes are found, the compatibility equations are solved giving local density ρ , velocity u , and pressure p . The left running characteristics (-) brings the pressure of the surroundings to each exit node. Before the update procedure values along this characteristic (density and velocity) is

taken to be the same as the values of the previous time level. Thus exit pressure is the only value imposed and all other variables are allowed to converge to their steady state values. However, this was the case for three dimensional runs. For 2-D case all the variables at the exit (point 2 in Fig. 3) were specified.

To summarize, in this method first the point-1 is located and the flowfield variables at point-1 are found. Then the plus Riemann invariant is determined as:

$$R^+ = u_1 + \frac{2}{\gamma-1} a_1$$

Then the point-2 is located and the minus Riemann invariant determined as:

$$R^- = u_2 - \frac{2}{\gamma-1} a_2$$

The conditions at point-4 are found as:

$$u_4 = 0.5 (R^+ + R^-)$$

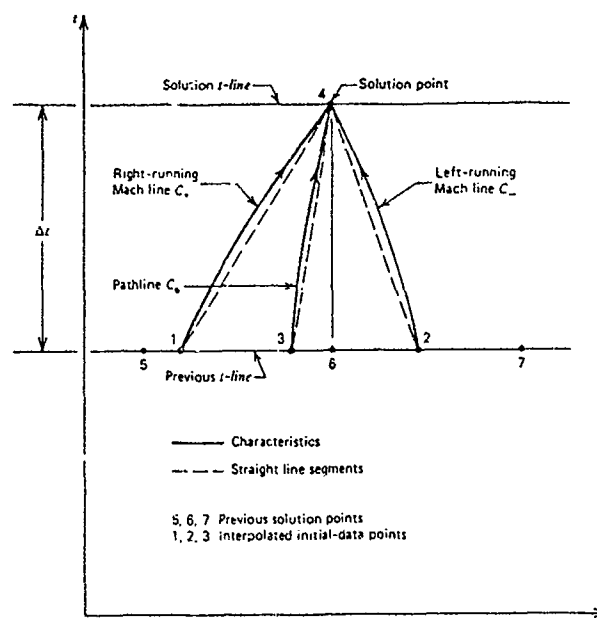


Figure 3. Finite difference grid for inverse characteristic boundary conditions³⁰.

$$a_4 = 0.5 \frac{\gamma-1}{2} (R^+ - R^-)$$

$$\rho_4 = \rho_2 \left(\frac{a_4}{a_2} \right)^{\frac{2}{\gamma-1}}$$

$$p_4 = \frac{\rho_4 a_4^2}{\gamma}$$

$$e_4 = \frac{p_4}{\gamma-1} + \frac{1}{2} \rho_4 (u_4^2 + v_4^2 + w_4^2)$$

Solid Walls

For these planes boundary conditions were specified as follows:

$$u_1 = v_1 = w_1 = 0,$$

$$p_1 = p_2$$

ρ_1 = Extrapolated from station 2 and station 3 by properly scaling with the local Jacobian.

Indices:

- 1: station on the wall,
- 2: second station above (below) the wall,
- 3: third station above (below) the wall.

Top Plane

For open top plane of 3-D case boundary conditions could be applied in two ways. First, the flowfield variables could be extrapolated from the station below. Second, the flowfield variables could be set equal to the freestream conditions. Both approaches were tested and found to be suitable. However, it was felt that the first approach under some conditions could lead to the divergence of the solutions. Then the second approach was preferred for the results which will be presented.

Side Planes

Initial runs of the three dimensional problem was performed by using a rectangular half grid. For the side

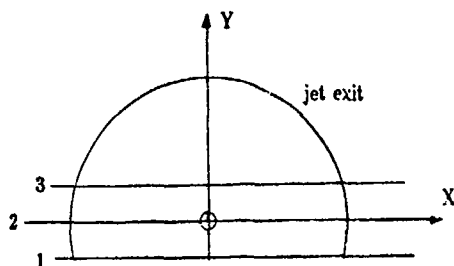


Figure 4. Application of the boundary conditions in the symmetry plane (not to scale).

plane which is away from the jet exit, flowfield variables were extrapolated from the neighbouring inner station. For the side plane which is next to the symmetry plane the boundary conditions were applied referring to Figure 4. as follows;

$$u_1 = u_3, v_1 = -v_3, w_1 = w_3, \rho_1 = \rho_3, e_1 = e_3.$$

Indices:

- 1: first station in Y direction,
- 3: third station in Y direction,

Turbulence Modelling

Two different turbulence models were used depending on the location. An algebraic turbulence model for curved jets proposed by Oh and Schetz¹⁴ was used for the jet region and Baldwin-Lomax²⁶ model was used for the remaining

part of the turbulent flow near solid boundaries. Oh and Schetz's model adopts the three dimensional, rectangular free jet model suggested by Sforza et al.²⁷

Computation of a Two Dimensional Jet in a Crossflow

Preliminary computations of a 2-D jet in a crossflow by using a grid with flat bottom showed singularities on surface pressure distribution. These preliminary runs were made for an arbitrary case for which a jet enters into a crossflow which is not bounded from above. Application of the boundary conditions for the preliminary run is shown in Fig. 5 and the surface pressure distribution is shown in

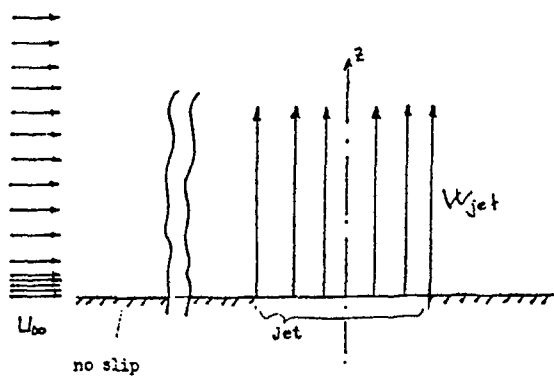


Figure 5. Application of the boundary conditions for the preliminary runs.

SLOT JET, MINF=0.1, MJET=0.4

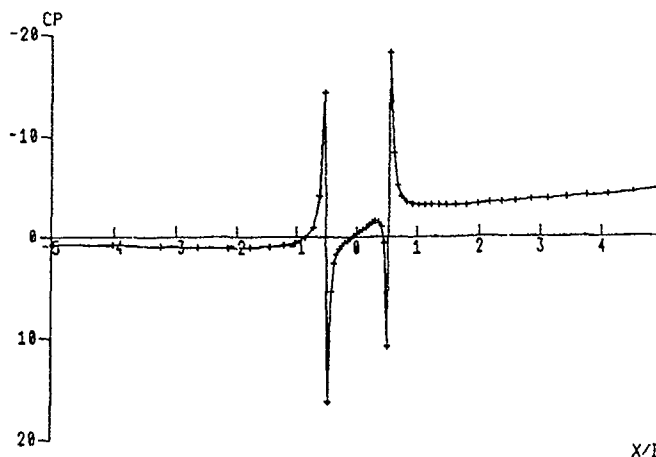


Figure 6. Surface pressure distribution obtained for a 2-D jet in a crossflow (not bounded from above)

Fig. 6. The two positive peaks seen at the edges of the jet exit can not be considered as physical. This result was probably due to imposing jet entrance boundary conditions in a non-physical manner. Then it was decided to make a new grid which has a cavity for the jet entrance. The 2-D jet in a crossflow results which will be presented here were obtained by using this new grid. Computations were made for a laminar ($\mu_t = 0$) and a turbulent jet in order to see the effect of turbulence modelling.

Experimental Data for Comparison

A case from the Mikhail, Chu, Savage³ experiments were chosen as the test case. Geometry and flowfield definition of these experiments are shown in Fig. 7. These are actually the flow visualisation experiments made in an open

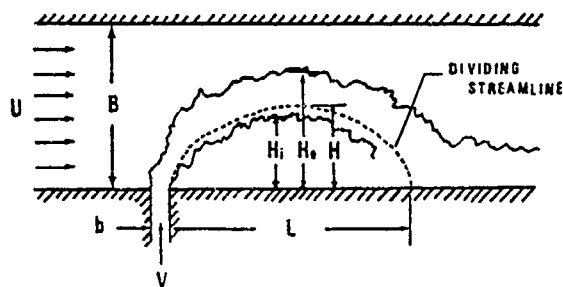


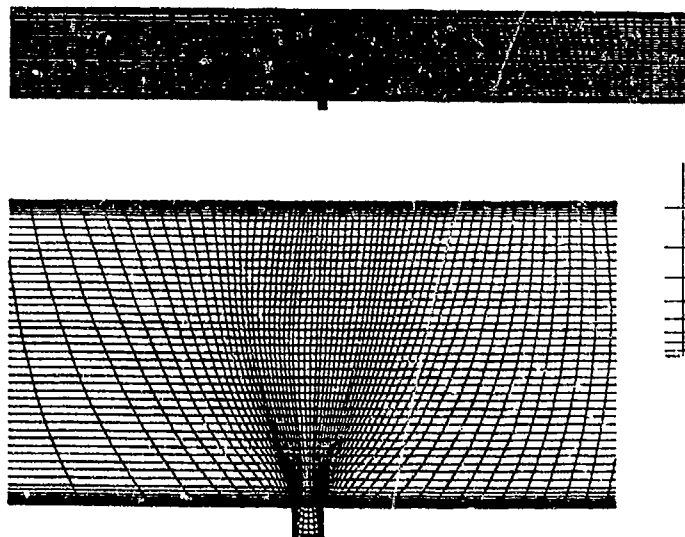
Figure 7. Geometry and flowfield definitions of Mikhail, Chu and Savage experiments³.

top water channel. It was stated³ that when the channel height was sufficiently high such experiments could represent 2-D flowfields. For the present computations jet width to channel width ratio (b/B) was chosen as 0.105 and jet to crossflow velocity ratio was chosen as 4. Thus the parameter:

$$\frac{V^2 b}{U^2 B} = 1.68.$$

Grid

The grid which has a cavity for jet entrance has the dimensions of $116 \times 5 \times 65$ in ξ , η , ζ directions respectively. In physical coordinates the grid extends in the range $-35 \leq x/b \leq 40$, $0 \leq z/b \leq 9.524$ (except the cavity), and $0 \leq y/b \leq 4$. Since it was made for the solution of a 2-D problem, the grid crosssections are identical in $y = \text{constant}$ planes. Details of this grid are presented in Fig. 8.



This is a mixed algebraic-elliptic grid. Some properties of the initial algebraic grid was preserved by solving the ϕ , ψ parameters of the elliptic grid generation program. For example $\xi = \text{constant}$ lines are parallel lines and the initial grid was totally conserved for the cavity region.

Computational Details

For the turbulent jet computations the turbulence models were applied as follows. First the Baldwin-Lomax²⁶ model permitted to work up till $z/d=5$. Then the curved jet model of Oh and Schetz¹⁴ overwrite for the regions of its applicability. In this way some sort of turbulence prediction was made for the entire jet and recirculation regions behind the jet entrance.

Application of the boundary conditions are shown in Figure 9. Characteristic boundary conditions were applied at the crossflow entrance and at the flow exit planes, but ordinary boundary conditions were applied at the jet entrance plane. A velocity profile was specified at the jet entrance. This profile is shown in Figure 10 together with the equivalent volume flow uniform profile. Magnitude of the flow exit velocity ($u = 9.071$) was found from a simple integral analysis using the incompressible continuity equation. The pressure coefficient at the infinity (crossflow entrance) was taken as zero. Then the pressure coefficient

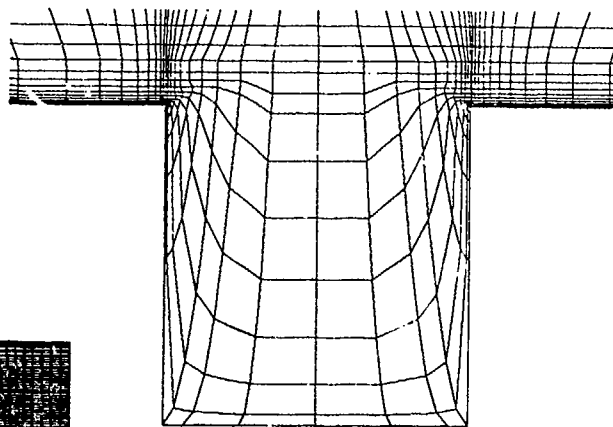


Figure 8. Grid for the 2-D jet, $116 \times 5 \times 65$.

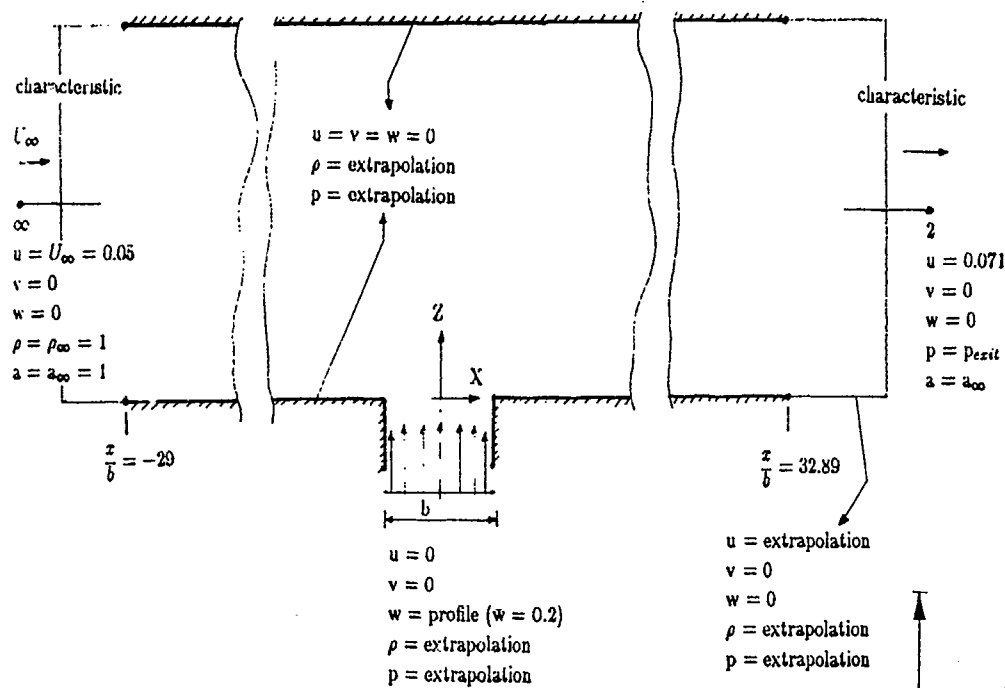


Figure 9. Application of the boundary conditions for the 2-D jet.

at the exit (point 2 in Figure 9) can be calculated from incompressible Bernoulli equation as ($C_{p,exit} = -1.016$). However, for this channel flow, viscous losses are important and the $C_{p,exit}$ was taken lower than the value calculated from the Bernoulli equation. In Figures 10 and 11 convergence histories for a 20000 iteration laminar ($\mu_t = 0$) and for a 20100 iteration turbulent runs are presented. In these figures the upper curve shows the convergence of the L2 norm of the residual and the lower curve shows the convergence of the maximum residual. For both cases and for the first 16000 iterations $C_{p,exit}$ was taken as $C_{p,exit} = -1.92$. For the first 12000 iterations the characteristic boundary conditions were applied as explained in the boundary conditions section. That means at the crossflow entrance the plus and minus Riemann invariants were calculated as

$$R_{\infty}^{+} = U_{\infty} + \frac{2}{\gamma - 1} a_{\infty}$$

$$R_2^{-} = u_2 - \frac{2}{\gamma - 1} a_2$$

and at the exit

$$R^{+} = u_1 + \frac{2}{\gamma - 1} a_1$$

$$R^{-} = u_2 - \frac{2}{\gamma - 1} a_2$$

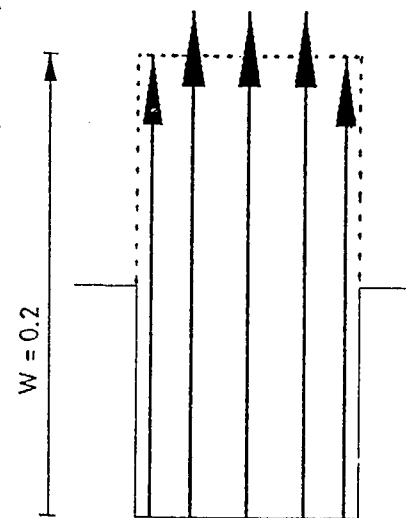


Figure 10. 2-D jet exit velocity profile, dotted lines show the equivalent volume flow uniform profile.

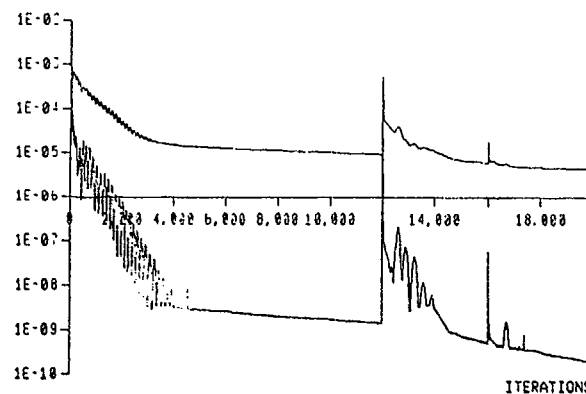


Figure 11. Convergence history for the 2-D laminar jet. Upper curve represents the L2 norm of the residual, lower curve represents the maximum residual.

However, when the surface pressure predictions checked for the laminar and turbulent cases these curves seemed like shifted upwards. Also there were two positive peaks right

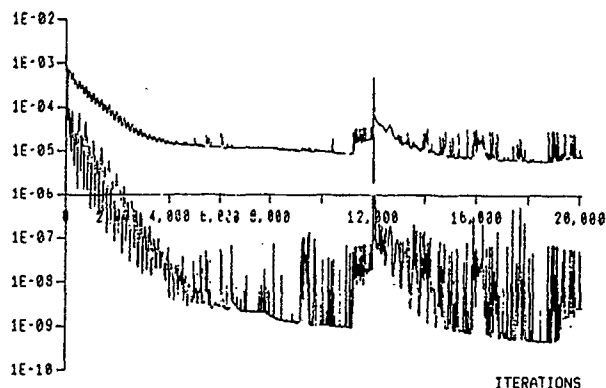


Figure 12. Convergence history for the 2-D turbulent jet. Upper curve represents the L2 norm of the residual, lower curve represents the maximum residual.

at the right and left boundaries. Then it was decided to give more weight to the specified ∞ and exit conditions. At the entrance in calculation of R_2^- , a_2 was replaced by a_∞ and at the exit in calculation of R^+ , a_1 was replaced by a_2 . After 16000th iteration it was observed this process was quite effective for shifting the curves downwards. We may say that particularly the change made at the exit plane was effective. Also the positive peak at the exit con-

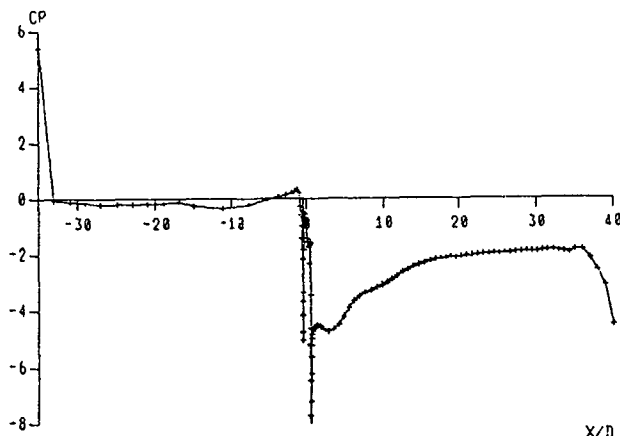


Figure 13. Pressure distribution prediction along x axis, 2-D, turbulent, after 20100 iterations.

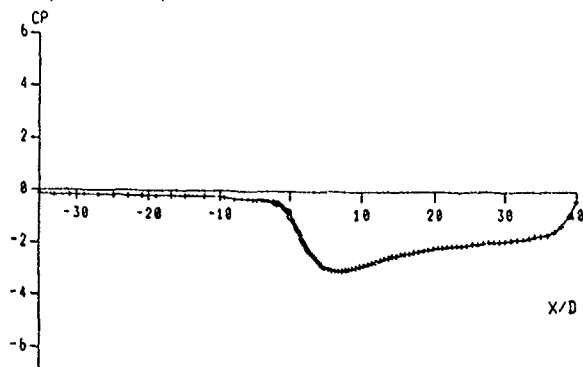


Figure 14. Pressure distribution in x direction, $z/b=4.76$ line 2-D, turbulent, after 20100 iterations.

verted itself to a negative peak (Figure 13) and its magnitude was much lower than the previous one. Considering the pressure peaks which occur at the flow entrance and exit boundaries, they are actually local singularities which are located at the corners of the computational grid. They may be due to the sudden application of the no-slip condition. They may also be due to the invalidity of the characteristic boundary conditions, which are based on inviscid equations, around these highly viscous regions. Nevertheless they may be considered as local singularities which are not harmful for the regions away from them. In Figure 14 the pressure distribution along the $z/b=4.76$ line is presented. This line is located at about the middle of the channel. Since it is away from the corners of the computational grid, no strange pressure peaks at the flow entrance and exit planes can be observed.

A 4000 iteration laminar run took about 3 hours and 42 minutes of CPU time and about 26 Megabytes of RAM at the M.E.T.U. machine (IBM-3090 180S, vector, single CPU). A 4000 iteration laminar run required 6 hours and 15 minutes CPU time at the TAI machine (IBM-3090 150E, scalar, upgraded). For a 4000 iteration turbulent run 7 hours and 6 minutes CPU time was needed at the TAI machine.

Results

In Figures 15 and 16 the streamlines obtained after 12000 and 20000 laminar ($\mu_t = 0$) iterations are presented. Size of the laminar bubble was growing with the iterations and it was not reached to its steady state size even after 12000 iterations. In Figures 17-18 the streamlines for the turbulent runs after 12000 and 20100 iterations are presented. The shape and the size of the turbulent bubble is quite different than the laminar bubble and it is quicker to reach its steady state form with the number of iterations. The big difference between the laminar and turbulent bubbles state the necessity of turbulence modeling, whether rough or accurate, for the prediction of these type of flow-fields. In Figure 19 the pressure distribution on the bottom surface (more correctly along x axis, $z/b = 0$) obtained after 20000 turbulent iterations is presented. Around the jet exit we observe two sharp negative pressure peaks at the both edges of the jet exit. These peaks can be considered as the corner effects. This figure should be compared with Fig. 6. Figure 6. shows the surface pressure prediction for a 2-D jet injected into a crossflow which was not bounded from above. Therefore, overall agreement of these two figures can not be expected. Here the purpose of comparison is related to the two positive pressure peaks which can be

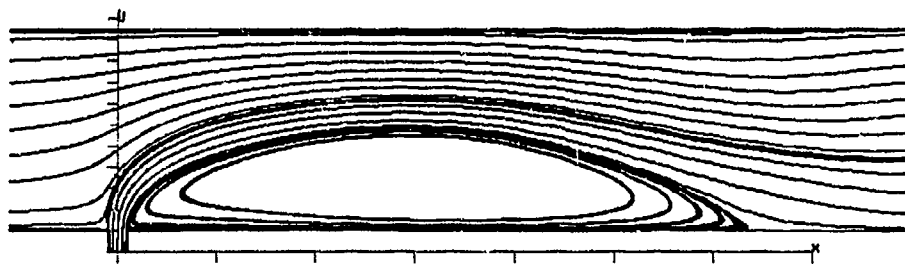


Figure 15. Streamlines, 2-D, laminar, after 12000 iterations.

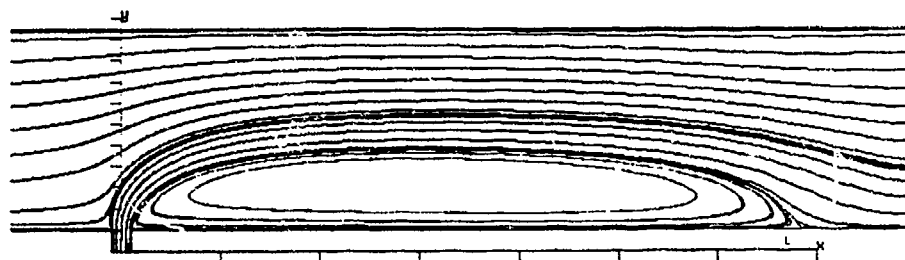


Figure 16. Streamlines, 2-D, laminar, after 20000 iterations.

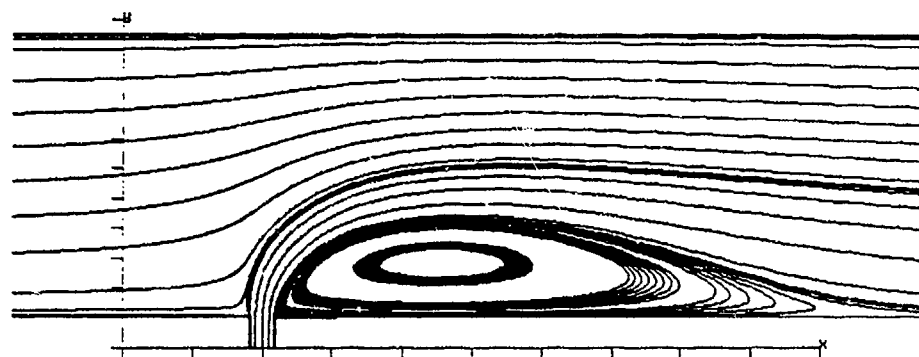


Figure 17. Streamlines, 2-D, turbulent, after 12000 iterations. .

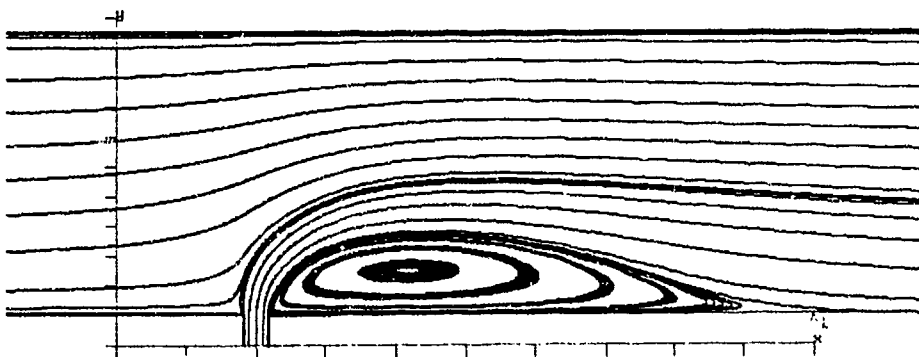


Figure 18. Streamlines, 2-D, turbulent, after 20100 iterations.

observed in Fig. 6 at the edges of the jet exit and next to the negative peaks. These two positive peaks can not be considered as physical. The pressure distribution shown in Fig. 6 was obtained by using a grid with flat bottom. Going back to the Figure 19 it can be observed that these very high positive peaks, which may be called as singularities, were removed by the utilization of the 2-D grid with cavity. In Figures 20-22 comparisons made with the available experimental data are shown. Only the results of flow visu-

alisation studies were available experimentally. In comparison of eddy shape factors (H_i/L) and eddy heights (H_i/B) the present results after 20100 laminar iterations and after 12000 turbulent iterations were in better agreement with the experiment than the present results after 20000 turbulent iterations (Figures 20 and 22). On the other hand, the laminar result did not agree with the experiment in comparison of jet widths, $(H_0 - H_i)/L$, while the turbulent results agreed well. The disagreement of the laminar result

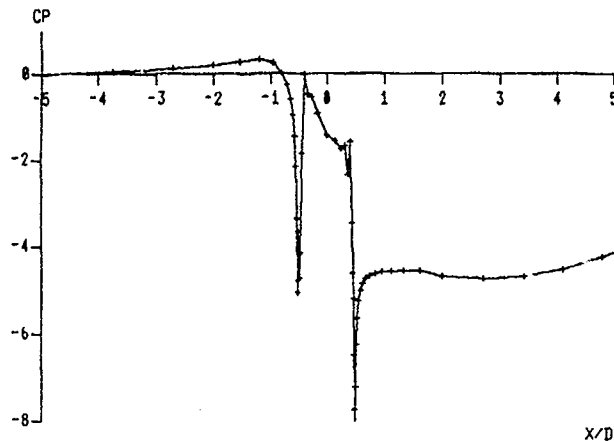


Figure 19. Pressure distribution along x axis, 2-D, turbulent, after 20000 iterations.

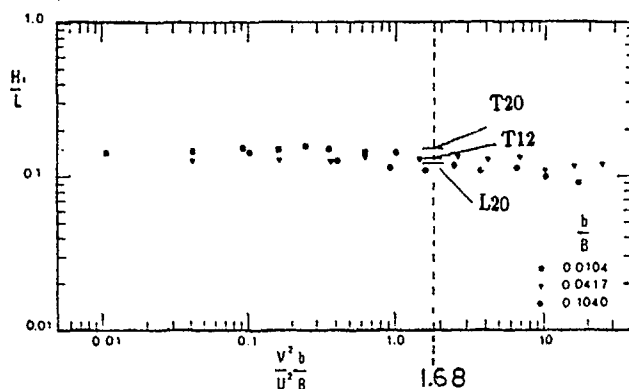


Figure 20. Comparison with the experiment³, eddy shape factor.

L20 : Laminar, after 20000 iterations.

T12 : Turbulent, after 12000 iterations.

T20 : Turbulent, after 20100 iterations.

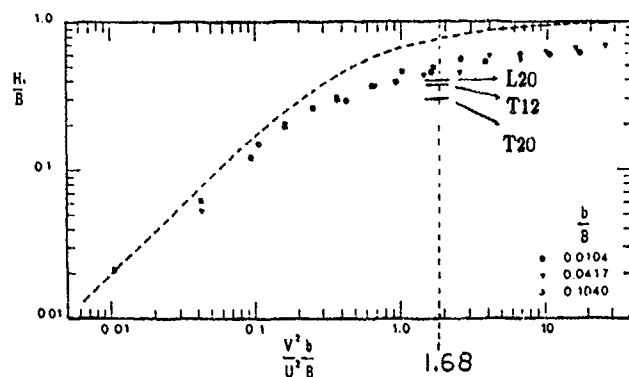


Figure 21. Comparison with the experiment³, eddy height.

L20 : Laminar, after 20000 iterations.

T12 : Turbulent, after 12000 iterations.

T20 : Turbulent, after 20100 iterations.

can particularly be attributed to the overprediction of the jet length L . Overall, the turbulent results after 12000 iterations were in best agreement with the experiment. The turbulent results after 20100 iterations were less successful

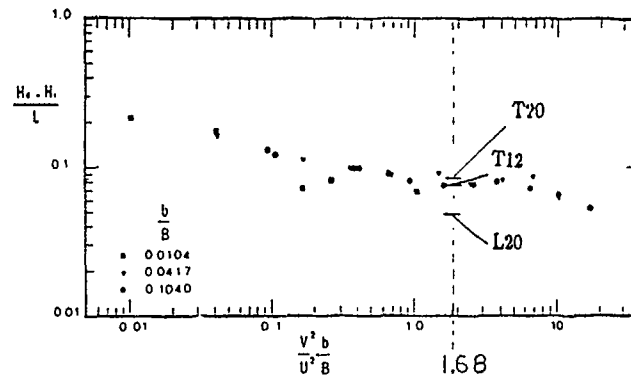


Figure 22. Comparison with the experiment³, jet width.

in prediction of H_i . This could be related to the accuracy of the turbulence modelling. Here it should be mentioned that experimental results were obtained by dye injection and the turbulent mixing of the dye may particularly make the measurement of H_i difficult.

Computation of a Three Dimensional Jet in Crossflow

Similar to the two dimensional case preliminary computations of a three dimensional jet in crossflow by using a rectangular grid with flat bottom showed singularities on surface pressure distribution. It was again decided to make a new grid with a cavity for the jet entrance. However, the results obtained by using the rectangular grid were in reasonably good agreement with the experimental results excluding the singularities. Therefore here, the results obtained by using both grids will be presented.

Experimental Data for Comparison

A case from the circular jet in crossflow experiments of Kavsaoğlu and Schetz²⁸ was chosen as the test case. For this experimental results the circular jet was injected from a flat plate in normal direction to the crossflow. The jet exit velocity profile was uniform with about 3 % turbulence level. In Ref. 28 this case was mentioned as the low turbulence case. Crossflow was also uniform and had very low turbulence level. The jet to crossflow velocity ratio was 4. Crossflow Mach number was $M_\infty = 0.05$ and the jet exit Mach number was $M_j = 0.2$. Reynolds number based on jet diameter and freestream velocity was 51400. The jet exit velocity was about 67 m/sec. Experimentally obtained velocity vectors in the jet centerplane and the surface pressure distribution results will be presented later in comparison with the numerical results.

Computations Made by Using a Flat Bottom Rectangular Grid

The specified conditions for these runs were as follows:

Freestream Mach Number: $M_\infty = 0.1$,

Jet Exit Mach Number: $M_j = 0.4$, based a_∞ ,

Jet to freestream velocity ratio: $R=4.0$

Reynolds number based on jet diameter

and the freestream velocity: $Re=51400$.

These conditions were in agreement with the experimental conditions except the Mach numbers were twice that of the experimental values. This was done because of using a compressible flow solver while trying to keep the flowfield still effectively incompressible.

Grid

A simple rectangular grid shown in Figures 23 and 24 was used. This is a half grid for the utilization of symmetry boundary conditions. In the X-Y plane the data points are clustered around the jet exit. Geometric stretching was used towards upstream, downstream and side. In the Z direction up to about $Z/D=2$ exponential stretching was used to capture the viscous layer on the surface. Then constant spacing was used up to about $Z/D=7.5$ and a larger constant spacing was used up to $Z/D=15$. This grid extends in the range $-12 \leq X/D \leq 22$, $-0.123 \leq Y/D \leq 6$ and $0 \leq Z/D \leq 15$. The total number of grid points is $59 \times 21 \times 45 = 55755$ in ξ , η , ζ directions respectively.

Computational Details

The turbulence models were applied as follows. First the Baldwin-Lomax²⁶ model worked up till $Z/D=7.5$. Then the curved jet model of Oh and Schetz¹⁴ worked for the jet region. In order to have a smooth μ_t distribution the final μ_t values for the jet region were determined by using a Harmonic averaging as follows;

$$\mu_t = \frac{2\mu_{t,Baldwin-Lomax}\mu_{t,curved-jet}}{\mu_{t,Baldwin-Lomax} + \mu_{t,curved-jet}}$$

The boundary conditions were applied as explained in the Boundary Conditions section. For the flow in plane the simple Riemann invariant type and for the flow out plane the inverse extrapolation type characteristic boundary conditions were applied. For the bottom solid walls the pressure and density were extrapolated and the no slip condition was applied. For the top plane and the side plane the flowfield variables were set equal to the values at the neighbouring inner planes. For the symmetry plane (see Figure 24), variables at the $K=1$ plane were set as follows; $\rho_1 = \rho_3$, $u_1 = u_3$, $v_1 = -v_3$, $w_1 = w_3$, $e_1 = e_3$. At the jet entrance ordinary (non-characteristic) boundary conditions

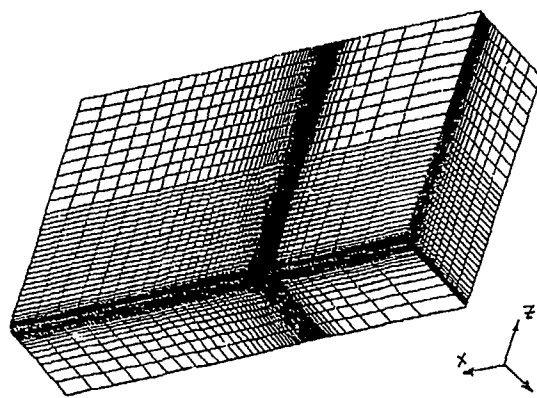


Figure 23. The rectangular grid for circular jet computations, $-12 \leq X/D \leq 22$, $-0.123 \leq Y/D \leq 6$, $0 \leq Z/D \leq 15$, ($59 \times 21 \times 45$).

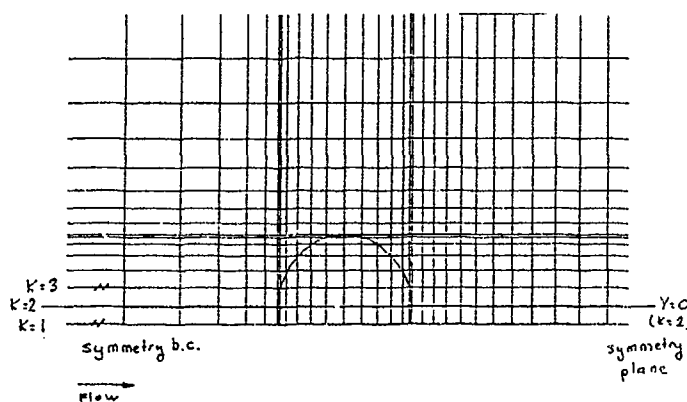


Figure 24. The rectangular grid for circular jet computations, X-Y plane, enlarged around the jet exit.

were applied. The pressure and density were extrapolated and a uniform velocity profile was specified. Looking at Figure 26, at the points which are on or inside the circle shown the jet entrance boundary conditions were specified. Diameter of this circle was 97 % of the actual jet diameter in order to compensate for the viscous boundary layer losses.

Convergence of the L2 norm of the residual is presented in Figure 25. For the first 3000 iterations it was a laminar run ($\mu_t = 0$). After 3000th iteration the turbulence models were applied and this shows itself with a peak in convergence history next to the 3000th iteration.

Results

In Figure 26 the surface pressure contours are presented in comparison with the experimental data²⁸. In this figure locations marked with 'G' represents the grid skewness effects on the surface pressure distribution. Going back to Figure 24 it can be seen that at these locations the grid lines have some skewness. In Figure 26 locations marked with 'S' represents the positive pressure singularity.

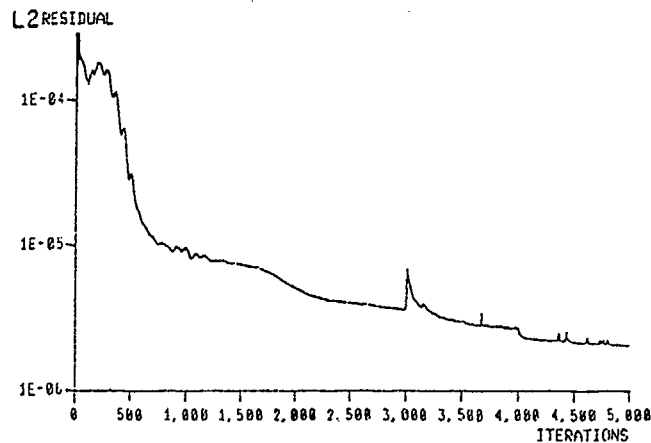


Figure 25. The convergence history for the circular jet runs using the rectangular grid.

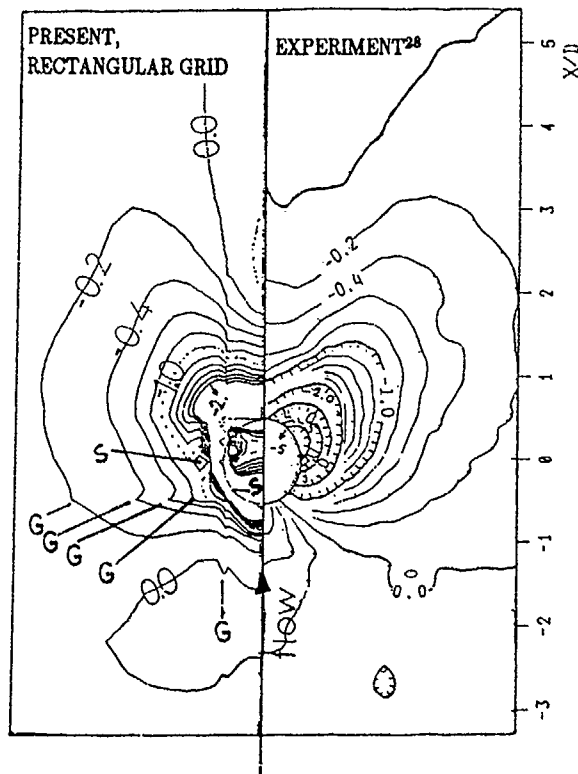


Figure 26. Circular jet surface pressure contours, after 5000 iterations, rectangular grid, in comparison with the experiment²⁸.

ties. Overall reasonable agreement with the experiment can be observed. Disagreements may be attributed to the grid skewness and singularities. For the wake region behind the jet effect of turbulence modelling should also be considered. In Figure 27 the velocity vectors in the jet centerplane are presented in comparison with the experimental data²⁸. The agreement can be considered as satisfactory.

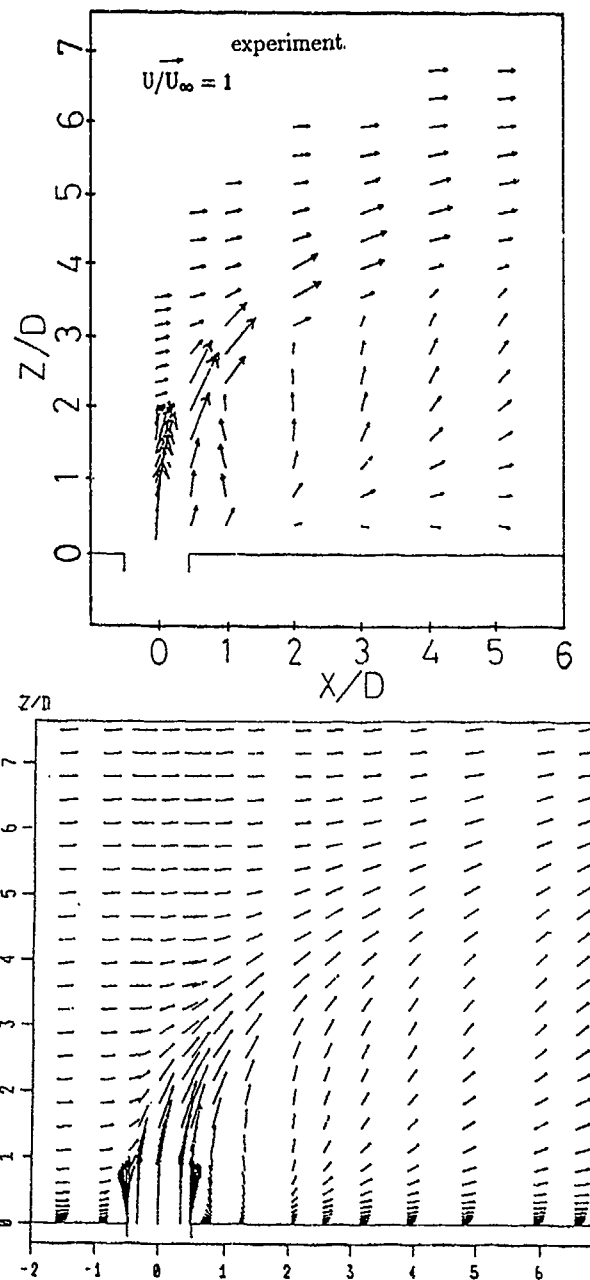


Figure 27. Circular jet velocity vectors in jet centerplane ($y/d=0$), after 5000 iterations, rectangular grid in comparison with the experiment²⁸.

Computations Made by Using a Grid with Cavity

The specified conditions for these runs were as follows:

Freestream Mach Number: $M_\infty = 0.075$,

Jet Exit Mach Number: $M_j = 0.3$, based a_∞ ,

Jet to freestream velocity ratio: $R=4.0$

Reynolds number based on jet diameter and the freestream velocity: $Re=51400$.

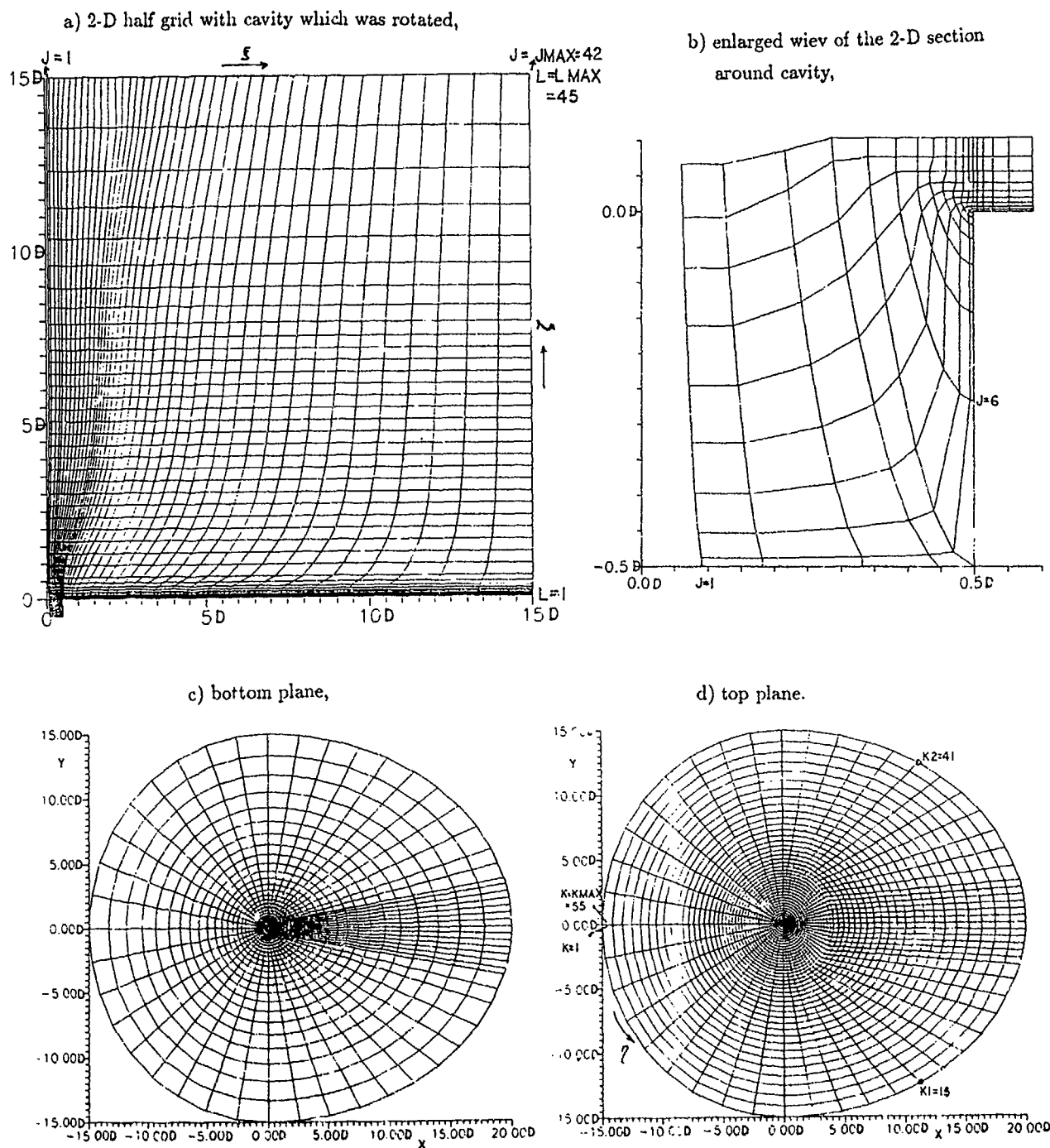


Figure 28. 3-D cavity grid with cavity used for circular jet in crossflow computations

Grid

In Ref. 34 circular jet in crossflow computations performed by using a half grid with cavity was reported. Half grid was used to benefit from the symmetry condition. That computations were not successful because the grid used had some skewness which effected the surface pressure predictions. Probably the easiest way to obtain a three dimensional cavity grid which doesn't have much skewness is to rotate a two dimensional half cavity grid around an axis.

For the present computations this approach was tested. Another benefit of rotating a two dimensional grid is to place more points around the jet exit than far away locations easily. Grid points were distributed more economically so a full three dimensional grid could be afforded instead of a half grid. In Figure 28-a the two dimensional half grid which was rotated is shown. In Figure 28-b enlarged view of this grid around the cavity is shown. In Figures 28 c and d the bottom and top views of the three dimensional grid

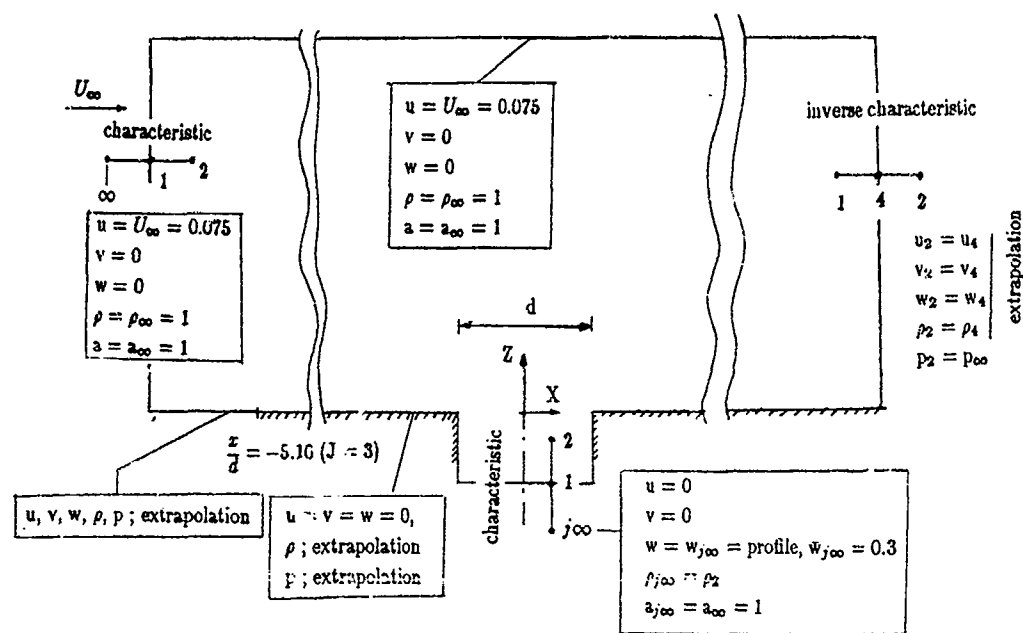


Figure 29. Application of the boundary conditions for the circular jet in crossflow computation.

obtained after rotation are shown respectively. In Figures 28-a and 28-b the ξ, η, ζ directions and distribution of corresponding J, K, L indices are also shown. During rotation the original two dimensional grid was also stretched for rear part of the jet exit.

Computational Details

The turbulence models were applied as follows. First the Baldwin-Lomax²⁶ model was applied over the flat plate up till $z/d = 2.0$ excluding the cavity region. Then the curved jet model of Oh and Schetz¹⁴ was applied for the curved jet region. No other turbulence predictions were made for the regions which were excluded by these two models such as the wake behind the jet.

Same with the experimental case²⁸ the jet to free-stream velocity ratio was 4 and the Reynolds number based on freestream velocity and the jet diameter was 51400. However the freestream and the jet Mach numbers were taken as 0.075 and 0.3 instead of the experimental 0.05 and 0.2. This was done so by expecting better results when a compressible flow solver used while keeping the flowfield effectively incompressible. Application of the boundary conditions are summarized in Figure 29. No slip condition was applied from $J=6$ till $J=37$. Riemann invariant type inflow boundary conditions were applied from $K=1$ till $K=K1$ and from $K=K2$ till $K=KMAX$ at the $J=JMAX$ surface (see Fig. 28). Rearplane inverse characteristic boundary conditions were applied from $K=K1+1$ till $K=K2-1$ at the

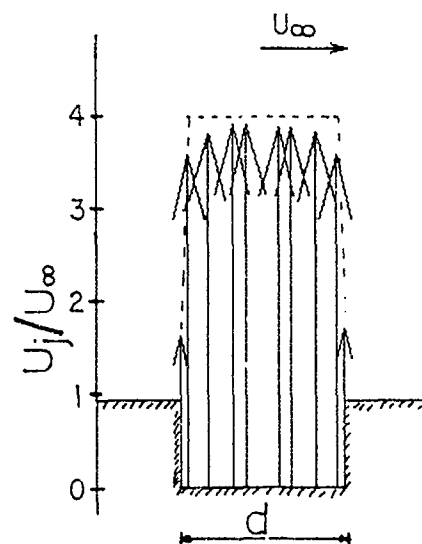


Figure 30. Circular jet exit velocity profile set by the application of characteristic boundary conditions.

$J=JMAX$ surface. Conditions at the top plane ($L=LMAX$) were set equal to the freestream conditions. For the jet entrance simple Riemann invariant type inflow characteristic boundary conditions were used. At the jet entrance a velocity profile was specified as infinity condition as shown by the dotted lines in Figure 30. This profile was then modified to the one shown by arrows by the application of Riemann invariant type boundary conditions as the velocity profile at the jet entrance plane (point 1 in Figure 29). The + Riemann invariant was obtained at point $j\infty$ and the - Riemann invariant was obtained at point 2 as;

$$R_{j\infty}^+ = w_{j\infty} + \frac{2}{\gamma-1} a_{j\infty}$$

$$R_2^- = w_2 - \frac{2}{\gamma-1} a_2$$

and the velocity and the speed of sound at point 1 was calculated as;

$$u_1 = 0.5 (R_{j\infty}^+ + R_2^-)$$

$$a_1 = 0.5 \frac{\gamma-1}{2} (R_{j\infty}^+ - R_2^-)$$

(see the Boundary Conditions section). For the two coinciding planes, $K=1$ and $K=KMAX$ density, velocity components and pressure was obtained by averaging the corresponding values from the $K=2$ and $K=KMAX-1$ planes. For the $J=1$ surface the application of the boundary conditions can be explained by the help of Figure 31. The flowfield variables (ρ , u , v , w , p and e) at point $(1,K,L)$ were obtained from the variables at point $(2,K,L)$ and at point $(2,KK,L)$ as follows;

$$\rho = \frac{\rho_1 r_2 + \rho_2 r_1}{r_1 + r_2}$$

$$u = \frac{u_1 r_2 + u_2 r_1}{r_1 + r_2}$$

$$v = \frac{v_1 r_2 + v_2 r_1}{r_1 + r_2}$$

$$w = \frac{w_1 r_2 + w_2 r_1}{r_1 + r_2}$$

$$p = p_1$$

$$e = \frac{p}{\gamma-1} + \frac{1}{2} \rho (u^2 + v^2 + w^2)$$

where ρ_1 , u_1 , v_1 , w_1 , p_1 are the variables at point $(2,K,L)$ and ρ_2 , u_2 , v_2 , w_2 , p_2 are the variables at point $(2,KK,L)$. Point $(2,KK,L)$ is at the opposite direction of point $(2,K,L)$ with respect to point $(1,K,L)$.

In Figure 32 the convergence history of these three dimensional computations can be seen. In this Figure the upper curve represents the L2 norm of the residual and the lower curve represents the maximum residual. These 3-D runs were performed at the IBM 3090 180S vector machine with single CPU of Middle East Technical University. By using the $42 \times 55 \times 45$ grid about 40 megabytes of RAM was needed and each 1000 iterations required about 3 hours and 52 minutes CPU time including two read operations for the solution and grid files and one write operation for the solution file.

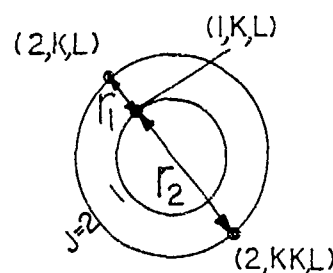


Figure 31. Application of the boundary conditions for the $J=1$ plane.

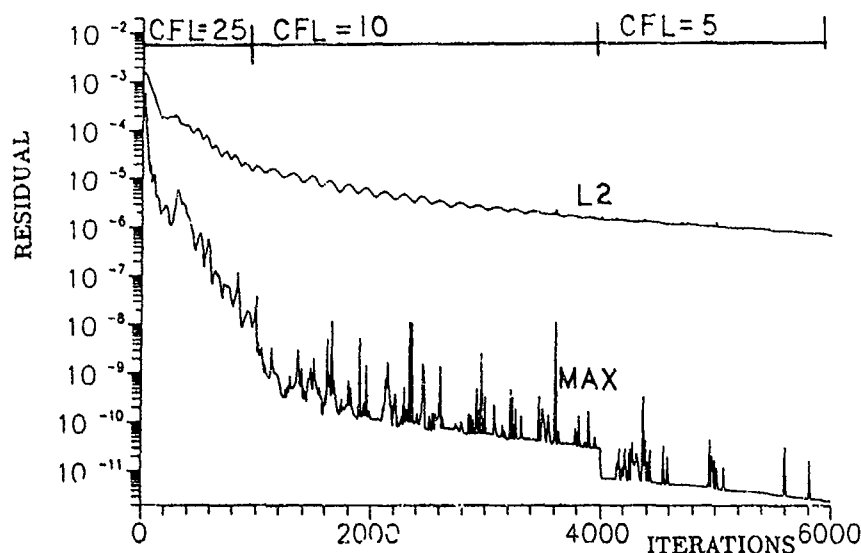


Figure 32. Convergence history for the circular jet in a crossflow computation.

Results

In Figure 33 the velocity vectors in jet centerplane ($Y/D = 0$), in Figure 34 the velocity vectors in the $X/D = 1.026$ plane are presented in comparison with the experimental results²⁸. In Figure 35 the velocity vectors in the $Z/D=0.61$ plane are presented. In general the agreement of the velocity vectors with the experimentally obtained velocity vectors are reasonably good. Note that velocity scales may be different in Figure 34. In Figure 36 computationally obtained surface pressure distributions are presented in comparison with the experimental data²⁸. In Figure 37

only the $C_p = -0.2, -1$ and -2 lines are compared with the experimental ones. -0.2 line extended to a larger region behind the jet and the experimental figures had some asymmetry. In general the agreements was reasonably good. In Figure 38 the present computational result was compared with the incompressible Finite Element simulation of Oh and Schetz¹⁴. Finite Element approach provided pressure contours free from oscillations. However, for the rear of the jet exit present computations agreed better with the experiment.

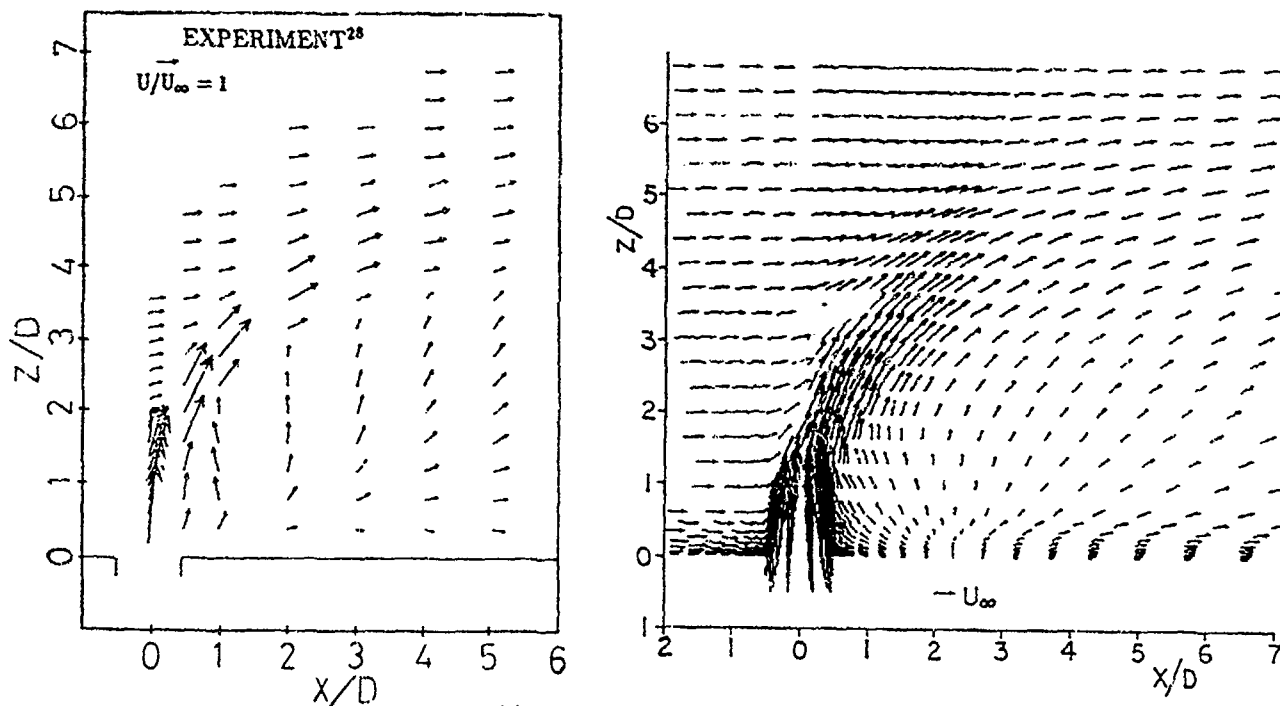


Figure 33. Velocity vectors in $Y/D = 0.0$ plane, (jet centerplane) in comparison with the experiment²⁸.

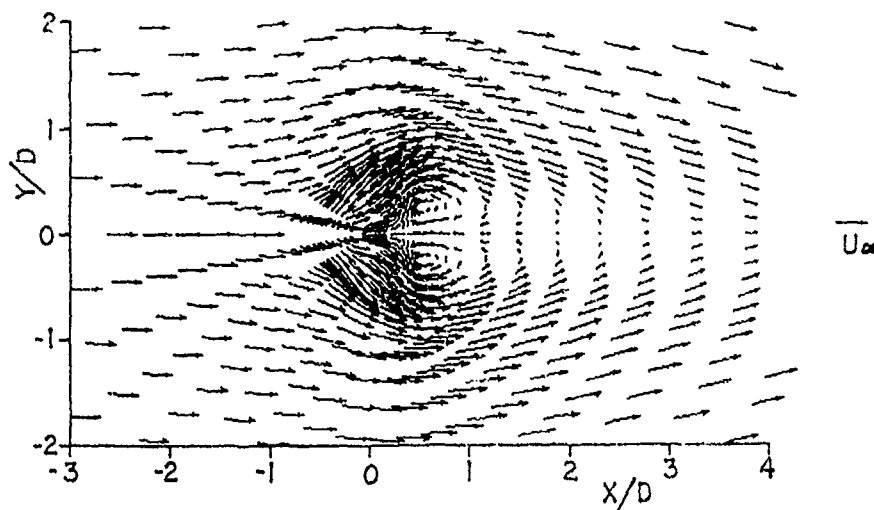


Figure 35. Velocity vectors in $Z/D = 0.61$ plane.

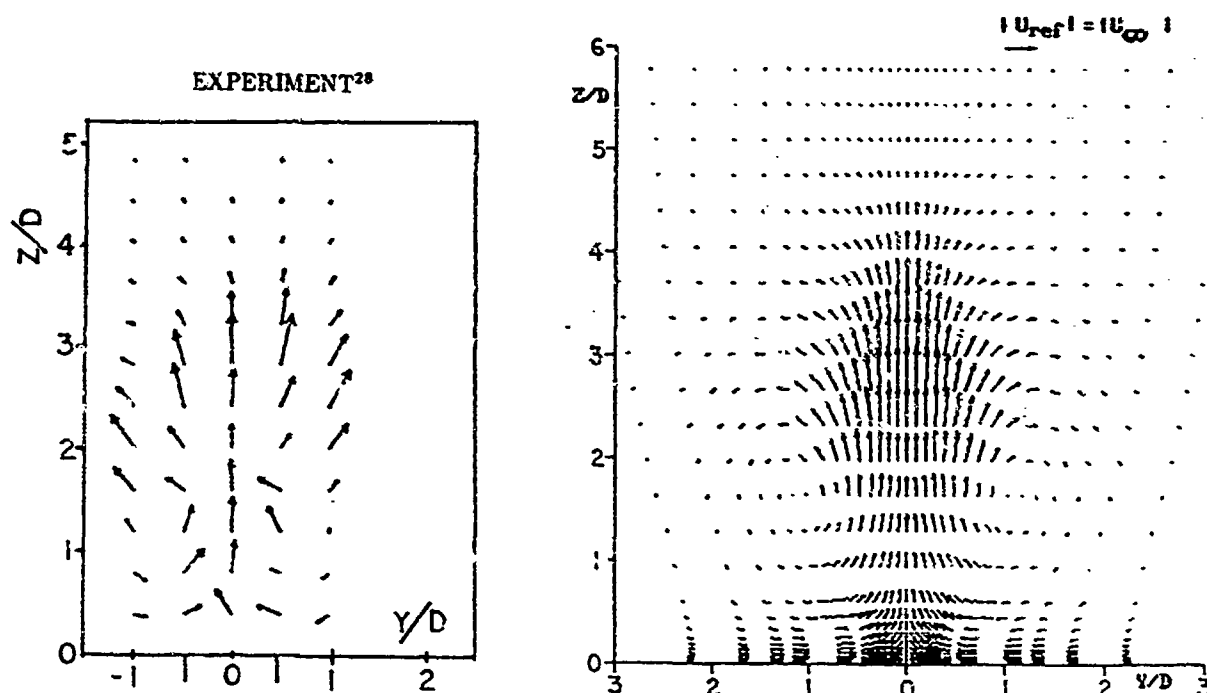


Figure 34. Velocity vectors in $X/D = 1.026$ plane in comparison with the experiment²⁸.

Discussion

In this study Navier-Stokes simulations of two and three dimensional jets were performed. The goal was to achieve some progress in the computation of VTOL aircraft aerodynamics. These type of flowfields are in general compressible in nature. In the present study a compressible flow solver was used but effectively incompressible flowfields were simulated to start and also to compare the results obtained with the available experimental data. Application of characteristic boundary conditions for the flow in and flow out planes were found to be useful to improve the convergence of the solutions. There are actually averaging processes between a point outside the computational grid (∞ point) and a point inside the computational grid (inner point) in order to set the conditions at a point on the boundary of the computational grid (boundary point). This way the boundary conditions are applied slowly and smoothly by the increasing number of iterations which is helpful for the convergence.

Characteristic boundary conditions utilizes the Riemann invariants. For flow in planes + Riemann invariant is calculated at the ∞ point and the - Riemann invariant is calculated at the inner point and both are assumed valid at the boundary point. In a previous study³⁴, it was also observed if in the calculation of - Riemann invariant taking the speed of sound from the ∞ point instead of the inner point could cause improvements in convergence. This may

be considered as giving more weight to the ∞ conditions in the averaging process. Another benefit of these boundary conditions is they set a velocity profile at the boundary plane which may be different than the specified profile at the ∞ plane and which is more realistic. This is particularly useful when no-slip condition is applied suddenly after the flow entrance.

When using a grid with flat bottom and specifying the jet entrance boundary conditions at the bottom plane suddenly, pressure singularities were obtained at the edges of the jet exit. These were local troubles and were not very harmful for the regions away from them. In the present study, due to the importance of flowfield very near the jet exit, cavity grid approach was tested. Making a cavity for the jet entrance was found to be successful to remove these pressure singularities. However, in a previous study³⁴ a three dimensional grid with cavity produced unsuccessful pressure predictions due to highly skew nature of the grid. In the present study a two dimensional cavity grid was rotated around an axis to obtain a three dimensional cavity grid. This produced much less skewness when compared to the grid used in Ref. 34 which made the pressure predictions more successful.

In the present study, locally valid algebraic turbulence models were used. In the computation of the jets in cross-flow problem the effects of turbulence models can be observed only after the perfect solution of the problems asso-

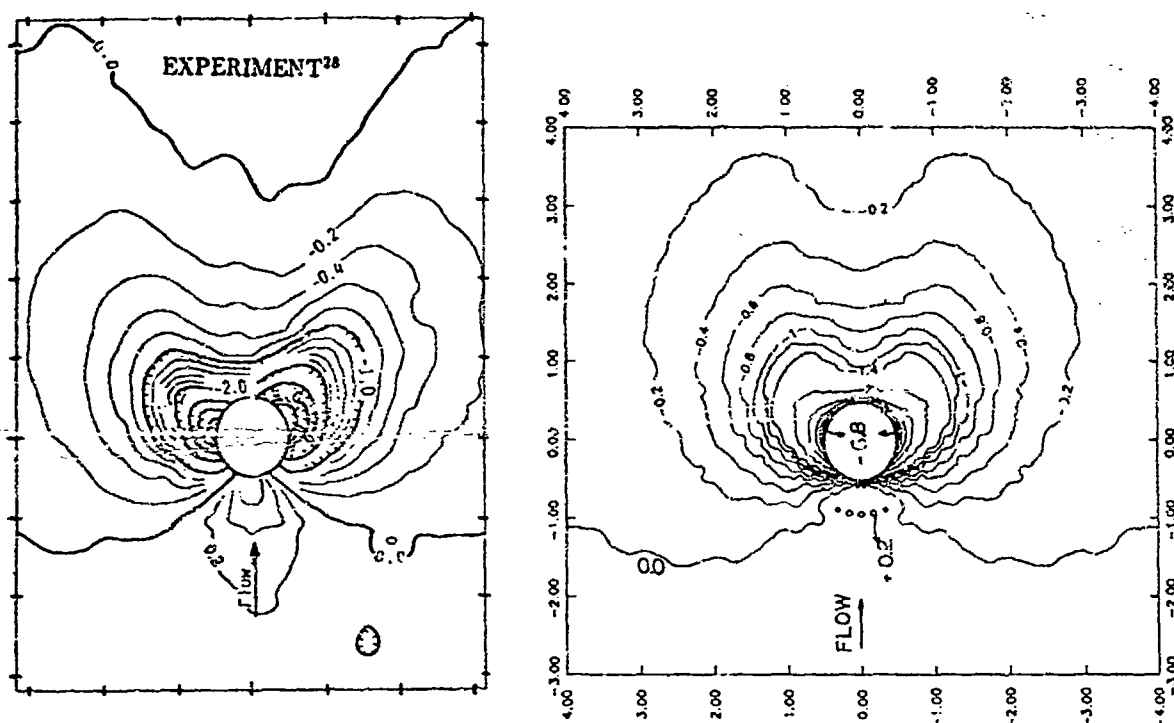


Figure 36. Surface pressure contours ($C_p = (p - p_\infty)/q_\infty$) in comparison with experiment²⁸.

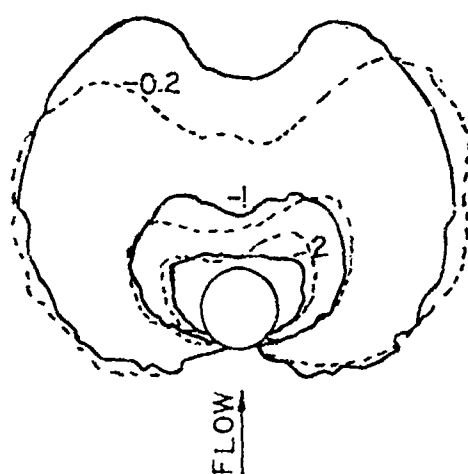


Figure 37. Comparison of the $C_p = -0.2$, -1.0 and -0.2 curves with the experiment²⁸, dotted lines represent experiment, solid lines represent present computation.

ciated with the grid and the boundary conditions. It also seems like further experimental studies are necessary to obtain the turbulence field. Experimentally obtained μ_t field can be plugged into the Navier-Stokes code and the results obtained can be used as a test case for the turbulence models.

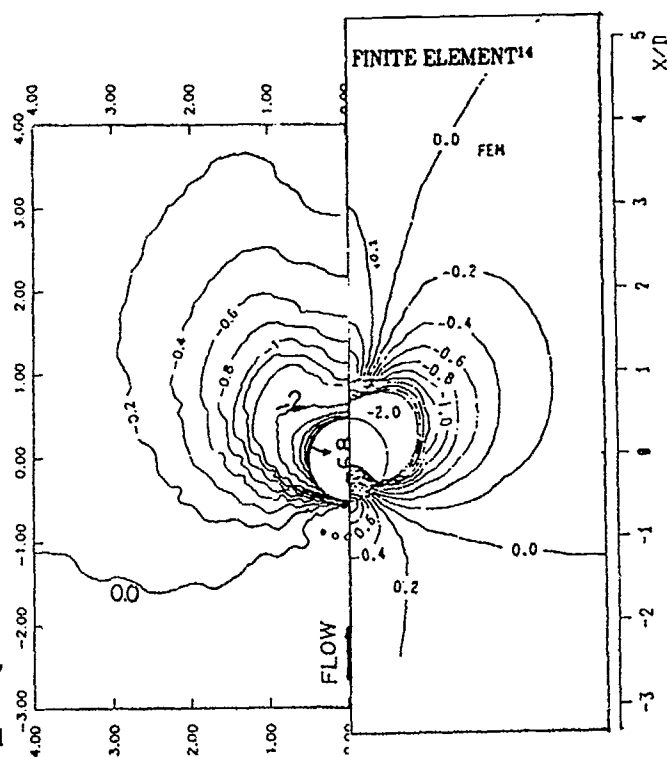


Figure 38. Comparison of the present surface pressure predictions with the incompressible Finite Element prediction of Oh and Schetz¹⁴.

Acknowledgement

Initially this research was supported by General Dynamics Forth Worth Division (GDFW) through a contract given to TUSAŞ Aerospace Industries (TAI). The technical monitor at GDFW was I. C. Bhateley. The technical monitor at TAI was M. O. Kiciman. The first two authors were participated in this project as consultants. The authors would like to acknowledge the help received on technical matters from Ü. Kaynak and M. Dindar. Thanks also go to C. Çıray, department head of M.E.T.U. Aeronautical Engineering department for his support, and to the staff of TAI and M.E.T.U. computer centers for their many help.

References

- ¹ Schetz, J. A., "Injection and Mixing in Turbulent Flow," Progress in Astronautics and Aeronautics, Vol. 68, AIAA, New York, 1980.
- ² Abramovich, G. N., "The Theory of Turbulent Jets," MIT, Cambridge, MA, 1960.
- ³ Mikhail, R., Chu, V. H. and Savage, S. B., "The Reattachment of a Two-Dimensional Turbulent Jet in a Confined Cross Flow," Proc. 16th IAHR Congress, Sao Paulo, Brazil, Vol. 3, 1975, pp. 414-415.
- ⁴ Rouse, H., "Diffusion in the Lee of a Two Dimensional Jet," Proc. 9th Cong. Int. Mec. Appl., Univ. Bruxelles.
- ⁵ Keffer, J. F. and Baines, W. D., "The Round Turbulent Jet in a Crosswind," Journal of Fluid Mechanics, Vol. 15, 1963, pp. 481-497.
- ⁶ Kamotani, Y., and Greber, I., "Experiments on a Turbulent Jet in a Cross-Flow," AIAA Journal Vol. 10, No. 11, 1972, pp. 1425-1429.
- ⁷ Moussa, Z. M., Trischka, J. W., and Eskinazi, S., "The Near Field in the Mixing of a Round Jet with a Cross-Stream," Journal of Fluid Mechanics, Vol. 80, p. 49, 1977.
- ⁸ Schetz, J. A., Jakubowski, A. K., and Aoyagi, K., "Surface Pressures Induced on a Flat Plate with In-Line and Side by Side Dual Jet Configurations," Journal of Aircraft, vol. 21, No. 7, 1984, pp. 484-490.
- ⁹ Kavsaoglu, M., Schetz, J. A., and Jakubowski, A. K., "Rectangular Jets in a Crossflow," Journal of Aircraft Vol. 26, No. 9, September 1989.
- ¹⁰ Lee, C. C., "A Review of Research on the Interaction of a Jet with an External Cross Stream," Brown Engineering Co., Tech. Note R-184, March 1966 (available from DDC as AD 630 294).
- ¹¹ Garner, J. E., "A Review of Jet Efflux Studies Application to V/STOL Aircraft," U.S. Air Force, Arnold Engineering Development Center TR-67-163, Sept. 1967 (available from DDC as AD 658 432).
- ¹² Perkins, S. C., Jr., and Mendenhall, M. R., "A Study of Real Jet Effects on the Surface Pressure Distribution Induced by a Jet in a Crossflow," NADSA CR-166150 (N81-23029), March 1981.
- ¹³ Crabb, D., Durao, D. F. G., and Whitelaw, J. H., "A Round Jet Normal to a Crossflow," Journal of Fluids Engineering, Transactions of the ASME, Vol. 103, March 1981, pp. 142-152.
- ¹⁴ Oh, T. S., and Schetz, J. A., "Finite Element Simulation of Complex Jets in a Crossflow for V/STOL Applications," Journal of Aircraft, Vol. 27, No. 5, May 1990.
- ¹⁵ Zhang X., and Hurst, D., "Surface Flow on a Flat Plate Induced by a Supersonic Jet Exhausting Normally into a Low Speed Crossflow," AIAA Paper 99-3011.
- ¹⁶ Chien, C. J. and Schetz J. A., "Numerical Solution of Three Dimensional Navier-Stokes Equations with applications to Channel Flows and a Buoyant Jet in a Cross-Flow," Journal of Applied Mechanics, Vol. 42, Sept. 1975, pp. 575-579.
- ¹⁷ McGuirk, J. J., and Rodi, W., "A Depth Averaged Mathematical Model for the Near Field of Side Discharges into Open-Channel Flow," Journal of Fluid Mechanics, vol. 86, part 4, pp. 761-781, 1978.
- ¹⁸ Patankar, S. V., Basu, D. K., and Alpay, S. A., "Prediction of the Three Dimensional Velocity Field of a Deflected Turbulent Jet," Journal of Fluids Engineering, Vol. 99, No. 4, 1977, pp. 758-762.
- ¹⁹ White, A. J., "The Prediction of the Flow and Heat Transfer in the Vicinity of the Jet in Cross Flow," American Society of Mechanical Engineers, ASME-80-WA/ht-26, 1980.
- ²⁰ Sykes, R. I., Lewellen, W. S., and Parker, S. F., "On the Vorticity Dynamics of a Turbulent Jet in a Cross Flow," Journal of Fluid Mechanics, Vol. 168, pp. 393-413.
- ²¹ Baker, A. J., Snyder, P. K., and Orzechowski, J. A., "Three Dimensional Near Field Characterization of a VSTOL Jet in Turbulent Crossflow," AIAA Paper 87-0051, Jan. 1987.
- ²² Mongia, H. C., Reynolds, R. S., and Srinivasan, R., "Multidimensional Gas Turbine Combustion Modelling: Applications and Limitations," AIAA Journal, Vol. 24, No. 6 1986, pp. 890-904.
- ²³ Holdeman, J. D., and Srinivasan, R., "Modeling Dilution Jet Flowfields," Journal of Propulsion and Power, Vol. 2, No. 1, 1986, pp. 4-10.

- ²⁴ Obayashi, S., Matsushima, K., Fujii K. and Kuwahara, K., "Improvements in Efficiency and Reliability for Navier-Stokes Computations Using the LU-ADI Factorization Algorithm", AIAA Paper 86-0338, Jan. 1986.
- ²⁵ Fujii, K. and Obayashi, S., "Practical Applications of New LU-ADI Scheme for the Three-Dimensional Navier-Stokes Computation of Transonic Viscous Flows", AIAA Paper 86-0513, Jan. 1986.
- ²⁶ Baldwin, B. S. and Lomax, L. S., "Thin Layer Approximation and Algebraic Model for Separated Turbulent Flows," AIAA Paper 78-257, 1978.
- ²⁷ Sforza, P. M., Steiger, M. H., and Trentacoste, N., "Studies on Three-Dimensional Viscous Jets," AIAA Journal Vol. 4, No. 5, 1966, pp. 800-806.
- ²⁸ Kavsaoğlu M. Ş., and Schetz J. A., "Effects of Swirl and High Turbulence on a Jet in a Crossflow," Journal of Aircraft, Vol. 26, No. 6, June 1989.
- ²⁹ Pulliam, T. H., "Euler and Thin Layer Navier-Stokes Codes: ARC2D, ARC3D", Notes for Computational Fluid Dynamics User's Workshop, The University of Tennessee Space Institute, Tullahoma, Tennessee, March 12-16, 1984.
- ³⁰ Zucrow, M. J., and Hoffman, J. D., "Gas Dynamics", volume 2, John Wiley and Sons, 1977, ISBN 0-471-018066-6.
- ³¹ Hoffman A. K., "Computational Fluid Dynamics for Engineers", 1990, Engineering Education System, Austin, Texas, 78713, USA.
- ³² Jordinson, R., "Flow in a Jet Directed Normal to the Wind", A.R.C. R. and M. 3074, 1956.
- ³³ Chassaing, P., George, J. Claria, A. and Sananes, F., "Physical Characteristics of Subsonic Jets in a Cross-Stream", Journal of Fluid Mechanics, Vol. 62, 1974, pp. 41-64.
- ³⁴ Kavsaoğlu M. Ş., Akmandor İ., Çiray S., Fujii K., "Navier-Stokes Simulation of Two and Three Dimensional Jets in Crossflow", AIAA Paper 91-1743, AIAA 22nd Fluid Dynamics, Plasma Dynamics & Lasers Conference, June 24-26, 1991, Honolulu, Hawaii.

Effects, Limits and Limitations of Spanwise Blowing

W. H. Staudacher
Head Pre-design and Design Analysis
Deutsche Aerospace AG
Military Aircraft Division
P.O. Box 80 11 60
D-8000 Munich 80
Germany

1. SUMMARY

Concentrated spanwise blowing over wings is a technique using mainly the secondary (= nonreactive) effects of a jet in crossflow, with the primary intention to generate and/or stabilize and control separated rolled-up leading edge vortex systems. This means an indirect application of a crossflow jet via triggering an other crossflow phenomenon, the L.E. vortex.

(1) Based on the results of extensive experimental research, the merits and shortcomings of this technique are overviewed concerning

- aerodynamic performance
- stability and control aspects

(2) The limits of aerodynamic efficiency are established on an empirical/theoretical basis and compared to experimental results. There is found a definite upper and lower boundary.

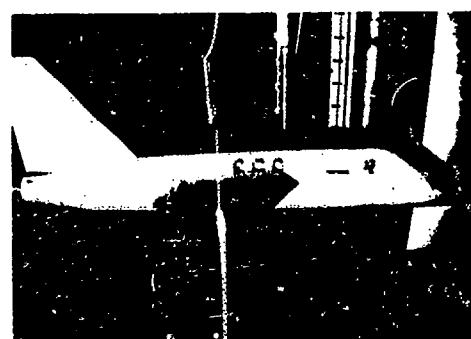
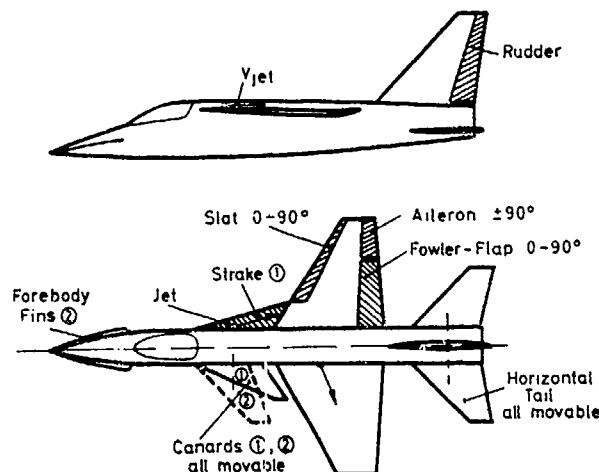
(3) The author's view is given concerning the practical (non-) applicability of this simple technique and the reasons for missing examples in operational aircraft are discussed via comparison to competitive approaches.

2. INTRODUCTION

The basic ideas of spanwise blowing came to appearance in the late 60-s, they can be attributed (to the author's knowledge) to J.J. Cornish and C.J. Dixon, both from Lockheed, USA, and Ph. Poisson-Quinton from O.N.E.R.A., France. Thus spanwise blowing may be regarded as the result of an ingenious transatlantic alliance.

The technique was "booming" then by many publications in the 1970's and it was at that time when the author himself came into the game (which does not mean that he claims the reason for that "boom"). Meanwhile, effects and efficiency of concentrated blowing are well established from the experimental side, spanning from improvements of performances (lift increase and drag reduction) to stability (around all axes depending on the location of the blowing jet over the wing, the tails or the body) and control augmentation (rudders and flaps). Some promising results will be repeated in the next

section headed "Effects". The following paragraph "Limits" will consider aerodynamic characteristics of this technique which have - in the author's opinion - contributed to its "Limitations" (say: missing practical application or even non-applicability?), which will be discussed in the concluding section from the view of the complete design.



3x3 m L.S. Tunnel, DFVLR Göttingen

Fig. 1 Pilot model

When in the course of this paper spanwise blowing is addressed, see Fig. 1, this always refers to a concentrated transversal jet, which is directed over the suction side of a lifting surface, blowing roughly parallel to its plane and leading edge. Thus we shall focus here on two effects, which may act separately or simultaneously depending on the type of the flow around the given wing planform:

- If the wing is exhibiting stable separated L.E. vortex systems by virtue of its geometry (e.g. on a slender delta-type or strake wing) then L.E. vortices may be manipulated by the presence of the spanwise jet.
- In the other case of a less slender and less swept wing (say: for arbitrary wing planforms) a similar vortex system can be generated, stabilised and controlled on this wing "naturally" nonexhibiting this type of separation.

Note that in the latter case spanwise blowing will not only introduce a global change of the wing upperside flow field but will also trigger this type of separation which is called "global" in the frame of the topology of 3-d separated flows.

3. EFFECTS

All the data presented in this paragraph were taken from the results of the former working group "Wings with Controlled Separation". The group's activities were directed on the experimental investigation of flows with stable L.E. vortex systems, especially on the development of strake wings (1969 - 1978) and on spanwise concentrated blowing (1975 - 1982).

Members of this team were individuals from DFLR (now DLR), the former companies MBB and VFW (both now DASA) and, temporarily, O.N.E.R.A., France, their work being sponsored at that time by the German Ministry of Defense. The working group "Wings with Controlled Separation" itself separated controlled (-loyal to its name-) after ten years activity in 1983. For detailed results concerning spanwise blowing the interested reader is referred to refs. [9 - 13, 16 - 19]

3.1 Approach

The experimental approach taken to optimize the effects of spanwise blowing comprised the following items of variation:

- wing geometry
 - trapezoidal wing (see Fig.1)
 - strake + trapezoidal wing (see Fig.1)
 - delta wing
 - clean or high-lift configuration
- blowing nozzle parameters
 - 6 chordwise positions housed in the wing/body juncture (see photo in Fig.1)
 - 41 positions above the outboard wing (see Fig.2)
 - 3 nozzle heights $Z_D/D = 1.0/1.5/2.0$
 - blowing angles (variable around two axes)
 - nozzle diameters ($D = 15\text{mm}$ or 7.5mm)
- blowing characteristics
 - intensity $0 < C_{\mu} \leq 0.4$
(blowing coefficient $C_{\mu} = 2 m_{\text{jet}} / \rho \infty V_{\infty}^2 (S_{\text{ref}})_{\text{wing}}$)
 - symmetrical/ asymmetrical blowing
 - blowing over flaps or rudders (aileron), see Fig.2
 - blowing simultaneously over strake and wing / wing and aileron or flap

- flow characteristics
 - low-speed $M \approx 0.2 / Re_c \approx 2.1 \cdot 10^6$
 - angle of attack $-5^\circ \leq \alpha \leq 90^\circ$
 - side-slip angle $-15^\circ \leq \beta \leq 15^\circ$

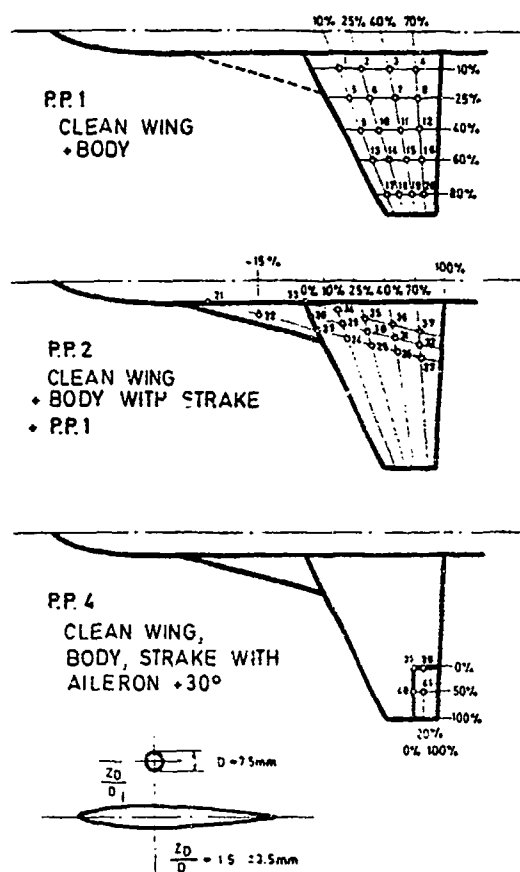


Fig. 2 Tested nozzle positions

The low-speed windtunnel tests were conducted in the 3x3m LS-tunnel of DLR Göttingen and in the large (transonic) facility S1 of O.N.E.R.A., Modane (pos. stall investigations). Detailed results can be taken from refs. [10, 11, 12, 17].

3.2 Effects for the Trapezoidal Wing

This wing has the following characteristics (see Fig.1)

- Aspect ratio $AR = 3.2$
- L.E.sweep $\varphi_0 = 32^\circ$
- Taper ratio $\lambda = 0.3$
- NACA 64 A 005.5 (mod.) wing section (twisted and cambered)

In Fig.3, the effect of varying the nozzle position in chordwise direction ($x/c = 0.1/0.25/0.40/0.75$) and over the exposed span ($y/s = 0.1/0.25/0.40/0.60/0.80$) is presented. The criterion used is the maximum induced lift increment given by the presence of the blowing jet. Nozzle height ($z_D/D = 1.5$) and

blowing direction (parallel to the surface and parallel to the L.E. hence $\varphi_D = 32^\circ$) were kept constant here as well as the blowing coefficient $C_{\mu} = 0.1$. Note that the data are representing pure aerodynamic interference effects of blowing as the nozzles were always mounted sting fixed. So direct reaction (thrust or lift-) effects were not measured. The best positions chordwise are varying between the leading edge and the 40 % chord position, and, as expected, the trend is for the more inboard locations of the blowing nozzle. Anticipating the result of the optimization of the nozzle positions housed in the wing/body juncture ($y/s=0$), which will be given next and which were actually obtained earlier, the locus of the total optimum is already shown (large circle at $y/s=0$ and $x/c=0.40$). The approach to this total optimum is depicted in Fig.4. Again, the same measure of improvement $\Delta(C_L C_{\mu})_{\max}$ is used. In Fig.4 the important part of the optimization process is given, i.e. the influences of the nozzle chordwise position x_D/c_r and the effect of nozzle sweep $\Delta\varphi_D$ ($\Delta\varphi_D$ counts positive when the nozzle is swept aft of the respective constant percent chord line, so that the resulting nozzle sweep $\varphi_D = \varphi_{(x/c)} + \Delta\varphi_D$). Finally the optimum position is found for:

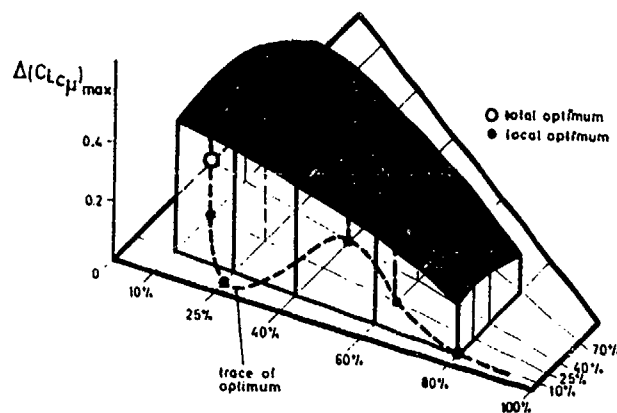


Fig. 3 Effect of nozzle position on outboard wing

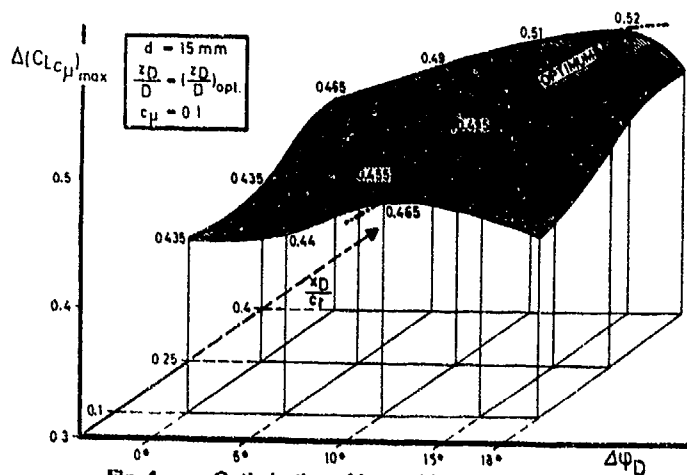


Fig. 4 Optimization of jet position and direction (blowing from the wing root)

- chordwise position at 40% root chord
- Blowing direction $\Delta\varphi_D = 15^\circ$, that is approximately parallel to the leading edge, hence $\varphi_D \approx \varphi_0 = 32^\circ$
- nozzle height $1.5\bar{\phi}$ ($Z_D/D = 1.5$).
- blowing angle relative to surface $\pm 1.5^\circ$, say parallel to the surface.

Nozzle height was found to have only marginal effects when varied in the range of $Z_D/D = 1.0 - 2.0$, inclination of the jet nozzle should not exceed $\pm 1.5^\circ$. For wings exhibiting a natural tendency to develop L.E. vortices due to their high sweep (delta-type and strakewings) the optimum position shifts forward ($\sim 10\%$ of root chord or extended root chord respectively), again blowing roughly parallel to the L.E. and the other parameters being unaltered. Note that this preference of the inboard position is a remarkable and rare result in aerodynamics: The most simple system (weight, structure, mechanical supply, complexity etc.) is also the aerodynamically most efficient one here.

Basic data of lift, pitching moment and drag for various blowing intensities C_{μ} are given in Fig.5, when applying the (nearly) optimum nozzle positions just derived for the clean trapezoidal wing (the slightly different nozzle height $Z_D/D = 2.0$ instead of 1.5 is not important).

The dominant effects are

- increase of maximum lift with simultaneous increase of angle of attack of maximum lift
- increasing lift curve slope, hence non-linear lift with increasing C_{μ} and α (the maximum local slope $dC_L/d\alpha$ rises from $3.4 \text{ l/rad}/C_{\mu}=0$ to $5.2 \text{ l/rad}/C_{\mu}=0.4$, that is more than 50%)
- for low angles of attack a small quasi camber effect is found (this will be analysed in Fig.6)
- this (quasi-) camber effect is not found in the pitching moment data (C_{m0} not altered), but increasing C_{μ} tends to linearize the data to higher a.o.a. and lift (constant neutralpoint)
- reduced lift dependent drag, the effect will be discussed later in Fig.7.

The afore mentioned quasi camber effect is shown in more detail in Fig.6a (for $C_{\mu} < 0.1$) and Fig.6b for high C_{μ} . Evidently the displacement effect of the transversal jet increases strongest for low C_{μ} as long as the convergent nozzle does not blow supercritical. This can be seen when comparing the results in Fig.6a for the small and the big nozzle. The smaller nozzle develops the highest gradients $\Delta C_L / \Delta C_{\mu}$. Both the nozzles being driven supercritically their slopes tend to converge, and both running highly supercritical (say $C_{\mu} = 0.08$ for the small nozzle and $C_{\mu} = 0.3$ for the big one) the effect seemingly comes to a stop. Indeed, the same effect was found for the other "camber"-effect noticed, namely the shift of the drag polar apex (which cannot be realized in the crude scale of Fig.5).

Its specific trend is given by Figs.6, too, when one takes $\sim 60\%$ of the ΔC_L -values depicted there.

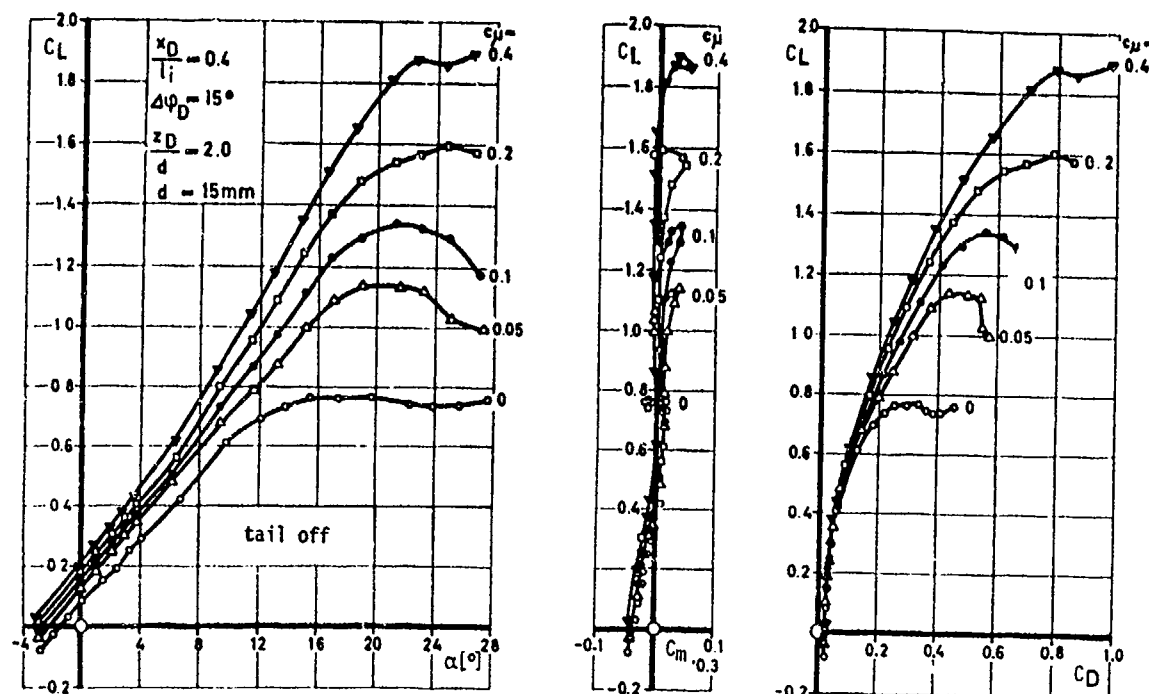


Fig. 5 Effects of spanwise blowing on lift, pitching moment and drag

The corresponding shift of minimum drag ΔC_{Dmin} and zerolift drag ΔC_{D0} could not be seen in Fig. 5, right hand graph. Analysis gave simple relations

- $\Delta C_{Dmin} \sim 0.033 C_\mu$ and
- $\Delta C_{D0} \sim 0.042 C_\mu$

They are averaged values for medium C_μ , for low $C_\mu < 0.05$ they tend to be higher, the opposite is true for $C_\mu > 0.05$, coming to a stop for $C_\mu > 0.4$ approximately. These characteristics are bound to type of planform and blowing direction. For practical purposes we can state that roughly 4% of the total jet momentum is transformed into aerodynamic drag by interference effects (viscosity plus displacement) at low α . As the nozzle was swept back here by $\sim 30^\circ$ ($\phi_D = \phi_0 = 32^\circ$) approximately 8% of the nominal propulsive nozzle thrust are lost. (Hopefully, the reader has recognized that this short excursion to drag-increase due to spanwise blowing is only justified by pure academic interest. Evidently it will not make sense from practical reasons to switch on the blowing system at low lift and a.o.a., where it would add drag by negative aerodynamic interference -simply speaking- before the crossover point of the respective drag polars is overstepped to gain L/D. Also, the argument that there is available excessive thrust from the blowing system's reactive force is poor, as there is no way to get power from the engine to drive the blowing nozzle without paying a higher loss in the former's gross thrust. Hence, pure aerodynamic reasoning turns out to be poor overall reasoning here)

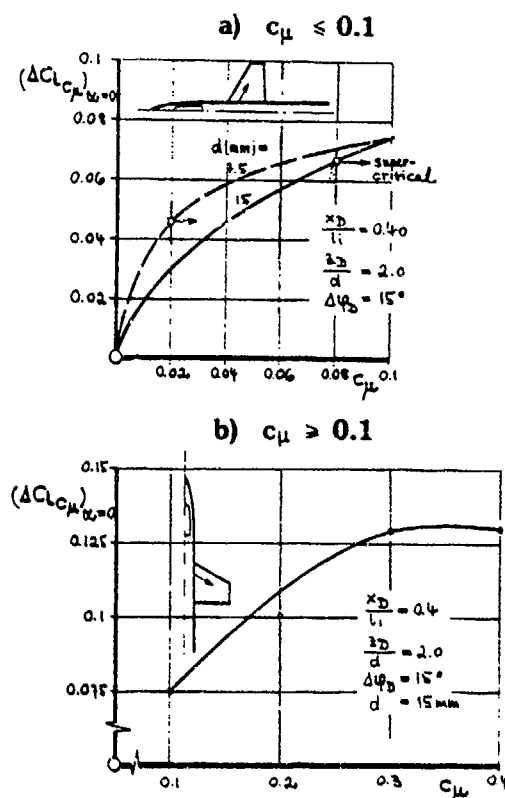


Fig. 6 Quasi-camber-effect of concentrated blowing on trapezoidal wing

In Fig.7 analysis of the lift dependent drag as affected by spanwise blowing is presented. The factor of induced drag $K = C_{Di}/C_L^2$ is plotted versus lift between the limits of ideal 100% L.E. suction and zero suction of the unblown basic wing ($AR = 3.2$). The basic wing ($C_{\mu} = 0$) shows the typical behaviour of a thin, moderately swept wing with small L.E. radius (better: low Reynoldsnumber based on the L.E. radius), thus exhibiting a "long bubble-type" separation with low drag-break lift coefficient $C_{Ldb} \approx 0.3$. Further indication of this special type of separation is found in the respective development of lift at high angles of attack as already shown in Fig.5.

When spanwise blowing comes into the game, the lift dependent drag is drastically reduced at high α (Fig.7). With increasing C_{μ} a "plateau" is developed which tends to lower K-levels and extends to increasing lift coefficients. This second "plateau" is typical for the effect of spanwise blowing as well as for the effect of a slender strake added to the basic wing (the curve for $C_{\mu} = 0.1$ /basic wing -see Fig.7- is practically duplicating the strake effect on lift and drag for a strake with 75° sweep and an area-ratio of 11%). Both the boundaries for zero and full suction, resembling the limits of the basic wing alone, are loosing their meaning when applied to cases with spanwise blowing. In fact, the "plateau" of reduced K-factors in the latter case always holds for zero-suction only and simply reflects the reduction of this specific K-factor, which is produced by the increase of lift curve slope due to blowing. Hence it reflects the reduced value of $1/C_{L\alpha}(\alpha, C_{\mu})$ which can be taken from the graph on the left side of Fig. 5. So the simulated gain of L.E. suction suggested by Fig.7 once more is the effect of additional nonlinear lift produced by a stable, separated vortex system manipulated by the blowing jet (or produced by a L.E. strake directly).

There is a third boundary plotted in Fig.7. It is given in advance of a result from para.4, when this limit will be derived for the case of C_{μ} tending to infinity.

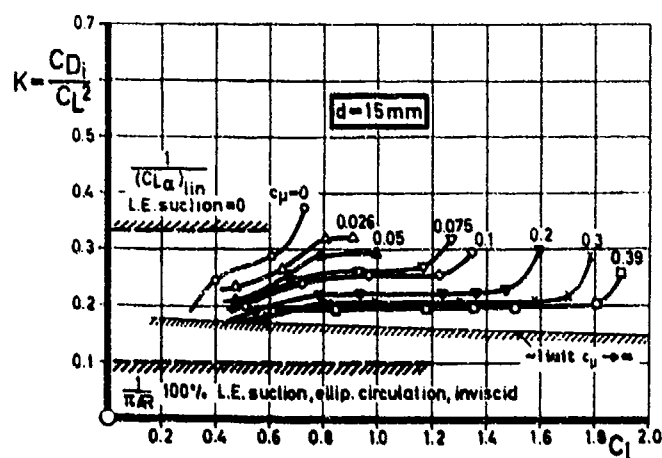


Fig. 7 Analysis of drag as affected by spanwise blowing (basic wing, strake off)

3.3 Comparison of Efficiencies

The primary design goal of the different blowing techniques (concentrated or distributed blowing, see e.g. [10, 23] and BLC-methods) is the enhancement of high-lift performance. So their intention may aim from the global modification of the wing flowfield (as presented so far) over concentrated blowing on flaps or rudder to blowing at distinct critical places for buffet suppression (ref. [14]). In the latter case the question is existing if this method is a meaningful measure of repair (when thinking of the system implications introduced then).

BLC methods will give a maximum of aerodynamic effects for a minimum of "jet" energy (reduced again by problems of complexity and reliability of the system), but usefulness is weak for slender, highly swept wings and for tailless configurations. In section 5 of this paper a discussion will be given of some general aspects concerning applicability.

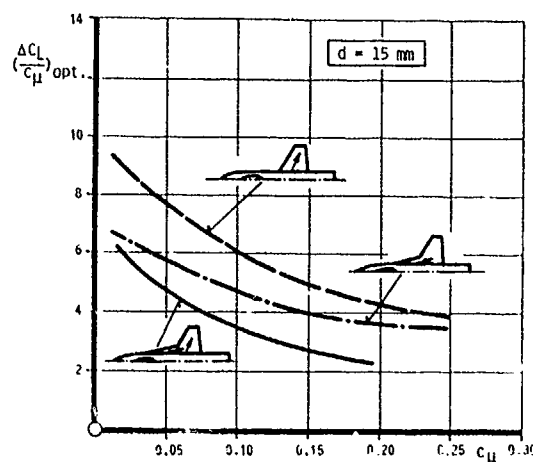


Fig. 8 Effects of wing planform and type of blowing

A simple figure of merit is the ratio $\Delta C_L / \Delta C_\mu$ quantifying the capability to transform jet momentum into useful aerodynamic lift. It will be used in the following two graphs. Note, that there are not measured any direct jet forces due to the blowing nozzle, the system being sting-mounted. For a complete analysis of effects see ref. [12]. In Fig.8 the efficiency ratio $\Delta C_L / \Delta C_\mu$ is compared for the clean configurations of the basic trapezoidal wing and the strake wing (strake wing = trapezoidal wing + strake with 75° L.E. sweep and $S_{exp, strake} = 11\%$ $S_{ref} = 13\%$ S_{exp}). Position and direction of the jet nozzle are: 10% of the extended root chord ($x_D/C_r = 0.1$) and $\varphi_D = 75^\circ = \varphi_{0, strake}$ for the strake wing / $x_D/C_r = 0.40$ / $\varphi_D = 32^\circ = \varphi_0$ for the basic wing. Total C_μ is constant for all cases ($= 0.1$), for combined blowing on the strake wing (see lower curve) the momentum was split equally for strake and basic wing. The general trend is found to be a gradual reduction of the relative gain in lift with increasing C_μ , an expected tendency when going from BLC efficiencies to supercirculation effects. Highest effectivity is found for the basic wing, that is for the case of generating and stabilising a L.E. vortex system on the less swept wing. For very high

blowing intensities actual efficiencies of the two wings are approaching one another. Combined blowing on the strake wing is the inferior method, which may be attributed to the disturbance of the dominating strake vortex system introduced by the less swept jet on the basic wing. All data are given for trimmed cases.

A similar comparison of blowing efficiency $\Delta C_L / \Delta C_{\mu}$ is given in Fig. 9, the two wings now in high-lift configuration (L.E. slats and T.E. fowler flaps deflected 25° and 30° down, respectively). Superiority of blowing on the basic wing has increased, generally the efficiencies are higher here when compared to the clean configurations in Fig. 8. For comparison two examples of constructed (elder) fighters with similar wing planforms are drawn in, both using BLC-techniques on the trailing edge flap (designated T.E.) or on the leading edge flap (L.E.). For small magnitudes of C_{μ} spanwise blowing is reaching the efficiency of the BLC variants (for this special criterion and trimmed (!) conditions, and not taking care of the difference in a.o.a.).

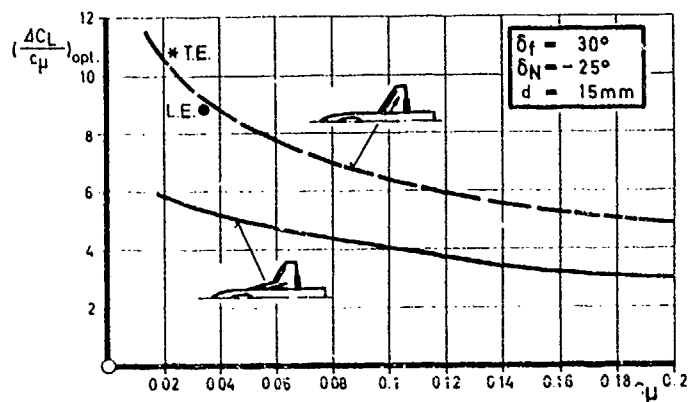


Fig. 9 Blowing efficiency on high lift configuration

3.4. Comparison of Roll Control Power

As mentioned before effects and efficiency of spanwise blowing nonlinearly are bound to high angle of attack flight conditions. This necessary coupling may prove to be a deficiency e.g. for high "g"-performance (at high dynamic pressure) and when thrust limited (sustained turn rates). But when attained performances are addressed this situation will change and that is especially true for high a.o.a. flight approaching post-stall conditions. One of the most striking examples for this aspect is shown in Fig. 10, when the aforementioned disadvantage turns into a profit.

In Fig. 10 roll power of a conventional aileron (curve no. (2)) is compared for non-blowing and blowing application (4). In the latter case a nozzle is used positioned slightly inboard (at 60% exposed span) and in front (at 25% local chord length) of the aileron (extending outboard of 65% span and having a depth of 25% chord). Only the right aileron is deflected 30° down and blowing is applied there. At medium a.o.a. the unblown aileron starts to stall and finally only $\sim 20\%$ of the original roll power is preserved when passing into the stall regime of the

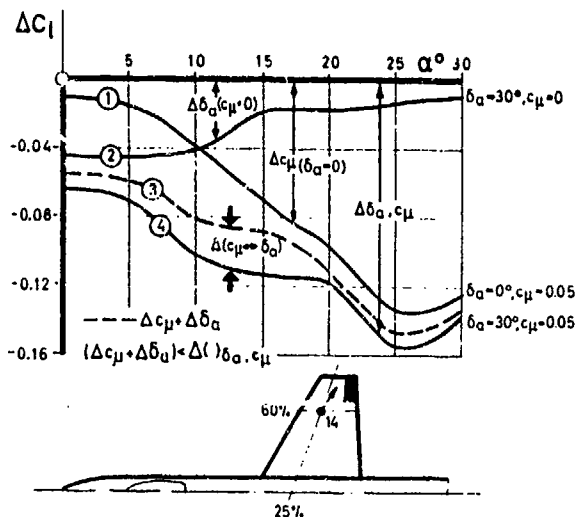


Fig. 10 Roll power due to aileron and/or spanwise blowing

wing ($\alpha > 20^\circ$), as given by curve (2). A highly reversed tendency is found when mere asymmetrical blowing (the aileron is set neutral) is applied, as presented by curve (1) (and $C_{\mu} = 0.05$). When the aileron is deflected in addition, the combined effects (blowing over the deflected aileron) give the characteristics of curve no. (4). Curve (3) was derived by simply adding the data of (1) plus (2), so the difference between (4) and (3) is presenting the small and positive interference effect added by spanwise blowing. Note that less than one half of the blowing intensity applied in this example would have restored a constant roll efficiency of the system (aileron + blowing) all over the angle of attack regime, and that it is spanwise blowing which will give this nice characteristics at high α . This is demonstrated in Fig. 11, now applying one-sided spanwise blowing from the wing root of the basic wing and the strake wing with very low blowing intensities ($C_{\mu} = 0.011$ and 0.016 respectively). In both cases the aileron (its effect is given for comparison) may only be used for fine-tuning purposes at high α .

This type of roll control will provide very attractive features not shown here:

- It is always a supporting lift increment which induces the high roll efficiency
- The reaction thrust of the nozzle will add a provers yawing moment (always true for the strake wing) and side force increment.

The table at the bottom of Fig. 11 gives the augmentation ratio of roll control due to asymmetrical spanwise blowing from the root, relative to a jet reaction control at the tip of the wing. Rolling moment coefficient C_l is referenced throughout to halfspan s . Efficiency is reduced for the strake wing to roughly 60% of the value found for the basic wing. This trend is expected considering the different natures of flow of the two wings and hence differing starting points for application of spanwise blowing, also resulting in distinct blowing sweeps. Nevertheless the technique is at least as attractive for the strake wing because its genuine high a.o.a. capacity lends itself to asymmetrical blowing to preserve roll control in this already given domain of strake induced high lift and α capacity.

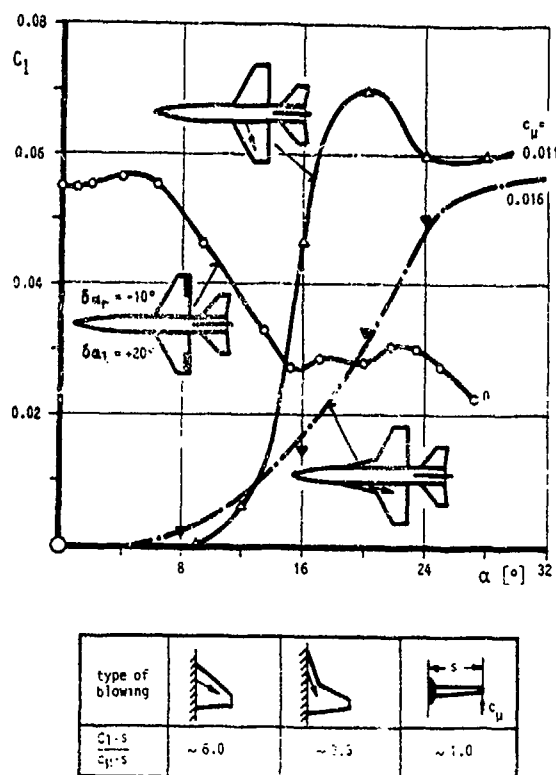


Fig. 11 Asymmetrical blowing from the root for roll control

3.5 Summary of Effects

Basic beneficial effects of concentrated spanwise blowing are summarized in Fig.12, the reader is referred to this chart.

- L i f t P r o d u c t i o n :
 - quasi camber effect at low α
 - nonlinear increase of Jet/vortex-induced lift with increasing a.o.a. and blowing intensity
 - increased $C_{L_{max}}$ and α_{max}
- D r a g D e v e l o p m e n t :
 - reduced lift dependent drag at higher incidences due to reduced a.o.a. for constant C_L :
 $\Delta C_D = -C_L(\tan \alpha_{C_{\mu}=0} - \tan \alpha_{C_{\mu}})$
 - less trim drag
- L o n g i t u d i n a l S t a b i l i t y :
 - linearized pitching characteristics at high a.o.a. (reduced pitch-up or-down characteristics)
 - basic stability (neutral point) and zero-pitching moment (center of pressure) unchanged
- L a t e r a l / D i r e c t i o n a l s :
 - increase of effective dihedral and directional stability and controllability at high a.o.a. by either direct effects (improved flow on the wing) or indirect effects (improved conditions in the wing wake = reduced side wash and increased dynamic pressure)

Fig. 12 Basic beneficial effects of concentrated spanwise blowing

4. LIMITS

The question addressed now is: to which lowest level we can reduce the factor of lift dependent drag $K = C_{D_L}/C_L^2$ when the blowing intensity C_{μ} tends to infinity.

Clearly this desire does not have a realistic background, it is neither practical nor practicable. C_{μ} is defined as the ratio of nozzle thrust divided by dynamic pressure times reference area (of the wing), so $C_{\mu} = 2m \cdot V_{jet}/(\rho \infty V_{\infty}^2 S_{ref})$. Now, V_{jet} is always a finite number, so the numerator is driven to infinity only by use of an infinitely large nozzle (which is not a practicable solution). On the other hand, the nominator reaches zero for $S_{ref} = 0$ or for zero speed (both solutions are practicable but not practical). To come out of this dilemma we'll escape into an experiment of thought and into simplification. Imagine that for $C_{\mu} \rightarrow \infty$ this spanwise directed jet momentum would drive the vortex system to infinity in the direction of span. For the limiting case of $C_{\mu} = \infty$ the effective aspect ratio of the wing $(AR)_{eff}$ would reach infinity then, independent of its geometric magnitude $AR = b^2/S_{ref}$. The lift curve gradient will be $C_{L\alpha} = (C_{L\alpha})_{2d} = 2\pi$ then and its reciprocal value $K (C_{\mu} \rightarrow \infty, \alpha \rightarrow 0) = 1/2\pi = 0.159$ is found as the lower boundary of induced drag for potential lift but zero L.E. suction. By introducing $(C_{L\alpha})_{2d} = 2\pi$ we confined ourselves to the case $\varphi_D = \varphi_0 = 0$, but the effect of sweep is accounted for when applying the well known $\cos \varphi$ correction term, see later Fig.13, $\alpha = 0$. It should be kept in mind that the imaginarity raised "effective" aspect ratio does not have any meaning for the potential theory limit of the 3-d wing induced drag (full suction, elliptic, circulation, inviscid $K = 1/\pi AR$), given in Fig.7 as the lower limit for the non-blown wing. But it is applicable to the lift development $C_{L\alpha} = f(AR_{eff})$.

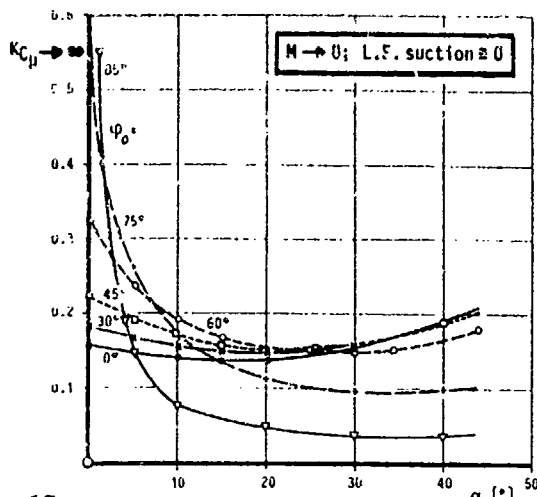


Fig. 13

Factor of induced drag for $C_{\mu} \rightarrow \infty$ as dependent on L.E. sweep φ_0 and a.o.a. α

The upper limit given in Fig.7 ($K = 1 / (C_L \alpha)$) linear for $C_{\mu}, C_L, \alpha \rightarrow 0$) remains realistic as the worst case for this planform exhibiting zero suction.

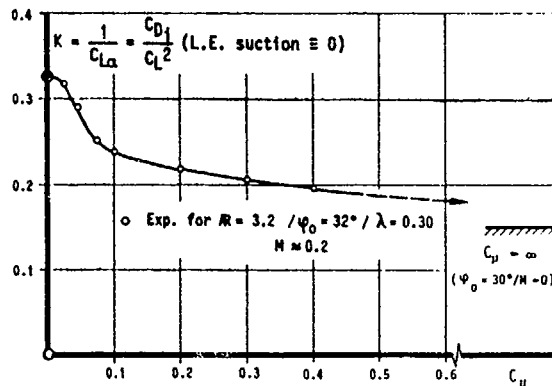
Up to now the potential theory lift of attached flow was taken into account not yet regarding the jet induced non-linear vortex lift. For the sum of potential and vortex lift we can apply the Polhamus Leading Edge Suction Analogy, the assumptions from above are fitting into its frame-work. We get for the total lift

- 1) $C_L = C_{Lp} + C_{Lv} = K_p \sin \alpha \cos^2 \alpha + K_v \sin^2 \alpha \cos \alpha$ with the notations given by Polhamus
- 2) $K_p = C_{Lp} / \alpha$
- 3) $K_v = K_p^2 (1/K_p - 1/\pi AR) / \cos \varphi_0$
Now let $C_{\mu} \rightarrow \infty$, so that $K_p \rightarrow (C_L \alpha)_{2d} = 2\pi$ (blowing parallel to the unswept L.E.), we get from 1)
- 4) $C_L = 2\pi (\sin \alpha \cos^2 \alpha + \sin^2 \alpha \cos \alpha)$,
 $K_p = K_v = 2\pi$
With the equation for lift dependent drag in the case of zero - L.E. suction $C_{DL} = C_L \tan \alpha$ we find
- 5) $C_{DL} = 2\pi \sin^2 \alpha (\sin \alpha + \cos \alpha)$
and for $K = C_{DL} / C_L^2 = \tan \alpha / C_L$
- 6) $K = [2\pi \cos^2 \alpha (\sin \alpha + \cos \alpha)]^{-1}$

This is the special case for $\varphi_D = \varphi_0 = 0$ in Fig.13, where the development of $K(C_{\mu} \rightarrow \infty)$ is presented as depending on α and $\varphi_D = \varphi_0$. The extrema of K are found by differentiating 6) with respect to α and $dK/d\alpha = 0$ gives a maximum for $\alpha = 90^\circ$ and $K_{max} = \infty$, the minimum is found for $\alpha = 15.7^\circ$ and $K_{min} = 0.139$ and $C_L = 2.0$. Note that for sweep angles less than 70° the magnitude of K_{min} is hardly affected by sweep, but the a.o.a. for K_{min} is driven to higher values with increasing sweep, the same is true for $C_L(K_{min})$, which tends to excessive magnitudes with increasing sweep and angle of attack. The latter effect is introduced by the unbroken contribution of nonlinear lift with increasing sweep and angle of attack due to the L.E. suction analogy (compare equations 1) and 3)).

Results are also shown in Fig.13 for low a.o.a and increasing sweep. Here the potential lift gradient K_p is reduced $K_p \sim 2\pi \cos \varphi$ and the vortex lift does not contribute very much to total lift ($K_v \sim \sin^2 \alpha$) so for $\varphi \rightarrow 90^\circ$ and $\alpha \rightarrow 0$ $K(C_{\mu})$ tends to infinity and $K(\alpha)$ is degenerating to the axis-system.

Let us now come to the realistic examples given in the preceding chapter. In advance of Fig.13 the limiting curve $K(C_{\mu} \rightarrow \infty)$ was already given in Fig.7 when analysing the effect of spanwise blowing on induced drag. This curve for the relevant basic wing ($AR = 3.2 / \varphi_0 = 32^\circ$) can be identified again in Fig.13 for $\varphi_0 \approx 30^\circ$. The lowest factor K was found the experiment for $C_{\mu} = 0.4$: $K \approx 0.2$.

Fig. 14 Comparison of limit $K_{C_{\mu} \rightarrow \infty}$ with experimental results

The experimental results for the development of K as a function of C_{μ} are presented in Fig.14, as taken from Fig.7 by crossplotting. The limit value is also plotted for this realistic configuration (but assuming $C_{\mu} \rightarrow \infty$), that is the above mentioned result from Fig.13, for $K_{min} = 0.15$. The experimental results may well indicate that the limit value established before will be approached in an asymptotic way, demonstrating again the wide range of applicability of Polhamus' L.E. suction Analogy. As J.E. Lamar admired the brightness of E.C. Polhamus' intuitive reasoning, when he established his suction analogy, the author cannot help but confess his admiration, that Polhamus' ideas continued to work even when the intuitive reasoning was further stressed "ad extensum" in this section.

5. LIMITATIONS and CONCLUSIONS

Let us start with some generic aerodynamic considerations about the lift production caused by spanwise concentrated blowing:

(A) Evidently this technique makes use of the second principle of dynamic lift as given by the separated stable vortex flow over wing upper surfaces. It is triggered here by the jet blowing parallel to the leading edge thus superposing a cross flow component, which in turn will generate the desired type of flow, globally differing from the classical attached (potential) flow (first principle). The contribution to lift introduced now is found to be proportional to α^2 , which means, that there is to expect an increased dominance of the wing's suction side when compared to the attached, rotation free flow of lift principle one. This strongly contrasts to the third principle - not being of any relevance here - given by super/hypersonic flow. Then, with increasing

Mach-number, the pressure-side of the wing is by far dominating, finally cumulating in the hypersonic shock-lift of waveriders.

It follows from this attempt to categorize, that spanwise blowing should be applied particularly for subsonic speeds which are offering the highest potential of negative pressure differences.

(B) Above statement of subsonic preference is strengthened further when the parameter C_{μ} (see before) comes into consideration again, C_{μ} being proportional to $1/M^2$ (for constant available jet momentum). Note that this holds also for the "effective" sweep introduced by blowing and necessary for the development of the desired vortex system. For a given swept wing and increasing Mach-number the nonlinear lift produced by blowing will be centered more inboard (and forward) relative to the low speed case. There might be introduced a pitch up tendency then.

This is leading over from the domain of speed to the domain of wing geometries favourable of spanwise blowing. High aspect ratio wings may be excluded in advance from the following reasons:

(C) They are bound to relatively thick wing sections from overall design aspects (loads, moments, weights). They'll have large nose radii thus exhibit T.E. separation at high α and are bound to attached flow around their L.E. from L/D reasons. They draw most profits from the first principle of aerodynamic lift.

From comfort and safety reasons the high α regime is avoided; to decouple lift from a.o.a. they use highly efficient flap systems. Thus aerodynamic, configurational and mission characteristics are opposing the principles of spanwise blowing, the effects and efficiency of which are coupled to the high a.o.a. regime ($\Delta C_L \sim \alpha^2$).

(D) Concentrated spanwise blowing underlies -as any blowing technique- a jet decay problem. Among others this will provoke the tendency of the jet to align with free stream direction. For a fixed wing area but increasing span (aspect ratio) decreasing portions of the wing will be influenced by the jet drifting inboard. This may cause a jet induced pitch up problem on a swept wing, similar to (B).

From this simple generic reasoning we can conclude for the domain of spanwise blowing:

- low speed regime / high angle of attack
- thin wings / moderate to low aspect ratio (say: fighter type wings / supersonic designs)

Having considered only aerodynamic characteristics so far, there is found a clear indication that spanwise blowing will lend itself to fighter-type aircraft (apart from applicability for transport-type configurations on their smaller lifting surfaces e.g. horizontal tails and canards or on heavy loaded parts like deflected T.E. flaps. In the latter case advantage of decoupling wing lift and a.o.a. is regained, but spanwise blowing

now is stuck with the problem, that it will pay with additional trim-drag for additional lift, comparable to BLC).

Having identified a bundle of aerodynamic improvements due to spanwise blowing pointing at application on fighter-type a/c, the question still is open, why there is not found an operative example. The reasons may become more plausible when the point of view is taken from the complete design. For instance the engine will come into the game then.

Spanwise blowing, i.e. its demand for pressurized air, should be taken into account already from the very beginning of engine design (intake, compressor as the supplier of blowing energy, engine control-hence the complete flow cycle). An add-on solution is very costly in terms of engine propulsion and handling, a 5% tapping of compressor flow for spanwise blowing may result in a loss of 10 - 15 percent of net propulsive force in this non adapted case (single cycle engine). Proper adaption will reduce this loss to roughly half the value, but, to the authors knowledge, adapted designs do not exist up to now.

A second region of "resistance" against application of spanwise blowing is found in mission and air-frame problems. The technique is bound to subsonic maneuvering and high a.o.a. thus to the flight regime, which is not limited by thrust (or drag) but is limited by available maximum aerodynamic lift of the (fighter-) configuration. This gives preference to the left and lower end of the flight envelope and to attained maneuver performances. It is questionable if the gain in lift attainable by spanwise blowing can be used for improvement of take-off and landing performances (exchange rate thrust versus lift in the former case and, in both cases, given limits of a.o.a. e.g. scrape angle). To get rid of this, one has to design higher (and more heavy) landing gears giving additional problems of housing these constructions, especially true for thin slender wings. A third and important argument against spanwise blowing is introduced by safety considerations, the effects of this technique being vitally bound to the operating engine. Engine out means blowing out and this may have catastrophic consequences in critical flight conditions (the same argument holds for BLC applications).

The "killer" argument against spanwise blowing is found in historical reasons. At the time s.b. came to appearance, the strake wing was in full development (F16, Northrop P530 Cobra, F18). This wing draws similar profits for the development of the stable separated vortex system just from its geometry, but allowing a much higher flexibility all over the speed regime (and not depending on the running engine). By virtue of its "natural" flow characteristics higher sustained and attained maneuver performances, lower buffet intensities, better transonic/supersonic accelerations (due to the lower wave drag) and less supersonic trim drag hence better L/D (due to smaller supersonic neutralpoint

shift) are presented by the strake when compared to the basic trapezoidal wing.

In Fig.15 the increment of maximum lift at subsonic speeds is presented, which is found experimentally when introducing -step by step and combined-spanwise blowing, high-lift flap systems and/or the strake. Note, that the increment due to blowing would reduce for higher M due to the proportionality of $C_{\mu} \sim 1/M^2$. Keeping this in mind the superiority of the strake wing is clearly evident and the contribution of spanwise blowing has to be measured relative to the level already given by the strake wing. Remember that this is also true for development of drag, as presented in Figs.5 and 7 for low speed, when the basic wing (plus blowing with $C_{\mu} = 0.1$) developed the same drag characteristics as given by the strake wing without blowing. For higher speed this equality of aerodynamic performance will quickly change to superiority of the strake wing.

Also it should be kept in mind that there is a definite lower boundary found, down to which spanwise blowing can drive the level of induced drag factor: $K(C_{\mu} \rightarrow \infty) \approx 0.15$ (see Figs.13,14). This limit is equivalent to a wing attaining 100% suction and having an aspect ratio $AR = 2.1$ only, a further but late hint for the a priori limited applicability of this technique.

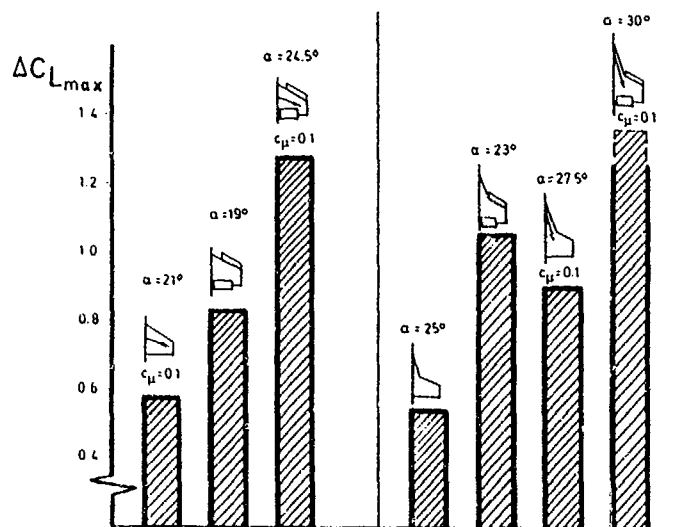


Fig. 15 Effects of strake, flap system and spanwise blowing (reference: clean basic wing)

PNEUMATIC MANAGEMENT OF BLUNTED-FOREBODY FLOW ASYMMETRY FOR HIGH-ANGLE-OF-ATTACK DIRECTIONAL CONTROL

by
Frederick W. Roos, Charles L. Magness, and Daniel V. Brown

McDonnell Douglas Aerospace
P.O. Box 516
St. Louis, Missouri USA 63166

SUMMARY

Low-speed experiments have been conducted to explore the effectiveness of combining nose bluntness, which suppresses the tendency toward flowfield asymmetry, and pneumatic flow-separation control, which triggers flow asymmetry, into a system of pneumatic side-force control for a slender forebody shape at high angles of attack (α). The basic forebody shape studied, a 20%-blunted, 3.5-caliber tangent ogive, developed no side force over the range $0 \leq \alpha \leq 60^\circ$. Slight blowing through either of two symmetrically positioned orifices at the blunt nose of the forebody produced a degree of flow asymmetry (and a corresponding side force) that depended on jet massflow rate within limits that varied with α , the specific jet configuration, and laminar vs. turbulent boundary-layer separation. Forward-blowing jets were found to be generally more effective than jets normal to the forebody surface in producing pneumatic side-force control.

INTRODUCTION

It has long been known that slender bodies of revolution, especially those having pointed noses, develop non-linear lift forces as well as very large side forces and yawing moments at high angles of attack (α), and that these characteristics are associated with asymmetry of the vortices formed by flow separation on the leeward side of such bodies.¹ The profound influence of minute nose-shape details on the development of large-scale flow asymmetry became quite evident in some of the earlier studies of vortex-dominated slender-body flows.²

In the design of current and future generations of high-performance aircraft, greatly-increased emphasis is being placed on controllability and maneuverability at very high α .³ Correspondingly, renewed interest has developed in the understanding, prediction, and control of high- α , vortex-dominated, fuselage-forebody flow fields.⁴ Employment of forebody vortex-flow asymmetry (and associated side forces) as a means of providing yaw authority for maneuvering at high α requires two essential characteristics. Firstly, the high- α flow about the forebody should, ideally, be naturally symmetric. Then, some means should be available to controllably perturb the flow into a state of asymmetry, favoring either side of the body, so as to induce a proportional side force (yawing moment).

It has been demonstrated that blunting a slender body of revolution suppresses the tendency of that body to develop asymmetric flow at high α .⁵ However, the fundamental instability of the slender-body vortex flow field remains, and it is possible for a small perturbation at the nose of such a blunted body to trigger flow asymmetry and the resulting lateral forces.⁶ The experiments described in the present paper constituted a study of the combination of blunting (to suppress flow asymmetry) on a 3.5 caliber tangent ogive forebody and blowing through small nose jets to introduce flow perturbation leading to controllable side forces, the latter based on the demonstrations by Malcolm et al.⁷⁻⁸ of the effectiveness of such jets in controlling vortex asymmetry. In principle, as suggested by the sketch in Fig. 1, it was expected that slight blowing through a jet on the right side of the nose would promote detachment of the separated-flow vortex on the right side of the forebody, leading to a leftward side force.⁹ (Here and elsewhere, right and left are intended in the sense of the view forward over the forebody nose.)



Fig. 1. Expected effect of nose jets in triggering separated-flow asymmetry on blunted tangent ogive forebody.

EXPERIMENTAL SETUP

The forebody experiments were conducted in the McDonnell Douglas Aerospace (MDA) Shear Flow Facility. In the test installation (Fig. 2), the strut-sting model-support system is attached to a turntable that provides angle-of-attack (α) variation. Aerodynamic loads were measured by an internal six-component strain-gage balance. The aerodynamic loads of primary interest here are normal force (C_N in coefficient form) and side force (C_Y). Note that the planform area A is the reference area used in the definition of all coefficients. The conventions employed for angles, forces, and signs are shown in Fig. 3. Flow-visualization images are acquired by a miniature video camera mounted on an offset from the sting; Fig. 4 shows

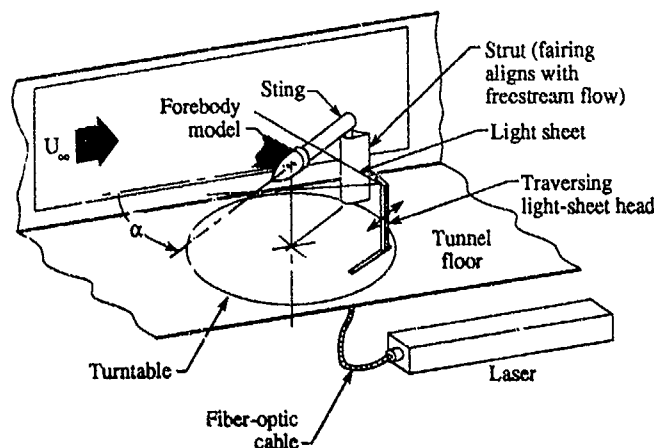


Fig. 2. Forebody test installation in MDA Shear Flow Facility.

Export authority: 22CFR125.4(b(13)).

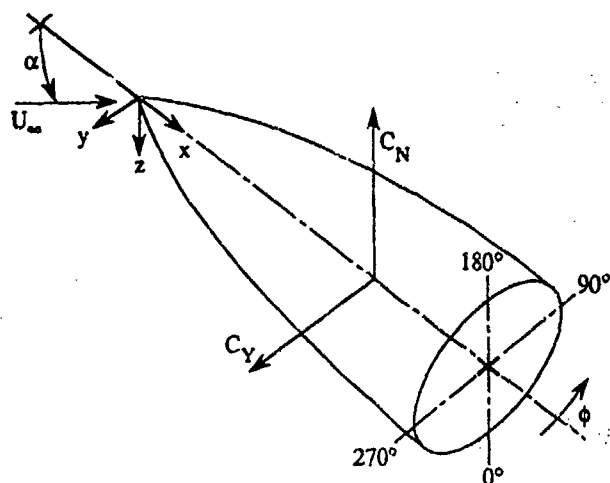


Fig. 3. Variables and sign conventions.



Fig. 4. View of model from video mini-cam.

the minicam view of a tangent ogive model. Vortex trajectories are determined by processing video frames of any particular flow cross section to identify the center of each vortex core. Such processing yields the vortex positions every one-third caliber along the body. For selected cases, flow field measurements were made with the MDA Three-Component Laser Doppler Velocimeter (LDV) System, shown in Fig. 5. This system is fully automated and provides highly resolved, interference-free data on the vortex velocity-field structure.

The model forebody tested was a 3.5-caliber tangent ogive having a base diameter, D , of 7.62 cm. The nose of the body was hemispherically blunted to a radius that was 20% of the base radius, i.e., $r_n/D = 0.10$. Several control-jet configurations were studied. In all cases, jet orifices were located axially at the point of tangency of the hemispherical nose and the tangent ogive surface. Azimuthally, the jets were usually positioned at $\pm 135^\circ$ from the windward meridian of the forebody (i.e., $\phi_j = \pm 135^\circ$). Figure 6 is a photograph of the nose of the model with forward-facing jets (jet axes parallel to the model centerline). Boundary-layer tripping techniques developed in the course of earlier forebody-flow-field investigations⁹ were employed to permit the study of cases of simulated-high-Reynolds-number fully turbulent flow separation. The head-on view of the model shown in Fig. 7 displays the longitudinal strips of #60 carborundum grit that functioned as crossflow boundary-layer trips at high α . Azimuthally, the grit bands were centered at $\phi = \pm 70^\circ$, and were approximately 10° wide. Axially, the grit bands originated at $x/D \approx 0.15$ and extended to the base of the model.

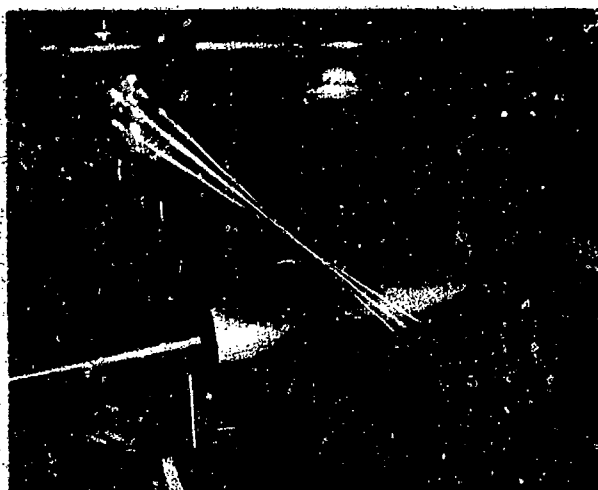


Fig. 5. MDA Three-Component Laser Doppler Velocimeter System mapping forebody flow field.

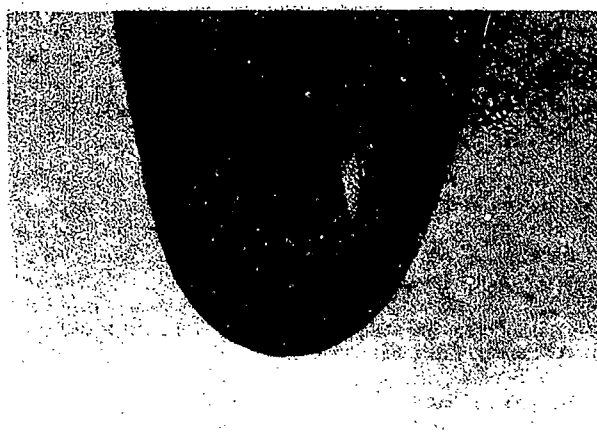


Fig. 6. Forward-blowing jet configuration on 20% blunted, 3.5D tangent ogive forebody.



Fig. 7. Head-on view of model with boundary-layer transition strips installed.

RESULTS

The basic effectiveness of nose bluntness in suppressing flow asymmetry is clearly shown in Fig. 8, which compares C_Y vs. α data for a pointed tangent ogive (reproduced from Ref. 9), the blunted tangent ogive (with $C_Y = 0$ for all α), and the blunted tangent ogive with a tiny hemispherical bump on one side of the nose. LDV velocity-field data taken in the blunted tangent ogive flow field at $\alpha = 45^\circ$ were used to evaluate axial vorticity over transverse planes at $x/D = 1.0, 2.0$, and 3.0 , where x is the axial distance aft of the virtual apex of the tangent ogive. The results are compared in Fig. 9 with corresponding data for the pointed tangent ogive. The symmetry of the flow field and vortex strengths for the blunted tangent ogive contrasts sharply with the pronounced asymmetry of the vortex flow field for the pointed body.

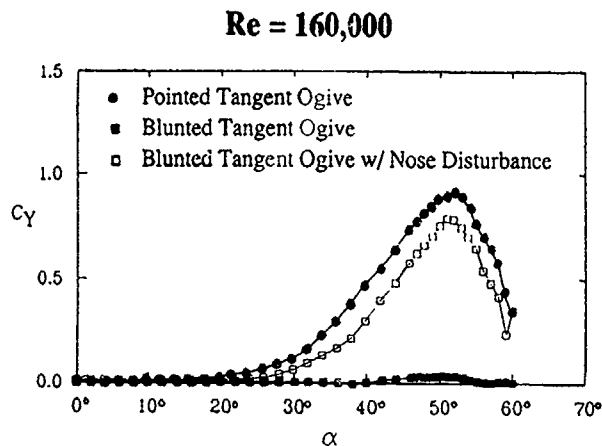


Fig. 8. Effect of blunting on side force for 3.5D tangent ogive.

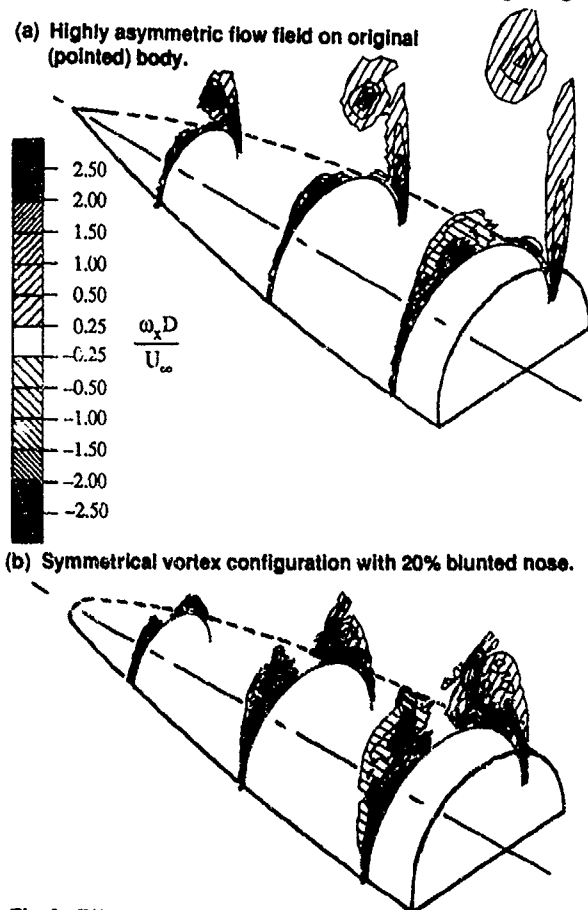


Fig. 9. Effect of bluntness on vorticity field above 3.5D tangent ogive forebody at $\alpha = 45^\circ$ (laminar separation).

Typical blowing results for the blunted tangent ogive with laminar separation are shown in Fig. 10, where the overall symmetry of effects produced by the two jets is evident (here and elsewhere, right and left are intended in the sense of a view forward over the forebody nose). The reason for the slight asymmetry in the C_Y curves for $55^\circ < \alpha < 60^\circ$ is not clear, although it may be associated with machining imperfections near the left jet orifice (refer to Fig. 6, remembering that the "left" jet is to the right in the photo). The effect on C_N and C_Y of blowing at various rates (right jet) is indicated in Fig. 11. Blowing rates are all defined in terms of a mass-flow coefficient, $C_{\dot{m}}$, rather than a momentum coefficient, C_{μ} , to emphasize the fact that it is the displacement effect of the jet flow, rather than any momentum-related entrainment and/or energizing effect, that is responsible for the phenomena demonstrated here. ($C_{\dot{m}} = \dot{m}_j / \rho_\infty U_\infty A$, where \dot{m}_j is the mass flowrate of the control jet.) Cross-plotting ΔC_Y vs. blowing rate (+ for right jet, - for left jet) for several α 's (Fig. 12) shows the basic characteristics of the pneumatic control. Within a range about $C_{\dot{m}} = 0$, the effect of blowing is proportional, up to limiting levels of ΔC_Y (with different maxima for each α).

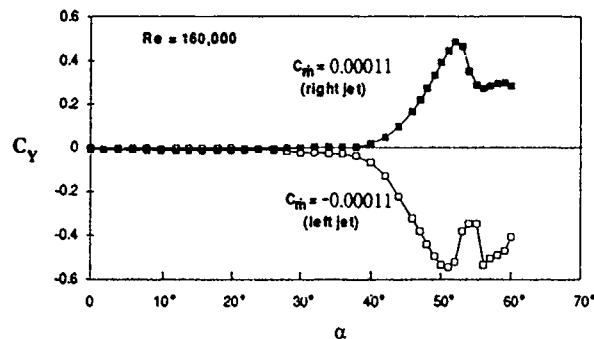


Fig. 10. Typical blowing results for blunted tangent ogive with laminar separation.

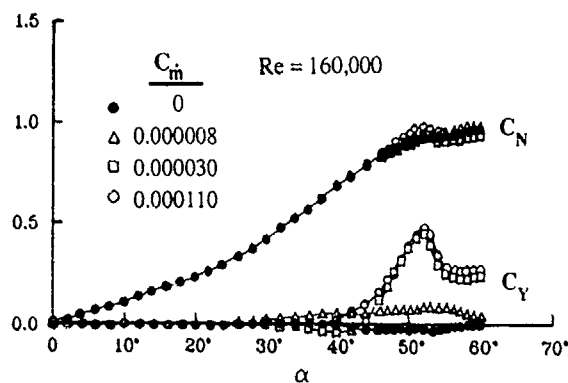


Fig. 11. Loads curves for range of right-jet blowing rates on blunted tangent ogive with laminar separation.

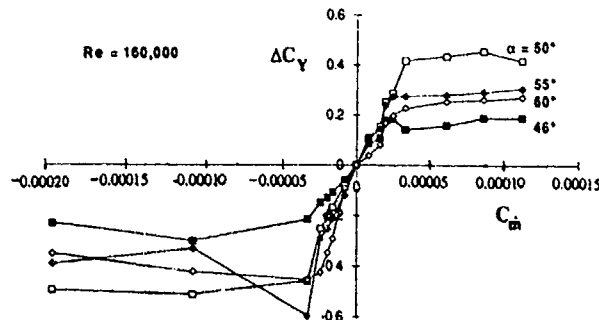


Fig. 12. Side-force control via forward-blowing jets on blunted tangent ogive with laminar separation.

Figure 13 shows that the blowing effectiveness is Reynolds-number-insensitive, further emphasizing that the blowing effect indeed scales with C_m rather than C_μ .

An alternative jet configuration involved jets at the same locations, but oriented normal to the forebody surface. Results obtained with this configuration are shown in Fig. 14, where the phenomenon we call "overblowing" is evident. For both + and - blowing at each α , ΔC_Y reaches a maximum for some range of C_m ; increasing C_m then produces a loss of ΔC_Y . We speculate that the greater momentum of the higher- C_m jets allows them to blow right through the region of effective interaction without stagnating, therefore producing no significant displacement effect on the local surface-boundary-layer flow.

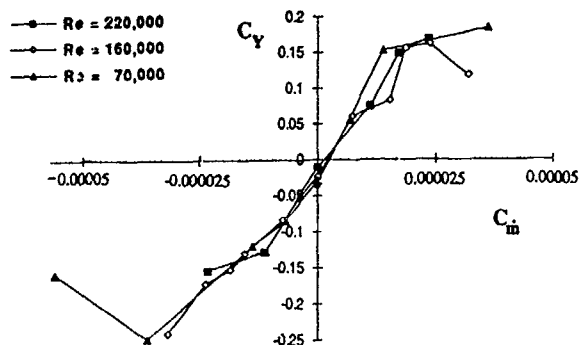


Fig. 13. Forward-blowing effectiveness on blunted tangent ogive with laminar separation at $\alpha = 46^\circ$ for various Reynolds numbers.

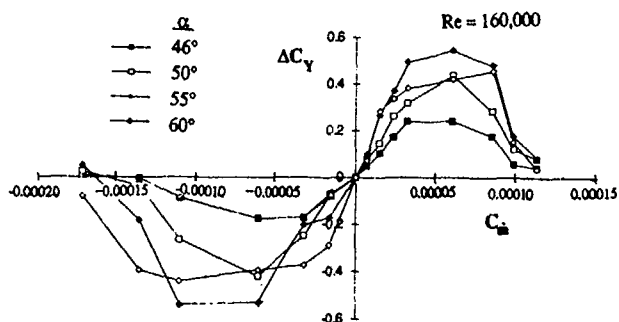


Fig. 14. Effectiveness of normal jets on blunted tangent ogive with laminar separation, showing "overblowing" effect.

That the nose-blowing does indeed induce vortex detachment, thus generating flow asymmetry, as intended (recall Fig. 1), is supported by the vortex-axis trajectories (derived from flow-visualization images) compared in Fig. 15. Clearly the blowing (from the right-side jet) causes the right side vortex to detach and the left-side vortex, which remains attached, to be drawn under the lifted-off vortex and to migrate toward the leeward meridian, all of which is consistent with the generation of positive C_Y (to the left).

Turbulent- and laminar-separation loads data (without blowing) are compared in Fig. 16. The pronounced reduction in C_N resulting from turbulent separation is characteristic of slender forebodies.^{2,11}

Turbulent-separation loads curves corresponding to various forward-blowing rates are presented in Fig. 17. Two features of the data curves in Fig. 17 differ from the corresponding laminar-separation data in Fig. 11. The maximum magnitudes of the blowing effects on C_N and C_Y are obviously greater when separation is turbulent. Also, the C_Y response to blowing first appears at considerably lower α for turbulent separation. Control-characteristic curves for two α 's with turbulent separation are plotted in Fig. 18, showing similar behavior to the laminar-separation case, i.e., a proportional effect range about $C_m = 0$, limited by maximum and minimum C_Y 's that depend on α .

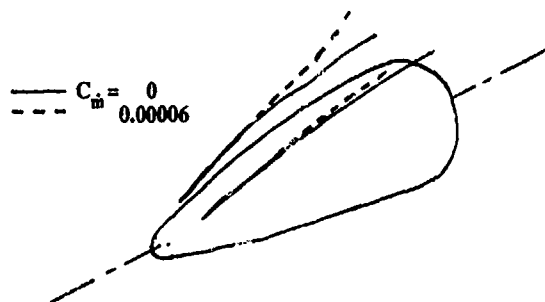


Fig. 15. Vortex trajectories above blunted tangent ogive with laminar separation at $\alpha = 50^\circ$, showing asymmetry induced by normal jet at right side of nose.

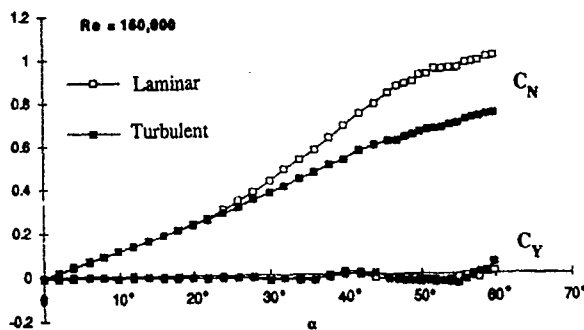


Fig. 16. Comparison of loads curves for blunted tangent ogive with laminar and turbulent separation.

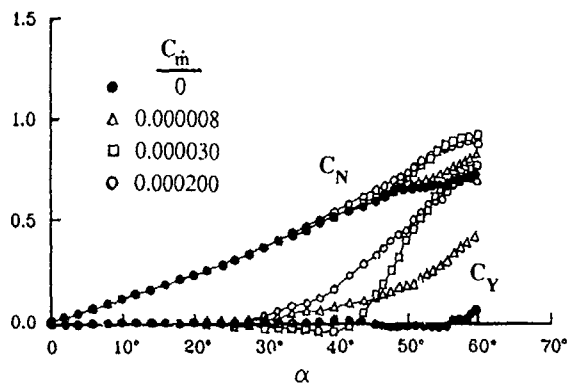


Fig. 17. Loads curves for range of right-jet blowing rates on blunted tangent ogive with turbulent separation.

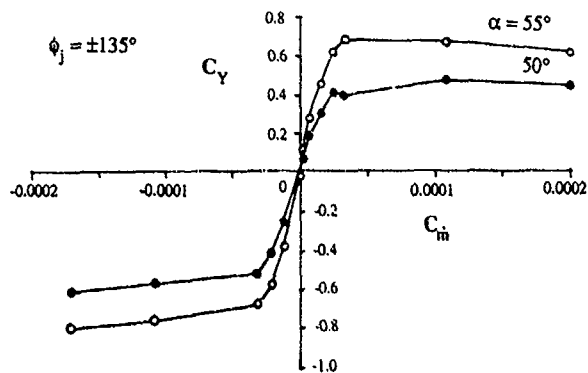


Fig. 18. Side-force control by forward-blowing jets at two angles of attack with turbulent separation.

The Reynolds-number-insensitivity evident in Fig. 19 shows both that the boundary-layer tripping is successful at these Reynolds numbers, and (again) that $C_{\dot{m}}$ is the appropriate blowing parameter.

Comparative effectiveness of pneumatic side-force control with laminar and turbulent boundary-layer separation is indicated in Figs. 20(a) ($\alpha = 50^\circ$) and 20(b) ($\alpha = 55^\circ$). At the lower α , blowing effectiveness is similar in the two cases. But at the higher α , the pneumatic-control effectiveness is much greater when separation is turbulent. This kind of variation underscores the importance of properly simulating the anticipated (full-scale) type of boundary-layer separation when attempting to evaluate unconventional flow-control methodologies.

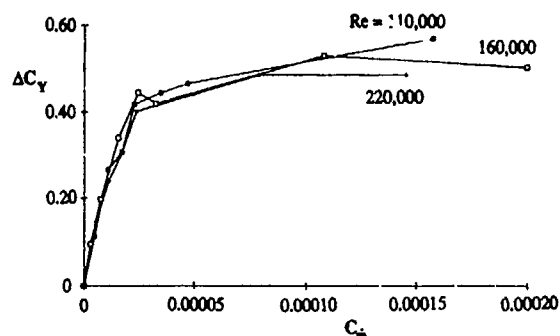


Fig. 19. Forward-blowing effectiveness with turbulent separation for several Reynolds numbers at $\alpha = 50^\circ$.

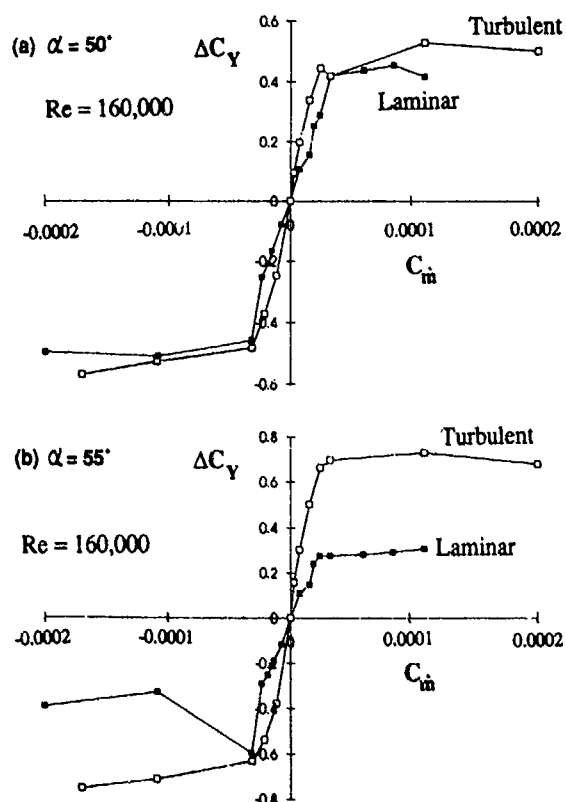


Fig. 20. Comparison of forward-blowing-jet effectiveness for laminar and turbulent separation at (a) $\alpha = 50^\circ$ and (b) $\alpha = 55^\circ$.

Several pneumatic-control jet configurations were studied with turbulent flow separation. Figure 21 shows results obtained with jets normal to the surface and turbulent boundary-layer separation. As was true with laminar separation (Fig. 14), it is again evident that the normal jets reach an "overblowing" condition. Blowing-flow-control effectiveness is compared for three jet configurations, all with fully turbulent separation, at $\alpha = 50^\circ$ in Fig. 22. Up to $C_{\dot{m}} = 0.00008$, it appears that the three jet configurations

are approximately comparable in effectiveness. The forward-blowing jets at $\phi_j = \pm 135^\circ$ produce the strongest response at low $C_{\dot{m}}$, whereas the forward-blowing jets at $\phi_j = \pm 105^\circ$ appear to yield the greatest overall ΔC_Y . Figure 23 presents additional comparisons of the two forward-blowing jet arrangements, further demonstrating the stronger response of the $\phi_j = \pm 135^\circ$ jets at low $C_{\dot{m}}$ and the greater ultimate effectiveness of the $\phi_j = \pm 105^\circ$ jets.

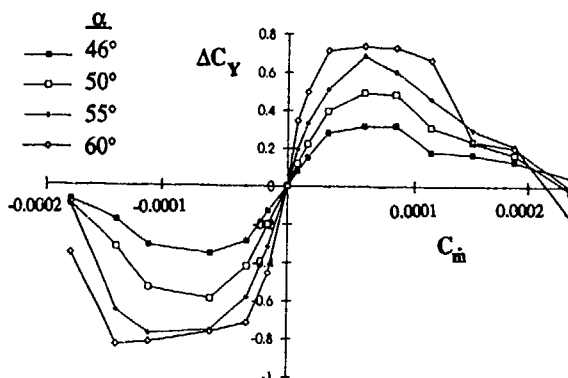


Fig. 21. "Overblowing" effect of normal jets with turbulent separation.

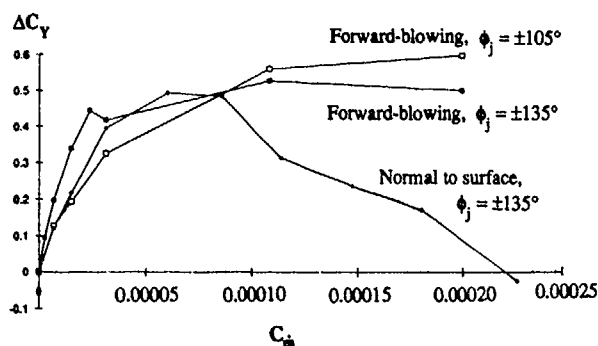


Fig. 22. Comparison of effectiveness of various jet configurations with turbulent separation at $\alpha = 50^\circ$.

Sensitivity of pneumatic-side-force-control effectiveness to sideslip was evaluated over the yaw-angle range $-15^\circ \leq \psi \leq 15^\circ$ with both laminar and turbulent separation. In each case, only the normal-jet configuration was studied. Results for $\alpha = 50^\circ$ are shown in Fig. 24, where it is evident that, regardless of the nature of the flow separation, the pneumatic-control capability exists throughout the indicated sideslip range.

CONCLUSIONS

A series of low-speed experiments has been conducted to explore the effectiveness of combining nose bluntness, which suppresses natural flowfield asymmetry, and pneumatic flow-separation control, which triggers asymmetry, into a system of pneumatic side-force control for a slender forebody shape at high angles of attack.

The forebody shape studied, a 20%-blunted, 3.5-caliber tangent ogive, was shown to develop no side force throughout the range $0 \leq \alpha \leq 60^\circ$, for both laminar and turbulent separation.

Slight blowing through either one of two symmetrically positioned orifices at the blunt nose of the forebody was shown to produce a degree of flow asymmetry (and a corresponding side force) that depended on jet massflow rate within maximum and minimum limits that varied with α , the specific jet configuration, and laminar vs. turbulent boundary-layer separation.

Forward-blowing jets were found to be generally more effective than jets normal to the forebody surface in producing pneumatic side-force control.

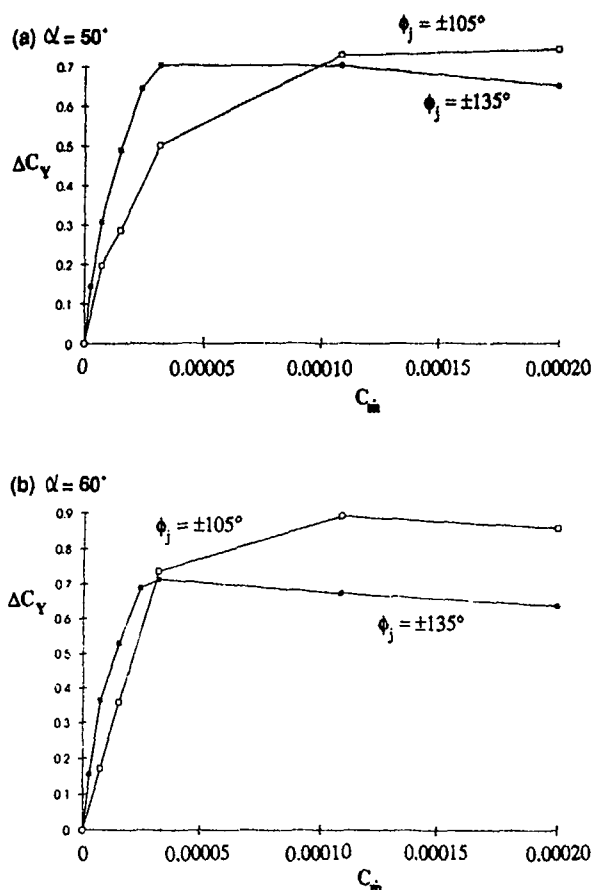


Fig. 23. Influence of azimuthal location on effectiveness of forward-blowing jets with turbulent separation at (a) $\alpha = 50^\circ$ and (b) $\alpha = 60^\circ$.

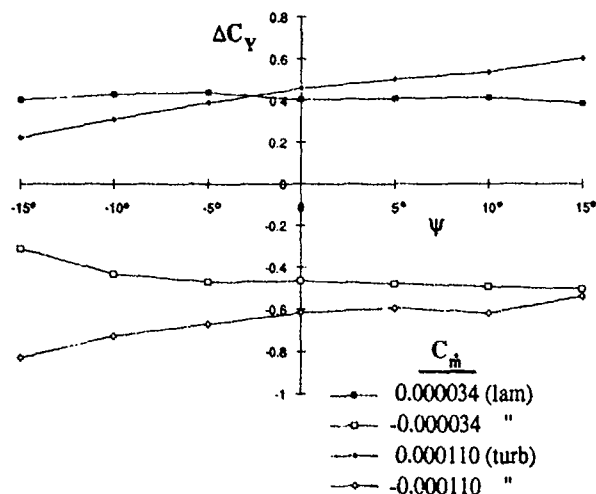


Fig. 24. Yaw influence on pneumatic side-force-control effectiveness at $\alpha = 50^\circ$, laminar and turbulent separation.

REFERENCES

1. Allen, H.J. and Perkins, E.W., "A Study of the Effects of Viscosity on Flow Over Slender Inclined Bodies of Revolution," NACA TR 1048, 1951.
2. Pick, G.S., "Investigation of Side Forces on Ogive-Cylinder Bodies at High Angles of Attack in the $M = 0.5$ to 1.1 Range," AIAA Paper No. 71-570, June 1971.
3. Skow, A.M. and Erickson, G.E., "Modern Fighter Aircraft Design for High-Angle-of-Attack Maneuvering," in High Angle-of-Attack Aerodynamics, AGARD LS-121, March 1982.
4. Chambers, J.R., Gilbert, W.P., and Nguyen, L.T., eds., "High-Angle-of-Attack Technology, Volume I," NASA CP - 3149, 1992.
5. Keener, E.R. and Chapman, G.T., "Onset of Aerodynamic Side Forces at Zero Sideslip on Symmetric Forebodies at High Angles of Attack," AIAA Paper No. 74-770, August 1974.
6. Moskovitz, C.A., Hall, R.M., and DeJarnette, F.R., "Effects of Nose Bluntness, Roughness, and Surface Perturbations on the Asymmetric Flow Past Slender Bodies at Large Angles of Attack," AIAA Paper No. 89-2236, September 1989.
7. Malcolm, G.N., Ng, T.T., Lewis, L.C., and Murri, D.G., "Development of Non-Conventional Control Methods for High-Angle-of-Attack Flight Using Vortex Manipulation," AIAA Paper No. 89-2192, September 1989.
8. Ng, T.T. and Malcolm, G., "Aerodynamic Control Using Forebody Blowing and Suction," AIAA Paper No. 91-0619, January 1991.
9. Roos, F.W. and Kegelman, J.T., "Aerodynamic Characteristics of Three Generic Forebodies at High Angles of Attack," AIAA Paper No. 91-0275, January 1991.
10. Kegelman, J.T. and Roos, F.W., "Influence of Forebody Cross-Section Shape on Vortex Flowfield Structure at High Alpha," AIAA Paper No. 91-3250, September 1991.
11. Lamont, P.J., "The Effect of Reynolds Number on Normal and Side Forces on Ogive-Cylinders at High Incidence," AIAA Paper No. 85-1799, August 1985.

ACKNOWLEDGMENT

This work was conducted under the McDonnell Douglas Independent Research and Development Program.

THEORETICAL AND EXPERIMENTAL INVESTIGATION OF A DELTA WING WITH TURBULENT LEADING-EDGE JETS

by

K.J. Craig and L. Roberts
Durand Bldg, RM 277
Stanford University
Stanford, CA 94305-4035
United States

D.I. Greenwell and N.J. Wood
School of Mechanical Engineering
University of Bath
Claverton Down
Bath BA2 7AY
United Kingdom

Summary

Control of the separated flow over a delta wing using Tangential Leading-Edge Blowing has been investigated experimentally and computationally. Tangential Leading-Edge Blowing describes the injection of momentum into the cross flow plane of the wing by thin Coanda wall jets located at the point of cross flow separation. The concept is shown to be capable of generating significant asymmetry in the vortical flowfield, and hence a lateral control capability, up to very high angles of attack. The primary effects of jet blowing have been modelled using a Navier-Stokes computation with an algebraic turbulence model.

Nomenclature

A_j	jet slot area
b	wing span
c	wing root chord
$C_{l\beta}$	roll moment due to sideslip
C_p	pressure coefficient
C_μ	blowing momentum coefficient
s	wing semi-span
S_{ref}	wing area
t	wing thickness
V_j	jet velocity
V_∞	freestream velocity
x	chordwise coordinate
x_{VB}	location of vortex burst
α	angle of attack
β	yaw angle
ρ	density
ϕ	roll angle

Introduction

It has long been known that because of boundary layer separation near the leading-edge, the flowfield of a delta wing is dominated by a pair of leading-edge vortices which add to the lift. At high angles of attack these vortices burst, sometimes asymmetrically; a phenomenon of particular importance to delta wing aircraft operating in this regime.

In this paper it is shown that the placement of a turbulent jet at the leading-edge of a delta wing greatly modifies, and even eliminates, the vortex pair at high angles of attack and may be used for the control of

such configurations. Navier-Stokes numerical solutions for a blunted delta wing of finite length are presented and include the effects of the jet on vortex breakdown on the wing. Experimentally, a similar configuration was investigated at the University of Bath and showed similar trends to those found in the computational work at Stanford University.

Tangential leading-edge blowing has as its origins the technique of circulation control as applied to two-dimensional aerofoils. Whereas, for aerofoils the injection of momentum produces motion of the rearward separation points to represent increased circulation at fixed geometric angle of attack, the injection of momentum into the cross flow of a delta wing produces an opposite result. For the delta wing configuration, motion of the separation points towards the leeward generator reduces the strength of the vortices as flow equilibrium is maintained.

Computational Programme

The concept of Tangential Leading-Edge Blowing with turbulent jets for a delta wing^[1] is illustrated in Figure 1a. Air is fed from a plenum inside the wing to form a jet which flows over the leading-edge, thereby causing a displacement and modification of the strength of the vortex. Asymmetric or one-sided blowing induces a rolling moment on the wing. The geometry for the thin-layer Navier-Stokes computation^[2] is shown in Figure 1b. It is a cropped 60° delta wing of constant thickness with a jet slot which extends approximately 85% of the length of the circular cross-section leading-edge. The jet slot grows linearly with distance, from 0.0003c to 0.001c, thereby preserving approximate conical similarity. This geometry is sufficiently simple for an algebraic grid combined with post-processing to provide 3-D viscous solutions. The grid is shown in Figure 2a and has approximately ½ million points. Stretching functions have been used to move grid points to high-gradient regions of the flow.

The numerical algorithm used to generate the flow is that developed by Steger et al^[3] - an implicit two factor scheme using a flux vector splitting to upwind difference the convection terms in the streamwise direction, with central differencing in the other direction. Artificial dissipation is used. A modified form of the two layer Baldwin-Lomax^[4,5] algebraic

turbulence model and an actuator plane concept⁽⁶⁾, as elaborated below, was used to model the flow including the turbulent jet.

The actuator plane concept was used to simplify grid generation in the vicinity of the origin of the jet. At the actuator plane the flow variables undergo a discontinuity within the boundary layer such that the jet is introduced while conserving mass and momentum (Figure 2b); this has been shown to give a good approximation to the jet and avoids the introduction of geometry changes due to the presence of the slot. It has the effect of changing the oncoming boundary layer profile to that of a jet at the location of the actuator plane. Jet blowing is characterized by the blowing momentum coefficient C_{μ} , defined as

$$C_{\mu} = \frac{\rho V_j^2 A_j}{\frac{1}{2} \rho V_{\infty}^2 S_{ref}}$$

The no-blowing case is considered first to illustrate the effect on the flowfield of increasing angle of attack and yaw. The case of jet blowing, with blowing coefficient C_{μ} , is then discussed for a fixed angle of attack, α and yaw angle, β .

(a) No Blowing

It can be seen by comparing Figures 3a and 3b that the effect of increasing angle of attack from 30° to 50° at zero yaw is to significantly change the leading-edge vortex, so that at the higher angle of attack the vortex burst takes place earlier with the burst extending over about $\frac{3}{4}$ of the length of the wing, compared with a minimal burst at 30° angle of attack. Shown are computed particle traces of the flow indicating that the vortex undergoes a sudden radial expansion at the burst location. Also computed (but not shown here) are the surface flow patterns for these conditions which show an inward movement of the lines of attachment indicating a displacement of the vortex for the higher angle of attack, together with a marked change of flow pattern near the trailing edge. Associated with the vortex burst is also a change in pressure distribution such that the vortex-induced suction peaks on the upper-surface are diminished; the result is a net loss of lift as the vortex burst becomes more prominent. These changes of pressure can be seen by comparing Figure 4a and 4b, which show the pressure changes radially to the surface at each location for several sections along the configuration.

The effect of non zero yaw is illustrated in Figure 5a, which shows particle paths for $\alpha = 30^\circ$ (which is before stall) and $\beta = 10^\circ$. The location of the vortex burst on the windward side is seen to move forward compared to that on the leeward side. The pressure distribution (Figure 5b) changes so that the leading-edge suction and the (unburst) vortex-induced suction peak on the

windward side are enhanced, giving a stabilising windward-side-up rolling moment. At higher angles of attack the effect is reversed as the windward side burst point moves forward, destroying the lift on that side.

(b) Blowing

The purpose of asymmetric jet blowing is to create a rolling moment and therefore permit control of the wing at high angles of attack. It should be possible to counter the effects of yaw discussed above, for example, by having the blowing create such a rolling moment. Figure 6a compares the particle paths for $\alpha = 30^\circ$, $\beta = 0^\circ$ for increasing amounts of blowing ($C_{\mu} = 0.01, 0.03$). It can be seen that the effect of blowing is to attach the flow on the blown side, effectively blowing the vortex to the unblown side where it overlaps the vortex that already exists on that side. Additional suction on the blown side and a resulting blown-side-up rolling moment is generated, which can be seen by comparing the spanwise pressure distribution at a given station (Figure 6b). Further increases in blowing (from $C_{\mu} = 0.03$ to $C_{\mu} = 0.06$) produce little further change in pressure distribution, so that blowing saturates the flow for $C_{\mu} > 0.03$.

An example of the combined effects of yaw and blowing is given in Figure 7 ($\alpha = 30^\circ$, $\beta = 10^\circ$, $C_{\mu} = 0.02$). There is a partially burst vortex on the unblown (windward) side and an attached flow on the blown (leeward) side. The resulting moment is shown in Figure 8 as a function of C_{μ} . It is seen that blowing ceases to be effective for $C_{\mu} > 0.03$, and that in this case the rolling moment due to yaw is only partially corrected by blowing. Also computed but not shown is a rolling moment reversal between $\alpha = 40^\circ$ and 50° . This reversal can be corrected by superimposing symmetric and asymmetric blowing as shown experimentally; however, only cases involving asymmetric blowing were computed.

Experimental Programme

A delta wing of similar geometry has been tested in the 2.1x1.5m low-speed wind-tunnel at the University of Bath. The wing geometry differed from that investigated computationally in having a thickness/chord ratio of 0.033 and a taper ratio of 0.2, as opposed to 0.061 and 0.3 respectively. Slot geometry was almost identical in terms of local slot height/chord ratio distribution. Aerodynamic loads were measured using an integral sting balance, and upper-surface and leading-edge pressures using a conventional Scanivalve system. Free stream speeds of between 20 and 30 ms^{-1} were typical. A more complete description of the experimental set-up may be found in Reference 7.

For comparison with the computational results presented above, the 'no-blowing' and 'blown' data-sets will be described separately.

a) No Blowing

Figure 9 illustrates the effect of angle of attack on upper and lower-surface spanwise pressure distribution at 50% chord, for zero yaw angle. The onset of vortex burst is reflected in the reduction in magnitude and widening of the vortex-induced suction peak^[6] at around 20°. The equivalent computational results (Figures 3 and 4) show similar behaviour, though with higher levels of leading-edge suction (due to increased wing thickness) and a later onset of vortex breakdown.

For non-zero yaw, Figure 10 shows the effect of increasing angle of attack at a constant roll angle ($\phi = +20^\circ$), corresponding to a gradually increasing sideslip angle (with the right or 'down' side into wind). At low angles of attack the windward side of the wing shows a stronger suction peak, primarily due to a difference in vortex core height rather than vortex strength, and giving a strong stabilising roll moment. As angle of attack increases, the windward vortex bursts ahead of the leeward side, due to the difference in effective leading-edge sweep angle, resulting in a destabilising contribution. At very high angles of attack the bursts reach the wing apex and the vortical flow subsides, leaving the stabilising lower-surface contribution dominant. The overall roll moment characteristic is illustrated by Figure 11 (adapted from Reference 9), showing 'effective dihedral' or roll moment due to sideslip as a function of angle of attack, with an unstable region due to vortex burst asymmetry.

Clearly, the unblown lateral characteristics are dominated by the vortex burst trajectory, which is a function primarily of sweep angle, but also of leading-edge shape, support interference, blockage and test conditions. The computational results show a breakdown-like phenomenon (Figures 3 and 5), but delayed by 10-20° compared with experimental and published (sharp-edged) data (Figure 12). This must be considered when comparing results, particularly for non-zero yaw where the later burst onset predicted computationally results in higher stable roll moments when unblown, as demonstrated by Figure 11.

b) Blowing

The effect of increasing right-side blowing on upper-surface pressures at fixed angle of attack is illustrated by Figure 13. At low angles of attack, with both vortices unburst, the vortex-induced suction peak on the blown side subsides as the vortex strength reduces. At a critical blowing level, the flow on the blown side is fully attached and the response to blowing saturates. The unblown side is unaffected. At a higher angle of attack, with burst vortices present, the blown vortex-

induced peak initially increases in strength as the burst moves aft followed by a reduction in magnitude and then saturation as before. However, an effect is now evident on the unblown side also, with a rapid increase in suction peak magnitude to an unburst maximum, indicating a strong coupling between the burst locations on the blown and unblown sides.

This coupling is seen more clearly in Figure 14, which shows the magnitude of the suction peak as a function of angle of attack and blowing. For blowing off, the suction peak increases with angle of attack, reaching a maximum as the burst passes and then subsiding to a fully separated flow. Symmetric blowing shifts this curve to the right, in a manner analogous to reducing the angle of attack of the vortical flow. For one-sided blowing, the blown side behaves in a similar fashion to the symmetric case, though with an earlier burst onset. The unblown side is unaffected at 'pre-burst' angles of attack, but displays a delayed burst onset. This asymmetry in burst location is similar to the effect of sideslip, with a change in effective leading-edge sweep^[10] corresponding to a shift of the flow 'centreline' away from the blown leading-edge.

The resultant roll moment characteristics are complex (Figure 15a), with a sign reversal in the vicinity of the stall angle. Several regions may be discerned in the characteristics (Figure 15b^[7]) and these can be related to the blowing effects discussed above. Region I, at low angles of attack, corresponds to completely attached flow on the blown side, with the response to blowing saturated. Roll moments are dominated by the 'potential flow' contribution of the jet-induced leading-edge suction, giving a trend approximated by $\sin^2\alpha$. At an angle of attack dependent on blowing level the blown vortex re-establishes, and the separation point moves rapidly from near the wing centreline to the vicinity of the leading-edge (Region II). A loss of leading-edge suction results, balanced by an increasing vortex contribution. While the net normal force contribution is maintained the overall roll moment decreases due to the different moment arms. Within region II a sub-region III is evident, corresponding to the onset of the blown vortex burst, where the roll moment is a complex function of asymmetry in both vortex strength and burst location. A sign reversal occurs, which is also predicted computationally, though at a higher angle of attack. By about 50°, both burst points reach the wing apex and the vortex contribution diminishes (Region IV). Although the remaining jet-induced leading-edge roll contribution is 'blown side up', a further roll reversal occurs. At very high angles of attack the outer flow separates ahead of the slot and all flow control is lost (Region V - 'slot stall'). A hysteresis loop is evident in this region, with onset appearing to be a function of Reynolds Number and leading-edge shape and sweep.

A comparison of these characteristics and local roll moments derived from integration of upper-surface

pressures (Figure 16) is illuminating. At lower angles of attack similar trends are shown, although at high angles of attack the roll reversal noted above in Region IV is not evident in the pressure data. The cause of this discrepancy was determined by flow visualisation (Figure 17) to be a large region of very unsteady, separated reverse flow at the tip on the blown side. This phenomenon was present throughout the angle of attack range tested and gives a very significant loss in roll control power which is not evident in the computational results. A possible cause is the strong end-vortex generated by a finite slot promoting separation aft of the slot and preventing the formation of a coherent tip vortex. The effect of tip geometry requires further investigation, but it is clear that to minimise losses, the slot should extend to the tip, with as small a tip chord as practicable.

Also evident from Figure 15 is a 'dead-band' in the roll response to blowing at lower angles of attack, possibly associated with the formation of the tip separation region. This may be alleviated by superimposing symmetric and asymmetric blowing, with a 'constant total blowing level' scheme found to be most efficient. This is illustrated by Figure 18, for a total jet momentum coefficient of 0.08. The dead-band is suppressed, while the roll reversal is reduced in magnitude and delayed in onset.

The effect of yaw (or roll angle) on lateral characteristics is shown in Figure 19, for a roll angle of $+20^\circ$. In general, recovery or 'out-of-roll' control power is increased while manoeuvre or 'into-roll' control is reduced, limiting maximum trimmable roll angles to around $\pm 15^\circ$; nevertheless, sufficient control power was available for a roll control system with a fully closed control algorithm to be implemented and the capability for control of wing rock demonstrated^[11]. The usable angle of attack range is limited by the onset of slot stall, but this could be extended by optimisation of the leading-edge profile. Alleviation of tip losses would also significantly increase roll authority.

Concluding Remarks

A combined computational and experimental program has investigated the control of a delta wing configuration using tangential leading-edge blowing. The primary effects of blowing of the turbulent jet have been explored computationally for a limited number of cases, while a more complete investigation has been undertaken experimentally.

It has been demonstrated that the effects of a turbulent jet blowing tangentially at the leading-edge of a delta wing, including the effects on vortex bursting, can be represented by computation of the Navier-Stokes equations using an algebraic turbulence model. The use of computation combined with the results of experiment can give a complete picture of the relevant

phenomena and permit control of the delta wings at high angle of attack.

References

1. Wood, N.J. and Roberts, L., "Control of Vortical Lift on Delta Wings by Tangential Leading-Edge Blowing", *Journal of Aircraft*, Vol 25 No 3, pp236-243, March 1988
2. Craig, K.J., "Computational Study of the Aerodynamics and Control by Blowing of Asymmetric Vortical Flows over Delta Wings", PhD Thesis, Stanford University, August 1992
3. Steger et al, "Flux-Split Algorithm for Numerical Simulation of Unsteady Viscous Flows", Proceedings of Workshop on CFD, U.C. Davis, 1986
4. Baldwin, B.S. and Lomax, H., "Thin Layer Approximation and Algebraic Model for Separated Turbulent Flows", AIAA-78-0257, January 1978
5. Degani, D. and Schiff, L.B., "Computation of Turbulent Supersonic Flows around Pointed Bodies having Cross Flow Separation", *J. of Comp. Phys.*, Vol. 66, pp173-196, 1956
6. Tavella, D.A., Schiff, L.B. and Cummings, R., "Pneumatic Vortical Flow Control at High Angles of Attack", AIAA 90-0098, January 1990
7. Greenwell, D.I. and Wood, N.J., "Static Roll Moment Characteristics of Asymmetric Tangential Leading-Edge Blowing on a Delta Wing at High Angles of Attack", AIAA-93-0052, January 1993, also accepted for *Journal of Aircraft*
8. Greenwell, D.I. and Wood, N.J., "Determination of Vortex Burst Location on Delta Wings from Surface Pressure Measurements", *AIAA Journal*, Vol 30 No 11, pp2736-2739, November 1992
9. Kraus, W., "X-31, Discussion of Steady-State and Rotary Derivatives", paper 13, AGARD CP-497, May 1991
10. Greenwell, D.I. and Wood, N.J., "Control of Asymmetric Vortical Flows", AIAA-91-3272, September 1991
11. Wong, G.S., Rock, S.M., Wood, N.J. and Roberts, L., "Active Control of Wing Rock of a Delta Wing at Post-Stall Using Tangential Leading-Edge Blowing", AIAA-93-0056, January 1993

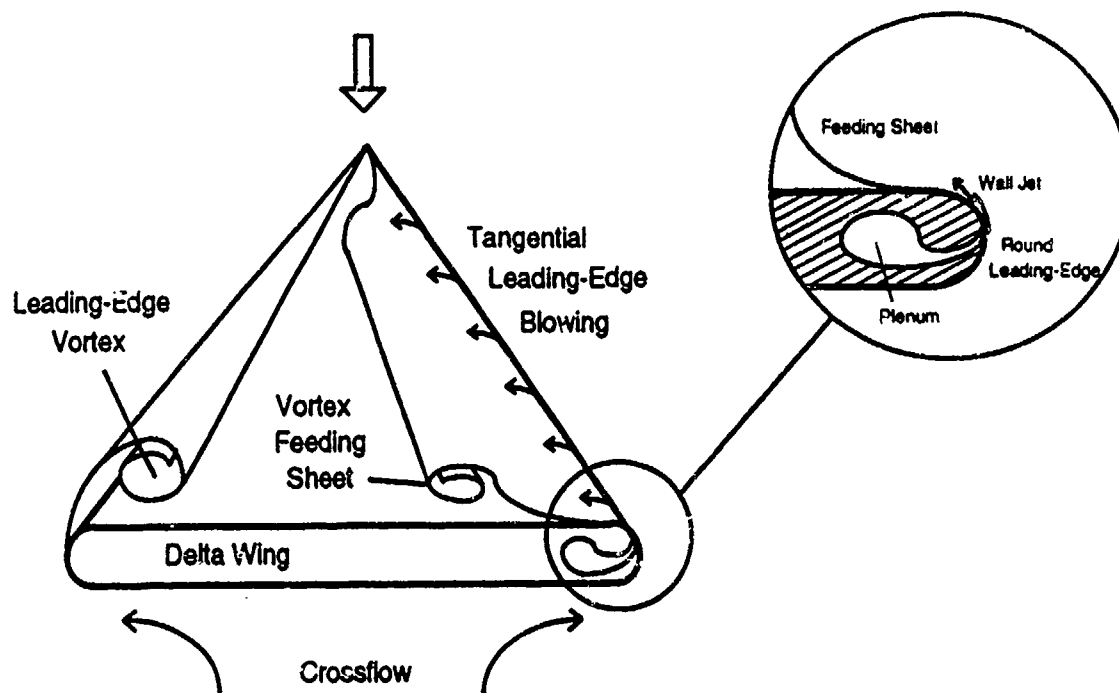


Figure 1a: Tangential Leading-Edge Blowing (TLEB)

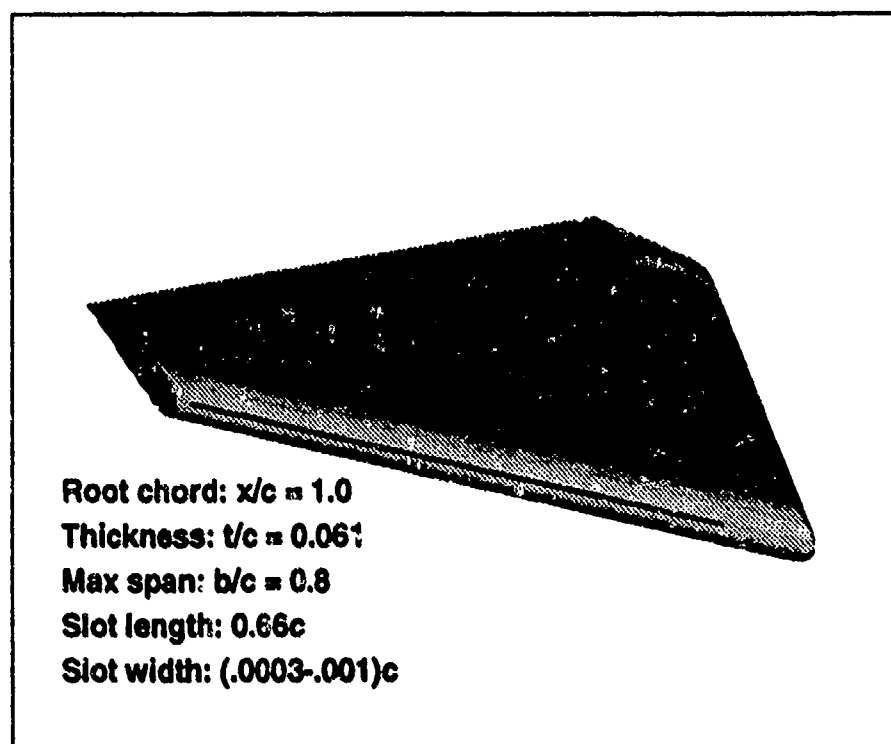


Figure 1b: Computed Geometry

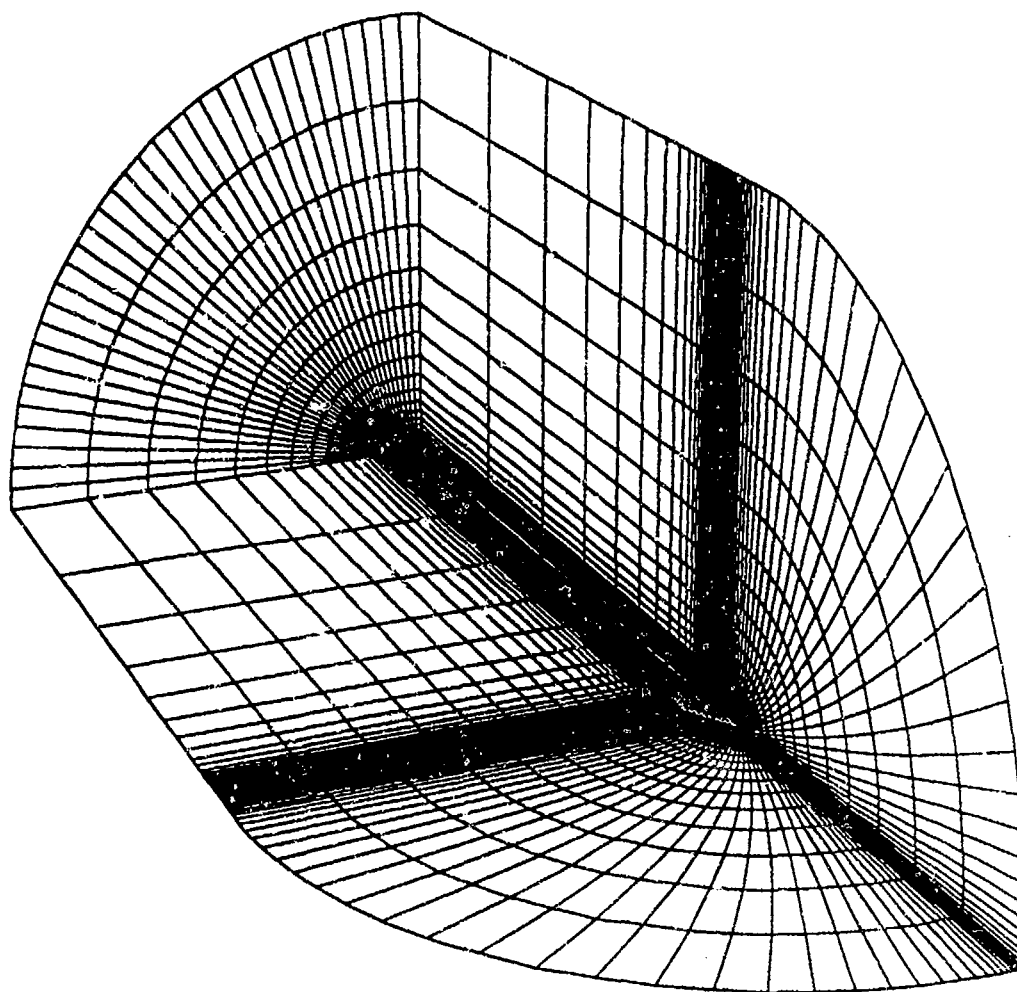


Figure 2a: Quarter Section of Whole Grid

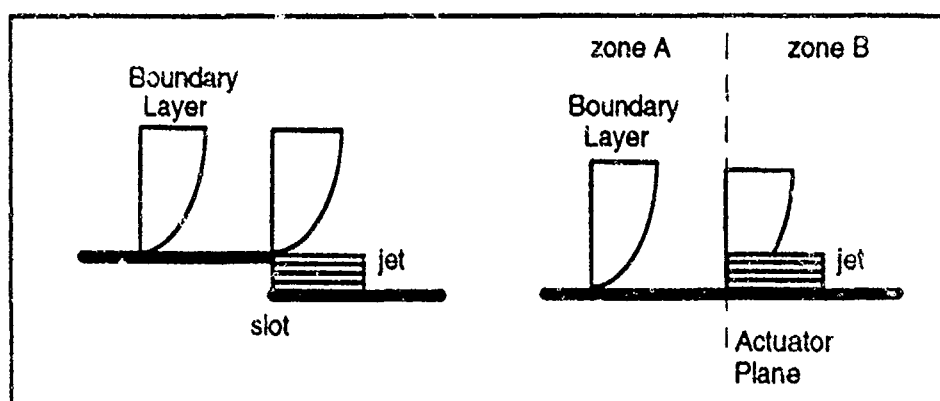


Figure 2b: Actuator Plane Concept

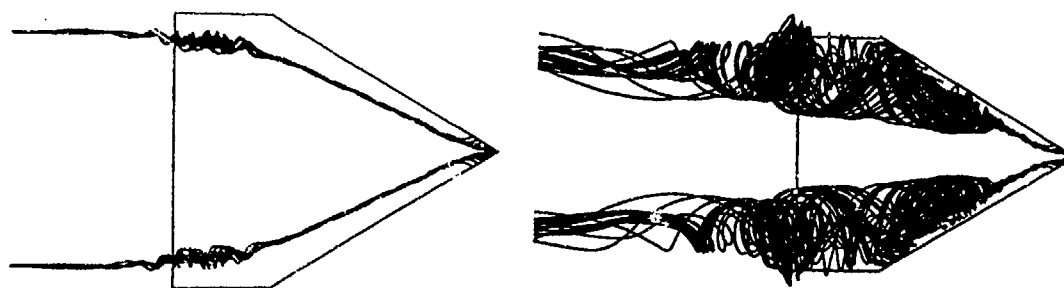


Figure 3: Effect of Angle of Attack on Computed Particle Traces at Zero Yaw ($\alpha = 30^\circ, 50^\circ$)

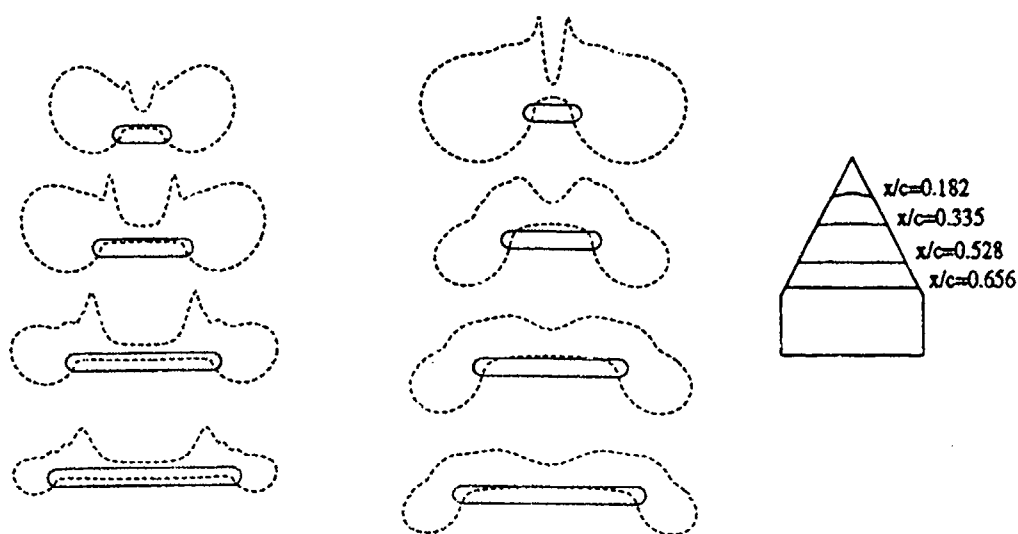


Figure 4: Effect of Angle of Attack on Normal Pressure Coefficient Distributions at Zero Yaw ($\alpha = 30^\circ, 50^\circ$)

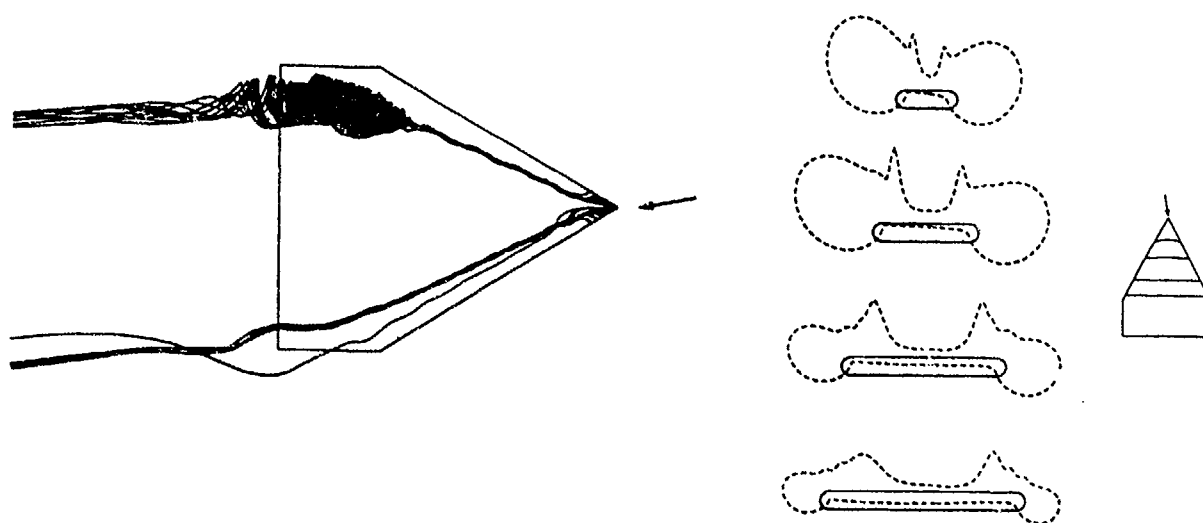


Figure 5: Effect of Yaw Angle on Computed Wing Flowfield ($\alpha = 30^\circ, \beta = 10^\circ$)

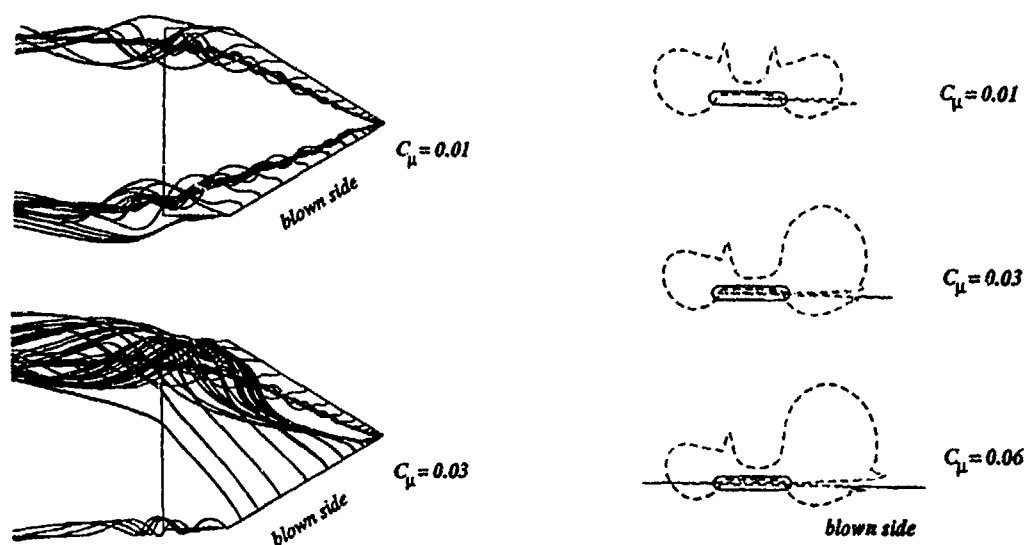


Figure 6: Effect of Increasing Right-Side Blowing on Computed Wing Flowfield ($\alpha = 30^\circ$, $C_\mu = 0.01$ to 0.06)

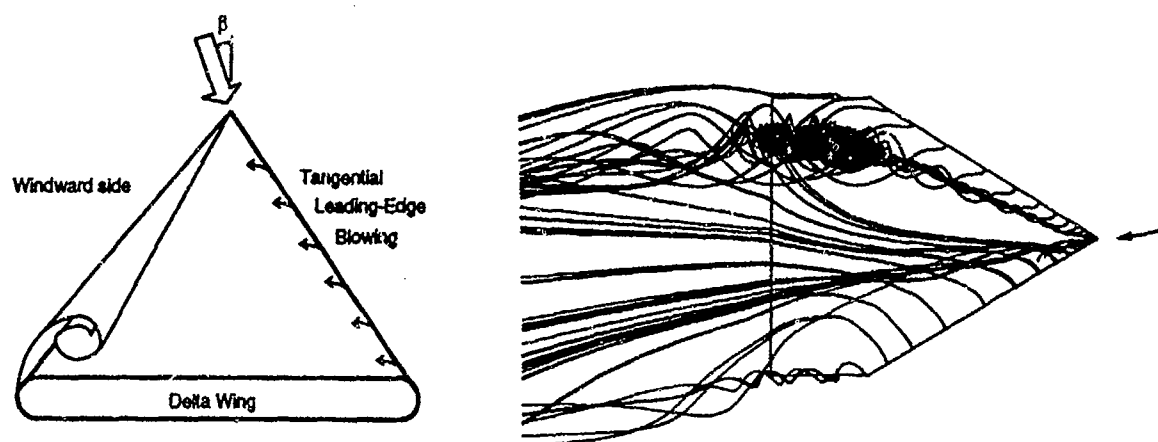


Figure 7: Effect of Combined Yaw and Blowing on Computed Particle Traces ($\alpha = 30^\circ$, $\beta = 10^\circ$, $C_\mu = 0.02$)

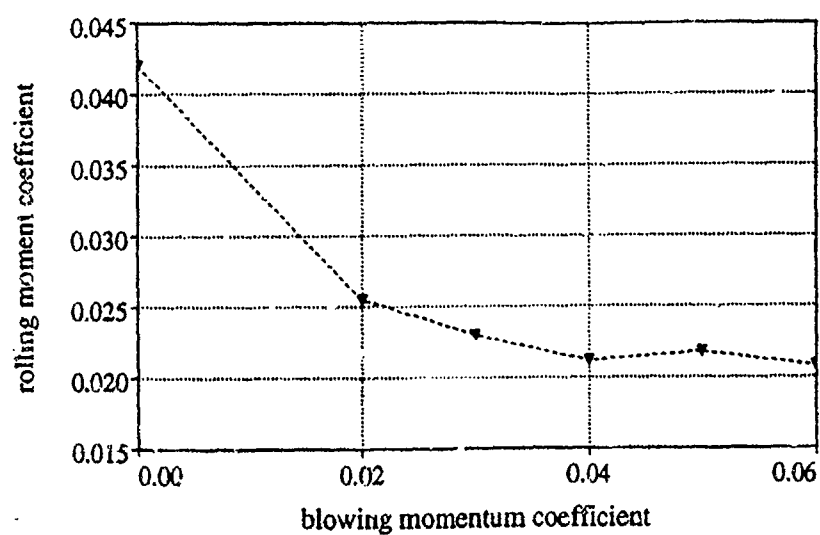


Figure 8: Computed Rolling Moment Coefficient as a Function of Blowing Momentum Coefficient ($\alpha = 30^\circ$, $\beta = 10^\circ$)

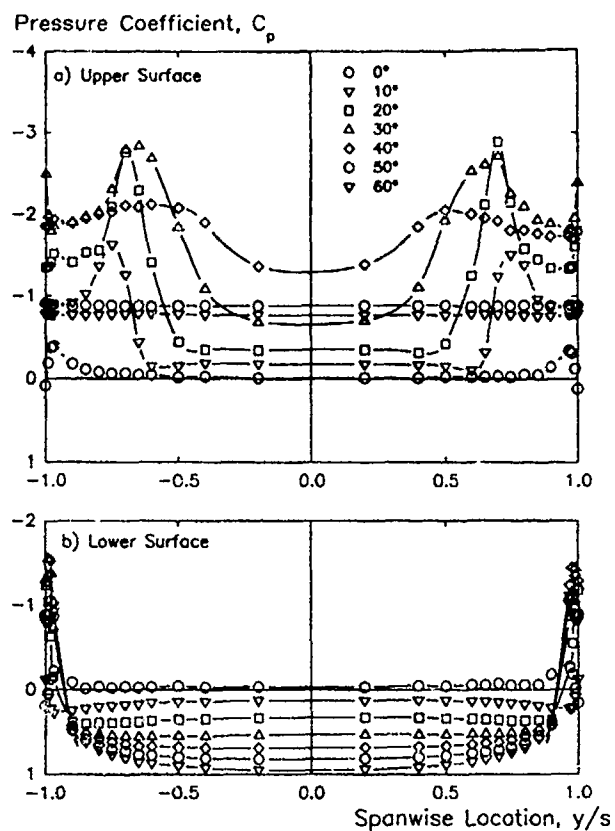


Figure 9: Effect of Angle of Attack on Upper and Lower-Surface Spanwise Pressure Distributions
(No Blowing, $\phi = 0^\circ$, $x/c = 0.5$)

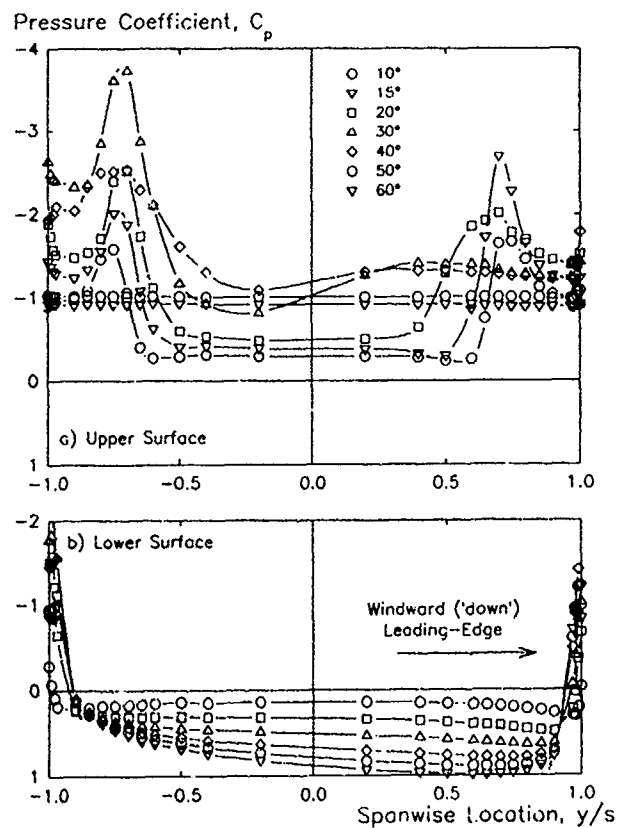


Figure 10: Effect of Angle of Attack and Roll Angle on Upper and Lower-Surface Spanwise Pressure Distributions
(No Blowing, $\phi = +20^\circ$, $x/c = 0.5$)

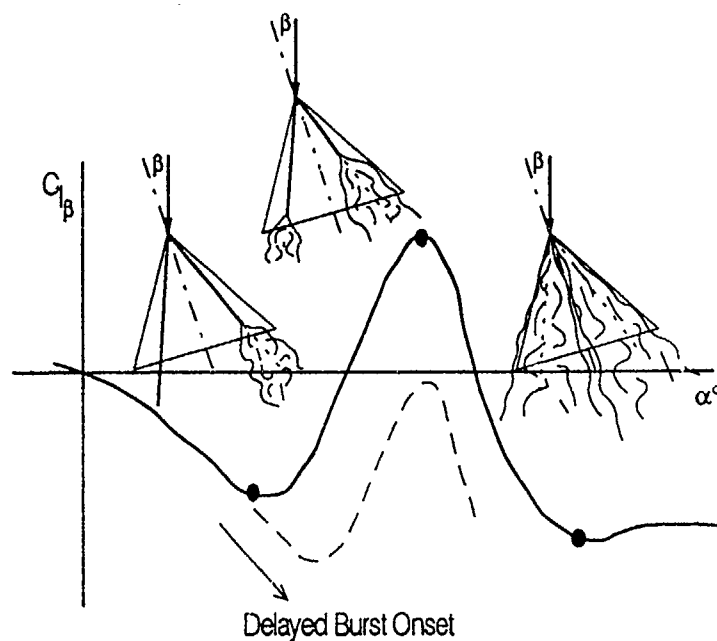


Figure 11: Typical Effective Dihedral Characteristics for Delta Wings^[9]

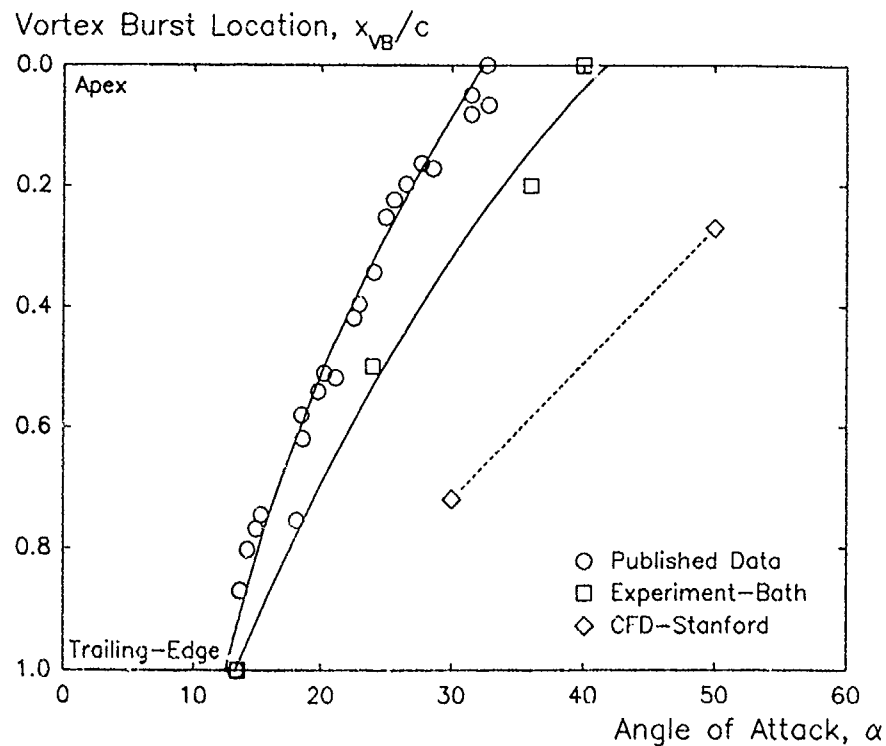


Figure 12: Comparison of Computed, Experimental and Published Vortex Burst Trajectories for 60° Delta Wings

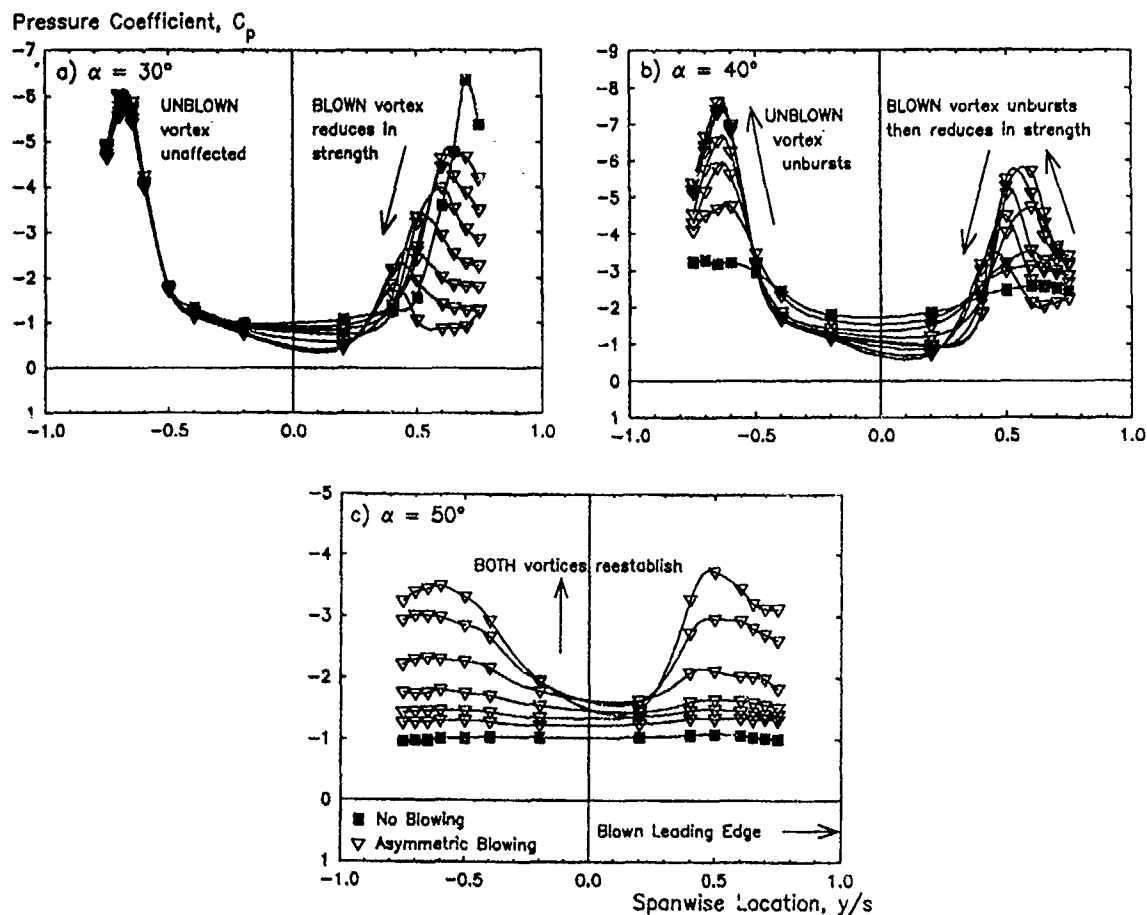


Figure 13: Effect of Increasing Asymmetric Blowing on Upper-Surface Spanwise Pressure Distributions (Right-Side Blowing, $x/c = 0.5$, $\alpha = 30^\circ$ - 50°)

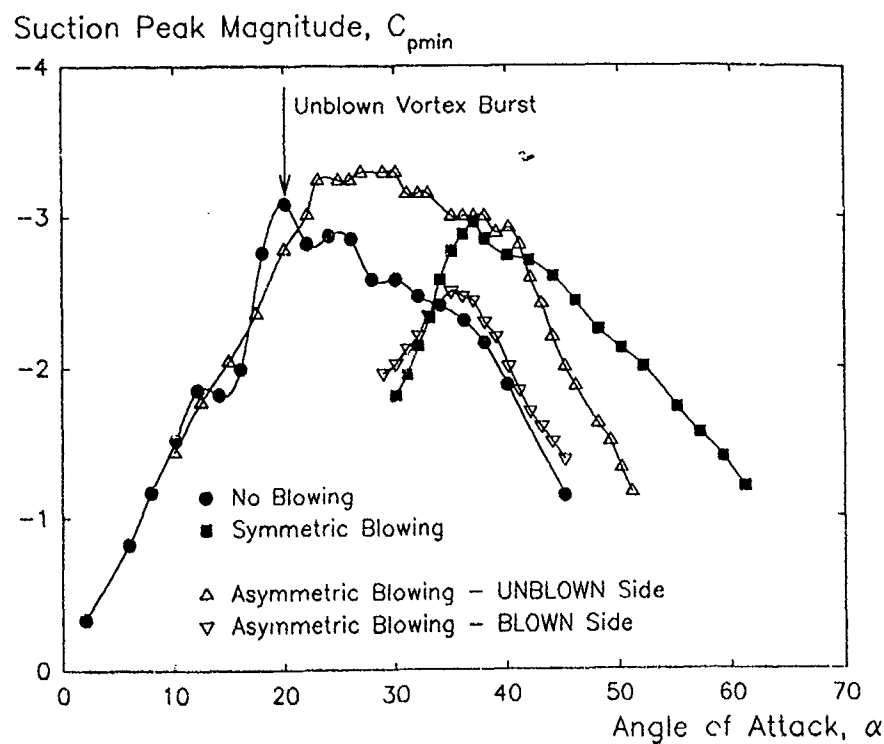


Figure 14: Effect of Blowing on Vortex-Induced Suction Peak Magnitude Variation with Angle of Attack

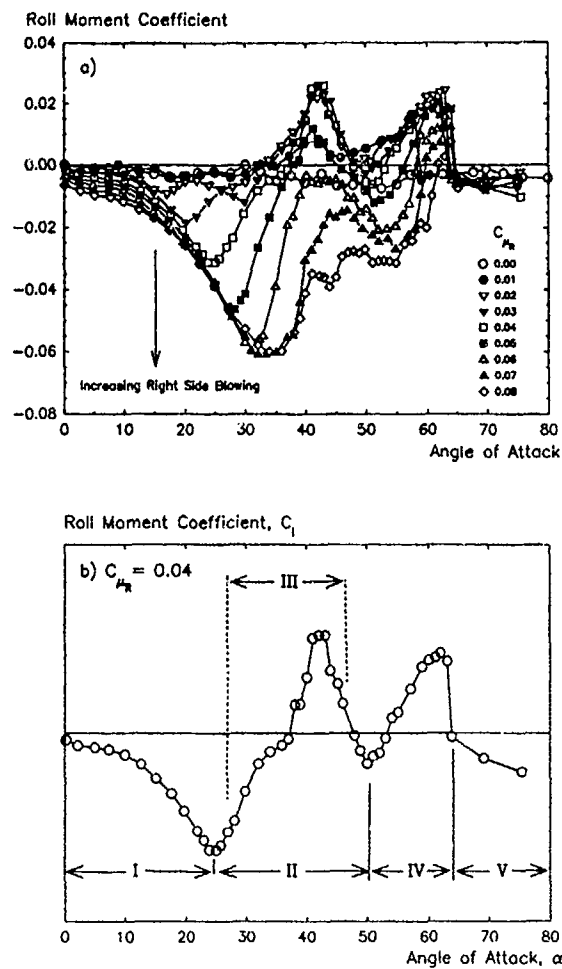


Figure 15: Roll Moment Characteristics of Asymmetric Blowing with Increasing Angle of Attack
 a) Increasing Right Side Blowing
 b) Typical Trend with Flow Regions Indicated

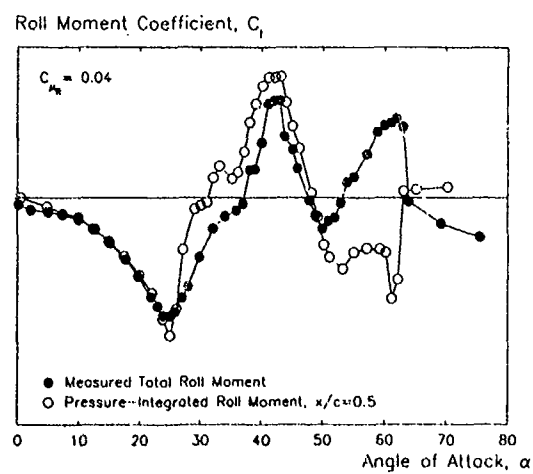
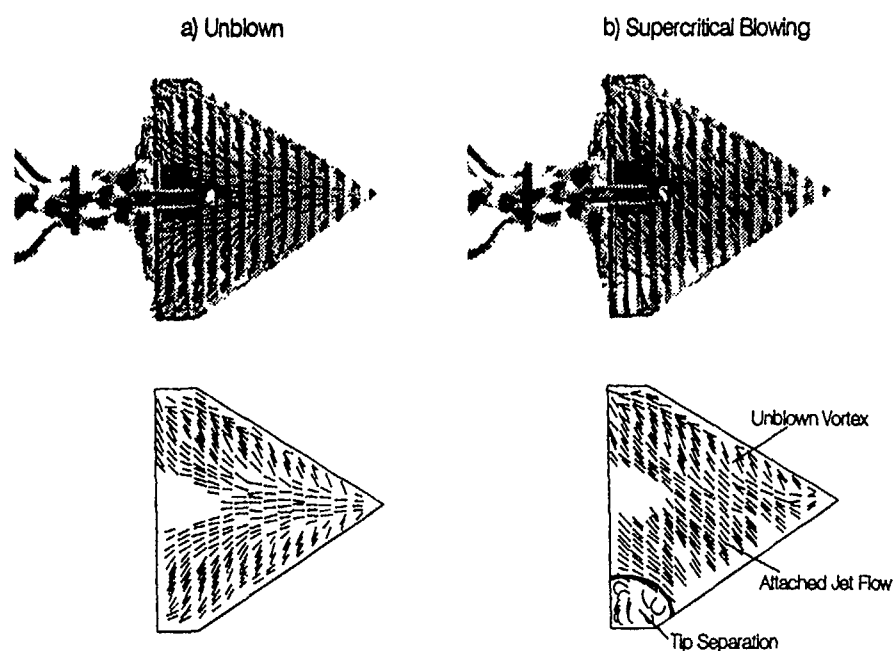
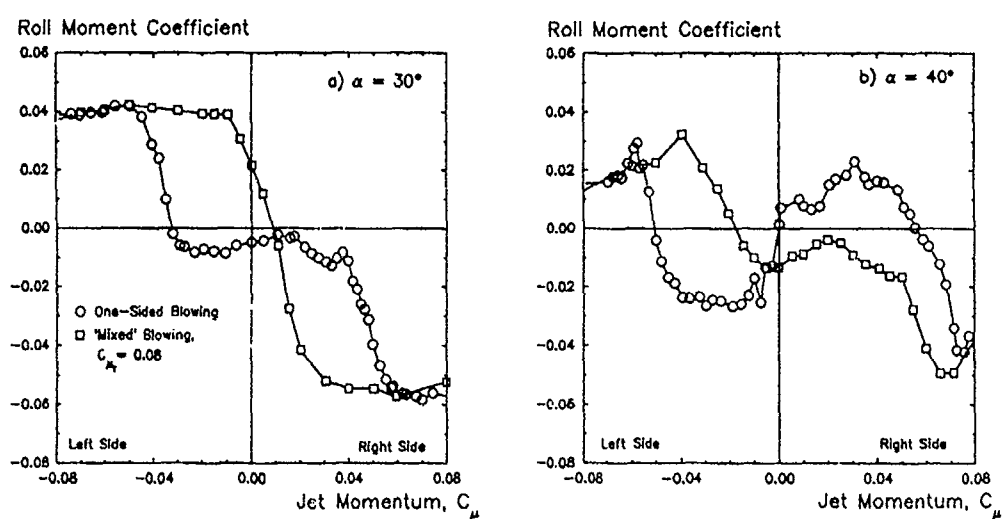
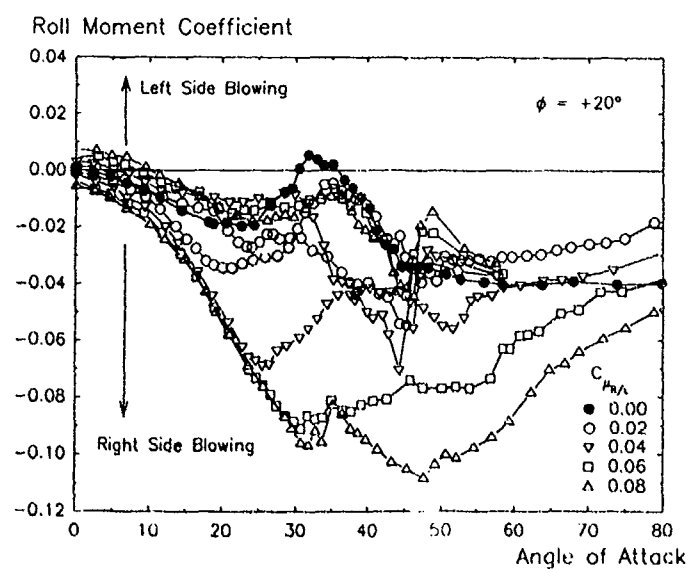


Figure 16: Comparison of Measured Roll Moment with Pressure-Integrated Local Roll Moment at $x/c = 0.5$

Figure 17: Wool Tuft Surface Flow Visualisation ($\alpha = 25^\circ$)Figure 18: Comparison of 'One-Sided' and 'Mixed' Blowing Schemes ($\alpha = 30^\circ, 40^\circ$)Figure 19: Effect of Roll Angle or Sideslip on Roll Control Power ($\phi = +20^\circ$)

RECENT DEVELOPMENTS IN THE SIMULATION OF STEADY AND TRANSIENT TRANSVERSE JET INTERACTIONS FOR MISSILE, ROTORCRAFT, AND PROPULSIVE APPLICATIONS

S. M. Dash, B. J. York, N. Sinha, R.A. Lee, A. Hosangadi, and D.C. Kenzakowski
Science Applications International Corporation
Propulsive Sciences Division
501 Office Center Drive, Suite 420
Fort Washington, PA 19034-3211 U.S.A.

SUMMARY

A review of recent activities focussed on the simulation of transverse jet interaction problems using advanced time-asymptotic and time-accurate Navier-Stokes methodology is presented. Missile work has involved the simulation of short-duration control jets issued from solid rocket motor nozzles. For the simulation of time-accurate particle-laden flows, a new Eulerian-based upwind/implicit particle-solver was developed and coupled with the gas-phase solver. Rotorcraft work has involved simulating the interaction of the exhaust plumes with the rotor wake and body aerodynamic flow. Hybrid vortex tracking/Navier-stokes methodology has been implemented with gridding of this complex 3D interactive flow being an issue of primary concern. Propulsive work has emphasized turbulence modeling. For scram-jet fuel-injection applications, compressible-dissipation extensions to the $k\epsilon$ model which provided marked improvements in simulating fundamental high-speed shear layers, have proven to work quite well for transverse jet injection.

1. INTRODUCTION

The authors have been involved in research and code development related to varied jet/plume interactive flowfield problems whose characterization is provided in Table I. While simple jet flows can thus be categorized, many realistic problems can involve the interaction of several classes of jets with distinguishing features often not readily apparent. For complex jet flows, time-asymptotic or time-accurate Navier-Stokes methodology is required and simulation issues involve numerics (e.g., gridding and grid resolution), physics modeling (turbulence and particulates) and thermochemistry. Since this Symposium focusses its attention to "jets in cross-flow," we will restrict attention to our recent activities in the third column of Table I, namely transverse jet problems.

Missile activities have involved simulating the interaction of propulsive and/or control jets with the aerodynamic flowfield. Such jets/plumes are chemically-reacting (viz, after-burning occurs with entrained air) and for solid propellant rocket motors, particle-laden. In an earlier AGARD paper [1] and a recent article on tactical missile plume/airframe interactions [2], capabilities for analyzing plumes issued from scarfed/bifurcated nozzles were described (Figure 1). This paper will focus on newer activities related to short duration control jets. Such jets, now being based on several newer missile systems (e.g., LOSAT, ERINT), issue from small, highly-energetic solid propellant rocket motors and contain significant loadings of metallic-oxide particu-

lates. New methodology developed to analyze this transient, two-phase problem will be described. The CRAFT 3D Navier-Stokes code [3-6] which utilizes implicit/upwind (Roe/TVD) numerics with multi-component gas-phase chemistry has been upgraded via incorporation of a new particulate solver [7] to analyze this complex flow problem. Applications to several unit problems and a generic Mach 2 missile flowfield problem will serve to illustrate this new capability.

Our work in rotorcraft has involved simulating the interaction of helicopter exhaust plumes with the vortical rotor wake, including wake/body interactions. The practical analysis of this complex 3D flowfield problem has entailed utilizing a hybrid approach which employs Lagrangian vortex tracking methodology coupled to a body potential solver for representing the rotor wake, combined with Euler/NS methodology for the plume/body analysis utilizing the rotor wake solution in a plane just under the rotor blades ("actuator disc" inflow boundary conditions). The PARCH 3D Navier-Stokes code [8,9] has been implemented which contains grid blanking capabilities (Figure 2) that facilitate the construction of computational grids for the helicopter problem. Grid embedding is utilized to concentrate grid points along the plume trajectory to obtain sufficient numerical resolution. This article will serve to illustrate the approach developed for a helicopter in hover and forward flight, showing the contributions of rotor wake and forward flight on the plume trajectory and structure. Full details of this approach are reported in other publications [10-12].

With regard to propulsive applications, the basic problem of transverse fuel injection in a supersonic environment was revisited. In earlier studies [1,2], difficulties were encountered using a basic $k\epsilon$ model associated with its inability to reproduce high Mach number compressibility effects. For simple shear layers and straightback round jets, success in analyzing high-speed problems was recently achieved via incorporating compressible-dissipation concepts of Sarkar and Zeman [13, 14] into a $k\epsilon$ framework [15-18]. For straightback jets, a systematic building-block approach has been followed using the blocks of data described in Table II to obtain a unified version of $k\epsilon$ which reproduced high-speed jet data and all subsets. While this approach has not been pursued for the transverse jet problem, preliminary applications of the new compressible-dissipation version of $k\epsilon$ ($k\epsilon_{CD}$) to this problem has provided significant improvements over the basic $k\epsilon$ model as will be discussed.

All the calculations described in this paper have been performed using the PARCH [8,9] and CRAFT [3-6] Navier-Stokes codes. The features of these codes are compared in Table III. PARCH has been utilized for steady flow problems while CRAFT has been used for transient flows. The reader is referred to the references for equations and details of the numerics employed. This paper will discuss transverse jet predictions made with PARCH and CRAFT for missile, rotorcraft and propulsive applications.

2. TACTICAL MISSILE APPLICATIONS

2.1 Angled Plumes from Scarfed Nozzles

In an earlier AGARD paper [1], our analysis of scarfed nozzle (Figure 1) plume/aerodynamic interactions for a generic missile configuration was discussed in some detail with calculations presented for Mach .6 conditions and 10° angle-of-attack using the PARCH NS code. More recently, predictions have been performed [19] simulating experiments of Aerospatiale at ONERA [20] for jets issuing from ogive/cylinders at various flight conditions. Figure 3 exhibits predicted Mach number contours and the grid implemented in the $y=0$ plane for a calculation at Mach 2. The air jet was inclined at 60° relative to the missile axis and was issued from a rectangular scarfed nozzle at an "average" Mach number of 2.5. The ratio of jet/freestream stagnation pressure was 28. The PARCH calculation implemented the basic $k\epsilon$ turbulence model and the wall boundary layer was not resolved (wall slip conditions were utilized).

In Figure 4, comparison of PARCH code cross-flow pressure predictions with data are shown in a plane located 6.5D downstream of the jet injection plane. The comparisons are quite favorable and indicate that the predicted jet penetrates somewhat more than observed in the experiments. Inclusion of a resolved boundary layer, improvements to the $k\epsilon$ model (see Section 4 of this paper), and a better representation of nozzle exit plane conditions (average properties were used as inflow conditions on the missile surface — actual conditions are variable) all need to be explored as to their influence on this prediction. Comparable comparisons with data were achieved for subsonic flight conditions [19].

2.2 Gas/Particle Interactions

Many tactical missile plumes of interest contain significant loadings of particulates which are not in equilibrium with the gas-phase and must be accounted for via the solution of dispersed-phase equations [21]. Since lateral control jets are of short duration, a new time-accurate particle-cloud solver was developed [7] which is compatible with the finite-volume implicit/upwind numerics in the CRAFT code. Its features are summarized in Table IV.

A basic test case of interest with one-way coupling (particulates do not influence gas solution) is that of the transverse particle jet with a uniform approach flow as schematized in Fig. 5. The gas phase approach flow is Mach 3, $P = 1$ atm, $T = 300^\circ\text{K}$. Aluminum oxide (Al_2O_3) particles are transversely injected at the same velocity and tempera-

ture as the approach gas. Time-asymptotic calculations for various particle sizes ($0.6\mu\text{m}$ - $600\mu\text{m}$) are shown in Fig. 6 obtained using a coarse 45×40 grid. The $0.6\mu\text{m}$ particles interact strongly with the uniform gas solution and are "flattened" against the solid boundary. The $600\mu\text{m}$ particles do not interact at all and penetrate through the computational domain. The $6\mu\text{m}$ and $60\mu\text{m}$ particles show intermediate levels of interaction with the gas.

To simulate time-accurate/finite-duration injection, the $6\mu\text{m}$ calculation was repeated with injection terminated after a short time interval. Referring to Figure 7, the transient particle-cloud is captured as it traverses through the flow following the same trajectory as for the steady calculation. Results with two-way coupling would be different for particles of significant loading since the particles disturb the gas-phase solution. However, these one-way coupling results give confidence that we are accurately simulating the unsteady convection of the particle cloud, and, that the particle cloud boundary is well captured without any oscillations — a problem with earlier non-upwind methods. Equivalent fully-coupled studies for transverse jet problems are described below.

A fully-coupled unit problem that was investigated was the perpendicular injection of a multi-phase jet into an external flowing stream. The wall has a length of 1m and the injection slot extends from 0.25m to 0.35m. The free-stream Mach number is 2.0, while the injected gas jet is sonic with the Al_2O_3 particles being fully equilibrated with the gas at injection. The pressure and temperature ratio between the jet and freestream is 2.0. The mass loading of the particles in the jet is 50 percent. We study the parametric effect of the particle size on the flowfield development by studying the injection of particles with three different sizes; $25\mu\text{m}$, $5\mu\text{m}$, and $2.23\mu\text{m}$. For reference, the corresponding single phase flowfield where the injected jet contains no particles was also computed. It is to be noted that the calculations shown here are inviscid and the upstream boundary layer is not simulated.

Figure 8 shows the Mach number and stagnation enthalpy (representative of gaseous species) contours for the single phase gas flowfield with no particles. The Mach number contours show a curved bow shock ahead of the injection. Upstream flow separation and the boundary layer are absent due to inviscid approximations. The jet expands around the downstream slot corner at $X = .35\text{m}$ and a low pressure zone is observed around the expansion point. The stagnation enthalpy contours show that the injected jet flattens out due to the large momentum of the oncoming freestream, and is completely bent back a short distance downstream of the injection.

We now study the effect of particle injection on the gas flowfield by injecting particles of $25\mu\text{m}$, $5\mu\text{m}$, and $2.23\mu\text{m}$ independently. Figures 9-11 show side-by-side particle and gaseous plume boundaries for the $25\mu\text{m}$ (Fig. 9), $5\mu\text{m}$ (Fig. 10), and $2.23\mu\text{m}$ (Fig. 11) cases. As shown in Fig. 9, the injection of the large $25\mu\text{m}$ particles has a negligible effect

on the gas flowfield. The particle path shows modest drag effects and a relatively minor deflection is observed. As the particle size is reduced to $5\mu\text{m}$ the interaction between the two phases becomes somewhat stronger. The particles are now strongly deflected and particle penetration gets substantially reduced when compared to the $25\mu\text{m}$ case. The gaseous jet penetration is not substantially different here than for the $25\mu\text{m}$ case, although significantly more heat transfer occurs as evidenced by the broad spread of the gaseous enthalpy contours. As the particle size is further reduced to $2.23\mu\text{m}$, the interaction between the gas and the particles becomes very strong (see Fig. 11). The particles deflect very strongly and the penetration of the particle-cloud is further reduced. Here, the particles serve to increase the gaseous penetration but the particle and gas-phase plume boundaries are still distinct indicating that this is still far from the equilibrium limit.

2.3 Transient Control Jet Missile Flowfield

The transient firing of a lateral control jet from a missile was simulated using the CRAFT code. A schematic of the jet-missile interaction flowfield is shown in Figure 12. The control jet is located midway down the missile at 10 radii. The grid points were clustered around the jet injection location to provide resolution in this region.

The freestream conditions are as follows:

Mach number = 2
Pressure = 1 atm
Temperature = 300°K

The control jet is injected with the following conditions:

$M_j = 3$
 $P_j = 20 \text{ atm}$
 $T_j = 3000^\circ\text{K}$

and is fired for 7.5 ms.

This case was performed with a 50% mass loading of $5\mu\text{m}$ Al_2O_3 particles in the jet. The particles were specified to be in equilibrium with the gas at the jet exit plane. Figure 13 compares gas-phase (stagnation enthalpy) and particle cloud plume boundaries, side-by-side, at 1, 3, 7, 8, 10 and 16 milli-seconds. The particle-cloud plume is seen to experience more penetration than the gaseous plume and after shut-off, it gets "blown downstream" more slowly due to lag effects (see contours at 16 milli-seconds). Complete details of this case are provided in Reference 5 including a description of phase change effects (liquid Al_2O_3 droplets undergo solidification at 2318°K). Note the presence of particles downstream of the injection location (associated with initial roll-up) even after shut-off at 7.5ms. The phase change zones are difficult to exhibit unless color contours are available.

3. ROTORCRAFT APPLICATIONS

3.1 Approach for Helicopter Plume Simulation

The accurate analysis of a helicopter flowfield (Figure 14) emphasizing plume simulation is a very complicated task.

The rotor flow, with respect to body-fixed coordinates is unsteady. As the rotor blades rotate, the lift forces acting on the blades generate a strong bound vortex at the tip of the blades. This complex vortex structure is convected to form the wake core. For multiple blades, vortex-vortex interactions occur. The fuselage immersed in this wake core experiences highly vortical downwash. As an added complexity, the fuselage itself is a complex geometry with attachments for the transmission bay, fixed wing stabilizers, engine nacelles, as well as armament. Since the engine is attached close to the fuselage, the jet plume is immersed in this highly vortical flow. The approach taken models the rotor wake and its interaction with the helicopter airframe using vortex-lattice/potential flow methodology as incorporated in the HELIWAKE code [22, 23]. Our numerical studies have indicated that while vortex-lattice/potential flow methodology can provide an adequate representation of the rotor wake downwash flow just under the rotor blades, the flow representation on and near the airframe surface is inadequately predicted.

In this approach, HELIWAKE defines rotor wake characteristics under the blades that account for wake/airframe interactions and Euler/Navier-Stokes (NS) methodology (PARCH) is utilized for the plume/wake/airframe interaction problem. The PARCH code grid patching/blanking capabilities (Figure 2) facilitate dealing with complex geometries (a single patched grid is used in contrast to multiple zonal blocks), and, an efficient diagonalized matrix inversion procedure provides reasonable CPU times. The three step procedure implemented to analyze the complete flowfield problem is as follows:

- (1) HELIWAKE provides a solution of the rotor wake/airframe interaction problem — this solution is utilized to provide a time-averaged "actuator disc" representation of the wake in a plane just under the rotor blades which is used as inflow boundary conditions for the Euler/NS solution. Figure 15 exhibits the HELIWAKE analysis of a helicopter in hover, while Figure 16 shows the actuator disc inflow conditions used for the Euler/NS solution in a plane under the blades.
- (2) PARCH is implemented in an Euler mode with a coarse grid to define the plume shape/trajectory. Figure 17 exhibits a typical grid and the grid patching implemented in one of the three coordinate directions.
- (3) PARCH is implemented in an NS mode using a two-equation turbulence model and grid embedding in the vicinity of the plume for adequate resolution.

3.2 Representative Plume Calculations

With the methodology described above, representative hover and forward flight predictions were performed to illustrate present capabilities. The helicopter geometry is prescribed in wireframe form from which an Euler grid is constructed using the GRIDGEN code in conjunction with a

surface decomposition procedure to aid in constructing the complex grid patching.

Figure 18 displays predicted temperature contours of the plume in hover while Figure 19 shows the trajectory (particle traces) of the exhaust. The predicted solution displays the normal "horseshoe-like" distortion of the plume immersed in a strong downwash. The temperature contours for the forward flight case showing the plumes are displayed in Figure 20, while the particle traces showing the plume trajectory are displayed in Figure 21. In contrast to the hover flowfield, the plumes are convected more aft than downward. A close-up view of the plume region displays an increase in static temperature in the region where the structure of the plume is distorted by the downwash (Figures 22 and 23). Figure 22 represents plumes in the hover flowfield while Figure 23 represents plume in the forward flight flowfield. The peak temperature on the blade advancing side is greater than the blade retreating side. This is because the jet exhaust in the blade advancing side is impeded by the downwash while the jet in the blade retreating side has less impedence. These calculations are not yet grid resolved and further work is required for their completion. Full details including color contour plots are available in Ref. 10, with further information also available in Refs. 11 and 12.

4. PROPULSIVE APPLICATIONS

4.1 Turbulence Model Upgrades

Following a systematic "building-block" approach, a new version of the $k\epsilon$ turbulence model ($k\epsilon CD$) has been formulated for high-speed jets and shear layers whose description and performance is provided in Refs. 15-18. This new model correctly predicts the observed decrease in mixing at higher convective Mach numbers and the associated decrease in velocity fluctuations and normal stresses (many sets of data have been investigated). The model is based on extensions of compressible-dissipation concepts proposed by Sarkar and Zeman [13, 14] whereby the dissipation, ϵ , is taken to be comprised of incompressible (ϵ_i) and compressible components ($\epsilon = \epsilon_i + \epsilon_c$) with the compressible component related to the local turbulent Mach number $M_t = \sqrt{2k}/a$, i.e., $\epsilon_c = \epsilon_i (1 + \alpha M_t^2)$ in Sarkar's formulation. The $k\epsilon CD$ model greatly improves upon the earlier $k\epsilon CC$ model of Dash et al. [24, 25] which also used M_t as a correlating parameter, but applied it to the turbulent viscosity, i.e., $\mu_t = C_\mu (M_t) \rho k^2/\epsilon$. Table V describes the $k\epsilon CD$ turbulence model. Figure 24 shows a comparison of its performance vs the earlier $k\epsilon CC$ model in predicting velocity fluctuations simulating recent experiments of Dutton and coworkers at the University of Illinois [26]. Both $k\epsilon CC$ and $k\epsilon CD$ predict the correct growth rate ($k\epsilon$, which is not shown, has a much larger spread and intensity levels comparable to $k\epsilon CC$) but $k\epsilon CD$ is seen to also predict the correct turbulent intensity. Comparable comparisons have been obtained with other data sets.

4.2 Two-Dimensional Transverse Fuel Injection Problem

Earlier predictions for a two-dimensional transverse jet interaction flowfield simulating the helium fuel injection experiment of Kraemer and Rogers [27] are exhibited in Figure 25, along with the experimental setup. Predictions made with the $k\epsilon$ turbulence model underestimated the lateral extent of the approach separation zone, indicating too fast a rate of mixing. A "capped" version of the $k\epsilon$ model that did not allow the turbulent viscosity, μ_t , to exceed 1000μ , produced results in better agreement with the data, indicating the requirement to incorporate compressibility effects into the turbulence model. Gridding was not an issue, as ascertained by grid convergence studies on both rectangular and adaptive grids.

We have revisited this transverse jet problem using the new $k\epsilon CD$ turbulence model. Figure 26 compares PARCH code $k\epsilon$ and $k\epsilon CD$ predictions simulating this experiment, both implementing the low Re Chien extension of $k\epsilon$ to analyze the near-wall region. The $k\epsilon CD$ predictions are significantly better than those of the $k\epsilon$ model. Figure 27 shows further improvements to the $k\epsilon CD$ prediction provided by the use of a solution adaptive grid. With the adaptive grid, the upstream solution improved but the downstream solution deteriorated. Also, some unsteadiness in the solution was observed which was probably dampened by the coarser original grid. Figure 28 compares the original non-adaptive and final adaptive grids utilized for these predictions. Figure 29 exhibits contours of Mach number and turbulence structure for the $k\epsilon CD$ prediction on the adaptive grid.

5. CONCLUDING REMARKS

This article has described transverse jet interaction flowfield solutions for problems associated with missile, rotorcraft, and propulsive applications. The PARCH and CRAFT Navier-Stokes codes have been utilized in the performance of these calculations. In the simplest of the problems exhibited, the 2D transverse helium jet of Section 4, turbulence modeling was the issue and the new $k\epsilon CD$ model was found to provide significant improvements over the basic $k\epsilon$ model. Vortical turbulence issues are anticipated in the helicopter plume problem and upgrades to $k\epsilon$ are anticipated as we progress further in this work. The unsteady lateral control jet did not implement a turbulence model — an Euler simulation with a dispersed particulate phase was described. For short duration transient flows, Reynolds-averaged turbulence modeling is not generally applicable and a large-eddy simulation (LES) approach is required. We have been pursuing such an approach for short duration interior ballistic gun chamber problems [28, 29] where thermochemical and multi-phase problems must be additionally addressed.

6. REFERENCES

- [1] Dash, S.M., Sinha, N., and York, B.J., "Computational Models with Advanced Thermochemistry for the Analysis of Missile/Plume Flowfield Interactions," AGARD Symposium on Missile Aerodynamics, AGARD CP-493, April 1990, pp. 31.1-31.30.

- [2] Dash, S.M. and Sinha, N., "Exhaust Plumes and Their Interaction with Missile Airframes: A New Viewpoint," *Tactical Missile Aerodynamics: Prediction Methodology*, Editor: M.R. Mendenhall, AIAA Tactical Missile Series, Vol. 142, Progress in Astronautics and Aeronautics Second Edition, 1992, Chapter 13, pp. 649-756.
- [3] Sinha, N., Hosangadi, A. and Dash, S.M., "The CRAFT NS Code and Preliminary Applications to Steady/Unsteady Reacting, Multi-Phase Jet/Plume Flowfield Problems," 19th JANNAF Exhaust Plume Technology Meeting, CPIA Pub. 568, May 1991, pp. 203-226.
- [4] Sinha, N., Dash, S.M., and Hosangadi, A., "Applications of an Implicit, Upwind NS Code, CRAFT, to Steady/Unsteady Reacting, Multi-Phase Jet/Plume Flowfields," AIAA-92-0837, AIAA 30th Aerospace Sciences Meeting, Reno, NV, January 6-9, 1992.
- [5] Hosangadi, A., Sinha, N., York, B.J., and Dash, S.M., "Progress Towards the Analysis of Transient Combusting, Multiphase Flows Using Upwind/Implicit Numerics," AIAA-93-0238, 31st AIAA Aerospace Sciences Meeting, January 11-14, 1993.
- [6] Sinha, N., Hosangadi, A., York, B.J., and Dash, S.M., "Recent Advances in the Simulation of Transient, Combusting, Multi-Phase Plume-Related Flowfields," 20th JANNAF Exhaust Plume Technology Subcommittee Meeting, Phillips Lab., Kirtland AFB, NM, February 9-11, 1993.
- [7] Hosangadi, A., Sinha, N., Dash, S.M., "Solution of Two-Phase Dilute Gas Particle Mixtures Using Upwind Finite-Volume Methodology," AIAA-92-0344, AIAA 30th Aerospace Sciences Meeting, Reno, NV, January 6-9, 1992.
- [8] Sinha, N., York, B.J., Ong, C.C., Stowell, G.M., and Dash, S.M., "3D Navier-Stokes Analysis of High-Speed Propulsive Flowfields Using the PARCH Code," AIAA-89-2796, Monterey, CA, July 1989.
- [9] Dash, S.M., Sinha, N., York, B.J., and Ong, C.C., "3D Navier-Stokes Analysis of Tactical Missile External/Plume Interaction Flowfields," JANNAF 18th Plume Technology Meeting, CPIA Pub. 530, November 1989, pp. 21-44.
- [10] Lee, R.A. and Dash, S.M., "Analysis of Helicopter Plumes Using Hybrid Vortex-Lattice/Navier-Stokes Methodology," Final Report, SAIC/FW TR-104, September 1992.
- [11] Lee, R.A. and Dash, S.M., "Helicopter Exhaust Plume Flowfield Simulation for SPIRITS-HC," presentation at EOATMUM92, Naval Air Warfare Center, Point Mugu, CA, Oct. 20-22, 1992.
- [12] Lee, R.A. and Dash, S.M., "Helicopter Plume Flowfield Simulation for Signature Prediction in SPIRITS-HC," 20th JANNAF Exhaust Plume Technology Meeting, Phillips Lab., Kirtland AFB, NM, February 9-11, 1993.
- [13] Sarkar, S. and Lakshmanan, B., "Application of a Reynolds Stress Turbulence Model to the Compressible Shear Layer," AIAA J., May 1991, pp. 743-749.
- [14] Zeman, O. "Dilatational Dissipation: The Concept and Application in Modeling Compressible Mixing Layers," Physics of Fluids, February 1990.
- [15] Dash, S.M., Walker, B.J., and Seiner, J.M., "A Building-Block Approach for Turbulence Model Validation/Upgrade Focussed on High-Speed Jet Flows," 19th JANNAF Propulsion Mtg., Feb. 24-27, 1992.
- [16] Dash, S.M., Sinha, N., and York, B.J., "The Critical Role of Turbulence Modeling in the Prediction of Supersonic Jet Shock Structure for Acoustic Applications," DGLR/AIAA 92-02-102, DGLR/AIAA 14th AeroAcoustic Conf., Aachen, Germany, May 11-14, 1992.
- [17] Dash, S.M. and Kenzakowski, D.C., "A Compressible-Dissipation Extension to the $k\epsilon$ Turbulence Model and Building-Block Data for its Validation," AIAA-92-2766, 1992 AIAA SDIO Technology Conference, May 19-21, 1992.
- [18] S.M. Dash, D.C. Kenzakowski, and R.A. Lee, "Simulation of High-Speed Jets: Turbulence and Two-Phase Flow Modeling," AIAA-92-3440, AIAA/SAE/ASME/ASCE 28th Joint Propulsion Conf., Nashville, TN, July 6-8, 1992.
- [19] York, B.J., Sinha, N., and Dash, S.M., "PARCH Computations of Inclined Jet Interactions with Ogive/Cylinder Airframe Flowfields," SAIC/FW TM-61, Sept. 1990.
- [20] Dormieux, M. and Mahe, C., "Calculs Tridimensionnels De L'Interaction D'un Jet Lateral Avec Un Ecoulement Supersonique Externe," AGARD Conference Proceedings Number 437, Validation of Computational Fluid Dynamics, May 1988.
- [21] Dash, S.M., Wolf, D.E., Beddini, R.A. and Pergament, H.S., "Analysis of Two-Phase Flow Processes in Rocket Exhaust Plumes," J. Spacecraft and Rockets, Vol. 22, May-June 1985, pp. 367-380.
- [22] Crimi, P., "Theoretical Prediction of the Flow in the Wake of a Helicopter Rotor," Parts 1 & 2, CAL Report Nos. BB-1994-S-1 & -S-2, September 1965 [Addendum, BB-1994-S-3/August 1966].
- [23] Jenkins, B.Z. and Marks, A.S., "Rotor Downwash Velocities About the UH-1M Helicopter - Flight Test Measurements and Theoretical Calculations," MICOM Technical Report RD-75-27, January 1975.
- [24] Dash, S.M., Weilerstein, G., and Vaglio-Laurin, R., "Compressibility Effects in Free Turbulent Shear Flows," Air Force Office of Scientific Research, TR-75-1436, August 1975.
- [25] Dash, S.M. and Wolf, D.E., "Interactive Phenomena in Supersonic Jet Mixing Problems, Part I: Phenomenology and Numerical Modeling Techniques," AIAA Journal, Vol. 22, July 1984, pp. 905-913.
- [26] Gruber, M.R. and Dutton, J.C., "Three-Dimensional Velocity Measurements in a Turbulent, Compressible Mixing Layer," UILU-ENG 92-4001, Univ. Illinois, Urbana, January 1992.
- [27] Kraemer, G.O. and Tiwari, S.N., "Interaction of Two-Dimensional Transverse Jet with Supersonic Mainstreams," NASA CR 175446, December 1983.
- [28] Hosangadi, A., Sinha, N., and Dash, S.M., "CRAFT Code Multi-Dimensional Simulation of ETC Interior Ballistics," 29th JANNAF Combustion Meeting, 19-23 Oct. 1992.
- [29] Sinha, N., York, B.J., Dash, S.M., Drabczuk, R., and Rolader, G.E., "Transient Simulation of Ram Accelerator Flowfields," 29th JANNAF Combustion Meeting, 19-23 Oct. 1992.

Table I. Basic Jet/Plume Flowfield Characterization

Problems	Straight-Back Jet/Mixing	Wall Jet	Transverse Jet
Internal Propulsive Problems	<ul style="list-style-type: none"> • Central Fuel Injection • Gas Turbine Core/Fan Mixing 	<ul style="list-style-type: none"> • Tangential Fuel Injection • Film Cooling of Propulsive Surfaces 	<ul style="list-style-type: none"> • Transverse Jet Injection
Missile Problems	<ul style="list-style-type: none"> • Tactical/Strategic Missile Plume <ul style="list-style-type: none"> - Single/Multi-Engine 	<ul style="list-style-type: none"> • Interceptor Window Film Cooling and Aero-Optics • Integrated Propulsive Systems (Ramjet/Turbofan) 	<ul style="list-style-type: none"> • Transverse (JI) Thrusters for Missile Control • Scarfed/Bifurcated Nozzle Exhausts
Aircraft Problems	<ul style="list-style-type: none"> • Aircraft Jet Exhausts <ul style="list-style-type: none"> - Single/Multi-Engine - Nonaxisymmetric 	<ul style="list-style-type: none"> • Plug Nozzles • Circulation-Control Airfoils • Integrated Propulsive Systems (Scramjet Exhaust) 	<ul style="list-style-type: none"> • V/STOL Aircraft • Helicopter Exhaust in Downwash

Table II. Building-Block Data for Straightback Jet Flowfields

<p align="center">- BUILDING-BLOCK 1 - LOW-SPEED PLANAR FREE SHEAR FLOWS</p> <ul style="list-style-type: none"> • ASYMPTOTIC <ul style="list-style-type: none"> - Velocity Ratio Effects (Rodi Correlation) - Density Ratio Effects (Brown/Roshko, etc.) • NON-ASYMPTOTIC <ul style="list-style-type: none"> - Initial Profile Effects - Free Stream Turbulence Effects - Pressure Gradient Effects • • • 	<p align="center">- BUILDING-BLOCK 2 - LOW-SPEED AXISYMMETRIC FREE JETS (WAKES)</p> <ul style="list-style-type: none"> • SELF SIMILAR BEHAVIOR/FARFIELD <ul style="list-style-type: none"> - Velocity Ratio Effects - Density Ratio Effects • TRANSITIONAL REGION + FARFIELD <ul style="list-style-type: none"> - Initial Profile Effects - Free Stream Turbulence Effects - Pressure Gradient Effects • • • • COMPLETE JET (BB/1 NEEDED)
<p align="center">- BUILDING-BLOCK 3 - HIGH-SPEED PLANAR FREE SHEAR FLOWS</p> <ul style="list-style-type: none"> • ASYMPTOTIC <ul style="list-style-type: none"> - Isoenergetic/One & Two Streams - Non-isoeenergetic/One & Two Streams • NON-ASYMPTOTIC <ul style="list-style-type: none"> - Initial Profile Effects - Free Stream Turbulence Effects - Wave/Shear Layer Interactions • • • 	<p align="center">- BUILDING-BLOCK 4 - HIGH-SPEED AXISYMMETRIC FREE JETS (WAKES)</p> <ul style="list-style-type: none"> • SELF SIMILAR BEHAVIOR/FARFIELD <ul style="list-style-type: none"> - Velocity Ratio/Density Ratio Effects - Compressibility (Mach Number) Effects • TRANSITIONAL REGION + FARFIELD <ul style="list-style-type: none"> - Balanced Pressure - Initial Profile, Free Stream Turbulence Effects - Imbalanced Pressure - Above Plus Wave/Shear Layer Interactions • COMPLETE JET (BB/3 NEEDED)

Table III. Features of PARCH and CRAFT Codes

FEATURE	PARCH	CRAFT
EQUATIONS	<ul style="list-style-type: none"> • 2D/AXI - 2D Code • 3D - 3D Code 	<ul style="list-style-type: none"> • 1D/2D/AXI/3D - Single Code
	<ul style="list-style-type: none"> • Euler/Thin Layer Options 	<ul style="list-style-type: none"> • Euler/Thin Layer Options
NUMERICS	<ul style="list-style-type: none"> • Finite-Difference Discretization with Finite-Volume Corrections to Cell Jacobians <hr/> <ul style="list-style-type: none"> • Beam-Warming Central Difference Algorithm/Diagonalized or Block Matrix Inversion <ul style="list-style-type: none"> - Jameson 2nd-/4th-Order Dissipation • Roe/TVD Run Option - for Perfect/Single-Component Gas <hr/> <ul style="list-style-type: none"> • Time-Asymptotic Numerics <ul style="list-style-type: none"> - Independent Time-steps - 2nd-Order Spatial Accuracy 	<ul style="list-style-type: none"> • Finite-Volume Discretization <hr/> <ul style="list-style-type: none"> • Roe/TVD Upwind Algorithm <ul style="list-style-type: none"> - Consistent for Real, Multi-Component Gas Mixtures - Standard Block or LU Matrix Inversion - Fully Implicit Including Source Terms <hr/> <ul style="list-style-type: none"> • Time-Accurate and Time-Asymptotic Numerics <ul style="list-style-type: none"> - 2nd-Order Temporal and Spatial Accuracy - Pseudo Time Iteration to Eliminate Approximate Factorization Errors
GRID AND BOUNDARY CONDITIONS	<ul style="list-style-type: none"> • Fixed Grid/Grid Blanking - Patching for Complex Geometries • Generalized Explicit BC 	<ul style="list-style-type: none"> • Dynamic Grid for Unsteady Flows with Moving Boundaries • Grid Blanking • Generalized Implicit BC
THERMO-CHEMISTRY	<ul style="list-style-type: none"> • Generalized Finite-rate, Matrix Split/Loosely Coupled • Equilibrium Air (Tannehill Fits) 	<ul style="list-style-type: none"> • Generalized Finite-Rate, Large Matrix/Strongly Coupled • Equilibrium Air (Tannehill Fits)
TURBULENCE	<ul style="list-style-type: none"> • $k\epsilon$ Turbulence Model <ul style="list-style-type: none"> - Loosely or Strongly Coupled to Fluid Dynamics - Chien Low Re Terms - Compressibility Corrections - 2D/AXI Jet Corrections 	<ul style="list-style-type: none"> • $k\epsilon$ Turbulence Model <ul style="list-style-type: none"> - Strongly Coupled to Fluid Dynamics - Compressibility Corrections - 2D/AXI Jet Corrections
MULTI-PHASE FLOW	<ul style="list-style-type: none"> • Equilibrated G/P Mixture • G/P Nonequilibrium Capability for Steady 2D/AXI Flows with No Recirculation 	<ul style="list-style-type: none"> • Generalized Steady/Unsteady G/P Nonequilibrium <ul style="list-style-type: none"> - New Conservative/Implicit Particle-Cloud Solver Using Higher-Order Upwind Numerics

Table IV. Features of the Particle-Cloud Solver

FEATURES	PARTICLE-CLOUD SOLVER
EQUATIONS	<ul style="list-style-type: none"> • 1D/2D/3D TIME MARCHING PARTICLE-CLOUD EQUATIONS • FULLY COUPLED PARTICLE DENSITY, VELOCITY, AND TEMPERATURE EQUATIONS • DRAG TERMS MODELED FOR NON-EQUILIBRIUM PARTICLE INTERACTIONS • DRAG RELATIONS OF HERMSEN AND HENDERSON AVAILABLE • PHASE CHANGE OF PARTICLES INCORPORATED
NUMERICS	<ul style="list-style-type: none"> • LIMITING PARTICLE STREAMLINE CAPTURED AS A DISCONTINUITY IN THE PARTICLE-CLOUD DENSITY • ROE TVD UPWIND ALGORITHM FULLY CONSISTENT WITH GAS PHASE NUMERICS • IMPLICIT TREATMENT OF PARTICLE SOURCE AND FLUX TERMS • ADI BLOCK INVERSION • TIME ACCURATE/TIME ASYMPTOTIC NUMERICS • NEWTON ITERATION TO REMOVE APPROXIMATE FACTORIZATION ERRORS
BOUNDARY CONDITIONS	<ul style="list-style-type: none"> • WALL WITH PARTICLES STICKING • WALL WITH PARTICLES SLIPPING • INFLOW • OUTFLOW

Table V. $k\epsilon$ CD Turbulence Model

The $k\epsilon$ CD turbulence model utilizes a "compressible" turbulent viscosity, μ_t , given by:

$$\mu_t = C_\mu \rho k^2 / (\epsilon_s + \epsilon_c)$$

The incompressible value of turbulent dissipation, ϵ_s , is obtained from the equation:

$$\rho \frac{D\epsilon_s}{Dt} = \frac{\partial}{\partial X_i} \left[\frac{(\epsilon_s + \epsilon_c)}{\epsilon_s} \frac{\mu_t}{\sigma_\epsilon} \frac{\partial \epsilon_s}{\partial X_i} \right] + \frac{\epsilon_s}{k} (C_1 \underline{P} - C_2 \rho \epsilon_s)$$

The compressible-dissipation, ϵ_c , is given by:

$$\epsilon_c = \epsilon_s \left[\alpha_1 \tilde{M}_T^2 + \beta \tilde{M}_T^4 \right]$$

where \tilde{M}_T includes a Zeman lag

$$\tilde{M}_T = M_T - \lambda$$

and the coefficients utilized are as follows:

$$\begin{aligned} \alpha_1 &= 1 \text{ (same as Sarkar)} \\ \lambda &= .1 \text{ (same as Zeman)} \\ \beta &= 60 \text{ (fits LaRC data the best)} \end{aligned}$$

The equation for turbulent kinetic energy, k , is given by:

$$\rho \frac{Dk}{Dt} = \frac{\partial}{\partial X_i} \left[\frac{\mu_t}{\sigma_k} \frac{\partial k}{\partial X_i} \right] + \underline{P} - \rho (\epsilon_s + \epsilon_c) + \overline{p' \theta'}$$

where the turbulent production, \underline{P} , in both the k and ϵ_s equations utilizes the compressible μ_t

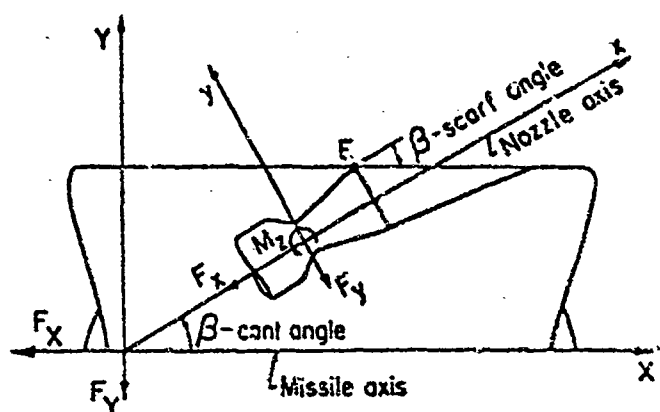


Figure 1. Schematic of Bifurcated/Scarfed Nozzle Casted at an Angle β Relative to the Missile Axis.

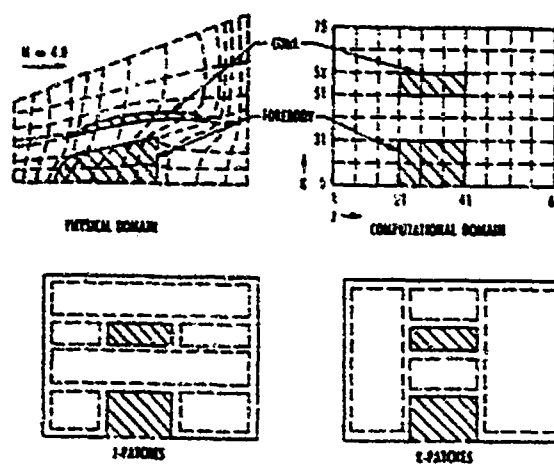


Figure 2. Patched Grid in Physical and Computational Domain.

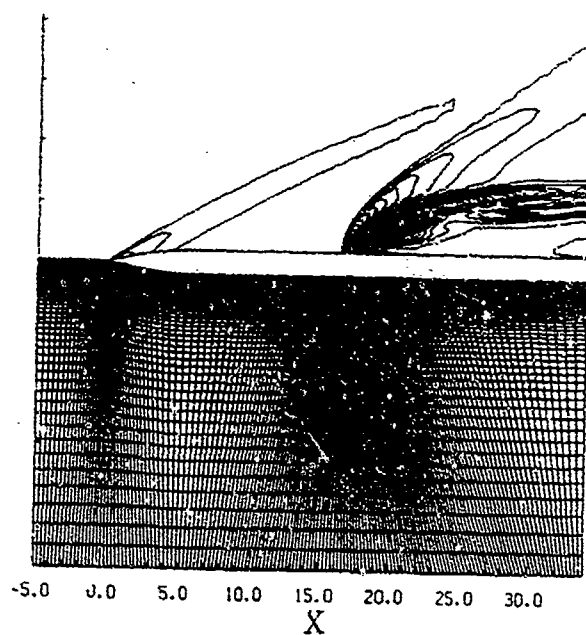


Figure 3. PARCH Mach Contours and Grid for Missile Plume/Airframe Prediction Compared with Aérospatiale/ONERA Data.

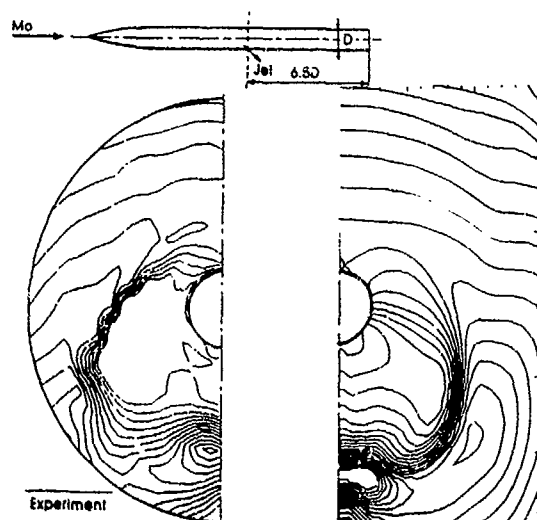


Figure 4. Preliminary Comparisons of PARCH predictions with Aérospatiale/ONERA Data for Mach 2 Missile with Mach 2.5 Highly Inclined Jet (using Roe/TVD Run Option).

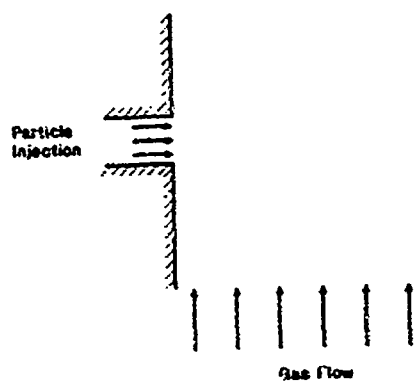


Figure 5. Schematic of Transverse Particle Jet Injection Problem.

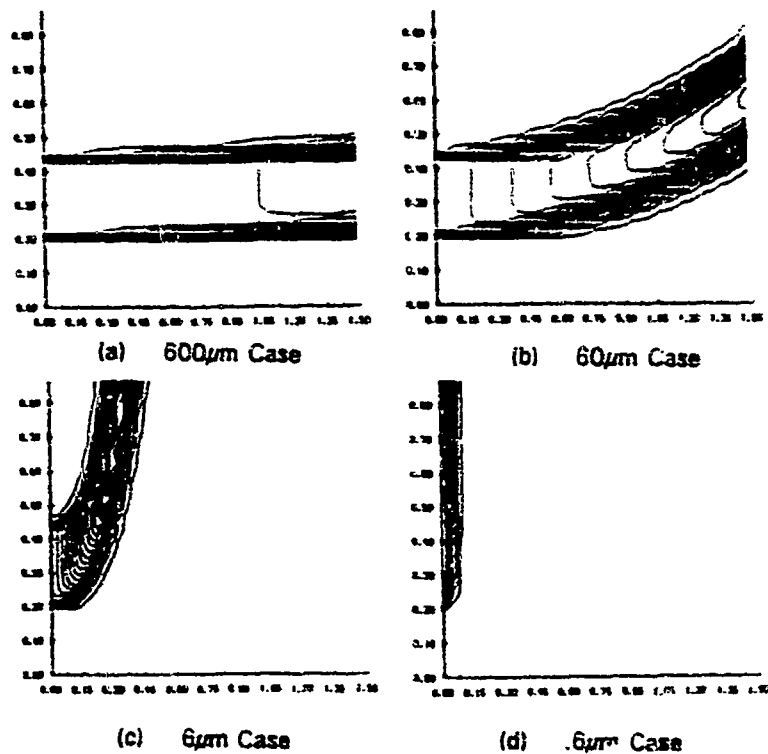


Figure 6. Particle-Cloud Density Contours for Time-Asymptotic Simulation of Transverse Jet Injection of Zirconium-Oxide Particles into Uniform Approach Gas Flow: (a) 600 μ m; (b) 60 μ m; (c) 6 μ m; and (d) .6 μ m.

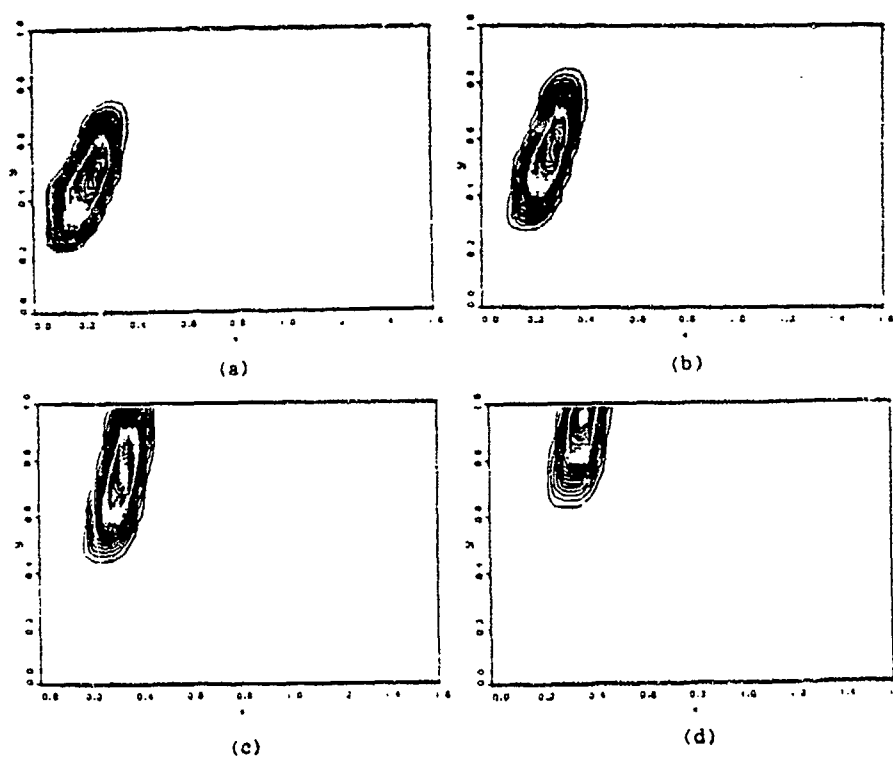


Figure 7. Particle-Cloud Density Contours at Several Times for Transient Transverse Injection Simulation, 6 μ m Zirconium Oxide Particles.

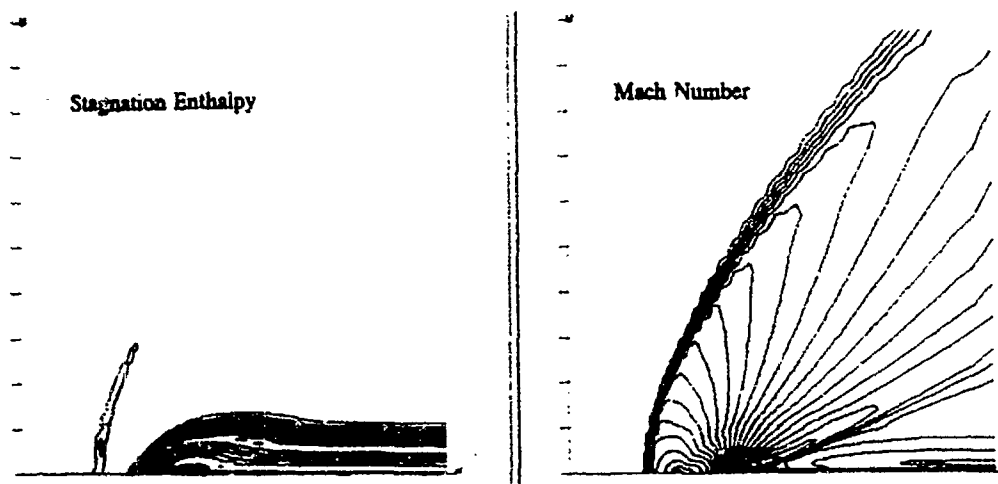


Figure 8. Transverse Injection Problem: Single Phase Mach Number and Stagnation Enthalpy Contours.

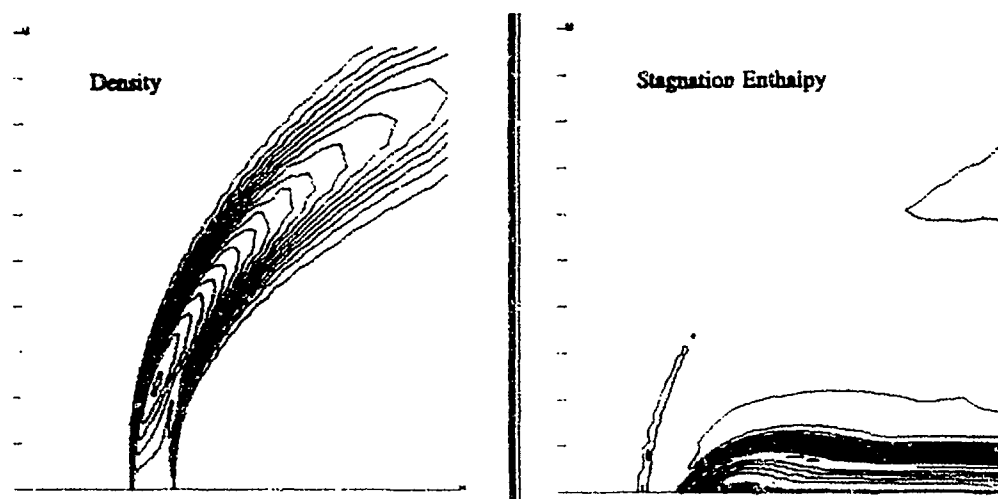


Figure 9. Particle-Cloud Density and Gas-Phase (Stagnation Enthalpy) Plume Boundaries for 25 μ m Case.

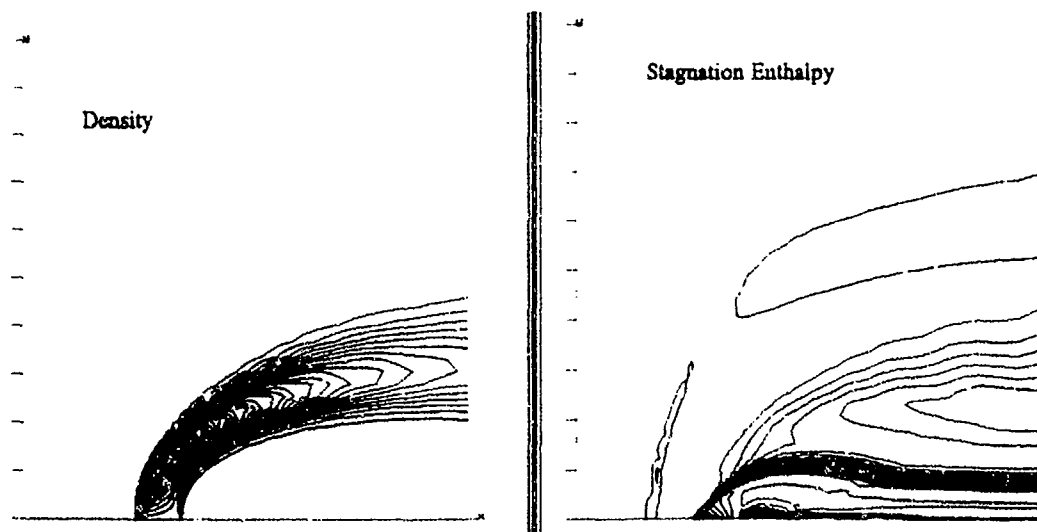


Figure 10. Particle-Cloud Density and Gas-Phase (Stagnation Enthalpy) Plume Boundaries for 5 μ m Case.

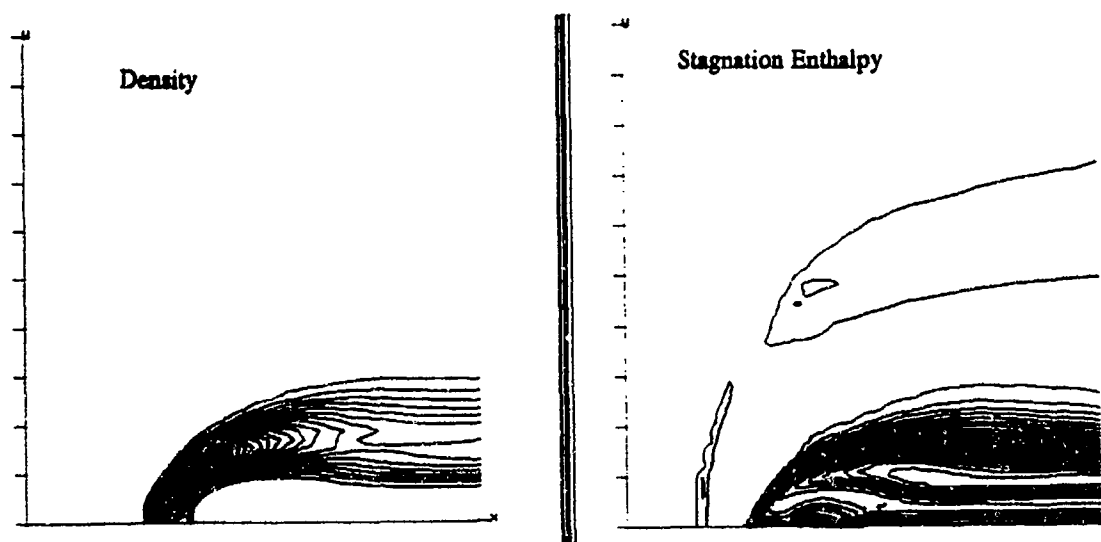


Figure 11. Particle-Cloud Density and Gas-Phase (Stagnation Enthalpy) Plume Boundaries for 2.23 μ m Case.

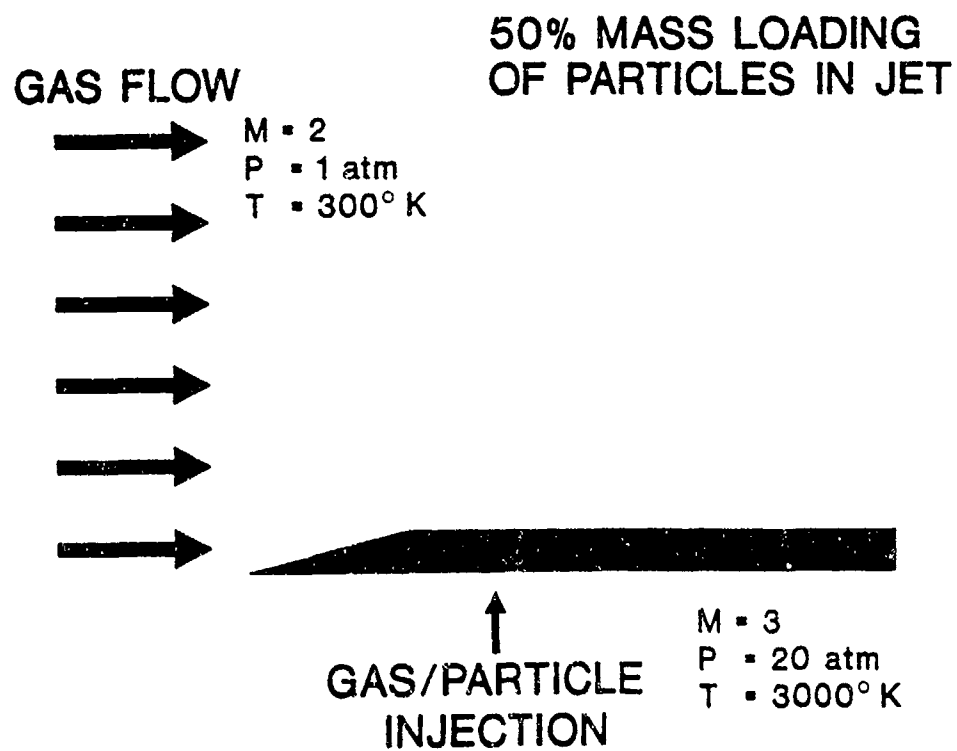


Figure 12. Schematic of Generic Jet/Missile Interaction Flowfield.

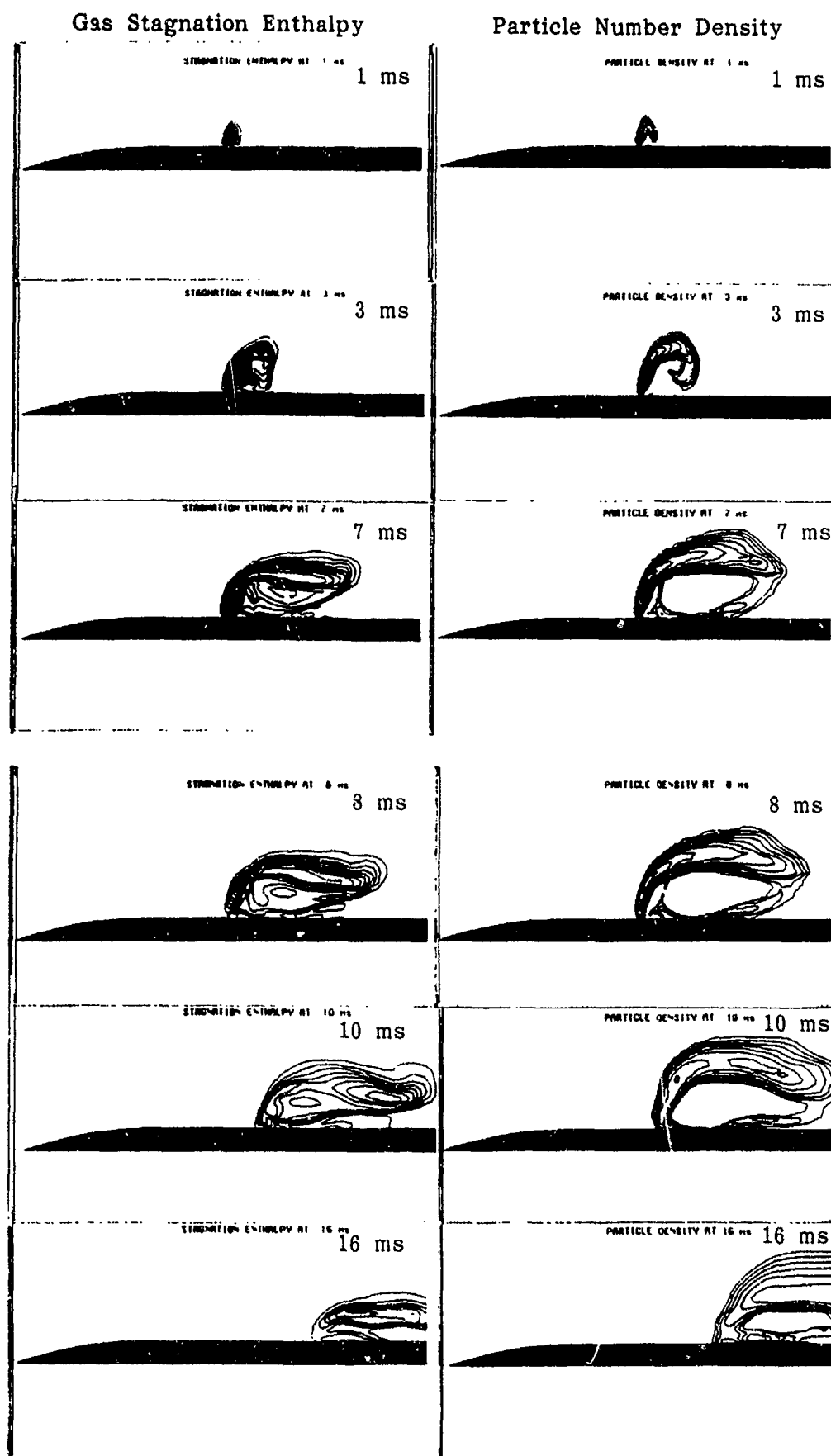


Figure 13. Gas-Phase (Stagnation Enthalpy) and Particle-Cloud Plume Boundaries at Selected Times for Transient Lateral Control Jet Problem.

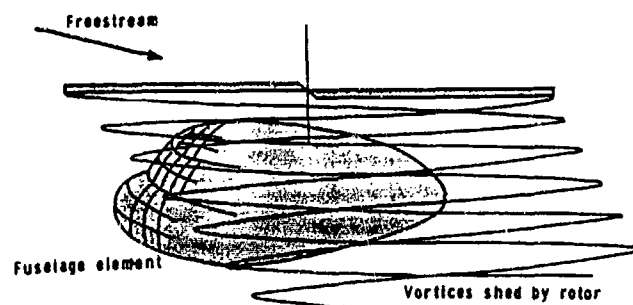


Figure 14. Schematic of Helicopter Flowfield.

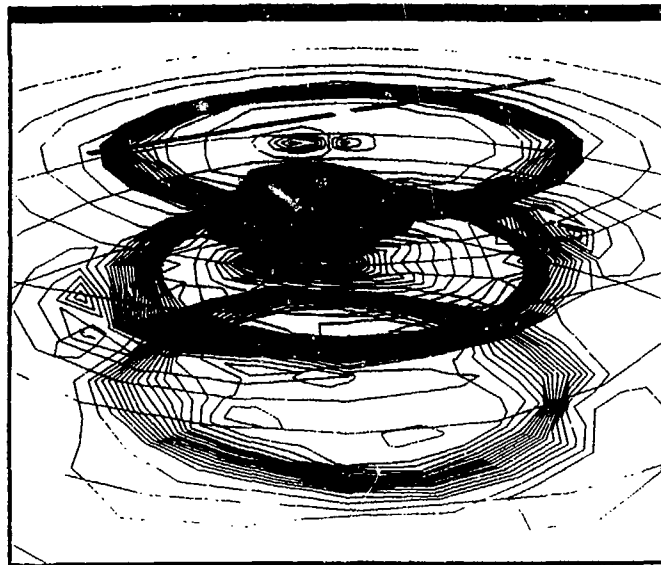


Figure 15. HELIWAKE Analysis of Helicopter Wake in Hover.

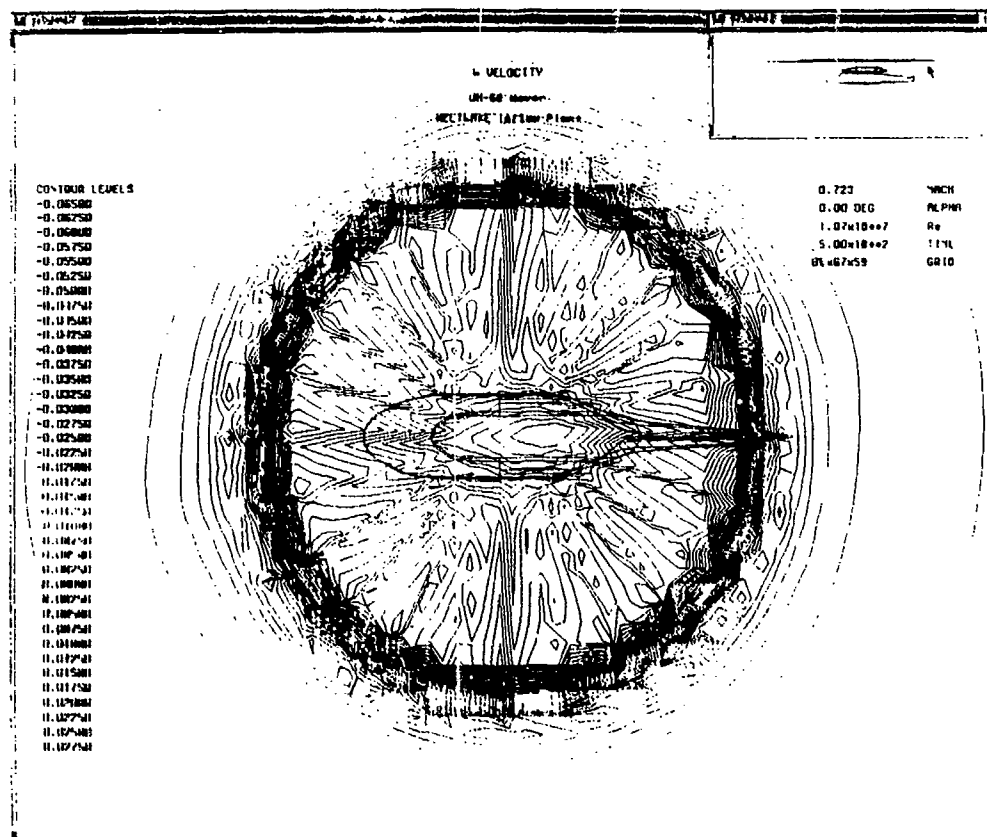


Figure 16. Hover Downwash Solution at HELIWAKE/PARCH Interface Plane.

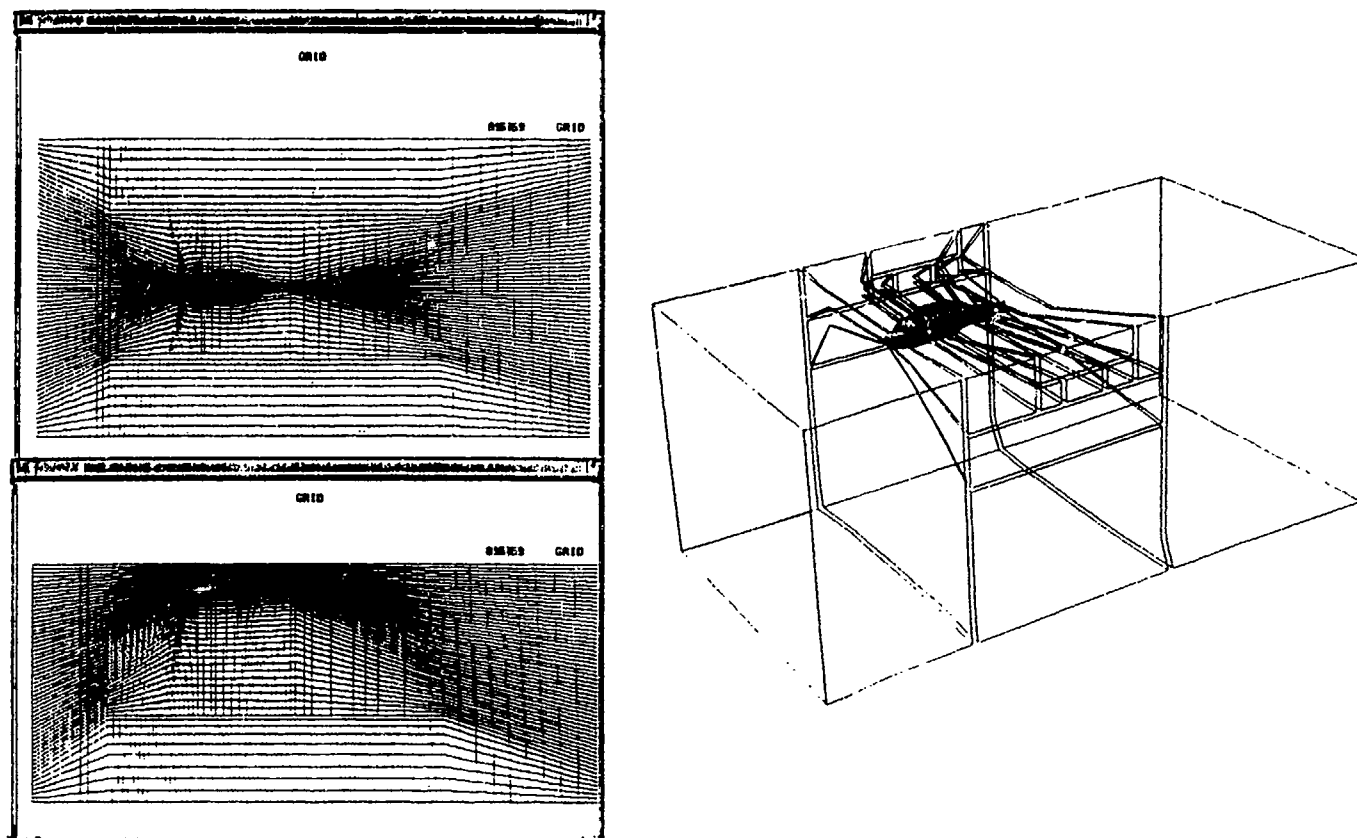


Figure 17. Baseline Grid and Patching in One of the Coordinate Directions.

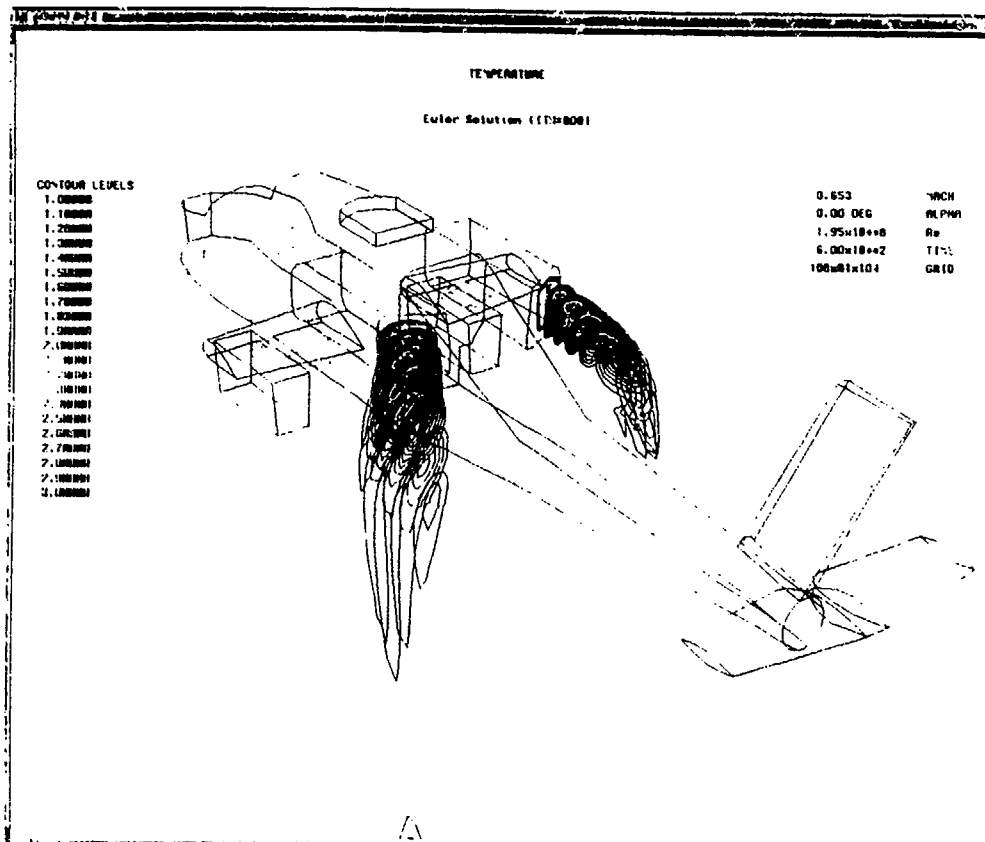


Figure 18. Temperature Contours of Helicopter Plumes in Hover.

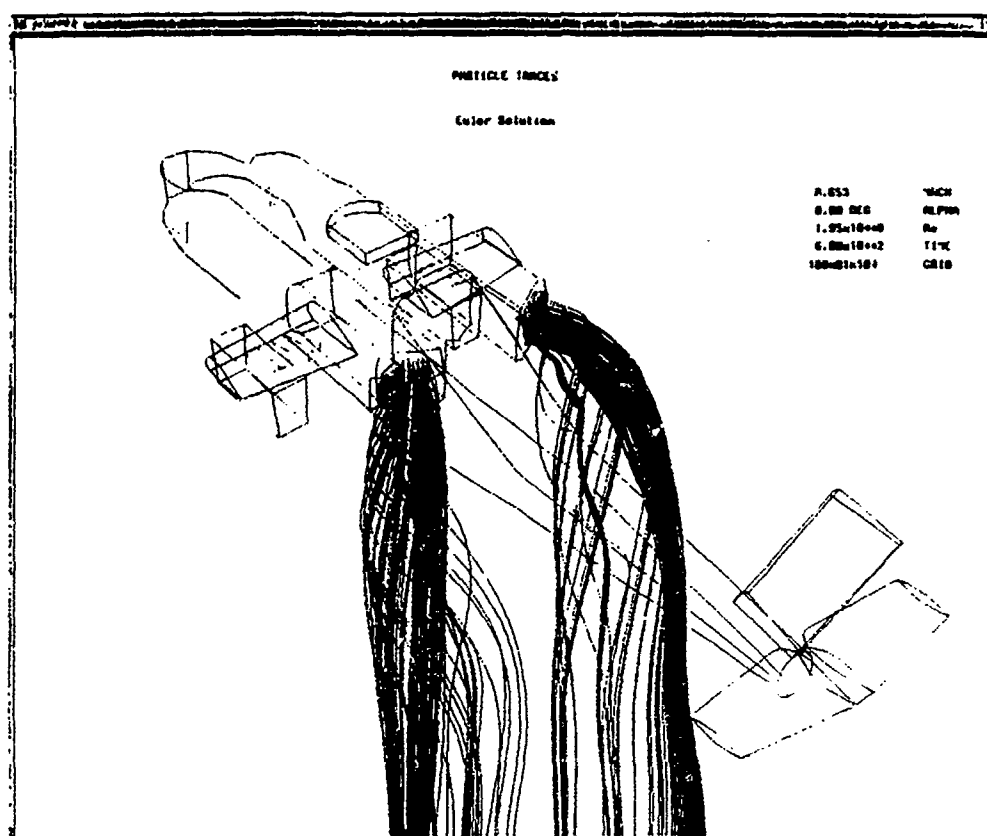


Figure 19. Streamline Traces of Helicopter Plumes in Hover.

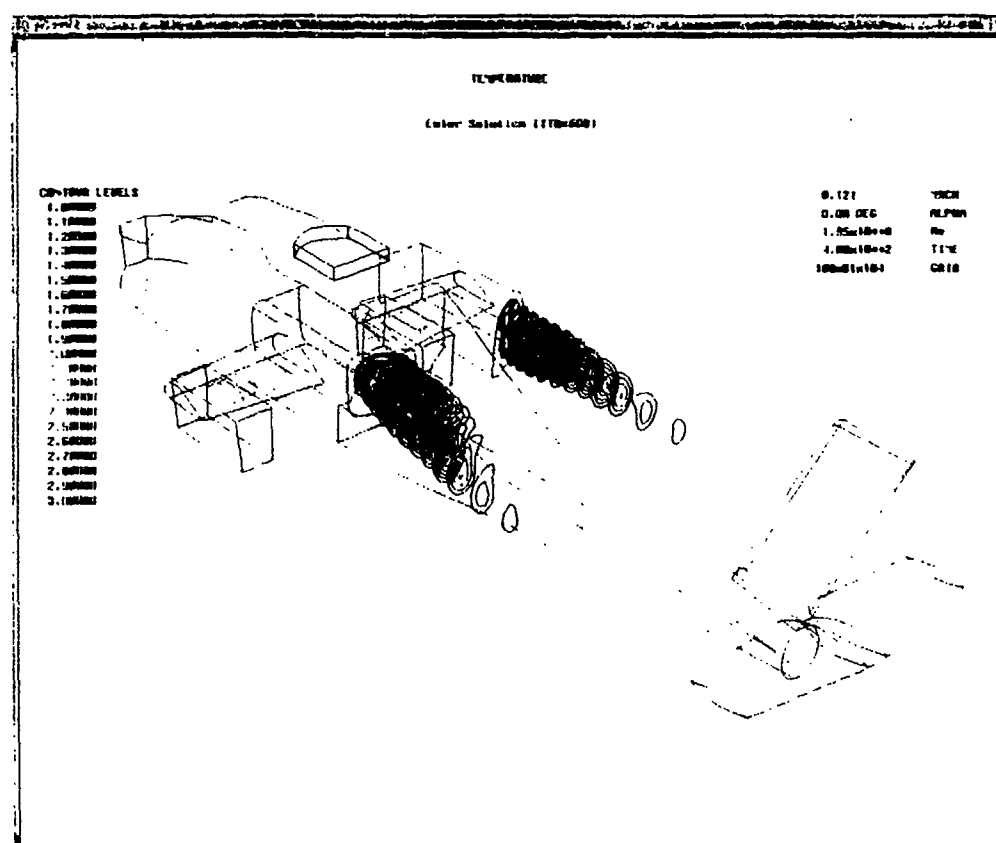


Figure 20. Temperature Contours of Helicopter Plumes in Forward Flight.

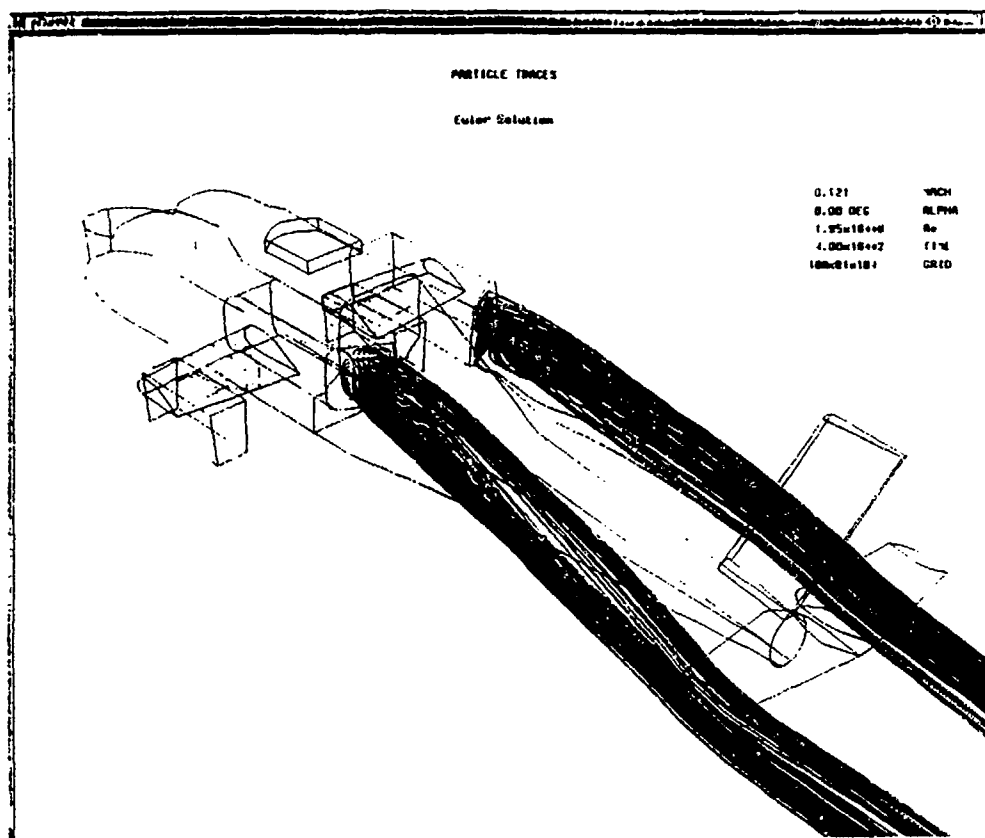


Figure 21. Streamline Traces of Helicopter Plumes in Forward Flight.

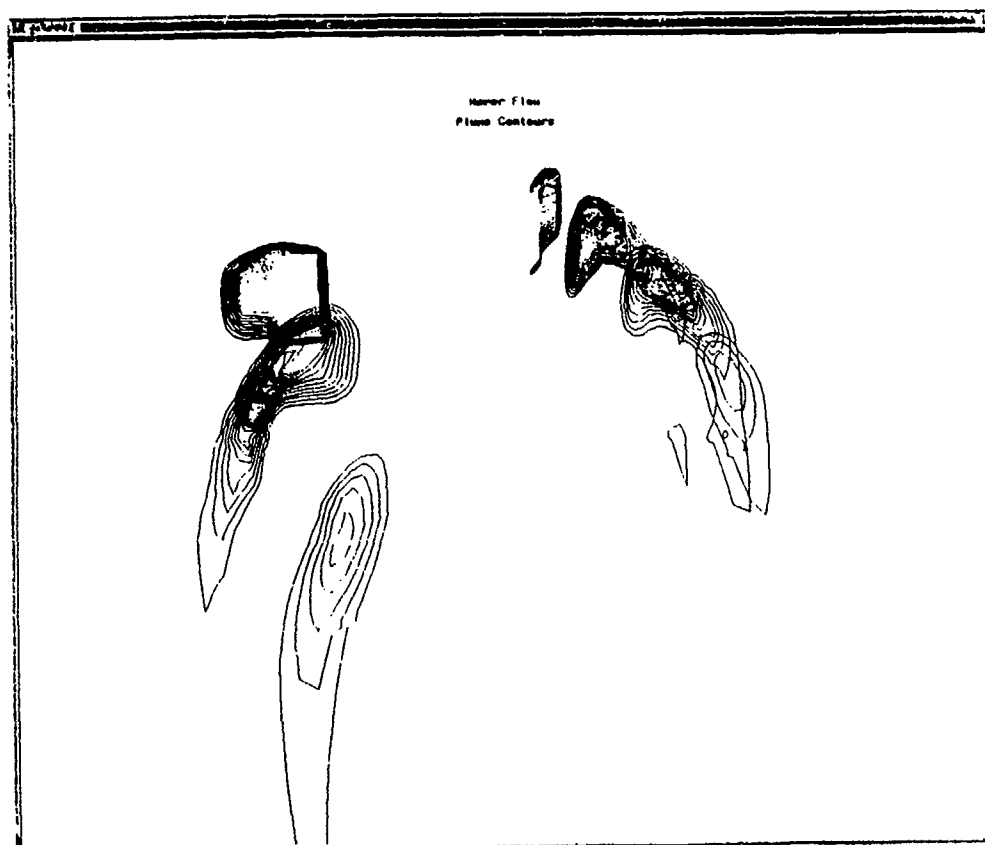


Figure 22. Close-Up View of Helicopter Plume Structure in Hover.

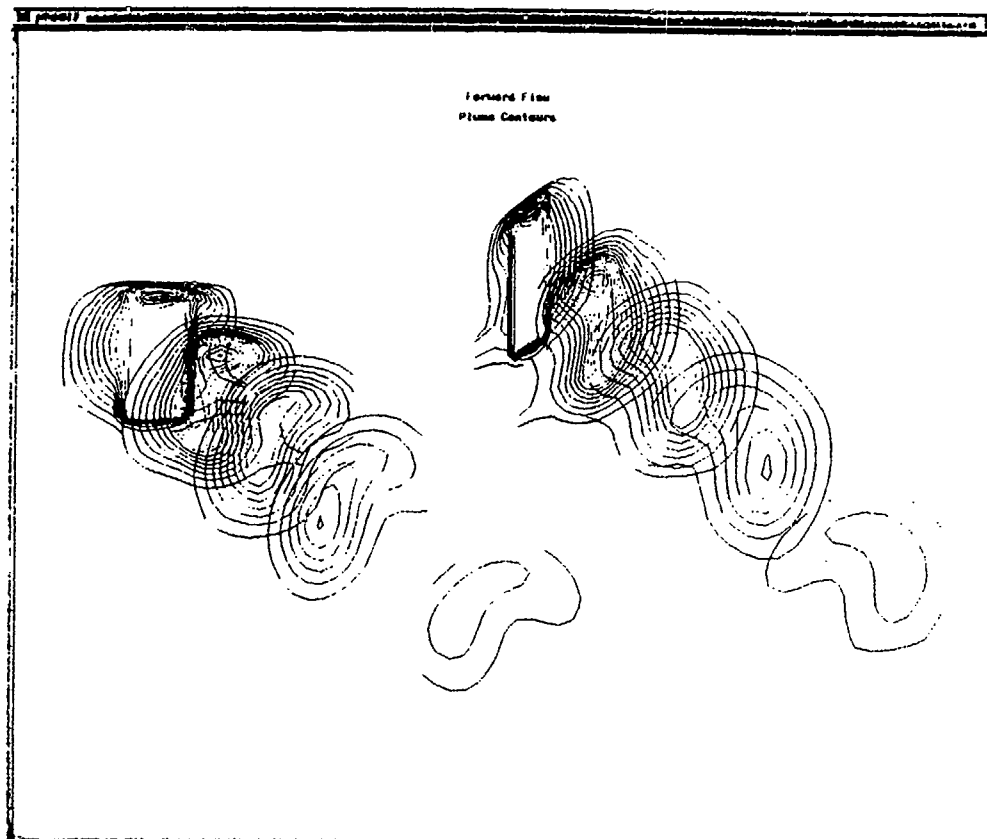
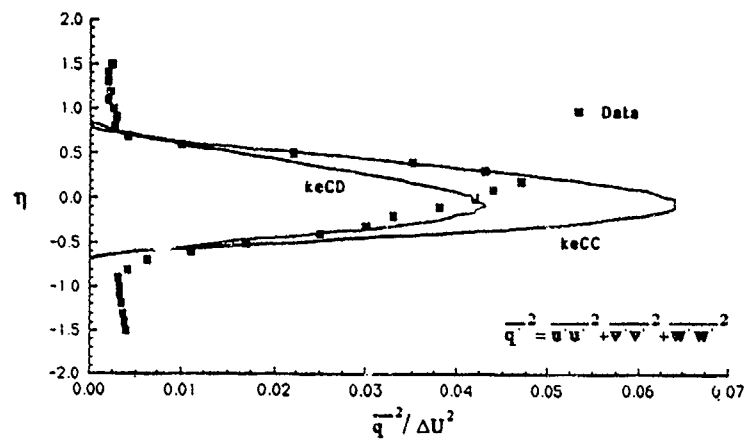


Figure 23. Close-Up View of Helicopter Plume Structure in Forward Flight.



Quantity	Primary Stream	Secondary Stream
Stagnation Pressures:	$P_{t1} = 552 \text{ kPa}$	$P_{t2} = 43.4 \text{ kPa}$
Stagnation Temperatures:	$T_{t1} = 279 \text{ K}$	$T_{t2} = 289 \text{ K}$
Static Pressures:	$P_1 = 40.3 \text{ kPa}$	$P_2 = 40.3 \text{ kPa}$
Freestream Velocities:	$U_1 = 543 \text{ m/s}$	$U_2 = 91.2 \text{ m/s}$
Static Temperatures:	$T_1 = 132 \text{ K}$	$T_2 = 285 \text{ K}$
Sonic Velocities:	$a_1 = 230 \text{ m/s}$	$a_2 = 338 \text{ m/s}$
Mach Numbers:	$M_1 = 2.36$	$M_2 = 0.27$
Freestream Densities:	$\rho_1 = P/RT_1 = 1.06 \text{ kg/m}^3$	$\rho_2 = P/RT_2 = 0.49 \text{ kg/m}^3$
Freestream Viscosities:	$\mu_1 = 9.10 \times 10^{-6} \text{ Pa-s}$	$\mu_2 = 1.77 \times 10^{-5} \text{ Pa-s}$

Figure 24. Comparison of Asymptotic Turbulence Intensity Profiles for the Gruber & Dutton High-Speed Shear Layer Case.

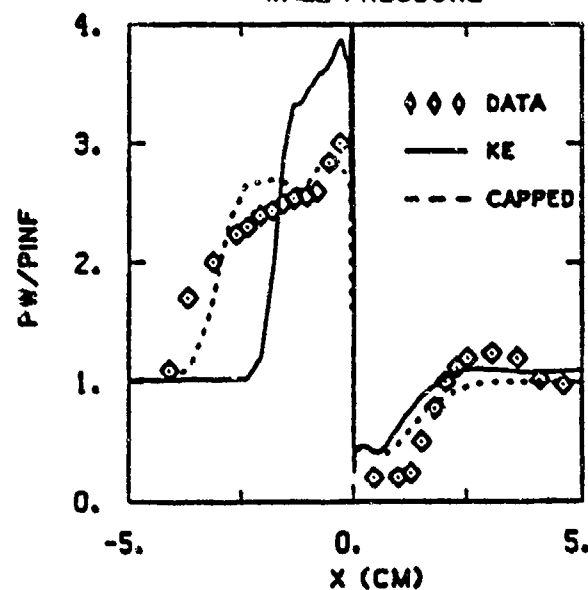
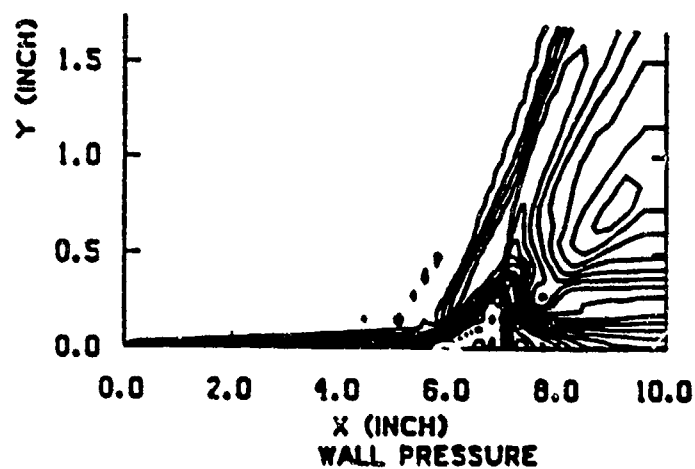
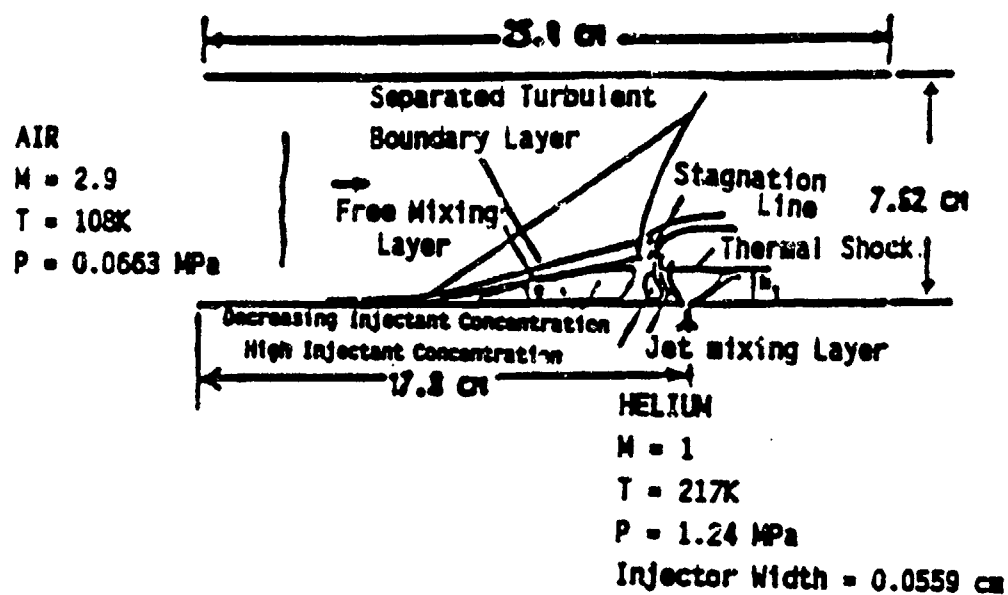


Figure 25. Planar Transverse Jet Interaction Problem, PARCH Mach Number Contours, and Comparison of PARCH Wall Pressure Predictions with Test Data.

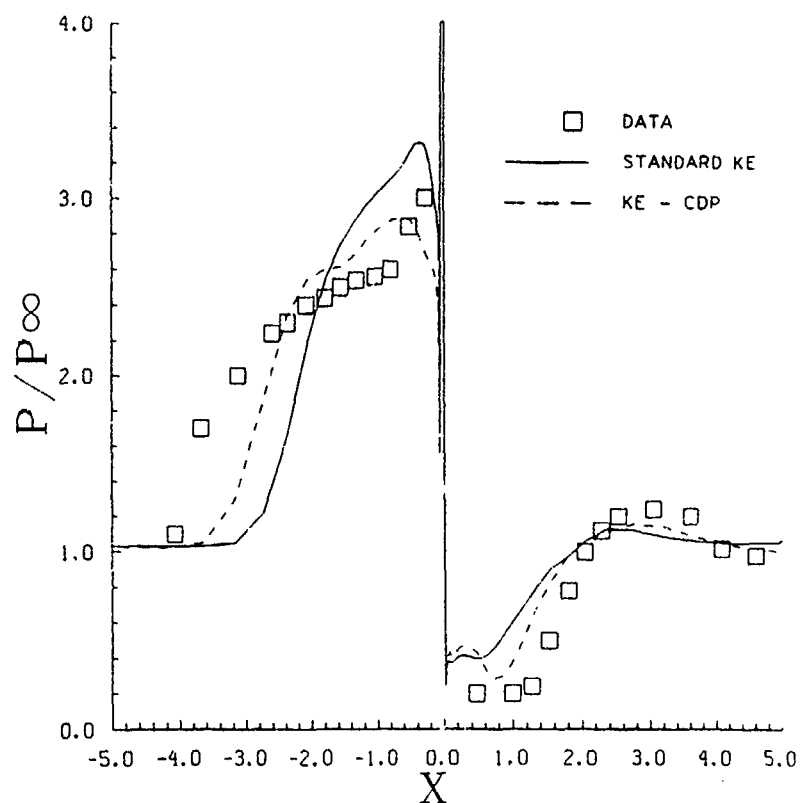


Figure 26. Comparison of Axial Pressure Profiles Predicted by $k\varepsilon$ and $k\varepsilon$ CD for the Transverse Jet Simulation.

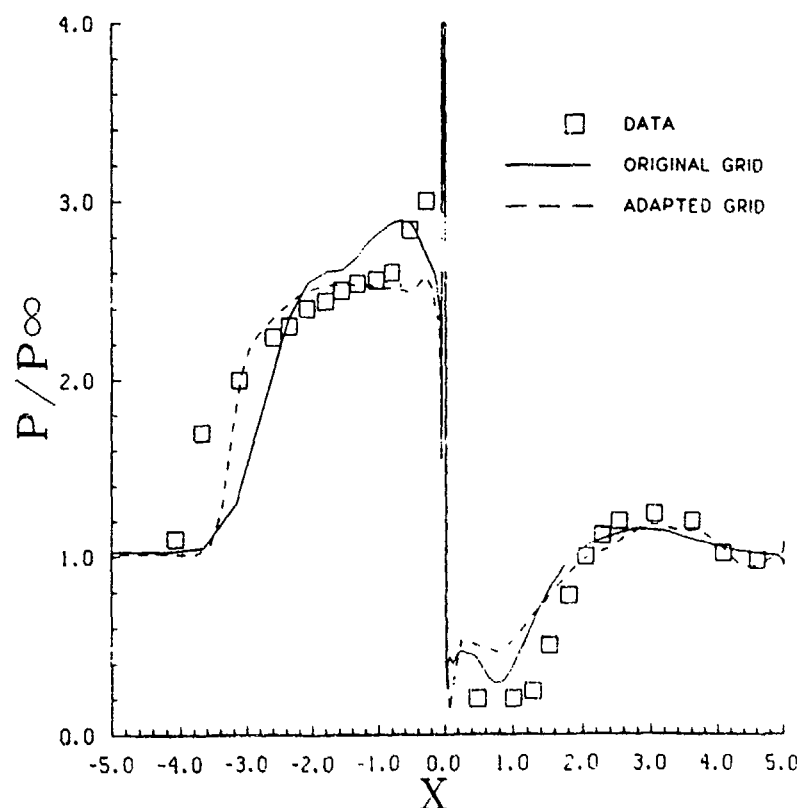


Figure 27. Effect of Using Grid Adaptation to Better Predict the Axial Pressure Distribution for a Transverse Jet Using the $k\varepsilon$ CD Turbulence Model.

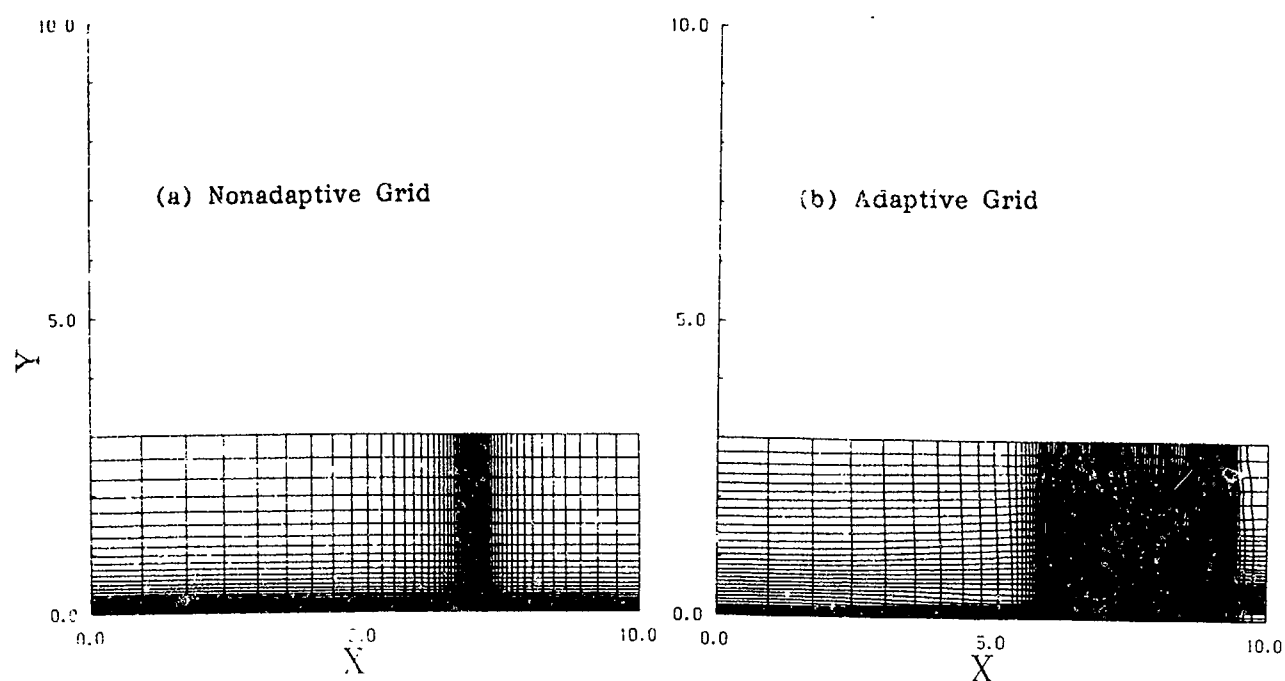


Figure 28. Grids Used for the Transverse Jet Calculation: (a) Non-Adaptive and (b) Adaptive.

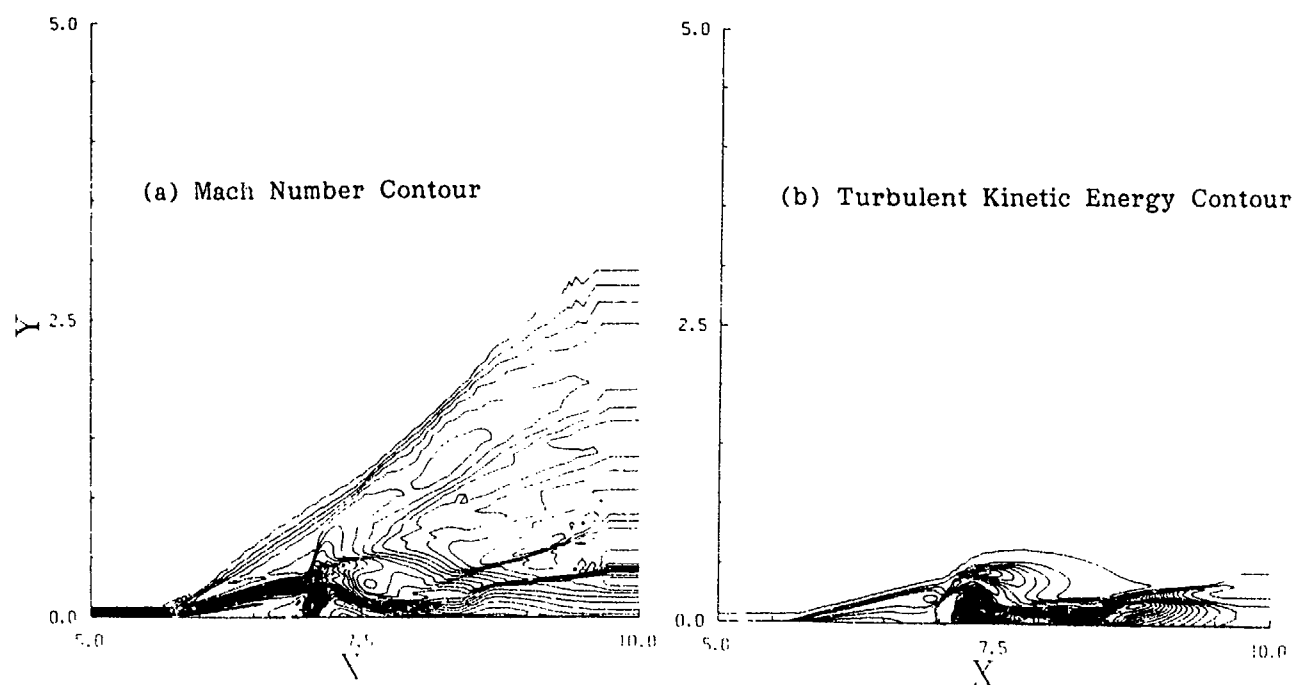


Figure 29. Contours of (a) Mach Number and (b) Turbulent Kinetic Energy for a Transverse Jet Using the $k-\epsilon$ CD Model and Adaptive Gridding.

NUMERICAL ASSESSMENT OF AERODYNAMIC INTERACTIONS ON MISSILES WITH TRANSVERSE JETS CONTROL

M. DORMIEUX - R. MARSAA-POEY

AEROSPATIALE-MISSILES
91370 Verrières-Le-Bulson - FRANCE

ABSTRACT

This paper deals with numerical studies made at AEROSPATIALE-MISSILES about aerodynamic interactions due to the use of pyrotechnical lateral force control. Calculations were performed in order to predict lateral jets interactions on two kinds of missiles: subsonic antitank and supersonic antimissile.

In the subsonic case, Euler and Navier-Stokes calculations were compared on a missile body test case. Then, Euler code was applied to an antitank missile configuration, and missile spinning effects were assessed.

In the supersonic case, jet stagnation temperature and jet species effects were studied on a surface-to-air missile.

1 - INTRODUCTION

Increasing needs for new missile systems with high performances have lead AEROSPATIALE-MISSILES to use pyrotechnical lateral force control for two kinds of missiles: subsonic antitank and supersonic antimissile.

However, presence of transverse jets close to the missile raises the problem of aerodynamic interactions. In this respect, use of lateral force control requires the ability to predict these aerodynamic phenomena.

This paper presents some calculations made around subsonic or supersonic missiles with transverse jets.

In the subsonic case, no numerical assessments was performed before the present one. Thus, a preliminary study on a missile body test case was made, and followed by calculations on an antitank missile with cold air jets.

In the supersonic case, AEROSPATIALE-MISSILES has acquired the ability to perform calculations around missiles with cold air jets since 1988 [5]. In this paper, calculations around a surface-to-air missile including jet stagnation temperature and jet species effects are presented.

2 - MISSILES IN SUBSONIC FLOWS

2.1 - Missile body test case

The aim of this preliminary study is to establish Euler and Navier-Stokes codes ability to predict aerodynamic interactions of a lateral jet with a missile body.

For this reason, calculations were made of an inclined lateral jet of cold air with an ogive-cylinder missile at zero angle of attack.

2.1.1 - Description of the test case

Experimental investigations of the flowfield around the missile body with a lateral jet were performed in the ONERA S2 wind tunnel at Modane.

Figure 1 illustrates the experimental set up. The missile body is a cylinder of diameter D equal to 0.1 meters, with a parabolic ogive of length equal to $3 D$. The jet issues from an axisymmetric nozzle inclined rearward at an angle of 60 degrees from the missile axis and located $8.5 D$ downstream of the nose. Ten 5-hole probes are disposed on crosswise sticks, which can be rotated around the body.

Experimental data acquisition was performed with this device in 3 planes respectively located $10 D$, $12 D$ and $15 D$ downstream of the nose. These probings were realised with a large number of freestream and jet conditions.

2.1.2 - Calculations performed

Calculations were made with the following freestream and jet conditions:

	Freestream	Jet
Mach number	0.8	2.5
Stagnation pressure	0.95 bar	22 bar
Incidence	0°	60°
Stagnation temperature	293 K	293 K

The nozzle exit section was simulated by a rectangular hole, the size of which was chosen to keep the flow rate through the section. As the configuration is symmetric, calculations were performed only on one half space.

Euler and Navier-Stokes turbulent calculations were made. The Euler calculation was made with Euler code SESAME, developed by ONERA [1], [2]. Euler equations are solved by SESAME with an explicit and centered numerical scheme (Lax-Wendroff-Ni). Scheme stability is provided by addition of artificial viscosity terms (Jameson-Schmidt). A grid of $122 \times 41 \times 34$ points was used as shown in figure 2. The Navier-Stokes calculation was performed by SAIC (Science Applications International Corporation, USA) with Navier-Stokes PARCH3D code [3]. Turbulent viscosity was obtained from the two-equation $k-\epsilon$ turbulence model. A Roe upwind scheme was used for this calculation, with a grid of $151 \times 71 \times 31$ points depicted in figure 2.

2.1.3 - Comparisons of calculations with experimental results

Comparisons of calculations with experimental data are displayed in the cross plane located at 12 D downstream from the nozzle.

We analysed the flowfield structure in this plane, established by experiment and calculations.

Figure 3 shows Ω_x (axial component of the vorticity vector) contours in the cross plane. Two contra-rotating vortices - one for each half plane - take place in the external flowfield. These vortices do result from the jet curvature and rounding by the external flow, and are clearly predicted by both calculations. Moreover, vortices location is very close to experimental results. However, Euler and Navier-Stokes calculations overestimate the vortices intensity by around 50 %. Another couple of vortices appear on experimental contours very close to the body. These vortices are detected by PARCH3D Navier-Stokes calculation, but not by SESAME Euler calculation.

Figure 4 shows Mach number contours in the cross plane. We observe from this figure that calculations are qualitatively close to experimental results, as far as the jet cross-section structure and size are similar. Mach number maximum value in the cross plane is well predicted by both calculations, with a difference to experimental results lower than 10%. This maximum location is nearly the same for experimental data and PARCH3D calculation. SESAME calculation locates this maximum about 0.5 D closer to the missile body than experimental results.

Stagnation pressure contours are shown in figure 5. The jet cross-section size is well predicted by calculations. The jet structure appears more complex than with other variables (Mach number or Ω_x). In each half plane, experimental results point out 3 extrema of stagnation pressure: one absolute minimum located in the vortex center (A), one local maximum below the minimum (B), and one absolute maximum above the minimum (C). These extrema are well predicted by the PARCH3D Navier-Stokes calculation, with the proper locations. The absolute maximum (C) value shows a difference equal to about 20% between the Navier-Stokes calculation and the experimental data. However, SESAME Euler calculations does not detect the absolute maximum (C). The local maximum (B) value is well predicted by Euler and Navier-Stokes calculations (with differences respectively lower than 20% and 5%).

In all cases, we note that the jet cross-section is rounder and more expanded for SESAME calculation than for PARCH3D one.

In a general way, it appears that a better agreement with experiment is obtained through Navier-Stokes calculation. However, Euler calculation is quite able to predict the flow structure and to give good results.

One quantitative criterion by which one can compare calculations is provided by integration of lift coefficient on the body. Results are shown on figure 6. However, we do not have any experimental results of this type to compare with calculations.

Curves obtained present similar trends in both cases - Euler or Navier-Stokes - and show a lift decrease located 2 D upstream from the nozzle due to an overpressure zone generated by the jet blockage effect. Immediately downstream the nozzle appears a lift increase created by the depression zone close to the body due to the jet. Further downstream, lift decreases because of jet vortical structures which affect the body surface.

Lift value C_z obtained 15 D downstream from the nozzle are the following ones: $C_z=0.48$ with SESAME and $C_z=0.55$

with PARCH3D. Thus, differences for C_z obtained between Euler and Navier-Stokes calculations remain moderate.

2.2 - Antitank missile application

Calculations were performed on a case of industrial interest, in order to study aerodynamic interactions created on an antitank missile with transverse jets propulsion and control. Euler equations were solved to have a low computation cost, as far as calculations on the missile body test case showed that Euler model was proper enough to describe interactions on missiles with jets.

2.2.1 - Description of the application

Figure 7 shows the antitank missile geometry. Propulsion unit is mounted at the front of the body, and nozzles - one in each half space - are located at the missile center of gravity. Each nozzle axis is inclined rearward so that thrust axial component contributes to accelerate the missile. Jets deflectors located at the nozzle exit section ensure missile steering. Missile spin rate ω around its axis permits to control the flight with two nozzles only. The hollow charge warhead is located at the missile rear, in order to have a sufficient distance between the nose and the warhead.

2.2.2 - Calculations performed

All calculations were made without incidence with a freestream Mach number equal to 0.3. Jet conditions were defined with a preliminary 3 D Navier-Stokes calculation of the flow into the nozzle with deflector. The nozzle exit section was simulated by a rectangular hole on the missile body, and jet conditions were imposed on this hole during the external calculations around the body.

Calculations were performed using Euler approximation with code SESAME, which permits to take into account the missile spinning effect by including inertial and Coriolis terms in Euler equations.

In this respect, three calculations were made:

- missile with jets without spinning effect,
- missile without jet with spinning effect,
- missile with jets and spinning effect.

Figure 7 shows the grid used for all calculations. Because of wings curvature and spinning effect, symmetry was not employed, and a grid of about 220000 points was generated.

Mach number contours in a transverse plane are shown in figure 8 for calculations performed with jets. Jet cross-sections are visible in each half plane, and located close to the wings. Without any spinning effect, one jet cross-section is approximately symmetrical to the other, some differences appearing due to wings curvature. When spinning effect is included in calculation, jet cross section structure does not change, but jet location is modified: jets turn around missile axis, and angular deviation obtained depends on the jet direction at the nozzle exit section compared to rotated external flow direction.

Figure 9 shows local normal forces on the wings due to external flow for the three calculations. Without spinning effect, interactions due to lateral jets create a depression - particularly on wings n° 3 and 4 - which was confirmed by wind tunnel results. With spinning effect and without jets, a normal force appears on each wing which induces a roll moment tending to slow down the missile spinning. With spinning effect and with jets, forces on the wings induce yaw

and pitch moments.

Phenomena included are clearly non linear because forces on the wings for the missile with spinning effect and jets are not obtained by simply adding up forces for the missile with spinning effect alone and for the missile with jets alone.

3 - MISSILES IN SUPERSONIC FLOWS

Application to a thrust-vector controlled anti-missile

The calculations presented in this paragraph differ from those of §2 by the supersonic upstream conditions, but also by the simulation of the jet stagnation temperature and the jet species effects.

3.1 - Description of the application

Figure 10 presents ASTER antimissile. It is a cruciform missile with four low aspect ratio wings and four control surfaces. The thrust-vector control is achieved by means of jets emerging from the lateral side of the wings.

The lateral force control configuration which has been calculated is a one jet configuration. The lateral jet emerges from the lateral side of the inferior wing (see fig.10, 11). For this configuration, two series of wind tunnel tests have been carried out: one with cold air jet, and the other with powder gas jet. These two kinds of tests are linked by criteria of similarity (conservation of nozzle thrust, exhaust section area, and expansion ratio). These criteria have been chosen in order to keep interactions as identical as possible between the two jets (especially in terms of jet penetration height). Experimentally small variations on aerodynamic coefficients are observed between the wind tunnel tests achieved with cold air jet and those achieved with powder gas jet.

We try to simulate these variations by modeling the powder gas jet as a perfect gas with the same specific heat ratio and the same molar mass. In other words, we try to explain these variations by jet stagnation temperature and jet species (specific heat ratio and molar mass) effects.

In this aim, the flow is modelised as an inviscid two-species perfect gas [6]. Euler equations are solved by the code FLU3M [4].

This model is of course not able to simulate certain physical phenomena: boundary layer, bow shock/boundary layer interaction, turbulent mixing layer between the jet and the external flow. However, it will be shown in the following that this model can be sufficient to predict the interactions in terms of aerodynamic coefficients.

3.2 - Previous calculations

Wind tunnel tests with a cold air jet had already been compared with numerical simulations using an inviscid one-species perfect gas model for the fluid. The comparisons in terms of aerodynamic coefficients were good [5].

The inviscid two-species perfect gas model had been previously validated on fundamental cases [6]. For the ASTER missile, we use now this model and simulate the powder gas jet as a perfect gas jet having the same specific heat ratio and the same molar mass.

3.3 - Present calculations and comparison with experiments

Four calculations have been performed corresponding to the

four following cases: without jet (available experimental forces), with a cold air jet (available experimental forces), with a hot air jet (no experimental data), with a perfect gas modeling the powder gas jet (available experimental forces). Cold air jet and hot air jet nozzle exit conditions differ only by the stagnation temperature.

We used a multidomain structured mesh made of 8 domains and about 400000 points (see fig.10).

Figure 11 shows a view of the wall pressure computed with the cold air jet and with the perfect gas modeling the powder gas jet.

Figure 12 shows calculations/experiments comparison and an interpretation of the results.

- Precision

Precision is computed by comparing normal force coefficient (CN) and the center of pressure abscissae (Zcp) for calculations and experiments (see fig.12).

For the cases without jet, with hot air jet and with a perfect gas modeling the powder gas jet, the error on CN is less than 7% and the error on Zcp is less than 0.25D (D diameter of the missile fuselage). The calculation with the cold air jet is a little less accurate (7% on the CN and 0.5D on Zcp).

- Interpretation

The interpretation is made by considering the differences on CN and Zcp/D between the 3 jet cases.

→ Effect of cold air jet (difference between the case with cold air jet and the case without jet):

the simulation of the effects of cold air jet is very good (error less than 2% on the ΔCN and 9% on the $\Delta Zcp/D$).

→ Effect of powder gas (difference between the cases with powder gas jet and cold air jet):

calculations show an effect as experiments do, that is to say, a slight increase in the normal force coefficient and a slight move of the center of pressure downstream.

It is interesting to evaluate the part of the jet stagnation temperature effect (difference cold air jet/hot air jet) and the part of the jet species effect (difference powder gas jet/hot air jet). In fact, we observe that the effect of stagnation temperature and species have the same weight (see fig.12).

3.4 - Flowfield analysis

We still have to understand how the jet species and the jet stagnation temperature locally act. In the following, we study some phenomena which are characteristic of the lateral jet in a supersonic crossflow: the bow shock ahead the jet, the Mach disk, and the jet location.

- Bow shock ahead the jet

On figure 13 are plotted against Z, for the 3 jets, the static pressure and the local normal force coefficient calculated along the intersection between the body and the symmetry plane.

Figure 14 compares, for the 3 jets, the pressure distribution in a transverse plane cutting the jet and located a little upstream of the nozzle center.

Between the cold air jet and the hot air jet on one side, and between the hot air jet and the powder gas jet on another side, we observe:

- a slight upstream shift of the bow shock and an increase in its curvature radius (see also fig.11)
- an increase in the local normal force coefficient in the region upstream the nozzle.

- Mach disk

Figure 15 compares the Mach number distribution in the

symmetry plane for the 3 jets. The Mach disk is located between the point where the Mach number reaches its maximum value and the point where it reaches its minimum value. The location of the first point stays the same for the 3 jets. The location of the second point moves a little upstream between the cold air jet and the hot air jet firstly, and between the hot air jet and the powder gas jet secondly. It seems difficult to conclude about the Mach disk location. It is all the more difficult since a good assessment of this location implies a more refined mesh [6].

- Jet location

The mass concentration of the jet is a well-adapted variable to pick out the jet location. It can be obtained in the present two-species Euler calculations.

Figure 16 shows the distribution of mass concentration of the jet species in a transverse plane located downstream of the nozzle. It appears that the jets shapes and heights of penetration are nearly the same for the 3 jets.

3.5 - Conclusions about stagnation temperature and jet species effects

The inviscid two-species gas model with a stagnation temperature effect gives a better assessment of the lateral powder gas jet interactions than the inviscid one-species gas model does.

It simulates the double effect of jet stagnation temperature and jet species, and shows that these two effects have the same weight.

Physically, these effects are characterized by:

- for the bow shock, slight upstream shift and increase in the curvature radius when stagnation temperature increased and when the hot air jet is replaced by a perfect gas modeling the powder gas jet
- for the jet location, no changes when jet stagnation temperature and species are modified.

Very recent fundamental experiments concerning the jet stagnation temperature effects have been carried out by ONERA [7]. They show the two trends above indicated.

4 - CONCLUSION

Calculations were performed around subsonic or supersonic missiles with lateral jets in order to predict aerodynamic interactions.

In the subsonic case, results obtained on a missile body test case show the ability of an Euler calculation to predict properly the external flowfield, although agreement with experiment is better when Navier-Stokes equations are solved. Euler calculations performed on an antitank missile first predicted downstream jets interactions on the missile, confirmed by wind tunnel results. Then, missile spinning effect was included in calculations, and results obtained show the influence of lateral jets interactions mixed with spinning effect on the missile global coefficients.

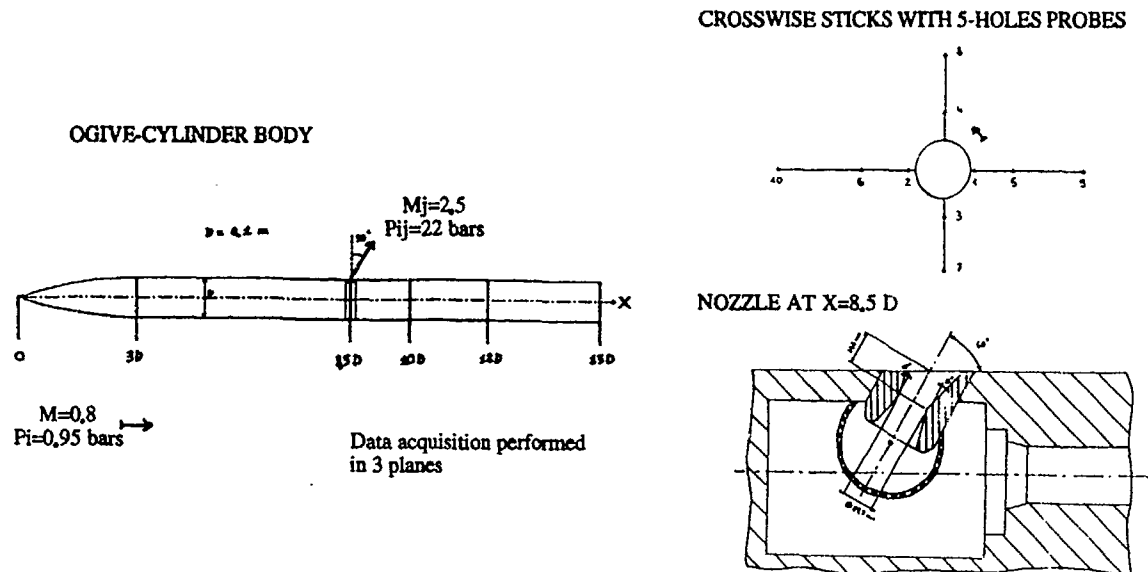
In the supersonic case, results of calculations performed around a surface-to-air missile showed that an inviscid two-species gas model simulates properly - in terms of aerodynamic coefficients - the effects of jet stagnation temperature and jet species, and that these two effects have the same weight.

ACKNOWLEDGEMENTS

This study was partly supported by French Ministry of Defence (D.R.E.T.).

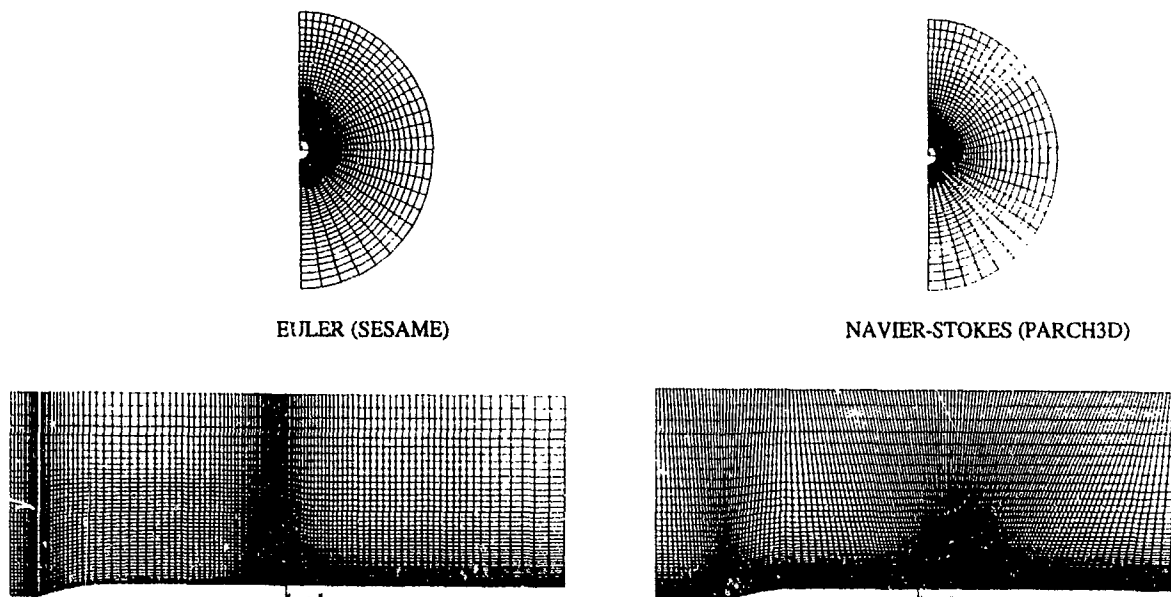
REFERENCES

- [1] - A. M. VUILLOT. "Multidomain3D Euler Solver For Flows in Turbomachines". Proceedings of the 9th ISABE Symposium, edited by S.S. BILLIG, AIAA Washington DC, Sept. 1989
- [2] - V. COUAILLIER. "Multigrid Method for Solving Euler and Navier-Stokes Equations in Two and Three Dimensions". 8th GAMM Conf. on Numerical Method in Fluid Dynamics, Delft (Holland), 27-29 Sept. 1989, ONERA
- [3] - B.J. YORK, N. SINHA, D.C. KENZAKOWSKI, S.M. DASH. "PARCH Code Simulation of Tactical Missile Plume/Airframe/Launcher Interactions". 19th JANNAF Exhaust Plume Technology Meeting, May 1991, CPIA Pub. 568, pp. 645-674
- [4] - Ph. GUILLEN, M. DORMIEUX. "Design of a 3D Multidomain Euler Code". Computational Mechanics Institute, Supercomputing in Fluid Flow, Boston. (1989).
- [5] - M. DORMIEUX, C. MAHE. "Calculs Tridimensionnels de l'Interaction d'un Jet Latéral avec un Ecoulement Supersonique Externe". AGARD-CP n°437, Lisbonne. (1988).
- [6] - M. DORMIEUX, Ph. GUILLEN, R. ABGRALL. "Numerical Simulation of Transverse Jet Flows by a Non Reactive Two Species Multidomain Euler Flow Solver". AIAA-90-0126, Reno.
- [7] - L. JACQUIN, P. GEOFFROY, G. LOSFELD, R. GAILLARD, R. MORELLE. "Etude Expérimentale à la Soufflerie S5Ch sur un Jet Transversal Supersonique Chauffé". RSP 3/2496AY, ONERA, Direction de l'Aérodynamique, Mars 1993.



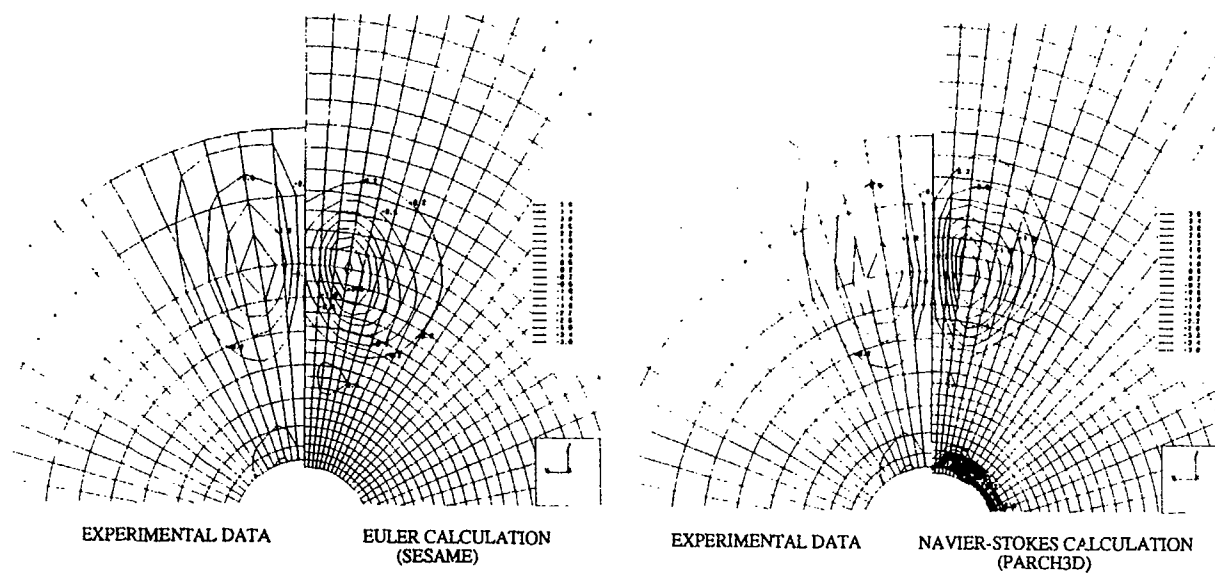
OGIVE-CYLINDER MISSILE:
WIND TUNNEL MODEL GEOMETRY

Fig. 1



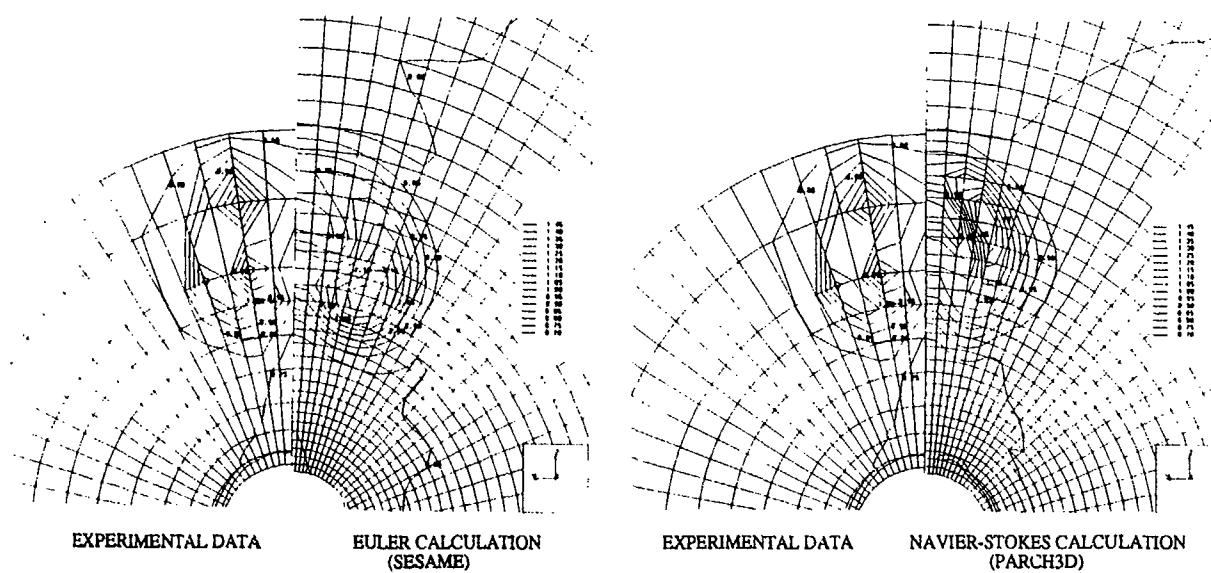
OGIVE-CYLINDER MISSILE:
GRIDS FOR EULER AND NAVIER-STOKES CALCULATIONS

Fig. 2



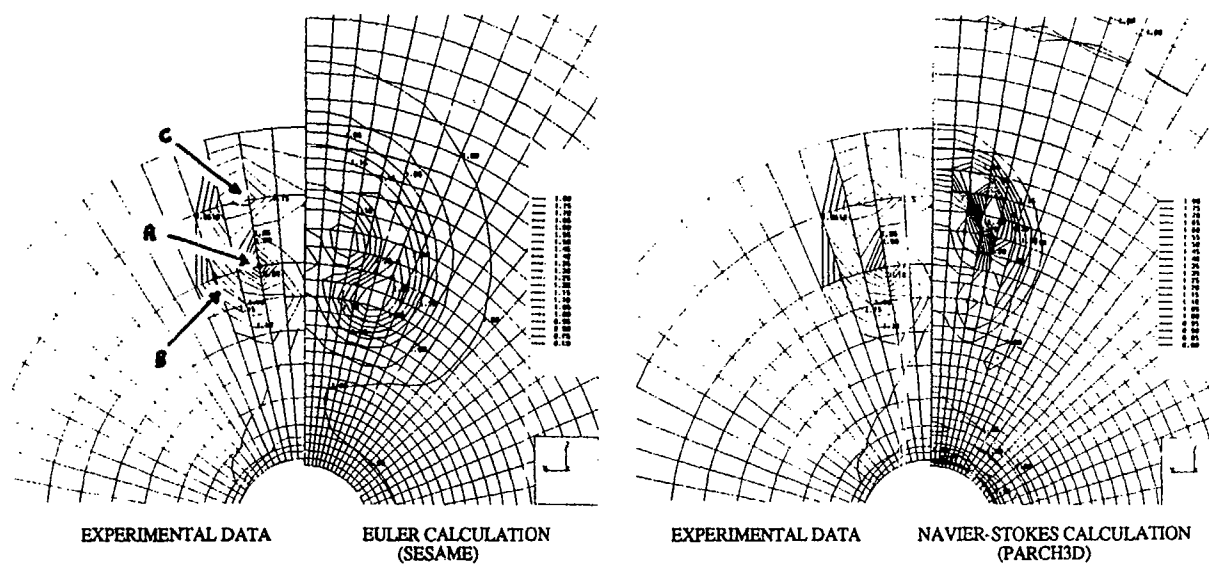
OGIVE-CYLINDER MISSILE:
 Ω_x CONTOURS IN THE CROSS PLANE AT $X=12 D$

Fig. 3



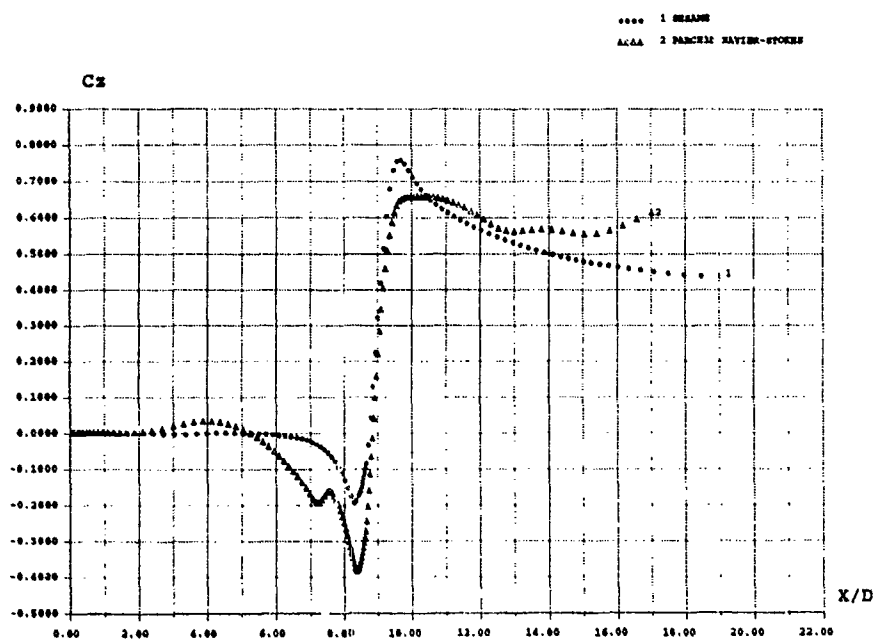
OGIVE-CYLINDER MISSILE:
 MACH NUMBER CONTOURS IN THE CROSS PLANE AT $X=12 D$

Fig. 4



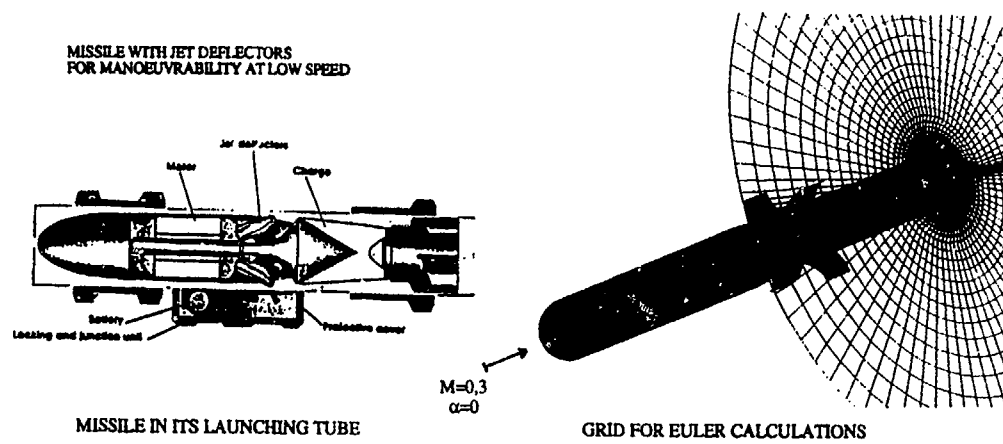
OGIVE-CYLINDER MISSILE:
STAGNATION PRESSURE CONTOURS IN THE CROSS PLANE AT $X=12 D$

Fig. 5



OGIVE-CYLINDER MISSILE:
INTEGRATION OF LIFT COEFFICIENT ON THE BODY (PRESSURE CONTRIBUTION)

Fig. 6



ANTITANK MISSILE

Fig. 7

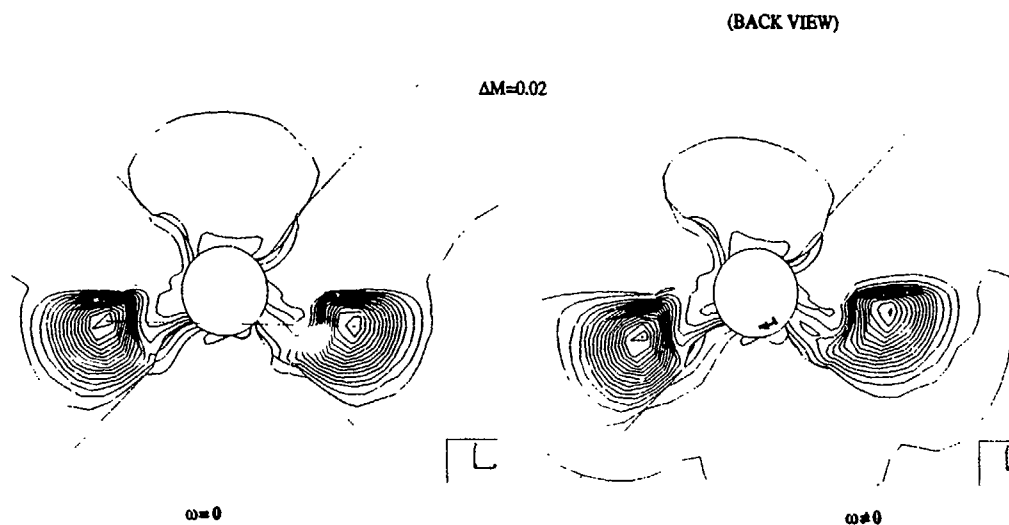
ANTITANK MISSILE:
MACH NUMBER CONTOURS IN A CROSS PLANE
(EULER CALCULATIONS)

Fig. 8

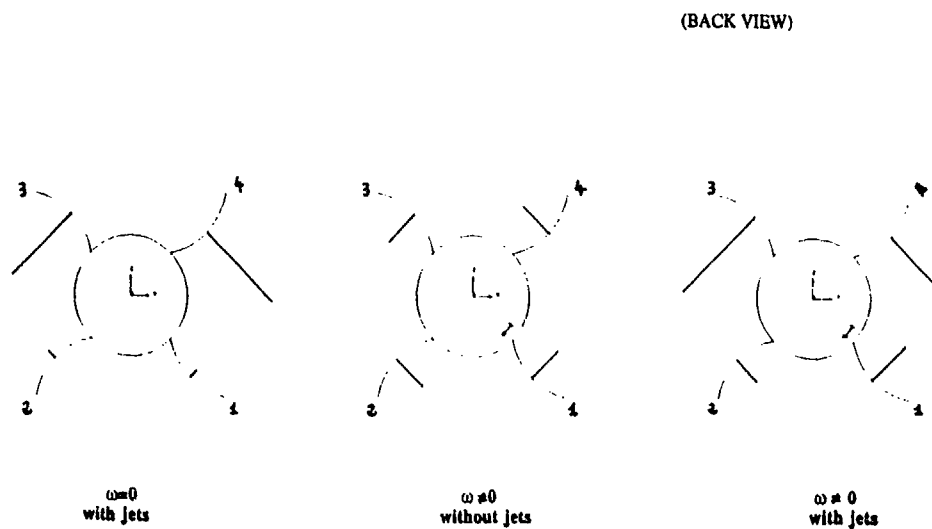
ANTITANK MISSILE:
NORMAL FORCE COEFFICIENTS ON THE WINGS
(EULER CALCULATIONS)

Fig. 9

AERODYNAMIC CONFIGURATIONS

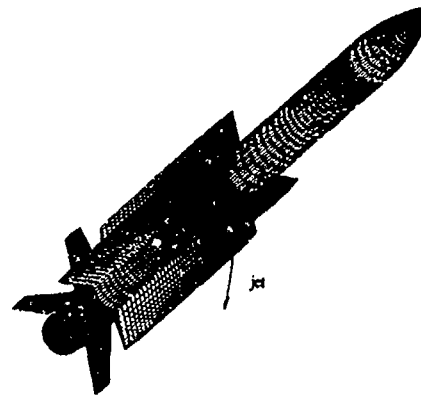
Upstream Conditions

$$M_0=1.6, \alpha=8^\circ$$

- without jet
- with a cold air jet
- with a hot air jet
- with a powder gas jet modelised as a perfect gas

MESH

Surface Mesh for Computations

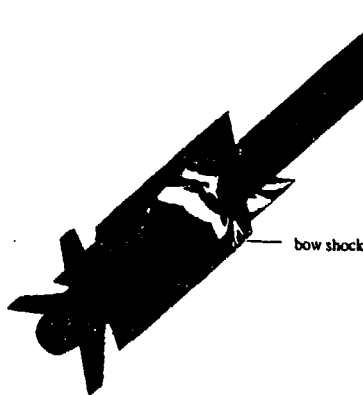


400000 mesh points (8 domains)

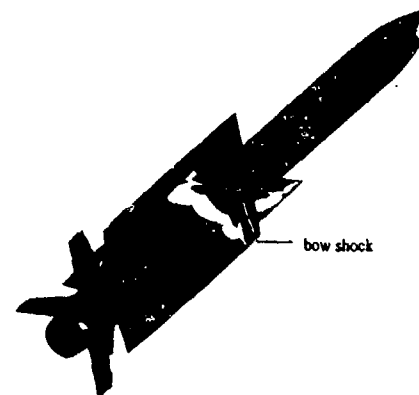
ASTER MISSILE
AERODYNAMIC CONFIGURATIONS AND MESH

Fig. 10

COLD AIR JET



POWDER GAS JET MODELISED AS A PERFECT GAS



ASTER MISSILE
COMPUTED WALL PRESSURE DISTRIBUTION
($M_0=1.6, \alpha=8^\circ$)

Fig. 11

PRECISION

	Without Jet	Cold Air Jet	Powder Gas Jet
$\Delta C_N / C_N$	5%	7%	7%
$\Delta Z_{cp} / D$	0.22	0.51	0.13

REPARTITION OF (JET) POWDER GAS EFFECTS VS (JET) COLD AIR EFFECTS

	Stagnation Temperature Effect	Species Effect
C_N	51%	49%
Z_{cp}	44%	56%

$$(\text{JET}) \text{ POWDER GAS EFFECTS} = (\text{JET}) \text{ STAGNATION TEMPERATURE EFFECT} + (\text{JET}) \text{ SPECIES EFFECT}$$

ASTER MISSILE
COMPUTED AERODYNAMIC COEFFICIENTS COMPARED WITH EXPERIMENTS
($M_0=1.6, \alpha=8^\circ$)

Fig. 12

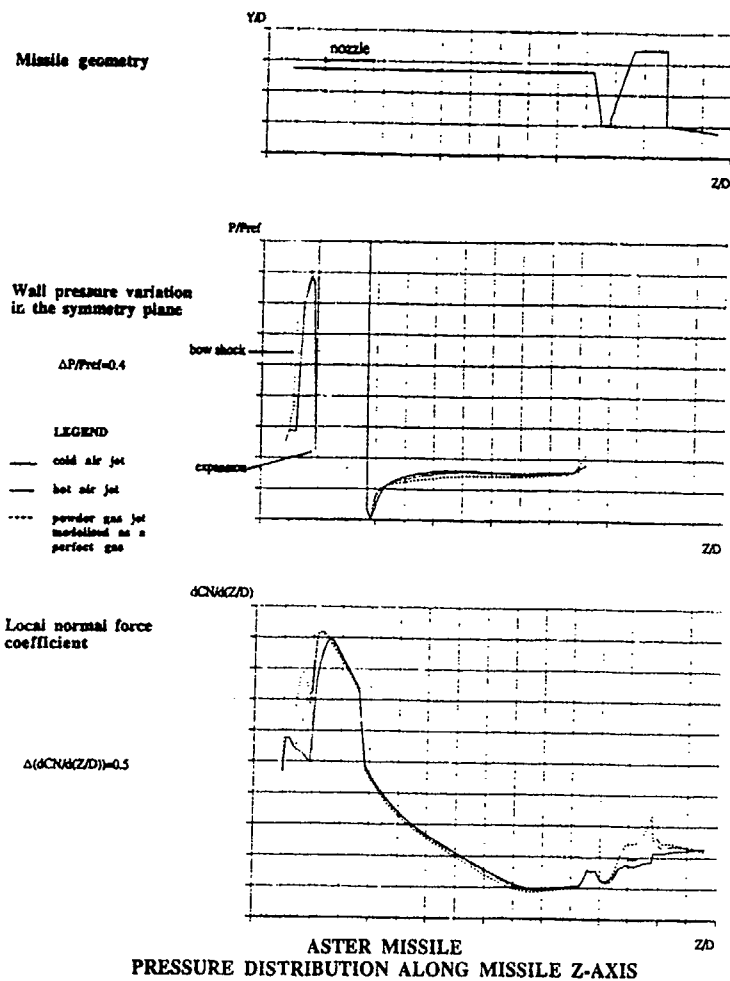


Fig. 13

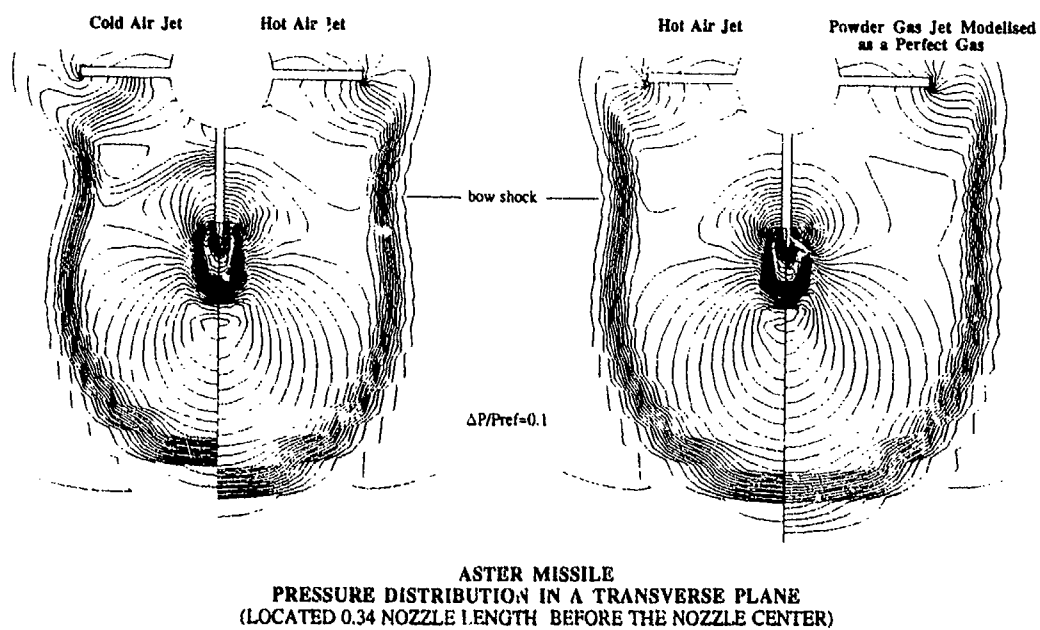
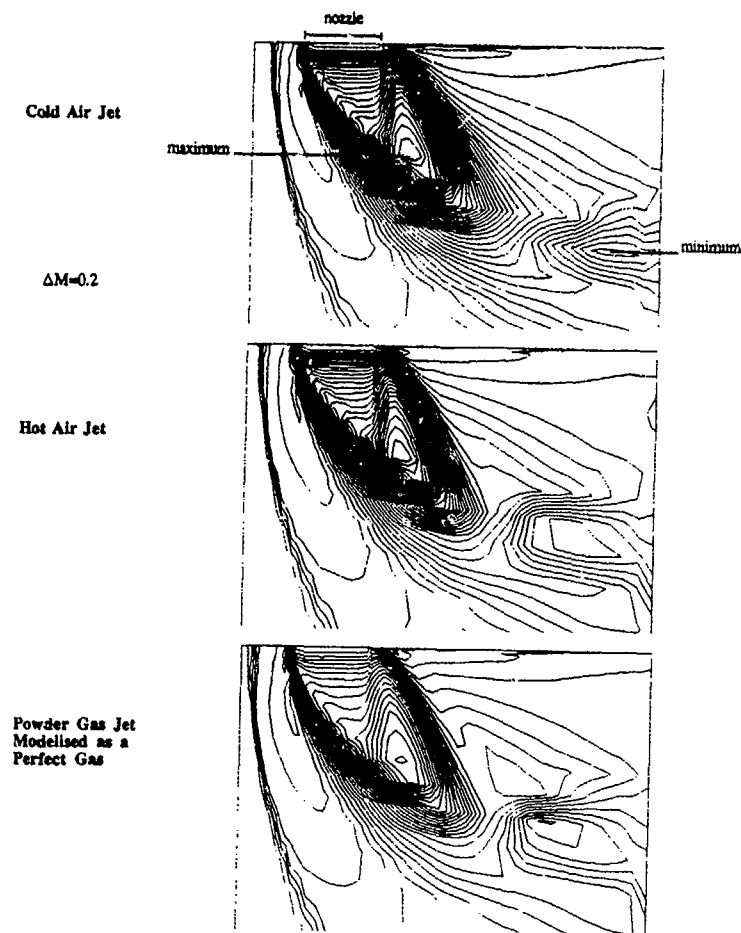


Fig. 14



ASTER MISSILE
MACH NUMBER DISTRIBUTION IN THE SYMMETRY PLANE

Fig. 15

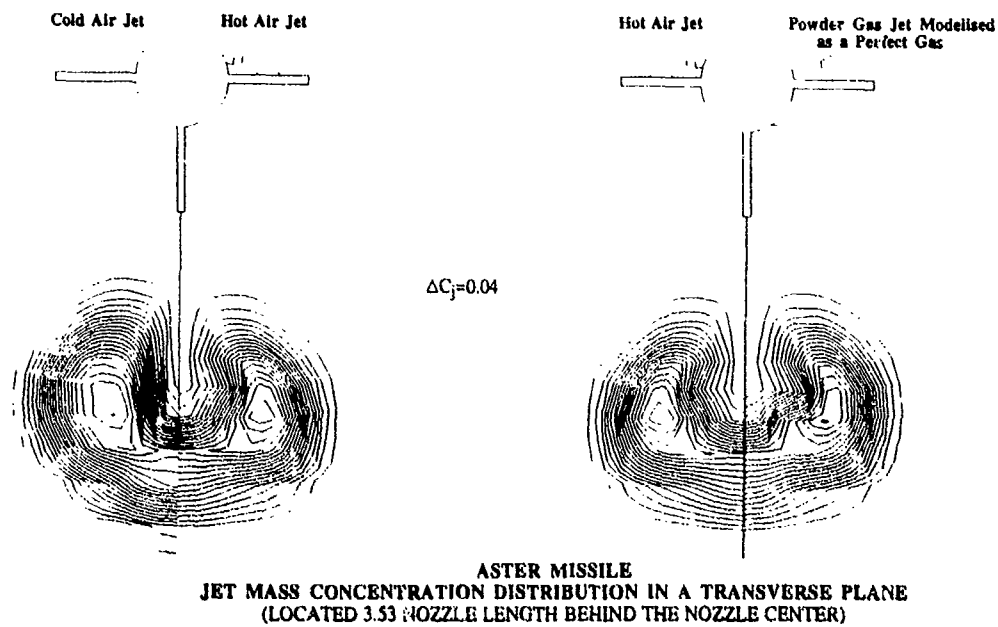


Fig. 16

FIRST EXPERIMENTAL ASSESSMENT OF RCS PLUME - FLOW FIELD INTERACTION ON HERMES LEADING EDGE THRUSTER CONFIGURATION

Th. Pörtner

DLR Institute for Experimental Fluid Mechanics
Bunsenstrasse 10, D-3400 Göttingen, Germany

1)

SUMMARY

Glow discharge flow visualization experiments are demonstrated which have been performed to enable a first assessment of the HERMES 1.0 leading edge thruster configuration concerning interference between the thruster plumes of the reaction control system (RCS) and the surrounding flow field.

The results of the flow visualization tests are presented in exemplary selected photographs. Additional Pitot pressure measurements support assumptions concerning interference induced pressure changes that may result from the observed significant flow field disturbances.

LIST OF SYMBOLS

A	area
C_D	nozzle discharge coefficient
d	diameter
l	length
M	Mach number
S_{ref}	reference area (wing area)
α_1	plume initial turning angle
γ	specific heat ratio
Φ	Momentum
Θ_{lim}	plume limit angle
Θ_N	nozzle lip angle

Subscripts

0	stagnation condition
1	windtunnel freestream condition
j	nozzle exit condition
$*$	nozzle throat values
N	nozzle
∞	free stream

¹⁾ This work is performed under CNES contract to DLR

1. INTRODUCTION

During the initial phase of reentry the control over a winged vehicle is to be achieved by the reaction control system (RCS). The efficiency of the involved control thrusters generally is adversely affected by interactions between the thruster plumes and the local flow field around the vehicle. As interaction effects are critical to safety and performance, it is necessary to achieve reliable prediction of the actual efficiency of a planned RCS configuration.

Before the tests that are reported in this paper available information on RCS interference showed the severity of the problem but it was restricted to the rear mounted RCS configuration of the US Shuttle. Quantitative interference results for the Shuttle cannot be transferred to HERMES due to the configurational differences. A theoretical analysis of the problem is defied by the complexity of the flow field, computational tools were not appropriate either, and so any statements on the RCS efficiency for HERMES were pure speculation. Consequently, the problem of RCS interference had to be accessed by experimental methods.

As a first step in the experimental approach flow visualization tests were performed on the 1991 RCS configuration. The simulation of the interference flow field was based on the scaling methods approved in the extensive NASA experiments concerning the Shuttle RCS.

In addition, exploratory Pitot pressure measurements were performed in proximity to the model surface which underline the visualization results by more quantitative information on the severity of the interaction. [1]

2. FLOW VISUALIZATION EXPERIMENTS

The glow discharge tests were performed in the V2G hypersonic vacuum tunnel with two main intentions:

- i) to show in what way the original shock system is changed by RCS thruster plumes, and,
- ii) to give first information on the severity of the interaction of a leading edge mounted thruster configuration.

It was decided to use a 1/90 scale plastic model of the HERMES 1.0 shape after preparatory experiments had secured that tunnel blockage in V2G can be excluded

for a model of that size. (Model length was $l = 162$ mm.)

2.1 General Simulation Aspects

External Flow Simulation

The operational altitude range of HERMES RCS is planned for initial reentry from 120 km down to at least 75 km altitude. The Mach number during this phase ranges from 20 to 27, and the Reynolds number based on the nominal vehicle length (15.5m) is 130 to 346000. The ambient pressure starts with 0.003 Pa in 120 km and ends up with 2.61 Pa in 75 km.

So the requirements for a free stream simulation of the entire operational range of the RCS system exceeds the capabilities of available windtunnels. However, as shown in [2] the main requirements for RCS simulation purposes can be sufficiently met in hypersonic vacuum tunnels.

The V2G tunnel provides high Mach numbers about $M=20$ to $M=22$, and a low static pressure level whereas Reynolds number duplication is possible only for a narrow altitude range about 92 km. The Reynolds number was about $Re = 30000$.)

During the present test program the usual stagnation chamber heating of the tunnel test gas was inhibited to avoid melting of the plastic model. So the external flow had intentionally to be replaced by a condensed flow which demanded some additional considerations on condensation effects.

Condensation Effects

The condensation of the tunnel flow reduces the Mach number and the Pitot pressure at the same time whereas the static pressure is increased. Isentropic expansion relations are not applicable to this flow. However, the product of static pressure and the square of the Mach number, which means the product of density and the square of the velocity, is not significantly changed by condensation. This means that the governing simulation parameter for RCS simulation, the momentum flux parameter (s.below), is also not seriously influenced by condensation.

So as the net effect of condensation on the simulation parameter is small, the simulation of the RCS interaction was carried out with the nominal free stream values for uncondensated flow.

For condensated flow preparatory visualization tests exhibited a slight outward displacement of the shock system. The shock patterns in principle remain unchanged but without condensation the lines would be slightly (about 10%) closer to the vehicle.

2.2 RCS Simulation

During the preparations for the tests the ERNO 400 N engine was replaced by a 600 N thruster from SEP. As no detailed information on this control thruster was available at that time the simulation design was based on the 400 N engine data. The higher thrust was accounted for by increasing the stagnation pressure of

the ERNO engine by a factor of 1.5, leaving all other data unchanged. In the model conical cold gas driven nozzles are integrated which are designed for Helium operation.

The simulation is based on the effective momentum flux ratio that is recommended by extensive NASA investigations, [3], and which is agreed upon as the best available scaling law for RCS simulation operations:

The effective momentum ratio is:

$$\frac{\Phi_j}{\Phi_\infty} = \frac{\gamma_j C_D P_j M_j^2 A_j}{\gamma_\infty P_\infty M_\infty^2 S_{ref}}$$

By the ambient pressure p_∞ this parameter is related to the entry trajectory. So each set of tunnel flow and model nozzle conditions refers to a special entry trajectory point.

The plume shape has been approximately matched with the empirical Latvala method [4]. According to this method the plume shape is defined by a circular arc of radius RPL and the initial turning angle of the plume boundary at the nozzle lip, α_1 . For Mach numbers above five the plume shape radius is mainly determined by the actual nozzle size. The initial turning angle can be adjusted approximately by the nozzle lip angle.

The following nozzle was used in the experiment:

nominal Mach number $M_{Exit} = 6.9$

$d^* = 0.60$ mm

$d_{Exit} = 2.89$ mm

$\Theta_N = 20.00^\circ$

$l_N = 3.146$ mm

This geometry was assumed the best compromise for the simulation of a wide range of reentry altitudes on one hand and workshop possibilities on the other hand. The nozzle exit diameter is only 6.16 % overscaled, the plume shape radius is 15 % smaller than scale, and the initial turning angle is slightly smaller than original: -0.12° for 100 km, and -6° for 74 km. So these values are close to scale requirements for all altitudes.

The nozzle discharge coefficient C_D in the momentum flux parameter is defined as the ratio of actual to theoretical thrust. It primarily applies to the stagnation pressure as it is assumed that the principle reason for the difference between a real nozzle and its theoretical performance is due to a loss in total pressure. That means all nozzle values can be calculated isentropically on the base of the corrected total pressure.

For practical reasons in the present tests the discharge coefficient was replaced by the ratio of actual to theoretical mass flow. This ratio was determined experimentally to a value of 91 %.

2.3 Technical Simulation Aspects

2.3.1 Model Technique

Fig.1 shows the positions of the RCS nozzles on the model. Although the original configuration has two thrusters each for yaw and pitch control the model is

equipped with only one yaw nozzle and one pitch/roll nozzle on the left side because during reentry simultaneous operation of two thrusters of a group is not planned. (At least this was the case at the time of the experiments.) As the front nozzle of each group has a greater effect on interaction it was decided to represent each nozzle group by its front nozzle.

In the model the two nozzles can be operated independent from one another but simulation of roll/yaw combined control is restricted to cases in which both thrusters have the same stagnation pressure.

Prints 1 to 3 show the construction process from the interior equipment to the final shape of the model. It is an important feature that all parts under supply pressure (up to 15 bar) are fabricated of metal, so that sealing problems arising from the plastic material of the outer model are avoided already by the design. During the experiment the model was highly stressed by temperature changes which led to a crack that separated the vehicle in the middle between nose and body flap. So the separation of the gas supply from the plastic fuselage secured the experiment.

Print 1 shows the two stagnation chambers of the nozzles which are arranged parallel to the longitudinal axis. They have an interior diameter of 6 mm (10 nozzle throat diameters) and are equipped with a pressure measurement tube, a gas supply tube and a thermocouple each. The tubes and the thermocouple wires are conducted through a stiff outer tube that extends out of the model base for sting mounting. The round metal plate at the base is the pole of the HF generator for the glow discharge of the flow field, whereas the metal star at the front end of the sting tube aids in fixing the whole construction group in the foundry form.

As the next step the front part of the model was casted into the form and cut off somewhat aft of the nozzle positions. Holes were drilled into this front part, aligned parallel to the longitudinal axis to serve as bearings for the metal stagnation chambers. These holes have to be positioned with high precision because the nozzle cones later are drilled into the casted model from outside, and it has to be sure that the throat diameter section of the nozzle is sufficiently short (0.2 mm are realized).

In print 2 the assembly of nose part and interior parts is shown. This assembly then is screwed into the foundry form to guarantee an exact position of the functional elements when casting the rest of the vehicle. In print 3 the final shape of the model after casting and nose finishing is to be seen. At last the nozzles are drilled into the exact positions and the model is sprayed with a conductive coating that is required for the HF glow discharge.

2.3.2 Experimental Setup

Print 4 shows the V2G tunnel with the model integrated into the test section. The vehicle is mounted onto a rear sting that is cranked in a way that the model center of projected area is located on the tunnel axis independent from roll angles. The supply tubes are conducted close to the lee side of the sting which itself is mounted onto an injection support which also allows electric angle of attack adjustment. The sting is also the phase pole of the HF generator, and it is insulated carefully

against the tunnel. For reasons of insulation half a meter of the metal supply tubes is replaced by thermoplastic tubes. The high quality of the glow discharge which is reached in this experiment is the result of proper adjustment concerning the HF equipment.

The nozzle stagnation pressure was controlled by an analogue pressure gauge that was linked directly to the stagnation chamber.

The camera was mounted on a massive tripod about half a meter from the model, equipped with a macro-objective of 55 mm focal length and a minimum diaphragm aperture of $f/32$.

2.4 Variation of Parameters

During the experiment the reentry attitude was not simulated directly. Instead, the stagnation pressure is varied from 15 bar via 10, 5, and 2 bar down to 1 bar. Tunnel stagnation pressures have been varied between 10 bar and 60 bar. The corresponding reentry altitudes then have been determined by calculation.

For each tunnel stagnation pressure single operation of the yaw nozzle, of the pitch/roll nozzle, and simultaneous operation of both nozzles at the same nozzle stagnation pressure have been visualized and photographed through the side window as well as through the top window of the test section.

The angle of attack was adjusted to $\alpha = 40^\circ$ and $\alpha = 30^\circ$, sideslip angles have been $\beta = 0^\circ$ and $\beta = 6^\circ$. In total a number of more than 300 photographs have been taken, including exposure variations.

2.4.1 Exemplary Photographs

From a number of 72 photographs in the original report a series of 12 pictures was selected as an absolute minimum for reproduction in this paper. These photographs show the RCS induced disturbances of the flow field and they should be sufficient to indicate the influence of altitude and sideslip angle. For one altitude, $H = 95.7$ km, an entire set of photographs concerning different RCS operation (yaw alone, pitch/roll alone, both simultaneously) is included. In this series, prints 7 to 12, the sideslip angle is $\beta = 6^\circ$, because the shock structure is more distinct with a sideslip angle.

Cases without sideslip angle (print 13 and 14) and an example for a lower altitude, $H = 86.9$ km, (print 15 and 16) are represented only by photos showing simultaneous operation of both nozzles. The shock system without RCS operation is shown as a reference case in prints 5 and 6.

Summarized Observations

An analysis of the flow visualization photographs (of the entire series) results in the following main observations.

An intersection between bow shock and plume shock occurs in all tested altitudes. In higher altitudes the bow shock of the vehicle vanishes downstream of the intersection point leaving an area of increased pressure, which can be concluded from the stronger light emis-

sion of the glow discharge in these regions. In the lower altitudes the plumes are much smaller and the plume shock is earlier deflected into the direction of the main flow. The original bow shock of the vehicle continues behind the intersection with the plume shock.

Especially for higher altitudes the top view pictures show that the yaw plume displaces the bow shock outward which indicates an upstream pressure increase on the fuselage in the sense of classical jet interaction.

The prints which show operation of both nozzles exhibit plume - plume interaction when they are compared to the prints with only one jet operating.

The sideslip angle increases the interaction of the plumes with the local flowfield. The pressure increase that is expected downstream of the shock intersection seems to be increased by the sideslip angle. It is not clear how strong the expected pressure increase will be for the winglet. Remember that the condensation widens the shock system so that (for sideslip angles) it is not sure whether the pressure increase region impacts more on the inner or more on the outer winglet surface. In cases without sideslip angle a direct impact of shocks on the winglet can be excluded.

A smaller angle of attack effects a stronger plume deflection and thus stronger pressure increments downstream of the jets. (No illustrating photographs in this paper)

Before the tests it was considered that upward firing of the pitch thruster could possibly widen the whole shock system of the vehicle which then would have effected a severe pressure increase on the windward side, counteracting the thrust moment. The tests proved that such a global displacement of the bow shock can be excluded.

3. EXPLORATION OF RCS INDUCED PRESSURE CHANGES

The glow discharge photographs demonstrated the disturbance of the flow field by the RCS plumes but the possibilities for an estimation of the actual changes of the surface pressure distribution based only on flow visualization are rather poor.

So it was decided during the experiment to perform at least exploratory pressure tests to obtain information on the change of the pressure level due to RCS interaction.

3.1 Pitot Pressure Measurements

To arrive at detailed information on the surface pressure distribution of course a model is necessary that is equipped with a sufficiently high number of static pres-

sure orifices. Such a model was not subject to the contract under which this work was performed and so Pitot pressure measurements were performed in proximity to the model surface instead.

Although the Pitot pressure cannot be directly converted into static pressure it is at least related to static pressure. The Pitot pressure is a function of $1/M^5$, whereas the static pressure is a function of $1/M^7$. Consequently, an increase of Pitot pressure that is effected by an interaction between plume flow and external flow indicates that there is also an increase in static pressure.

The Pitot probe was adjusted in 6 leeward and in 6 windward positions, aligned parallel to the longitudinal axis of the model.

Pressure Results

The tests exhibited most significant changes in pressure level on the leeward side. The highest increase was + 486 % for an altitude of 99 km on the upper wing near the pitch nozzle. On the outward surface of the winglet an increase of + 26 % for the same altitude was indicated. Moreover, a strong interaction between yaw and pitch/roll thruster plumes on the leeside.

Generally, the yaw interaction is stronger than the pitch/roll interaction. In all cases the interaction decreased with falling altitude, which is in agreement with the corner flow experiments of Allegre at SESSIA, and, which is in contradiction to Monte Carlo calculations of Aerospatiale.

The pressure results for the windward side show less interaction effects but here more refined methods of measurement are required.

This exploratory test showed that interference induced disturbance moments are very likely. The results confirm the conclusions drawn from the visualization tests. Further investigations require more detailed static pressure measurements.

4. CONCLUSIONS

The glow discharge flow visualization photographs demonstrate the significance of the RCS / external flow field interaction and show that disturbance moments are very likely. The exploratory Pitot pressure tests confirm the assumptions concerning interference induced moments by more quantitative results.

The experiments clearly show that RCS interference remains a subject to further investigations. The next step in the experimental approach is to build a new HERMES model with updated thruster configuration and with a number of static pressure orifices in selected surface locations ²⁾

²⁾ Presently, experiments with such a model are under progress in the V2G tunnel under Technical Assistance contract to CNES.

5. REFERENCES

1. Pörtner, Th., Boettcher, R.-D. "RCS/External Flow Field Interference - Flow Visualization Experiments", DLR-IB 222-92 A17, also as HERMES Technical Assistance Document H-NT-0-2042-DLR, Aug. 1992.
2. Pörtner, Th. "RCS/External Flow Field Interference", DLR-IB 222-91 A14, also as HERMES Technical Assistance Document H-NT-0-2026-DLR, April 1991.
3. Rausch, J.R. "Space Shuttle Orbiter Rear Mounted Reaction Control System Jet Interaction Study, Final Report", NASA CR-151481, May 1977, DLR-IB 222-91 A14, also as HERMES Technical Assistance Document H-NT-0-2026-DLR, April 1991.
4. Latvala, E.K. "Spreading of Rocket Exhaust Jets At High Altitudes", AEDC TR-59-11, June 1959.

FIGURES AND PHOTOGRAPHS

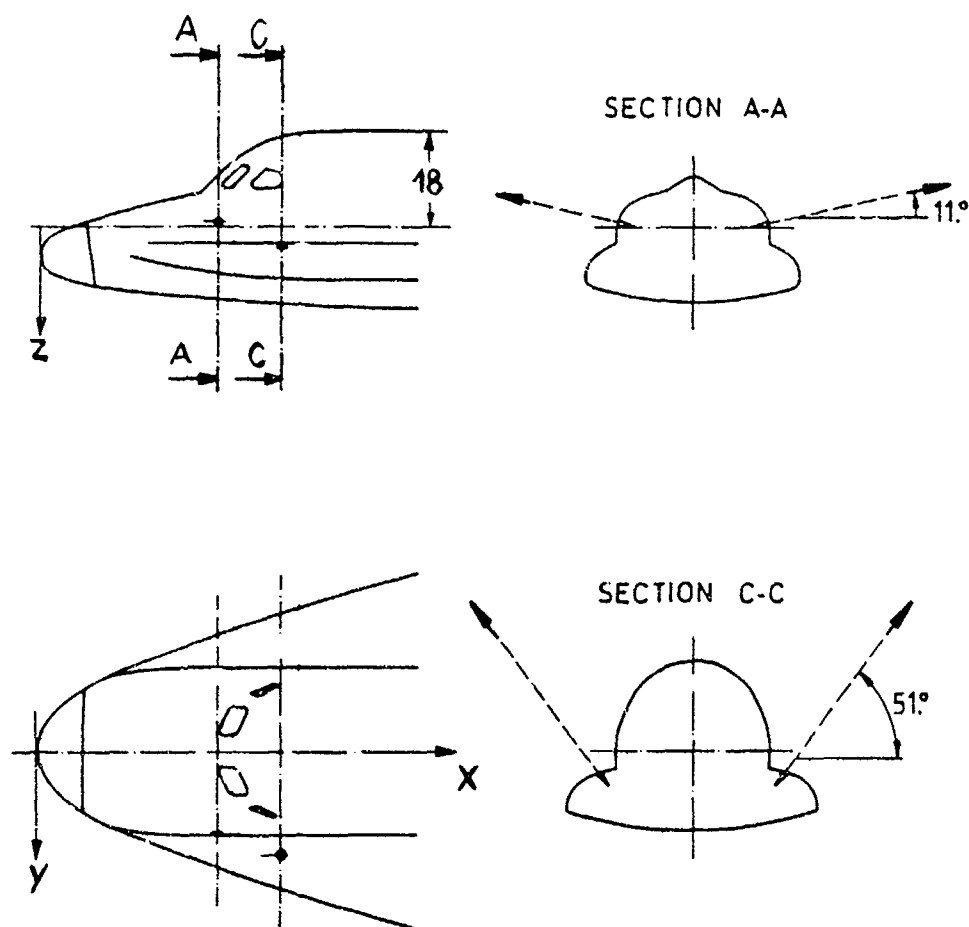
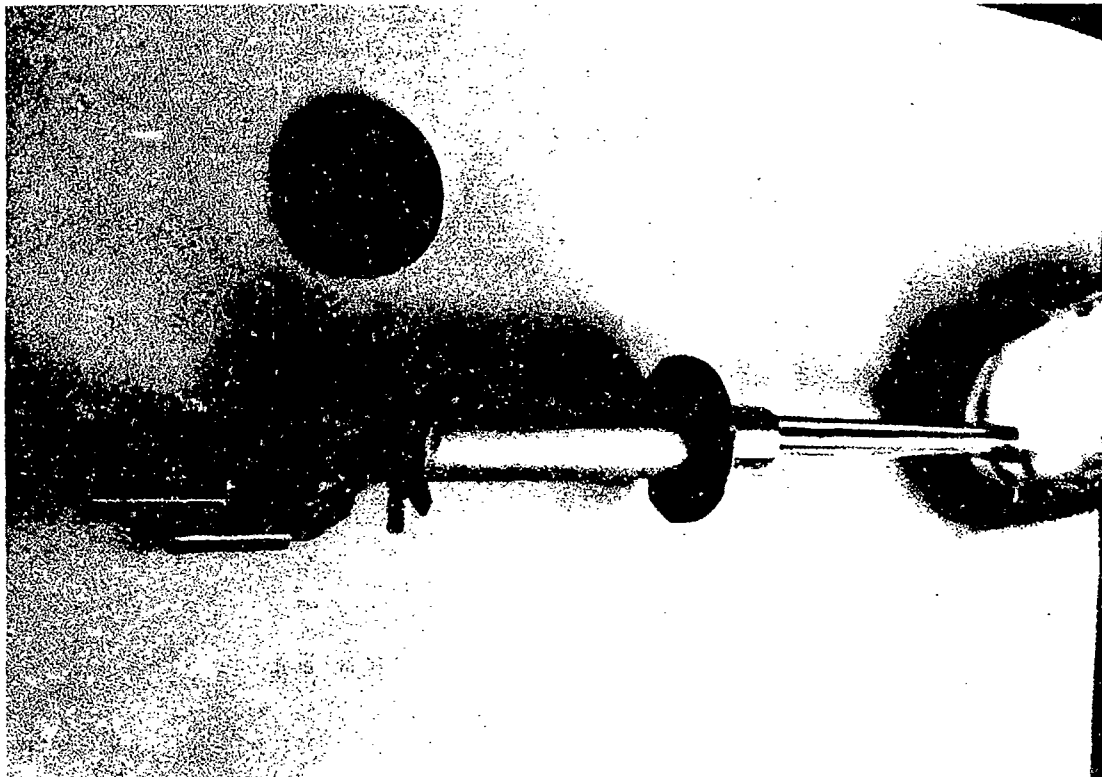
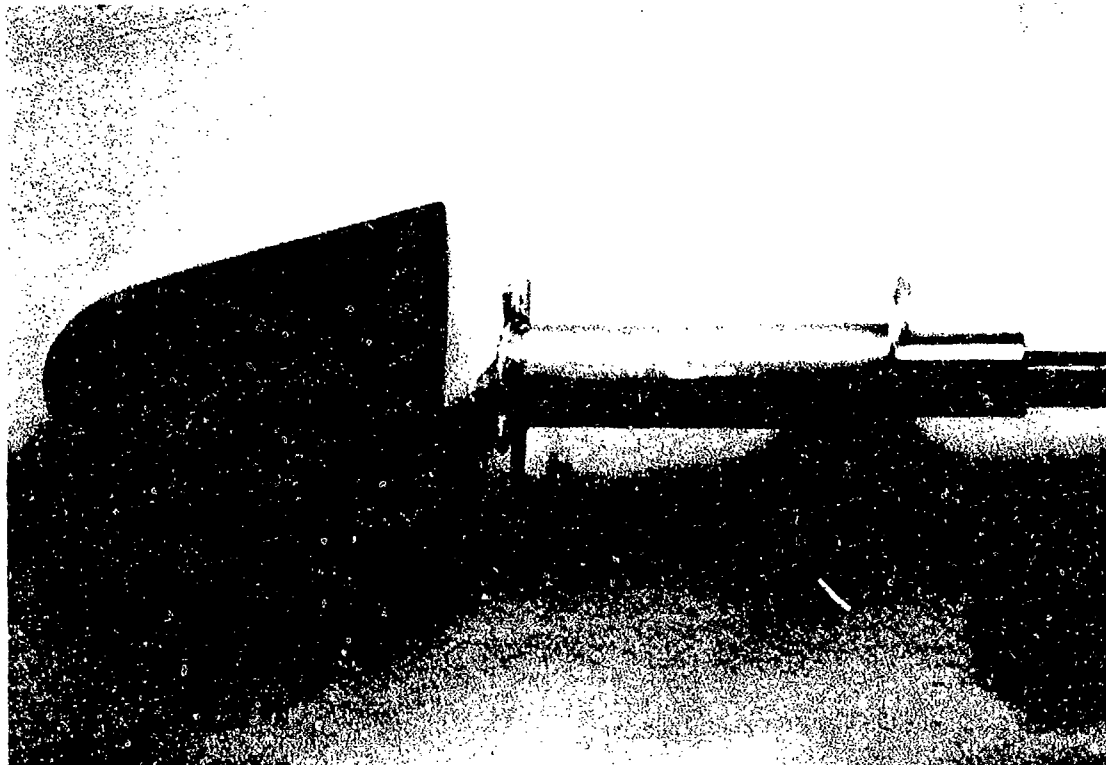


Fig.1: HERMES 1.0, positions of RCS model nozzles (1991 configuration)



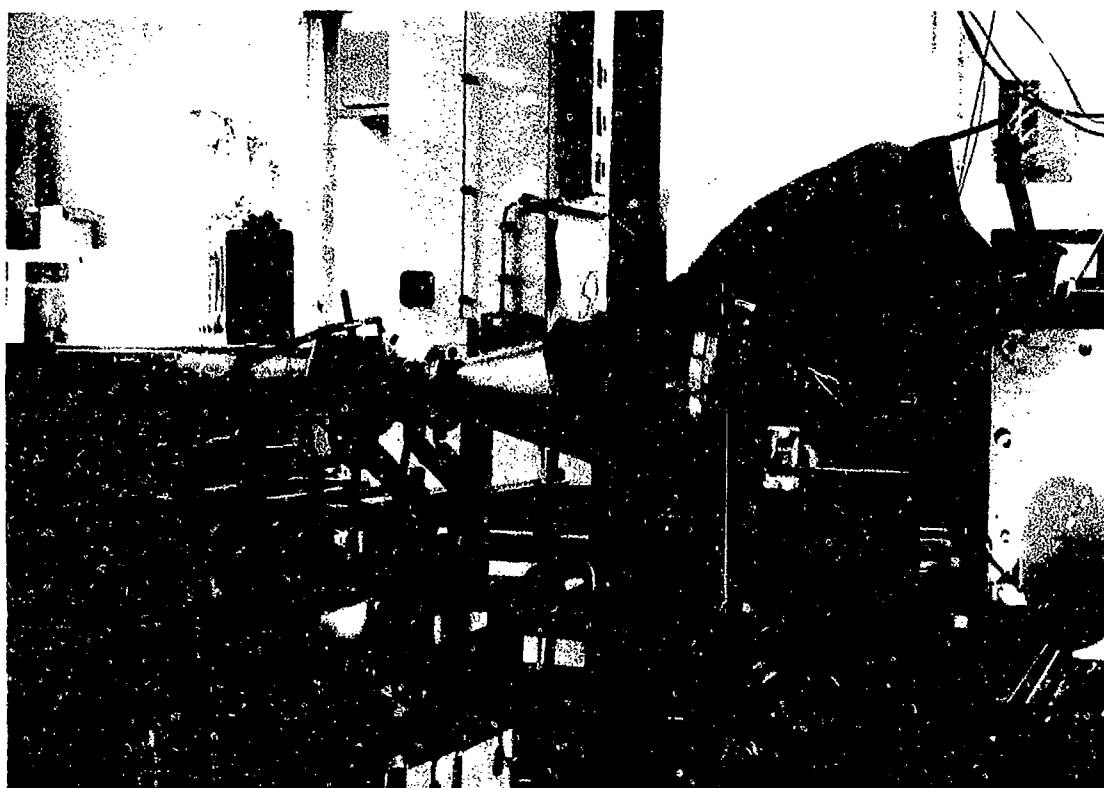
Print 1: Interior equipment of the HERMES RCS flow visualization model



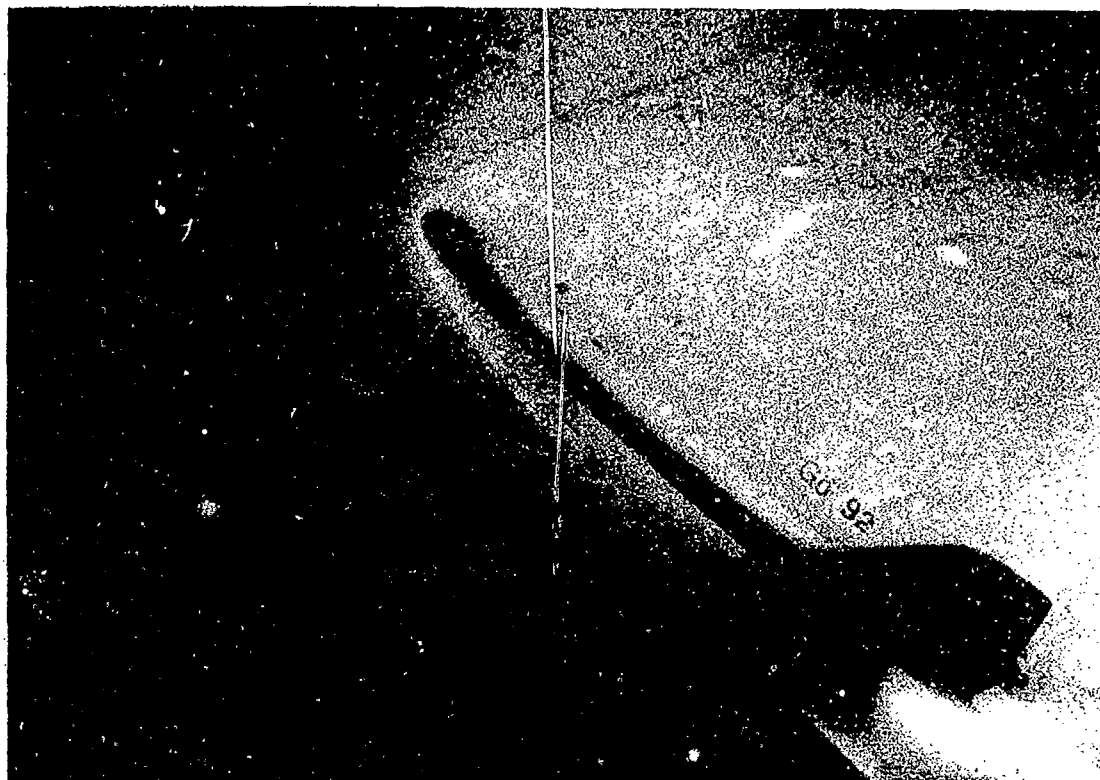
Print 2: Assembly of nose section and interior equipment



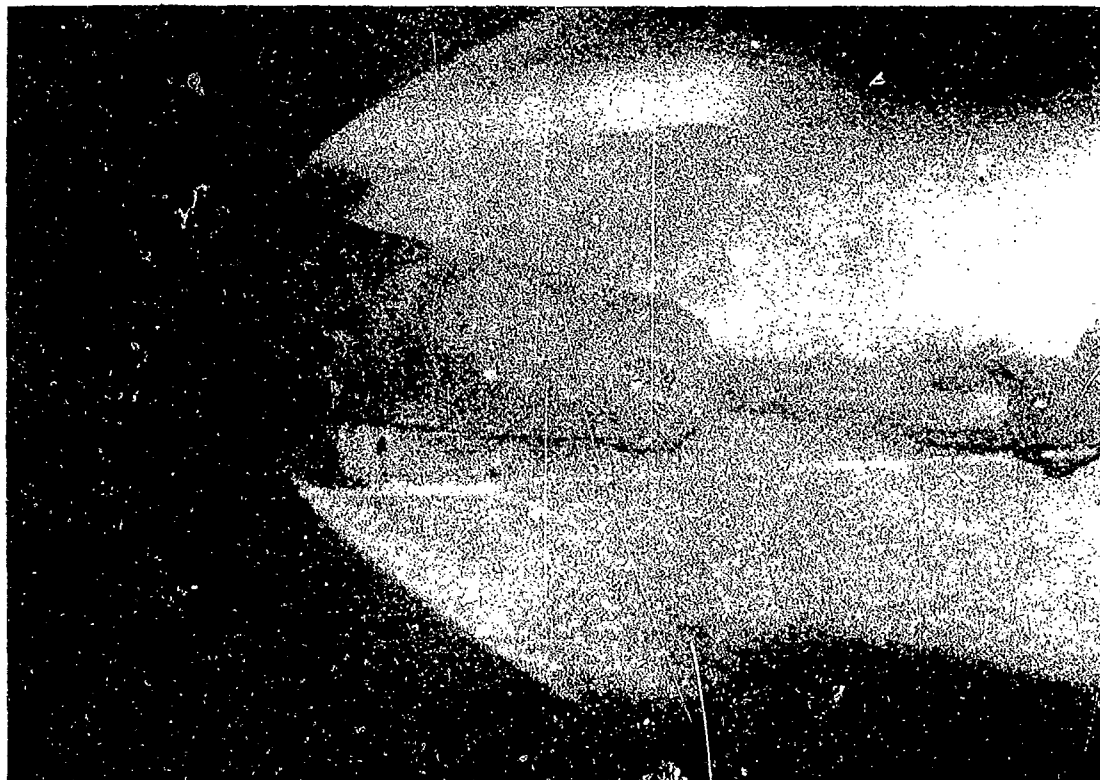
Print 3: Final assembly of model before conductive coating



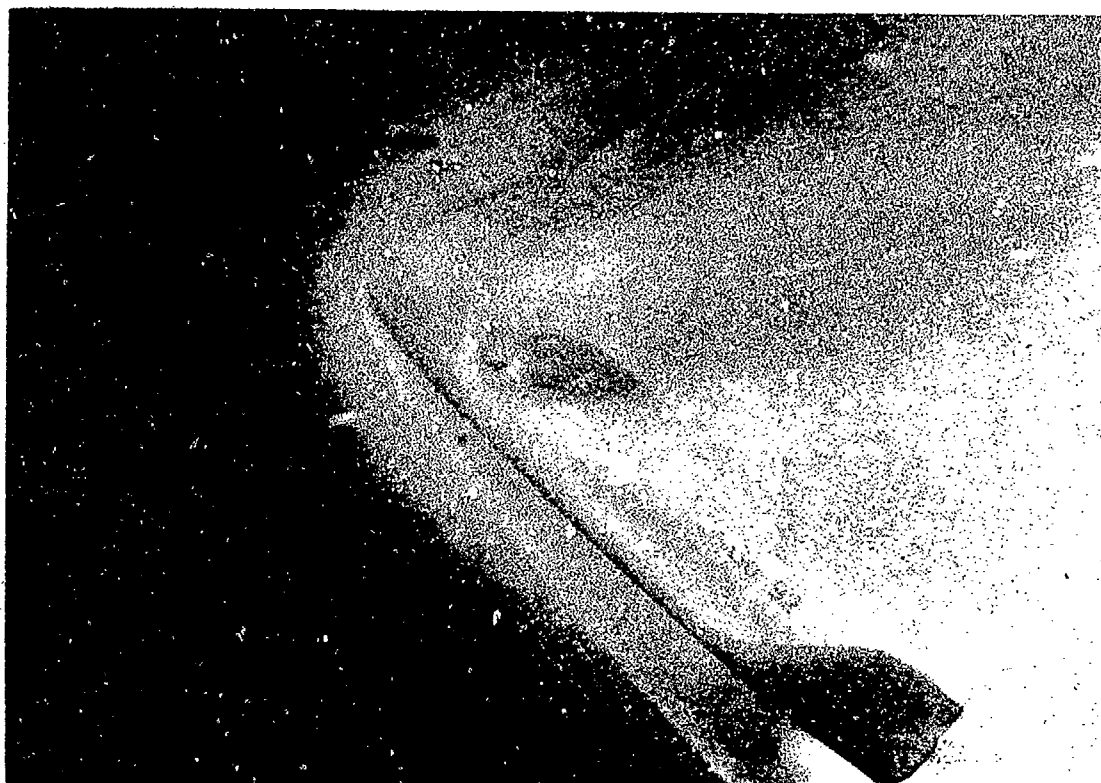
Print 4: Experimental setup



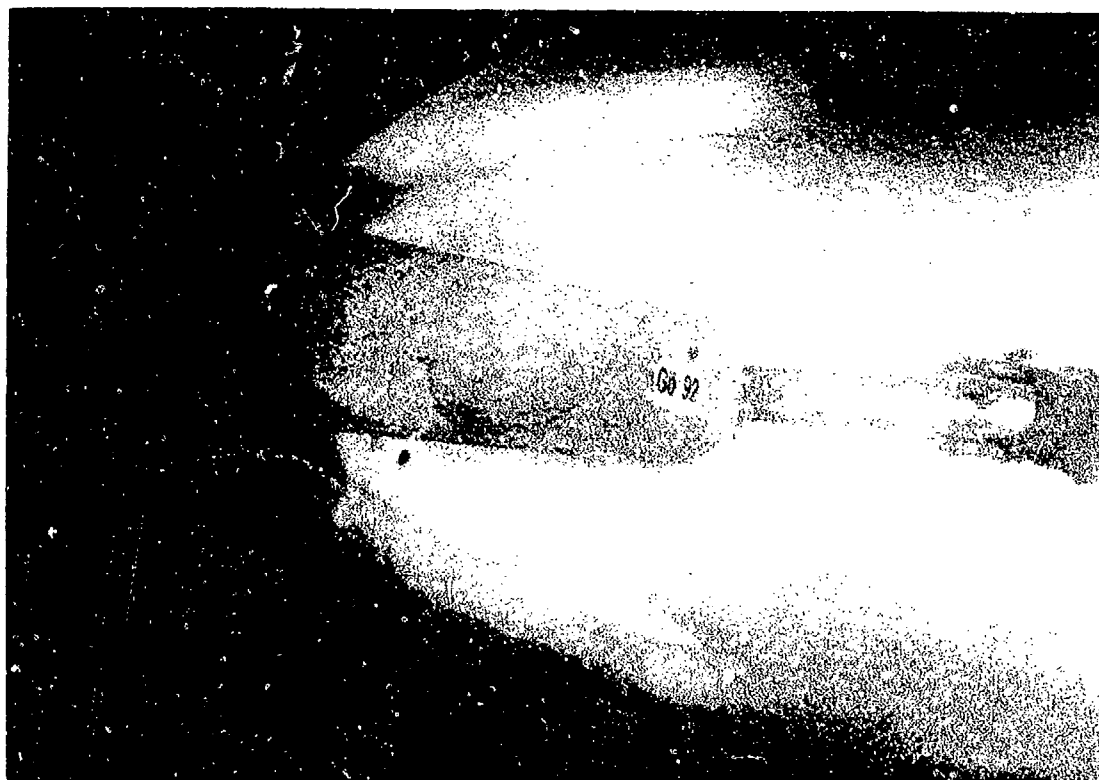
Print 5: $\alpha = 40^\circ$, $\beta = 6^\circ$, $P_{0j} = 25$ bar , side view, no RCS operation



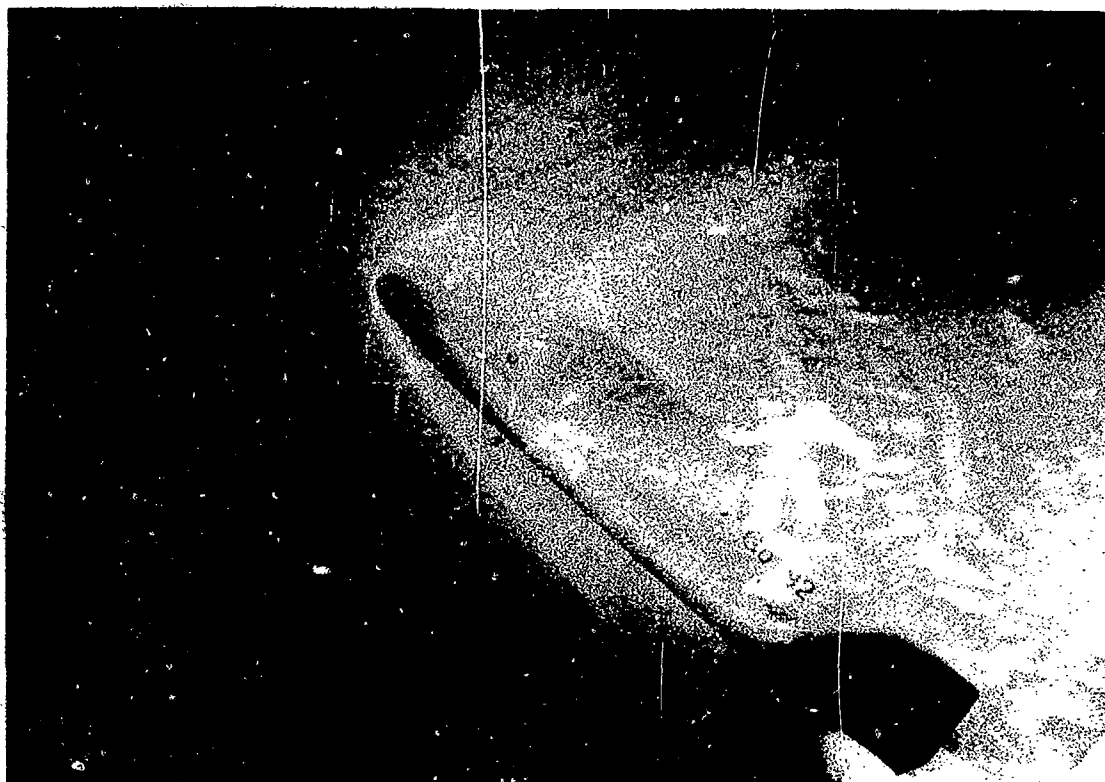
Print 6: $\alpha = 40^\circ$, $\beta = 0^\circ$, $P_{0j} = 10$ bar , top view, no RCS operation



Print 7: yaw nozzle, $\alpha = 40^\circ$, $\beta = 6^\circ$, $H = 95.7$ km, side view



Print 8: yaw nozzle, $\alpha = 40^\circ$, $\beta = 6^\circ$, $H = 95.7$ km, top view



Print 9: pitch nozzle, $\alpha = 40^\circ$, $\beta = 6^\circ$, $H = 95.7$ km, side view



Print 10: pitch nozzle, $\alpha = 40^\circ$, $\beta = 6^\circ$, $H = 95.7$ km, top view



Print 11: both nozzles, $\alpha = 40^\circ$, $\beta = 6^\circ$, $H = 95.7$ km, side view



Print 12: both nozzles, $\alpha = 40^\circ$, $\beta = 6^\circ$, $H = 95.7$ km, top view



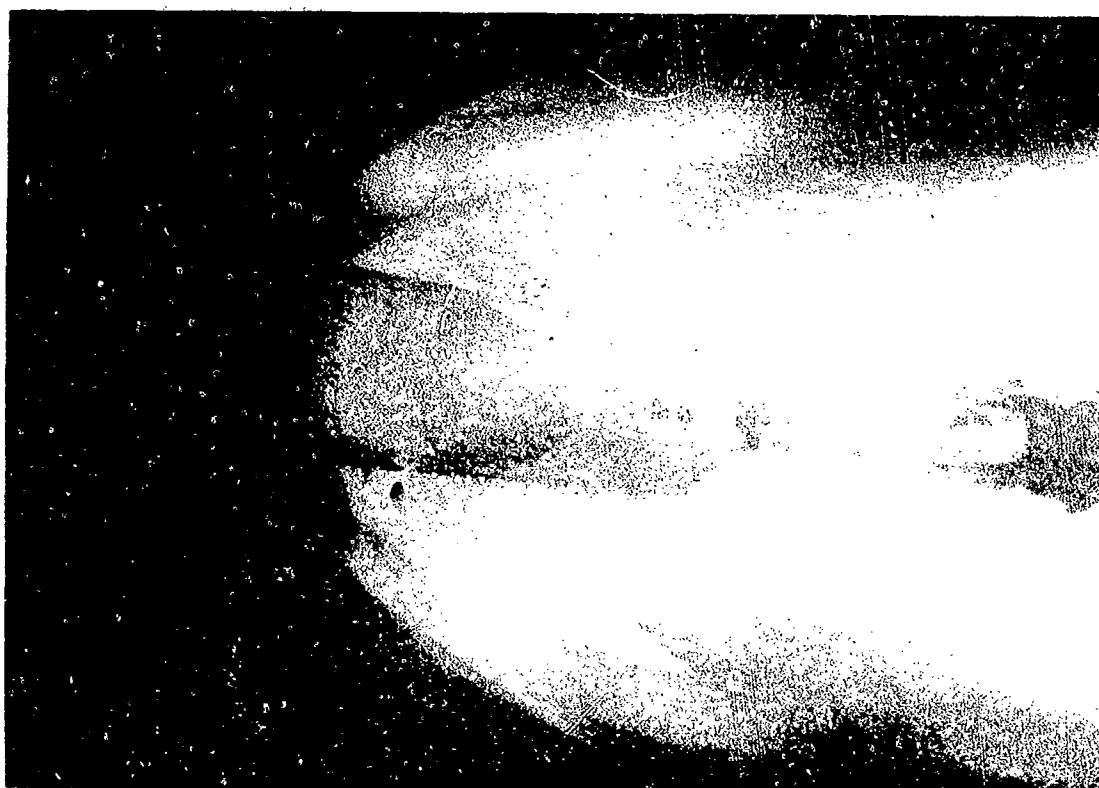
Print 13: both nozzles, $\alpha = 40^\circ$, $\beta = 0^\circ$, $H = 95.7$ km, side view



Print 14: both nozzles, $\alpha = 40^\circ$, $\beta = 0^\circ$, $H = 95.7$ km, top view



Print 15: both nozzles, $\alpha = 40^\circ$, $\beta = 6^\circ$, $H = 86.9$ km, side view



Print 16: both nozzles, $\alpha = 40^\circ$, $\beta = 6^\circ$, $H = 86.9$ km, top view

Numerical Simulation of a Powered-Lift Landing

Kalpana Chawla

MCAT Institute

M.S. 258-1, NASA Ames Research Center

and

William R. Van Dalsem

M.S. T045-2, NASA Ames Research Center

Moffett Field, California 94035-1000

U.S.A

1. SUMMARY

The flow field about a delta wing equipped with thrust reverser jets in slow speed flight near the ground has been computed. Results include the prediction of the flow about the delta wing at four fixed heights above the ground, and a simulated landing, in which the delta wing descends towards the ground. Comparison of computed and experimental lift coefficients indicates that the simulations can capture at least the qualitative trends in lift-loss encountered by thrust-vectoring aircraft operating in ground effect.

2. INTRODUCTION

Thrust vectoring can be used to improve short field, up-and-away, and post-stall maneuvering performance of high-performance aircraft. When vectored thrust is used to meet short runway requirements, as in the case of the Harrier AV-8B, a complex fluid dynamics interaction between the vectored jets, the ground, and the airframe is encountered. This flow field can put the aircraft at risk due to lift loss and hot-gas/debris ingestion. As a result of these risks, operational flexibility and performance may be reduced. Experiments performed by Paulson and Kemmerly¹ at NASA Langley's Vortex Research Facility (VRF) indicate that for a STOVL (Short Take-Off and Vertical Landing) configuration the magnitude of the loss in wing-borne lift is a strong function of its rate of descent. Although this phenomenon is not fully understood, it is known that during a landing with a rapid rate of descent, the lift loss is much less than in the case of a low (or zero) rate of descent. It is conjectured that at rapid rates of descent, insufficient time exists for the complete ground vortex structure to form under the aircraft. A computational study has been carried out to predict the lift-loss experienced by aircraft using thrust-vectoring in ground effect, and to understand the differences in flow physics in the straight-and-level flight and the

descent cases.

To understand the jet related flow physics of the suck-down phenomenon, Van Dalsem^{2,3} conducted a numerical study of the impingement of an unsteady three-dimensional jet on a ground plane, in cross-flow, by solution of the Reynolds-averaged Navier-Stokes equations. This work simulated the experimental work of Stewart, Kuhn and Walters.⁴ Insights into the impinging jet flow physics, for example, the sensitivity of ground vortex location to the level of mixing in the wall jet were obtained in this work.³ Also the computed ground vortex locations and the pressure coefficient distribution compared well with the experimental data. This effort quantified the ability of Computational Fluid Dynamics (CFD) to predict the strength and location of the primary features of the impinging jet flow-field.

To understand the suck-down effect, it was required to introduce an airframe in the above study, so that the interaction of the jets with the ground and the airframe could be studied. To concentrate resources on resolving the complex flow physics, flow was computed about a simple configuration consisting of a delta planform with two jets in ground effect (Refs. 5-7). The experimental work of Paulson and Kemmerly¹ had indicated that the flow about this configuration produces much the same flow physics as the flow about even a very complex and realistic configuration, such as an F-18 in ground effect. The non-time-accurate simulations of flow past the delta wing showed the capability to capture jet impingement/entrainment, ground vortex formation, and the ability to predict lift loss in ground proximity.⁵⁻⁷

In the present paper, time-accurate simulations of both straight-and-level and descending flight profiles are presented. Both the mean and unsteady characteristics of these flows are analyzed. Of particular interest is the flow unsteadiness due to apparent instabilities in the jet and ground vortex structures. Analysis of lift coefficient and pressure histories and extensive flow visualization are used to develop an understanding of the relationship between the observed

forces on the delta wing and the flow dynamics.

3. COMPUTATIONAL MODEL

The computational model consists of a 60° delta wing in a free-stream Mach number of 0.064 (70 ft/sec), and chord length (31 in.) based Reynolds number of 1.2 million, in ground effect. The wing is equipped with two choked thrust reverser jets (diameter 0.6 in.) exiting from jet pipes at an angle of 45° to the delta wing and at NPR (nozzle pressure ratio) of 1.8. These geometrical and flow conditions correspond to the conditions in the wind-tunnel and VRF experiments used for the validation of this study. The computational model duplicates the wind-tunnel conditions for straight-and-level flight (Fig. 1). In the wind-tunnel simulations of the straight-and-

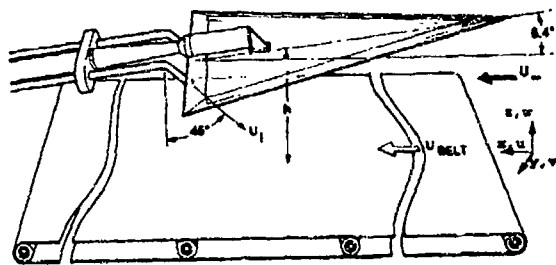


Fig. 1: The Wind-Tunnel setup.

level flight cases, the floor of the wind-tunnel is replaced by a moving belt to remove the boundary layer absent in flight tests. Identical procedure is followed in the computational model.

For the descent simulation there are some differences in the conditions between the computational model and the VRF experiment. In the VRF experiments, the delta wing is suspended from a cart that moves horizontally on rails, while the descent is simulated by the horizontal motion of the wing above a slanted ground board (Fig. 2). The VRF test sec-

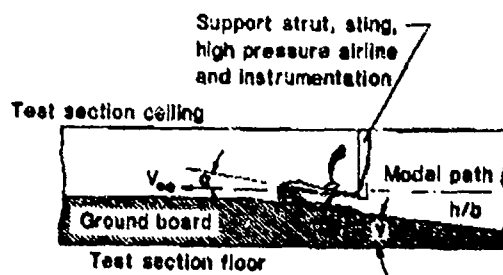


Fig. 2: The Vortex Research Facility setup.

tion is 150 ft. long. The ground board for the first 100 ft. of the test section is slanted upwards and the last 50 ft. is horizontal thus allowing simulation of descent followed by straight-and-level flight. In the computational model, the delta wing remains stationary and the free-stream moves over it, while the

descent is simulated by moving the ground upwards. The ground grid is moved up at the effective experimental descent rate of Mach no. 0.004475 (4.9 ft/sec). For the descent simulations, the descent is started at $h/b = 1.0$ as opposed to the experimental starting height of $h/b = 2.0$ (where h is the height of the delta wing measured at two-thirds of the chord above the ground, and b is the wing span) to lower computational expense. The experimental data shows small differences between descending and straight-and-level lift coefficients at $h/b = 1.0$, indicating that there should be little difference between the static and dynamic flow structures at this height. Therefore, the descending case can be initialized using the flow field for straight-and-level flight at $h/b = 1.0$ without introducing significant errors.

3.1 Grids

The accuracy of the simulation of a complex flow problem, such as under study here, depends strongly upon the choice of grids. The straight-and-level flight simulations were performed using grids that would be extendible to the descent case. Body-conforming grids were generated about the delta wing, the jet pipe, and the ground to resolve the boundary-layers, and an overset "jet" grid was used to resolve the jet (Figs. 3, 4, 5). The mated delta-wing, jet, and pipe grids overset a ground grid. The overset topol-

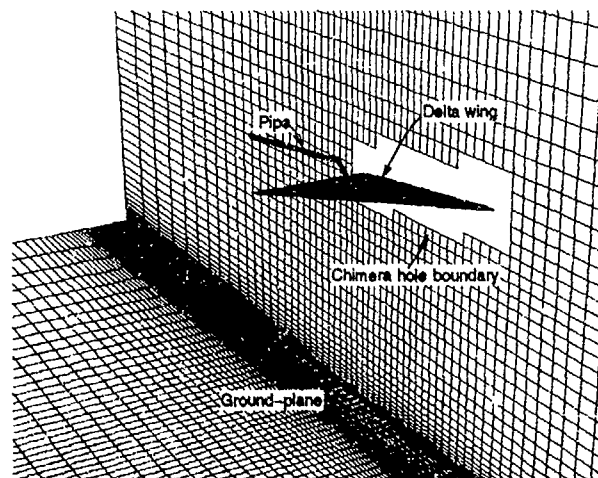


Fig. 3: The ground-plane grid.

ogy allows relative motion of component grids and thus efficiently manages grid points for moving-body simulations. It has been used in the past to simulate store separation⁸ and the separation of the Solid Rocket Boosters from the Shuttle/Main Tank assembly.⁹ Here, the descent is simulated by moving the ground grid in the upward direction. The data transfer between the grids is achieved using a new implementation¹⁰ of a grid communication scheme referred to as the Chimera scheme.¹¹ Using this scheme, solutions are computed independently on all the grids. Overset/overlapping grids feel the influence of other grids via hole and outer boundaries. Hole

boundaries are artificial boundaries in grids. The solution is ignored on all points within a hole boundary as this area/volume is either overset by a solid body (hole made by delta wing in the ground and the jet grids), or it is resolved by a finer grid (hole made by the jet grid in the ground grid). In the straight-and-level flight computations, the interpolation coefficients required for grid communication at the outer and the hole boundaries are computed just once. However, for the descent simulation they have to be recomputed periodically due to the relative motion of grids.

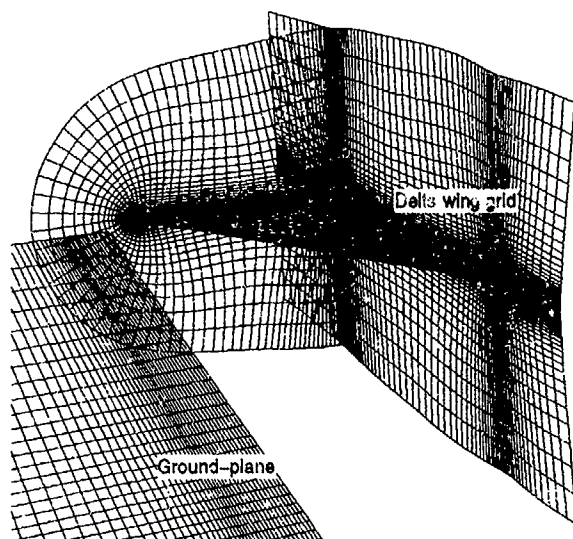


Fig. 4: The delta wing grid.

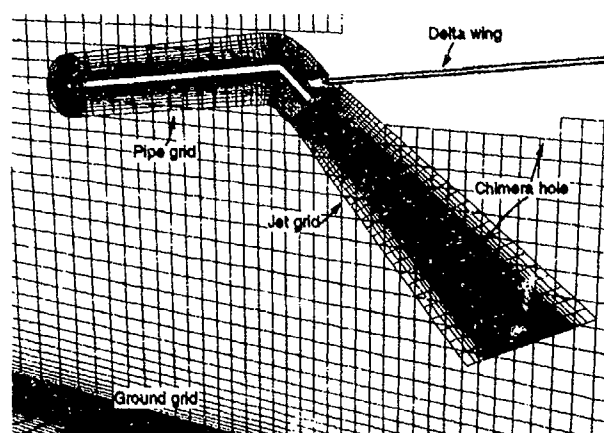


Fig. 5: The pipe and the jet grids.

3.2 Numerical Algorithm

Time-accurate computations were carried out on a Cray-YMP by solving the three-dimensional Navier-Stokes equations, using the OVERFLOW¹² code, on overset grids. Flow was computed on one half of the configuration with the assumption of symmetry about the x-z plane. The equations are discretized by using a diagonalized three-factor scheme,¹³ which is second-order accurate in space, and at most first-order accurate in time. Higher-order time accuracy

is possible by using subiterations. The code is used to solve the conventional dependent variable vector $[\rho, \rho u, \rho v, \rho w, e]^T$ where ρ is density, u, v , and w are Cartesian velocity components, and e is the total energy per unit volume. Speed of sound, delta wing centerline chord, free-stream density, and $\gamma \times$ pressure (γ is specific heat ratio for air) are used as reference quantities.

3.3 Boundary Conditions - Straight-and-level flight cases

Ground grid inflow and jet exit values are specified to match the wind-tunnel conditions. The ground plane moves at the same velocity as the free stream to remove the boundary layer effects. A no slip condition is used at the delta wing and pipe surfaces. On solid surfaces, density is extrapolated from one grid point away and pressure is computed by solving the normal momentum equation. All variables are extrapolated at the ground grid outflow plane.

3.4 Boundary Conditions - Descent cases

In the VRF experiments, the delta wing moved relative to the ground, however in these simulations the delta wing remains stationary and the free-stream moves over it. The inflow boundary conditions on the ground grid are specified to match the delta wing velocity (70 ft/sec), and sea-level density and pressure. Additionally, the co-ordinate transformation between the VRF setup and the computational model requires that the floor of the computational ground grid move at the same speed as the free-stream. All other boundary conditions are specified in a similar manner as for the straight-and-level flight cases.

4. RESULTS

4.1 Parametric Studies

Parametric computational studies were performed utilizing the straight-and-level flight setup to evaluate the effect of grid density. It was determined that the computed lift is a strong function of the jet trajectory. In turn, it was found that the jet trajectory can be heavily influenced by the level of grid refinement. It was found that no practical Cartesian ground plane grid could support the experimentally observed jet trajectory. Rather, the total jet momentum would decay rapidly with distance from the nozzle exit, and the jet would finally become so weak that it would be deflected downstream by the oncoming flow. This was in distinct disagreement with the experimental flow visualizations of Paulson.¹ It is for this reason that the jet grid was added to the computational model. With the jet grid, and low levels of spatial numerical dissipation, the jet penetrates far upstream, impacts the ground plane, and spreads to form a thin wall jet. The high speed and large surface area of the wall

jet result in significant flow entrainment. Because the entrained flow accelerates, a low static pressure region forms under the delta wing, and lift loss occurs. The results of these parametric studies were used to select the grid topology and density for all work presented here.

For the descent simulations, additional two-dimensional parametric studies were carried out to determine the effect of time step Δt on simulations involving moving grids by descending a two-dimensional center section of the delta wing in ground effect. It was shown that for a high value of Δt (1.0), the ground cushion effect may not be captured. For smaller time steps ($\Delta t=0.5$), the solution indicates increased lift with ground proximity based on conventional ground effect. Further reductions in time step indicate convergence of lift histories and do not show any new flow physics. In these simulations, a $\Delta t = 0.002$ is used due to stability considerations. The above study shows that the chosen time step is small enough to accurately capture the flow features in the descent simulation.

4.2 Test Case Studies

Visualizations of the flow about the delta wing at $h/b = 0.25$ and 1.0 for straight-and-level flight are presented in Plate 1. The instantaneous streamlines passing through the nozzle exit plane indicate that at $h/b = 1.0$ the jet does not have sufficient momentum to impact the ground. As a result, the level of flow entrainment is low and little lift loss is encountered. However, at $h/b = 0.25$ the jet does impact the ground and, as described above, significant flow entrainment occurs, a low pressure pocket forms under the delta wing, and significant lift loss is encountered. Because of the care taken in minimizing computational errors due to numerical dissipation and grid resolution, the predicted lift coefficients are in reasonable agreement with experimental data (Fig. 6).

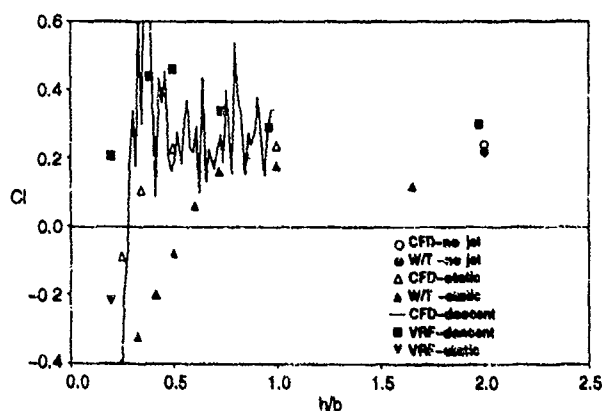


Fig. 6: Comparison between the experimental and computational C_l values.

The experimental values obtained from the VRF were smoothed by Paulson and Kemmerly (Ref. 14)

following the procedure outlined in Fig. 7. The computed data presented in Fig. 6 for the descent case has been filtered so as to match the sampling rate of the experimental data. However, no smoothing procedure similar to the experimental procedure (Fig. 7) has been carried out.

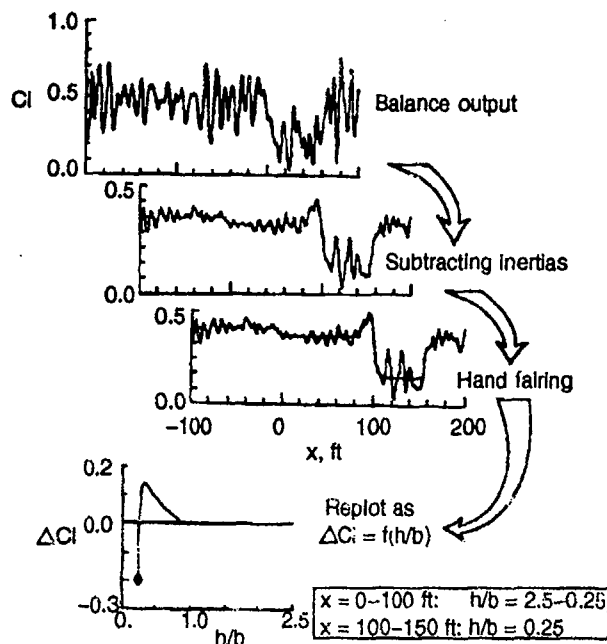


Fig. 7: VRF raw data processing.¹⁴

At higher heights above the ground, insignificant differences are observed between the straight-and-level flight and the descent cases. The gross flow features and mechanism of lift loss are same for both the cases. The descent lift curve indicates increased lift between $h/b = 0.5$ and 0.4 due to the conventional ground cushion effect. However as the delta wing approaches the ground, differences become apparent as indicated by higher value of C_l at $h/b = 0.35$ for the descent case as compared to the straight-and-level flight case.

The computed time histories of the lift-coefficient for both the straight-and-level flight at various heights above the ground (Fig. 8) and the descent case (Fig. 9) show large temporal variations and increased amplitude in lift oscillation with ground proximity. Preferred frequencies of these oscillations are

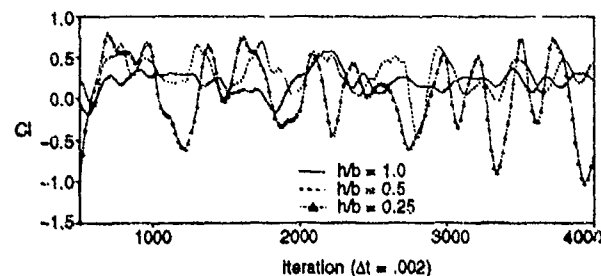
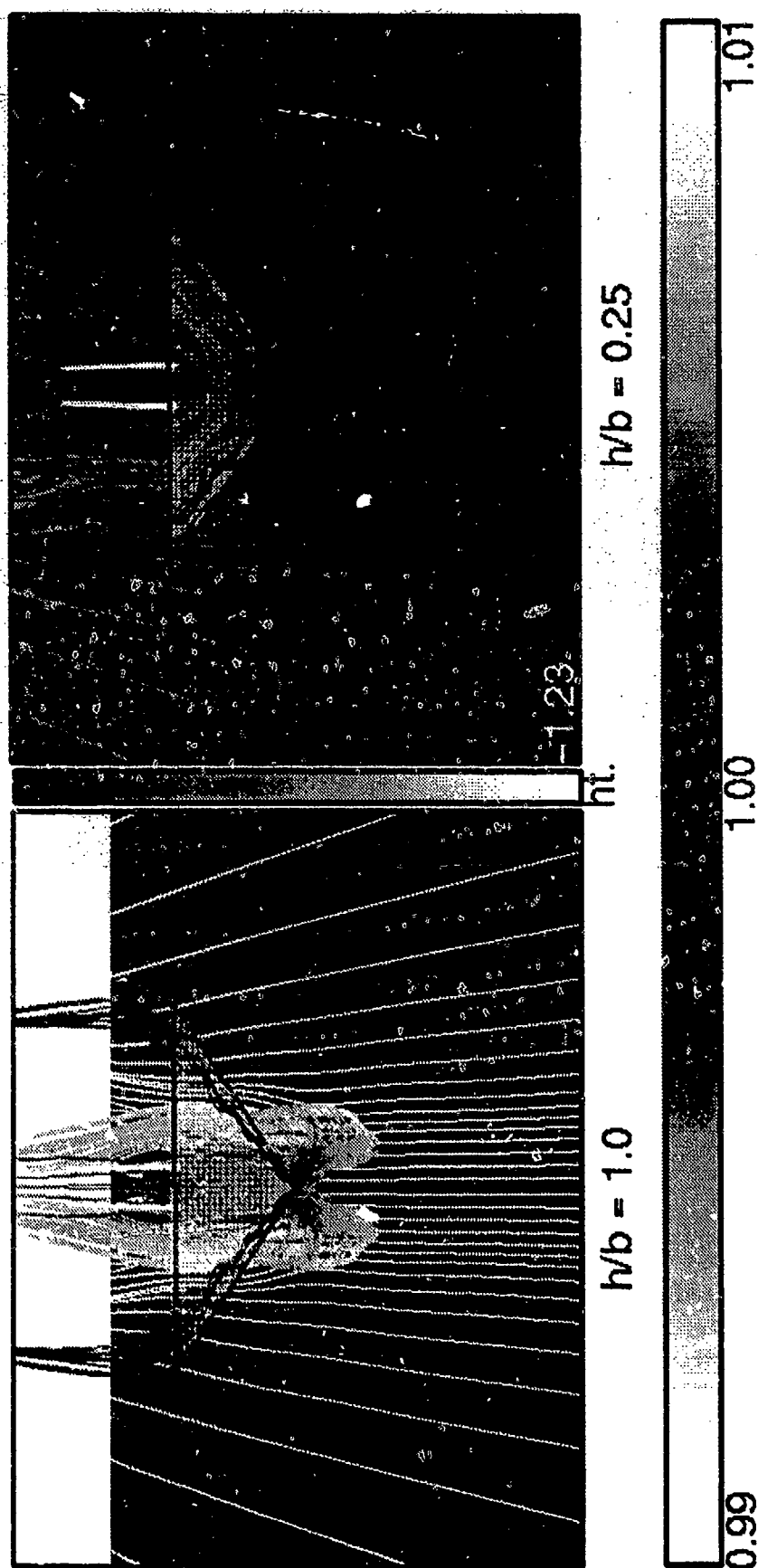


Fig. 8: The lift history of the straight-and-level flight cases.



Particle traces shaded by height; ground shaded by normalized pressure.

Plate 1: Comparison of particle traces for straight and level flight.

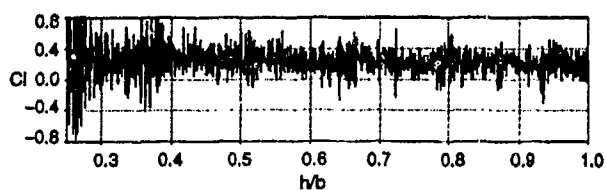


Fig. 9: Lift history of the descent case.

identified by computing power spectra of the time-varying lift histories (Fig. 10, 11). Power of all spectra presented in this work has been normalized using maximum power. For the descent case, the spectra are obtained over segments of descent (Fig. 11).

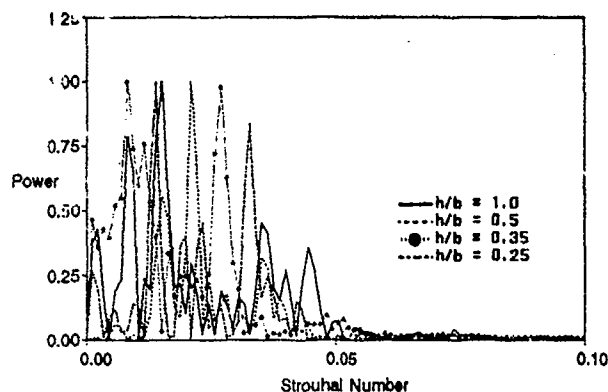


Fig. 10: Power spectra of lift history for the straight-and-level flight cases.

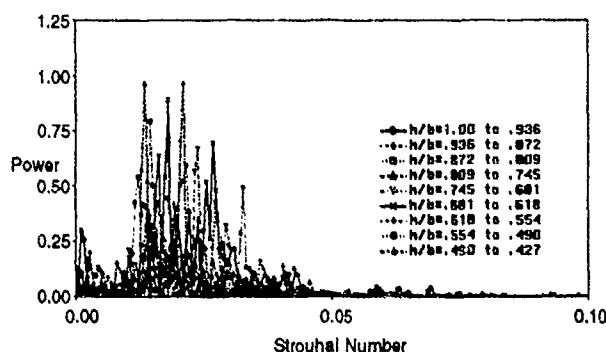


Fig. 11: Power spectra of lift history for the descent case.

These spectra indicate that preferred frequencies are confined in the narrow range of Strouhal number = 0.015 to 0.030. ($St. = f D_j / U_j$, where D_j and U_j are jet diameter and velocity respectively)

Flow visualizations indicate a number of flow features that could cause large temporal variations and increased amplitude in lift oscillation with ground proximity. For example, vortices shedding from the jet lip interact in non-periodic, almost random pairings; as a result the jet strength and trajectory vary with time. The jet oscillates both laterally, towards and away from the symmetry plane, and in the streamwise direction. There is also evidence of a complex Kármán vortex street shedding behind the dual

jet configuration. Finally, the ground vortex height oscillates.

To determine if the ring vortex dynamics causes the observed variation in lift, temporal variations in pressure at the jet lip and four diameters downstream are analyzed (Fig. 12, 13). Power spectra of these pres-

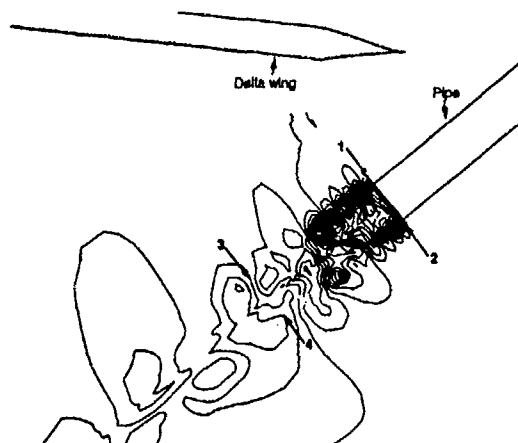


Fig. 12: Vortex shedding at the jet lip: Probe locations.

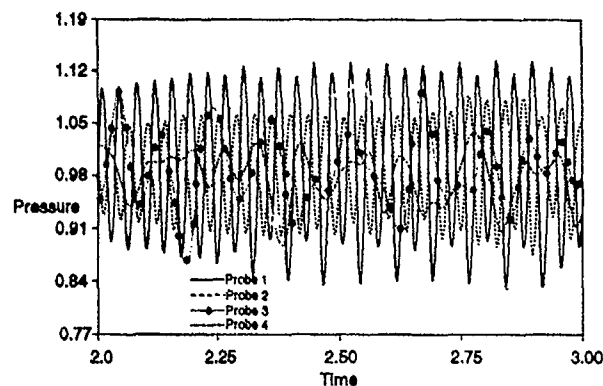


Fig. 13: Pressure samples at the jet probe locations.

sure histories, presented in Fig. 14 indicate an initial shedding frequency of $St. = 0.53$ at the jet exit, dropping to a vortex passage frequency in the range of 0.1 to 0.2 by four diameters downstream. Although the initial shedding frequency is lower than the experimentally observed frequencies (probably due to the large time-step and inadequate grid resolution), the observed passage frequency (0.1 to 0.2) near the end of the potential core is within the range of experimentally observed ring vortex Strouhal numbers, as compiled by Gutmark.¹⁵ The reduction in frequency as the probe is lowered from the jet lip to four diameters downstream is attributed to vortex pairings observed in flow visualizations. Because the range of observed frequencies due to the ring vortex dynamics is much higher than the observed time period in the lift variations, it is unlikely that the ring vortex structures are the dominant cause of the lift oscillations.

To determine if the lift oscillations are related to the lateral/streamwise jet oscillations, the temporal variation of the pressure field on the under surface

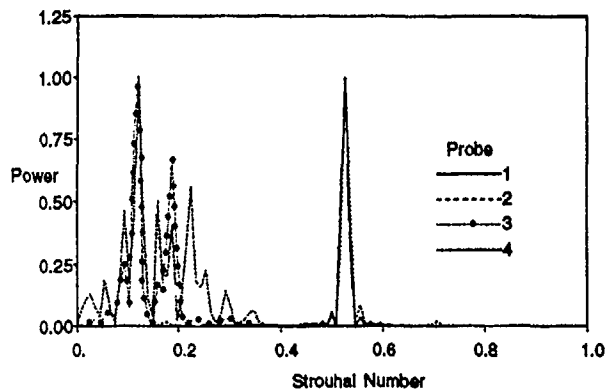


Fig. 14: Power spectra of pressure sampled at the jet probe locations.

of the delta wing is visualized. Concentric pressure waves emanating from the jet region move along the under-surface of the delta wing (Plate 2). Pressure distribution on the under-surface of the delta wing is shown at two different steps corresponding to instances when the under-surface is dominated by the high pressure and low pressure regions respectively of the pressure wave (Plate 2). Flow visualizations indicate that lift oscillates in synchrony with the movement of peaks (high-pressure) and troughs (low-pressure) of the pressure wave on the under-side of the delta wing. Based on this, it appears that the lift oscillations are related to these pressure waves. These waves are similar in shape and magnitude to the pressure waves observed on the ground plane (Plate 1) as well.

The history of the pressure variations at four points on the ground plane are presented in Fig. 15. These pressure histories were extracted as the delta wing descended through $h/b = 0.35$. Spectra analysis of

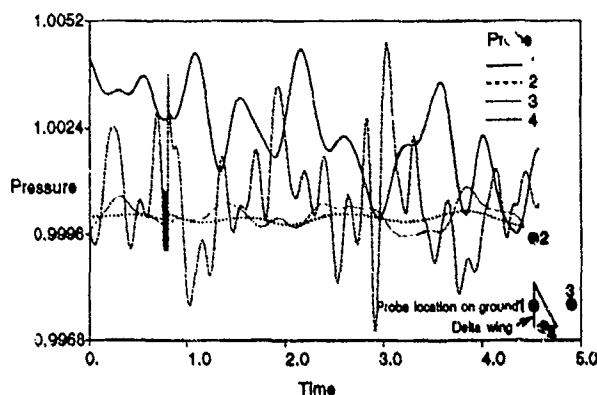


Fig. 15: Pressure samples at the ground probe locations.

these histories, presented in Fig. 16, show a preferred frequency of $St. = 0.015$, which is within the range of lift oscillation frequency. Because of this match in frequency, and the observation that the pressure waves only exist when the jets are present, and also they emanate from the jet vicinity, it appears that the lift oscillations are due to large scale motions of

the jet and jet-induced flow structures.

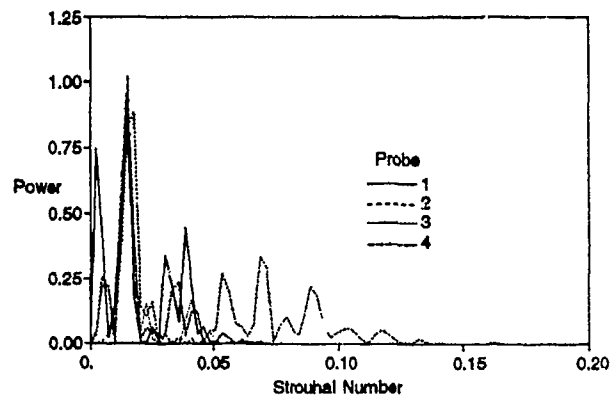


Fig. 16: Power spectra of pressure sampled at the ground probe locations.

The very low frequency ground vortex oscillations ($St. = f D_j/U_j = 0.006$) observed by Cimbalá et al.¹⁷ suggest that lift oscillations could be related to ground vortex oscillations. These low-frequency oscillations, referred to as "ground vortex puffing," are caused when the ground vortex first grows and then, when it can no longer retain its structure, collapses. However, in these computations, the ground vortex appears only at lower heights (Fig. 17, 18), yet the same narrow range of low-level-frequency lift oscillations occur over the range of computed heights. For this reason, it appears the lift oscillations are not related to ground vortex puffing.

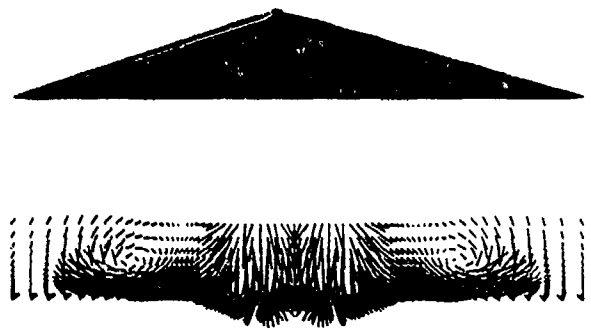


Fig. 17: Front view of the ground vortex.

There is evidence of a Kármán vortex street behind the dual jet. The frequency of this vortex street has yet to be determined, however, the shedding frequency for a Kármán vortex street for flow past a circular cylinder (jet in this case) for similar Reynolds numbers (jet-diameter-based) is in the range of $St. = 0.18$ to 0.20 .¹⁸ The computed lift oscillation frequency range corresponds to free-stream velocity based $St. = 0.23$ to 0.46 . This frequency range is very close to the expected vortex street fre-

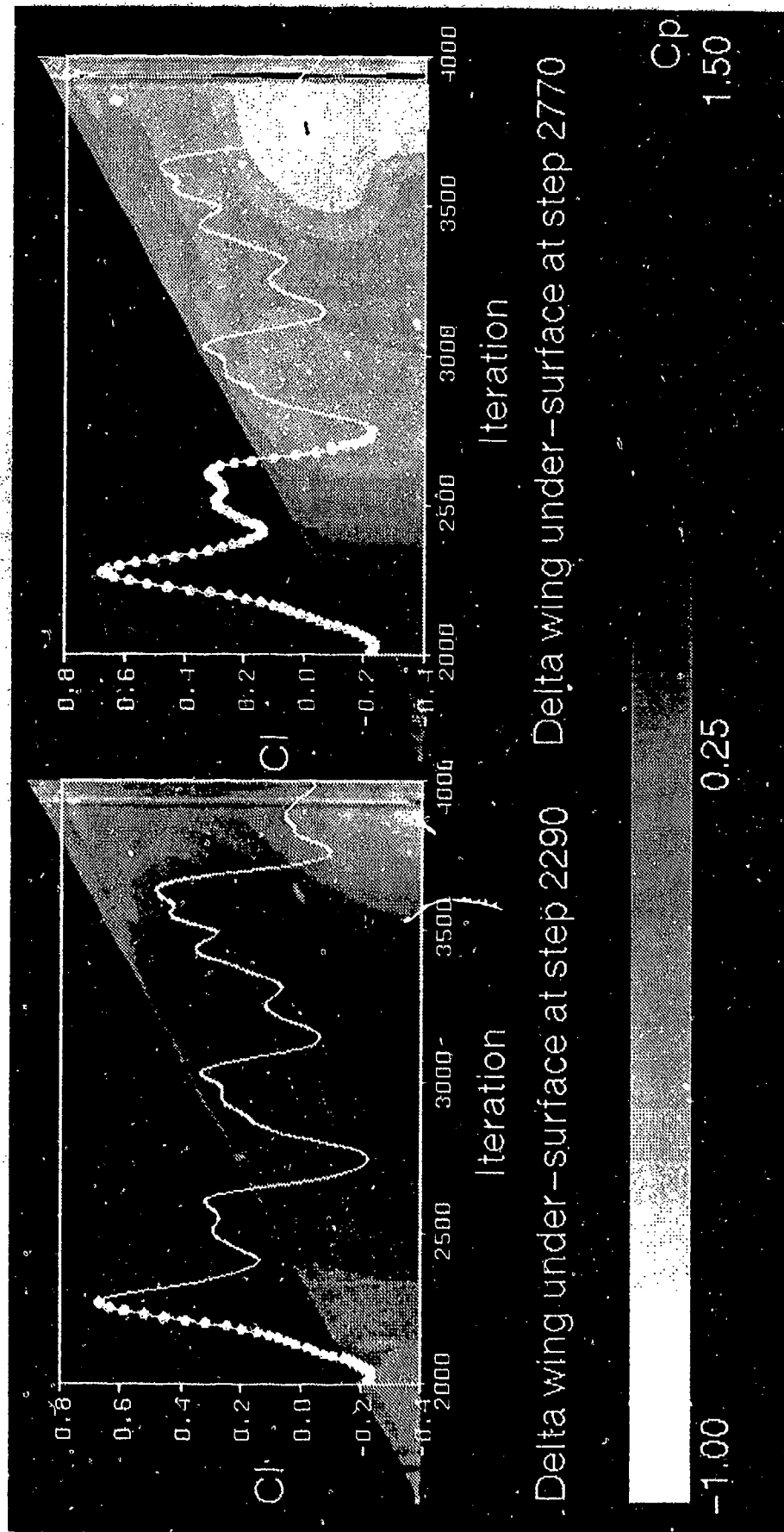


Plate 2: Correspondance of Cp and Cl oscillation at $h/b = 0.35$.

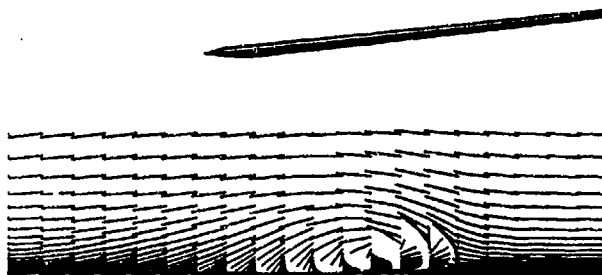


Fig. 18: Side view of the ground vortex.

quency. However, the position of the Kármán vortex street past the trailing edge of the delta wing makes it an unlikely feature that can affect the lift oscillations. Further, no correlation has been found between the wave-like nature of the pressure field on the under-surface of the delta wing and the Kármán vortex street.

The computational simulation captures the qualitative physics, as indicated by typical lift-coefficients at high h/b values and low lift-coefficient values at lower heights indicating suck-down (Fig. 6). Computed values fall within the data discrepancy band in the two experimental facilities (note C_l difference between the VRF and W/T results for $h/b = 1.0$ and $h/b = 0.25$). Quantitatively, the CFD simulation under-estimates the lift loss for straight-and-level flight cases. This could be due to the lack of a turbulence model in these simulations. Inclusion of a turbulence model would have increased the jet spreading and resulted in increased flow entrainment. No turbulence model was included in these simulations due to lack of a rational approach to apply an algebraic turbulence model to a flow of this complexity. A higher order two-equation model, for example a $k-\epsilon$ model, would have pushed the computational cost beyond what could be accommodated.

5. CONCLUSIONS

Lift loss in ground proximity, as may be encountered during STOL operations, was computed by solving flow past a delta wing with thrust reverser jets in the straight-and-level and descent flight profiles.

Efforts were made to minimize numerical errors due to grid resolution and time step. Overset grids were used to capture the jet trajectory. Two-dimensional parametric studies were carried out to determine the effect of time step Δt on simulations involving moving grids. The computed unsteady result (descent case) showed convergence for smaller values of Δt and indicates that for higher Δt , the ground cushion effect

may not be captured. The time-step used in these simulations was sufficiently small to capture the descent related flow features.

The time-accurate computations for the straight-and-level flight were performed for a number of heights ($h/b=1.0, 0.5, 0.35$, and 0.25) above the ground. The computations over-predict the lift coefficient, however flow physics corresponding to lift loss with increased ground proximity is captured.

The time-accurate simulation of the descent from $h/b = 1.0$ to $h/b = 0.25$ captures the initial increased lift due to the conventional ground cushion effect followed by lift loss due to the suck-down effect as the delta wing approaches the ground. The computed lift coefficients are in fair agreement with the experimental values.

Both the straight-and-level flight and descent simulations exhibit high levels of unsteadiness. Spectra of the lift histories indicate preferred frequencies in the narrow range of $St. = .015$ to $.03$ for the straight-and-level flight over all computed heights. The same range of frequencies is preferred when spectra are computed over segments of the descent.

Efforts were made to understand the unsteady flow structures which produce the lift oscillations. The ring vortex shedding frequencies were deemed too high to cause the lift oscillations. Kármán vortex street was ruled out as the feature causing lift oscillations due to its position beyond the trailing edge of the delta wing. Further, no correlation could be found between the wave-like nature of the pressure distribution on the under-surface of the delta wing and the ground, and the vortex street.

Presence of a "wave-like" pressure field in the vicinity of the jet indicates that the jet oscillations result in moving pressure waves. It was shown that the lift oscillation frequency is related to the frequency of these waves. Analysis of the temporal variations of pressure at various locations on the ground indicated frequencies within the range of the lift oscillation frequencies. Based on this, it was concluded that the lift oscillations are due to large scale motions of the jet and jet-induced flow structures.

Ground vortex was ruled out as the cause of lift oscillations as it appears only at lower heights. Lift oscillations, however, over same range of preferred frequencies appear even at higher heights (e.g. $h/b = 1.0$). It is conjectured that ground-vortex-puffing type of flow physics occurs in the vortex formed behind the jet causing its size to oscillate, and resulting in lift oscillations.

6. References

- ¹ Paulson, J. W. and Kemmerly, G. T., "An Assessment of Ground Effects Determined by Static and Dynamic Testing Techniques," Ground Vortex Workshop, NASA Conference Publication 10008, NASA Ames Research Center, 1987.
- ² Van Dalsem, W. R., "Study of Jet in Ground Effect with Crossflow Using the Fortified Navier-Stokes Scheme," AIAA Paper 87-2279, 1987.
- ³ Van Dalsem, W. R., Panaras, A. G., and Steger, J. L., "Numerical Investigation of a Jet in Ground Effect with a Crossflow," SAE Paper 872344, 1987.
- ⁴ Stewart, V. R., Kuhn, R. E., and Walters, M. M., "Characteristics of the Ground Vortex Developed by Various V/STOL Jets at Forward Speed," AIAA Paper 83-2494, 1983.
- ⁵ Chawla, K., Van Dalsem, W. R., and Rao, K. V., "Simulation of a Delta Wing with Two Jets in Ground Effect," Computing Systems in Engineering, 1, pp. 483-494, 1990.
- ⁶ Chawla, K., Van Dalsem, W. R., and Rao, K. V., "Numerical Study of a Delta Planform with Multiple Jets in Ground Effect," SAE Paper 892283, 1989. Also in SAE 1989 Transactions, Journal of Aerospace, Section I, pp. 1555-1567.
- ⁷ Chawla, K., Van Dalsem, W. R., and Rao, K. V., "Simulation and Analysis of a Delta Planform with Multiple Jets in Ground Effect," AIAA Paper 90-0299, 1990.
- ⁸ Dougherty, F. C. and Kuan, J. H., "Transonic Store Separation Using a Three-Dimensional Chimera Grid Scheme," AIAA Paper 89-0637, 1989.
- ⁹ Meakin, R. L. and Suhs, N. E., "Unsteady Aerodynamic Simulation of Multiple Bodies in Relative Motion," AIAA Paper 89-1996, 1989.
- ¹⁰ Meakin, R. L., "A New Method for Establishing Inter-Grid Communication among Systems of Overset Grids," AIAA Paper 91-1586, 1991.
- ¹¹ Benek, J. A., Buning, P. G., and Steger, J. L., "A 3-D Chimera Grid Embedding Technique," AIAA Paper 85-1523, 1985.
- ¹² Buning, P. G. and Chan, W. M., "OVERFLOW/F3D User's Manual," NASA Internal Memorandum, NASA Ames Research Center, Moffett Field, CA, March 1991.
- ¹³ Pulliam, T. H. and Chaussee, D. S., "A Diagonal Form of an Implicit Approximate Factorization Algorithm," Journal of Computational Physics 39, pp. 347-363, 1981.
- ¹⁴ Kemmerly, G. T. and Paulson, J. W., "Investigation of a Moving-Model Technique for Measuring Ground Effects," NASA Technical Memorandum 4080, January 1989.
- ¹⁵ Gutmark, E. and Ho, C. M., "Preferred Modes and the Spreading Rates of Jets," Physics of Fluids, 26, pp. 2932-2933, 1983.
- ¹⁶ Schlichting, H., Boundary Layer Theory, McGraw Hill Book Company, pp. 32, 1979.
- ¹⁷ Cimbala, J. M., Billet, M. L., and Gaublumme, D. P., "Experiments on the Unsteadiness Associated with a Ground Vortex," Journal of Aircraft, 28, No. 4, pp. 261-267, 1991.

A STUDY OF JET EFFECT AND GROUND EFFECT INTERFERENCE ON A STOL FIGHTER

by

David J. Moorhouse
Wright Laboratory
Wright-Patterson AFB
2645 Fifth St
Ohio 45433-7922
United States

James G. Reinsberg
Frank J. Shirk
McDonnell Douglas Aerospace
St Louis
Missouri
United States

INTRODUCTION

The STOL and Maneuver Technology Demonstrator (S/MTD) program was structured to investigate, develop and validate through analysis, experiment and flight test, four specific technologies related to providing current and future high performance fighters with both STOL capability and enhanced combat mission performance. The four technologies are:

- Two-dimensional thrust vectoring and reversing exhaust nozzle
- Integrated Flight/Propulsion Control (IFPC) System
- Advanced Pilot Vehicle Interface
- Rough/soft field landing gear.

In addition to the required technologies, all-moving canard surfaces were also incorporated into the baseline F-15B (see Figure 1). As stated previously, the intent of the demonstration program was to validate specific technologies, it was neither a prototype nor an explicit research program. Starting with an existing aircraft, many wind tunnel tests were performed to define the incremental effects of the specific technology items. Thrust reversing was achieved by blocking the nozzle exit area and exhausting the flow through vane packs on top and bottom of the engine. In the Short Landing (SLAND) mode the engines were at full military RPM and all exhaust flow was diverted through the vane packs. The aircraft made the final approach with the reverser vanes pointed aft to provide forward thrust. At touchdown, the vanes quickly swing forward to orient the exhaust flow to provide reverse thrust for the rollout (see Figure 2). A significant amount of wind tunnel testing was devoted to measuring jet effects at all conditions but definition of jet effects in ground effect received particular emphasis.

Reference 1 documented the development of the S/MTD configuration with details on the wind tunnel data and control laws. Data was presented on the jet effects in ground effect that were predicted. Special control logic was defined to mitigate strong nose-up pitching moments as thrust reversing was initiated after touchdown. A special ground-handling mode was also incorporated for the rollout phase. The flight testing, completed since Reference 1, produced some surprising results. The object of the present paper is to document that experience. Data from Reference 1 will be summarized briefly for completeness. Pertinent flight test experience will be presented, with results of an innovative analysis technique developed by the contractor. Lastly, future requirements will be discussed.

DESIGN REQUIREMENTS

As much as possible, the program requirements were stated in operational terms rather than design parameters. As an example: "A design requirement and technology driver for this program is to takeoff with payload and land with a ground roll (including dispersion tolerances) of 1500 feet or less under adverse weather conditions (night, in wet, gusty weather)". These dimensions form implicit, and very stringent, requirements on flight path control and touchdown dispersion. Longitudinal touchdown dispersion is typically measured in hundreds of feet - a significant proportion of the available length. The specified length of 1500 ft, therefore, became a design requirement on precision of airspeed and flightpath control. Lateral and directional flying qualities design requirements are dictated by the 50 ft. runway width in conjunction with specified crosswind, turbulence and windshear (numerical values given in MIL-F-8785C). The severity of this requirement applies throughout a STOL approach and flare to ground rollout. This last phase is also

aggravated by the necessity for high values of reverse thrust and specified slippery surface conditions coupled with crosswinds.

The reverser flow was to provide pitch, yaw and roll control functions. The intent was stated to be "to enhance stability and controllability of the aircraft in the STOL operating mode both in flight and on the ground". The actuation rates, however, were dictated by a requirement to go "from the nominal steady state approach position to full reverse or to maximum dry forward thrust in less than one second". The intent of this requirement was to minimize delay in obtaining reverse thrust for stopping or forward thrust for a go-around. The fallout was a control bandwidth more than adequate for all other control functions.

WIND TUNNEL TEST RESULTS

This section summarizes results from References 1-3. From Reference 2, for low speed wind tunnel tests using a fixed ground board, the S/MTD thrust reversers were found to induce:

- a. Small lift and negligible pitching moment increments in free air.
- b. Increasing lift and pitching moment increments during transition into ground effect.
- c. Large lift losses and nose-up pitching moment increments at landing gear height. These increments varied with the lower vane angle, velocity, nozzle pressure ratio and sideslip angle.
- d. Non-linear horizontal tail effectiveness characteristics in all flight regimes.
- e. Negligible changes in lateral stability in free air.
- f. Large increases in lateral stability at landing gear height.
- g. Changes in directional stability and rudder effectiveness, which were strongly affected by the upper vane angle. These changes were independent of the height above the ground.
- h. Large favorable yawing moment increments with differential upper vane deflection.

Moving Model Test Approach

The Vortex Research Facility (VRF) at the NASA-Langley Research Center was used for the study discussed in Reference 3. The test region of the VRF was modified to incorporate a 150-foot long ground plane near the center of the test section. The ground board consisted of two parts: a ramp which was inclined upward 4° for a distance of 100 feet, followed by a horizontal section which extended for an additional 50 feet. The height of the model over the fixed horizontal portion of the ground board was horizontal portion of the ground board was set by adjusting the length of the model support strut. As the model moved horizontally over the inclined portion, the distance from the ground board to the model reduced, thereby simulating an approach along a glide slope of 4° with rate of descent dependent on the test velocity. After moving across the ramp, the model passed over the horizontal section to simulate roll-out or constant altitude flight (see Figure 3).

Figure 4 illustrates some of the important differences between conventional static ground effects test methods and the moving model method. Static test techniques involve setting a model at a given height above the ground plane, allowing the flow field to reach a steady state, and measuring the aerodynamic loads. The moving-model technique, on the other hand, involves measuring the aerodynamics while the model is in motion and the flow field is in a dynamic state, similar to conditions in an actual approach. Simulations of normal approaches (without thrust reversers) have indicated only small, but discernable, differences in model aerodynamics measured statically and at various rates of descent. With thrust reversers or similar jet devices operating, however, the two techniques could yield significantly different results. Scaling considerations are discussed in Reference 4.

Comparison of Moving Model to Static Results

There are three major differences between the static wind-tunnel database and the measurements made using the moving model at the VRF. The first principal difference is that the VRF data accurately simulates the time dependent aerodynamic effects related to rate of descent and ground plane interaction with the exhaust plume. The second principal difference is that the static measurements were

made in the presence of a ground boundary layer which has been shown to have a significant impact on the development of the ground vortex created by vectored jets near a ground plane. This impact is detailed in Reference 5. In short, the presence of a ground boundary layer allows the ground vortex to penetrate significantly farther upstream (approximately 30 percent) than would be possible in its absence. Finally, since the VRF simulates the flight path angle on approach, the incidence angle between the plume and the "horizontal" ground plane is reduced at the same angle of attack. This reduced incidence angle alters both the jet to ground impingement angle and the jet point of contact with the ground plane. These three major differences are believed to be the source of the differences between the two data sets discussed below. For the data shown in Figures 5 through 9 the angle of attack was 12° , the flaps and ailerons were set at 20° , the canard at -13° and the horizontal tail at 2° . These were approximately the approach conditions of the S/MTD aircraft when entering ground effect.

In Figure 5, the lift increment in ground effect for the approach configuration has been plotted for Lower Vane Angles (LVA) of 45° and 60° . As height decreases to touchdown height the static wind-tunnel data consistently predicts a greater lift increment due to ground effect than that predicted by the VRF data set. This difference is attributed to the effects of rate-of-descent modeling in the VRF. Once at the minimum ground height for some time, the results from the VRF testing are seen to have the same steady state lift increment levels as those in the wind-tunnel database.

As the thrust reverser vanes were vectored farther forward, the presence of the ground boundary layer is seen to have a greater effect. This is illustrated in Figure 6. For LVA of both 80° and 110° not only is the lift increment different as h/b reduces to the minimum ground height, but also, the steady state levels measured once the models were at that minimum height are different. The reason for the differences at the minimum ground height is believed to be due to the presence of a ground boundary layer in the wind tunnel testing. The differences at the other ground heights are due to both rate-of-descent modeling in the VRF and

the presence of a ground boundary layer in the wind tunnel testing - these two effects can not be separated for this particular set of data.

The differences in pitching moment are similarly illustrated in Figures 7 and 8. The thrust reverser configuration LVA = 45° and LVA = 60° are shown in Figure 7. At LVA = 45° , much like the results seen for the lift coefficient, the wind tunnel database predicts greater nose-down pitching moment than the dynamic measurements from the VRF as the model height is reduced to the minimum ground height. However, once at that height for some time, and the VRF flow field transitions to a steady state, the level of nose-down pitching moment measured by the two techniques are nearly equal. Again this difference at heights greater than that corresponding to wheel touchdown is attributed to the modeling of a rate of descent in the VRF testing.

As the thrust reverser jet is vectored further to LVA = 60° , the comparison is similar down to a model height to wing span of approximately 0.3. Below that height the wind-tunnel database indicates that the configuration experiences progressively less nose-down pitching moment as the model approached the ground. This is, again, believed to be due to the presence of the ground boundary layer in the wind tunnel testing. This boundary layer allows the thrust reverser jets to penetrate farther upstream before forming the ground vortex. In this situation it is believed that the ground vortex has developed under the horizontal stabilizer and the low pressure vortex has reduced the lift on that surface. The greater penetration of the ground vortex also induced greater upwash at the wing. The net effect is as seen in Figures 5 and 7: increased steady state pitching moment increment and no difference in lift increment between the VRF data and the wind-tunnel database.

The effect of the ground boundary layer is even more pronounced as the thrust reverser jets are vectored further forward. This is presented in Figure 8. In these configurations, more upwash might be induced at the canard in the wind tunnel database than was indicated in the VRF results because the ground vortex could not penetrate as far upstream in the absence of a ground boundary layer.

It is concluded in Reference 3 that, relative to the conventional

static wind tunnel ground-effects tests, the rate-of-descent modeling produced substantially less lift increase in ground effect, more nose-down pitching moment, and less increase in drag. These differences became more prominent at the larger reverser vane angles. The results of the moving model technique indicate no safety-of-flight problems with the lower reverser vectored up to 80° on approach. They also indicate that the S/MTD configuration could employ a nozzle concept using lower reverser vane vector angles up to 110° on approach if a procedure were adopted in which rate of descent was not arrested near the ground and if inlet reingestion were found not to pose a problem. These moving model tests, however, were performed too late for consideration in the S/MTD development.

The control laws were designed, using the static wind tunnel data, to avoid uncontrollable nose-up pitching moments. The philosophy was based on the belief that this was a conservative approach. The lower vane deflection was scheduled with both pitch attitude and speed, plus a stabilator/canard pitchdown bias was introduced to provide a rapid (2 seconds) and repeatable nose-down rotation to a three-point attitude.

RESULTS

Initial Flight Experience

In May and June, 1990, five landings were made in the SLAND mode yielding unexpected results. Shortly after touchdown, the aircraft experienced a high initial nose-down pitch rate that had the potential to bottom out the nose gear (see Figure 9).

The abrupt nose down pitch rate (15.5 deg/sec max) can be seen to develop approximately 0.25 seconds after the 6deg/sec pitch down command is engaged. Figure 9 shows that this acceleration begins to develop well after the stabilator and canard have begun to travel on their rate limit due to the pitchdown command. Neglecting aerodynamic lag, this indicated that these control surfaces are not the dominant effector of pitch acceleration. Further, at the point in time at which the pitch acceleration abruptly changes ($T=61.350$ sec), the aircraft is airborne from the initial ground contact bounce (no gear forces) and the rotating vanes are producing a nose up

direct jet moment. Based on a pitch acceleration of 36 deg/sec², the conclusion was that the lower vanes are inducing a nose down pitching moment coefficient of approximately -0.2 at a lower vane angle of 75°. Note that this acceleration remains roughly constant through nose wheel contact at $T=61.625$ sec. After subtracting the direct jet moment at nose wheel contact, a residual nose down pitching moment coefficient of -0.1 remains at a lower vane angle of 85°. In contrast, the pitching moments predicted by the low speed jet effects wind tunnel test were +0.06 and +0.15 for the 75° and 85° vane conditions. These observations seem to be consistent with the formation of a high pressure "bubble" under the aft portion of the empennage and horizontal tails. This "bubble," or stagnant flow region, may also explain why the stabilators appear so ineffective during this period of time.

In hindsight, results from the low speed jet effects wind tunnel program were deficient in that no testing was performed between 65 and 80°, which seems to be the region where a nose down moment is indicated. Finally, Reference 3 indicates the fixed ground boards may not be suitable for "static" powered model testing. That is, testing where the model is allowed to come to steady-state conditions and the data points are an average of several samples. A short ground board was chosen to minimize boundary layer effects, but boundary layer removal may have been required. Also, the reference indicates that sink speed, and presumably dynamics in general such as pitch rate, play an important role in measured data. These conclusions are supported by our test results.

The analysis was clever in that it capitalized on the bounce which consistently occurred just after touchdown. During this bounce, the main gear unloaded and the aircraft was airborne for 0.25-0.50 seconds. Since all the gear is unloaded, gear loads are zero and do not contribute to the aircraft force and moments. Gear loads could not be measured when the gear was in contact because of damage to strut strain gage instrumentation. The pitch acceleration during this time was relatively constant and could be used to compute a total aircraft pitching moment. Direct jet effects were calculated and subtracted from the moment, leaving only an aerodynamic contribution. Since the analysis had also shown the lower vane to be the most powerful

effector during this part of the landing, the aerodynamic pitching moment is approximately the lower vane induced effect.

A second effect occurred during ground rollout with thrust reversing, the S/MTD aircraft experienced a rather vigorous 1/3 hertz limit cycle pitch oscillation if braking was not used. An example of this phenomenon is shown in Figure 10. The oscillation was not predicted by the simulation model at these speed/vane angle/nozzle pressure ratio combinations, and it quickly damps below a dynamic pressure of 30 psf. Control law AOA is a likely candidate as the forcing function since it is fed back to the lower vanes through the pitch up protection schedule and it also fades to zero at 30 psf. As shown in Figure 11 braking increases the system damping to an acceptable level. But in the event of wet/icy runway conditions or anti-skid failure, this damping would cease to exist. Also note that the pitch rate has stopped increasing, and actually begun to decrease, before the lower vanes were pulled back by the control law pitch up protection schedule. This implies that the vane induced nose up moment is stable with AOA, and this trend was predicted by the low speed jet effects test for the 110 degree lower vane angle.

Software Redesign

The second effect was the easiest to cure since the braking effect indicated that damping was the solution. Pitch rate feedback was added to the lower vane schedule. This change was completely successful and is not discussed further.

The key to solution of the first effect was obviously to achieve a more optimum movement of the lower vanes from touchdown forward to the reverse thrust position. The original control logic included a one-second delay to avoid the predicted nose-up pitching moments at the forward deflections. The excessive nose-down pitch that was experienced indicated a heuristic solution. The redesigned control law eliminated the time delay before forward vane movement. A capability to hold the lower vane deflection at different fixed values was also included as an option selectable by the pilot. A second redesign was also prepared, with the delay increased to two seconds ("just in case"). Landing ground roll would have been

increased, but this version was not tested because of the success of the other version. Figure 12 shows the reduction in pitch rate achieved by eliminating the one-second time delay.

Second Flight Test

A pilot procedure during landing was developed that extended the amount of time the aircraft was airborne during the bounce, compared to typical landings, and ensured the lower vanes were positioned at the limit during the bounce (see Figure 13). The procedure consisted of approaching at steeper glide slopes and pulling the throttle to reverse prior to touchdown. These landings were characterized by high vertical velocities at touchdown and peak nose down pitch rates comparable to those obtained with the old control law Operational Flight Program (OFP). The pilots referred to these landings as "crash and go's".

The SLAND landings suitable for comparison to off-line Six Degree of Freedom (SDF) predictions are both full stop landings and SLAND touch-and-go's performed with Dial-A-Gain (DAG) Sets 9-11. These DAGs limit the lower vane forward deflection during ground rollout. Airframe characteristics and atmospheric conditions were obtained from the onboard flight data rather than relying on the individual flight reports.

Before the SDF time histories could be compared to flight results, three modeling adjustments were made to bring SDF in line with flight data. Adjustments were made to braking effectiveness, engine thrust level, and aerodynamics just prior to touchdown. The aerodynamic adjustments were required to attain the appropriate touchdown speed with properly positioned control surfaces. The aerodynamic adjustments did not involve lower vane induced effects and were ramped out as AOA went to zero.

A comparison of SLAND landings to SDF predictions using this aerodynamic database is presented in Figure 14. Note that even though several seconds of trajectory are presented, the only valid time span for comparison of pitch characteristics is during the aircraft bounce when the gear is unloaded. This corresponds to the time when the peak nose down pitch accelerations occur during the time history. In general these comparisons show that the aircraft had higher nose down pitch accelerations than predicted during

the bounce. Analysis from the initial flight tests concluded that the actual lower vane induced effects were more nose down than predicted by the wind tunnel results. Although adequate for qualitative comparisons, the remainder of the time history is influenced by a gear model which, due to lack of loads data because of damaged strut strain gage instrumentation, was never updated for flight results.

ANALYSIS

The flight test data were reviewed to see which landings had pitch characteristics that would lend themselves to analysis for extraction of ground induced effects. Recall that the landing trajectory needed to exhibit relatively constant pitch acceleration while the aircraft was airborne during the bounce. The review identified an SLAND with the old control law OFF from Flight 1672 and four SLAND landings made with DAG #9-#11 from Flights 1716 and 1717. Pitch acceleration was determined by computing the gradient of the pitch rate trajectory during the time span of the aircraft bounce when the gear was unloaded. Figure 15 presents these pitch acceleration characteristics. In addition, the nose up pitch acceleration obtained when DAG #7-#11 were disengaged during the ground rollout of Flight 1719 are included. Note that the new OFF was so successful in improving the pitching characteristics during thrust reversing landings that none of the pitch acceleration trajectories of any SLAND landing without DAG #9-#11 engaged were suitable for this analysis.

The total aircraft pitch acceleration is a result of both aerodynamic and propulsive effects. The aerodynamic pitching moment was obtained by subtracting pitching moment due to direct vane thrust from the product of the total aircraft pitch acceleration and the pitch moment of inertia. The moments due to vane thrust were computed from the normal and axial components of vane gross thrust at the centroid of the vanes and the moment arm to the aircraft cg. Since the left bottom vane gross thrust normal component was unavailable, thrust data from the right vane was used for components of both sides. If the time slice of interest included a "step" in the thrust data component, an average value was used for that component.

The flight derived aerodynamic pitching moment coefficients are compared to wind tunnel predictions of the lower vane induced effects in Figure 16. The aerodynamic pitching moment includes the pitch moment due to ground induced effects, stabilator, canards, etc. However, the analyses concluded that the ground induced effects were the major contributor. The moments are referenced to 28 percent MAC. These wind tunnel predictions were included in the aerodynamic data base used to generate the SDF trajectories that showed higher than expected nose down pitch accelerations during thrust reversing landings.

The coefficient comparison shows the flight derived pitching moment is significantly more nose down than the wind tunnel data. As a result, the pitchdown control logic, which was designed to overcome expected strong nose up lower vane induced effects, was effectively over-designed.

Hindsight

The initial analyses with the static wind tunnel data indicated that it would not be possible to allow the lower reverser vanes to go forward immediately after touchdown. The predicted nose-up pitching moments exceeded the aerodynamic control capabilities. At a minimum, this would have caused the nozzle structure to contact the runway. Designing to prevent this from happening appeared to be a conservative approach. As we have seen, this conservatism could have erred in the opposite direction by causing nose-gear damage.

CONCLUSIONS

The STOL & Maneuver Technology Demonstrator was designed to achieve short landing performance using reverse thrust. final approach and touchdown were made with engine exhaust flow passing through reverser vane packs on top and bottom of the exhaust nozzle. The vanes rotated to direct the exhaust flow forward after touchdown. The original design incorporated a one-second delay before vane movement in order to avoid strong nose-up pitching moments predicted by static wind tunnel tests. Actual flight experience showed more nose-down pitching moments and the delay was eliminated to complete a successful flight test program. A wind tunnel test with a moving model simulated the motion effects of approaching a runway. This test produced results very consistent with the actual

flight test data.

REFERENCES

1. Moorhouse, D.J., J.A. Laughrey and R.W. Thomas, "Aerodynamic and Propulsive Control Development of the STOL and Maneuver Technology Demonstrator" AGARD Conference Proceedings CP-465, October 1989.
2. Blake, W.B., "F-15 S/MTD Low Speed Jet Effects Wind Tunnel Test Results", NASA Conference Proceedings CP10008, 1987 Ground Vortex Workshop, April 1987.
3. Kemmerly, G.T., "A Comparison of the Ground Effects Measured with and Without Rate-of-Descent Modeling on the F-15 S/MTD Configuration", AIAA Paper No. 89-3280, August 1989.
4. Kemmerly, G.T., "Dynamic Ground Effect Measurements on the F-15 STOL and Maneuver Technology Demonstrator (S/MTD) Configuration", NASA Technical Paper 3000, June 1990.
5. Steward, M., and G.T. Kemmerly, "Characteristics of the Ground Vortex formed by a Jet Moving Over a Fixed Ground Plane", AIAA Paper No. 89-0650, January 1989.

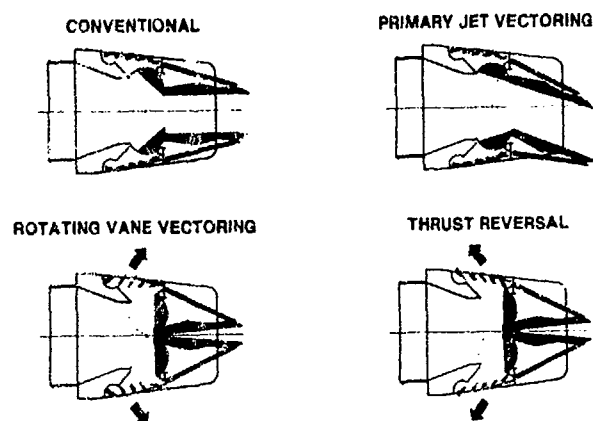


Figure 2. Nozzle Operating Modes

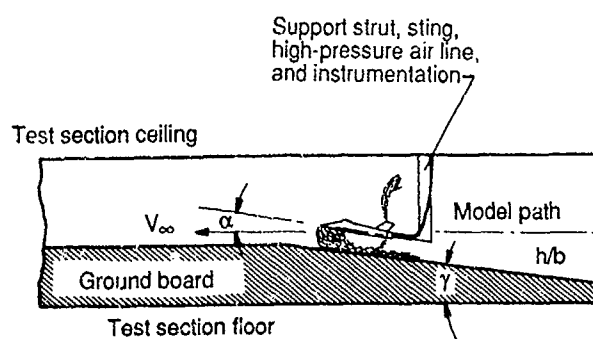


Figure 3. VRF Test Section (Ref. 3)

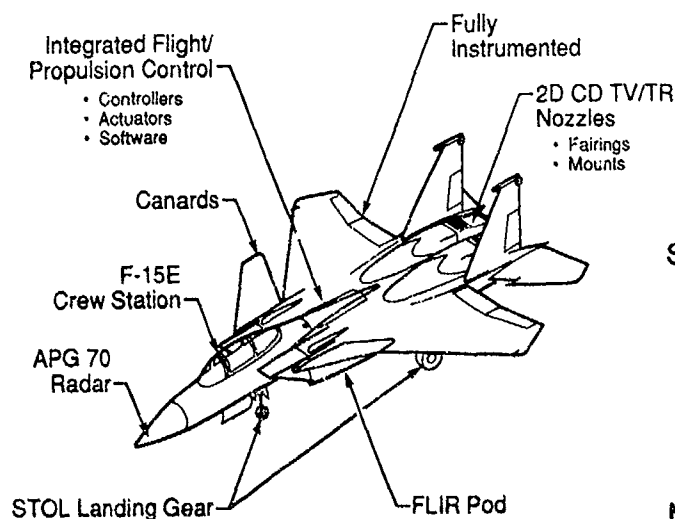
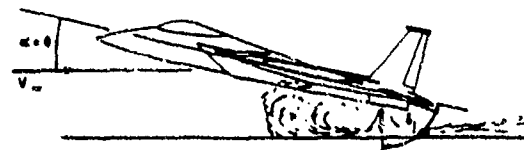


Figure 1. S/MTD Configuration

Steady State: $\gamma=0$, $\alpha=12$, $\theta=12$ deg



Moving Model: $\gamma=-4$, $\alpha=12$, $\theta=8$ deg

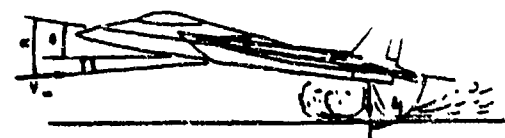


Figure 4. Dynamic vs Steady State Ground Effects

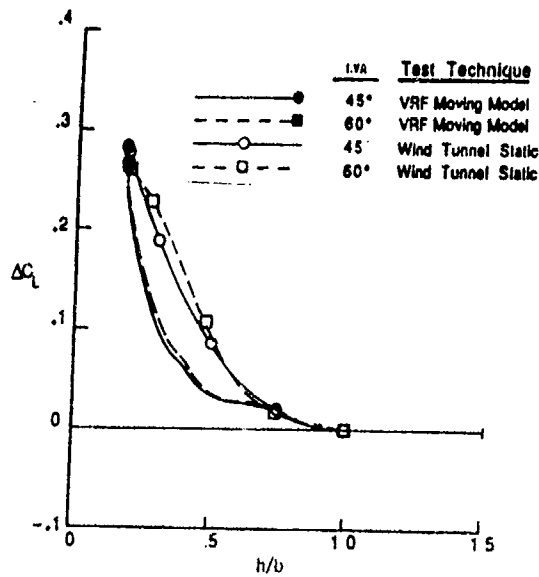


Figure 5. Comparison of Dynamic and Steady State Lift Coefficients (Ref. 3)

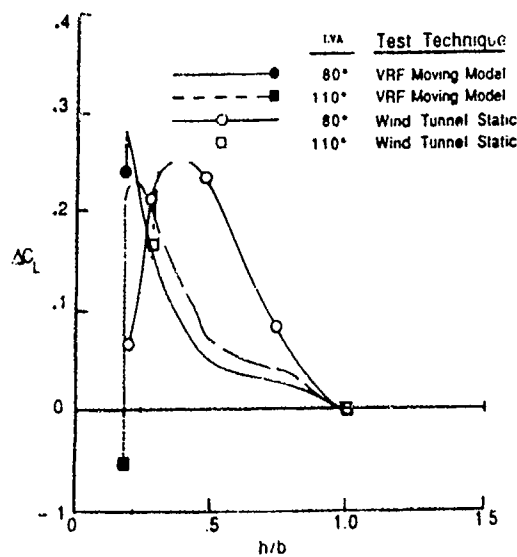


Figure 6. Comparison of Dynamic and Steady State Lift Coefficients (Ref. 3)

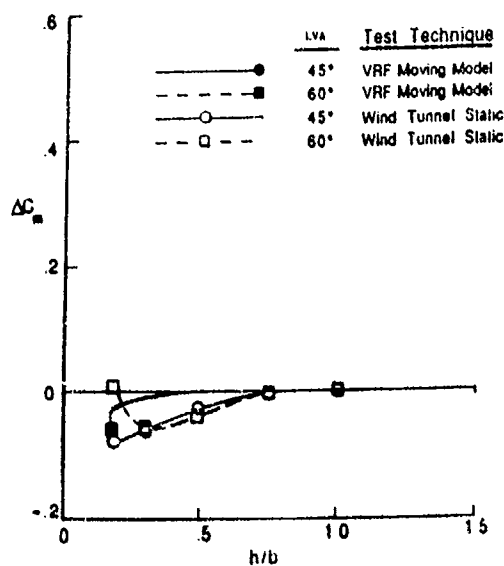


Figure 7. Comparison of Dynamic and Steady State Pitching Moments (Ref. 3)

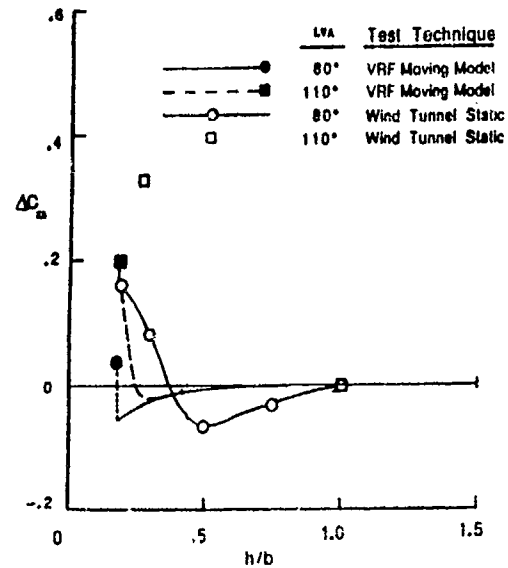


Figure 8. Comparison of Dynamic and Steady State Pitching Moments (Ref. 3)

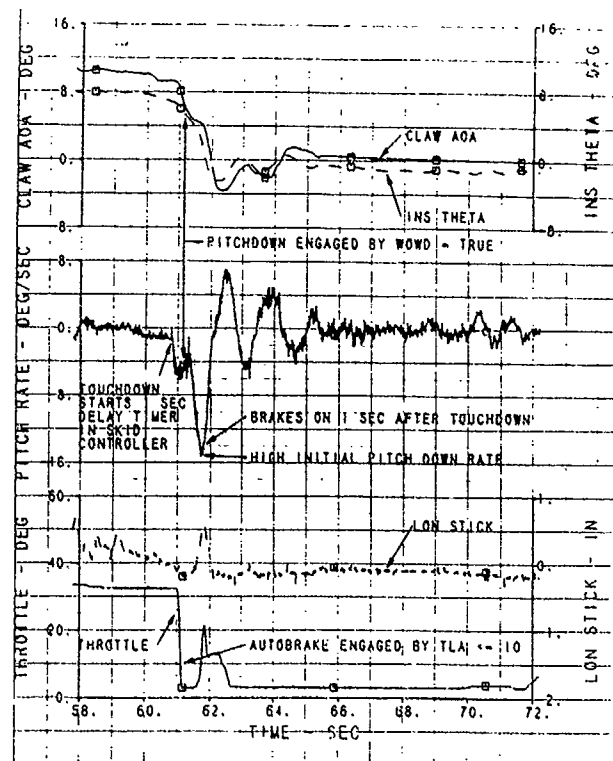


Figure 9. Typical Touchdown Dynamics

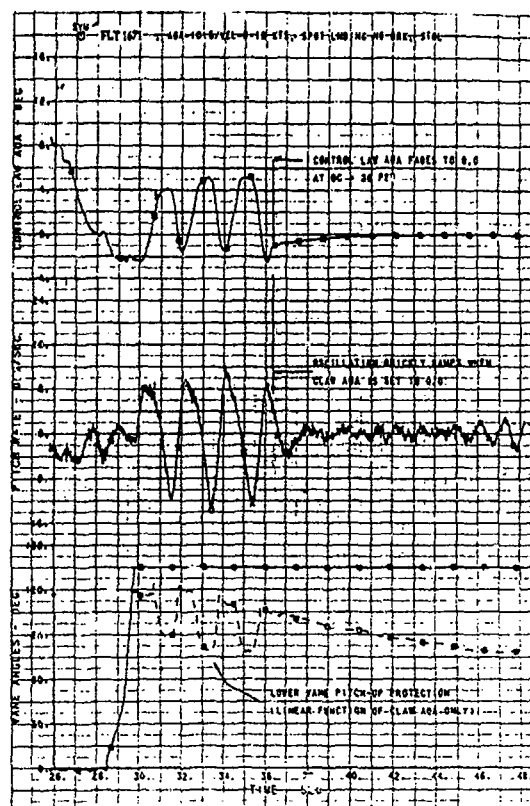


Figure 10. Pitch Oscillation During Ground Rollout

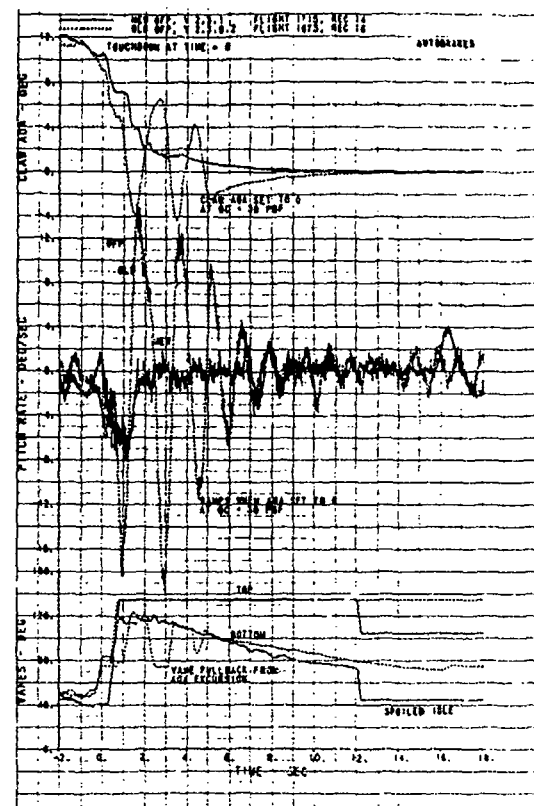


Figure 12. Improved Landing Dynamics With New OFF

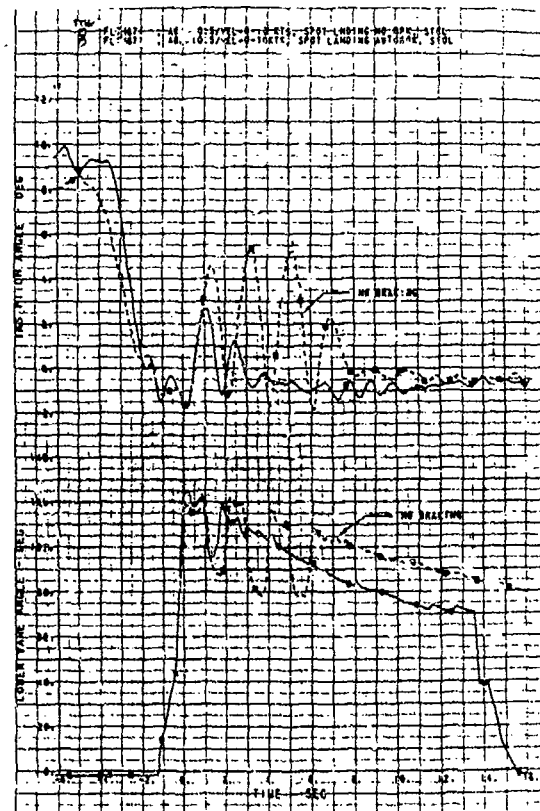


Figure 11. Effect of Braking on Pitch Oscillations

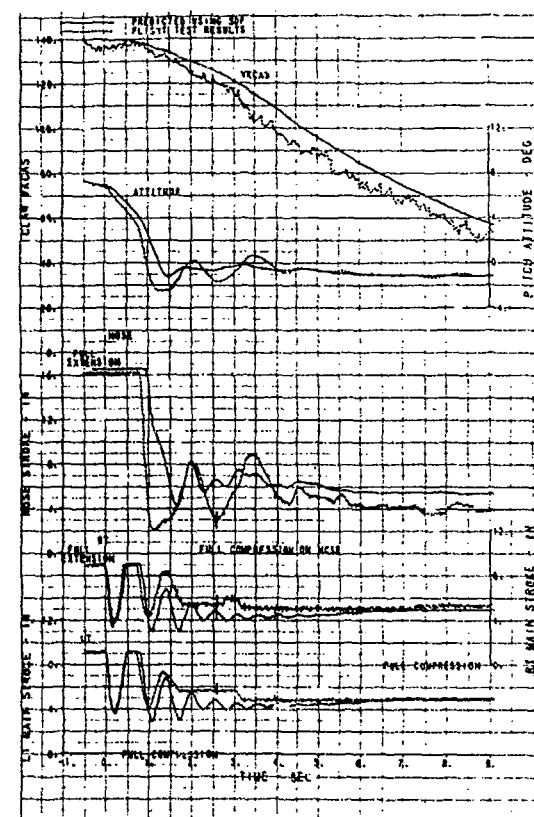


Figure 13. Enhanced Bounce Characteristics

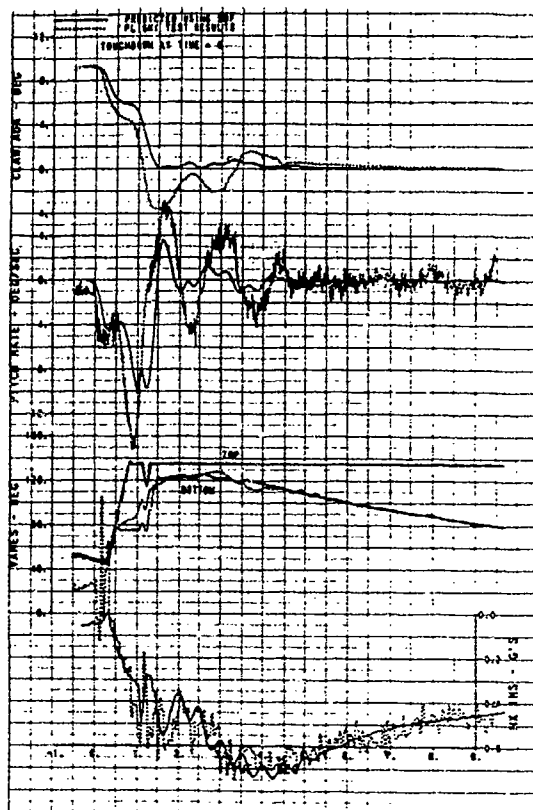


Figure 14. Flight Dynamics vs Prediction

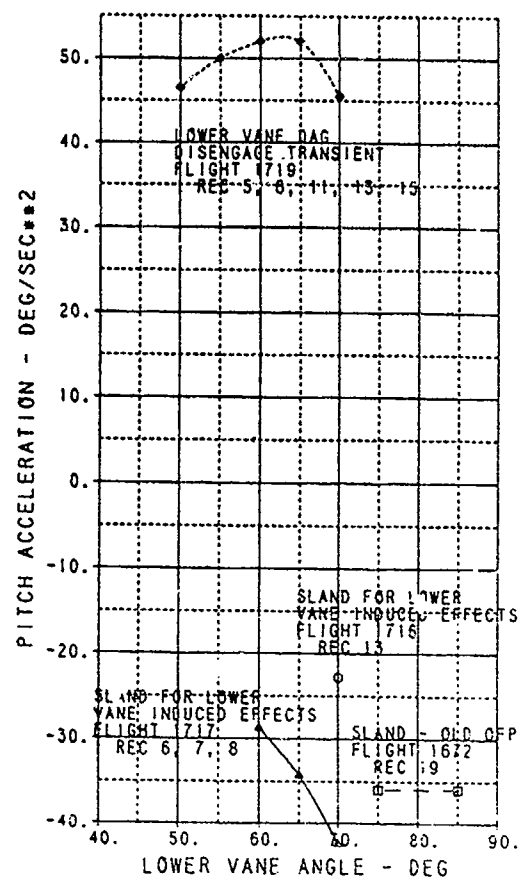


Figure 15. Pitch Acceleration Characteristics

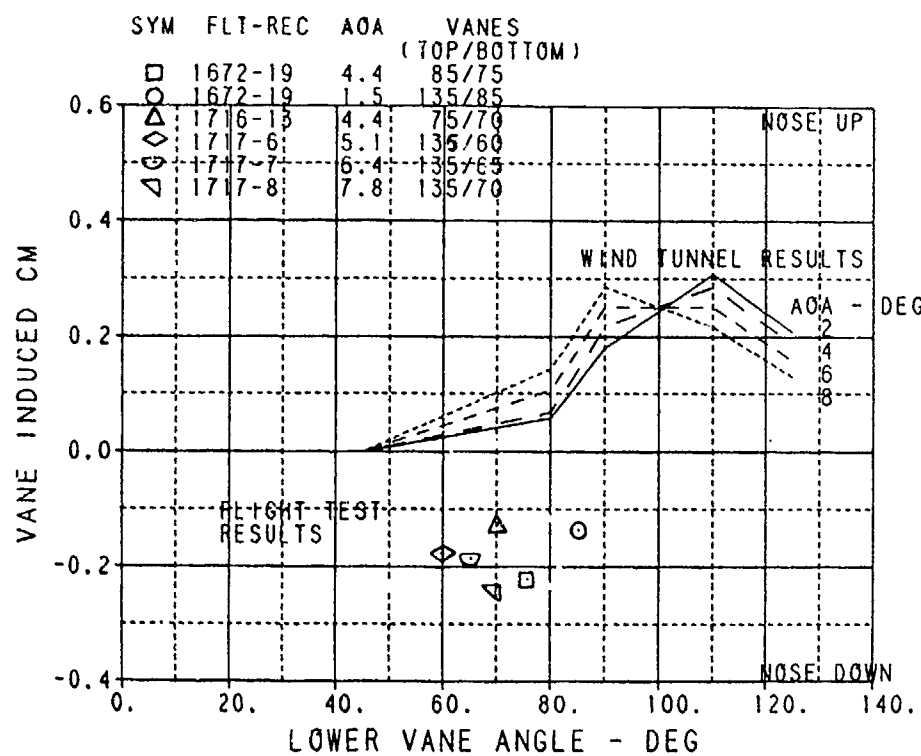


Figure 16. Flight and Wind Tunnel Induced Pitching Moments

TRANSITIONAL FLIGHT CHARACTERISTICS OF A GEOMETRICALLY SIMPLIFIED STOVL MODEL

Karlin R. Roth
NASA Ames Research Center
Mail Stop 247-2
Moffett Field, CA 94035-1000
USA

SUMMARY

The transitional flight characteristics of a geometrically simplified Short Take-Off Vertical Landing (STOVL) aircraft configuration were measured in the NASA Ames 7-by 10-Foot Wind Tunnel. The experiment was designed to provide detailed data for evaluating the capability of computational fluid dynamics methods to predict the important powered lift flow parameters. The model consists of a 60° cropped delta wing planform; a blended fuselage; and tandem, circular, high pressure air jets that exit perpendicular to the flat lower surface. Freestream Mach number is limited to a maximum of 0.2. Model angle of attack ranges from -10° to +20°. The nozzle pressure ratios of both jets are varied between 1 and 3, and the jet exit temperatures are maintained at near ambient conditions. Detailed surface pressure measurements show that suction pressure peaks located on the upper surface of the wing during conventional wingborne flight for angles of attack greater than 5° move to the wing lower surface at angles of attack less than 0°. A reduction in these suction pressure peaks is observed when the lift jets are operating. With sonic jet exit conditions, a freestream Mach number of 0.14, and 0° angle of attack, the jet-induced suckdown is equivalent to a 3.7° reduction in angle of attack. Schlieren, laser light sheet flow visualization and total pressure measurements in the jet plumes provide a description of the three-dimensional jet efflux flowfield.

LIST OF SYMBOLS

b	Wing span, 68.580 cm (27.000 in)
c	Model length, 76.200 cm (30.000 in)
C_L	Lift coefficient, $L/q_\infty S$
C_D	Drag coefficient, $D/q_\infty S$
C_p	Pressure coefficient, $(p - p_\infty)/q_\infty$
D	Drag, N (lbs)
D_j	Jet exit diameter, 3.048 cm (1.200 in)
L	Lift, N (lbs)
M	Mach number
NPR	Nozzle pressure ratio, p_t/p_j
p	Pressure, kPa (psf)
q	Dynamic pressure, kPa (psf)
S	Wing planform area, 29.61 square centimeters (3.19 square feet)
T	Thrust, N (lbs)
V_e	Effective velocity ratio, $(q_\infty/q_j)^{0.5}$
x, y, z	Cartesian coordinates with origin at the model nose-tip
α	Angle of attack, degrees
β	Yaw angle, degrees
ΔL	Jet induced suckdown load, N (lbs)

Subscripts

j	Denotes jet exit condition
t	Denotes stagnation condition
∞	Denotes freestream conditions

1. INTRODUCTION

During the transition from hover to wingborne flight, Short Take-Off and Vertical Landing (STOVL) aircraft rely on the direct thrust of lift jets to supplement the aerodynamic wing lift. The interaction of the lift jets with the flow over the airframe produces a complex, three-dimensional flowfield that impacts the overall aerodynamic performance of the aircraft¹. Thus, proper design of STOVL aircraft requires adequate understanding of the magnitudes and physics of the aerodynamic/propulsive interaction.

The present investigation of the transitional flight characteristics of a geometrically simplified STOVL aircraft is part of a combined computational and experimental program whose goal is to validate the Navier-Stokes flow code designated OVERFLOW² for powered lift applications. The computational approach builds on experience obtained from earlier computations of basic components of the powered-lift flowfield³⁻⁶. One of these component flows, the subsonic jet in crossflow, defined as a round jet exhausting perpendicularly through a flat plate into a crossflow, isolates the physics of the lower surface aerodynamic/propulsive interaction during transition flight. Navier-Stokes simulations⁴⁻⁶ of the jet in crossflow showed favorable agreement with measurements presented by Fearn and Weston⁷⁻¹⁰ for the jet trajectory, the properties of the contrarotating vortex pair and the pressure distribution on the planar surface surrounding the jet. Recent grid refinements and the addition of turbulence modeling to this model have improved its performance¹¹. Specifically, the refined computations capture small scale flow features such as the horseshoe vortex system upstream of the jet and achieve improved agreement of the plate pressure distribution in the region within two diameters of the jet exit.

The quality of the jet in crossflow results provided encouragement to extend the application to a representative STOVL aircraft. A geometrically simplified STOVL model was selected for testing and simulation. The model geometry, a cropped delta wing with a blended fuselage and tandem circular jets, minimizes geometric modeling complexity while retaining the lift-jet/aerodynamic-surface interaction physics. Closely coupled planning of the experiment and the computations provides a unique opportunity to critically assess the performance of the numerical model.

Computational fluid dynamics (CFD) solutions provide a detailed description of the flow, including the computational variables of density, the three components of momentum and the total energy, at finely spaced mesh points in the flowfield. To gain similar insight into the flow, experimental data used for comparisons must be consistent in form and detail with the CFD¹²⁻¹⁴. Hence, a powered lift CFD validation experiment must examine more than the traditional aerodynamic performance parameters such as total lift and drag. Measured boundary conditions, including precise model definition; upstream, downstream and wall conditions; and jet exit conditions are needed to initialize the computation. Next, flowfield measurements in critical locations, for example the decay rate of the jet core, are needed to verify the predicted flow physics. Finally, detailed measurements such as velocity and Reynolds stresses are needed to improve physical modeling techniques particularly in separated flow regions such as the wake of the lifting jets.

In this paper, descriptions of the model and test procedures are given. Selected measurements of the transitional flight characteristics of the STOVL aircraft configuration are reported. These results include aerodynamic force coefficients, surface pressures and jet exit and flowfield surveys. In addition, flow visualization is used to provide a partial description of the three-dimensional flow physics. Suitable validation requires comprehensive data which adequately characterizes a few representative test conditions. As a result, emphasis is placed on presenting the detailed flow data acquired with a freestream Mach number of 0.14, an angle of attack of 10° and sonic, ambient temperature jet exit conditions.

2. APPARATUS AND TECHNIQUES

2.1 Facility

The test was conducted in the NASA Ames 7- by 10-Foot Wind Tunnel Number 1. The facility is a closed test-section, single-return atmospheric tunnel with approximately 10% air exchange. A comprehensive description of the wind tunnel as well as flow quality data is presented in Reference 15. Test section blockage for the model and its support system is 2% at $\alpha = 20^\circ$.

2.2 Model Description

The STOVL configuration model consists of a numerically-defined flat-bottom airfoil shape with a cropped delta wing planform, a blended fuselage wing junction, and tandem circular jet nozzles which exit from the wing lower surface. The wing planform is similar to the STOVL E-7A configuration¹⁶ while the lift jets are representative of the high pressure ratio, small jet engines to be utilized on future STOVL aircraft. The leading edge radius varies smoothly from 2.54 mm (0.100 in) at the nose to 0.36 mm (0.014 in) at the wing tip. Rounded leading edges and smooth body contours minimize the geometric modeling complexity.

Views of the model from the top and side are sketched in Figure 1. The model has an overall length of 76.200 cm (30.000 in), a span of 68.580 cm (27.000 in), a leading edge sweep angle of 60.00° and a trailing edge sweep angle of -10.98° . The planform area for the wing, S , is 29.61 square centimeters (3.19 square feet). The top of the

model is a fiberglass shell which attaches to the aluminum bottom plate. The model is instrumented with 281 static pressure ports located on the model surface with 88 taps on the upper surface, 63 taps clustered radially around the front jet, 62 taps clustered radially around the rear jet and the remaining taps distributed on the lower surface.

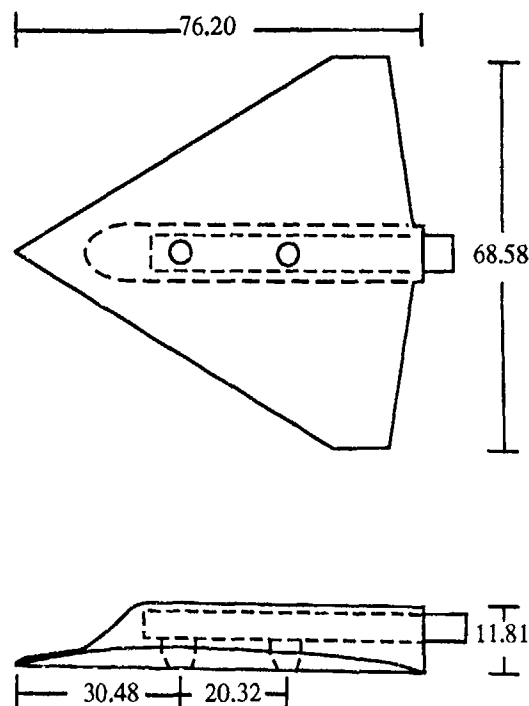


Fig. 1 STOVL CFD Model geometry. Top and side views. Dimensions are in centimeters.

The blended fuselage contains the plenum, an internal balance, two jet nozzles and six, 48- port electronically scanned pressure modules. Each of the jet nozzles has an exit diameter $D_j = 3.048$ cm (1.200 in), a length of 4.666 cm (1.837 in) and a contraction ratio of 1.417 to 1. Both jets exit perpendicular to the lower surface of the model. Perforated plates placed between the plenum and the nozzles help to provide uniform flow distribution at the nozzle exits. A Kiel probe with a co-located thermocouple is mounted in each of the nozzles to provide reference jet pressure and temperature data. The probe is located upstream of the nozzle contraction, approximately 0.6 jet diameters from the exit, and has a probe tip diameter of $0.079 D_j$. The jet exits are centered on the symmetry plane, $y/b = 0$. The upstream jet is at $x/c = 0.400$, and the downstream jet is at $x/c = 0.667$ measured from the front of the model to the center of the jet. Heated, high pressure air is supplied to the model plenum and ejected through the nozzles. The plenum and nozzles are designed so that the jet thrust is isolated from the internal force balance. The internal balance measures aerodynamic forces on the wing.

The model support system for installation in the 7- by 10-Foot Wind Tunnel is shown in Figure 2. The model support system is comprised of the internal plenum, the sting assembly and the vertical and horizontal supports. This system is attached to the existing 7- by 10-Foot Wind

Tunnel model supports. In this photograph, the model is mounted to the sting with the wing span oriented in the vertical direction. Measurements were also made with the wing inverted.

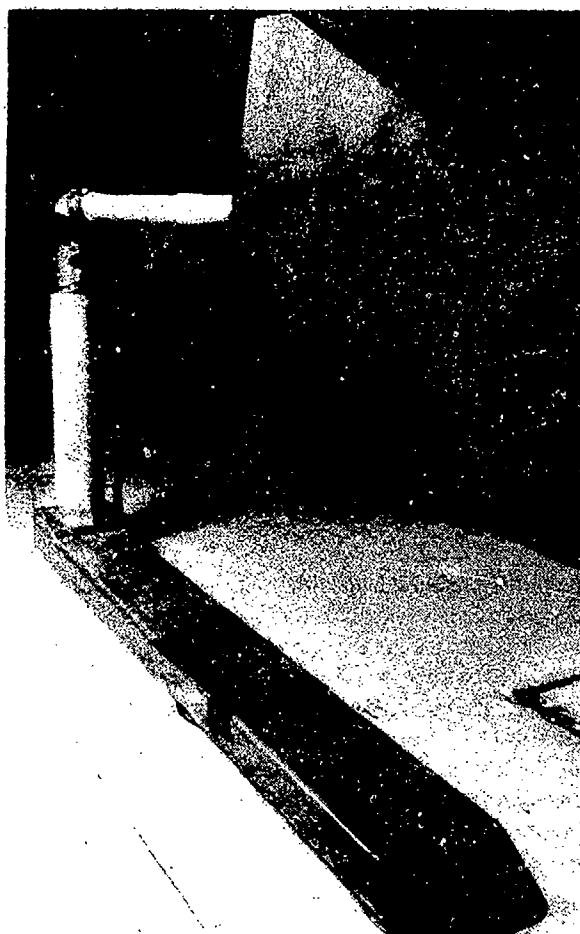


Fig. 2 Wing vertical installation in the 7-by 10-Foot Wind Tunnel.

2.3 Instrumentation and Data

2.3.1 Data System. A dedicated data acquisition system was used to simultaneously sample the 28 channels of analog test data and to acquire surface pressure data from the pressure measurement system. Data reduction was performed on the same computer.

2.3.2 Balance. Forces and moments were measured using an internal, 2.54 cm (1.00 in), six-component force balance. An accuracy of 0.5% of the full scale gauge limits was attained for the force and moment measurements. Gauge limits are 890 N (200 lbs) for normal, axial and side forces and 271 N-m (200 ft-lbs) for rolling moment.

2.3.3 Pressures and Temperatures. The electronically scanned pressure modules and all pressure tubing for the 281 surface pressure ports were internal to the model. Calibrations showed the electronically scanned pressure modules were accurate to 0.1% full scale. The transducers

used ranged from 2,491 kPa (10 inches of water) in the expected low pressure regions to 17.24 kPa (2.5 psi) transducers in the regions near the jet exits.

All nozzle pressure measurements were made using 690 kPa (100 psia) pressure transducers. Nozzle temperatures were measured using 38°C (100°F) copper constantin thermocouples.

A five-hole directional pressure probe instrumented with 6.895 kPa (1,000 psid) pressure transducers and a micropitot probe instrumented with a 690 kPa (100 psia) pressure transducer were used for flow surveys. Both probes were positioned using a three-axis, remotely-controlled survey apparatus. Positioning accuracy for the probes was ± 0.3 mm (± 0.01 in) for the nozzle surveys and ± 1.3 mm (± 0.05 in) for boundary condition surveys across the test section. Calibration of the five-hole probe showed that flow angularity measurements were accurate to approximately $\pm 0.5^\circ$.

2.3.4 Laser. A three-dimensional orthogonal laser system was developed and utilized for laser light sheet and schlieren flow visualization during the transitional flight test. Optical access is provided from the top and both sides of the test section.

3. RESULTS AND DISCUSSION

Force and pressure measurements for the STOVL model over a range of angles of attack were acquired for approximately 30 combinations of freestream Mach number and jet nozzle pressure ratio (NPR). These measurements were made with the model wing oriented vertically in the test section. Ambient temperature was maintained at the jet exits for all measured conditions. The range of the test parameters is summarized in Table 1.

Table 1 also outlines a particular set of flow conditions selected for detailed flow measurement and future CFD simulation. The detailed measurements were acquired with the model wing inverted in the test section. Specifically, this case, which represents decelerating transition or short landing conditions, has both jets operating with a 10.0° angle of attack, a freestream dynamic pressure of 1.44 kPa (30.0 psf) and a NPR of approximately 1.9. At $\alpha = 10^\circ$, wing vortices are located on the upper surface. For $q_\infty = 1.44$ kPa (30.0 psf), or equivalently $M_\infty = 0.14$, the convergence rate for the OVERFLOW algorithm is not significantly affected by low freestream speeds. Finally, for NPR greater than or equal to 1.89, the jets are choked at the exits. This simplifies jet exit boundary conditions since the flow in the nozzle, upstream of the sonic jet exit is unaffected by the external flowfield. At these conditions, the effective velocity ratio, V_e , which is the dominant parameter for the jet flow, is approximately 0.15 for the front jet and 0.14 for the rear jet. Jet penetration into the crossflow is not affected by the presence of the tunnel walls for these velocity ratios.

Table 1. Test Parameters.

VARIABLE	RANGE	DETAILED CASE
Number of jets	0, 1 or 2	2
Angle of attack, α	-10° to $+20^\circ$	$+10^\circ$
Yaw, β	0° to 5°	0°
Freestream dynamic pressure, q_∞	0.48 kPa to 2.39 kPa	1.44 kPa
Freestream Mach number, M_∞	0.08 to 0.18	0.14
Nozzle pressure ratio, NPR	1.0 to 3.3	1.9 (Front nozzle) 2.0 (Rear nozzle)
Effective velocity ratio, V_e	0, 0.05 to 0.32, ∞	0.15 (Front nozzle) 0.14 (Rear nozzle)

3.1 Lift-Jet Impact on Vehicle Performance

3.1.1 Thrust Measurements. An independent nozzle calibration test was conducted to measure the jet thrust. For calibration, the plenum and nozzles were mounted on a static calibration stand. Forces and moments were measured using a 3.81 cm (1.50 in) six-component force balance. The accuracy for these measurements is 0.5% of the full scale gauge limits; gauge limits are 2224 N (500 lbs) for normal force, 1334 N (300 lbs) for axial force (thrust direction), 1112 N (250 lbs) for side force and 91 N-m (67 ft-lb) for rolling moment. Thrust is plotted versus the reference nozzle pressure ratio of the rear jet in Figure 3. Reference NPR is based on the Kiel probe pressure measurement within the nozzle. In the figure, data plotted from two different runs demonstrates the repeatability of the thrust measurement. In addition, small changes in the high pressure air temperature (ambient $\pm 5^\circ\text{F}$) do not significantly affect the measurement.

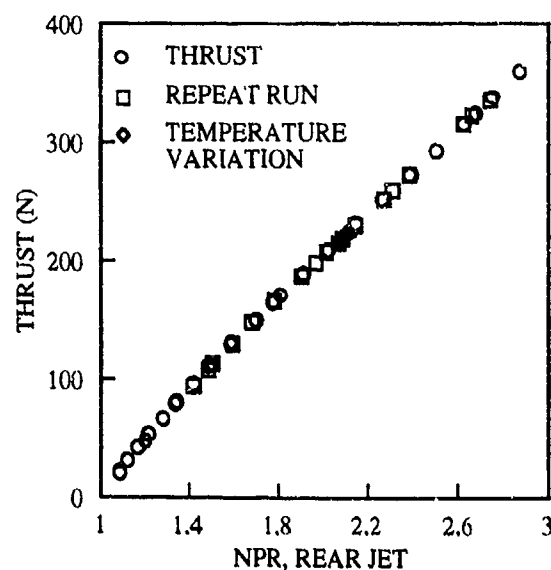


Fig. 3 Jet thrust measured on calibration stand.

Due to the pressure drop within the plenum between the front and rear jet offtakes, for all measured conditions the rear jet supplies a greater percentage of the total thrust. When the front jet is choked, $\text{NPR} = 1.9$, the rear jet is underexpanded with $\text{NPR} = 2.0$. At this condition, a total of 209 N (47 lbs) of thrust is generated by the two jets with the rear jet supplying 53.5% of the total thrust. This thrust imbalance between the front and rear jet varies with pressure. Throughout this paper, results are referenced to the rear nozzle conditions.

3.1.2 Forces and Moments. Integrated aerodynamic performance parameters including lift and drag globally characterize aircraft performance even though they do not provide detailed insight into the flow physics. For example, total lift nondimensionalized by thrust, L/T , is plotted as a function of the effective velocity ratio for the rear jet in Figure 4. All data in the figure is for $\alpha = 10^\circ$ and rear jet $\text{NPR} = 2.0$. Total lift includes the aerodynamic wing lift, L_{wing} , suckdown loads from the jet induced lift loss, ΔL , and the component of jet thrust in the lift direction, $T \sin(90^\circ + \alpha)$. Aerodynamic wing lift is defined as the lift generated by the wing under the same flight conditions without lift jets. Measured lift includes the aerodynamic wing lift and suckdown. Thus,

$$L/T = (L_{\text{wing}} + \Delta L)/T + \sin(90^\circ + \alpha)$$

For comparison, an ideal curve, constructed using the wing lift measured with jets off and the thrust at the corresponding jets-on condition, is plotted in Figure 4. Clearly, the jets induce a lift loss on the wing, and the lift loss increases with the freestream dynamic pressure. Examination of the data for $V_e = 0.14$ demonstrates the agreement between data acquired with the wing vertical and with the wing inverted. A similar jet induced lift loss is reported by Kuhn and Stewart¹⁷ for a flat-plate model having the identical planform, nozzle and plenum design as the STOVL configuration used in this investigation.

The strong effect of the jet-induced suckdown is shown in Figure 5 where L/T is plotted for angles of attack between

-10° and $+20^\circ$. For this data, NPR was set to 2.0 at the rear nozzle. For the jet off case, there is practically no lift, $C_L = 0.05$, when $\alpha = 0^\circ$. This suggests that L/T would be slightly above unity with operational jets; however, for both jets operating, $L/T = 0.76$ at $\alpha = 0^\circ$. This loss of lift is due to the suckdown induced by the jets ($\Delta L/T$) and is equivalent to a 3.7° reduction in angle of attack.

Drag polars are presented in Figure 6 with and without the lift jets. A comparison of the total lift and drag with the measured forces on the wing excluding the lift and drag increments due to thrust is also made for the jets-on case. The total lift and drag increase with jets on for positive angles of attack; total lift increases and drag decreases at negative angles of attack. At increased lift coefficients, the horizontal component of thrust contributes the deceleration increment to the drag coefficient. The STOVL configuration model has a minimum drag at $\alpha = 1^\circ$ without jets and at $\alpha = -3^\circ$ with jets.

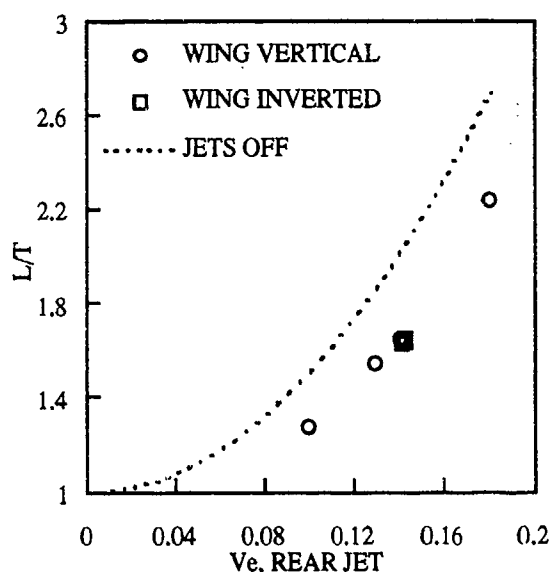


Fig. 4 Influence of effective velocity ratio variation on lift. $\alpha = 10^\circ$, rear jet NPR = 2.0

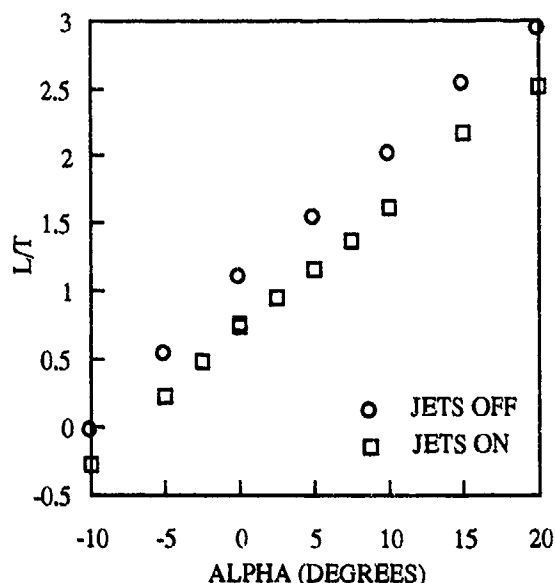


Fig. 5 Jet-induced lift loss. $q_\infty = 1.44$ kPa (30.0 psf), rear jet NPR = 2.0

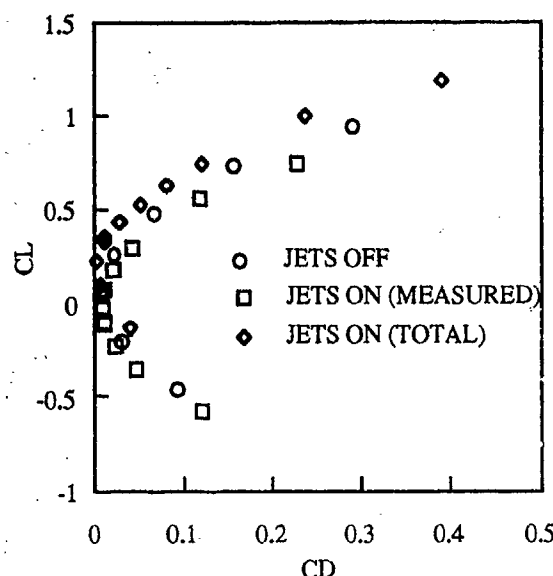


Fig. 6 Drag Polars. $\alpha = 10^\circ$, $q_\infty = 1.44$ kPa (30.0 psf). Rear jet NPR = 2.0 for jets on.

3.1.3 Surface Pressures. The surface pressure distribution provides a more useful measurement for comparison with CFD than the integrated aerodynamic coefficients because specific flow features can be identified. Upper and lower surface pressure distributions are presented in Figures 7 through 10. In each plot, data is for the detailed case identified in Table 1.

High suction pressure peaks are located on the upper surface of the vehicle with jets off for angles of attack greater than 5° . These suction peaks move to the lower surface at decreased angles of attack. In Figure 7, a series of pressure coefficient plots for the upper surface with $\alpha = 10^\circ$ at stations $x/c = 0.267, 0.400, 0.533, 0.667$ and 0.800 shows the impact of the lift jets on the leading edge suction. At the forward most station, $x/c = 0.267$, which is ahead of the front jet, no jet-induced effects on the suction pressure are present. All other stations show that the leading edge suction pressure is reduced by the jets. The greatest magnitude of the leading edge suction pressure is in the vicinity of the front jet. Aft of the rear jet, the suction is slightly reduced and the jet induced effects are decreased. Pressure measurements along the upper surface symmetry plane, $y/b = 0$, show almost no influence of the jets (Figure 8).

Lower surface pressure distributions taken with spanwise cuts through the center of each jet and with a chordwise cut taken through both jets in the symmetry plane are plotted in Figures 9 and 10. During conventional wingborne flight (jets off) the lower surface pressures are nearly equal to the freestream static pressure. In contrast, during powered-lift flight, the jets induce higher pressures upstream and lower pressures to the side and downstream of the jets. Notably, the suckdown effects are stronger near the front jet than near the rear jet. Trends of the pressure distribution near the jets agree with the data presented by Kuhn and Stewart¹⁷ as well as with previous experimental studies of two jets exiting from a flat plate, for example References 18 and 19.

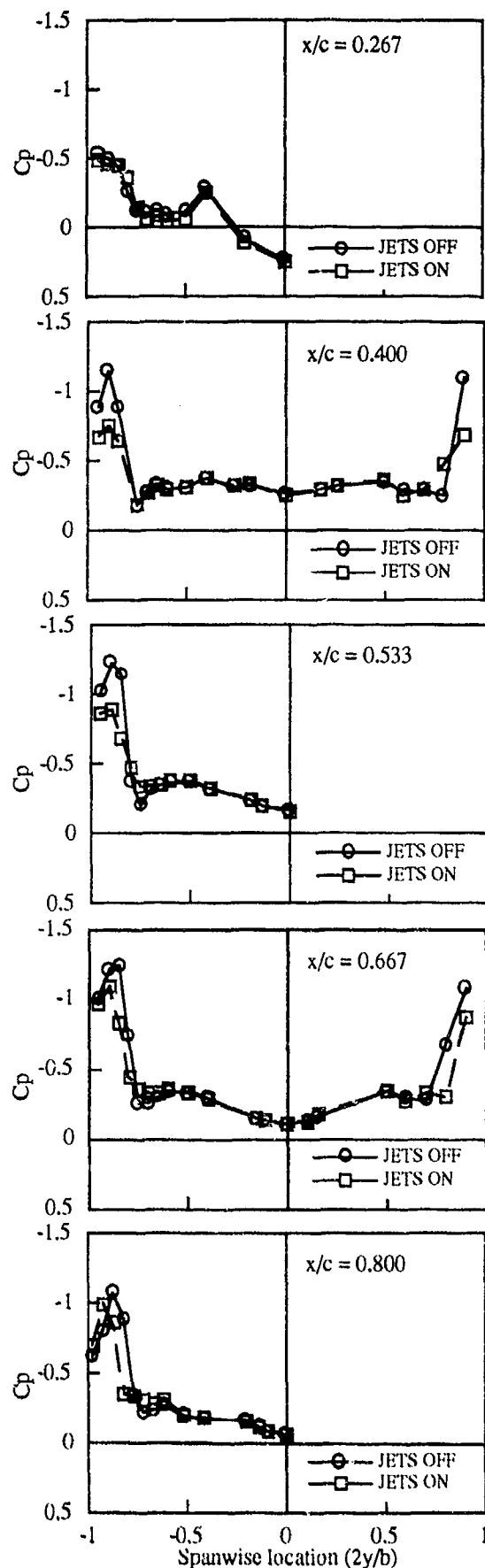


Fig. 7 Upper surface pressure distribution. $\alpha = 10^\circ$, $q_\infty = 1.48$ kPa (30.9 psf). Rear jet NPR = 2.0 for jets on.

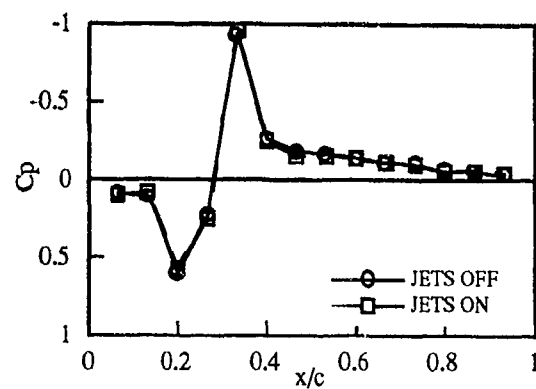


Fig. 8 Upper surface pressure distribution in the symmetry plane. $\alpha = 10^\circ$, $q_\infty = 1.48$ kPa (30.9 psf). Rear jet NPR = 2.0 for jets on.

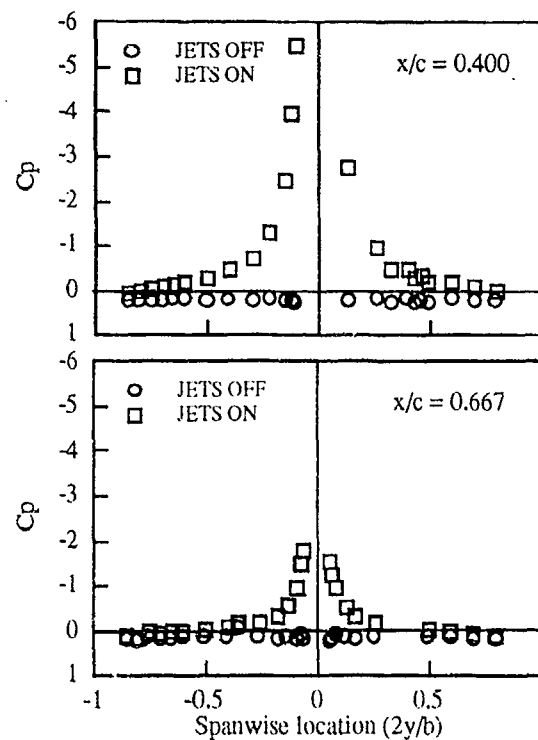


Fig. 9 Lower surface pressure distribution. $\alpha = 10^\circ$, $q_\infty = 1.48$ kPa (30.9 psf). Rear jet NPR = 2.0 for jets on.

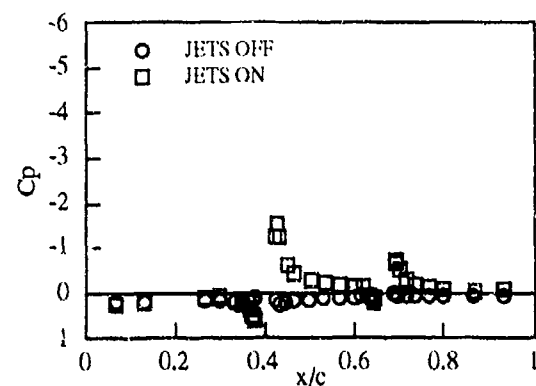
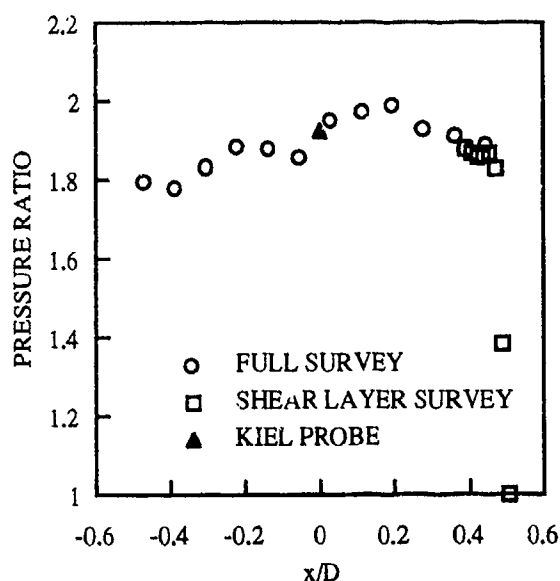


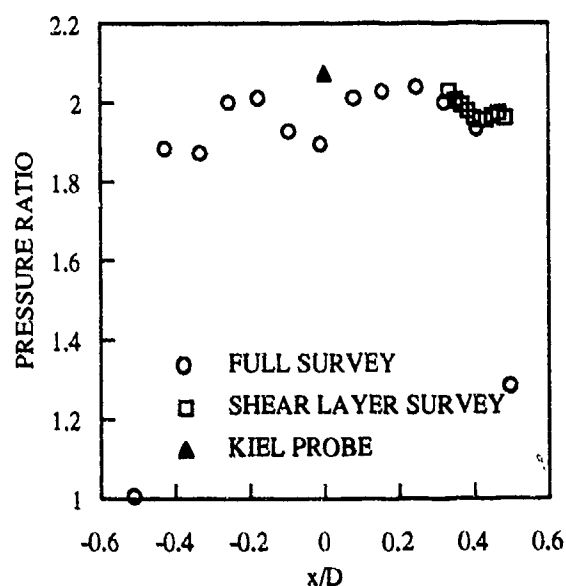
Fig. 10 Lower surface pressure distribution in the symmetry plane. $\alpha = 10^\circ$, $q_\infty = 1.48$ kPa (30.9 psf). Rear jet NPR = 2.0 for jets on.

3.2 Lift-Jet Characteristics

3.2.1 Jet Exit Conditions. Correct specification of the jet exit boundary conditions is critical for computation of powered lift flows. As a minimum, two thermodynamic variables and one dynamic variable, for example, total pressure, temperature and the velocity profile, must be input to the OVERFLOW code. Often, these parameters are not available from experiments and create uncertainty in the code verification process. In this experiment, total pressure surveys in the plane of the jet exit were made to verify the reference pressures measured with the nozzle Kiel probes. The surveys were made at static tunnel conditions. Measurements were taken in a rectangular grid that was dimensioned by D_j and centered at the origin of each nozzle. Spacing between measurements was held at a constant $0.083 D_j$ (2.54 mm or 0.10 in).



a) Front nozzle.



b) Rear nozzle.

Fig. 11 Nozzle exit pressures in the symmetry plane.

The pressure ratios for the symmetry plane surveys of the front and rear jets are plotted in Figure 11(a) and (b). For each jet, the reference Kiel probe measurement is plotted at $x/D_j = 0$. Finely spaced measurements near the edge of the jet shear layer at the aft side of each nozzle are also presented. Both jets exhibit nonuniform total pressure profiles. The nonuniformities in the exit pressure distribution are attributed to the presence of the nozzle Kiel probe as well as to internal flow disturbances due to the plenum geometry. Additional jet exit data is reported in Reference 20.

3.2.2 Schlieren Visualization with No Crossflow. During the nozzle calibration, color schlieren photographs were taken of the jets with no crossflow for nozzle pressure ratios between 1 and 3. Figure 12 is a schlieren photograph taken with the rear jet at $NPR = 2.0$. In this photo, the STOVL model shell is removed and the model plenum is mounted on the calibration stand. The jets exhaust upward with the front jet located on the left. No shocks are visible in the front jet which has a reference $NPR = 1.9$ while the rear jet is characterized by shock patterns. Thus, the flow visualization confirms the nozzle instrumentation readings. Furthermore, the photograph shows that the jet core for the front jet extends approximately 5 jet diameters from the exit and the rear jet core extends slightly farther. Also, at distances of 1, 2 and 4 jet diameters from the exit, the jet plume has spread to approximately 1.4, 1.8 and 2.2 jet diameters. Each of these features was quantified using total pressure measurements of the jet plumes.

3.2.3 Schlieren Visualization with Forward Flight. Flow visualization also provides a qualitative description of the three-dimensional flowfield with two jets exhausting into a crossflow. A black and white schlieren photograph of the jets with $\alpha = 10^\circ$, $q_\infty = 1.47$ kPa (30.7 psf), rear jet $NPR = 2.0$ and front jet $NPR = 1.9$ is presented in Figure 13. As before, the front jet is to the left. The flat surface seen at the top of the photograph is the lower surface of the STOVL model. Flow from the front jet exhausts into the crossflow and is deflected by it. The trajectory of the front jet is quite similar to the trajectory for a single jet in crossflow with an effective velocity ratio of 0.15. Comparison with the front jet shows that the rear jet penetrates further into the flow before it is deflected. There are two reasons for this behavior. First, the rear jet has a lower effective velocity ratio ($V_e = 0.14$). In addition, it is partially shielded from the freestream by the front jet. Thus, the rear jet actually sees a dynamic pressure that is less than freestream.

Vertical, tornado-like vortices were observed in the wakes of both the front and rear jets and appeared to move downstream. These vortices are apparent in the wake of the front jet in the photograph presented in Figure 13. Although visualization of these vortices was somewhat random, they were observed in schlieren photographs for all jet nozzle pressure ratios tested. Similar wake vortices were observed in water tunnel flow visualization of a delta wing configuration with tandem jets²¹ which resembles the STOVL configuration studied in this test. Wake vortices were also observed in water tunnel flow visualization of a single jet in crossflow²²⁻²³. It is believed that the wake vortices evolve from the reorientation of boundary-layer vorticity at the sides of the

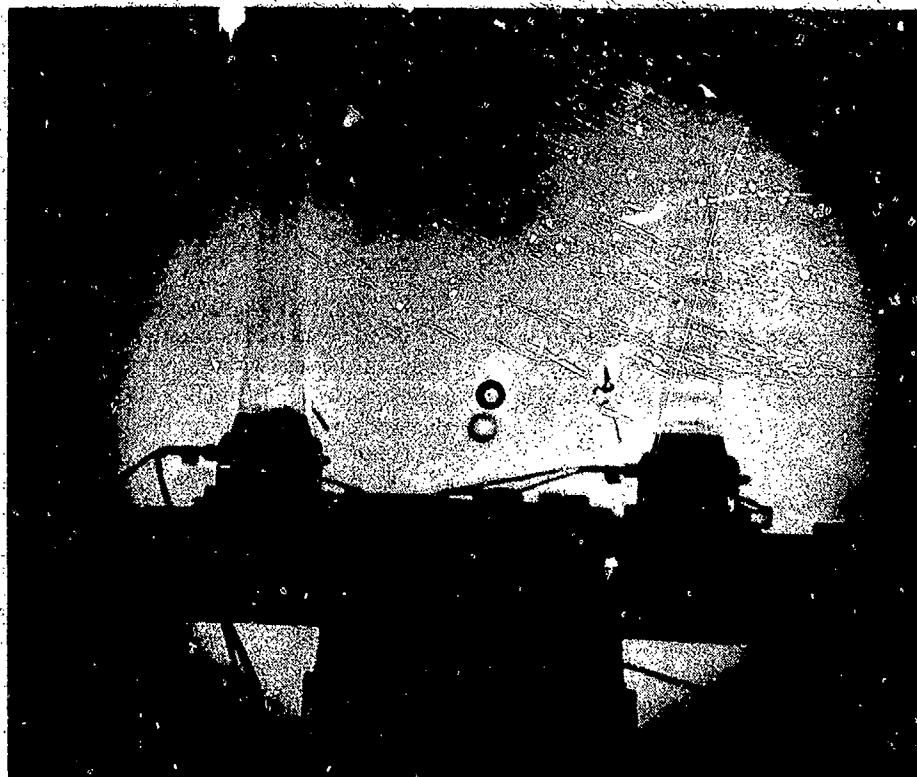


Fig. 12 Schlieren photo of jets on the thrust calibration stand. $q_\infty = 0.0$ kPa Front jet NPR = 1.9 and rear jet NPR = 2.0

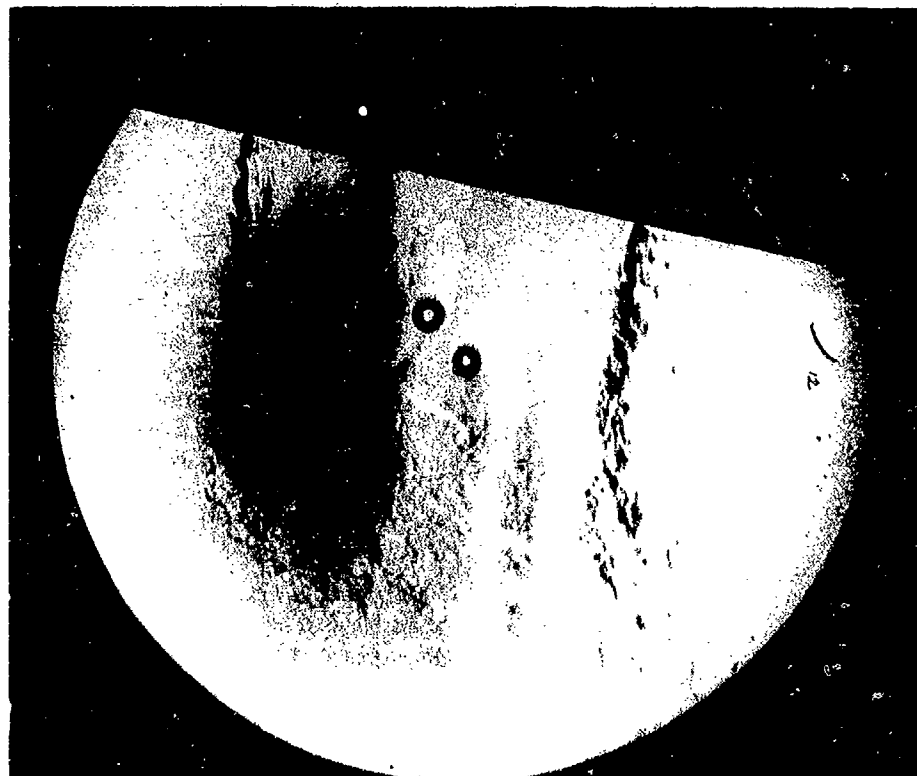


Fig. 13 Schlieren photo of model with jets exiting from the lower surface into the crossflow. $\alpha = 10^\circ$, $q_\infty = 1.47$ kPa (30.7 psf). Front jet NPR = 1.9, and rear jet NPR = 2.0



(a) Origin of front jet.



(b) Midway between front and rear jets.



(c) Origin of rear jet.

Fig. 14 Laser light sheet photos taken in a plane perpendicular to the freestream from downstream of the model. $\alpha = 10^\circ$, $q_\infty = 0.48$ kPa (10.1 psf). Front jet NPR = 1.3 and rear jet NPR = 1.4

jet exit and that stretching of the vorticity field, particularly in the vertical direction behind the jet, produces the concentrated vertical vortices. The impact of this unsteady phenomena on the aircraft flight performance is unknown.

3.2.4 Laser Light Sheet Visualization. Cross-sections of the jet plumes were visualized using a laser light sheet oriented perpendicular to the freestream. Three light sheet planes, positioned at the center of the front jet exit ($x/c = 0.400$), midway between the front and rear jets ($x/c = 0.533$) and at the center of the rear jet exit ($x/c = 0.667$), were used. The flow was visualized with the model at $\alpha = 10^\circ$. Photographs with a 1/15 second exposure time were taken from a location downstream of the model. For the light sheet visualization, smoke was introduced into the flow from a tube located in the settling chamber upstream of the test section. In order to provide a relatively even smoke distribution in the test section, the freestream dynamic pressure was limited to 0.5 kPa (10 psf). The photographs presented in Figure 14 (a) to (c) were taken with $q_\infty = 0.48$ kPa (10.1 psf), front jet NPR = 1.3 and rear jet NPR = 1.4. These conditions provide effective velocity ratios of 0.14 and 0.11 for the front and rear jets respectively. For comparison with the aerodynamic performance data presented for the detailed case, this condition gives $L/T = 1.36$, $C_L = 0.24$ and $C_D = 0.04$. Figure 14 (a) shows evidence of the front jet penetrating into the freestream. In Figures 14 (b) and (c), the existence of the contrarotating vortex pair in the plume of the front jet is established.

4. CONCLUSIONS

Measurements for a generic STOVL configuration were made in the NASA Ames 7- by 10-Foot Wind Tunnel. The effect of the effective jet velocity ratio and the model attitude on the vehicle performance was determined using the measurements of jet thrust, model forces and surface pressures. For conventional wingborne flight, suction pressure peaks are located on the upper surface of the wing for angles of attack greater than 5° and move to the wing lower surface at angles less than 0° . The magnitude and location of the leading edge suction pressures are affected by the lift jets. With sonic jet exit conditions, a freestream Mach number of 0.14 and a 0° angle of attack, the jet-induced suckdown is equivalent to nearly a 4° reduction in angle of attack. Force measurements, detailed pressures and flowfield data combine with the flow visualization to provide a database that is well-suited for the development and validation of powered-lift computational algorithms.

5. REFERENCES

- ¹Margason, R. J. and Kuhn, R. E., "Application of Empirical and Linear Methods to VSTOL Powered-Lift Aerodynamics," SAE Paper 872341, Dec. 1987.
- ²Renze, K. J., Buning, P. G. and Rajagopalan, R. G., "A Comparative Study of Turbulence Models for Overset Grids," AIAA Paper 92-0437, Jan. 1992.
- ³Van Dalsem, W. R., "Study of Jet in Ground Effect with a Crossflow Using the Fortified Navier-Stokes Scheme," AIAA 87-2279-CP, Aug. 1987.

⁴Roth, K. R., Fearn, R. L. and Thakur, S. S., "Evaluation of a Navier-Stokes Prediction of a Jet in a Crossflow," *J. Aircraft*, Vol. 29, No. 2, pp. 185-193, Mar.-Apr., 1992.

⁵Roth, K. R., "Influence of the Thin-Layer Approximation on Jet in Crossflow Computations," AIAA Paper 90-3056, Aug. 1990.

⁶Roth, K. R., Fearn, R. L. and Thakur, S. S., "A Numerical Study of the Contrarotating Vortex Pair Associated with a Jet in a Crossflow," AIAA Paper 88-0448, Jan. 1988.

⁷Fearn, R. L. and Weston, R. P., "Vorticity Associated with a Jet in a Crossflow," *AIAA J.*, Vol. 12, No. 12, Dec. 1974, pp. 1666-1671.

⁸Fearn, R. L. and Weston, R. P., "Induced Pressure Distribution of a Jet in a Crossflow," NASA TN D-7616, July 1975.

⁹Fearn, R. L. and Weston, R. P., "Induced Velocity Field of a Jet in a Crossflow," NASA TP-1087, May 1978.

¹⁰Fearn, R. L. and Weston, R. P., "Velocity Field of a Round Jet in a Crossflow for Various Jet Injection Angles and Velocity Ratios," NASA TP-1506, Oct. 1979.

¹¹Chiu, S., Roth, K. R., Margason, R. J. and Tso, J., "A Numerical Investigation on a Subsonic Jet in Crossflow", accepted for the AIAA 31st Aerospace Sciences Meeting, Reno, NV, Jan. 1993.

¹²Bradley, R. G., "CFD Validation Philosophy," Paper No. 1, AGARD CP-437, Vol. 1, *Validation of Computational Fluid Dynamics*, May 1988, Lisbon, Portugal.

¹³Marvin, J. G., "Accuracy Requirements and Benchmark Experiments for CFD Validation," Paper No. 2, AGARD CP-437, Vol. 1, *Validation of Computational Fluid Dynamics*, May 1988, Lisbon, Portugal.

¹⁴Marvin, J. G. and Holst, T. L., "CFD Validation for Aerodynamic Flows -- Challenge for the '90's," AIAA Paper 90-2995, Aug. 1990.

¹⁵Wadcock, A., "The NASA Ames 7-Foot by 10-Foot Wind Tunnel -- Present Flow Quality and Recommendations for Improvement," Analytical Methods Report 8705, July 1987.

¹⁶Foley, W.H., Sheridan, A.E. and Smith, C.W., "Study of Aerodynamic Technology for Single-Cruise Engine V/STOL Fighter/Attack Aircraft," NASA CR-166268, Feb. 1982.

¹⁷Kuhn, R. E. and Stewart, V. R., "Effect of Forward Speed and Jet Arrangement on Jet Induced Suckdown and Fountain Effects," KSA Report 92-2, Apr. 1992.

¹⁸Schetz, J. A., Jakubowski, A. K. and Aoyagi, K., "Surface Pressures Induced on a Flat Plate with In-Line and Side-by-Side Dual Jet Configurations," AIAA Paper 83-1849, July 1983.

¹⁹Fricke, L. B., Wooler, P. T. and Ziegler, H., "A Wind Tunnel Investigation of Jets Exhausting into a Crossflow," Vol. 1, AFFDL-TR-70-154, Dec. 1970.

²⁰Roth, K. R., "A Powered Lift Experiment for CFD Validation," AIAA Paper 91-1731, June 1991.

²¹Miller, L. S., Papadakis, M. and Klausmeyer, S., "Flow Visualization for a STOVL Aircraft in Ground Proximity," AIAA Paper 91-0769, Jan. 1991.

²²Fric, T. F. and Roshko, A., "Structure in the Near Field of the Transverse Jet," 7th Symposium on Turbulent Shear Flows, Aug. 1989.

²³Shi, Z., Wu, J. M. and Wu, J. Z., "Symmetric and Asymmetric Jets in a Uniform Crossflow," AIAA Paper 91-0722, Jan. 1991.

EFFECTS OF FREE-STREAM TURBULENCE ON A JET IN A CROSS FLOW

T.H. Toften

A.E. Holdo

D. Kapfer

University of Hertfordshire

Aeronautical Dept.

Hatfield Herts AL10 9AB, U.K.

1. SUMMARY

At present there is limited information available on effects of free-stream turbulence intensities and scale on both the time average and instantaneous development of a jet in a cross flow. The aim of this study was to investigate such effects on both entrainment and mean path of the jet using primarily experimental methods.

The experimental part consisted of measurements using hot wire anemometers, thermocouples and a nine hole vortex probe as well as observations with a colour Schlieren system on a jet issuing from a circular aperture in a flat plate. The jet Reynolds numbers of the tests were in the region 2×10^4 – 8×10^4 and the flow could be considered as incompressible for all cases tested.

The use of both a visualisation technique as well as quantitative measurements have proven to be helpful in the description of free-stream turbulence effects. Although it should be noted that some quantitative data can be inferred from the Schlieren observations.

The results show that there are clear effects due to variations in free-stream turbulence on the development of the jet. The effects within the range of variation in free-stream turbulence intensity and length scale of the investigation are manifest in terms of all main jet characteristics. These characteristics are the rate of entrainment, the mean jet path and the strength of the main jet vortices.

The observed effects are significant, but at present there are no direct trends in the results with increasing or decreasing turbulence scales or intensity to help propose the primary mechanisms involved in the effects. This is the subject of further investigations at the present time.

2. INTRODUCTION

There are many cases of practical interest when the free-stream turbulence intensity of the cross flow is high and when the corresponding turbulence length scales are larger than the exit diameter of the jet. Typical examples are jets exposed to atmospheric wind only, and jets entering wake or share layer regions. The first case is possibly only of limited significance for vertical take off and hovering, but the second case may well take place during manoeuvring of an aeroplane and could be important.

A jet in a cross flow is a combination of an undisturbed jet flow and a wake. For a jet in calm ambient the entrainment rate is changing with the turbulence

intensity, which have been shown by many authors [10]. The free-stream turbulence alter the shape of the share layer in a wake flow. Hence, different turbulence scale and intensity in both the jet exit and the free-stream should could a change in the development of a jet in a cross flow.

Effects due to free-stream turbulence have been observed on bluff bodies by several investigators. The effect of turbulence has been manifest through changes in the base pressure [3][6]. Variations from high to low turbulence intensity has altered the base pressure of rectangular shaped prisms as much as 75%. An explanation of these effects have been offered by Hunt [5]. His theory suggests that the effect is primarily due to stagnation line turbulence and its effect on separated share layer turbulence and consequently the share layer curvature.

Earlier investigations of jets in a cross flow has been performed under different conditions of free-stream turbulence, like field studies in the atmosphere, laboratory studies in different type of wind tunnels and water tanks. In the literature the results from many of these observations deviates for drag and entrainment which have not been estimated explicitly taking the effect of free-stream turbulence into account. The effects of increased free-stream turbulence intensity reported by Wark and Foss [8] are less penetration and more unsteady behaviour of the jet. Ramsey and Goldstein [7] states intermittence of the flow, and anisotropy in the turbulence structure has been reported by Crabb, Durão and Whitelaw [4].

At present there is limited information available on effects of free-stream turbulence in the cross flow on both the time average and instantaneous development of jets in a cross flow with varying turbulence intensities and scale. The aim in the study was to investigate such effects on both entrainment and mean path of the jet using primarily experimental methods.

3. APPARATUS AND SYSTEM SET-UP

3.1 The Test Rig

The test rig used in the experiments consisted of a plate, a nozzle and an air supply system. The plate was placed on the floor of an open return wind tunnel with the nozzle mounted flush with the plate surface and perpendicular to the cross flow. The low speed wind tunnel had a working section of 1250x1555mm (HxW).

The aluminium plate 20x764x1525mm (HxWxL) was machined 15° underneath to have a sharp leading edge. The upper surface had a polished finish and was slightly curved at the leading edge to avoid separated flow. The plate was supported on four adjustable legs about 100mm above the floor of the wind tunnel. The results from initial measurements has shown good agreement with the logarithmic boundary layer theory [14].

The aluminium nozzle was shaped to minimise the jet exit velocity profile, and had an outlet diameter (D) of 30mm. It was located on the plate symmetry line 220mm downstream the leading edge, as shown in figure 1. The nozzle was mounted flush with the upper plate surface without touching the plate. In the small gap at the surface a thin layer of insulating smooth filling was used, and the larger gap underneath was ventilated by the cross flow to avoid heat transfer. A thermocouple was placed inside the nozzle to measure the jet exit temperature. The results from initial measurements has shown a flat uniform profile at the jet exit with a nearly constant turbulence intensity of 1.5% for all exit velocities used [14].

The air supply system comprised of a centrifugal fan with a 3" valve to adjust the flow rate. The fan was connected to a heater-box built by welded steel plates and an ordinary cooker-element. A calibrated flow nozzle was located between the fan and the heater-box to measure the flow rate. All connections were made using insulated 2" steel pipes.

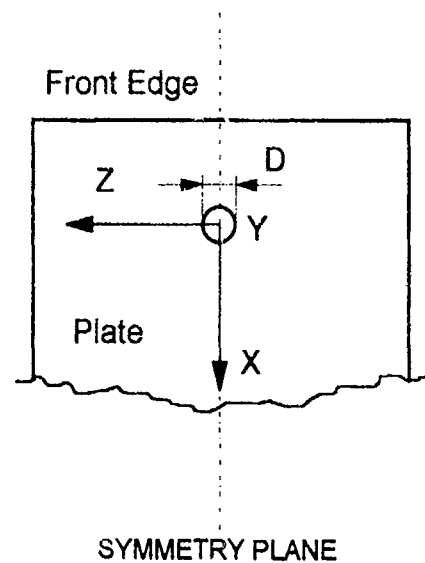


Figure 1.
The test rig.

3.2 Hot Wire Instrumentation

A standard 5µm tungsten single hot wire connected to a DISA 55M10 CTA-bridge and DISA 55M01 main unit was logged on a PC using an analogue to digital (A-D) converter and PCLAB software. A DISA 55D25 Auxiliary unit was used to low pass filter the signals at 1kHz and give suitable voltage offset for the A-D converter. The hot wire was logged at 2kHz using 12288

samples with a resolution of 4096 digital steps in a range of 2.5V. Calculation of velocities were performed in a subroutine based on calibration data to allow measurements in the full range down to zero. The system error estimated using this technique was less than 2% for the mean velocity.

3.3 The Vortex Probe

An eight hole vortex probe was constructed and calibrated following the concept of Freestone [1]. The probe was built of eight 45° cut medical hypodermic needles with an outer diameter of 0.5mm. Two tubes were secured together in parallel to make a yaw-probe with the openings pointing 45° outward. The four pairs were evenly spaced on the periphery to form a circle with a diameter of 2.5mm. In addition a ninth tube with a straight cut was placed in the centre of the circle.

The resulting nine hole vortex probe could directly measure the vortex strength and all velocity components. The vortex probe and a stationary pitot tube were connected to a SCANIVALVE ZOC16 and a SETRA 261 pressure transducer, which was operated from a PC using PCLAB software. The transducer had an error of less than 1% at full scale of ±1246Pa. Initial measurements [14] resulted in 500 samples as an optimum for removing noise and vibration.

3.4 Thermocouples

A 180x180mm (HxW) mesh with an even spacing of 20mm in each direction was constructed by soft soldering 3mm squared brass rods together. In each local corner 100mm long cu-coated welding sticks with a diameter of 2mm were soldered on perpendicular to the mesh plane. K-type thermocouples were placed at the tip of the sticks forming a 10x10 grid. The thermocouples were connected to a SCHLUMBERGER 3531 data acquisition system. The connector 35303A had a built in cold junction (ambient temperature) circuit. Number of samples used was 50 at a speed of 40/s for time mean measurements and 500/s for instantaneous measurements, with an overall error less than 0.7%.

3.5 The Schlieren system

The Schlieren system used in this work is basically described in i.e. Vasil'ev [11] as a Z-system, which was composed of a light transmitter, two 203mm high-quality cylindrical concave Schlieren mirrors, and a receiver. In addition a directional and sensitivity controller was specially developed to the system. Those units are described in Settery [13]. The observations were photographed with a camera at the exit of an open cascade wind tunnel.

4. EXPERIMENTAL PROCEDURE

The difference in turbulence intensity and scale were created by use of two wooden grids at two different locations in the open return wind tunnel. The large grid was made of 51x19mm wood with a squared spacing of 152mm, whilst the small grid was made of 19x19mm

wood with a squared spacing of 761mm.

Two different locations were chosen, the first at the entrance of the tunnel upstream the jet exit and the second location closer to the jet. A third grid was used in a cascade tunnel and was made of 2mm plastic with 14mm squares. This gave the following different test cases listed in table 1 together with the free-stream turbulence intensities at different locations downstream:

Test-Case	Grid-Type	Location X/D	Turbulence intensity[%]			
			X/D=1	3	10	30
TG0	No grid		0.93	0.91	0.76	0.62
TG1	Plastic	-9.7		2.2		
TG2	Small	-58	4.8			
TG3	Large	-58	9.0	8.5	7.3	5.6
TG4	Small	-10.3	18.7	15.3	10.6	6.1
TG5	Large	-10.3	24.7		16.6	

Table 1.

Test cases and the free-stream turbulence intensity.

In the hot wire measurements a single wire was pointing upstream the tunnel using either horizontal or vertical alignment of the wire. For each case a calibrated hot wire was placed in the vicinity to the plate at zero flow to read the offset into the computer. With the jet air supply valve closed, the wind tunnel was then adjusted for 2.5m/s using the hot wire (except in an extraordinary test case using 10m/s). Next the jet exit velocity was adjusted according to a digital manometer connected to the flow nozzle. The hot wire was traversed manually in the XY-plane only (plane of symmetry) and all data was logged by the computer for calculation of mean and RMS values. Some of the measurements were also passed over to a Fast Fourier Transformation (FFT) procedure for analyses of the frequency spectrum and the turbulence length scales involved. The hot wire measurements were carried out at $X=1, 3, 10$ and 30 jet exit diameters (D) downstream the jet exit for velocity ratios of $R=U(\text{Jet exit})/U(\text{Cross flow})=4, 7$ and 10 . All test cases were carried out, but not for every combination as shown in table 1.

For the vortex probe measurements the zero offsets were taken with no flow in the wind tunnel placing the calibrated probe at the plate. With the jet valve shot, the velocity in the tunnel was adjusted to 10m/s with a pitot tube and a digital manometer. The pressure transducer was calibrated, and the static pressure was given to the computer. The offset of all the flow angles caused by manufacturing and positioning the probe was optimised by adjusting the probe and repeat the readings of the cross flow until minimum average values could be given to the computer. Finally the jet exit flow was then adjusted for $R=4$ using the flow nozzle and the digital manometer, and the measurements could be carried out for $X=1, 3$ and $10 D$. The probe was aligned horizontally pointing upstream for case TG0 and TG4 and traversed in the YZ-plane. In addition

measurements with vertical alignment of the probe pointing downward in negative Y-direction were carried out for case TG0 at $X/D=1$ to detect the secondary vortices, as shown in figure 2.

For temperature measurements the velocity in the wind tunnel was adjusted to 2.5m/s without turbulence grid (TG0) using a pitot tube and a digital manometer. Because the heater box had no temperature adjustments the jet exit velocity was pre-set and the system left for a long time to obtain constant conditions. The temperature mesh was placed in the YZ-plane with the first column of thermocouple at $Z=0$ and traversed in the Y-direction. The measurements were taken at $X=1, 3, 10$ and $30 D$. The turbulence grid was placed in the tunnel and the wind tunnel velocity adjusted before the measurements were repeated for TG4. This procedure was carried out for momentum ratios $N=27$ and 74 with jet exit temperatures of 210°C and 160°C (Froude number 49 and 84) respectively.

The visualisation performed using the colour Schlieren method was carried out using a cascade wind tunnel. A transparent grid with 12.7mm (0.423D) squares was used as a reference showing up on the photographs.

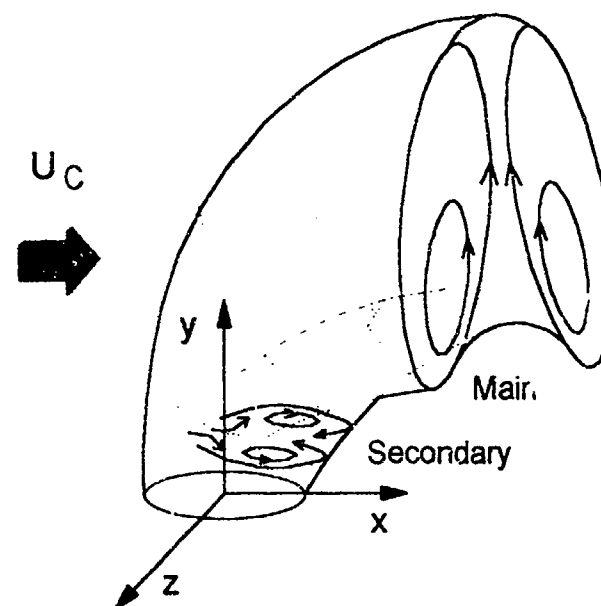


Figure 2.
Main and secondary vortices for a jet in a cross flow.

5. EXPERIMENTAL RESULTS

5.1 Hot Wire Measurements

Typical results from the hot wire measurements for mean velocities at the centre plane (symmetry plane) are shown in Figure 3 A and B. The local mean velocities using a horizontal and a vertical aligned hot wire are called total velocity U_j and horizontal velocity U_x respectively. The velocities shown in figure 3 have been normalised by the free-stream velocity U_c .

The total velocity profiles show two local maximum and two local minimum both for U_j and U_x . The values in

the upper maximum was never exceeded by the lower maximum and therefore called the absolute maximum. The upper local minimum on top of the jet flow caused by stagnation of the cross flow was called stagnation minimum. The stagnation minimum retained the same position and magnitude for both U_j and U_x , and was found for all velocity ratios R in all the test cases. The stagnation minimum values decreased (getting closer to U_c) for decreasing velocity ratio.

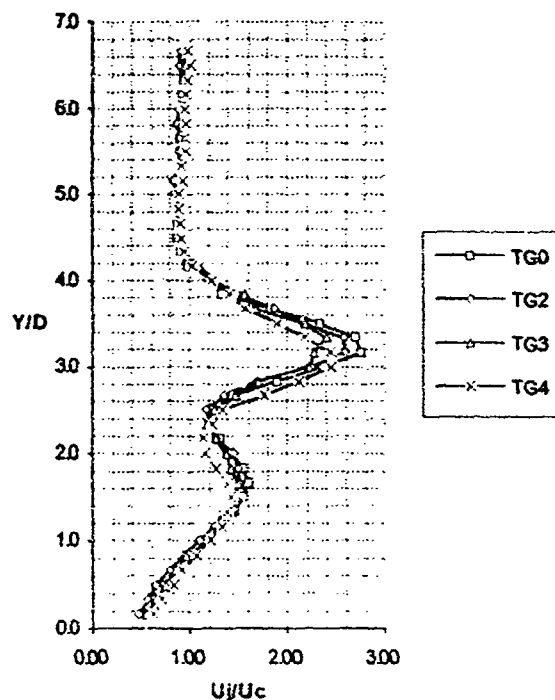


Figure 3A.
Mean velocity profiles U_j for R 4 at X/D 1.

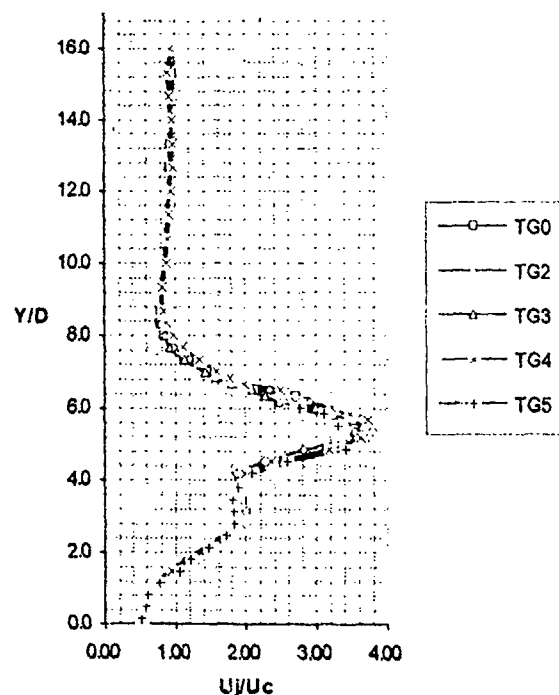


Figure 3B.
Mean velocity profiles U_j for R 7 at X/D 1.

The values also decreased downstream, and therefore no stagnation minimum could be found at X/D 30 for all R and X/D 10 for R 4.

The absolute maximum was found at all X/D for all velocity ratio R with same position for U_j and U_x . An exception was for R 10 at X/D 30 where no measurements could be taken because the jet was too close to the ceiling of the wind tunnel. The values of U_j and U_x in the absolute maximum increased for increasing velocity ratio, and U_j decreased faster downstream relative to U_x . Because of this U_j and U_x merged downstream for the absolute maximum. The downstream distance X/D for the merging point increased for increasing velocity ratio. It was found between X/D 3 and 10 for R 4 and between X/D 10 and 30 for R 7. At X/D 30 for R 4 no minimum or maximum could be found, and the velocity profiles was fully merged for U_j and U_x .

No trend was found in the Y -position of the velocity profiles to separate the different test cases. A decreasing total velocity with increasing turbulence intensity in the free-stream could be observed at the absolute maximum. This trend was found at X/D 1 for all R with an increasing effect for decreasing velocity ratio, and therefore also could be seen at X/D 3 for R 4. The effect was much stronger for $TG4$ than in the other test cases as shown in figure 1. The effect was not obvious further downstream for higher velocity ratio. No such trend could be found for the velocity U_x in the absolute maximum.

The local maximum value of U_j indicated the maximum of the vertical velocity component U_y . The value of U_y was found to be of the same magnitude as U_x absolute maximum. The same trend for increased free-stream turbulence, as found for the total velocity U_j at the absolute maximum, was also found for U_j (or U_y) at the local maximum. The value of U_y between the local maximum and up to Y between the absolute maximum and stagnation minimum was nearly constant. Except at X/D 1 where U_y increased as a result of vertical inertia forces from the jet exit momentum. The increase of U_y in this region was stronger for increasing velocity ratio, and could therefore also be observed at X/D 3 for R 10.

Typical results of velocity rms values from the hot wire measurements are shown in figure 4 A and B. The root mean square values of the velocity fluctuations measured with a horizontal and a vertical aligned wire are called RMS and RMS_x respectively. The values in figure 4 have been normalised by the free-stream velocity U_c .

The profiles for RMS and RMS_x fully merged downstream between X/D 3 and 10. The merged profiles had one maximum called absolute maximum, and was always located in the shear layer of U_x between the U_x local minimum and absolute maximum. The rms values in the absolute maximum decreased downstream, and

increased for increasing velocity ratio. At the same Y location as the U_j local maximum the rms values changed to increase more rapid up to the absolute maximum.

At X/D 1 the RMS had two maximum. The distance Y/D between them increased with increasing velocity ratio. The local minimum was centred between the two maximum and was located at the U_j absolute maximum.

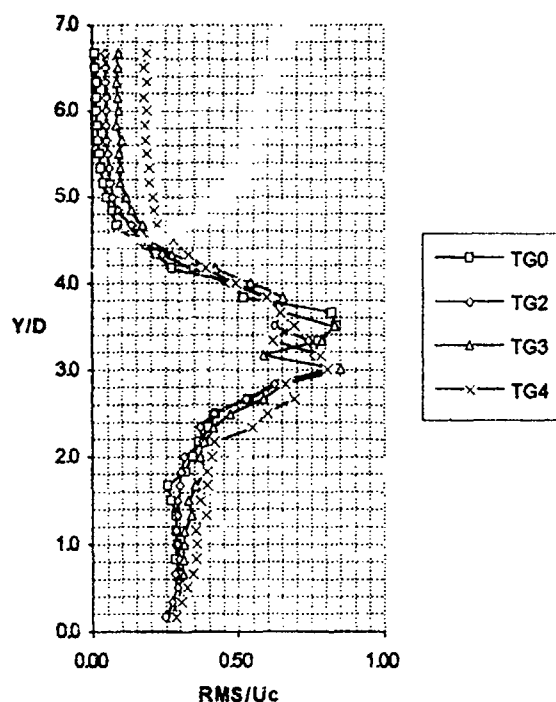


Figure 4A.
RMS profiles for R 4 at X/D 1.

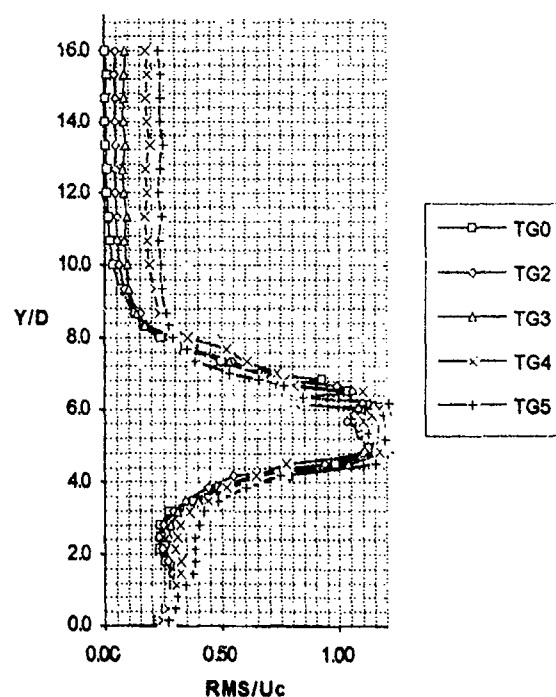


Figure 4B.
RMS profiles for R 7 at X/D 1.

The value of the upper maximum was more unstable and less than for the lower maximum called absolute maximum. An other local minimum closer to the plate was found at the same location as the local maximum for U_j .

At X/D 1 the RMSx gave one maximum here called absolute maximum at the same location as the absolute maximum of RMS. The value of the RMSx at the absolute maximum was less than the value for RMS. Closer to the plate the RMSx curve gave a local maximum and minimum at the same location as for U_j local maximum and minimum.

At X/D 3 the values of RMS and RMSx were located between X/D 1 and 10. The local maximum for RMS found at X/D 1 could not be observed clearly at X/D 3, but the values at the absolute maximum was unstable. The RMS and RMSx values increased for increasing turbulence level in the free-stream for all the cases at all locations in X and Y with strongest effect upstream.

5.2 Vortex Probe Measurements

Essential for the measurements was to define and locate the centre of the vortices involved in the flow. Since only time mean measurements were performed, only one side of the symmetry plane was investigated. In this work the centre of the main vortices was defined as flowing parallel with the cross flow (figure 2), which is where both the pitch angles ALPHA and the yaw angles PHI change sign from positive to negative or vice versa using a horizontal aligned probe.

Typical results for ALPHA and PHI used to locate the main vortices centres are shown in figure 5. It can also be seen that the vortices were not rotational symmetrical. Comparing all the results for ALPHA and PHI the shape of the vortices were more narrow in the Z-direction relative to the Y-direction (more oval) upstream than downstream.

Testcase	X/D	Y/D	Z/D	U_v/U_c	Vorticity
TG0	1	1.4	1.3	0.92	400
TG0	3	2.7	1.7	0.88	110
TG0	10	4.8	1.9	0.92	50
TG4	3	2.8	1.7	0.84	90
TG4	10	4.8	1.8	0.87	40

Table 2.

Location and strength of the main vortices centres for velocity ratio R 4. U_v is the velocity located at the centres.

At the Z-position of the vortices centres ALPHA and PHI had a maximum and a minimum. Comparing the absolute values of ALPHA in the maximum and the minimum gave a larger angle in the maximum upstream at X/D 1 and equal values further downstream.

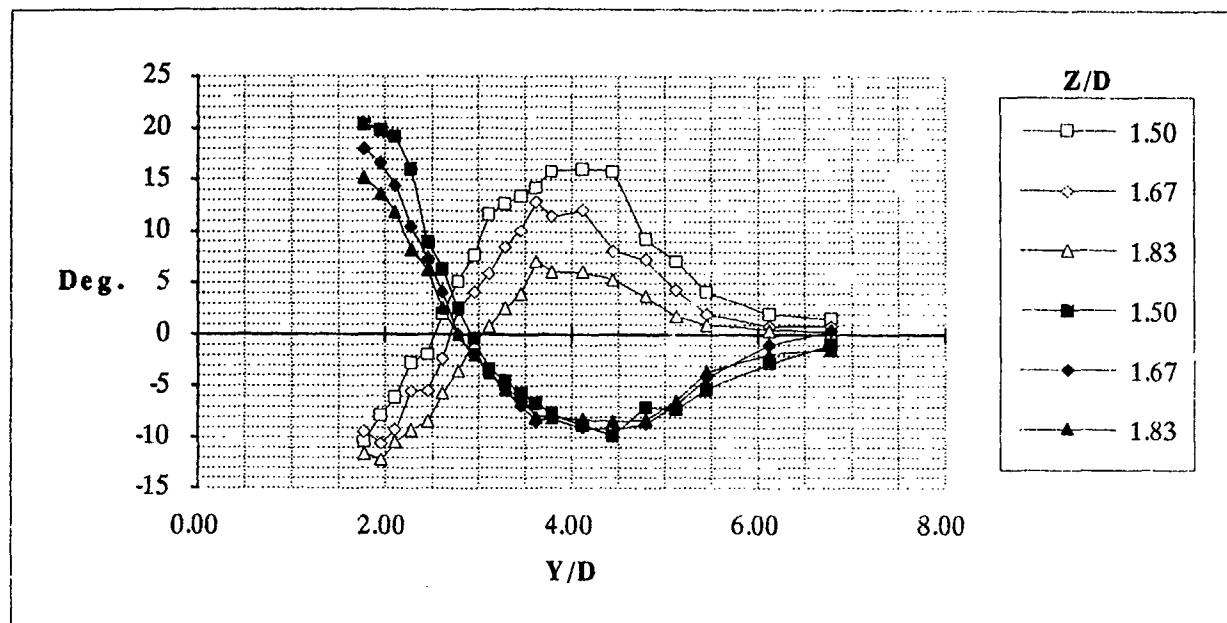


Figure 5.
Alpha (white symbols) and Phi (black symbols) for R 4
at X/D 3.

A similar comparison for PHI gave a larger angle in the minimum upstream at X/D 1 and a smaller value (nearly the half) in the minimum further downstream. The effect of increased turbulence in the free-stream could be seen for PHI as slightly less absolute values in the maximum and minimum. The vortices centres found are listed in table 2.

The main vortices centres were observed to be located at the same Y-position as for the U_j local maximum where U_y obtain the maximum value. The results from the velocity U_v at the main vortices centres and the measured vortices strength are listed in table 2. An increase in free-stream turbulence resulted in weaker main vortices.

The vortex probe could also detect the regions upstream in the wake where the flow was reversed. In this area the secondary vortices were measured aligning the probe vertically at X/D 1. The secondary vortices centres were found at Y/D 1.8 and Z/D 0.47 and are defined as a vortex flowing parallel with the jet exit. These vortices are the recirculation behind the jet caused by the cross flow shown in figure 2. No further investigations were performed for the secondary vortices.

5.3 Temperature Measurements

Typical plots from the temperature contours measured are shown in figure 6 A and B. The temperatures in the measurements were normalised by $T = (T_{\text{probe}} - T_{\text{ambient}}) / (T_{\text{jet exit}} - T_{\text{ambient}}) * 100$ to be comparable with concentrations (when neglecting heat transport at the plate and buoyancy effects).

For both test case (TG0 and TG4) the highest temperature at the symmetry plane upstream was found to correspond with the mean Y-position of U_j absolute

maximum measured with the hot wire. The Y-position for test case TG4 was higher than for TG0, but was within the same variance as found in the test cases of the trajectory measured for U_j absolute maximum with the hot wire. Further downstream ($X/D > 3$ for N 27 and $X/D > 10$ for N 74) the Y-position of symmetry plane maximum temperatures was found below the trajectory for U_j absolute maximum. The distance between the two maximum increased downstream and also with decreasing momentum ratio, but did not move below the centres of the main vortices. For N 27 at X/D 30 the Y-position was close to the main vortices centres and was the only location where the kidney shape had nearly disappeared in the measurements.

The position of the absolute maximum temperatures in the YZ-planes were found at the symmetry plane for test case TG4 at all X-positions. But for test case TG0 the absolute maximum was located at the symmetry plane only at X/D 1, and approached the main vortices centres as the jet was flowing downstream. The highest absolute temperatures was found in test case TG0, but the difference between the two test cases was less than 1% downstream X/D 3. Measured with the 1% temperature contour line the total width of the jet (in Z) was close for both test cases at all X-positions. The total height of the jets (in Y) were larger in test case TG4 than in test case TG0. Upstream at X/D 1 the differences in height were located in the upper half of the jets.

5.4 Schlieren Visualisation

The photographs of jets in cross flow using the Schlieren method gave the trajectory of the temperatures as well as the main and secondary vortices. Turbulence length scales could also be directly measured and the flow was always highly intermittent as shown in photograph 1. The main vortices could be observed initiating at the sides of the jet exit ($Z/D < 0.5$) a distance up from the plate dependent on the momentum ratio.

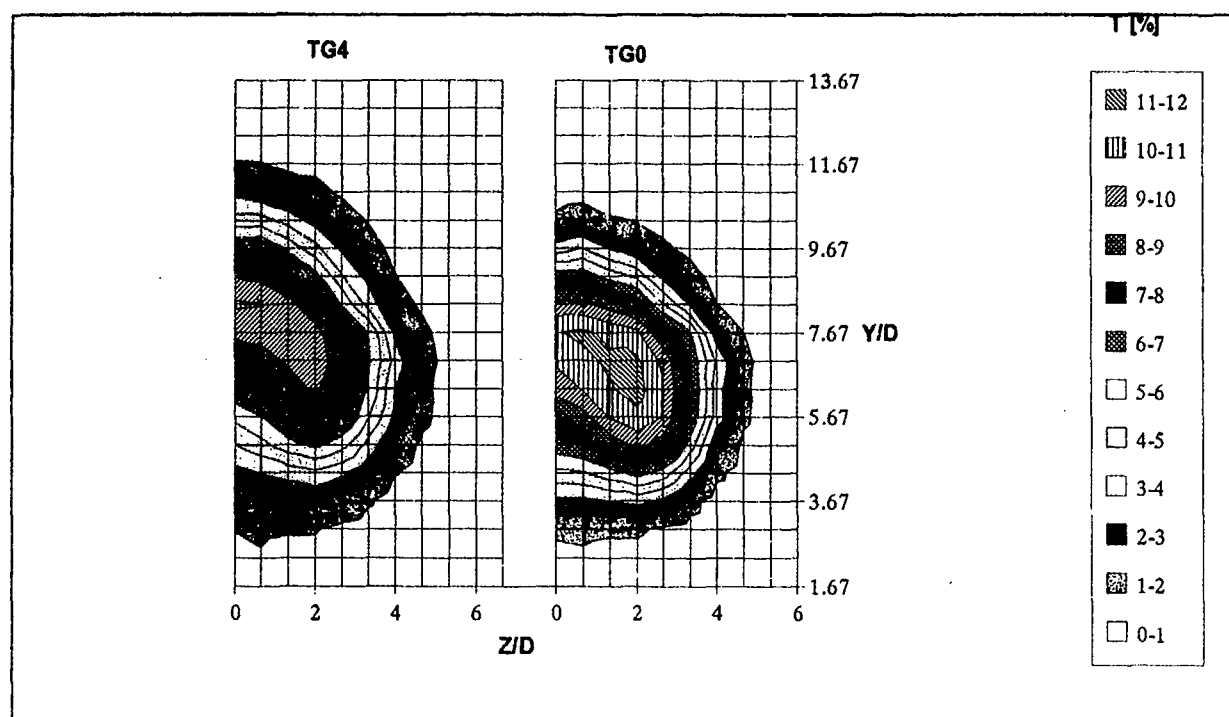


Figure 6A.
Temperature contours [%] for R 4 at X/D 10.

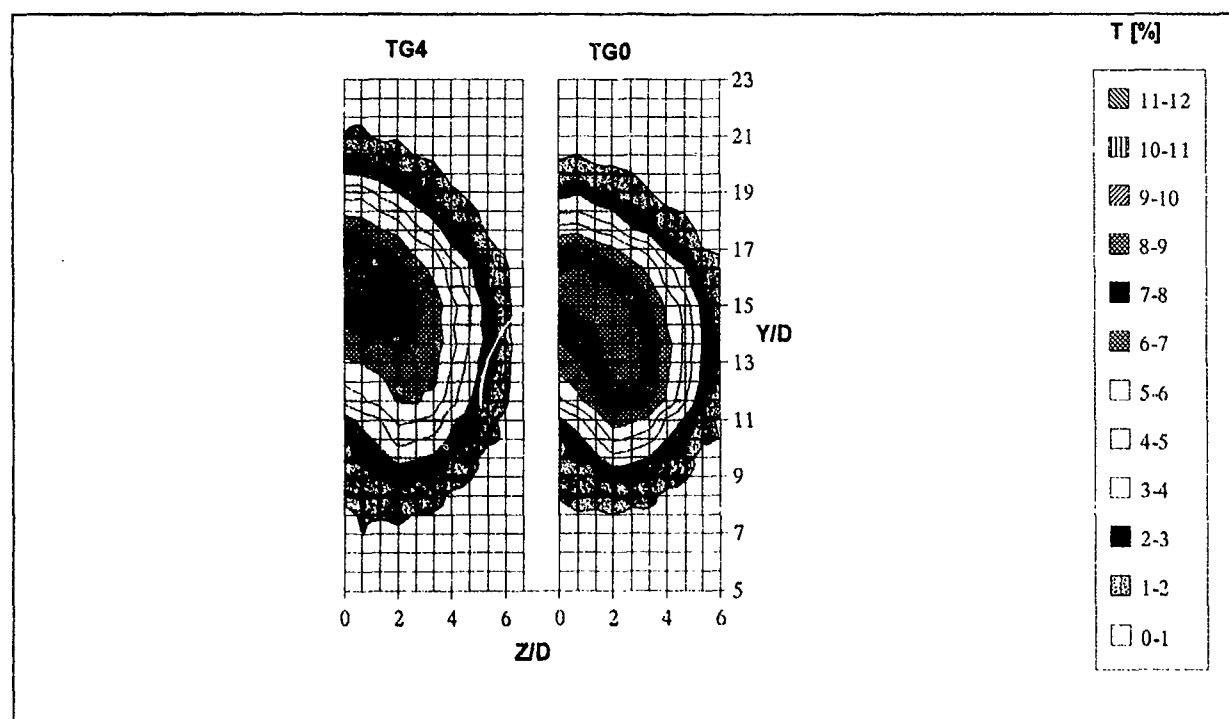


Figure 6B.
Temperature contours [%] for R 7 at X/D 10.

6. DISCUSSION

The blockage of the wind tunnel can be seen in figure 1 from the hot wire measurements of the stagnating cross flow. The velocity of the cross flow reached the free-stream velocity at relatively high distance above the jet flow, but can be seen not to interfere with the ceiling of the tunnel. For the highest velocity ratio 10 the jet was actually hitting the ceiling at X/D 30 and therefore no measurements could be taken there.

Many of the hot wire measurements were taken in regions of the flow where a standard hot wire is not suitable because of the RMS-values being too high and thereby interference with the probe support [9]. In these regions the measurements should not be used directly, but will show relative values for the different test cases. Almeida [12] has shown that a pulsed hot wire could improve direct measurements in such regions.

The position of the U_j absolute maximum measured with the hot wire at the symmetry plane have been compared in figure 7. Each X-position has between 5 and 9 points for each velocity ratio tested. The mean of these points have been drawn by a trajectory line. Many of the points does not show very well because they are located too close to each other, but give an idea of the variation. The overall standard deviation for all points on the trajectory was calculated to 0.30 diameter in Y-position. No trend was found in the trajectory of the jet for different level of turbulence in the free-stream.

Inaccuracies could also have affected the results shown in figure 7 due to positioning the hot wire. About 2000 manual traversed readings were taken, and about 10 errors were corrected when they were done. It could easily be one or two more, and the whole profile would jump in the Y-direction. However most of the traversing steps was $D/6$ and therefore causing a variation less than the calculated overall error level. The main cause to the variation in all the results is therefore assumed to be the reading error of the digital manometer used in the measurements for the flow nozzle (deviation in velocity ratio).

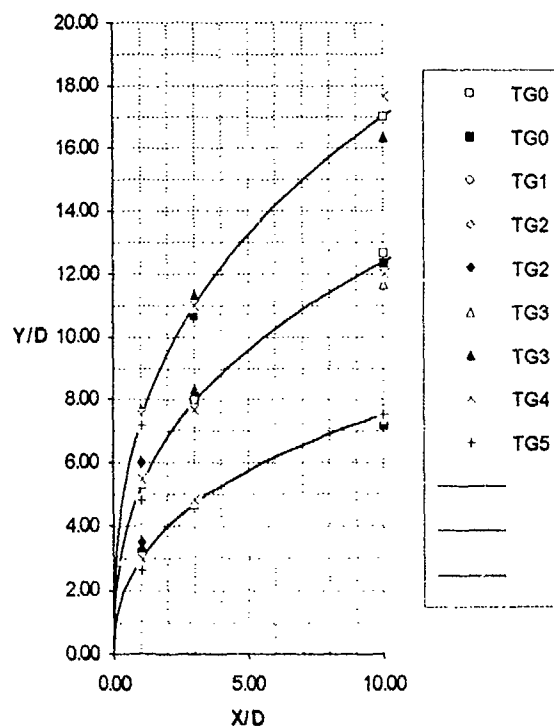


Figure 7.
Trajectories of U_j absolute maximum for R 4, 7 and 10.
(Black symbols for U_x).

The trend found in the hot wire velocity measurements caused by the free-stream turbulence did seem to have a connection with the strength of the main vortices. This is because both the values in the local maximum and the absolute maximum shows decreasing U_y with increasing turbulence level. The trend was relative small compared to the error level and therefore a connection was difficult to calculate for the cases tested out. Direct

vorticity measurements with velocity ratio of 4 indicates a constant reduction of about 20% downstream for an increase in free-stream turbulence intensity of about 20% at the jet exit. The effect was within the error level for velocity ratio 10, but could be registered for the highest free-stream turbulence tested.

The measurements performed using the vortex probe confirms the effect of free-stream turbulence found using the hot wire. The results did not show any difference for the trajectory of the main vortices, but indicates weaker main vortices for higher level of turbulence in the free-stream. The measurements of a secondary vortex pair at $X/D = 1$ confirms the observations in the Schlieren visualisation. This means the main vortices are not initiated by the recirculation behind the jet, but connected and located with the centre outside the secondary vortices. Hence the initiating of the main vortices are located at the sides of the jet (say $X/D < 0.5$) and the strength is dependent on the exact X-location and the momentum ratio.

The error level using the vortex probe was much higher than for the hot wire. The main reason is the calibration error estimated to about 10% mainly due to manufacturing of a relatively small probe. The error level increased with increased pitch and yaw angles found upstream the flow. Further downstream at the Z-location of the main vortices centres the pitch angle was small compared to the system and reading error, and therefore less reliable. Hence the vortices strengths and Z-positions listed in table 2 should only be used as an indication showing a trend in the results. At the main vortices centre the gradients $\partial\Phi/\partial Y \gg \partial\Phi/\partial Z$ and $\partial\Phi/\partial Z \ll \partial\Phi/\partial Y$ in the measurements as seen in figure 5. Therefore the error level in the Y-position of the main vortices centres was detected with much higher accuracy than the rest of the results using the vortex probe.

The mechanism of the main effect of free-stream turbulence is most possibly a change in the initial point of the main vortices at the sides of the jet. As a parallel to flow around bodies the separation point is triggered at different locations as a result of an increase in free-stream turbulence. For a jet in a cross flow the location of the initial point seems to move downstream with increasing turbulence in the free-stream, because this can explain less vortices strength. It is also likely to assume there is no effect of free-stream turbulence that can cause the initial point to move vertically in Y. Because this would have been detected in the analysis of the trajectories.

The temperature measurements also confirm less strong main vortices with increased free-stream turbulence. The contours shows that the absolute temperature maximum moves towards the main vortices centres for less free-stream turbulence. The only reason for this must be that the vortices are stronger, and the same effect could be seen regardless of velocity ratio tested.

The rise in the trajectory with increased turbulence level in the free-stream seen in the temperature measurements could be due to a higher level of error in velocity ratio. The reading error is considerably increased compared to the hot wire measurements and is mainly due to use of the digital manometer in conjunction with a pitot static tube in the wind tunnel to adjust the speed. In the hot wire measurements the calibrated wire was used to set the speed of the cross flow, and sampling lowered the error to an acceptable level. The free-stream velocity U_c used was about 2.5m/s which was in the lower range for the digital manometer. Initial testing on the precision of the digital manometer has shown an error of 13% in pressure in this range which could have caused the effect seen for the trajectory. However the measurements were taken in two series without adjusting the velocity ratio, and therefore one incorrect adjustment of the velocity ratio cause the same result to show at all X-positions. Taken these errors into account the observed rise in the trajectory is questionable, and also shown not to exist in the measurements carried out with both the hot wire and the vortex probe.

Also found in the temperature measurements was a temperature local maximum on top of the jet at $X/D = 1$ for higher free-stream turbulence. The reason for this could be explained by the local maximum in RMS found in the hot wire measurements at $X/D = 1$. Andreopoulos and Rodi [2] has explained how the stability parameter $S = (\partial v / \partial x) / (\partial u / \partial y)$ introduced by Bradshaw can be used to show that the deflection of the jet at this location are de stabilising the jet.

It appears that increased free-stream turbulence could amplify this effect for the jet to become more intermittent, and thus the occurrence of the local maximum in the temperature. The local maximum temperature seems to be smoothed out by the vortices further downstream.

Finally, the Froude numbers of 49 and 84 for the two momentum ratios tested does not seem low enough to have caused buoyancy effects in this study.

7. CONCLUSIONS

The effect of free-stream turbulence on a jet in a cross flow have been investigated for velocity ratios of 4-10 and turbulence intensity of 1-25% using primarily experimental methods. The results have shown the following trends:

VORTICITY

Increased turbulence in the free-stream resulted in a reduction of the main vortices strength that remains relative constant downstream. The effect decreased with decreasing velocity ratio.

DRAG FORCES AND TRAJECTORY

Maximum mean velocity in the flow decreased with increasing free-stream turbulence as a result of the change in strength of the main vortices. The jet did not

change velocity parallel to the cross flow with changes in free-stream turbulence, and therefore the drag forces deflecting the jet remained unchanged. The trajectories for the maximum mean velocity and the main vortices centres did not change due to different free-stream turbulence.

TURBULENCE AND INSTABILITY

RMS of all velocities in the jet at the symmetry plane increased with increasing free-stream turbulence. The increase was less for higher RMS values in the jet. At the exit the deflection of the jet caused instability and maximum peaks in RMS that was closer and interfering more with the jet centre for less velocity ratio. The instability and increase in turbulence in the flow did not change the momentum (change the trajectory) for different level of free-stream turbulence, and therefore did not change the vorticity.

HEAT TRANSPORT AND ENTRAINMENT

The heat transport was changing with the level of turbulence in the free-stream. The location of maximum concentration in the jet was located at the symmetry plane for high free-stream turbulence and at the centres of the main vortices for lower level of free-stream turbulence. This effect did not change the level of maximum concentration and was independent of the velocity ratio. Because of the higher vorticity for lower free-stream turbulence the entrainment increased at the symmetry plane and caused an decrease of the concentration here. Higher free-stream turbulence and less vorticity should therefore caused less entrainment and higher concentration, but this was balanced by more entrainment due to a higher turbulence level in the jet and more instability.

The mechanism causing the reduction in vorticity could be a displacement in the initial point of the main vortices, and is therefore recommended for further investigation. In atmospheric boundary layer the lateral instability is expected to be higher than in this investigation, and therefore give different results.

8. ACKNOWLEDGEMENT

This work has been carried out with the support of The Research Council of Norway (NFR), Department of Scientific and Industrial Research (NTNF), as a PhD grant.

9. REFERENCES

Conference Proceedings

1. Freestone, M.M., "Approximate Measurements of Stream wise Vorticity in Aeronautical Flow by Simple Pressure probe", I.Mech.E.-Hatfield Conference. Developments in Measurements and Instrumentation in Engineering, 11-13 Sept. 1985.

Periodical Articles

2. Andreopoulos, J. and Rodi, W., "Experimental Investigation of Jets in a Cross flow", *J.Fluid Mech.*, Vol. 138, 1984, pp 93-127.
3. Bearman, P.W., "Some Measurements of the Distortion of Turbulence approaching a two dimensional Bluff Body", *J.Fluid Mech.*, Vol. 53, 1972, pp 451.
4. Crabb, D., Durão, D.F.G. and Whitelaw, J.H., "A Round Jet Normal to a Cross flow", *Transaction of ASME, J. of Fluids Eng.*, Vol. 103, 1981, pp 142-153.
5. Hunt, J.C.R., "A theory of Turbulent Flow around two dimensional Bluff Bodies", *J.Fluid Mech.*, Vol. 65, 1973, pp 625.
6. Lee, B.E., "The effect of turbulence on the surface pressure field of a square prism", *J.Fluid Mech.*, Vol. 69, 1975, pp 263.
7. Ramsey J.W. and Goldstein, R.J., "Interaction of a Heated Jet with a Deflecting Stream", *Transaction of ASME, J. of Heat Transfer*, Vol. 93, November 1971, pp 365-372.
8. Wark C.E. and Foss, J.F., "Thermal Measurements for Jets in Disturbed and Undisturbed Cross wind Conditions", *AIAA Journal*, Vol. 26, No. 8, 1988, pp 901-902.

Books

9. Bradshaw, P., "An Introduction to Turbulence and its Measurements", Academic Press, London 1971.
10. Skåret E., "Ventilation Techniques", The Norwegian Institute of Technology, HVAC Division, Trondheim 1986.
11. Vasil'ev, L.A., "Schlieren Methods", Israel Program for Scientific Translations, Keter Publishers LTD., London 1971.

Reports

12. Almeida, H.M.S., "Study of the Interaction of a Jet and a Uniform Stream using Pulsed-Wire Anemometry", PhD-thesis, University of London, December 1985.
13. Settery, G., Final year project report for the BSc degree in Aeronautical Eng., University of Hertfordshire, 1985.
14. Toften, T.H., PhD-thesis in preparation, University of Hertfordshire, 1993.



Photography 1.

Schlieren visualisation of a jet in a cross flow for N 14.

ANALYSIS OF COOLING JETS NEAR THE LEADING EDGE OF TURBINE BLADES

by

E. Benz and S. Wittig

University Karlsruhe, Kaiserstrasse 12, W - 7500 Karlsruhe, Germany

A. Beeck

ABB Power Generation Ltd, CH - 5401 Baden, Switzerland

L. Fottner

University of the Armed Forces Munich, W - 8014 Neubiberg, Germany

Summary

Film-cooling air ejection affects the aerodynamics of turbine blades by the mixing of the coolant with the mainstream as well as by the interaction between the jet and the boundary layer. In the present paper, these effects are studied experimentally and numerically. The results show that the flow in the coolant channel is strongly affected by the main flow around the blade, leading to significant deflection of the coolant air jets.

To account for these interactions between the cooling jet and the main flow in the numerical predictions, a multi-block technique is applied. With this technique very complex but structured geometries can be modelled by simply attaching grids of the different subdomains. For the present investigations, these subdomains are the two coolant channels at the leading edge and the main flow around the blade.

For adaption to the curved geometry of such a turbine blade, a non-orthogonal body fitted grid is used for solving the time average two- or three-dimensional compressible Navier-Stokes equations by a finite volume method. The turbulence is taken into account by the standard k, ϵ -model. For discretization of the convective terms the Monotonized-Linear-Upwind scheme (MLU) is used. The pressure-velocity coupling is achieved by the SIMPLEC-algorithm for compressible flows.

The calculated results are compared with experimental investigation performed with a L2F-system at a large scaled turbine blade. Three typical blowing ratios are presented. Due to the simultaneous calculation of the coolant flow and the main flow, good agreement was obtained.

Nomenclature

a, q	geometric quantities
a_i	coefficients in difference equation
h	enthalpy
p	pressure
ρ	density
u, v, w	velocity components
U, V, W	contravariant velocity components
k	turbulent kinetic energy
ϵ	dissipation rate of k
$\sigma_k, \sigma_\epsilon, C_1, C_2, C_\mu$	Konstants of $k - \epsilon$ model
ϕ	dependent variable
x, y, z	axis of cartesian coordinate system
ξ, η, ζ	axis of curvilinear coordinate system
J	Jacobian of transformation
μ	turbulent viscosity
Γ	effective viscosity
M	blowing ratio ($M = \rho_j V_j / \rho_\infty V_\infty$)
Ma	Mach-number
Re	Reynolds-number
s	surface coordinate
t	pitch of the blade row
β	flow angle
γ	slot angle

Indices

i	coordinate direction
i, j	tensor indices
j	jet
1	cascade inlet
2	cascade outlet
DS	pressure side
SS	suction side
s	stagger
th	theoretic

UniBw München Institut für Strahlantriebe		High-Speed Cascade Wind Tunnel	1985
test section data:		supply units:	wind tunnel data:
Mach number	$0.2 \leq Ma \leq 1.05$	evacuating unit	AC electric motor
Reynolds number	$0.2 \cdot 10^6 \text{ m}^{-1} \leq Re/l \leq 18.0 \cdot 10^6 \text{ m}^{-1}$	$P_1 = 30 \text{ kW}$ $P_2 = 20 \text{ kW}$	axial compressor
degree of turbulence	$0.4\% \leq Tu_1 \leq 7.5\%$	boundary layer suction	6 stages
upstream flow angle	$25^\circ \leq \beta_1 \leq 155^\circ$	(centrifugal compressor)	air flow rate
blade height	300 mm	additional air supply	$\dot{V}_{\max} = 30 \text{ m}^3/\text{s}$
test section height	235 mm - 510 mm	(screw compressor)	total pressure ratio
			$(p_{11}/p_K)_{\max} = 2.14$
			number of revolutions
			$n_{\max} = 6300 \text{ min}^{-1}$
			tank pressure
			$p_K = 0.04 - 1.2 \text{ bar}$

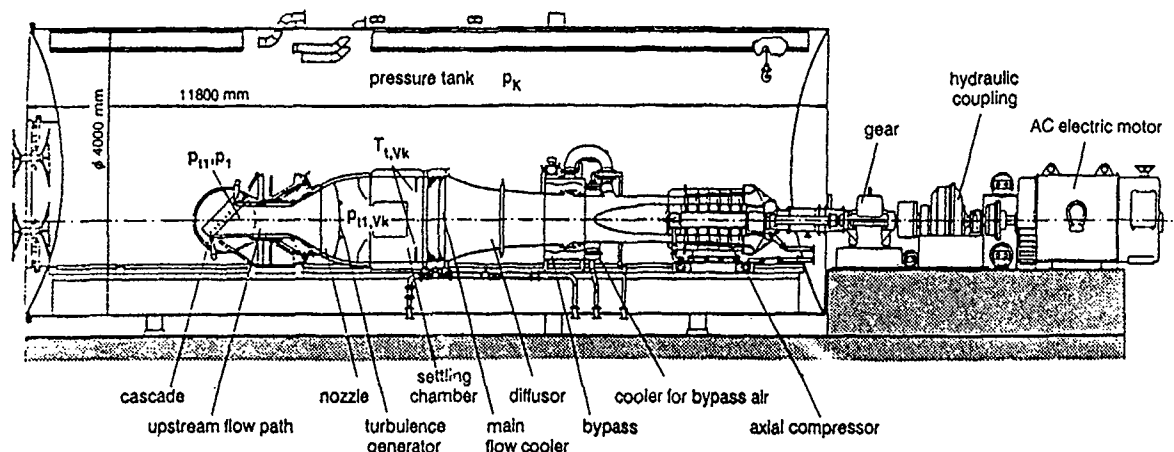


Figure 1: High speed wind tunnel

Introduction

The flow characteristics of a jet in a crossflow is of general importance in a wide range, such e.g. dispersal of pollutants, the aerodynamics of VSTOL-aircrafts, the mixing in combustors and the film-cooling of turbine blades and combustor-chambers. Besides the geometric conditions the momentum flux ratio respectively the blowing rate are the main parameters which describe the flow. Many fundamental experimental and numerical studies to the different applications and therefore to the different geometric boundary conditions are found in literature (e.g. Bergeles et al. (1976), Crabb et al. (1981), Noll (1992)).

In the field of turbomachinery high momentum jets are used to stabilize the flame and to dilute the hot gases. Due to the high turbulence intensities generated by the impinging jets excellent mixing as well as high intensity combustion is achieved. The interaction of such jets in the primary zone of a combustor was studied by Noll (1992), Jeckel et al. (1992).

In contrast, film cooling of combustor-chambers and turbine blades is attained by low momentum jets through holes and slots. The design of a film-cooling configuration has to be optimized with respect to the best suitable blowing rate in order to maintain the coolant near the wall and with respect to the optimal placement of the holes for the specific blowing rate to achieve best cooling efficiency. In general, the coolant flow of turbine blades is injected in streamwise direction, except in the leading edge region where jets are directed against the mainflow. In addition, the strong pressure gradients in the stagnation region have to be considered.

Many aerodynamic and heat transfer investigations on turbine blade film cooling are found in the literature which help to understand the main phenomena. However, investigations of film cooling in the leading edge of turbine blades rarely appear. The present study of a large scaled model turbine blade provides an important contribution to a better understanding of the flow-phenomena at the leading edge of a film cooled turbine blade. Detailed experimental results carried out with a Laser Transit Velocimeter are compared with numerical results. Due to the elliptic behaviour of the flow in the vicinity of the film-cooling

Ma_1	=	0.37	l	=	250mm
Ma_2	=	0.95	t/l	=	0.714
Re_1	=	$3.7 \cdot 10^5$	b_s	=	73°
Re_2	=	$6.95 \cdot 10^5$	s/l_{SS}	=	0.02
β_1	=	133°	s/l_{DS}	=	0.03
β_2	=	28.3°	β_s/l	=	0.01018
$\Delta\beta$	=	104.7°	γ_{SS}	=	55°
γ_{DS}	=	70°	h	=	300mm

Table 1: Design Data of the Turbine Cascade

holes, it turns out that the complete Navier-Stokes respectively the Reynolds-averaged equations (Benz and Wittig (1992)) have to be solved also for the flow inside the injecting holes.

Experiments

The high pressure turbine cascade (Fig. 2) was designed for two dimensional turning of 104.7° and for an isentropic Mach number of $Ma_{2th} = 0.95$. The Reynolds number was $Re_{2th} = 6.95 \cdot 10^5$. The cascade consists of three large scaled turbine blades. The leading edge region was fitted with slots in spanwise direction close to the stagnation line as a two-dimensional model of ejection holes.

Table 1 gives the aerodynamic and geometric data.

The experiments were carried out in the high speed cascade wind tunnel of the University of the Armed Forces Munich (Fig. 1). This facility operates continuously and allows the independent variation of Mach number and Reynolds number by changing the pressure level of the surrounding tank (Scholz et al. (1959), Sturm et al. (1985)). A turbulence grid was installed upstream of the cascade in order to generate a design turbulence level of about 8 % (Kiock et al. (1985)).

To achieve a constant pressure distribution over the inlet area, adjustable guide vanes are mounted at the cascade end. Therefore similar flow conditions could be attained for all three blades. The centre blade was equipped with tapings in the midspan region of the blade. Glass windows were installed in the front part of the side walls of the cascade for Schlieren observations and laser anemometry.

The mainstream air had a total temperature of 313 K, while the cooling air temperature was about 30 K lower. The cooling air is delivered from a separate screw compressor. The mass flow rate was measured by an orifice plate (DIN).

For wake traverse measurements, a wedge probe was used (Scholz (1956), Römer et al. (1988)) at

32 % of the chord axially downstream of the trailing edge plane. From the surface pressure distribution, the surface Mach number distribution was evaluated with the assumption of constant total pressure.

The flow field around the leading edge region was measured in detail by use of a Laser Transit Velocimeter (Schodl (1974)). This measuring technique is non intrusive and allows measurements very close to the wall (about 50 microns) as well as in regions with large velocity gradients i.e. in the jet boundary, near the stagnation point or in the region between reverse flow and main stream.

Due to the small probe volume ($0.17 \cdot 0.2 \cdot 0.008 \text{ mm}^3$) a very high resolution of the flow field with the jets, the stagnation area, the boundary layer, and even in recirculation regions could be achieved.

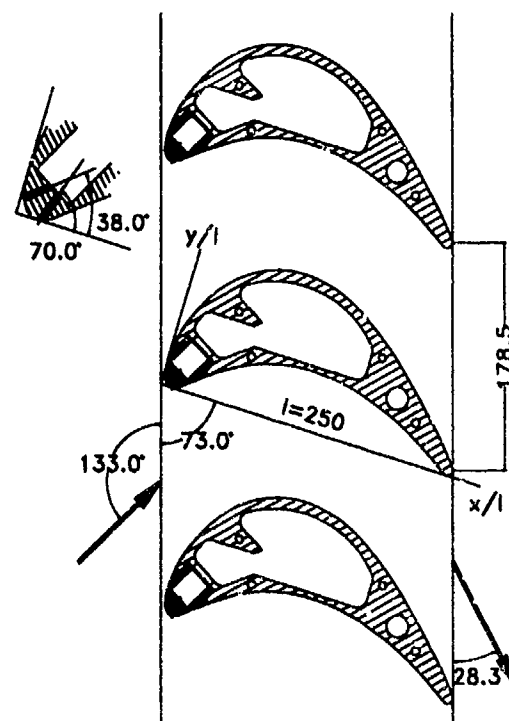


Figure 2: High pressure turbine-cascade

Numerical method

Governing equations and turbulence modeling

The Navier-Stokes-equations of a compressible fluid were used in the present study. For turbulent flow calculations the Reynolds-averaged equations are solved. The governing equations can be written in Cartesian tensor form as:

Mass

$$\frac{\partial}{\partial x_i}(\rho u_i) = 0 \quad (1)$$

Momentum

$$\frac{\partial}{\partial x_i}(\rho u_i u_j) = -\frac{\partial p}{\partial x_j} + \frac{\partial}{\partial x_j} \left[\mu \left(\frac{\partial u_i}{\partial x_j} + \frac{\partial u_j}{\partial x_i} - \frac{2}{3} \frac{\partial u_k}{\partial x_k} \delta_{ij} \right) - \overline{\rho u_i' u_j'} \right] \quad (2)$$

Energy

$$\frac{\partial}{\partial x_i}(\rho u_i h) = \frac{\partial}{\partial x_i} \left(\frac{\mu}{Pr} \frac{\partial h}{\partial x_i} \right) - \overline{\rho u_i' h'} + S_h \quad (3)$$

Gas State

$$p = \rho R T \quad (4)$$

To evaluate the stress terms, two transport equations for the turbulent kinetic energy k and its rate of dissipation ϵ are solved.

$$\frac{\partial}{\partial x_i}(\rho u_i k) = \frac{\partial}{\partial x_i} \left(\frac{\mu_t}{\sigma_k} + \mu \right) \frac{\partial k}{\partial x_i} - G_k - \rho \epsilon \quad (5)$$

$$\frac{\partial}{\partial x_i}(\rho u_i \epsilon) = \frac{\partial}{\partial x_i} \left(\frac{\mu_t}{\sigma_\epsilon} + \mu \right) \frac{\partial \epsilon}{\partial x_i} + \frac{\epsilon}{k} C_1 G_k - C_2 \rho \frac{\epsilon^2}{k} \quad (6)$$

The eddy viscosity is related to the turbulent kinetic energy and the dissipation rate by

$$\mu_t = C_\mu \frac{k^2}{\epsilon} \quad (7)$$

The well known k, ϵ -model is used in the standard form with the wall-function approach.

Discretization and numerical solution

The transformation of the governing equations into a body-fitted-coordinate system (ξ, η, ζ) leads to the following general linearized form of the governing equations:

$$\begin{aligned} \frac{\partial}{\partial \xi}(\rho U \phi) + \frac{\partial}{\partial \eta}(\rho V \phi) + \frac{\partial}{\partial \zeta}(\rho W \phi) = \\ + \frac{\partial}{\partial \xi} \left[\frac{\Gamma}{J} \left(q_{11} \frac{\partial \phi}{\partial \xi} + q_{12} \frac{\partial \phi}{\partial \eta} + q_{13} \frac{\partial \phi}{\partial \zeta} \right) \right] \\ + \frac{\partial}{\partial \eta} \left[\frac{\Gamma}{J} \left(q_{21} \frac{\partial \phi}{\partial \xi} + q_{22} \frac{\partial \phi}{\partial \eta} + q_{23} \frac{\partial \phi}{\partial \zeta} \right) \right] \\ + \frac{\partial}{\partial \zeta} \left[\frac{\Gamma}{J} \left(q_{31} \frac{\partial \phi}{\partial \xi} + q_{32} \frac{\partial \phi}{\partial \eta} + q_{33} \frac{\partial \phi}{\partial \zeta} \right) \right] \\ + J \cdot S(\xi, \eta, \zeta) \end{aligned} \quad (8)$$

In Eq. 8 ϕ represents the dependent variables u, v, w, k, ϵ , and h . J is the Jacobian of the transformation and Γ the effective viscosity. The contravariant velocity components U, V, W which determine the convective flux normal to the volume face are derived from the cartesian velocity components. More details can be found in Benz et al. (1992), Wittig et al. (1987) and Peric (1985)).

By the finite volume discretization method the differential equation is transformed into an algebraic equation. For the discretization of the diffusive terms a central-difference scheme is used, whereas for the convective terms a high-resolution-scheme is incorporated. The high-resolution-scheme used here is the Monotonized-Linear-Upwind-scheme (MLU) proposed by Noll (1992). The MLU-scheme is derived from the monotonized-central-difference scheme, originally proposed by Van Leer (1977). In contrast to the widely used QUICK-scheme the MLU-scheme is free from over- and undershoots. That means it is bounded and of second-order accuracy in smooth regions of the flow and degenerates to first-order accuracy at local extremes. The MLU-scheme was successfully used for a variety of computations of combustor flows (Noll (1992)) and turbine flows (Benz et al. (1992)).

The pressure-correction method used for the coupling of the velocity and pressure field was originally developed (Patankar 1980) for staggered grid arrangements to prevent 'checkerboard' pressure-velocity oscillations. In the present method all variables are located at the same cell centered position. To avoid non-physical oscillation of flow variables a similar interpolation than the practice of Hsu (1981) and Rhie and Chow (1981) is used here. To account for the compressibility in the pressure-correction

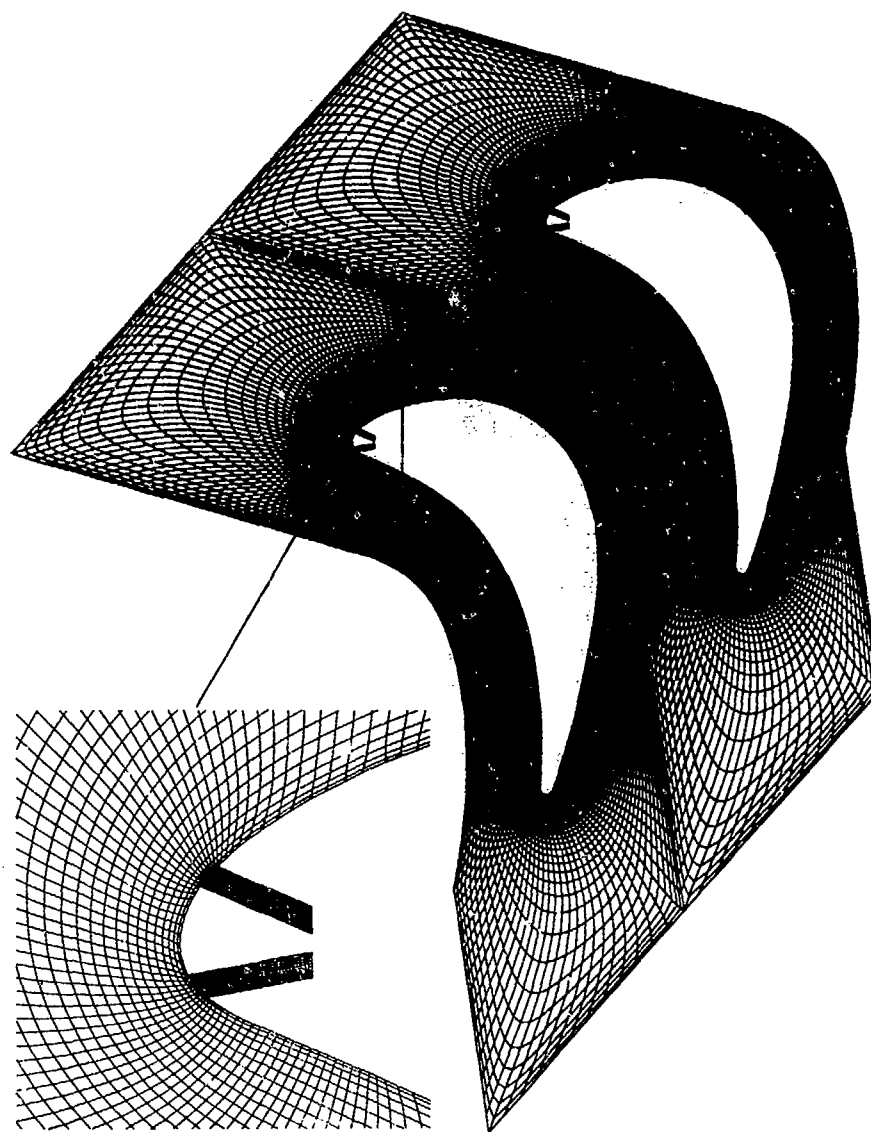


Figure 3: O-grid with two H-grids

algorithm the density-changes are incorporated in the pressure-correction equation. The one step SIMPLEC-algorithm for compressible flows (Doormal et al. (1984), Doormal et al. (1987)) is used here.

For the solution of the system of the algebraic equations the generalized conjugate gradient (CG) iterative procedure, described in detail by Noll et al. (1992), was employed. The CG-method was tested in a variety of computations of typical complex gas-turbine-combustor flows and was found to be very efficient and robust.

Multi-block method, Grid attaching

By the use of a multi-block method a complex geometry can be subdivided into simple blocks. Therefore,

the prediction of very complex geometries becomes feasible which are impracticable using a single structured body fitted grid. The domain-decomposition method, respectively multi-block technique applied here, is based in contrast to other methods on periodic boundary conditions.

In the numerical code the periodic boundary conditions are incorporated in a very general form to enable the connection of any cell-surface of a control volume to another control volume. Therefore, for predicting the flow in turbine- or compressor-stages all classical grids such as H-, C-, O-, I-grids can be chosen. For the present calculations, where the leading edge region is of major interest, an O-grid was used to resolve the blunt leading and trailing edges of a turbine blade.

Due to the general implementation of the periodic

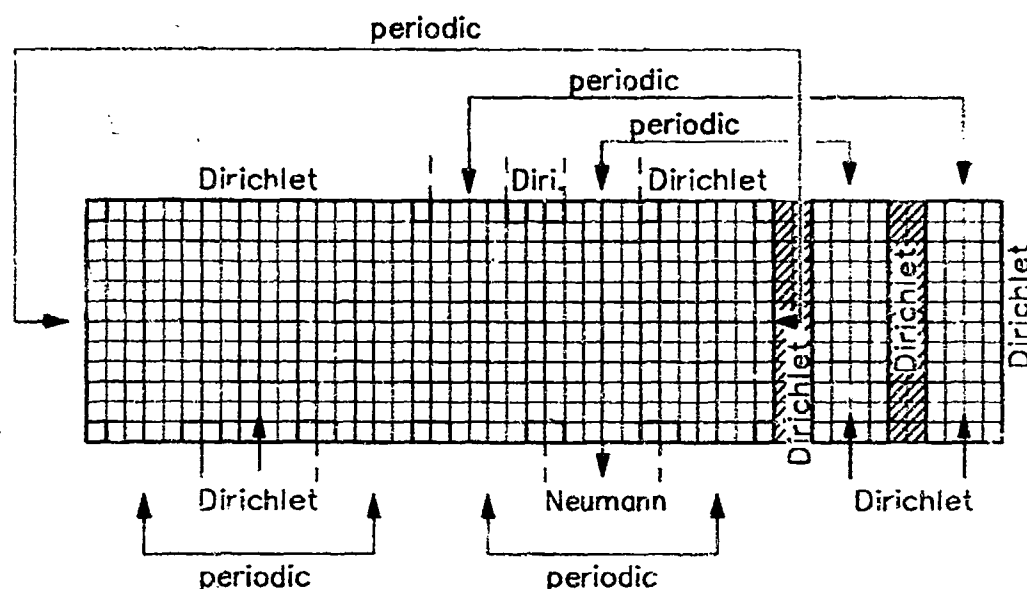


Figure 4: Computational grid

connections, different structured grids can be attached (Benz et al. 1992). That means that this multi-block method resulting from the universal implementation of the periodic boundary conditions needs no additional changes in the solution algorithm.

In Fig. 3 the single O-grid around the blade together with two attached H-grids for the discretization of the film cooling slots is shown. The number of gridpoints of the O-grid is 211×42 . The three grids consist of approximately 10.000 points. A detailed view of the leading edge (Fig. 3) gives an impression of the fine resolution of the interesting region. In Fig. 4 a schematic of the computational domain is shown. The arrows are indicating the periodic connections. The left part represents the logical region of the O-grid with its periodic connections. The two H-grids are placed on the right side. In addition several Neumann- and Dirichlet-boundaries are marked representing various inlet, outlet and wall boundaries of the domain.

Results

The aerodynamic behaviour of the film cooling ejection in the stagnation region and its influence on the loss coefficient was discussed already by Beeck et al. (1992). In this paper here, detailed comparison between measured and predicted results for three typical blowing ratios are presented.

It was shown in our last papers (Beeck et al. (1992), Benz, Wittig (1992)) that the velocity profile at the

slot exit strongly depends on the mass-flux ratio. From fundamental experimental studies of a single low momentum jet normal to the cross flow (Bergles et al. (1977), Andreopoulos (1982) and Crabb et al. (1981)) the existence of a strong non-uniform velocity profile at the exit of the pipe due to the variation of the pressure field in the vicinity of the hole is well known.

Therefore, it is not possible to find suitable boundary condition at the slot exit when the prediction starts there. As mentioned before in contrast to other investigations in the present study the computational domain includes the film cooling slots where the jet flow boundary conditions are easily specified.

In the present study in the slot a uniform velocity profile is specified, corresponding to the blowing ratios $M=0.47$, $M=0.78$ and $M=1.14$ which is a suitable assumption.

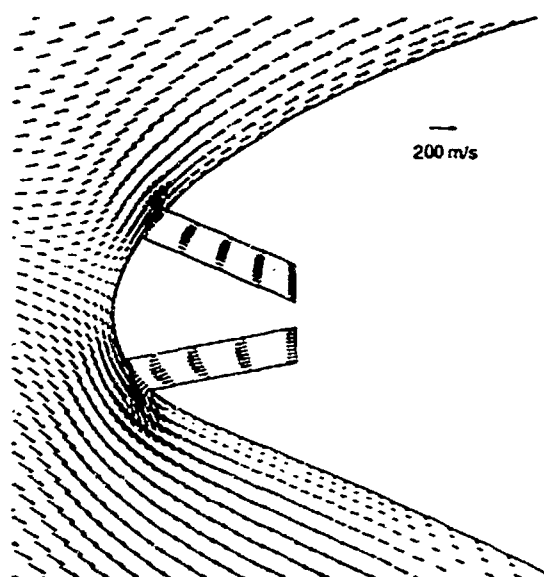
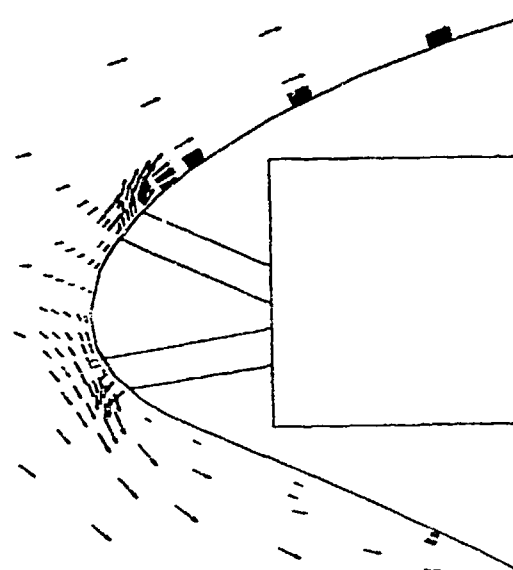
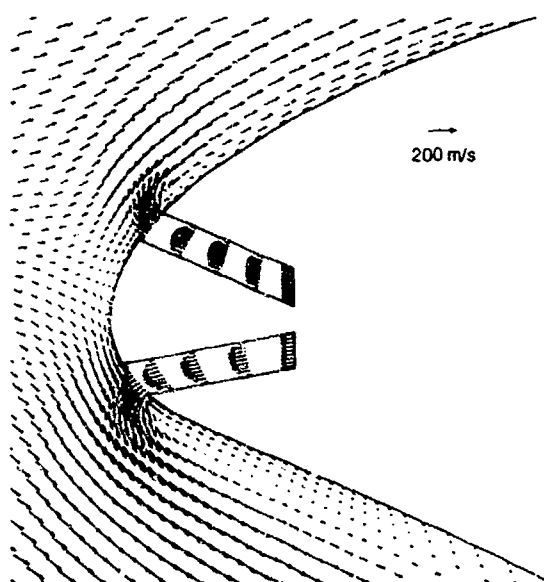
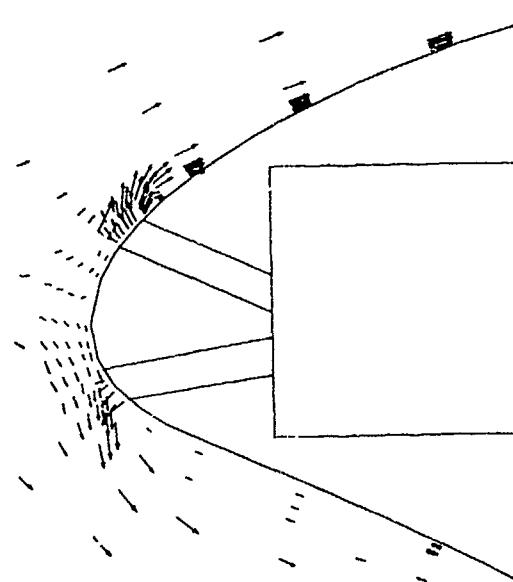
In the following figures the predicted and measured velocity vectors for the three mass-flux ratio are compared. For reasons of clarity only every tenth grid line of the predicted results in the slots is plotted and also in measurements some vectors are not shown.

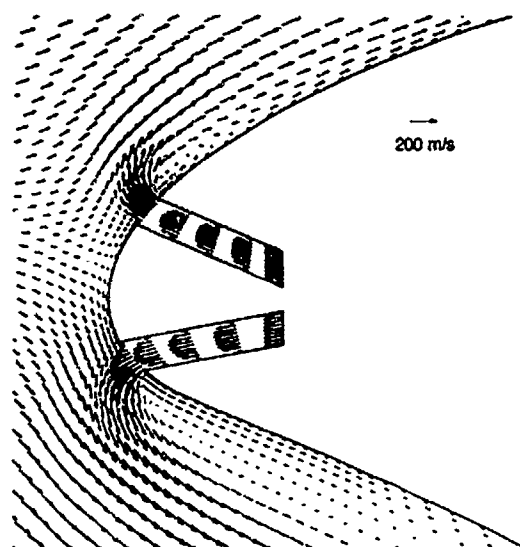
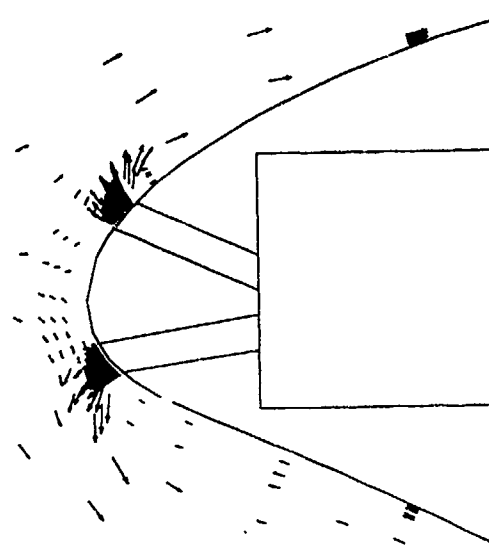
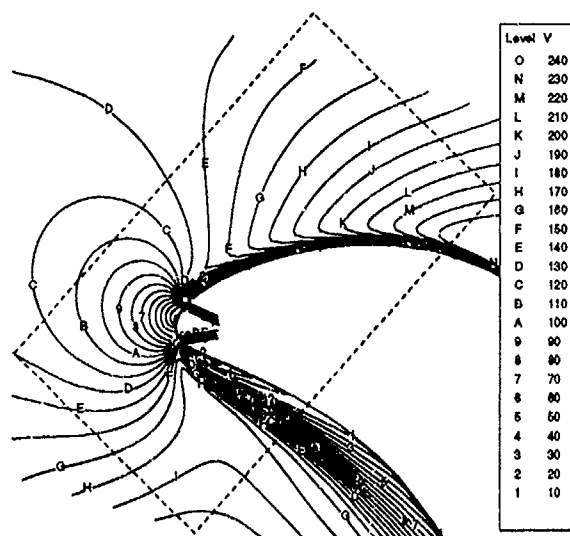
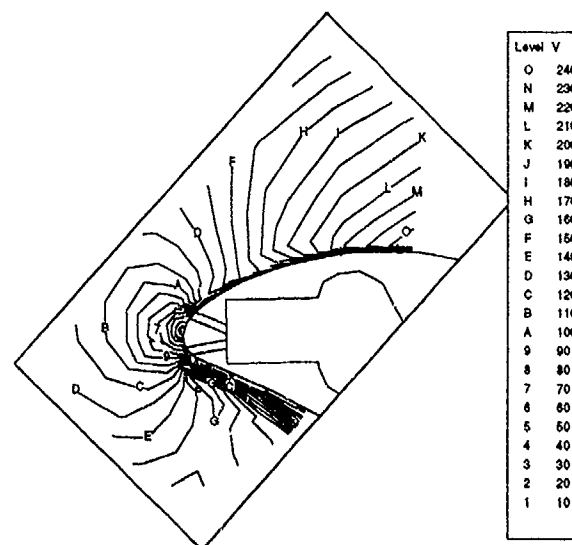
The measurements show, except for the smallest blowing ratio, flow separation on the suction side as well as on the pressure side of the blade. On the pressure side for the blowing ratio $M = 0.47$ no separation occurs. Due to the acceleration on the suction side, the separation there is much smaller than on the pressure side. The predicted results are an excellent agreement with measurements. Note, e.g. that for $M=0.47$ on the suction side also no flow separation on the suction side was predicted.

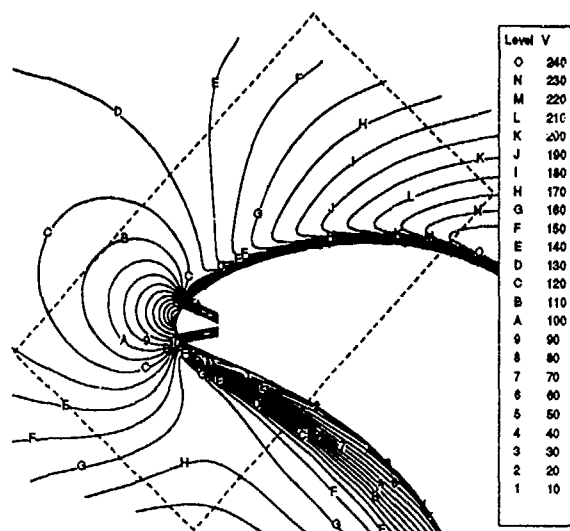
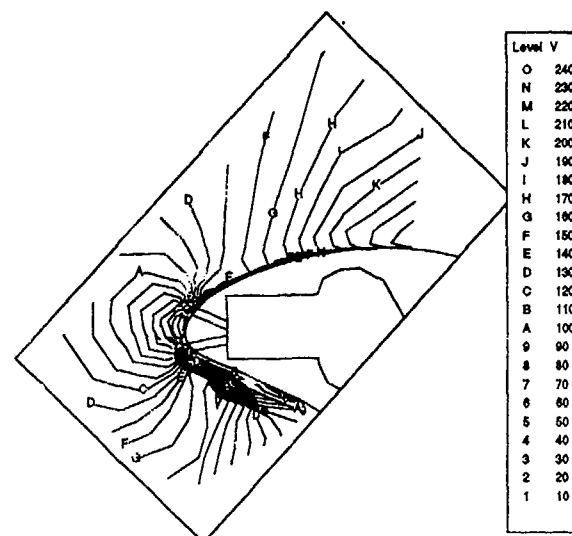
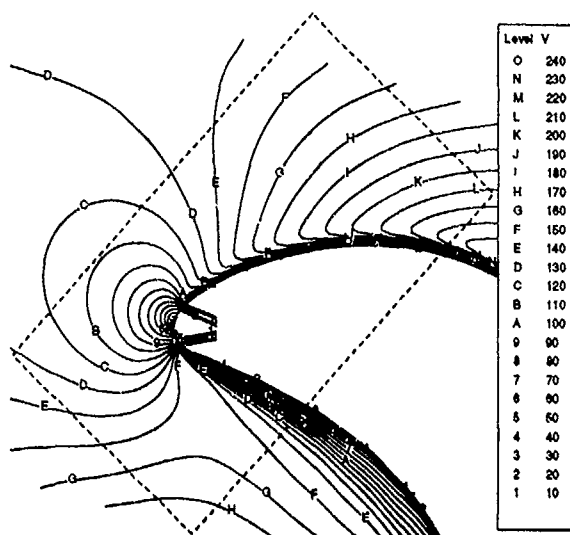
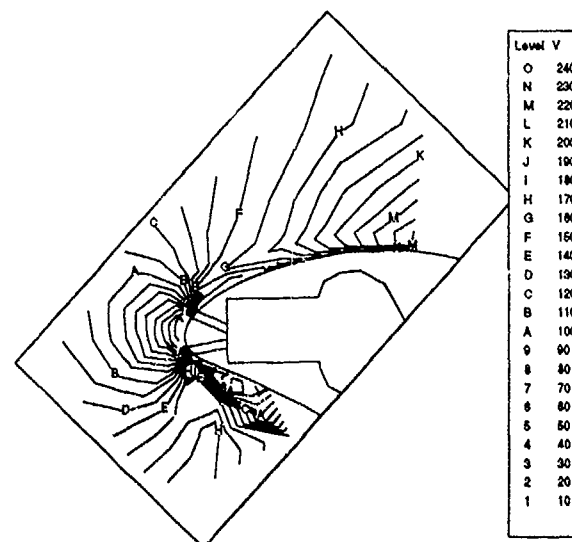
As expected at the slot exit a strong distortion of the velocity profile is to be detected. With increasing blowing ratio the deformation of the profile diminishes. For all blowing ratios the predicted non-uniform velocity profile at the slot exit agrees well with the measurements.

In addition, if the coolant mass-flux is low ($M=0.47$), a blockage of the slot by the main flow occurs leading to a strong acceleration on the downstream side in the slot. As shown by numerical calculations (Benz et al. (1992)) and by experiments (Andreopoulos (1983)) a small separation on the upstream side in the slot or hole is established due to the blockage of the flow.

The vector plots and the isolines of the velocity indicate that the measured separation is thicker than the calculated. This can be explained by the three dimensional flowpattern causing a flow below the jets in spanwise direction of the blade.

Figure 5: Predicted velocity vectors, $M=0.47$ Figure 7: Measured velocity vectors, $M=0.47$ Figure 6: Predicted velocity vectors, $M=0.76$ Figure 8: Measured velocity vectors, $M=0.76$

Figure 9: Predicted velocity vectors, $M=1.14$ Figure 11: Measured velocity vectors, $M=1.14$ Figure 10: Predicted velocity contours, $M=0.47$ Figure 12: Velocity contours, $M=0.47$

Figure 13: Predicted velocity contours , $M=0.76$ Figure 15: Velocity contours, $M=0.76$ Figure 14: Predicted velocity contours , $M=1.14$ Figure 16: Velocity contours, $M=1.14$

Conclusions

The flowfield generated by film cooling injection in the stagnation region of a high pressure turbine blade has been investigated experimentally and numerically. The measurements show for all blowing ratios separation downstream of the slots. Except for the smallest blowing ratio $M=0.47$ on the suction side no separation was found. For all blowing ratios the velocity profile at the slot exit shows a strong distortion. Additionally, for small blowing ratios a blockage of the slot by the main flow occurs resulting in an increased distortion of the velocity profile.

Due to this distinct elliptic behaviour of the interaction of the film-cooling air and main flow it is necessary, to use a fully elliptic Navier-Stokes-code for the prediction. Moreover, the coolant flow in the slot and the main flow has to be calculated simultaneously. As shown, these are the conditions for predicting the measured flow phenomena of film cooling at turbine blades and the excellent agreement of the predicted results with the measurements.

References

- [1] Andreopoulos, J. (1983): Measurements on a pipe flow issuing perpendicular into a cross stream, *J. Fluids Eng.*, Vol. 104, pp. 493-499
- [2] Bauer, H-J. (1989): Überprüfung numerischer Ansätze zur Beschreibung turbulenter elliptischer Strömungen in komplexen Geometrien mit Hilfe konturangepaßter Koordinaten, Dissertation, Universität Karlsruhe, Institut für Thermische Strömungsmaschinen
- [3] Beeck, A. (1992): Strömungsfelduntersuchungen zum aerodynamischen Verhalten eines hochbelasteten Turbinengitters mit Kühlluftausblasung an der Vorderkante, Dissertation Universität der Bundeswehr München, Institut für Strahltriebwerke
- [4] Beeck, A.; Fottner, L.; Benz, E.; Wittig S.: (1992) The aerodynamic effect of coolant ejection in the leading edge region of a film-cooled turbine-blade, presented at the AGARD Meeting : 'Heat-Transfer and Cooling in Gas Turbines' October 1992, Antalya, Turkey
- [5] Benz, E.; Wittig, S. (1992): Prediction of the interaction of coolant ejection with the mainstream at the leading edge of a turbine blade: Attached Grid Application, *Int. Sym. Heat Transfer in Turbomachinery*, August 24-28, Athens, Greece
- [6] Bergeles, G.; Gosmann, A.D.; Launder, B.E. (1976): The near-field character of a jet discharged normal to the main stream, *J. Heat Transfer*, Vol. 98c, pp. 373-378
- [7] Crabb, D.; Durao, D.F.G.; Whitelaw, J.H. (1981): A round jet normal to a crossflow, *J. J. Fluids Engg.*, Vol. 103, pp. 142-153
- [8] Hsu, C. (1981): A curvilinear-coordinate method for momentum, heat and mass transfer in domains of irregular geometry, PhD Thesis, University of Minnesota
- [9] Jeckel, R.; Noll, B.; Wittig S. (1992): Three-dimensional time-resolved velocity measurements in a gas turbine model combustor, *Symp. on Appl. Laser Technologies* Lissabon, 20-23 July
- [10] Kiock R., Laskowski G., Hoheisel H. (1982): Die Erzeugung höherer Turbulenzgrade in der Meßstrecke des Hochgeschwindigkeits-Gitterwindkanals Braunschweig zur Simulation turbomaschinenähnlicher Bedingungen DFVLR FB 82-25, Braunschweig
- [11] Noll, B. (1992): Evaluation of a bounded high resolution scheme for combustor flow computations, *AIAA-Journal*, Vol. 30, No. 1
- [12] Noll, B.; Wittig, S. (1992): A generalized conjugate gradient method for the efficient solution of three dimensional fluid flow problems, *Numerical Heat Transfer*, Vol. 20 No. 2, pp. 207-221
- [13] Patankar, S.V. (1980): *Numerical Heat Transfer and Fluid Flow*. Hemisphere Publishing Corporation
- [14] Peric, M. (1985): A finite volume method for the prediction of three-dimensional fluid flow in complex ducts, PhD Thesis, University of London
- [15] Rhie, C.; Chow, W.L. (1983): Numerical study of the turbulent flow past an airfoil with trailing edge separation, *AIAA Journal*, Vol.21, No.11
- [16] Römer N., Ladwig M., Fottner L. (1988) : Measuring Techniques at the High Speed Cascade Wind Tunnel of the University of the Federal Armed Forces Munich, 9th Symposium of Measuring Techniques for Transonic and Supersonic Flows in Cascades and Turbomachines, Oxford

[17] Schodl R. (1974) :
On the Development of a New Optical Method for
Flow Measurements in Turbomachines, ASME-paper
74-GT-157

[18] Scholz, N. (1956) :
Über die Durchführung systematischer Messungen
an ebenen Schaufelgittern, Zeitschr. Flugw. 4 , Vol.
10

[19] Scholz N., Hopkes U. (1959):
Der Hochgeschwindigkeits-Gitterwindkanal der
Deutschen Forschungsanstalt für Luftfahrt Braun-
schweig, Forschung auf dem Gebiet des Ingenieur-
wesens, Bd. 25, pp. 79-93

[20] Sturm W., Fottner L. (1985):
The High-Speed Cascade Wind Tunnel of the Ger-
man Armed Forces University Munich, 8th Sympo-
sium of Measuring Techniques for Transonic and
Supersonic Flows in Cascades and Turbomachi-
nes, Genua

[21] Van Doormaal, J.P.; Raithby, G.D. (1984):
Enhancements of the simple method for predicting
incompressible fluid flows, Numerical heat transfer,
Vol.7, pp.147-163

[22] Van Doormaal, J.P.; Raithby, G.D.; McDonald,
B.H. (1987):
The segregated approach to predicting viscous com-
pressible fluid flow, Transactions of the ASME,
Vol.109, April

[23] Van Leer, B. (1977):
Towards the ultimate conservative difference scheme
III. Upstream-centered finite difference scheme for
ideal compressible flow, Journal of Computational
Physics 23, pp. 263-275

[24] Wittig, S.; Bauer, H.J., Noll, B. (1987):
On the application of finite-difference techniques for
the computation of the flow field in gas turbine com-
bustors with complex geometries, AGARD Propul-
sion and Energetics, 70th Symposium on combustion
and fuels in gas turbine engines, AGARD CP No.
422

Navier-Stokes Analysis of a Swirling Jet in Crossflow

Hüseyin Yağcı*
TUSAŞ Aerospace Industries,
P.K. 18, 06690, Kavaklıdere,
Ankara, TURKEY

Mehmet Şerif Kavsaoğlu**
Middle East Technical University
Dept. of Aeronautical Engineering
06531 Ankara, TURKEY

Abstract

Flowfield of a subsonic swirling jet injected into a subsonic crossflow was computed by using a three dimensional Navier-Stokes code (LANS3D)¹. Baldwin-Lomax² turbulence model and the algebraic curved jet turbulence model of Oh and Schetz³ were used depending on the location in the flowfield. Characteristic boundary conditions based on Riemann invariants were utilised for the flow in and out planes. A single block grid with a cavity at the jet entrance was used.

Introduction

In this computational study a swirling subsonic jet injected into a subsonic crossflow was analysed. For comparison a test case was selected from the circular jet in crossflow experiments of Kavsaoğlu and Schetz⁴. This test case was described as the 58 % swirl case with jet to freestream velocity ratio of 4⁴. A three dimensional, thin layer, Reynolds averaged, compressible Navier-Stokes solver (LANS3D)^{1,5} was used. This program solves the Navier Stokes equations written in strong conservation form by using an LU-ADI factorization algorithm with diagonally dominant LU factorization. The algebraic turbulence model suggested by Oh and Schetz³ was used in the jet region. Baldwin-Lomax² model was used for the other viscous turbulent flow areas which are not covered by the first model. For the flow in planes the Riemann invariants based characteristic boundary conditions and for the flow out planes inverse characteristic boundary conditions were utilized. The detailed description of the application of these boundary conditions were given elsewhere⁶. Out of experience gained from previous studies⁶ it was decided to use a grid with cavity at the jet entrance for more realistic interaction of the jet with crossflow. In Figure 1 flowfield description of a round jet injected into a crossflow can be seen⁷. This figure also describes the coordinate system used for the presentation of present results.

Experimental Data For Comparison

For the test case selected a swirling circular jet was injected from a flat plate into a crossflow perpendicularly⁴. These experiments were performed in a uniform flow, low turbulence, subsonic wind tunnel of 1.8 m * 1.8 m test section. Jet to freestream velocity ratio was 4. Swirl was introduced

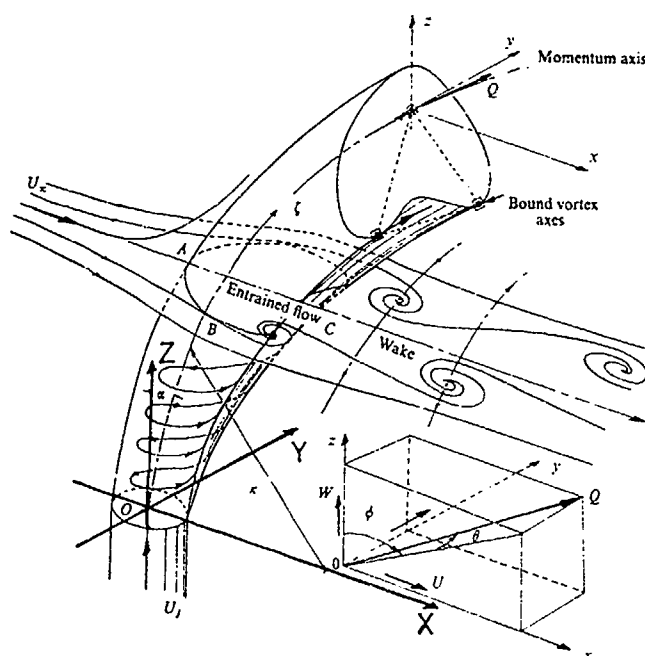


Figure 1. Flowfield description of a round jet in crossflow⁷.

by tangential air injection at a location upstream of the contraction used before the jet exit. Swirl ratio was defined as the ratio of the swirl component of velocity at $r/D \approx 0.41$ to the average total velocity measured at the jet exit. Where r is the radius measured from the jet center at the exit and D is the diameter of the jet exit. Swirl ratio was measured when the crossflow was off and with the above definition it was 58 %. Boundary layer on the flat plate was tripped before the jet entrance and had a turbulent velocity profile around the jet entrance. Jet exit velocity was about 67 m/sec. The experimental jet entrance velocity profile which was measured when crossflow was off is given in Figure 4 in comparison with the velocity profile used as boundary condition for the computation. Jet exit Mach number was about 0.2 and the Reynolds number based on crossflow velocity and the jet diameter was about 51400.

*Research Engineer

**Associate Professor

Grid

A three dimensional perspective view of the grid used is shown in Figure 2-a. This grid was obtained by rotation of a two dimensional half grid around the jet axis. This grid had a cavity at the jet entrance. In Figure 2-b the enlarged view of the two dimensional half grid at the cavity location is shown and in Figure 2-c the top view of this grid can be seen. The grid was stretched and the grid points were more densely located at the rear of the jet entrance. Additional figures describing this grid was given in paper 25 of this symposium⁶. This grid was extended from -15 D to 20 D in x direction, from -15 D to 15 D in y direction and from -0.5 D to 15 D in z direction where D being the jet exit diameter. The size of the grid was 42*55*45 points in ξ, η, ζ directions.

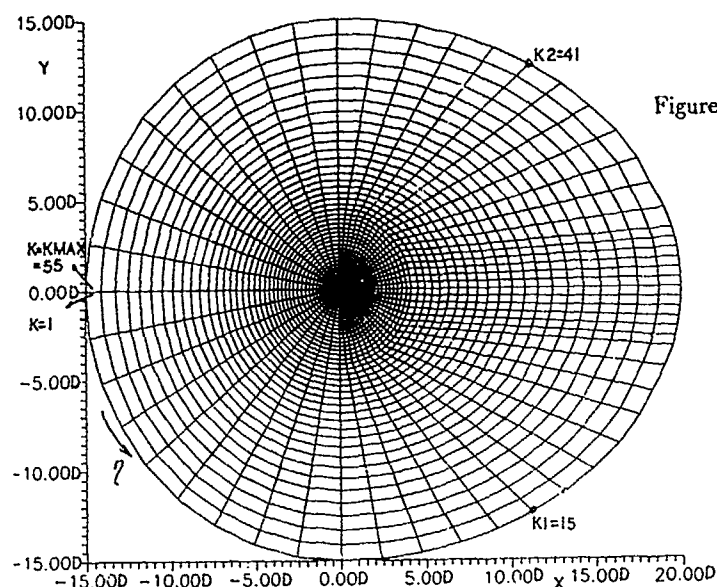


Figure 2-c. Top view of the grid.

Boundary Conditions

Application of the boundary conditions are described in Figure 3. At the bottom plane no slip condition was applied from $J=6$ to $J=37$ (see Figures 2, 3 and Figure 28 of Ref. 6). At the top plane freestream conditions were forced. At the outer side surface ($J=JMAX$) inflow characteristic boundary conditions were applied from $K=1$ till $K=15$ and from $K=41$ till $K=KMAX=55$, outflow (inverse) characteristic boundary conditions were applied from $K=16$ till $K=40$ (see Figure 2-c). Inflow and outflow characteristic boundary conditions were described in detail in Reference 6. For the inner side surface ($J=1$) flowfield variables were interpolated from the neighbouring points as described in Figure 31 of Ref. 6 and the related formulations given there. For the jet entrance plane inflow characteristic boundary conditions were applied as follows. The R_+ Riemann constant was found from the

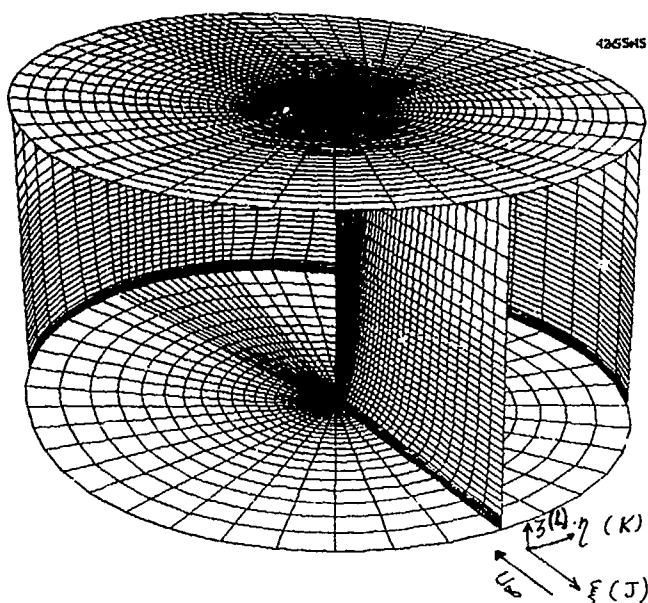


Figure 2-a. Three dimensional perspective view of the grid.

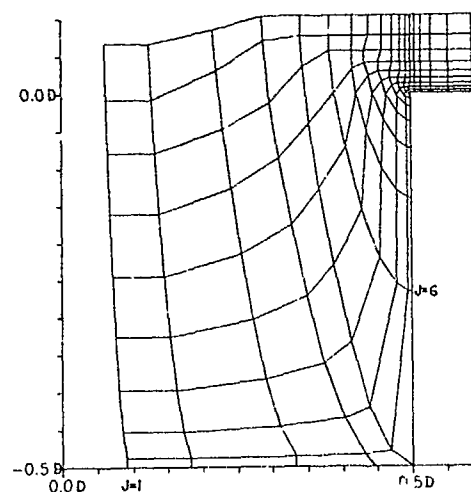


Figure 2-b. A two dimensional section view of the grid enlarged around the cavity.

specified infinity conditions. R_- was extrapolated from the interior of the flow domain. At ∞ , $u_{j,\infty}$, $v_{j,\infty}$, $w_{j,\infty}$ were specified according to the experimental jet exit velocity profile⁴. Jet to freestream velocity ratio was set as:

$$\frac{w_{j,\infty}}{U_\infty} = 4.0.$$

Swirl component of velocity was defined as:

$$V_{j,s,\infty} = \sqrt{u_{j,\infty}^2 + v_{j,\infty}^2}$$

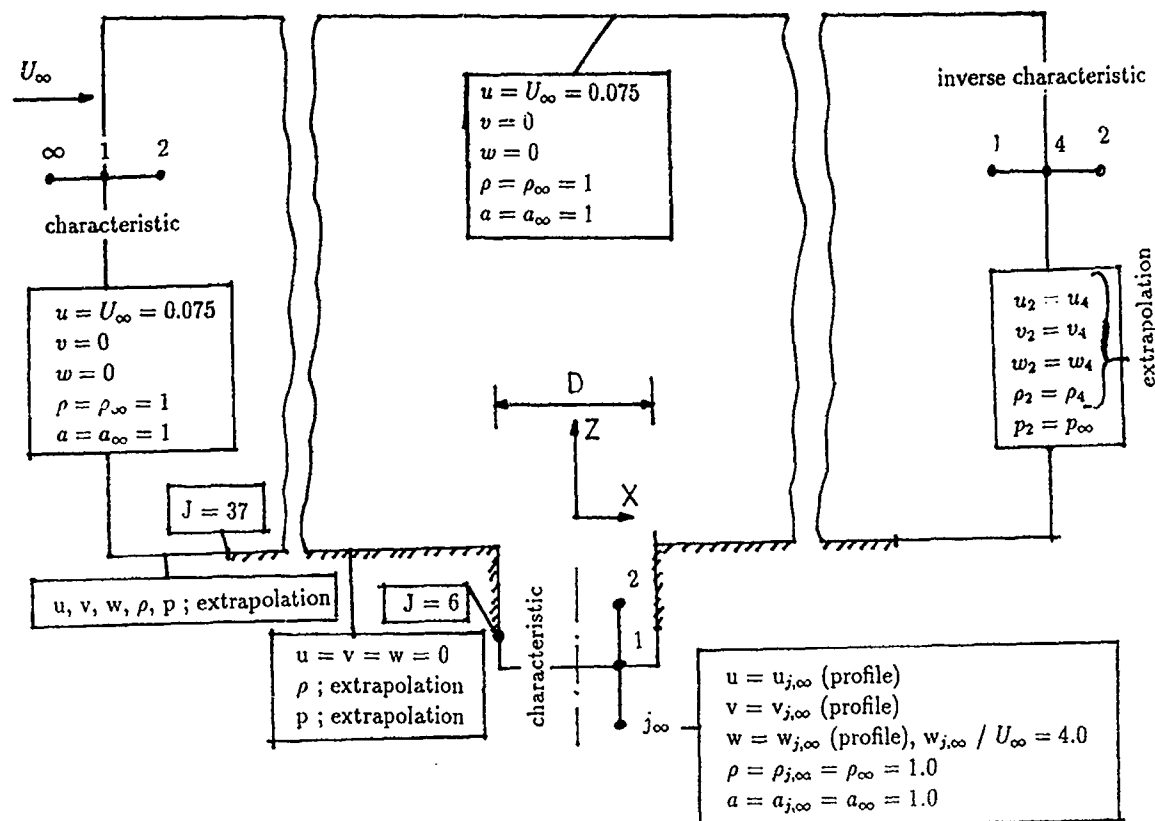


Figure 3. Application of the boundary conditions.

Total velocity was defined as:

$$V_{j,TOT,\infty} = \sqrt{w_{j,\infty}^2 + V_{j,\infty}^2},$$

$a_{j,\infty} = 1.0$ and $\rho_{j,\infty} = 1.0$ was accepted same with that of crossflow infinity conditions. Alternatively from Figure 3. $\rho_{j,\infty} = \rho_2$ could also be written but, this was not done. From Figure 3. the boundary conditions were set as follows. First the + and - Riemann invariants were calculated.

$$R_{\infty}^+ = V_{j,TOT,\infty} + \frac{2}{\gamma-1} a_{j,\infty}$$

$$R_2^- = w_2 - \frac{2}{\gamma-1} a_2$$

then,

$$V_{TOT,1} = 0.5 (R_{\infty}^+ + R_2^-)$$

but, instead of

$$a_1 = 0.5 \frac{\gamma-1}{2} (R_{\infty}^+ - R_2^-)$$

$$a_1 = a_{j,\infty} = 1.0$$

was taken. From isentropic relations,

$$\frac{\rho_1}{\rho_{\infty}} = \left(\frac{a_1}{a_{\infty}} \right)^{\frac{2}{\gamma-1}}$$

From, $a_{\infty} = 1$ and $\rho_{\infty} = 1$

$$\rho_1 = a_1^{2/(\gamma-1)}$$

then,

$$p_1 = \frac{\rho_1^{\gamma}}{\gamma}$$

$$e_1 = \frac{p_1}{\gamma-1} + 0.5 \rho_1 V_{TOT,1}^2$$

After obtaining the total velocity at point 1 the x, y, z components of the total velocity were obtained as follows;

$$u_1 = V_{TOT,1} * \frac{u_{j,\infty}}{V_{j,TOT,\infty}}$$

$$v_1 = V_{TOT,1} * \frac{v_{j,\infty}}{V_{j,TOT,\infty}}$$

$$w_1 = V_{TOT,1} * \frac{w_{j,\infty}}{V_{j,TOT,\infty}}$$

Indices:

1: first station in Z direction,

2: second station in Z direction,

∞ : infinity,

j: jet.

In Figure 4 the velocity profile given as the jet entrance boundary condition is shown in comparison with the experimentally measured one⁴. The solid lines show the conditions

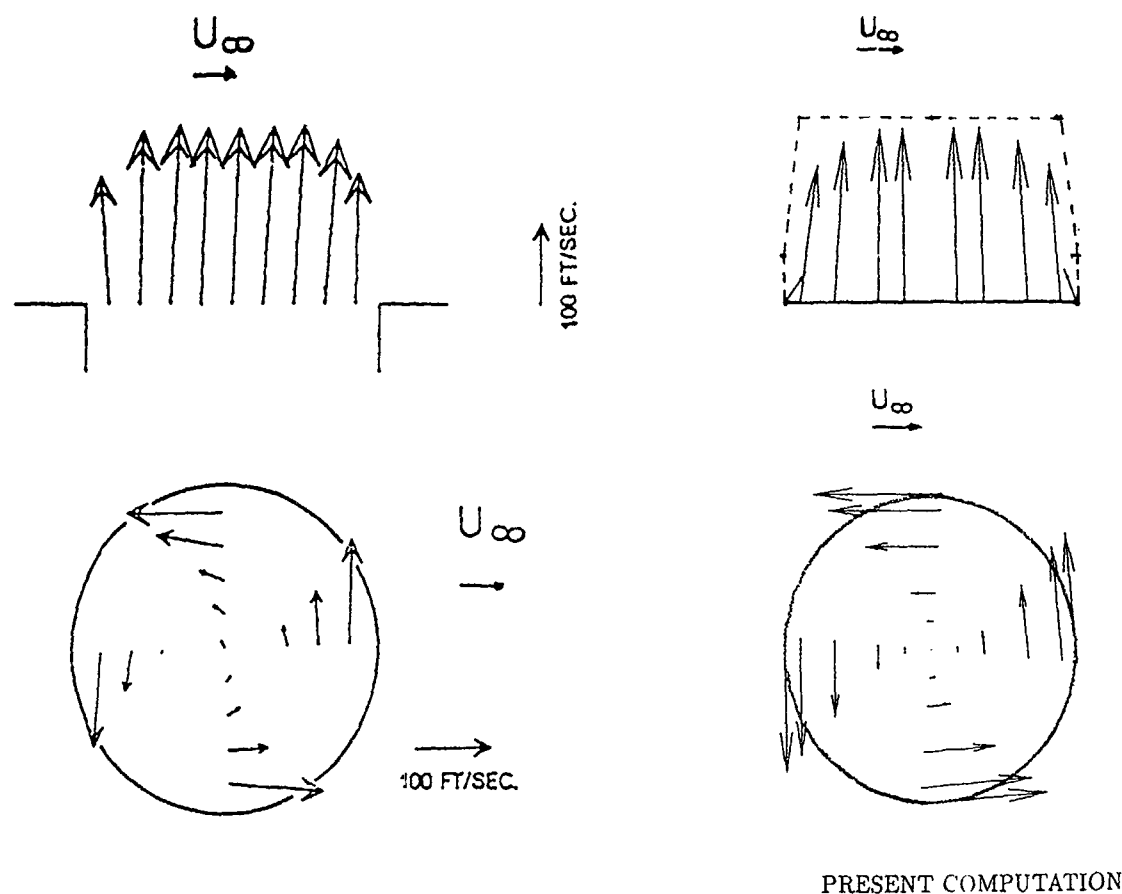


Figure 4. Swirling jet exit velocity profile in comparison with the experimental profile⁴, dotted lines show the profile specified as infinity condition.

at point 1, which is the actual computational boundary, and the dotted lines show the conditions at point j_∞ (see Figure 3). It can be seen that the specified profile at j_∞ was modified at point 1 by the application of characteristic boundary conditions.

Computational Details

The turbulence models were applied as follows. First the Baldwin-Lomax² model was applied over the flat plate up till $z/d = 2.0$ excluding the cavity region. Then the curved jet model of Oh and Schetz³ was applied for the curved jet region. No other turbulence predictions were made for the regions which were excluded by these two models such as the wake behind the jet.

Same with the experimental case⁴ the jet to freestream velocity ratio was 4 and the Reynolds number based on freestream velocity and the jet diameter was 51400. However the freestream and the jet Mach numbers were taken as 0.075 and 0.3 instead of the experimental 0.05 and 0.2. This was done so by expecting better results when a compressible flow solver used while keeping the flowfield effectively incompressible.

Computations were performed at the IBM 9021-500 vector computer installed at the TUSAŞ Aerospace Industries (TAI). Results which will be presented were obtained after 6000 iterations. For 6000 iterations L2 norm of the residual was dropped from 10^{-2} to 10^{-6} . For $42 \times 55 \times 45$ grid points one iteration lasted about 13 seconds CPU time.

Results

In Figure 5 the velocity vectors in jet centerplane ($Y/D = 0$), in Figure 6 the velocity vectors in the $X/D = 1.026$ plane are presented in comparison with the experimental results⁴. Note that the direction of the swirl component of velocity is the same with the direction of the freestream; for negative Y/D values. This should be considered particularly when viewing Figure 6. In Figure 7 the velocity vectors in the $Z/D = 0.61$ plane are presented. In general the agreement of the velocity vectors with the experimentally obtained velocity vectors are reasonably good. In Figure 8 computational obtained surface pressure distributions are presented in comparison with the experimental data⁴. In this figure computational $C_p = \text{const.}$ lines were drawn with $\Delta C_p = 0.2$ intervals

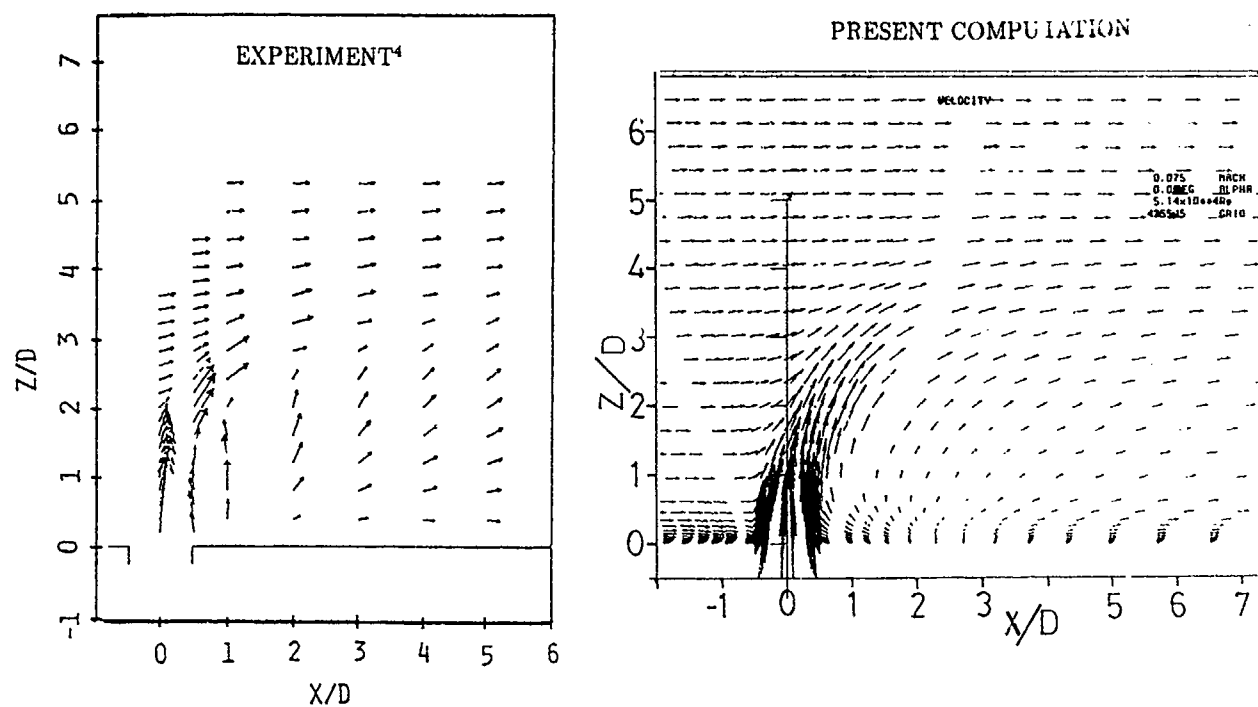


Figure 5. Velocity vectors in $Y/D = 0.0$ plane, (jet centerplane) in comparison with the experiment⁴.

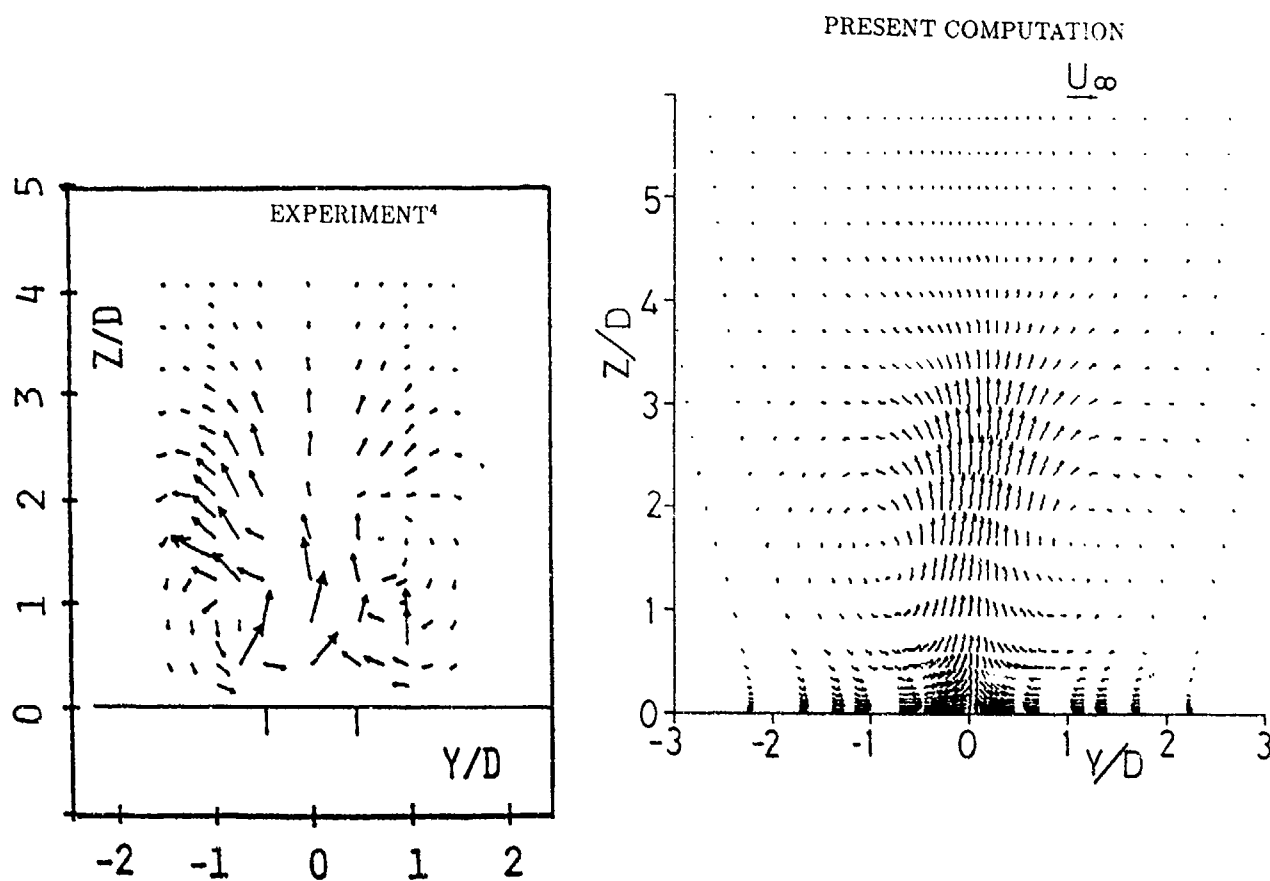
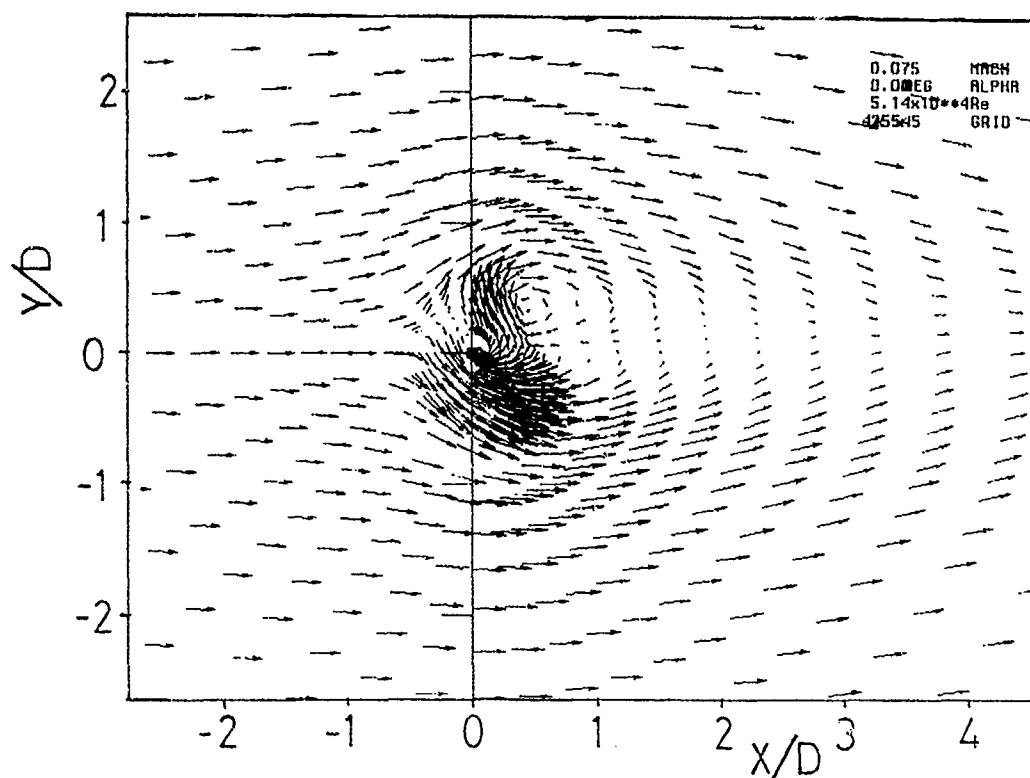
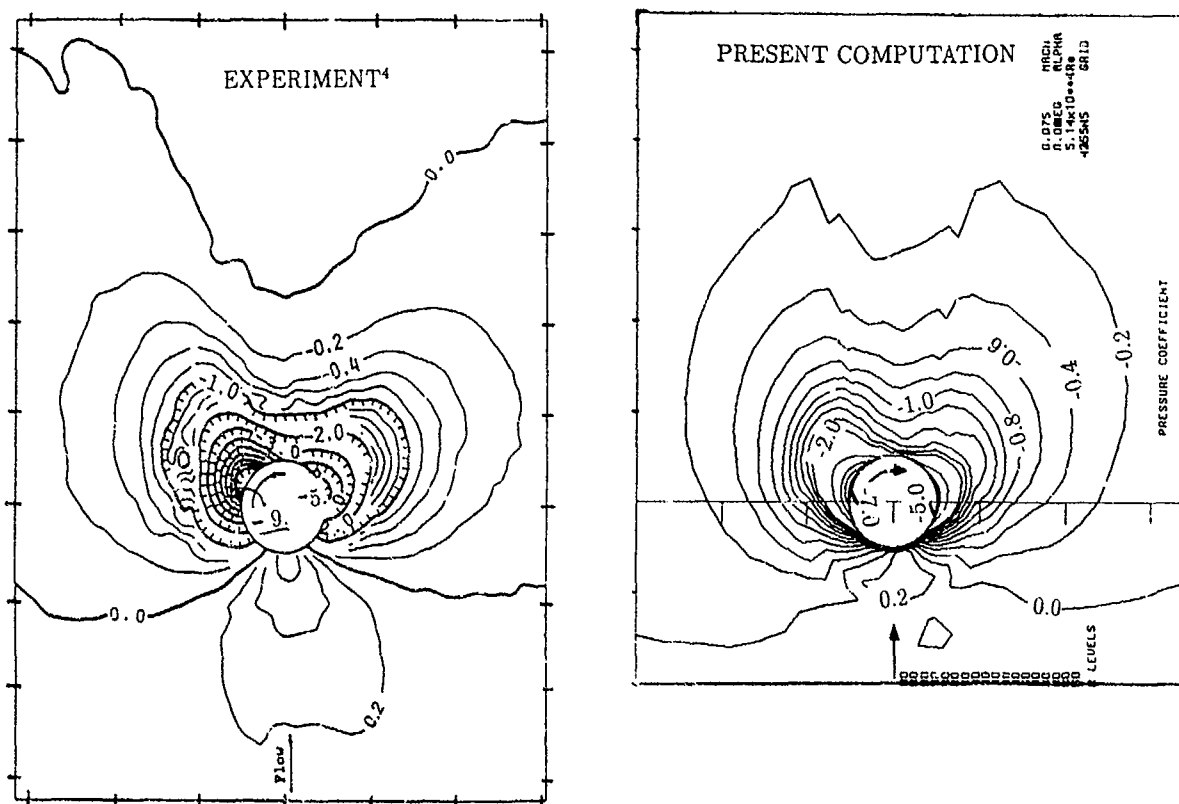


Figure 6. Velocity vectors in $X/D = 1.026$ plane in comparison with the experiment⁴.

Figure 7. Velocity vectors in $Z/D = 0.61$ plane.Figure 8. Surface pressure contours ($C_p = (p - p_\infty)/q_\infty$) in comparison with experiment⁴.

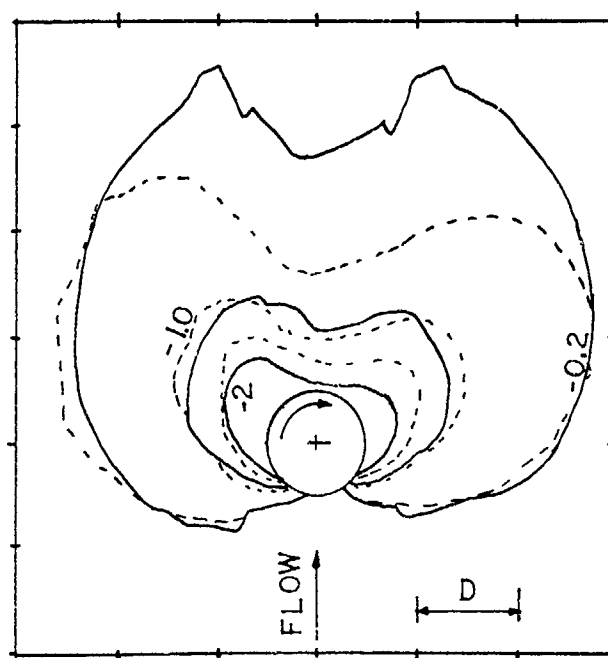


Figure 9. Comparison of the $C_p = -0.2$, -1.0 and -2.0 curves with the experiment⁴, dotted lines represent experiment, solid lines represent present computation.

between $C_p = 0.2$ and $C_p = -2.0$, and with $\Delta C_p = 1.0$ intervals between $C_p = -2.0$ and $C_p = -7.0$. Experimental result showed stronger asymmetry particularly at the immediate vicinity of the jet exit. In Figure 9 only the $C_p = -0.2$, -1.0 and -2.0 lines are compared with the experimental ones. Computationally obtained -0.2 line extended to a larger region behind the jet. $C_p = -1.0$ lines agreed reasonably well.

Discussion

In this study thin layer Navier Stokes analysis of a swirling jet in cross flow was performed. Based on previous experience⁶ Riemann invariant type inflow characteristic boundary conditions were applied at the flow in planes of both jet and crossflow and inverse characteristic boundary conditions were applied at the flow out plane. Again, based on previous experience⁶ a single block grid which had a cavity for the jet entrance was used. Algebraic turbulence models were utilized. Baldwin-Lomax² model was used for flow over solid surfaces and algebraic curved jet turbulence model of Oh and Schetz³ were used for the jet dominated regions. Asymmetric nature of the flowfield was predicted. Velocity vectors agreed reasonably well with the experiment⁴. Experimentally

obtained surface pressures⁴ showed asymmetric pressure distribution which was felt particularly at the near vicinity of the jet exit. Computationally obtained surface pressure distribution agreed well with the experiment in some regions. Agreement was weaker at the immediate vicinity of the jet exit where experiment showed stronger asymmetry. This may be due to grid skewness and/or turbulence modelling at this region. Also, since swirl introduces a strong shear flow in directions not normal to the wall, a full Navier Stokes solution could be more appropriate rather than thin layer. The second disagreement was at the rear of the jet exit where the com-

putationally obtained $C_p = -0.2$ line extended to a larger region behind the jet when compared to the experimental one⁴. A similar result was obtained after the computation of a nonswirling jet in crossflow using the same flow solver, same grid and similar boundary conditions⁶. This could be due to the turbulence modelling. A more appropriate model for this wake region is needed. It should be mentioned that experimentally obtained turbulence data is strongly needed for test of turbulence models used for computation of jets in crossflow.

Acknowledgement

The authors would like to thank Dr. Kozo Fujii of Institute of Space and Astronautical Science (JAPAN) for permission to use LANS3D code. The authors would like to acknowledge the help received on technical matters from Dr. Ünver Kaynak and Mustafa Dindar of Tusaş Aerospace Industries (TAI), TURKEY.

References

- 1 Fujii, K. and Obayashi, S., "Practical Applications of New LU-ADI Scheme for the Three-Dimensional Navier-Stokes Computation of Transonic Viscous Flows", AIAA Paper 86-0513, Jan. 1986.
- 2 Baldwin, B. S. and Lomax, L. S., "Thin Layer Approximation and Algebraic Model for Separated Turbulent Flows," AIAA Paper 78-257, 1978.
- 3 Oh, T. S., and Schetz, J. A., "Finite Element Simulation of Complex Jets in a Crossflow for V/STOL Applications," Journal of Aircraft, Vol. 27, No. 5, May 1990.
- 4 Kavsaoglu M. S., and Schetz J. A., "Effects of Swirl and High Turbulence on a Jet in a Crossflow," Journal of Aircraft, Vol. 26, No. 6, June 1989.
- 5 Obayashi, S., Matsushima, K., Fujii K. and Kuwahara, K., "Improvements in Efficiency and Reliability for Navier-Stokes Computations Using the LU-ADI Factorization Algorithm", AIAA Paper 86-0338, Jan. 1986.
- 6 Kavsaoglu M. S., Akmandor İ., Çiray S., Fujii K., "Navier-Stokes Simulation of Two and Three Dimensional Jets in Crossflow, Effects of Grid and Boundary Conditions", Paper No. 25 presented at the AGARD symposium on Computational and Experimental Assessment of Jets in Cross Flow, 19-22 April 1993 Winchester, United Kingdom.
- 7 Moussa, Z. M., Frischka, J. W., and Eskinazi, S., "The Near Field in the Mixing of a Round Jet with a Cross-Stream," Journal of Fluid Mechanics, Vol. 80, p. 49, 1977.

Etude expérimentale sur les interactions entre un jet supersonique chauffé transversal et un écoulement supersonique externe

R. Gaillard, P. Geffroy, L. Jacquin et G. Losfeld

Office National d'Etudes et de Recherches Aéronautiques
Direction de l'Aérodynamique ONERA
BP 72 Châtillon Cedex-France

1. Résumé

Ce papier présente les techniques mises en oeuvre ainsi qu'un ensemble de résultats obtenus lors d'une expérimentation menée à la soufflerie S5ch de l'ONERA sur le cas d'un jet transversal de nombre de Mach égal à 2, fortement chauffé, débouchant dans un écoulement perpendiculaire de même nombre de Mach. L'écoulement est qualifié au moyen d'une sonde 5 trous miniature, par des thermocouples et par vélocimétrie laser tridirectionnelle. Les effets de la température sur les propriétés moyennes et turbulentes du jet sont discutées. Des strioscopies éclairées sont également présentées. Elles mettent en évidence la nature fortement instationnaire de cette interaction.

2. Introduction

Dans le cadre des applications au pilotage par jet, l'ONERA mène depuis quelques années des activités expérimentales et numériques sur le thème des jets transversaux supersoniques. En particulier, plusieurs expériences ont été effectuées à la soufflerie supersonique S5 du centre de Chalais sur le cas de jets débouchant perpendiculairement de plaques planes. Dans les systèmes de pilotage, les jets sont constitués de gaz très chauds issus d'impulseurs à poudre. Dans les expériences de laboratoire, ces jets sont souvent simulés par des éjections de gaz froid léger (hélium par exemple). Cette démarche s'appuie sur le principe d'une analogie entre les gaz chauds et les gaz légers, analogie qui n'a jamais été réellement validée. L'un des objectifs de cette nouvelle expérience est de fournir des informations précises sur l'influence de la température sur l'interaction entre des jets de même espèce (ici de l'air). Des essais ultérieurs sur l'interaction entre des gaz différents permettront alors d'évaluer les limites de cette analogie.

Au delà de ce problème particulier, l'expérience décrite ici fournit de multiples éléments sur les propriétés aérodynamiques générales du jet transversal supersonique [Ref 1].

Ce papier présente une partie des résultats obtenus, tout en mettant l'accent sur les éléments techniques et métrologiques particuliers qui ont été développés pour cette expérience.

3. Dispositif expérimental

Le dispositif est schématisé sur la figure 1. Le jet, de nombre de Mach égal à 2, débouche d'une plaque plane dans une demi-tuyère de même nombre de Mach. Il est alimenté par de l'air comprimé réchauffé à l'aide d'une canne chauffante schématisée sur la figure. Cette canne contient un faisceau de six tubes métalliques résistants, mis sous tension électrique, dans lesquels circule l'air d'alimentation de la tuyère. L'alimentation électrique est assurée par un transformateur fournissant une puissance nominale de 80 kW. La partie basse de la canne chauffante est refroidie par une circulation d'eau.

Ce système permet de réguler continuellement la température d'arrêt du jet jusqu'à des valeurs d'environ 1200K. Les principaux paramètres de cette expérience sont résumés ci-dessous.

Jet :

- Diamètre : $d_j = 11$ mm.
- Nombre de Mach : $M_j = 2$.
- Pression d'arrêt : $p_{ij} = 5$ b
- Température d'arrêt : $T_{ij} = 310, 620, 930$ °K
- Densité : $\rho_j = 1.29, 0.65, 0.43$ kg/m³.
- Vitesse de sortie : $U_j = 526, 744, 911$ m/s.

Écoulement extérieur :

- Hauteur demi-veine : $H = 150$ mm
- Largeur demi-veine : $L = 300$ mm
- Nombre de Mach $M_\infty = 2$.
- Pression totale : $p_{i\infty} = 0.5$ b
- Température totale : $T_{i\infty} = 310$ °K.
- Densité : $\rho_\infty = 0.129$ kg/m³
- Vitesse : $U_\infty = 526$ m/s

Table 1 : Conditions génératrices

Dans la suite, les trois jets expérimentés seront identifiés par le rapport de température $R_T = T_{ij}/T_{\infty}$ qui varie de 1 à 3.

Comme pour le cas d'une interaction incompressible, les lignes principales d'un jet transversal supersonique (trajectoires moyennes, par exemple) dépendent principalement du rapport des flux de quantité de mouvement. Dans notre expérience, les nombres de Mach étant égaux et les gaz de même composition (air), ce paramètre se réduit au rapport des pressions statiques :

$$R^2 = \frac{\rho_j U_j^2}{\rho_{\infty} U_{\infty}^2} = \frac{P_j}{P_{\infty}} = 10 \quad (1)$$

Le jet est sous-détendu.

4. Visualisations

Les lignes principales de cette interaction sont schématisées sur la figure 2. Certains de ces éléments sont caractérisés par la strioscopie continue de la figure 3 ainsi que par la tomoscopie de la figure 4. La tomoscopie est effectuée dans un plan transversal situé à $x/d_j = 5$ à l'aval de l'éjecteur, en introduisant de l'eau pulvérisée uniquement dans l'écoulement extérieur. Les phénomènes observés sont typiques de ce genre d'écoulement (cf. par ex. [Ref 2]). Il s'agit ici du cas iso-énergétique ($R_T = 1$), mais le réchauffement ne modifie pratiquement pas les résultats (cf. [Ref 1]).

Sur la figure 3, on identifie le choc détaché, la structure "en lambda" de l'interaction entre ce choc et la couche limite, et dans le jet lui-même, la focalisation des ondes de compression terminée par un disque de Mach. Sur la figure 4, on observe la trace du choc de tête ainsi que celle du choc de recompression qui se développe sous le jet. Ce choc, qui est vertical à $x/d_j = 5$, redresse l'écoulement extérieur après la détente consécutive au contournement du jet. Ce dernier est caractérisé par l'absence de traceur. On peut aussi noter l'allure perturbée de la couche limite ainsi que la présence des tourbillons en fer à cheval qui se développent à partir de la base du jet.

Des strioscopies éclairs, d'une durée de 20ns, ont été réalisées à l'aide d'un matériel Impulsphysic (cf. [Ref 1]).

La figure 5 montre un cliché obtenu pour le jet iso-énergétique ($R_T = 1$). Cette photo peut être directement comparée à son homologue "stationnaire" de la figure 3. Les figures 6 et 7 montrent deux photos relatives au cas du jet chauffé à 930K ($R_T = 3$). Ces deux photos correspondent à un réglage différent des couteaux strioscopiques. Les trois strioscopies éclairs montrent que le jet transversal est soumis à

d'intenses phénomènes instationnaires.

Tout d'abord, des instabilités violentes se développent dans la couche de mélange du jet. En comparant la trajectoire des structures turbulentes associées à ces instabilités avec l'allure du barillet de sous-détente du jet, on constate que cette agitation turbulente n'affecte que la partie amont de la couche de mélange initialement cylindrique. Ce développement asymétrique de la turbulence pourrait être relié aux effets centrifuges associés à la courbure du jet. En effet, dans la partie amont de la couche de mélange le moment angulaire de l'écoulement décroît dans le sens positif du rayon de courbure. Il s'agit là de conditions favorables pour le développement d'instabilités centrifuges. Par opposition, le moment angulaire augmente dans la partie aval de la couche de mélange. La turbulence est donc ici soumise à une courbure stabilisante. Cette interprétation simplifiée considère le cas de couches de mélange planes. Elle ne constitue donc qu'un élément très partiel des mécanismes tridimensionnels qui régissent l'évolution de la nappe du jet cylindrique défléchi. Par exemple, la partie de la couche de mélange située sous le jet est ici fortement tridimensionalisée par le développement des tourbillons de sillage (cf. section 5). L'absence de turbulence sous le jet résulte certainement plus de ces effets tridimensionnels complexes que d'une "restabilisation" centrifuge.

Comme le montrent les figures 5 et 6, les instabilités amonts de la couche de mélange sont couplées à une propagation acoustique intense dans l'espace compris entre le jet et le choc détaché (l'augmentation du contraste sur la figure 7 permet d'accentuer le champ turbulent, mais elle efface en même temps les fines discontinuités qui caractérisent les ondes). Ces ondes semblent provenir de la région de l'éjecteur, juste derrière la partie droite du choc. On observe aussi que le choc détaché est fortement perturbé par l'interaction avec les ondes. Un phénomène équivalent a été observé dans un jet supersonique d'hélium [Ref 3].

En comparant les deux figures, on voit que l'accroissement de la température du jet s'accompagne d'une intensification de la propagation acoustique. On note en particulier que les ondes se propagent plus en aval et que le choc détaché est plus perturbé. Ces mécanismes et leur dépendance vis à vis de la température peuvent s'interpréter comme suit. On peut supposer qu'on est ici en présence d'ondes de Mach engendrées par les structures turbulentes. La courbure de ces ondes peut alors résulter de celle des trajectoires des sources turbulentes ainsi que de la variation de la célérité du son derrière le choc détaché. Dans le cadre de ce scénario, la propagation de ces ondes est alors régie par le nombre de Mach convectif défini comme le rapport entre la vitesse de convection des structures et la célérité du son dans

l'espace compris entre le jet et le choc. Cette célérité étant indépendante de la température du jet, le nombre de Mach convectif dépend donc essentiellement de la vitesse de convection des structures. Cette vitesse de convection augmente avec la vitesse du jet, donc avec la température. Ceci peut alors expliquer l'intensification du mécanisme propagatif entre le cas $R_T=1$ et le cas $R_T=3$. Des mesures sont en cours pour analyser plus en détail ces mécanismes instationnaires.

5. Champ moyen

Le champ moyen de ces écoulements a été caractérisé à l'aide d'une sonde 5 trous miniaturisée (d'un diamètre de 1.5 mm) et avec des thermocouples. Les procédures d'étalonnage de la sonde 5 trous sont décrites dans la référence [4]. Des thermocouples (Thermocoax) ventilés et non-ventilés ont été utilisés. Comme expliqué dans la référence [1], dans un écoulement aussi tridimensionnel et turbulent, les résultats fournis par la sonde non-ventilée s'avèrent plus facile à analyser.

Quatre demi-plans transversaux à l'aval de l'éjecteur ($x/d_j=5, 10, 15$ et 17.5) ont été sondés sur un maillage fin ($2.5 \times 2.5 \text{ mm}^2$). Les sondages ne sont pas poursuivis au delà de $x/d_j=17.5$, car l'écoulement est alors perturbé par le choc détaché qui est réfléchi par la paroi supérieure de la veine.

Des résultats typiques déduits de ces sondages sont présentés sur les figures 8 et 9 sous la forme d'une juxtaposition du cas iso-énergétique ($R_T=1$, partie droite des figures) et du cas du jet chauffé à 930K ($R_T=3$, partie gauche). La figure 8 montre le flux de quantité de mouvement, ρU_0^2 où U_0 désigne le module de la vitesse; la figure 9 montre la composante axiale du rotationnel, Ω_x . Ces deux quantités sont normalisées à l'aide de paramètres relatifs à l'écoulement externe, $\rho_\infty U_\infty^2$ pour la quantité de mouvement, et $2U_\infty d_j$ pour le rotationnel ($2U_\infty d_j$ évalue la vorticité associée au contournement d'un cylindre de diamètre d_j par un écoulement plan de vitesse U_∞).

5.1 Quantité de mouvement

Sur la figure 8 on observe un déficit de quantité de mouvement très marqué, sous le jet, dans la zone où se forment les tourbillons. Dans les plans $x/d_j=15$ et 17.5 , on peut identifier la réflexion du choc détaché. Au delà de $x/d_j=15$, cette onde réfléchie impacte la partie supérieure du jet qui correspond à la zone où ρU_0^2 atteint son maximum. Des lignes de discontinuité apparaissent sur cette figure. A $x/d_j=5$, on identifie une ligne horizontale aux alentours de $z=20\text{mm}$. Cette ligne pourrait correspondre à la surface de glissement associée à la ligne de rattachement entre le choc de tête et le choc de

séparation (point triple). A $x/d_j=10$, on observe la marque verticale du choc de recompression schématisé sur la figure 2 et visualisé sur la figure 4. L'identification de ce choc de recompression dans les sondages plus aval est plus difficile (cf. [Ref 1]).

Enfin, on voit que la température n'a pratiquement aucun effet sur le flux de quantité de mouvement. Seules de légères différences apparaissent dans le dernier plan de sondage ($x/d_j=17.5$) : on note une légère déformation des lignes iso-valeurs ainsi que le retour plus précoce du choc détaché.

5.2 Tourbillons

Sur la figure 9, l'allure des iso-valeurs de la composante longitudinale du rotationnel illustre la transformation rapide de la nappe tourbillonnaire du jet en un couple de tourbillons contrarotatifs parfaitement défini. L'origine et les mécanismes qui régissent l'établissement de ces tourbillons n'ont jamais été totalement clarifiés. Conformément au schéma de la figure 10, une interprétation possible consiste à relier directement ces tourbillons à la nappe tourbillonnaire issue de l'intérieur de l'éjecteur. La "visualisation" des tourbillons au moyen d'un sondage tel que celui de la figure 9, correspondrait alors à une coupe effectuée au travers d'un amalgame d'anneaux tourbillonnaires issus de l'éjecteur. Ces anneaux subissent un violent étirement sous l'effet de l'entraînement par l'écoulement extérieur. Comme montré dans la référence [5], ce principe est compatible avec l'évolution de l'intensité des tourbillons mesurée dans certaines expériences. Il semble compatible, aussi, avec les analyses théoriques et numériques des références [6] et [7]. Notons que la strioscopie fortement contrastée de la figure 7 montre une structuration horizontale de l'écoulement qui n'est pas sans point commun avec le schéma de la figure 10. On note aussi sur la figure 9 la présence des tourbillons en "fer à cheval" qui résultent de la rotation et de l'étirement des lignes tourbillonnaires autour de la base du jet (cf. figures 2, 4 et 10).

Concernant l'effet de la température, on voit que l'accroissement de la vitesse du jet avec R_T s'accompagne, logiquement, d'une intensification de Ω_x . On est cependant frappé par la similitude entre les positions et les formes des lignes iso-valeurs. On remarque seulement une légère élévation de la trajectoire des tourbillons avec R_T .

Enfin, on s'attend à ce que les tourbillons de sillage annihilent progressivement les tourbillons en "fer à cheval", qui sont moins intenses, et de signe opposé. Cela peut expliquer la diminution de l'intensité de ces tourbillons secondaires lorsque R_T augmente.

L'influence de la température sur les tourbillons contrarotatifs de sillage est illustré de façon

différente, sur la figure 11 à travers l'évolution longitudinale de la circulation de chaque tourbillon, $\Gamma(x)$, et l'évolution de l'impulsion du système formé par les deux tourbillons, $I(x)$. Ces paramètres sont définis de la façon suivante :

$$\Gamma(x) = \int_C U \cdot dl = \int_{-\infty}^{\infty} \int_{-\infty}^{\infty} \Omega_x dydz \quad (2)$$

$$I(x) = 2 \int_{-\infty}^{\infty} \int_{-\infty}^{\infty} \rho y \Omega_x dydz \quad (3)$$

où y et z sont les coordonnées transversales et verticales. Sur la figure 11(b), $I(x)$ est normalisé par l'impulsion verticale du jet, évaluée ici par $I_0 = \rho_j U_j^2 A_j / U_\infty$ avec $A_j = \pi d_j^2 / 4$. L'impulsion d'un système contrarotatif plan ne peut décroître que sous l'effet des flux turbulents à travers sa frontière (ovale de Kelvin). Ici, bien que les tourbillons de la figure 9 ne soient pas pleinement bidimensionnels, ce paramètre peut permettre de caractériser l'effet global de la diffusion turbulente sur le système formé par les deux tourbillons. La circulation de chaque tourbillon individuel décroît sous l'effet de la diffusion interne des tourbillons puisque celle-ci s'accompagne d'un transfert de rotationnel de signe inverse à travers le plan de symétrie du système ($y=0$). Ce phénomène n'affecte pas l'impulsion.

La figure 11(a) montre que la circulation Γ décroît rapidement selon x et que son niveau augmente avec R_T . Parallèlement, la figure 11(b) montre que l'impulsion du sillage tourbillonnaire se stabilise à une valeur égale à environ la moitié de I_0 . On note que, malgré l'accroissement de Ω_x avec la température, l'impulsion présente un comportement inverse : l'impulsion des tourbillons à $R_T=3$ est inférieure d'environ 15% à celle obtenue dans le jet iso-énergétique $R_T=1$. Conformément à la relation (3), ce comportement résulte d'une variation de la distribution du rotationnel, et surtout de la décroissance de la masse volumique de l'écoulement chaud. Selon l'interprétation de ce paramètre donnée plus haut, ce comportement traduit une intensification globale, avec l'élévation de la température, de la diffusion turbulente qui affecte le système tourbillonnaire.

Enfin, la figure 12 présente le résultat des sondages au thermocouple, sous la même forme que les figures 8 et 9. On note la forme initialement cylindrique des iso-températures d'arrêt pour $R_T=3$ et sa déformation progressive sous l'effet des tourbillons de sillage. Le déficit de température d'arrêt observé dans la zone tourbillonnaire du jet iso-énergétique est la manifestation du déséquilibre entre les mécanismes diffusifs qui affectent l'énergie dans le cas où le

nombre de Prandtl diffère de l'unité [Ref 1]. Il s'agit ici du même mécanisme que celui rencontré dans les couches limites compressibles.

6. Mesure par vélocimétrie laser

Nous avons également sondé le jet iso-énergétique et le jet chauffé à 930K à l'aide du banc de vélocimétrie laser tridirectionnelle de l'ONERA. Le principe de ce banc est exposé dans la référence [8]. Le système comprend deux sources laser argon de 15 W. Les longueurs d'onde verte et bleu de l'une des sources sont utilisées pour mesurer les composantes longitudinales et verticales de la vitesse instantanée. Ces faisceaux suivent une direction perpendiculaire à l'axe de la veine. Quant à la mesure de la troisième composante, elle s'appuie sur l'utilisation d'un couple de faisceaux violets délivrés par la seconde source. Ces faisceaux convergent vers le point de mesure avec un angle de 45° par rapport à l'axe optique des autres faisceaux. Les signaux délivrés par les photomultiplicateurs sont traités analogiquement par des compteurs DANTEC LD 55 et par une interface de simultanéité ONERA. Les principaux paramètres de fonctionnement du vélocimètre sont résumés ci-dessous.

Composantes	bleue	verte	Violette
	488nm	515nm	475nm
Focale (m)	1	1	1.5
Interfrange (μ m)	16.67	16.67	18.75
Nbre de franges	24	24	16
Dimension du			
Volume de mesure	400	400	300
(μ m)			
Fréquence de Bragg	10	10	10
(MHz)			

Table 2 : Configuration du banc laser

L'ensemencement est effectué avec des particules polydispersées d'oxyde de magnésium (MgO), de diamètre moyen égal à environ 0.4 μ m. La masse volumique de ce produit est égale à 3500kg/m³. Deux systèmes d'ensemencement permettent d'introduire les particules de façon indépendante à l'amont de la canne chauffante et dans le convergent de la veine d'essai.

6.1 Limitations

La mesure par vélocimétrie laser 3D est ici soumise à toutes les limitations inhérentes à cette technique : 1) pénétration optique et particules virtuelles, 2) domaine des vitesses, 3) problèmes d'ensemencement. On trouvera dans la référence [1] un exposé détaillé de ces limitations et des moyens utilisés pour les minimiser. On se limitera ici à quelques principes généraux.

Concernant le premier point, la disposition des

faisceaux évoquée ci-dessus correspond à un compromis entre la pénétration optique et la minimisation du biais de mesure consécutif à la création de particules virtuelles (cf. [9], [1]). Des hublots spéciaux ont été implantés dans la veine S5 pour faciliter le sondage des quatre plans étudiés ci-dessus avec cet arrangement optique.

Le vélocimètre a par ailleurs été configuré pour permettre de couvrir au mieux le domaine des vitesses à mesurer. Il faut noter que ce domaine peut être localement très étendu. C'est le cas notamment dans le plan de symétrie $y=0$, près de l'éjecteur, là où les vitesses verticales induites par les tourbillons peuvent être aussi importantes que les vitesses longitudinales. La mesure dans ces conditions nécessite un contrôle strict du domaine de fonctionnement qui est déterminé par le défilement des franges, et la valeur des fréquences du filtrage passe-bande.

Le problème de l'ensemencement est certainement le plus délicat. Les particules sont en effet soumises, d'une part à des effets centrifuges violents dans la zone d'éjection et dans le sillage tourbillonnaire, et d'autre part à des mécanismes d'intermittence turbulente très marqués. Ces deux phénomènes ont été étudiés en détail dans la référence [1], notamment grâce à une comparaison entre les résultats déduits d'ensemencements séparés ou simultanés des deux écoulements. Quelques résultats typiques sont présentés sur les trois figures suivantes.

La figure 13, relative au jet iso-énergétique, illustre la présence d'une zone non-ensemencée dans le premier plan de sondage : quel que soit le mode d'ensemencement utilisé (par le jet, par l'écoulement extérieur, ou simultanément par les deux écoulements), il existe une zone commune, située "sous le jet", où le traceur ne pénètre pas. Ici, compte tenu de leur inertie, les particules intérieures et extérieures sont centrifugées.

La figure 14 montre une comparaison entre les iso-valeurs de la composante axiale du rotationnel déduites des mesures stationnaires et des mesures laser dans le plan $x/d_j=10$. Les deux écoulements sont ensemencés de façon simultanée. Par rapport aux résultats des sondages stationnaires, la vélocimétrie laser déforme la distribution des lignes iso-rotationnel et minimise le niveau du maximum. On peut montrer que ces distorsions traduisent, d'une part une centrifugation des particules dans les tourbillons, et d'autre part un traînage excessif des particules à la traversée du choc de recompression identifié sur la figure par un trait vertical (voir figure 8). Le lecteur attentif notera des différences entre le résultat "sonde 5 trous" présenté sur cette figure et le résultat correspondant de la figure 9 ($x/d_j=10$, figure de droite). En effet, pour effectuer la comparaison de la figure 14, Ω_x est calculé sur le même maillage que

celui de la vélocimétrie laser. Or ce maillage est deux fois plus lâche que celui des sondages stationnaires ($5 \times 5 \text{ mm}^2$). Ces différences reflètent donc l'influence du maillage de sondage sur le résultat du calcul du rotationnel.

Enfin la figure 15 illustre les difficultés que pose le caractère intermittent du champ turbulent dans certaines zones de l'écoulement. On compare ici les niveaux de la composante verticale du tenseur de Reynolds $\overline{w^2}$ et celui de la composante croisée \overline{uw} , mesurées sur l'axe de symétrie $y=0$ à $x/d_j=5$ en ensemencant séparément ou simultanément les deux écoulements. Les ensemencements séparés fournissent des résultats très différents : localement, $\overline{w^2}$ varie du simple au double et \overline{uw} change carrément de signe. Le résultat des ensemencements simultanés se situe entre ces deux limites, à un niveau qui dépend de la contribution relative de chaque population de particules. Il est toutefois impossible de contrôler, et même de définir, un équilibre entre les deux populations (cf. [Ref 10]). L'ensemencement mixte représente donc un compromis aléatoire. Ces différences ne sont dues que partiellement aux effets inertiels des particules. En fait, on peut montrer qu'il ne font que traduire la nature intermittente du mélange turbulent, c'est à dire la coexistence locale de deux "familles" de fluide différentes. Ce phénomène, déjà présent dans les couches de mélange rectilignes (cf. [Ref 10]), est ici accentué par les effets de centrifugation déjà évoqués à propos des strioscopies éclairées : conformément au schéma simplifié de la figure 15, le fluide issu de l'éjecteur, et les particules qu'il transporte, sont soumis aux effets d'une courbure destabilisante alors que le fluide issu de l'extérieur est redressé par une courbure stabilisante. Les mesures reflètent ces différences de comportement. En d'autres termes, même si le traceur possédait les mêmes caractéristiques inertielles que le fluide, on pourrait s'attendre à observer le même type d'écarts. De nouveau cette interprétation fait l'impasse sur le caractère tridimensionnel de l'écoulement qui doit jouer un rôle tout aussi important, notamment à travers l'action des tourbillons.

Ces diverses limitations sont d'autant plus aiguës que l'on se rapproche de l'éjecteur. Elles rendent vaines toutes tentatives de sondage dans la région proche de l'éjecteur. On peut enfin montrer que les erreurs introduites par ces divers biais s'amenuisent rapidement au delà de $x/d_j=10$ [Ref 1].

6.2 Résultats

Les résultats complets fournis dans la référence [1] comprennent les six composantes du tenseur de Reynolds. Nous nous limiterons ici à la figure 16 qui présente une confrontation entre les taux de turbulence locaux q/U_0 ($q^2 = u^2 + v^2 + w^2$, $U_0^2 = U^2 + V^2 + W^2$) mesurés dans le jet iso-énergétique et dans le jet chauffé à 930K (par

ensemencements mixtes). A $x/d_j=5$, on retrouve la zone non-ensemencée identifiée sur la figure 13. Cette zone est légèrement plus étendue dans l'écoulement chaud. On est de nouveau frappé par la similitude entre les deux écoulements au niveau de cette variable adimensionnelle. On note le niveau important des taux de turbulence relevés : des maxima d'environ 25% s'établissent dans la zone tourbillonnaire et se conservent loin en aval. Ces valeurs, fortes en regard des écoulements cisailés rectilignes usuels (jets, couche de mélange plane), reflètent le brassage intense imprimé par les tourbillons de sillage. La vitesse moyenne locale U_0 étant une fonction croissante de la température, l'identité des niveaux de q/U_0 correspond donc à une intensification logique de l'énergie turbulente avec la température. Cela est conforme avec la décroissance de l'impulsion relevée précédemment.

7 Conclusions

Des visualisations et des sondages à la sonde cinq trous, au thermocouple et au vélocimètre laser tridirectionnel, ont été effectués dans une interaction entre un jet transversal sous-détendu chauffé, de température variable, et un écoulement supersonique perpendiculaire. Les nombres de Mach des deux écoulements sont égaux à 2 et le rapport de détente est fixé à 10.

Les résultats montrent que les caractéristiques moyennes de l'écoulement (trajectoires moyennes, chocs, détentes...) sont peu sensibles à la température d'arrêt du jet. Une turbulence très intense est maintenue par l'action de brassage des tourbillons de sillage. La turbulence s'amplifie avec l'accentuation des gradients cinématiques résultant de l'élévation de la température du jet, mais même à ce niveau de description, le jet chauffé présente un degré de similitude remarquable avec le jet de référence iso-énergétique.

Les mesures par vélocimétrie laser, sont particulièrement délicates dans ce type d'écoulement. On a évoqué ici certaines difficultés rencontrées lors de la réalisation de cette phase de l'expérience.

Enfin, des visualisations rapides ont montré que cette interaction est fortement instationnaire. La turbulence est déséquilibrée par des effets centrifuges (déflexion du jet, tourbillons de sillage). On observe également le jet et le choc de tête. Il semble que ces ondes correspondent à des ondes de Mach engendrées par les instabilités turbulentes convectées dans la partie amont de la couche de mélange du jet.

Ces divers résultats soulignent la complexité de cet écoulement fondamental, dont l'étude revêt une grande importance pour diverses applications aéronautiques (pilotage par force directe, mélange et

combustion). Le dispositif implanté à la soufflerie S5, ainsi que les moyens de mesures mis en oeuvre, constituent un environnement expérimental privilégié pour l'étude de cet écoulement.

Remerciements : Cette étude a été réalisée grâce au soutien financier de la DME/STSMT, au titre de la convention n° 91-70-501.

8. References

- [1] Jacquin L., Geffroy P., Losfeld G., Gaillard R. & Morelle R., "Etude expérimentale à la soufflerie S5ch sur un jet transversal supersonique chauffé", RSF ONERA 3/2496 AY, mars 1993.
- [2] Spaid F.W. & Cassel L.A., "Aérodynamique interference induced by reaction control", AGARD - AG.173
- [3] Papamoschou D., Hubbard D.G. & Lin M., "Observation of supersonic transverse jets", AIAA-91-1723.
- [4] Gaillard R., "Etalonnage et utilisation de sondes 5 trous", 7th symposium on "measurement techniques for transonic and supersonic flows in cascade and turbomachinery", paper 19 pp 1-10, 1983.
- [5] Jacquin L., "Phénoménologie et modélisation simplifiée du sillage tourbillonnaire engendré par un jet transversal", soumis à La Recherche Aérospatiale.
- [6] Coelho S.L.V. & Hunt J.C.R., "The dynamics of the near field of strong jets in crossflows", Journal of Fluid Dynamics, 200, pp 95-120, 1989.
- [7] Sykes R.I., Lewellen W.S. & Parker S.F., "On the vorticity dynamics of a turbulent jet in a cross flow", journal of Fluid Mechanics, 168, pp 393-413, 1986.
- [8] Boutier A., "Laser Velocimetry", VKI Lecture Series on "Measurement techniques for hypersonic flows", Rhône-Saint-Genève, 28 mai-1 juin 1990.
- [9] Boutier A., Pagan D. & Soulevant D., "Measurements accuracy with 3D laser velocimetry", Int. Conf. on Laser Anemometry, Advances and Application, 16-18 december 1985, Manchester, ONERA TP n°1985-171.
- [10] Geffroy P., Blin E., Jacquin L., D'Humières C., Soulevant D. & Micheli F., "Mesures par vélocimétrie laser dans la couche de mélange d'un jet supersonique de révolution", RT ONERA 52/1147 AY, octobre 1991.

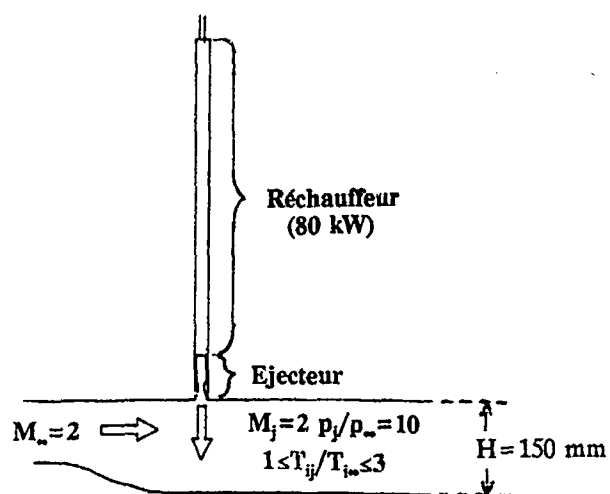


Fig.1 : Schéma du montage

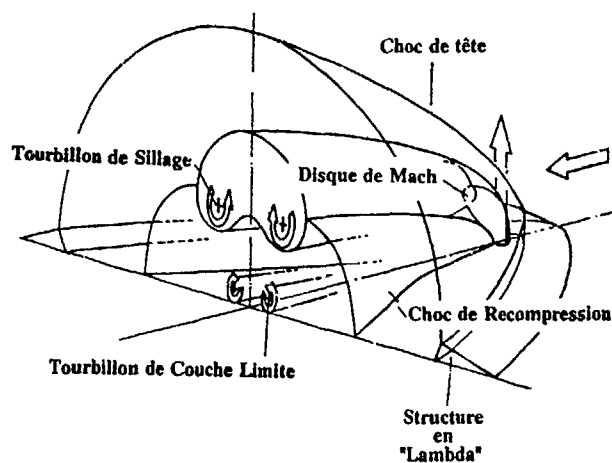
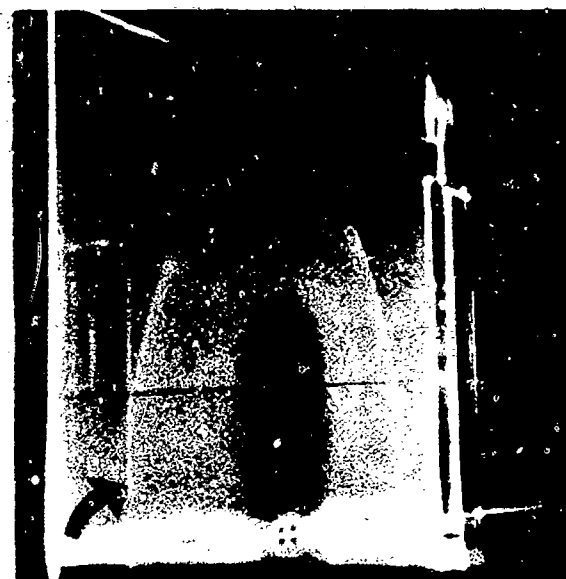
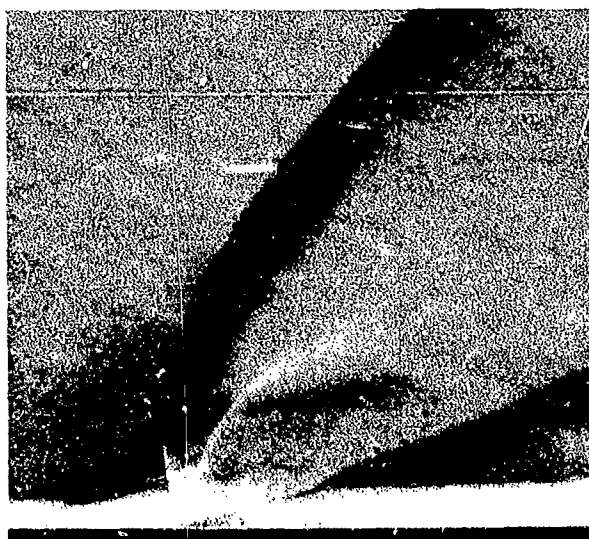
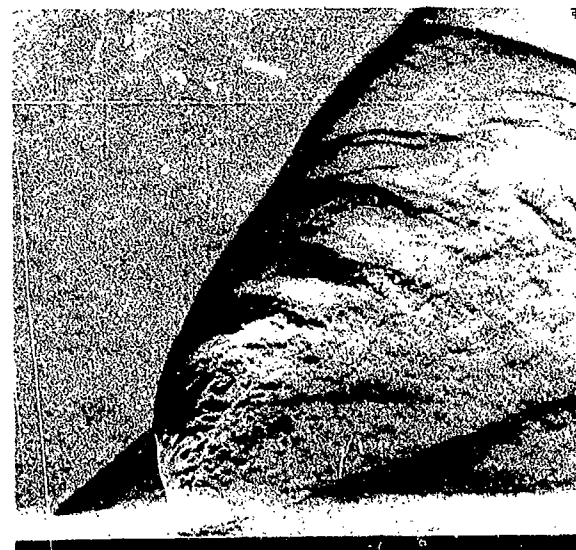


Fig.2 : Phénoménologie de l'écoulement

Fig.4 : Tomoscopie laser dans le plan $x/d_j = 5$ Fig.5 : Strioscopie éclair 20ns (cas $T_i = \text{cte}$)Fig.3 : Strioscopie continue (cas $T_i = \text{cte}$)Fig.6 : Strioscopie éclair 20ns (jet chaud $R_T = 3$)

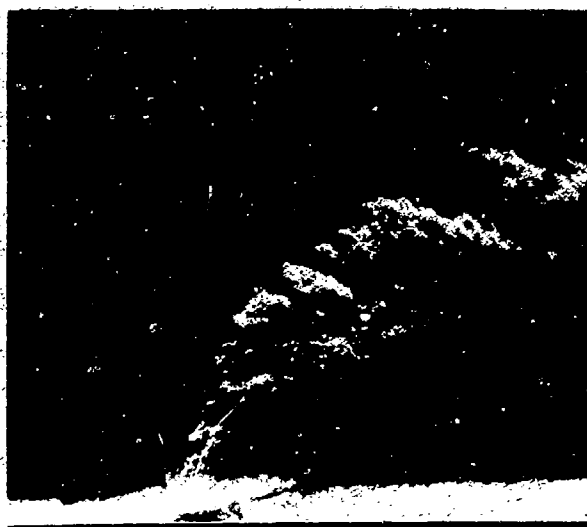
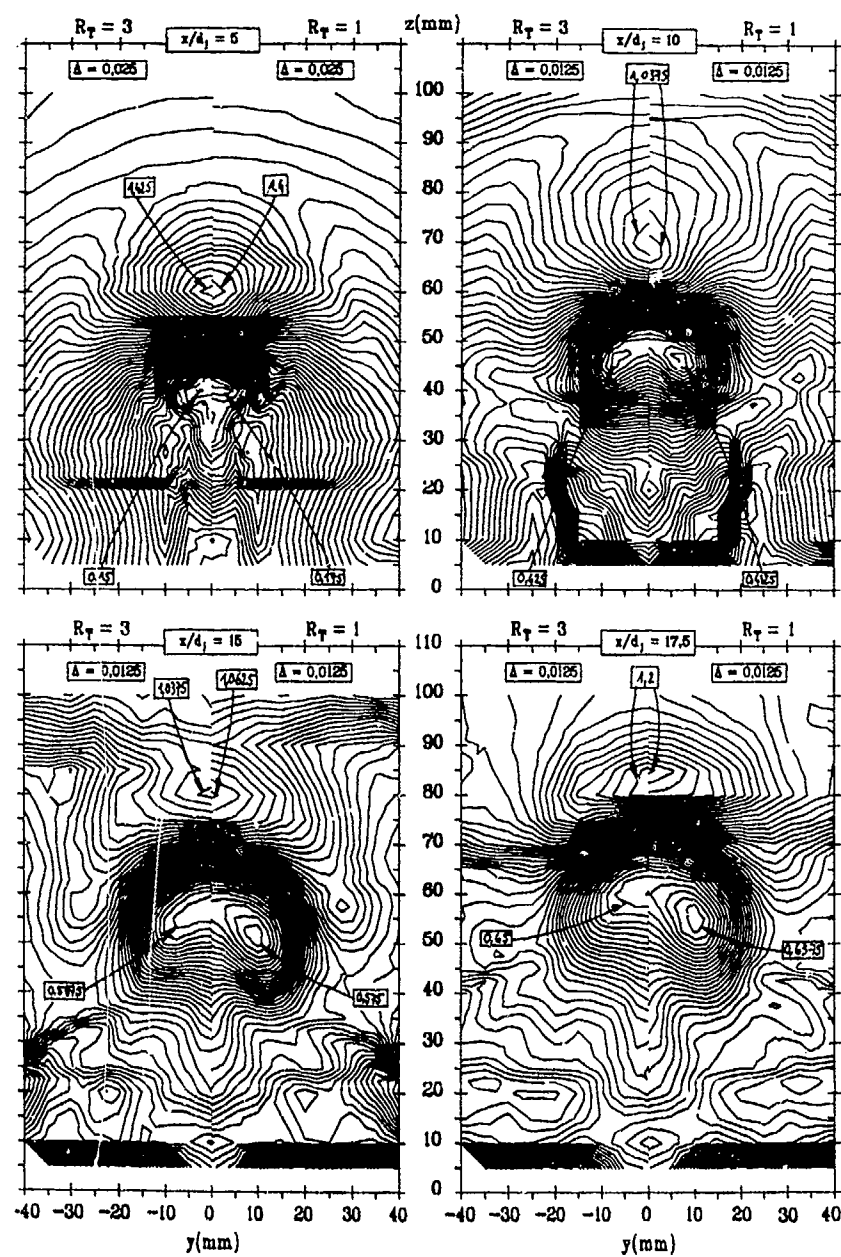


Fig.7 : Strioscopie éclair 20ns à fort contraste
(jet chaud $R_T=3$)



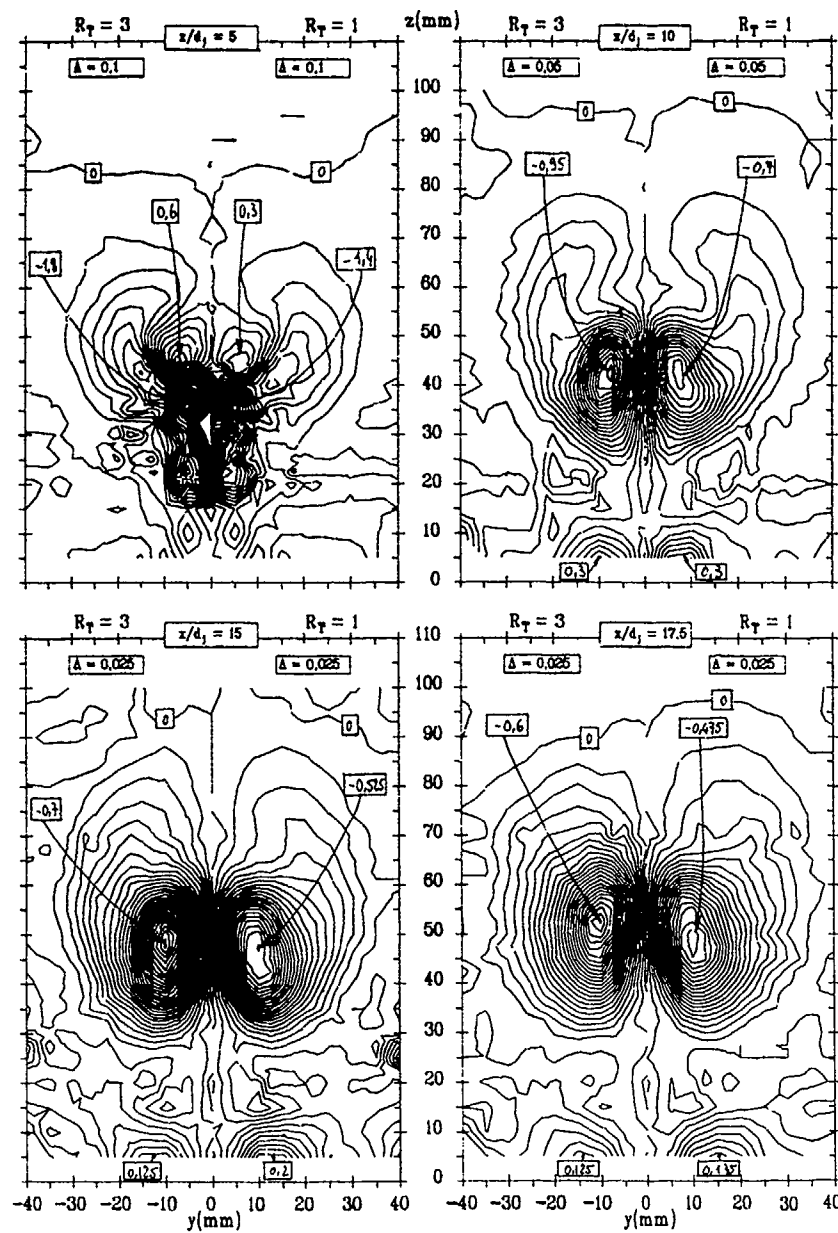


Fig.9 : Composante longitudinale du rotationnel $\Omega_x/2U_\infty d_j$ mesuré dans le jet iso-énergétique ($R_T=1$, partie droite des figures) et dans le jet chauffé à 930K ($R_T=3$, partie gauche)

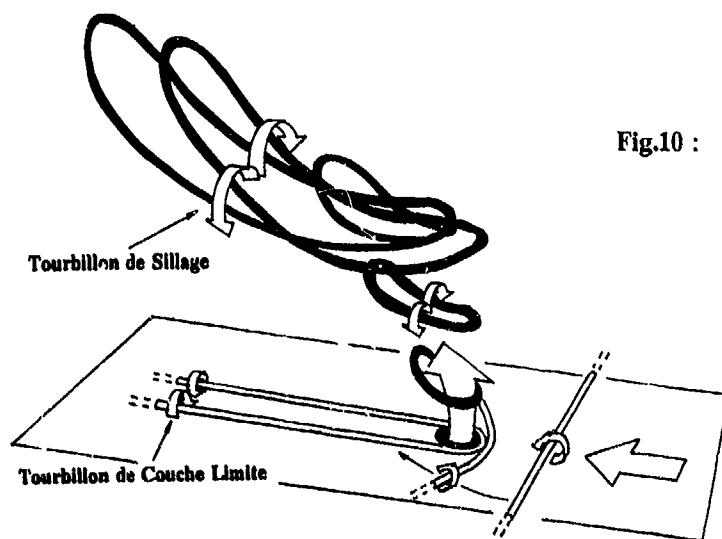


Fig.10 : Un schéma phénoménologique de la formation des tourbillons dans le sillage du jet

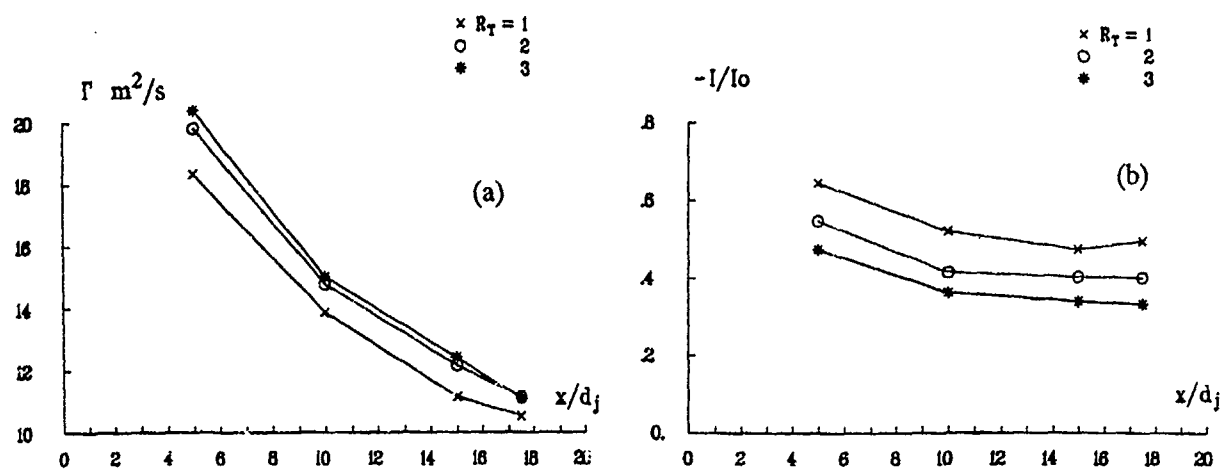


Fig.11 : Caractérisation globale des tourbillons :
 (a) évolution longitudinale de la circulation
 des tourbillons pour les trois températures;
 (b) évolution longitudinale de l'impulsion
 du système contrarotatif

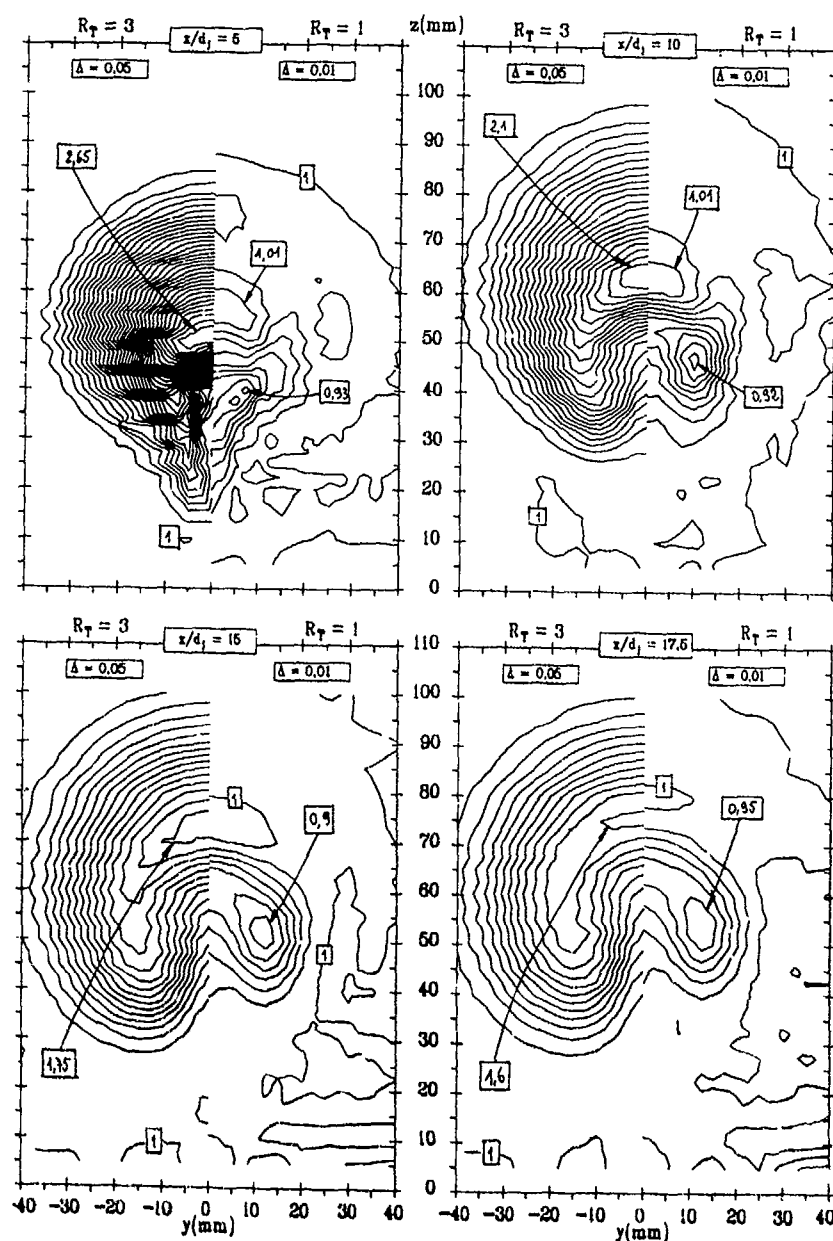
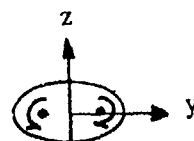


Fig.12 : Température d'arrêt $T_i/T_{i\infty}$ mesurée dans le jet iso-énergétique et dans le jet chauffé à 930K

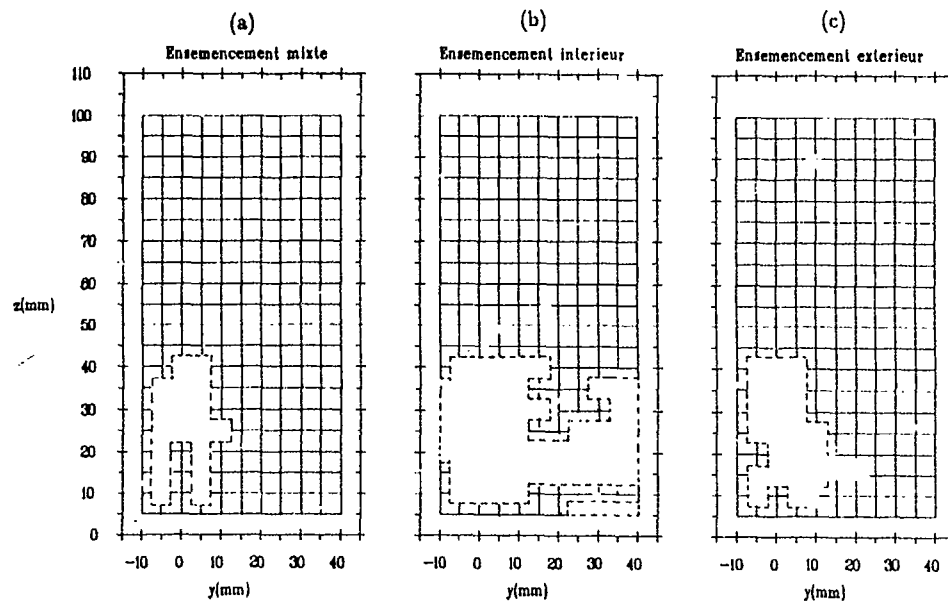


Fig.13: Zones sans particule à $x/d_j=5$ dans le jet iso-énergétique selon le mode d'ensemencement

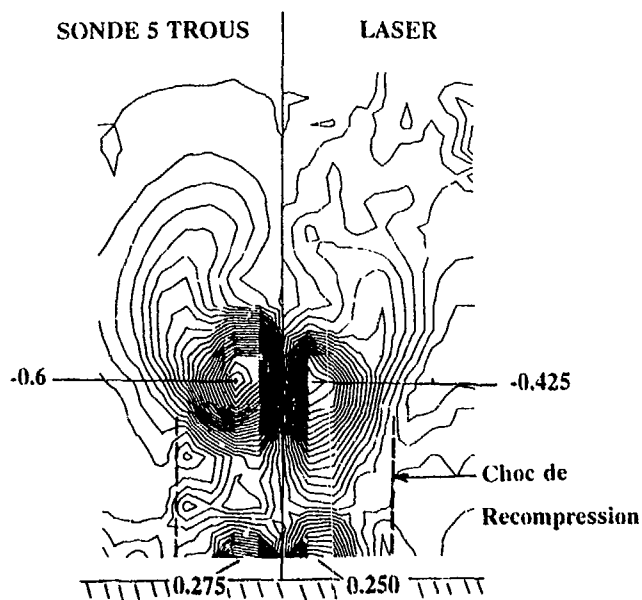


Fig.14 : Composante longitudinale du rotationnel $\Omega_x/2U_\infty d_j$ mesurée dans le jet iso-énergétique à $x/d_j=10$: confrontation mesures pitot-mesures laser

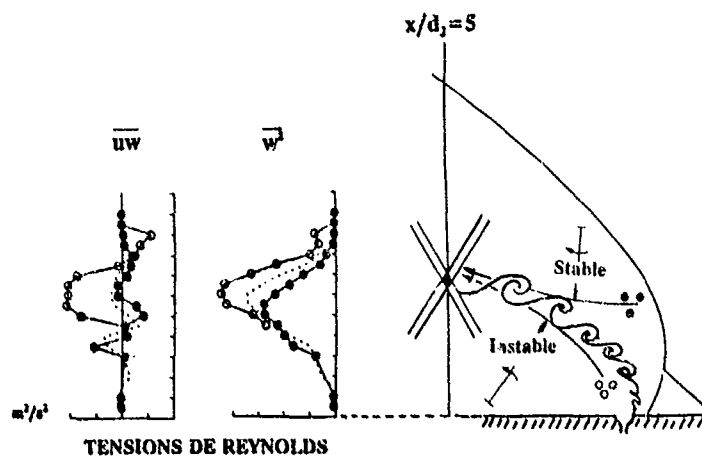


Fig.15 : Comparaison entre les valeurs de deux tensions de Reynolds mesurées à $x/d_j=5$ sur l'axe vertical de symétrie $y=0$, en ensençant soit le jet (symboles ajourés), soit l'écoulement extérieur (symboles pleins), soit les deux simultanément (pointillés)

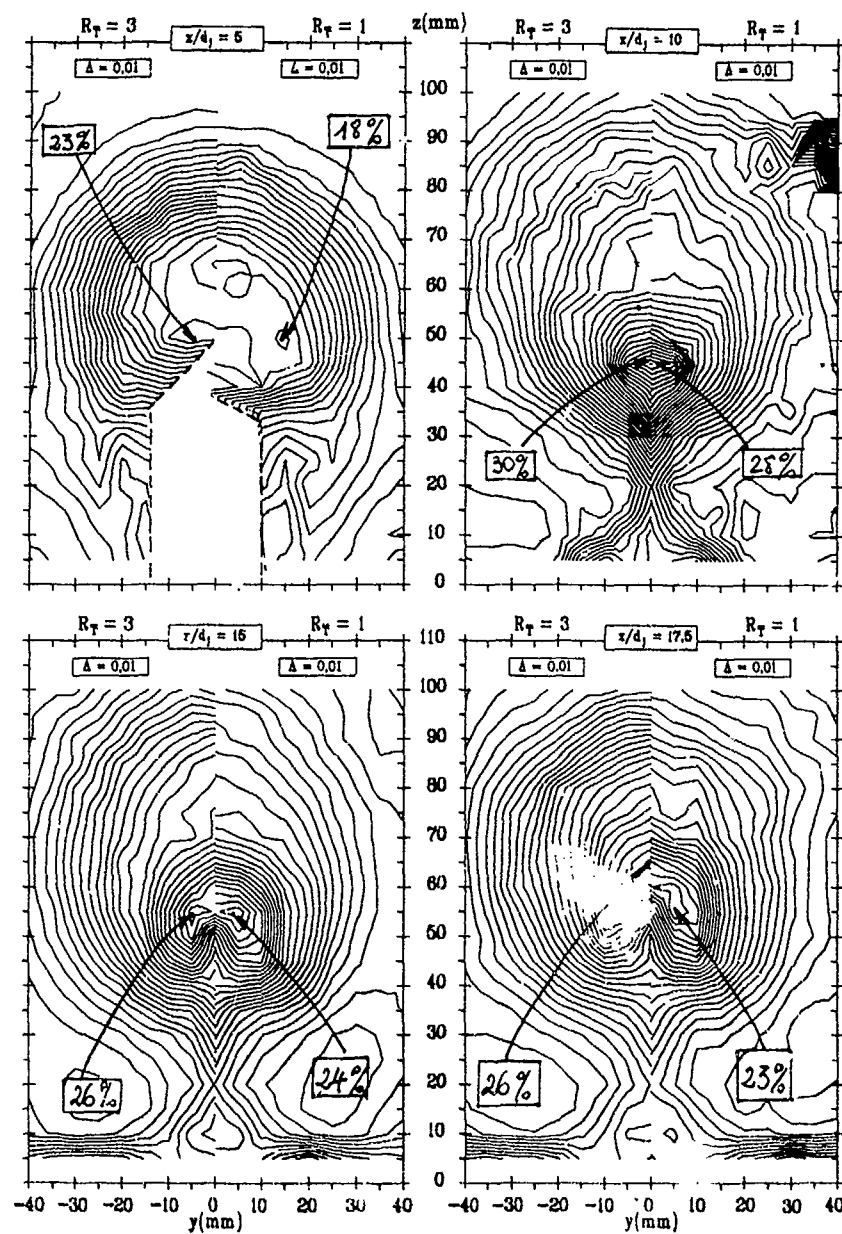


Fig.16 : Taux de turbulence q/U_0 mesuré dans le jet iso-énergétique et dans le jet chauffé à 930K

INCLINED AIR-JETS USED AS VORTEX GENERATORS TO SUPPRESS SHOCK-INDUCED SEPARATION

H H Pearcey
K Rao#
D M Sykes

Department of Mechanical Engineering and Aeronautics
City University
Northampton Square
London EC1V 0HB
UK

SUMMARY

Experiments have been performed to assess the effectiveness of air-jet vortex generators as alternative to vanes in suppressing shock-induced separation. It is shown that a single jet inclined to the plane of the surface and skewed to the direction of the undisturbed stream produces a single strong vortex and can therefore be treated as the equivalent of a single vane. It follows that jets can be installed in arrays to correspond to arrays of vane vortex generators.

A spanwise array of jets is shown to produce closely similar results to an array of co-rotating vane vortex generators of the type that has now been used in very many applications to suppress the effects of shock-induced separation. Air-jet vortex generators should therefore be equally effective in practice and may have significant inherent advantages for many applications.

The vortex generators were effective for shock-upstream Mach numbers up to and beyond 1.6. The maximum effectiveness occurred close to the generators but they remained reasonably effective for a range of shock positions of up to 50% chord.

Some initial pointers are given on the influence of certain design parameters and on what considerations would apply in tailoring the jets to specific applications.

LIST OF SYMBOLS

c	aerofoil chord
M	Mach number
M_L	local Mach number upstream of shock waves
p	static pressure on aerofoil surface
p_1	value of p immediately upstream of shock
p_2	value of p immediately downstream of shock (see Fig 7)
p_{TE}	value of p at the trailing-edge position
p_0	stagnation pressure
x	chordwise distance along the surface of the aerofoil

x_{sh}	position of the shock (see Fig 7)
θ	angle at which the jet exit is skewed to the direction of the undisturbed stream
θ_s	value of θ above which a single vortex occurs instead of a pair (see Fig 2)
ϕ	angle at which the jet exit is pitched to the plane of the surface

LIST OF CONTENTS

1.	Introduction
2.	The mechanism of vortex formation
3.	Details of the experiments
4.	The development of separation in the absence of boundary-layer control
5.	The overall contrast with separation suppressed
5.1	With vane vortex generators
5.2	With air jet vortex generators
6.	More specific comparisons between the effectiveness of air jets and vanes
6.1	Fixed shock position and strength
6.2	Shock pressure rise
6.3	Overall pressure rise and shock movement
7.	The influence of certain jet parameters
7.1	Exit mass-flow rates (hence vortex size and strength)
7.2	Skew angle
7.3	Pitch angle
8.	Concluding remarks
9.	Acknowledgements
10.	References

1. INTRODUCTION

Boundary-layer control by an array of longitudinal vortices trailing over the surface has been widely used for more than thirty years as a means of suppressing separation and its effects.

Small vanes normal to the surface have so far been used as the vortex generators. These have been both convenient to apply and effective, and, so, the alternative possibility of using inclined air jets has not been exploited in practice although it has long been known to have potential advantages over the vanes^{1,2}. For example, the air-jet vortex generators would normally be used near the extremities of the flight envelope, when separation was imminent; drag penalties would thus be avoided for other conditions. Also, air-jets would not become

Now with Airbus Industrie.

ineffective, as vanes would, when submerged by local regions of separation or extra thick shear layers; the jets could penetrate into the outer regions of higher velocity to form their vortices. Furthermore, the controllability of air-jets leads to opportunities of extending the application from the specific suppression of separation to its more general active control for flight control purposes.

The work described in this paper was commissioned by British Aerospace plc to re-examine the possibilities for air jets and to extend previous studies to include rectangular as well as circular exits, and angles of skew (downstream inclination) as well as pitch in the cross-plane only.

Attention was focused on the effects of shock-induced separation because these have been the subject of many of the practical applications of vane-type vortex generators; significant delays of buffet onset have featured in the benefits, as have control of stall development, elimination of wing rocking and improvement in control effectiveness.

The effectiveness of air-jets has been assessed in the present experiments by direct comparison with that of vanes and so can be related to the extensive experience from the application of vanes.

The research has been described more fully Dr Rao in his PhD thesis⁽⁹⁾.

2. THE MECHANISM OF VORTEX FORMATION

A jet inclined in pitch to the surface but aligned to the undisturbed flow in the plane normal to the surface is well known to produce a pair of counter-rotating vortices (Fig 1(a)). The vorticity is introduced by the initial deflection of the approaching streamlines (which deflection is of course sheared in the boundary layer) and enhanced by the subsequent entrainment by the jet.

With the jet directed across the flow ($\theta = 90^\circ$, Fig 1(b)), it appears that the enhanced entrainment on the leeward side introduces a marked differential strengthening of the vortex on that side which then sweeps the weaker one around and into itself. The net result is that a single stronger vortex replaces the two counter-rotating ones that are formed by the "in-line" jet.

Unlike the counter-rotating pair of vortices that transport each other outwards, the single vortex trails downstream close to the surface keeping much of the jet fluid with it. Each jet then becomes the equivalent of a single vane vortex generator and they can be used in rows to form arrays of boundary-layer controlling vortices.

It was these fully cross-flow jets that were introduced by Wallis⁽²⁾ as the air-jet alternative to vanes and that Pearcy⁽¹⁾ and his colleagues found to produce similar but somewhat less favourable effects than vane-type generators.

Subsequently, Freestone⁽⁴⁾ at City University showed that the single vortex could be strengthened still further if the cross-flow jet was also turned part way into the stream direction (see Fig 1(c), skew angle $90^\circ > \theta > 0^\circ$). He also suggested that rectangular exits might be preferable to circular ones.

Rao⁽³⁾ used an experimental hydraulic analogy to study qualitatively the effects of jet skew direction and exit velocity. His results are shown schematically in Fig 2. The pair of vortices is converted into a single stronger one for all skew angles above a certain value θ_c , but the formation does depend on the exit velocity being greater than a critical value which varies with skew angle. The minimum occurs for a skew angle of about 45° .

At any given skew angle greater than θ_c , the strength of the single vortex is increased as exit velocity is increased above the critical value.

More recently both Henry⁽⁵⁾ and Zhang⁽⁶⁾ have developed numerical models for the vortex generation and have reproduced the observed contrast between the vortex pair of the "in-line" jet and the single vortex of the skewed jet (Figs 3a and 3b).

3. DETAILS OF THE EXPERIMENTS

It was felt that the applicability of the results would be best secured by reproducing as nearly as possible the approach that had been followed in the early tests on vane vortex generators at the National Physical Laboratory; these tests had provided the basis for design guidelines⁽¹⁾ that had stood the test of so many practical applications since then. In this way, the present results on air-jet vortex generators could be related directly to the extensive experience with vane vortex generators.

A half-aerofoil, or bump (Fig 4) was fitted to span one wall of the City University's 200 mm x 250 mm induced-flow transonic wind-tunnel⁽⁷⁾. The tunnel-wall boundary layer approaching the model was removed by suction just upstream of the leading edge to allow a thin turbulent boundary layer to develop over the model itself. This together with the choice of aerofoil shape to ensure the development of Type A shock-induced separation rather than Type B (see Section 4) should be sufficient, as it was in the early N.P.L. tests, to ensure that the results are relatively insensitive to scale effects and that the conclusions should therefore be relevant to full-scale applications.

The aerofoil shape was of the same derivation as that used in the N.P.L. tests but with thickness increased to yield higher local Mach numbers and hence more severe shock-induced separation and more severe test for the vortex generators. Two thickness/chord ratios were used, namely 10% and 14% based on the maximum thickness of the half aerofoil. The aerofoil chord was 305 mm.

The tunnel wall opposite the model was solid, again following the early N.P.L. tests. The effects of blockage interference were by-passed by confining the analysis to the local flow on the aerofoil (see below).

The model was constructed with an internal plenum chamber to duct air to the jets. The jet exits were formed in plugs inserted from the surface and rotatable to the required skew angle, θ , from 45° to 90° . The jet exits were rectangular and either 7.6 mm x 1.6 mm or 12.7 mm x 1.6 mm. Two sets of plugs were made for the smaller exits, with pitch angles, ϕ , of 30° and 45° . Only one set, $\phi = 30^\circ$, were used for the larger exits.

Jet exit velocities were controlled (but not measured) by control of plenum pressure, p_B , which was varied between stagnation pressure, p_0 , (one atmosphere) and $1.8 p_0$.

There were 9 jets uniformly spaced across the span of the model (Fig 4) all of the same orientation to produce an array of co-rotating vortices of equal strength, this being the arrangement normally used to control shock-induced separation over a wide range of shock positions as required in the present case.

The performance of the air-jet systems was assessed against that of a co-rotating vane system chosen from the earlier work to perform well in such circumstances. The individual vanes were rectangular, 3 mm high, 12 mm long, spaced at 25.4 mm and inclined at 20° to the undisturbed stream ($h = 0.01c$, $l = 4h$ and $s = 8.5h$ in the notation of reference 1). This spacing coincides with that of the air jets.

Air jets and vanes were also located at the same chordwise position, namely, 35% chord from the leading edge and 5% chord upstream from the point at which the shock first formed. By the highest speed of the tests, the shock had moved to within about 10% chord of the trailing edge and so the total range of shock positions was from 5 to 55 vane heights downstream from the generator position.

Surface static pressure holes were provided at close intervals along the centre span of the model. They were connected to an array of tubes that could be clamped during the short run and then sensed sequentially using a Scani-valve and transducer. The signals were recorded on disc for subsequent analysis.

The interpretation of the shock-wave boundary-layer interaction and vortices was assisted by other flow observations not reproduced. These observations included schlieren photography and detailed surveys made by a pitot rake located at 60% chord from the leading edge and four spanwise stations in the interval between the spanwise position of one jet exit and the next.

4. THE DEVELOPMENT OF SEPARATION IN THE ABSENCE OF BOUNDARY-LAYER CONTROL

Distributions of surface pressure are shown in Fig 5(a) for a sequence of increasing tunnel speeds starting from M, that for which the shock wave is located at 0.43 chord with a local Mach number immediately upstream of 1.34. A local separation bubble was already present at the foot of the shock and this spread progressively rearwards with each of the first few stages of the sequence - as the upstream Mach number increased - to reach the trailing edge by stage N in the sequence.

This is the typical Type A development⁽⁸⁾ which is not influenced by a rear separation spreading forwards from the trailing edge, as in Type B, and therefore not much subject to scale effects.

The rate of pressure recovery downstream of the shock is significantly reduced from point N onwards.

The rearward movement of the shock is halted during the initial development of the separation

but recommences after N, allowing the local supersonic flow to develop upstream. The maximum local Mach number increases to 1.51 during the sequence, but the separation at the foot of the shock restricts the pressure rise through the shock to a near constant value. As a result, the shock downstream pressure falls instead of rising as would be expected for a sequence with increasing shock-upstream Mach number (falling p_1) in the absence of separation.

Three related but distinct effects of separation are thus evident, namely,

1. an initial pause and subsequent resumption in the natural rearward movement of the shock;
2. a fall in shock downstream pressure, p_2 , or a locus of p_2 rising up the page;
3. a marked fall to near zero in the rate of pressure recovery downstream of the shock.

These same features are present, Fig 6(a), but in somewhat more severe form, for the 14% thick bump for which shock upstream Mach number increases to a maximum of 1.71.

5. THE OVERALL CONTRAST WITH SEPARATION SUPPRESSED

5.1 With vane vortex generators

The contrast, Fig 5(b) (10% thick bump) and Fig 6(b) (14% thick bump), is marked in all three features noted above. The shock now moves progressively over the surface, the pressure rise through the shock is significantly greater, and the rate of pressure rise downstream of the shock is also restored.

5.2 With air-jet vortex generators

The results shown in Figs 5(c) for the 10% thick bump, and in 6(c) for the 14% thick bump have been selected from the range available for air-jet vortex generators to show that closely similar, and in some cases better, overall control was achieved by the air jets.

6. MORE SPECIFIC COMPARISONS BETWEEN THE EFFECTIVENESS OF AIR-JETS AND VANES

6.1 Fixed shock position and strength

Each of Figs 7 and 8 shows a group of three pressure distributions selected respectively from Figs 5(a), (b) and (c) and 6(a), (b) and (c). In each case, results are compared for a fixed shock position (hence fixed shock strength) and show how the suppression of separation by boundary-layer control increases both the pressure rise through the shock and the rate of recovery downstream. The air jets give a slightly greater improvement than the vanes for the 10% thick bump (Fig 7) but almost identical ones for the 14% thick bump (Fig 8).

6.2 Shock pressure rise

The chordwise distribution of local supersonic Mach number traced out upstream of the shock as it moves rearward over the surface, see Figs 5 and 6, is a function only of the aerofoil shape; it is not affected by the boundary-layer control save in its extent. It thus forms a locus of shock-upstream pressure, p_1 , that is the same for all tests on each of the 10% thick and 14% thick bumps in turn.

Thus, the increases in shock-pressure rise

achieved by the application of vortex generators are shown by the position of the p_2 locus as in Figs 9 and 10, respectively for the two bumps.

For the 10% thick bump, the initial increase in p_2 (that is, for shocks near the generators) is slightly better for the air jets than for the vanes. But for the 14% thick bump, the vanes give the slightly greater initial improvement. In all cases, for both vanes and air jets, the degree of improvement begins to decrease as the shock moves downstream away from the generators, presumably as the vortex strength is dissipated. This decrease is noticeably less for the air jets than for the vanes.

The value of p_2 for any given pressure distribution is defined by the intersection of the rapid pressure rise for (or the onward projection of it) with the much slower downstream rise (or the backward projection of it). For the vortex generators, Figs 5(b), 5(c), 6(b) and 6(c), the definition is less precise for the later stages of the sequence than for the earlier ones. This is probably because a local separation is then present at the foot of the shock with almost immediate re-attachment; the re-attachment pressure rise would thus be included in the definition of "shock-pressure rise". This is not thought to detract from the relevance of p_2 as an indicator of the effectiveness of the air-jet vortex generators. It has not done so in the past in the numerous applications of vane vortex generators.

6.3 Overall pressure rise and shock movement

Indeed there are some circumstances for which the overall pressure rise from upstream of the shock to the trailing edge would be a measure of the effectiveness of the boundary-layer control; it is, for example, an indication of the degree to which boundary-layer growth is constrained.

The overall pressure rise could be displayed by plotting p_{TE} as a function of shock position, or vice versa, again because the locus of p_1 is fixed for a given aerofoil shape. This has the advantage, as in Figs 11 and 12, of illustrating also the manner in which the shock moves over the surface as p_{TE} is decreased.

For example, for both bumps without vortex generators, the near fixed location of shock for the initial range of p_{TE} is clearly shown. This is reproducing the initial pause in the natural shock movement that was noted in Section 4 to be one of the principal features in the development of separation and that occurs as the separation bubble at the foot of the shock spreads towards the trailing edge.

Both the vanes and the effective air-jets represented in Figs 11 and 12 eliminate the shock pause to give a progressive shock movement towards the trailing edge.

7. THE INFLUENCE OF CERTAIN JET PARAMETERS

7.1 Exit mass flow rates (hence vortex strength and size)

Although mass flow rates were not measured, comparative values can be inferred from the fact that the pressure ratio from the plenum chamber to the jet exit into the local supersonic flow was never less than 3. The jet exits were therefore almost certainly choked. It is thus reasonable to assume for present purposes that the exit mass

flow rate was proportional to both exit area and plenum pressure.

On this basis, the comparative exit mass flow rates for the various configurations tested are as indicated in the Table, where m is the lowest value.

	10% thick bump	14% thick bump
Small exits		
$p_0/p_\infty = 1.2$	m	m
1.6	1.3 m	1.3 m
Large exits		
$p_0/p_\infty = 1.0$	1.4 m	-
1.2	1.7 m	1.7 m
1.5	-	2.1 m
1.8	2.5 m	-

The influence of these variations is assessed from their effect on the movement of the shock with respect to p_{TE} , see Figs 13 and 14.

The differences are best displayed in Fig 14 for 14% thick bump for which the vortices have to counter the more severe separation. Overall, and in the main, the effectiveness of the air-jet vortex generators increases progressively as the exit mass-flow rate increases, presumably because vortex strength increases. This dependence has since been demonstrated by the numerical models of Henry⁽⁵⁾ and Zhang⁽⁶⁾.

For the maximum mass-flow rate, the effectiveness of the air jets is very similar to that for vanes except that a limited shock pause occurs at 0.8 chord. The dependence on exit mass-flow rate seems to become anomalous in this region in that, if anything, the systems with larger mass-flow rate are less effective. Rao⁽³⁾, with the assistance of detailed surveys through the vortices, deduced that this is because the diameter of the vortices was initially larger and that the spreading as they were convected downstream led to interaction and mutual dissipation between adjacent vortices, much as occurs for co-rotating vane vortex generators if the vanes are too closely spaced⁽¹⁾.

Similar inferences can be drawn from the results for the 10% thick bump, Fig 13, with one qualification. All the results for air-jet systems are grouped closely for the initial stages in the sequence of shock positions; all are slightly better than vanes. For the larger exits (and mass-flow rates), the effectiveness again falls off, judging from the shock pause, when the shock reaches around 0.75c, presumably again because of the mutual interaction of adjacent vortices. In this case, though, for the largest mass-flow rate of all, 2.5 m (large exits, $p_0/p_\infty = 1.8$), effectiveness is restored over the full range of shock positions. It is not clear whether this is because the vortices were initially tighter (smaller) as well as stronger or some of the jet momentum is somehow retained for this higher exit pressure.

Two other features of the results for the 10% thick bump are noteworthy. For these shock strengths (local upstream Mach number of around 1.45), and shock waves within about 40% chord of the generator position, relatively small exit mass-flow rates can be effective. The results for ram air ($p_0/p_\infty = 1.0$, large exits, mass-flow rate 1.4 m) correlate with the others on the

basis of mass-flow rate; although, if a long range of effectiveness is required it would seem better to use smaller exits with higher exit pressures.

7.2 Skew angle

Tests on the 10% thick bump with large exits and $p_b = 1.8 p_o$, Fig 15, indicated little difference between skew angles of 45° and 60° but a slight deterioration at 75°.

7.3 Pitch angle

Tests on the 14% thick bump with small exits and $p_b = 1.6 p_o$, Fig 16, suggested that a pitch angle of 45° might give slightly better results for the shock positions nearer the generators. There was no difference at the larger distance.

8. CONCLUDING REMARKS

The results confirm that air jets inclined to the plane of the surface and skewed to the direction of the undisturbed stream can be an effective alternative to vane vortex generators in suppressing the effects of shock-induced separation. Each jet produces a single strong vortex and is therefore the equivalent of a single vane. Just as for vanes, they can be arranged to produce rows of either co-rotating vortices or counter-rotating pairs.

The degree to which the effects of separation were suppressed was indicated by significant increases in shock pressure rise and downstream pressure recovery and by the restoration of the natural shock movement over the surface (with increase of free-stream Mach number). The results achieved in all these detailed respects were closely similar to those achieved by a system of co-rotating vanes known to have been effective in a wide range of practical applications.

It follows that air jets can be considered with confidence for similar applications in the future and for others for which vanes might incur unacceptable drag penalties or be inappropriate or ineffective for some specific reason (eg if embedded in thick shear layers or separated flow).

The confidence is underlined by the fact that the present tests were as near as possible in all respects to the early NPL tests⁽¹⁾ on vanes and which have formed the basis for so many of the full-scale applications since. The broad principles for designing and scaling specific applications would be similar.

Co-rotating vortices were chosen for the present tests because they remain close to the surface as they trail downstream from the generator position and so remain effective for a wide range of shock positions. This range was up to 50% of the aerofoil chord in this instance, although maximum effectiveness occurred in the first part of this range.

The experiments covered a range of shock strengths also, with upstream Mach numbers up to 1.65. For the upper part of this range (1.45 to 1.65), the effectiveness of the jets increased with exit mass-flow rate, with one important proviso (see below). For weaker shocks within 40% chord of the generators, effectiveness was relatively insensitive to exit mass-flow rate.

The proviso is that the stronger (and larger) vortices created by the larger exit mass-flow

rates spread as they trail downstream causing mutual dissipation if they are too closely spaced initially. There is thus an important interplay between spacing and vortex strength in achieving effectiveness for a range of shock positions.

The spacing, exit area and blowing pressure would presumably be tailored to specific applications. For the present tests, the area of the choked exits was either 0.0014c or 0.0024c per unit span, with blowing pressure ranging from stagnation pressure to 1.8 times that. Ram air gave good results for shock upstream Mach numbers up to 1.45, within a chordwise range of 40%. Judging from recent successful experience with very small vane vortex generators (sub boundary layer vortex generators)⁽⁶⁾ it is possible that smaller exits and hence smaller exit mass flow rates would be effective for specific applications in which boundary-layer control was required for smaller ranges of shock position and/or shock strength.

9. ACKNOWLEDGEMENTS

We are pleased to acknowledge that the work was sponsored by British Aerospace - under a contract controlled by the then Military Division - and that the results are now published with the permission of the successor British Aerospace Defence Ltd (Military Aircraft Division). We remain grateful for Dr David Laughler's initial suggestion of reviving interest in air-jet vortex generators as an alternative to vanes and for Mr Cliff Bore's advice during the progress of the work. Dr Mike Freestone and Mr Rod Lomas, both erstwhile colleagues at City University, respectively made many important scientific and technical contributions.

10. REFERENCES

1. Pearcey, H H Shock-induced separation and its prevention by design and boundary-layer control (Part IV of Boundary-layer and Flow Control, Ed Lachmann, Pergamon Press, Oxford, 1961).
2. Wallis, R A and Stuart, C M On the control of shock induced boundary-layer separation with discrete air jets (A.R.C. Report 19, 865, 1958).
3. Rao, M K An experimental investigation of the use of air-jet vortex generators to control shock-induced boundary-layer separation (PhD Thesis, City University, 1988).
4. Freestone, M M Preliminary tests at low speed on vorticity produced by air-jet vortex generators (City University, RM Aero 85/1 1985).
5. Henry, F S and Pearcey, H H A numerical investigation of the

- flow downstream of an array of pitched and skewed air jets issuing into a turbulent boundary layer with application to air-jet vortex generators (submitted to AIAA).
6. Zhang, X
Computational analysis of co- and contra-rotating longitudinal vortices in a turbulent boundary layer. (AIAA Paper 93-3035).
7. Sykes, D M
The slotted wall transonic wind tunnel
8. Pearcey, H H
Osborne, J and Haines, A B
at The City University. (City University RM Aero 69/3, 1969.)
The interaction between local effects at the shock and rear separation. (AGARD C.P. No 35, 1968).
9. Holmes, A E
Hickley, P K
Murphy, W R and Hilton, D A
The application of sub-boundary layer vortex generators to reduce canopy 'Mach rumble' interior noise on the Gulfstream III, (AIAA Paper 87-0084, 1987).

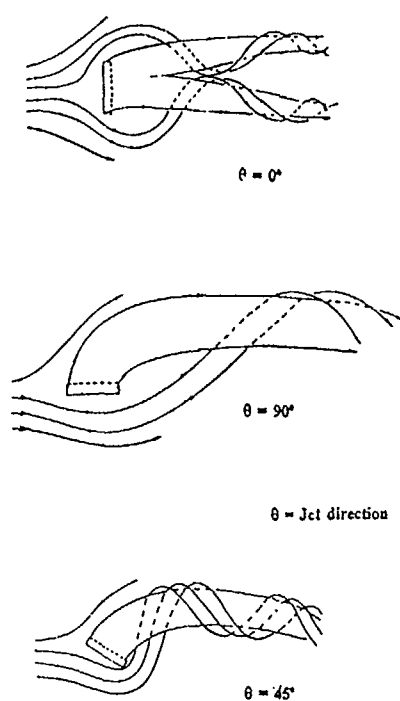


Fig 1 Effect of jet direction on vortex formation

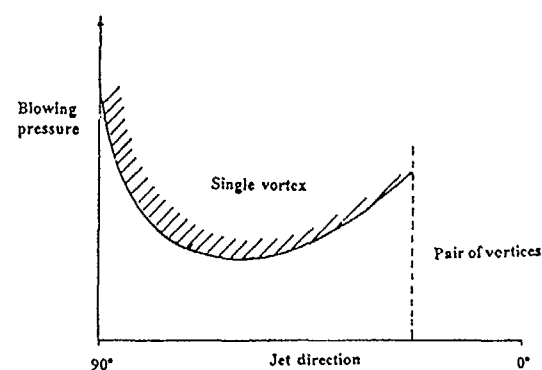


Fig 2 Sketch showing the variation in critical blowing pressure with jet direction (hydraulic analogy)

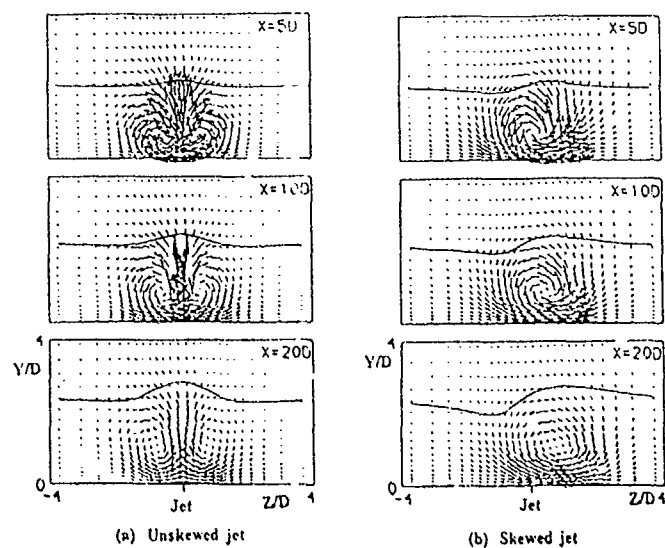
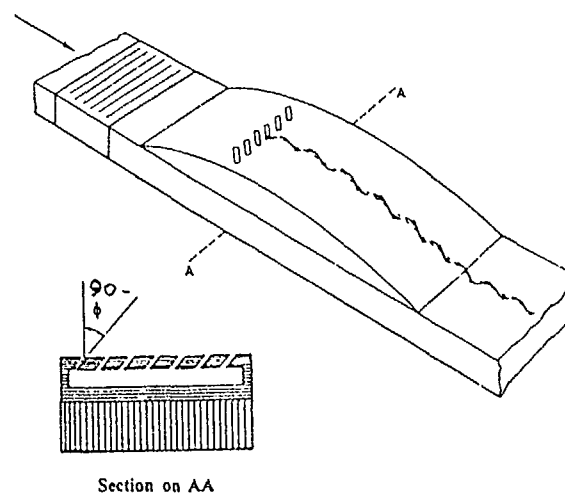
Fig 3 Numerical model of vortex formation
(from Zhang, Ref 6)

Fig 4 The full-span half aerofoil

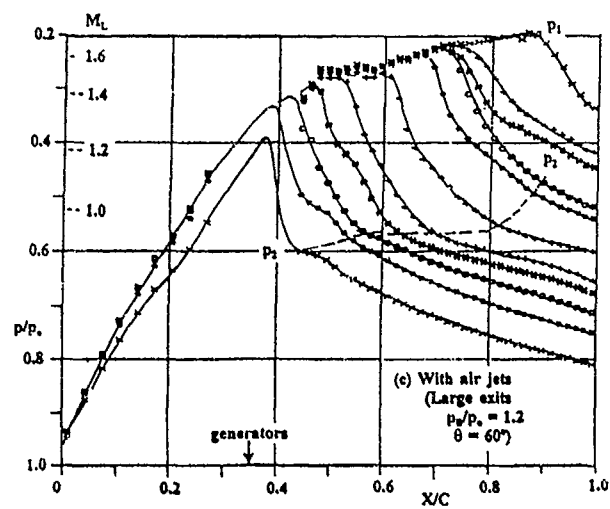
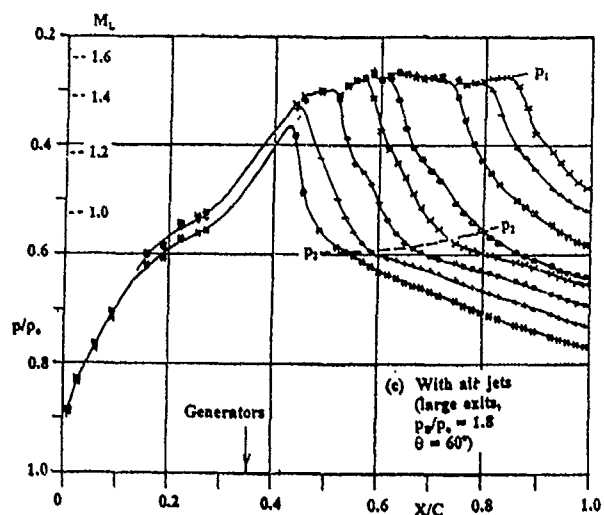
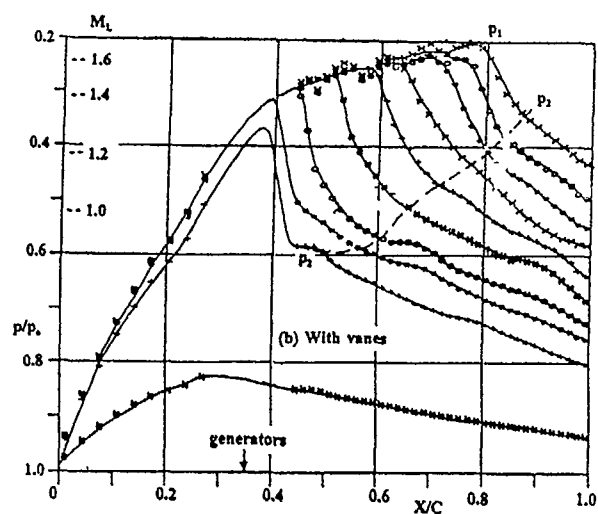
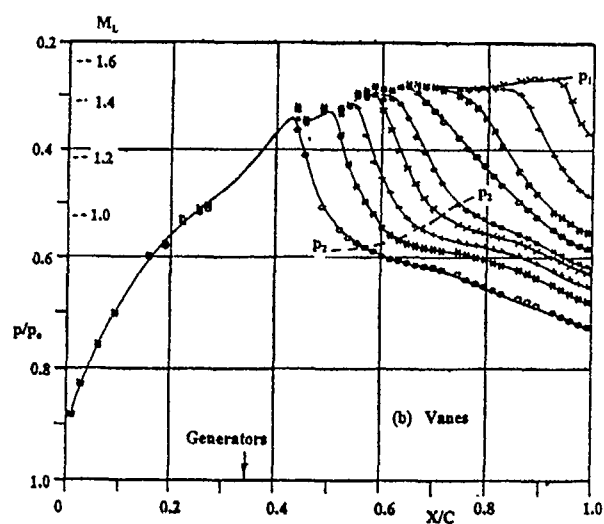
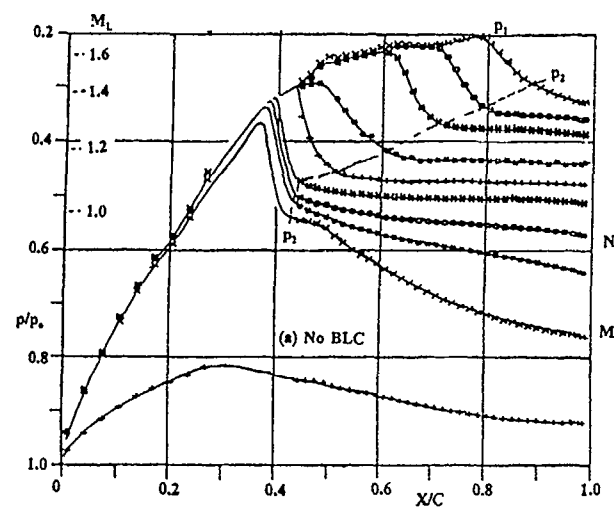
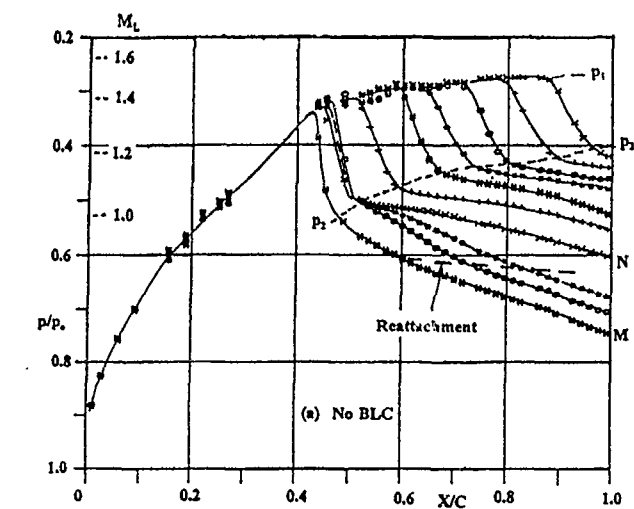


Fig 5 Surface pressure distributions for the 10% thick bump

Fig 6 Surface pressures for the 14% thick bump

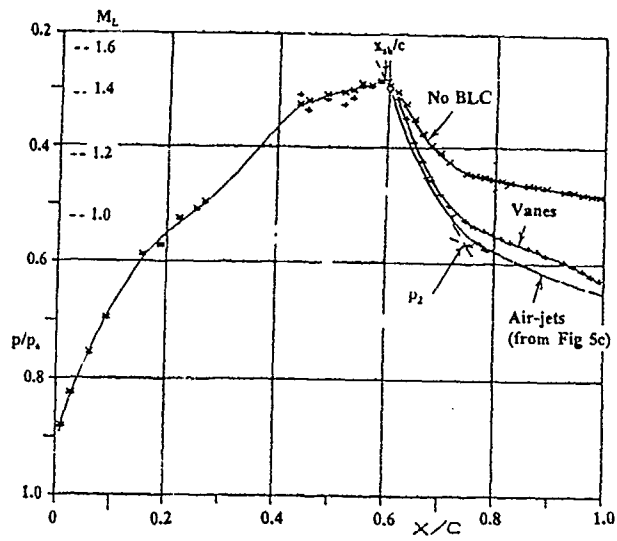


Fig 7 Effect of vortex generators on pressure distribution for fixed shock position; 10% thick bump

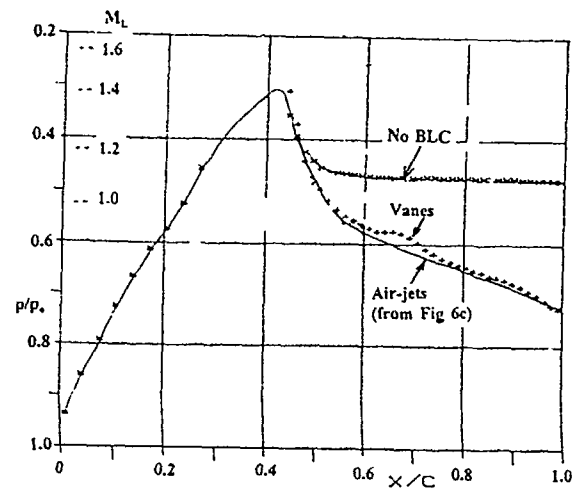


Fig 8 Effect of vortex generators on pressure distribution for fixed shock position, 14% thick bump

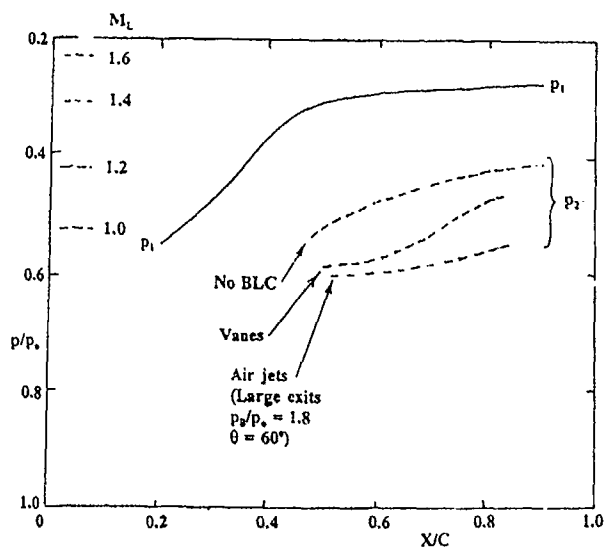


Fig 9 Effect of vortex generators on shock pressure rise ($p_2 - p_1$); 10% thick bump

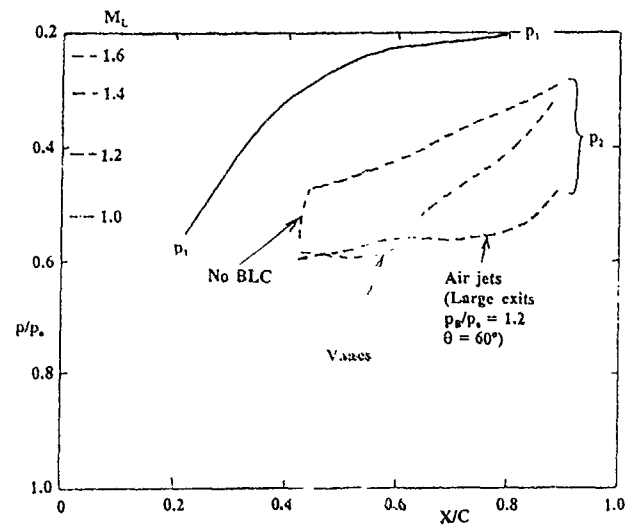


Fig 10 Effect of vortex generators on shock pressure rise ($p_2 - p_1$); 14% thick bump

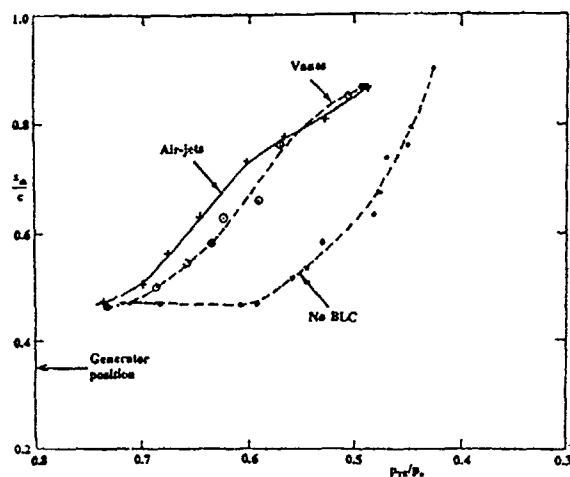


Fig 11 Effect of air-jets on shock position; 10% thick bump; large exits
 $\phi = 30^\circ$, $\theta = 60^\circ$, $P_0/P_\infty = 1.2$

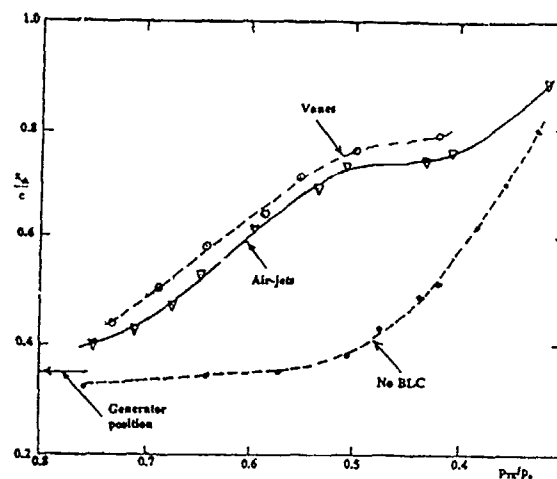


Fig 12 Effect of air-jets on shock position; 14% thick bump; large exits
 $\phi = 30^\circ$, $\theta = 60^\circ$, $P_0/P_\infty = 1.2$

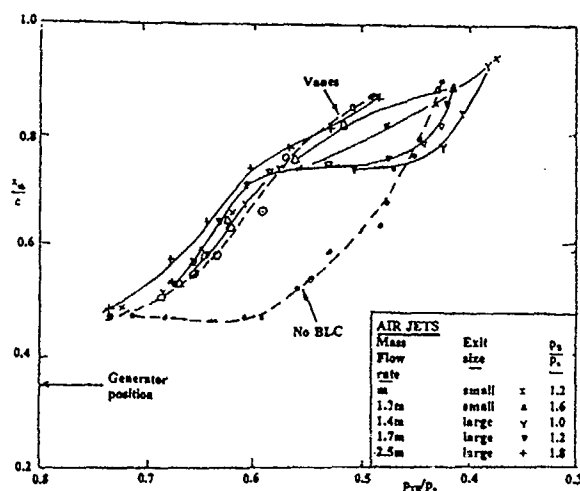


Fig 13 Effect of exit mass-flow rate on shock position; 10% thick bump;
 $\phi = 30^\circ$, $\theta = 60^\circ$

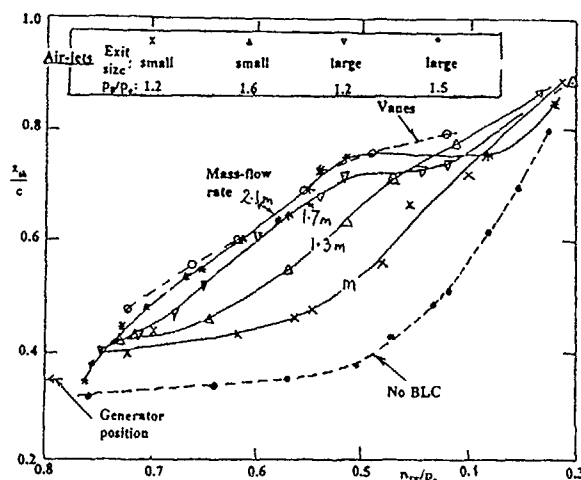


Fig 14 Effect of exit mass-flow rate on shock position; 14% thick bump;
 $\phi = 30^\circ$, $\theta = 60^\circ$

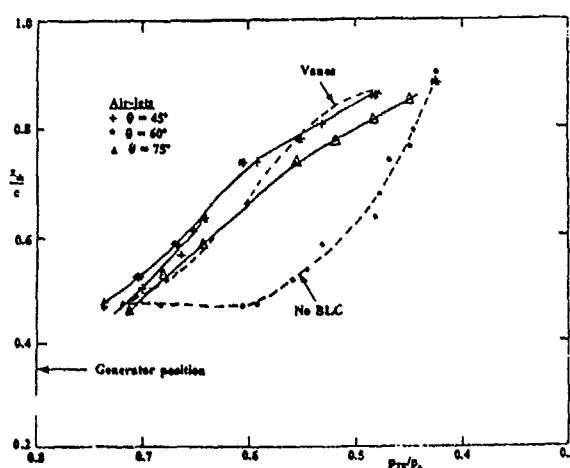


Fig 15 Effect of skew angle, θ , for large exits; $P_0/P_\infty = 1.8$; 10% thick bump

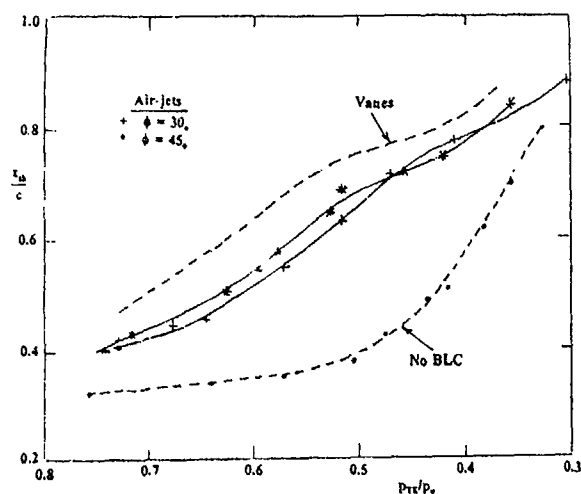


Fig 16 Effect of pitch angle, ϕ , for small exits; $P_0/P_\infty = 1.6$; 14% thick bump

GENERAL DISCUSSION

Professor Cantwell, Stanford University, US

It is a pleasure now to introduce Len Roberts. Len did his Ph.D. at the University of Manchester in 1955 where he was a student of Sir James Lighthill. He went on following that to a period as Instructor at MIT. From MIT in 1957 he moved to the Langley Research Center where he worked on hypersonic flows, problems of ablation and heat transfer, during the height of the rocket program, I suppose. That was just before Sputnik. Len was a rising star and in 1969 he spent a year at Stanford University and in 1970 he became Director of Aeronautics and Flight Systems at NASA Ames. Then in 1980 he joined the faculty of Aeronautics and Astronautics at Stanford University where I have since had the pleasure of his collegiality. In 1983 he became the Director of the Joint Institute for Aeronautics and Acoustics. He is a fellow of the AIAA and in 1978 he received the NASA Distinguished Medal. In addition, many people here know him personally since he was a member of the AGARD Fluid Dynamics Panel from 1980 to 1986. From 1984 to 1986 he was the Chairman of the Fluid Dynamics Panel. It is a great pleasure to welcome Len Roberts who will give the evaluation.

Professor Roberts, Stanford University, US

Thank you very much Brian. I see by the program it is my turn to evaluate what has just happened. I am not in a very good position to do that just a half an hour later, but I will try. The Symposium consisted of about 37 papers which have been grouped for the purpose of review. Following the general observations, I will review the program in these categories and end up with some conclusions and recommendations.

The Symposium included papers which ranged from an understanding of the basic structure of the jet and the cross-flow to those concerned with experimental and computational methods for determining the interactions to papers which treated the more practical aspects such as thrust vectoring, impingement and exhaust gas injection, vehicle control including hypersonics, and internal flows. A review of the history of jets in a cross-flow was given in the opening paper by Rich Margason. This traces the development of the interaction over the past 50 years with its application to such diverse fields as plume dispersion, combustion fuel injection, reaction control of missiles and aircraft, to its most celebrated application, V-STOL aircraft in transition flight. Primary emphasis in this presentation was placed on tracing our evolving understanding, experimentally and computationally, of the flowfield structure. Many of the papers, particularly those on flow structure and on experimental and computational methods, and on turbulence modeling, were presented by researchers from universities, while important contributions from the national laboratories and industry were made on the more practical problems associated with vehicle development. While substantial progress was reported on both experimental and computational aspects of the steady flow, less was reported on unsteady problems and more effort must be applied to this latter subject before a full understanding of future V-STOL vehicles or of the control of jet flows can be claimed. In view of their historical involvement in the development and deployment of the Harrier Aircraft and its derivatives, a preponderance of papers from the UK and the USA was found with some papers from Germany, France, Belgium and Turkey and no papers from other countries in NATO. Although much of the Conference was inherently oriented toward military aircraft application, it should be realized that the future needs of civil aircraft will involve such subjects as aero acoustics in the future and that they may influence the direction of research.

With respect to flow structure, the sessions 2, 5 and 12 comprised 9 papers covering both experimental and computational studies of subsonic and supersonic jets in the cross-flow. In paper 3 the unsteady pressure was measured at high Reynolds number for a supersonic jet including effects of the oncoming boundary layer to identify variations in the sound pressure level with jet pressure ratio and the jet mode, (subsonic, under and over expanded jets), giving multiple mode surface pressure fields. The effects of the oncoming turbulent boundary layer were not large in this paper.

Paper 4 is concerned with the unsteady generation and convection of vorticity in the wake using a fluorescent dye and laser cross-sectioning techniques, allowing the concentration field in the wake to be reconstructed. The study confirmed and elaborated earlier conclusions that the vorticity emanated from the wall boundary layer.

In paper 5 the separated flow structure caused by a rectangular jet was investigated experimentally for several parameters of the jet. The Reynolds number, Mach number, vector angle, upstream boundary conditions and so on. The results are displayed showing the separated wake behind the jet occurring when the jet is pointed upstream and downstream, giving different frequencies for the flow. In paper 12, two studies were reported; a visualization study, using colored dye, in a water tunnel, and a flying hot wire study using a low speed tunnel, to investigate the counter-rotating pair that results from the

interaction of the jet with the cross-flow. They show the importance of the separation position in the jet exit tube to the subsequent development of the vortex flows. Jumping to paper 14, a completely different application is investigated: the creation and diffusion of a phyto-plankton plume by large populations of filter-feeding animals in estuary regions. The effect of bed clams was simulated by large numbers of siphon pairs which alter the mixing characteristics of the phyto-plankton depleted fluid. Variations in concentration were found as a function of size and height changing the effect of surface roughness and results were explained in terms of jet-stream velocity ratio.

In paper 39 experimental studies of the heated supersonic jet flowing cross-wise to a supersonic stream was undertaken in the S5 tunnel at ONERA. The shock and vorticity structure were shown at Mach 2 with emphasis on the effects of heating which are small, and of turbulence. The use of air jets to suppress shock-induced separation on aircraft wings or empennages was explored in paper 40 where a comparison is made of vane-type vortex generators. It was found that the air jet allows a greater pressure rise through the shock which now progresses continually over the surface and allows an increase in the downstream pressure recovery at high α . In attempting to summarize the sessions on Flow Structures, it should be said that the CFD comparison with experimental measurements shows good agreement when the flow is dominated by inviscid effects. However, when turbulence plays an important part agreement depends on the turbulence model chosen and this can effect some of the inviscid features. For example, the position of the horseshoe vortex in the impinging jets against a flat plate. Nevertheless, our understanding of the flow structure for steady flows has progressed to the point of application to several problems in aerodynamics in addition to the traditional V-STOL application. Furthermore, our progress and understanding of unsteady phenomena continues and should be further pursued, particularly in the context of the enhanced mixing. The sessions on Experimental and Computational Methods and on Turbulence, Sessions 3 and 8, comprise 7 papers and also covered the subject of jets in a cross-flow, which concentrated on techniques, both experimental and computational, and on turbulence modelling required for a good description of this interaction. In paper 6 experiments conducted in a wind tunnel with Planar Laser Induced Fluorescence using acetone as a tracer gave the scalar mixing of the jet concentration and showed images of the structure not previously reported. The use of smoke illuminated by a laser beam to visualize in real time and measure the twin jets flowing normally into the cross-flow was reported in paper 7. Differences were found in the widely spaced twin jet configuration compared to the single jet configuration. Measurement variations were found of the probability density, the energy spectra and the interface location and gave a detailed mapping of the single and twin jet cases the tandem and inline cases. Notably absent in the measured spectra was evidence of periodic vortex shedding, as reported by earlier works. Paper 8 gave good examples of using LDV in a water channel to investigate the behavior of twin jets. This research concentrated on turbulent measurements required for the validation of CFD codes.

On the computational side, paper 22 reported a numerical investigation using different boundary conditions and two turbulence models, the Baldwin Lomax and the Baldwin Barth models with the thin layer Navier Stokes results showing good agreement with pressure measurements. The calculation used two grids, a cartesian grid and a cylindrical grid for the far and near fields respectively, and successfully showed the presence of a horseshoe vortex near the wall, and its influence on the pressure distribution as well as the usual dominant features, the contra-rotating vortices and downstream circulation. In paper 23, computational results were obtained for a single and multiple jet with emphasis on the influence of the turbulence model closure on the results. It was claimed that the results are in better agreement with experiment if the Reynolds stress model, given by Gibson and Launder, is used in conjunction with a near wall log-wall base model as opposed to the simpler $k-\epsilon$. The comparison shows that the use of the former turbulence model produces a ground vortex in better agreement with experiment. Results are presented for several fundamentally different 3-D geometries and underscore the importance of the choice of turbulence model closure. Similar conclusions regarding the importance of choice of turbulence model were shown in paper 24, which I believe was motivated by the behavior of gas turbine combustors. While agreement with experiments was not particularly good, it appears that some improvement was obtained when the second moment closure model was used for turbulence. The effect of grid geometry and boundary conditions were investigated in paper 25, where 2-D and 3-D jets were considered. Results were compared using algebraic turbulence models with previous experiments and good agreement is claimed for the gross features.

To summarize these sessions, it is clear that we now have good techniques to both measure and compute flows, certainly external flows. These are important tools, non-invasive experimental techniques used with good computational techniques. The long pole in the tent is still turbulence modelling. I suspect that this will hold up final progress toward getting full agreement between theory and experiment.

Sessions on the practical applications to military aircraft comprised seven papers and concerned thrust vectoring, jet impingent and exhaust gas reingestion. The empirical modelling of the interaction between a thrust reverser jet and an external flow was undertaken in paper 9 where the efficiency of the thrust reverser was determined as a function of door design including its opening angle. The influence of the

door and sideplates on the penetration of the jet and the vortex strength were determined. In paper 10 the jets were represented by a distribution of doublets, sources and sinks. The vortex path is described empirically. The model was then incorporated into a panelling method to give the interference forces and moments on wings and tails as functions of the jet placement, the jet velocity ratio and wing aspect ratio in the low speed transitional phase of flight. The control of thrust vectoring by injection was investigated in paper 11 for a hypersonic aircraft. Two-D Euler calculations were carried out to investigate subsonic and supersonic injection of the aircraft's forebody boundary layer into the nozzle flow. This allows a determination of the effects of injection on thrust vector due to changes in pressure and temperature in the nozzle. The stability of the aircraft with α is improved by injection. Paper 15 reviewed past and current experimental studies for the ground vortex produced by jet impingement using fixed ground boards, moving ground belts and moving model tests to give the gross effects of the vortex on the aerodynamics of a generic wing/body configuration. Large effects on forces and moments of ground effects were observed. Paper 16 performed experiments to determine the scaling parameters for exhaust reingestion for STOL aircraft and in particular, addressed the question of buoyancy on Mach number scaling versus pressure ratio scaling in this context. It was concluded that for the descent mode of a whole aircraft model the differences in flow field did not appreciably change engine face conditions, thus confirming the scaling parameters originally derived by Cox.

In paper 17 the subject of hot gas ingestion was further pursued and the influence of the direction of head-wind on engine performance degradation was addressed. The effect of buoyancy and pressure ratio were considered for Harrier type and A-STOVL supersonic exhaust engines with a conclusion that hot gas reingestion is head-wind dependent for some configurations, and increases with nozzle pressure ratio. Importantly, for full-scale model comparisons ingestion is stochastic in nature and requires the use of statistical methods in its analysis. In paper 18 for A-STOVL aircraft unsteady effects of reingestion were considered and the use of statistical techniques was made to describe the presence of large-scale unsteady streaks of hot gas entering the intake. The analysis has been applied to reingestion with under-fuselage diverter arrangements and also provided some insight into flow mechanisms using model conditions at nozzle pressure ratios different from full scale while maintaining dynamic similarity.

Sections 4 and 6 underscored the importance of good experimental testing in such practical problems as combustion mixing or hot gas reingestion, as evidenced by papers 17 and 18, in conjunction with adequate analysis of the unsteady effects of such phenomena on engine and vehicle performance. Although substantial progress has been made on the numerical analysis of relatively simple geometries for the purpose of conceptual design, experimental testing and the use of appropriate scaling laws together with engineering analysis will continue to be important for the development of full-scale aircraft.

I turn now to vehicle control, including hypersonics. The sessions on the use of jets to control vehicle motion, including hypersonic vehicles, consisted of 12 papers. Regarding the interaction of jet flows with the hypersonic stream, sets of experimental data for trailing edge jets on a 60 degree wing, and for transverse jets in a corner, were given in paper 19. For the delta wing experiment, two jets, symmetrically placed on the wing, were used and the efficiency of the jets, which depend on the interaction with the hypersonic flow, was determined in terms of the jet momentum and the jet position as well as the angle of attack. An enhanced normal force and rolling moment were produced for angle of attack less than 20 degrees. For the corner flow, Mach 20, the induced wall pressures that result from interaction with the control plumes was found by varying the stagnation pressure of the control jet. These induced pressures result from separation of the corner flow. The investigation of interactions between the jet and a hypersonic stream are continued in paper 20 which used a flat plate approximately 20 cm long in an isentropic light piston tunnel of Mach number of about 7 and Reynolds number of about 4 times a million meters. Results in 3-D for different injection gases showed a dependence on upstream separation and on a local flow structure generally and on the ratio of specific heats for the gas. Comparison of these features for the 3-D flow field were made with 2-D results previously reported. In paper 21, a unique model mounting support for the ISL shock tunnel was described which allows Mach number, Reynolds number and velocity of the hypersonic flow to be produced for millisecond force measurement. Typical interaction coefficients in excess of two were measured, depending on the location and number of nozzles used and the shape of the surface with which they interact.

Turning now to the lower Mach number flows, paper 26 gave a summary in the form of an historical review of the use of spanwise blowing to produce an improvement in the post-stall aerodynamic performance and the stability and control of wings. The conclusions are based on an empirical analysis and the use of spanwise blowing on current and past operational aircraft. The blunting of the forebody of an ogive-cylinder at high angle of attack in low speed flow suppresses the tendencies to develop spurious forces and moments. Proportional side force was produced experimentally by blowing small nose jets for the purpose of control in paper 27 where it was shown that such blowing controls the vortex behavior. Results were given for laminar separation for the blunted configuration in terms of a mass-blowing coefficient and turbulent results were presented using boundary layer tripping techniques showing greater blowing effectiveness for this case and particularly for forward blowing jets. This paper,

although not presented, will appear in the proceedings. In paper 28 a delta wing rather than a blunted cone is used with blowing at the leading edge of the wing, that is blowing tangentially around the blunted leading edge. It was shown experimentally that blowing is similar at a high angle of attack to a reduction in angle of attack, and a reduction in sweep angle in that both tend to reduce the effect of vortex burst on loss of lift. Computation of vortex bursting was carried out using the thin layer Navier Stokes equation and the effects of blowing as well as angles of attack and yaw on the flow over the delta wing were given. The experimental and computational work showed that control by producing a rolling moment is effected so that wing rock can be eliminated.

In paper 29 a general numerical simulation was used with Navier Stokes codes to describe how jet interactions can play a dominant part in the control of missiles and propulsive devices. A computational scheme was presented which accounts for the presence of heavily laden particulates in the transverse jet. A compressible dissipative $k-\Sigma$ model, $Cd(k\Sigma)$ was used. In addition, the simulation of helicopter plume interactions with a downwash was considered using Lagrangian vortex tracking procedures with the Navier Stokes methodology. In paper 30, the aerodynamics of lateral control jets on a missile were determined. These were determined numerically for both subsonic and supersonic flow using overlapping grids to conduct the Navier Stokes computation with generally good agreement with experimental results. In paper 31 experimental results were presented on visualization tests of the use of control jets for the Hermes spacecraft. Simulation based on NASA's momentum flux parameters for this configuration was based on scaling laws derived from the Shuttle spacecraft reaction control system. Additionally, exploratory pressure measurements were made to describe the jet interactions with the surface. Returning to the subject of vehicle control at low speed, paper 32 gives a numerical simulation of powered flight on a simplified V-STOL configuration, including the lift loss that occurs during descent and its dependence on the behavior of the ground vortex that appears under the vehicle. Time accurate simulations using the Cray supercomputer of both straight and level flight and descending flight are presented. A set of overlapping grids was used, a ground jet and delta wing grids which required an upgrading of communication between grids. In the descent case it was found that a number of flow features could cause temporal variations in ground surface pressure, that is pressure waves and oscillations in lift when the vehicle is in ground proximity. These include vortex shedding from the jet lip causing jet oscillations, both laterally and streamwise, oscillations in the ground vortex height, and evidence of Karman vortex shedding behind the jet. Comparison of the Strouhal numbers, isolated the cause of these oscillations as probably being associated with the variations emanating from the lip of the jet. Fair agreement was found with the previously determined experimental lift coefficient, with the primary effort made to understand the unsteady flow features. The practical problems of reducing landing ground roll for the F-16 aircraft was reported in paper 33 which analyzed experimentally the use of thrust reversers for this purpose. The effect on pitching moment was explored, particularly, and it was found that a large nose-up pitching moment was experienced on the wind tunnel model at forward deflection of the lower thrust reverser vane. This effect together with the results using the short ground board in the wind tunnel influenced the design of the control system used in flight. Subsequent flight tests results showed that a nose-down rotation was produced during landing. These results of jet ground forces were very different from those predicted. Control laws were updated to reflect these effects, particularly as they affected the thrust reverser operation. The experimental and computational methods used in a STOLV takeoff study based on a cropped delta wing with tandem jets was reported in paper 34. Experimentally, at a maximum of free stream Mach number of 0.2 and a maximum nozzle pressure ratio of 3, forces and moments of steady and unsteady pressures together with surveys near the tunnel wall were measured to verify the boundary conditions used in the computations. Comparisons were made for particular set of flow conditions and with choked jets. Gross features such as coefficients of lift and pitching moment were found and the computation evaluated through detailed comparisons including the pressure distribution. LDV and Schlieren photographs were also used. The papers in the vehicle control sessions indicate that the use of jets is promising for increased vehicle control and maneuvering at all speeds, but that near the ground, thrust vectoring involves more complex aerodynamic phenomena than was first realized, despite the success of the Harrier operating partly in this regime.

Finally, Session 10, devoted to internal flows including turbine cooling, was concerned with experimental and computational approaches to the effects of free stream turbulence, space averaging of multiple jets, flow inside cooling channels and swirling jets. Paper 35 on the effects of stream turbulence investigated, primarily experimentally, its influence on entrainment and mean path of the slightly heated jet at low jet Mach number. Results show that there are effects of free stream turbulence intensity and jet development although the trends are insufficiently clear to suggest the primary mechanisms involved. Paper 37 considered the application of turbine cooling by air injection. Experimental and computational studies indicated that flow inside the cooling channel was influenced by the main flow around the airfoil, thus requiring gridding inside the channel. Good agreement of separation with the laser measurements was found when simultaneous calculation of the airflow and the internal flows were carried out. Paper 38 computed the effect of the swirl on a jet using algebraic turbulence models with the thin layer Navier Stokes equations. I have some conclusions and recommendations. The first conclusion is a general one;

- (1) Today's technology adequately meets the needs for the successful development of military subsonic exhaust V-STOL aircraft; that additional technology is required for the application to aircraft control by solely pneumatic means, and that other applications, for example, environmentally clean combustion, may be equally important in the future.
- (2) Agreement between experiment and computation in describing flow structure is generally good for most gross inviscid features of simple flows. Agreement on the finer details depends upon the choice among several turbulence models; the unsteady interaction of the jet with neighboring surfaces and the mixing process in combustion need more research.
- (3) There recently have been major improvements in the use of LDV and in non-invasive techniques more generally, and significant progress in the use of CFD. Detailed agreement may not always be necessary, depending on the application, and further development of both techniques should be encouraged.
- (4) In practical applications, there is good agreement on the primary effects on current vehicles, but their impact on future vehicles is not as well known, that is, particularly for supersonic exhaust vehicles.
- (5) The use of jets for vehicle control appears promising at all speeds when conventional aerodynamic forces are not available. The interaction of the aerodynamics and the control laws is particularly important to be pneumatic control of vehicles, and further attention must be given to a proper understanding of this interaction.
- (6) Further improvement in the understanding of internal flows, particularly the mixing process, is needed and can bring about gains in propulsive efficiency of aircraft engines, but also can be applied in other ways.
- (7) Blade cooling seems to be modelled well, if adequate care is taken to include the internal channels of the flow cooling system.

I think that is about as much as I have in the way of conclusions and I am not prepared to answer any questions regarding this review.

Professor Cantwell

Now the meeting is open for discussion and I would like to remind you once again to say your name and affiliation clearly and to try and speak as slowly and carefully as you can for the translators.

Professor Jimenez, Escuela Tecnica Superior de Ingenieros Aeronauticos, SPAIN

You mentioned several times that some of the computations are still not working, could you be a bit more explicit of which aspects of the computation are missing something?

Professor Roberts

I have the general impression that the gross features of the flow can be predicted using almost any turbulence model, the K- ϵ or perhaps one of the higher order turbulence models, but the details of flow, the degree of separation and the presence of the vortical structure in detail is not given very well by any turbulence model, and any turbulence model is no better than the K- ϵ model, although it is claimed to be otherwise.

Professor Cantwell

That is something to pursue; is the Reynolds stress transport approach better?

Professor Lilley, Southampton University, UK

I would like to congratulate Len Roberts for his presentation of the conclusions of this meeting. There are, however, certain matters concerning jets in a cross flow, and, their applications in respect to the validation of the performance of full-scale vehicles which should be emphasised. My impression, gained from this meeting, is that in part of this flow, where the flow is reasonably steady, we find that the computed flow agrees very well with experiment. But in many of these particular flows there are gross unsteady features, especially in the downstream wake. The problem then, and one which worries me, is how we can recognise these regions of gross unsteadiness from the steady flow computations, or how to introduce unsteady methods of computation. One point I would like to stress is that we have found this unsteadiness from doing experiments. If we had been relying entirely on computation we probably would not have realized that the unsteadiness was there. Therefore, the message is quite clear, that in the future we must continue with experiment on at least some of these particular flow fields to really understand the unsteadiness and to investigate the nature of that unsteadiness. If we know that the flow is unsteady, or part of the flow field is unsteady, it is quite clear that in computation we have got to have unsteady methods. Short of full Navier Stokes solutions it would seem that our only hope forward is not

via current turbulence models, but possibly via Large Eddy Simulation (LES). We have heard at this meeting of the large time scales that are required for such calculations. Short of computations with LES we have got to rely on experiment. This is a very important conclusion. Certainly what I have said applies to single jets, and of course once we get into the problem of tandem jets and spanwise jets, the problem gets even more complicated, and the regions of gross unsteadiness increase. Again, as a final conclusion, whatever we do in relation to improving our computational methods, we must have experiments available for validation, and validation is one of the key words in this game.

Professor Cantwell

I noticed the other day on the technical tour they had a figure showing a plot of the turbulence level in the fountain. I think I remember turbulence levels near the centerline on the order of 0.6, possibly related to flapping back and forth of the jet. Maybe I could generalize that point and ask if we would like to discuss whether, in order to make further progress on predictive methods, it is really essential to go to unsteady calculations. Is there any more to be gained from using stationary mean flow turbulence models?

Professor Ciray, Middle East Technical University, TU

During the presentations, we have seen work done mostly on diagnostics. This part was particularly impressive since they were clearly showing the unsteady character of the flow. Indeed, as has been pointed out by Professor Lilley and Professor Cantwell, this unsteadiness presently is one of the key features that future investigations may be oriented. The turbulence level of 60% that you have mentioned, whether it should be called a turbulence or a rapidly fluctuating flow is something to be seen. My thought is that an unsteady turbulence flow associated with LES (Large Eddy Simulation) type model apparently is a need for understanding and deciding about these kinds of flows.

Dr. Dash, Science Applications International Corporation, US

I think that we are facing a very difficult situation because large eddy simulation involves many different scales. I think that we are really talking about, in these flows, flows with two different scales, scales of unsteadiness that might be acoustic unsteadiness and then turbulence scales that are quite different. I think overall we will need a hybrid type of approach. We are using unsteady Navier Stokes methodology and generally we seek time-asymptotic solutions that really never get to a steady state. The codes do have the possibility if they will run. They will have to be run a little differently than we run them now. In many ways of running these codes we run them to force them to steady state and we use accelerator strategies. Now if instead of running the codes that way we do take a time accurate approach, we work towards achieving steady-state solutions, I think that we will find some of the oscillatory behavior. As long as we can separate frequencies, if it is low frequency oscillations, I think we can use conventional Reynolds-averaged concepts and some of the other structure will be more wave or acoustic structure. If we are into high frequencies, such as screech tones and things like that, we have no way of doing it. I think there is room both for Reynolds stress or $k-\epsilon$ type modelling as well as unsteady simulations for certain classes of flows. The CFD community has to be extremely careful in how one looks at problems. We have CFD codes, particularly the day that we put time into the codes is the day that we all have to start becoming extremely careful in looking at what that time does. We have a lot of young and inexperienced people working with CFD codes trying to get that solution to converge and yet there is something that is bouncing up and down in the solution. Often we find that as we try to improve our solutions by tightening up the grid, that a solution that looked good and was nice and steady, suddenly goes unsteady because we have hit those scales. We have lost the numerical damping. The other caution is in how one puts in the turbulence modelling. If one puts it in brute force at the beginning of the calculation, one can suppress the ability for the flow to actually go unsteady. There has to be great care in the application of CFD. There is room for both types of models in certain classes of calculations.

Professor Cantwell

People who do LES speak of using coarse grain methods or under-resolved LES methods. They are out there, but they also require extreme care and understanding as to whether what you are computing actually has some physical meaning.

Professor Ciray

If I may continue on the unsteadiness: from time to time, I and other people got the impression that the unsteadiness is essentially due to the wake flow behind the jet. So this, in a sense, brings the idea of Karman vortex street, and it has been mentioned in many places. Perhaps, the periodicity of the flow can roughly be judged. This period or this frequency can be used in splitting the flow into what we call the steady periodic plus the turbulence. This may be a point for future calculation basis.

Professor Cantwell

A question is how clearly periodic is the Karman shedding in these cross flow jets? How clean a harmonic, it looks kind of broad band to me.

Professor Kind, Carleton University, Canada

My feeling is that we may be dealing with two or more kinds of, shall we say, unsteadiness, sometimes periodic analogous to the Karman vortex street and sometimes another kind. I think that the periodic and similar kinds of unsteadiness can be picked up with unsteady Navier Stokes methods with basically a turbulence model, in other words, without the necessity for large eddy simulation. I think there are other problems, for example, where you have two jets impinging and producing a fountain, where the unsteadiness is from a different source, perhaps from the large scale structures in the flow, the structures that relate to intermittency. One jet may be on a low and the other on a high, they interact and the fountain is driven back and forth, fluctuating in space because of the large scale more or less stochastic, as opposed to periodic, structures as opposed to periodic. There may be other phenomena; Dr. Dash alluded to acoustic coupling phenomena. I don't think we can think in terms of only one source of unsteadiness.

Professor Jimenez

I just want to point out that large eddy simulation is nothing else than non-steady the Navier Stokes equations with a turbulent model underneath. I don't think there is any contradiction between using LES and doing what you are saying, it is essentially the same thing. It is just a question of where you do your filtering and at what side you do your filtering. You say, below this is turbulence, above this large scale.

Dr. Dash

It is quite a different type of filtering. In standard turbulence modelling or Reynolds averaged turbulence modelling, we decompose into $U + U'$; U could be a function of X and t , but U' is supposedly a fluctuating component that we then form Reynolds stresses from. In the other (LES), it is a spatial type of decomposition. We decompose into resolvable and unresolvable and the feeling is that for many of these problems with true unsteadiness, we do have to use an LES approach, but an LES approach is very complicated. For example, we could have regions where we have wall boundary layers, but we may have some jets as well, and it could be that we would like to use a conventional turbulence model in the boundary layer and just restrict the full LES to regions that are truly unsteady. I think that we are going to need hybrid methodology to try and do things from an engineering point of view. Full LES is very problematic because LES involves other types of instabilities and it is a very sensitive type of methodology. One would have a very difficult time trying to do a very simple shear layer problem with LES because the whole instability process has to come through that LES methodology. It is not an easy approach if one wanted to work a problem that truly was a steady problem and all the unsteadiness was on a real turbulent scale. It is a very difficult problem. One has to force the motion to bring in these eddies. There a conventional turbulence model would be a much easier approach. If one has a flow dominated by large eddy structures, that is where a large eddy simulation approach would make more sense. I think it is where one can see true unsteadiness, flapping, these types of motions, that we need LES and applying a conventional turbulence model there would actually damp those motions. I think we are going to need very creative and zonal approaches and try to restrict LES to where we see true unsteadiness. We try to say we will use full LES for full flow problems. I don't think that is ever going to be feasible.

Professor Jimenez

What you are saying is that you can't apply LES blindly. You cannot apply anything blindly. What you are requesting basically, is LES applied with intelligence. The flow structures we want to resolve are different in different places, which is true of any flow; a wall flow, for instance, or any inhomogeneous flow, as a jet or a boundary layer. It is a question of names, we shouldn't argue too much over that.

Professor Cantwell

Can I throw an added complexity into that. If you are going to go to the effort of doing LES, how important is it to also resolve the acoustic field. Normally LES computations don't do that and acoustics plays an important role. If you are going to make that kind of effort, probably you will have to anticipate needing to do both.

Professor Lilley

I am pleased, Mr. Chairman, that the question has been raised about the need for the study of the noise radiated from many of these particular flows. I would like to briefly mention that the structural engineer needs to know the magnitude and spectrum of the fluctuating pressures on surfaces adjacent to these flows. It is very necessary to have knowledge of the full range of the acoustic modes incident on such surfaces. It is only then that the structural engineer will be able to design the appropriate optimum structure to withstand the acoustic loading. These acoustic modes are dependent on the flow geometry and the exhausts are very hot when the design problem involves not only acoustic fatigue but also that relating to heat lag. The unsteady flow problem adjacent structures is a very important one.

Professor McGuirk, Loughborough University of Technology, UK

I just want to return to the original argument and support Dr. Dash's claim that what we need is a hybrid

approach. I don't think that we needed to come to this conference to find out that turbulent flows are unsteady, the question is to what extent does that unsteadiness need representing in what detail in any calculations that we should do which are then truly predictive. Before we all go off and do LES calculations, I think we have seen a challenge to LES in this conference in terms of this turbulence intensity in the fountain. It is quite clear that a $k-\Sigma$ model will give you a turbulence level of about 20% in the fountain, a Reynolds stress improves on that and gives you 30%, but you are still a long way short of what is measured when you average over all scales. But we don't know whether an LES will give you the 50 or 60%. Someone needs to do an LES calculation and time average the time dependent predictions that the LES gives to see whether it will give a time averaged 60% level of turbulence intensity. That is quite an expensive calculation to do. I think that this conference says it should be done, and if it is successful, then for those circumstances under which one needs to know about that contribution to the fluctuations to the unsteadiness from the large scale, then LES will be a tool that one needs to use. I think that the reingestion papers show that that is not the only thing you need to know. Knowing what the time mean ingestion is also very useful to a designer. I think that the time average models can give already some useful indications on that.

Professor Cantwell

While you have got the microphone, let me bring another point into this. There was some discussion during the talks about buoyancy parameterization. When and under what circumstances does buoyancy play a role, in say hot gas reingestion. Are there circumstances where buoyancy in and of itself, that is the rising of warm fluid in a quiescent flow in some way, becomes important in the reingestion problem.

Professor McGuirk

I will give you my opinion. The parameter which scales the buoyancy effects is the Froude number and a derivative of that is what was used. First of all, I don't think that you should exclude gravitational acceleration because that is the interaction between fluid density differences with the gravitational acceleration that gives you your buoyancy effects. What the Froude number does is to scale that force due to density differences and to weight differences essentially, against the inertia differences. I think the velocities are always sufficiently high in reingestion - impingement type problems that in spite of the density differences the buoyancy, in my opinion, is always negligible. Therefore, I don't see a point of scaling an effect that is not actually there in practice.

Professor Cantwell

So what you are saying is a reingestion problem occurs close enough to the ground so that velocities are high enough so that inertial forces dominate buoyancy forces, but if you had for example, an incredibly quiet day higher up, the buoyancy dominates.

Professor McGuirk

I think that that is what has been described as far field ingestion. I think that it has also been said by several people that that is not really the design limiting problem, it is the near field ingestion that is the killer, as it were. Under those circumstances the buoyancy isn't really dominant or influential at all.

Mr. Curtis, British Aerospace, UK

Jim wouldn't expect me not to have a comment on this. I agree that in the time mean jet flow fields that the velocities are too high. I think that you saw in some of our video footage that within the very unsteady nature, within some of the large eddies which break off from some of these ground jet flows, that we do actually have some very low velocities which are of the same order as the free stream velocity which is very low. You get to the stage where the buoyancy probably does have an effect. I would like to see some CFD calculations where they can model some of these pockets of hot gas and then switch off gravity and then show me that there is no effect. When Jim can do that, then I will believe him, up till that time I shall remain skeptical.

Professor McGuirk

I think that is challenge number 2 for the LES people because I think that what Peter is asking for which is a fair request if he has got the money, is for someone to do an LES calculation which will predict the small eddies and the one-off events and to repeat the LES calculation with and without gravity to see if the behavior of the small eddies which are being reingested actually changes when you remove the gravitational field. That is the only way I think that we will get a handle on that because Peter's suspicions are exactly that, they are suspicions. I don't think that you know that you have got the eddies which have sufficiently low velocity and sufficiently low density, sufficiently high weight differences that they are affected by buoyancy, it is a suspicion at the moment.

Professor Cantwell

So we have LES, acoustics, buoyancy.

Professor Jimenez

I have to say that DNS people or LES people are not able to do that. It is still very far away. You are asking too much. You are asking now for a calculation that has to worry about the near field, and then of something that is far enough for buoyancy to be important. It is a challenge.

Dr. Dash

I wonder if I could throw out another more general question and that is, where is the future of this view; where is the future of jets and cross flow. Should future research be predicated on applications to V-STOL or should we be trying to take a broader view.

Professor Jimenez

Roberts said something about mixing and combustion and I think that should be discussed here. Whether there are important applications to the problem of making things burn better.

Dr. Dash

I think that the missile community is interested in these attitude control jets and getting fast response for missiles so that is another problem area. That is still a fairly active problem area and an area that is poorly understood.

Dr. Naumann, French-German Research Institute ISL, FR

I think it is as well the fast response of high velocity vehicles as the constraint that is imposed on those vehicles from the aerothermodynamics, because in dense atmosphere aerodynamic heating is extremely severe even for moderate flight velocities. At velocities above 1500 meters per second in main sea level, you will even get steel almost to melt, and so you must clean your surface as well as possible. You must try to dispose of thin structures, and side-jet control may be the only possible way to get those missiles with a minimum of drag and with a maximum of heat resistivity to its aim.

Mr. Margason, NASA Ames Research Center, US

Having worked in V/STOL for the better part of the last 30 years, I think that there will not be a lot of JICF activity related to V/STOL in the future given the change in the world political situation. We have one activity, STOVL-Strike Fighter (SSF) in the U.S. that has been initiated by the ARPA, which will probably be active over the next several years as a project for the defense industry to stress some new concepts and perhaps replace some airplanes when they eventually wear out. For other opportunities, I think that the JICF problem is related to turbine engines for several applications, to some environmental problems, and to missile reaction controls. I also think that the JICF problem is interesting in that it applies the computational procedures to very difficult flows where it may provide an understanding of the strengths and weaknesses of particular computational codes. There are several numerical representations of turbulent flow before we get too wrapped around this large eddy simulation application for turbulent flow, I think that there is quite a bit of room to fully evaluate the computations that we are capable of doing now, both from a time average and an unsteady point of view. We can obtain appropriate experimental data to assess the usefulness of existing computational methods and use this as an opportunity to determine limits on where they should be applied and where they shouldn't be. There are a lot of relatively inviscid flow regions for the JICF problem where we can do a pretty good job. As we get into the viscous regions immediately behind the jet, however, where there is a lot of flow separation, I think that there is still room for a lot of learning from the existing methods. Some systematic work would be useful for many other applications as well.

Professor Cantwell

Should we be pushing harder toward doing some full Reynolds stress transport modelling?

Mr. Sacher, DASA, PBM, GE

Addressing your last question, where is the future in jets in cross flows. I don't believe too much in V-STOLs because this is something that we have explored in the past. What I was missing in the program was the field of applications of thrust vectoring for manoeuvring. There are many attempts in developing thrust vectoring nozzles used in flight, and this could really be seen as jets being in cross flow because in V-STOL we have the jet but no cross flow. What was the reason for the program committee not to include at least one session on those important applications?

Professor Cantwell

I don't think that we got any papers on it.

Mr. Sacher

Did you make a request?

Professor Cantwell

I believe it was one of the areas we argued for to be included in the basis of the meeting.

Mr. Sacher

But in terms of engineering applications that seems to be one of the most important applications that could be seen in the future.

Professor Cantwell

Item 2 in the announcement is Thrust Vectoring and Vehicle Control. We got papers on vehicle control but nothing on thrust vectoring.

Mr. Sacher

Maybe we should have addressed the PEP community. I know that GE and Pratt & Whitney are developing such type of vectoring devices quite heavily.

Professor Cantwell

Are there any other comments in that regard?

Professor Slooff, National Aerospace Laboratory NLR, NE

I was about to throw a similar pebble in the pond and perhaps cause a few ripples. I want to refer to one of Len Roberts remarks. It seems that we have a deficiency in our knowledge in the area of the control over vehicles with thrust vectoring. I am referring to incidents like with the YF 22 for example, where we seem to have a situation of unpredictable non-linear instabilities in the combined aerodynamic, thrust vectoring propulsion and flight control systems. I think there is a general deficiency in our knowledge and capabilities in that area. This is, of course, a multidisciplinary problem, but with a very strong aerodynamic aspect in it. I think the aerodynamic community perhaps should take the lead in trying to solve this. I don't have any suggestions in how to address this problem. Can we and should we try for experimental simulations with all those systems coupled in the windtunnel, is that feasible? Or should we try to aim for numerical simulations? What is the feasibility of that and in what time frame. Or, perhaps most likely, should we try to follow both lines? I would like to hear some comments and suggestions from the audience on that subject.

Mr. Bowers, Wright Laboratories, WL/FIMA, US

I would like to suggest one way to go down that path, and it is not unique to this community. It is characteristic of many communities. It is time once again to get the CFD and the design people together. We can't afford 300 hours on a Cray for one solution. Some of these tools are applicable to shorter term design projects, but they cannot be expensive.

Also, the CFD community needs to understand what the design community wants. There is still a gulf between the two sides. Until they get closer together we are going to do large complicated computations that can't be used by the people that are working on these control laws.

Professor Cantwell

Are there any other comments with regard to Professor Slooff's remarks, or Peter Sacher's. I don't know why we didn't get papers on that subject. The announcement was certainly circulated widely. As you all know, you all get thick envelopes full of announcements to send to everyone that you know. Why we didn't find some papers coming in on that is a little bit of a mystery, even if it was specifically spelled out as one of the terms that we wanted to look at.

Mr. Selegan, Wright Laboratories, WL/FIM, US

Probably one of the reasons that you didn't get responses is that right now in the US we are starting two programs and planning a third. The first one is the GE thrust vectoring nozzle on an F-16. That will be done by the Airforce. The second program is a complementary one with Pratt & Whitney on the STOL F-15. Both of these programs are Risk Reduction Programs for the following program which will be called PACIR, Propulsion Aerodynamic Control Program. I think that part of the problem might have been timing. We were in the middle of a source selection and evaluation and we are going back to the table on that so, probably you didn't get a response cause everybody is holding their cards close to their vest at this time.

Professor Cantwell

Maybe to continue with this, if there are these programs coming up, should we look at this as a potential area for a symposium. Maybe this is an area, thrust vectoring in and of itself. Would there be enough material there for a symposium.

Mr. Selegan

That may be in the future, and in fact the PACIR program is being somewhat touted and pushed as an international program with international involvement. The details have to be worked out, but we are working down that international route for that program.

Mr. Margason

There is another thrust vector problem that is being worked on using the F18 at Dryden where they have paddles in the exhaust for manoeuvring at high angle of attack. That is another program, but it is early in the flight program and sufficient data simply has not been generated yet to provide a story. There was a considerable amount of wind tunnel work done in the 1970's and early 1980's, and most of that has already been reported. Now there are a few new flight programs so it is again probably an issue of timing on presenting results of the thrust vector application.

Professor Cantwell

Any further comments about the future of this field? It looks like thrust vectoring is one area where it does have a future.

Professor Roberts

I have a question generally for the audience, rather than a comment. Does any organization have plans to do work that is not V-STOL oriented, that is more oriented toward the environment or some other application of the kinds of tools that we have now?

Dr. Smith, Stanford University, US

I am certainly no expert on funding, but my advisor Godfrey Mungal at Stanford University has just received funds from the Gas Research Institute to study the mixing combustion of jets in crossflow.

Professor Cantwell

Someone, I think Len, may have said that we have good techniques for measurement and computation, is that a fair statement, particularly with regard to measurement? Where should the experimental techniques development be?

Mr. Margason

When I was looking at the data for the review paper, I was hoping that I would find quite a bit of laser velocimetry data to identify that would be suitable for comparison with computational results as part of evaluating current methods. The thing that surprised me was how limited the existing LV data is on the jet. Of course, we have to recognize that LV data by its nature at least with current systems, is time averaged data over days and days and days by the time you get a few decent cross-sections. There was a several year effort at Ames in the 7x10 tunnel to get LV data, but it was really more of a development of the LV instrument by the developers of that instrument rather than a fluid mechanics investigation of the jet in cross flow. Out of that I could only identify about 6 cross sections that were taken at one jet condition and that is hardly an extensive technique. There is development going on of Doppler global velocimeters which would give you the promise of taking a light sheet across a jet flow like this and give you instantaneous data at that point in time. The fact that there is so little experimental data available out there of a detailed flow field nature leads me to the conclusion that either the methods are not mature or we haven't adequately exploited them for this problem. I would say that there is probably quite a bit of room for effort experimentally to get detailed measurements that are suitable for comparison with computation.

Professor Cantwell

We have a couple of comments now. Let me go to the very back for the first one.

Professor Monismith, Stanford University, US

I am a little bit surprised in the review that PIV (particle image velocimetry) wasn't mentioned in context for experimental measurement. I think it is something that is really exploding now and offers the promise of very detailed instantaneous flow field measurements. The way it is proceeding you will be able to get averaged data that is probably comparable to LVA data but now for maybe 1024 x 1024 fields in planes and other people are doing holography and a variety of things. I think it is something that could really be exploited for this flow. It is a good flow to test it on in fact.

Dr. Naumann

The main problem that you have to face with laser Doppler velocimetry or even with particle image velocimetry is, that you have particles of a certain size, and if you want to detect turbulence and rapid fluctuations there is some indication that your measurements are not true. In our department there are investigations to find out how the particles are influenced by the motion, and we have seen small vortices in hypersonic shear layers which are completely depleted from particles. So you have regions where you have no measurements, and other regions, where you can measure but the particles have another path than the flow. A possible means to come on with this is to use the laser Doppler velocimeter as it is developed in the ISL, which uses the constant scattered light of many very small particles that are running through the measuring volume, and which are surely better following the flow than few comparatively large Mie scatterers. We have also another development on the way to make with these small particles Doppler pictures; not particle displacement velocimetry, which also needs quite large particles, but

Doppler pictures which give the velocity in a plane.

Professor McGuirk

In terms of measurements that are required, I think that there have been two suggestions emerging from the discussion in terms of doing more calculations. One is to do more calculations using Reynolds stress transport type turbulence models and the other is to do LES calculations. Both of these require different kinds of measurements. To validate the calculations done with Reynolds stress transport models means measuring the individual Reynolds stresses. It means not only LDV but the 3-d LDV so that you can actually get the correlations out. I think it is only just in the last few years that the 3-d LDV systems are starting to be used in anger. But I certainly would agree with Dr. Margason that there is certainly a need to do more of that. Then I want to also agree with a comment made that PIV is probably going to be the validation tool for LES that LDF is for the time-averaged turbulence models.

Professor Monismith

Regarding the difficulties of using PIV and LDA in these flows - I guess it is the advantage of low speed, particularly water channel flows, at least as far as elucidating the structures present in the flow which there seem to be still a lot of debate about what is actually going on from a pretty basic standpoint. Low speed gas or water tunnel experiments should be very good with PIV or LDA. I think it is maybe the more engineering hypersonic and supersonic cases are going to be tougher.

Professor Cantwell

I have a comment about Reynolds stress transport models. The modeled terms in that approach involve velocity gradients and products of the pressure with velocity gradients. Measurements of velocity gradients and pressure are going to be required to really check directly with the model terms in that approach. We are a long way from that even using PIV.

Dr. Woodward, Defence Research Agency DRA, UK

Unfortunately I have not been fortunate enough to be present to hear most of these papers, but listening to the discussion, I thought it might be interesting that I have just received from a UK member of the FDP Working Group 14, which is the working group which is working on an experimental data base for CFD validation, a proposal for another working group to work on providing a comparable data base for time dependent flows, and talks about oscillatory flows, periodic flows, generally unsteady flows which is the sort of categorization I have been picking up from listening from the discussion. My question really is, listening to the later remarks about PIV and laser Doppler velocimetry is do we actually have the experimental capability to make the measurements which would provide a set of validation results which we could rely on and secondly, if we can do that, what do we need to put in place? Do we have the data already or do we need to do some new experiments? I wonder whether that would be a note on which to end the discussion.

Professor Cantwell

So we are talking about DES, Direct Experimental Simulation. Do we have the techniques for doing DES. We have measurements in a plane using PIV, but DES really requires a fully three dimensional measurement, especially if you want to generate velocity gradient information. There are techniques people are working hard on, I would say, and they are mostly in the form of holographic particle imagery and multiple sheet particle imagery.

Professor Onorato, Politecnico di Torino, IT

I think that we possess this technique, but the limitations are those techniques can be easily applied to very slow motion fluid. The limitations are due to the, let me say, the cost of the few high speed telecameras that we can buy today and are due to light problems for such techniques. We need high power, neodymium yag lasers, things like that, but in principle such techniques are under development.

Professor Cantwell

I think that is a good note on which to end the discussion. Before I finish though, I would like to say some thanks. First, and really these are my thanks from the Program Committee, first to Len Roberts for the hard work in being the Technical Evaluator. That really is a tough job to sit through every talk, take an interest in every talk, write notes on every talk and then immediately after the last talk get up and talk about the talks. That is not an easy thing to do and we appreciate your efforts. Finally, I would like to thank all the authors. Some of you may or may not be aware that we actually set something of a record in this meeting in that all but one of the papers which will appear in the proceedings are in hand. I don't think that has ever happened before. Someone earlier said that that might be a record for AGARD. So on that basis let's give ourselves all a hand. Finally, I would like to introduce Professor Slooff who will close the meeting.

Professor Slooff

Thank you Brian. Well, ladies and gentlemen I am afraid that this really is the end of four days of

intensive jet work. Judging by the general level of attendance and the lively discussion, I think that this meeting was very successful, and clearly it would not have been possible without the help and dedication of several people. In the first place we have to thank our UK hosts for inviting us to the charming city of Winchester, with the excellent facilities here in the Guild Hall. In particular, we have to thank our local coordinator Dr. David Woodward and the UK national coordinator Mrs. Sheila Martin who took care of all the preparations including the impressive air display of the Harrier and the technical tour and exhibition at Farnborough. David and Sheila, we thank you very much for all of that. We also thank the city of Winchester, its Pubs, the Mayor in particular, for the hospitality and the fine reception we had earlier this week in this Guild Hall. I am sure I am speaking on behalf of the ladies if we also thank Mrs. Woodward for setting up such a splendid program for our companions and for providing such beautiful weather with it. Now switching to the primary reason for our presence here, that is of course, the symposium, I would like to thank the co-chairmen of the symposium, Professor Cantwell, Professor Ciray and Professor Jimenez for their initiative and their efforts and compliment them on the success of this meeting. We already thanked Professor Roberts for his on-the-spot technical evaluation; it has already been mentioned that you had the toughest job of all of us, but we also know that you gladly accepted it as an excuse for working again with the panel. Thanks again, Len, for your help and your skillful evaluation. Thanks are also due for the indispensable help of a number of people who have done everything to run this meeting smoothly, firstly the interpreters, Mrs. Day and Squadron Leader Smeeton. I am sure that we must have driven you crazy with all of our technical slang words and with all the different accents that we have exposed you to, and we thank you very much for taking care of your difficult job. The audio visual aids have been taken care of by Mr. Moir, Mr. McComb and also we had secretarial support from Mrs. Simpson and Mrs. Moir. We all thank you for your help in having this meeting run smoothly. Last but certainly not least, we have to thank the panel executive, Dr. Winston Goodrich and his secretary Anne-Marie Rivault for their very professional, efficient and friendly support. Winston, we know that this is your last meeting as an Executive, and I am personally very sorry about it, as are many of us. You have done a terrific professional job over the past four years, and last but not least, you are a very nice guy. We wish you all the best in your new job with NASA.

It remains to thank you all for your interest in this meeting. We thank Drs. Margason and Perry, the invited speakers, and all others authors for presenting their papers and all of you for your contributions to the discussion. I call your attention to our future activities and ask you to communicate them to your colleagues. I wish you all a safe journey home.

REPORT DOCUMENTATION PAGE			
1. Recipient's Reference	2. Originator's Reference	3. Further Reference	4. Security Classification of Document
	AGARD-CP-534	ISBN 92-835-0720-7	UNCLASSIFIED/ UNLIMITED
5. Originator	Advisory Group for Aerospace Research and Development North Atlantic Treaty Organization 7 Rue Ancelle, 92200 Neuilly sur Seine, France		
6. Title	COMPUTATIONAL AND EXPERIMENTAL ASSESSMENT OF JETS IN CROSS FLOW		
7. Presented at	the Fluid Dynamics Panel Symposium held in Winchester, United Kingdom, 19th—22nd April 1993.		
8. Author(s)/Editor(s)	Various		9. Date November 1993
10. Author's/Editor's Address	Various		11. Pages 492
12. Distribution Statement	There are no restrictions on the distribution of this document. Information about the availability of this and other AGARD unclassified publications is given on the back cover.		
13. Keywords/Descriptors	<div style="display: flex; justify-content: space-between;"> <div> Cross flow Jet flow Jets Aerodynamics Flow distribution </div> <div> Thrust vector control Hypersonic flow Exhaust systems Computational fluid dynamics </div> </div>		
14. Abstract	<p>The 37 papers prepared for the AGARD Fluid Dynamics Panel (FDP) Symposium on "Computational and Experimental Assessment of Jets in Cross Flow" that was held 19th—22nd April 1993 in Winchester, United Kingdom are contained in this report. In addition, the Technical Evaluation Report — aimed at assessing the success of the Symposium in meeting its objectives and its relevance to the technical needs of the aerospace community — is included in this report along with an edited transcript of the General Discussion held at the end of the meeting which addressed issues raised during the Symposium.</p> <p>The primary objective of the Symposium was to provide a forum for assessing advances made in the technology and application of jets in cross flow which have occurred since the last meeting on this subject, held by the FDP in 1981. Major topics covered included enhanced descriptions of the fundamental flow structure of jets in cross flow, experimental methods, thrust vectoring, jet impingement and exhaust gas reingestion, hypersonic crossflow, and numerics and turbulence modelling.</p>		

<p>AGARD Conference Proceedings 534 Advisory Group for Aerospace Research and Development, NATO COMPUTATIONAL AND EXPERIMENTAL ASSESSMENT OF JETS IN CROSS FLOW Published November 1993 492 pages</p> <p>The 37 papers prepared for the AGARD Fluid Dynamics Panel (FDP) Symposium on "Computational and Experimental Assessment of Jets in Cross Flow" that was held 19th-22nd April 1993 in Winchester, United Kingdom are contained in this report. In addition, the Technical Evaluation Report — aimed at assessing the success of the Symposium in meeting its objectives and its relevance to the technical needs of the aerospace community — is included in this report along with an</p> <p>P.T.O.</p>	<p>AGARD-CP-534</p> <p>Cross flow Jet flow Jets Aerodynamics Flow distribution Thrust vector control Hypersonic flow Exhaust systems Computational fluid dynamics</p>	<p>AGARD Conference Proceedings 534 Advisory Group for Aerospace Research and Development, NATO COMPUTATIONAL AND EXPERIMENTAL ASSESSMENT OF JETS IN CROSS FLOW Published November 1993 492 pages</p> <p>The 37 papers prepared for the AGARD Fluid Dynamics Panel (FDP) Symposium on "Computational and Experimental Assessment of Jets in Cross Flow" that was held 19th-22nd April 1993 in Winchester, United Kingdom are contained in this report. In addition, the Technical Evaluation Report — aimed at assessing the success of the Symposium in meeting its objectives and its relevance to the technical needs of the aerospace community — is included in this report along with an</p> <p>P.T.O.</p>	<p>AGARD-CP-534</p> <p>Cross flow Jet flow Jets Aerodynamics Flow distribution Thrust vector control Hypersonic flow Exhaust systems Computational fluid dynamics</p>
<p>AGARD Conference Proceedings 534 Advisory Group for Aerospace Research and Development, NATO COMPUTATIONAL AND EXPERIMENTAL ASSESSMENT OF JETS IN CROSS FLOW Published November 1993 492 pages</p> <p>The 37 papers prepared for the AGARD Fluid Dynamics Panel (FDP) Symposium on "Computational and Experimental Assessment of Jets in Cross Flow" that was held 19th-22nd April 1993 in Winchester, United Kingdom are contained in this report. In addition, the Technical Evaluation Report — aimed at assessing the success of the Symposium in meeting its objectives and its relevance to the technical needs of the aerospace community — is included in this report along with an</p> <p>P.T.O.</p>	<p>AGARD-CP-534</p> <p>Cross flow Jet flow Jets Aerodynamics Flow distribution Thrust vector control Hypersonic flow Exhaust systems Computational fluid dynamics</p>	<p>AGARD Conference Proceedings 534 Advisory Group for Aerospace Research and Development, NATO COMPUTATIONAL AND EXPERIMENTAL ASSESSMENT OF JETS IN CROSS FLOW Published November 1993 492 pages</p> <p>The 37 papers prepared for the AGARD Fluid Dynamics Panel (FDP) Symposium on "Computational and Experimental Assessment of Jets in Cross Flow" that was held 19th-22nd April 1993 in Winchester, United Kingdom are contained in this report. In addition, the Technical Evaluation Report — aimed at assessing the success of the Symposium in meeting its objectives and its relevance to the technical needs of the aerospace community — is included in this report along with an</p> <p>P.T.O.</p>	<p>AGARD-CP-534</p> <p>Cross flow Jet flow Jets Aerodynamics Flow distribution Thrust vector control Hypersonic flow Exhaust systems Computational fluid dynamics</p>

<p>edited transcript of the General Discussion held at the end of the meeting which addressed issues raised during the Symposium.</p> <p>The primary objective of the Symposium was to provide a forum for assessing advances made in the technology and application of jets in cross flow which have occurred since the last meeting on this subject, held by the FDP in 1981. Major topics covered included enhanced descriptions of the fundamental flow structure of jets in cross flow, experimental methods, thrust vectoring, jet impingement and exhaust gas reingestion, hypersonic crossflow, and numerics and turbulence modelling.</p> <p>ISBN 92-835-0720-7</p>	<p>edited transcript of the General Discussion held at the end of the meeting which addressed issues raised during the Symposium.</p> <p>The primary objective of the Symposium was to provide a forum for assessing advances made in the technology and application of jets in cross flow which have occurred since the last meeting on this subject, held by the FDP in 1981. Major topics covered included enhanced descriptions of the fundamental flow structure of jets in cross flow, experimental methods, thrust vectoring, jet impingement and exhaust gas reingestion, hypersonic crossflow, and numerics and turbulence modelling.</p> <p>ISBN 92-835-0720-7</p>
<p>edited transcript of the General Discussion held at the end of the meeting which addressed issues raised during the Symposium.</p> <p>The primary objective of the Symposium was to provide a forum for assessing advances made in the technology and application of jets in cross flow which have occurred since the last meeting on this subject, held by the FDP in 1981. Major topics covered included enhanced descriptions of the fundamental flow structure of jets in cross flow, experimental methods, thrust vectoring, jet impingement and exhaust gas reingestion, hypersonic crossflow, and numerics and turbulence modelling.</p> <p>ISBN 92-835-0720-7</p>	<p>edited transcript of the General Discussion held at the end of the meeting which addressed issues raised during the Symposium.</p> <p>The primary objective of the Symposium was to provide a forum for assessing advances made in the technology and application of jets in cross flow which have occurred since the last meeting on this subject, held by the FDP in 1981. Major topics covered included enhanced descriptions of the fundamental flow structure of jets in cross flow, experimental methods, thrust vectoring, jet impingement and exhaust gas reingestion, hypersonic crossflow, and numerics and turbulence modelling.</p> <p>ISBN 92-835-0720-7</p>